SEVENTH INTERNATIONAL SYMPOSIUM ON APPLICATIONS OF LASER TECHNIQUES TO FLUID MECHANICS

VOLUME I

July 11th to 14th 1994
Lisbon, Portugal

SEVENTH INTERNATIONAL SYMPOSIUM ON APPLICATIONS OF LASER TECHNIQUES TO FLUID MECHANICS

VOLUME I

July 11th to 14th 1994
Lisbon, Portugal

SEVENTH INTERNATIONAL SYMPOSIUM ON APPLICATIONS OF LASER TECHNIQUES TO FLUID MECHANICS

PREFACE

The proceedings volumes I and II comprise the papers that were accepted for presentation at the **Seventh International Symposium on Applications of Laser Techniques to Fluid Mechanics** held at *The Calouste Gulbenkian Foundation in Lisbon*, during the period of July 11 to 14, 1994. The prime objective of this Seventh Symposium is to provide a forum for the presentation of the most advanced research on laser techniques for flow measurements, and reveal significant results to fluid mechanics. The applications of laser techniques to scientific and engineering fluid flow research is emphasized, but contributions to the theory and practice of laser methods are also considered where they facilitate new improved fluid mechanic research. Attention is focused on laser-Doppler anemometry, particle sizing and other methods for the measurement of velocity and scalars such as particle image velocimetry and laser induced fluorescence.

The papers comprising the formal record of the meeting, were selected following high standard reviews, by members of the Advisory Committee, from approximately 300 extended abstracts submitted for presentation at this meeting.

Volume I comprises the papers to be presented during the first and second days of the Symposium, namely July 11th and 12th, while Volume II includes the papers of the following days, Wednesday, July 13th, and Thursday, July 14th.

We would like to take this opportunity to thank those who assisted us. The assistance provided by the Advisory Committee is highly appreciated. We are highly indebted for the financial support provided by the Sponsoring Organizations that made this Symposium possible. Many thanks are also due to the secretariat of the Symposium, Graça Pereira, Carlos Carvalho, Anabela Almeida and Luísa Martins.

THE ORGANIZING COMMITTEE

ORGANIZING COMMITTEE

- **R.J. Adrian**
  Department of Theoretical and Applied Mechanics
  University of Illinois at Urbana - Champaign
  Urbana, Illinois 61801
  USA

- **D.F. G. Durão**
  Department of Mechanical Engineering
  Instituto Superior Técnico
  Av. Rovisco Pais
  1096 Lisboa Codex
  PORTUGAL

- **F. Durst**
  Lehrstuhl fur Stroemungsmechanik
  University of Erlangen - Nurenberg
  Egerlandstrasse 13
  D-8520 Erlangen
  GERMANY

- **M. V. Heitor**
  Department of Mechanical Engineering
  Instituto Superior Técnico
  Av. Rovisco Pais
  1096 Lisboa Codex
  PORTUGAL

- **M. Maeda**
  Department of Mechanical Engineering
  Keio University
  1-14-1 Hiyoshi, Kohuku
  Yokohama 223
  JAPAN

- **J.H. Whitelaw**
  Imperial College of Science, Technology and Medicine
  Department of Mechanical Engineering
  Exhibition Road
  London SW7 2BX
  ENGLAND

ADVISORY COMMITTEE

SPONSORING ORGANIZATIONS

- Associação para o Desenvolvimento do Instituto Superior Técnico *ADIST*
- Banco Comercial Português, *BCP*
- Câmara Municipal de Lisboa
- Centro de Termodinâmica Aplicada e Mecânica dos Fluídos da Universidade Técnica de Lisboa, *CTAMFUTL*
- DHL
- Direcção Geral de Turismo
- European Research Office: United States Army, Navy and Air Force Departments
- Fundação Luso Americana para o Desenvolvimento *FLAD*
- Fundação Calouste Gulbenkian
- Instituto Superior Técnico, *IST*
- Instituto Tecnológico Para A Europa Comunitária, *ITEC*
- Junta Nacional de Investigação Científica e Tecnológica, *JNICT*
- Air Portugal *TAP*

LIST OF CONTENTS

VOLUME I (SESSION 1-20)

Session 1. PLENARY SESSION

1.1• A Phase Screen Approach to Non-Particle Laser Anemometry, **L. Lading, S. Hanson and R.V. Edwards**

1.2• Gaussian Beam Errors in Phase Doppler Anemometry and Their Elimination, **G. Gouesbet and G. Grehan**

1.3• Characteristics of Counter-Gradient Heat Transfer in a Non-Premixed Swirling Flame,**Y. Hardalupas, M. Tagawa and A.M.K.P. Taylor**

1.4• A High-Speed Processing System for Holographic Particle Image Velocimetry, **C.D. Meinhart, D.H. Barnhart and R.J. Adrian**

Session 2. COMBUSTION I

2.1• Flame Front Characteristic Measurements in Turbulent Premixed Combustors, **D. Veynante, J.M. Duclos, J. Piana and X. Montazel**

2.2• LDV Measurements of Turbulent Length Scales in a Combusting Flow with Two-Point Correlations, **D. Trimis, A. Melling and F. Durst**

2.3• Flame Structure Characterization Based on Rayleigh Thermometry and Two-Point Laser-Doppler Measurements, **D. Duarte, P. Ferrão and M.V. Heitor**

2.4• Simultaneous Velocity and Temperature Measurements in Turbulent Flames Obtained by Coupling LDV and Numerically Compensated Fine-Wire Thermocouple Signals, **F. Neveu, F. Corbin, M. Perrin and M. Trinite**

2.5• Simultaneous Measurements of Temperature and OH Concentration Fields in Turbulent Combustion Using One Single Laser Source, **S. Kampmann and A. Leipertz**

2.6• Application of CARS on Temperature Measurements in a Turbulent Premixed Reactive Flow, **Y. Kawaguchi and K. Kontani**

Session 3. ROTATING MACHINES I

3.1• Considerations Involving the Application of the Laser Doppler Velocimetry Technique to Measurements within a Radial Inflow Turbocharger, **M.J. O'Rourke and D.W. Artt**

3.2• Laser Doppler Velocimeter Measurements in a Centrifugal Ventricular Assist Device, **M. Pinotti, N. Paone, and E.P. Tomasini**

3.3• Application of a Multi-Angle Laser-2-Focus Velocimeter to Unsteady Flow Measurements in a Centrifugal Compressor, **A. Sugiyama, S. Obi, M. Maeda and I. Ariga**

3.4• The Study of Internal Recirculation in Rotodynamic Pumps, **K. Weiss and B. Stoffel**

3.5• Secondary Flow Measurements in a Mixed Flow Pump Using Laser Velocimetry, **K. Brun, R.D. Flack and S.B. Ainley**

3.6• Data Reduction Procedures For Laser Velocimeter Measurements in Turbomachinery Rotors, **J. Lepicovsky**

Session 4. WALL FLOWS

4.1• Low Reynolds-Number Effects in a Turbulent Boundary Layer, **C.Y. Ching, L. Djenidi and R.A. Antonia**

4.2• Measurements of the Structure of a 3-D Turbulent Boundary Layer Using a 5-Velocity-Component Laser Velocimeter, **M.S. Ölçmen and R.L. Simpson**

4.3• Study of Turbulent Channel Flow at Moderate Reynolds Numbers with Particle Image Velocimetry and Proper Orthogonal Decomposition, **Z.C. Liu, R.J. Adrian and T.J. Hanratty**

4.4• LDA Velocity Profile Measurements of a Non-Newtonian Slurry with Various Yield Stresses in Turbulent Pipe Flow, **J.T. Park, T.A. Grimley and R.J. Mannheimer**

4.5• Turbulent Pipe Flow Characteristics of Lw Molecular With Shear-Thinning Fluids, **A.S. Pereira and F.T. Pinho**

4.6• Annular Flow of Shear-Thinning Fluids with Centrebody Rotation, **M.P. Escudier and I.W. Gouldson**

Session 5. MANUFACTURERS' TECHNICAL PRESENTATION

Session 6. COMBUSTION II

6.1• Mixing Characterization in Semi-Industrial Natural Gas Flames Using Planar MIE-Scattering Visualization, **J. Dugué, A. Mbiock and R. Weber**

6.2• Application of Laser Diagnostics to Studies of Fluid Dynamic/Combustion Interactions, **K.C. Schadow, E. Gutmark, T.P. Parr, D.M. Hanson-Parr, K. Yu**

6.3• Development of an Uv-Laser-Diagnostic System for Combustion Research Under Zero-Gravity at Drop Tower "Bremen", **C. Eigenbrod, J. König, T. Bolik, T. Behrens, F. Dinkelacker, H.J. Rath, T. Schröder, H. Albrecht, D. Müller and W. Triebel**

6.4• Optical Registration of Combustion to Detonation Transition in Gas Flow, **N. Smirnov and M. Tyurnikov**

Session 7. JETS AND CROSS FLOWS

7.1• Fine Scale Velocity Measurements in a Turbulent Jet in a Confined Crossflow, **G. Catalano, J. Mathis and K. Chang,**

7.2• An Inclined Turbulent Jet into a Cross-Flow of Lower Density, **F. Peña and T. Arts**

7.3• Non-Circular Turbulent Jets in a Cross Flow, **V. Sivadas, B. Pani and K. Bütefisch**

7.4• Flow in a Duct and Through a Hole in a One Wall, **L. Martins and J.H. Whitelaw**

7.5• Turbulent Flows in 2-D and 3-D Simulated SDR Combustors, **T. Liou, Y. Wu and H. Lee**

Session 8. DATA PROCESSING I

8.1• Quantization of Doppler Signals: how many bits are needed?, **K. Andersen and A. Host-Madsen**

8.2• Running Fourier Transform and Multilinear Time Frequency Representation in the Analysis of a Doppler Signal, **S. Camporeale and A. Cenedese**

8.3• Time-Frequency Analysis and Measurement Accuracy in Laser Doppler and Phase Doppler Signal Processing Applications, **K.M. Ibrahim and W. Bachalo**

8.4• Cross Spectral Analysis Using Laser Doppler Anemometry, **J. Fitzpatrick and C. McDonnell**

Session 9. COMBUSTION III

9.1• Microscopic Structures in Turbulent Diffusion Flames by Laser Rayleigh Pyrometer, **T. Ida and K. Ohtake**

9.2• Temperature Measurements by Laser Rayleigh Scattering in Counterflow Diffusion Flames: T. Croonenbroek, F. Aguerre, P. Versaevel, **J.P. Martin, N. Darabiha and J.C. Rolon**

9.3• Velocity and Temperature Characteristics of Jet Diffusion Flames in Mutual Interaction, **M.V. Heitor, A.L. Moreira and A.C. Pires**

9.4• Flux Measurement of O_2, CO_2 and NO in Oil Furnace, **Y. Ikeda, N. Kawahara and T. Nakajima**

9.5• Comparison of CARS Measurements, Modelling Predictions and Suction Probe Temperature Data on a 6 MW_t Reburning Boiler, **A. Ferrante, M. Gaudio, M. Martano, A. Perrini, A. Soranno and R. Sorrenti**

Session 10. ROTATING MACHINES II

10.1• Development of an Advanced LDA Technique for the Determination of Boundary Layer Profiles on a Rotor, **C. Swales, M. Lowson, and R. Barrett**

10.2• The Interaction of the Trailing Vortex Streams From Rushton Turbine Blades, **K.C. Lee, K. Rutherford and M. Yianneskis**

10.3• LDA Measurements around Hovering Rotor Blades and Correlation with Local and Overall Airloads, **E. Berton, D. Favier, C. Maresca and M. Nsi Mba**

10.4• Laser Sheet Velocimetry Measurements of Rotor Craft Blade-Vortex Interaction, **M. Horner, J. Stewart, R. McGalbraith, I. Grant, F. Coton and G.H. Smith**

10.5• Measurements of the Flow Around Wind Turbine Rotors by Particle Image Velocimetry, **I. Grant, G. Smith, D. Infield, X. Wang, Y. Zhao, S. Fu and E. Owens**

Session 11. DATA PROCESSING II

11.1• A New Method for Estimation of Turbulence Spectra for Laser Doppler Anemometry, **A. Host-Madsen**

11.2• The Limitations in High Frequency Turbulence Spectrum Estimation Using The Laser Doppler Anemometer, **A. Host-Madsen, C. Caspersen**

11.3• Assessment of 3-D Spectral Bias in LDV, **D. Lee and H. Sung**

11.4• Estimation of Spectral Power Density of Turbulence for Flow Field in a Defibrator, **R. Karvinen, H. Ihalainen, P. Saarenrinne, S. Soini and S. Vienola**

Session 12. COMBUSTION IV

12.1• Laminar Spray Flame Oscillation, **Y. Levy and B. Golovanesky**

12.2• Phase Doppler Velocimetry Measurements in Counterflow Spray Flame, **F. Lacas and P. Versaevel**

12.3• Simultaneous Measurement of Droplet Size, Velocity and Temperature in a Swirl-Stabilized Spray Flame, **S.V. Sankar, D.H. Buermann, K.M. Ibrahim and W.D. Bachalo**

12.4• Structure of Spark-Ignited Spherical Flames Propagating in a Droplet Cloud, **F. Akamatsu, K. Nakabe, M. Katsuki, Y. Mizutani and T. Tabata**

12.5• Combination of Deflection, Scattering/Extinction and Diffraction Measurements for the Analysis of Soot Particle Temperature, Size and Shape, **B. Mandel and B. I. Neichen**

12.6• Two-Dimensional Mie Scattering Technique for Spray Diagnostics Under Running Engine Conditions, **K. Münch and A. Leipertz**

Session 13. SEPARATED FLOWS

13.1• The Turbulent Flow in a Channel with Large-Amplitude Wavy Surfaces, **G.P. Almeida, D. Durão and M.V. Heitor**

13.2• An Experimental Study of the Flow Upstream of a Circular Cylinder, **H. Nigim and C. Tropea**

13.3• Flow Structure Near The Front Edge of an Ice Cover, **J.G. Eriksson and R.I. Karlsson**

13.4• Turbulent Shear Flow Over the Repeated Two-Dimensional Square Ribs on Ground Plane, **S. Okamoto, K. Tsunoda, T. Katsumata, D. Suzuki and N. Abe**

13.5• Investigations of Flow-Field for Sudden-Expansion Pipe with Transverse Side-Flows, **A. Wang, S. Jow and C. Lin**

13.6• LDA Measurements in the Near-Wall Region of an Axisymmetric Sudden Expansion, **I. Lekakis, F. Durst and J. Sender**

Session 14. OPTICS I

14.1• Direction Sensitive LDA Using a Single High-Frequency Pulsed Diode Laser and a Single Photodetector, **H. Wang, H. Müller, V. Strunck and D. Dopheide**

14.2• Brillouin Frequency Shift LDA, **H. Többen, H. Müller and D. Dopheide**

14.3• Investigation of the Adaptive Laser Doppler Anemometer, **B. Rinkevichius**

14.4• LDV-System with Frequency Shift Using Two Modes of a Nd:YAG Micro Crystal Laser, **R. Kramer, H. Müller, D. Dopheide, J. Czarske and N.P. Schmitt**

14.5• The Realization of a Continuously Tuneable Optical Frequency Shift LDV-System at Green Wavelength for Highly Turbulent Flows Using Diode Pumped Nd: YAG Lasers and Monolithic Ring Frequency Doublers, **R. Kramer, H. Müller, D. Dopheide**

14.6• Fibre-Optic Bundle Beam Delivery System for High Pulse Energy Laser PIV Illumination, **D. Anderson, J. Jones, W. Easson and C. Greated**

Session 15. COMBUSTION V

15.1• Instantaneous Velocity Measurements in Premixed Flames Using on-Line PIV, **M. Mungal, L. Lourenço and A. Krothapalli**

15.2• Simultaneous 2D Measurements of Flame Front Propagation by High Speed Tomography and Velocity Field by Cross-Correlation PIV, **B. Lecordier, M. Mouqallid and M. Trinité**

15.3• Velocity Measurements in Turbulent Premixed Flames by LDV and PIV, **N. Paone**

15.4• Flame Front Visualization By OH LIF and C2 Emission in Axisymmetric Laminar Methane-Air Premixed Flames, **J., K. Mokaddem, M. Perrin, J. Rolon and H. Levinsky**

Session 16. VORTICES & BREAKDOWN

16.1• Taylor Vortices in Shear-Thinning Liquids, **M. Escudier, I. Gouldson and D. Jones**

16.2• LDA Measurements of Confined Vortex Breakdown Generated by a Rotating Cone, **D. Durão, J. Pereira, J. Sousa and T. Pereira**

16.3• LDV Measurements on the Laminar-Turbulent Transition in Spherical Couette Flow, **C. Egbers, W. Beyera, A. Meijering and H. Rath**

16.4• LDA and LIF Experiments on a Quasi-Periodic and Complex Flow in a Cyclone, **M. Fokke, T. Liem, J. Derksen and H. den Akker**

Session 17. OPTICS II

17.1• Scanning Laser Doppler Probe for Profile Measurements, **V. Strunck, G. Grosche and D. Dopheide**

17.2• Simultaneous Multi-point Laser Velocimetry Using Holographic Optical Element Lens, **Medhat Azzazy**

17.3• The Effect of Laser Beam Orientation on the Accuracy of 3D LDA Measurements within an Annular Test Facility, **J. Carrotte and K. Britchford**

17.4• A General Procedure for Calculating and Correcting the Displacement of Laser Beams Passing Through Plane and Cylindrical Windows Using a Three Component Laser-

Doppler Anemometer For Turbomachinery Applications, **A. Doukelis, M. Founti, K. Mathioudakis and K. Papailiou**

Session 18. TWO PHASE FLOW INSTRUMENTATION I

18.1• Experimental Investigations on the Effect of Trajectory Dependent Scattering on Phase Doppler Particle Sizing With a Standard Instrument, **M. Willmann, R. Kneer, L. Eigenmann, R. Koch, S. Wittig and E. Hirleman**

18.2• Measurement of Bubbles by Phase Doppler Technique and Trajectory Ambiguity, **G. Gréhan, F. Onofri, T. Girasole, G. Gouesbet, F. Durst and C. Tropea**

18.3• Dual-Mode Phase Doppler Anemometry, **C. Tropea, T. Xu, G. Gréhan, F. Onofri, and P. Haugen**

18.4• Correction of Particle Size Distributions from PDA-Measurements for Continuous Distributions Less than 10 um, **S. Schabel, A. Doieu, and F. Ebert**

18.5• A Contribution to the Study of PDA Sensitivity of the Phase-Diameter Relationship to the System Parameters, **J Garcia, J. Lagranja, and L. Aísa**

Session 19. SWIRLING FLOWS

19.1• Route to Chaos for a Swirling Flow in an Open Cylindrical Container With a Rotating Bottom, **H. Sheen, D. Young and T. Hwu**

19.2• Confined Mixing Between a Compressible Central Jet and a Swirling Co-Flowing Outer Stream, **S. Favaloro and F. Brizuela**

19.3• Experimental Studies of Confined Turbulent Swirling Flows, **M. Wessman, J. Klingmann and B. Norén**

19.4• Axial and Tangential Velocity Components at the Exhaust End of a Highly Complex Cyclonic Flow, **P. Yazdabadi, A. Griffiths and N. Syred**

Session 20. SCALAR MEASUREMENT I

20.1• Pure Rotational CARS Method for Temperature of Gas Mixture, **Y. Hara, T. Fujimoto, T. Ni-Imi and S. Ito**

20.2• Comparision of the LIF and DFWM Techniques for the Detection and Imaging of Nitrogen Dioxide, **B. Mann and F. White**

20.3• Multi Directional Laser Absorption Technique for Simultaneous Determination of Temperature and Concentration within a Shocked Gaseous Interface, **G. Jourdan, A. Touat, I. Chemouni and L. Houas**

20.4• 20.4• A Shock Tube of CN Emission in Titan Radiative Environment, **M. Billiotte, L. Labracherie, M. Dumitrescu, L. Dumitrescu R. Brun, D. Zeitoun, L. Houas and M. Baillion**

20.5• Flow Density Visualization Enhancement to the Warwick Solid State 3D PIV System, **M. Funes-Gallanzi and P.J. Bryanston-Cross**

VOLUME II (SESSION 21-39)

Session 21. TWO PHASE FLOW INSTRUMENTATION II

21.1• Investigation of Polydisperse Spray Interaction Using an Extended Phase-Doppler Anemometer, **G. Brenn, J. Domnick, F. Durst, C. Tropea and T. Xu**

21.2• Examination of the Rainbow Position of Optically Levitated Droplets for the Determination of Evaporation Rates of Droplets, **N. Roth, K. Anders, A. Frohn**

21.3• A New Technique to Measure Refractive Index With Phase Doppler Anemometry, **H. von Benzon, T. Nonn and P. Buchave**

21.4• Phase Doppler Anemometry With Dual Bursts Technique for Particle Refractive Index Measurements, **F. Onofri, G. Grehan, G. Gouesbet, T. Xu, G. Brenn and C. Tropea**

21.5• Simultaneous Determination of Temperature and Size of Droplets from the Rainbow, **J. van Beeck and M. Riethmuller**

Session 22. PARTICE TRACKING VELOCIMETRY, PTV

22.1• Lagrangian Study of Convective Boundary Layer Using Image Analysis, **A. Cenedese and G. Querzoli**

22.2• Flow Measurements Close to the Free Air/Water Interface, **J. Dieter, R. Bremeyer, F. Hering and B. Jähne**

22.3• PTV Measurement on a Rotating System Using Semiconductor Laser and CCD Camera, **H. Koyama, K. Fujimura, T. Uemura, H. Sung and J. Hyun**

22.4• Quantitative Visualization of Velocity Distributions in Flow, **I. Shimizu, K. Suzuki and N. Akino**

22.5• Flow Tagging in Water Using Photo-Activated Non intrusive Tracking of Molecular Motion (PHANTOMM), **W. Lempert, S. Harris, K. Magee, C. Burchan, D. Saville, R. Miles, K. Gee and R. Haugland**

22.6• Measurement of 3-D Velocity Fields in a Square Duct Using A Stereo Color-Coded Particle Tracking Velocimetry, **Tzong-Shyan Wung**

Session 23. DATA PROCESSING III

23.1• Application of Kalmen Reconstruction to Laser-Doppler Anemometry Data for Estimation of Turbulent Velocity Fluctuations, **H. van Maanen and H. Tulleken**

23.2• LDA Signal Reconstruction: Application to Moment and Spectral Estimation, **E. Müller, H. Nobach and C. Tropea**

23.3• Heterodyning and Quadrature Signal Generation: Advantageous Techniques for Applying New Frequency Shift Mechanisms in the Laser Doppler Velocimetry,

H. Müller, J. Czarske, R. Kramer, H. Többen, V. Arndt, H. Wang and D. Dopheide

23.4• ASIC Based Processing Unit in the Miniature LDA Sensor Concept, Using Minimal Cross-Correlation, **S.M. Damp**

23.5• A Comparison Between Two Different Laser Doppler Anemometer Processors in the Low Turbulence Regime, **C. Caspersen**

Session 24. TWO-PHASE FLOW INSTRUMENTATION III

24.1• A Rigorous Procedure for Design and Response Determination of Phase Doppler Systems, **A. Naqwi and R. Menon**

24.2• Experimental and Theoretical Studies of the Sources of Uncertainties in a Phase Doppler System, **M. Seidel, M. Ziema, A. Naqwi and F. Durst**

24.3• Improving the Accuracy of Particle Sizing Techniques Using the Light Scattered from Single Particles, **M. Bohan and T. Claypole**

24.4• Coherent Scattering in Phase Doppler Interferometry: Effects on Spray Characterization, **S. Sanker, K. Ibrahim and W. Bachalo**

24.5• Integral Doppler Spectra Due to the Particles Size-Velocity Correlation in Two-Phase Flows, **V. Kononenko and B. Rinkevichius**

24.6• A Miniaturized Instrument to Measure Particles From 2*um* to 5000 *um*, **C. Wood and C. Hess**

24.7• Measurements of Size and Velocity of Arbitrary Shaped Particles by a LDA Based Shadow Image Technique, **H. Morikita, K. Hishida and M. Maeda**

Session 25. FREE FLOWS

25.1• Three-Component LDA Measurements of Mean Turbulence Quantities, Time and Spatial Correlation Functions in the Wake of a Flat Plate in an Adverse Pressure Gradients, **M. Tummers, P. Narayana and D. Passchier**

25.2• An LDA Based Method for Accurate Measurement of the Dissipation Rate Tensor With Application to a Circular Jet, **G. Johansson and J. Klingmann**

25.3• Velocity Characteristics of Flow With and Without Swirl Around a Disk with a Central Jet, **D. Durão, C. Freek and J. Pereira**

25.4• Laser Sheet Tomography of Jet Flows, **P. Larsen, L. Böhme and E. Andresen**

25.5• Two-Dimensional Gas Concentration Measurement in a Large Low Speed Wind Tunnel Using Light Scattering By Small Particles, **Bernd Leitl**

25.6• Concerning Taylor Time and Length Scale Estimates Made from Single and Two-Point Correlation LV Measurements, **L. Benedict, P. R. Yearling and R. Gould**

Session 26. PARTICLE IMAGE VELOCIMETRY, PIV

26.1• High Speed Scanning 3-D Particle Image Velocimetry Technique, **Y. Guezennec, Y. Zhao and T. Gieseke**

26.2• Multiple Light Sheet Particle Holography For 3-D Flow Velocimetry, **H. Hinrichs and K. Hinsch**

26.3• An In-Line, Stereoscopic, Colour PIV System for 3-Component Velocity Measurements with Ambiguity Resolution, **I. Grant, S. Fu, X. Pan, X. Wang and A. Aroussi**

26.4• The Accuracy and Reliability of PIV Measurements, **A. Host-Madsen and D. McCluskey**

26.5• Near Field Structure of a Supersonic Jet: "On-Line" PIV Study, **A. Krothapalli, D. Wishart and L. Lourenço**

26.6• Precision Whole-Field Velocity Measurements With Frequency-Scanned Filtered Rayleigh Scattering, **R. Miles, J. Forkey, N. Finkelstein, W. Lempert**

Session 27. TWO-PHASE FLOW I

27.1• Laser Shadowgraphy of the Breakup of a Liquid Sheet Downstream of a Model Prefilming Airblast Atomiser, **M. Adzic, I. S. Carvalho and M.V. Heitor**

27.2• Measurement of Velocity Profiles in a Falling Liquid Film in Counter current Annular Flow, **W. Pun, C. Lorencez, M. Kawaji, G. Karini, F. Kaminaga, H. Akimoto and Y. Sudo**

27.3• Annular Two-Phase Flow Sauter Mean Diameter Measurements--Comparison With Predictions, **C.J. Bates and R. Ayob**

27.4• Velocity and Particle Size Measurements in a Two-Phase Flashing Jet, **R. Balachandar, S. Mulpuru and H. Ungurian**

Session 28. BEND FLOWS

28.1• The Experimental Study on the Characteristics of Turbulent Polymer Solution Flow in a 180 Degree Square Sectioned Bend, **F. Tong, S. Houjung**

28.2• Flow Structure in Meandering Channel for Overbanks Flows, **K. Shiono, Y. Muto, H. Imamot and T. Ishigaki**

28.3• Velocity Measurements in a Rotating 'U' Bend Using a Stationary Fibre Optic LDA Probe, **S. Cheah, H. Iacovides, D. Jackson, H. Ji and B. Launder**

28.4• Visualization and Measurement of Velocity Profile in Pulsatile Flow Through U-Bend Using Laser-Induced Fluorescence Method, **K. Ohba, H. Kamino and T. Takegami**

28.5• 3-Dimensional Laser Doppler Measurements in a Curved Flume, **R. Booij and J. Tukker**

Session 29. SCALAR MEASUREMENT II

29.1• A Real-Time Free-Surface Elevation Mapping Technique, **D. Dabiri, X. Zhang and M. Garib**

29.2• An Optical Method For Determining The Geometric Characteristics of Liquid Films Flowing Around A Horizontal Tube, **P. Speck, M. Khan, P. Desevaux and P. Panday**

29.3• Application of Laser Induced Fluorescence For Measuring the Thickness of Liquid Films on Transparent Walls, **J. le Coz, C. Catalano, T. Baritaud**

29.4• A LIF Technique for the Measurement of Concentration Profiles in the Aqueous Mass Boundary Layer, **T. Münsterer and B. Jähne**

Session 30. OPEN FORUM

Session 31. TWO-PHASE FLOW II

31.1• Behaviour of Spray Particles in the Surroundings of a Bluff-body, **O. Nishida, H. Fujita, W. Harano, K. Fukuzato and H. Ohkawa**

31.2• Experimental Study on Controlling Size-Distribution of Droplets by Multi-Spray, **M. Higuchi, T. Shirakawa, H. Morikita, K. Hishida and M. Maeda**

31.3• LDA Measurements of Turbulent Air-Solid Suspension Flow in a 90° Bend of Square, ***B. Hiwatika, Y.D. Tridimas and N.H. Woolley***

31.4• Pneumatic Particle Conveyance in Pipe Bend: Simultaneous Two Phase PIV Measurements of the Slip Velocity Between the Air and Particle, **M.L. Jakobsen, D.R. McCluskey, W.J. Easson, D.H. Glass and C. A. Greated**

31.5• Measurement of Pseudo-Turbulence in Bubbly Flows By Phase Doppler Anemometry, **A. Cartellier and Img. Legi**

Session 32. HOLOGRAPHIC INTERFEROMETRY & TOMOGRAPHY

32.1• High Resolution, Time-Resolved Optical Absorption Tomography, **A.J. Daiber, L. Hesselink**

32.2• Mass Transfer Measurement by Holographic Interferometry for a Jet Impinging on a Flat Surface at Moderate Reynolds Numbers, **N. Macleod and J.J. Nebrensky**

32.3• Tomographic High-Speed Digital Holographic Interferometry Measurements in Free-Jet Flows, **B.H. Timmerman and D.W. Watt**

32.4• Three Components Velocity Measurements in a Connective Fluid by Holographic Interferometry, **N. Andrès, M.P. Arroyo and M. Quintanilla**

32.5• Measurements of Flow Velocity and Temperature Using Laser Photo-Thermal Effect With a Differential Interferometer, **N. Nakatani and T. Oshio**

Session 33. ENGINES I

33.1• Simultaneous Two Component Velocity and Dropsize Measurements in a Combusting Diesel Fuel Spray, **G. Picher and G. Wigley**

33.2• Correlation Between the Characteristics of an IDI Diesel Spray Measured with PDA and Instantaneous Conditions in the Nozzle, **J.M. Desantes, J. Arrègle and J.V. Pastor**

33.3• Manifold Injection and the Origin of Droplets at the Exit of an Inlet Valve, **M. Posylkin, A.M.K. Taylor and J.H. Whitelaw**

33.4• Experiments With Valve Shrouds and Secondary Fuel Injection for Lean Burn, **C. Arcoumanis, D. Hull, J.H. Whitelaw and C.H. Xu**

33.5• Comparison of In-Cylinder Scavenging Flows in a Two-Stroke Cycle Engine Under Motored and Fired Conditions, **P.C. Miles, R.M. Green and P.O. Witze**

Session 34. TWO PHASE FLOWS III

34.1• Particle Flow Diagnosis in Powder Injection Laser Alloying Process, **C. Herschkorn, J. Lascu, P. Gougat, D. Kechemair and R. Prud'homme**

34.2• The Application of a Holografically Shaped Laser Beam for Light Scattering Studies During Particle Breakup, **J.J.F. Strecker and P. Roth**

34.3• Microprojectile Velocities in a Gas Driven Launcher, **A.L. Duval, N.W. Page and K. Bremhorst**

34.4• Laser Holographic Studies on Deformation and Fragmentation of Droplets in their own Vapor, **G. Zerf and K. Hornung**

34.5• Single Particle Operations by LDA-Assisted Electrodynamic Thermogravimetry, **M. d'Amore, G. Donsi, P. Giordano and G. Raso**

34.6• Phase-Doppler Anemometrie (PDA) - A New Tool for Monitoring Thermal Spraying, **R. Zeller, J. Domnick, E. Schubert, H.W. Bergmann and F. Durst**

Session 35. PIV & PTV SIGNAL PROCESSING

35.1• A Fast Data Acquisition System for Digital PIV: Application to Fully-Developed and Transition Turbulent Pipe Flow, **J. Westerweel, A.A. Draad, J.G. Th. van der Hoeven and J. van Oord**

35.2• A Compact and Simple all Optical Evaluation Method for PIV Recordings, **A. Vogt, J. Kompenhans and F. Reichel**

35.3• A New Paradigm for Particle Tracking Velocimetry, Based on Graph-Theory and Pulsed Neural Network, **D. Derou and L. Herault**

35.4• The Application of the Neural Network Technique to the Analysis of Particle Tracking (PIV) Images Obtained in Flows with a Directional Ambiguity, **I. Grant, X. Pan and A. Aroussi**

35.5• Error Analysis for PIV Recording Utilizing Image Shifting, **I.M. Raffel and J. Kompenhans**

35.6• The Importance of Image Shifting to the Applicability of the PIV Technique for Aerodynamic Investigations, **J. Kompenhans and M. Raffel**

35.7• High Accuracy Techniques Applied to the Extraction of Absolute Position Estimation in 3D PIV, **M. Funes-Gallanzi and P.J. Bryanston-Cross**

Session 36. ENGINES II

36.1• Simultaneous Measurement of Inlet Flow and Valve Motion in Internal Combustion Engines by Laser Doppler Techniques, **N. Paone, C. Santollini and E.P. Tomasini**

36.2• Investigation of the Flows Through Two Production Catalytic Converters, **D.P.E. Foster, K.C. Lee, M. Yianneskis and G. Ganti**

36.3• Phase-Doppler Characterization of a Diesel Spray Injected into a High Density Gas under Vaporization Regimes, **A. Coghe and G.E. Cossali**

36.4• LDV Measurements in Non-Stationary Turbulence in a Compressed Jet-Flow, **H.J. Nuglisch, J. Borée, G. Charnay and D. Veynante**

36.5• PDA Analysis of Transient Spray Flows Initiated From Air Assisted Injector, **T. Obokota, H. Tanaka and T. Koyama**

Session 37. PIV APPLICATIONS

37.1• PIV Measurements in Simulated Microbursts, **E.K. Longmire and A. Alahyari**

37.2• A Study of an Inclined Cylinder Wake Using Digital Particle Image Velocimetry, **L.J.W. Graham and J. Soria**

37.3• Investigation of the Local Flow Topology in the Vicinity of a Prosthetic Heart Valve by Using Particle Image Velocimetry, **F. Hirt, Z. Zhang and E. Jud**

37.4• Comparison of PIV Data With Hot-Wire Measurements and Calculations Obtained for Instabilities in a Flat Boundary Layer, **M. Fischer**

37.5• Full-Field Cross Flow Measurements in a Bank of Rods Using Particle Image Velocimetry, **Y.A. Hassan, R. Martinez, W.D. Schmidl and O.G. Philip**

Session 38. AERODYNAMICS

38.1• Experimental Study of the Dynamic Stall Process on a Pitching Airfoil by Means of Laser Sheet Visualization and PIV Measurements, **P. Wernert, G. Koerber, F. Wietrich, M. Raffel and J. Kompenhans**

38.2• Embedded LDA Technique Applied to the Boundary-Layer Separation Measurement on Oscillating Airfoils, **D. Favier, M. Pascazio and C. Maresca**

38.3• A Phase Locked High Speed Real-Time Interferometry System for Large Amplitude Unsteady Flows, **M.S. Chandrasekhara, D.D. Squires, M.C. Wilder and L.W. Carr**

38.4• Investigation of the Unsteady Diffuser Flow in a Radial Pump, **K. Eisele, Z. Zhang, F. Muggli**

38.5• The Application of 3D Laser-Doppler Anemometry to Large Scale Flow Measurements on a Formula 1 Racing Car, **C. Saunders, J. Rickards, C. Swales, R.V. Barrett**

Session 39. COMPLEX FLOWS

39.1• Measurements of Velocity and a Passive Scalar in an Isothermal Flow Model of a Pressurized-Coal Combustor, **M. Bodegon, A. Moore, A.M.K.P. Taylor and J.H. Whitelaw**

39.2• Investigation of Particle Flows in a Top-feed Shell Boiler Using Laser Sheet Illumination, **J. Stroud**

39.3• Velocity Characteristics of the Crossflow over Tube Bundles, **S. Balabani, G. Bergeles, D. Burry and M. Yianneskis**

39.4• LDA Study of Turbulent Flow in a Staggered Tube Bundle, **K. E. Meyer and P. Larsen**

39.5• Automatic Computer-Based Non-Intrusive Temperature Measurements in a Counterflow Heat Exchanger, **M.J. Braun, M. Dzodzo, S.B. Lattime and R. Krstic**

AUTHORS' INDEX

Session 1.
Plenary Session

A PHASE SCREEN APPROACH TO COLLECTIVE LIGHT SCATTERING; RESOLVING TEMPORAL FLUCTUATIONS

**Lars Lading, Robert V. Edwards*
and Steen Hanson**

Association Euratom - Riso National Laboratory
Optics and Fluid Dynamics Department
Risø National Laboratory
DK-4000 Roskilde, Denmark

ABSTRACT

Velocity measurements based on the transport of turbulence induced refractive index structures are investigated. Particle scattering is assumed to be negligible. The scattering from collective structures is analyzed with a phase screen model. A system based on reference beam detection and combining Doppler and time-of-flight concepts may provide the best spatial resolution and utilize a broad band region of the high frequency turbulence for light scattering. In the optical region it is so that a long wavelength is preferable and reference beam detection is necessary. An potential hybrid system for plasma diagnostics is presented. It is shown that time resolved measurements may be possible.

1 INTRODUCTION

Laser anemometry based on particle scattering is well established. However, in certain fluids particles cannot be present at all, or the concentration is very low. In a fusion plasma there are no large scattering particles; in high speed wind tunnels the concentration of particles may be extremely low. In such systems it may be possible to measure transport properties of large scale fluctuations on the basis of light scattering/diffraction from small scale structures convected by the larger scales.

Light scattering from collective structures has been utilized for velocity measurements. Radar scattering from refractive index fluctuations in the atmosphere have been used for the measurement of velocity on very large scales. Strauch (1985). Simple configurations based on visible light have been devised for measuring *cross wind* velocities, Clifford, Ochs, and Wang (1975). For diagnostics in connection with plasma fusion configurations similar to the original reference beam laser Doppler anemomenter have been applied, Slusher and Surko (1978), Truck et al (1991). The method has recently been applied to the measurement of fluid velocity in high speed wind tunnels, Grésillon et al (1992).

We shall briefly discuss scattering from refractive index fluctuations. The essential types of fluctuations encountered are identified. The nonpropagating types of fluctuations may be used for measuring the fluid velocity.

The trade offs in terms of optical wavelength, spatial resolution, measurement configuration, and turbulence parameters are discussed.

The reference beam LDA has so far been the configuration that has been applied. Direct detection (as commonly used in LDA based on particle scattering) can only be applied in cases with very strong fluctuations. Surprisingly it is so that the longer the optical wavelength is the better is the spatial resolution. However, even at the wavelength of the CO_2 laser (10.6 μm) the resolution along the optical axis is inadequate. We are here proposing a system that combines the time-of-flight configuration with the Doppler system. Such a system provides for a significantly better spatial resolution and does also utilize a larger part of the spectral content of the refractive index fluctuations.

Time resolved measurements have so far to our knowledge not been performed with this type of scattering. We are briefly outlining the considerations on which the feasibility of time resolved measurements can be decided. It is shown that even in a fusion plasma time resolved measurements may be possible.

2 BASIC CONCEPTS, DEFINITIONS, AND ASSUMPTIONS

Light scattering in fluids may be classified as either inelastic or elastic. Fluorescence and Raman scattering are examples of inelastic scattering. These types of scattering are well suited to identify the chemical composition of the medium. Fluorescence may also be applied to velocity measurements in high speed flows, Hanson (1994) or even in particle LDA. The intrinsic spectral broadening of this type of scattered light is in general so large that only supersonic velocities can be accurately measured.

* Permanent address: Chemical Engineering Department
Case Western Reserve University
Cleveland, OH 44106, USA

Quasi-elastic scattering is scattering where a possible shift in frequency only is caused by the movement (velocity) of the scatterer and not by a change in the quantum-mechanical state of the particle. This type of scattering is the basis for laser anemometry but also for measuring diffusion and molecular dynamics. However, incoherent molecular scattering will in general give a spectral broadening proportional to the thermal velocity of the molecules. In most flows this type of broadening is much larger than the fluid velocity making it unsuited for anemometry.

Despite the large thermal velocity of molecules *collective* light scattering may provide a signal with a spectral width much smaller than the thermal broadening. Collective scattering is scattering from a large number of scatterer that in some way supports a large scale (large compared to the mean free path) scattering structure. A sound wave may be an example of such a wave structure. It is necessary that the spatial scale of the structure is larger than the mean free path.

In laser anemometry as well as in other types of measurements based on quasi-elastic scattering the light collection and detection mode may be either coherent or incoherent. Let us assume a large number of particles in the measuring volume. Coherent detection implies that the photocurrent is proportional to the squared sum of the fields from the particles, i.e. that

$$i \propto \left| \sum_i U_i \right|^2 . \qquad (1)$$

We note that the photocurrent contains a sum of contributions from the individual particles plus a sum of cross-beat terms. Coherent detection requires that the phase fronts are parallel over the detector area implying a small collector aperture. Incoherent detection implies that

$$i \propto \sum_i |U_i|^2 . \qquad (2)$$

In this case the collector aperture is very large and the cross particle contributions vanish. Incoherent detection is in general not feasible if collective scattering is to be applied.

In the case of a very high particle concentration it may be preferable to apply a continuum model. We shall do that and consider the random fluctuations of the refractive index.

We summarize this section by the following definitions:
Collective light scattering is scattering/diffraction from random fluctuations of the refractive index of a medium through which light is propagating.
Dynamic light scattering: Scattering where the frequency shift (or broadening) exclusively is caused by the motion of the scatterer(s).

Applying this type of scattering and detection we may measure transport of refractive index fluctuations, which may represent

- materials transport,
- propagating waves or,
- convection of small scale turbulence by larger scales.

Applications are found in several quite different areas, e.g. velocimetry (anemometry), waves in bulk media and on surfaces (visco-elastic), diffusion, and particle sizing.

3 A CONTINUUM MODEL BASED ON PHASE SCREENS

We shall here outline a model for calculating the photocurrent and its correlation function. A so-called *phase screen* model is applied (originally introduced by Lee and Harp (1969)) in order to analyze wave propagation through random media; the phase screen model is also used in the analysis of thick holograms).

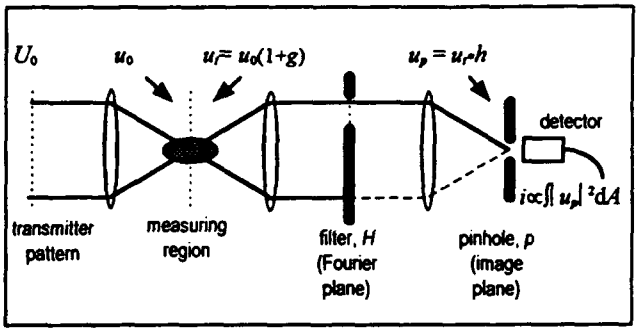

Figure 1. Fourier optical model. For the reference beam LDA the transmitter pattern consists of two parallel beams of which the top beam is much stronger than the bottom beam.

3.1 The Photocurrent

The analysis is based on a Fourier optical model as shown in Fig. 1. (Lading, Mann, and Edwards). The field in the measuring plane is given by the Fourier transform of the transmitted field pattern. The interaction region is divided into a number of screens perpendicular to the optical axis (Fig.2). Screen j is assigned a transmission function given by

$$t_j = \exp\{jk\Delta z \Delta n_j(x,y)\} \cong \exp\{ik\Delta z\}(1 + i\Delta z \Delta n_j(x,y)) \quad (3)$$

The field out of screen j is

$$u_{out,j} = (u_{in,j} t_j) * h_{\Delta z}, \qquad (4)$$

where

$$h_{\Delta z} = \frac{\exp\{ik\Delta z\}}{2\pi i(\Delta z / k)} \exp\left\{ -\frac{1}{2} \frac{x^2 + y^2}{i\Delta z / k} \right\}. \qquad (5)$$

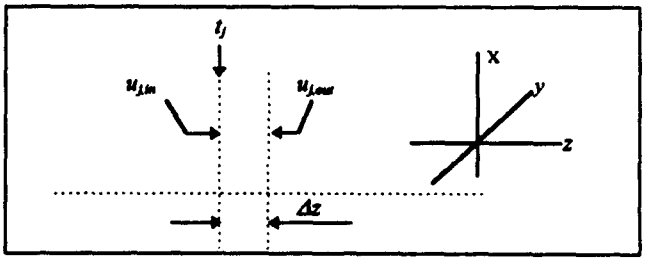

Figure 2. Phase screen.

Summing the contributions from all the phase screens letting Δz go to zero and the number of screens go to infinity yields an expression for the total field. The field is referred to the measuring plane. Convoluting with the filter function h and multiplying with the pinhole function p gives the field on the detector. Squaring and integrating over the detector area gives the photocurrent.

The photocurrent contains in general three terms (as in normal particle laser anemometry):

1. A dc current with no information about the dynamics of the measuring object.
2. A 'homodyne' term caused by interference between purely scattered/diffracted beams.
3. A 'heterodyne' term caused by mixing between scattered/diffracted light and reference beam(s).

The first term is unavoidable since the photocurrent cannot be negative. The second term is the dominating dynamic part of the photocurrent in most laser anemometry systems based on particle scattering and here the mixing does only occur between beams scattered by the same particle. Non-particle laser anemometry may be based on either the second or the third term, but the third term is often preferred because a parametric amplification of the signal is obtained since the amplitude of the dynamic part of the photocurrent is given by the product of the scattered field and the reference field. This may be necessary if a wavelength is applied where no photomultipliers or avalance diodes are available (e.g. at the wavelength of the CO_2 laser). It is also so that the statistics of the photocurrent is simpler if the third term is the dominating dynamic component.

3.2 The Correlationfunction

The correlationfunction is evaluated using the same procedure as in Lading, Mann, and Edwards (1989). For the reference beam mode (heterodyne) we get that the correlation function is

$$R(\tau) \propto \int_{x\text{-}y\ \text{plane}} S(\mathbf{q},\tau)|F(\mathbf{k})|^2 \,\mathrm{d}\mathbf{k}, \qquad (6)$$

where $S(\mathbf{q},\tau)$ is the 2D spatial Fourier transform of the 2D space-time correlation for the phase perturbations. $|F(\mathbf{k})|^2$ is an instrument function given by the dynamic part of the field distribution in the measuring volume.
where

$$\mathbf{k} = (k_x, k_y) \text{ and } k_z = 2\pi/\lambda.$$

For the homodyne mode we get

$$R(\tau) = \left| \int_{x\text{-}y\ \text{plane}} S(\mathbf{q},0)|U(\mathbf{k})|^2 \,\mathrm{d}\mathbf{k} \right|^2 + 2\left| \int_{x\text{-}y\ \text{plane}} S(\mathbf{q},\tau)|U(\mathbf{k})|^2 \,\mathrm{d}\mathbf{k} \right|^2 . \qquad (7)$$

Note that in Eq. (7) $R(\tau)$ is given directly by the first order space-time correlation, whereas in Eq. (8) it is given by a more complicated expression of the first-order correlation.

Now, the expressions are given by the 2D correlation function for the refractive index fluctuations, but the measurements are here anticipated to be performed in a 3D medium. In the analysis of beam propagation through turbulent media it is customary to assume δ-correlation along the optical axis (i.e. no width of the correlation function in the z-direction). This may be legitimate if the interaction region is much larger than the beam diameters and the spatial wavelength of the turbulence that are considered. However, this is not the case here. Other investigators, Grésillon (1992), have used the 3D correlation. However, we find that neither is in general correct. Being short of a rigorous procedure we shall do the following: phase screens with a spacing smaller than the selected wavenumber are added coherently, whereas screens with a spacing larger than the selected coherence length are added incoherently.

The spectrum of the refractive index fluctuations (from which the spectrum for the phase perturbations is obtained) will in general contain two terms: (1) a term that does not propagate relative to the fluid with a coherence time given by the thermal diffusivity, and (2) a term given by propagating sound waves in general with a very small damping.

4 SPECIFIC CONFIGURATIONS

Let us investigate specific configurations and compare them in relation to spatial resolution and signal strength.

4.1 The Reference Beam Doppler Configuration

The principles of the configuration is illustrated in Fig. 3. The transmitter is essentially as for a homodyne mode LDA except for the fact that one of the transmitted beams is much weaker than the other. The detection is done in the direction of the weakest of the transmitted beams. The dynamic part of the signal is then given by scattered light from the strong beam that is heterodyned with directly transmitted light of the weak beam. (The configuration is similar to the very first Laser Doppler Velocimeter). The few practical implementations that so far have appeared are all using a CO_2 laser (λ = 10.6 μm). The fringe spacing has to be selected so that it is larger than the Kolmogorov length scale; otherwise the system will not be able to detect any (weak) turbulence induced refractive index fluctuations.

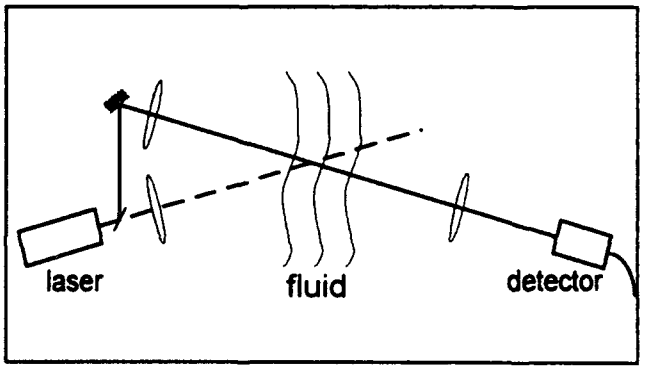

Figure 3. Basic scheme of a reference beam Doppler configuration. The actual implementation may be quite different. Frequency shift is generally applied and proper spatial mode matching should also be ensured.

Let the fringe spacing be Λ and the optical wavelength λ. The angle θ between the two transmitted beams is then given by

$$\theta = \tfrac{1}{2}\sin^{-1}(\lambda/\Lambda). \tag{8}$$

The spatial resolution along the optical axis, $\pm \Delta z$, is

$$\Delta z = 2r_0 \frac{\Lambda}{\lambda}, \tag{9}$$

where $2r_0$ is the beam diameter in the measuring plane. We note that a large optical wavelength implies a good spatial resolution!

The system shown in Fig. 3. is sensitive to refractive index fluctuations in a spatial region with a spatial center frequency given by $2\pi/\Lambda$ and a relative bandwidth of Λ/r_0.

4.2 The Time-of-flight Configuration

A so-called time-of-flight configuration (also called a two-spot system) has been applied as an alternative to the LDA in some cases where a good spatial selectivity along the optical axis is mandatory. Since it is a major problem with non particle laser anemometry to obtain a good spatial resolution along the optical axis it could be worth while to investigate the feasibility of the laser time-of-flight anemometer (LTA). The principles of an LTA for nonparticle laser anemometry could be envisaged to be as illustrated in Fig. 4. Scattered/diffracted light from the two focal regions should heterodyne with the directly transmitted light on the detectors. However, for scattering/diffraction caused by a weak phase object this will not happen. This is essentially the same problem as the classical phase contrast problem. Unfortunately, the same remedy cannot be applied here to cure the problem.

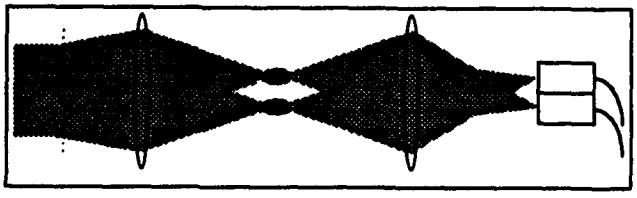

Figure 4. An envisaged LTA for non-particle laser anemometry. However due to the fact that the signal caused by weak phase perturbations is in phase quadrature with the directly transmitted beams the system cannot operate in a reference beam mode.

Let us briefly illustrate the problem: the transmission function of a weak phase object can be approximated as follows

$$e^{i\phi(x,y)} \cong 1 + i\phi(x,y). \tag{10}$$

The problem is that because of the i in front of $\phi(x, y)$ the signal is in phase quadrature with the reference. The phase contrast principle applied in microscopy to solve this problem cannot be applied here (Lading 1983). Introducing a spatial carrier frequency by tilting the reference beam will work - but then it becomes an LDA.

Away from the fundamental phase quadrature problem it is also problematic to have the full power of the directly transmitted beams impinge on the detectors; they may be damaged by the power.

4.3 A Hybrid Configuration

Let us summarize the features of the LDA and the LTA respectively. This is done in the table 1. Each of the two spots of the LTA have a diameter equal to the fringe spacing of the LDA. This implies that the spatial bandwidth of the LTA is much larger than the bandwidth of the LDA. The focal depth of a focused single mode beam is

$$\Delta z = 2\pi r_0^{\,2} / \lambda \tag{11}$$

giving a length for the LTA much smaller than the intersection region of the two intersecting beams of an LDA. The directional sensitivity is small for a two spot system because a structure contributing to the signal has to pass both beams. Elliptic spots may enhance the acceptance angle, but it cannot be $\pm$ 180° as for an LDA with frequency shift.

Table 1. Comparing an LDA with an LTA.

	LDA	LTA
bandwidth	small	large
spatial resolution	poor	good
directional sensitivity	small	high
reference beam	controllable	fixed

The problem with the LDA in the present context is that a large number of fringes is needed in order to allow for a good frequency estimate. This implies a spatial resolution that is unacceptable in relation to many applications. Note here that the fringe spacing has to be larger than the smallest turbulence scale. The LTA could provide an order of magnitude better spatial resolution and it would utilize a larger part of the turbulence spectrum; however, under most conditions it is insensitive to the type of disturbances that here provides the signal.

In order to obtain some of the advantages of the two systems we propose a hybrid configuration: A dual LDA system where each fringe pattern only has - say - 3-4 oscillations. The velocity is not determined from the frequency, but from the time of flight between the two fringe patterns. The system is illustrated in Fig. 5.

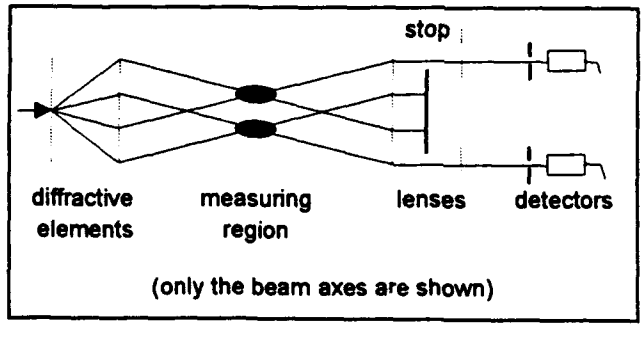

Figure 5. A hybrid LTA/LDA configuration. A diffractive element (to the left) generates four beams. A second element refracts and focuses these beams into two spatially separated fringe patterns, each with only a few fringes. The beams that impinge on the detectors will heterodyne with the scattered light from the two other beams. The reference beam is much weaker than the beams from which scattered light is utilized.

For a laser anemometer we can define a *code* that is a function that defines the way in which the velocity information is encoded into the system. For an LDA the code is a wave packet; for an LTA it consists of two displaced peaks. The code of the hybrid system is shown in Fig. 6. It consists of two displaced wave packets each with only a few oscillations.

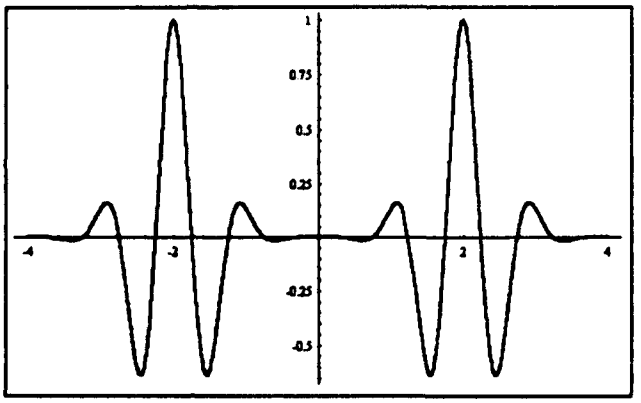

Figure 6. The intensity distribution as seen by the detectors of a hybrid laser anemometer - the *code* of the system.

In Fig. 7 is shown a spatial turbulence spectrum . Also shown are the 'filters' of the LDA and the hybrid system, respectively. The filters select the spectral regions from which refractive index perturbations can contribute to the signal. It is seen that the LDA selects a much narrower region than the hybrid system. For a given spatial resolution this implies that the hybrid will give a much stronger signal. However, if the purpose of a given investigation is to investigate the propagation of different spatial wavenumbers a narrow spatial frequency range is mandatory. For 'frozen' turbulence a large spectral region must be preferable.

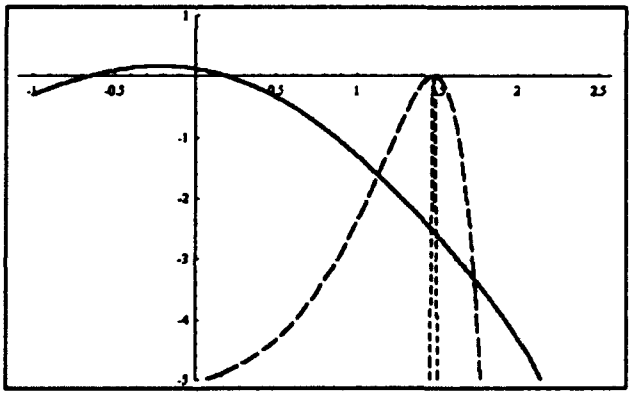

Figure 7. A turbulence spectrum (solid line) with the filter functions of an LDA (the narrow filter) and a hybrid LA, respectively. Notice that the hybrid utilizes a much larger part of the turbulence spectrum. (Log-log plot).

In discussing the spectral regions of the turbulence spectrum we must remember that the purpose may be to get information about the turbulence - possibly about its temporal evolution. With the present scheme it is so that we can only 'track' turbulence in a spectral region below that which gives rise to the signal: the high frequency turbulence serves the same purpose as particles do in normal laser anemometry.

5 TIME RESOLVED MEASUREMENTS

The signals of the systems considered here are in priciple continuous. Thus, time resolved measurements are potentially possible. The situation is similar to normal laser anemometers operating with many particles in the measuring volume. The statistics of especially LDA systems have been investigated in great detail over the years. Some of the results are adaptable to the systems considered here. We shall use the results of Lading and Edwards (1993).

In the type of systems considered here there are two fundamental stochastic processes that may limit the performance: the photon noise and the random process of the signal itself. In addition to these processes other types of fluctuations may hamper the performance. For reference beam systems it is often so that laser noise (caused by powersupply ripples, mode competition, intermode beats, mechanical instability . . .) is the limiting factor. However, we shall here assume that an adequately quite laser is available.

The relative measurement uncertainties can be expressed as follows:

fluctuations of the scattering/diffracting object itself;	*relative variance* $\approx 1/N$
photon noise (additive here)	*relative variance* $\approx \dfrac{\kappa^2}{\langle n_s \rangle}\dfrac{1}{N}$

The relative variance is the variance of the velocity estimate normalized by the square of the true velocity, i.e. $\mathrm{var}\{\hat{v}\}/v^2$. N is the number of degrees of freedom over which the averaging takes place, defined by the product of signal bandwidth times averaging time (assuming that the averaging time is larger than the reciprocal signal bandwidth). n_s is the number of detected scattered photons within the coherence time of the signal (= 1/signal bandwidht, also equal to the transit time through the illuminated volume(s)). κ is the reciprocal number of fringes in the measuring volume (LDA), or the ratio between beam radius and beam spacing (LTA).

Now, in order to perform time resolved measurements the averaging time must of course be smaller than the time scale of the fluctuations to be resolved. In order to get the best temporal resolution the photon noise should be negligible relative to the intrinsic signal fluctuations, i.e.

$$\kappa^2 / \langle n_s \rangle << 1. \qquad (12)$$

6 A SPECIFIC EXAMPLE FOR PLASMA TURBULENCE

Turbulence in fusion plasmas is of major concern because it has an essential impact on the confinement and

stability of the plasma. It also represents a type of fluid where no particles are to appear. We believe that some of the considerations relevant for plasma measurements may also be relevant for measurements in other types of fluids. Going through the calculations is beyond the limitations of this presentation. However, we shall summarize the numbers we arrived at in table 2. (An overview of the problems is given by Callen, Carreras, and Stambaugh (1992)).

Table 2. Potential parameters for a plasma diagnostic set-up

Relative refractive index fluctuations $\Delta n/n$	10^{-5}
Fraction of refractive index fluctuations utilised	10^{-3}
Velocity	10^{4} m/s
Overall efficiency	10 %
Laser Power	5 Watts
# photons/coherence time of signal	20
focal (intersection) regions	0.5 mm × 30 mm
wavelength of spatial filter	0.25 mm
spacing between focal regions	30 mm
transmitter/receiver spacing	3 m
transmitter aperture	300 mm
receiver aperture	2×100 mm
laser power	2 W

Since $\kappa<1$ and the number of estimated scattered photons within the coherence time of the signal is larger than unity, time resolved measurements appear feasible (Eq. 12).

7 CONCLUSION

Principles of non-particle laser anemometry have been discussed. A novel hybrid laser anemometer configuration is identified in order to enhance the spatial resolution and overcome the phase detection problem. A potential application to diagnostics in a fusion plasma is discussed and it is shown that time resolved measurements may be possible.

It should be mentioned that a number of important problems to non-particle laser anemometry have either only been mentioned briefly or not mentioned at all. Most important is the problem of separating propagating and non-propagating refractive index fluctuations.

REFERENCES

Callen, D.C., Carreras, B.J., and Stambaugh, R.D. (1992), Stability and Transport Processes in Tokamak Plasmas, Physics Today, January, pp. 34-42.

Clifford, S.F., Ochs, G.R., and Wang, T.I. (1975), Optical wind sensing by observing the scintillations of a random scene, Appl. Opt., vol.14, pp. 2844-2850.

Grésillon, D., Bonnet, J.P., Cabrit, B., and Frolov, V. (1992), Collective Light Scattering and the Diagnostics of Velocity Fluctuations in Transonic Flows, Sixth Int. Symp. Appl. Laser Tech. Fluid Mech. pp 2.6.1. - 2.6.6.

Lading, L., (1983), Estimating time and time-lag in time-of-flight velocimetry, Appl. Opt., vol. 22, pp. 3637-3643.

Lading, L. and Edwards, R.V., Laser velocimeters: lower limits to uncertainty, App. Opt. , vol. 32, No. 21 July 1993.

Lading, L., Mann, J.A., and Edwards, R.V. (1989), Analysis of a surface-scattering spectrometer, J. Opt. Soc. Am. A. vol. 6., No. 11, November 1989.

Lee, R.W. and Harp, J.C. (1969), Proc. IEEE vol. 57, 375.

Patrie, B.J., Seitzman, J.M., and Hanson, R.K. (1994), Instantaneous 3-Dimensional Flow Visualization by Rapid Acquisition of Multiple Planar Flow Images, Opt. Eng., Mar. 1994, vol. 33, No. 3, pp. 975-980.

Slusher, R.E. and Surkom C.M. (1978), Phys. Rev. Lett. 40, p. 400.

Strauch, R.G. (1985), Radar wind Profilers, Proc. NASA Symp. on Global Wind Measurements, July 29 - August 1, Columbia, MD, pp. 133-137.

Truck, A. et al, "ALTAIR: An infrared laser diagnostic on the TORE SUPRA tokamak, Rev. Sci. Instrum. vol. 63, pp. 3716-3724 (1992).

GAUSSIAN BEAM ERRORS IN PHASE-DOPPLER ANEMOMETRY AND THEIR ELIMINATION.

G. GOUESBET, G. GREHAN.

Laboratoire d'Energétique des Systèmes et Procédés,
INSA de ROUEN, URA.CNRS.230, CORIA.
BP08, 76131, Mont-Saint-Aignan Cédex, France.
Tel: (33) 35 52 83 87, Fax: (33) 35 52 83 90

Abstract

GLMT (generalized Lorenz-Mie theory) and its applications to the design of phase-Doppler instruments are discussed. A particular emphasis is stressed on Gaussian beam errors (trajectory ambiguity effects) and their elimination. Very recent concepts, even if not yet fully developed and/or implemented, are discussed too.

1 Introduction

A basic rule of science is to permanently take care of the necessary dialogue between theory and experiments. As a special case, this rule must obviously be satisfied in the field of opticle particle sizing (and characterization). However, most of the modern intruments used in this field rely on the interaction between laser beams (Gaussian beams, laser sheets, top-hat beams, to name a few) and particles (such as spheres or cylinders). Until recently, the required dialogue was therefore essentially forbidden by the fact that available theories assumed that the illumination beam was a plane wave, for instance in LMT (Lorenz-Mie theory) describing the interaction between a plane wave and a sphere. In the eighties neverteless, LMT has been generalized to GLMT describing the interaction between an arbitrary illuminating beam and a sphere. Thanks to GLMT, the required dialogue between theory and experiments has been restored. The aim of this paper is to review applications of GLMT to the analysis of phase-Doppler instruments, and in particular to the study of Gaussian beam defects and their elimination. Some connected topics will also be considered, such as the study of laser sheets or the development of the theory of interaction between an arbitrary incident beam and an infinite cylinder.

Even if GLMT is now essentially completed, many avenues remain to be explored. An increasing number of researchers is now following these avenues on a fundamental point of view. A still larger number of researchers is working on the applications of GLMT to concrete problems. In this paper, we shall try, beside the main objective presented by the title, to inform the reader about the more recent news. This would be impossible if we decided to go into details. Therefore, it has been decided that this paper would be written essentially in a qualitative way, dismissing in particular any mathematical expression (and figures). But, on the other hand, the reader is directed on the literature from which he could accede, hopefully, to any desired information. In other words, this paper is a guide to a sightseeing tour, not the tour by itself.

The paper is organized as follows. Section II is devoted to the GLMT itself. Section III is devoted to phase-Doppler instruments, Gaussian beam effects and their elimination. Section IV is devoted to connected topics and contain possibly some prospective ideas, trying to somehow forecast what we could expect from the near future. Section V is a conclusion.

2 Generalized Lorenz-Mie theory

GLMT describes the interaction between an arbitrary incident beam and a sphere, using partial wave expansions. The first archival paper is Ref (1) although the existence of this theory and some early results may be found in Ref (2). The development of the theory took about ten years, and may essentially be considered as completed after Refs (3,4). A rather recent exhaustive review of GLMT and applications is available from Ref (5).

A major issue to which much effort is still devoted is the speeding-up of numerical computations. For a long time, the most difficult task from this point of view has been the numerical evaluation of beam shape coefficients which may be considered as generalized Fourier coefficients expressing the partial wave expansions of the incident beam. A breakthrough has been the introduction of the so-called localized approximation in Ref (6), for the so-called beam waist center case, generalized in Ref(7) to the case of an arbitrary location of the particle, i.e.for the so-called off-axis case. An efficient algorithm to evaluate the beam shape coefficients in the framework of the localized approximation is discussed in Ref (8).

Although the accuracy of the localized approximation was very good (typically one part per 10^5), a drawback has been a lack of rigorous mathematical justification. A first step toward such a justification has been achieved by Lock in the on-axis case by using a stationary phase method (Ref 9). Unfortunately, the same method could not be extended to the general so-called off-axis case, even leading there to conflicting results, likely meaning that the success of the proof was in part incidental. By using another technique relying on Taylor expansions, a final proof of the validity of the localized approximation has afterward been obtained for both the on-axis and the off-axis cases (Refs 10,11), with, as a by-product, a very refined understanding of the nature of laser beams (Ref 12). The use of the localized approximation to handle GLMT allows fast and systematic study of phase-Doppler instruments, with a reasonable amount of CPU time. Furthermore, algorithm improvements are likely not exhausted. Let us for instance mention Ref (13) which implements a substantial amount of such improvements, in particular within the framework of the localized approximation. A pertinent example is given in which the Gaussian beam program runs about 70 times slower than the corresponding plane wave program. It may be forecasted that the combination of further improvements in software, and hardware, should make the difference between GLMT and LMT computational times fairly unessential within a few years. The same might become true if we compare GLMT and geometrical optics, with the advantage that GLMT is a rigorous theory.

3 Gaussian beam defects in phase-Doppler instruments

3.1 Generalities.

Phase-Doppler anemometry (PDA), an extension of laser Doppler velocimetry (LDV), is nowadays the most popular technique for simultaneously measuring the size and the velocity of individual particles. Examples of pioneering and significant papers are Refs (14)-(17), among many others. The principle of the technique may possibly be summarized as follows. Let us consider two interfering laser beams B1 and B2, and a spherical particle crossing the fringe control volume. At a point P in space, waves W1 and W2 scattered by the particle from the incident beams B1 and B2 respectively, interfere together. The resulting wave at point P is obtained by summing the amplitudes of the waves W1 and W2. After evaluating intensities and integrating on the surface of a detector D, one finds that the detected signal is characterized by a phase P. Let us now consider two detectors D1 and D2 leading to phases P1 and P2, respectively. Then, under some ideal circumstances, including the plane wave character of the incident beams, it has been predicted that the phase difference (P1-P2) is related to the particle diameter through a linear relationship.

The physical process aforementioned is amenable to a full theoretical simulation when a light scattering theory is used. Such scattering theo-

ries may be LMT, geometrical optics, or GLMT. LMT is a rigorous theory but, being limited to the plane wave case, it cannot predict the influence of the Gaussian character of the incident beams. This Gaussian character may be implemented in geometrical optics. But geometrical optics is not a rigorous theory with the consequence that the induced loss of accuracy may possibly be dramatic in some cases, although, in other cases, it can be quite insignificant. Finally, GLMT is a rigorous theory which correctly incorporates the Gaussian character of the incident beams. The price to pay is more extensive computational times but, as discussed previously, this drawback is likely to be somewhat provisional. Geometrical optics and LMT have been applied to phase-Doppler instruments in earlier stages. The first applications of GLMT to PDA dates back to 1990 (18).

3.2 Gaussian beam defects

In many cases, the size of the scatter centers is not small enough with respect to the beam size, i.e. the incident beams cannot be safely considered as being plane waves. Then departures from the linear phase/diameter relationship may be observed, possibly leading to considerable errors in diameter measurements. Nowadays this phenomenon is referred to as a trajectory ambiguity effect (TAE) or, to better stress the origin of the problem, as a Gaussian beam defect (GBD).

TAE has been theoretically predicted by Bachalo and Sankar by using geometrical optics (19), and then confirmed by using GLMT (20). A simple qualitative explanation may be provided in terms of the competition between refracted and reflected rays induced by the Gaussian profile (5). Following these preliminary observations, a considerable systematic effort has been devoted to the analysis of TAE and to their elimination as testified by Refs (21)-(32). Remedies are discussed in the next sub-section.

3.3 Elimination of Gaussian beam defects

A rather exhaustive list of remedies to Gaussian beam defects is given below. Details may be found in Refs (21)-(32). Basically, remedies may be splitted in two individual classes, one corresponding to the optimization of the optical design, and the second to the refinement of the data processing. Of course, there exists also an hybrid class in which both optical design optimization and signal processing refinement may cooperate.

(i)It is possible to manipulate the incident beam polarizations in order to modify the balance between reflected and refracted contributions as suggested by Saffman et al (33,34). This strategy relies on the basic idea that interferences between reflected and refracted components spoil the desired linear relationship between phases and diameters. This concept has been investigated by using GLMT (25). The conclusion is that doing so it is possible to improve the quality of the measurements but not necessarily in an effective enough way.

(ii)It has been suggested to use a discrimination criterion relying on the measurement of two phase differences, P12 from detectors D1 and D2, and P13 from detectors D1 and D3. Then the discrimination to retain or reject measurements is based on the value of the ratio P12/P13. A GLMT-analysis of this concept is for instance given in Refs (22,25). Again, improvements are observed but not effective enough.

(iii)Let P be the plane defined by the incident laser beams. The analysis of Gaussian beam defects then demonstrates that good measurements are obtained when the detectors and the particle are on the same side with respect to P. Conversely, departures from the ideal relationship arise when the detectors and the particle are located on opposite sides. Then, we may use an optical design in which two detector assemblies are used, symmetrically located with respect to P. The use of two symmetric assemblies ensures that there will always be one assembly for which relationships are satisfactory. Furthermore, the comparison between the two responses allows one to determine which response is correct. This technique is effective, although it increases the complexity of the instrument. Details are available from Refs (21,25,27).

(iv)Among many possibilities, Doppler signals may be analysed by using a discrete Fast Fourier

Transform (DFFT), leading to the evaluation of the Doppler frequency, i.e. to the measurement of one velocity component of the scatter center. In the phase-Doppler technique, one may rely on the use of an extended version generating a cross-spectral density (CSD) function, allowing the evaluation of the frequencies from detectors D1 and D2 and of the phase difference between both signals (35). Because CSD does not analyse phase evolution in the case of Gaussian beam defects, it may lead to significant errors in diameter measurements by averaging phase differences along the duration of the signals. Therefore, the use of a wavelet transform which has temporal localization properties may allow the detection of phase evolution in a signal, and therefore provide a discrimination procedure (36,5). It must be however noted that a systematic investigation of this concept has not yet been carried out.

(v)In the standard design, the detectors are located outside of the plane defined by the incident laser beams, and particles pass through the control volume, essentially perpendicularly to the non moving fringes. As discussed above, such a design is subject to Gaussian beam defects. This is due to the fact that trajectories are parallel to isophase lines. Therefore, the phase is constant but depends on the particle location.

In the so-called planar system, conversely, the detectors are located in the same plane than the incident beams. In this case, the particles cross the isophase lines. Therefore, there is a phase evolution along the burst but, limiting data processing to the part of the signal around the maximum, it is possible to show that the measured phase corresponds to the plane wave case predictions (26,28,32). In this case, TAE elimination is obtained by an appropriate modification of the optical design with respect to the standard system. A similar effect may also be obtained by an appropriate design of a two-colour PDA standard system (37), leading to a design which may be called the modified standard system. It is also possible to use a two-colour dual-mode system, combining a planar system based on one colour and a modified standard system based on another colour (38). An advantage of this dual-mode technique is that it allows a measurement of the particle refractive index, of sufficient quality for material recognition. Furthermore, each colour component of the system determines a diameter, i.e. actually a curvature radius, therefore leading possibly to non sphericity identification.

All the above techniques based on modifications of the optical design and/or on data processing refinements are devoted to the elimination of TAE considered as defects. On the other hand, TAE also contain relevant information and, therefore, instead of working towards their elimination, it might be very advisable to recover, if possible , the information that they contain. This different attitude leads to the so-called dual-burst system.

3.4 Taking advantage of TAE

In the dual-burst system, the control volume is choosen very small, therefore enhancing TAE to better take advantage of the information that they carry. Apart of that, the optical design may be either a planar system or a modified standard system, but data processing is carried out by recording the phase evolution along the duration of the signal. Then, the theoretical analysis, confirmed by experiments, shows that one part of the signal is free of TAE while another part, easily identified, contains extra information associated with TAE. Therefore, we may measure velocities and diameters by analyzing the TAE free part of the signal. The other part, conversely, is shown to contain information on refractive indices. Also, non sphericity, as well as inhomogeneity, information could possibly be recovered (29).

4 Connected topics

We end this paper by briefly mentioning a few connected topics relevant to particle characterization.

4.1 Laser sheets

Although phase-Doppler instruments rely on the use of Gaussian beams, there may be advantages in using laser sheets. Laser sheets may be obtained by transforming Gaussian beams with the

aid of a cylindrical lens. Laser sheets are for instance used in particle image velocimetry, for polarization ratio measurements , for measuring wall shear stress in a turbulent boundary layer , for particle sizing, or for studying droplet distribution effects on planar laser imaging of sprays (39-45). Therefore, GLMT has been specified to the case of laser sheets and used to investigate some optical characterization problems (46-53). The use of laser sheets in phase-Doppler instruments might be an interesting prospect.

4.2 Stratified spheres

In the previous subsection, GLMT has been specified to the case of laser sheets. It does not change the GLMT framework which is insensitive to the nature of the incident beam (GLMT is an arbitrary beam theory). Considering a new kind of beam however requires some extra-work associated with the knowledge of the electromagnetic description of the beam, to be used as an input in GLMT. Instead of changing the nature of the beam, we may consider other cases than the classical homogeneous sphere assumed in LMT and GLMT. Then, for each of these other cases, a new theory must be built.

The simplest case is the stratified sphere which preserves the spherical symmetry enjoyed by GLMT. The theory of interaction between an arbitrary incident beam and a stratified sphere has indeed been recently completed (54). Relying on the plane wave case, we may forecast many applications of this theory to optical characterization, in particular in combusting systems which induce temperature gradients inside droplets (see for instance 55). The development of phase-Doppler instruments to the study of stratified spheres might then be another interesting prospect.

4.3 Cylinders

Many particles are not spheres nor even stratified spheres. It is therefore somewhat of an unpleasant state of affair that most of our experimental techniques have to assume that we deal with spherical particles, even if they are not. This attitude may lead to the so-called spherical chicken syndrome as defined by B.H.Kaye (56),i.e. to misleading measurements and physical models. A possible way to escape of this problem is to develop the phase-Doppler instruments in such a way that they could provide non sphericity information as previously discussed. Another way is to develop other instruments less sensitive to non sphericity. There, a good candidate is the so-called top-hat beam technique which allowed rather successful measurements on irregular particles, such as sand particles (57-60,20,12, and references therein). Other techniques are the Visible Infra-red Double Extinction (VIDE) technique to investigate the case of large optical thicknesses, or quasi-elastic light scattering spectroscopy devoted to ensemble measurements on submicronic particles (61,62, and references therein).

Another approach is to start a systematic study of well defined shapes. After spheres, and stratified spheres, the best candidate to investigate seems to be the infinite cylinder. Many potential applications can be expected. Examples are the control of the production of glass wool for thermal isolation, of optical fibers for data transmission, or the study of pulverization processes when droplets are produced by instabilities acting on an initial liquid jet. Another promising remark is that many particles, even if they are not infinite cylinders, may locally look like an infinite cylinder when they are illuminated by focused beams. Therefore, this special case of a regular particle might also help to study a class of irregular particles, including sinuous fibers.

Concerning phase-Doppler instruments, it appears pretty sure that the extension of this technique from spheres to cylinders should lead to significant results. On the theoretical side, let us mention that the theory of interaction between an arbitrary incident beam and an infinite cylinder is under construction. However, the problem appears much more complicated than expected as testified by Refs (63-65). In particular, the basic so-called separability theorem used in designing both LMT and GLMT looks like failing for the cylinder problem. A pure mathematical work concerning this theorem is therefore likely to be compulsory, such as discussed in Ref (66). The construction of the GLMT basically required

one decade. It is hoped that the completion of the cylinder problem will be less time demanding. In any case, we may forecast future interesting developments in this topic, both from an experimental and a theoretical point of view.

5 Conclusion

One of the major recent news concerning phase-Doppler anemometry has been the uncovering of the existence of trajectory ambiguity effects (Gaussian beam defects) which may lead to dramatic measurement errors if the optical design and the data processing are not set up in an appropriate way. These effects, first revealed by theoretical investigations, have been experimentally confirmed. At first sight, this is bad news. In particular, it is quite possible that some data displayed in the literature are erroneous due to the lack of knowledge on these effects.

A strong and systematic effort has therefore been devoted to the analysis of these effects, and to their elimination. Several new optical designs, possibly associated with refined data processing, actually allow one to cure them. May be more interesting, TAE, first considered as a nuisance, may also be considered as a chance because they carry extra information that we may recover, therefore opening new possibilities.

Finally, related topics have been considered, namely the specification of GLMT to the case of laser sheets,its generalization to the case of stratified spheres, and the challenging problem of interaction between arbitrary shaped beams and infinite cylinders.

6 References

1. G. Gouesbet, G. Gréhan, Sur la généralisation de la théorie de Lorenz-Mie, Journal of Optics (Paris), 13,2,97-103, 1982.

2. G. Gréhan, G. Gouesbet, C. Rabasse, The computer program Supermidi for Lorenz-Mie theory and the research of one-to-one relationships for particle sizing. Proceedings of the symposium on long range and short range optical velocity measurements, Institut franco-allemand de Saint-Louis, 15-18th sept. ,1980.

3. G. Gouesbet, B. Maheu, G. Gréhan, Light scattering from a sphere arbitrarily located in a Gaussian beam, using a Bromwich formulation, Journal of Optical Society of America A, 5,9,1427-1443, 1988.

4. B. Maheu,G. Gouesbet,G. Gréhan, A concise presentation of the generalized Lorenz-Mie theory for arbitrary location of the scatterer in an arbitrary incident profile, Journal of Optics (Paris), 19,2, 59-67,1988.

5. G. Gouesbet, Generalized Lorenz-Mie theory and applications, Plenary lecture, Third international congress on optical particle sizing, August 23-26,1993, Yokohama, Japan, Proceedings, republished in Particle and Particle Systems Characterization, 11, 22-34, 1994.

6. G. Gréhan, B. Maheu, G. Gouesbet. Scattering of laser beams by Mie scatter centers : numerical results using a localized approximation, Applied Optics, 25,19,3539-3548, 1986.

7. G. Gouesbet,G. Gréhan, B. Maheu, A localized interpretation to compute all the coefficients gnm in the generalized Lorenz-Mie theory, Journal of Optical Society of America A, 7,6,998-1007, 1990.

8. K. F. Ren, G. Gréhan, G. Gouesbet, Localized approximation of generalized Lorenz-Mie theory. Faster algorithm for computations of the beam shape coefficients, Particle and Particle Systems Characterization, 9, 2, 144-150, 1992.

9. J. A. Lock, The contribution of high-order rainbows to the scattering of a Gaussian laser beam by a spherical particle, Journal of Optical Society of America A, 10, 4, 693-706, 1993.

10. J. A. Lock, G. Gouesbet, A rigorous justification of the localized approximation to the beam shape coefficients in generalized Lorenz-Mie theory, I. On-axis beams, To be published in Journal of Optical Society of America A.

11. G. Gouesbet, J. A. Lock, A rigorous justification of the localized approximation to the beam shape coefficients in generalized Lorenz-Mie theory, II. Off-axis beams, To be published in Journal of Optical Society of America A.

12. G. Gouesbet, J. A. Lock, G. Gréhan, Do you know what a laser beam is?, Proceedings of

the seventh workshop on two-phase flow predictions, Erlangen, Germany, April 11-14, 1994.

13. J. A. Lock, An improved Gaussian beam scattering algorithm, under preparation.

14. F. Durst,M. Zare, Laser Doppler measurements in two-phase flows. Proceedings of the LDA-symposium, Copenhagen, 1975, pp 403-429.

15. W. D. Bachalo, M. J. Houser, Phase-Doppler spray analyzer for simultaneous measurements of drop size and velocity distributions, Optical Engineering. 23, 583-590, 1984.

16. M. Saffman, P. Buchhave, H. Tanger, Simultaneous measurement of size, concentration and velocity of spherical particles by a laser Doppler method, in R. J. Adrian, D. F. G. Durao, F. Durst, Mishina, J. H. Whitelaw (edts), laser anemometry in fluid mechanics-II, Ladoan-Lisbon, 1984, pp85-104.

17. S. A. M. Al-Chalabi, Y. Hardalupas, A. R. Jones, A. M. K. P. Taylor, Calculation of the calibration curves for the phase-Doppler technique, comparison between Mie theory and geometrical optics, in G. Gouesbet,G. Gréhan (edts), optical particle sizing : theory and practice, Plenum Press, New-York, pp 107-120, 1988.

18. G. Gréhan, G. Gouesbet, F. Vannobel, J. B. Dementhon, Generalized Lorenz-Mie theory : an application to phase-Doppler technique. Proceedings of the fifth international symposium on applications of laser anemometry to fluid mechanics, Lisbon, Portugal, July 9-12, 1990.

19. W. D. Bachalo, S. V. Sankar, Analysis of the light scattering interferometry for spheres larger than the light wavelength, Proceedings of the fourth international symposium on applications of laser anemometry to fluid mechanics, Lisbon, 1988.

S.V. Sankar and W.D. Bachalo, Response characteristics of phase Doppler particle analyzer for sizing spherical particles larger than the wavelength, Applied Optics, vol. 30, n 12, 1487-1496, 1991.

S.V. Sankar, A. Inenaga and W. D. Bachalo, Trajectory dependent scattering in phase doppler interferometry: minimizing and eliminating sizing error, Proceedings of the sixth international symposium on applications of laser anemometry to fluid mechanics, Lisbon, Portugal, July 20-23, 1992.

20. F. Corbin, G. Gréhan, G. Gouesbet, Top-hat beam technique : improvements and application to bubble measurements, Particle and Particle Systems Characterization, 8, 222-228, 1991.

21. G. Gréhan, G. Gouesbet, A. Naqwi, F. Durst, Evaluation of phase-Doppler systems using generalized Lorenz-Mie theory, international conference on multiphase flows, university of Tsukuba, Japan, Sept 24-27, 1991. Proceedings.

22. G. Gréhan, G. Gouesbet, A. Naqwi, F. Durst, On elimination of the trajectory effects in phase Doppler systems, 5th European symposium on particle characterization, Nrnberg, March 1992, Proceedings, pp 309-318.

23. G. Gouesbet, A. Berlemont, P. Desjonquères, G. Gréhan, On modelling and measurement problems in the study of turbulent two-phase flows with particles, Sixth workshop on two-phase flow predictions, Erlangen, March 23-26, 1992. Proceedings : Forschungszentrum Jlich GmbH, bilateral seminar of the international bureau, 14, 1993, pp 365-387, M. Sommerfeld, editor.

24. A. Naqwi, M. Ziema, G. Gréhan, G. Gouesbet, Accuracy considerations in the optical design of phase Doppler systems, Same as Ref 24, pp 412-420.

25. G. Gréhan, G. Gouesbet, A. Naqwi, F. Durst, Trajectory ambiguities in phase-Doppler systems : use of polarizers and additional detectors to suppress the effect. Sixth international symposium on applications of laser techniques to fluid mechanics, Lisbon, July 20-23, 1992, proceedings.

26. Y. Aizu, F. Durst, G. Gréhan, F. Onofri, T. H. Xu, PDA- systems without Gaussian beam defects, Proceedings of the third international congress on optical particle sizing, August 23-26, Yokohama, 1993.

27. G. Gréhan, G. Gouesbet, A. Naqwi, F. Durst, Particle trajectory effects in phase-Doppler systems : computations and experiments, Particle and Particle Systems Characterization, 10,332-338, 1993.

28. Y. Aizu, J. Domnick, F. Durst, G. Gréhan, F. Onofri, Hui-He Qiu, M. Sommerfeld, Tien-Hua Xu, M. Ziema, New generation of phase-Doppler

instruments for particle velocity, size, and concentration measurements, Particle and Particle Systems Characterization, 11, 43-54, 1994.

29. F. Onofri, G. Gréhan, G. Gouesbet, T. H. Xu, G. Brenn, C. Tropea, Phase-Doppler anemometry with dual-burst technique for particle refractive index measurements, present conference.

30. G. Gréhan, F. Onofri, T. Girasole, G. Gouesbet, F. Durst, C. Tropea, Measurement of bubbles by phase-Doppler technique and trajectory ambiguity, present conference.

31. G. Gréhan, G. Gouesbet, A. Naqwi, F. Durst, Trajectory ambiguities in phase-Doppler systems : study of a near-forward and a near-backward geometry, To be published in Particle and Particle Systems Characterization.

32. Y. Aizu, F. Durst, G. Gréhan, F. Onofri, T. H. Xu, PDA-systems without Gaussian beam defects, To be published in ASME journal.

33. M. Saffman, P. Buchhave, H. Tanger, Simultaneous measurement of size, concentration, and velocity of spherical particles by a laser Doppler method, in R. J. Adrian, D. F. G. Durao, F. Durst, Mishina, J. H. Whitelaw (eds) : Laser anemometry in fluid mechanics-II, Ladoan-Lisbon, 1984, pp 85-104.

34. M. Saffman, The use of polarized light for optical particle sizing, in R. J. Adrian, T. Asanuma, D. F. G. Durao, F. Durst, J. H. Whitelaw (eds) : Laser anemometry in fluid mechanics-III. Selected papers from the third international symposium on applications of laser anemometry to fluid mechanics, 1986.

35. J. Domnick, H. Ertel, C. Tropea, Processing of phase-Doppler signals using the cross-spectral density function, in applications of laser anemometry to fluid mechanics, R. J. Adrian, T. Asanuma, D. F. G. Durao, F. Durst, J. H. Whitelaw (eds), Springer-Verlag, 1989.

36. F. Onofri, C. Roze, G. Gréhan, Traitement des signaux phase- Doppler et ADL sujets aux effets de trajectoire, analyse par ondelettes, Proceedings des 9èmes journées sur les aérosols, Paris, Dec 8-9, 1992.

37. T. H. Xu, C. Tropea, Improving performance of two-component Phase Doppler anemometers, accepted for publication in Measurement Science Technology.

38. C. Tropea, T. Xu, G. Gréhan, F. Onofri, P. Haugen, Dual-mode - phase-Doppler anemometry, present conference.

39. R. J. Adrian, Scattering particle characteristics and their effect on pulsed laser measurements of fluid flow : speckle velocimetry vs. particle image velocimetry. Applied Optics, 23, 1690-1691, 1984.

40. R. J. Adrian, The role of particle image velocimetry in fluid mechanics, in : optical methods and data processing in heat and fluid flow, London, April 1992, pp 1-6.

41. C. H. Ryan, A. Pal, W. Lee, R. J. Santoro, Droplet distribution effects on planar laser imaging of sprays, Atomisation and sprays, 2, 155-177, 1990.

42. A. Naqwi, W. C. Reynolds, L. W. Carr, Dual-cylindrical wave laser Doppler method for measurement of wall shear stress, in Adrian, Durao, Mishina, Whitelaw (eds) : laser anemometry in fluid mechanics-II, Ladoan-Instituto superior tecnico, Lisbon, 105-122, 1986.

43. A. Naqwi, X. Z. Liu, F. Durst, Dual-cylindrical wave method for particle sizing, Particle and Particle Systems Characterization, 7, 45-53, 1990.

44. A. Naqwi, X. Z. Liu, F. Durst, Evaluation of the dual-cylindrical wave laser technique for sizing of liquid droplets, Particle and Particle Systems Characterization, 9, 44-51, 1992.

45. C. F. Hess, Poster at the 2nd international congress on optical particle sizing, Tempe, Arizona, USA, March 190. Company Metro-laser.

46. K. F. Ren, G. Gréhan, G. Gouesbet, Laser sheet scattering by spherical particles, Proceedings of the sixth international symposium on applications of laser techniques to fluid mechanics, Lisbon, July 20-23, 1992.

47. J. Mroczka, K. F. Ren, G. Gréhan, G. Gouesbet, Particle sizing by using polarisation ratios, on the use of laser sheets, first international conference-workshop on modelling in measurement processes, June 7-9, Technical University of Wroclaw, Szklarska-Poreba, Poland, proceedings, 1993.

48. G. Gréhan, K. F. Ren, G. Gouesbet, A. Naqwi, F. Durst, Application of the generalized

Lorenz-Mie theory to multiphase flows experimental techniques, Ninth symposium on turbulent shear flows, Kyoto, Japan, August 16-18, 1993, Proceedings, paper 27-1-1.

49. G. Gréhan, K. F. Ren, G. Gouesbet, A. Naqwi, F. Durst, Evaluation of particle sizing technique based on laser sheets, Third international congress on optical particle sizing, August 23-26, Yokohama, Japan, Proceedings, 1993.

50. K. F. Ren, G. Gréhan, G. Gouesbet, Laser sheet scattering by spherical particles, Particle and Particle Systems characterization, 10, 332-338, 1993.

51. G. Gréhan, K. F. Ren, G. Gouesbet, A. Naqwi, F. Durst, Evaluation of a particle sizing technique based on laser sheets, Particle and Particle Systems Characterization, 11, 101-106, 1994.

52. K. F. Ren, G. Gréhan, G. Gouesbet, Evaluation of laser sheet beam shape coefficients in generalized Lorenz-Mie theory by using a localized approximation, To be published in Journal of Optical Society of America A.

53. K. F. Ren, G. Gréhan, G. Gouesbet, Symmetry relations in generalized Lorenz-Mie theory, To be published in Journal of Optical Society of America A.

54. F. Onofri, G. Gréhan, G. Gouesbet, Electromagnetic scattering from a multilayered sphere located in an arbitrary beam, submitted to Applied Optics.

55. L. Kai, P. Massoli, A. D'Alessio, Studying inhomogeneities of spherical particles by light scattering, 3rd international symposium on optical particle sizing, Yokohama, Japan, pp 135-143, 1993.

56. B. H. Kaye, A random walk through fractal dimensions, VCH, 1989.

57. D. Allano, G. Gouesbet, G. Gréhan, D. Lisiecki, Droplet sizing using a top-hat laser beam technique, Journal of Physics : Applied Physics, 17,1,43-58, 1984.

58. G. Gréhan, G. Gouesbet, Simultaneous measurements of velocities and sizes of particles in flows using a combined system incorporating a top-hat beam technique. Applied Optics, 25,19, 3527-3538, 1986.

59. R. Kleine, G. Gouesbet, B. Rück, Lokale, optische Messungen von Teilchengeschwindigkeiten, Teilchengrssenverteilungen und Teilchenkonzentrationen. Sensor 82. Essen, January 12-14, 1982. Proceedings.

60. G. Gréhan, G. Gouesbet, R. Kleine, V. Renz, I. Wilhelmi, Corrected laser beam techniques for simultaneous velocimetry and sizing of particles in flows and applications. Third international symposium on applications of laser anemometry to fluid mechanics, Lisbon, July 7-9, 1986. Proceedings.

61. J. B. Guidt, G. Gouesbet, J. N. Le Toulouzan, An accurate validation of visible infra-red double extinction simultaneous measurements of particle sizes and number-densities by using densely laden standard media, Applied Optics, 29, 7, 1011-1022, 1990.

62. N. Lhuissier, G. Gouesbet, M. E. Weill, Extensive measurements on soot particles in laminar premixed flames by quasi-elastic light scattering spectroscopy, Combustion science and technology, 67, 17-36, 1989.

63. G. Gouesbet, G. Gréhan, Recent advances in generalized Lorenz-Mie theory and applications. Third European aerosol conference 93, Universitt Duisburg, Oct 4-8, 1993, seminar : trends in aerosol research. Proceedings of the seminar of the Sonderforschungbereich 209, Universitt Duisburg Gesamthochschule, A. Schmidt-Ott, ed, pp 17-23.

64. G. Gouesbet, G. Gréhan, Interaction between shaped beams and an infinite cylinder, including a discussion of Gaussian beams, to be published in Particle and Particle Systems Characterization.

65. G. Gouesbet, G. Gréhan, Interaction between a Gaussian beam and an infinite cylinder, using non-sigma separable potentials, submitted to Journal of Optical Society of America A.

66. G. Gouesbet, The separability dogma revisited with applications to light scattering theory, submitted to Journal of Optical Society of America.

CHARACTERISTICS OF COUNTER - GRADIENT HEAT TRANSFER IN A NON - PREMIXED SWIRLING FLAME

Y Hardalupas, M Tagawa*, A M K P Taylor

Department of Mechanical Engineering, Imperial College of Science, Technology & Medicine, London SW7 2BX

*Department of Mechanical Engineering, Nagoya Institute of Technology, Gokiso-cho, Showa-ku, Nagoya 466, Japan

1 INTRODUCTION

1.1 The Flow Considered

There is now an extensive body of literature which documents that the turbulent fluxes of heat and momentum in premixed flames may frequently arise in the counter-gradient direction (e.g. Heitor et al., 1987; Ferrão & Heitor, 1993). The observation has consequences for both the interpretation of reaction rates, stability limits and also for the mathematical modelling of these fluxes in the context of, say, CFD predictions of such flames. The origin of the phenomenon is the interaction between mean pressure gradients, arising in the flow due either to mean streamline curvature or because of acceleration of gases across the flame front, and the density of hot packets of fluid which become preferentially accelerated relative to cold ones (e.g. Bray & Libby, 1991). The phenomenon is particularly stark in premixed flames because, in most technical applications, the temperature of the gases is sharply bimodal with a cold entry at the temperature of the reactants and a hot one corresponding to the products. The phenomenon also arises in non-premixed flames and has been found by Takagi et al. (1984) in confined, swirling non-premixed flames, where the swirl imparted to the combustion air provides a strong radial mean pressure gradient which acts on the flame sheet at which mixing between the cold reactants and the hot products occurs.

1.2 The current contribution

The configuration of a swirling annulus of combustion air surrounding a coaxial stream of fuel arises in many technical contexts, such as the combustion chambers of gas turbines and the burners in utility boilers. Further investigation of the magnitude and occurrence of counter-gradient diffusion in non-premixed flames is warranted and the purpose of this paper is to demonstrate the existence of counter-gradient diffusion of heat flux in a swirling non-premixed burner, fitted with a diffuser, fired by natural gas. The distinguishing feature from the investigation of Takagi et al. (1984) is that, here, apart from the presence of the diffuser and the subsequent unconfined flame, the swirl number of the combustion air was sufficiently large to generate a large internal recirculation zone.

2 EXPERIMENTAL METHOD

2.1 Experimental Configuration

The burner geometry is shown in figure 1: the burner geometry is identical to that used by Milosavljevic et al. (1990) and its description will not be repeated here, except to remark that the swirl number (defined using the ratios of the axial fluxes of angular and axial momentum) was continuously variable from zero to a value beyond unity. The burner was operated at an air flow rate of 900 l/min, resulting in a high cold-flow Reynolds number, and at a gas flow rate corresponding to an equivalence ratio of 0.85.

2.2 Instrumentation

The turbulent heat flux was measured by means of a digitally compensated thermocouple and a single channel laser Doppler anemometer, as shown schematically in figure 2. The basic features of compensation have been described by Heitor (1985) and recent analysis for non-premixed flames has been provided by Mastorakos (1993)

3 RESULTS

The complete paper will present radial profiles of: the three components of the mean and rms values of the axial, radial and azimuthal (swirl) velocities, of the corresponding values of the shear stress $\overline{uv}$, of the mean and rms temperature and of the heat fluxes, $\overline{ut}$ and $\overline{vt}$ as a function of axial location downstream of the exit of the quarl up to 1.5 diffuser exit diameters. Figure 3 presents a sample of the radial profiles of mean temperature and of radial heat flux which shows the presence of counter-gradient turbulent transport.

To know in detail the quantitative contributions of each fluid motion classified in the (v, t) plane to the turbulent heat flux $\overline{vt}$, we use the weighted pdf of vt, $W_{\hat{v},\hat{t}}(\hat{v},\hat{t})$, defined by (Nagano & Tagawa, 1988)

$$W_{\hat{v},\hat{t}}(\hat{v},\hat{t}) = \int_{-\infty}^{\infty} \hat{v}\,\hat{t}\,P(\hat{v},\hat{t})\,d\hat{t}$$

where $\hat{.}$ denotes normalisation by the rms value of the variable and $P(v, t)$ represents the joint probability distribution function of fluctuations of radial velocity and temperature. The results of $P(\hat{v},\hat{t})$ are shown in figure 4(a) and (b) for y = 3 and x/R = 0.1 and y = -5 mm and 0.5 which are locations where the time-averaged values of heat flux are in the gradient and strong counter-gradient directions, respectively: figures 5(a) and (b) show the calculated values of $W\hat{v},\hat{f}$ $(\hat{v},\hat{t})$. Note that *second* and *fourth* quadrant contributions are expulsion and entrainment type motions and counter-gradient flux can occur only when the contribution of these quadrants is dominated by that from the *first* and *third* quadrant motions, as in figure 5(b). Thus, although an analysis similar to Bray and Libby – appropriately modified for diffusion flames – may explain counter gradient diffusion in swirling flames, the explanation is however applicable only in the region where the effects of entrainment on the flow characteristics are negligible. Counter-gradient diffusion helps to "trap" hot products inside the recirculation zone and thus to stabilise the flame.

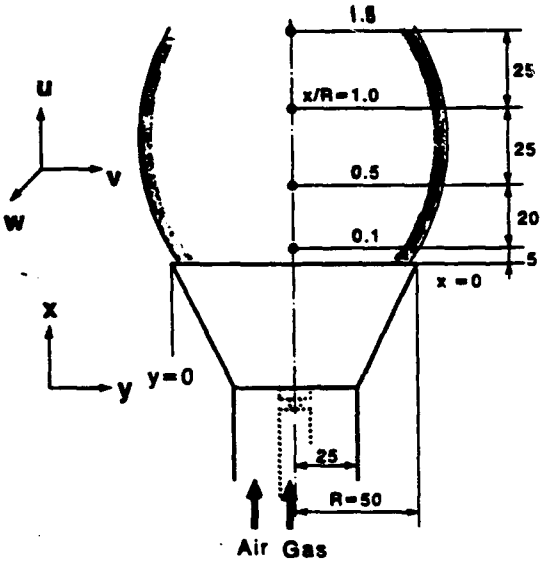

Fig. 1 The burner geometry

REFERENCES

Bray, K N C, Libby, P A, 1991. Premixed turbulent combustion. In Fluid Dynamical Aspects of Combustion Theory (M Onofri and A Tesei, eds.), pp. 113 - 140, Longman.

Ferrão, P, Heitor, M V, 1993. Turbulent mixing and non-gradient diffusion in baffle-stabilised flames. *Paper 28-2-1* in Ninth Symposium on Turbulent Shear Flows, Kyoto, Japan.

Heitor, M V, 1985. Experiments in turbulent reacting flows. Ph D Thesis, University of London.

Heitor, M V, Taylor, A M K P, Whitelaw, J H, 1987. The interaction of turbulent pressure gradients in a baffle-stabilised premixed flame. J Fluid Mech., vol. 181, 387 - 413.

Mastorakos, E, 1993. Turbulent combustion in opposed jet flows. Ph D Thesis, University of London.

Milosavljevic, V D, Taylor, A M K P, Whitelaw, J H, 1990. The influence of burner geometry and flow rates on the stability and symmetry of swirl stabilized non-premixed flames. Comb Flame, 80, 196 - 208.

Nagano, Y and Tagawa, M, 1988. Statistical charactersitics of wall turbulence with a passive scalar. J Fluid Mech., vol. 196, 157 - 185.

Takagi, T, Okamoto, T, Taji, M and Nakasuji, Y, 1984. Retardation of mixing and counter-gradient diffusion in a swirling flame. Twentieth Symposium (International) on Combustion, pp. 251 - 258. The Combustion Institute, Pittsburgh.

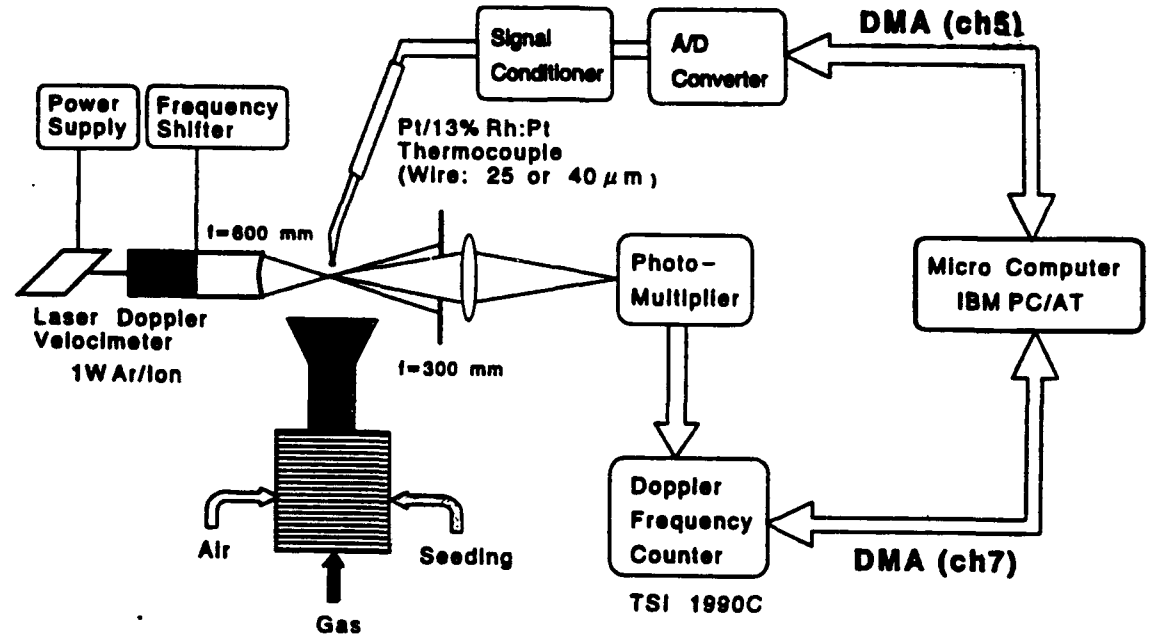

Fig. 2 Digitally compensated thermocouple and a single channel laser Doppler anemometer.

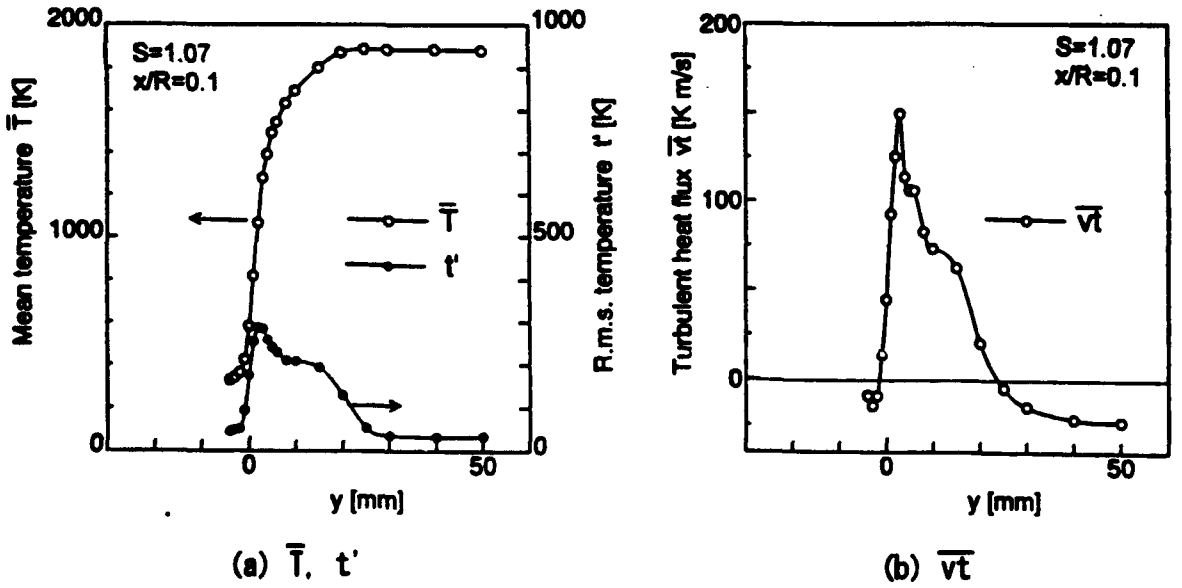

Fig. 3 Radial profiles of mean temperature and of radial heat flux which shows the presence of counter-gradient turbulent transport. Swirl number was 1.07, x/R ≈ 0.1.

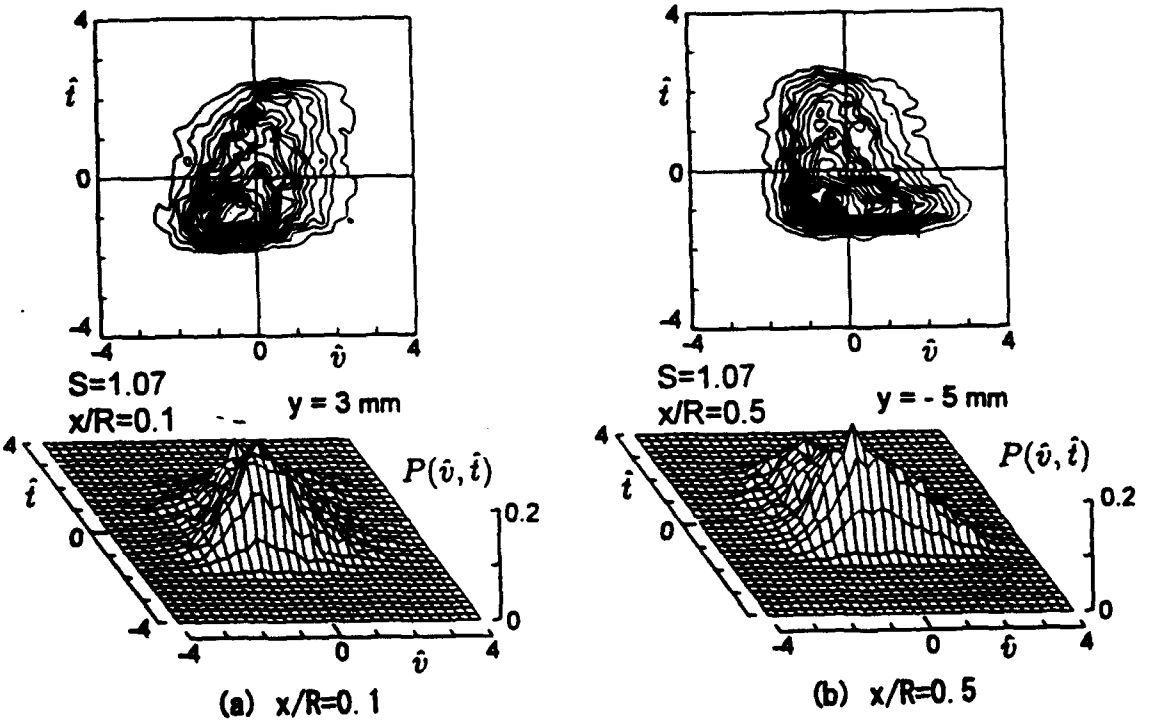

Fig. 4(a) and (b) Normalised joint probability distribution of radial velocity and temperature, $P(\hat{v},\hat{t})$ for y = 3 and x/R = 0.1 and y = -5 mm and 0.5 which are locations where the time-averaged value of heat flux *is in the gradient and strong counter-gradient directions, respectively.*

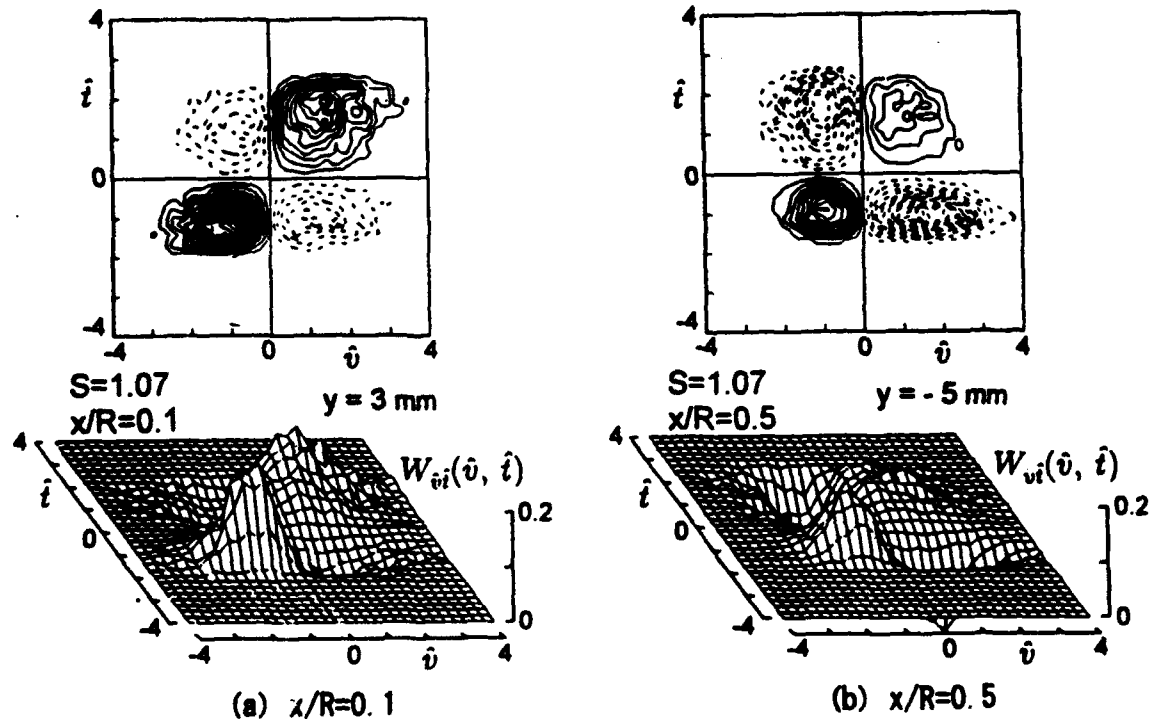

Fig. 5(a) and (b) Normalised, *weighted* joint probability distribution of radial velocity and temperature, $W\hat{v},\hat{t}(\hat{v},\hat{t})$, corresponding to fig. 4 (a) and (b).

AN INTERROGATION AND VECTOR VALIDATION SYSTEM FOR HOLOGRAPHIC PARTICLE IMAGE FIELDS

C.D. Meinhart†, D.H. Barnhart‡ and R.J. Adrian†

†Department of Theoretical and Applied Mechanics
‡Department of Electrical and Computer Engineering
University of Illinois, Urbana, IL USA

ABSTRACT

A holographic particle image velocimetry (HPIV) system has been developed to measure instantaneously all three components of velocity at order 10^6 points in a three-dimensional volume. A high speed interrogation system and an automated vector validation system is incorporated to make this measurement technique applicable to turbulence research. The procedure by which holographic particle images are analyzed to obtain the three-dimensional velocity measurements from a single hologram, and how these measurements are validated using automated statistical algorithms is described in this paper.

1. INTRODUCTION

The physics of turbulence can be better understood when the instantaneous three-dimensional structure is captured by measuring all three components of velocity in a three-dimensional volume with high spatial and velocity resolution. Over the past several years, two-dimensional PIV techniques have been used to measure two-dimensional slices of turbulence structures at relatively high Reynolds numbers. Holographic PIV is an extension of the standard two-dimensional PIV technique to three dimensions, enabling the three-dimensional structure of high Reynolds number turbulent flows to be measured.

The analysis of large three-dimensional holographic image fields using correlation techniques requires large numbers of computations. For example, the analysis of a $100 \times 100 \times 100$ mm^3 volume, with 1 mm grid spacing, requires 10^6 two-dimensional correlations. If a conventional interrogation system can process 1-4 vectors per second using a pixel resolution of 128×128, it would take between 70 and 300 hours of processor time to analyze a 10^6 vector field. This is an unacceptably long time, especially if one wishes to interrogate many such fields. Therefore, an eight array parallel processor system has been developed which is capable of analyzing 100 vectors per second using 128×128 single-frame cross-correlations (see, Meinhart *et al.* 1993). This corresponds to analyzing 10^6 vectors in less than 3 hours.

Once the image fields have been interrogated, the resulting vector maps contain spurious vectors. These vectors are the result of noise in the correlation functions of the image fields during interrogation and they must be removed before the velocity fields can be considered valid measurements. It is both time consuming and tedious to sort through 10^6 vectors and remove the erroneous vectors manually. Therefore, an automated vector validation process has been developed, which uses algorithms to analyze statistically the reliability of each velocity measurement. When a vector is deemed erroneous, it is tagged and then removed automatically. The result is a fully reliable three-dimensional velocity field consisting of order 10^6 three-dimensional velocity vectors.

2. ANALYSIS OF HOLOGRAPHIC IMAGE FIELDS

2.1 Holographic Image Recording

The holographic imaging system is described in detail by Barnhart *et al.* (1994). This system records four distinct holographic images, two stereo views at the two different times t_1 and t_2, on a single holographic plate. The stereo views are used to reconstruct the image field from two different perspectives, providing displacement information in all three directions. Exposures from times t_1 and t_2 are recorded with separate reference beams. This enables the exposures to be reconstructed individually and cross-correlated.

2.2 Holographic Image Acquisition

Figure 1 shows the optics and the computer system used for reconstruction, acquisition and interrogation of the holographic image fields. The interrogation involves three steps; (1) measuring the two-dimensional displacements of the images that are recorded and reconstructed through L_{12}-P_1-L_{11}, (2) measuring of the two-dimensional displacements of the images that are recorded and reconstructed through L_{22}-P_2-L_{21}, (3) validation of the two-dimensional fields to remove erroneous velocity measurements and (4) combining the two sets of two-dimensional measurements to obtain the three-dimensional displacements. This procedure is similar to stereo PIV using two-dimensional photographic recording (Prasad *et al.* 1993).

During the first interrogation, the optical path through L_{12}-P_1-L_{11} is blocked so that only the particles images recorded through L_{22}-P_2-L_{21} are reconstructed. The images from t_1 and t_2 are reconstructed and digitized separately, using computer controlled switching between reference beams R_1* and R_2*, which is synchronized with the image capture of the frame grabber. These image fields are then double-frame cross-correlated, using the system described by Meinhart *et al.* (1993), to determine the two-dimensional displacement field of the images as viewed through L_{22}-P_2-L_{21}, see Figure 1. This procedure is repeatedly applied to the entire reconstructed image volume by scanning the CCD camera over many X-Y planes.

The entire volume is then re-analyzed, except that the optical path through L_{22}-P_2-L_{21} is blocked so that only particle images recorded through L_{12}-P_1-L_{11} are reconstructed, digitized and interrogated. The resulting two-dimensional displacement measurements are validated using the automated routines to remove erroneous measurements. The two-dimensional displacements fields are then combined to obtain all three displacement components on a three-dimensional grid. This procedure is referred to as *stereo-stereo holography*, because it involves recording the images stereoscopically and reconstructing them stereoscopically. It is not the same as reconstructing a single holographic image and viewing it stereoscopically.

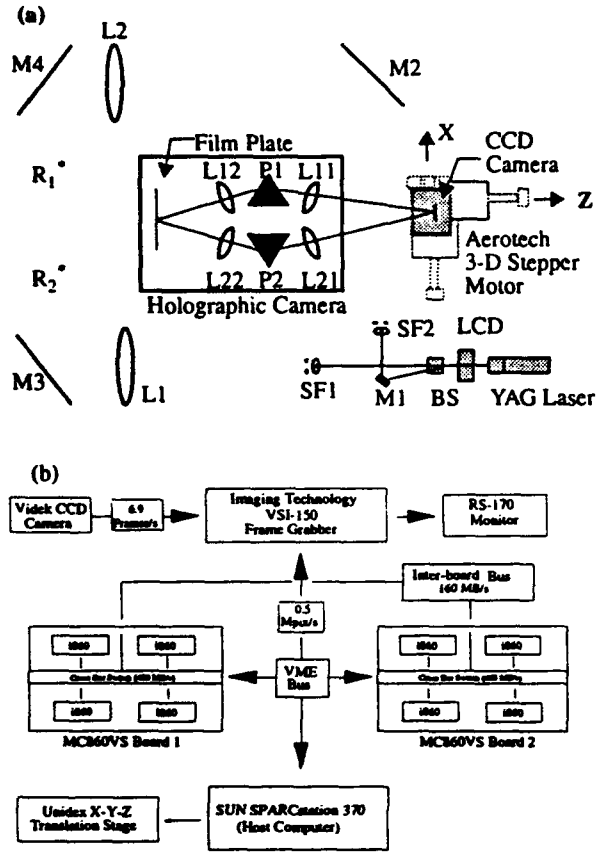

Figure 1. Schematic of reconstruction and interrogation of holographic images. (a) Optics configuration (top view), (b) Computer configuration (reproduced with permission from Meinhart *et al.* 1993).

The displacement of the holographic images at each interrogation spot is found by double-frame cross-correlating the images of the first exposure I_1 and the second exposure I_2,

$$C(s) = \int I_1(X)\, I_2(X+s)\, dX. \qquad (1)$$

Figure 2 shows the autocorrelation *R(s)* of the superposed image fields $I_1 + I_2$, and the cross-correlation *C(s)* of the image fields I_1 and I_2. Clearly, the height of the noise peaks compared the signal peak (labeled C_D and R_D+) is much lower for cross-correlation than autocorrelation. This is an important part of the holographic interrogation system, because in demanding situations, it provides more reliable velocity measurements than autocorrelation. In addition, double-frame cross-correlation eliminates the need for artificial image shifting when the displacement vector is near-zero or negative. (See Keane and Adrian, 1992, for a detailed discussion of the theory of cross-correlation of PIV image fields.)

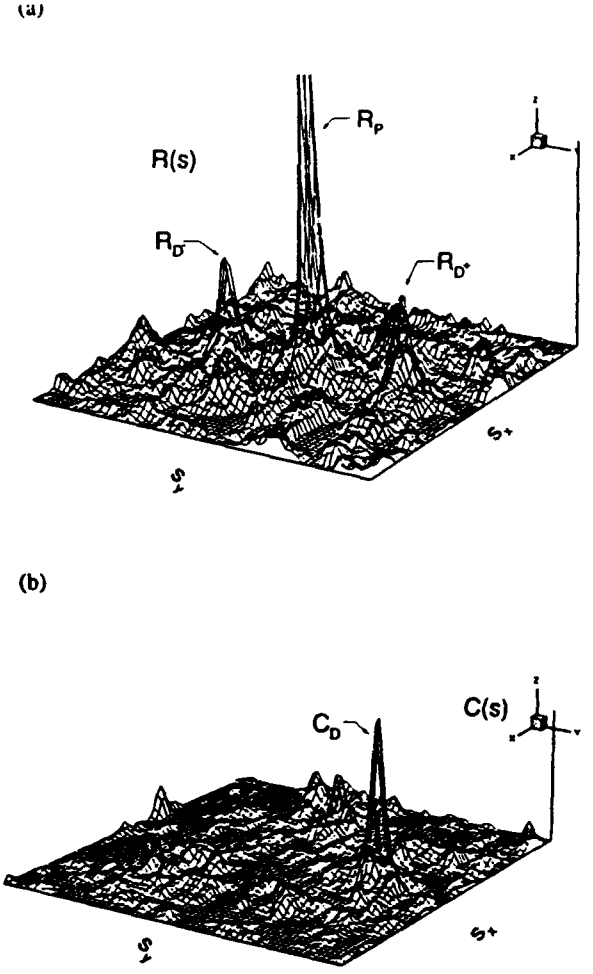

Figure 2. Correlation functions of holographic particle images: (a) autocorrelation, (b) double-frame cross-correlation.

3. VECTOR VALIDATION

3.1 Introduction

The system used to validate the large numbers of vectors generated by holographic image fields is discussed below. It uses algorithms to statistically analyze the reliability of each velocity measurement, remove erroneous measurements and replace empty grid points with alternatively measured vectors.

In order to accomplish this task, a two-stage strategy is used. The first step is to remove all or nearly all the erroneous vectors. Next replacements are sought to fill the empty grid points by evaluating the reliability of alternatively measured vectors, (i.e. the second and third highest displacement peaks in the correlation function of the image field) based on information from reliable neighboring vectors.

An interpolation scheme is then used to fill in empty grid points that are absent of velocity data with information from the neighboring velocity field. The vector fields are them smoothed by convolving them with a Gaussian kernel.

3.2 Removal of Erroneous Measurements

When removing erroneous vectors, it is important to remove all the outliers, even at the expense of sacrificing a few valid vectors. If the opposite viewpoint is adapted where one tries to retain all the valid vectors with the possibility of retaining a few outliers, the outliers that are large in magnitude, will likely corrupt flow statistics calculated from the resulting vector field.

We use three automated techniques, that are based upon the spatial relationships between in-plane velocity vectors, to remove erroneous measurements in PIV vector fields: (1) *tolerance removal*, (2) *magnitude difference removal* and (3) *quality removal*. An additional technique known as *stereo matching* is used for stereo PIV image fields.

Tolerance removal. Tolerance removal is considered a global technique because its criteria is based upon statistical quantities that are spatially averaged over the entire vector field, as opposed to statistics averaged locally in space. A tolerance is placed by requiring the vectors to be within a specified number of standard deviations from the mean, where the standard deviation (rms) and mean are estimated by using an x-line-average, a y-column-average or averaging in both the x and y directions over the entire field. Global averaging decreases the effect of the nearby erroneous vectors on the statistics. In extreme situations, however, numerous outliers can adversely effect the statistics, causing unreasonably large values in the estimated rms velocities, which limits the effectiveness of the tolerance removal technique. In these situations, it becomes necessary to artificially impose reasonable limits on the rms velocities, to enhance the effectiveness of the tolerance removal technique.

Typically, tolerance values of 3.5 - 4.0 are used, that is velocity vectors that are more than 3.5 - 4.0 standard deviations from the mean are removed. Poisson statistics suggest that if a data point is more than three standard deviations from the mean, then there is less than a 1 in 20 chance of it being good, regardless of the probability distribution function (Bedat and Piersol, 1986).

Magnitude difference removal. Magnitude difference removal is a local technique that mathematically defines how well a particular *vector in question* fits in with its surrounding neighborhood. This is considered a local technique because it is primarily dependent upon the vectors in the immediate neighborhood. Figure 3 shows the spatial relationship of a vector in question and its surrounding 3 x 3 neighborhood. The velocity vector of the neighborhood is estimated by calculating the median[1] of the neighborhood for each velocity component. The median is a more robust average than the other more conventional linear averages such as the mean (Westerweel 1994). If a neighborhood contains several erroneous vectors that are large in size, the mean average of the neighborhood will be an inaccurate estimate of the actual neighborhood velocity, while the median average may essentially be unaffected by the neighborhood outliers.

We define the magnitude difference Md as,

$$Md = \sqrt{\frac{(u-u_{med})^2}{u_{rms}^2} + \frac{(v-v_{med})^2}{v_{rms}^2}}, \qquad (3.1)$$

where u, v are the horizontal and vertical components of the vector in question, u_{med} and v_{med} are the components of the neighborhood median velocity. The velocity difference between the horizontal and vertical components of velocity between the vector in question and its neighborhood are normalized by their respective components of globally averaged rms velocity, u_{rms} and v_{rms}. The magnitude difference is the Euclidean norm of the normalized velocity components and it defines a functional that is an estimate of how well a vector fits in with its neighborhood.

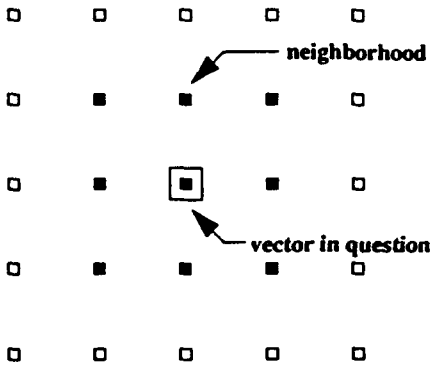

Figure 3. Vector grid showing the 3 x 3 neighborhood of a vector in question for the magnitude difference vector removal technique.

By specifying a high and a low value of magnitude difference, all the velocity measurements are divided into three categories; erroneous vectors, questionable and reliable, according to Figure 4. When the magnitude difference routine is executed, the erroneous vectors are removed, the reliable vectors are retained and the questionable vectors are sent to the *vector-checker*.

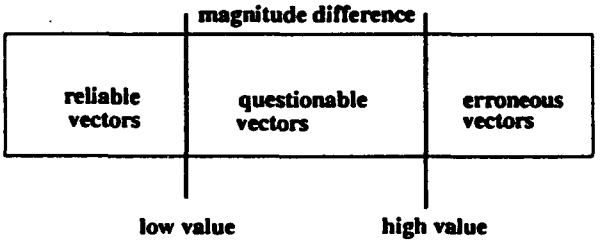

Figure 4. Division of vectors into the three categories of reliable, erroneous and questionable, based upon the magnitude difference criterion.

The vector checker is PIV's answer to a spelling checker found on most word processors. The idea is that there may not be a clear-cut mathematical line separating good vectors from bad vectors, but instead, a gray area between good and bad vectors where vectors are considered questionable. While it may be difficult to develop an automatic algorithm that can determine whether a borderline vector is reliable or erroneous, it is much easier for an algorithm to seek out and identify questionable vectors, the display them at the center of the computer screen and to prompt the user for a keep or remove decision. This utility makes it possible to cast judgement on many vectors in just a few seconds. The vector checker utility is only used as a last resort in difficult situations, when it is not possible to remove all the bad vectors with automatic routines.

Quality removal. The quality of a vector is measured in the correlation plane during interrogation, and is defined as the ratio of the height of the highest displacement correlation peak to the second highest displacement correlation peak. Since the quality is a measure of the signal-to-noise ratio, it should be a good criterion for estimating the reliability of the measurement.

1. The median technique was suggested by Jerry Westerweel.

Experience shows, however, that quality is in fact a poor measure of vector reliability (Westerweel 1994). While it is true that nearly all bad vectors have quality values only slightly larger than unity, it turns out that reliable measurements can often have qualities with similar values to that of erroneous measurements. Therefore, quality is usually not used in validating PIV measurements.

Stereo matching. In stereo PIV, all three components of velocity are calculated by measuring the two in-plane components of velocity from each of two perspectives and combining them to obtain all three components of velocity (Prasad *et al.* 1993). The system of equations used to combine the two perspectives is over constrained, thereby over specifying one component of velocity. In our situation, the vertical component of velocity measured separately from the right and left perspectives of the hologram should agree to within the accuracy of the HPIV measurement technique. Erroneous measurements are identified when the difference between the two vertical components of velocity at a given point is greater than some specified value, when normalized by a characteristic velocity.

3.3 Replacement with Alternatively Measured Vectors

The second part of the validation strategy is to replace the empty grid points with alternatively measured good vectors. The alternative replacement algorithm fills empty grid points with alternatively measured velocity vectors if the alternatively measured vectors satisfy both a global criterion and a local criterion. The global criterion requires that the alternatively measured vectors (the Choice 2 or Choice 3 vectors) reside within a user specified tolerance. The local criterion requires the successful replacement vector to have a lower magnitude difference value than all the other alternatives. In other words, an empty grid point is filled with an alternatively measured velocity vector, if the alternatively measured vector is within a specified tolerance and fits in well with its neighborhood.

3.4 Interpolation

Isolated empty grid points that have reliable and well represented surrounding neighborhoods can be assigned an estimated velocity, u', based upon a weighted spatial average of the neighborhood,

$$u'(x') = \int w(x - x')\, u(x)\, dx, \qquad (2)$$

where the weighting function, $w(x - x')$, is a Gaussian or a similar type function. A convolution-type average is typically less sensitive to noise than the median average and utilizes more information from neighboring velocity vectors than a simple bilinear interpolation. The convolution integral is evaluated in fully three-dimensional space for holographic vector fields and in two-dimensional space for standard PIV vector fields.

If empty grid points exist within the neighborhood, those points are excluded from the calculation. The reliability of the neighborhood estimate is ensured by requiring that a specified percent of the neighborhood velocity vectors are present before the empty point is assigned the estimate u'.

3.5 Low-pass Spatial Filtering

The previous sections have discussed the nonlinear filtering techniques used to remove erroneous measurements and to replace alternatively measured velocity vectors. A linear low-pass filter can also be applied to the velocity field by convolving it with a Gaussian kernel given by,

$$G(x - x') = exp\left(-\frac{(x - x')^2}{x_k^2}\right). \qquad (3.2)$$

where x and x' are the spatial coordinate vectors, x_k is size of the kernel. This convolution is evaluated in three-dimensional space for holographic vector fields. The Gaussian filter removes high frequency noise from the velocity measurements which can be a result of random white noise generated by film grain noise and pixel digitization during interrogation.

3.6 Batch Mode Execution

Once a sequence of vector validation routines along with their operating parameters are found to work well for several two-dimensional planes of a three-dimensional HPIV vector field, they are stored in a macro file. An entire holographic vector field consisting of ~10^6 vectors can be validated automatically in about 3 hours by executing the validation program in batch mode.

3.7 Vector Validation Example

Typically, the mode of operation for validating three-dimensional holographic vectors is to: (1) use stereo-matching to remove vectors whose vertical components of velocity do not agree, (2) apply the tolerance removal technique to remove erroneous vectors that have very large magnitudes, (3) apply the magnitude difference technique to remove erroneous vectors that do not fit in well with the neighboring vectors, (4) replace the empty grid points with alternatively measured vectors (where applicable), (5) reapply tolerance and magnitude difference to remove any erroneous vectors not previously removed or incorrectly added during Step 3, (6) three-dimensionally interpolate and smooth velocity fields (where applicable).

The performance of this sequence of operations was evaluated by applying the automated routines to a typical two-dimensional PIV vector field using steps (2)-(5) and then comparing those results to a manual validation of the same vector field. Figure 5 shows the velocity field before and after the sequence of automated operations. The performance of each operation and the convergence to the manually validated field is displayed in Figure 6. Fifty five percent of the erroneous vectors were initially removed during interrogation, because there was not an adequate signal peak detected in the correlation function. After applying tolerance removal (Step 2) and then magnitude difference (Step 3), 93% and 97% of the erroneous vectors were removed, respectively. The replacement with alternatively measured vectors routine (Step 4) replaced 95% of the Choice 2 and Choice 3 vectors that were reliable measurements. Magnitude difference was then applied for the second time (Step 4); it removed 100% of the erroneous measurements.

The sample vector field used here contains roughly 10 000 grid points, out of which the automated removal routines correctly removed 100% (387 vectors) of the erroneous vectors, and the automated replacement routine correctly replaced 95% (93 vectors) of the reliable Choice 2 and Choice 3 vectors. The only error was that the automated routines failed to replace two Choice 2 vectors and two Choice 3 vectors. The performance of the automated routines displayed in Figure 6 is not always achieved, but it is characteristic of most PIV vector fields, when data dropout is not too severe.

4. HPIV MEASUREMENTS OF A JET FLOW

Figure 7 is an HPIV vector field, covering a volume of 24.5 × 24.5 × 60 mm^3, of air flow issuing from a 76 mm turbulent pipe at Reynolds number $Re = U_B D/\nu = 6000$. The interrogation spots are 0.87 mm^3 and overlapped by 50% in all three directions, giving nearly 400 000 three-dimensional velocity measurements, fully resolving the turbulent motion. The interrogation and vector validation system described in this paper allows velocity measurements such as the one presented in Figure 7 to be obtained from interrogating holographic particle images, with just a few hours of computer time.

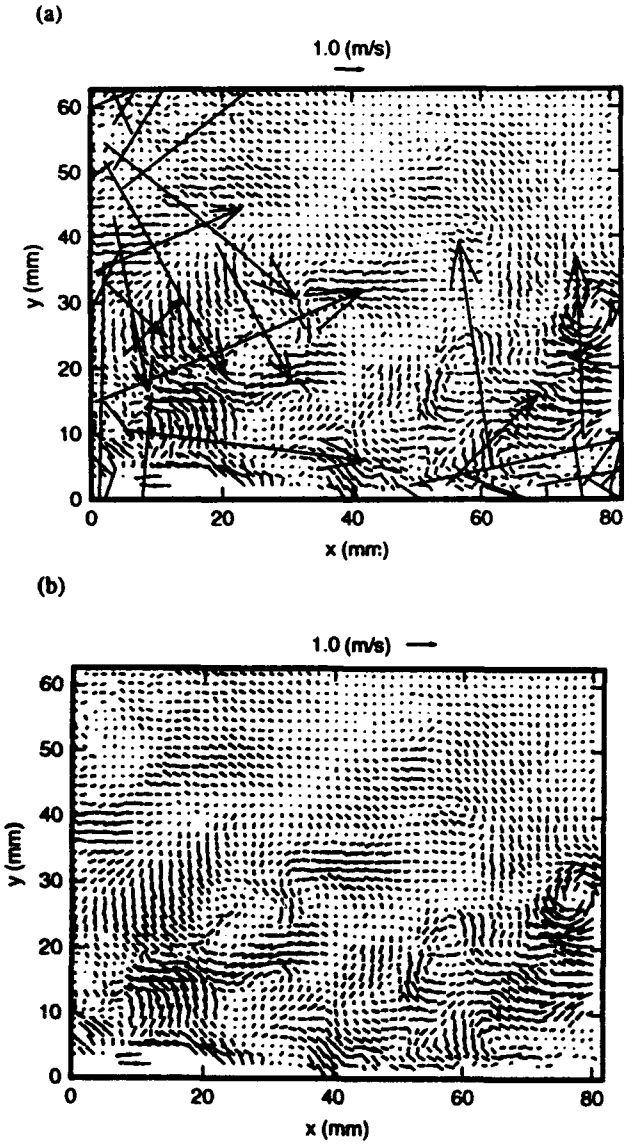

Figure 5. Typical PIV velocity vector field: (a) before automatic data validation, (b) after data validation.

5. CONCLUSION

Holographic particle image velocimetry is used to measure over 400 000 three-dimensional velocity vectors in a three-dimensional volume. This technique is made feasible by incorporating a high-speed parallel processing system to analyzed over 100 vectors per second, using 128 × 128 double-frame cross-correlations. By using double-frame cross-correlation instead of autocorrelation, a larger percentage of reliable vectors is obtained, because cross-correlation has a greater signal-to-noise ratio.

Automated vector validation routines have been developed that remove efficiently erroneous velocity measurements, which result from noise in the correlation functions during interrogation. These validation routines make it possible to validate millions of PIV velocity vectors in just a few hours. Test results show that, for a typical two-dimensional vector field, decisions made by the automated validation routines agree well with independently made manual decisions.

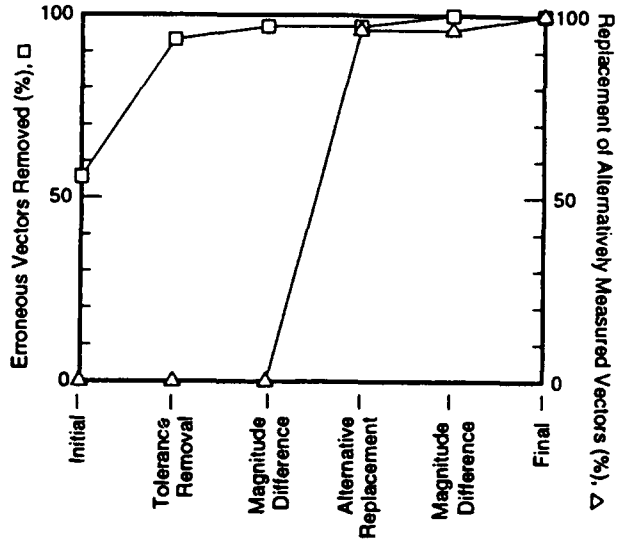

Figure 6. Performance of a typical vector validation sequence. This graph shows the effect of the various automated validation routines on the percent of erroneous vectors removed and the percent of alternatively measured vectors. Convergence to 100% is achieved when the automated routines agree completely with manual decisions.

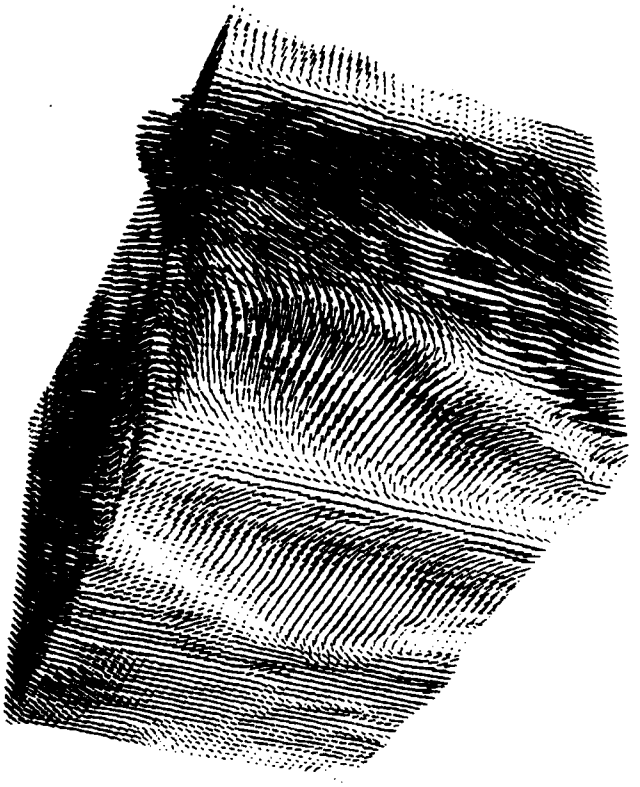

Figure 7. Three-dimensional holographic velocity vector field.

ACKNOWLEDGEMENT

This research was supported by the Office of Naval Research Grant N00014-90-J-1415 and a grant from TSI, Inc.

REFERENCES

Adrian, R. J. 1991. Particle Imaging Techniques for experimental fluid mechanics. *Annu. Rev. Fluid Mech.*, Vol. 23, pp. 261-304.

Barnhart, D. H., Adrian, R. J. and Papen, G. C. 1994. Phase-conjugate holographic system for high resolution particle image velocimetry. *Jour. of Appl. Optics, in print.*

Bendat, J. S. and Piersol, A. G. 1986. Random data analysis and measurement procedures, 2nd Ed., *John Wiley & Sons, Inc.* New York.

Keane, R. D. and Adrian, R. J. 1992. Theory of cross-correlation analysis of PIV images, *Appl. Sci. Res.*, Vol. 49, pp. 191-215.

Meinhart, C. D., Prasad, A. K., Adrian, R. J. 1993. A parallel digital processor system for particle image velocimetry. *Meas. Sci. Technol.*, Vol. 4, pp. 619-626.

Prasad, A. K. and Adrian, R. J. 1993. Stereoscopic particle image velocimetry applied to liquid flow, *Exp. in Fluids*, Vol. 15, pp. 49-60.

Westerweel, J. 1994. Efficient detection of spurious vectors in particle image velocimetry data. *Exp. in Fluids, in print.*

Session 2.
Combustion I

LDV MEASUREMENTS OF TURBULENT LENGTH SCALES IN COMBUSTING FLOW WITH TWO-POINT CORRELATIONS

D. Trimis, A. Melling, F. Durst

Lehrstuhl für Strömungsmechanik, Universität Erlangen-Nürnberg
Cauerstr. 4 / 91058 Erlangen, Germany

ABSTRACT

A simple two-point-LDV-setup for the determination of the turbulent length scales in an axisymmetric burner and the co-flowing air jet was designed, built and tested under isothermal and combusting conditions. Representative measurements of spatial correlation coefficients for different flow configurations are presented and discussed. Grid induced turbulence of different length scales is the main parameter distinguishing the flow configurations, resulting in different types of flames for otherwise identical boundary conditions. The accuracy of the two-point measurements is also discussed.

1. INTRODUCTION

Length scales are important parameters for the description of turbulent transport processes. They can be directly obtained by measuring the spatial correlation function of the flow velocity, or by invoking Taylor' s hypothesis [see Tennekes & Lumley 1972]. The latter can be used only for the estimation of the longitudinal spatial correlation in the direction parallel to the main flow, from the autocorrelation function in a single measuring point. Cenedese et al. (1991) made an experimental test of the validity of Taylor's hypothesis in a turbulent channel flow and found out that only the microscales are sufficiently described by the "frozen flow" assumption. Romano (1993) pointed out that Taylor's hypothesis is only reasonable for high Reynolds numbers. This brief discussion shows the necessity of obtaining the spatial correlation function of the flow velocity in a direct way, by simultaneous multiple point measurements. In most cases 2-point measurements are applied. The traditional hot-wire technique has the disadvantage in the case of longitudinal correlations, that the wake generated by the first wire affects the second ; the method can therefore be applied only for transverse correlation measurements. In combusting flows, however, only optical techniques such as Laser Doppler Velocimetry can be applied. Until now several 2-point LDV systems using various optical configurations have been implemented. Nakatani et al. (1985) realised a system with several pairs of beams generated by a diffraction grating. Other researchers used 2 independent systems with different wave-lengths, e.g. Romano (1993), Cenedese et al. (1991), Johns et al. (1986). Fraser and Bracco (1988) developed a 2-point single probe-volume LDV system by collecting the scattered light from different positions within an elongated probe volume. Benak et al. (1992) developed a compact fiber optic 2-point LDV sensor operating in backscattering for use in I.C. engines. Pfeifer (1986) suggested a system which creates a second measuring volume by refocusing the divergent beams from the first measuring volume back into the flow, by means of a spherical mirror. Finally Benak et al. (1993) discussed the choice of a suitable estimator for the spatial -temporal correlation function from 2-point LDV measurements with special emphasis on the slot correlation and on the interpolation schemes for an equidistant lag time processing, while Romano (1993) preferred to obtain the cross-correlation coefficient from the cross-spectral power density function of the resampled 2-point velocity data at equidistant intervals.

In the present work a simple 2-point-LDV-setup for the determination of the transverse spatial correlations in an axisymmetric burner and the coflowing air jet was designed, built and tested under isothermal and combusting conditions. The parameters affecting the accuracy of the 2-point measurements are discussed and a correction scheme for the accurate estimation of the cross-correlation coefficient is proposed.

2. EXPERIMENTAL SETUP

The experiments were carried out in a concentric jet which can be operated either isothermally or with combustion of the gas exiting the central pipe, which has a diameter of 30mm after a 4:1 contraction. A blower in the outer pipe (160mm diameter after a 4:1 contraction) delivers an air flow as a mantle around the central flow. Honeycombs and two screens in the outer pipe ensure a controlled turbulence level and swirl-free flow. For combustion tests dry air and methane are mixed in a pre-chamber connected to the central pipe. Flow controllers in the two gas lines ensure a flow uncertainty of maximum ±1% with a reproducibility of ±0.25%. A flame trap (1000 holes with 1 mm diameter in a 4 mm thick plate) is included in the central pipe. At the outlet of the central pipe different grids can be installed, which produce different scales of turbulence in the central stream. The grid size is the main parameter of the present experiment. The premixed flame has a height of 600 mm with the flame front in the region up to 120 mm above the burner.

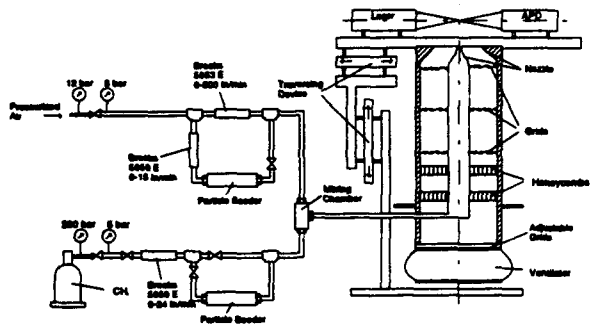

Fig. 1 Schematic diagram of the experimental setup

The optics for the LDV-setup (Fig.2) consist of a 10 mW He-Ne laser (2), the transmitting optics (6) with a 50 mm beam separation and a 310 mm transmitting lens, and the receiving optics in forward scattering mode with a 150 mm lens (10) and an Avalanche Photo Diode (APD) with a 200 µm pinhole (11). A beam collimator was built using two lenses, one 50 mm (4) and one 200 mm (5), in order to reduce the size of the measuring volume and improve the spatial resolution. The measuring volume has a diameter of 75 µm and a length of 900 µm in this configuration.

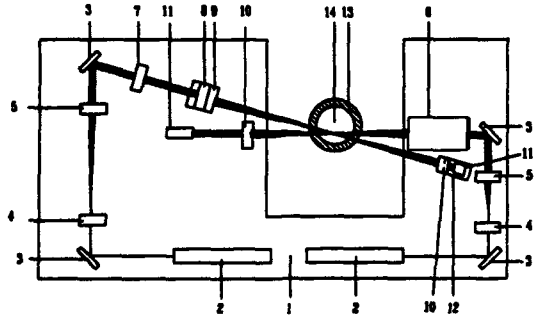

1. Optical table
2. 10 mW He-Ne Laser
3. Mirror
4. Lens 50mm
5. Lens 200mm
6. Sending optics
7. 50mm beam splitter
8. Sending lens 310mm
9. Microtraversing table
10. Receiving lens 150mm
11. Photodetector (APD)
12. Microtraversing table
13. Outer nozzle
14. Inner nozzle

Fig.2 Schematic diagram of the LDV - setup

A second system was designed and built using the same optical parameters as the first one, but with the sending optics lying on the opposite side of the first system. This second system also works in the forward scattering mode with the same receiving optics parameters as the first one. The sending lens (8), the receiving lens (10) and the APD (11) of the second system are mounted on microtraversing devices (9,12) in order to traverse the second measuring volume relative to the first one.

The second system was designed in order to make a 2-point correlation of the velocity signals possible. The measurements begin with the two measuring volumes overlapping each other ($\delta r=0$) and then the autocorrelation function $\rho(\delta r)$ is measured for different $\delta r'$ s. The two systems both work in forward scattering mode but the one opposite to the other in order to avoid cross-talk in the case of overlapping measuring volumes, i.e. when the measuring volumes overlap, one system should receive signals in backscattering, which is about 100-1000 times weaker than forward scattering; no crosstalk is then detectable due to the low power of the laser sources used.

For the LDV-signal processing, two TSI 1980B counter processors with a DOSTEK 1400A interface card installed in an IBM compatible PC were used. This system can simultaneously acquire data from two LDV-systems. Furthermore a user-defined coincidence window can be set, such that each pair of 2-point measurements can be regarded as coincident. The entire optical setup is located on a three dimensional traversing device driven by stepper motors. The stepper motors are controlled with an interface card in the PC. The overall accuracy of the traversing device is 5µm in every direction. For the inner flow, MgO seeding particles of approximately 1µm diameter were used, originating from cyclone-type particle seeders. For the outer flow, glycerine particles in a water solution of 1:8 coming from an atomizer were used. The resulting signal quality was good in all regions, except in the interaction region between outer flow and outer cone of the burnt gas. In this region, the glycerine particles possibly evaporated and the data rate was massively reduced.

For the adjustment of the 2-point LDV probe a special procedure was developed to satisfy two conditions:

1) For $\delta r=0$, the two measuring volumes should overlap
2) When traversing the second system (both sending and receiving optics), the optical adjustment of this system should remain stable.

The $\delta r=0$ adjustment of the 2-point LDV-probe proved to be very tricky and sensitive to disturbances. A 30µm pinhole was centred on the inner stream nozzle, and the sending optics of both systems were adjusted with micro-traversing devices, until all four laser beams passed through the pinhole. A second check to assure the quality of the adjustment consisted of checking if both systems could receive signals in backscattering under the following conditions:

a) the amplification of the receiving APD of one system was high.
b) the laser source of the same system was turned off.

In order to assure stable optical alignment, when traversing the second LDV-system, a second receiving lens was used. A projection of the measuring volume on the entire APD sensitive surface was possible (about 0.5 mm), resulting in insensitivity of the receiving optics to small misalignments of the optical path due to small traversing inaccuracies, when the second system was traversed relative to the first one. The effect of the collimator adjustment in the accuracy of the measurements is very critical. The best method to adjust the collimator is to perform measurements in a laminar flow and adjust the collimator lens separation with a micro-positioner until the measured RMS reaches the lowest possible value. If this adjustment has not been performed, uncorrelated noise caused by the divergend fringe pattern destroys the correlation measurements.

In order to make 2-point correlations without using signal reconstruction methods such as those proposed by Veynante and Candel (1988) or Chao and Leu (1992), the two LDV-systems were operated in the "coincidence" mode, i.e. the LDV-signals were evaluated only if both systems received a LDV-signal within a small time window, which was set in these experiments to 10μs, i.e. much shorter then the smallest time scale of the flow. However if not only the spatial but also the temporal cross-correlation is of interest, either a slot correlation of the velocity pairs as proposed by Mayo (1975) or a signal reconstruction method has to be applied.

In the case of $\delta r=0$, the two systems give signals for the same particles resulting in a sufficient data rate of coincident signals. In the case where $\delta r \neq 0$ the individual data rates have to be high enough in order to get a sufficient coincidence data rate. This task is difficult especially for combusting flows in which the flame front illumination reduces the data rate. For the required data rate two new APD's were used with the following advanced features:

a) The frequency response was limited to 5 MHz (-3dB) in order to improve the amplification characteristics.

b) A resistor of high value was connected in series with the APD sensor, in order to protect the amplifier from saturation in the case of large particles. In the case of smaller particles, the APD sensor has a high resistance itself, so that the main part of the supply voltage remains on the APD sensor. This results in a non-linear behaviour of the APD-sensor, i.e. for higher intensities the amplification is lower. This allows higher amplification levels (important for smaller particle signals) without saturation due to larger particles.

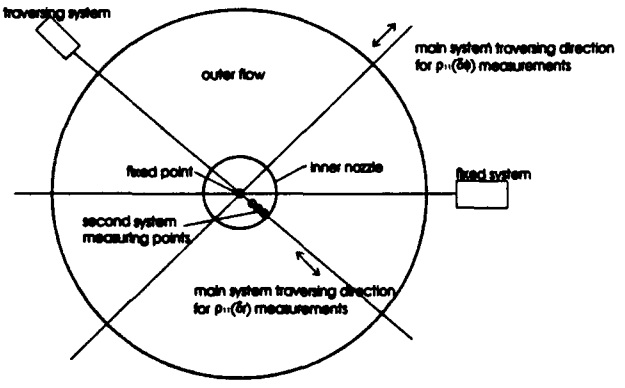

Fig.3 Different traversing options for length-scale measurements

The axial symmetry of the flow permitted different correlation coefficients to be measured. In order to measure the $\rho_{11}(\delta r)$ correlation coefficient the main traversing unit was traversed in a plane perpendicular to the jet axis and parallel to the axis of the second LDV-system traversing mechanism. For the measurement of $\rho_{11}(\delta\phi)$ the main traversing unit was traversed in a plane perpendicular to the jet axis and perpendicular to the axis of the second LDV-system traversing mechanism. In figure 3, the different traversing configurations can be seen. For the measurement of $\rho_{11}(\delta x)$ (δx being in the axial direction) the time delay correlation function from one system could be used under the assumption that Taylor's hypothesis is valid.

3. PARAMETERS AFFECTING THE ACCURACY OF THE 2-POINT PROBE

The transverse spatial correlation coefficient between velocity fluctuations u_1' and u_2' separated by a distance δr perpendicular to the velocity components was measured:

$$\rho_{12}(\delta r) = \frac{\overline{u_1' u_2'}}{\left(\overline{u_1'^2 u_2'^2}\right)^{1/2}} \qquad (1)$$

The integral length scale Λ characterizing the large eddies which are important for turbulence production is found from

$$\Lambda = \int_0^\infty \rho(\delta r) d\delta r \qquad (2)$$

In the vicinity of $\delta r = 0$ $\rho(\delta r)$ follows the form of a downward opening parabola, i.e.

$$\rho(\delta r)\big|_{\delta r=0} = 1 - \frac{\delta r^2}{\lambda^2} \qquad (3)$$

where the Taylor microscale λ which characterizes the turbulence scales in the inertial subrange is defined by the intersection of this parabola with the axis $\rho = 0$.

The correlation coefficient at $\delta r = 0$ is a good criterion for the quality of the 2-point probe since $\rho(0)$ should be 1. The accuracy requirements for correlation measurements are very stringent. The correlation is performed on the velocity fluctuations, which are in general smaller than the mean velocities, and is affected by the following factors:

- optical and electronic noise which is not correlated with the signal
- spatial resolution of the LDV system in comparison with the length scales to be resolved
- the coincidence window width, or the temporal resolution of the signal reconstruction method, in comparison with the time scale to be resolved
- cross-talk between the two measuring volumes

Preliminary tests with the 2-point probe at $\delta r = 0$ showed that positions with low turbulence intensity values had lower correlation coefficients than highly turbulent positions. In order to understand this behaviour the following experiment was performed. A sine wave generator with amplitude and frequency modulation was connected to the two TSI 1980B counters. The frequency modulation (FM) resulted in an adjustable pseudo-"turbulence intensity" and the amplitude modulation (AM) resulted in burst signals in order to operate the single measurement per burst mode of the counter. The correlation coefficient of the frequency fluctuations was calculated and can be seen in figure 4.

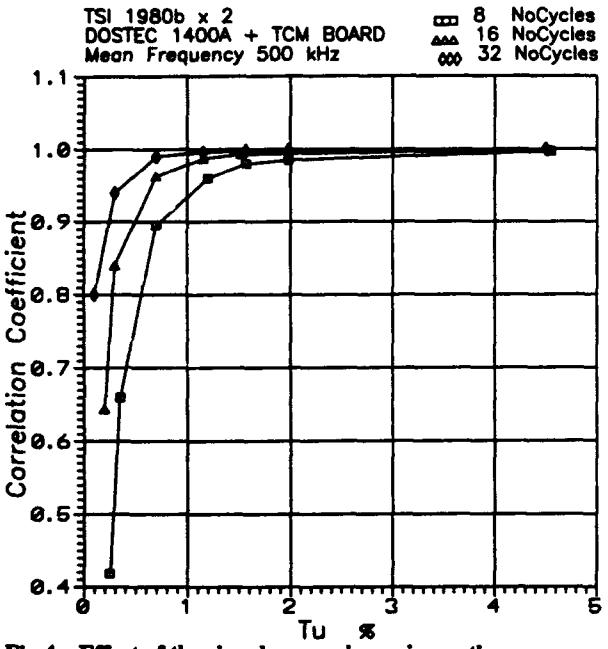

Fig.4 Effect of the signal processing noise on the correlation coefficient for different turbulence intensities

The main result of this experiment is that in regions with low turbulence intensity (less than 1 %), the accuracy of the correlation measurements is not good because of the relatively high level of uncorrelated noise. The number of cycles used for the counter signal processing plays an important role in the achieved accuracy. In the present experiment, the diameter of the measuring volume (resulting from the desired spatial resolution) and the fact that no Bragg-cells were used limited the number of cycles used for the counter signal processing to 16. In this approach, however, only the electronic and digitization noise in the signal processing units is considered.

In the real case (see fig. 5) other noise sources also exist: from the APD's, and from other light sources, etc.

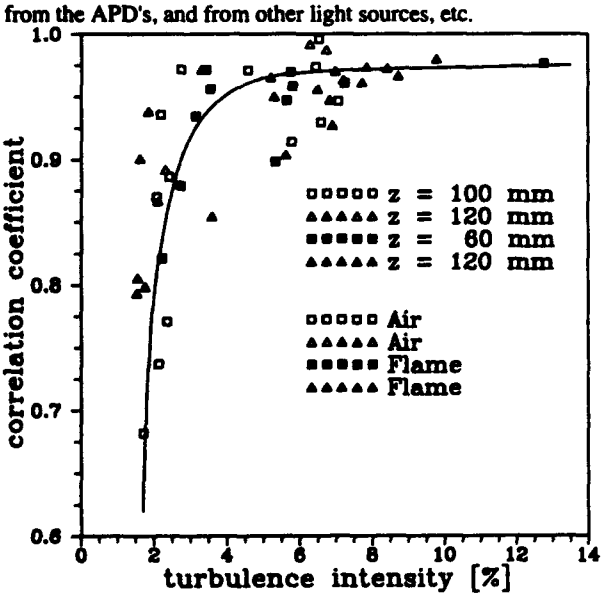

Fig. 5 Measured correlation coefficients for δr=0 in different locations and conditions

Because of the uncorrelated noise the correlation coefficient at zero separation (δr=0) is less than one measured. Hence the scales that are calculated from the measured correlation coefficient function $\rho(\delta r)$ with formulas (2) and (3) cannot be accurate. A procedure for the exact estimation of the correlation coefficient, based on the work of van Maanen et al. (1975), who proposed a cross-correlation technique for the reduction of the ambiguity noise in LDV, was used in this study. The measured velocity u(t) as a function of time consists of the following parts:

$$u(t) = \overline{U} + u'(t) + u_n(t) \tag{4}$$

where $\overline{U}$ is mean velocity, $u'(t)$ are the velocity fluctuations and $u_n(t)$ the noise of the entire system. The measured apparent velocity fluctuations $u'_m(t)$ are:

$$u'_m(t) = u'(t) + u_n(t) \tag{5}$$

The measured correlation coefficient $\rho_{12m}(\delta r)$ consequently is different than the one from equation (1):

$$\rho_{12m}(\delta r) = \frac{\overline{u'_{1m} u'_{2m}}}{\left(\overline{u'^2_{1m}}\,\overline{u'^2_{2m}}\right)^{1/2}} \tag{6}$$

The following relations between the measured and the exact values can be derived under the assumption that the noise components u_{1n} and u_{2n} are not correlated to any other quantity except each one with itself:

$$\overline{u'_{1m} u'_{2m}} = \overline{(u'_1 + u_{1n})(u'_2 + u_{2n})} = \overline{u'_1 u'_2} \tag{7}$$

$$\overline{u'^2_{1m}} = \overline{(u'_1 + u_{1n})^2} = \overline{u'^2_1} + \overline{u^2_{1n}} \tag{8}$$

$$\overline{u'^2_{2m}} = \overline{(u'_2 + u_{2n})^2} = \overline{u'^2_2} + \overline{u^2_{2n}} \tag{9}$$

From the relations (7)-(9) one can see that the cross-correlation $\overline{u'_1 u'_2}$ is measured accurately also in the presence of noise, but the normal stresses of the velocity in the two points are larger by the RMS of the uncorrelated noise $\overline{u^2_{1n}}$ and $\overline{u^2_{2n}}$ and affect the denominator of the correlation coefficient. The measured RMS of the uncorrelated noise $\overline{u^2_{1n}}$ and $\overline{u^2_{2n}}$ can be obtained from the measurement for zero separation δr=0. In this case the following relations are valid:

$$\overline{u'^2_1}\Big|_{\delta r=0} = \overline{u'^2_2}\Big|_{\delta r=0} = \overline{u'_1 u'_2}\Big|_{\delta r=0} = \overline{u'_{1m} u'_{2m}}\Big|_{\delta r=0} \tag{10}$$

$$\overline{u^2_{1n}}\Big|_{\delta r=0} = \overline{u'^2_{1m}}\Big|_{\delta r=0} - \overline{u'_{1m} u'_{2m}}\Big|_{\delta r=0} \tag{11}$$

$$\overline{u^2_{2n}}\Big|_{\delta r=0} = \overline{u'^2_{2m}}\Big|_{\delta r=0} - \overline{u'_{1m} u'_{2m}}\Big|_{\delta r=0} \tag{12}$$

Thus, since from the measurement at zero separation the RMS of the noise for each LDV channel is known the correlation coefficient can be corrected also for separations δr≠0 , under the

assumption that the RMS of the noise remains unchanged for both channels. This assumption is valid for the system, which measures at the fixed point and almost valid for the second system if the separation distance is small. In this discussion we have neglected the "noise" originating from the finite size of the measuring volume which will be somehow correlated. If the spatial resolution is good compared to the smallest scales of the flow, then this effect can be neglected.

4. EXPERIMENTAL RESULTS AND DISCUSSION

Measurements were performed at a Reynolds number of about 7500 (based on the inner pipe diameter) for three cases:

- no grid installed
- a coarse grid installed (0.75 mm thick, 3.5 mm mesh size)
- a fine grid installed (0.35 mm thick, 1.5 mm mesh size)

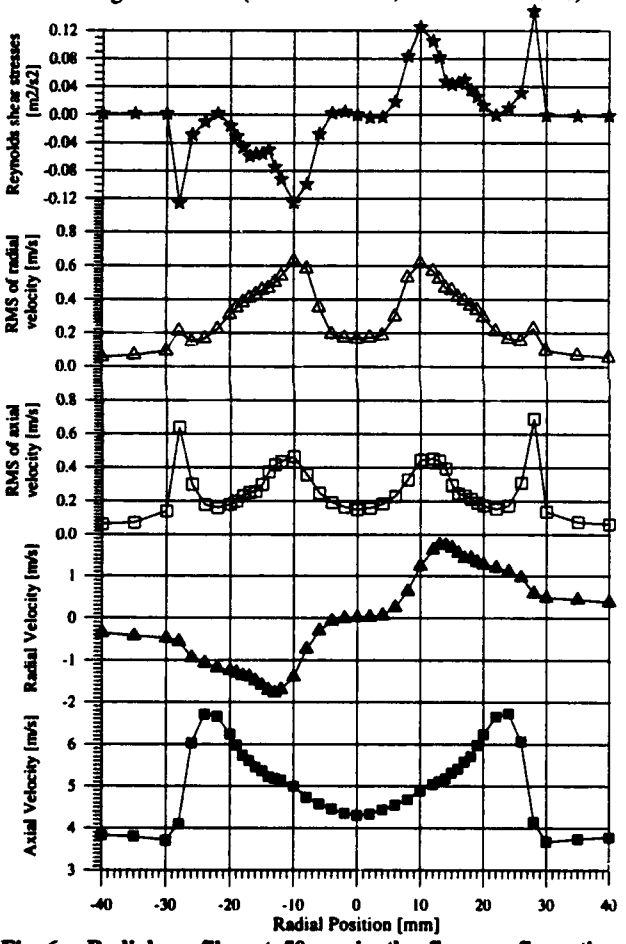

Fig. 6 Radial profiles at 50mm in the flow configuration with coarse grid

The velocity of the inner stream was 3.6 m/s . The energy release rate of the flame was 8kW with a stoichiometric methane-air mixture. The outer flow velocity was set for all flow configurations to 3.6 m/s, before ignition, at the radial position 30mm and axial position 10mm after the nozzle exit. The room temperature was about 25° C. In order to get an overview of the flow field, two-component LDV measurements were performed in a radial region of -40mm - +40mm and an axial region of 10 - 140mm from the nozzle exit at 665 points for all three flow configurations. The profiles of the mean axial and radial velocity, and the normal and the shear stresses, are given in figures 6 and 9 for the same axial position at which correlation measurements were made, under combusting conditions.

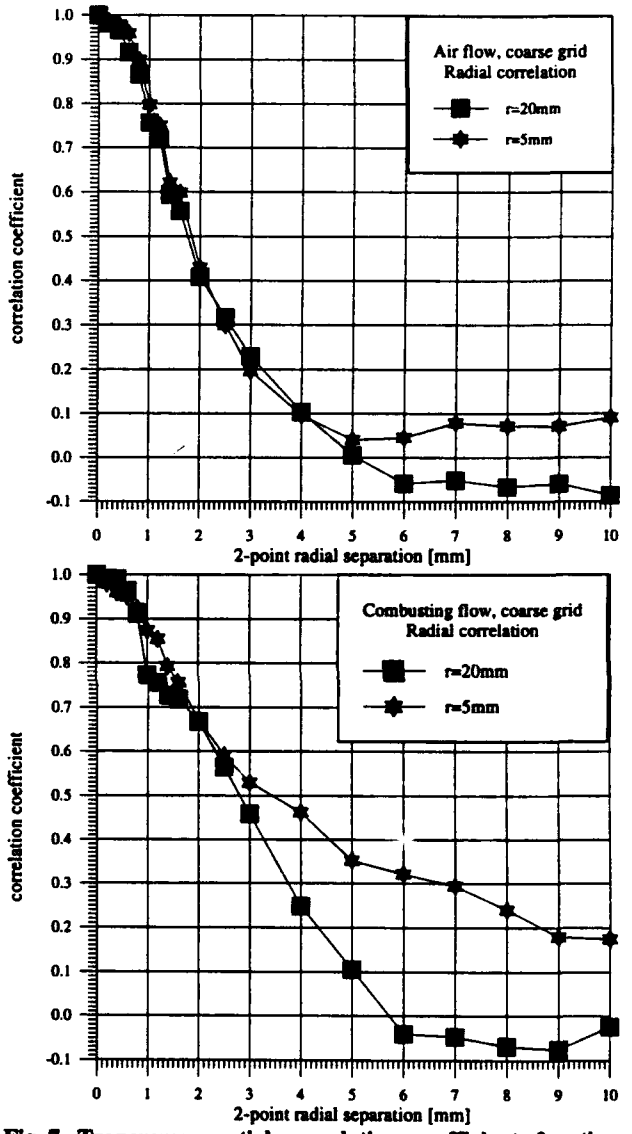

Fig. 7 Transverse spatial correlation coefficient function (radial) in the flow configuration with coarse grid for the isothermal and the combusting case

For both flow configurations with combustion the flame structure is similar but quantitative differences in the mean velocities, the Reynolds stresses and the region sizes are revealed in figures 6 and 9. In general the flow of the unburnt gases in the middle accelerates before the flame front as shown by the axial velocity profiles because of the increasing temperature and decreasing density. The burnt gases also accelerate. The development of a shear layer between the outer cone of the burnt gases and the outer flow is shown in figures 6 and 9 and is particularly marked in the profiles of RMS axial velocity and Reynolds shear stresses.

The axial position in which the flame front ends is about 110-120mm for the case without a grid, 80-90mm for the case with the coarse grid and 90-100mm for the case with the fine grid. The turbulent flame speed can be calculated from the angle of the flame front (as defined by the height of the flame and the diameter of the inner nozzle) and the mean velocity at the outlet of the inner nozzle. According to this procedure the turbulent flame speed is:

- without a grid: ~0.5 m/s
- with the coarse grid: ~0.7 m/s
- with the fine grid: ~0.6 m/s

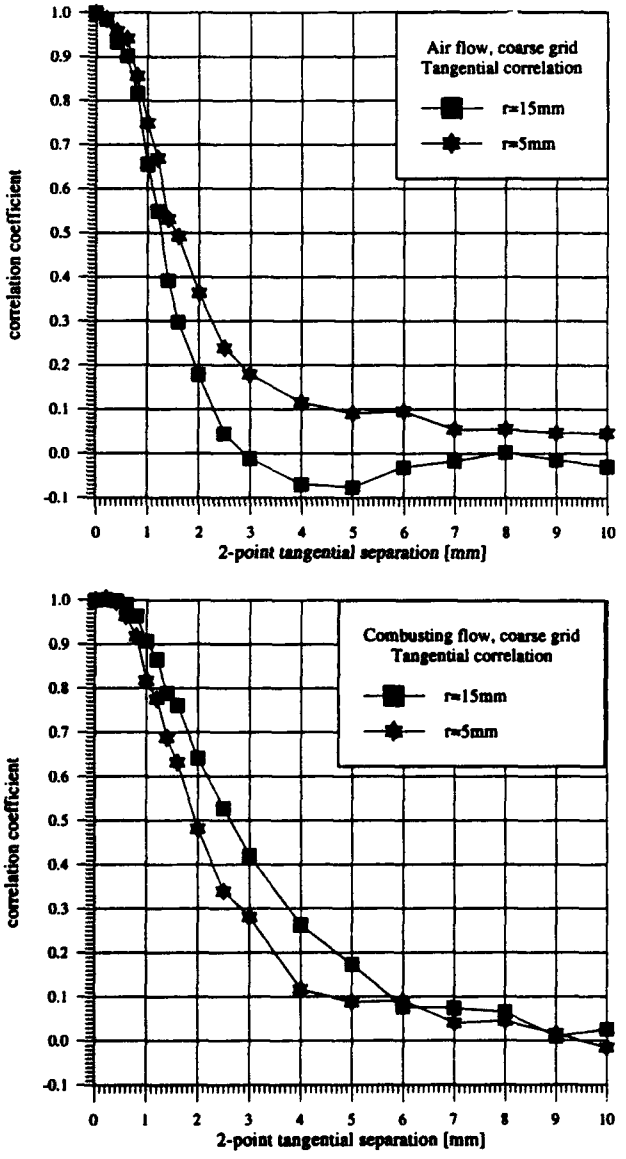

Fig. 8 Transverse spatial correlation coefficient function (tangential) in the flow configuration with coarse grid for the isothermal and the combusting case

Representative 2-point measurements at an axial position of 50mm after the outlet of the central pipe were performed and are presented in figures 7-8 and 10-11 for the flow configurations with coarse and fine grid installed in the central pipe. For each flow configuration two radial positions of the fixed measuring volume were examined, i.e. one before the flame front in the inner stream and one just after the flame front in the cooling region of the combustion products. For each of the positions of the fixed measuring volume, both the radial and the angular (tangential) correlation coefficient functions were measured. The corrections described by equations (7) to (12) were applied. The '2-point distance' δr between the two measuring volumes was normally varied up to 10 mm but the experimental facility allowed a maximum δr of 15mm. In order to understand the effect of combustion on the spatial correlation of the velocity fluctuations the same measurements were repeated under isothermal conditions for otherwise identical boundary conditions.

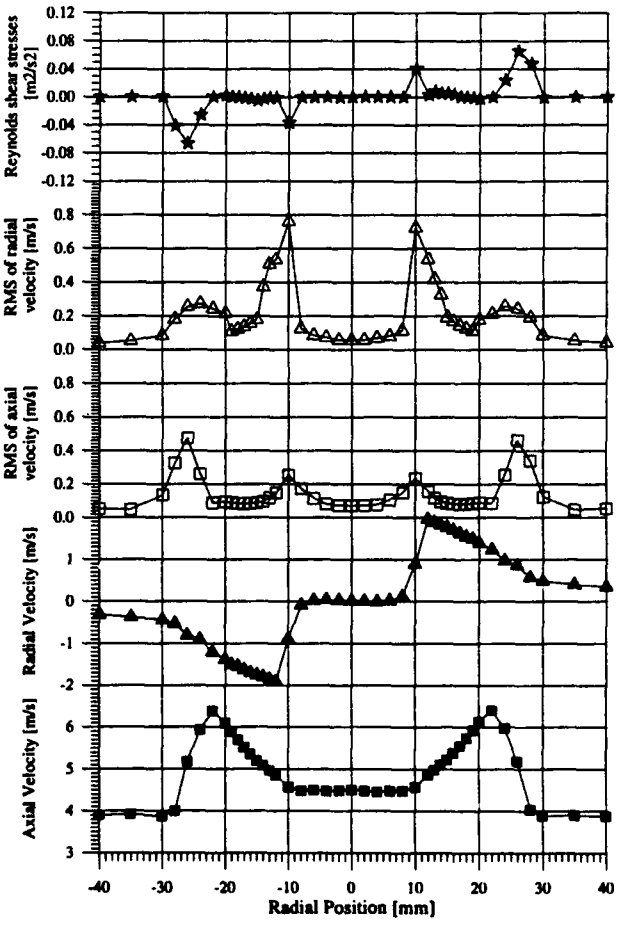

Fig. 9 Two-component measurements of the axial profile of 50mm in the flow configuration with fine grid

Referring to figures 7,8,10 and 11, the measured correlation coefficients do not always have the classical shape with an asymptotic approach to zero. This is a consequence of non-homogeneous turbulence and sometimes the correlation falls to zero only for δr larger than 10 mm, where the measuring volumes are in flow regions with completely different flow structures. Integrating under the correlation coefficient curve to

determine the integral length scale is in these cases not feasible. The determination of the Taylor microscale is also very sensitive to small errors in the correlation coefficient near the origin.

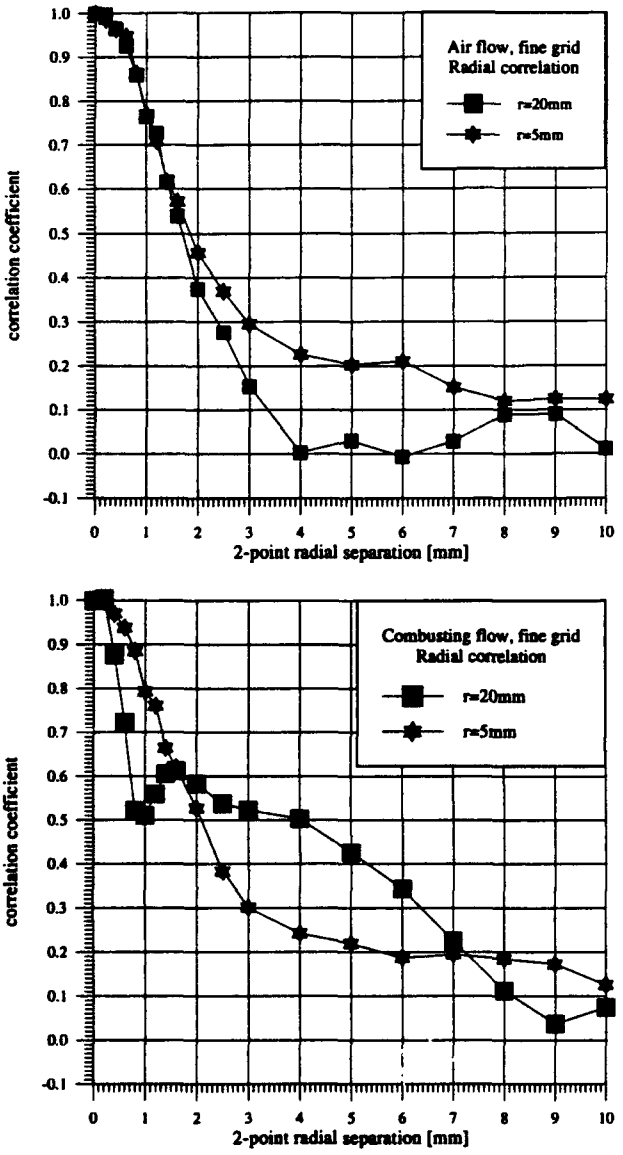

Fig. 10 Transverse spatial correlation coefficient function (radial) in the flow configuration with fine grid for the isothermal and the combusting case

The comparison between the cases of the isothermal and the combusting flow shows that the scales for the fixed measuring volume at the radial position of 5mm (before the flame front) are approximately equal. This means that combustion does not affect the flow upstream of the flame front. Downstream of the flame front (r=15mm or 20mm) the scales change significantly. In general the integral scales are larger due to an overall expansion of the flow.

The comparison between the two combusting cases shows that in the case of the fine grid the radial correlation after the flame front decays rapidly (small Taylor microscale), while in the case of the coarse grid the behaviour is not significantly different before and after the flame front. This could mean that the larger eddies of the coarse grid "survive" on their way through the flame front, while the smaller eddies of the fine grid are destroyed. The corresponding Reynolds shear stress (axial-radial) profiles show that for the fine grid the shear stress is significantly lower than for the coarse grid, although the normal stresses are of the same order of magnitude.

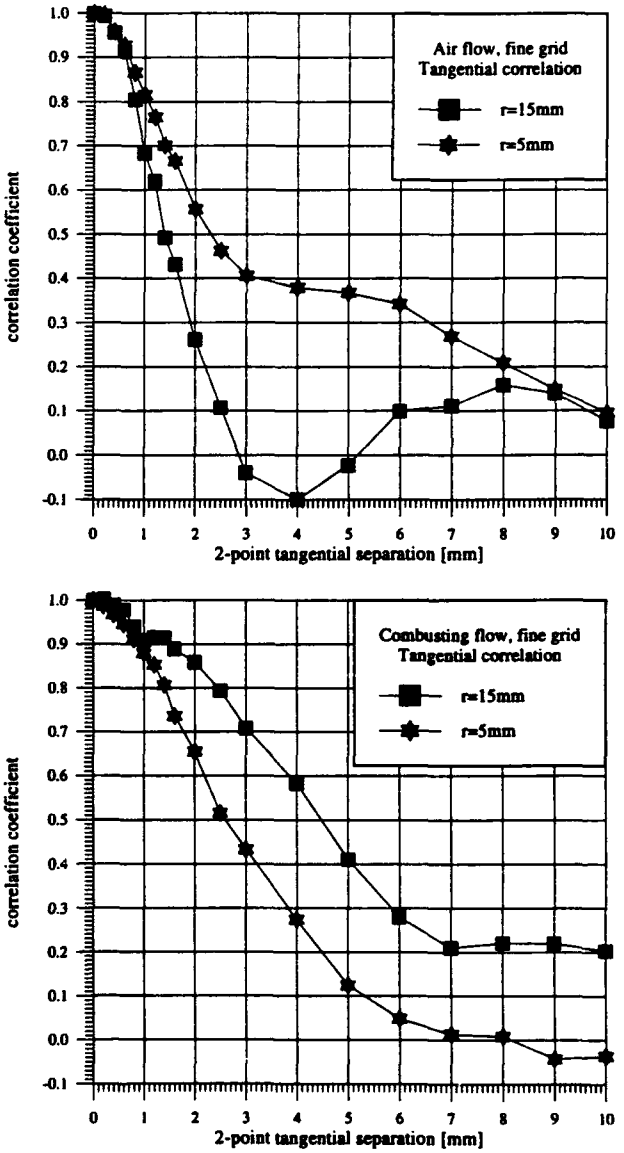

Fig. 11 Transverse spatial correlation coefficient function (tangential) in the flow configuration with fine grid for the isothermal and the combusting case

The tangential correlations show that the microscales do not change significantly in this direction, but the integral scales expand. The expansion of the integral scales in the tangential direction is more evident in the case of the fine grid, for which the microscales in the radial direction were destroyed, than for the coarse grid.

The high quality of the flow is confirmed by the excellent symmetry or anti-symmetry of the two-component LDV-results.

5. CONCLUSIONS

A simple two-point-LDV-setup using the same wavelength and optical parameters for both measuring volumes was designed, built and tested under isothermal and combusting conditions. The parameters affecting the accuracy of two-point measurements and the role of uncorrelated noise were discussed. A correction for the uncorrelated noise has been proposed. Representative measurements for different flow configurations of a turbulent flame indicate that spatial velocity correlation coefficients can be measured with well designed two-point LDV systems. The integral and microscales of turbulence can in principle be deduced from these correlations to assist the understanding of the turbulent transport phenomena in combusting flows. In practice, however, the complicated form of the correlation coefficient curves in non-homogeneous turbulence may prevent a reliable determination of the turbulence scales even with correlation data of high quality.

ACKNOWLEDGEMENTS

The authors would like to thank the EU for the financial support of this work within the framework of the JOULE I programme, contract No JOUE-CT91-0077 "Study of turbulent transport phenomena in combustion" . The support of the student Mr. O. Pickenäcker in building and testing the 2-point probe is also highly appreciated.

REFERENCES

Benak, M., Sturm, M., Tropea, C., Nobach, H., Fuchs, W., Müller, E., 1993, Correlation Estimators for Two-Point Laser-Doppler-Anemometry, SPIE Vol. 2052 Laser Anemometry Advances and Applications, pp.613-621.

Benak, M., Koenig, M., Melling, A., Stieglmeier, M., Tropea, C., 1992, Zweipunkt-LDA-Fasersonde zur Erfassung von Längenmaßen turbulenter Strömungen, Workshop: Lasermethoden in der Strömungsmeßtechnik, Inst. für Hydromechanik, Univ. Karlsruhe, Sept. 29-30.

Cenedese, A., Romano, G. P. and F. Di Felice, F. 1991, Experimental testing of Taylor's hypothesis by LDA in highly turbulent flow, Experiments in Fluids vol. 11, pp. 351-358.

Chao, Y. C. and Leu J. H. 1992, A fractal reconstruction method for LDV spectral analysis, Experiments in Fluids vol. 13, pp. 91-97

Fraser R. A. and Bracco F. V. 1988, Cycle-resolved LDV integral length scale measurements in an I.C. engine, Intenational Congress and Exposition, Detroit, Michigan, SAE Technical Paper Series, Nr. 880381

Johns, R. J. R., Pitcher, G. F. and Winklhofer, E. 1986, Measurement of spatial correlations in a turbulent flow with a two-component backscatter LDA system, Third Int. Symp. on Applications of Laser Techniques to Fluid Mechanics, Lisbon

van Maanen, H.R.E., van der Molen K. & Blom J. 1975, Reduction of ambiguity noise in laser-doppler-vlocimetry by a crosscorrelation technique, Proc. of the LDA-Symposium, Copenhagen, pp.81-88.

Mayo, W. T. Jr., 1975, Modelling of laser velocimeter signals as triply stochastic Poisson processes, Proc. of Minnesota Symp. on Laser Doppler Anemometry, Univ. of Minnesota, Bloomington, MI.

Nakatani, N., Tokita, M., Maegawa, M. & Yamada, T. 1985, Multipoint LDVs using phase defraction gratings and optical fiber probes - measurements of coherent structures in premixed flame, Proc. of the 2nd Inter.ASME Laser Anemometry Symposium, Miami, 1985, (ASME) FED-vol. 33, pp.111.

Pfeifer, H.S. 1986, Correlation and spectral density measurement by LDA, ISL-CO 244, ISL St.Louis, France.

Romano, G. P. 1993, Two points velocity measurements using LDA: spatial and temporal analysis in a turbulent boundary layer, Laser Anemometry Advances and Applications, vol. 2052, pp. 597-604.

Tennekes, H., Lumley, J. L., 1972, A first course in turbulence, MIT Press, Cambridge, Massachusetts, London.

Veynante, D. and Candel S. M. 1988, Application of non linear spectral analysis and signal reconstruction to laser Doppler velocimetry, Experiments in Fluids vol. 6, pp. 534-540.

FLAME STRUCTURE CHARACTERIZATION BASED ON RAYLEIGH THERMOMETRY AND TWO-POINT LASER-DOPPLER MEASUREMENTS

D. Duarte, P. Ferrão, and M.V. Heitor

Technical University of Lisbon
Instituto Superior Técnico
Dept. of Mechanical Engineering
Av. Rovisco Pais
1096 Lisboa Codex, PORTUGAL

ABSTRACT

Turbulent premixed flames stabilized in a bluff-body are experimentally investigated in order to discuss flame structure and morphology. Integral scales were measured within the reacting flow, based on the integral of the lateral velocity correlations obtained by using two laser-Doppler velocimetry systems. The quantitative results obtained are compared with flame shadowgraphs and complemented with simultaneous measurements of time-resolved velocity and temperature obtained by combining laser-Doppler velocimetry and laser-Rayleigh scattering. The results are used to quantify the relative magnitudes of the terms involving the balance equations of momentum, turbulent kinetic energy and heat flux. In addition, the interaction of pressure gradients and temperature fluctuations is shown to affect the heat release in the flame studied, revealing the existence of large zones characterized by non-gradient scalar fluxes.

1. INTRODUCTION

In the past many attempts have been performed to extend the knowledge on laminar flames and non-reacting fluid mechanics, to turbulent combustion, but turbulent mixing in flames is altered by the accompanying heat release and can, as consequence, be qualitatively different from that occurring in non-reacting flows. Examples include counter-gradient diffusion, e.g. Libby and Bray (1981), Bray et al. (1985), in either confined non-premixed swirling flames, Takagi et al. (1985), or in unconfined premixed flames, Heitor et al. (1987), Ferrão and Heitor (1993).

Although turbulent flames are characteristic of most of the industrial burning devices, their physical structure cannot be regarded as completely understood at the present. As pointed out by Borghi (1985), the detailed study of the fine-scale fluctuating structure of turbulent flames is very difficult to investigate experimentally and, consequently, theoretical studies based on physical assumptions suffer from lack of validation. This is the main motivation of the work reported in this paper.

The discussion on turbulent flames structure and morphology emerged from the fifties when turbulent flames were divided in two different categories, namely "wrinkled laminar flames" and "distributed reaction zones". Work performed during the sixties in Russia, e.g. Schelkin (1968) and Talantov et al. (1969), suggested that turbulent flames could be represented by either regimes, depending on the magnitude of turbulent intensity and the turbulent scales compared to laminar flame velocity and thickness. The need for an intermediate combustion regime was emphasized by Zimont et al. (1979), who justified the introduction of the "thickened -flame regime".

It is now generally accepted that the definition of turbulent combustion regimes according to the flame structure and morphology is based on the magnitude of turbulent intensity and the turbulent scales compared to laminar flame velocity and thickness. The resulting diagrams representing the combustion regimes, e.g. Borghi (1985), are frequently used, although they should be analysed with care and require the quantification of characteristic scales which are not generally easy to measure. It should be noted that the boundaries between combustion regimes are not as sharp as derived from physical analysis as discussed, for example, by Poinsot et al. (1991), through the direct numerical simulation of a flame front under strong curvature effects. The experimental work reported in this paper intends to contribute with quantitative data on these aspects, and includes the characterization of a flame in the "distributed reaction zone" regime. The main characteristics theoretically associated with this regime are analyzed and compared to the experimental data obtained.

The work follows that of Ferrão and Heitor (1993), which has assessed the extent to which a laser-Doppler velocimeter, LDV, may be used for the analysis of turbulent heat transfer in strongly sheared disc-stabilized propane-air flames through its combination with laser-Rayleigh scattering. The present paper complements this information and reports measurements of lateral integral scales within the reacting flow.

The remainder of this paper includes three sections. The experimental techniques are briefly discussed in the next section. The results obtained are presented and discussed in the third section and the last section summarizes the main conclusions.

2. FLOW CONFIGURATION AND EXPERIMENTAL METHOD

The analysis considered in this paper refers to a premixed propane-air flame stabilized on a disc of D = 0.056m diameter located at the exit section of a contraction with a diameter of 0.080m. The flame is open to the atmosphere to facilitate optical access. The annular bulk velocity at the trailing edge of the disc was equal to 19.5 m/s, resulting in a Reynolds number based on the disc diameter of 71,000. For the experiments reported here, the equivalence ratio was 0.60 and the corresponding adiabatic flame temperature is 1717 K. The rear stagnation point of the flame is located at an axial position of 110 mm, or x/D= 2.0.

The instrumentation used in this work is based on the combined LDV/LRS system schematically represented in Fig. 1a), which uses a single laser light source (5W Argon-ion laser), the details of which can be found in Ferrão (1993).

The velocimeter was based on the green light (514.5 nm) of the laser and was operated in the dual-beam, forward scatter mode with sensitivity to the flow direction provided by a rotating diffraction grating. The calculated dimensions of the measuring volume at e^{-2} were 606 μm and 44 μm. The Rayleigh scattering system was operated from the blue line (488 nm) of the same laser source, which was vertically polarized and made to pass through a 5:1 beam expander. The light converged in a beam waist of 50 μm diameter, and was collected at 90° from the laser beam direction, through a slit of 1μm. The collected light was filtered by a 1 nm interference filter and passed through a polarizer in order to increase the signal-to-noise ratio. A calibration procedure was implemented in order to compensate for number density dependence on the chemical composition. The uncertainty on the average temperature was quantified as 4%.

For the measurements of spatial velocity correlations, the laser light source was operated in multiline and the LRS optical system was replaced by a second dual-beam laser velocimeter mounted on a positioning system which allows the displacement of the control volume of this system relative to that described before, figure 1b). This second LDV was based on the green light (514.5 nm) of the laser and operated in backscatter mode, with sensitivity to the flow direction provided by a bragg cell. Two interference filters of 1nm bandwith were used in each optical collection systems, in order to avoid optical interference between the two systems.

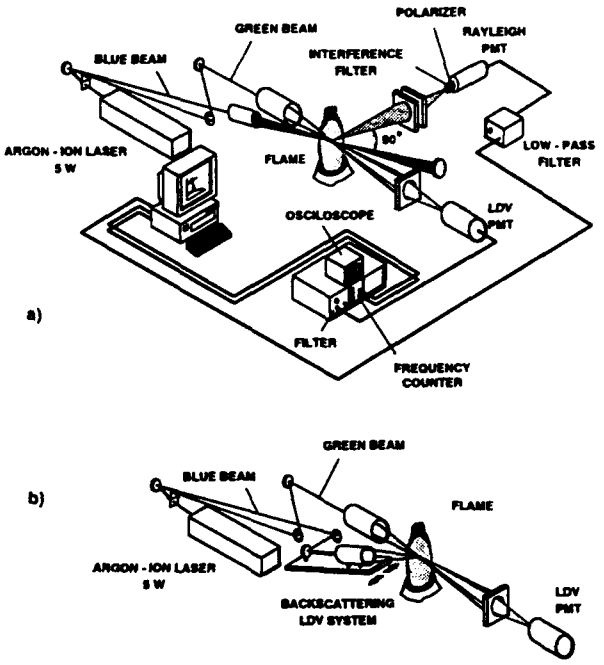

Figure 1. Schematic diagram of the instrumentation used:
a) combined LDV/Rayleigh scattering system
b) velocity correlation measuring system

Two frequency counters (DANTEC, model 55L96) were used to process the Doppler signals and a maximum coincidence time of 1μs was used to decide upon the simultaneity of the measurements. Each measurement was based in a population of N=6144 valid simultaneous velocity time series.

Correlation measurements at small separations can be expected to be influenced by the spatial resolution of the system. However, this does not noticeably affect the determination of the integral length scales, which are the purpose of the present work. The consequence of the limited spatial resolution is that the velocity correlation measured for nominally zero separation is never equal to unity. In practice, this is mainly because the measuring values are bigger than the smaller scales of the flow.

The experimental procedure included the measurement of the axial velocity fluctuations with the two LDV systems, respectively u_1 and u_2, at each measuring location, ζ, which was followed by successive displacement, ζ, of the backscatter system up to a maximum distance ℓ of 17 mm. This procedure allowed

the measurement of the lateral velocity correlation coefficient, $g(r,\zeta,)$ for a location r, defined as :

$$g(r,\zeta) = \frac{1}{(N-1)} \frac{\overline{u_1'(r)\, u_2'(r+\zeta)}}{\sqrt{\overline{u_1'^2(\zeta)}}\sqrt{\overline{u_2'^2(r+\zeta)}}}$$

were $\widetilde{u_1''}$ represents the turbulent velocity fluctuations of u_1 .

For the results reported here, the velocity correlations obtained were divided by the value measured at zero separation, which was generally about 0.7.

3. EXPERIMENTAL RESULTS AND DISCUSSION

The analysis and discussion of the experimental results presented here is divided in three parts. The first discusses the measurements of the lateral velocity correlation coefficient and the evaluation of the integral scales along the flame. The values obtained are used to define the combustion regime representative of the flame, which is compared to theoretical considerations. The last section summarizes the main mechanisms inherent to the turbulent transport of kinetic energy and heat fluxes in the flames considered.

3.1. Integral scales of turbulence

The integral length scale of turbulence is, to a certain extent, a measure of the longest connection, or correlation distance, between the velocities at two points of the flow field. It is reasonable to expect, as pointed out by Hinze (1975), that the degree of correlation will decrease as the distance between the two measuring points, ζ, is increased and that, beyond some finite distance, L, this correlation will be practically zero. Thus, the integral length scale of turbulence, l, is defined by:

$$l = \int_0^{\infty} g(\zeta)\, d\zeta = \int_0^{L} g(\zeta)\, d\zeta$$

The measurements of the lateral velocity correlation coefficient were performed in several radial positions located at two characteristic axial locations of the flame studied, namely at the rear stagnation point, x/D=2.0, and at the location of maximum width of the recirculation zone, x/D=1.2. Some results obtained for $g(\zeta)$ at different points for each location are represented in Figs. 2 and 3.

The shape of $g(\zeta)$ is qualitatively similar for all the conditions studied, but it can be clearly concluded that there are considerable differences in the values of the integral length scale of turbulence. The lateral velocity correlation coefficient rapidly decreases to zero in the points located at the reacting shear layer, as represented in Fig.3, while within the recirculation zone the correlation do not reach zero within the measuring distance.

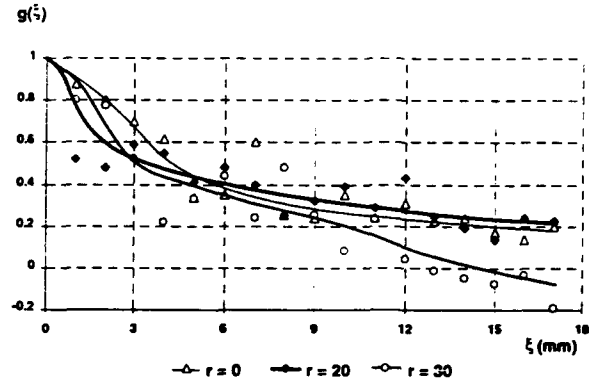

Figure 2. Lateral velocity correlation coefficient obtained at the rear stagnation point, x/D=2.0

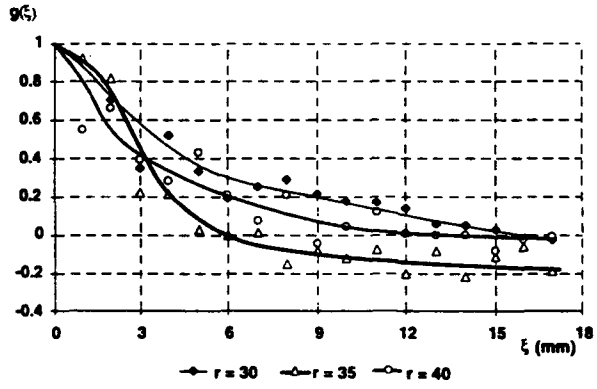

Figure 3. Lateral velocity correlation coefficient for the axial location of, x/D=1.2

The results can be used to obtain of the length scales and the turbulence intensity characteristic of each location measured, as represented in Table 1, where l_f and s_L represent the laminar flame thickness and velocity, respectively. It is shown that the length scales inside the recirculation zone are of about 10-12 mm and decrease to about 3-4 mm within the reacting shear layer. These units may be compared with the qualitative information provided by the shadowgraphs of Fig. 4, although this technique integrates over the line of sight and the information along that line is not unique and must be considered with some precaution.

X/D	r (mm)	l (mm)	u´ (mm)	u'/s_L	l/l_F	Ka	Da
1.2	0	12	4	27	30	25	1
1.2	15	9	4	27	23	29	1
1.2	30	5	4	27	13	39	1
1.2	35	3	2	13	8	18	1
1.2	40	4	2	13	10	15	1
2.0	0	8	4	27	20	31	1
2.0	15	7	4	27	18	33	1
2.0	30	4	3	20	10	28	1

Table 1- Integral length scales and characteristic parameters.

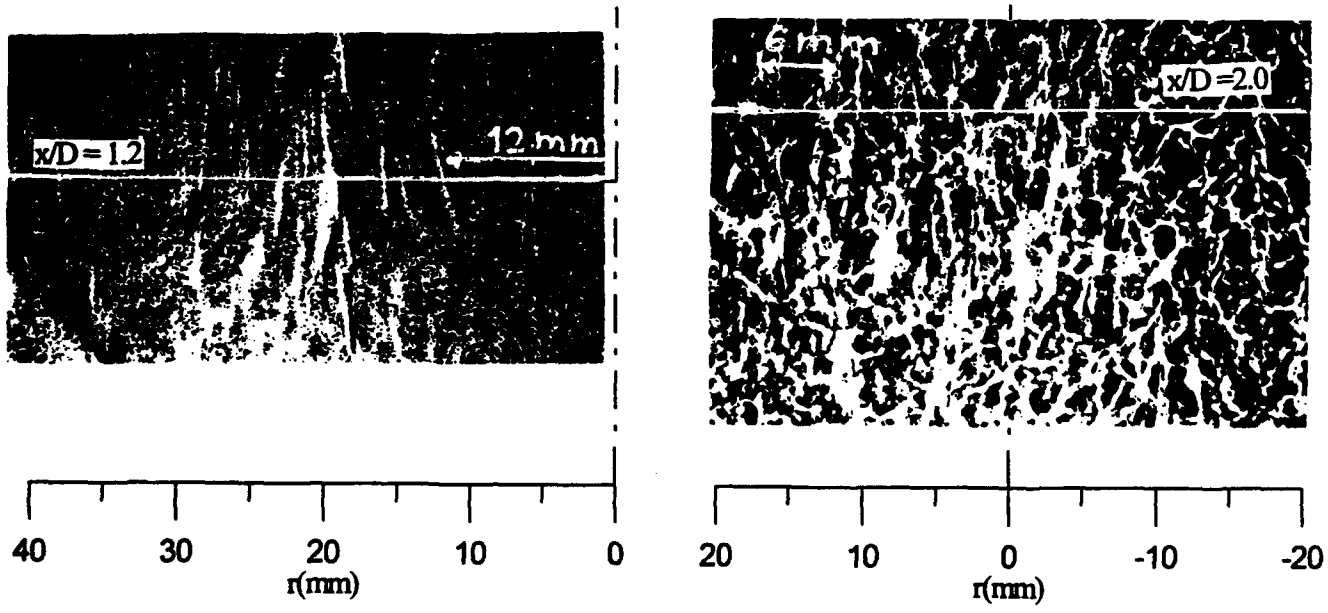

Figure 4. Shadowgraphs of the flame studied

Nevertheless, qualitative information on integral scales derived from Fig.4 agrees with the results reported in Table 1. Once the technique is sensitive to the second derivative of the index of refraction, i.e. the density, the results suggest the existence of regions of strong curvature of the flame front.

3.2. Combustion regime characterization

The non-dimensional Damköler (Da) and Karlovitz (Ka) numbers reported for the flame studied are presented in Table 1, and show that the flame is in the transition of the "distributed reaction zone" regime, because Da≈1 and Ka>1. At this combustion regime, thin reaction zones may be generated locally and quenched by flame stretching, thus characterizing a turbulent flame as a thickened-wrinkled flame with possible extinctions, Borghi (1985). As a consequence, the probability of finding gases in an intermediate state is not negligible, which means that a probability density function of temperature in any point should have a near bimodal shape with a significant population between combustion reactants and products.

This analysis was experimentally validated from the simultaneous velocity-temperature measurements performed in the reacting shear layer and shown in Fig.5, which represents the joint probability density function of velocity and the progress reaction variable, $c=(T-T_0)/(T_{ad}-T_0)$. The results confirm that the reacting shear layer is characterized by large temperature and velocity fluctuations were local extinction in the inner

reaction layer is expected to occur due to straining caused by the small eddies. The results validate the theoretical analysis available for the combustion regime identified before.

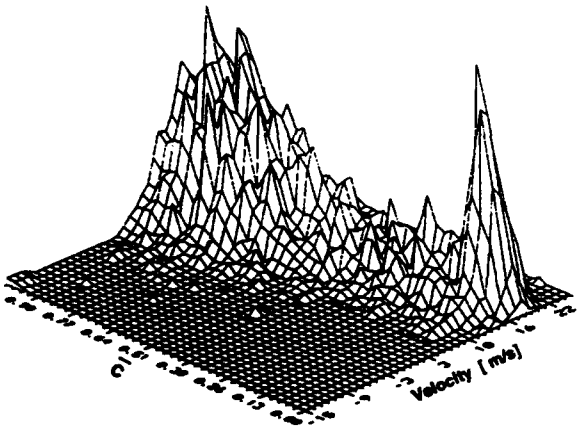

Figure 5. Typical joint probability density function of velocity and progress reaction variable for the reacting shear layer

3.3. Balance equations for Turbulent Kinetic Energy and Heat fluxes

This section gives details of the characteristics of the flame at X/D=1.2, and summarizes the main mechanisms inherent to the transport of turbulent kinetic energy and heat fluxes. Fig. 6 represents the mean velocity, progress reaction variable and turbulent velocity fluctuations across this axial section of the flame. It can be concluded that the recirculation zone is characterized by homogeneous temperatures and that its limit is located at r/D=0.4. The maximum turbulence intensity occurs at the location of the maximum gradients of mean velocity as predicted by gradient models, and the turbulence is not isotropic, as the axial velocity fluctuations in the shear layer is about twice the intensity of the radial and the tangential velocity fluctuations.

The terms in the transport of axial and radial momentum have been calculated from the measurements and are shown in Figs. 7 and 8. The mean pressure gradients have been found by addition and are dominated by the difference between two large terms, namely the convection terms (also the diffusion term in the balance of radial momentum). The pressure gradients represent an important source or sink of radial momentum, which is to be expected because of the large streamline curvature.

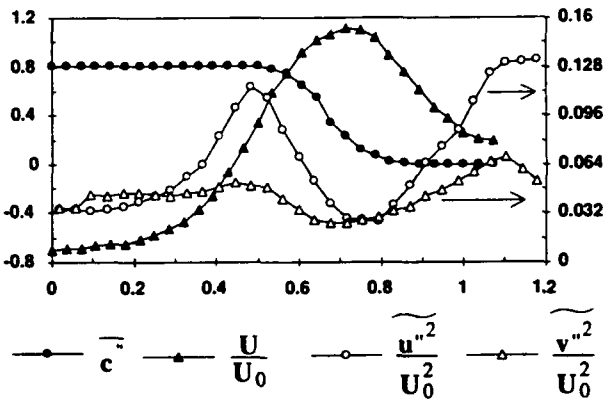

Figure 6. Radial profiles of mean velocity, progress reaction variable and turbulent velocity fluctuations for the axial location of x/D=1.2

The mean pressure gradient also appears in the transport equations for turbulent kinetic energy, whose most significant terms are represented in Fig.9. In the core of the annular jet, turbulence production by normal stresses *is negative and convection* is the largest term and represents a loss. In the shear layer, the major contribution to the production of turbulent kinetic energy is due to the interaction between shear stresses and shear strains. The production by the interaction of pressure gradients and velocity fluctuations is negligible all over the flow field.

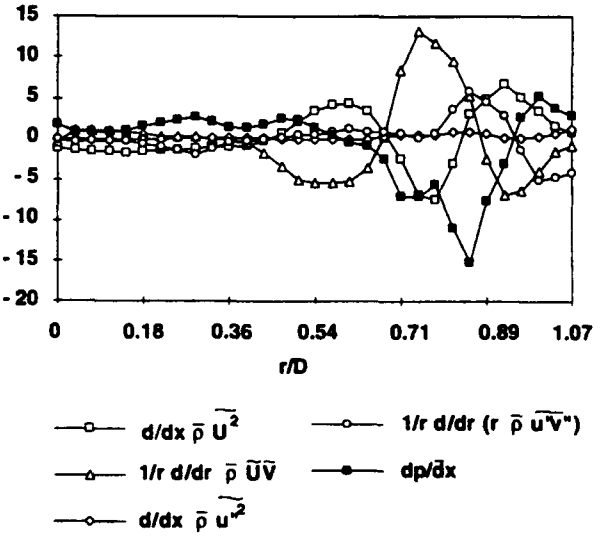

Figure 7. Terms involved on the balance equation of axial momentum

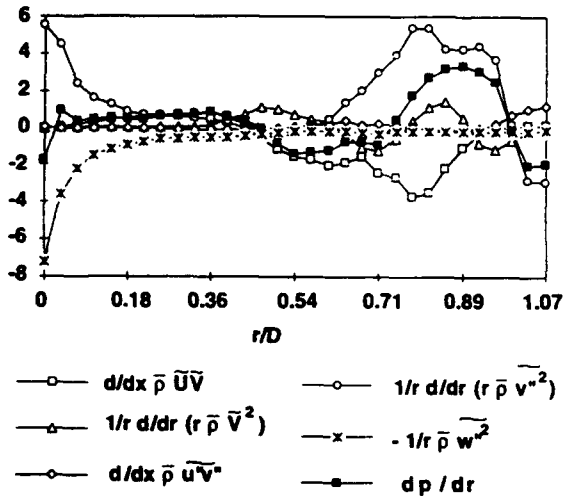

Figure 8. Terms involved on the balance equation of radial momentum

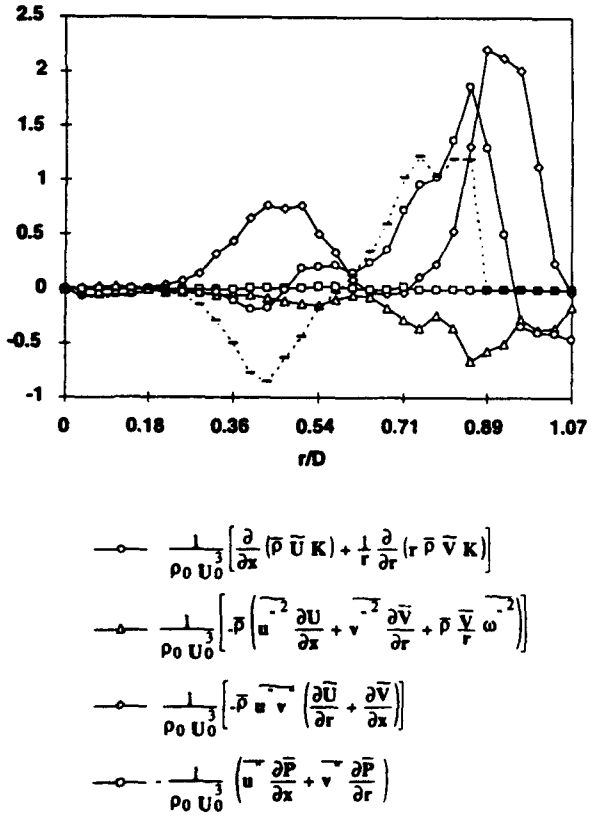

Figure 9. Terms involved on the balance equation of turbulent kinetic energy

The turbulent axial and radial heat fluxes measured with the LDV/LRS system across this axial location are represented in Fig.10 and are restricted to the thin zone along the shear layer where the radial gradients of mean temperature are large. These quantities represent the exchange rate of reactants responsible for the phenomena of flame stabilization and the results show that the axial fluxes are higher than the radial values. This reveals non-gradient transport of heat, as the isotherms in this location are axially aligned. It should be noted that radial fluxes are positive, as expected in a recirculating flame (Heitor et al., 1987).

The flame is then stabilized by the heat transfer between the hot products and the cold reactants with the sign of the radial heat flux opposite to that derived from gradient-transport models. Similar behaviour has been observed in the turbulent premixed flames of Ferrão and Heitor (1993) Heitor et al. (1987) and has also been predicted analytically by Bray et al. (1985).

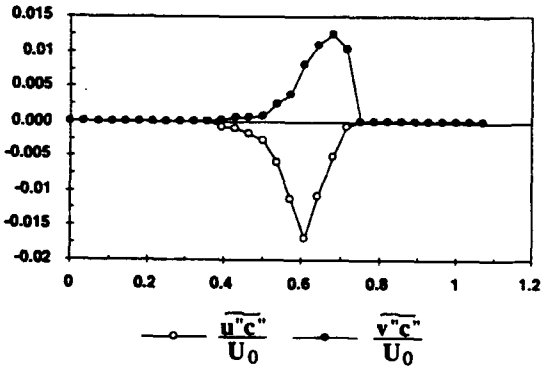

Figure 10. Axial and radial velocity correlation components

The non-gradient heat transport has been associated to the preferential deceleration of the light products of combustion relative to the cold reactants, due to the interaction between the mean adverse pressure gradients, typical of the present recirculating flow, and the large density fluctuations characteristic of reacting flows. This can be confirmed by the analysis of the terms involved in the transport equations for the axial and radial heat flux that are represented in Figs. 11 and 12, respectively. The evidence is that the interaction between the mean adverse pressure gradients and the large temperature fluctuations that occur in the present flame is important and influence the turbulent heat transport in recirculating flames.

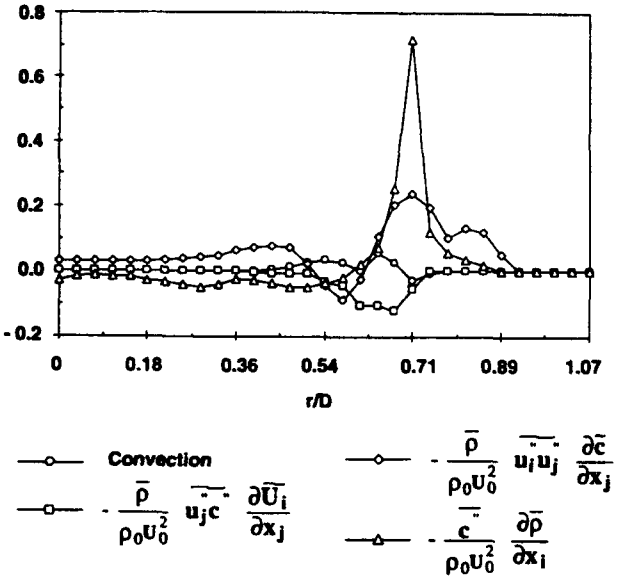

Figure 11. Terms involved on the balance equation of axial heat flux

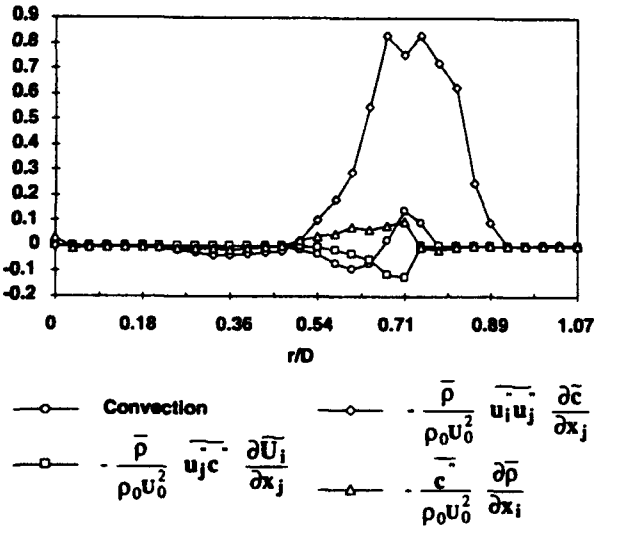

Figure 12. Terms involved on the balance equation of radial heat flux

4. CONCLUSIONS

Time-resolved simultaneous measurements of velocity and temperature, together with those of the spatial correlations of velocity, have been obtained by combining laser-Doppler velocimetry and laser-Raleigh scattering and using two laser velocimeters, respectively, in a turbulent recirculating premixed propane-air flame.

The spatial velocity correlations within the flow were used to analyze the extent to which turbulent mixing interacts with combustion, changing the flame structure and morphology. The experimental results were used to validated currently accepted theoretical descriptions of turbulent combustion regimes.

The velocity-scalar correlations measured were used to quantify the relative magnitudes of the terms involving the balance equations of momentum, turbulent kinetic energy and heat flux. It was concluded that the interaction of pressure gradients and temperature fluctuations is shown to affect the heat release in the flame studied, revealing the existence of large zones characterized by non-gradient scalar fluxes.

ACKNOWLEDGMENTS

The assistance of Messrs. Carlos Carvalho and Jorge Coelho in the preparation of this paper is gratefully appreciated. Financial support has been provided by the SCIENCE programme of the DGXII of the European Commission, under the contract SC1-0459.

REFERENCES

Borghi, R. (1985). "On the Structure and Morphology of Turbulent Premixed Flames". Recent Advances in the Aerospace Sciences, Ed.Corrado Casci, Plenum Publishing Corporation : 117-137.

Bray, K.N.C., Libby, P. and Moss, J.H. (1985). "Unified Modelling Approach for Premixed Turbulent Combustion - Part I: General Formulation". Comb. & Flame, 61: 87-102.

Ferrão P. and Heitor M.V. (1992). "Simultaneous Measurements of Velocity and Scalar Heat Transfer in Recirculating Flames" 6th Symposium on Applications of Laser Techniques to Fluid Mechanics, 20-23 July, 1992.

Ferrão, P. (1993). "Análise Experimental de Chamas Turbulentas com Recirculação". Ph.D Thesis, Technical University of Lisbon (In Portuguese).

Ferrão, P. and Heitor, M.V. (1993). "Turbulent Mixing and Non-Gradient Diffusion in Baffle-Stabilized Flames". "Turbulent Shear Flows-9", ed. Springer Verlag, Japan: 28-2.

Heitor, M.V., Taylor, A.M.K.P. and Whitelaw, J.H. (1987). "The Interaction of Turbulence and Pressure Gradients in a Baffle-Stabilized Premixed Flame". J. Fluid Mechanics, 181: 387-413

Hinze, J.O. (1975). Turbulence, 2nd Edition. McGraw-Hill.

Libby, P. and Bray, K.N.C. (1981). "Counter-Gradient Diffusion in Premixed Turbulent Flames". AIAAJ., 19 : 205-213

Poinsot, T., Veynante, D. and Candel, S. (1991). "Quenching Process and Premixed Turbulent Combustion Diagrams". Journal of Fluid Mech., 228:561-606.

Schelkin, K.I. (1968). "Combustion Hydrodynamics". Fiz. Goreniya Vzryva, 4 : 455-468.

Takagi, T., Okamoto, T., Taji, H. and Nakasuji, Y. (1985). "Retardation of Mixing and Counter-Gradient Diffusion in a Swirling Flame". Twentieth Symposium (Int'l) on Combustion, The Combustion Institute: 251-258

Talantov, A., Ermolac, V.H., Zotin, V.K. and Petrov, E.A. (1969). "Laws of Combustion of a Homogeneous Mixture in a Turbulent Flow". Comb. Explos. Schock Waves, 5 : 73-75.

Zimont, V.L. (1979). "Theory of Turbulent Combustion of a Homogeneous Fuel Mixture at High Reynolds Numbers", Fiz. Goremiya Vzryva, 15 : 23-32.

SIMULTANEOUS VELOCITY AND TEMPERATURE MEASUREMENTS IN TURBULENT FLAMES OBTAINED BY COUPLING LDV AND NUMERICALLY COMPENSATED FINE-WIRE THERMOCOUPLE SIGNALS

F. Neveu*, F. Corbin*, M. Perrin** and M. Trinité*

* C.N.R.S. - CORIA Université de ROUEN CEDEX
76821 MONT SAINT-AIGNAN - FRANCE

** GAZ DE FRANCE - Research and Development Division 361, Avenue du Président Wilson
93211 LA PLAINE SAINT-DENIS - FRANCE

ABSTRACT

The temperature and velocity are simultaneously measured in a turbulent nonpremixed flame. The goal of the method is to use two independent techniques while minimising pre-setting at the time of acquisition. All the data reductions are made by post-processing, time coincidence between the two velocity components, numerical compensation for thermocouple signal, temperature signal reconstruction for the $u'\theta'$ correlation. By using a computer, one can remake the data-processing to point out the influence of reduction parameters on the RMS or cross-correlation values. For example, by modifying the coincidence window, one can see the biases or time integrating effects. In the same way, the thermocouple time constant can be adjusted with respect to velocity and temperature. An application of this technique is given on a turbulent non-premixed methane-air flame from a bluff-body type burner. Coupling between aerodynamic and combustion are quantified. The mechanism of flame stabilisation by reignition of the downstream reaction zone can be explained.

1. INTRODUCTION

The simultaneous measurement of velocity and temperature in turbulent flame provides a better understanding of coupling between aerodynamics and combustion. Same, mathematical models (like R_{ij} models) must be validated by this type of measurements. In particular, for intermittent flames, data for cross-correlation between velocity and temperature are necessary, along with information on large scale structures. To carry out these experiments, we use an association of two techniques, Laser Doppler Velocimetry (LDV) and numerically compensated fine-wire thermocouple.

Today, measurement of the velocity by LDV is well established. However, when studying a turbulent diffusion flame, some difficulty remains to measure in the mixing zone, due to unequal seeding of the two streams (Labbaci *et al.* 1988). For temperature, non intrusive optical methods are promising. But these techniques, such as CARS, have a poor spatial resolution and are not presently time resolved (Goss *et al.* 1988). For Rayleigh scattering, presence of particles limits coupling with LDV (Dibble *et al.* 1981). Then, in spite of its limitations, the thermocouple technique is the most adapted method to be coupled with LDV (Yanagi & Mimura 1981, Heitor *et al* 1985).

One of the particularity of this work is to combine two opposite methods in the way data acquisition should be made. A fixed sampling rate of the temperature signal is needed for numerical compensation whereas velocity is sampled with random particle arrivals. With a dedicated electronic, a simultaneous acquisition of temperature and velocity signal can be obtain (Heitor *et al.* 1985), but this approach requires many electronics communications between the temperature and LDV acquisition systems. Another way to acquire temperature and velocity in time coincidence, is to independently measured temperature and velocity and then, by a post-processing, mathematically reconstruct (Wills 1991) the temperature signal for each velocity component. This method is used here for calculating the temperature/velocity cross-correlations.

The velocity component's acquisition is made independently on each channel, to keep all the validated bursts on the two channels in a given measurement time. The time coincidence between the two components is achieve by a post-processing on a computer. We discuss below what this type of velocity acquisition and processing can provide (Carey 1986).

A brief explanation of the thermocouple time constant measurement and interactive numerical compensation are also given.

Mean, RMS and cross-correlation fields of u, v, θ measured in a Bluff-Body stabilised flame are presented in Figures.

2. EXPERIMENTAL APPARATUS AND METHOD

2.1 Velocity Measurement

For the two velocity component measurements a two colors, dual beam, real fringe in backscatter mode TSI LDV system is used. The table 1, gives its principal characteristics. Axial velocities are measured using the green line and the radial components with the blue line from an argon-ion laser (1.5 Watt). After the beam splitter, 40 MHz Bragg-cells are used to eliminate directional ambiguity in each component. The photomultiplier output signals are analysed by two TSI 1990C processors. The MI 990 multi-channel interface enables data transfer from counters into computer memory through direct memory access (DMA). This interface is also used to give the time between data (TBD), providing time series data.

2.2 Temperature Measurement

The temperature fluctuations are measured with a fine wire thermocouple of fifty micrometer diameter (Pt-Rh 6/30%). The thermocouple junction is made by welding with a capacitive discharge. Reproductive junction without bead are made with this technique.

Optics (TSI)				
half angle		κ (°)	4.95	
focal	f	(mm)	476	
wavelength	l	(nm)	514.5	488
number of fringes			19	18
fringe spacing	d_f	(μm)	2.98	2.87
volume diameter	d_m	(μm)	55.5	52.6
volume length	l_m	(μm)	580.	549.
Acquisition (TSI)				
counter processors		1990C (X2)		
timers		1995B (X2)		
interface		MI 990		
Seeding				
PALAS (RBG 1000) brush seeders for air and methane jets, ZrO_2 particles < 1 μm (DEGUSA)				
LDV Pre-setting				
Number of cycles/burst			16	16
Comparison		(%)	1	1
HI Limit Filter		(MHz)	20	20
LO Limit Filter			1	1

Table 1. Principal characteristics of LDV system

A correct length *l* of the wire (12 mm) is used to make heat conduction losses negligible ($l/lc > 10$ where *lc* is the cold length $lc = (\alpha\tau)^{0.5}$, α is thermal wire diffusivity and τ the thermocouple time constant, Paranthoën *et al*, 1982). The fine wire is flame welded on two 250 μm diameter intermediate support wires. Then, these last wires are also welded on end support wires of 500 μm diameter (see Figure 1). This design is intended to reduce support wire wake and to minimise the distance between the ceramic support exit and the probe volume while keeping a good probe rigidity. The thermocouple signal is first amplified (x 100) by a low noise preamplifier (Stanford Research 512) before been digitised with a 12 bit digital oscilloscope (Nicolet 4094C).

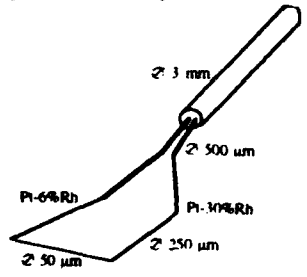

Fig. 1 Thermocouple design.

The axial distance between the thermocouple junction and the LDV probe volume was less than 1 mm. The influence of this distance on the $\overline{u'\theta'}$ correlation was clearly discuss by Heitor *et al* (1985) and are taken into account.

2.3 Acquisition Control

A software has been developed, under Microsoft Windows 3.1, to control the data acquisition and storage (Corbin *et al*, 1992). The computer operates in DMA mode to get measurements from the two LDV channels with random arrival, while the thermocouple signal is regularly sampled and stored by an independent digital oscilloscope. The temperature and velocity synchronisation is also take on by the software which drives the oscilloscope trigger and the DMA transfer of the LDV system.

The number of samples stored by the oscilloscope is 15872. Then, for a 5 kHz sampling rate, the time duration of a data acquisition is limited to 3.1744 seconds. The low thermocouple sampling rate is a compromise between time duration of data acquisition (to resolve low frequency fluctuation) and the LDV sample size. During this time, we acquire all the validated Doppler bursts on each channel without any time coincidence control and then increasing the data rate (Carey 1986). This type of acquisition is advantageous in the recirculation zone where the particles concentration is low. When the oscilloscope has finished one acquisition, the computer stops the DMA transfer and the temperature data are transferred from the oscilloscope to the PC through an IEEE 488 interface. A "real time" visualisation of the mean and fluctuations velocity profiles on the computer screen provides a monitoring of the measurement in progress.

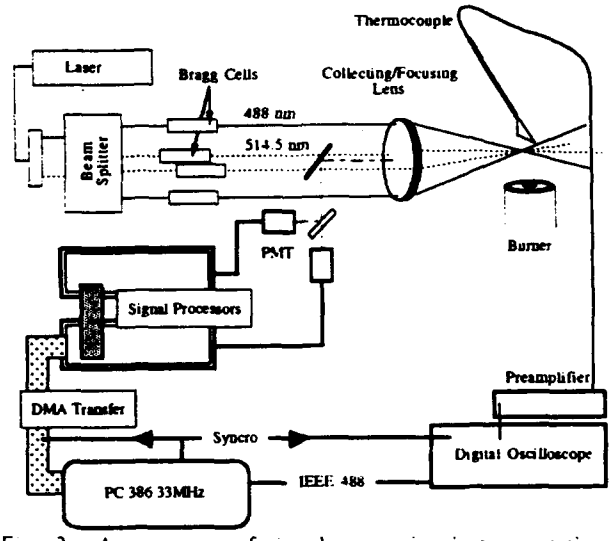

Fig. 2 Arrangement of signal processing instrumentation

When all the measurements are achieved throughout the flame field, the data processing is carried out by a dedicated software on a SUN work station.

3. DATA REDUCTION PROCESSING

3.1 Velocity Time Coincidence

Because each velocity component are measured independently from each other, a coupling in time between

the two components is necessary to calculate the $\overline{u'v'}$ correlation.

To find time coincidence between $u(t)$ and $v(t)$ we used a very simple algorithm. Its principle is to scan if, inside a time window of size Δt, there is measured points on both series. If they exist, these velocities are say to be in coincidence with the other. Then we move the window along the time series data for an other coupling research. If, in the coincidence window, more than one data point exists, the mean value is calculated and stored, created a low pass filter. The advantages of this procedure are to keep all the validated burst of the data acquisition and to control coincidence bias. Nowadays, with the continuous computer technology progress, this type of processing can be done without excessive computer time.

3.2 Temperature Signal Processing

Numerical compensation. The gas temperature fluctuations are calculated from the simplified energy balance equation:

$$T_g = T_w + \tau \frac{\partial T_w}{\partial t} \quad (1)$$

where T_g is the gas temperature and T_w the thermocouple temperature. The thermocouple time constant depends on temperature, velocity and gas composition (Heitor *et al*, 1985). A numerical compensation was preferred to an analogue circuit because it can take into account some of these dependencies (Heitor *et al*, 1985), as the gas temperature with iterative loop and the velocity by the instantaneous LDV measurement for time constant adjustment.

Time constant measurement. The thermocouple time constant was measured by the laser heating method (Nina *et al*, 1985). The thermocouple is placed in a laminar heated gas flow at temperature T_g. With a laser sheet (7 Watt), the thermocouple junction temperature is increased to temperature T_h. Then, a shutter is triggered and blocks the laser beam, while the decreasing temperature signal is store by a digital oscilloscope. The time constant is then calculated from this signal.

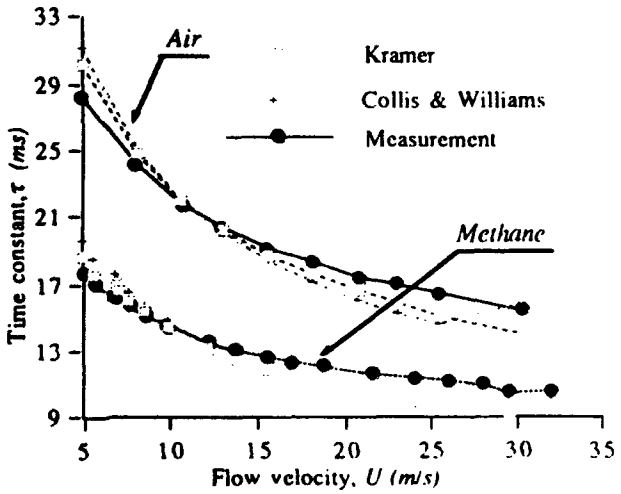

Fig. 3 Time constant evolution for an air and methane flow.

A comparison of the measured and theoretical value time constant is shown for air and methane flow (T_g = 480 K). We notice a ratio between measured air and methane time constant of approximately 0.65, as previously observed by Heitor *et al* (1985) (Figure 3). This is due to the large heat conductivity (λ) difference

$$\frac{\tau_{CH4}}{\tau_{air}} \approx \frac{\lambda_{air}}{\lambda_{CH4}}.$$

In Figure 3, to calculate the theoretical values of time constant:

$$\tau = \frac{\rho C_p d^2}{4 Nu \lambda_g}$$

the Nusselt number is evaluated by the Kramers (1946) and Collis & William (1959) laws. Thermophysical properties of gases are estimated using Touloukian (1970, 1975) tables. Given the small differences between measured and calculated time constant values, we use the Kramers expression to compute the Nusselt number. To take into account local gas composition, the mean concentration values of methane are used to adjust time constant at each measurement location.

3.3 Temperature-Velocity Correlation

To calculated the $\overline{v'\theta'}$, $\overline{u'\theta'}$ correlation or to determine the joint probability distribution, we apply first the Nyquist interpolation formula to reconstruct the thermocouple signal (Wills, 1991) at the time of the velocity measurement and then the numerical compensation algorithm. The interpolation formula is:

$$T_w(t) = \sum_{k=-\infty}^{+\infty} T_w(k) \frac{\sin(\pi f_e t - k\pi)}{\pi f_e t - k\pi}$$

coupled with a fast algorithm to accelerate the series convergence (Boyd 1992). The only restriction to use the reconstruction is that the signal should not contain frequency greater than half the sampling frequency. That can be guaranteed by using a high order Butterworth digital filter. This method provides calculation of the temperature-velocity correlation on all the validated burst and not only on the velocity measurements in time coincidence.

4. MEASUREMENTS IN A NONPREMIXED TURBULENT FLAME

4.1 Flow Configuration

Axisymmetric Bluff-Body burners have been investigated, in previous studies, for different configurations (Scheffer *et al* 1987, Kelly *et al* 1989, Perrin *et al* 1990, Namazian *et al* 1993). In this study, one of the configurations was used, with a blockage ratio of 83%. This burner consisted of a central 5.4 mm diameter methane-supply tube, located in the center of a 50 mm cylindrical bluff body. The annular air jet outer diameter was 55 mm. The exit bulk velocity is 7.5 m/s for the air jet and 21 m/s for the methane jet.

4.2 Mean and RMS

The flame length is about 50 cm, but the measurement zone investigated is limited to [5, 160] mm from the

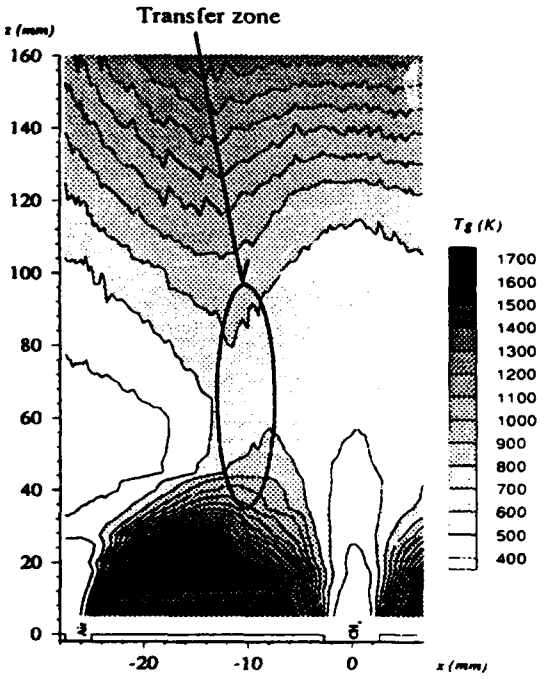

Fig. 4 Mean temperature, combustion in the recirculation zone in the first 35 mm then partial extinction [40-100] mm and the reignition zone.

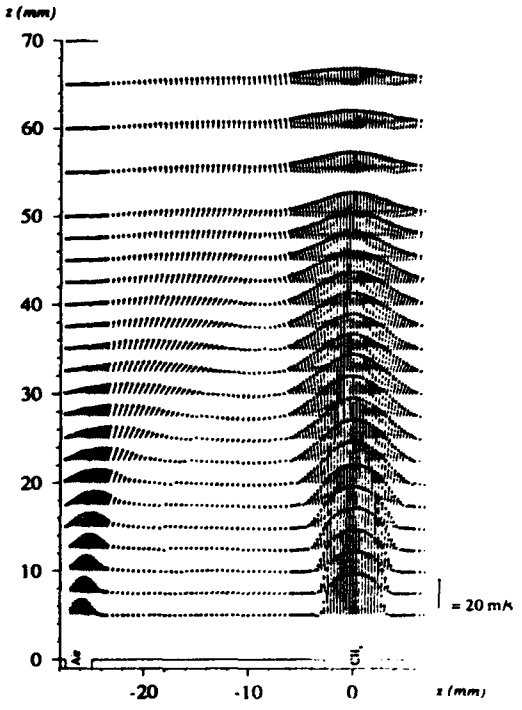

Fig. 5 The velocity fields show the recirculation zones of air and methane flow and the methane jet penetration. The air flow turn in clockwise while methane flow in anticlockwise.

burner exit for the axial distance and to [-27.5, 7] mm for the radial distance. In this domain, we could observe two combustion zones in the flame: one in the recirculation zone and another higher in the flame. By a careful visual observation, one can notice stretched flame packets escaping from the recirculation zone and transported further downstream through an extinction zone. This phenomenon is confirmed by analysing the mean temperature field (see transfer zone in Figure 4). These packets have a preferential transfer path, at ≈ -10 mm from the axis burner, that can be seen on Figure 4 with the contour lines ([584, 676] K) at x ≈ -10 mm, z ≈ 70 mm location. Then, the recirculation zone plays a critical role in reignition of the second combustion zone.

The mean velocity field, of the Figure 5, clearly shows the recirculation zone of the air and methane flow. The high radial velocity gradient near the methane jet exit is well resolved by the adapted fine mesh.

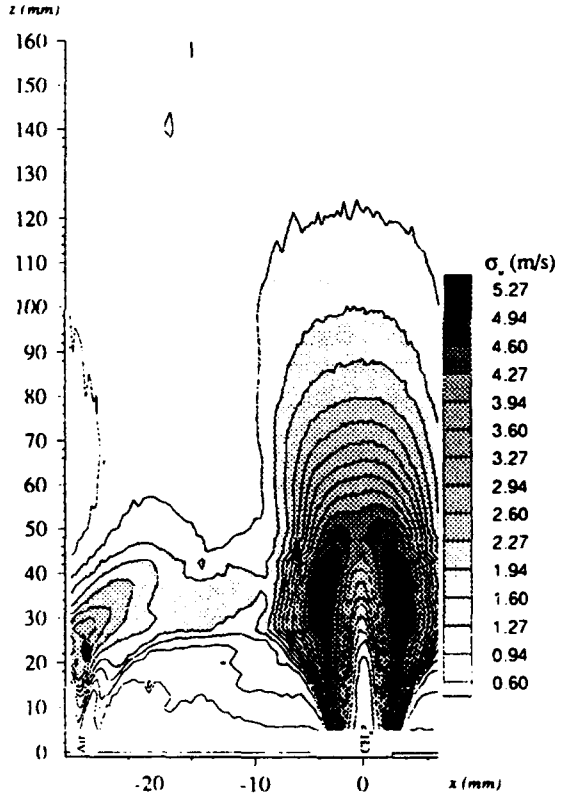

Fig. 6 Axial velocity fluctuations.

As shown by Figure 6, the velocity fluctuation level in the recirculation zone are very low and the maximum RMS is found in the methane shear layer. The same factor 2, in favour of axial fluctuation, between the two velocity fluctuations is found, as Sheffer *et al* (1987), in the shear zone of the methane jet.

During the experience no particles accumulation on the fine wire for a [5-110] mm axial distance from exit burner was noticed, the turbulent flow appeared to clean the thermocouple. At the opposite, for the distance over 110 mm,

the turbulence level became low and a cleaning of the thermocouple was frequently needed.

4.3 Evolution of the Velocity Statistics with the Time Coincidence Window

For all these tests, the measurements are taken at 7 mm from the burner exit and without combustion. At this height, the air jet, recirculation zone and the methane jet are clearly distinct on the mean velocity profiles.

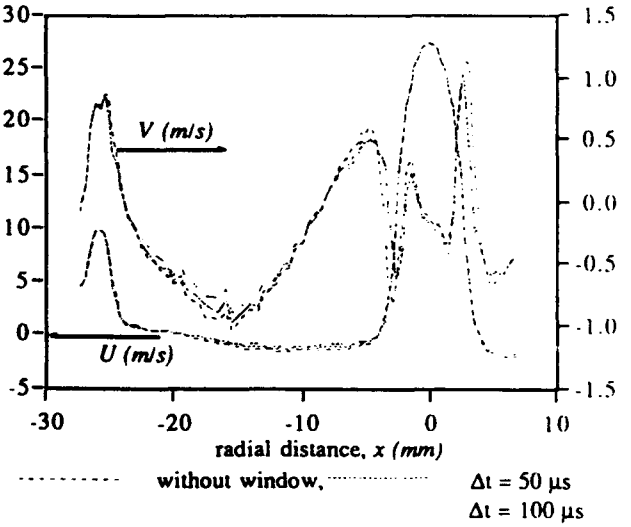

Fig. 7 Mean axial (U) and radial (V) velocity profiles for different time coincidence window sizes.

Figure 7 shows that the size of coincidence window has no significant effect on the mean profiles (for the studied range).

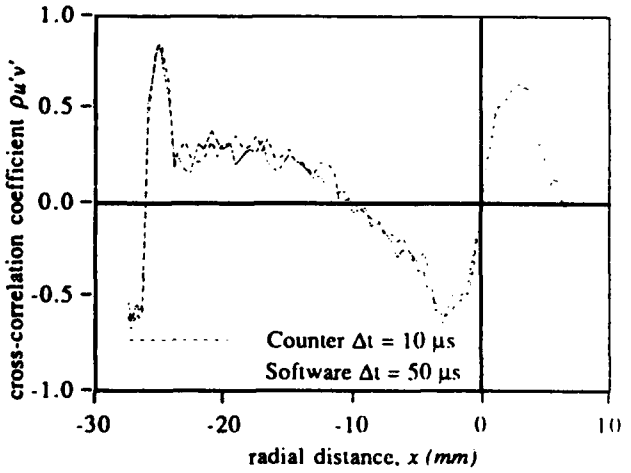

Fig. 8 Comparison between velocity cross-correlation coefficient given by counters and by our software.

A comparison is also given for the $\rho_{u'v'} = \overline{u'v'} / \left(\overline{u'^2}\,\overline{v'^2}\right)^{1/2}$ correlation found with coincidence selected from the counters and the coincidence made by our method (see Figure 8). With this procedure it is also possible to verify if the velocity samples used for the coincidence are randomly selected (bias problem). Figure 9 shows, that in shear zones, RMS values computed with all samples (σ_u,) may be different from those obtained from coincident samples (σ_{uc}). In the high shear layers, where small scales of turbulence are dominant, σ_{uc} is higher the σ_u. In the opposite, in the recirculation zone, σ_{uc} is lower than σ_u. Then, the time coincidence procedure behaves differently depending on the turbulence scale distribution in the velocity sample.

4.4 Temperature fluctuations

From the transfer equation (1) we define η, the numerical compensation efficiency as the effective fractional energy temperature spectrum restored by the numerical compensation on the energy temperature spectrum restored by an ideal compensation up to a fixed frequency. The efficiency is a function of the signal sampling frequency, the type of computation method used to calculated $\partial T_w/\partial t$, and the level of the background noise (Neveu 1993).

$$\eta(\omega) = \frac{\int_0^{\omega} \left| \frac{1}{1+(\omega\tau)^2} \right| \left| 1+(\omega\tau)^2 \left(\frac{\sin \omega T_e}{\omega T_e} \right)^2 \right| d\omega}{1.\omega} \qquad (2)$$

where T_e is the sampling period and ω the pulsation ($2\pi f$).

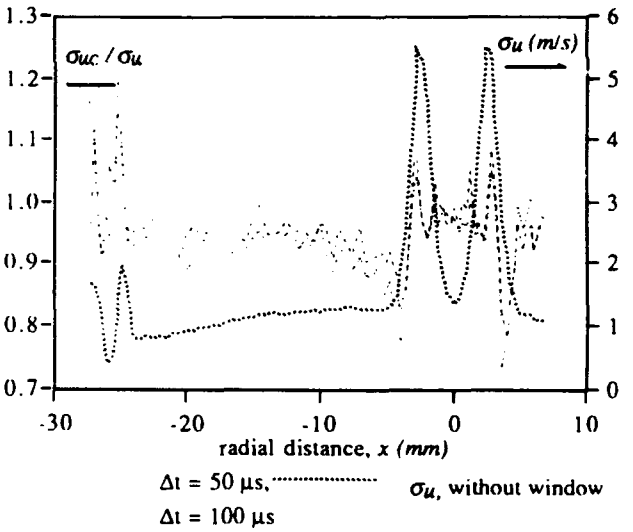

Fig. 9 Influence of the time coincidence window on the axial RMS velocity. σ_{uc} is the RMS after coincidence.

The relation (2) is calculated with a classical central difference derivative scheme:

$$\frac{\partial T}{\partial t} \equiv \frac{T_{n+1} - T_{n-1}}{2\Delta t}$$

and with the assumption that τ is constant. Figure (10) shows the previous relation and, for example, for a 5 kHz sampling rate signal, up to 1 kHz, the thermocouple can restore about 85% of the total initial energy.

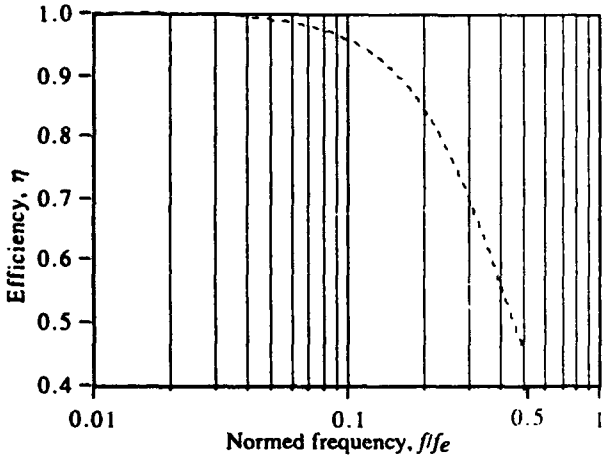

Fig. 10 Numerical compensation efficiency, *fe* is the sampling frequency.

The use of higher order to calculated the temporal derivative, $\partial T_w/\partial t$, increase the efficiency of the numerical compensation up to 97% (below 1 kHz), but became very sensitive to the background noise (Neveu 1993).The question is to know what are the contribution of the high frequencies in the total energy of the temperature spectrum. Heitor *et al* (1985) compares the cumulative spectrum of the signal measured and compensated with a 15 and 40 µm thermocouple.

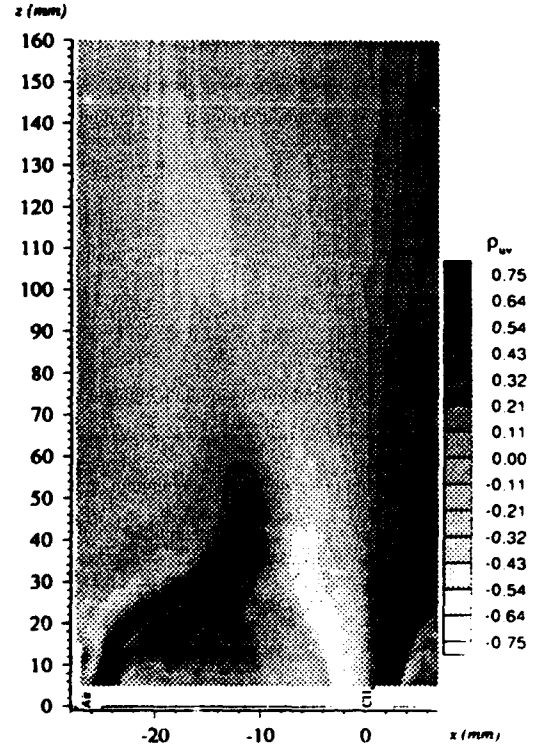

Fig. 11 Velocity cross-correlation coefficient, for a 50 µs time coincidence window.

The energy difference found between the two wires is 5% and, below 1 kHz, the energy is about 90% of the total energy. The same type of comparison is made by Talby *et al* (1990) between a platinum cold wire (0.63 µm) and a compensated thermocouple (50 µm) in a strongly heated turbulent jet. They found that, below 1 kHz the variance contribution is 93 % of total energy and shows a good similarity between cold wire and compensated thermocouple spectrum. We can reasonably estimate that, with the 5 kHz sampling rate and with the thermocouple time constant adjustment with velocity and temperature, the maximum energy restored is about 80% of the initial total energy.

4.5 Temperature and velocity coupling

To calculate the cross-correlation velocity coefficient (ρ_{uv}) we used the technique previously describe, with a coincidence window of 50 µs.

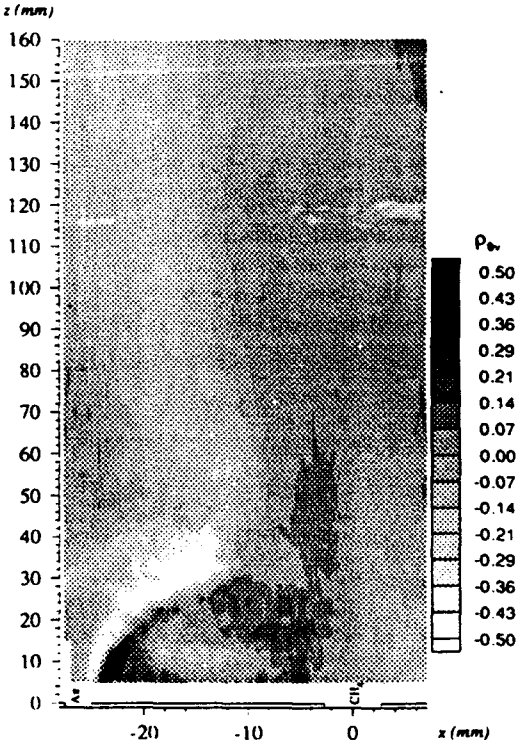

Fig. 12 Radial velocity-temperature cross-correlation coefficient.

The correlation values show the recirculation zone curvature (see Figure 11). The coupling between the two velocity components is very important along the recirculation zone and near the same flame packet transfer zone previously described.

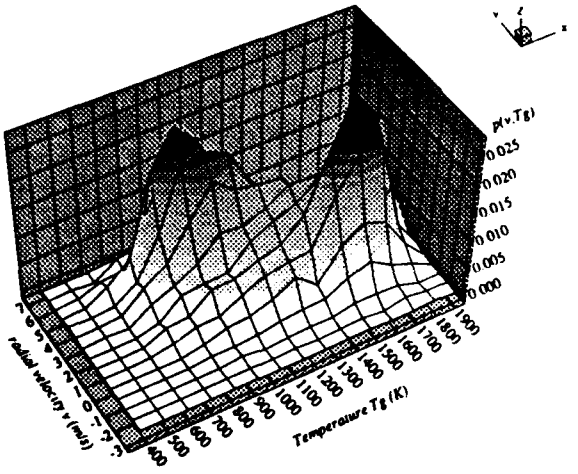

Fig. 13 Joint probability distribution $p(v, Tg)$ of radial velocity and temperature (x = -17 mm, z = 30 mm).

The Figure 12 shows that radial velocity fluctuations inside the recirculation zone are of the same sign of the temperature fluctuation. On the upper side of the recirculation zone the two fluctuations are in opposite sign. The joint probability distribution of Figure 13 shows two distinct peaks resulting of the intermittent nature of the flow in the transfer zone. A first peak is centred at high temperature (1700 K) and low radial velocity (1 m/s) while a second one is centred at low temperature (1000 K) and high radial velocity (5 m/s).

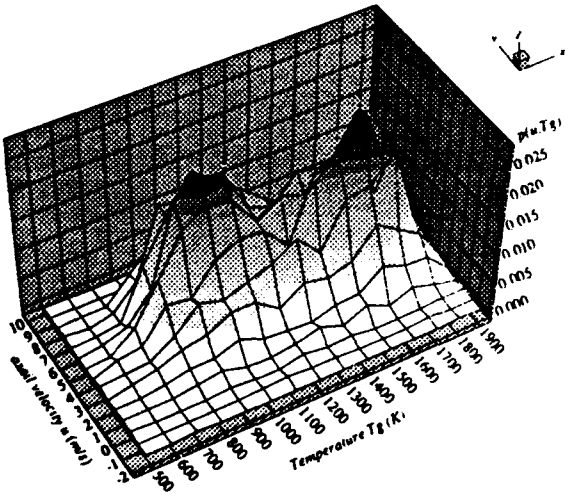

Fig. 14 Joint probability distribution $p(u, Tg)$ of axial velocity and temperature (x = -17 mm, z = 30 mm).

The same shape is observed for the joint probability distribution $p(u, Tg)$ on Figure 14, where the two peaks are located for slightly different axial velocities (4 and 5.5 m/s). The joint probability $p(u, v)$ shows that the lowest axial velocity is associated with the lowest radial velocity and the highest axial velocity is associated with the highest radial velocity. Then, we can conclude that the flame packets escape from the recirculation zone when the velocity vector is nearly parallel to the axial axis (u = 4 m/s, v = 1 m/s, Tg = 1700K).

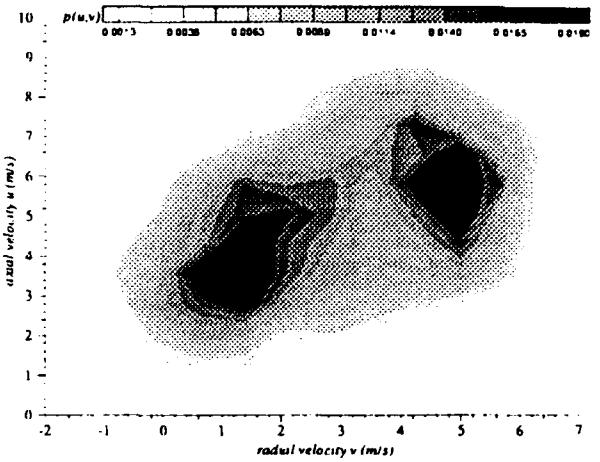

Fig. 15 Joint probability distribution $p(u, v)$ of axial and radial velocity (x = -17 mm, z = 30 mm).

The phenomena visually observed in §4.2 is confirmed and quantified by our measurements and analysis. Furthermore, the reignition mechanism is characterised.

SUMMARY

The simultaneous measurement of velocity and temperature in turbulent nonpremixed flame was made by use of LDV and numerically compensated fine wire thermocouple.

- Independent acquisition on each LDV channel is used to keep all the validated burst, while thermocouple signal is sampled with a fixed frequency. All data processing is carry out after acquisition by a dedicated software, providing more control on parameters such as RMS velocity time constant adjustment, coincidence window.
- The simultaneous velocity and temperature measurement gives information on how the temperature fluctuations are dependent of velocity.
- Numerous studies were made on Bluff-Body stabilised flames by several authors using classical diagnostic techniques. For the configuration studied in this paper, an extinction zone separating two combustion zones was observed. By coupling two classical methods and using extensive computerised post-processing, we have demonstrate the mechanism of flame reignition in the second reaction zone of a Bluff-Body flame by packets transport though an extinction zone.

REFERENCES

Boyd J. P. (1992): A fast algorithm for Chebyshev, Fourier, and sinc interpolation onto an irregular grid. Journal of Computational Physics. 103, pp 243-257.

Carey C. (1986): Statistical bias of the data from two-channel Laser Doppler Anemometer Systems. 3th Int. Symp. Appl. Laser Anemometry to Fluid Mech., Lisbon paper 3.4.

Collis D. C. and Williams M.J. (1959): Two-dimensional convection from heated wires at low Reynolds numbers. J. Fluid Mech. vol. 16, pp. 357-384.

Corbin F., Paue B. and Trinité M. (1992): Automatisation des mesures de vitesse en velocimetrie laser: application à la cartographie et au suivi de lignes de courant. 3ème Congrès Francophone de Velocimetrie Laser, 21-24 Septembre Toulouse France.

Dibble R. W., Rambach G. D., Hollenbach R. E. and Ringland J. T. (1981): Simultaneous measurement of velocity and temperature in flames using LDV and CW laser Rayleigh thermometry. Proc 7th Biannual Symp. on turbulence, Rolla Missouri.

Goss L. P., Trump D. D. and Roquemore W. M. (1988): Combined CARS/LDA instrument for simultaneous temperature and velocity measurements. Exp. Fluids 6, pp 189-198.

Heitor M. V., Taylor A. M. K. P. and Whitelaw J. H. (1985): Simultaneous velocity and temperature measurements in a premixed flame. Exp. Fluids. 3, pp 323-339.

Hilaire C., Filtopoulos E. et Trinité M. (1991): Mesure de température dans les flammes turbulentes. Revue Générale de Thermique n° 354-355, pp 1-8.

Kelly J., Namazian M., Scheffer R. W. and Perrin M. (1989): Characterization of nonpremixed turbulent bluff-body flames. Annual Report GRI, GRI.88/0168.

Kramers H. (1946): Heat Transfer from spheres to flowing media. Physica XII no 2-3, pp. 61-80.

Labbaci K., Trinité M., Stepowski D. (1988): Comparison of velocity statistics as obtained by different averaging procedures in a turbulent diffusion flame. 4th Int Symp. Lisbon, Portugal.

Namazian M., Kelly J., Periera J, Scheffer R. W. and Filtopoulos E. (1993): Characterization of nonpremixed turbulent bluff-body flames. Annual Report GRI Contract No. 5086-260-1250.

Neveu F. (1993): Mesure de température par thermocouple à fil fin, étude de la compensation numérique. CORIA-GDF research contract - Progress Report GAZ DE FRANCE-DR-CERSTA n°93.185.

Nina M. N. R. and Pita G. P. (1985): Measurements of fluctuating gas temperatures using compensated fine wire thermocouples. Agard Conference. Proc. 65th Propulsion and Energetic Panel Symposium, Bergen (Norway).

Paranthoën P., Petit C. and Lecordier J. C. (1982): The effect of the thermal prong-wire interaction on the response of a cold wire in gaseous flows (air, argon and helium). J. Fluid Mech. vol. 124, pp 457-473.

Perrin M., Kelly J.T., Namazian M. and Schefer R.W. (1990): Effect of confinement and blockage ratio on nonpremixed turbulent bluff-body burner flames. 23rd Int. Symp. on Combust. Orléans.

Scheffer R. W., Namazian M. and Kelly J. (1987): Velocity measurements in turbulent nonpremixed bluff-body stabilized flame. Combust. Sci. and Tech. Vol 56, pp 101-138.

Talby R., Anselmet F. and Fulachier L. (1990): Temperature fluctuation measurements with fine thermocouple. Exp. Fluids. 9, pp 115-118.

Touloukian Y. S., Liley P. E. and Saxena S. C. (1970): Thermal conductivity Non-metallic liquids and gases. Thermophysical Properties of Matter. The TPRC Data Series, vol. 3. IFI/Plenum.

Touloukian Y. S., Saxena S. C. and Hestermans P. (1975): Viscosity. Thermophysical Properties of Matter. The TPRC Data Series, vol. 11. IFI/Plenum.

Wills J. A. B. (1991): Data sampling and data recovery. Exp. in Fluids. 12, pp 23-28.

Yanagi T. and Mimura Y. (1981): Velocity-Temperature correlation in premixed flame. 18th Symp. (Intl) on Combustion.pp 1031-1039.

SIMULTANEOUS MEASUREMENTS OF TEMPERATURE AND OH CONCENTRATION FIELDS IN TURBULENT COMBUSTION USING ONE SINGLE LASER SOURCE

S. Kampmann and A. Leipertz

Lehrstuhl für Technische Thermodynamik (LTT),
Universität Erlangen-Nürnberg, Erlangen, Germany

ABSTRACT

A method for the simultaneous detection of the two-dimensional (2D) temperature and the 2D OH concentration distributions in a high turbulent premixed flame inside a contained combustion chamber is presented. The temperature information is obtained by Rayleigh scattering and the OH concentration from laser-induced predissociated fluorescence (LIPF). A newly designed detection optics for the separation of the synchronously induced Rayleigh and fluorescence signals allows the use of only one single laser source in combination with only one single 2D detector.

1. INTRODUCTION

In technical combustion systems high turbulent premixed flames are of increasing importance due to their low NO_x emissions. The investigation of the interaction between turbulence and combustion kinetics in premixed flames requires the knowledge of the instantaneous temperature field and of the OH concentration field as well. From accurately measured and spatially resolved temperature distributions flame thickness can be evaluated to show the influence of the turbulence on the combustion process in the context of a diagram which has been introduced by Borghi (1988) in order to characterize different areas of turbulent premixed combustion. However strong turbulence can also result in flame quenching, which may cause wrong interpretation of the temperature data if not taken into account appropriately.

The measured concentration of the OH radical can be used as an indicator for intensity of the reaction taking place and thus for the reaction zone. Therefore the simultaneous measured OH distribution is a necessary information for the interpretation of flame thickness data considering flame quenching.

Investigations have to be performed at similar operating conditions as used in technical flames, e.g., high pressure and according containment geometry, if the transferability of the results should be guaranteed. Therefore the appropriate diagnostic technique must be applicable also to contained combustion chambers which allows operation under those similar conditions.

2. TWO-DIMENSIONAL RAYLEIGH THERMOMETRY

The applicability of 2D Rayleigh scattering for gas thermography in laboratory flames has been shown nearly one decade ago by Long et al. (1985). Recently Kampmann et al. (1993) presented for the first time its use in a contained technical flame for the investigation of temperature structures in an industrial double cone swirl combustor. The Rayleigh signal was generated by a pulsed frequency doubled Nd:YAG-laser and detected with an ICCD slow-scan camera. Interferences of the Rayleigh scattered light with glare from burner surfaces and Mie scattered light from dust particles could be reduced by using high efficient filter elements in the gas supplies and by a sophisticated design of the optical access to the combustion chamber. Figure 1 shows schematically the experimental situation and the orientation of the light sheet and the observation direction in combination with to the combustion chamber.

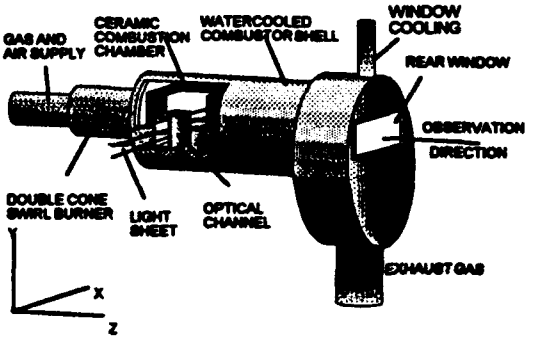

Fig. 1:Scheme of the combustion chamber with optical access

The extension of this technique to the UV for a more efficient generation of the Rayleigh signal due to the $1/\lambda^4$ relation of the Rayleigh cross section was recently done by Kampmann et al. (1994) using a KrF excimer laser source (λ=248nm). The accuracy of the temperature data being evaluated from the shot-noise limited Rayleigh signals was about ±5 % for a typical combustion temperature of 1550 K. As an example Figure 2 shows one typical result when crossing the flame front within an instantaneous temperature distribution at one particular position in the turbulent flame.

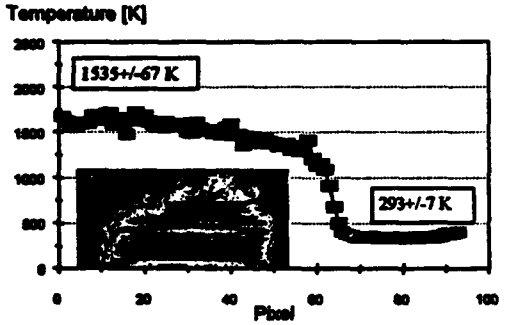

Fig. 2 Cross section through the flame front indicating the accuracy of the excimer laser Rayleigh probe for instantaneous temperature fields measurements

3. SIMULTANEOUS 2D RAYLEIGH AND OH PLANAR LASER-INDUCED FLUORESCENCE MEASUREMENTS

Planar laser-induced fluorescence (LIF) measurements of the OH radical by the excitation with a KrF excimer laser has been used successfully for the determination of flame structures and reaction zones in laboratory flames as well as in technical applications by Versluis et al. (1992) and Koch et al. (1993) making use of the predissociated fluorescence technique (LIPF) introduced by Andresen et al. (1988).

For collecting well evaluable Rayleigh signal intensities an UV-telescope with high aperture (f/1.0) had to be used for the combined Rayleigh/LIPF measurements.

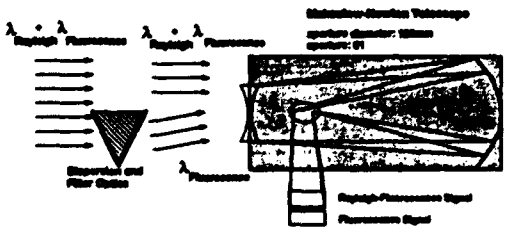

Fig. 3: Scheme of the detection arrangement

A refractive filter optics has been developed in order to separate the Rayleigh signal from the OH fluorescence

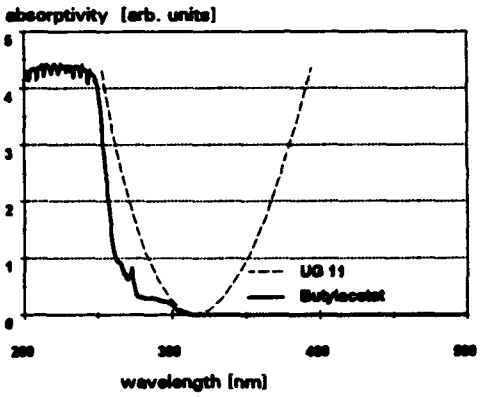

Fig. 4: Absorption spectra for butylacetat and the used colour glas filter

signal in front of the telescope. Figure 3 shows a scheme of the choosen optical configuration. A prism was formed with two parallel plates of fused silica. The volume between the plates was filled with butylacetate, which acts as a longpass filter at a cutoff wavelength at 250 nm (see Fig. 4). This prism is placed in front of the telescope in such a way that it covers only a part of the aperture. The other part of the signal which passes the uncovered area of the aperture will unaffectedly be imaged on the array detector placed behind the telescope and gives thus a combined Rayleigh/LIF signal distribution $I_{Ray,LIF}(x_1, y_1)$. From that part of the signal which is detected through the prism, the Rayleigh signal is absorbed and the transmitted LIF signal is deviated, which results in a LIF signal distribution at a new location on the detector $I_{LIF}(x_2, y_2)$. However, for temperature evaluation the pure Rayleigh signal distribution $I_{RAY}(x_1, y_1)$ has to be known. If the ratio of the LIF signal at location 1 to the LIF signal at location 2 can be measured

$$R = \frac{I_{LIF}(x_1, y_1)}{I_{LIF}(x_2, y_2)} \qquad (1)$$

the pure Rayleigh signal can be calculated from the simultaneously collected data by

$$I_{Rayleigh}(x_1, y_1) = I_{Ray,LIF}(x_1, y_1) - R \cdot I_{LIF}(x_2, y_2) \qquad (2)$$

The required temperature fields can be calculated from these data sets following the method presented by Fourguette et. al. (1986). In order to measure the ratio R one UG11 filter was used in front of the array detector. This filter blocked the Rayleigh contribution of the combined Rayleigh/LIF signal (see Fig. 4) providing the same transmission at both signal paths. R can be determined from the resulting LIF signals alt both locations. Variations of R could easily be achieved by adjusting the position of the prism in front of

the telescope. As best done we regard a LIF signal as low as necessary and a combined Rayleigh/LIF signal as high as possible for reliable temperature information.

The Rayleigh signal, however, can also be interfered by resonant fluorescence signals. There are two possible ways to overcome this problem:

a) Using a weak excitation transition, so that the interference is negligible. This however works only with detector systems with high dynamic range, e.g., slow-scan CCDs, as the wavelength shifted fluorescence signal becomes also smaller and has to be detected together with the Rayleigh signal within the dynamic range of the CCD detector.

b) Estimation of the contribution of the resonant fluorescence signal by two measurements of the scattered light intensities at laser wavelength in a laminar flame, for one tuning the laser on an OH excitation wavelength and for one tuning it off. The difference of the signal intensities gives the intensity of the resonant fluorescence signal. This can be taken into account appropriately by the knowledge of the wavelength shifted fluorescence distribution.

4. FIRST RESULTS

First measurements have been performed in the turbulent combustion field of a technical burner of Asea Brown Boveri (ABB) which has been described by Kampmann et al. (1993) elsewhere. The detected signals were generated by a laser pulse of 140mJ. The best spatial resolution of our detector system was calculated to be 140 µm per pixel.

Figure 5 shows the first results of our simultaneous Rayleigh/LIF experiments. Picture part (a) exhibits the combined Rayleigh/LIF signal distribution, picture part (b) the LIF distribution alone. From these data the pure Rayleigh signal distribution was reconstructed, from which the temperature distribution could be calculated, which is shown in picture part (c).

A comparison of the temperature distribution (c) and the OH concentration field (b) shows very good agreement in the observed structures. At locations where ignition temperature is reached also OH starts to appear and increasing concentration indicates the higher combustion intensity.

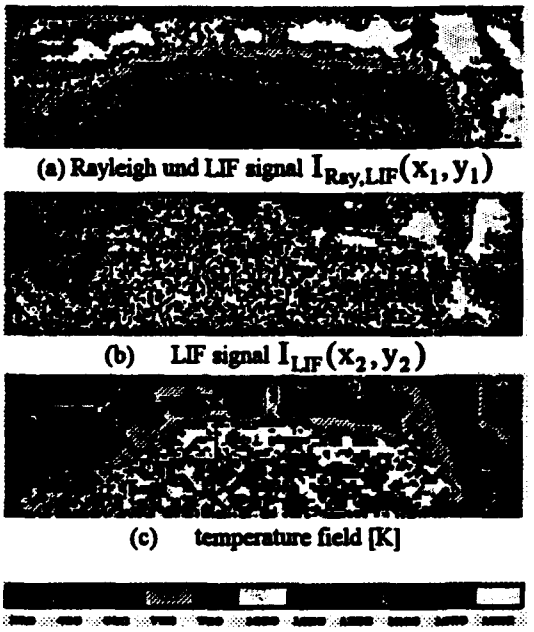

Fig 5: Results of the simultaneous measurements

ACKNOWLEDGEMENTS

The authors gratefully acknowledge financial support for parts of the work by the Deutsche Forschungsgemeinschaft, by the Bundesministerium für Forschung und Technologie and by the Max-Buchner Forschungsstiftung. They also thank for the very fruitful cooperation they have with Drs. K. Döbbeling, W. Polifke, J. Haumann, and Th. Sattelmayer of the Aerodynamic Group of Asea Brown Boveri Research Center, Baden/Dättwil (Switzerland), who also provided the technical burner and the combustion chamber for this investigation.

REFERENCES

Andresen, P., Bath, A., Gröger, W., Lülf, H.W., Meijer, G. & ter Meulen, J. J. 1988, Laser Induced Fluorescence with Tunable Excimer Lasers as a Possible Method for Instantaneous Temperature Field Measurements at High Pressures: Checks with an Atmospheric Flame, Appl. Optics, Vol. 27, p. 365

Borghi, R. 1988, Turbulent Combustion Modelling, Progr. Energy Combustion Science, Vol. 14, 245

Fourguette, D.C., Zurn, R.M. & Long, M.B. 1986, Two-Dimensional Rayleigh Thermometry in a Turbulent Nonpremixed Methane-Hydrogen Flame, Combust. Science and Technology, Vol. 44, p. 307

Kampmann, S., Leipertz, A., Döbbeling, K., Haumann, J. & Sattelmayer, Th. 1993, Two-Dimensional Temperature Measurements in a Technical Combustor with Laser Rayleigh Scattering, Appl. Optics, Vol. 32, p. 6167

Kampmann, S., Seeger, T. & Leipertz, A. 1994, Simultaneous CARS and 2D Laser Rayleigh Thermometry in a Contained Technical Swirl Combustor, submitted for publication (March 1994)

Koch, A., Chrysostomou, A., Andresen, P. & Bornscheuer, W. 1993, Multi-Species Detection in Spray Flames with Turnable Excimer Lasers, Appl. Physics B, Vol. 56, p. 156

Versluis, M., Boogaarts, M., Klein-Douwel, R., Thus, B., de Jongh, W., Braam, A., ter Meulen, J.J., Meerts, W.L. & Meijer, G. 1992, Laser-Induced Fluorescence Imaging in a 100kW Natural Gas Flame, Appl. Physics B, Vol. 55, p. 167

APPLICATION OF CARS ON TEMPERATURE MEASUREMENTS IN A TURBULENT PREMIXED REACTIVE FLOW

Y. Kawaguchi and K. Kontani

Mechanical Engineering Laboratory,
Agency of Industrial Science and Technology, MITI
Tsukuba, 305 JAPAN

ABSTRACT

In this study, a high-resolution coherent anti-Stokes Raman spectroscopy (CARS) system was developed for use in combustion thermometry. This system is characterized by a folded BOX-type beam crossing geometry and multiplexed signal acquisition. Although a complicated experimental system is necessary for these features, this system has high spatial and temporal resolutions, which provide for a more reliable measurement of the temperature in turbulent flames.

In this project, careful consideration was given to developing the CARS system. In parallel to this, calculated CARS spectra were generated based on the physical constants and transfer functions of the experimental facilities.

The applicability of this system for temperature measurement has been tested in a premixed turbulent flame. Based on the method of full fitting with calculated spectra, experimental CARS spectra were analyzed. There was good coincidence between the experimental and calculated spectra over a wide range of temperatures. The correspondence between mean flame temperatures obtained by CARS and those by fine wire thermocouple were also good.

1. INTRODUCTION

In past research, Kawaguchi and Hama (1988) have made velocity measurements in a hydrogen combustor using a laser Doppler anemometer in order to investigate the combustor's performance from the stand point of fluid dynamics. They found that the quick expansion caused by rapid combustion of hydrogen mixture greatly affects the mean velocity streamline in the flame holder. This streamline perturbation was closely related to flame stability, which is especially important in determining the range of applicability of hydrogen combustors. At the same time, variations of turbulence intensity and length scale distributions were observed in reactive cases when compared to nonreactive cases. The analytical study to find the cause of the velocity field alteration was potentially insightful, but a complete analysis was not conducted there because the authors had no information about either the instantaneous temperature or concentration at that time.

Due to recent developments in laser technology, optical techniques for scalar quantity measurements are progressing rapidly. CARS is one such technique, and it is applicable for gas temperature measurements in relatively high temperature regions, such as combustion (Eckbreth et. al. 1979). Such techniques will likely give additional information on scalar quantities, and when they are combined with velocity measurements, they help to get a more complete view of the complicated processes of combustion in industrial facilities.

CARS is similar to LDA in its outlook. Both CARS and LDA use excitation laser beams and analyze scattered light. Being optical diagnostics, they have similar advantages such as non-invasive characteristics and high temporal and spatial resolutions. But they differ on the basic principle of light scattering. LDA is based on Mie-scattering and is classified as elastic scattering. The instrumentation for LDA is sophisticated but relatively simple and the resultant data have a linear relation with velocity, making it easy to interpret. In contrast, CARS is based on the Raman scattering process and the resultant data contain information of molecular species. Therefore, CARS requires a more complicated data processing procedure, namely interpretation of spectra based on simulated spectra. Because of this requirement, spectral simulation of CARS will be described first.

2. SPECTRAL SIMULATION OF CARS

Calculated CARS spectra are necessary for analyzing the experimentally obtained CARS spectra. This is due in part to complications caused by nonlinear characteristics of CARS. Since the number density of molecules is a function of temperature, the shape of CARS spectra have a temperature dependency-this is the principle of CARS thermometry. But measurement of the shape of a spectrum, such as band width or proportion, is a complicated function of temperature, which depends on the experimental facilities used. Therefore, a set of calculated CARS spectra, obtained using transfer functions of

the experimental facilities, is needed for reliable spectral analysis.

Although a number of articles which describe CARS spectrum modeling exist (Hall, 1979, Eckbreth, 1988), only a brief description will be given here. The resonant contributions to the third-order nonlinear electric susceptibility $\chi^{(3)}$ can be expressed as a sum over neighboring transitions, and the full CARS susceptibility may be expressed as:

$$\chi^{(3)} = \sum_j \chi_{rj} + \chi_{nr} = \sum_j K_j \frac{\Gamma_j}{2\Delta\omega_j - i\Gamma_j} + \chi_{nr} \quad (1)$$

where the j summation is over all Q-branch vibration-rotation transitions in the vicinity of $\omega_1 - \omega_2$, and ω_1 and ω_2 are wave numbers of pump and probe beams respectively. Γ_j is the homogeneous line width estimated by the full width at half maximum, and $\Delta\omega_j$ is the detuning $\omega_j - (\omega_1 - \omega_2)$. For the line widths, Γ_j, $0.1\,cm^{-1}$ was given for room temperature and a $T^{-1/2}$ temperature dependency was assumed.

Calculations were made for N_2. As reported in Hall (1979), in an atmospheric flame, the resonant CARS contribution from N_2 will be much stronger than the non-resonant contribution χ_{nr}, therefore χ_{nr} was eliminated in this study. The first step in calculation of the resonant term χ_r, was to calculate the total energy using the following equation:

$$E = E_v + E_r = \omega_e(v+\frac{1}{2}) - \omega_e x_e (v+\frac{1}{2})^2 + B_v(J(J+1)) - D_v(J(J+1))^2 \quad (2)$$

$$B_v = B_e - \alpha_e(v+\frac{1}{2})$$

where optical constants are shown in Table 1, in unit of cm^{-1}. From the energy difference between upper and lower vibration-rotation states, ω_j was determined. Next, K_j was determined from the population using Boltzmann's statistics and dependency on nuclear spin.

The frequency distribution of the scattered power for finite laser line width can be described by the convolution integral,

$$I(\omega_3) = K \int \left|\chi^{(3)}(\omega_3' - \omega_{1a} - \omega_{1b} + \omega_2)\right|^2 \times f_1(\omega_{1a})\, f_1(\omega_{1b})\, f_2(\omega_2)\, f_3(\omega_3 - \omega_3') \times \delta(\omega_3' - \omega_{1a} - \omega_{1b} + \omega_2)\, d\omega_{1a}\, d\omega_{1b}\, d\omega_2\, d\omega_3' \quad (3)$$

ω_e	$\omega_e x_e$	B_e	α_e	D_v
2358.57	14.324	1.99824	0.017318	5.76E-6

Table 1 Optical constants of N_2

where $f_1(\omega_1)$ and $f_2(\omega_2)$ are, respectively, the power distribution of pump and probe beam, respectively, and $f_3(\omega_3 - \omega'_3)$ is the slit function of the spectrometer system. Triangular-shaped functions were used and the widths are given in Table 2.

A computer program was developed to calculate the right side of equation (3). As a result of the nonlinearity of CARS, the effect of spectral interference between neighboring transitions and between resonant and non-resonant contributions to $\chi^{(3)}$ in equation (1) may be significant. Therefore, careful selection of both wave number resolving power is important to accurately the CARS spectrum. In this study, 2000 points were used to cover the region from 2250 to 2350 cm^{-1} of Raman shift.

The calculated results are shown in Figure 1 in steps of

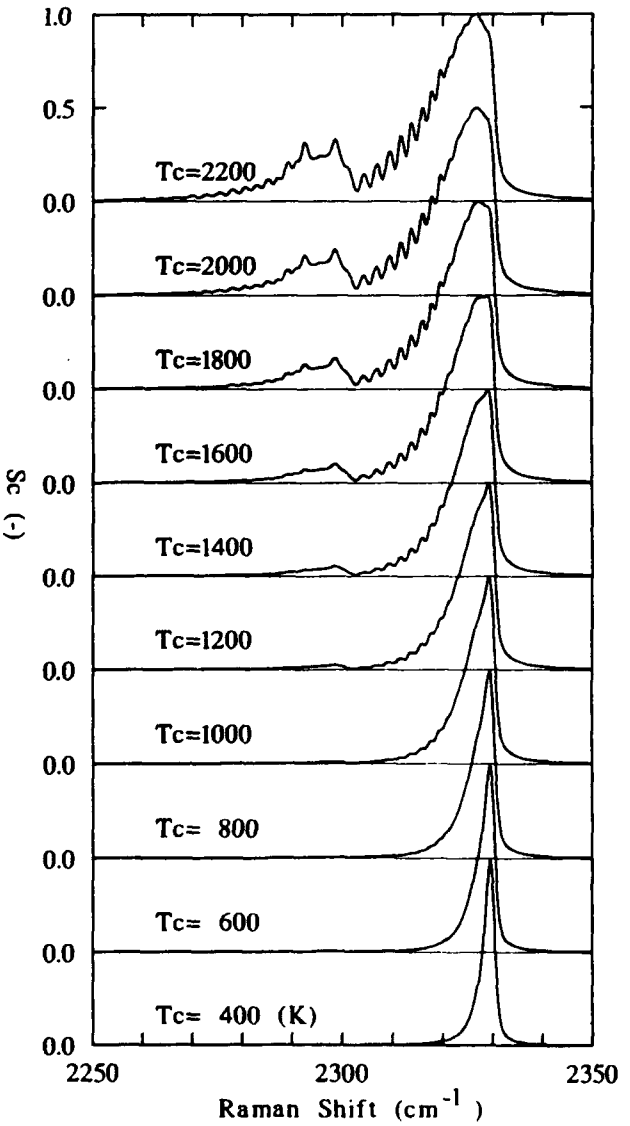

Fig 1 Calculated results of CARS spectra

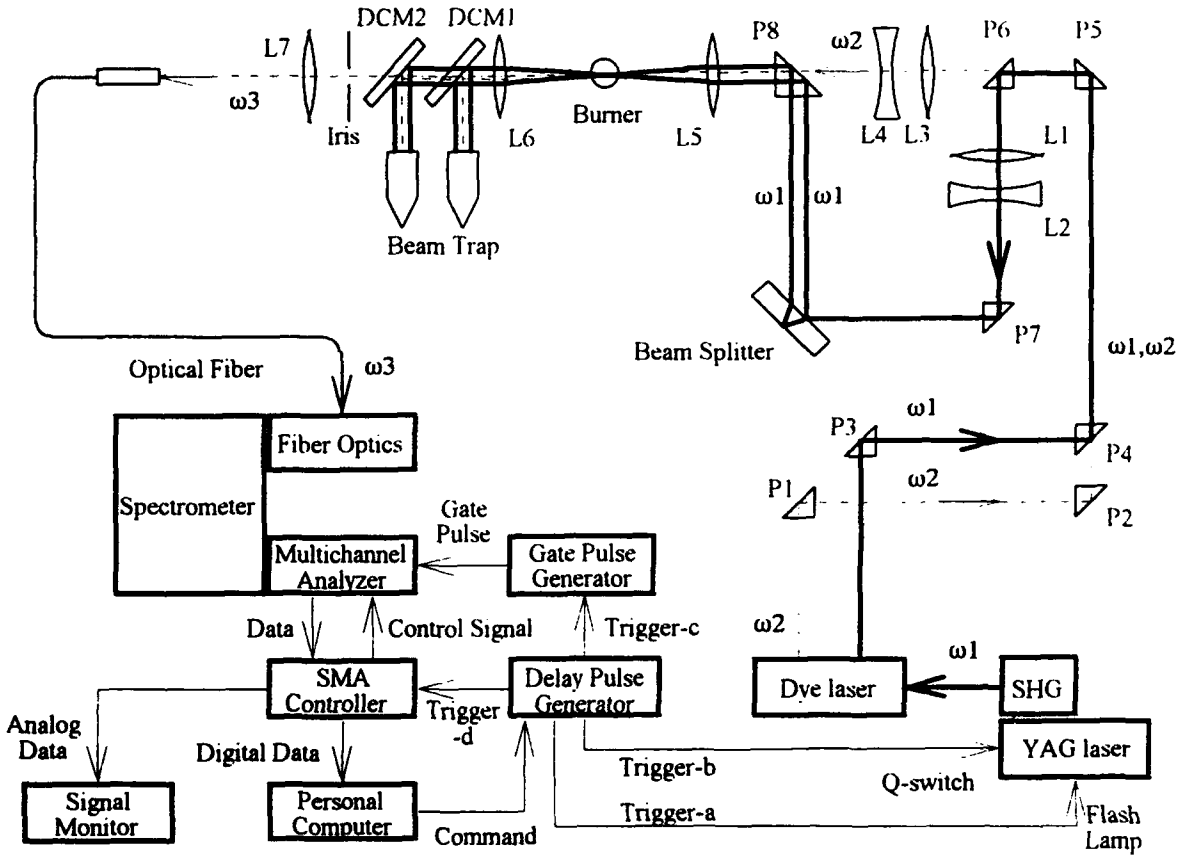

Fig. 2 Experimental arrangement of the CARS system

200K. The calculated spectra are similar in shape to Hall's results (Hall, 1979). However, a slight difference can be seen due to differences in the assumed shape and width of $\int_1$, $\int_2$ and $\int_3$. The calculated spectra in this section was used for spectral fitting described in section 4.

From these results, it is seen that there are three features in the shape of CARS spectra calculated at high temperature.

a) The band-width of the main peak located near 2330cm^{-1} increases with increase in temperature.

b) Small peaks, due to rotational transitions, appear at Raman shifts of 2300-2320cm^{-1}, and at temperatures beyond 1200K.

c) A small secondary band appears near 2280-2300cm^{-1} when the temperature exceeds 1200K.

Feature a) occurs at temperatures below 1000K. Therefore, this feature can be used at relatively low temperatures, where b) and c) characteristics are not prominent.

3. EXPERIMENTAL APPARATUS AND PROCEDURE

3.1 CARS Optical System

Figure 2 illustrates the setup of CARS thermometry system employed in this work. The system is composed of two lasers, transmitting and receiving optics, a spectrometer, controllers and a personal computer. The pump laser and probe laser parameters, and spectrometer characteristics of this experiment are summarized in Table 2.

Pump Beam	Source	YAG Second Harmonics
	Wave Length	532 nm
	Band Width (FWHM)	0.03 nm
	Pulse Energy	135 mJ
Probe Beam	Source	R610,R640 Mixed Dye Broad Band Emission
	Wave Length	607 nm
	Band Width (FWHM)	5.1 nm
	Pulse Energy	37mJ
Spectrometer System	Spectrometer	f=800 mm, Double
	Detector	Diode Array, 512ch/12.5mm
	Image Intensifier	Double MCP
	Dispersion	0.383 cm^{-1}/ch

Table 2 Lasers and spectrometer parameters

A frequency-doubled pulsed Nd:YAG laser (SL-803, Spectron Laser Systems) and a broad-band dye laser (SL-4000G, Spectron Laser Systems) were used for the pump and probe sources, respectively. The produced 1064nm beam in YAG laser was frequency doubled to 532nm, and a nominal output pulse energy of 330mJ was obtained. The dye laser,

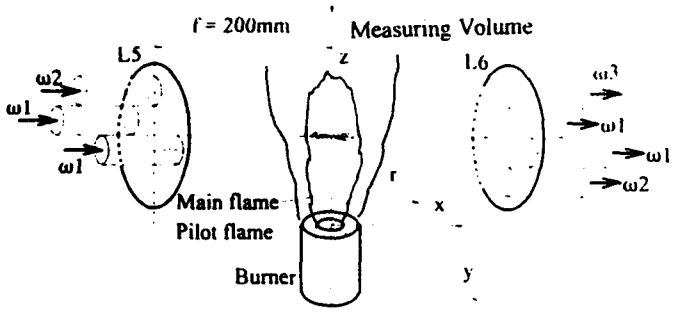

Fig. 3 Folded BOXCARS beam alignment

having a transversely pumped oscillator dye cell and two longitudinally pumped amplifier dye cells, was excited by a portion of the Nd:YAG laser output. The dye laser was carefully tuned to match the requirement for N_2, Q-branch thermometry by adjusting the concentration of two kinds of laser dyes, i.e. Rhodamine 610 Chloride and Rhodamine 640 Chloride in methanol. As the power and transverse mode of the dye laser beam output is very sensitive to misalignment, the optical components in the dye laser were carefully adjusted before every experiment.

A plane view of the optical system used for this experiment is also shown in Figure 2. Prisms (P1 to P8) were used to transfer the beams. After passing through a telescope (L1 and L2), the pump beam (ω_1) shown by the solid line was divided into two parallel beams at the beam splitter and transferred to a collimating lens (L5). A half-reflection coated optical parallel was used for the beam splitter. The probe beam (ω_2, shown by a dotted line) passes over P4 and P6, and also passes through a telescope (L3 and L4).

Figure 3 shows the close up view near the measuring volume of CARS. To tune the system, each of three beams was aligned parallel to the x-axis shown in Fig. 3, between P8 and L5, which is found using a mirror and screen placed in a remote position. If the three beams have parallel wavefronts and are aligned parallel to each other, by definition all the beams will have their waist at the crossing point in the burner. However, due to wavefront sphericity of pump and probe beams, their waists are not coincident at the crossing point. The adjustable telescopes in each beams were used to eliminate this effect and to position the beam waist at the crossing point. The waist position was monitored by a small sheet of paper inserted near the focus. The intensity of cracking sound, at each laser shot, changes when the paper is moved back and forth in axial direction. At the waist position, the sound becomes loudest.

Due to the wavelength difference between ω_1 and ω_2, slight misalignment of the crossing point can occur due to chromatic aberration in L5. In order to obtain precise geometrical arrangement of beams near the crossing point, a three dimensional record of beam spots was obtained. To record this, a sheet of exposed photographic printing paper and a transversing stage were used. When the paper was moved at a slight angle to the beam axis by the transversing stage, a series of spots burnt by the laser were recorded. This enabled precise alignment to be made.

The phase matching arrangement used for this study is called 'folded BOXCARS' and is shown in Figure 3. In this arrangement, two pumping beams, ω_1 and a probe beam ω_2, are collimated by a front lens L5, which has a focal length of 200mm. The crossing angle α between ω_1 and ω_2 was 2deg. A large α can reduce the size of the measuring volume, but it weakens the signal. One advantage of folded BOXCARS is the complete angular and spatial separation of the CARS beam. From this perspective, a large α also helps to confirm the separation of CARS signal from ω_1 and ω_2.

After passing through the measuring point, the four beams, including ω_3 were recollimated by a lens L6, having the same focal length as L5. Pumping and probe beams were filtered out by two identical dichroic mirrors, which had coatings for short wavelength transmission and long wavelength reflection. The cutoff wavelength was selected to ensure N_2 CARS separation from ω_1 and ω_2. An iris was also applied for spatial separation of ω_3. After passing the iris, the CARS signal was launched into an optical fiber and transferred to the spectrometer system.

A multiplexed spectral acquisition system composed of a Czerny-Turner spectrometer (CT-80D, JUSCO) and a spectrometric multichannel analyzer (SMA, D/SIDA-D512, Princeton Instruments) was employed in order to detect the full CARS spectrum for each individual laser pulse. The width of N_2 Q-branch CARS spectrum was relatively narrow, with a typical value between 20-50cm^{-1}. Since precise analysis of this region is necessary for CARS thermometry, large dispersion of the spectrometer is needed. The spectrometer employed was a the modified double-monochromator having a focal length of 0.8m and a f-number of 6.8. In combination with the SMA, which has a double row of 512 pixel linear diode arrays, the dispersion turned out to be 0.383cm^{-1}/channel and was satisfactory for purposes of this experiment. At the same time, sensitive and high S/N detectors were important to discriminate elusive CARS signal from high temperature gas. Therefore, a SMA having a double MCP intensifier was used. A delay pulse generator (DG535, Princeton Instruments) initiated digitization and storage of the data in the personal computer (PC9801, NEC). This generator also triggered the flash lamp and Q-switch of YAG laser, and the gating of the SMA.

The recorded dataset was analyzed by an engineering work station (AXP-3000/400, Digital Equipment Corp.) using data processing programs.

3.2 PREMIXED BURNER

The burner used in this experiment (Figure 4) was specifically designed to maintain uniform experimental conditions and help researchers to conduct bench-mark testing of measurement

techniques (Yoshida, 1987a). Detailed characteristics of the velocity field, including the Reynolds stress distribution, have been reported by Maeda (1987). Flow rates of air and main fuel was measured and controlled by mass flow meter/controllers (F100/200, Oval Engng. Corp.). Conditions relating to fuel and air flow are summarized in Table 3. These coincide with those suggested in the literature (Yoshida, 1987a).

The burner was mounted on a three dimensional transversing stage (LTS+Mark-14, Sigma Koki Co.). The location of the CARS measuring volume was fixed to the floor and position of the burner was changed to measure spatial distribution of temperature. All measurements in this work were made at 60mm downstream from the burner outlet where the temperature was measured by Asanuma (1987) and Yoshida (1987b) with a fine wire thermocouple.

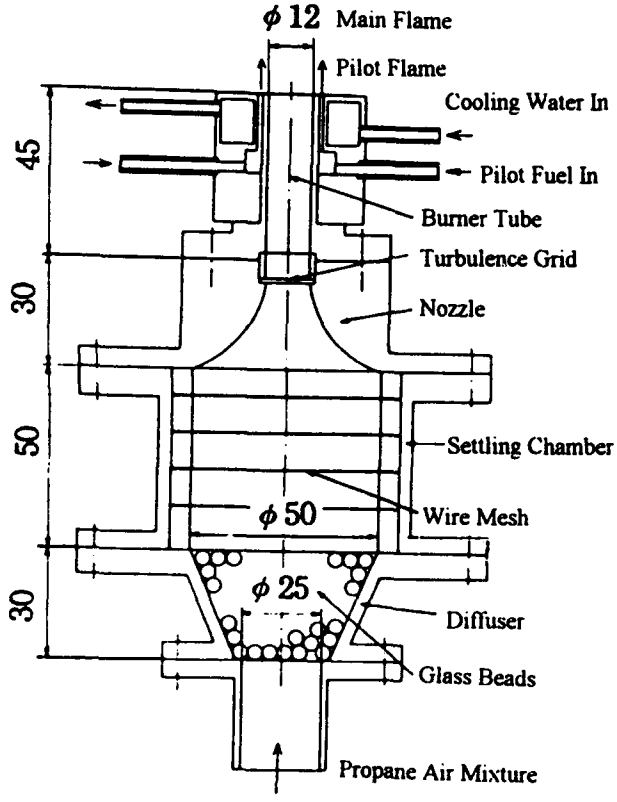

Fig. 4 Premixed burner

Main Flame	
Fuel	Propane
Mean velocity of Mixture at Outlet	4.64 m/s
Equivalence Ratio	0.73
Flow rate of Air	5.08E-4 m^3/s
Flow rate of Fuel	1.55E-5 m^3/s
Pilot Flame	
Fuel	Methane
Flow rate	6.67E-6 m^3/s

Table 3 Experimental condition of flame

4. RESULTS AND DISCUSSION

4.1 POSSIBLE ERROR SOURCES OF CARS THERMOMETRY

Experimentally obtained spectra always contain some errors. When the distortion of the spectra is large, subsequent analysis may result in unrealistic temperature if it is not conducted carefully. Most of the distortion is recognizable through some standard in the processing program, but compensation or reconstruction of the signal is almost impossible. Therefore, optimization of the system, based on preliminary experiments and careful investigation of data, is necessary before main experimental runs can start. Typical distortions, probable causes and appropriate countermeasures are discussed.

a) Poor alignment of optics. Excessively weak signal was observed due to poor alignment of optics or lasers. Step by step alignment of all components are needed in this case. Generally, air at room temperature produces an intense N_2 CARS signal. Once a weak signal can be found observed, intensifying it is simplified.

b) Effect of high temperature. Generally, high temperature gas produces weak signal. The relation between the excitation laser power, number density of molecules and intensity of CARS signal can be expressed as follows,

$$I_{\omega 3} \propto I_{\omega 1}^2 I_{\omega 2} N^2 \qquad (5)$$

where, $I_{\omega 1}$, $I_{\omega 2}$ and $I_{\omega 3}$ and intensities of pumping, probing and CARS beams respectively. N is the number density of molecules under observation. In an isobaric state, N is inversely proportional to absolute temperature. Therefore, the intensity of CARS generally becomes weak at high temperatures. Although this effect cannot be avoided in high-temperature measurements, potential errors due to low S/N ratio should be expected. The noise appearing in spectral domain could be misunderstood to be characteristics of high temperature, such as main band broadening or secondary peaks. Therefore, very weak signals comparable to noise, signal has biasing effect which acts to increase the resultant temperature. When the signal magnitude reaches the photon counting level, distortion of the spectral shape cannot be avoided without accumulating multiple signals.

c) Beam steering due to temperature gradient. Weak signals intermittently observed in the flame. This was probably the result of the effect of high temperatures described in b), as well as beam steering caused by large refractive index gradients. These two effects are difficult to separate.

d) Saturated data signal. Constant occurrence of this phenomenon was avoided by reducing the gain of SMA. In practice, intermittent appearance of intense signals from low temperatures could be observed. In this case, saturated signals were discarded before data processing.

e) Breakdown. As seen from equation (5), high laser power helps to produce an intense CARS signal. But too much power can cause a breakdown in the measurement volume, making CARS measurements impossible. Breakdown is indicated by a 'snapping' sound and a white spark produced near the focal point.

f) Shot-by-shot fluctuation of spectra due to fluctuation of the dye laser profile. This effect can be estimated by measuring a steady-state sample, such as air at room temperature. Generally, compensation of this distortion can be made by using a reference cell. But to achieve identical phase-matching in measurement volume and reference cell was difficult for the multi-mode laser employed in this experiment. Since much improvement could not be attained due to this limitation, a reference cell was not used in this study.

g) Bias due to large measuring volume. A biasing effect can occur when a large measuring volume relative to the characteristic temperature scale is used. In this situation, the measuring volume can be occupied by high and low temperature regions simultaneously. In such case, the intense CARS signal from the low temperature region dominates that of the high temperature region. Therefore, the resulting CARS signal is biased towards the lower temperature. In this study, this effect was observed when the focal length of L5 was changed to 500mm and the measuring volume was larger than that described in section 3.1

h) Bias due to ensemble-averaging. When the spectrum was obtained by accumulation of signals from multiple shots of the laser, and the temperature fluctuation of the sample was large, a biasing effect similar to g) could occur. In such case, the resultant temperature was lower than the mean temperature.

Most of these effects could be avoided or minimized by preliminary experiments. Sometimes, one error factor was eliminated at the cost of increasing another type of error. For example, the effect of low S/N ratio b) was eliminated by multiple data acquisition, but then the biasing effect described in h) can occur. Generally, g) and h) should be estimated considering the type of object to be measured.

4.2 EXPERIMENTAL CARS SPECTRA

Figure 5 shows the radial variation of CARS spectra obtained in the flame. Signals from 50 laser pulses were accumulated to obtain each spectrum. As described in the previous section, the number of pulses were determined from the measuring object. In this case, temporal temperature fluctuation was not large except for a small region of flame. The number of pulses was optimized through the preliminary experiments. As stated in the previous section, the size of the measuring volume was critical.

In spite of the severe conditions, i.e. folded BOX optical alignment and multiplexed data acquisition, the quality of observed CARS spectra was adequate. The shape of the spectra obtained between 4 and 10mm clearly shows the high temperature characteristics in the calculated spectra described in section 2. It is characterized by a widening of the main band, appearance of rotational structure, and a secondary peak appearing around a Raman shift of 2300 cm^{-1}.

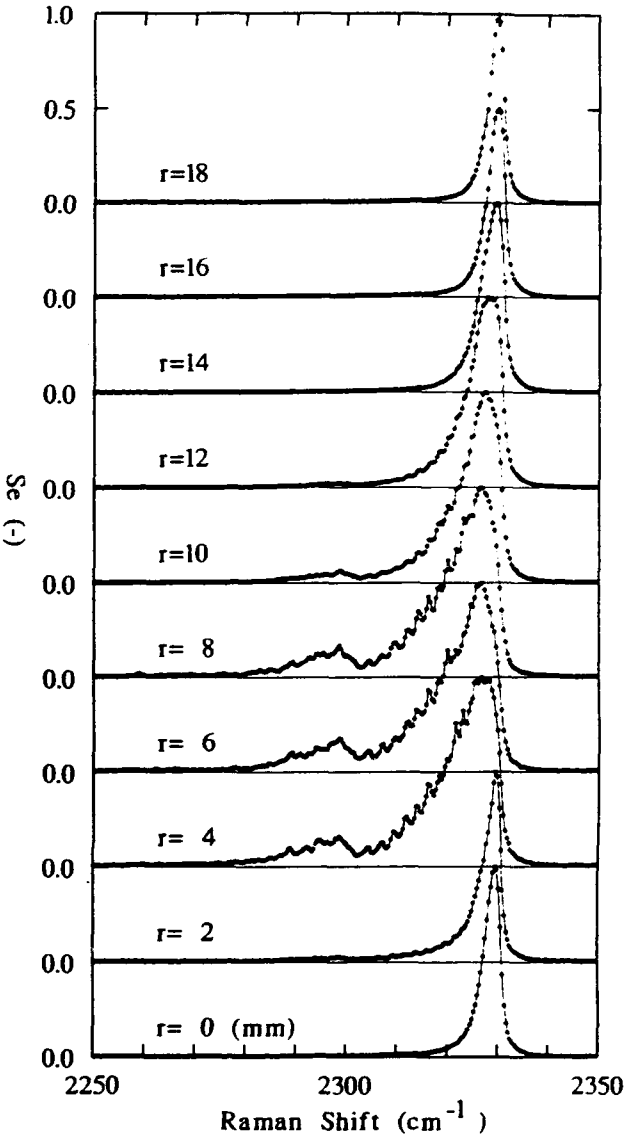

Fig. 5 Experimental CARS spectra in flame

4.3 SPECTRAL MATCHING PROCEDURE

The recorded experimental spectra were examined individually to identify distorted spectra. Probable courses of the spectral distortion have been discussed in Section 4.2. After rejecting the distorted data, the remaining data were analyzed using a computer program. For the analysis of experimentally obtained CARS signals, a full-fitting method was selected. This program calculated an integrated residual defined as follows.

$$R(T_c) = \int_{\omega_s}^{\omega_e} (S_e(\omega) - S_c(\omega, T_c))^2 \, d\omega \qquad (6)$$

where ω_s and ω_e were 2250 and 2350cm^{-1} respectively. S_c and S_e are the calculated and experimental spectra, respectively. The estimated temperature T_e was given as the temperature which produced the minimum R. Since the theoretical spectra are given in increments of 100K, interpolation was made around the minimum of R.

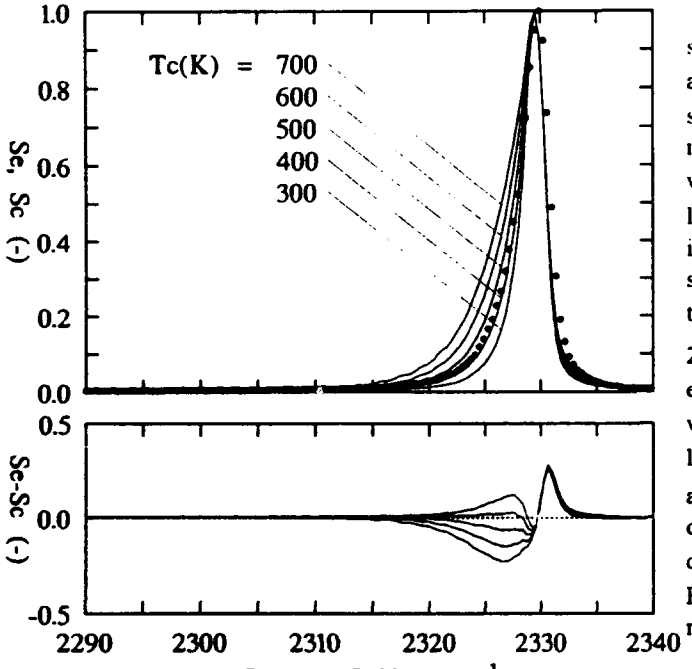

Fig. 6 Comparison of experimental spectrum S_e at r=19mm (dot) and calculated spectra S_c(line)

This calculation can be used not only to determine probable temperature but also to estimate the quality of CARS spectra obtained. If a spectrum can be found which completely matches S_c, R_{min} becomes 0. However, for a distorted spectrum, R_{min} is always larger than that of a non-distorted spectrum. Therefore, R_{min} provides one way to evaluate the quality of CARS spectra.

In Figures 6 and 7, S_e and a group of S_c are shown at the same scale. The differences between S_e and each of S_c are also shown in these figures. Ideally, $S_e - S_c$ should show a small value over a wide range of Raman shift, when the optimum S_c is found. Figure 6 shows the comparison of S_e, which was obtained at r=19mm and a group of S_c, which was selected from the calculated library. In upper half of Figure 6, it is seen that the correspondence between the experimental spectrum and calculated one for T_c=400K is good. Looking at the differential spectra, a prominent peak of $S_e - S_c$ appears at 2331cm^{-1}. Around 2327cm^{-1}, the difference of $S_e - S_c$ is either negative or positive, depending on T_c. It is found that when an appropriate S_c is chosen, the residual caused by the latter peak or valley can be minimized. Although the reason of a peak at 2331cm^{-1} remains is unknown, this peak is independent of T_c, however this peak only acts to offset R and does not affect the optimum choice of S_c. In case shown in Figure 6, interpolation of residuals R from 300, 400 and 500K resulted T_e=422K.

Figure 7 shows similar comparison for S_e obtained at r=6mm. In this case, special characteristics of high temperature were obvious in the experimental spectrum; therefore, S_c at

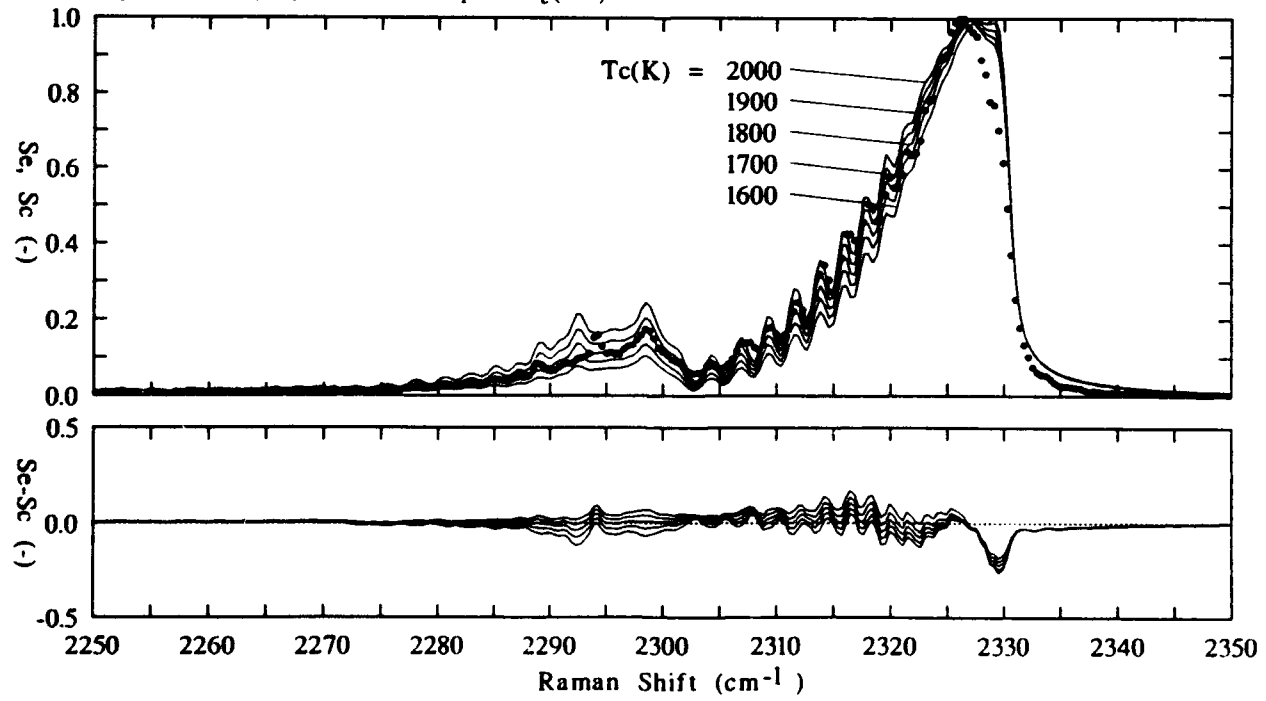

Fig. 7 Comparison of experimental spectrum S_e at r=6mm (dot) and calculated spectra S_c (line)

relatively high temperature such as T_c=1800K, corresponds to experimental one. The computer algorithm makes final choices in the balance of secondary peak appearing from 2290 to 2303cm^{-1}, the region between 2305 to 2325cm^{-1} where rotational transition is observed, and the valley seen at 2329cm^{-1}. And this choice does not give large discrepancy from human inspection, that can be seen from the figure.

4.3 MEAN TEMPERATURE IN PREMIXED FLAME

The experimentally determined mean temperature profile at 60mm downstream of burner outlet is shown by open circles in Figure 8. This temperature is determined as a mean of ten data, each are based on 50 shots of laser pulse. The length of error bar around the circle indicates twice of root mean square of data fluctuation. As each data was composed of multiple shots, the rms is not intensity of fluctuating temperature but ambiguity of determining mean temperature. Results from fine-wire thermocouple measurements by Asanuma (1987) and Yoshida (1987b) are also shown by solid and dotted lines. Temperatures obtained by CARS corresponds those by fine wire thermocouple very well.

There is a low temperature region near the burner axis, where the combustion is not completed. Relatively high and constant temperature is observed between the radial positions of 4 and 8mm, where reacted gas is flowing. Between these two regions, a layer having high mean temperature gradient is observed. This layer corresponds to wrinkled flame zone and high temperature fluctuation was observed here by Yoshida (1987b). In this region, error bar of CARS measurement is extending. Although this fluctuation is not corresponding to the temperature fluctuation directory, it is seen that the ambiguity of mean temperature is affected by fluctuating temperature.

5. CONCLUSIONS

A CARS system having features of a folded BOX-type beam crossing geometry and a multiplexed signal acquisition system was developed in the purpose of thermometry in combustion. Detailed experimental considerations were also made on developed CARS system. Discussion on probable error source and its countermeasure was also made. The applicability of this system was tested in a premixed turbulent flame. The temperatures determined by CARS was compared to the results of fine wire thermocouple.

In spite of the severe conditions, the quality of experimental CARS spectra was adequate. There were good correspondence between experimental and calculated CARS spectra from 400K to 1900K. This correspondence over a wide range of temperature suggests validity of present experimental and analytical scheme. The agreement between mean flame temperatures obtained by CARS and those by fine wire thermocouple were also good.

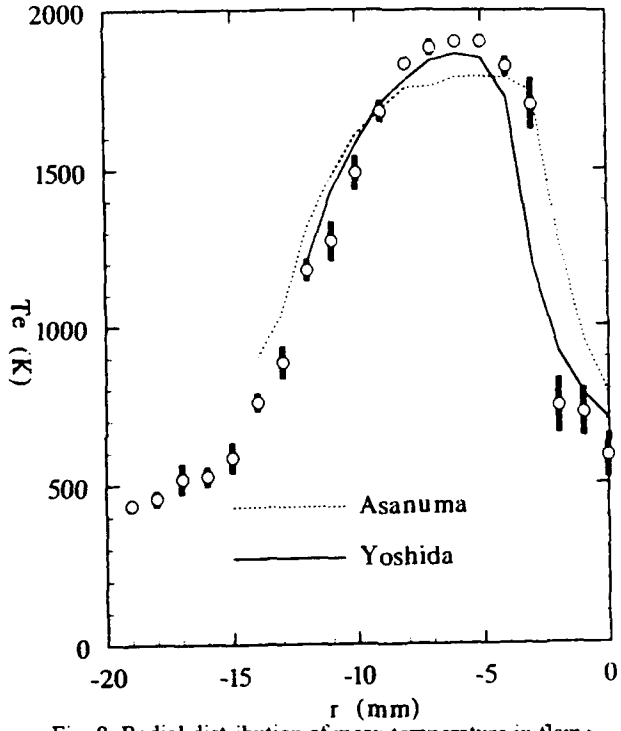

Fig. 8 Radial distribution of mean temperature in flame

REFERENCES

Asanuma T., 1987, Measurement of Temperature Distribution, in Diagnostics and Modeling of Combustion, ed. Iinuma K. et. al., pp. 357-358, JSME, (in Japanese)

Eckbreth, A. C., Bonczyk P. A. and Verdieck J. F. 1979, Combustion Diagnostics by Laser Raman and Fluorescence Techniques., Prog. Energy Comb. Sci. Vol. 5, pp. 253-322

Eckbreth, A. C. 1988, CARS in Laser Diagnostics for Combustion Temperature and Species, pp. 220-300, Abacus Press, Kent, UK

Hall, R. J. 1979, CARS Spectra of Combustion Gases. Combustion and Flame, vol. 35, pp. 47-60

Kawaguchi, Y. and Hama, J. 1989, Measurement of Turbulent Characteristics of Premixed Hydrogen Flame in a Sudden Expansion Type Flame Holder, Proc. Int. Conf. Dynamic Fluid Measurement and its Applications, Beijing, pp. 127-132

Maeda, M., 1987, Measurement of Velocity component by a miniature 2 color 4 beam LDV probe, in Diagnostics and Modeling of Combustion, ed. Iinuma K. et. al., p. 353, JSME

Yoshida T., 1987a, Outline of Standard Burners, ibid., pp. 351-352

Yoshida T., 1987b, Measurement of Velocity and Temperature using LDV and Thermocouple, ibid., pp. 359-360

Session 3.
Rotating Machines I

CONSIDERATIONS INVOLVING THE APPLICATION OF THE LASER DOPPLER VELOCIMETRY TECHNIQUE TO FLUID MEASUREMENTS WITHIN A RADIAL INFLOW TURBOCHARGER ROTOR

Mr M. J. O'Rourke and Dr. D. W. Artt

Department of Mechanical Engineering
The Queens University of Belfast

ABSTRACT

This paper describes a method by which velocity measurements were obtained within the exducer section of a radial inflow turbine rotor utilising a laser Doppler velocimeter. The problems associated with the application of a velocimeter to such a harsh environment are highlighted and the authors, through a careful consideration of the characteristics of the radial turbine have shown that unique techniques can be developed to facilitate the requirements of the velocimeter. This is illustrated by the development of a solid particle seeding system and also by the adoption of a fluorescence technique, which enabled near wall measurements to be made. The success or otherwise of the various techniques adopted is discussed.

1. INTRODUCTION

In the modern day research and development of turbomachinery, the numerical solution of the 3 dimensional Reynolds averaged Navier-Stokes equations is becoming an ever increasingly important design tool. However before such solutions can be reliably used, validation with experimental results is essential. Recent advancements in the laser Doppler velocimetry technique have resulted in its utilisation to obtain velocity measurements within the various turbomachinery components upon which the accuracy of these numeric codes can be gauged.

Whilst the laser Doppler technique is non-intrusive to the flow there are however many practical problems associated with its application to turbomachinery, many of which have been reviewed by Strazisar (1986). Many of these problems are highlighted to the extreme in the small diameter (less than 150mm) radial inflow turbine rotor. Coupled with this is the fact that a dearth of quantitative information exists as to the nature of the flow field within, Kitson *et al* (1991), Ahmed *et al* (1991), Benisek and Struble (1990) and Benisek and Spraker (1987).

With the aforementioned in mind, a research project was undertaken with a view to obtaining velocity measurements upon which a numerical solution could be validated.

2. LASER DOPPLER VELOCIMETRY

Laser Doppler velocimetry is a technique which as its name suggests utilises the Doppler effect to measure the velocity of particles entrained within a fluid. If the particles are of a sufficiently small size then it can be assumed that their velocity is representative of the fluid velocity within which they are moving. The laser Doppler velocimeter used in the current work is shown diagramatically in Figure 1. Its principle of operation can be explained briefly as follows: Two monochromatic laser beams having a common source (514.5 nm), hence coherent, are focused so as to intersect forming a region, ellipsoidal in shape, referred to as the 'measuring or probe volume'. Within the measuring volume superposition of the incident laser beams results in the formation of a fringe pattern, consisting of parallel planes of varying light intensity, as shown in Figure 2. A seed particle traversing these fringes will scatter a finite signal of varying intensity, known as the Doppler signal or Doppler burst. This signal when collected contains all the essential information from which the velocity of the particle can be estimated. The component of velocity measured is in the plane of the two incident laser beams, along a perpendicular to their common axis. In the velocimeter system used the lens which gathers the scattered light (receiving lens) is housed in a probe which also contains the focusing lens (transmitting lens) of the incident laser beams. This arrangement is referred to as backscatter and unfortunately the intensity of the scattered light is weakest in this set-up. A photomultiplier is used to convert the scattered optical signal to an electrical signal and is subsequently processed by electronic equipment. For a detailed explanation of laser velocimetry see Durst et al (1981).

3. PRACTICAL IMPLEMENTATION OF LASER VELOCIMETRY

There are many common problems associated with the application of laser anemometry in measuring the velocity of fluid flows. In most applications an artificial seed material needs to be introduced. This seed material must fulfil a number of requirements: It must be of sufficient size to faithfully follow the variations in the flow velocity. It also must scatter light of sufficient intensity to be detected by

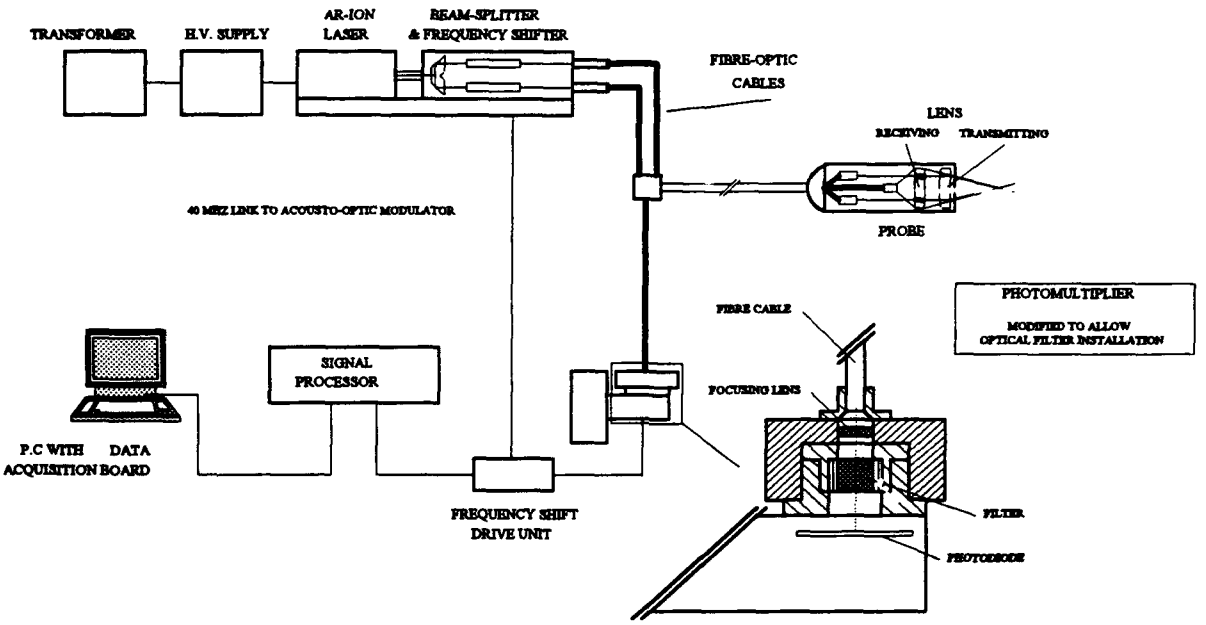

Figure 1 The laser Doppler velocimetry system

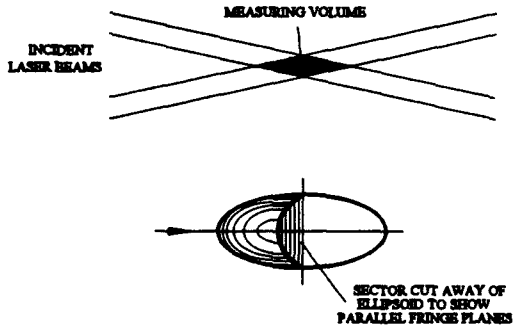

Figure 2 The measurement or probe volume

modern equipment. Furthermore it is necessary to provide an optical path by which the incident laser beams of the velocimeter reach the measurement control volume and by which the scattered light passes to the receiving optics. In most cases this is via glass or perspex windows fitted into the boundary of the control volume. However the use of glass windows leads to further problems. Firstly, depending on the seed material used, a deposit may occur on the window which will eventually block the optical path. Secondly, it is an inherent property that when the measuring volume is located close to the window, reflection of the incident light beams will occur from the surface of the windows, known as 'flare'. In the case of a velocimeter operating in backscatter, the flare will mix with the scattered light from the seed particles. This is referred to as signal noise and often can obscure the weaker scattered light signal. A similar problem which is general to many applications occurs when measurements are made in close proximity to boundary walls. Again light reflected from the incident laser beams striking the boundary walls is present in the signal as noise and as before may obscure the Doppler signal.

It is clear therefore that any successful application will require consideration of the above problems, producing an adequate seed material and reducing the noise level associated with flare to give an optimum value of the signal to noise ratio.

4. PROBLEMS ASSOCIATED WITH THE APPLICATION OF LASER DOPPLER VELOCIMETRY TO A RADIAL TURBINE ROTOR

Laser Doppler velocimetry measurements in a radial turbine rotor offer additional problems to the above. The physical makeup of the turbine rotor requires the strobing of a velocimeter which operates in backscatter as a means of collecting data within the rotating passages. At the high rotational speeds associated with turbomachinery, design of electronic strobe units can be difficult. The size and nature of the seed particles is critical to success. Rapid rates of acceleration coupled with the influence of high centripetal forces require that the seed particles must be maintained below 1 μm. However particles below 0.5145 μm (the laser light wavelength) scatter light of intensity often insufficient to be detected. This lower limit however is not critical but if all particles were below it then no signal would be detected at all.

Additional requirements of a seed material are that they must not combust in the hot gases, often in the range of 873 K passing through the turbine. Generally solid particles are therefore required. It is possible however to carry out cold flow testing at gas temperatures which would permit liquid seeding to be used. Fouling of the optical access window then

becomes a major problem restricting the experimental time before a window needs to be removed and cleaned.

Further fouling of the optical access windows may occur as a result of other contaminants, i.e. soot contained within the working fluid or as has occurred in the current project, oil from the bearing housing of the turbocharger rotor.

It is therefore a complex problem to design a test facility upon which laser Doppler velocimeter tests can be carried out successfully. All of the above problems must first be overcome.

5. THE TEST FACILITY AT QUEENS UNIVERSITY

In designing the current test facility at Queens a solution to each problem was sought as it was encountered. The existing test facility is shown in Figure 3. The basic unit consisted of a proprietary turbocharger as shown in Figure 4.

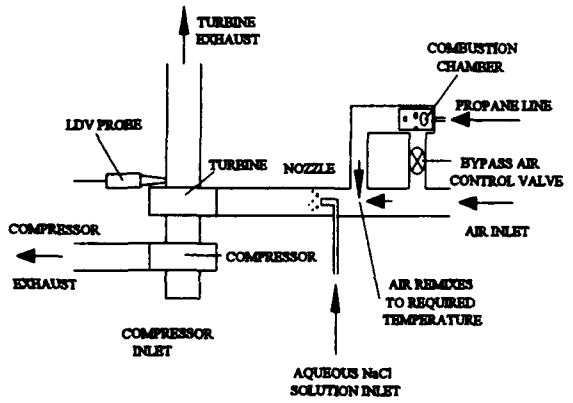

Figure 3 Turbine test facility

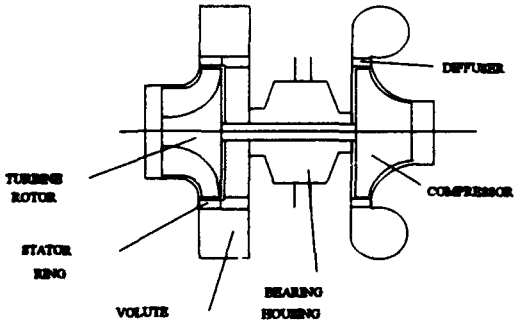

Figure 4 Cross-section of turbocharger unit

Table 1 Details of turbine test rotor

design speed	65 000 RPM
overall diameter	112 mm
blade tip at inlet	15 mm
exducer diameter	100 mm
number of blades	14

The turbine rotor under test had the specifications shown in Table 1. Propane gas, combusted in a supply of air obtained from an industrial screw compressor was used to drive the turbine and exhausted to the atmosphere downstream. The work output from the turbine was absorbed by the centrifugal compressor which acted as a dynamometer. In the following the solution to the various problems, both practical and technical is described.

5.1 Seeding

In designing the seeding system the characteristics of the radial turbine were utilised. Seed particles conforming to the required dimensions were formed by evaporating atomised droplets of an aqueous solution of common salt, NaCl, within the hot inlet turbine gases to give crystals of salt. These droplets were produced and introduced to the flow by a standard Monarch F-80 fuel nozzle positioned a distance upstream of the turbine. The evaporation of the droplets resulted in a temperature drop in the region of the nozzle and the nozzle was positioned well upstream of the turbine inlet so that the fluid was fully mixed out at turbine inlet. The size of the salt crystals was controlled by varying the upstream temperature of the working fluid. Figure 5 shows a diagram of the seeding system.

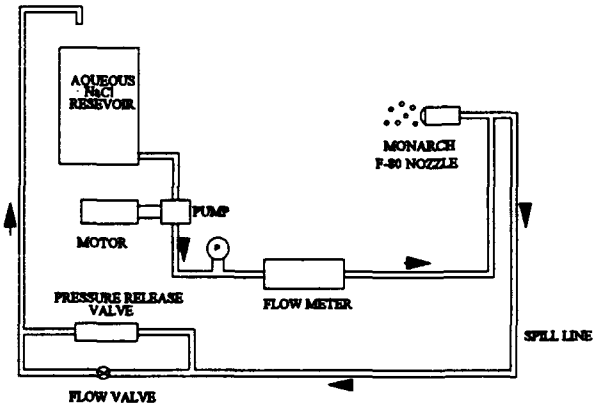

Figure 5 Aqueous NaCl Seeding System

A major advantage of the seeding system that has been designed is that the whole mass flow through the turbine rotor was seeded as opposed to the partial seeding of the flow obtained by the more common method of point injection. With point injection the seed inlet is positioned upstream of the rotor wheel at the inlet to one of the stator nozzle passages. As each blade passage passes the seeded nozzle, an amount of seed is carried inside the rotor passage by the air mass flow and passes down through the passage to outlet. In preliminary tests carried out using point injection it proved difficult to ensure that the seeding within the rotor passage coincided with the measurement volume of the velocimeter. This problem was heightened by fluctuations in the rotational speed of the rotor due to changes in turbine inlet temperature. Furthermore,

point injection proved inflexible when a number of different measurement stations were required to be considered or when the rotor test speed was to be varied.

5.2 By-Pass Combustion Chamber

With no by-pass line in the turbine air supply line, initial testing at low turbine inlet temperatures proved difficult. Firstly, combustion was unstable and difficult to maintain and secondly, but more importantly, the combustion of the propane was unclean and fouling of the optical access window resulted. A by-pass line with control valve was then added to the test facility to allow the propane to be burned at a more suitable temperature.

5.3 A Fluorescence Technique to Aid Near Wall Measurements

To aid near wall measurements to be made, a fluorescent technique was developed which again utilised the characteristics of the turbine. The principle of the technique was based on the fluorescent compound Rhodamine 6G found as an ingredient in fluorescent paints. Figure 6 shows the absorption and fluorescence spectrum of this compound. The wavelength of the laser light used in this project, 514.5 nm, falls within the absorption spectrum. Any light, with wavelength falling within the absorption spectrum, illuminating Rhodamine 6G is absorbed by the compound which then emits light at wavelengths within the fluorescence spectrum.

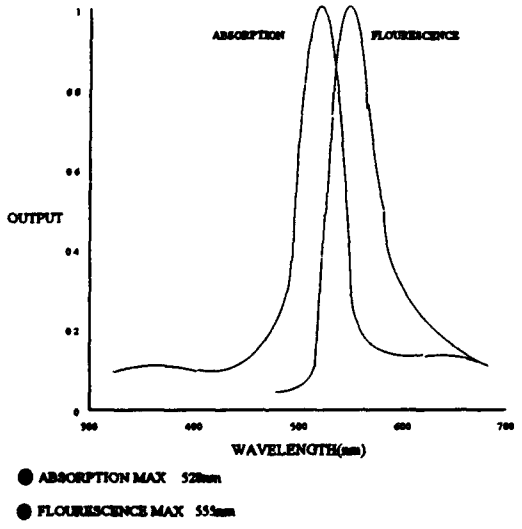

Figure 6 Absorption and emmision spectrum of Rhodamine 6G

To apply the technique required that the surfaces near which laser Doppler velocimeter measurements were to be made were coated with a paint containing the Rhodamine 6G ingredient. The incident laser beams of the velocimeter were absorbed by the paint and fluorescence occurs. By choice of a suitable optical bandpass filter placed in the receiving optics the fluorescence wavelengths were filtered out leaving only the required Doppler signal. One problem which may exist in general applications is that a laser beam falling consistently on the same spot of paint would cause the paint to burn. However in a rotating rotor the incident beams are only striking the same point for a finite time once every revolution, certainly not sufficiently long enough to burn the paint at the laser powers required for laser Doppler velocimetry.

5.4 Off-Axis Collection of Doppler Signal

As a solution to the problem of flare at the optical access window, off-axis collection was incorporated. This can be understood by a consideration of Figure 7. The path of the reflected laser light is so as it does not pass into the receiving optics. Care needed to be taken when positioning the measurement volume as the effects of refraction at the glass window caused translation of the measuring volume.

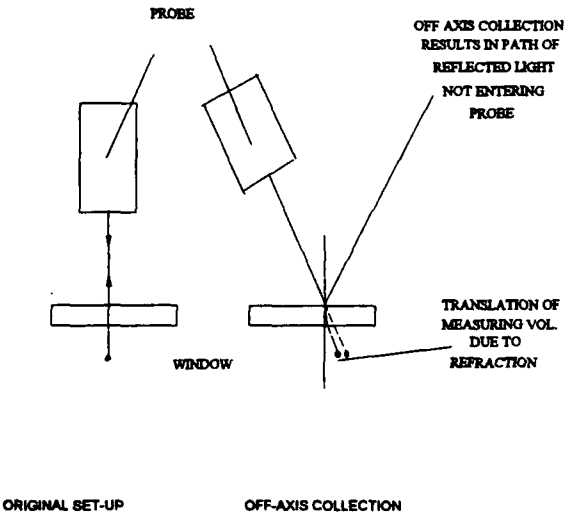

Figure 7 Off axis collection of scattered light

6. EXDUCER MEASUREMENTS

Preliminary tests results have been carried out within the exducer section of the rotor to determine the effectiveness of the above techniques.

A specimen of seed particles was collected under test conditions just downstream of the rotor outlet and examination under a microscope revealed that the majority (greater than 95%) were of sub-micron size.

The effectiveness of the fluorescence technique was estimated by observing the level of noise on an oscilloscope, firstly with the filter in line and secondly with it removed. The filtered signal noise level was reduced to within 20 % of its unfiltered value (in determining this the peak transmittance of the filter which was 50 % of the incident light intensity, was taken into account). Measurements were obtained up to 0.5 mm from the blade surfaces.

7. DISCUSSION

The effectiveness of the test facility thus far has been encouraging in view of the preliminary measurements that have been made. Measurements were achieved within a distance of 0.5 mm of the blade surfaces thus proving the success of the fluorescence technique. However there are a few drawbacks with the technique. Firstly a suitable high temperature fluorescent paint has of yet not been obtained and a standard fluorescent paint of the type used by model makers has instead been used. The maximum working temperature of this paint has been found to be 393 K and as a result cold flow testing had to be carried out operating at an inlet temperature of 373 K. Furthermore, it was noticed that when carrying out off design tests, that abrasion of the paint on the blade surfaces at the rotor inlet occurred. This was most likely due to seed particles impinging on the blade surfaces. However further downstream, where the authors are most interested in the flow patterns, the paint remained unaffected.

The cost of an optical filter with a bandwidth suitable for use in the technique was extremely cheap, in the range of £50stg for a filter with centre wavelength of 514.5 nm and bandwidth of 10 nm. The power of the transmitted light through the filter however was reduced by 50 %. As a result signals of weak intensity were lost. This problem could be somewhat counteracted by increasing laser power so as the intensity of the scattered light was increased. With more common methods of flare reduction, such as the use of a matt black paint to coat the blade surfaces, increasing laser power results in a reduction of the signal to noise ratio. However the effect here was to increase fluorescence which was then filtered out and ultimately the effect on signal to noise ratio was little.

The use of the salt particles as a means of seeding has proved most satisfactory. The vast majority of the particles are below 1 μm and are therefore suitable for velocimetry measurements. However for those that are not the counter processor used in the velocimetry system possessed an amplitude filter which effectively neglected signals above a certain intensity i.e. those from the largest particles. By optimising laser power and the amplitude filter suitable data rates were obtained for tests to be carried.

The mechanism by which the salt particles were produced remains unclear. It is suspected that at suitable concentrations, 22.2 cc of NaCl per litre H_2O, that individual atomised droplets of the aqueous NaCl form a number of solid crystal particles of NaCl whose size and hence number depends on the rate of evaporation of the H_2O. This in turn is controlled by the upstream temperature and the mass flow of the air through the turbine. However at concentrations of NaCl in excess off 30.0 cc per litre H_2O it was found that many larger particles began to form as well as the smaller particles. It was suspected that this resulted from too high a concentration of salt particles within the inlet flow with a subsequent agglomeration of particles. A limiting concentration of the salt solution was therefore realised.

8. CONCLUSIONS

Implementation of the laser Doppler velocimetry technique to particular applications often requires the ingenuity of the test operator to create a test facility upon which valid velocity measurements can be made. In the case of a radial inflow turbine many problems associated with the application of the technique have been highlighted in the former. By utilising the characteristics of the radial inflow turbine the authors have created a suitable test facility upon which laser Doppler Velocimetry can be carried out.

REFERENCES

Ahmed, N. A., Foster, C. P. & Elder, R. L. 1991, Laser Anemometry in Turbomachines, Journal of Aerospace Engineering, Proc Instn Mech Engrs, Vol 205, pp. 1-12.

Benisek, E. F. & Struble, A. G. 1990, Laser Velocimeter Measurements in a Turbocharger Turbine, Proc Instn Mech Engrs, C405/009, pp. 1-6.

Benisek, E. F. & Spraker, W. A. 1987, Laser Velocimeter Measurements at the Rotor Inlet of a Turbocharger Radial Inflow Turbine, Presented at the Third International Symposium on Laser Anemometry, FED-Vol 55, pp. 207-213.

Durst, F., Melling, A. & Whitelaw, J. H. 1981, Principles and Practice of Laser Doppler Anemometry, Academic Press, London.

Kitson, S. T., Maguire, J. M., Langdon, P. J., Varo, R. G. and Shaw, G. D. 1991, The Computational Experiment Applied to Aerodynamic Design and Analysis of Turbomachinery, 67th Symposium of the AGARD Propulsion and Energetics Panels on advanced Instrumentation for Aero Engine Components, Philadelphia, Pennsylvania, May 19-23.

Strazisar, Anthony J. 1986, Laser Fringe Anemometry for Aero Engine Components, International Congress and Exposition, Detroit, Michigan, NASA TM-88798.

LASER DOPPLER VELOCITY MEASUREMENTS IN A CENTRIFUGAL VENTRICULAR ASSIST DEVICE

M. Pinotti, N. Paone* and E. P. Tomasini*

Departamento de Energia, UNICAMP, Campinas SP, Brazil.
* Dipartimento di Meccanica, Univ. Ancona, Ancona, Italy.

ABSTRACT

The present work describes the use of the laser Doppler velocimeter as a tool for flow mapping in a complex geometry such as vaneless centrifugal blood pump. A typical in vitro test bench was assembled with some characteristics for optical measurements of flow velocity. Due to the complex geometry, refractive index matching was obtained by assembling around the pump a Plexiglass box filled with the working fluid. The measurements reveal that the constrained forced vortex technology, in which this pump is based, provides pumping action in a restricted area in the core of the pump.

1. INTRODUCTION

The reasons for exploring the applicability of centrifugal pumps as a heart assist device were the problems associated to the use of the pulsatile pneumatic artificial ventricule. Saxton and Andrews (1960) pointed out that the big size, the high power requirements and the accelerated degradation of plastic components after many hours of use were the main limitations of pulsatile devices. At present, among the currently available devices, centrifugal blood pumps receive special attention for their simplicity, relatively low cost of utilization and low hemolysis level. The constrained vortex technology, used in the construction of vaneless centrifugal pumps (Kletchka et al, 1975), has eliminated the need for the vanes, and the blood, gently pumped by the action of its viscosity, may circulate in the system with low doses of anticoagulants. However, all these important features are not enough to guarantee mechanical reliability and low blood cells damage in the long term operation. Additionally, an optimal situation in which the volume of blood needed for operation (prime's volume) is minimal and performance is maximum have not been achieved yet.

It is known that proper development of centrifugal blood pumps requires four tools:

• Hydraulic measurements, which gives a basic feeling on pump performance and a global value of its efficiency.

• Computational Fluid Dynamics (CFD), which helps to determine problem areas, but cannot yet be applied for quantification of blood trauma.

• Flow visualization and local velocity measurement, which require high investment for each tested version, but may verify computer calculations and give data on regions that are not accessible to numerical simulations.

• In vitro blood tests, which provide reliable data of the overall performance, but no direct information on regional influences.

For pump development all these four methods should be combined to get an overall understanding of the investigated device. A very useful feature resulting from the use of CFD is providing information of the flow in a ventricular assist device, even if it does not exist physically. Due to the complexity of such devices, successfull attempts of CFD have been overshaded by the lack of experimental confrontation.

Flow visualization and velocity measurements have been described in the literature for pulsatile heart assist devices (Baldwin et al, 1990; Jin & Clark, 1993; Bertram & Nugent, 1993). Recirculating and stagnant flows were possible to observe in a sac-type pneumatically driven device and in a pusher plates pump. For nonpulsatile devices, Schima et al 1993 have described flow visualization in an upscale model of impeller centrifugal pump. In such type of device, the presence of extremely high velocity gradients in the vicinity of the vanes limits the application of CFD methods and, consequently, flow measurements using a non-invasive technique is recommended.

In the case of vaneless centrifugal pumps, numerical models are stable enough to provide information about the flow in the device and may be compared to experimental measurements obtained from Laser Doppler Velocimeter. (LDV).

To provide information regarding the flow in a vaneless centrifugal pump (rotating concentric cones), which are not available in the open literature, a test circuit was assembled with special characteristics for optical measurements. The present work describes the use of the LDV technique as a tool for flow mapping and the procedures to obtain the refractive index matching between the working fluid and the pump are discussed.

2. MATERIALS AND METHODS

2.1. The Device

The device studied is commonly used in ventricular assistance and in cardiopulmonary bypass procedures. The pump is formed by three concentric cones (Fig. 1) assembled on a magnetic rotor. A magnet at the base of the cones is married to a console magnet. The console turns the magnets and the cones

spin. As the cones rotate, energy is imparted to the fluid in two forms, potential energy (pressure), and kinetic energy (flow). The multiple cones assembly is to increase the internal surface area which provides an increasing of the energy imparted to the fluid. At the pump's suction inlet, the negative pressure, caused by centrifugal effects, induces the blood flow into the pump's rotating channels. Then, the momentum imparted by the rotating surfaces is transmitted to the blood by the fluid-surface interaction due to viscous drag. There is also fluid-fluid interaction in the bulk of the fluid where an interplay between viscous forces and inertia forces exists to balance the pressure gradient established within the rotating channels. The magnitude of the viscous and inertia forces depends on flow regime. The pumping action occurs due to the centrifugal force induced by the rotational speed of the fluid, and the magnitude of the pressure gradient depends on the magnitude of the through flow and rotational speed of the disks.

Finally, at the end of the rotating channels, the fluid is led to the exit tube by a voluta type channel in the pump's housing.

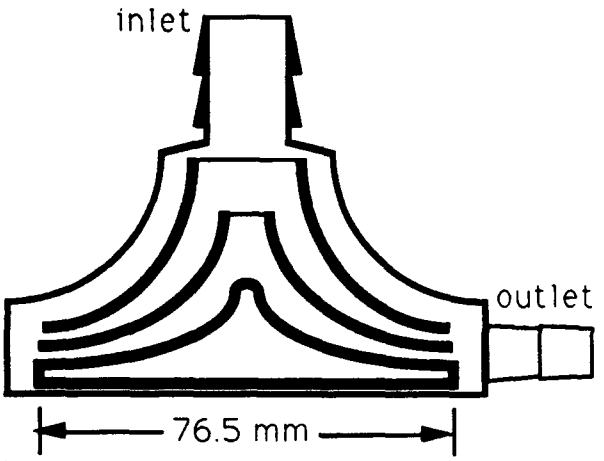

Fig. 1 - Schematic representation of the vaneless pump (multiple smooth rotating cones).

2.2. The experimental system and the measurement technique.

A typical in vitro test bench was assembled in order to reproduce flow resistance of a circulatory system. Figure 2 depicts schematically the test circuit.

Flow rate is monitored by a turbine flow meter (6), whose uncertainty is around 0.3%. Flow rate can be regulated by a flow resistor (5). Pump rotating speed can be varied by controlling the excitation voltage of the brushless DC motor in the console (4) and it is measured by an optical proximity sensor installed on the pump rotor. Pressure rise across the pump is monitored by a U-tube differential manometer (7).

Main difficulty in performing velocity measurements inside the vaneless pump is related to its small dimensions and very complex geometry. Only a non invasive measurement technique, as LDV, can be employed for velocity measurement in such flow. Nevertheless, pump geometry imposes the application of a Refractive Index Matching (RIM) technique to access, with the LDV measurement volume, the inner regions of the pump. In fact, its double curvature and the difference between refractive index of air, plexiglass and the working fluid would produce fringe distortion, affect probe volume location or even impair its formation inside the pump. For these reasons the working fluid was prepared in order to have the same refractive index of the pump's constructive material (Plexiglass).

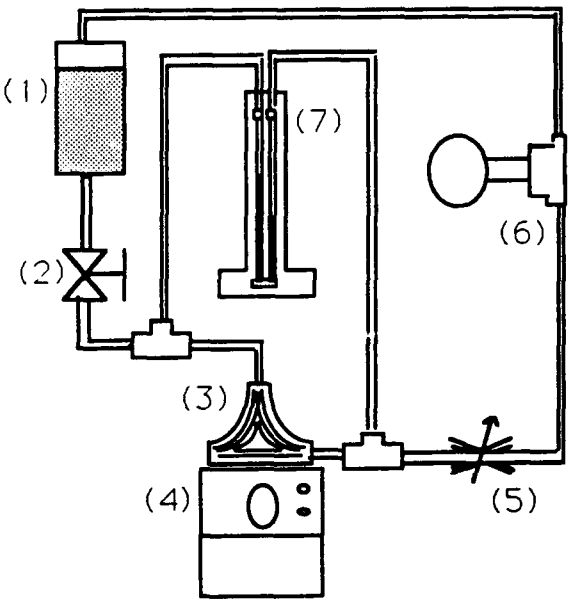

Fig. 2- The test circuit. (1) cylindrical tank, (2) control valve, (3) centrifugal pump, (4) control unit, (5) flow resistor, (6) turbine type flow meter and (7) U-tube differential manometer.

Although proper refractive index matching between working fluid and device was obtained, a suitable system of reference was difficult to be adopted because of the complex geometry of the pump. Futhermore, refraction at the curved external walls of the pump distorts significantly the measurement volume dimension, orientation and fringe pattern itself. The elimination of curved boundary between regions of different refractive index (air and Plexiglass) was possible by means of a prismatic box filled with the working fluid assembled externally to the pump's housing. This procedure allows the utilization of a cartesian-based system of reference and eliminates distortions of the measurement volume. Figure 3 shows the prismatic transparent box installed around the pump and the relative position of the cartesian reference frame. The dashed line indicates the Z position where the measurements, presented in this work, were performed.

By employing this technique, no corrections were used for the measured velocity data and the measurement volume position could be easily determined by knowing refractive index of the fluid/Plexiglass relative to air.

The working fluid (79% saturated aqueous solution of NaI, 20% glycerine and 1% distilled water, by volume) was chosen to match transport properties of blood and optical properties of Plexiglass. At 25°C, the blood analog fluid has an absolute viscosity (η) of 4.2×10^{-3} kg/ms (measured with a rotoviscometer at shear rates of 1000 and 2000 s^{-1}) and density (ρ) of 1682.9 kg/m^3 , resulting in a kinematic viscosity (ν) of 2.5×10^{-6} m^2/s. The measured refractive index of the solution is 1.486 (± 0.006), which matches accurately the refractive index of Plexiglass.

Such fluid at 25°C satisfies Reynolds similitude to blood at 37°C.- its kinematic viscosity is similar to the blood at shear rates above 500 s^{-1}.

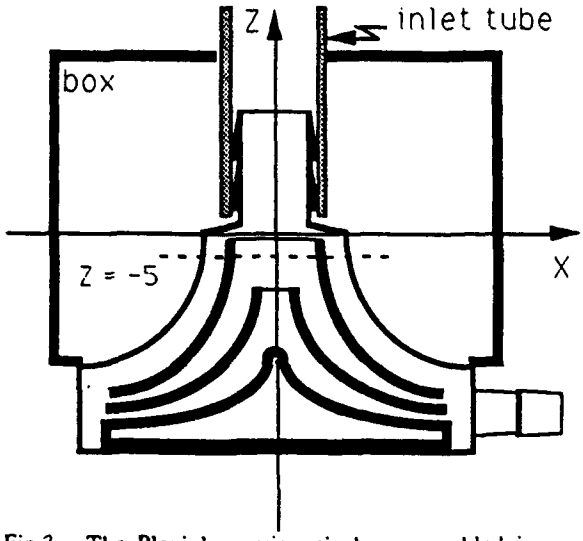

Fig.3 - The Plexiglass prismatic box assembled in pump's housing. The whole pump, immersed in a box filled with the working fluid allows the utilization of the cartesian system of reference.and renders refraction possible only across flat surfaces.

A four beam Ar^+ ion based LDV system was used in a backscatter configuration for two component velocity measurements. For each component, the beams of identical wavelenghts were crossed at their beam waists to form an ellipsoidal measurement volume. With a 160 mm focal lenght len, the resulting ellipsoid, computed inside the pump, had diameter of 0.0781 mm and lenght of 0.9779 mm. The dimensions of the measurement volume are sufficiently small, compared to channel width, to resolve axial and radial velocity profiles along the X axis and to resolve axial and tangential velocity profiles along Y axis.To measure negative velocities, Bragg cells were used to shift the frequency of one of the two beams for each component by 40 MHz. The two sample volumes were coincident and were oriented so that orthogonal velocity components were measured.

Velocity data are collected with no reference to rotor angular position, due to its symmetry. A fiber optic probe was used for beam delivery; its optical axis is aligned to the Y axis of the pump reference frame. Quality of refractive index matching can be experimentally obseved by looking at beams shone across the pump cones - they remain straight and reflections at each cone surface are minimized.

Measurement volume is moved across the pump by a three axis traversing system. Motions along X and Y axis are driven by step motors (± 0.01 mm uncertainty), while Z motion is manually controlled (± 0.05 mm). Alignment is performed with respect to the external box and to the inner walls of the pump's housing. It should be stressed that these pumps, being manufactured in Plexiglass by a casting technology, exhibit large geometric tolerances.

Signals are processed by two burst spectrum analyzers, operated in a burst mode, due to scarse natural seeding density. The sampling rate of the LDV was dependent on the rate of occurence of the Doppler bursts and the power of the photomultipliers. In the experiments, without added seeding particles, data rate was generally in the range between 20 and 150 Hz depending in the location of the measurement volume (low rates in the near-wall regions). In order to sample a statiscally meaningful population at each measurement point, 10000 data were collected and processed to compute mean and RMS velocity.

Although refractive index matching is achieved with less than ±1% uncertainty, coincidence of the blue (488nm) and green (514.5nm) measurement volumes was observed not to be good when beams cross more than six plexiglass surfaces and consequently, reducing validated data rate if measurements are taken in coincidence mode. Therefore, this first investigation is performed without imposing coincidence on Doppler signals.

Special attention should be paid to practical measurements problems which arise if the working fluid is in contact with air and polychromatic light, due to rapid oxidation which leads the redution of its optical transmission coefficient for the blue and green light. If such thing happens data rate and signal to noise rate drop and measurements cannot be taken. The fluid degradation was delayed by assembling a hermetic test circuit and protecting it from polychromatic light.

3. RESULTS

The objectives of the measurements presented in the this work are twofold: to evaluate the effects of the rotational speed of vaneless cones on the flow and to observe possible regions of undesirable recirculating flow.

It has been experimentally observed that the red blood cells (RBC) damage in a shear flow is due to two factors acting at the same time: the level of shear stress and the exposure time of the cell membrane to these forces (Leverett et al, 1972;.Sutera, 1977; Blackshear & Blackshear, 1987). Hence, a low level of hemolysis can be expected in flows with high shear stress if the exposure time is short enough. Conversely, high level of hemolysis can be expected in flows with low shear stress if the exposure time is long enough. A desirable feature in a blood pump would be low shear stress and short exposure times. Evidently, these two characteristics are difficult to be found at the same time because short exposure time means incresing shear stresses in the flow. Therefore, an optimal compromise between them should be achieved.

The measurements were performed in the x-y plane at z = -5 mm, taken as reference the cartesian system of Fig. 3. The flow resistor was regulated to impose a resistance of 122×10^6 N s m^{-5} (1220 dyn s cm^{-5}) to reproduce a typical level of systemic vascular resistance. Rotational speed of 1800 and 3000 rev/min were switched in the console to generate flow rates of 2.2 and 3.9 l/min, respectively - typical values for adult ventricular assistance.

In figs. 4, 5 and 6, internal boundary of the stationary walls (pump's housing) and the rotating cone are represented by straight lines intercepting X axis at -13 and 13 mm (thick lines), and, at -8.9 and 8.9 mm, respectively.

The particles of the fluid follows a spiral trajectory inside the pump. The driving force of such flow are the viscous drag,which accelerates the fluid along divergent channels and the pressure gradient induced by the costrained forced vortex. The pressure gradient, established between the outlet and the inlet of the pump is balanced by the viscous and inertial forces of the flowing fluid. Therefore, in regions of the flow where this balance is not verified, i.e. near a stationary wall, a backflow may occur.

Once established, such flow pattern may be easily observed in the axial velocity profile. This velocity component

(parallel of Z axis) gives information on the pumping action in the plane of measurements and has the same orientation displayed in fig. 3 - upward positive.

Figure 4 shows the axial velocity profile along the X axis. In the external channel formed by a stationary and a rotating walls (X < -8.9 and X > 8.9), the velocity profile which has similar profiles for both rotational speed is oriented upward, denoting a backflow. The presence of a stationary wall and the divergent geometry of the channel make that the positive pressure gradient, between inlet and outlet, became high enough to overcome the fluid forces, therefore inducing backflow. From basic fluid mechanics theory (Schlichting, 1979) it is known that boundary layer thickness for a stationary wall in a rotating fluid is twice the thickness for the case of a rotating wall in a stationary fluid. This may be the reason for the asymmetry of the axial velocity - negative velocities more pronunciated in the wall side - profile in the external channel.

On the other hand, inside the rotating cone (-8.9 < X < 8.9), the flow is clearly downward and the profile reveals the action of the interplay between viscous drag (pumping driving force) and centrifugal forces in the region near the rotating surfaces, and pressure induced gradient in the core of the flow.

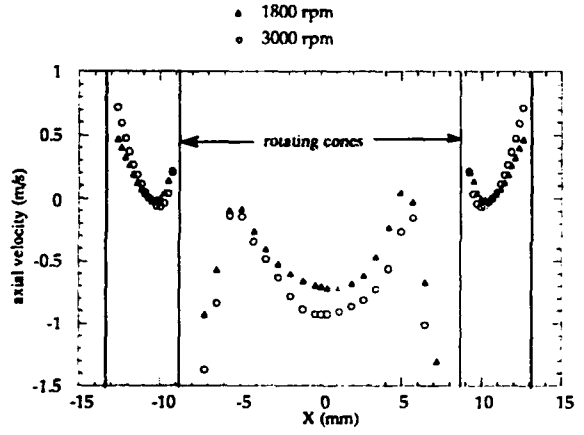

Fig. 4 - Axial velocity along X axis at Z = -5 mm The balance between viscous/inertial forces and the established pressure gradient along the pump determines the signal of the axial velocity.

Radial velocity is parallel to the X axis and its orientation is the same displayed in fig. 3 (positive values are left-to-right direction). This component gives information on the flow across the channel and low values are expected to be found. At 1800 rev/min, radial velocity profile displays a discrete symmetry in the central channel. As the rotational speed increases (3000 rev/min), the effects of misalignements of the rotor shaft leaves its signature on the radial velocity profile. The flow in this region is influenced by the vortex induced by the rotating channel and by the disturbance due to the rotating edge of another cone few milimeters below. Such disturbance is due to the increasing pumping action which acelerates the fluid in the core of the established vortex and, at the same time there is a flow rearrangement due to the presence of the rotating cone which induces the fluid towards itself. Additionally, the presence of another rotating channel few milimeters below the measurement plane induces a stagnation region in the border of the induced vortex. It should be noticed that "stagnation region" means that there is no flow downward or upward, and obviously a fluid particle maintains its tangential velocity describing a circular pathline.

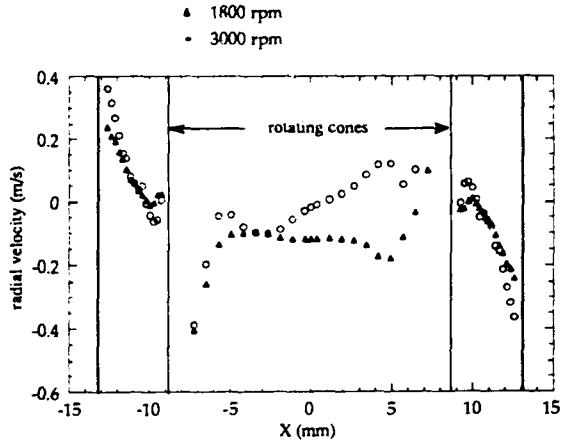

Fig. 5 - Radial velocity. The increasing of the rotational speed reveals a misalignement in the rotor shaft.

It may observed that the actual pumping effect of the rotating cone occurs in a restricted area in the core of the flow, where the radial and tangential components vanishe and the axial velocity reaches its maximum levels. In the border of this region, called constrained forced vortex, exist radial and tangential velocity gradients which render possible the mass conservation in this pump section.

The tangential velocity profile is displayed in Fig. 6, below. It was possible to measure the tangential velocity of the rotating cone. As expected, the tangential component reaches its maximum values in the rotating wall and decreases as the measurement volume is placed away from the cone. In the vortex core the tangential velocity profiles exhibits the same pattern with values near zero. This is not verified in the external channel, formed by a rotating and a stationary wall. The profiles are similar, but the values of the tangential velocity are greater for 3000 rev/min. The ratio between the measured tangential velocity for both operational situations in the each grid position is about 5/3, the same ratio between the rotational speed imposed to the cones (3000/1800).

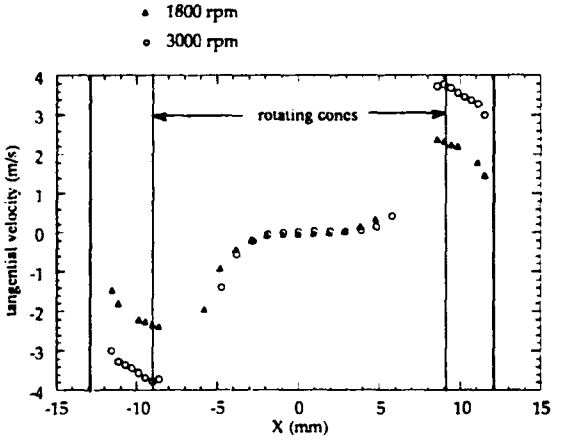

Fig 6 - Tangential velocity. The profile at the center of the pump reveals the pumping action of the constrained forced vortex.

4. CONCLUSION

This paper reports preliminary measurements in a nonpulsatile ventricular assist device. A test circuit was designed to reproduce the flow resistance of an adult human and to allow optical measurement of the velocity field by LDV. Special attention has been devoted to develop a working fluid which matches transport properties of blood and provides refractive index matching necessary for using optical measurement techniques in complex geometry. The influence of the rotational speed on the axial, radial and tangential profiles are displayed and reveals that the pumping action of the vaneless centrifugal pump is restricted to a region where the constrained forced vortex is established. The measurements performed in this preliminary study provide precious information on the regions in which mechanical damage of blood components may occur and they may give directions to future tests.

ACKNOWLEDGEMENTS

This work was partially financed by CNPq - Brasilia (Brazilian Research Council), grant n° 201586/92 assigned to Marcos Pinotti. The contribution of F. Sgarbi, S. Evangelisti and V. Ponzio to the construction of the experimental setup and to the measurements is gratefully acknowledged.

REFERENCES

Baldwin, J.T., Deutsch, S., Geselowitz, D.B.& Tarbell J.M. 1990, Estimation of Reynolds stresses within the Penn State left ventricular assist device, Trans ASAIO , vol. 36, pp M274-M278.

Bertram, C.D.& Nugent, A.H. 1993, Flow visualisation and measurements in a cardiac assist device, SPIE vol. 2052 Laser Anemometry Advances and Applications , pp 203-209.

Blackshear, P.L. & Blackshear, G.L. 1987. Mechanical Hemolysis,in Handbook of Bioengineering, eds. R. Skalak & S. Chien, pp 15.1-15.19, McGraw Hill, New York.

Jin W.& Clark C. 1993, Experimental investigation of unsteady flow behaviour within a sac-type ventricular assist device (VAD), J Biomechanics , vol. 26, n 6, pp 697-707.

Kletschka, H. D., Rafferty, H., Olsen, D.A., Clausen, E.W., Hubbard, L.C., Robinson, A.R.& Larson, W.H. 1975, Artificial Heart: Development of efficient atraumatic blood pump. A review of the literature concerning in vitro testing of blood pumps for hemolysis, Minnesota Med, pp. 757-781.

Leverett L. B., Hellums J. D., Alfrey C.P.& Lynch B.C. 1972, Red blood cell damage by shear stress, Biophys J , vol. 12, pp 257-273.

Rand R.P. 1964, Mechanical properties of red cell membrane. Part 2 Viscoelastic breakdown of the membrane, Biophys J , vol. 4, pp 303-316.

Saxton, G.A. & Andrews, C.B. 1960. An ideal heart pump with hydrodynamic characteristics analogous to the mammalian heart. Trans ASAIO , vol. 6, pp. 288-290.

Schima H., Huber L., Glekas J.P., Siegl H., Muller M.R., Wieselthaler G., Losert U. , Thoma H.& Wolner E. 1993. Three aproaches for flow evaluation in centrifugal blood pumps: numerical calculation, visualization and in-vitro thrombus formation. Artificial Organs , vol. 17, n 6, p 471 (abstract).

Schlichting H. 1979, Boundary-Layer Theory, pp 229 - 230, Mc Graw-Hill, New York.

Sutera, S.P. 1977, Flow-induced trauma to blood cells, Circ res, vol.41, n 2, pp 2-8.

APPLICATION OF A MULTI-ANGLE LASER-2-FOCUS VELOCIMETER TO UNSTEADY FLOW MEASUREMENTS IN A CENTRIFUGAL COMPRESSOR

Akihiro SUGIYAMA, Shinnosuke OBI, Masanobu MAEDA and Ichiro ARIGA

Department of Mechanical Engineering, Keio University
3-14-1 Hiyoshi, Kohoku-ku, Yokohama 223, Japan

ABSTRACT

The paper presents the turbulent flow measurements in a vaned diffuser passage associated by intense turbulence due to the wake of impeller blades. A multi-angle laser-2-focus velocimeter, that is suitable to measuring high-speed flows with strong variation of flow direction, is used together with a novel digital signal processing technique. From the ensemble averaging of the velocity signals as synchronized with the impeller-blade motion, it has been confirmed that the periodic fluctuation of velocity vector due to the impeller wake persists in the middle of the diffuser passage, and it is transferred downstream with the speed which is comparable to the local flow velocity.

INTRODUCTION

It has been clarified that about one-third of the whole stage losses takes place in the diffuser passage (Agrawal, et al., 1991). The detailed flow measurement in the diffuser is therefore of great engineering importance, and a number of studies on internal flow have been undertaken for optimum design of turbo-machines. Among other complex flow characteristics in the diffuser, the rolls of periodic fluctuation occurring in diffusers are not sufficiently understood, although the extremely strong fluctuations in a diffuser of centrifugal compressor have been recognized as a result of characteristic wake of impeller vanes (Krain, H., 1981).

Because of the high velocity and fluctuation, the measurement of the flow field in the compressor should be undertaken by advanced velocimeter. The multi-angle laser-2-focus velocimeter (MALV) is a variant of laser two focus velocimeter (L2F), that takes the advantage of L2F for high-speed flow measurement and enables the instantaneous velocity vector measurements by using a pair of four-channel Si-avalanche photodiode arrays. Because the direction of the flow can be relatively easily determined, the extreme preciseness in manufacturing the optical probe, usually required for rotating the probe to determine the flow direction, is not necessary, and the system can be relatively easily miniaturized by using e.g. a laser diode and Si-avalanche photodiodes instead of the gas laser and photo-multipliers. These advantages of the MALV have enabled the application to the flow measurements in a centrifugal compressor whose complex geometry makes it difficult for conventional velocimeters to get an efficient access of the measuring probe.

The present paper documents the preliminary results from a course of study in clarifying the complex turbulent flow field associated with the phenomena of rotating stall in a radial compressor. Once the stall occurs, the flow field is set under the subject of the strong fluctuation with a dominating frequency of stall rotation. The establishment of the flow measuring technique that takes into account the periodic nature of the flow field is therefore desired. Apart from the rotating stall, the flow field in the diffuser part is strongly affected by the wake of impeller blade, which is also of great engineering interest.

The objective of the present study is two fold: The primary purpose is the application of the recently developed MALV system to the measurements of flows in turbomachinery. To clarify the time-dependent feature of the flow in the diffuser passage. is the secondary purpose. The discussions will be made on the basis of the ensemble-averaging of the periodic flow field, and the characteristic behavior of the periodic fluctuation will be compared with the time-averaged flow field.

MALV-SYSTEM

Optical Arrangement

The optical arrangement of the present system is schematically shown in Fig. 1 (a). A 40mW-infrared (λ=780nm) laser diode (SHARP Inc., LT025MD) was used as light source. The originally plane-polarized light was changed into circular-polarized beam by $\lambda/4$-plate (LP), after collimated by the lens 1.

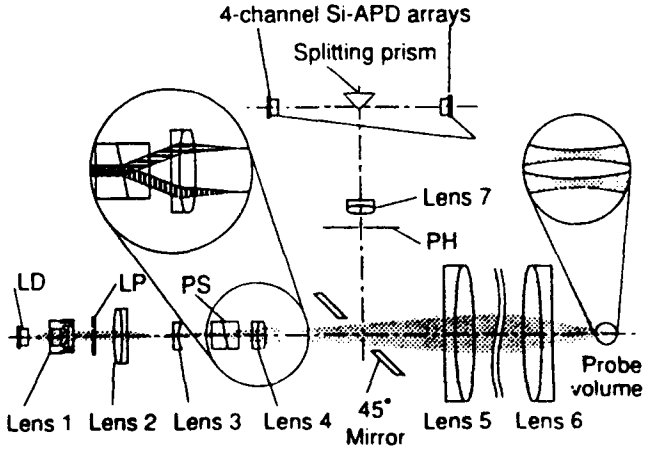

Fig. 1 (a): A schematic of MALV optical system

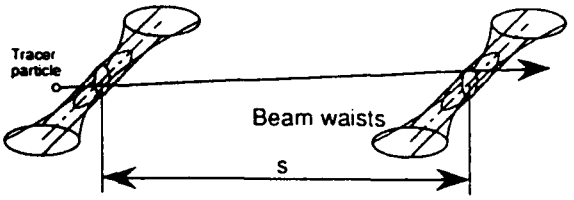

Fig. 1 (b): MALV probe

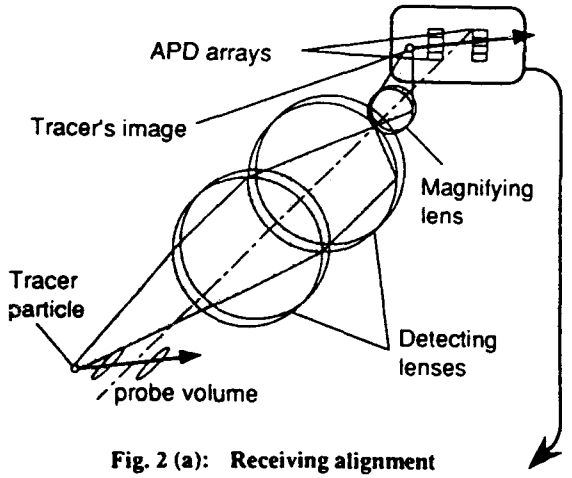

Fig. 2 (a): Receiving alignment

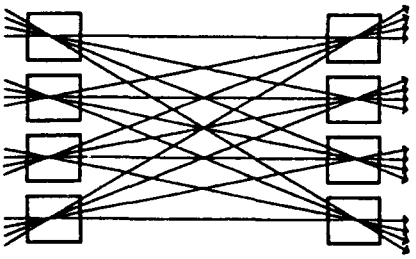

Fig. 2 (b): Detection of direction by APD arrays

The laser beam was divided by a Wollaston-prism (PS) into two beams that splits a circular-polarized beam into plane-polarized two beams of equal intensity which have polarization planes perpendicular to each other. Both of them were focused by lens 4, and then projected by transmitting lenses (lens 5, 6) to form the probe volume.

Figure 1 (b) shows the probe volume of MALV. The probe volume was consisted from two beam waists with the beam distance S of 405 μm. Because the laser diode has the beam with ellipse-like cross-section, both of the two beam waists had elliptical cross section with their longer axis set perpendicular to the line connecting them.

Scattered lights were detected by the four-channel Si-avalanche photo diode (APD) arrays in backward mode as shown in Fig. 2 (a). The optical image of the two elliptic-sectioned beam waists were projected individually onto the two APD arrays in the manner as illustrated in the figure. The path of the tracer particle through the probe volume could be determined by monitoring the channel of diode-array covering each beam waist. Once the location of the particle in the probe volume was known, the flow direction could be evaluated by

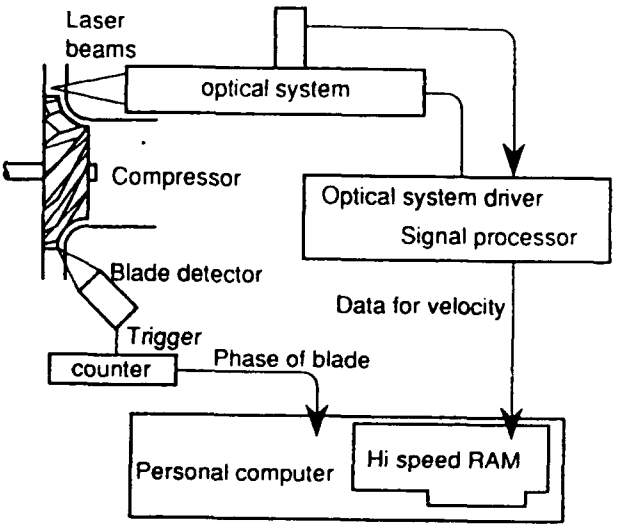

Fig. 3: Synchronizing system to blade phase

comparing the channel number of the two APD arrays (Fig. 2 (b)). The pitch between detectable directions was a function of the magnification. The arrangement with the pitch of 3 degrees was adopted in the present study.

Signal Processing

The detected signal pulses were digitized by the 4-channel amplifier and comparator before transferred to the memory unit in personal computer through a high speed memory board.

There is two methods to acquire particle flight time. One is the so-called time-of-flight method (TOF) which measures the time interval between passing of two foci directly, and the other is the cross correlation method which takes a time correlation between signals of two foci. Since the number density of tracer particle is low in the present case, the TOF method is adopted rather than the cross correlation method.

SIGNAL SYNCHRONIZATION

In order to capture the periodic fluctuation component induced by moving blades, ensemble averaging of the signals were undertaken in synchronization to the blade angles, see Fig. 7. As shown in the timing diagram, Fig. 8, the scattered light from compressor blades was taken by a blade detector for starting time counter, and the arrival time of the tracer particle was stored together with the velocity signal. The counter was reset by the next impeller blade. The ensemble averaging of the data is performed for a fixed blade phase angle, with each window covering one fifth of the blade interval.

The periodically fluctuating flow velocity with magnitude V and direction α may be decomposed into three components as

$$\left.\begin{aligned} V &= \bar{V} + \tilde{V} + V' \\ \alpha &= \bar{\alpha} + \tilde{\alpha} + \alpha' \end{aligned}\right\} \quad (1)$$

with the quantities with ¯ denote time-averaged component, and those with ~ and ′ correspond to the periodic and turbulent fluctuation components, respectively.

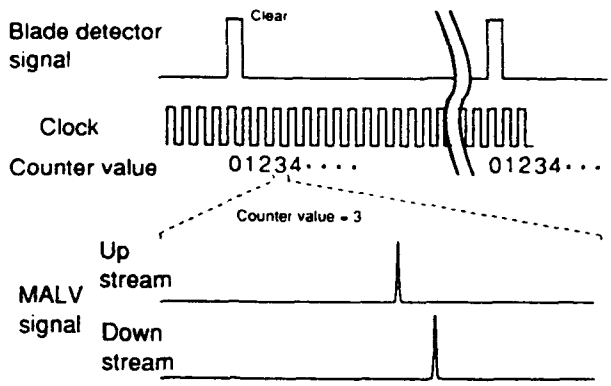

Fig. 4: Encoding timing diagram

TEST RIG

Flow System

Figure 5 shows the flow system. The compressor inlet was opened to the air, and outlet flow was exhausted to the atmosphere through the pipe with a control valve. A 140KW blower supplied air into a turbine on the same axle of the compressor. Figure 6 shows the test centrifugal compressor. The impeller had 14 blades and rotated at up to 10000rpm in the present study. The diffuser had 11 straight vanes. The diffuser axial passage width b was 16mm, and all measurements were performed on the middle plane, i. e. $z/b = 0.5$, with z being the axial location from the shroud wall. The diffuser vanes were fixed on the shroud side, and their height h was 8mm. The other configuration of the diffuser is summarized in Table 1.

In the present study, the measurements were performed under the conditions presented in Table 2. The flow coefficient Φ is defined as

$$\Phi = \frac{U_1}{U_2} \tag{2}$$

with U_1 being the bulk mean velocity in radial direction which is calculated from the measured volume flow rate Q as

$$U_1 = \frac{Q}{2\pi r_t b} \tag{3}$$

and U_2 denotes the tip speed of the impeller.

Test Section

The details of the test section is shown in Fig. 6; a close-up view of the measuring section is presented in Fig. 6(b). The diffuser shroud wall at the corresponding location was replaced by an optical flat acrylic window. The velocity along the arcs with constant radius, r = 125, 130, 135 and 140mm, are measured, and especially at four measuring points P1, P2, P3 and P4, which are aligned to the centerline of the diffuser channel, the periodic velocity motion was analyzed in detail.

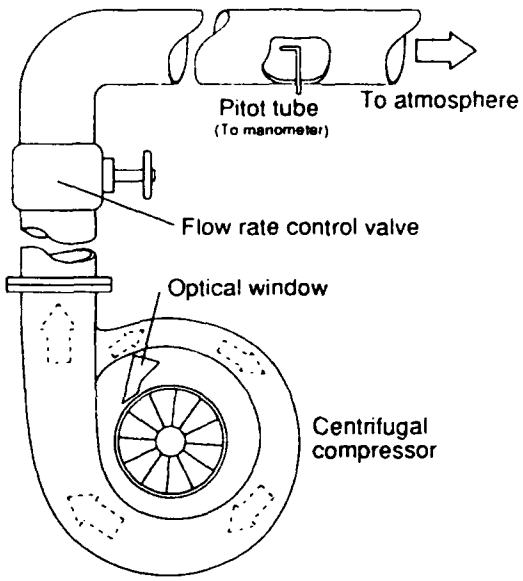

Fig. 5: Flow system

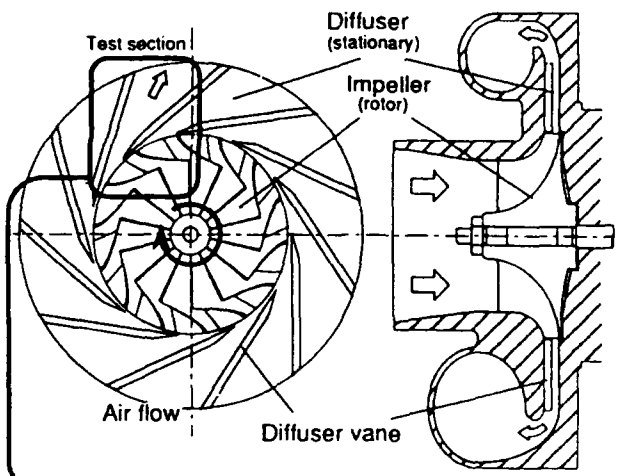

Fig. 6 (a): Test centrifugal compressor

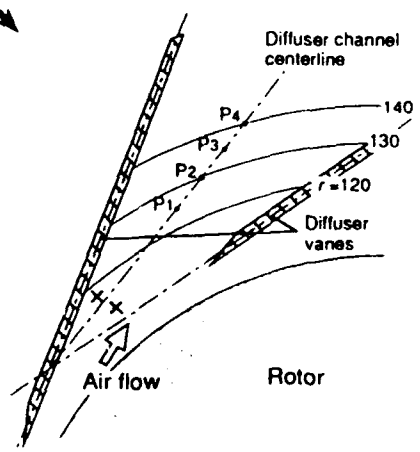

Fig. 6 (b): Test section

Table 1. Geometric configuration of the diffuser

Parameter	Dimension
Inlet radius (r_i)	98 [mm]
Outlet radius (r_o)	180 [mm]
Diameter ratio (r_o/r_i)	1.84
Axial width (b)	16 [mm]
Vane height (h/b)	0.5
Vane thickness	2.5 [mm]
Vane length	110 [mm]
Vane number	11
Channel divergence angle	33 [deg.]
Vane setting angle	10 [deg]

Table 2. Experimental conditions

Parameter	Condition 1	Condition 2
Number of revolution [rpm]	4500	10000
Rotor tip speed U_2 [m/s]	46.2	102.6
Blade motion frequency [Hz]	1.1×10^3	2.3×10^3
Blade motion period[ms]	0.95	0.43
Flow coefficient Φ	0.3	0.3

RESULTS AND DISCUSSION

Time Averaged Flow Field

Figure 7 shows the vector map of time averaged velocity field ($\bar{V}$, $\bar{\alpha}$) in the diffuser channel for the both of two conditions. The lengths of the velocity vectors are normalized by the rotor tip speed U_2. It seems that the mean flow direction is almost conform to diffuser channel centerline, and there is a similarity between the two flow fields (a) and (b).

The turbulence intensity (RMS value of V without phase-averaging) and fluctuation in the velocity vector direction α are presented at the four measuring positions P1 to P4 in Fig. 8. The RMS of the turbulent velocity fluctuation reaches about 20 percents of the local velocity at each points for the both conditions. For the condition 1, it is seen that the RMS value is nearly constant throughout the channel, while turbulence motion seems to increase gradually along the flow direction for the condition 2

Periodically fluctuating

Figure 9 presents the RMS value of the periodic fluctuation in velocity vector magnitude and its direction. The magnitude of the fluctuation is of one order smaller as compared with the turbulent component. For the condition 1, both the velocity fluctuation and the fluctuation of direction decrease monotonously in downstream direction. On the other hand, it is seen that the RMS of velocity for the condition 2 indicates more complex feature. The flow direction drops rapidly at point P4 for the condition 2. Taking into account the relatively mild variation of the turbulent fluctuation components of V and α, it is understood that the organized fluid motion caused by the wake of the impeller blade is diminished more rapidly than turbulent fluctuation.

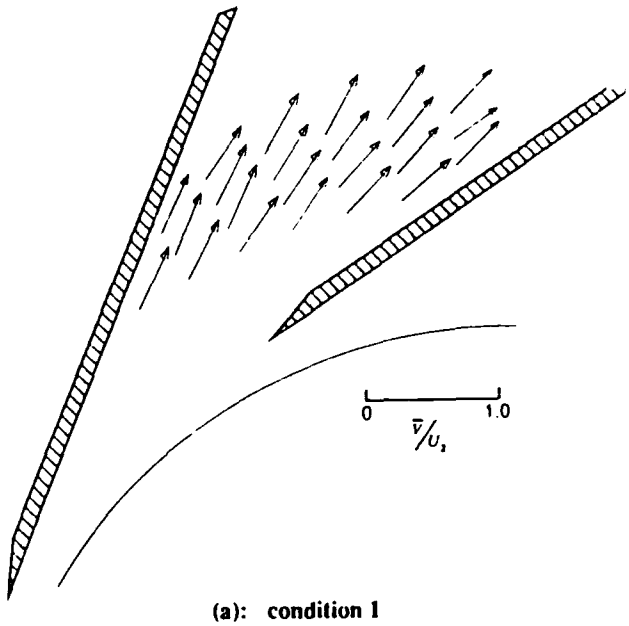

(a): condition 1

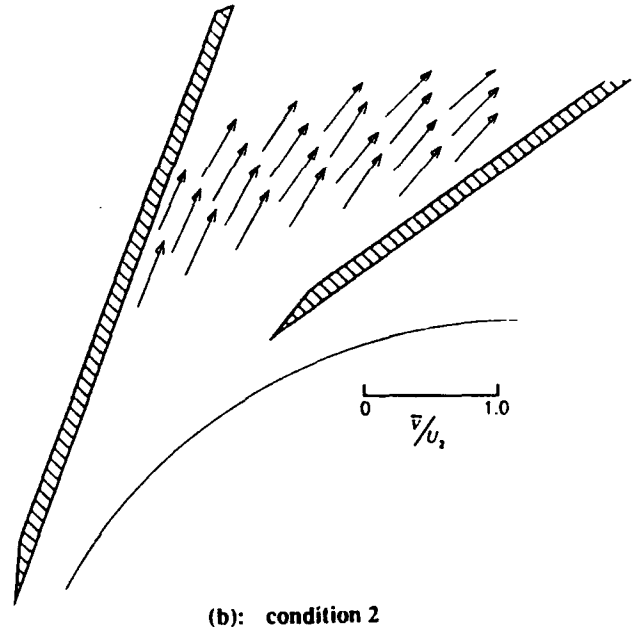

(b): condition 2

Fig. 7: Mean velocity vectors

The temporal variation of periodical fluctuation is presented in Fig. 10; (a) shows the flow velocity fluctuation $\tilde{V}$ and (b) shows the flow direction fluctuation $\tilde{\alpha}$ for the condition 1 as a function of dimensionless time T defined as $T=t/t_b$, with t_b: being the period of the blade motion. 1 cycle of the rotor blade motion is equal to 0.95ms. It is clearly seen that the flow fluctuates with the same frequency as the blade cycle. The flow direction fluctuation has particularly large correlation to the motion of rotor blades, with the maximum direction difference being 4 degrees at each locations, P1 to P4.

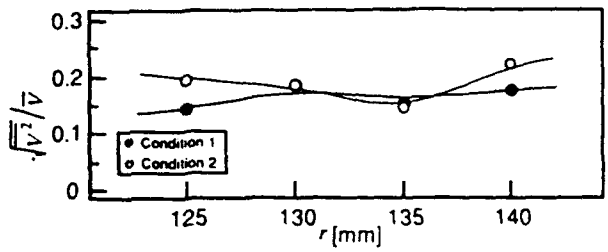

Fig. 8 (a): RMS of V

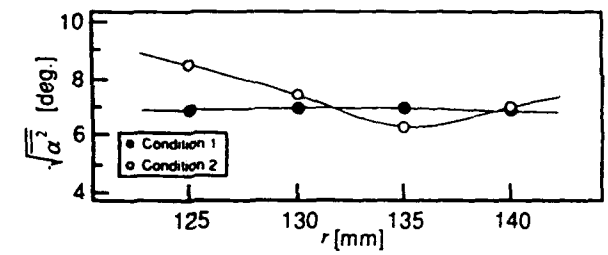

Fig. 8 (b): RMS of α

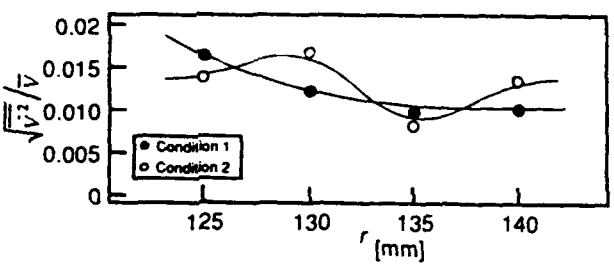

Fig. 9 (a): RMS of velocity fluctuation $\tilde{V}$

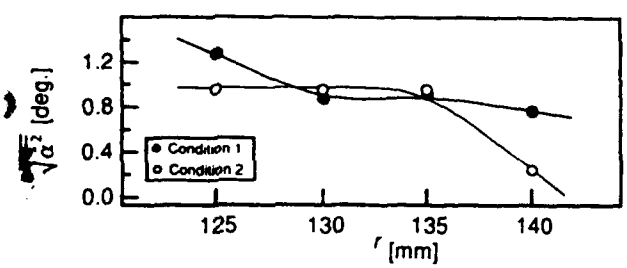

Fig. 9 (b): RMS of flow direction fluctuation $\tilde{\alpha}$

It is further observed that the velocity and/or direction fluctuation at four locations are in sequential manner, i.e. the periodic motion is transferred to downstream with a constant velocity. The corresponding figures for the condition 2 are presented in Fig. 11. In this case, 1 cycle is equal to 0.43ms. It is seen that there is a similar tendency as has been observed in the condition 1 in terms of the clear periodicity and shift of profiles in the sequential manner.

In order to analyze the propagation of periodical fluctuation more quantitatively, the correlation between fluctuation at different points are evaluated. The correlation function R_{cr} is defined as:

$$R_{cr}=\frac{\overline{\tilde{\alpha}_1(T)\cdot\tilde{\alpha}_2(T+\tau)}}{\sqrt{\overline{\tilde{\alpha}_1}^2}\sqrt{\overline{\tilde{\alpha}_2}^2}}. \qquad (4)$$

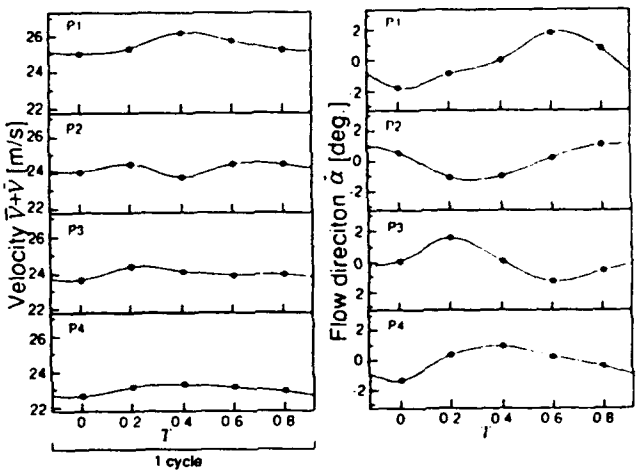

(a): velocity fluctuation $\tilde{V}$ (b): direction fluctuation $\tilde{\alpha}$

Fig. 10: Flow fluctuation (condition 1)

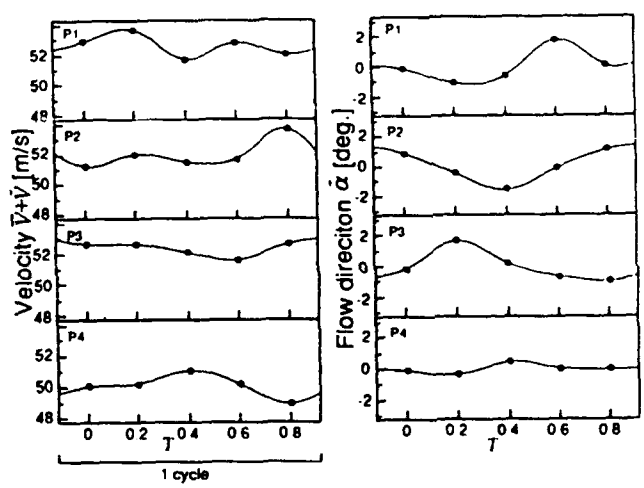

(a): velocity fluctuation $\tilde{V}$ (b): direction fluctuation $\tilde{\alpha}$

Fig. 11: Flow fluctuation (condition 2)

where $\tilde{\alpha}_{(T)}$ is the instantaneous value of $\tilde{\alpha}$ at a time instant T. The time-average is approximated by the ensemble average of the product $\alpha_1 \cdot \alpha_2$ obtained at five discrete time instants as

$$\overline{\tilde{\alpha}_1(T_n)\cdot\tilde{\alpha}_2(T_n+\tau)}\approx\frac{1}{m}\sum_{n=0}^{m-1}\left[\tilde{\alpha}_1(T_n)\tilde{\alpha}_2(T_n+\tau)\right]. \qquad (5)$$

where m is the number of time intervals within 1 cycle (m= 5). By applying Eq. (4) to the quantities at different time instants, the space-time correlation can be evaluated.

In order to examine the analogy between the flow fields for two different conditions, the cross correlation of the corresponding quantities are calculated for the same spatial location and same time instant. The results indicate that the average of cross correlation functions at τ = 0 was 0.76, thus confirming that there is a high correlation between the flow fields, in spite of the large difference (2.2 times) in rotating frequency.

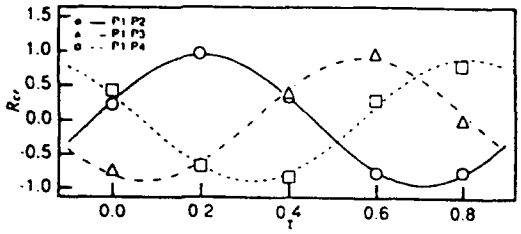

(a): Condition 1

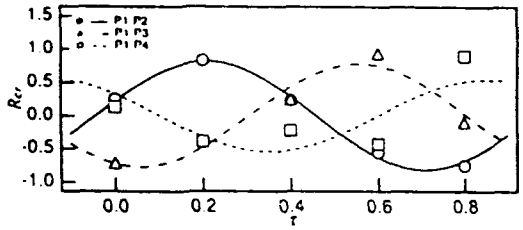

(b): Condition 2

Fig. 12: Space-time correlations R_{cr} between point P1 and other point

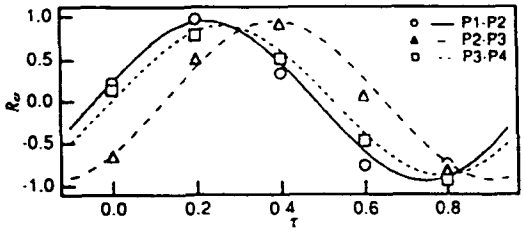

(a): Condition 1

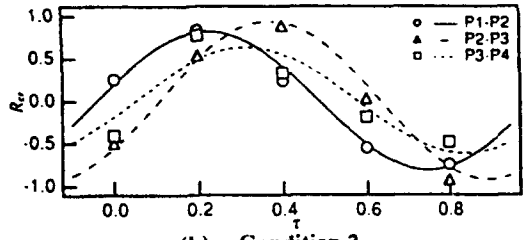

(b): Condition 2

Fig. 13: Space-time correlations R_{cr} between next measuring point

The space-time correlations R_{cr} between measuring points P1-P2, P1-P3, as well as P1-P4 are calculated and presented in Fig. 12. The lines connecting the plots are the sinusoidal functions obtained by least square fitting on the basis of the fixed time period, which is equal to the interval of blade motion, and varying amplitude and phase difference. It is indicated that the correlations between each measuring points are equally high, implying that the periodic motion persists throughout the measuring location, although there is a slight decrease in the amplitude of R_{cr}.

Figure 13 shows the space-time correlation function between the successive two measuring points, P1-P2, P2-P3, and P3-P4 for each conditions. Because the spatial intervals between the measuring points are constant, the inspection of these correlations make it possible to estimate the transfer rate of periodical fluctuation and its variation in the streamwise direction. As seen in these figures, every correlation has its peak in the range of $2.0 \leq \tau \leq 4.0$, and dividing the distance between the measuring points by the time interval, the propagating velocity can be evaluated to be approximately 1.0 ~ 1.9 times the mean flow velocity and it is the same for the both conditions.

CONCLUDING REMARKS

The application of the multi-angle laser-2-focus velocimeter (MALV) to the measurements of the unsteady flow in a diffuser of centrifugal compressor has been performed by taking into account the periodic flow fluctuation due to the wake of the impeller blades. Although the MALV must be used as a conventional L2F velocimeter under a few operations for the measurements due to strong turbulence, the flows with maximum more than 8 degrees of variation in velocity vector direction could be successfully measured by MALV with only few rotations of the optical probe per one measuring point.

It is confirmed that the measured flow fluctuations has appreciable periodic fluctuations; its magnitude in terms of the flow direction reaches up to degrees at maximum from peak to peak. The RMS of flow direction fluctuation which correlates between the blade motion and the flow direction decreases with the increasing RMS of turbulent fluctuation in downstream direction for the higher rotor revolution. The fluctuation is transferred in downstream at a rate which is of same order as the local mean velocity. The same tendencies have been observed for different impeller rotation speed in terms of the phase angle of the periodical fluctuation as well as its transmitting rate.

ACKNOWLEDGEMENT

The authors are grateful to Mr. T. Mimura, under graduate student of Dept. Mechanical Engineering, Keio University, for his assistance in performing the experiments. The kind help in modifying the test rig by Mr. M. Nakamura of IHK corporation is also acknowledged.

NOMENCLATURE

N:	Number of impeller revolution
r:	Radial position
T:	Dimensionless time
t:	Time
t_b:	Period of impeller blade motion
U_2:	Impeller tip speed
V:	Flow velocity
α:	Flow direction
Φ:	Flow coefficient
τ:	Dimensionless time-lag
$\bar{}$:	Mean component
$\tilde{}$:	Periodical fluctuation component
$'$:	Turbulent component'

REFERENCES

Agrawal, D. P., Yahya, S. M., and Thankappan, K. V., 1991, "Effect of Inlet Velocity Distribution on the Vaned Radial Diffuser Performance" ASME Fluid Machinery Forum, FED-Vol. 119, pp. 71-75

Baghdadi, S., (1977) "The Effect of Rotor Wakes on Centrifugal Compressor Diffuser Performance — A Comparative Experiment" ASME Journal of Fluids Engineering, Vol.99, pp. 45-52

Krain, H., (1981) "A Study on Centrifugal Impeller and Diffuser Flow" ASME Journal of Engineering for Power, Vol. 103, No.4, pp. 688 697

Ohmura, K., Hishida, K. and Maeda, M., (1992) A Multi-Angle Laser two-focus Velocimeter using Photo Diode Arrays, Proc. Int. Sym. Appl. Laser Techniques to Fluid Mechanics, Lisbon, Portugal, paper 14-1.

Schodl, R., (1980) "A Laser-Two-Focus(L2F) Velocimeter for Automatic Flow Vector Measurements in the Rotating Components in Turbomachines" J Fluids Engineering, Vol. 102, pp. 412-419.

Schodl, R. and Förster, W., (1988) "A multi color fiber optic laser two focus velocimeter for 3-dimensional flow analysis" Proc. 4th Int Sym Appl Laser Techniques to Fluid Mechanics, 11-14 July 1988, Lisbon, Portugal

SECONDARY FLOW MEASUREMENTS IN A MIXED FLOW PUMP USING LASER VELOCIMETRY

Klaus Brun, Research Engineer
Ronald D. Flack, Professor and Chairman
Steven B. Ainley, Graduate Research Assistant

Department of Mechanical, Aerospace, and Nuclear Engineering
University of Virginia, Charlottesville, VA 22903 USA

ABSTRACT

A laser velocimeter was used to measure the secondary flow field in the mid and exit planes of an automotive torque converter pump. Four significantly different pump and turbine speed operating conditions of the torque converter were tested. Results showed counter-clockwise circulating secondary flow in the pump mid plane and clockwise circulating secondary flow in the exit plane for all torque converter operating conditions. Typical secondary velocity magnitudes were 1.0 m/s, while typical through flow velocities were 1.5 m/s. From the measured velocities the average flow vorticity was calculated. The magnitudes of the dimensional secondary velocity and the average flow vorticity were seen to decrease with decreasing pump speed in both the mid and exit planes. Also, the highest average vorticity and secondary flow magnitudes were observed for a low turbine/pump speed ratio.

1. INTRODUCTION

The standard automotive torque converter is a recirculating hydrodynamic, mixed flow turbomachine (containing both axial and radial flow) with three independent elements that govern the internal flow field. These elements are the pump, which energizes the working fluid and is connected to the automobile's engine, the turbine, which absorbs the fluid energy and drives the transmission shaft, and the stator, which redirects the fluid to obtain zero flow incidence into the pump at a specific design speed ratio (for the remainder of this manuscript speed ratio is defined as the turbine rotational speed divided by the pump angular speed). The pump and the turbine are rotating at different speeds, while the stator is either locked or allowed to float freely, depending on the particular design and application.

Due to the significant curvature of the flow path (forcing the fluid to complete two 180 degree turns axially) and the different angular speeds of the elements the flow field is highly three dimensional. The three dimensional flow in the torque converter can be divided into meridional and non-meridional (secondary) velocity components. Secondary flows in the torque converter pump are undesirable since they cause viscous energy losses and do not contribute to the pumping process. Thus, to optimize future torque converter pump designs (and minimize internal flow losses) a thorough understanding of the internal secondary flow field is necessary. The aim of this research is to identify, document, and analyze secondary flows in the mixed flow pump for several different operating conditions of the torque converter.

1.1 Previous Studies of Torque Converter Internal Flows

A comprehensive review of relevant torque converter literature was included in papers by Bahr et al. [1991] and Gruver et al. [1994]. For the sake of brevity only a few significant papers are reviewed herein.

The average velocity flow field in the stator of an automotive torque converter was described by Bahr et al. [1991]. For their research, a torque converter was machined entirely from Plexiglas and a one directional laser velocimeter was employed to measure the flow field. Detailed velocity profiles for five planes in the stator and for two speed ratios were presented. Separation was observed in the stator for both the 0.065 and 0.8 speed ratios.

Gruver et al. [1994] and Brun et al. [1994] used the same experimental facility to determine the flow field in the pump of an automotive torque converter. Velocity vector plots for the inlet, mid-, and exit planes were presented for the 0.065 and 0.800 speed ratios. Separation regions were observed at the core-suction side in the pump mid- and exit planes for the 0.065 speed ratio. Circulatory secondary flow was observed for both speed ratios in the mid- and exit planes.

The unsteady torque converter turbine inlet flow field was measured by Brun and Flack [1993]. A method to analyze the unsteady flow field in any rotating turbomachine element was developed and applied to the torque converter. Strong influence of the pump on the turbine inlet flow field, with a jet/wake region migrating through the turbine inlet at the blade interaction frequency, was demonstrated.

By and Lakshminarayana [1991,1993] measured average static pressures on the blades of an automotive torque converter stator and pump, respectively. Their results showed that the static pressure distribution is generally poor at the blade core section and that centrifugal force has a dominant effect on the static pressure rise in the pump. Later, By et al. [1993] developed a three-dimensional viscous flow code to predict the flow field of a torque converter pump. Results showed that the pump rotation has a major effect on the secondary flow field.

Browarzik and Grahl [1992] used hot film anemometry to examine the flow field at the inlet and outlet of the pump and turbine of the torque converter. A frequency spectrum showing the relative magnitudes of velocities at the turbine exit is presented. Further research was recommended.

1.2 Objectives

For this research the same experimental facility as described by Bahr et al. [1991], Gruver at al. [1993], and Brun et al. [1993] was utilized to measure the secondary flow field in the pump mid and exit plane (for the remainder of this paper, the secondary flow is defined as the velocity components normal to the through flow direction). Four significantly different operating conditions were tested. Velocity vector plots of the secondary flow results are included herein. Based on the measured velocities the average flow vorticities were determined. This paper provides the most complete and detailed data of the secondary flow field in the torque converter pump published to date. Results presented offer not only a basic understanding of the torque converter pump flow field, but also serve as a benchmark for mixed flow turbomachinery computational flow codes.

2. EXPERIMENTAL FACILITY AND DATA ACQUISITION

The overall schematic of the experimental test rig is shown in Figure 1. The torque converter test fixture, the support system, laser velocimeter, and data acquisition system will be discussed below.

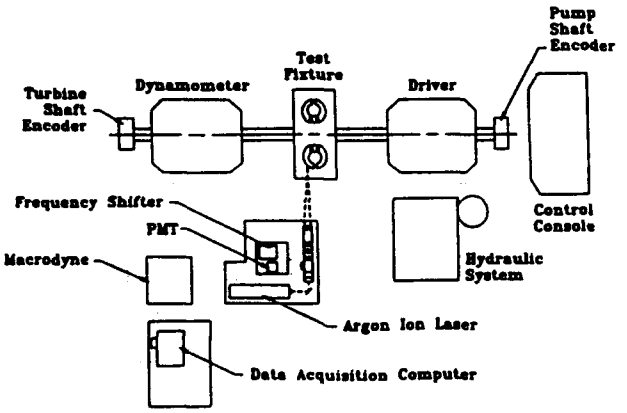

Figure 1: Overall Schematic of Experimental Test Rig

2.1 Torque converter

A standard automobile torque converter geometry was completely machined from Plexiglas and installed in an oil filled Plexiglas containment box, which is optically accessible from all sides. Figure 2 shows a cross-section of the torque converter geometry used for this research. The full diameter of the torque converter is 230 mm. Shellflex 212 oil was used as the flow medium within the converter. This oil has an index of refraction of 1.489 at 25° C and 1.480 at 50° C. The specific gravity is 0.9 at 16° C, and the viscosity varies from 19 cSt at 40° C to 4 cSt at 100° C. The oil was seeded with metallic coated glass particles of 12 μm diameter. The oil was chosen to match the index of refraction of the Plexiglas (1.490). However, perfectly matching the index of refraction of the oil and the Plexiglas was impossible because of thermal transients and gradients in the oil during torque converter operation and because of birefringent properties of Plexiglas, especially after machining. Since all laser beams had to cross through five or more Plexiglas-oil interfaces at sometimes high angles of incidence, crossing more than two beams during the measurement time interval at one location was usually impossible. Hence, multidirectional laser velocimetry was unsuitable.

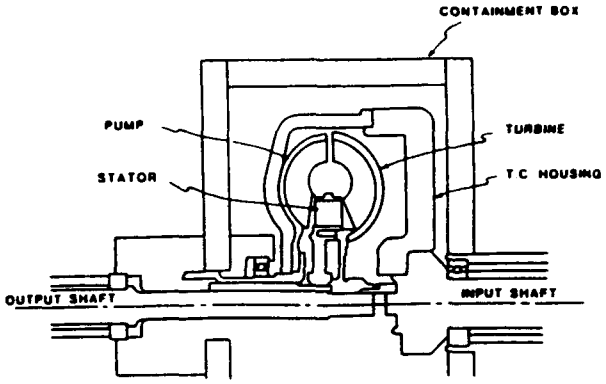

Figure 2: Cross-Section of Torque Converter

2.2 Torque converter support system

The torque converter pump was driven by a 18 kW motor, with the turbine output power absorbed by a 130 kW capacity eddy current dynamometer. A hydraulic system cooled and lubricated the driver, absorber and test fixture. The torque converter pump and turbine rotational speed were monitored and controlled to within 1 rpm. Temperatures and pressures in the torque converter, containment box, and hydraulic system as well as input and output torques were also monitored and recorded.

2.3 Laser velocimeter system

The one-directional frequency shifted, back scatter laser velocimeter system used for this research is shown in Figure 3. A 2 Watt Argon-ion laser was operated at 50 mW and at a wavelength of 514.5 nm. Two different transmitting lenses (focal lengths 250.8 mm or 350 mm) and a mirror were used to access the torque converter from three Cartesian angles to independently obtain the three dimensional velocity field. The beam separation was 40 mm and the frequency shift was 40 MHz. The backscattered light was collected by the photo-multiplier tube, downshifted to 2 MHz, bandpass filtered to eliminate the pedestal and other spurious frequencies, and then transmitted to the burst counter processor. To measure the three different velocity components realigning the optics was

necessary. The transmitting and receiving optics were mounted on a motor driven mill table such that the probe volume could be accurately moved in all three orthogonal directions. The position was monitored using linear encoders and a digital readout (accuracy 0.005 mm).

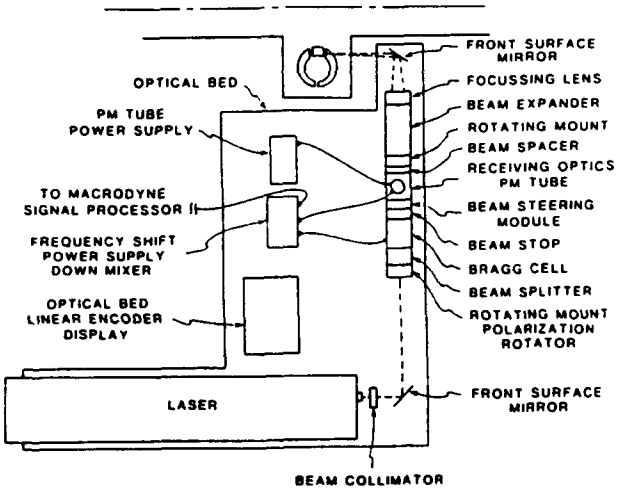

Figure 3: Laser Velocimeter System

2.4 Data acquisition system

A commercially available burst counter was used to process velocity signals. The bursts were validated using a minimum threshold setting to eliminate low amplitude noise and using a 5/8 peak counter-comparator to eliminate multiple particle signals. Validated signals were digitized and transmitted to a 486 microcomputer, where a high speed digital I/O card was used for data collection. The photomultiplier tube high voltage setting and the burst processor minimum threshold setting were adjusted to achieve a high data rate of valid signals. A 10-bit digital shaft encoder (1024 angular sectors) was used to measure the angular position of the torque converter pump at the instant that valid velocity signals were collected. The shaft encoder angular positions were also read into the computer using the digital I/O card.

2.5 Data acquisition

The torque converter pump consisted of 27 identical blade passages each with an angular resolution of 37 sectors. Each blade passage was defined by a pressure, suction, core and shell side as shown in Figure 4. Velocities were measured at 9 core to shell side positions in the pump mid and exit planes. As the pump rotated by the stationary laser velocimeter 37 blade-to-blade positions (for 27 blade passages) were accessed at each measurement location. Thus, a 37*9 measurement grid was obtained for each blade passage. The velocity profiles for the 27 blade passages were shown to be identical within their uncertainty and, hence, could be superimposed and averaged. For 90% of the measurement grid positions more than 150 valid velocity samples were collected; sufficient samples for a high confidence in the average velocities. Table 1 shows the torque converter operating conditions for which measurements were taken. All rotational speeds are given in revolutions per minute (rpm).

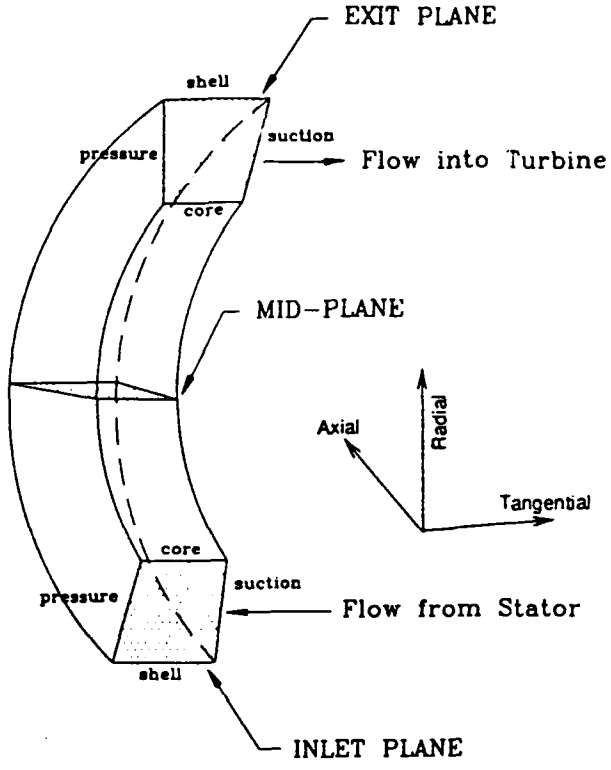

Figure 4: Schematic of Pump Blade Passage

Table 1: Test Conditions

	Cond #1	Cond #2	Cond #3	Cond #4
Speed Ratio:	0.800	0.800	0.800	0.065
Pump Speed:	1100	550	314	809
Turbine Speed:	880	440	251	52

The entire experimental facility and data acquisition procedure were described by Bahr et al. [1991], Gruver et al. [1993], and Brun et al. [1993]. The detailed dimensions of the torque converter and passage geometries were given by By and Lakshminarayana [1993]. Thus, the measurement geometry and test conditions can be reconstructed from the above references.

3. RESULTS AND DISCUSSION

Secondary velocities are presented and analyzed for the four above mentioned torque converter operating conditions. Results are given for both the mid and exit planes of the pump. All velocities are shown relative to the rotating frame. Also, the average vorticity and secondary flow magnitude is derived from the experimental data for all measurement conditions.

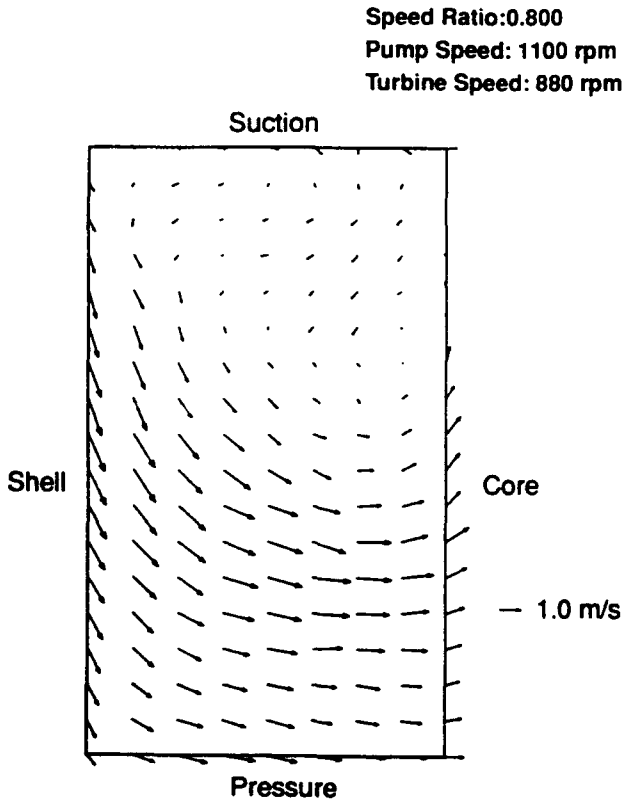

Figure 5: Secondary Flow Velocity Vectors for Operating Condition #1, Pump Mid Plane

3.1 Secondary flow results in the mid plane

Figures 5 through 8 show velocity vector plots for the pump mid plane. The secondary flow for the operating condition #1 (0.8 speed ratio, 1100 rpm pump speed) is presented in Figure 5. As can be seen, secondary flows in the mid plane have a strong counter-clockwise rotational circulation. Peak velocities of 1.9 m/s are observed near the pressure and shell sides, while smallest velocities of 0.2 m/s are located near the suction side. Since the fluid is rotating around the shaft of the torque converter and is also being turned from axial to radial and back to axial flow (the blade passage curvature), a combined effect of the coriolis and centrifugal forces as well as shear forces on the fluid are postulated to be responsible for this circulation.

Similar secondary flow velocity profiles can be seen in Figures 6 and 7 for torque converter operating conditions #2 and #3, respectively. For these cases the speed ratio was maintained at 0.8 but the pump speed was reduced to 550 rpm and 314 rpm, respectively. Figures 6 and 7 show that the general circulating flow field trends are similar to the previous case, but the overall velocity magnitudes are lower. Peak secondary velocities are 1.1 m/s and 0.8 m/s for conditions #2 and #3, respectively. A direct comparison of Figures 5, 6, and 7 shows that the secondary flow magnitudes decrease with pump rotational speed, but the center of circulation remains stationary over the range of pump speeds.

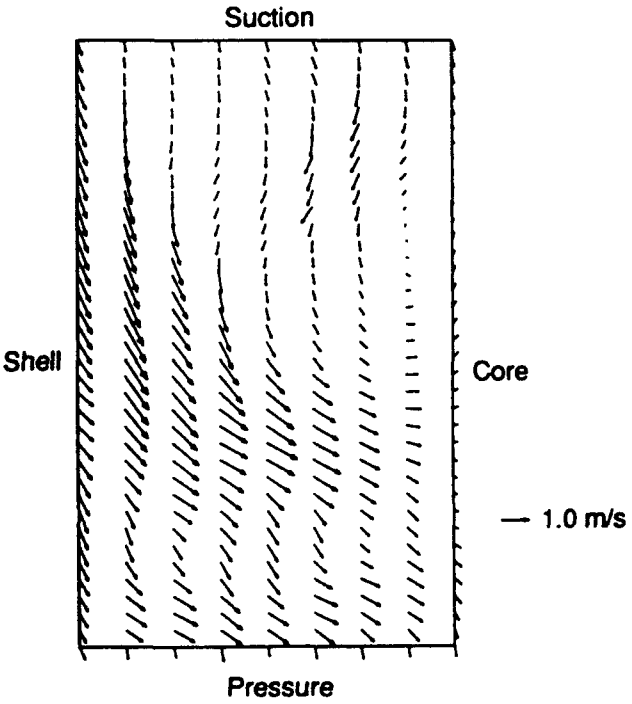

Figure 6: Secondary Flow Velocity Vectors for Operating Condition #2, Pump Mid Plane

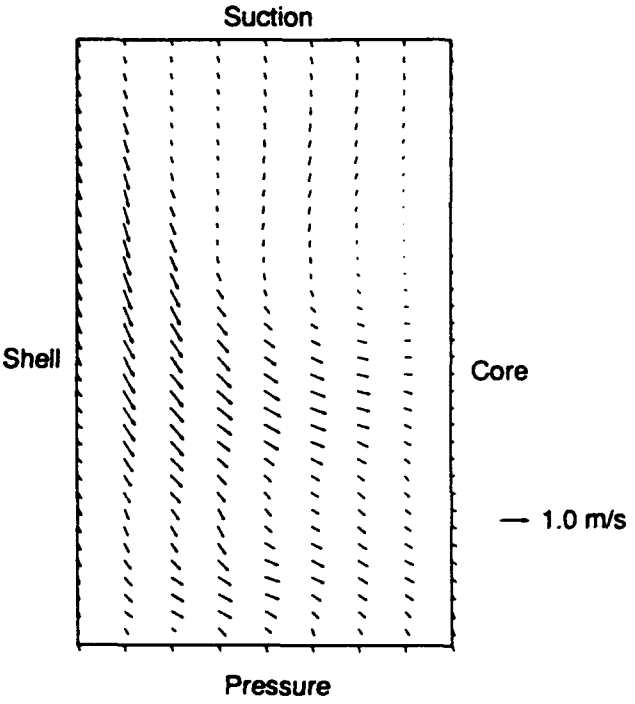

Figure 7: Secondary Flow Velocity Vectors for Operating Condition #3, Pump Mid Plane

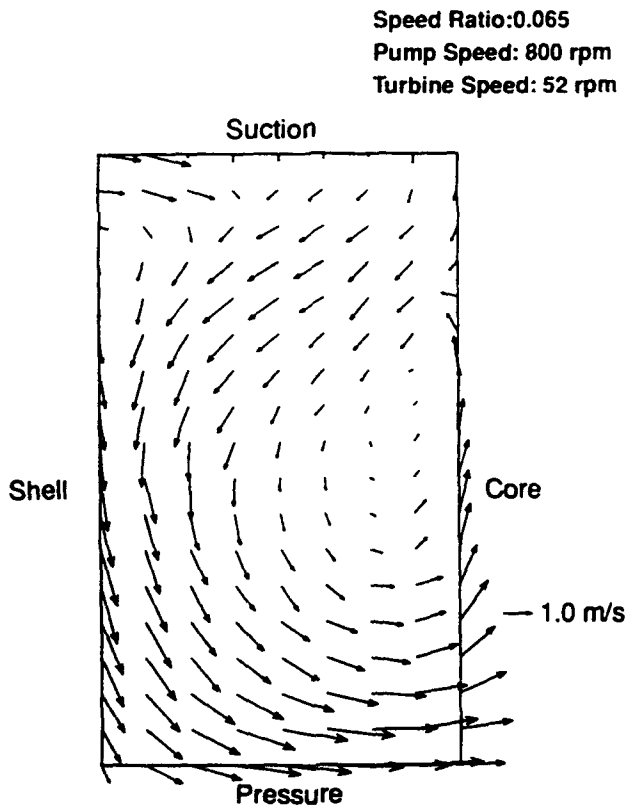

Figure 8: Secondary Flow Velocity Vectors for Operating Condition #4, Pump Mid Plane

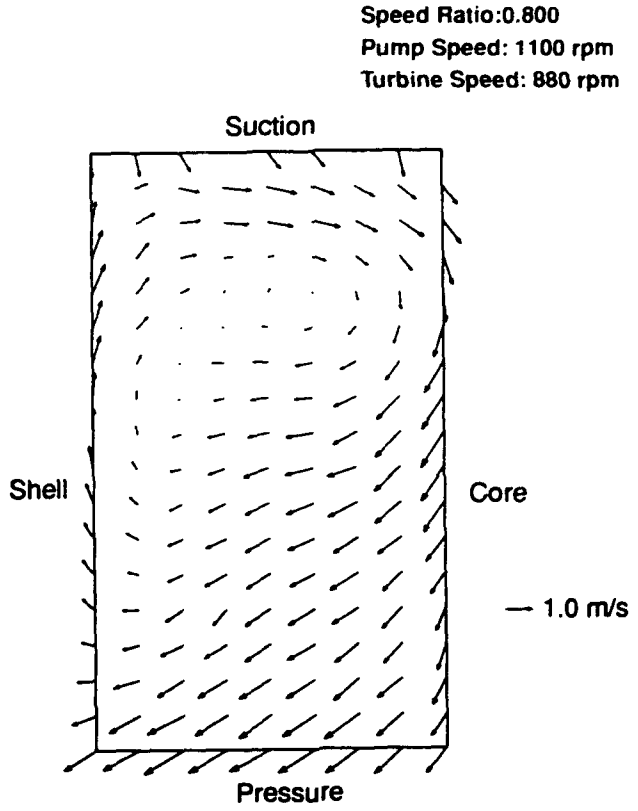

Figure 9: Secondary Flow Velocity Vectors for Operating Condition #1, Pump Exit Plane

The flow field for operating condition #4 is shown in Figure 8. For this case the speed ratio was lowered to 0.065 and the pump speed was 800 rpm. As a consequence, the torque converter operation is significantly different from the previous cases. The secondary flow is still circulating counter-clockwise, but the general flow trends are dissimilar from conditions #1, #2, and #3. The center of circulation is shifted toward the middle of the blade passage and peak secondary velocities of 1.7 m/s are now located near the pressure and core corner.

3.2 Secondary flow results in the exit plane

Vector plots of the secondary flow field in the pump exit planes are presented in Figures 9 through 12. Again, all 4 operating conditions are analyzed. Figure 9 shows the secondary flow for condition #1. A strong circulatory flow pattern in the clockwise direction is observed. One should note that the counter-clockwise circulating flow from the mid plane has reversed rotational directions between mid and exit plane and is circulating clockwise in the exit plane. This trend is consistent for all 4 operating conditions. The center of circulation for this case is located near the suction side. Maximum and minimum secondary flow velocities for condition #1 are 1.4 m/s and 0.1 m/s, respectively.

Figures 10 and 11 show the pump exit flow field for operating condition #2 and #3, respectively. For both cases the center of circulation is located close to the shell side and highest velocities are seen at the pressure and suction sides. Peak secondary velocities are 0.8 m/s and 0.4 m/s for condition #2

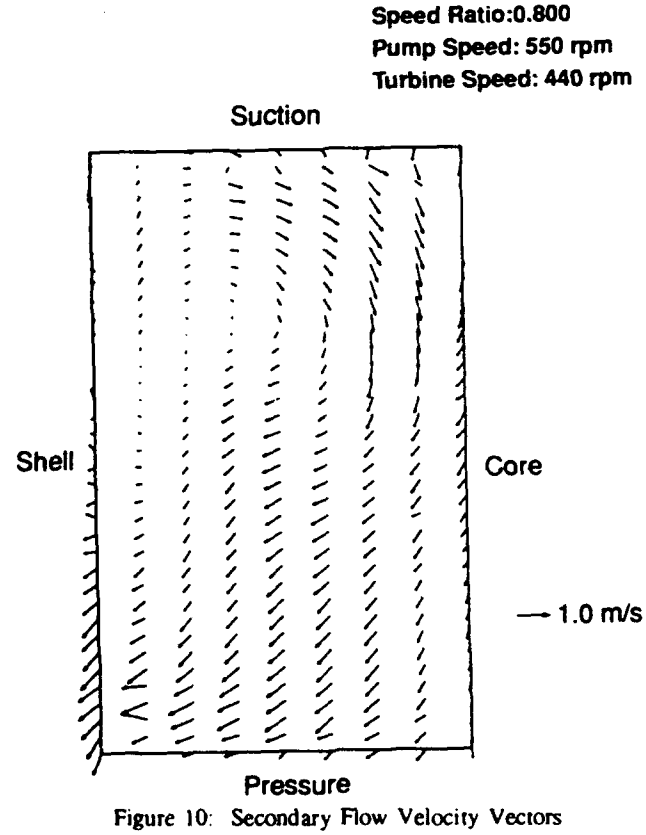

Figure 10: Secondary Flow Velocity Vectors for Operating Condition #2, Pump Exit Plane

and #3, respectively. By comparing Figures 9, 10, and 11 one can observe that lowering the pump rotational speed significantly affects the secondary flow field in the pump exit. As the pump speed is lowered the center of circulation shifts from the passage center to the shell side. Also, similarly to observations in the mid plane, the overall secondary flow velocity magnitudes in the exit plane decrease with pump rotational speed.

Finally, Figure 12 shows the pump exit secondary flow for operating conditions #4. The overall flow characteristics are significantly different from the previous exit plane cases. Highest secondary velocities (1.7 m/s) are observed at the pressure-core corner, while lowest velocities (0.0 m/s) are near the suction side. As previously noted, altering the speed ratio significantly affects the secondary flow field characteristics.

3.3 Average secondary and through flow velocity magnitudes

The average through flow velocity magnitude was measured by Ainley [1994] and is included here as a comparison for general flow trends. Table 2 shows through flow results for the mid and exit planes.

Table 2: Average Through Flow Velocity (m/s)

(Turbine rpm)/(Pump rpm)	Mid Plane	Exit Plane
880/1100 (Condition #1)	1.6	1.7
440/550 (Condition #2)	0.6	0.7
251/314 (Condition #3)	0.3	0.3
52/800 (Condition #4)	2.2	2.5

The average secondary flow velocities were calculated by integrating the magnitudes of the measured secondary velocities (in the rotating frame) across an entire plane and dividing it by the number of measurement locations. Average secondary flow velocities were then normalized by the through flow velocities from Table 2. Both dimensional and non-dimensional average secondary flows are presented in Table 3 (non-dimensional values are in brackets).

Table 3: Average Secondary Velocity (m/s), [Normalized Average Secondary Velocity]

(Turbine rpm)/(Pump rpm)	Mid Plane	Exit Plane
880/1100 (Condition #1)	1.0 [0.65]	0.5 [0.27]
440/550 (Condition #2)	0.7 [1.06]	0.4 [0.60]
251/314 (Condition #3)	0.4 [1.10]	0.2 [0.72]
52/800 (Condition #4)	1.2 [0.55]	0.8 [0.30]

Results from Table 3 show that for the 0.8 speed ratio the average secondary velocities decrease with decreasing pump speed. This would be expected because the through flow also decreases with decreasing pump speed. Generally, the secondary flow magnitude is observed to be smaller in the exit plane than the mid plane. Normalized velocities for the 0.8 speed ratio increase from 0.65 to 1.10 in the mid plane and from 0.27 to 0.72 in the exit plane as the pump speed decreases. Thus, the

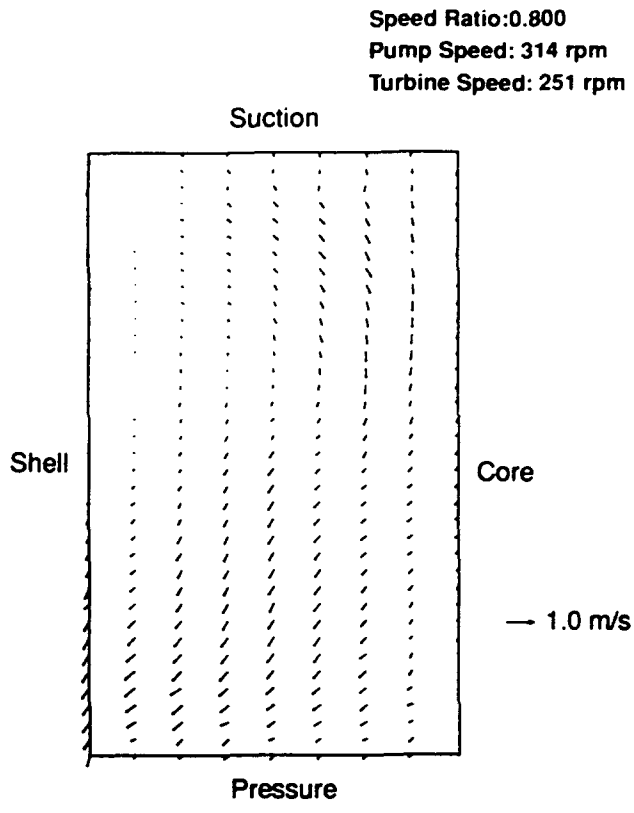

Figure 11: Secondary Flow Velocity Vectors for Operating Condition #3, Pump Exit Plane

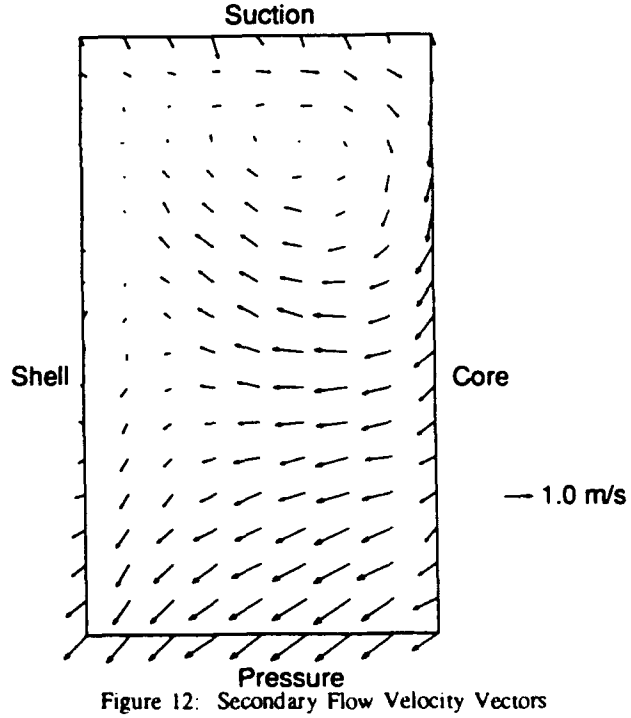

Figure 12: Secondary Flow Velocity Vectors for Operating Condition #4, Pump Mid Plane

through flow and secondary flow components are of similar magnitude in the mid plane, while in the exit plane the through flow velocity dominates.

In both mid and exit planes the dimensional average secondary velocities are highest for the 0.065 speed ratio, while the normalized average secondary velocity is lowest for this case. Similarly to the 0.8 speed ratio, the normalized average secondary velocity is seen to decrease between mid and exit planes, but, unlike the 0.8 speed ratio case, for the 0.065 speed ratio the through flow velocity is dominant in both planes.

3.4 Secondary flow vorticity

Since rotating circulatory flow patterns were observed in the mid and exit planes for all 4 measurement conditions, a logical choice to quantify the secondary flow field is the vorticity. The average vorticity, ξ, of a plane is calculated from the following equation,

$$\xi = -\frac{1}{A}\iint(\nabla \times V)\cdot dA = -\frac{1}{A}\iint(\frac{\partial v}{\partial x} - \frac{\partial u}{\partial y})dA$$

where V is the total local velocity vector, u is the core to shell velocity, v is the pressure to suction velocity, and A is the area of the plane. Both u and v are in the local rotating frame. The local coordinates x and y are defined as the core to shell and pressure to suction directions, respectively. One should note that the average vorticity also equals the negative flow circulation, $-\Gamma$, divided by A. The average vorticity equation can be discretized as follows:

$$\xi = -\frac{1}{A}\sum\sum[(\frac{v_{i+1}-v_i}{x_{i+1}-x_i} - \frac{u_{j+1}-u_j}{y_{j+1}-y_j})\cdot(x_{i+1}-x_i)\cdot(y_{j+1}-y_j)]$$

This expression is evaluated by integrating the measured secondary flows across an entire plane. To non-dimensionalize the vorticity it was divided by the average through flow (Table 2) and multiplied by the core-shell blade length. Average vorticities are presented in Table 4.

Table 4: Average Vorticity (1/s), [Normalized Average Vorticity]

(Turbine rpm)/(Pump rpm)	Mid Plane	Exit Plane
880/1100 (Condition #1)	117.6 [1.49]	-144.5 [-1.45]
440/550 (Condition #2)	83.1 [2.42]	-40.9 [-1.04]
251/314 (Condition #3)	21.5 [4.12]	-20.6 [-1.06]
52/800 (Condition #4)	150.1 [1.33]	-71.2 [-0.49]

The results in Table 4 are consistent with observations of the secondary flow plots in Figures 5 through 12; in the mid plane the flow is counter-clockwise (positive vorticity, negative circulation) and in the exit plane the flow is clockwise (negative vorticity, positive circulation). For the 0.8 speed ratio (Conditions #1, #2, and #3) the magnitude of the dimensional vorticity in both planes is seen to decrease with the pump rotational speed. Also, in the mid plane the normalized vorticity increases with increasing pump speed, while in the exit plane the normalized vorticity decreases with increasing pump speed.

The strongest dimensional counter-clockwise circulating flow in the mid plane is at the 0.8 speed ratio (Condition #1), while in the exit plane the strongest clockwise circulating flow is at the 0.065 speed ratio (Condition #4). The lowest magnitude of the normalized vorticity is observed in both planes for the 0.065 speed ratio.

4. SUMMARY AND CONCLUSIONS

The secondary flow field in the mid and exit plane of an automotive torque converter pump was analyzed for four significantly different torque converter operating conditions. Velocities were measured in the stationary frame using a laser velocimeter and then translated into the relative rotating frame using digital pump shaft encoder information. From the measured velocities 2-D vector plots were generated and average vorticities were calculated. Important conclusions drawn from this research are:

- Significant secondary flows were observed in the torque converter pump mid and exit plane at all operating conditions.
- In the pump mid plane the secondary flow field circulated counter-clockwise for all measurement conditions, while the pump exit secondary flow field circulated clockwise for all measurement conditions.
- In the mid plane the secondary and through flow velocities have similar magnitudes, while in the exit plane the through flow velocities dominate.
- The dimensional average secondary flow velocities and flow vorticity decrease with decreasing pump speed for a constant speed ratio of 0.8.
- Normalized average secondary velocities were seen to increase with decreasing pump speed for the constant 0.8 speed ratio for both planes. Also, the normalized vorticity increased with increasing pump speed in the mid plane, while it decreased with increasing pump speed in the exit plane for this case.
- For the 0.8 speed ratio the center of circulation location in the midplane was not affected by the pump speed, while in the exit plane the center of circulation was seen to shift from the passage center to the shell side as the pump speed was decreased.
- Lowering the speed ratio significantly affected the overall velocity trends of the secondary flow field and the location of the center of circulation in both the mid and exit planes. In both planes the highest dimensional average secondary velocity was observed for the 0.065 speed ratio case.

ACKNOWLEDGEMENTS

This research was sponsored in part by General Motors Corporation NAO Engineering Center in Warren, MI, the GM Powertrain Division in Ypsilante, MI, and Rotating Machinery and Controls (ROMAC) Industrial Research Program at the University of Virginia. The authors wish to express their gratitude to Don Maddock for his support and suggestions.

REFERENCES

Ainley, S.B. 1994, Laser Velocimetry Measurements in the Stator and Pump of an Automotive Torque Converter, MS Thesis, University of Virginia, Charlottesville, Virginia, USA..

Bahr, H.M., Flack, R.D., By, R.R., and Zhang, J.J. 1990, Laser Velocimeter Measurements in the Stator of a Torque Converter, SAE Paper No. 901769, SAE 1990 Transactions, Journal of Passenger Cars, Vol. 99, Section 6, pp. 1625-1634.

Browarzik, V., and Grahl, K.G. 1992, Non-Steady Flow Measurements Inside a Hydrodynamic Torque Converter, ASME Paper No. 92-GT-161.

Brun, K., and Flack, R.D. 1993, Transient Velocity Measurements in a Turbomachine with Independently Rotating Components, Fifth International Conference on Laser Anemometry, SPIE Conference Proceedings, Vol. 2052., pp. 419-426.

Brun, K., Flack, R.D., and Gruver, J.K. 1994, Laser Velocimeter Measurements in the Pump of an Automotive Torque Converter: Part II - Unsteady Measurements, ASME Paper No. 94-GT-48, accepted for publication in the ASME Transactions, Journal of Turbomachinery.

By, R. R., and Lakshminarayana, B. 1993, Measurement and Analysis of the Static Pressure Field in a Torque Converter Pump, 2nd ASME Pumping Machinery Symposium, FED-Vol. 154, pp. 253-264, to be published in ASME Transactions, Journal of Fluids Engineering.

By, R.R., Kunz, R.F., and Lakshminarayana, B. 1993, Navier Stokes Analysis of the Pump Flow Field of an Automotive Torque Converter, 2nd ASME Pumping Machinery Symposium, FED-Vol. 154, pp. 264-274, to be published in ASME Transactions, Journal of Fluids Engineering.

Gruver, J.K., Flack, R.D., and Brun, K. 1993, Laser Velocimeter Measurements in the Pump of a Torque Converter Part I - Average Measurements, ASME Paper No. 94-GT-47, accepted for publication in the ASME Transactions, Journal of Turbomachinery.

DATA REDUCTION PROCEDURES FOR LASER VELOCIMETER MEASUREMENTS IN TURBOMACHINERY ROTORS

J. Lepicovsky

NYMA, Inc.
NASA LeRC Group
Brook Park, OH 44142, U.S.A.

INTRODUCTION

Blade-to-blade velocity distributions based on laser velocimeter data acquired in compressor or fan rotors are increasingly used as benchmark data for the verification and calibration of turbomachinery computational fluid dynamics (CFD) codes. Using laser Doppler velocimeter (LDV) data for this purpose, however, must be done cautiously. Aside from the still not fully resolved issue of the seed particle response in complex flowfields, there is an important inherent difference between CFD predictions and LDV blade-to-blade velocity distributions. CFD codes calculate velocity fields for an idealized rotor passage. LDV data, on the other hand, stem from the actual geometry of all blade channels in a rotor. The geometry often varies from channel to channel as a result of manufacturing tolerances, assembly tolerances, and incurred operational damage or changes in the rotor individual blades.

In high speed fans at certain operating conditions, the rotors exhibit noticeable differences among the velocity fields of individual rotor blade channels. Figure 1 serves as an example. The figure, which presents an extreme case of a high speed fan rotor operating at off-design conditions, shows axial velocity distributions in each of the 44 rotor blade channels (notice that the velocity was measured in 43 out of 44 channels). The differences in axial velocity profiles among individual blade channels are striking.

Understandably, in a situation like that in Figure 1, the question which immediately arises is which blade channel is the "right" one to use for CFD code verification; or alternately, should the channel velocity profiles instead be first averaged over the rotor and then the resulting average channel distribution used. A follow-up question is how faithfully the resulting average velocity profile represents the "correct" velocity distribution for the given operating conditions. In essence, the question is how much "agreement" or "disagreement" is required or should be tolerated in comparison with the CFD predictions to approve a particular CFD code as a reliable tool for a given task.

To responsibly approach the questions raised above, it must be understood how the laser velocimeter (LV)

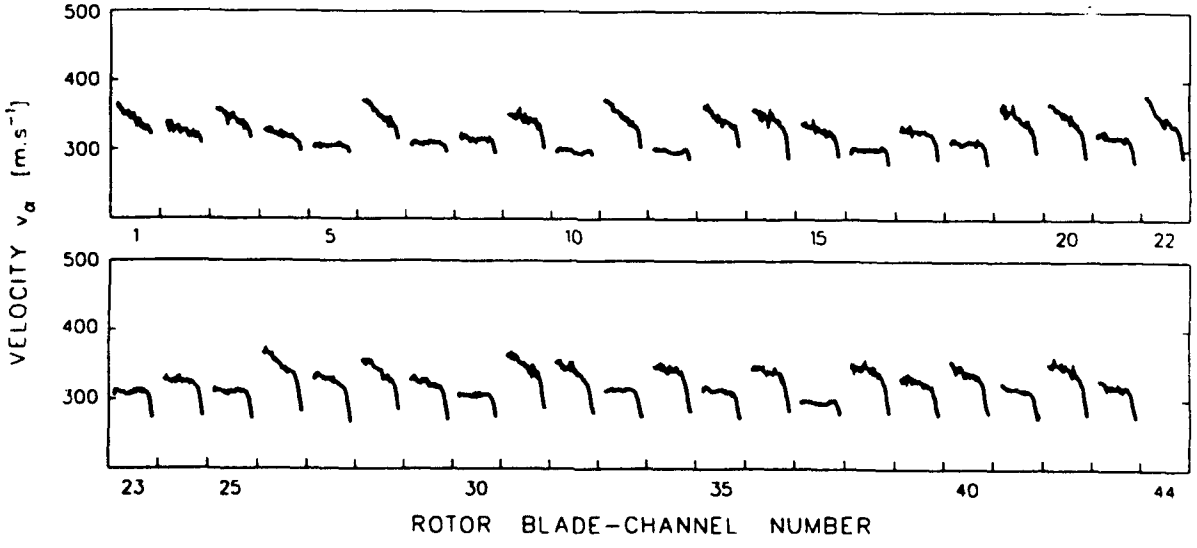

Figure 1. Axial velocity distribution for off-design operation in a high speed fan rotor.

results were generated. A common approach to acquiring periodic data is to employ conditional sampling and ensemble averaging procedures. Ensemble averaging of LV data acquired in a spinning rotor can be done in several ways. In the early days the LV system was "turned on" only for a selected angular position of a rotor to record velocity values at that particular location in the rotor. With the advent of accurate rotary encoders, much more efficient data acquisition was possible. An LV system "works continuously", and a recorded and validated LV velocity sample is immediately tagged with a particular angular position generated by the rotary encoder. Currently, the two basic approaches are either blade-channel conditional sampling or rotor conditional sampling. In the blade-channel sampling procedure, the rotary encoder is restarted at the beginning of every blade passage. Consequently, ***each LV data sample*** has the same "weight" in the procedure that generates the resulting blade-channel velocity profile. In the rotor sampling approach, the rotary encoder is restarted by each rotor revolution. In this approach ***each blade channel velocity distribution*** "weighs" equally during the averaging over the entire rotor when the resulting blade-channel velocity profile is generated. It is the goal of this paper to describe and discuss the data reduction procedure used by the author for LV data acquired recently in the rotor of a high speed fan.

THE NATURE OF LV MEASUREMENTS IN SPINNING ROTORS

A specific feature of laser velocimeter measurements made in spinning rotors is that the "probe traversing" in the circumferential direction is provided by the rotation of the rotor. As depicted in Figure 2, in the relative frame of a spinning rotor, the LV probe first moves from the center of the first blade (point C_1) to cross the first blade suction surface (point S_1), then passes by the blade channel centerline (point C_0) to cross the pressure surface of the second blade (point P_2), and finally moves by the center of the second blade (point C_2) to repeat the same sequence for the following blade channel. The circumferential traversing of the LV probe is therefore determined by the rotor rotation; as a result, the instantaneous pitchwise position of the LV probe can be predicted. On the other hand, an LV velocity data sample is acquired only when a seed particle crosses the LV probe and its signal is validated by the LV circuitry, which unfortunately, cannot be predicted. As a consequence, LV velocity data are acquired randomly. Care must be exercised to correctly locate the randomly measured flow velocity samples with respect to a moving blade channel.

A typical LV data set contains a very large number of velocity samples (*80 000* to *100 000* for the case of the presented data). The flow velocity samples, acquired in a random sequence during a time interval of several thousands of rotor revolutions, were rearranged by the post-processing procedure based on one of the ensemble averaging methods and are presented as a velocity distribution along the blade-channel pitch. Figure 3 is an example of such a velocity distribution. The distribution follows the time sequence along the LV probe trace line indicated in Figure 2. The depicted velocity profile is not a result of only one blade-channel crossing. The profile shown here as a continuous curve actually consists of discrete LV velocity samples acquired randomly along the rotor circumference. To generate the resulting velocity profile, the radial, axial, and instantaneous circumferential LV probe positions must be known with sufficient accuracy [Lepicovsky (1993)].

Many equally important conditions must be met to successfully conduct LV measurements in a fan or a compressor stage. Two of these conditions are the existence of the LV probe (measurement volume) and its visibility. Both the existence of the LV probe and its visibility are affected by obstacles in the optical path (e.g., rotor blades). The obstacles for the transmitting optics determine the probe's existence; the obstacles in

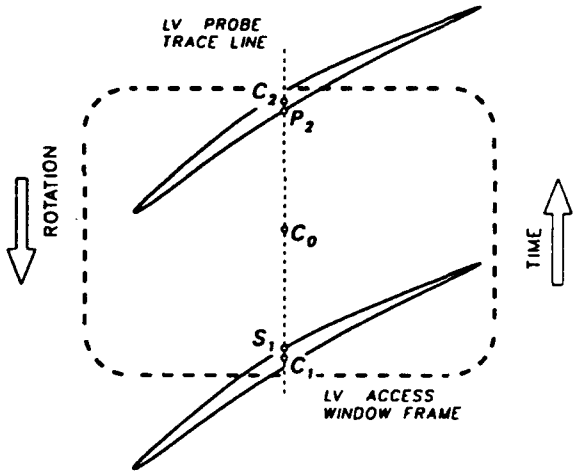

Figure 2. LV probe trace line.

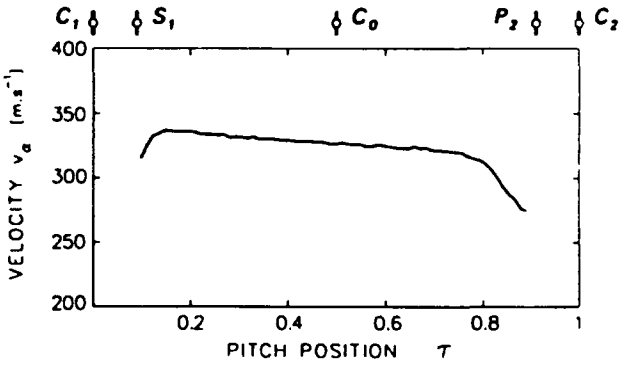

Figure 3. Blade-to-blade axial velocity distribution.

the path of the receiving optics determine the probe visibility [Lepicovsky (1993)]. Full probe visibility implies that there is no interference between the light-collecting cone of the receiving optics and either the fan casing or the rotor-blade geometry. In a blade tip region, these two conditions are satisfied provided there is a suitable access window in the fan casing. Deeper in the blade channel, however, the blade geometry may significantly restrict the region where the LV probe exists or is visible (optical shading).

The ranges of visibility and existence for the LV probe must be determined to distinguish between regions where the LV signal could originate only from the seed particles and those regions where the LV signal could also be generated from the LV probe interference with blade surfaces [Lepicovsky (1993)]. Occasionally, such signals may satisfy the validation criteria of an LV processor and they can be accepted as valid velocity data. Of course, if an LV processor validates any signal which did not originate from the visibility region, that signal must be rejected from the procedure that generates flow velocity profiles.

THE RANDOMNESS OF THE LV DATA

To illustrate the random nature of LDV signals, Figure 4 depicts a time interval of one revolution of a high speed fan rotor. A time scale at the bottom of the figure indicates the time elapsed from the beginning of the particular revolution. Utilizing the same data set already shown in Figure 1, the figure shows a time sequence of recorded LV data samples taken during the 61st revolution of the fan rotor after the onset of the LV data acquisition process. To record a sufficient number of LV velocity samples for the entire data set, the LV data were recorded over an interval of *48.4 s*, which was equal to *10 414* rotor revolutions. The total number of recorded LV samples was *94 164*, thus giving an average LV data rate of *1.95 kHz*. As seen in Figure 4, however, there were *30* LV data samples recorded during this particular revolution, which translates to a momentary LV data rate of *6.5 kHz*. Even though the LV data rate during the 61st revolution was more than three times higher than the average data rate, it was not high enough for us to be able to record at least one velocity sample in each blade channel of the fan rotor (44 blades). Consequently, a data reduction procedure must properly reconstruct the blade-to-blade velocity distributions from a very sparsely populated data sequence. In order to place the random LV samples at correct pitch positions in a particular rotor blade channel, the LV signal is tagged with the instantaneous angular position of the rotor. For the case under discussion, the angular resolution of the tagging electronics was *0.1 dg*, thus giving 82 positions per one rotor blade channel pitch. The LV data recorded for rotor blade channels 6 through 11 during the 61st revolution are shown in Figure 5 (circular markers) together with the velocity distributions generated later from all the LV data acquired for the given fan operating conditions (as already shown in Figure 1). Again, the time scale in this figure shows the time elapsed from the beginning of this particular revolution of the fan rotor.

CONDITIONAL SAMPLING

In order to construct the velocity distribution in a spinning rotor, the LV data must be acquired using a conditional sampling technique. Conditional sampling of LV data, described in detail by Strazisar & Powell (1981)

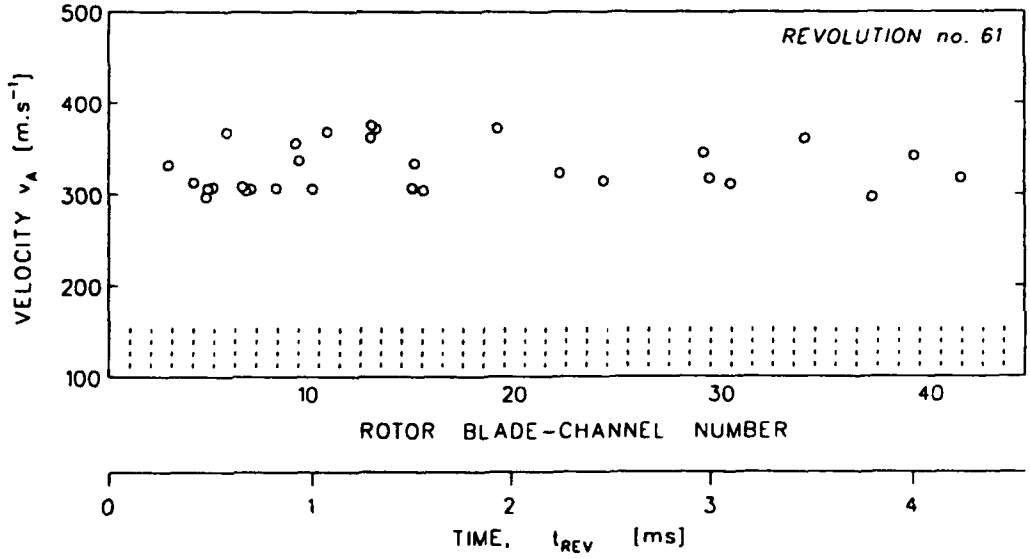

Figure 4. Sequence of LV samples recorded for one revolution of the fan rotor.

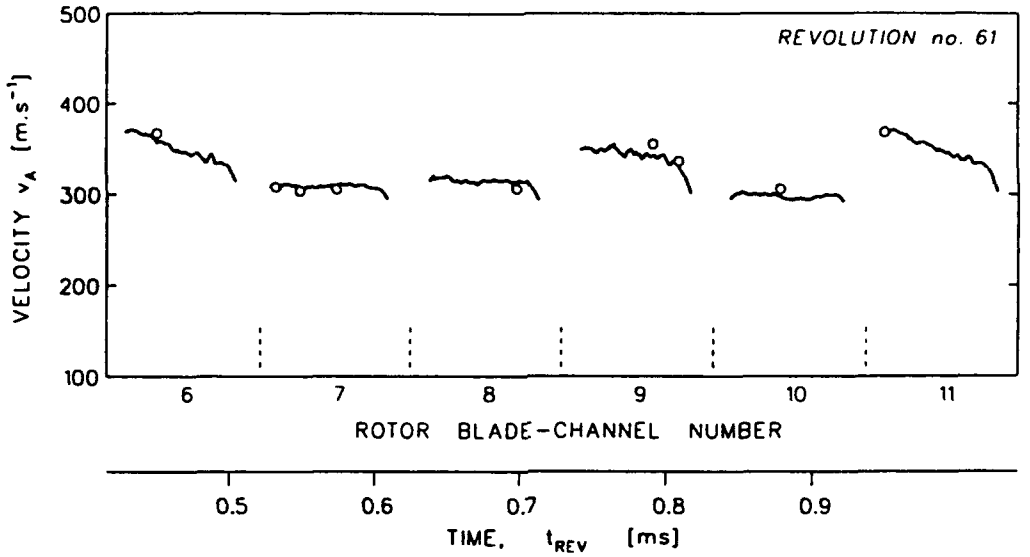

Figure 5. Sequence of LV samples recorded during one passage of six rotor blade channels.

and Lepicovsky & Bell (1984), can be triggered either by a blade passage (channel sampling) or by a rotor revolution (rotor sampling). Using true blade-channel sampling, each blade when passing by the LV probe repeatedly initiates a time sequence of the LV data acquisition. In this way, all LV data recorded in different blade channels are "piled up" into a single file representing an average blade channel width. Consequently, blade-channel sampling results in a blade-to-blade averaged velocity distribution over an average single blade channel (Figure 3). In contrast, for rotor sampling, the sequence of recorded LV data is repeatedly initiated by each rotor revolution and the LV data are "piled up" into a single file representing the entire circumference of the rotor (Figure 1). Thus, rotor sampling results in an averaged velocity distribution over the entire circumference of the rotor. A pseudo blade-channel sampling method utilizes LV data acquired in the rotor sampling mode; however, the sequence of recorded LV data is divided into segments equal to one blade-channel pitch flyby interval and then the LV data are "piled up" into a single file equal to the width of a rotor blade channel.

Each of the sampling methods has its advantages and problems. For example, to construct a blade-to-blade velocity distribution using the blade-channel sampling; only a moderate number of LV samples needs to be acquired. Therefore, this approach can be used to advantage for the cases of limited memory capacity of the data acquisition electronics, cases of low LV data rates, or cases when the total time of data acquisition is restricted by the operating conditions of a tested hardware. However, the need to repeatedly initiate the data acquisition sequence by each blade passage restricts this method to cases with a low blade passing frequency e.g., Lepicovsky & Bell (1984). The rotor sampling approach, on the other hand, requires large memory capacity for the data collection device and a high LV data rate. The major advantage of this approach is that the data allow inspection of changes of the velocity patterns from channel to channel. This approach, however, requires a large number of LV samples to be collected, which means longer data acquisition times and a large memory capacity. The pseudo blade-channel sampling approach tries to utilize advantages of both previously discussed methods. The drawback of this method is the decreasing accuracy of LV data placement at correct pitch positions with an increasing time interval from the instant of the once-per-revolution (OPR) triggering signal which repeatedly restarts the rotary encoder. The OPR signal also controls encoder's "speed". Consequently, the encoder is locked to the previous revolution time and "does not know" the immediate rotor speed, which may slightly vary. Larger velocity variations are flagged by the end-of-revolution encoder count, and the LV data for such revolution will be discarded. However, for velocity variations within the encoder limits even small deviations from the correct pitch positions may strongly affect the velocity and velocity unsteadiness values, especially in regions of high velocity gradients in the vicinity of blade surfaces. The data discussed in this paper were acquired using the rotor sampling mode. The results, shown here, were generated using either the rotor sampling or pseudo blade-channel sampling approaches. The term blade-channel sampling in the following sections actually refers to the pseudo blade-channel sampling method.

CLEANING PROCEDURES FOR LV TURBOMACHINERY DATA

Spurious and statistically insignificant data entries should be removed from an LV data set at the onset of the data reduction procedure. Three data "cleaning"

schemes were employed in our approach: (1) histogram clipping, (2) ensemble clipping, and (3) visibility clipping.

Histogram Clipping

The first cleaning procedure, called histogram clipping, is based on a population cut-off limit of a velocity histogram generated from all acquired LV samples disregarding the time sequence (instantaneous angular position) of their acquisition. It is a common approach in non-periodic flows outside turbomachinery measurements to use velocity histograms for judging the quality of the collected LV data [Petrie *et al* (1988)]. For turbomachinery data, such an approach is usually not adopted [Strazisar *et al* (1989)] because the value of the overall data velocity histograms for interpreting rotor or blade velocity distributions is questionable. In non-periodic flows with constant mean velocity, the velocity histograms are used to estimate the mean velocity value and the root-mean-square (RMS) value of velocity deviations from the mean (σ) of the flow in question. After that, all velocity samples which deviate more than $\pm 3\sigma$ from the mean are discarded for their statistical insignificance. In turbomachinery rotor flows, however, the value of local mean velocity is not constant but depends on the particular pitch position inside the blade channel. For the rotor flows measured in the non-rotating frame, the local mean velocity is a strong function of time; it is periodic with the blade passing frequency. The variability of the mean velocity of rotor flows is the reason why the overall velocity histograms cannot be used in the same manner as is common in non-periodic flows. Still, the velocity histogram plays an important role in the procedure for cleaning LV data from rotor flows. The overall data histogram can be used to eliminate LV data with low statistical significance based on the ***velocity bin population*** value rather than on the deviation from the mean.

The overall data velocity histogram, generated for a velocity resolution of *1* $m.s^{-1}$, is shown in Figure 6. To enhance the visibility of the sparsely populated velocity bins, the histogram is replotted in Figure 7 utilizing a logarithmic scale on the ordinate. The population cut-off limit for data cleaning was selected to be *1%* of the population of the most populated velocity bin. The limit was *21* in this particular case. The cut-off limit can be set independently or it can be related to some fraction of the most populated velocity bin. For pure Gaussian distributions, the population cut-off limit and the RMS value are mathematically related. For skewed histograms of turbomachinery rotor flows, the relation between the population cut-off limit and RMS values is not straightforward. The author's experience is that the population cut-off limit should not be less than *10* velocity samples per bin.

Ensemble Clipping

The cleaning procedure to follow the histogram clipping is applied either to the channel or rotor data sets, depending on which type of sampling was employed. For channel sampling data sets, all of the acquired LV samples were allocated to particular pitch positions in a single blade channel (Figure 8). After that, the data subsets at each of the recorded pitch positions (82 in the described case) were treated separately. Since the data were acquired in the sampling mode synchronized with the blade passing frequency, the time dependence of the velocity signals with respect to the rotor motion was removed and the individual velocity data sets at each pitch position can be treated as having constant mean velocities. Velocity histograms for each data subset were generated and the mean values and the root-mean-square

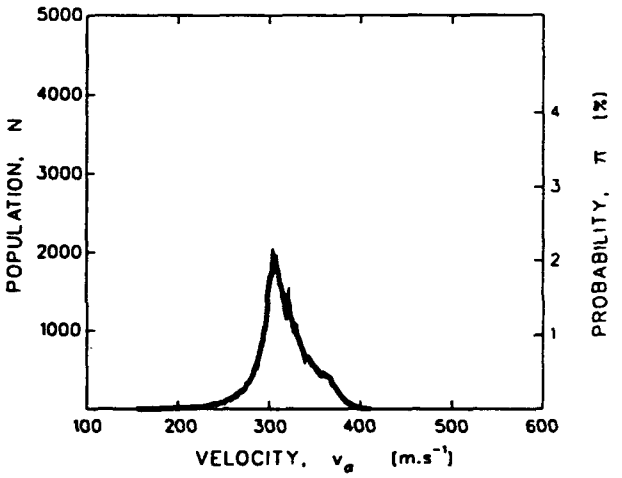

Figure 6. Over-all data velocity histogram of recorded LV samples.

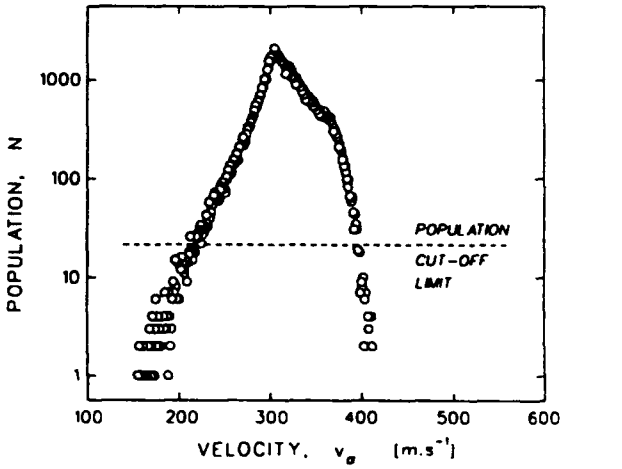

Figure 7. Population cut-off limit of a velocity histogram.

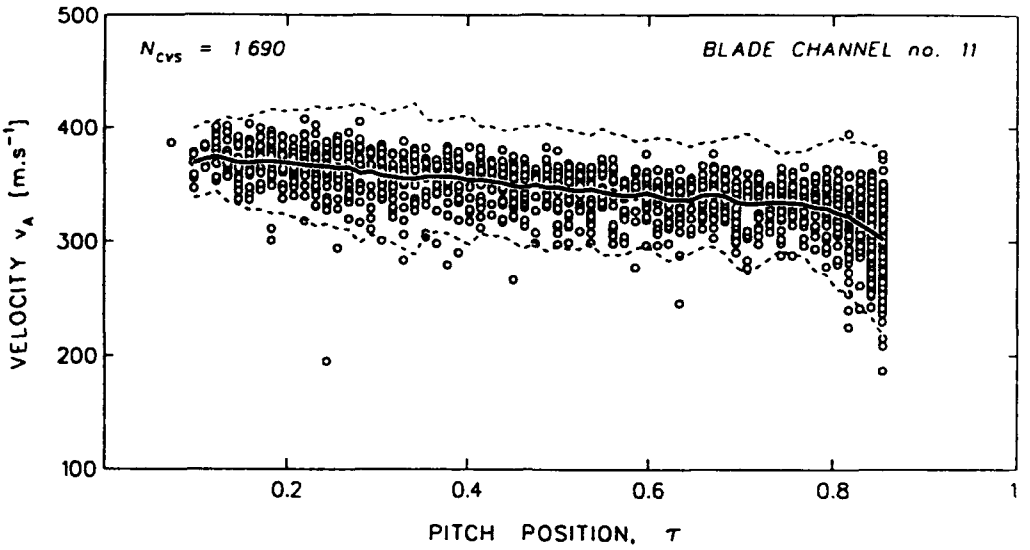

Figure 8. LV samples recorded in a channel sampling mode.

standard deviations (RMS) were calculated for each of the data subsets. The resulting mean velocity values along the blade-channel pitch are shown in Figure 8 by a solid line; the dotted lines show the $\pm 3\sigma$ (standard deviations) of individual data subsets at each of the 82 pitch positions. Then, all the velocity samples outside of the $\pm 3\sigma$ band were rejected for their low statistical significance, and both mean and RMS values were calculated again for the remaining velocity samples. Next, a population cut-off threshold was set for the blade-channel data ensemble for the entire blade-channel. Again, the cut-off threshold can be set arbitrarily or it can be related to the most populated subset at any of the pitch positions. Usually, the cut-off threshold is equal either to *1 %* of the population of the most populated data subset or to a minimum of *10* velocity samples, whichever is greater. All data subsets with populations less than the selected threshold were eliminated because of their low statistical significance.

The procedure of ensemble clipping for rotor sampling data sets is similar to the previous procedure for channel clipping; however, in this case, it is repeated separately for each blade channel in the rotor. The individual rotor blade channels have a lower data population than was the case of the single blade channel for the channel sampling; therefore, the population cut-off threshold is lower than in the case of blade-channel sampling. For the current data, the cut-off limit for the rotor sampling procedure was set to *5* velocity samples. Elimination of some of the data subsets at some of the pitch positions for rotor clipping could lead to gaps in the velocity distribution for some of the blade channels, which is a trade-off with data reliability. The resulting data file represents the velocity distribution for the entire rotor for an average revolution of the rotor (Figure 1).

Visibility Clipping

Visibility clipping is the last cleaning procedure applied to the LV data. Its purpose is to eliminate LV samples which could possibly originate from the LV probe and blade surface interaction (blade flash). It is based on mapping the rotor blade channel in terms of LV probe visibility. By masking the LV data with a visibility map, the LV samples at pitch positions close to blade surfaces, which could originate from the blade surface reflections, are eliminated. The visibility clipping procedure is performed in the data post processing. Visibility clipping is discussed in detail by Lepicovsky (1993) and is mentioned here only for the sake of completeness.

THE BLADE-CHANNEL VERSUS ROTOR SAMPLING APPROACH

The cleaned LV data consist of individual data subsets for each position along a blade-channel pitch or the rotor circumference. The individual data subsets contain information about the velocity distribution (mean values) as well as the velocity unsteadiness distribution (standard deviation values). The velocity information can be used for comparison with the CFD predictions. The data generated by the channel sampling can be used directly since they depict velocity or velocity unsteadiness distributions over a single rotor blade channel (Figure 9). The data generated using the rotor sampling (Figure 1), however, must first be averaged over the entire rotor. The resulting single channel distributions are shown in Figure 10. The vertical bars at pitch positions of τ = *0.2, 0.4, 0.6,* and *0.8* indicate the range of average axial velocity values in individual rotor blade channels as reported in Figure 1. As can be seen by comparing the

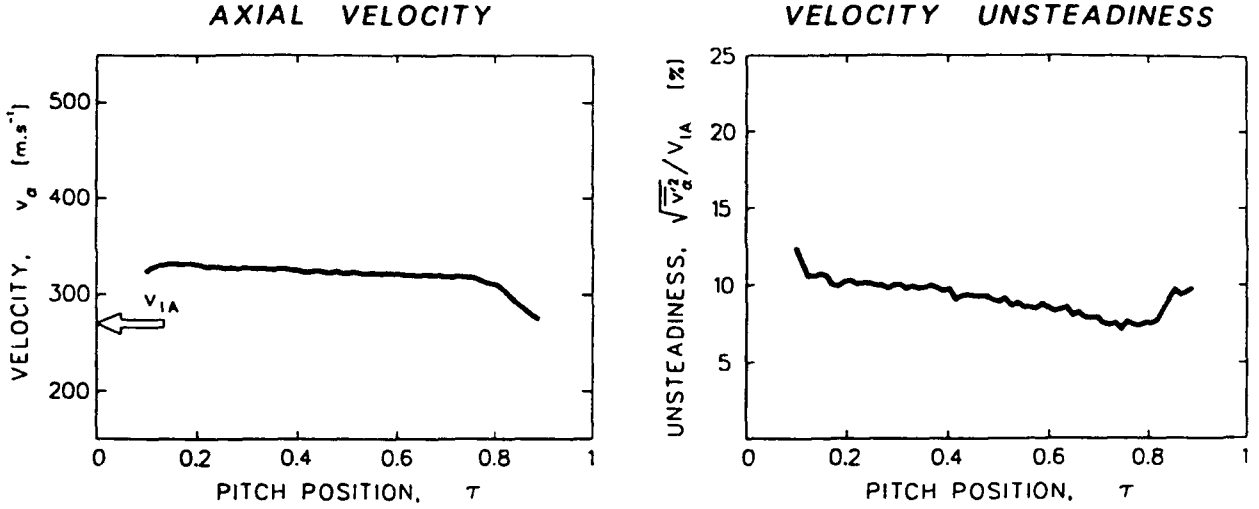

Figure 9. Velocity and velocity unsteadiness distributions generated using the blade-channel sampling mode.

lefthand sides of Figures 9 and 10, there is practically no difference between both velocity distributions, and it appears they can be used interchangeably. This conclusion seems to be true even for large channel-to-channel differences for cases of data sets with sufficiently high populations of LV samples. In our case the above conclusion was valid for measurements with at least 25 LV samples per pitch location and blade channel (rotor sampling). Even though there are no visible differences in velocity distributions for the blade-channel and rotor sampling approaches, rotor sampling should be preferred because it allows inspection of channel-to-channel differences (Figure 1). However, for cases of low data rates and a small number of acquired samples with very uniform rotor flowfields, blade-channel sampling can be safely used.

Contrary to the velocity case, there are noticeable differences for distributions of velocity unsteadiness generated by these two methods. The velocity unsteadiness levels generated by the blade-channel sampling method are visibly higher (righthand side of Figure 9) than those resulting from the rotor sampling method (righthand side of Figure 10). Clearly, the rotor sampling procedure followed by averaging over the entire rotor removes the channel-to-channel deterministic and periodic fluctuations from the resulting velocity unsteadiness distribution. Consequently, the resulting velocity unsteadiness distribution contains only random velocity fluctuations, which approximate flow turbulence intensity [Lepicovsky (1986)]. In most cases, however, the resulting unsteadiness levels are still slightly higher than the flow turbulence true levels because of the contaminations resulting from the nonuniformity of seed particle sizes and the effects of uncertainty in determining

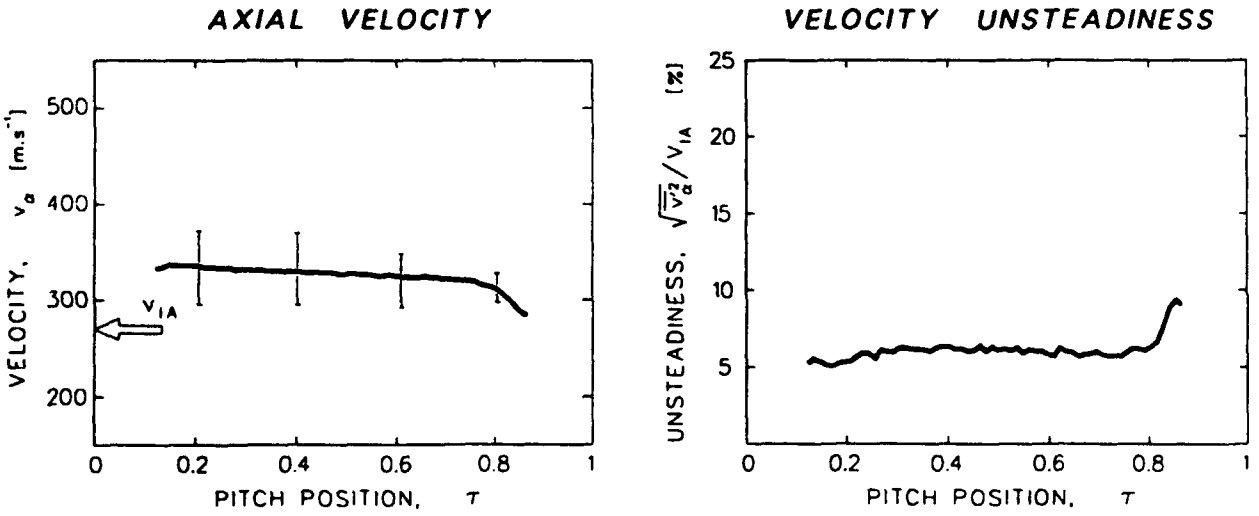

Figure 10. Velocity and velocity unsteadiness distributions generated using the rotor sampling mode.

the pitch position (especially in the regions of high velocity gradients). In any case, the average velocity unsteadiness for the rotor sampling (as shown in the righthand side of Figure 10) is a measure of velocity fluctuations in the rotating system (inside the spinning rotor), while the velocity unsteadiness distribution for the channel sampling (the righthand side of Figure 9) is a measure of velocity fluctuations felt on nonrotating elements in the flow path behind the rotor. The velocity unsteadiness, shown in Figure 9, determines the maximum amplitude of the excitation force for flow-induced vibrations on nonmoving structural components.

A strong argument in favor of the rotor sampling approach is the ability to capture the flowfield over the entire rotor, as shown in Figure 1. The range of velocity differences among individual rotor channels generated using rotor sampling is summarized in Figure 11. The velocity profile in the upper left corner shows the resulting average blade-to-blade velocity distributions. The subplot in the upper right corner shows velocity profiles from all rotor channels simply "piled-up" on each other. The remaining two subplots show five "low" and five "high" rotor channels plotted separately (but not averaged). The high and low channels were determined based on the value of average velocity in each individual blade channel. The figure demonstrates that for the particular fan operating conditions, the velocity level difference among individual rotor blade passages reached up to *80 m.s^{-1}*, which is *25 %* of the average mid-channel axial velocity, and that the velocity distribution for "low" channels exhibited a different trend across the blade channel than the velocity distribution for the "high" channels. Channel-to-channel velocity variations were observed for most of the fan operating regimes investigated; in a majority of cases, the variations were substantially smaller than that depicted in Figure 1. In any case, however, the variation pattern was always the same; it is that the same blade channels were always either "high" or "low" regardless of the operating conditions. The repeatability of the nonuniformity pattern indicates that the velocity channel-to-channel variations were connected to the differences in the geometry of individual blade channels.

CONCLUSIONS

The acquired LV data shed new light on the flow physics of high-speed fan rotors. The recorded channel-to-channel velocity variations are important information which must be taken into consideration when using the experimental data to evaluate the accuracy of CFD codes. The information about channel-to-channel variations cannot be derived from the CFD methods since it stems from the actual rotor geometry, while the CFD predictions are based on an idealized rotor passage.

The ability of rotor sampling to capture the channel-to-channel velocity variations is an important factor in favor of the rotor sampling approach. It is the author's view that rotor sampling should be preferred even though it is more demanding on a high LV data rate and a large memory capacity of the data acquisition electronics. The total number of acquired LV samples must be sufficiently high to secure enough velocity data per pitch position in each rotor channel for the resulting data to be statistically significant.

Finally, there is no universal answer to what data reduction procedure should be used for data comparison

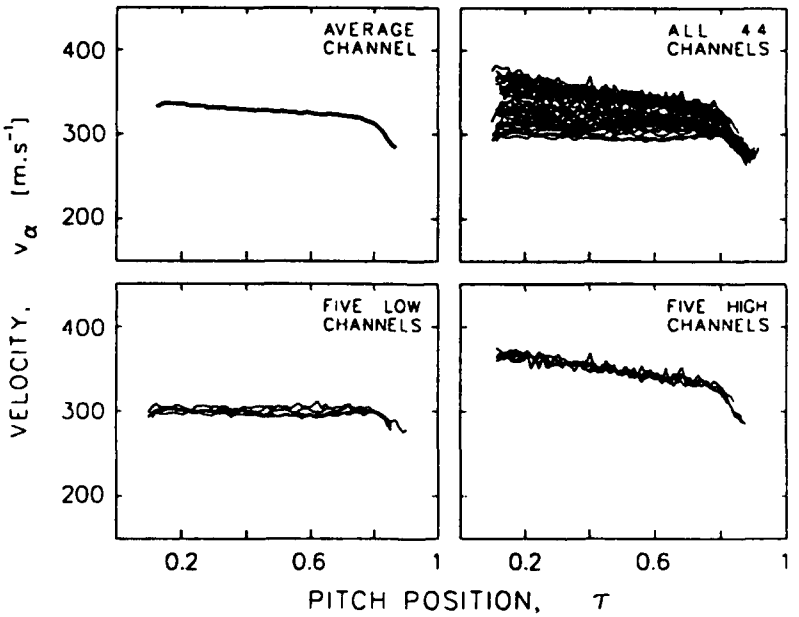

Figure 11. Channel-to-channel velocity variations.

with the CFD predictions. It should be judged case by case. Obviously, for flow conditions as depicted in Figure 11, it makes little sense to spend excessive effort trying to adjust the CFD predictions to every detail of the experimental data. Rather, the comparison should focus on trends in the velocity flowfield development and on comparison with global flowfield characteristics.

Acknowledgement

The experimental part of the work was performed under contract NAS3-25266 managed by Sverdrup Technology, Inc. The author is grateful to Dr. L.J. Bober of the Turbomachinery Technology Branch of NASA Lewis Research Center for his continuous support and encouragement during the course of this project.

References

Lepicovsky, J. 1993, Coupling of Laser Velocimeter Data With a High Speed Fan Rotor Geometry, Proceedings of the 2nd ISAIF, Prague, vol. 2, pp. 347-353.

Strazisar, A.J. & Powell, J.A. 1981, Laser Anemometer Measurements in a Transonic Axial Flow Compressor Rotor, ASME Journal of Engineering for Power, vol. 103, pp. 424-429.

Lepicovsky, J. & Bell, W.A. 1984, Aerodynamic Measurements about a Rotating Propeller with a Laser Velocimeter, Journal of Aircraft, vol. 21, pp. 264-271.

Petrie, H.L., Samimy, M. & Addy, A.L. 1988, Laser Doppler velocity bias in separated turbulent flows, Experiments in Fluids, vol. 6, pp. 80-88.

Strazisar, J.A., Wood, J.R., Hathaway, M.D. & Suder, K.L. 1989, Laser Anemometer Measurements in a Transonic Axial-Flow Fan Rotor, NASA TP-2879.

Lepicovsky, J. 1986, Laser Velocimeter Measurements of Large-Scale Structures in a Tone-Excited Jet," AIAA Journal, vol. 24, pp. 27-31.

Session 4.
Wall Flows

LOW-REYNOLDS-NUMBER EFFECTS IN A TURBULENT BOUNDARY LAYER

C. Y. Ching, L. Djenidi and R. A. Antonia

Department of Mechanical Engineering
University of Newcastle, NSW 2308, Australia

Abstract

Low-Reynolds-number effects in a zero pressure gradient turbulent boundary layer have been investigated using a two-component LDV system. The momentum thickness Reynolds number R_θ is in the range 400 to 1320. The wall shear stress is determined from the mean velocity gradient close to the wall, allowing scaling on wall variables of the inner region of the layer to be examined unambiguously. The results indicate that, for the present R_θ range, this scaling is not appropriate. The effect of R_θ on the Reynolds normal and shear stresses is felt within the sublayer. Outside the buffer layer, the mean velocity is more satisfactorily described by a power-law than by a logarithmic distribution.

1 Introduction

The direct numerical simulation (DNS) boundary layer data of Spalart (1988) for R_θ in the range 300 to 1410 show that scaling on wall variables u_τ and ν (u_τ is the friction velocity and ν is the kinematic viscosity) is generally inappropriate for the inner region of the layer. Significant R_θ effects on the wall-normalized turbulence quantities are evident; these effects often extending down to the wall. The wall-normalized Reynolds stresses exhibit different Reynolds number dependences, the w'^+ component (u, v, w denote the velocity fluctuations in the streamwise (x), wall-normal (y) and spanwise (z) directions respectively; the prime denotes an rms value, and the superscript + denotes normalization by the wall variables) being the most affected. Spalart's results show that, while u'^+ has a distinct peak at $y^+ \approx 15$, the peaks in v'^+, w'^+ and $-\overline{u^+v^+}$ are much broader, and their y^+ locations increase with R_θ. Similar low Reynolds number effects in the inner region of a fully developed turbulent channel flow have been observed both in experimental and DNS data (Kim et al., 1987; Wei and Willmarth, 1989; Antonia et al., 1992). Antonia and Kim (1993), using the channel flow DNS data, examined the near-wall behaviour of the various turbulence quantities and showed that the Reynolds number effects were most pronounced at the wall.

There is as yet no fully satisfactory explanation for these effects. Spalart (1988) attributed the effect to the inactive motion (Townsend, 1961; Bradshaw, 1967). Wei and Willmarth (1989) suggested two possible reasons: an increased vortex stretching with Reynolds number and a direct interaction between inner-region structures from opposite channel walls. Antonia et al. (1992), by introducing a small amount of heat at one of the walls in experiments and simulations, dismissed the direct interaction explanation as unlikely. They also found no significant evidence for attributing low Reynolds number effects to the inactive motion, arguing instead that the active motion should be the major contributor to the Reynolds shear and normal stresses in the inner region. Antonia and Kim (1993) concluded that low-Reynolds-number effects could be explained in terms of an intensification of the vortices in the wall region, noting however, that the average location and diameter of the vortices, when expressed in wall units, remain approximately unchanged.

Low Reynolds number effects can also be discerned on the mean velocity. Spalart's data, when plotted in the form $(y^+ d\overline{U}^+/dy^+)$ versus y^+, suggest that R_θ effects extend into the inner region. Also, from such a plot, Spalart inferred that the log region disappears at $R_\theta \leq 600$. Arguments for a log region are strictly tenable only at infinite Reynolds number (e.g. Sreenivasan, 1990), and there is no *a priori* reason for it to be valid at low Reynolds numbers. On the other hand, the arguments for a power law, $\overline{U}^+ = Cy^{+\alpha}$, which are as convincing as those for a log region (Barenblatt, 1993; George and Castillo, 1993), are valid at finite Reynolds numbers and should be more relevant

for low R_θ boundary layers. In the outer region, the strength of the wake $\Delta\overline{U}^+$, defined by Coles (1962) as the maximum deviation of the velocity profile from the log region, has been shown to decrease for values of $R_\theta < 6000$ (most of the decrease occuring for $R_\theta < 2000$), and is often cited as an important indicator of low Reynolds number effects. However, in the light of the previous comments on the log region, $\Delta\overline{U}^+$ is unlikely to provide a reliable measure of low Reynolds number effects on the outer region.

The main aim of this study is to investigate low Reynolds number effects on the inner region of a turbulent boundary layer by exploiting the advantages of LDV in this region. At present, there are very few reliable measurements in the near-wall region of a turbulent boundary layer. This is primarily due to the difficulties associated with hot-wire anemometry in this region (e.g. see Antonia, 1993). Karlsson and Johansson (1988) showed that reliable near-wall data could be obtained using LDV, but presented boundary layer data only for $R_\theta = 2400$. In particular, LDV allows the wall shear stress to be estimated from the mean velocity gradient close to the wall (see Djenidi and Antonia, 1993). This is important when enquiring into the relevant scaling for both mean velocity and turbulence intensities in the inner layer.

2 Experimental Details

The experiments were performed in a closed circuit constant-head vertical water tunnel (Zhou and Antonia, 1992) shown schematically in Fig. 1. The vertical 2 m high working section (250 mm square cross section) is made of 20 mm thick clear perspex. One of the walls of the working section, which is removable, was used as the smooth wall. A roughness strip, which was made up of 4.5 mm high pebbles glued onto a 30 mm wide perspex strip, was recessed into a groove about 100 mm downstream from the exit of the contraction and used to trip the boundary layer. The measurement station was located about 1 m downstream of the roughness strip. Flow visualization performed by injecting dye through a hole in the wall indicated the boundary layer to be turbulent at this station for a freestream velocity, U_1, as small as 0.08 m/s. The maximum value of U_1 is about 0.5 m/s. The freestream turbulence intensity is less than 0.5% for all values of U_1. The pressure gradient was checked by measuring U_1 at several axial locations and found to be negligibly small ($U_1 dU_1/dx \approx 5.5 \times 10^{-4}$ ms^{-2} for a freestream velocity of about 0.22 m/s). Measurements were performed at eight values of R_θ in the range 400 to 1320, corresponding to a range of 0.08 to 0.45 m/s for U_1.

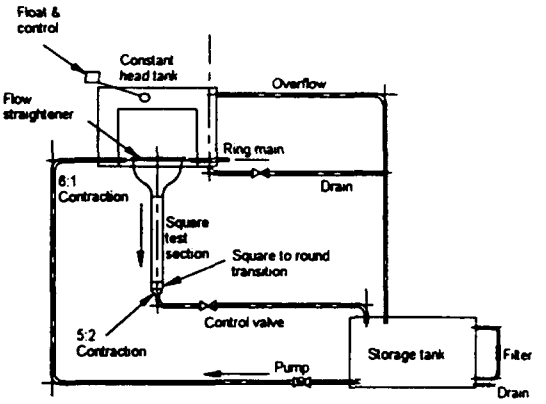

Figure 1: Schematic of water tunnel

The mean velocity at the centerline of the tunnel, measured prior to and after each velocity profile measurement, was found to be nearly constant, thus confirming the stability of the tunnel during the relatively long experimental times ($\approx$ 8 hours for one profile).

A three-component fibre optic LDV system (5W Ar-Ion) was used in forward scatter mode. Only two-component measurements (for $u - v$ or $u - w$) were performed. Since the refractive index effects are wavelength dependent, the two pairs of beams with the closest wavelengths (in this case, blue and violet with wavelengths 488 and 476.5 nm respectively) were used. For the $u - v$ measurements, the measuring volumes had their largest dimension oriented along the spanwise direction in order to optimize the spatial resolution in the wall-normal direction. In this configuration, the beam closest to the wall (used for the wall-normal component) was centered using a pair of prisms, and the probe was slightly tilted ($\approx 2°$) with respect to the z-direction in order to obtain measurements very close to the wall. With the diameter of the beam crossing ellipsoid being 0.04 mm and the measured friction velocity in the range 0.004 to 0.02 m/s, the spatial resolution in the wall- normal direction was in the range 0.16 to 0.8 wall units. For the $u - w$ measurements, the length of the measuring volume (0.5 mm) was perpendicular to the wall, resulting in a poorer spatial resolution (in the wall-normal direction) in this case. The probe was traversed using a three-dimensional computer-controlled traversing system, with a minimum step length of 0.025 mm in all three directions.

Enhanced Burst Spectrum Analyzers (BSA) were used for processing the photo multiplier signals. The two-component measurements were made in the coincidence mode, except very close to the wall where the data rates fall off quite steeply. In the coincidence mode, the two BSAs process the electrical signals only

when a particle simultaneously crosses the two measuring volumes, allowing a more reliable measurement of the Reynolds shear stress $-\overline{uv}$. Very close to the wall, operation in the coincidence mode was not feasible because of the very low data rates (note that no seeding was used). In this case, in order to improve the data rates, the BSAs were operated in the private mode. Typical data rates in the outer part of the boundary layer were about 200 Hz, falling off to about 10 Hz very close to the wall. In the outer part of the boundary layer, 20000 samples were collected at each measurement point and this was reduced to 5000 samples very close to the wall.

3 Determination of u_τ and Mean Velocity Profiles

To examine the inner scaling laws unambiguously, an accurate estimate of the friction velocity is of paramount importance. However, the accurate determination of the friction velocity for low R_θ turbulent boundary layers is not trivial. At low R_θ, there is no rigorous basis for the log region, and the Clauser-plot technique would therefore be ineffective. A reliable method of estimating u_τ is to measure the mean velocity gradient, $d\overline{U}/dy$, at the wall. Djenidi and Antonia (1993) determined u_τ, with an estimated uncertainty of $\pm 3\%$, by fitting a straight line to their near-wall LDV data for $y^+ < 2.5$ on the basis that the DNS data of Kim et al. (1987) and Spalart (1988) indicate that $d\overline{U}^+/dy^+$ has decreased to about 0.97 at $y^+ \approx 2.6$, i.e. 3% below the wall value.

For all R_θ, it was possible to measure $\overline{U}^+$ down to about $y^+ \approx 1$, which enabled u_τ to be estimated using the method of Djenidi and Antonia (1993). An initial estimate of u_τ was obtained by fitting a least squares straight line to the near-wall $\overline{U}$ data. The origin for the velocity profile was estimated by extrapolating this line to $\overline{U} = 0$; this location was always within ± 0.075 mm of the initial estimate of the origin (inferred by visual inspection of the intersection of the laser beams as they approached the perspex wall and of the analogue signals from the BSA's). From the initial estimate of u_τ, the physical values of y were converted to y^+ and the linear fit was re-done in the region $y^+ \leq 2.5$. The second (and final) estimate of u_τ was typically 5% larger than the first estimate; further iterations showed no change in the value of u_τ.

Normalized mean velocity profiles (Fig. 2; only three profiles are shown for clarity) show the same trend as the DNS profiles of Spalart. While the experimental data closely agree with the DNS data throughout the layer at the higher Reynolds number, they are slightly

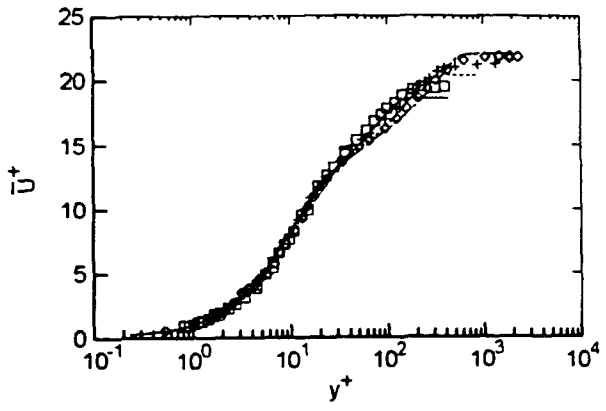

Figure 2: Mean velocity. $\diamond$, R_θ = 1316; +, 765; $\square$, 400; — - —, DNS 1410; ----, 670; ——, 300.

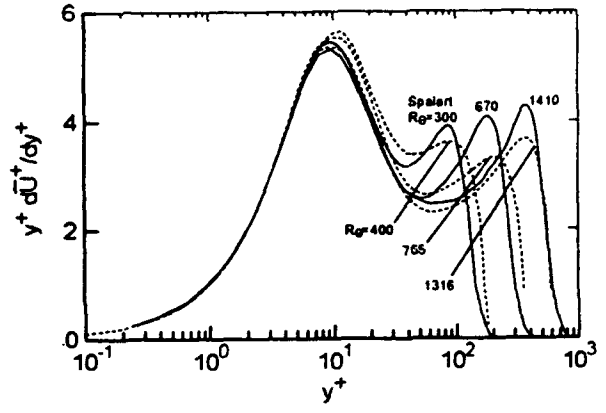

Figure 3: Distribution of $(y^+ d\overline{U}^+/dy^+)$. ——, DNS; ----, experimental.

higher than the DNS data at the lower Reynolds numbers for $y^+ > 30$. There appears to be good collapse of the profiles in the region $y^+ \leq 30$; a Reynolds number dependence is discernible for $y^+ > 30$. Note that only the collapse in the region $y^+ \leq 2.5$ is "forced" in view of the way in which u_τ is determined.

To accentuate the effects of R_θ on the mean velocity, especially in the inner region, $(y^+ d\overline{U}^+/dy^+)$ is plotted against $(\ln y^+)$ (Fig. 3). Such a plot also allows a critical examination of the log region; a log region should appear as a plateau in the curve (see Spalart, 1988). The derivative $d\overline{U}^+/dy^+$ was determined after first applying a curve fit to the data for $\overline{U}^+$. This was done via the calculation method of Bisset and Antonia (1991), which combines an eddy viscosity relation for the inner region and an empirical wake function for the outer region; the assumptions on which the calculation is based are not of particular relevance in the present context since the main interest here is to ob-

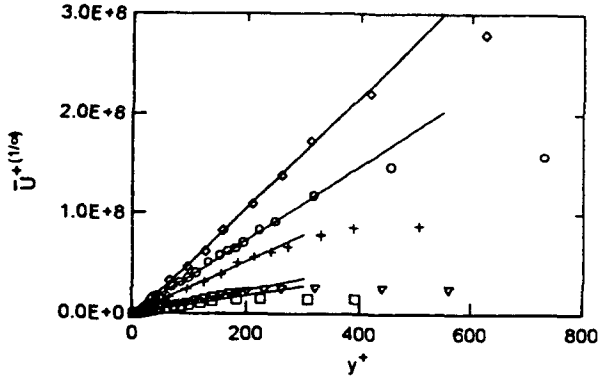

Figure 4: Mean velocity plotted in the form of a power-law. ◇, $R_\theta = 1316$; ○, 979; +, 765; ▽, 509; □, 400.

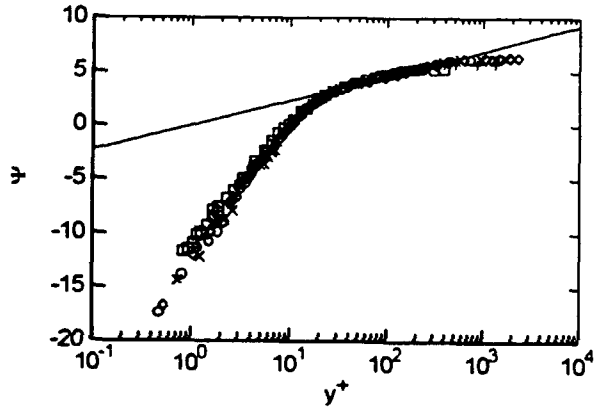

Figure 5: Mean velocity plotted as a function $\Psi \equiv 1/\alpha \ln \overline{U}^+/C$. Symbols as for Fig. 4; ——, $\Psi = \ln y^+$.

tain a reliable curve fit to $\overline{U}^+$ in order to estimate $d\overline{U}^+/dy^+$ (thus avoiding the need to differentiate the $\overline{U}^+$ data). No significant plateau is evident in any of the $y^+ d\overline{U}^+/dy^+$ profiles. Instead, all the profiles exhibit a local minimum, indicating that the logarithmic region is either very narrow or non-existent. As the Reynolds number decreases, the local minimum increases and its location shifts to a smaller value of y^+. For $R_\theta = 400$, the minimum occurs at $y^+ \approx 40$, while for $R_\theta = 1320$, it is at $y^+ \approx 60$. The distributions of $y^+ d\overline{U}^+/dy^+$ suggest that the effect of R_θ on $\overline{U}^+$ is discernible for $y^+ \gtrsim 8$, i.e the effect extends well into the buffer layer.

The mean velocity data are plotted in the form $(\overline{U}^+)^{1/\alpha}$ versus y^+ (Fig. 4) to ascertain whether a power-law distribution of the form

$$\overline{U}^+ = C y^{+\alpha} + D \quad , \tag{1}$$

is applicable. Based on the corrections to the classical Kolmogorov-Obukhov exponents 2/3 and 5/3, Barenblatt (1993) conjectured that the exponent α should be inversely proportional to the logarithm of the Reynolds number. A specific form of the conjecture, based on that used by Barenblatt (1993) for pipe flow, i.e.

$$\alpha = \frac{3}{(2 \ln R_\delta)} \quad , \tag{2}$$

where R_δ ($\equiv U_1 \delta/\nu$) is the boundary layer thickness Reynolds number, was used to determine α. Straight lines are observed over an extensive y^+ range for all R_θ, indicating that: (a) the mean velocity distribution outside the buffer layer, and extending into the outer layer, appears to be well represented by a power-law, and (b) the value of α appears to be consistent with (2). It is also seen that, when extrapolated, the straight lines in Fig. 4 (obtained by a least squares fit to the data after first eliminating the data points close to the wall and to the boundary layer edge), nearly pass through the origin indicating that $D \approx 0$. A quasi-universal form of the power-law can be obtained by defining a new function Ψ (Barenblatt and Prostokishin, 1993),

$$\Psi \equiv \frac{1}{\alpha} \ln \frac{\overline{U}^+}{C} = \ln y^+ \quad . \tag{3}$$

The mean velocity data are plotted in the form Ψ versus y^+ in Fig. 5, and for $y^+ > 25$, there is good collapse of the data onto the line $\Psi = \ln y^+$. The power-law is observed to extend well into the outer layer. Although the profiles deviate from the line $\Psi = \ln y^+$ for $y^+ < 25$ — this is expected since (1) is not supposed to be valid close to the wall anyway - there is still an apparently good collapse of the data down to the sublayer. This is because there is, in general, a good collapse of $\overline{U}^+$ vs y^+ in the range $y^+ < 25$ (see Fig. 2), and the variation of α and C over the present R_θ range is small enough ($0.158 < \alpha < 0.179$ and $7.51 < C < 8.03$) to show an apparent collapse of the data. The arguments for a power-law are based on the assumption that viscosity exerts a non-trivial influence on the mean velocity; if α asymptotes to a non-zero constant, the log-law would not be strictly valid, and the traditional asymptotic arguments for the boundary layer would need to be re-examined. The skin friction law corresponding to the power-law (1) can be obtained (by extrapolating to $y = \delta$) as:

$$\frac{u_\tau}{U_1} = \frac{1}{\exp(3/2\alpha)} \left(\frac{\exp(3/2\alpha)}{C} \right)^{1/(1+\alpha)} \tag{4}$$

For all R_θ, the experimental values of u_τ are within ±3% of those obtained with Eq. (4). This good agreement suggests the possibility of using (4) as a means of estimating the friction velocity, especially at low Reynolds numbers.

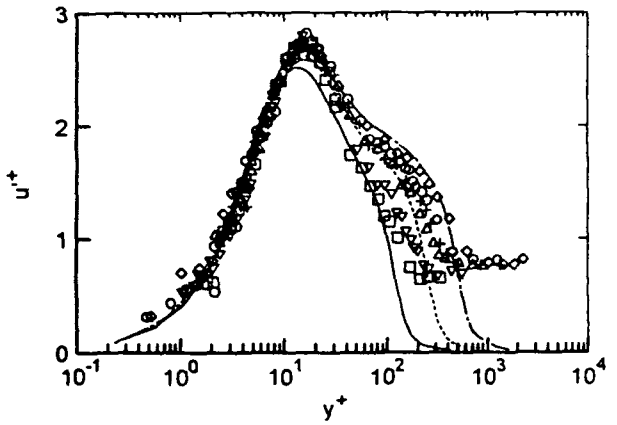

Figure 6: rms longitudinal turbulence intensity. ◇, R_θ = 1316; ○, 979; +, 765; △, 729; ▽, 509; □, 400; — - —, DNS 1410; - - - -, 670; ——, 300.

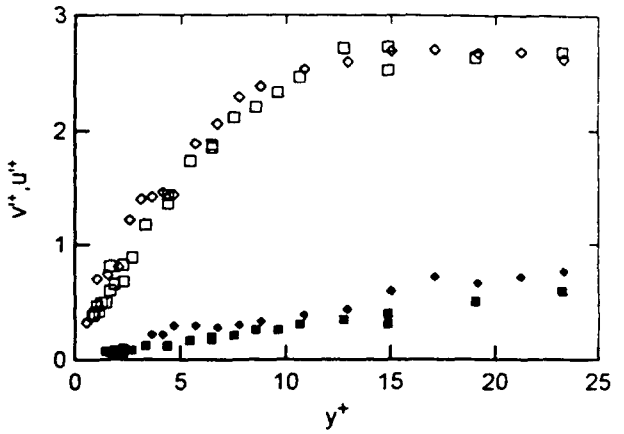

Figure 7: Near-wall data for u'^+ and v'^+. ◇, R_θ = 1316; □, 400. Open symbols for u'^+, solid symbols for v'^+.

4 Turbulence Measurements

One measure of the uncertainty in the Reynolds stress measurements in the near-wall region — there is a marked decrease in the signal-to-noise ratio as the wall is approached because of the decrease in the velocity itself, and the large amount of extraneous light (reflected from the wall) collected by the receiving optics — was provided by the scatter inferred from the repetition of measurements at the same point. This uncertainty was estimated at ±4%, while the uncertainty in u_τ is ±3% (see Djenidi and Antonia, 1993); this yields an uncertainty of ±5% (see Moffat, 1988) for the wall-normalized quantities. An additional uncertainty in the results is that due to the correct location of the origin; this is estimated at ±0.025 mm (the minimum resolution of the traversing system), corresponding to y^+ in the range 0.1 to 0.5. Although the absolute error in the location of the origin is small, this is highlighted in the near-wall region because of the logarithmic scale for y^+.

All of the u'^+ profiles (Fig. 6) have a discernible peak at about $y^+ = 15$; this location is consistent with that found for the DNS data of Spalart (1988). The magnitude and y^+ location of the present u'^+_{max} is also in good agreement with the hot-wire data of Purtell at al. (1981) (these are not shown to avoid overcrowding). However, the nearly constant peak magnitude of about 2.75 is at variance with the systematic increase observed in the DNS data. For $y^+ > 15$, there is a generally systematic increase in u'^+ with R_θ at any given y^+; also, u'^+ falls off less rapidly with y^+ as R_θ increases. It is difficult to discern a Reynolds number effect from the above figure in the region $y^+ < 15$. However, when only the near-wall data at the two extreme values of R_θ are plotted (Fig. 7), a systematic

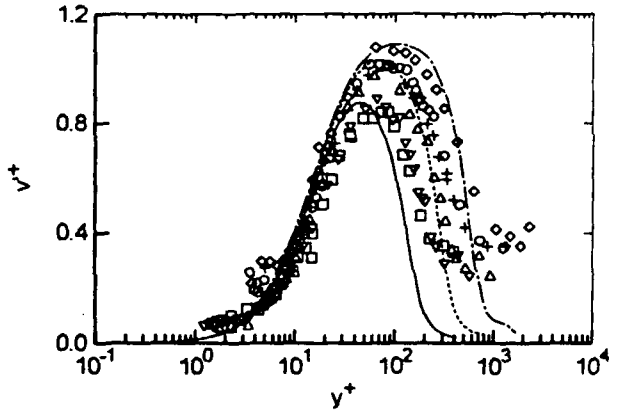

Figure 8: rms normal turbulence intensity. Symbols and lines as for Fig. 6.

increase with R_θ is noticeable for both u'^+ and v'^+. The increase in v'^+ extends to larger values of y^+ than that in u'^+. In contrast to u'^+, the peak in v'^+ (Fig. 8) is much broader, and the magnitude and y^+ location of v'^+_{max} increase with R_θ. While the peak in u'^+ occurs in the inner layer, the peak location for v'^+ occurs in the range $70 < y^+ < 100$. A systematic increase in v'^+ with R_θ is observed for $y^+ > 15$, the increase being more pronounced than for u'^+. While it is difficult to discern any R_θ effects in the region $y^+ < 15$ from Fig. 8, the results in Fig. 7 indicate that the R_θ effects on v'^+ extend into the sublayer. Profiles of w'^+ are shown in Fig. 9, and for the range of y^+ in which the measurements were performed, show a systematic increase with R_θ. Note that relative to u'^+ and v'^+, the DNS data show that the effect of R_θ on w'^+ is much larger in the near-wall region. Despite the lack of near-wall measurements for w'^+, this trend is also evident in the experimental data; close to the wall, the poor spatial

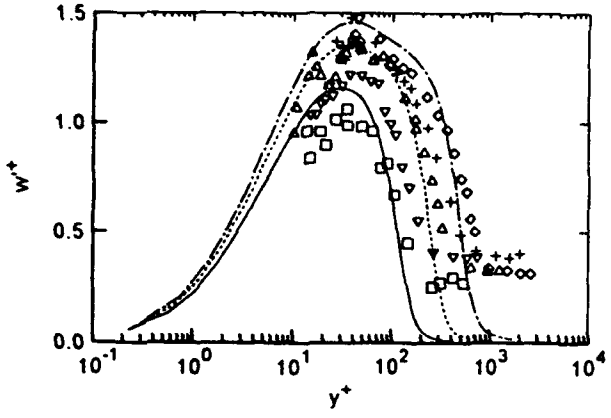

Figure 9: rms spanwise turbulence intensity. Symbols and lines as for Fig. 6.

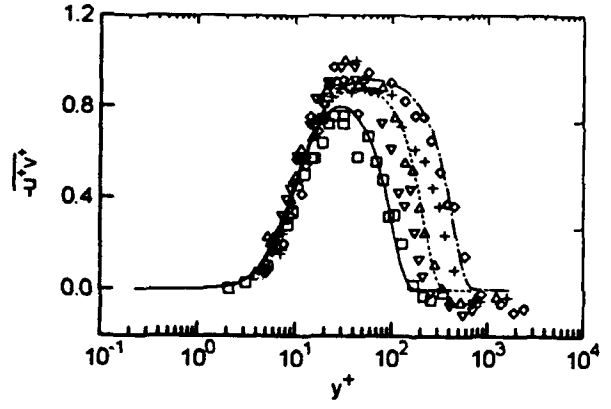

Figure 10: Reynolds shear stress. Symbols and lines as for Fig. 6.

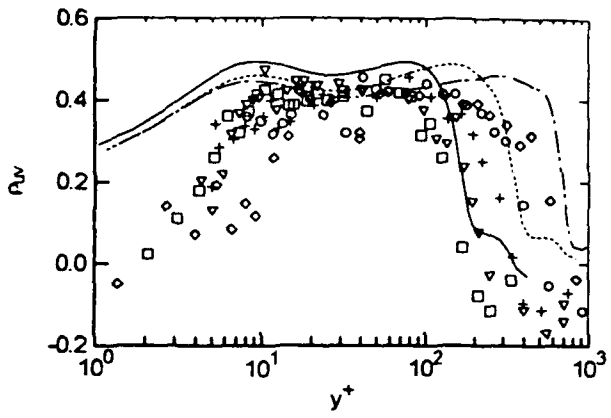

Figure 11: Correlation coefficient between u and v . Symbols and lines as for Fig. 6.

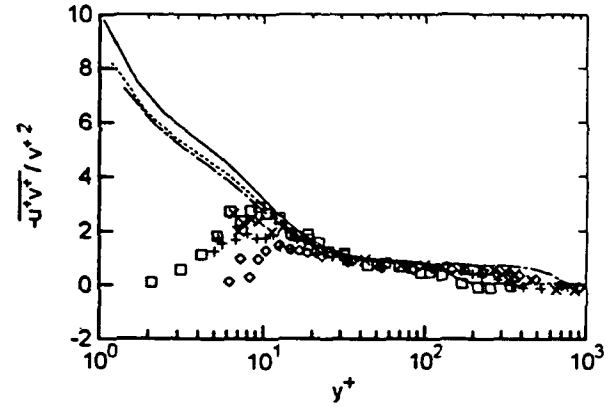

Figure 12: Distribution of $-\overline{uv}/\overline{v^2}$. Symbols and lines as for Fig. 6.

resolution in the wall-normal direction compounded by the glare of the laser beams as they hit the wall (this is far more intense than the light scattered from the measuring volume) makes it difficult to obtain good measurements. A peak in w'^+, albeit a broad one, is discernible in the range $30 < y^+ < 60$.

Distributions of the Reynolds shear stress $-\overline{u^+v^+}$ are presented in Fig. 10. The profiles show good agreement with the DNS data, and like v'^+, systematically increase with R_θ for $y^+ > 15$. Within the experimental uncertainty, it is difficult to determine any R_θ effects in the region $y^+ \leq 15$; in this case, the problems are exacerbated because of the difficulty of making coincidence mode measurements close to the wall. The peak in $-\overline{u^+v^+}$ is broader than that for v'^+, and both its magnitude and y^+ location, notwithstanding the difficulty of defining this peak, increase with R_θ. However, the y^+ location ($30 < y^+ < 60$) of $-\overline{u^+v^+}_{max}$ is smaller than that for v'^+_{max}. The correlation coefficient ρ_{uv} ($\equiv -\overline{uv}/u'v'$) displays a plateau with a value of about 0.4, starting at $y^+ \approx 10$ and extending well into the outer layer (Fig. 11). The scatter in the data makes it difficult to discern any systematic Reynolds number dependence for this parameter. However, the DNS data show a decrease in ρ_{uv} with an increase in R_θ throughout the layer. Profiles of $-\overline{uv}$ normalized by $\overline{v^2}$ are presented in Fig. 12. The departure of the experimental data from the DNS data for $y^+ < 15$ is attributed to the difficulties in the $-\overline{u^+v^+}$ measurements in this region. There appears to be good collapse of the profiles in the range $15 < y^+ < 100$. This reflects the fact that the increase in $-\overline{u^+v^+}$ with R_θ in this range is almost perfectly offset by that of v'^+, suggesting that the mechanism responsible for the increase in $-\overline{u^+v^+}$ with R_θ must be the same as that for v'^+. This is plausible since the active motion should be the major contributor to both v'^+ and $-\overline{u^+v^+}$ (u'^+ receives contributions from the inactive motion - see Antonia et al., 1992), and the increase in these quantities is attributed to an intensification of the active

motion with R_θ (Antonia and Kim, 1993).

As the freestream is approached, the values of u'^+, v'^+ and w'^+ (Figs. 6, 8 and 9) are at variance with the actual freestream turbulence intensity of about 0.5% (measured by Djenidi and Antonia (1993) using a 15 mW He-Neon one-component TSI system, and confirmed in this study by measuring u' and v' using a DANTEC 1D probe). Our investigations show that this is directly attributed to noise (the most likely cause is a poor alignment of the beam waists within the probe) picked up by the 2D probe when the actual rms-to-mean values $(u'/\overline{U})$ are small. The probe used is a DANTEC 85 mm probe with a beam expander, and the beam separation distance was found to have a significant effect on this apparent turbulence intensity. Higher rms values were measured when the beam separation distance was reduced. Profiles of the Reynolds stresses measured with different beam separation distances showed that this effect decreases as $(u'/\overline{U})$ increases, and is not discernible when the value is greater than about 8%; the inner layer is thus relatively free of this error. The slightly negative values of $-\overline{u^+v^+}$ in the freestream (Fig. 10) are also spurious and are likely due to a slight misalignment of the beams with respect to the streamwise and wall-normal directions and/or a poor alignment of the beam waists within the probe.

5 Conclusions

1. As has been previously observed by Spalart (1988) using direct numerical simulations, there are significant low Reynolds number effects on all the Reynolds stresses. The near-wall data for u'^+ and v'^+ show that the effect extends well into the sublayer, indicating that, in the range $400 \leq R_\theta \leq 1320$, scaling on wall variables is, in general, not appropriate.

2. The dependence of each wall-normalized quantity on the Reynolds number is different. While the peak in u'^+ is distinct and its magnitude and y^+ location are nearly constant, the peaks in v'^+, w'^+ and $-\overline{u^+v^+}$ are much broader and both the magnitude and location increase with R_θ.

3. There appears to be good collapse of the $-\overline{uv}$ profiles when normalized by $\overline{v^2}$ in the range $15 < y^+ < 100$, indicating that the increase in $-\overline{u^+v^+}$ with R_θ is almost perfectly offset by that of v'^+ in this region. This is consistent with the notion that the active motion is the major contributor to both v'^+ and $-\overline{u^+v^+}$, and that the increase in these quantities is attributed to an intensification of the active motion with R_θ.

4. The profiles of $(y^+ d\overline{U}^+/dy^+)$ suggest that R_θ effects on the mean velocity may be felt down to $y^+ \approx 8$. Outside the buffer layer, the mean velocity is well described by a power-law, as opposed to a universal log-law, implying that viscous effects are non-negligible.

Aknowledgements

The support of the Australian Research Council is gratefully acknowledged.

References

Antonia, R. A. : 1993. Direct Numerical Simulations and Hot Wire Experiments : A Possible Way Ahead? In *New Approaches and Concepts in Turbulence*, (ed. T. Dracos and A. Tsinober), Birkhauser Verlag, Basel, Switzerland, 349-365.

Antonia, R. A. and Kim, J. : 1993. Low Reynolds Number Effects on Near-Wall Turbulence, *J. Fluid Mech.* [to appear]

Antonia, R. A., Teitel, M., Kim, J. and Browne, L. W. B. : 1992. Low-Reynolds-Number Effects in a Fully Developed Turbulent Channel Flow, *J. Fluid Mech.*, **236**, 579- 605.

Barenblatt, G. I. : 1993. Scaling Laws for Fully Developed Turbulent Shear Flows. Part 1. Basic Hypotheses and Analysis, *J. Fluid Mech.*, **248**, 513-520.

Barenblatt, G. I. and Prostokishin, V. M. : 1993. Scaling Laws for Fully Developed Turbulent Shear Flows. Part 2. Processing of Experimental Data, *J. Fluid Mech.*, **248**, 513-520.

Bisset, D. K. and Antonia, R. A. : 1991. Mean Velocity and Reynolds Shear Stress in a Turbulent Boundary Layer at Low Reynolds Numbers, *Aeron. Quart.*, **95**, 244-247.

Bradshaw, P. : 1967. 'Inactive' Motion and Pressure Fluctuations in Turbulent Boundary Layers, *J. Fluid Mech.*, **30**, 241-258.

Djenidi, L. and Antonia, R. A. : 1993. LDA Measurements in a Low Reynolds Number Turbulent Boundary Layer, *Expts. in Fluids*, **14**, 280-283.

Coles, D. E. : 1962. The Turbulent Boundary Layer in a Compressible Fluid. *Rand Report R-403-PR.*

Erm, L. and Joubert, P. N. : 1991. Low Reynolds Number Turbulent Boundary Layers, *J. Fluid Mech.*, **230**, 1-44.

George, W. K. and Castillo, L. : 1993. Boundary Layers with Pressure Gradient : Another Look at the Equilibrium Boundary Layer. In *Near-Wall Turbulent Flows*, (ed. R. M. C. So, C. G. Speziale and B. E. Launder), Elsevier Science Publishers, 901-910.

Karlsson, R. I. and Johansson, T.G. : 1988. LDV Measurements of Higher Order Moments of Velocity Fluctuations in a Turbulent Boundary Layer. In *Laser Anemometry in Fluid Mechanics III* (ed. R. J. Adrian et al.), Ladoan - Instituto Superior Tecnico, Portugal, 273-289.

Kim, J., Moin, P. and Moser, R. : 1987. Turbulence Statistics in Fully Developed Channel Flow at Low Reynolds Number, *J. Fluid Mech.*, **177**, 133-166.

Moffat, R. J., 1988: Describing the Uncertainties in Experimental Results, *Experimental Thermal and Fluid Science*, **1**, 3-17.

Purtell, L. P., Klebanoff, P. S. and Buckley, F. T. : 1981. Turbulent Boundary Layers at Low Reynolds Numbers, *Phys. Fluids*, **24**, 802-811.

Spalart, P. R. : 1988. Direct Simulation of a Turbulent Boundary Layer up to $R_\theta = 1410$, *J. Fluid Mech.*, **187**, 61-98.

Sreenivasan, K. R. : 1990. The Turbulent Boundary Layer. In *Frontiers in Experimental Fluid Mechanics* (ed. M. Gad-el-Hak), pp.159-210, Springer-Verlag.

Townsend, A. A. : 1961. Equilibrium Layers and Wall Turbulence, *J. Fluid Mech.*, **11**, 97-120.

Wei, T. and Willmarth, W. W. : 1989. Reynolds-Number Effects on the Structure of a Turbulent Channel Flow, *J. Fluid Mech.*, **204**, 57-95.

Zhou, Y. and Antonia, R. A. : 1992. Convection Velocity Measurements in a Cylinder Wake, *Expts. in Fluids*, **13**, 63-70.

STUDY OF TURBULENT CHANNEL FLOW AT MODERATE REYNOLDS NUMBERS WITH PARTICLE IMAGE VELOCIMETRY AND PROPER ORTHOGONAL DECOMPOSITION

Z. -C. Liu[1,2], R. J. Adrian[1], T. J. Hanratty[2]

[1] Department of Theoretical and Applied Mechanics,
University of Illinois, Urbana IL 61801 USA.
[2] Department of Chemical Engineering,
University of Illinois, Urbana IL 61801 USA.

ABSTRACT

An experimental study of turbulent flow in a channel has been performed using PIV at Reynolds numbers of Re_h = 5378 and 29935 based on the half-channel height, h, and the bulk velocity, u_b. Two-point spatial correlations have been calculated from the measured fluctuating velocity fields. Proper orthogonal decomposition (POD) has been employed to calculate the eigenvalue and eigenfunctions of each eigenmode for the experimental PIV data. The results show that the eigenfunctions and the eigenvalue spectra in the outer region of channel flow when scaled by outer variables are independent of Reynolds number. A few lower eigenmodes are the main contributors of the turbulent kinetic energy and turbulent intensity of the turbulent channel flow.

1. INTRODUCTION

The turbulent structure in the outer region of a flow past a wall is not as well understood as in the near wall region. The linear variation of the characteristic length scale of turbulence with distance from the wall in the log-layer is an accepted concept in wall turbulence. However the interpretation of this concept in terms of turbulence structure is not established. It is interesting to find more experimental evidence of such behavior in the log-layer. This paper presents results of a study of the structure of the outer region of turbulent channel flow, with PIV, at much larger Reynolds numbers than is feasible in present DNS.

The PIV technique provides turbulent fluctuating velocity field measurements and enables one to study the structures of turbulent motion (Adrian 1991). The Reynolds numbers of present studies are moderate, Re_h = 5378 and 29935. The spatial resolution of PIV in these two cases is good enough to study turbulent scales. It is not fine enough to resolve the very small scales and the near wall region without using higher magnification in the optics. In the present work conventional two-dimensional PIV is used to study two velocity components in streamwise and wall-normal directions. Sixty to one hundred PIV photographs were taken and interrogated for each of the two Reynolds numbers. The fluctuation field was calculated for each realization. Observations of these flow fields through low-pass filtering show that in the outer region large scale motions are associated with large turbulent kinetic energy and Reynolds stress events. Their dimensions are about 1/4 of the channel height in wall normal direction and over 2 channel heights in the flow direction.

Two-point correlation functions over a wide region can be calculated directly from PIV data. Since two-point correlations contain important information about the coherent structures of turbulent flow field, it is attractive to pursue proper orthogonal decomposition (POD), an elegant technique to decompose turbulent flow field, using two-point correlation data to study turbulent structures. The detail description of POD can be found in Lumley (1967, 1981) and a recent review paper by Berkooz *et al* (1993). The results of the present investigation on flows at two different Reynolds numbers indicate that in the outer region of wall turbulent flow both eigenfunctions and eigenvalue spectra do not change with Reynolds number if scaled with outer variables. The low modes are energetic and can be associated with the large scale motions.

2. TURBULENT CHANNEL FLOW

The experimental research was carried out in a flat-wall, closed-flow loop water channel with a rectangular cross section of 48.75 mm high (y), 609.6 mm wide (z) and 15.24 m long (x). The test section was located 200 channel heights downstream from the entrance, where the flow was fully developed. Tap water, cleaned with 3 μm filters, was used as test fluid to fill the channel. The test section had 5.5 cm x 15 cm optical windows on both sides and a 10.5 cm x 15 cm optical window on the top, which allowed a laser light sheet to illuminate a normal plane of the flow and a camera to record the flow velocity field. The temperature of the fluid in channel was controlled during experiments to maintain constant flowrate for all runs. A sketch of the channel is shown in Fig.1. A detailed description is given in a thesis by Niederschulte (1989).

The choice of seed particles is an essential factor for a good recording, and it leads to results with high accuracy. They should be small enough to follow

the fluid and large enough to provide strong light scattering from the laser light sheet (Adrian 1991) . Aluminum oxide particles of 9.5 micron nominal size were chosen based on these considerations and were seeded in the fluid at a concentration of approximate 15 particles per mm^3.

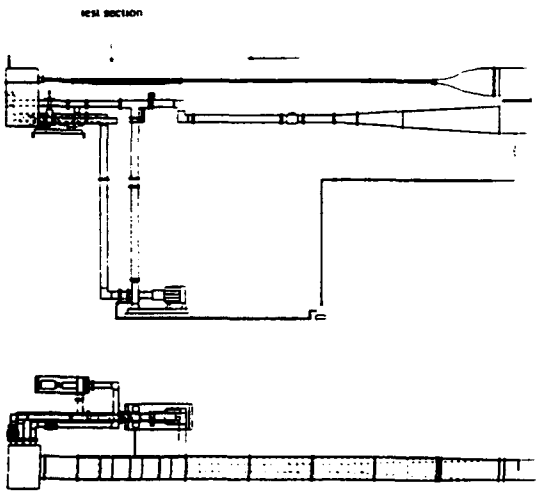

Fig. 1 Turbulent channel flow system

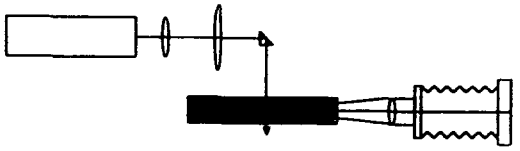

Fig. 2 PIV optical setup

An Apollo ruby laser of model 22HDX with double pulses of 2J of energy each was employed as the light source. The time duration was 30 ns for each pulse. The optical system used in this study is sketched in Fig. 2. The light sheet forming optics are composed of a cylindrical lens with 100 mm focal length and a spherical lens with 787.5 mm focal length. It provides an illuminated region 0.8 mm thick in the spanwise direction and approximate 120 mm wide in streamwise direction in the flow. Double images of particles were photographed, using a 4 x 5 inch format camera with a f/9 Schneider lens, and recorded on Kodak 4415 film with a magnification of 0.97. The diffraction limited particle image size was approximately 32 μm. The maximum errors in this system due to the refractive index of water and due to a perspective effect (Adrian 1991) are 0.17% and 0.6%, respectively, of the bulk velocity over the entire recorded flow field, which are small and acceptable. The experimental techniques have been detailed previously in Liu *et al* (1991).

Experiments were performed at Reynolds number $Re_h = u_b h/\nu = 5378$ and 29935, where u_b is the bulk velocity, h is the half channel height and ν is the kinematic viscosity. They correspond to $Re_\tau = u_\tau h/\nu = 315$ and 1414, respectively, where $u_\tau = (\tau_w/\rho)^{1/2}$ is the friction velocity calculated using measurements of bulk velocity and Dean's correlation of the friction coefficient (Dean 1978). The viscous length scales, ν/u_τ, were 77.5 μm and 17.2 μm for these two Reynolds numbers. The bulk velocities of these two cases were 212 mm/s and 1074 mm/s. The pulse separations of the laser pulses were determined from bulk velocity to be 1.2 ms and 0.24 ms, to allow the mean displacement of a particle-image pair to be approximately 0.25 mm, a quarter of the interrogation spot size, thereby satisfying the 'one-quarter rule' for double-pulsed autocorrelation PIV to achieve a high detection rate during interrogation (Keane and Adrian 1990).

3. PIV MEASUREMENTS

The analyses of PIV photographs were carried out with an interrogation system, described by Meinhart *et al* (1993), which contains a host workstation, SUN 4/370, with eight high-speed Mercury array processors, MC860. A Videk Megaplus CCD camera with 1320 x 1035 pixels of resolution was used to acquire images from interrogation spots. An Imaging Technology VSI-150 frame grabber digitizes the images at a frequency of 20 MHz. This system can calculate over 100 velocity vectors in a second. It takes 2 to 3 minutes to interrogate one PIV photograph. A single-frame double-exposure cross-correlation technique, which significantly improves the signal-to-noise ratio over autocorrelation (Keane and Adrian 1992), was used to interrogate 60 to 100 PIV photographs for each Reynolds number. The sizes of the first and second windows of cross-correlation were 128 pixels and 64 pixels in streamwise and normal directions respectively. The size in normal direction with stronger velocity gradient is chosen half of that in streamwise direction in order to reduce errors due to the strong wall-normal velocity gradient. The offset of two windows was set to be 28 pixels at first to match the displacement of the image pair. It was adaptively adjusted during interrogation to follow the change of the local displacements of image pairs. The dimensions of interrogation spot were Δx=1.6 mm, Δy=0.8 mm and Δz=0.8 mm in the fluid, which form a interrogation spot volume of 1.024 mm^3. It then contains about 15 particles in this volume and satisfies the requirement of obtaining a valid detection probability at least 90% (Keane and Adrian 1990).

The raw vectors after interrogation were cleaned up with an automatic post-interrogation procedure that replaced bad vectors with alternatives from other correlation peak measurements. A gaussian low-pass filter with a width of 0.75 grid size was used to remove noise present in the vector field. The ensemble-averaged velocity of the flow field was computed by averaging the measured velocity vectors along line of constant y in all PIV photographs. Turbulent fluctuation is obtained by subtracting the total velocity field from the ensemble

mean velocity. Fig. 3a and 3b show two instantaneous turbulent fluctuating velocity fields for Re_h = 5378 and 29935. The coordinates in the figures are in viscous wall units. The flow direction is from left to right. For low or high Reynolds numbers the center line of the flow is at y_c^+ = 315 or 1414 and the first grid point from the lower wall is at y_1^+= 5.3 or 23.8. The resolution is (Δx^+, Δy^+, Δz^+) = (20.6, 10.3, 10.3) or (93.0, 46.5, 46.5) in terms of wall unit, and ($\Delta x/h$, $\Delta y/h$, $\Delta z/h$) = (0.065, 0.032, 0.032) in terms of the outer length-scale for both Reynolds numbers. The resolution in the y-direction for the high Reynolds number was not enough to resolve the buffer layer region and very small scales.

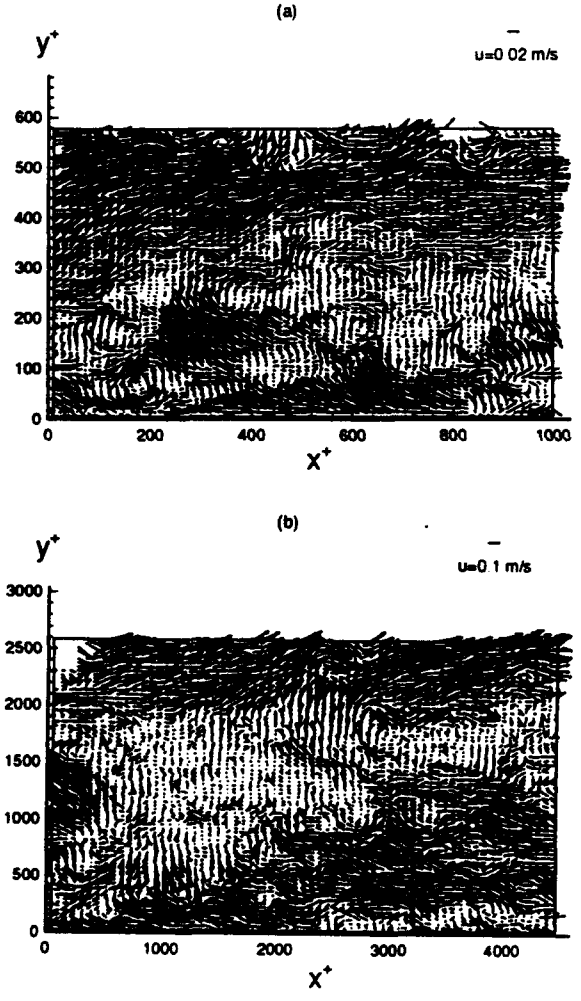

Fig. 3 Fluctuating velocity fields of channel flow obtained from PIV measurements. The bottom wall is located at y^+=0 and top borders of the vector maps are close to the upper wall of the channel. (a) Re_h = 5378, (b) Re_h = 29935.

As seen in previous PIV studies in the same channel in a streamwise-normal plane at a low Reynolds number Re_h = 2872 by Liu *et al* (1991), the most frequently appearing structures in almost every PIV realization in the region of $y^+ < 100$ are low momentum fluid moving away from the wall and high momentum fluid moving toward the wall. These motions could be related to ejection and sweep events. They meet together and create a sharp shear layer inclined to the wall with an angle of less than 45^0. The shear layer can be caused to roll up at downstream by down coming fluid from the outer region to form a spanwise vortex. This kind of coherent structure can also be found in flow fields at Re_h = 5378 and 29935, but not very often. The most striking structures of flows at moderate Reynolds numbers are the large scale streamwise motions with low momentum fluid or with high momentum fluid. Studies of low-pass filtered fields, show that these large structures are associated with the production of large amount of turbulent kinetic energy and Reynolds stress (Hanratty *et al*, 1993). The dimensions of these events are roughly independent of Reynolds number; they extend over about 1/4 of the channel height in the log-layer in the normal direction and over two channel heights (beyond the photograph) in streamwise direction. They are scaled with the outer length scale and do not change much with Reynolds numbers.

Two-point spatial correlations, $R_{ij}(y,y')$ and $R_{ij}(r_x,y,y')$, were computed for two Reynolds numbers, where r_x, y, y' are the space separations between two points in x-direction and their y-locations, $i, j = u$ or v. Figure 4 shows the two-point correlation coefficients of $R_{uu}(y,y')$ with r_x = 0 for Re_h = 5378. Three curves are plotted for the fixed point at 3 locations, y'/h = 0.114, 0.476, 0.50. The abscissa is y/h, the locations of the other point. Contours of correlations $R_{uu}(r_x,y,y')$ are plotted in Fig. 5a for Re_h = 5378 and Fig. 5b for 29935. The fixed points are at y'/h = 0.25 and on the ordinate are locations of the other points. The positive or negative r_x/h indicate the other point to be in the downstream or upstream side. These figures show that the dimension of the coherent motion is quite large and consistent with observations from filtered fluctuating velocity fields. It is interesting to note that the strong correlations appear to incline forward from the wall at an angle of approximately 10^0 and that the correlations with upper half channel flow become slightly negative, as can be seen in Fig. 4 also.

4. PROPER ORTHOGONAL DECOMPOSITION OF TURBULENT CHANNEL FLOW

The proper orthogonal decomposition was proposed by Lumley (1967) in an effort to extract coherent structures in turbulent flows with objective definition. The structure is selected when it has the largest mean square projection on the turbulent velocity field. This results in an eigenvalue problem, a Fredholm integral equation whose kernel is the two-point correlation tensor of the turbulent velocity field. The solution of the equation is an orthonomal set of deterministic eigenfunctions which are empirical and associated with coherent structures. It is believed that, if a structure contributes a majority of the turbulent kinetic

energy or Reynolds stress, it will dominate the two-point correlation statistics in an average sense. Therefore, information about the structure will be retained in the correlation tensor.

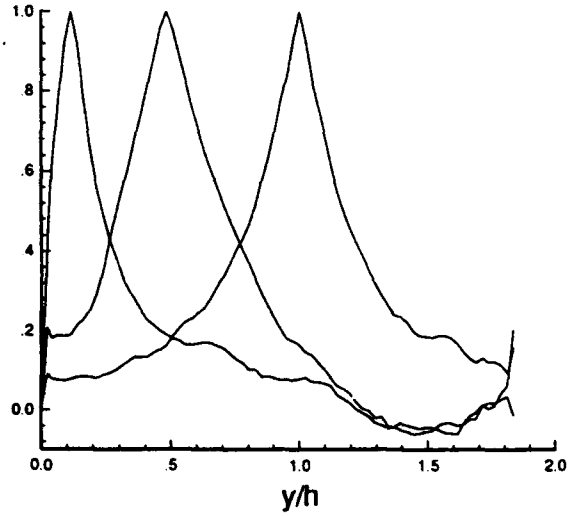

Fig. 4 Two-point correlation coefficients, $R_{uu}(y,y')/u_{rms}(y)\,u_{rms}(y')$ at $Re_h = 5378$.

The two-point correlation tensor was calculated from the PIV measurements as mentioned above. Since the realizations studied here are only two-dimensional the eigen-equation can be solved for only two components of eigenfunction. For the first step the one-dimensional (the inhomogeneous y- dimension only) POD was performed in a domain of half channel height for two Reynolds numbers using the computed correlation tensor of each component (Liu *at al*, 1994).

The eigen-equation reads:

$$\int_0^h R_{ii}(y,y')\varphi_i^{(n)}(y')dy' = \lambda_n \varphi_i^{(n)}(y). \qquad (1)$$

where

$R_{ii}(y, y') = < u_i(x,y,z,t)\, u_i(x,y',z,t) >$, $i = u$ or v.

$\phi_i^{(n)}(y)$ is the n^{th} order eigenfunction with an eigenvalue of λ_n. The eigenvalues represent the energy associated with the corresponding eigenmodes. They are ordered so that $\lambda_n \geq \lambda_{n+1}$. The lowest eigenmode will contribute the largest energy to the flow field. Based on this modal decomposition in the eigenfunctions a velocity field that is a member of the ensemble can be reconstructed:

$$u_i(x,y) = \Sigma_n a_n(x)\, \phi_i^{(n)}(y). \qquad (2)$$

The coefficient a_n can be evaluated using the orthogonality of the eigenfunction set and the realization itself. The total turbulent kinetic energy and Reynolds stress of the flow field can also be calculated by a diagonal decomposition:

$$< u_i^2(x,y,z,t) > = \Sigma_n \lambda_n [\phi_i^{(n)}(y)]^2. \qquad (3)$$

$$< u_i(x,y,z,t)\, u_j(x,y,z,t) > = \Sigma_n \lambda_n \phi_i^{(n)}(y)\, \phi_j^{(n)}(y). \qquad (4)$$

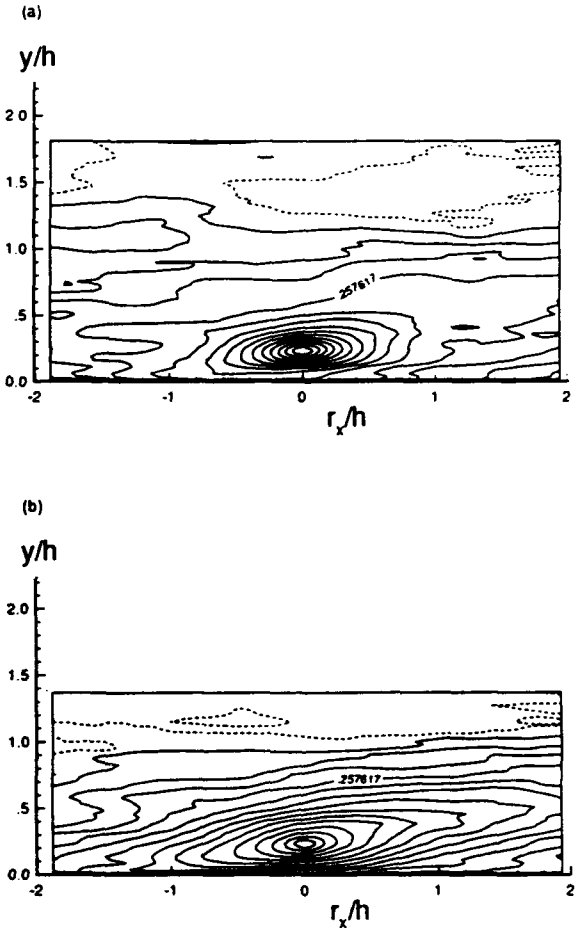

Fig. 5 Contours of two-point correlation functions, $R_{uu}(r_x,y,y')$. at $Re_h = 5378$ (a) and 29935 (b). Solid line contours are positive and dash line contours are negative.

When the decomposition is done for two velocity components the phases between eigenfunctions of two components are obtained. They are needed when carrying out calculations of the contributions to Reynolds stress from equation (4). Different decomposition domains can also be selected, such as the near wall region or the full channel height. If POD is carried out in two dimensions, Fourier decomposition should be used in the homogeneous streamwise direction, since the POD in the homogeneous direction will be reduced to Fourier decomposition.

Fig. 6 and 7 present the eigenfunctions and eigenvalue spectra of POD applied to PIV data of turbulent fluctuating fields. They are dimensionalized by outer layer length scale h (the half channel height) and the friction velocity, u_τ (Liu *et al*, 1994). Fig. 6a and 6b show the u- and v- components of the eigenfunction of order n = 3 for Re_h = 5378 and 29935. The eigenfunctions exhibit almost the same modal structure in the outer region, even though the Reynolds numbers are 5.5 times one another. The u- eigenfunctions are clearly dependent on Reynolds number in the near wall region. The modal orders n are related to a sequence defined as the number of the zero crossings of the eigenfunction in the domain and are equal to the number of half-cycles in the domain h. Fig. 7 presents the eigenvalue spectra for two Reynolds numbers. The similarity of low modes at different Reynolds numbers is evident. They are independent of Reynolds number. The spectrum of high modes for high Reynolds number is much broader than for the low Reynolds number. It shows significant Reynolds number effect on high modes. These results provide a credible test of the conjecture made by Chambers *et al* (1988) in the study of spectra of Bergers equation that the real turbulence might also obey a generalized law of Reynolds number similarity. At the high mode numbers shown in Fig. 7 the high Reynolds number spectrum starts to drop down, possibly because the resolution in the PIV measurements is not fine enough.

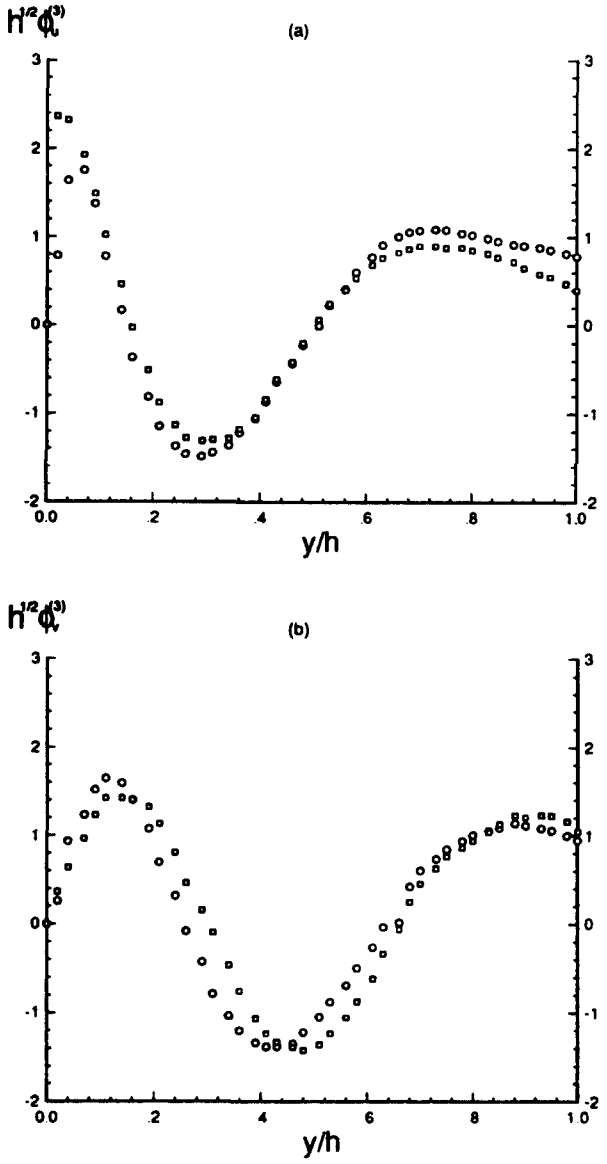

Fig. 6 One-dimensional eigenfunctions of u- component (a) and v- component(b) at Re_h = 5378 (circles) and 29935 (squares).

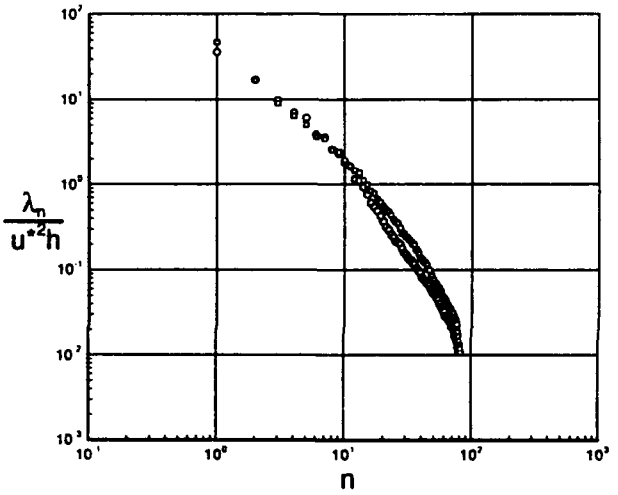

Fig. 7 Eigenvalue spectra of one-dimensional POD at Re_h = 5378 (circles) and 29935 (squares).

The dominant eigenmode contributes a large portion of the total turbulent kinetic energy and the Reynolds stress. The eigenmode of lowest order carries 35% of the total energy and 61% of Reynolds stress for Re_h = 5378, and 40% of total energy and 48% of Reynolds stress for Re_h = 29935. Figure 8 demonstrates the contribution of eigenmodes to turbulent kinetic energy at Re_h = 5378. Term N is the number of the first low modes involved. It can be seen that the first five low eigenmodes carry 74% and the first twelve low modes carry 90% of the total energy. The lower modes are more energetic and have less zero crossings. They could be associated with the streamwise large scale motions observed from PIV fluctuating velocity fields (Hanratty *et al* (1993). The results agree well with results at Re_τ =180 presented by Moin and Moser (1989). For comparison, the following Table 1 lists the contributions of the first three eigenmodes to the turbulent kinetic energy E and to the Reynolds stress P.

Re_τ	180 **	315 *	1414 *
λ_1/E	0.32	0.35	0.406
λ_2/E	0.16	0.166	0.145
λ_3/E	0.08	0.0954	0.0773
λ_1/λ_2	2.0	2.1	2.8
P_1/P	0.66	0.61	0.477

Table 1. Contributions of the one-dimensional eigenmodes to energy and Reynolds stress. *: present study, **: Moin and Moser (1988)

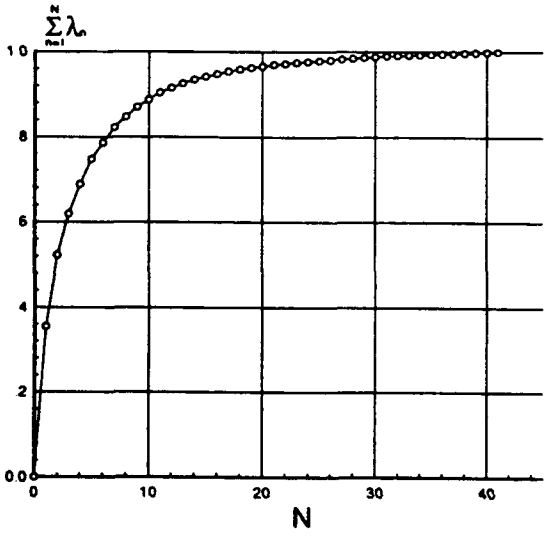

Fig. 8 Contributions of first N lowest eigenmodes at Re_h = 5378 to turbulent kinetic energy.

5. CONCLUSIONS

PIV measurements of turbulent flow in a channel have been made in a streamwise-normal plane at moderate Reynolds numbers, Re_h = 5378 and 29935, corresponding to Re_τ = 315 and 1414. Most of the fluctuating velocity fields show streamwise large scale motions with a length scale of over two channel heights in streamswise direction and approximately a quarter of the channel height in normal direction. Two-point correlations were computed from ensembles of the fluctuation fields for two Reynolds numbers. The contours of correlation support observations of length scale of large scale motions seen in the fluctuating velocity fields .

The proper orthogonal decomposition of two-dimensional PIV data has been successful. The present results are consistent with those from DNS data (Moin and Moser 1989, Sirovich *et al* 1991). The one-dimensional POD results presented in this paper substantiate the conjecture that the real turbulence obeys a generalized law of Reynolds number similarity made by Chambers *et al* (1988). It will be important that one can predict the similar behavior of modal structures over a large Reynolds number range.

The dominant eigenmode contributes a large amount of turbulent kinetic energy and Reynolds stress. A few of the lower eigenmodes dominate the energy and turbulent production. They could be associated with the observations of streamwise large scale motions. The results of contributions from first three eigenmodes to total turbulent kinetic energy and Reynolds stress agree well with those published by Moin and Moser (1989).

ACKNOWLEDGMENTS

This work was supported by ONR N00014-93-1-0552, NSF CTS 92-00936 and Petroleum Res. Fund for Amer. Chem. Soc. Project #35913

REFERENCES

Adrian, R. J. 1991, Particle-imaging techniques for experimental fluid mechanics, Ann. Rev. Fluid Mech., vol. 23, pp. 261-304.

Berkooz, G., Holmes, P., Lumley, J.L. 1993, The proper orthogonal decomposition in the analysis of turbulent flows. In Ann. Rev. Fluid Mech, vol. 25, 539-575.

Chambers, D.H., Adrian, R.J., Moin, P., Stewart, D.S., and Sung, H.J. 1988, Karhunen-Loeve expansion of Burger's model of turbulence, Phys. Fluids, vol. 31, pp. 2573-2582.

Dean, R. B. 1978, Reynolds number dependence of skin friction and other bulk flow variables in two-dimensional rectangular duct flow, J. of Fluids Engineering, vol. 100, pp. 215-223.

Hanratty, T. J., Adrian, R. J., Liu, Z. C., Brook, J., Papavassiliou, D., McLaughlin, J. 1993, Recent results on the structure of wall turbulence, Ninth Symposium on "Turbulent Shear Flows", 11-3-1--11-3-3, Kyoto, Japan.

Keane, R.D., Adrian, R.J. 1990, Optimization of particle image velocimeters. Part 1: double pulsed systems, Meas. Sci. Technol., vol. 1, pp. 1202-1215.

Keane, R.D., Adrian, R.J. 1992, Theory of cross-correlation analysis of PIV images, Applied Scientific Research. vol. 49, pp.191-215.

Liu, Z.-C., Landreth, C.C., Adrian, R.J., Hanratty, T.J. 1991, High resolution measurement of turbulent structure in a channel with particle image velocimetry, Exp. Fluids, vol. 10, pp. 301-312.

Liu, Z.-C., Adrian, R.J., Hanratty, T.J. 1994, Reynolds-number similarity of orthogonal decomposition of the outer layer of turbulent wall flow. TAM Report No.748 UILI-ENG-94-6004, Feb. Also to appear in Phys. Fluids.

Lumley, J.L. 1967, The structure of inhomogeneous turbulent flows. In Proc. Intl. Coll. on the Fine-Scale Structure of the Atmosphere and its Influence on Radio Wave Propagation. (Dokl. Nauk., Moscow, p.166-178.

Lumley, J.L. 1981, Stochastic Tools in Turbulence. Academic, New York.

Meinhart, C.D., Prasad, A.K., Adrian, R.J. 1992, Parallel digital processor system for particle image velocimetry, Meas. Sci. Tech. vol. 4, pp. 619-626.

Moin, P., Moser, R. D., 1989, Characteristic-eddy decomposition of turbulence in a channel, J. Fluid Mech., vol. 200, pp.471-509.

Niederschulte, M.A. 1988, Turbulent flow through a rectangular channel, Ph.D. thesis, University of Illinois, Urbana, Il.

Sirovich, L., Ball, K. S., Handler, R. A., 1991, Propagating structures in wall-bounded turbulent flows, Theoretical and computational Fluid Dynamics, vol.2 pp. 307-317.

TURBULENT PIPE FLOW CHARACTERISTICS OF LOW MOLECULAR WEIGHT SHEAR-THINNING FLUIDS

A. S. Pereira
Departamento de Engenharia Química, Instituto Superior de Engenharia do Porto
Rua de S.Tomé, 4200 Porto CODEX, Portugal

F. T. Pinho
Departamento de Engenharia Mecânica e Gestão Industrial
Faculdade de Engenharia, Rua dos Bragas, 4099 Porto CODEX, Portugal

ABSTRACT

A miniaturised fibre optic Laser-Doppler anemometer and a differential pressure transducer were used to carry out detailed hydrodynamic measurements in a fully developed turbulent pipe flow with 0.4% to 0.6% by weight shear-thinning aqueous solutions of a methylhydroxil cellulose of molecular weight equal to 6,000 kg/kmole (Tylose MH 10000K from Hoechst).

In spite of undetectable elasticity in oscillatory and creep flow tests and of their low molecular weight, these solutions exhibited drag reductions of up to 35% relative to a newtonian fluid flow at the same wall Reynolds number, and of about 25% relative to the inelastic shear-thinning friction correlation of Dodge and Metzner (1959) at the same generalised Reynolds number, respectively.

The low molecular weight polymer solutions were also observed to delay transition from the laminar to the turbulent regime as intensively as reported before by Pinho and Whitelaw (1990) with heavier and more elastic solutions of cellulose, and we may tentatively conclude that this transition delay is a shear-thinning rather than an elastic effect.

1. INTRODUCTION

In the past the investigation of non-Newtonian wall-dominated flows has been mostly concerned with the study of the drag reduction phenomena and the understanding of the effects of elasticity and variable viscosity on their turbulent characteristics, but the fluids under scrutiny normally were made with additives of molecular weight over 10^5 kg/kmole (Berman (1978), Allan *et al* (1984) at very dilute concentrations. More recently Pinho and Whitelaw (1990) and Escudier *et al* (1992) investigated the turbulent pipe flow of shear-thinning polymer solutions with viscosity power law indices between 0.39 and 0.90 which also showed drag reduction and the validity of Virk's asymptote for variable viscosity fluids.

Elasticity in turbulent pipe flow manifests itself in a reduction of the friction coefficient, and according to Hinch (1977), Tabor *et al* (1989) and more recently Kostic (1994) amongst others, this is related to a strong strain imposed elongation of the molecules and its effect on the extensional viscosity, thus leading to an anisotropic viscosity. Therefore, it is logic to expect that small light molecules may be inelastic and will show no drag reduction. The experiments of Lodes and Macho (1989) with aqueous solutions of a 19.000 kg/kmole partially saponificated polyvinylacetate with different degrees of hydrolysis have reported drag reductions close to the maximum predicted by Virk's asymptote (Virk *et al*, 1970), but did not report any turbulence field data, and the authors speculated on a different origin for the elastic behaviour of the fluid without proper evidence. Therefore, the purpose of this work is to investigate the turbulent characteristics of shear-thinning fluids, of molecular weight lower than 10,000, in a pipe flow.

2. EXPERIMENTAL SET UP

The flow configuration, fully described in Pereira (1993), consisted of a long 26 mm inside diameter vertical pipe with a square outer cross section to reduce diffraction of light beams. The fluid circulated in a closed circuit, pumped from a 100 litre tank through 90 diameters of pipe to the transparent acrylic test section of 232 mm of length, and a further 27 diameters down back to the tank, with the flow controlled by two valves. A 100 mm long honeycomb was located 90 diameters upstream of the test section to help to ensure a fully developed flow in the plane of the measurements.

Four pressure taps 65 mm apart were drilled in the test section and the upstream pipe and were used for the pressure loss measurements. Equal longitudinal pressure gradients were measured between any two consecutive taps, thus ensuring that the connection between the brass pipe and the test section was well done and within the machining tolerances of $\pm$ 10 μm, and caused no detectable harm to the flow condition. This, together with equal velocity measurements at two different far apart within the test section, confirmed a fully developed flow situation there.

The pressure drop was measured by means of a differential pressure transducer from Rosemount, model 1151 DP 3S and its output was sent to a computer via a data acquisition board Metrabyte DAS-8 interfaced with a Metrabyte ISO 4 multiplexer, both from Keithley. The overall uncertainty of the pressure measurements was less than 1.2 Pa, which is about 1.6% and 5% for high and low pressure differences, respectively.

A fiber optic laser-Doppler velocimeter from INVENT, model DFLDA was used for the velocity measurements, with a 30 mm probe mounted on the optical unit. Scattered light was collected by a photodiode in the forward scatter mode, and the main characteristics of the anemometer are listed in table I and described by Stieglmeier and Tropea (1992). The signal was processed by a TSI 1990C counter interfaced with a computer via a DOSTEK 1400 A card, which provided the statistical

quantities. The data presented in this paper has been corrected for the effects of the mean gradient broadening and the maximum uncertainties in the axial mean and rms velocities at a 95% confidence level are of 2% and 3.1% on axis respectively, and of 2.8% and 7.1% in the wall region. The uncertainty of the radial and tangential rms velocity components is 4.1% and 9.4% on axis and close to the wall, respectively.

The velocimeter was mounted on a milling table with movement in the three coordinates and the positional uncertainties are of ± 200 and ± 150 μm in the axial and transverse directions, respectively.

Table I - Laser-Doppler characteristics

Laser wavelength	827 nm
Laser power	100 mW
Measured half angle of beams in air	3.68
Size of measuring volume in water at e^{-2} intensity	
minor axis	37μm
major axis	550μm
Fringe spacing	6.44μm
Frequency shift	2.5 [illegible]Hz

3. FLUID PROPERTIES

Aqueous solutions of a methil-hydroxil cellulose from Hoechst, Tylose MH 10000K, with a molecular weight of 6,000 kg/Kmole were investigated. Prior to the hydrodynamic measurements, the 0.4%, 0.5% and 0.6% by weight concentration Tylose solutions were characterised for their transparency, viscometric viscosity, dynamic viscosity, creep compliance and resistance to degradation. The biocide Kathon LXE from Rohm and Haas was added at 0.02% by weight to prevent bacteriological deterioration and the solutions were prepared with tap water.

The rheological characterisation of the fluids was carried out in a rheometer from Physica, model Rheolab MC 20, made up of an universal measurement unit UM/MC fitted with a low viscosity double-gap concentric cylinder system and a cone-plate system. The rheometer could be both stress and shear rate controlled and viscosities up to the maximum shear rate of 5230 s^{-1} could be measured, with an uncertainty of less than 3.5%.

The viscometric viscosity of the three solutions at 25°C are plotted in figure 1 together with the fitted Carreau viscosity model and its parameters are listed in Table II.

$$\mu = \mu_0 \left[1 + (\lambda\dot{\gamma})^2\right]^{\frac{n-1}{2}} \qquad (1)$$

Table II- Parameters of the Carreau model for the viscosity of the Tylose MH 10000K solutions at 25° C.

Concentration	μ_0 [Pa.s]	λ [s]	n	$\dot{\gamma}$ [s^{-1}]
0.4%	0.0208	0.0047	0.725	6.1 a 4031
0.5%	0.0344	0.005	0.660	6.1 a 4031
0.6%	0.0705	0.0112	0.637	6.1 a 4031

The fluids circulated in the rig for periods of less than 21 hours, during which the viscometric viscosity decreased by 10% due to the mechanical deterioration. The resistance to mechanical degradation of Tylose was three times longer than the lifetime of the CMC solutions, of molecular weight of 300,000, used by Pinho and Whitelaw (1990), under similar conditions.

The oscillatory and creep tests that were carried out could not detect any elasticity within the instrument accuracy.

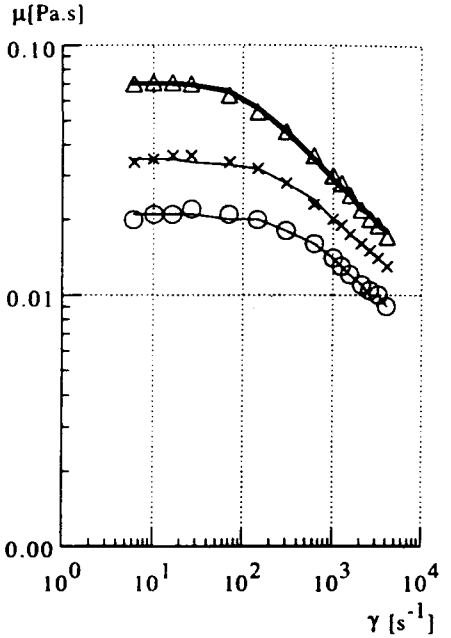

Figure 1- Viscosity and ajusted Carreau model to the 25° C Tylose solutions data. O- 0.4%; x-0.5% and Δ- 0.6%.

4. RESULTS AND DISCUSSION

Figures 2 and 3 show the Darcy skin-friction coefficient ($f_D=2\Delta pD/\rho U_b^2 L$) versus generalised and wall Reynolds numbers respectively, and illustrates the behaviour of the non-Newtonian solutions under laminar, transitional and turbulent flow conditions. The use of the generalised Reynolds number, as defined by Dodge and Metzner (1959), is appropriate in laminar flow and collapses the experimental data on the Newtonian relationship $f_D=64/Re_{gen}$ within the experimental uncertainty (figure 2). The Darcy friction (f_D) coefficient law for inelastic shear-thinning fluids based on the generalised Reynolds number (equation 2), is also included for comparison and shows that a drag reduction exists for the Tylose solutions.

$$\sqrt{\frac{1}{f_D}} = \frac{2}{n^{0.75}} \log\left[Re_{gen}\, f_D^{\frac{2-n}{n}}\right] - \frac{1.204}{n^{0.75}} + 0.602\, n^{0.25} - \frac{0.2}{n^{1.2}} \qquad (2)$$

However, for the turbulent regime the wall viscosity is a preferred parameter to define the Reynolds number, because it is in the wall region that viscous forces are most important. The same data of figure 2 is plotted again in figure 3 using the wall Reynolds number together with the newtonian Prandtl-Kárman law and Virk's (1975) maximum drag reduction asymptote. The newtonian data is consistent with previous results and confirms that the flow is close to being fully developed at high Reynolds numbers. Although not conclusive, the drop of the ratio of centreline to bulk velocity (U_0/U_b) with Reynolds number of figure 4 indicates that the flow condition is fully developed, or

close to it, for the maximum flow rate with the various polymer solutions.

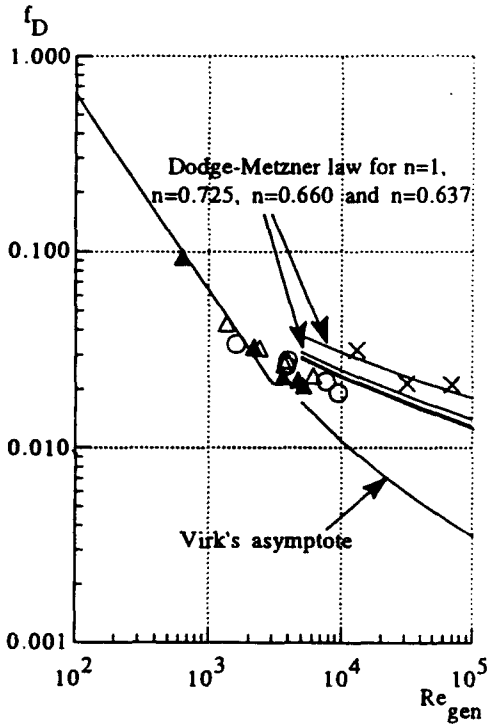

Figure 2- Darcy friction factor versus generalised Reynolds number. X Water, O Tylose 0.4%, Δ Tylose 0.5% and ▲ Tylose 0.6%. n - viscosity power law index.

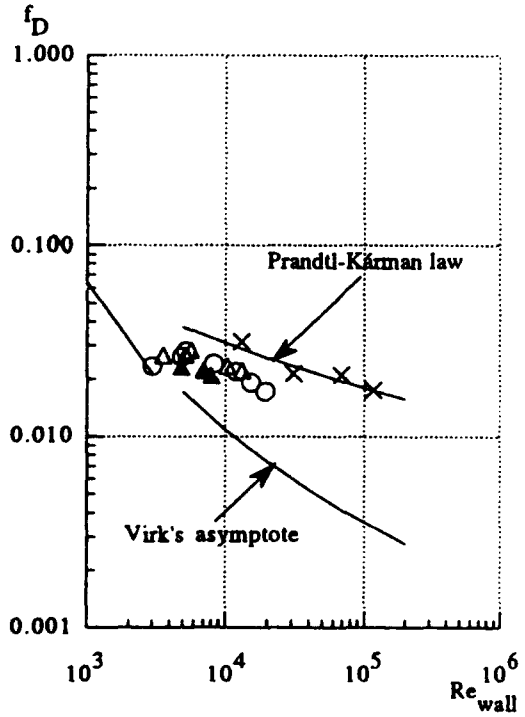

Figure 3- Darcy friction factor versus wall Reynolds number. X Water, O Tylose 0.4%, Δ Tylose 0.5% and ▲ Tylose 0.6%.

Figures 2 and 3 clearly emphasize the main conclusion of this work; in spite of the very low molecular weight of Tylose the aqueous solutions of this polymer exhibit drag reduction and this is consistent with the mean velocity profiles in wall coordinates shown below. The reduction of the friction factor is not a consequence of the shear-thinning characteristic of the polymer solutions, as can be seen in the comparisons figure 2 with Dodge and Metzner (1959) friction law for inelastic shear-thinning fluids. Maximum drag reductions of 30% to over 35% were measured relative to a newtonian flow at constant wall Reynolds number for the 0.4 and 0.6% Tylose solutions, which corresponded to about 20 to 27% if compared on the basis of a constant generalised Reynolds number. The drag reduction of Tylose was about half that reported to occur with the low elasticity shear-thinning high molecular weight CMC solutions of Pinho and Whitelaw (1990) which reached Virk's asymptote.

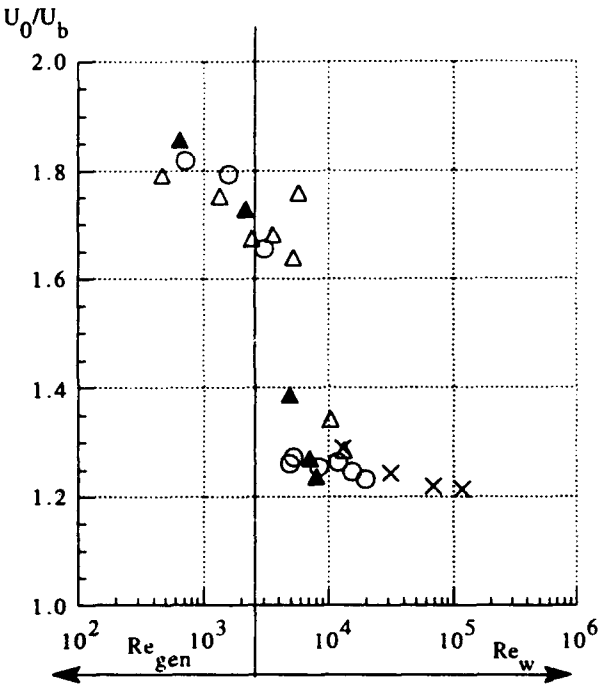

Figure 4- Ratio of centreline to bulk velocity versus generalized and wall Reynolds number for X Water, O Tylose 0.4%, Δ Tylose 0.5% and ▲ Tylose 0.6%.

Local measurements of the mean velocity and of the root-mean-square of the velocity fluctuations of the 0.4% by weight Tylose MH 10000K solution are shown in figures 5 to 7 which include some non-newtonian data taken from Pinho and Whitelaw (1990) concerning aqueous solutions of CMC (sodium carboxymethil cellulose) grade 7H4C from Hercules, with a molecular weight of around 3×10^5, i.e., about 50 times heavier than the Tylose solutions used in this work.

The axial mean velocity profile of the 0.4% Tylose at a Reynolds number of 3,030 in figure 5 is clearly not turbulent. The flow at the Reynolds number of 4,920, in spite of a low value of the ratio U_0/U_b in figure 4 and the mean velocity profiles of figures 5 and 6 which could indicate turbulent flow, does not seem to be under such flow condition as the exceedingly high velocity fluctuations of figures 7a) to c) suggest. For this flow condition the turbulence is much higher

than that for higher Reynolds numbers, and this can be associated with flow intermittency. Normal Reynolds stresses are known to increase gradually with the decrease in Reynolds number. Wei and Willmarth (1989), but for this low Reynolds number range the variations should not be so intense as observed here, unless the flow is within a transitional condition with intermittency contributing decisively to turbulence broadening. Actually this seems to be the case here as confirmed in figure 4 which shows a delayed transition with the non-newtonian fluids, a behaviour beautifully investigated by Wójs (1993).

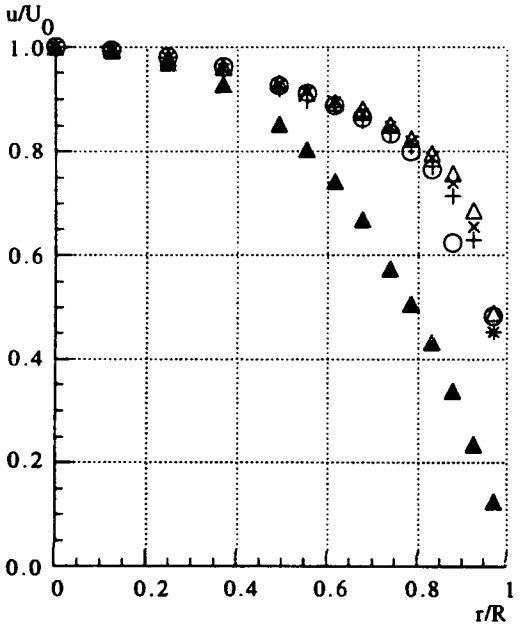

Figure 5- Axial mean velocity profile in physical coordinates for the 0.4% Tylose solutions. ▲ Re_w= 3030, O Re_w= 4920, + Re_w= 11930, X Re_w= 15400 and Δ Re_w= 19570.

The axial mean velocity profiles in wall coordinates of the 0.4% Tylose solutions in figure 6 are consistent with the drag reduction because they are shifted upwards from the newtonian log law, in a way which is proportional to the drag reduction intensity. This is better understood from the comparison with the 0.1% and 0.2% CMC data of Pinho and Whitelaw (1990) which were reported to have drag reductions of 47% and 64%, respectively. The more intense drag reductions of these heavy polymers imply a larger shift from the newtonian log law than that of the light Tylose solutions. Figure 6 also shows that the slope of the velocity profiles become steeper with drag reduction, especially at higher values of drag reduction, close to Virk's asymptote.

The normal Reynolds stresses of the Tylose solutions have a behaviour which is intermediate to the newtonian and the high molecular weight and intense drag reducer CMC solutions. The axial component of the Reynolds stress of the 0.4% Tylose solutions is not so high close to the wall as with the 0.2% CMC solutions, the one that is closer to the 0.4% Tylose in terms of viscous characteristics, and at the centre of the pipe the turbulence is not so damped, as shown in figure 7 a). Drag reduction is known to intensify axial turbulence close to the wall (Allan *et al* (1984) and is associated with a decrease of transverse turbulent transport. With drag reductions which are intermediate between those of the CMC solutions and the

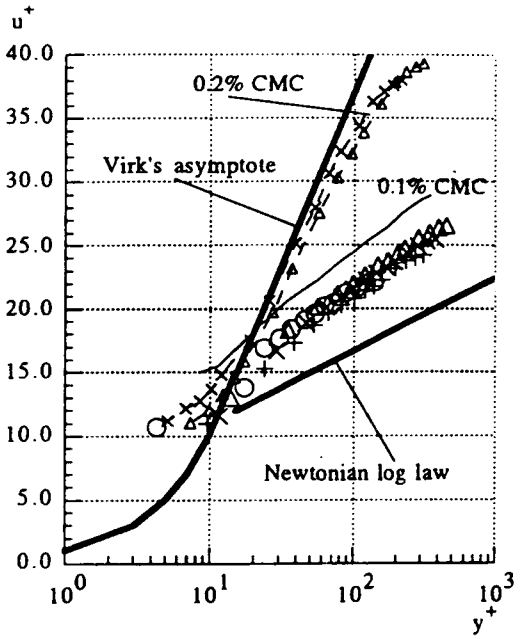

Figure 6- Axial mean velocity profile in wall coordinates for the 0.4% Tylose solutions. O Re_w= 4920, + Re_w= 11930, X Re_w= 15400 and Δ Re_w= 19570. From Pinho and Whitelaw (1990) -Δ- 0.2% CMC at Re_w= 18260,-x- 0.2% CMC at Re_w= 11770,—— 0.1% CMC at Rew= 16800.

newtonian fluid, it is expected that the profiles of the rms *velocities reflect* this behaviour, as happens here. The axial turbulence profiles show a small Reynolds number effect with the flow at a Reynolds number of 11,930 having marginally higher values than the flow at a higher Reynolds number.

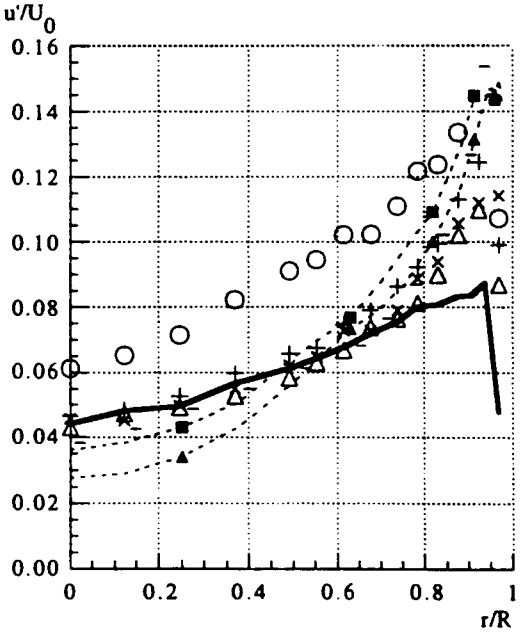

Figure 7a) Axial rms velocity profile in physical coordinates for the 0.4% Tylose solutions. O Re_w= 4920, + Re_w= 11930, X Re_w= 15400 and Δ Re_w= 19570.—— Water Re= 117500. From Pinho and Whitelaw (1990) -▲- 0.2% CMC at Re_w= 18260,- ■ - 0.2% CMC at Re_w= 11770, • 0.1% CMC at Re_w= 16800.

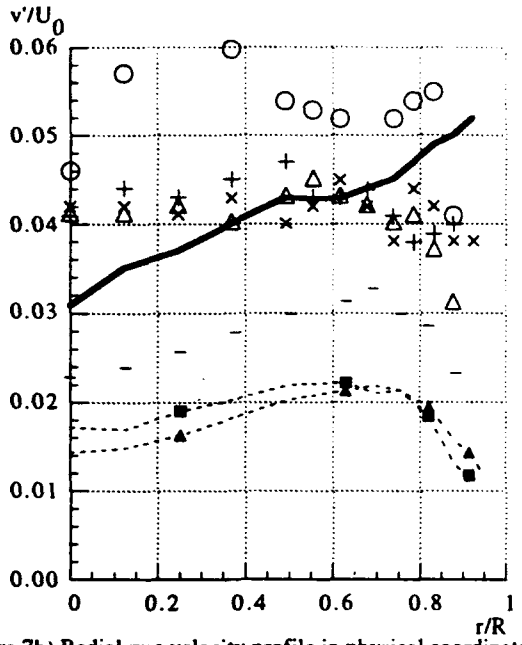

Figure 7b) Radial rms velocity profile in physical coordinates for the 0.4% Tylose solutions. O Re_w= 4920, + Re_w= 11930, X Re_w= 15400 and Δ Re_w= 19570. —— Water Re= 117500. From Pinho and Whitelaw (1990) -▲- 0.2% CMC at Re_w= 18260,- ■ - 0.2% CMC at Re_w= 11770, * 0.1% CMC at Re_w= 16800.

The radial and azimuthal components of the rms of the fluctuating velocity of the 0.4% Tylose fluids in figures 7 b) and c) agree with the previous observations, showing less dampening than those of the CMC solutions. However there is a major difference between the Tylose and the CMC curves: although intense dampening of the transverse turbulence is observed with the Tylose and CMC solutions in the near-wall region in relation to the water flows, in the centre of the pipe there is no reduction of turbulence with the Tylose, and in fact the opposite occurs. Radial and tangential rms velocities hardly increase from the centre of the pipe to the wall, remaining almost constant within 80% of the radius, and decreasing only on the final 20% near the wall. The high radial and tangential turbulence in the center of the pipe could be due to the reported delay in transition together with a Reynolds number effect. This means that Reynolds number and transitional effects with the non-newtonian Tylose solutions occur over a wider range of Reynolds numbers than with the water flows. For the water flows at Reynolds numbers between 30,000 and 117,500 the turbulence profiles hardly change, and agree well with data from Lawn (1971) indicating fully developed turbulent flow in all conditions. Besides, as already mentioned, Reynolds number effects with newtonian fluids are not so intense as observed here with the non-newtonian fluids.

It is clear that the effects of drag reduction on the turbulence characteristics of the low molecular weight polymers are localised in the wall region, whereas for the high molecular weight solutions they span over the whole pipe, and this effect is not restricted to the transverse components of turbulence. In the centre of the pipe the axial component of turbulence of the Tylose solutions is similar to the newtonian values whereas the CMC axial turbulence intensity is attenuated.

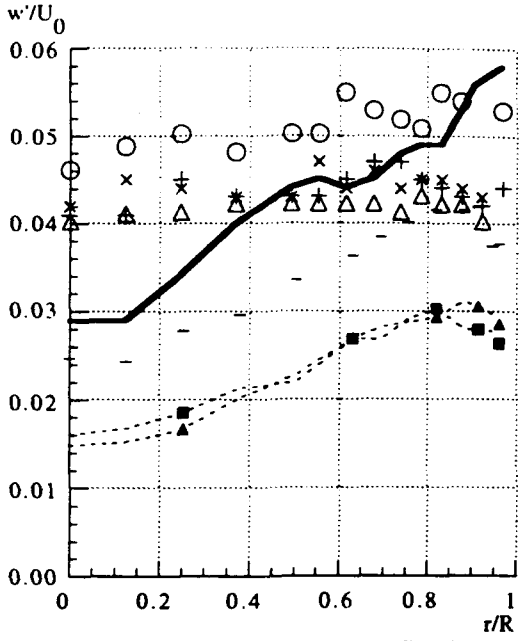

Figure 7c) Azimuthal rms velocity profile in physical coordinates for the 0.4% Tylose solutions. O Re_w= 4920, + Re_w= 11930, X Re_w= 15400 and Δ Re_w= 19570. —— Water Re= 117500. From Pinho and Whitelaw (1990) -▲- 0.2% CMC at Re_w= 18260,- ■ - 0.2% CMC at Re_w= 11770, * 0.1% CMC at Re_w= 16800.

5. CONCLUSIONS

Aqueous solutions of a very low molecular weight polymer were rheologically characterised to be shear-thinning and inelastic in creep and oscillatory flows. In spite of this, they exhibited drag reductions of up to 35% in a turbulent pipe flow, as compared to the newtonian friction law and a delay in transition proportional to the polymer concentration.

The drag reduction was accompanied by a reduction of the turbulence, especially in the transverse directions. However, these effects were not so intense as previously observed with high molecular weight shear-thinning polymer solutions and were mostly concentrated on the wall region.

One has to conclude from this work that linear molecules suffer the effects of elongational viscosity increase, or any other mechanism that causes turbulent drag reduction and the decrease of transverse turbulence, even for very small molecular sizes.

ACKNOWLEDGEMENTS

The authors would like to thank Instituto Nacional de Investigação Científica- INIC, INEGI (Instituto de Engenharia Mecânica e Gestão Industrial) and Laboratorio de Hidráulica da Faculdade de Engenharia for financing the rig, lending some equipment and providing building space for the rig, respectively. We also appreciate Hoechst, Portugal and Horquim, Portugal for offering us the polymers and additives.

REFERENCES

Allan, J. J., Greated, C. A. and McComb, W. D. 1984. Laser-Doppler Anemometer Measurements of Turbulent Structure in Non-Newtonian Fluids. J. Phys. D: Appl. Phys., vol. 17, pp. 533 - 549.

Berman, N. S. 1978. Drag Reduction by Polymers. Ann. Rev. Fluid Mech., vol. 10, pp. 47-64.

Dodge, D. W. and Metzner, A. B. 1959. Turbulent Flow of Non-Newtonian Systems. AIChE J., vol. 5, pp. 189-204.

Escudier, M. P., Jones, D. M. and Gouldson, I. 1992. Fully Developed Pipe Flow of Shear-Thinning Liquids. Proc. 6th Int. Symp. on Appl. Laser Techniques to Fluid Mech., Lisbon, paper 1.3.

Hinch, E. J. 1977. Mechanical Models of Dilute Polymer Solutions in Strong Flows. Phys. Fluids, vol. 20, pp. S22-S30.

Lawn, C. J. 1971. The Determination of The Rate of Dissipation in Turbulent Pipe Flow. J. Fluid Mech., vol. 48, pp. 477-505.

Lodes, A. and Macho, V. 1989. Scale Effects in Polymer Solution Pipe Flow. Exp. in Fluids, vol. 7, pp. 383-387.

Pereira, A. S. 1993. Rheological and Hydrodynamical Characteristics of Low Molecular Weight Non-Newtonian Fluids in Pipe Flows. MSc. Thesis (in Portuguese), Univ. Porto.

Pinho, F. T., and Whitelaw, J. H. 1990. Flow of Non-Newtonian Fluids in a Pipe. J. Non-Newt. Fluid Mech., vol. 34, pp. 129-144.

Stieglmeier, M. and Tropea, C. 1992. A Miniaturized, Mobile Laser- Doppler Anemometer, Applied Optics, vol. 31, pp. 4096.

Tabor, M., Durning, C. J. and O'Shaughnessy, B. 1989. The Microscopic Origins of Drag Reduction. Internal Report of University of Columbia, Depts. of Applied Physics, Applied Chemistry and Chem. Eng., NY 10027.

Virk, P. S., Mickley, H. S. and Smith, K. A. 1970. The Ultimate Asymptote and Mean Flow Structure in Tom's Phenomena. J. Appl. Mech., vol. 37, pp. 488-493.

Wei, T. and Willmarth, W. W. 1989. Reynolds Number Effects on The Structure of a Turbulent Channel Flow. J. Fluid Mech., vol. 204, pp. 57- 95.

Wójs, K. 1993. Laminar and Turbulent Flow of Dilute Polymer Solutions in Smooth and Rough Pipes. J. N-Newt. Fluid Mech., vol. 48, pp. 337- 355.

ANNULAR FLOW OF SHEAR THINNING LIQUIDS WITH CENTREBODY ROTATION

M P Escudier and I W Gouldson

University of Liverpool, Dept of Mechanical Engineering,
P O Box 147, Liverpool, L69 3BX, England.

SUMMARY

Radial distributions of the axial and tangential components of velocity and rms velocity fluctuations are presented together with friction factor versus Reynolds number (f-Re) data for Newtonian and shear-thinning liquids in laminar, transitional and turbulent flow in an annular geometry with a rotating centrebody of diameter ratio 0.506.

In all flow regimes, the global influence of centrebody rotation is most apparent for the Newtonian fluid where the friction factor increases appreciably with rotation speed. The non-Newtonian fluids show less of an increase due to rotation than the Newtonian fluid.

LDA measurements of the tangential velocity reveal three distinct regions across the radial gap with a central region of almost constant velocity which diminishes in magnitude as the Reynolds number increases.

Axial velocity measurements show little deviation from what would be expected for the case without centrebody rotation. In turbulent flow axial velocity fluctuations show a progressive decrease with increasing Reynolds number. Suppression of tangential velocity fluctuations is found for the polymeric liquids, especially at high Reynolds numbers where the influence of centrebody rotation is reduced.

Over a limited range of (low) Reynolds number and rotation speeds, the generation of Taylor vortices produces complex flow patterns. Limited measurements are reported for the vortex advection speed.

1. INTRODUCTION

With the exception of the very recent paper of Nouri and Whitelaw (1993), no other detailed experimental studies of the flow of non-Newtonian fluids in an annulus with centrebody rotation have been reported. Wroński and Jastrzębski (1990 a) have used a mass-transfer technique to investigate the stability of helical flow in concentric annular channels of radius ratio 0.66, 0.8 and 0.86 with relatively high concentrations of carboxymethylcellulose (CMC) and methylcellulose. The same authors (1990 b) concluded that the mass transfer rate could be correlated with the results for Newtonian liquids using a mean apparent viscosity value. There is considerably more theoretical work, inevitably confined to the laminar flow regime. Recent work includes that of Bittleston and Hassager (1992) and of Malik and Shenoy (1991), both concerned with generalised annular Couette flow of shear-thinning liquids. Of more direct relevance is the paper of Lockett et al (1992), concerned with the stability of inelastic non-Newtonian liquids in Couette flow, as well as the more extensive study of Lockett (1992) which considers the more general situation of combined axial and rotational motion.

In this paper we present measurements of the variations in flow structure with flowrate and rotation speed for a Newtonian liquid (glucose) and two shear-thinning liquids (CMC and Xanthan gum).

2. EXPERIMENTAL SET UP

Measurements were carried out in a 5.7m length of precision-bore glass tubing (100.4mm ID ± 0.1mm) with a nominally concentric thin-walled stainless steel centrebody (50.8mm OD) giving a radius ratio of 0.506. Rotation of the centrebody was provided by a DC Neco motor and gearbox, monitored by an optical encoder giving a resolution of 0.1rpm and a range of 0-126rpm. Axial flow was provided by a Mono progressive cavity pump (max flowrate $0.025m^3/s$), supplied by a 500ℓ stainless steel tank. Three accumulators located immediately after the pump outlet functioned to remove pulsations in the flow prior to the test section. Volumetric flowrate measurements were taken using a Fischer and Porter electromagnetic flowmeter (max capacity $0.0333m^3/s$) incorporated into the return arm of the flowloop, downstream of the test section. Validyne pressure transducers (3448 Pa and 862 Pa fsd) were used to measure pressure drops along the test section to

determine the average wall shear stress τ_s. Temperature measurements were taken using a platinum resistance thermometer (±0.1°C) located in the end housing downstream of the test section. Measurements of axial and tangential velocities as functions of radial and axial location were made using a Dantec Fibreflow laser Doppler anemometer system with a measuring volume length in water of 0.19mm. For a few measurements, a second LDA system was employed to permit cross-correlation measurements of the velocities at two locations separated axially by 10 mm and azimuthally by 90°, the azimuthal separation necessitated by the physical size of the probe head. To achieve minimal refraction and minimise misalignment of the beams a flat-faced optical box was positioned over the pipes and filled with castor oil which had a refractive index close to that of the glass (R_n=1.478). A 125um filter was incorporated into the system within a bypass loop allowing filtering of the water prior to the addition of polymer.

Measurements of the rheological characteristics of the liquids used were made using a Carri-Med CSL 100 controlled-stress rheometer. Both cone and plate and parallel-plate geometries were employed for the fluid characterization. Fluid refractive indices were determined using an ABBE 60/ED high accuracy refractometer.

3. TEST FLUIDS : PREPARATION AND RHEOLOGY

The non-Newtonian liquids used were aqueous solutions of CMC (0.2% w/w) and Xanthan gum (0.15% w/w) with a 1:1 w/w glucose/water mixture with viscosity 0.01 Pa.s to provide a basis for comparison. 700ℓ of each fluid was prepared by filtering tap water prior to the addition of the polymer or glucose. To prevent bacteriological degradation of the fluid a small quantity (100ppm for CMC and Xanthan gum; 200ppm for glucose/water) of formaldehyde was added. Seeding particles (Timiron MP-1005, mean diameter approx 20μm) at a concentration of 1ppm were added to improve the LDA signal/noise ratio and data rate.

The viscometric characteristics of the two polymers are shown in **Figure 1**. The power-law behaviour of CMC is well represented (for $\dot{\gamma} > 200\ s^{-1}$) by $\mu = (\lambda_n \dot{\gamma})^{n-1}$ with λ_n = 0.239 s and n = 0.69. A better representation of the CMC viscosity data over the entire range of shear rates is given by the Cross model

$$\frac{\mu - \mu_\infty}{\mu_o - \mu_\infty} = [1 + (\lambda_c \dot{\gamma})^n]^{-1}$$

with μ_o = 0.0346 Pa.s, μ_∞ = 0.001 Pa.s, λ_c = 0.0165 s and n = 0.66. For Xanthan gum the viscosity is best described by the Sisko model,

$$\mu = \mu_{ref} (\lambda_s \dot{\gamma})^{n-1} + \mu_\infty$$

with n = 0.407, λ_S = 12.1 s, μ_∞ = 0.0014 Pa.s and μ_{ref} = 1 Pa.s. As well as power-law behaviour over a wide range of shear rates, Xanthan gum also exhibits a measurable degree of viscoelasticity. For the evaluation of Reynolds and Taylor numbers, shear rates for the determination of the fluid viscosity μ were obtained using the average surface shear stress determined from the axial pressure gradient and viscometric data for the particular fluid in use.

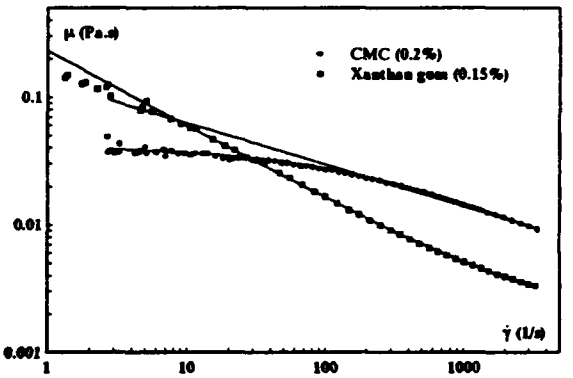

Figure 1. Viscosity vs shear rate for CMC and Xanthan gum.

4. RESULTS

The global influence of centrebody rotation for each of the test fluids is apparent from the friction factor vs Reynolds number data shown in **Figure 2** and the normalised axial velocity fluctuations at ξ = 0.8 shown in **Figure 3**. The velocity fluctuations are used to monitor the change from laminar flow through transition to fully developed turbulent flow. For comparison purposes, curves representing standard friction-factor correlations for fully developed flow of a Newtonian fluid in an annulus with radius ratio 0.5 and no centrebody rotation are included in **Figure 2** as follows

f = 23.9/Re (laminar)

$\frac{1}{\sqrt{f}}$ = 4 $\log_{10}$ (1.343 Re $\sqrt{f}$) - 1.6 (turbulent) Jones and Leung (1981)

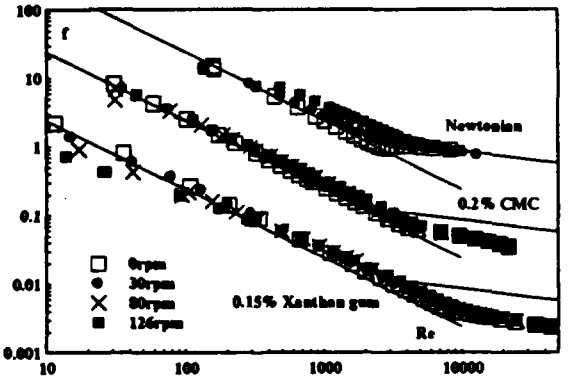

Figure 2. f vs Re for Newtonian fluid, CMC and Xanthan gum (note shifted origins).

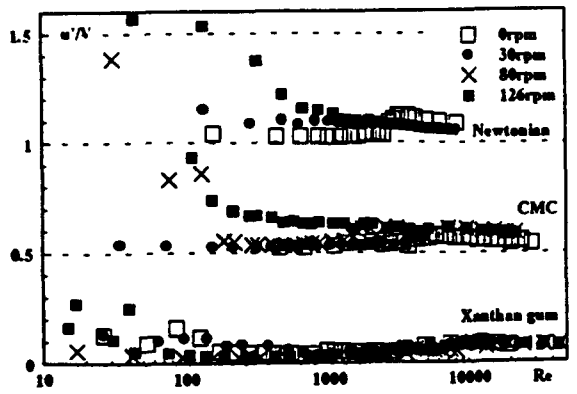

Figure 3. Velocity fluctuations vs Re for Newtonian fluid, CMC and Xanthan gum (note shifted origins)

Only in the absence of rotation for the glucose/water mixture is there a clear transition from laminar to turbulent flow. The increase in friction factor at the highest rotation speed is also most marked for this fluid whereas for, the shear-thinning liquids, the global effect of rotation is marginal and in the turbulent-flow regime **Figure 2** shows that the degree of drag reduction for the two polymers is essentially unaffected by rotation. From **Figure 3** it is seen that for each fluid there is an increase in the intensity of the velocity fluctuations in the laminar regime as the rotation speed is increased.

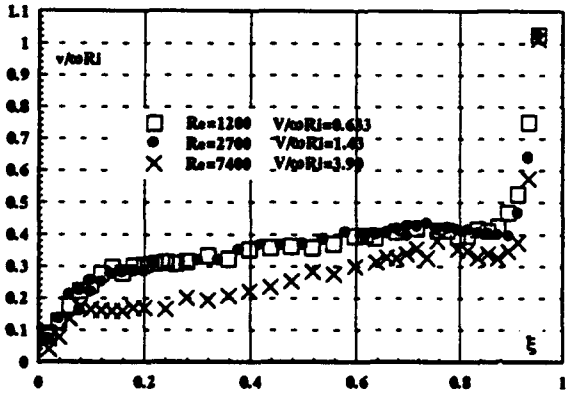

Figure 4. Tangential velocity profiles for Newtonian fluid.

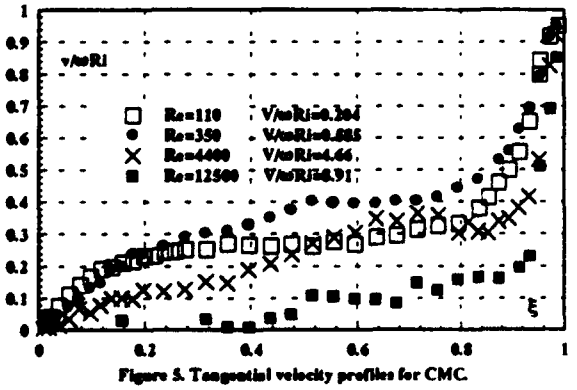

Figure 5. Tangential velocity profiles for CMC.

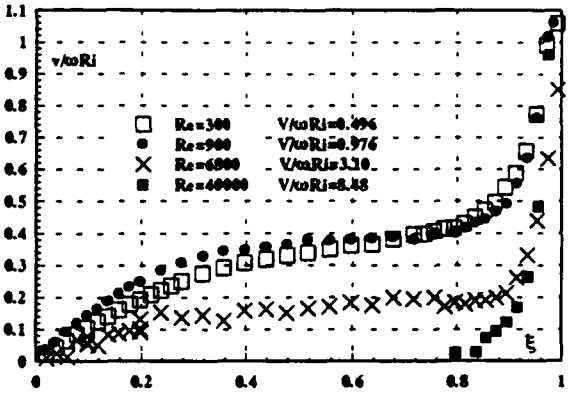

Figure 6. Tangential velocity profiles for Xanthan gum.

All subsequent figures refer to data for the highest rotation speed (126 rpm) as the bulk Reynolds number is varied.

In contrast to the negligible influence on the f-Re data, rotation has a dramatic influence on the flow structure, as revealed by the LDA measurements of axial and tangential mean velocities and velocity fluctuations. In all cases, the tangential velocities (**Figures 4-6**) reveal a triple-layer structure. Nouri and Whitelaw (1993) report very similar observations for their measurements for a Newtonian fluid and for CMC in the turbulent-flow regime. Limited measurements showing the triple-layer structure for turbulent airflow in a narrow annulus were also reported by Simmers and Coney (1979). Perhaps surprisingly, the theoretical work of Bittleston and Hassager (1992) revealed that laminar flow of a Bingham plastic in an annulus also exhibits a triple-layer structure. Over much of the central region of the annulus, the tangential velocity is almost constant at a level which diminishes with increasing Reynolds number. At the highest Reynolds numbers, penetration of the influence of rotation is increasingly limited to an inner layer and for Xanthan gum the tangential velocity at Re = 40,000 was too small to measure for $\xi < 0.8$. Close to the centrebody, the velocity increases across the inner layer to match the peripheral speed. As is typical of shear flows generally, this inner layer thickness decreases with increasing Reynolds number. It is also seen that the inner-layer thickness for the two shear-thinning fluids is roughly double that for the glucose/water mixture. Although the outer layer is of comparable thickness to the inner layer in each case, the gradients are less steep because the maximum velocity in the central layer is approximately 0.4 ωR_i.

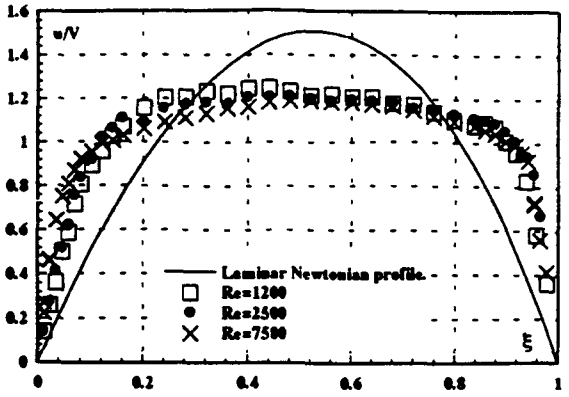

Figure 7. Axial velocity profiles for Newtonian fluid.

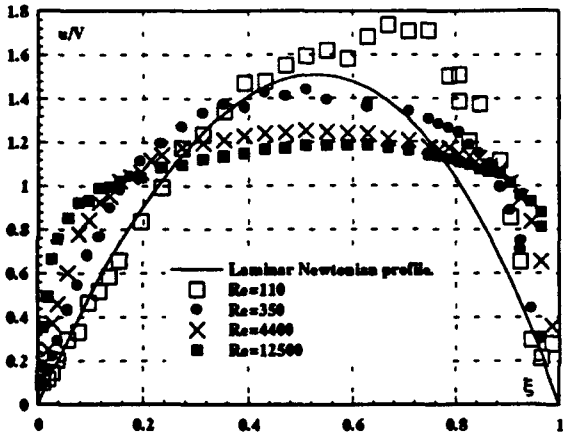

Figure 8. Axial velocity profiles for CMC.

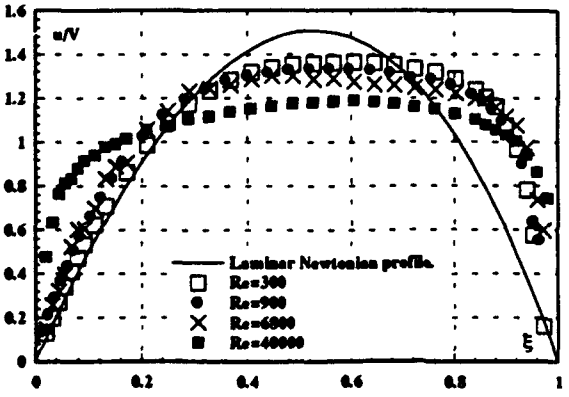

Figure 9. Axial velocity profiles for Xanthan gum.

With the exception of the aqueous solution of CMC at Re = 110, the axial velocity distributions (**Figures 7-9**) are little different from what would be expected in the absence of rotation: i.e. a progressive flattening of the profile with increasing Reynolds number. The apparently spurious behaviour for CMC at the lowest Reynolds number is a consequence of averaging the axial velocities associated with the interior circulation of Taylor vortices which are transported axially by the bulk flow.

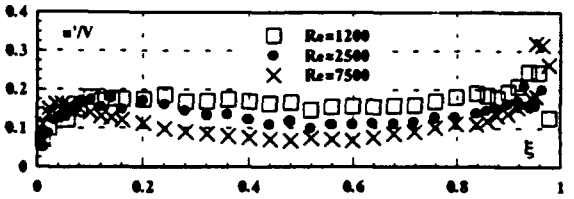

Figure 10. Axial velocity fluctuations for Newtonian fluid.

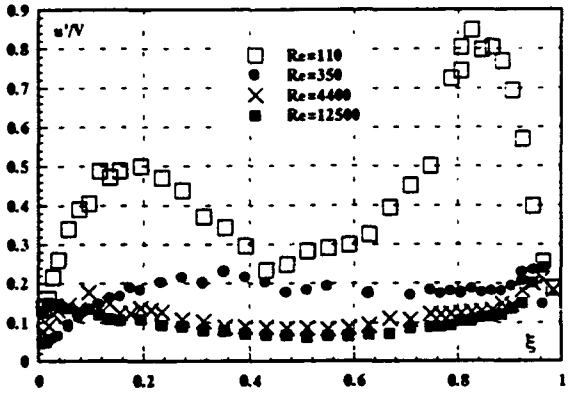

Figure 11. Axial velocity fluctuations for CMC.

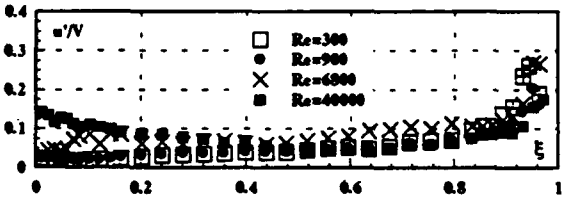

Figure 12. Axial velocity fluctuations for Xanthan gum.

Even clearer evidence for the presence of Taylor vortices for the low Reynolds number CMC flow is seen in the axial velocity fluctuations (**Figure 11**). Two peaks close to ξ = 0.2 and 0.8 again represent the time-averaged effect of the internal recirculating motion of the Taylor vortices as they are transported axially. With the added exception of the highest Reynolds number (40,000) for Xanthan gum, (**Figure 12**) in all other cases the axial velocity fluctuations show a progressive decrease with increasing Reynolds number. This too is ascribed to the very complex but well defined structures which are generated by the centrebody rotation at the lower Reynolds numbers. For Xanthan gum with Re = 40,000, the situation is representative of a fully turbulent flow for which the centrebody rotation has little influence outside a thin inner layer, as was already evident from the corresponding tangential velocity profile in **Figure 6**.

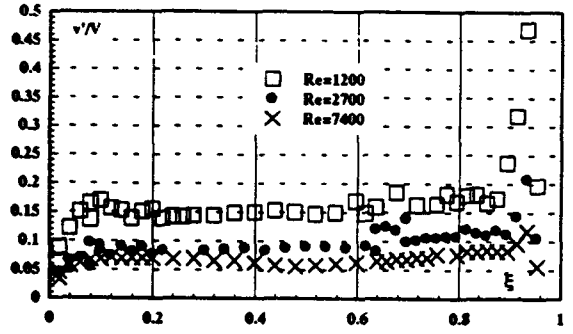

Figure 13. Tangential velocity fluctuations for Newtonian fluid.

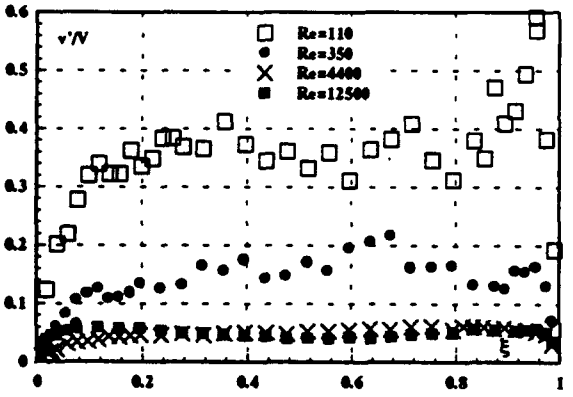

Figure 14. Tangential velocity fluctuations for CMC.

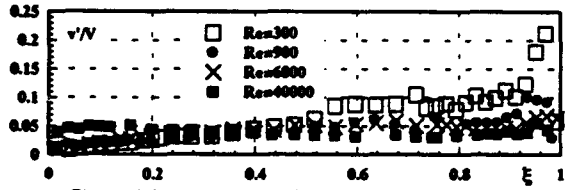

Figure 15. Tangential velocity fluctuations for Xanthan gum.

Figures (13-15) refer to the tangential velocity fluctuations. It is well established that for turbulent flow of polymeric fluids (such as Xanthan gum and CMC), drag reduction under turbulent pipe-flow conditions is invariably accompanied by suppressed levels of tangential turbulent velocity fluctuations. This behaviour is also evident here, except for the high fluctuation levels at the lower Reynolds numbers associated with complex vortical structures induced by the centrebody rotation. As already seen, the radial penetration of the rotational influence for the higher Reynolds numbers is much reduced and turbulent fluctuations are again suppressed.

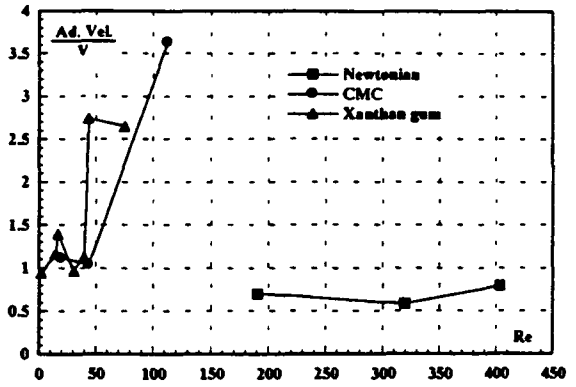

Figure 16. Advection velocities for Newtonian fluid, CMC and Xanthan gum.

Limited investigations into the structural flow changes at low but increasing bulk velocity were carried out using two identical LDA probes with the probe volumes a set distance apart (10 mm). Physical limitations meant that the probes had to be placed at 90° to each other ie. vertical and horizontal. The velocity-time signals generated by the two probes were correlated against each other to give a time spacing between the flow passing each probe and hence an advection velocity for the cell structure. **Figure 16** shows the change with Reynolds number in the advection velocity normalised with the bulk flow velocity. The normalised advection speed is seen to increase from a value of about unity to values above 2.5 for both CMC and Xanthan gum, indicating a change from a toroidal to a spiral structure. However, it would require three simultaneous measurements to determine advection speed, cell size and spiral pitch and this was not possible. The value of unity at the lower Reynolds number is consistent with the visual estimates of Synder (1962) which gave an average value for a Newtonian fluid of 1.2 at Reynolds numbers less than 16. For the Newtonian fluid the signals at higher Reynolds numbers than those shown did not reveal a periodic structure which could be used to determine advection speed.

5. CONCLUSIONS

The combination of an imposed bulk flow through an annulus, centrebody rotation and the influence of non-Newtonian fluid rheology produces a range of complex flow behaviour. Little can be learned from global measurements (frictional pressure drop versus flow rate) alone since the influence of rotation is generally small for all flow conditions. However from detailed measurements of the axial and tangential velocity components, both mean and fluctuating, it is possible to identify specific flow characteristics, including axially translating Taylor vortices, a triple-layer mean flow structure and suppression of tangential turbulence fluctuations for high Reynolds number turbulent flow of the non-Newtonian fluids.

NOMENCLATURE

f	friction factor $2\tau_s/\rho V^2$
n	power-law exponent
$\dot{Q}$	volumetric flow rate (m^3/s)
r	radial location in annulus (m)
Re	bulk flow Reynolds number $2\rho V(R_o - R_i)/\mu$
R_i	outer radius of centrebody (m)
R_o	inner radius of outer wall of annulus (m)
u	mean axial velocity component (m/s)
u'	rms value of fluctuating axial velocity (m/s)
v	mean tangential velocity component (m/s)
v'	rms value of fluctuating tangential velocity component (m/s)
V	bulk axial velocity $\dot{Q}/\pi(R^2_o - R^2_i)$ (m/s)
λ_c	constant in Cross model (s)
λ_n	constant in power-law model (s)
λ_s	constant in Sisko model (s)
$\dot{\gamma}$	shear rate (1/s)
μ	characteristic fluid viscosity (Pa.s)
μ_o	zero shear-rate viscosity
μ_{ref}	reference viscosity (1 Pa.s)
μ_∞	infinite shear-rate viscosity (Pa.s)
ξ	non-dimensional radial location $(R_o - r)/(R_o - R_i)$
ρ	fluid density (kg/m^3)
τ_s	average surface shear stress (Pa)
ω	centrebody rotation speed (rad/s)

REFERENCES

Bittleston, S.H. and Hassager, O. 1992. Flow of viscoplastic fluids in a rotating concentric annulus. J. Non-Newtonian Fluid Mech. Vol 42. pp 19-36.

Lockett, T.J. Numerical simulation of inelastic non-Newtonian fluid flows in annuli. PhD Thesis. Imperial College of Science, Technology and Medicine. August 1992.

Lockett, T.J., Richardson, S.M. and Worraker, W.J. 1992. The stability of inelastic non-Newtonian fluids in Couette flow between concentric cylinders: a finite-element study. J. Non-Newtonian Fluid Mech. Vol 43. pp 165-177.

Jones, O.C. and Leung, J.M.C. 1981. An improvement in the calculation of turbulent friction in smooth concentric annuli. Trans. ASME. J. Fluids Eng. Vol 103, (1981), pp 615-623.

Malik, R. and Shenoy, U.V. 1991. Generalised annular Couette flow of a power-law fluid. Ind. Eng. Chem. Res. Vol 30. pp 1950-1954.

Nouri, J.M. and Whitelaw, J.H. 1993. Flow of Newtonian and non-Newtonian fluids in a concentric annulus with rotation of the inner cylinder. Imperial College, Dept of Mech Eng, TF/93/1.

Simmers, D.A. and Coney, J.E.R. 1979. The experimental determination of velocity distribution in annular flow. Int. J. Heat and Fluid Flow. Vol 1, No 4, pp 177-184.

Synder, H.A. 1962. Experiments on the stability of spiral flow at low axial Reynolds numbers. Proc. Roy. Soc. A Vol 265, pp 198-214.

Wroński, S. and Jastrzębski, M. 1990 a. Experimental investigations of the stability limit of the helical flow of pseudoplastic liquids. Rheologica Acta. Vol 29. pp 453-461.

Wroński, S. and Jastrzębski, M. 1990 b. Mass transfer in the spiral flow of a pseudoplastic liquid. Int. J. Ht. and Mass Transfer. Vol 33, No (1). pp 1-7.

Session 5.
Manufacturers' Technical Presentation

MANUFACTURER'S TECHNICAL PRESENTATION

SESSION 5

Monday, March 11th, 1994 (14:30 - 15:50)

Company	Title	Speaker
AEA	To be Announced	To be Announced
AEROMETRICS	To be Announced	To be Announced
DANTEC MT A/S	To be Announced	Kristian Askegaard
DANTEC/INTEC	To be Announced	To be Announced
LSTM	Ultrasonic Standing Wave Particle Positioner for scattering experiments and PDA-Alignment	Prof. F. Durst
POLYTEC GmbH	New Developments in the Laser Velocimeter Using Laser Diodes	Dr. Helmut Selbach
TSI	Innovative Technology Implementations for Velocity and Size Measurements	Dr. Rajan Menon
OXFORD LASERS	To be Announced	To be Announced
OPTIMAGE	To be Announced	To be Announced
OPTICAL FLOW SYSTEMS	To be Announced	To be Announced
JENOPTIC TECHNOLOGY	To be Announced	To be Announced

Session 6.
Combustion II

MIXING CHARACTERIZATION IN SEMI-INDUSTRIAL NATURAL GAS FLAMES USING PLANAR MIE-SCATTERING VISUALIZATION

Jacques Dugué, Aristide Mbiock and Roman Weber

International Flame Research Foundation
IJmuiden, The Netherlands

ABSTRACT

The present work is concerned with the application of planar Mie scattering visualization for the characterization of mixing in semi-industrial natural gas flames. Time-averaged conserved scalar data are derived from the analysis of large sequences of instantaneous planar Mie scattering images. The assumptions of fast and irreversible chemistry (mixing controlled by turbulent diffusion) and a unit Lewis number allow the derivation of a monotonic relation between the number density of inert seeding particles in the natural gas jet and a conserved scalar. Ensembles of instantaneous conserved scalar images are processed to extract time-averaged parameters which include the mean and fluctuating scalar field, the intermittency and unmixedness factors, the scalar dissipation field and spatial correlations.

1. INTRODUCTION

The Mie scattering technique has been extensively applied to derive scalar data and to characterize mixing in small scale isothermal and combusting flows since the early sixties (Becker et al (1963), Ebrahimi and Kleine (1977), Kennedy and Kent (1978), and Mansour et al (1988)). The technique provides concentration data when one of the fluids entering a mixing region is seeded with small marker particles. The light scattered by the marker particles crossing a light beam is ideally proportional to the local particle number density. The Mie scattering technique is usually implemented for single-point measurement using a focused laser beam and a photodetector for the collection of the laser light scattered from the measurement volume. Over the last decade, advances in laser, camera and computer technology have enabled the implementation of Mie scattering for planar measurements in combusting flows using sheet illumination and line or rectangular array detectors.

In the present study, planar Mie scattering visualization has been further demonstrated for application in industrial-scale cold flows and gas flames over flow areas as large as one square meter. The natural gas stream is seeded with micron-size zirconium oxide particles. Images of the instantaneous particle concentration field are recorded with a black and white CCD camera synchronized to the pulses of a Nd:YAG laser. The camera gating time of 1 μs is short enough to suppress the flame radiation of even the most luminous flames and allows the recording of scattered laser light alone. The signal spatial resolution is determined by the laser sheet thickness and the camera magnification; it is typically of the order of 1 mm^3. Computer analysis of large ensembles of instantaneous images allows the extraction of many time-averaged parameters. They include the mean and fluctuating conserved scalar field, the average scalar dissipation field, the unmixedness and intermittency factors, and the scalar spatial correlations. The objectives of this paper are to present the implementation of the technique for conserved scalar measurements in large scale natural gas flames and to discuss its inaccuracies and limitations. Results of an application in a 3 MW natural gas flame are presented.

2. MEASUREMENT PRINCIPLE

2.1 The Mie Scattering Technique

The application of the Mie scattering technique to concentration measurements has been documented in detail by Becker et al (1967 and 1977), Shaughnessy and Morton (1977) and Stepowski (1992) and will only be briefly recalled here. Assuming ideal conditions, the instantaneous light-scatter signal I is proportional to the number of scattering particles in the control volume. It is easy to show that the signal I is also related to the conserved scalar Z based on the mass fraction of seeded nozzle fluid according to:

$$I \propto \rho Z$$

The conserved scalar Z is also strictly equivalent to the mixture fraction. It takes the value of one for pure nozzle fluid and zero for pure external fluid. Normalizing the signal so that I equals one in the potential core of the nozzle fluid outlet ($Z = 1$), we obtain:

$$I / I_o = \rho Z / \rho_o$$

This relation implies the validity of a number of assumptions:

- there is no multiple scattering and no optical attenuation
- the particle concentration is low enough not to alter the properties of the seeded fluid
- the marker particles have a monosize distribution, or at least a size distribution that does not vary in space
- the scattering cross section of the marker particles remains constant in the temperature range covered
- the seeding concentration at the nozzle outlet is constant
- the light sheet intensity does not vary over time and space
- the molecular diffusivity coefficients of fuel and air are equal
- the molecular and thermal diffusivities are equal (Lewis number =1)
- the tracer particles are free of inertial effects (no particle slip) and faithfully follow the mixing and diffusion of the nozzle fluid molecules .

Proper experimental care must be applied to ensure that deviations from these assumptions do not cause excessive measurement inaccuracies. The effect of light absorption, which is not insignificant in large scale flows, can be quantified and corrected in the image calibration procedure. The non-uniform light sheet intensity also needs to be accounted for when using a diverging light sheet to illuminate a large flow cross section.

2.2 Molecular Diffusion Effects

A crucial assumption necessary to derive the fuel mixture fraction from the Mie scattering signal is that marker particles mix and diffuse like fuel molecules. According to the data of Becker (1977), the diffusivity of 1 μm particles in air at 300 K is 2.7 x 10^{-7} cm^2/s. This value is to be compared with the molecular diffusivity coefficients of air and methane in air which, at ambient temperature, are 0.21 and 0.23 cm^2/s, respectively. At 1000°C, they increase to 2.0 and 2.3 cm^2/s, which are many orders of magnitude higher than the particle effective diffusivity. Thus, in flows where molecular diffusion accounts for a significant part of the mixing process, planar Mie scattering visualization of a seeded flow leads to an overestimation of the gradients in the mixture fraction field. The significance of molecular diffusion at the flame scale reported here has been assessed using the approach of Stårner and Bilger (1983). The turbulent Reynolds number in the natural gas jet self-similar region, calculated from the measured RMS fluctuating velocity and outer scale jet width, has a value of 6200. This results in a turbulent diffusivity of 1120 cm^2/s, which is at least two orders of magnitude higher than the molecular diffusivities of air or natural gas at flame temperatures. Therefore, in large scale flows where mixing is controlled by turbulence, the inaccuracies induced by molecular diffusivities and particle effective diffusivity are negligible.

2.3 Fast Chemistry Limit

In combustion systems involving mixing of a seeded fuel stream with an oxidant stream, the instantaneous Mie scattering signal is proportional to the product of the conserved scalar and the density. Thus, calculation of the conserved scalar requires the simultaneous measurement of the instantaneous particle number density and the flow temperature. As shown by Kennedy and Kent (1978), Bilger (1989) and Stepowski (1992), a simplification to this requirement is often introduced when combustion can be described using the fast chemistry approach. The assumptions implied are infinitely fast and irreversible chemical reactions (at least for the major species), equal diffusivities of the fuel and oxidant, unit Lewis number and adiabatic equilibrium. These assumptions are usually valid in large scale flames (high Reynolds and Damköhler numbers) where mixing is controlled by turbulent diffusion. The instantaneous relationships relating the temperature and the calibrated Mie scattering signal to the mixture fraction are shown in Figure 1. The function relating the calibrated signal to the conserved scalar depends on the air and natural gas inlet temperatures (F=0 and F=1), the adiabatic flame temperature, and the mixture fraction at stoichiometry (F_{st}).

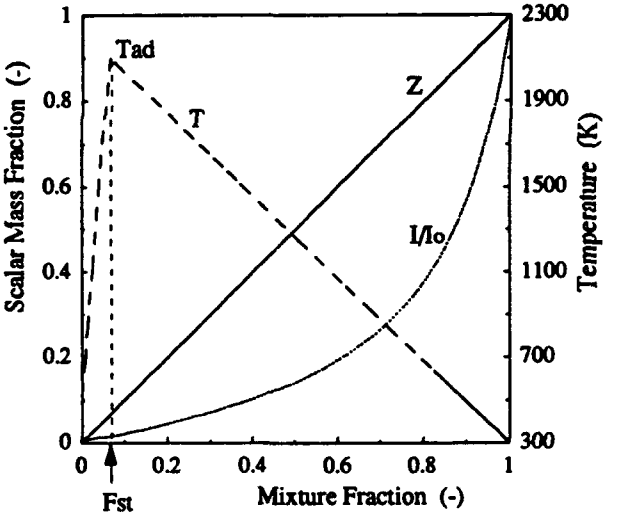

Fig. 1 Instantaneous relations for infinitely fast and irreversible reactions

3. EXPERIMENTAL

3.1 Furnace Configuration and Optical Setup

The experiments were carried out in a 6 x 2x 2 m furnace equipped with a 4 MW natural gas burner (Bertolo et al (1993)). A NOx reduction technique was implemented by splitting the natural gas input between a primary injector located at the center of the burner quarl and eight secondary axial injectors located at the quarl periphery. Flame stability

was provided by a large primary injector blockage ratio (BR=0.65) and a medium combustion air inlet swirl level (So=0.57). The experiments reported here were performed at a thermal input of 3 MW with 80% of the total natural gas flow injected through the secondary jets. This staging ratio corresponded to the maximum NOx reduction achievable without loss of flame stability. Based on these inputs and a nozzle diameter d_o of 9 mm, the jet outlet velocity U_o was 175 m/s and the resulting Reynolds number was 103,000.

The laser sheet was produced by expanding the beam of a pulsed Nd:YAG laser through a cylindrical lens. The laser produced 25 pulses per second at a wavelength of 532 nm and with an energy of 190 mJ per pulse. As shown in Figure 2, the laser sheet was introduced under the furnace outlet and its plane crossed the burner and the top and bottom jet axes. Collimation of the beam waist was achieved with two spherical lenses (f_1 = -150 mm, f_2 = 400 mm) located in front of the laser at 14 m from the burner wall. The light sheet was produced with a cylindrical lens (f_3 = -25.4 mm) located in front of the furnace back wall, at 6.5 m from the burner wall. The measured laser sheet thickness was 1.2 mm and was verified to be constant over the imaged area. The natural gas jets were seeded with sub-micron zirconium oxide particles using a cyclone design identical in principle to the one described by Glass and Kennedy (1977). The particles were classified in a size range of 0.3 to 2.0 μm. The Mie scattering intensity was collected with a black and white, fixed gain, non-interlaced image-intensified CCD camera which was gated at 1 μs. The CCD camera was externally triggered by the laser pulses. The short gating time enabled blocking of the flame radiation and recording of scattered laser light alone. The camera optics were equipped with a 40 nm bandwidth filter for suppressing the infra-red radiation incident onto the image intensifier and the CCD sensor. The standard video signal was fed to a S-VHS video recorder and was later digitized by a frame grabber over an array of 768 by 512 pixels. The 16 MB store board coupled to the grabber board enabled the acquisition of series of 32 consecutive images. The image processing analysis was performed over an ensemble of 350 images.

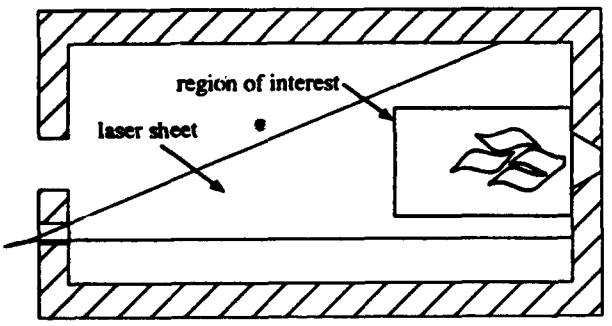

Fig. 2 Laser sheet setup in furnace

3.2 Experimental Resolution

The spatial resolution of the measurements depends on the size of the laser sheet volume imaged per pixel. The imaging region covered a field of view of 450 x 300 mm which was digitized over a detector array of 768 x 512 pixels. The measured laser sheet thickness was 1.2 mm. Thus, the measurement volume size per pixel was 0.586 x 0.586 x 1.2 mm^3. Since the Nyquist sampling theorem states that the maximum detectable spatial frequency is half the sampling frequency, the size of the smallest resolvable structure is two pixels large, or 1.2 mm. If a high spatial resolution is preferred over a large field of view, a smaller measurement volume can be achieved by using a higher optical magnification and smaller laser sheet thickness. Ultimately, the maximum spatial resolution is determined by the need to have a sufficient number of particles in the measurement volume not to invalidate the assumption of marker continuum. This practical limit is usually close to the smallest scale of turbulence. The measurement spatial resolution should be compared to the smallest length scale of gradients in the conserved scalar field. Recent measurements by Buch and Dahm, (1991) and Southerland and Dahm (1994) report that the scalar diffusion scale thickness is given by $\lambda_D \approx 11.2\ \delta\ Re_\delta^{-3/4}\ Sc^{-1/2}$ where δ is the local lateral scale of the jet and $Re_\delta = u\ \delta / \nu_\infty$ is the outer scale Reynolds number. Dimensional reasoning indicates that in the far field of a round jet, the outer scale Reynolds number is constant (Dahm and Dimotakis (1990)). Since the jet lateral dimension scales as $\delta \approx 0.44$ x and this flow has a Schmidt number near unity, the scalar diffusion scale thickness increases as $\lambda_D \approx 4.93\ x\ Re_\delta^{-3/4}$. The axial distance x is measured from the nozzle outlet. For the present experiments, the Reynolds number Re_δ was calculated at x = 150 mm (17 d_o) using the laser visualization and velocimetry measurements. With a centerline mean velocity of 52 m/s and a full local jet width of 62 mm, the outer scale Reynolds number is 17900. Thus, the scalar diffusion scale thickness varies from 0.32 mm for x = 100 mm to 1.3 mm for x = 400 mm. This indicates that the measurement spatial resolution is not small enough to resolve the smallest gradient scales in the scalar field except at distances larger than 40 nozzle diameters (x=360 mm).

3.3 Data Reduction

The procedure used to extract instantaneous conserved scalar data from the raw Mie-scattering images can be outlined as outlined below. First, the images are rescaled so that the maximum signal intensity measured in the jet potential core corresponds to 100% and the minimum signal intensity corresponds to 0. The zero Mie-scattering signal is defined as the mode of the image histogram in the background region. Second, the images are corrected for non-uniform light sheet illumination and for light absorption. This correction is

performed using a reference image computed from the laser sheet intensity profiles in the axial and radial direction and an average extinction coefficient. These coefficients were determined experimentally by averaging the images obtained with homogeneous seeding and no flow in the furnace. They agreed well with values calculated theoretically from the laser sheet geometry and the estimated particle size and concentration in the furnace. Performing these two image calibration steps provides calibrated, normalized particle number density images which range from 100% in the natural gas jet potential core to 0 in the combustion air stream. The third step consists in applying the fast chemistry limit relations previously described to extract the instantaneous temperature and conserved scalar fields. These relations require as inputs the natural gas and combustion air inlet temperatures, the adiabatic flame temperature, and the stoichiometric mixture fraction. Because this procedure yields the instantaneous normalized particle number density, the conserved scalar and temperature fields, averaging can be performed using the Reynolds or Favre definition. The various mean parameters derived from the instantaneous conserved scalar images are presented in the results section.

3.4 Error Analysis

The measurement random and bias errors in the Mie scattering signal have been estimated by recording the laser sheet in a uniformly seeded volume in the absence of any convection. The random error at a fixed pixel position, measured by calculating the rms noise level of the image sequence, was found to be 1.8% of the maximum dynamic range. This random error is the result of fluctuations in the seeding density, and electronic noise in the CCD camera and frame grabber. The random error of a time-averaged parameter decreases with the square root of the number of samples. Thus, for a sequence of 350 images, the random noise level on the calibrated particle number density is of the order of 0.1% of the full scale. The total error of the mean particle number density was estimated by averaging a sequence of images corrected for non-uniform illumination and light absorption. The total error, measured by taking the rms of the mean image histogram, was found to be 5% of the maximum dynamic range. The systematic errors which are caused by optical attenuation, non-uniform light illumination and non-linear camera response provide the largest contribution to the mean number density error. Because image averaging does not reduce the bias errors, the bias errors on the instantaneous images are also about 5%. Figure 3 shows how a 5% error on the particle number density propagates in the calculations of the temperature and conserved scalar. It shows that the absolute inaccuracy on the conserved scalar and temperature is inversely proportional to the number density. It reaches 0.03 and 0.23 for normalized number densities of 0.4 and 0.05, respectively.

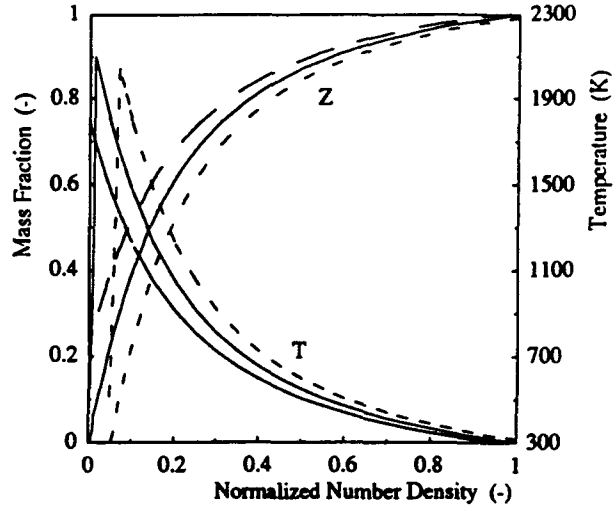

Fig. 3 Absolute inaccuracies on the mean conserved scalar and temperature for ±5% error on the raw signal (—— : +5%, - - - : -5%, —— : true signal)

4. RESULTS

Figure 4 displays a Mie-scattering image taken from the ensemble of images analyzed. Because the laser pulse is only 7 ns long, these images reveal the instantaneous distribution of the marker particles over the laser sheet. The field of view of 450 x 300 mm covers one of the eight jets located at the quarl periphery and extends up to 38 nozzle diameters in the axial direction. No obvious artifact can be detected in the Mie-scattering images other than the light sheet reflection on the burner front wall. The background of the images is uniform in the whole region of interest which includes the near burner zone and excludes the front wall reflections (right side of the nozzle on Figure 4). Furthermore, it was verified that with the laser shutter closed, the images were uniformly dark and showed no residual flame emission.

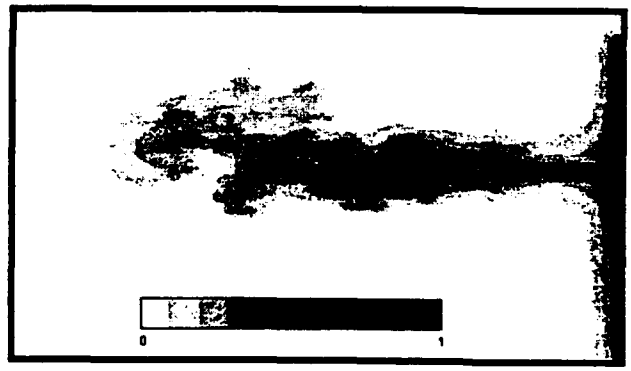

Fig. 4 Mie scattering visualization of the instantaneous particle distribution in a natural gas jet

Figures 5 and 6 display the mean and rms scalar image fields obtained from a sequence of 350 images following the data reduction procedure described above. The jet asymmetry can be attributed to its interaction with the external recirculation zone which enhances the jet radial expansion towards the furnace walls. As expected, the RMS scalar field displays zero fluctuations in the jet potential core and maximum fluctuations in the mixing layer.

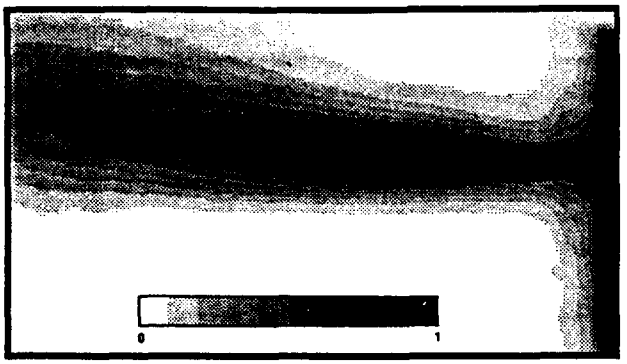

Fig. 5 mean conserved scalar field

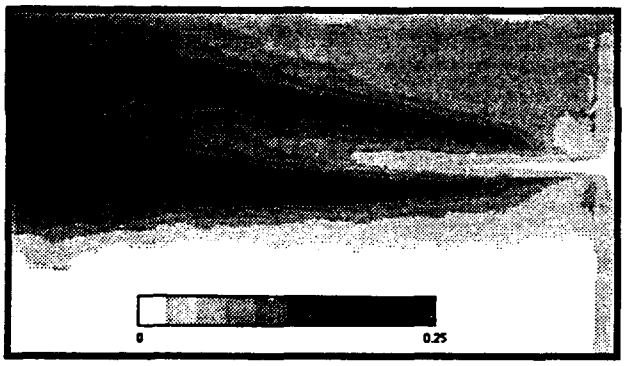

Fig. 6 RMS fluctuations in conserved scalar field

Self-similarity of the conserved scalar field was assessed by normalizing the radial conserved scalar profiles with the maximum value of the scalar on the radial profile. Figure 7 displays the normalized scalar field. The 50% normalized mean scalar lines can be used to define the jet half width, and in the selfsimilar region, the angle of spread of the jet and the rate of entrainment.

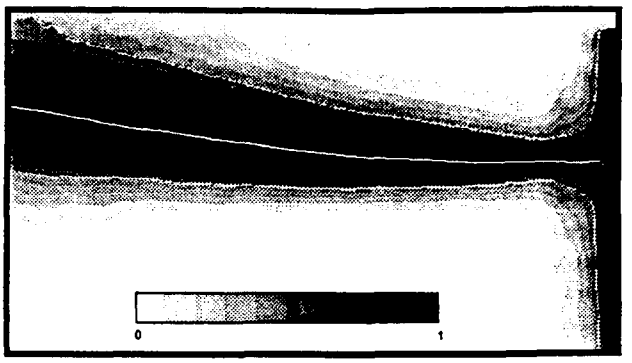

Fig. 7 Normalized mean scalar field

Figure 8 shows plots of the normalized mean scalar profiles for seven traverses from the nozzle outlet (x/d_O= 4, 10, 15, 20, 25, 30, and 36). The radial position is normalized by the distance from the nozzle outlet to the traverse. In order to compare the experimental results with data from the literature, the solid line corresponding to the curve fit $\bar{Z}/\bar{Z}_o = \exp\left(-54(r/x)^2\right)$ is also shown. For the side of the jet expanding towards the centerline (positive radii on Figure 8), self-similarity is reached after an axial distance of 20 nozzle diameter from the nozzle outlet. The very good agreement observed between the self-similar profiles and the experimental curve fit is encouraging and seems to indicate a satisfactory accuracy of the Mie scattering technique, at least for the mean conserved scalar results.

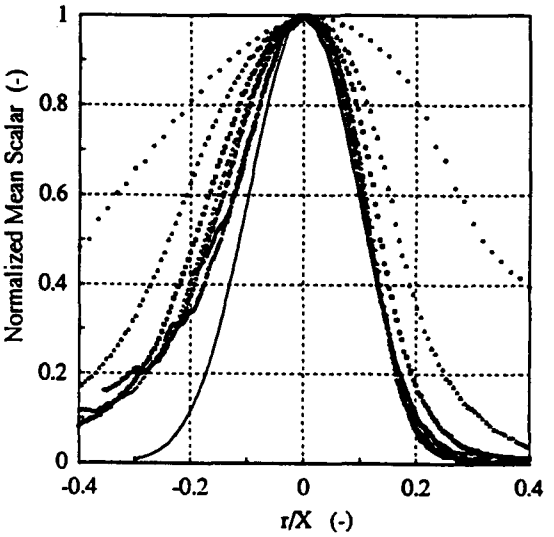

Fig. 8 Normalized radial profile of mean scalar

The intermittency factor is defined as the probability that the scalar concentration is greater than zero. In the presence of noise, the intermittency is simply equal to the fraction of time the scalar concentration is above the noise level (Chigier, (1981)). The intermittency factor provides insight into the process of entrainment by indicating the location and extent to which ambient fluid penetrates into the mixing layer. An intermittency factor of 0.5 can be used to define the jet turbulent boundary, and it also coincides with the region where the difference between Reynolds and Favre averages is largest. Because the entrainment process is accomplished mostly through large eddies, the determination of the intermittency field does not require a spatial resolution of the same order as the smallest scales of turbulence.

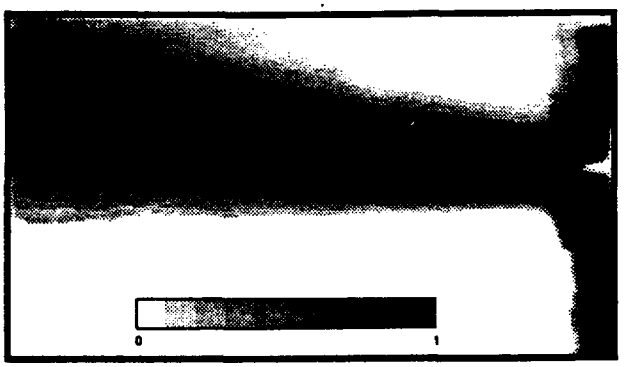

Fig. 9 Intermittency

The unmixedness factor was calculated using the definition of Chigier (1981):

$$UM = \frac{\int_{T_1}\left(Z-\bar{Z}_f\right)dt_1+\int_{T_2}\left(\bar{Z}_f-Z\right)dt_2}{\left(1-\bar{Z}_f\right)T_1+\bar{Z}_f T_2}$$

The mean scalar $\bar{Z}_f$ corresponds to the far field concentration which is reached after complete mixing between the fuel and the combustion air. It is calculated from the burner inputs and the fuel air requirements; it corresponds to the mixture fraction reached in the flue gas and is taken here as 0.055. The time intervals T_1 and T_2 correspond to the conditions $Z > \bar{Z}_f$ and $Z < \bar{Z}_f$, respectively. The unmixedness describes the extent of mixing between the seeded stream (natural gas) and the non-seeded stream (combustion air). When natural gas and combustion air are completely mixed, there is no fluctuation of concentration and the unmixedness is zero. The flow is completely unmixed (unmixedness is one) when the concentration fluctuates between zero (pure air) and one (pure fuel). It is clear that the unmixedness is zero when the flow is completely mixed at the scale corresponding to the experimental spatial resolution. The extent of mixing at the molecular level cannot be measured when collecting a signal from marker particles. However, as discussed earlier, the contribution of molecular mixing in large scale flames is very small when compared to turbulent diffusivitiy.

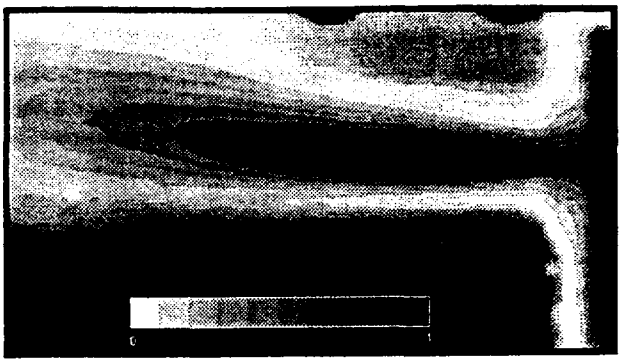

Fig. 10 Unmixedness

The instantaneous scalar dissipation rate is expressed in cartesian coordinates as:

$$\chi = 2D\cdot\left(\left(\frac{\partial Z}{\partial x}\right)^2+\left(\frac{\partial Z}{\partial y}\right)^2+\left(\frac{\partial Z}{\partial z}\right)^2\right)$$

where D is the molecular diffusivity of methane in air and was taken as 0.2 cm^2/s. The instantaneous scalar dissipation rate is in units of s^{-1}. In this work, the third component is not accessible and the dissipation rate was calculated using only the first two dimensional gradients of the conserved scalar. It must be noted that accurate, quantitative measurements of the scalar spatial gradients require the experimental resolution to be close to the scalar diffusion scale. Since this was not the case in these experiments, the scalar dissipation results are underestimated. The mean dissipation rates shown in Figure 11 are qualitatively consistent with the results reported by Namazian et al (1988) and Feikema and Driscoll (1992). The scalar dissipation reaches high values in the mixing layer of the natural gas jet close to the nozzle, at the interface between the natural gas and the ambient fluid. At higher axial locations, the dissipation levels decay and the maximum values of the radial profiles gradually move closer to the jet axis. The local scalar dissipation rate is an important parameter because it describes the local mixing intensity and shows where the mixing energy is spent. This information helps verify and optimize the burner mixing characteristics. In the present application, the maximum levels of scalar dissipation are encountered in a region of low oxygen concentration which corresponds to flue gas entrained from the external recirculation zone into the natural gas jets. The initial mixing of natural gas with flue gas delays mixing between natural gas and air and results in low peak flame temperatures and low NO_x emissions.

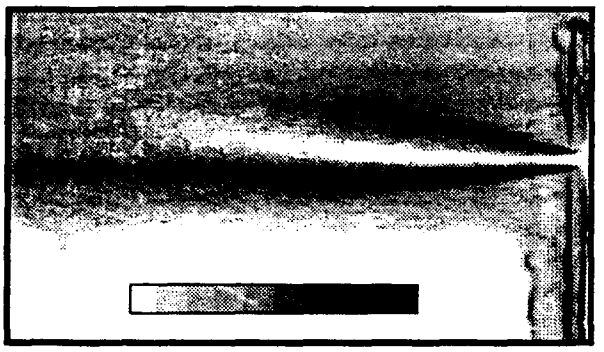

Fig. 11 Log of the mean scalar dissipation field

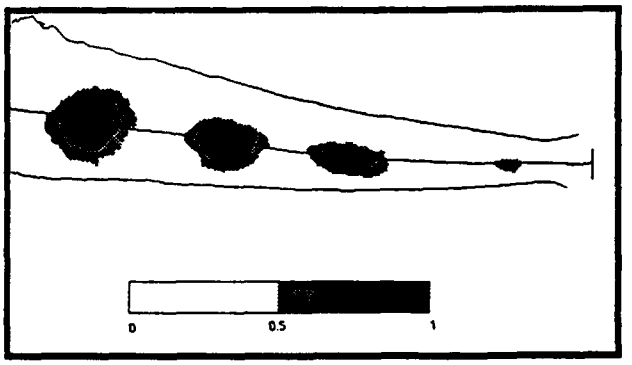

Fig. 12 Scalar spatial correlations at selected locations

The spatial correlation of the scalar field was calculated at selected locations in the flow and is displayed in Figure 12. The spatial correlations show the length scales over which the scalar fluctuations are correlated. The spatial correlations at the spatial distances δx, δy from the fixed locations (x_O,y_O) are the intercorrelation coefficients between the points $Z(x_O,y_O)$ and $Z(x_O+\delta x,y_O+\delta y)$. They are given by:

$$Cor(x_o,\delta x,y_o,\delta y)=\frac{Cov\left(Z(x_o,y_o),Z(x_o+\delta x,y_o+\delta y)\right)}{\left(Var\left(Z(x_o,y_o)\right)\cdot Var\left(Z(x_o+\delta x,y_o+\delta y)\right)\right)^{0.5}}$$

The covariance between $Z(x_O,y_O)$ and $Z(x_O+\delta x,y_O+\delta y)$ is defined by:

$$Cov\left(Z,Z^{\delta}\right)=\overline{Z(x_O,y_O)\cdot Z(x_O+\delta x,y_O+\delta y)}$$

The variance $Var\left(Z(x_o,y_o)\right)$ is simply the square of the RMS fluctuations of Z at the positions (x_O,y_O). As pointed by Schefer et al (1988), the 0.5 contour line provides a close approximation of the integral length scale of turbulence. Because the spatial correlation characterizes the turbulence macroscale, its accurate determination does not require a spatial resolution as high as for the dissipation measurements. It can be further noted from the normalized mean scalar field shown in Figure 7 and the spatial correlations shown in Figure 12 that the radial integral length scale is close to half the jet width. As indicated earlier, the jet width is defined as the distance between radial locations at which the scalar has decreased to half the maximum value.

5. CONCLUSIONS

Experiments in a 3 MW natural gas flame have shown that Planar Mie scattering visualization is a simple and effective tool for mixing characterization in semi-industrial scale flames. The fast and irreversible chemistry approach is well suited to relate the number density of inert seeding particles in a combusting natural gas jet to a conserved scalar. Computer analysis of large ensembles of instantaneous images allowed the extraction of many time-averaged parameters which include the mean and fluctuating conserved scalar field, the average scalar dissipation field, the unmixedness and intermittency factors, and the scalar spatial correlations. Two main limitations in the method presented can be identified. One is the lack of measurement accuracy in the low mixture fraction range which limits the usability of the technique to the fuel rich zone. The second limitation is the difficulty of resolving the smallest scales of turbulence. This is mostly a concern when measuring parameters such as the scalar dissipation which has a diffusion scale close to the Kolmogorov length scale.

Despite these limitations on spatial resolution and absolute accuracy, the planar Mie-scattering visualization technique provides unprecedented insight in the mixing characteristics of large scale natural gas flames. It should prove a valuable tool for assessing and comparing the mixing characteristics of semi-industrial natural gas burners.

ACKNOWLEDGMENTS

The authors gratefully acknowledge the IFRF Members and the Gas Research Institute (GRI) of Chicago for their financial support as part of the Scaling 400 study. The IFRF Joint Committee is acknowledged for permission to publish this paper. Further thanks are due to Henk Horsman for his continuous contributions to this experimental work.

REFERENCES

Becker, H.A., Hottel, H.C. & Williams G.C. 1963, Mixing and flow in ducted turbulent jets. *9th Symp. (Int.) on Combustion*, pp. 7-20.

Becker, H.A., Hottel, H.C. & Williams G.C. 1967, On the light-scatter technique for the study of turbulence and mixing. *Journal of Fluid Mechanics*, vol 30, part 2, pp 259-284.

Becker, H.A. 1977, Mixing, concentration fluctuations, and marker nephelometry. *Studies in Convection.*, vol.2, edited by B.E. Launder

Bertolo, M., Sayre, A., Dugué, J. & Weber, R. 1993, Scaling characteristics of aerodynamics and low-NOx properties of industrial natural gas burners. IFRF Doc No F40/y/12.

Bilger, R.W., 1989, Turbulent diffusion flames. *Annual Rev. Fluid Mechanics*. 21, pp 101-135.

Buch, K.A. & Dahm, W.J.A. 1991, Fine scale structure of conserved scalar mixing in turbulent shear flows: Sc » 1, Sc ≈ 1 and implications for reacting flows. Report No. 026779-5, The University of Michigan.

Chigier, N. 1981, *Energy, Combustion and Environment*, McGraw-Hill, New-York

Dahm, W.J.A. & Dimotakis, P.E. 1990, Mixing at large Schmidt number in the self-similar far field of turbulent jets. *Journal of Fluid Mechanics*, vol. 217, pp. 299-330.

Dowling, D.R. & Dimotakis, P.E. 1988, On mixing and structure of the concentration field of turbulent jets. *Proceedings of the 1st National Fluid Dynamics Congress*, New-York.

Drake, M.C., Bilger, R.W. & Stårner, S.H. 1982, Raman measurements and conserved scalar modelling in turbulent diffusion flames. *19th Symp. (Int.) on Combustion*, pp. 459-467.

Ebrahimi, I. & Kleine, R. 1977, The nozzle fluid concentration field in round turbulent free jets and jet diffusion flames. *16th Symp. (Int.) on Combustion*, pp. 1711-1723.

Feikema, D.A. & Driscoll, J.F. 1992, Scalar dissipation rate measurements in initially on-premixed turbulent shear layers using Rayleigh imaging. *Proc. 6th Int. Symp. on Appl. of Laser Techniques to Fluid Mechanics*, Lisbon.

Friehe, C.A., Van Atta, C.W. & Gibson, C.H. 1971, Jet turbulence: dissipation rate measurements and correlations. AGARD Turbulent Shear Flows, CP-93, pp 18-1 to 18-7.

Glass, M. & Kennedy, I.M. 1977, An improved seeding method for high temperature laser Doppler velocimetry. *Combustion and Flame*, vol 29, pp 333-335.

Kennedy, I.M. & Kent J.H. 1978, Measurements of a conserved scalar in turbulent jet diffusion flames. *17th Symp. (Int.) on Combustion*, pp. 279-287.

Mansour, M.S., Bilger, R.W. & Dibble, R.W. 1988, Raman/Rayleigh and Mie scattering measurements in a reverse flow reactor close to extinction. *22nd Symp. (Int.) on Combustion*, pp. 711-719.

Namazian, M., Schefer, R.W. & Kelly J. 1988, Scalar dissipation measurements in the developing region of a jet. *Combustion and Flame* 74, pp 147-160.

Schefer, R.W., Namazian, M. & Kelly, J. 1988, Structural characteristics of lifted turbulent-jet flames. *22nd Symp. (Int.) on Combustion*, pp. 833-842.

Shaughnessy, E.J. & Morton, J.B. 1977, Laser light-scattering measurements of particle concentration in a turbulent jet. *Journal of Fluid Mechanics*, vol 80, part 1, pp 129-148.

Southerland, K.B. & Dahm, W.J.A. 1994, Four-dimensional laser induced fluorescence study of the structure of molecular mixing in turbulent flows. AIAA 94-0820, January 10-13, Reno

Stårner, S.H. & Bilger, R.W. 1983, Differential diffusion effects on measurements in turbulent diffusion flames by the Mie scattering technique. *Progress in Astronautics and Aeronautics*, New-York.

Stepowski, D. 1992, Laser measurements of scalars in turbulent diffusion flames. *Prog. Energy Comb. Science*, vol 18, pp. 463-491.

APPLICATION OF LASER DIAGNOSTICS TO STUDY FLUID DYNAMIC/COMBUSTION INTERACTIONS

K. C. Schadow, E. J. Gutmark, T. P. Parr, D. M. Hanson-Parr, and K. H. Yu

Research Department, Code C02392
Naval Air Warfare Center Weapons Division,
China Lake, CA 93555-6001

ABSTRACT

Laser diagnostics were utilized to study the development of large-scale structures and their break-down into fine-scale turbulence in nonreacting and reacting shear layers. Of particular interest were shear-flow/combustion interactions to provide the basic understanding for passive and active combustion control. The paper describes accomplishments in three projects which were performed (1) investigation of the three-dimensional interactions between large-scale spanwise vortices and streamwise vortices, (2) control of soot formation by acoustic forcing of air and fuel flow, and (3) identification and control of large-scale structures in supersonic jets.

1. INTRODUCTION

Reacting turbulent jets are governed by the interaction of fluid dynamics, chemical reaction and heat release (Broadwell and Dimotakis, 1986). The fluid dynamics involved in these types of flows are related to a mixing layer flow which is governed by large-scale vortices. The roll-up and growth of these vortices are determined by instability forces and mutual interactions (Brown and Roshko, 1974). The large-scale structures entrain flow from the two sides of the shear layer and mix the flow at both large and small scales, leading to the molecular mixing necessary for reaction. The development of large-scale vortices in the shear layer is influenced by the reaction through heat release and density gradients. In turn, the vorticity controls the reaction by the turbulent mixing process (Mungal and Dimotakis, 1984).

In a plane mixing layer, the development of three-dimensional small-scale fluctuations could be related to the streamwise vortices which have been shown to develop concomitantly with the spanwise large coherent structures (Bernal, 1981 and Metcalfe et al, 1987). In axisymmetric flames, this process is associated with coherent axisymmetric vortices. Browand and Laufer (1975) observed the formation of four to nine lobes in a circular jet and suggested that the disintegration of the large structures into small-scale turbulence is due to the amplification of the azimuthal instability.

The evolution of azimuthal structures on coherent initially axisymmetric vortices was observed both in cold flow (Browand and Laufer, 1975) and reacting flows in flames (Chen and Roquemore, 1986, Settles, 1985, and Gutmark et al, 1989a).

The present paper describes two and three-dimensional near field structure of a reacting jet using Planar Laser Induced Fluorescence (PLIF). The evolution of this flow and its interaction with the combustion process are not fully understood. The understanding of this process is important for practical application such as the mechanism leading to combustion instability, and can help in developing methods for enhancing energy release and reducing the formation of soot.

For soot formation control, an annular diffusion flame was used which allowed independent acoustic forcing of the central air and circumferential fuel. The forcing introduced coherent vortices into the flow and allowed complete control of fuel injection into the vortex shedding process.

The relation between soot formation, the vortical structures, and fuel injection location during active control of this flame was investigated using advanced diagnostics, such as PLIF (Planar Laser Induced Fluorescence) and PIV (Particle Imaging Velocimetry). The diagnostics were phase locked to the vortex evolution cycle. This allowed the entire time evolution of the mixing and combustion processes to be imaged.

Laser diagnostics are also an important tool in supersonic flow research. Since large-scale vortical structures and their dynamics play a central role in turbulent incompressible mixing, considerable research effort has been directed toward identifying similar structures in compressible shear layers. For large-scale structure studies in compressible shear layers, planar visualization is an essential tool because naturally occurring structures are often three-dimensional and poorly organized. Thus, laser-assisted flow visualization techniques are well suited for such studies.

A planar Mie-scattering technique was used in visualizing Mach 2 jets which were discharged either freely or inside a co-flowing Mach 1.3 jet. The objectives were to identify large-scale structures in the initial shear layers of supersonic jets and to develop new means for controlling the large-scale structures.

2. EXPERIMENTAL SET-UP

2.1 3-D Imaging

A system for PLIF imaging of OH radicals in flames using a XeCl excimer laser at 308 nm was used (Fig. 1) (Gutmark et al, 1989b). The laser beam was expanded into a planar sheet, passed through the flow perpendicular to the axis for azimuthal structures measurements. The resonance fluorescence from OH was imaged with a gated intensified diode array camera. The sheet was approximately 0.5 mm wide.

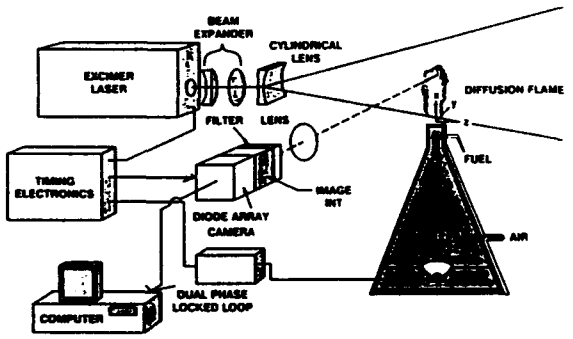

Fig. 1. Experimental Set-Up For PLIF Imaging in 2-D.

The air issued at a velocity of 5 m/s from a 22 mm diameter circular nozzle yielding a Reynolds number in the range of 350 to 4000, based on the shear layer thickness, exit velocity, and the kinematic viscosity of the air at room temperature. Propane was injected circumferentially around the air jet nozzle into the initial shear layer, via 24 1.6 mm diameter holes, on a 23.5 mm diameter circle, which are slightly angled into the shear layer. The fuel exit velocity was 0.2 m/sec. The initial rms level measured at the exit of the nozzle on the centerline was 3.6 percent.

The flow was excited by a set of four speakers mounted in an acoustic resonating chamber which was used as a settling chamber as well. The speakers were driven at controlled frequencies and amplitudes using a dual phase locked loop and audio power amplifier. To construct the turbulent structure at a specific phase, the laser system was phase locked to acoustic excitation of the flame jet. The phase angles between the forcing signal and the laser could be varied in a full cycle range. The speakers force, and phase lock, only the longitudinal mode of the jet.

The azimuthal structure was stabilized by vortex generators in the jet boundary layer upstream of the exit. Previous experiments (Gutmark et al, 1989a) showed that the preferred azimuthal structure has a five-fold symmetry. Therefore, a set of five pairs of split delta-wings were installed at the exit. Two configurations of wings were tested. One generates "mushroom" like vortices and the other a "delta wing" type vortex pair. The triangles forming the semi-delta wing had a base of 4 mm and an apex angle of 30°.

2.2 Soot Control

The apparatus diagram for the soot control experiments in shown in Fig. 2. The diffusion flame burner was the same as the one used for the 3-D visualizations. It was forced at a Strouhal number of 0.73 (100 Hz) by a single acoustic driver, and a coaxial fuel injection ring fed by a plenum forced by two acoustic drivers at either 100 Hz (single phase injection) or 200 Hz (dual phase injection). The fuel to air ratio was varied from 0.8 to 1.4 to simulate differing soot formation conditions. The centerline velocity at the nozzle exit was 3.0 m/sec; the unforced (natural) rms was 4.5%, the forced rms was 30%. The Reynolds number based on the exit diameter was 3700.

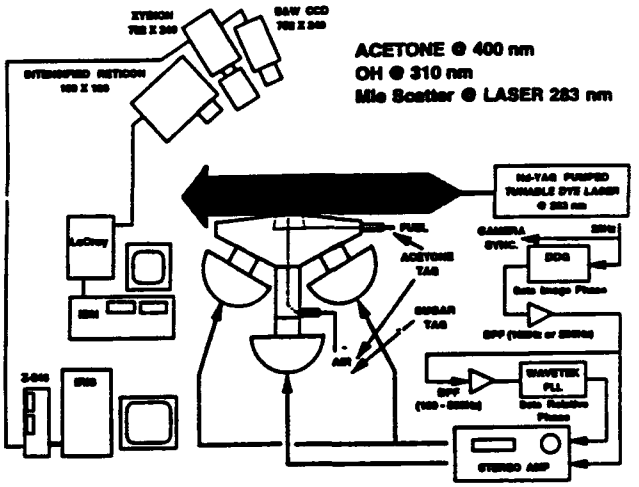

Fig. 2. Schematic of the Experimental Arrangement for Soot Control.

A Nd^{+3}-YAG pumped dye laser with nonlinear crystal doubling was tuned either on or close to (but off) the (1,0) A-X transition of OH radicals located near 283 nm and two cameras simultaneously monitored selected combinations of two of four scalars: OH, soot, fuel, and air. The pairs of scalar images were combined into four scalar images by making use of the phase locked imaging.

Table 1 shows the permutations of scalar measurements. The two cameras used were a Xybion™ ISG-240 gated image intensified 752 x 480 CCD and a gated intensified Reticon™ 100 x 100 diode array. Both cameras were gated for about 50 nsec to encompass the laser pulse but reject flame chemiluminescence. The flows were tagged with either fine sugar particles, monitored with Mie scatter using an 283 nm interference filter, or with acetone, monitored via laser induced fluorescence (Lozano et al, 1992). Acetone has a broad absorption peak centered at 275 nm; when pumped at 283 nm it produces a broad induced fluorescence peak centered at 400 nm and extending from 320 nm to about 600 nm. Acetone PLIF was monitored with a 400 nm interference filter having a 65 nm FWHM. OH was imaged via fluorescence from the (1,1) A-X band selected using a 311 nm, 10 nm FWHM interference filter, and soot was monitored using Mie scatter at 283 nm.

Images from the two gated cameras were acquired using two computers, a transient digitizer, and frame grabber.

Instantaneous phase sampled velocity vector fields were measured in cold flow using a PIV setup. PIV is the measurement of local flow velocities by following the movement of seed particles with time. The light source was an unmodulated fiber optic microscope illuminator (tungsten incandescent bulb). Timing was controlled by

Table 1. Test Conditions.

Camera 1 (Reticon™)	Camera 2 (Xybion™)	OH Resonance	Flame
OH (LIF)	Fuel (acetone)	on	on
Soot (Mie)	Fuel (acetone)	off	on
Fuel (Mie)	Air (acetone)	off	off
OH (LIF)	Air (acetone)	on	on
Air (Mie)	Fuel (acetone)	off	off
Air (Mie)	Fuel (acetone)	off	on
OH (LIF)	Soot (Mie)	on	on

gating the Xybion™ camera. The output of the fiber optic illuminator was loosely focused into a relatively wide (5 mm) light sheet using a cylindrical lens.

The flow associated with this flame is highly complex due to the strong vorticity and, it turns out, strong entrainment, leading to regions of reversal. Therefore the PIV technique had to allow for resolution of the direction ambiguity. The camera was gated with a dash-dot pattern. Thus the particle track images consist of lines followed by dots making direction analysis unambiguous.

Powdered milk sieved to below 74 m was utilized for seeding in the cold flow tests.

2.3 Supersonic Jets

The blow-down supersonic jet stand is shown in Fig. 3. Axisymmetric converging-diverging nozzles were used. The exit design Mach number was 2.0 for the inner nozzle when the specific heat ratio γ of the gas was between 1.3 and 1.5. The outer nozzle design Mach number was 1.3 for gases with γ in the similar range. Either air or ethylene-oxygen combustion products were used for the inner jet. When combustion products were used, nitrogen was added to control the exit temperature and γ. The outer jet used only air.

The near field of supersonic jets was visualized for four different cases. Table 2 shows the flow conditions which include the Mach number (Ma), exit temperature (T) and specific heat ratio (γ) for the jets and the convective

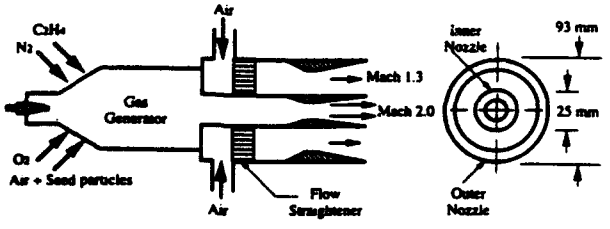

Fig. 3. Supersonic Coaxial Jet Set-Up.

Mach number (M_C) for the shear flow. The convective Mach numbers are based on the velocity difference between the free streams and the large-scale structures (Bogdanoff, 1983, and Papamoschou and Roshko, 1988).

The inner jet was seeded with condensed ethanol droplets (Clemens and Mungal, 1991) for cold nonreacting flows and 0.3 μm aluminum oxide (Al_2O_3) particles for hot reacting flows. The amount of seeding varied depending on the flow conditions but the total mass flux of the seed material was less than 0.5 % of the inner jet gas flow. For typical cases the calculated number density was in excess of 10^4 *particles/mm*^{3}.

A copper vapor laser (20 *nsec* pulses; 4 *mJ/pulse*; 511 and 578 *nm*) was used as the light source. The laser beam was shaped into a thin sheet and was traversed across the jet along the center axis illuminating a cross section. A CCD camera, mounted at a perpendicular angle from the laser sheet, was used to collect the seed-particle-scattered light.

3 RESULTS AND DISCUSSION

3.1 Three Dimensional Imaging

The three-dimensional image of the phase-locked structures was reconstructed from multiple planar slices measured at different axial locations. Using this technique it was possible to follow the generation of streamwise vortices in the braid region, their growth and subsequent interaction with the large-scale spanwise vortices.

The streamwise vortices which were generated by the semi-delta wings had a strong effect on the flow structure. Figure 4 shows the two-dimensional images of radial cross-sections of the jet obtained at increasing axial distances from the flameholder. The initial "braid" region acquires a pentagonal shape due to the flow induced by the streamwise vortices. The shape of these vortices become more evident as the axial distance grows and the axial vortices develop (x/D = 0.62). A close-up phase-averaged

Table 2. Flow Conditions

Case	Inner Jet			Outer Jet			Shear Flow	
	Ma_1	T_1 (K)	γ_1	Ma_2	T_2 (K)	γ_2	M_{C1}	M_{C2}
1	2.0	160	1.4	1.3	210	1.4	0.23	0.23
2	2.0	1800	1.3	1.3	220	1.4	1.16	1.10
3	2.0	160	1.4	0	300	1.4	0.85	0.85
4	2.0	1300	1.3	0	300	1.4	1.36	1.31

figure of the streamwise vortices is shown in Fig. 5. The "mushroom" shape of the streamwise vortex is evident in the image. Moving further downstream into the spanwise vortex region, x/D = 0.94 (Fig. 4), it becomes pinched off with a five-fold symmetry, which is related to the longitudinal structures. The interaction between the streamwise vortices and the spanwise coherent structures results in a deformation of the latter and then breakdown to smaller scales. Studying the variation of the stack of radial slices along the axis shows the three-dimensional character of this jet.

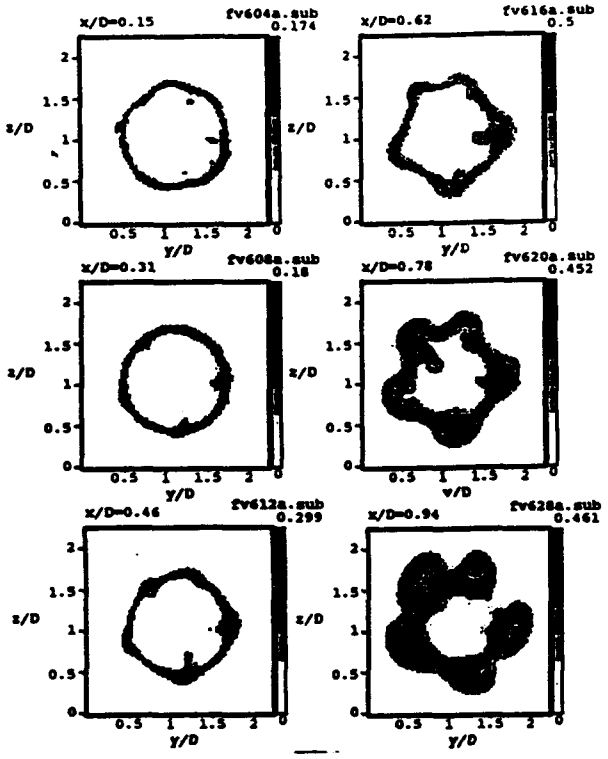

Fig. 4. Multiple Axial Planar Cross-Section Used to Reconstruct a 3-D Image. Azimuthal structure stabilized by semi-delta wing ("mushroom" type vortex). Spanwise structure forced at St = 0.49.

3-D images of the flow were constructed from 20 two-dimensional planar images using *Stans Surf* rendering software (Wu and Hesselink, 1988). The perspective views of the flames forced by the "mushroom" type vortices and by the "delta" type vortices are shown in Figs. 6 and 7, respectively. The rendering was done using the phase-averaged set of data, resulting in a relatively smooth interpolated surface. The transition from the streamwise structures to the spanwise pinched vortices is clear in these images. There are some differences between the two flames structures due to the two types of vortex generators. However, the coherence of both the spanwise and streamwise structures obtained by using the combined active and passive forcing is sufficient to obtain a consistent structure. The roll-up location and the spatial positioning of the bulges and ridges remain essentially fixed in space. This fact suggests that the stabilization by the vortex generators and the forcing was highly efficient.

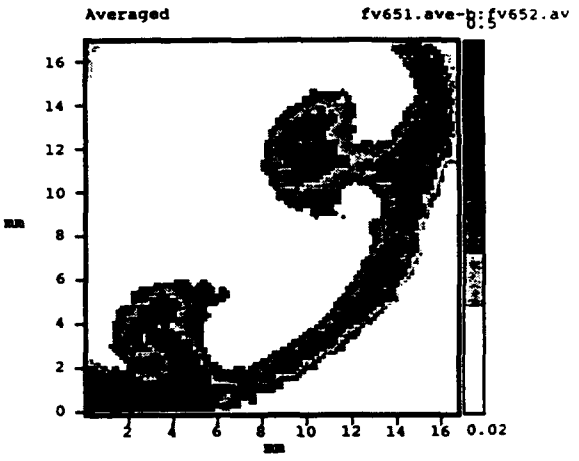

Fig. 5. Close Up Cross Sectional Cut in Streamwise "Mushroom" Type Vortices in "Braid" Region.

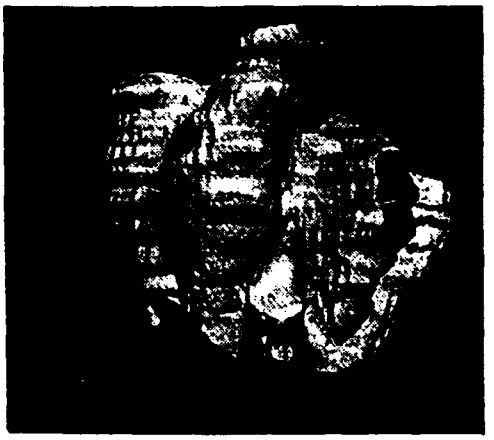

Fig. 6. Phase Averaged 3-D Image of the Azimuthal Structures in the Flow, With Streamwise "Mushroom" type vortices.

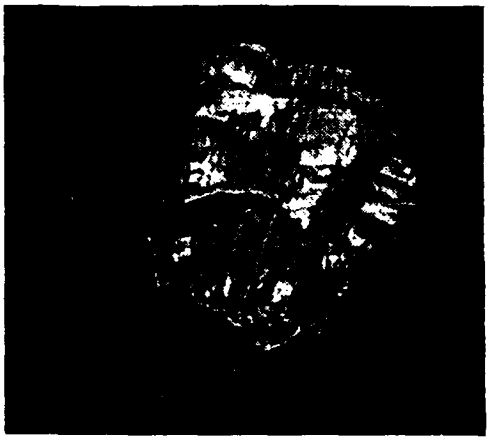

Fig. 7. Phase Averaged 3-D Image of the Azimuthal Structures in the Flow, With Streamwise "Delta type" vortices.

Horizontal cut (Fig. 8) through the center of the spanwise structures shows the pinched structure with reaction zones only at the outer parts of the vortex, where the high turbulence level concentrates.

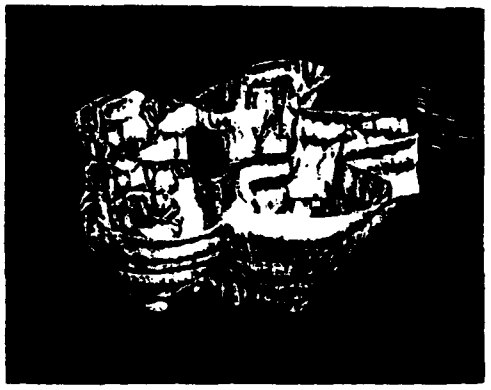

Fig. 8. Horizontal Cut Through the Phase Averaged 3-D Image of the Azimuthal Structures in the Flow, With Streamwise "Mushroom" type vortices.

3.2 Control of Soot Formation

Since the downstream soot production is controlled by upstream mixing we undertook imaging at a magnification level high enough to follow the mixing process within the first vortex formation region. Results from the simultaneous dual parameter PLIF measurements are shown in Figs. 9 through 12. Two sets of experiments were performed to control the soot formation. In the first set (Figs. 9 and 10) the fuel was injected once in every air vortex cycle. This method was successful in soot reduction but did not enhance the energy release. In the second set (Figs. 11 and 12) the fuel was injected twice per air vortex cycle. It resulted in a decrease in soot and an increase in energy release as measured with average temperature profiles (not shown).

The frames of Fig. 9 (single phase injection) show that for the low soot fuel phase angle the fuel is injected into the incipient vortex rollup and homogeneously mixed with the air vortex yielding intense reaction downstream as shown by the OH region above the vortex area. The dynamic sequence (computer generated movie) showed this even more clearly than the still images. The images corresponding to the high soot flame (Fig. 10) and the corresponding movie show that when the fuel is injected out of phase with the air vortex cycle, the air vortex formation is partially inhibited, and the fuel remains unmixed in pockets between air vortices resulting in alternating regions of high and low stoichiometry. This leads to poor combustion and high soot production. The reaction region as indicated by the OH is primarily at the external shear layer of the jet where the fuel is mixed with the external air. This flame has a very high sooting level, which was not clearly visualized in Fig. 10 as the soot was concentrated above the field of view of the images.

Figures 11 (low soot phase angle) and 12 (high soot phase angle) show the results for dual phase injection. Fuel is injected twice per air vortex shedding. Figure 11, low soot case, shows that the first fuel injection, which is synchronized with the formation of the incipient vortex, mixes homogeneously and initiates intense combustion downstream of the vortex. The second injection penetrates the jet and brings the fuel into the lean combustion products of the prior vortex. The process therefore emulated staged combustion without mechanical stages. This configuration leads to high soot reduction as well as and increase in energy release rate close to the flame holder (as evidenced by thermocouple profiles).

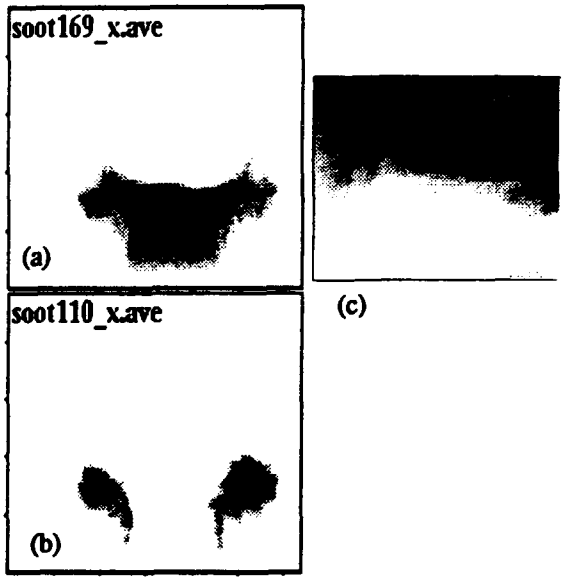

Fig. 9. PLIF and Mie Images From Single Phase Injection for Low Soot Case. (a) Air, (b) Fuel, and (c) OH.

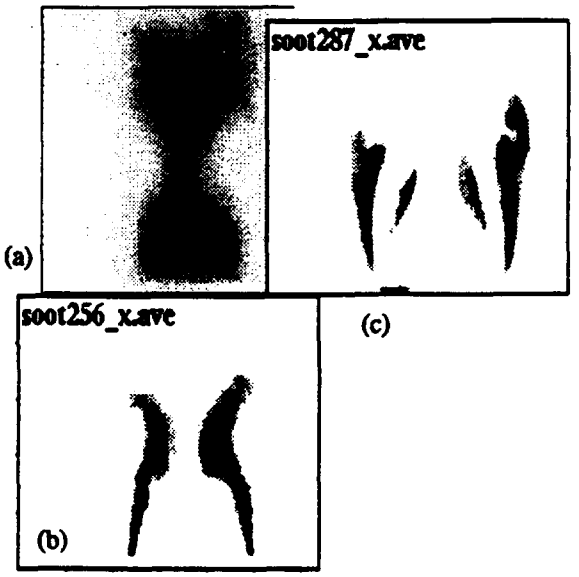

Fig. 10. PLIF and Mie Images From Single Phase Injection for High Soot Case. (a) Air, (b) Fuel, and (c) OH.

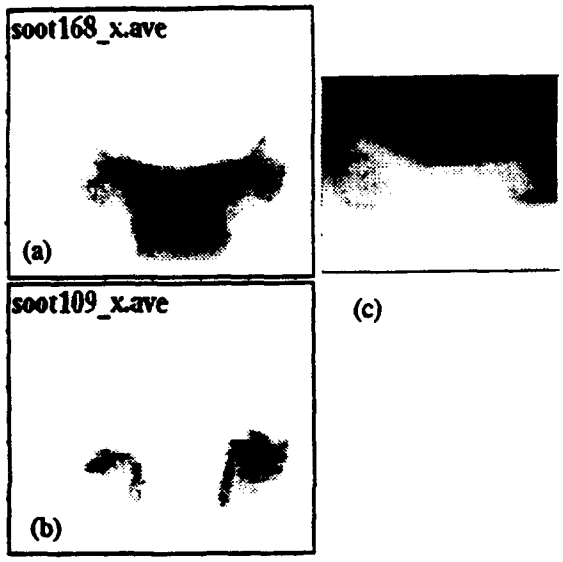

Fig. 11. PLIF and Mie Images From Dual Phase Injection for Low Soot Case. (a) Air, (b) Fuel, and (c) OH.

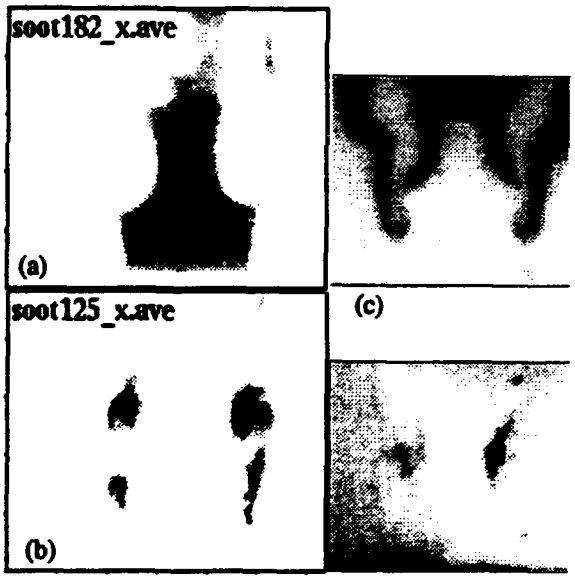

Fig. 12. PLIF and Mie Images From Dual Phase Injection for High Soot Case. (a) Air, (b) Fuel, (c) OH, and (d) Soot.

The injection sequence which results in a highly sooting flame (Fig. 12) occurs out of phase with the air vortex formation. The first fuel injection misses the air vortex and stays unmixed while also partially suppressing the roll-up of this air vortex. The second fuel injection enters the void between the air vortices and stays separated from the air. The rich mixture results in the formation of soot at this point as shown by the black spots. Temperature profiles also show the energy release rate to be lower in this case.

Later experiments showed that a portion of the soot reduction effect seen in the experiments was caused by strong entrainment of surrounding air with subsequent reduction in the fuel to air ratio. The dual phase case, especially, creates high periodic, and even high net entrainment just above the nozzle exit plane. Figure 13 shows the PIV measured cold flow velocity vector field map under the low soot case of dual injection. The vorticity is clearly evident. Also evident is a very strong entrainment of surrounding air at the base of the flame under the first vortex. The average centerline velocity is about 3.5 m/sec yet the net average entrainment velocity near the exit is as high as 1 m/sec. The entrainment under the second vortex is much weaker due to a stagnation region from centerline flow moving outward between the vortices.

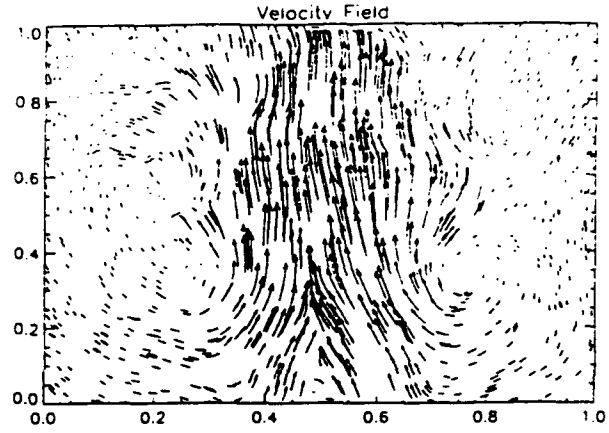

Fig. 13. PIV Measure Velocity Vector Field for Dual Phase Injection, Low Soot Case.

3.3 Large-Scale Structures in Supersonic Jets

The supersonic jets were visualized using Mie-scattering technique and the large-scale structures were identified from the images. Figure 14 shows the coaxial jet images corresponding to Cases 1 and 2. Large-scale structures are much more coherent at the lower convective Mach number (Case 1). By applying Fourier transform to the digitized intensity along the streamwise direction, it was possible to quantify the wavelength of the coherent structures. Figure 15 illustrates how the streamwise wavelength was deduced from the spectral peaks.

The coherent structure wavelength increased with the inner nozzle lip thickness. The dependence was nearly linear. The results were normalized with the wake characteristic parameters yielding Strouhal frequency, $St = tU_C/\lambda U_\infty$, where t is the lip thickness, U_C is the coherent structure convection velocity, λ is the wavelength, and U_∞ is the free stream velocity. Among the five different lip thicknesses that were tested, the lip thickness of 2.0 mm resulted in "best" organized structures with highest spectral peaks.

The total pressure profiles were measured at a distance of 1.5 mm downstream of the nozzle exit plane. Average velocity profiles for the wake flow downstream of the lip were obtained from the pressure profiles. A linear stability analysis was performed for the shear flow profiles at each side of the wake using the two-dimensional Rayleigh equation. The details of the analysis can be found in Gutmark et al (1993). The most amplified frequencies from the

stability analysis were compared with the wavelength-based measurements, and the results are shown in Fig. 16 as a function of the lip thickness. Near the lip thickness of 2.0 mm, there was a particularly good agreement between the most amplified frequencies and the measured frequency. This suggests that the unusually high degree of coherence, found in the large-scale structures for this condition, is the result of a possible resonant interaction between the instabilities associated with the two shear layers and the lip-created wake.

Lastly, a passive control of large-scale structures was demonstrated in free jet shear layers using specially designed cavities which were placed at the jet exit. Figure 17 shows the instantaneous flow images for natural jets and cavity-forced jets. There was a significant increase in the shear layer spreading rate with the cavity-actuated forcing. The maximum increase was about 50 to 300% depending on the flow condition.

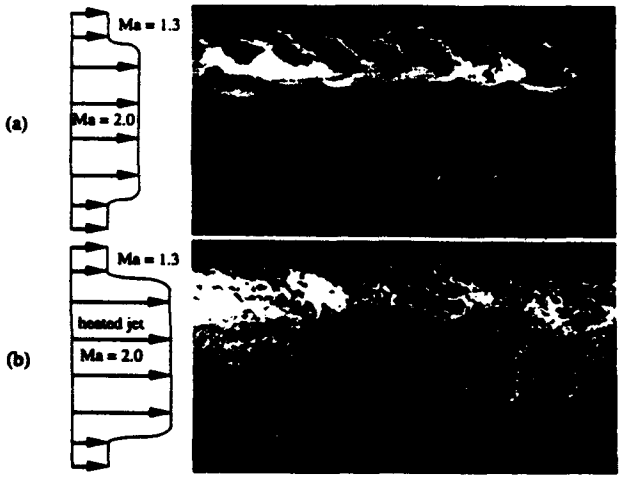

Fig. 14. Planar Mie-Scattering Images of Supersonic Coaxial Jets Corresponding to (a) Case 1, and (b) Case 2 Flow Conditions.

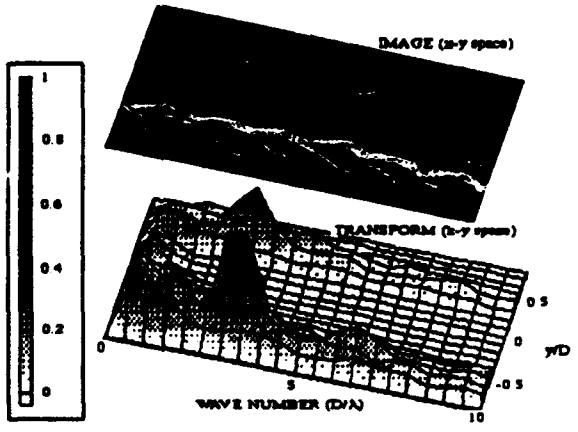

Fig. 15. Spectral Intensity Map Obtained From FFT Processing.

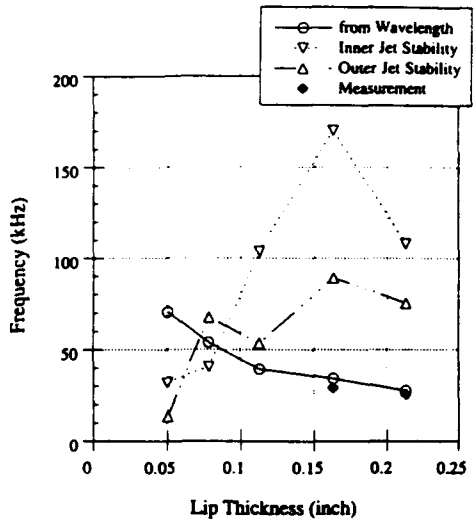

Fig. 16. Comparison of Most-Amplified Shear Layer Frequencies With Measured Coherent Structure Frequency.

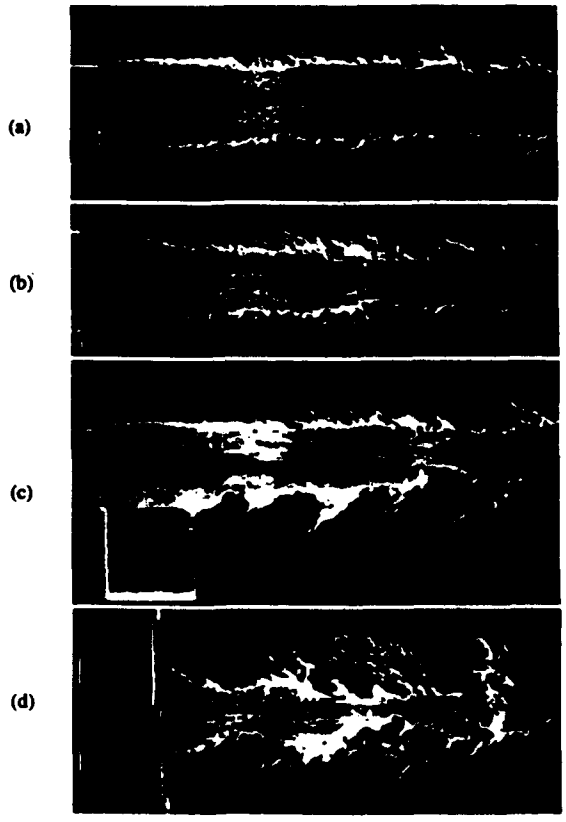

Fig. 17. Comparison of Natural Jets at (a) Mc = 0.85 and (b) Mc = 1.36 With Cavity-Forced Jets at Corresponding Flow Conditions (c) and (d), Respectively.

REFERENCES

Bernal, L.P. 1981, The Coherent Structure of Turbulent Mixing Layer, Ph.D. Thesis, California Institute of Technology.

Bogdanoff, D.W. 1983, Compressibility Effects in Turbulent Shear Layers, AIAA J., Vol. 21, pp. 926-927.

Broadwell, J.E. & Dimotakis, P.E. 1986, Implications of Recent Experimental Results for Modeling Reaction in Turbulent Flows, AIAA J., Vol. 24, p. 875.

Browand, F.K. & Laufer, J. 1975, The Role of Large-Scale Structures in the Initial Development of Circular Jets, Turbulence in Liquids, (J. L. Zakin, and G. K. Patterson, eds., Princeton, N.J.), p. 333.

Brown, G.L. & Roshko, A. 1974, On Density Effects and Large Structures in Turbulent Mixing Layers, J. Fluid Mech., Vol. 64, p. 775.

Chen, L.D. & Roquemore, W. R. 1986, Visualization of Jet Flames, Combust. and Flame, Vol. 66, p. 81.

Clemens, N.T. & Mungal, M.G. 1991, A Planar Mie Scattering Technique for Visualizing Supersonic Mixing Flows, Exp. in Fluids, Vol. 11, pp. 175-185.

Gutmark, E., Parr, T.P., Parr, D.M. & Schadow, K.C. 1989a, Azimuthal Structure of an Annular Diffusion Flame, Combust. and Flame, Vol. 75, p. 229.

Gutmark, E., Parr, T.P., Parr, D.M. & Schadow, K.C. 1989b, Planar Imaging of Vortex Dynamics in Flames, J. of Heat Transfer, Vol. 3, p. 148.

Gutmark, E., K. Yu, K. & Schadow, K.C. 1993, The Effect of Nozzle-Lip Wake on the Structure, Stability, and Pressure Fluctuations of Coaxial Supersonic Jets, AIAA-93-4363.

Lozano, A., Yip, B. & Hanson, R.K.. 1992, Acetone: A Tracer for Concentration Measurements in Gaseous Flows by Planar Laser-Induced Fluorescence, Exp. in Fluids, Vol. 13, p. 369.

Metcalfe, R.W., Orszag, S.A., Brachet, M.E., Menon, S., & Riley, J.J. 1987, Secondary Instability of a Temporally Growing Mixing Layer, J. Fluid Mech., Vol. 184, p. 207.

Mungal, M.G. & Dimotakis, P.E. 1984, Mixing and Combustion with Low Heat Release in a Turbulent Shear Layer, J. Fluid Mech., Vol. 148, p. 349.

Papamoschou, D. & Roshko, A. 1988, The Compressible Turbulent Shear Layer: An Experimental Study, J. Fluid Mech., Vol. 197, pp. 453-477.

Settles, G.S. 1985, Color Coding Schlieren Techniques for the Optical Study of Heat and Fluid Flow, Int. J. Heat & Fluid Flow, Vol. 6, p. 3.

Wu, K. & Hesselink, L. 1988, Computer Display of Reconstructed 3-D Scalar Data, Appl. Optics, Vol. 27, p. 395.

DEVELOPMENT OF AN UV-LASER-DIAGNOSTIC SYSTEM FOR COMBUSTION RESEARCH UNDER ZERO-GRAVITY AT DROP TOWER "BREMEN"

Ch. Eigenbrod, J. König, T. Bolik, T. Behrens, F. Dinkelacker, H. J. Rath
ZARM - Center of Applied Space Technology and Microgravity,
Universität Bremen, Am Fallturm 1, D-28359 Bremen, Germany

H. Albrecht, D. Müller, Th. Schröder, W. Triebel
Institut für Physikalische Hochtechnologie, Helmholtzweg 4,
D-07743 Jena, Germany

ABSTRACT

The application of modern laser diagnostical measurement techniques for combustion research in earth-based laboratories has brought essential experimental progress. In this paper the development of an UV-laser system is described, which for the first time will allow the application of two dimensional laser spectroscopic measurement techniques for experiments at drop tower "Bremen". The laser system will be integrated at the top of the drop tower; the laser beam follows the falling drop capsule and enters it from above. The drift between capsule and laser beam has to be compensated with an accuracy in the sub-mm range.

Described are the laser-, control-, detection- and data acquisition systems, first results of the experimental properties and planned applications for experiments at the drop tower "Bremen".

1. INTRODUCTION

Combustion experiments under buoyancy-free conditions can give important insight into the detailed physical and physico-chemical processes of combustion, since the overlapping effect of buoyant convection can be eliminated (Sacksteder 1990). As a representative for many important technical problems, the study of evaporation, self ignition and burning of single droplets can be mentioned, where under normal gravity conditions convectional effects prevent detailed investigation of the interacting two-phase processes. Under strongly reduced gravity conditions these processes can be experimentally investigated in detail (Kumagai and Isoda 1957, Choi *et al* 1990, Sato 1993, Chauveau *et al* 1994), and compared with detailed numerical simulations (Ristau *et al* 1993).

Experiments under reduced gravity conditions can be conducted in orbiting spacecraft, in parabolic flights and in ground-based drop towers. While spacecraft experiments allow long experimental times they are extremely expensive and quite inflexible compared to ground based facilities. The drop tower in Bremen offers experimental times of 4.7 seconds, which is sufficiently long for droplet combustion experiments. Residual acceleration levels are below 10^{-5} g_o (Dittus and Rath 1993).

Up to now, the measurement techniques applied to these experiments were restricted to intrusive probing techniques, photography, videofilming and interferometric devices (e.g. Tanabe *et al* 1994), since microgravity facilities provide strongly restricted limits to payload mass, volume, power consumption and mechanical strength. In this paper an advanced experimental set-up is presented, which for the first time will allow the application of modern laser spectroscopic measurement techniques such as two-dimensional laser-induced fluorescence (e.g. Kychakoff *et al* 1984, Arnold *et al* 1989) to strongly reduced gravity combustion experiments at drop tower "Bremen". Since this laser system might have wide applications for experiments under microgravity in different fields of combustion research and fluid mechanics, details of the technical solution are presented here.

2. DESIGN BENCHMARKS

Constraints on the experimental set-up for the use of laser-spectroscopical techniques in the drop tower Bremen are:

- Limited space and load in the drop capsule (diameter 70 cm, height 150 cm and load up to 200 kg for the experimental arrangement).
- Sufficient mechanical stability of the optical and electronical arrangement. During the deceleration phase the drop capsule has to withstand up to 30 g. Since this acceleration force is nearly constant over a 0.2 second period (Dittus and Rath 1993) it is possible to use carefully adapted standard instrumentation.
- Since an UV-laser system cannot be integrated in the drop capsule the laser beam has to be directed from a location outside of the evacuated tower into the falling drop capsule. For that purpose the divergency of the laser beam has to be minimized for use at all positions along the trajectory of the falling drop capsule from 5 to 115 m.
- The drift between drop capsule and laser beam has to be compensated with an accuracy in the sub-mm range, since the light sheet must be focused on a defined position within the experimental apparatus.
- The data acquisition rate must be as high as possible, since the experimental time is below 5 seconds and experiments cannot be repeated very often.

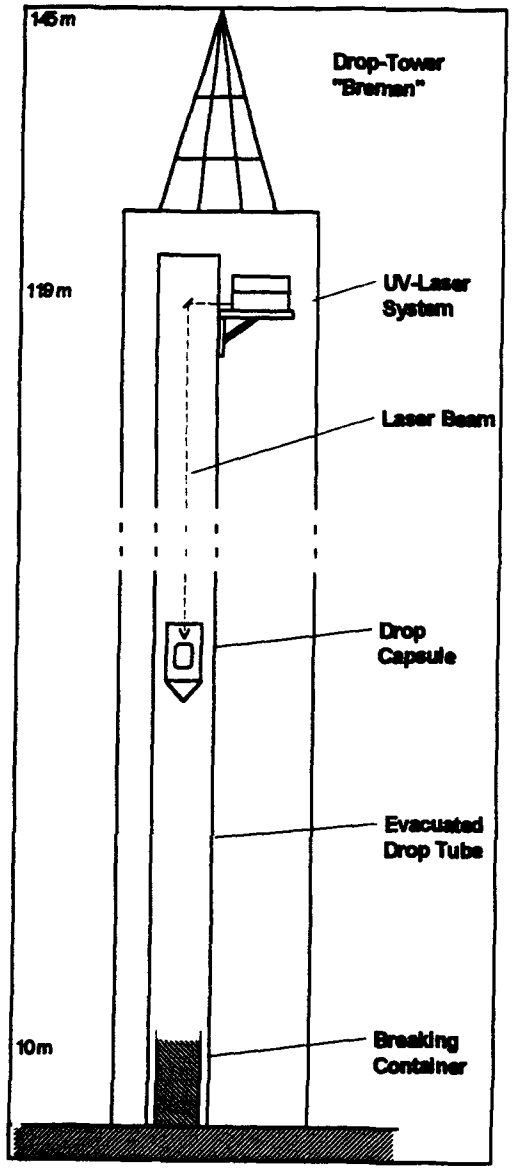

Fig. 1: Integration of the UV-excimer laser system on the drop tower "Bremen"

3. TECHNICAL SOLUTION

Two UV-excimer laser are used in an oscillator- amplifier arrangement (Lambda Physics LPX 120i, LPX 220i) equipped with an external narrowband unit using a tunable Littrow grating. With this equipment high repetition rates of 250 Hz can be combined with high energies up to 350 mJ per pulse and tunable narrowband properties to obtain high temporal and spectral resolution.

The laser system will be integrated at the top of the drop tower, mounting the laser to the inner evacuated drop tube. The laser beam follows the falling drop capsule and enters it from above through a quartz window (Fig. 1). Details of the optical arrangement are shown schematically in Fig. 2. In order to fix the position of the laser beam within the experimental apparatus (e.g. the combustion chamber) with an accuracy in the sub-mm range the drift between capsule and laser beam has to be compensated. Experiments in the drop tower have shown that this drift, in the range of 20 mm, is induced by oscillations of the concrete drop tower, from momentum of the release mechanism and from improperly compensated coriolis force. The positioning system is based on a guiding HeNe-laser beam which is coupled coaxially into the optical path of the excimer laser, and on a positioning unit at the top of the drop capsule. With two beam splitter plates the HeNe-laser beam is directed on two planar position sensing detectors (PSD). A control unit drives two motorized mirrors with two axes of rotation each. Thus the lateral and the angular drift between the drop capsule and laser beam can be compensated.

In order to minimize the divergency of the laser beam over a range of 5 to 115 m the beam is widened from its original shape of about 5 x 20 mm to about 25 x 25 mm by means of a telescope, since diffraction-based divergency is inversly proportional to the width of the beam. The telescope consists of a horizontally arranged cylindrical lens (f = -886 mm), a vertically arranged cylindrical lens (f = -250 mm) and one spherical

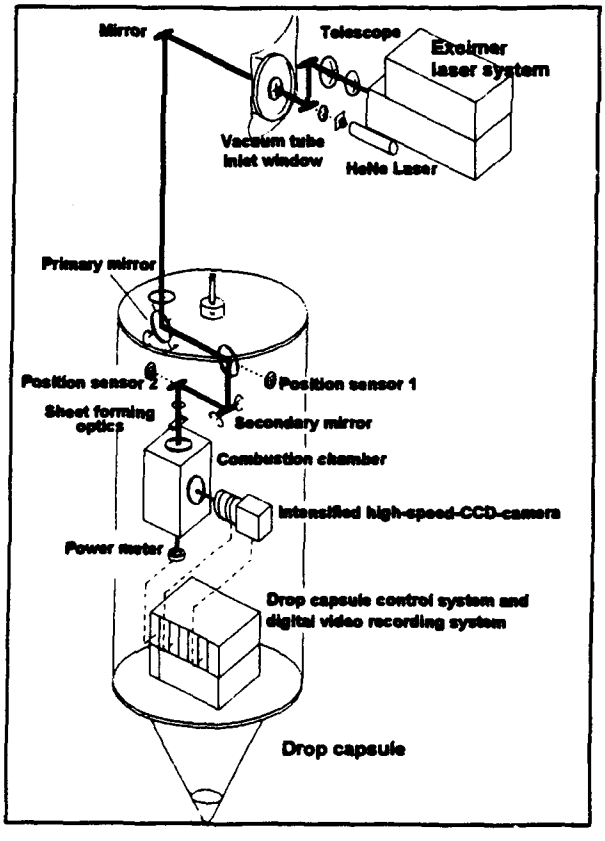

Fig. 2: Schematics of the optical arrangement at the top of the drop tower and within the drop capsule

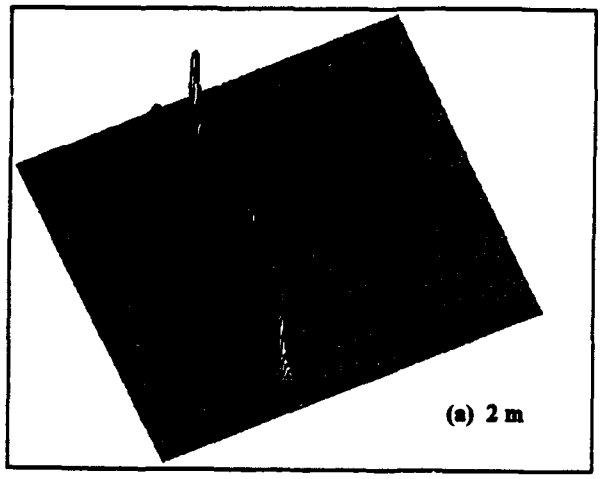

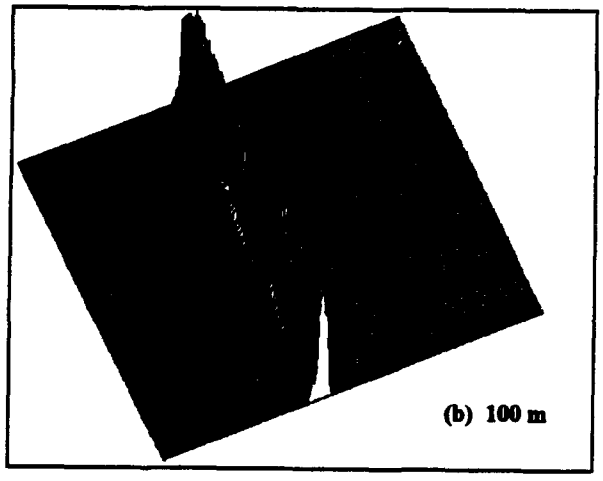

Fig. 3: Intensity distribution showing the beam profile of the excimer laser beam, focused to a two-dimensional light sheet (a) 2 m behind the laser, (b) 100 m behind the laser. The repetition rate of the laser was 200 Hz. The images show the good quality of the light sheet.

lens (f = 1000 mm). Measurements of the beam profile at distances up to 115 m from the laser show that the width is always below 30 mm. Spatial fluctuations in the beam profile are strongly reduced when the laser beam is focused to a two-dimensional light sheet, using a suitable cylindrical telescope (f_1 = 370 mm, f_2 = - 62 mm), which later will be integrated into the drop capsule behind the positioning unit. In Fig. 3 single-pulse examples of the light sheet profiles are shown. The two-dimensional light sheet has a height of about 25 mm and a width below 500 µm (FWHM).

In order to enable the investigation of rapid instationary processes like auto ignition phenomena within the drop time of 4.7 seconds the frame rate of the laser diagnostic system is maximized to 250 frames per second. To achieve this an image intensified CCD camera with 256 x 256 squared pixel (Dalsa) is tuned to a frame rate of 250 frames per second. Using an 8 bit A/D converter with 18 MHz sampling rate, a high speed video-interface and an EISA bus-based PC system (486 DX) up to 128 MBytes data can be stored during the drop time directly on the random access memory (RAM) of the PC. Image acquisition and data storage equipment are integrated within the capsule. Immediately after finishing the drop experiment the image data can be transferred via a telemetry line to a large data storage outside the drop tube. From here a first evaluation of the obtained raw image data is possible, and extensive automatized digital image processing can be done.

For triggering the image acquisition system by the laser-pulse a fast UV-photodiode is used within the drop capsule. With temporal pulse-to-pulse fluctuations (jitter) of the laser below 3 ns, a pulse length below 20 ns, a temporal drift due to the moving capsule below 1 ns per pulse and a gate time of the image intensifier of 100 ns it is possible to trigger the acquisition of an image with the previous laser pulse.

First applications in the drop tower "Bremen" are planned for experiments on droplet ignition, where laser induced fluorescence of hydroxyl radicals can give important information to be compared with detailed numerical simulations.

Further applications might be:

- 2 D - Measurements of the interaction of two or more droplets during ignition, flame spread and burning, which is an important step in understanding the processes of spray combustion.
- Measurement of the flamefront structure of flat-plate diffusion flames in buoyant free surrounding (Joulain 1993).
- 1 D - Raman / Rayleigh Spectroscopy for simultaneous measurement of different major species and temperature (Starner *et al* 1990) focusing the laser sheet to a focal line and using an OMA system, where the emission wavelength is measured against the spatial coordinate with high temporal resolution.
- 2 D - flowfield measurements like particle tracking velocimetry (PTV, e.g. Barker and Fourney 1977) or laser speckle velocimetry (LSV, e.g. Merzkirch 1990, Kemmerich *et al* 1994) for various applications in fluid mechanics under microgravity conditions, where small seeding particles can be illuminated stroboscopically with the planar laser light sheet, so that the two velocity components in this plane can be measured simultaneously.
- Use of the UV laser beam for photochemical processes (e.g. photopolymerization) under microgravity conditions (Sturm *et al* 1992).

ACKNOWLEDGEMENT

We thank the German Space Agency DARA for financial support (FKZ 50 WP 9251-9).

REFERENCES

Arnold A., Becker H., Ketterle W., Monkhouse P., Suntz R., Köllner M., Wolfrum J., 1989, Einsatz von Ultrakurzzeit- und UV-Lasersystemen zur mehrdimensionalen Fluoreszenzdiagnostik industrieller Verbrennungsprozesse, VDI Berichte 765

Barker D.B., Fourney M.E., 1977, Measuring fluid velocities with speckle patterns, Opt. Lett. 1, 135

Chauveau C., Chesneau X., Gökalp I., 1994, High pressure vaporization and burning of methanol droplets in reduced gravity, AIAA Paper No. 94-0430

Choi M. Y., Dryer F. L., Haggard J. B., 1990, Observations on a Slow Burning Regime for Hydrocarbon Droplets: n-Heptane / Air Results, Twenty-Third Symposium (International) on Combustion / The Combustion Institute, 1597-1604

Dittus H., Rath H. J., 1993, Mikrogravitation im freien Fall, Phys. Blätter 4, 307

Joulain P., 1993, Diffusion Flame Combustion in Oxidizing Flow, Microgravity Science and Technology V/4, 178

Kemmerich T., Saß V., Rath H. J., 1994, Simultaneous investigation of the temperature and the velocity fields in an open cavity under microgravity, 123. TMS Annual Meeting, San Francisco

Kumagai S., Isoda H., 1957, Sixth Symposium (International) on Combustion / The Combustion Institute, 726

Kychakoff G., Howe R., Hanson R., 1984, Quantitative flow visualisation technique for measurements in combustion gases, Appl. Optics 23, 704

Merzkirch W., 1990, in Ruck B. (Ed.): Lasermethoden in der Strömungstechnik, AT-Fachverlag Stuttgart

Ristau R., Nagel U., Iglseder H., König J., Rath H. J., Nomura H., Kono M., Tanabe M., Sato J., 1993, Theoretical and Experimental Investigations on Droplet Evaporation and Droplet Ignition at High Pressures, Microgravity Science and Technology VI/4, 223-228

Sacksteder K.R., 1990, The Implications of Experimentally Controlled Gravitational Accelerations for Combustion Science, Twenty-Third Symposium (International) on Combustion / The Combustion Institute, 1589-1596

Sato J., 1993, Studies on Droplet Evaporation and Combustion in High Pressures, AIAA Paper No. 93-0813

Starner S. H., Bilger R. W., Dibble R. W., Barlow R. S., 1990, Some Raman / Rayleigh / LIF Measurements in Turbulent Propane Flames, Twenty-Third Symposium (International) on Combustion / The Combustion Institute, 645

Sturm D., Müller R., Meier M., Rath H. J., 1992, Photoinitiated Polymerization of Acrylates in the Absence of Gravitational Forces, Proc. 18th International Symp. on Space Technology and Science, Kagoshima, Japan

Tanabe M., Kono M., Sato J., König J., Eigenbrod Ch., Rath H.J., 1994, Effects of Natural Convection on Two Stage Ignition of an n-Dodecane Single Fuel Droplet, accepted for Twenty-Fifth Symposium (International) on Combustion / The Combustion Institute

Session 7.
Jet and Cross Flows

AN INCLINED TURBULENT JET INTO A CROSS-FLOW OF LOWER DENSITY

Fernando López Peña
Universidad Politécnica de Madrid, Escuela Universitaria de Ingeniería Técnica Aeronáutica
Plaza del Cardenal Cisneros 3. 28040 Madrid, Spain

Tony Arts
von Karman Institute for Fluid Dynamics
Chaussée de Waterloo 72, 1640 Rhode-Saint-Genese, Belgium

ABSTRACT

The flow field generated by an inclined jet coming into a cross stream of lower density is experimentally investigated by means of a two components Laser Doppler Velocimeter. The similarity parameters are selected to correctly simulate the film cooling characteristics observed in a high pressure gas turbine. The study is made in a large flat plate model. The density differences between the coolant and the main flow occuring in the turbine are simulated by using a mixture of air and a heavier gas at the injection. The experimental apparatus, the measurement technique, and a selection of the obtained results are presented. Special emphasis is put on the description of the apparatus specifically developed for the present work. It mainly concerns the coolant flow generation as well as the seeding systems for the jet and for the main flow.

SYMBOLS

I	Momentum flux ratio ($\rho_i V_i^2/\rho_o V_o^2$)
M	Mass flux ratio ($\rho_i V_i/\rho_o V_o$)
R	Density ratio
Tu	Turbulence Level
	Subscripts:
i	At the injection
o	Free stream

1. INTRODUCTION.

The flow field generated by a jet emerging into a main stream is characteristic of many cases of technological interest, such as VSTOL aircraft aerodynamics during take-off or landing, the mixing process taking place in combustors, the dispersal of pollutants in the environment, or the film cooling of gas turbine blades and combustion chambers. These applications, among others, made this type of flows the subject of many experimental, computational and theoretical studies. A summary of the material published about this topic was presented by Marganson (1993). In most of the above mentioned applications the injected and mean flows have different densities. This difference in density affects the injected flow momentum and, consequently, the flow field characteristics are modified. Despite the similarities existing between the above listed applications, the variation of some parameters may drastically change the character of this type of flows. This is, for instance, the case of the injection through an orifice in a wall versus the injection through a long chimney into the atmosphere. In the former case the presence of the wall and the interaction between the injected flow and the incoming boundary layer strongly characterize the flow while in the latter case both influences simply do not exist. The complex topology of the main flow field generated by a jet emerging from a hole in a wall into a cross stream has been described, among other authors, by Andreopoulos and Rodi (1984). The description of the instantaneous flow field corresponding to the application under investigation in the present contribution is given by Kelso et al. (1993).

An experimental study on this type of flow field is presented here. Similarity parameters are chosen to approach those observed in the cooling of high pressure gas turbine blades. In a gas turbine blade, the differences in temperature between the coolant and the main flow can produce a ratio of densities as high as 2. In the present investigation this difference on densities is achieved by using a mixture of air with a heavier gas at the injection. The use of gases with different compositions for the injection and the mean flows prevents the employ of hot-wires to perform aerodynamic measurements because in such a situation the hot wire heat transfer depends upon more than one independent variable. The logical choice is therefore a Laser Doppler Velocimeter. A two components LDV, provided by DANTEC, was used.

2 EXPERIMENTAL APPARATUS.

The Low Turbulence Win Tunnel (LT1) of the von Karman Institute was used to perform the present experimental investigation. It is an aspirating open type wind tunnel with a 0.35 m x 0.8 m x 2 m test section. The test surface was an instrumented flat plate, installed into the test section. The injection was made through a hole drilled along the central line of the plate. The injected fluid was a mixture of air with a heavier gas. The gas selected for this purpose is SF_6. A schematic view of the installation is presented in Figure 1. The

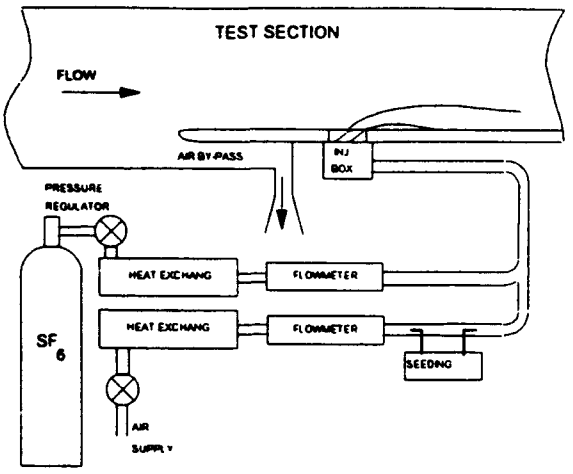

Fig. 1 Generation of the coolant flow.

mass flow and density of the mixture could be independently selected by changing the flow rates of the air and the SF_6. Two valves were used to regulate these flow rates. Each valve was mounted in series with a heat exchanger and a flowmeter. The heat exchangers were used to reduce the drop in temperature caused in the working gases by their expansion from the supply. The flowmeters, of the laminar type, are used to control the flow rates. The particles seeding system will be described in a further section.
The following operating conditions were selected:

- 5 m/s wind tunnel air velocity.
- Ejection hole of 12 mm of diameter and inclined 35 degrees.
- 4×10^3 Reynolds number.
- 9 mm thick incoming laminar boundary layer.
- Turbulent jet.
- 1, 1.5 and 2 ejection to main stream density ratios.

The use of laminar oncoming boundary layer and flow interacting with a turbulent jet allows an easy discrimination of the flow region affected by the coolant injection by measuring the turbulence intensity. This latter will be the only parameter used in the present paper for the discussion of the results. Other aspects of this investigation were discussed earlier by the present authors (1993). Pietrzyk et al. (1989) and Sinha et al. (1990) performed a similar investigation but they considered a turbulent incoming boundary layer.

The measurements were made with a two-component fiber optic LDV system from DANTEC. This system was operated in a two color mode with beam wavelength values of 514.5 nm and 488.0 nm. It was driven by a Spectraphysics 2016 Argon Ion laser with a 5W output power. A frequency shift of 40 MHz was introduced in one beam of each component. Two burst spectrum analyzers (BSA) were used for Doppler signal processing. These commercial LDV processors do not work directly on the Doppler signal but on its power spectrum. Information about the operating principle of these processors is given by Lading (1987).

Measurements with the LDV system were performed for different coolant flow conditions in planes normal to the jet. Since the generated flow field is clearly three dimensional, all measurement points were interrogated two times; once from one side of the test section and once again with the optical probe placed inside the test section, downstream of the ejection hole. In this way the three dimensional flow field could be quantified with a two components measurement system. Unfortunately, one of the shear stresses could never be measured with this procedure while, on the other hand, one velocity component and one normal stress were measured twice. Two different focusing lenses were used with the emitting-receiving optical probe. A lens of 600 mm focal length was used to measure through the facility lateral wall and a second lens of 400 mm focal length was used to measure inside the test section. The first lens focal length allows to measure further than the middle of the test section, while the smaller diameter of the second lens minimized the flow perturbation and the blockage effects inside the facility. Two independent traversing mechanisms were developed to position the probe. The first mechanism was placed at the lateral wall and the second is on top of the test section. Both mechanisms allowed the positioning of the probe along three axis. The positioning along the vertical axis was electrically controlled whereas the displacements along the other two axis were performed manually. The displacement precision was 0.5 mm following the facility main axis and 0.02 mm along the other two directions.

Two different seeding systems were simultaneously in use (Fig. 2). One seeded the air in the mainstream and the other seeded the gas mixture of the jet. Both seeding system were specifically designed for this application. Special care was taken in obtain similar particle size distribution and density of particles in both seeded flows. A bias error would otherwise appear in the measurements along the mixing layer where particles coming from both generators are present. The mainstream seeding was made with small dropplets obtained by condensation of propylene glycol. A mixture of propylene glycol and air was sprayed on top of a heated plate inside the particle generator. The vapor was collected and sent through a large flexible pipe into an array of vertical tubes located in front of the inlet of the wind tunnel. These tubes were perforated along their length with holes of 4 mm of diameter, their spacing was 80 mm. The air-glycol vapor came out through these holes and condensed in the atmosphere. In this way a cross sectional area of 600 mm x 600 mm was correctly

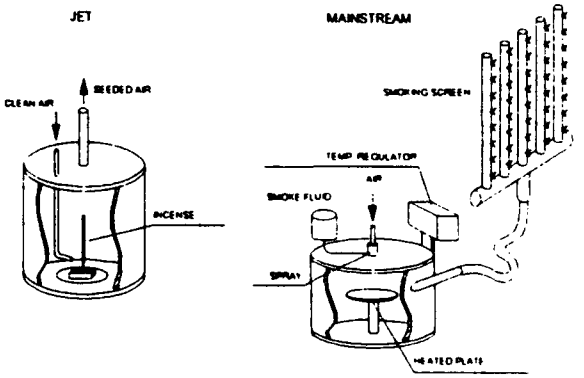

Fig. 2 Particle generators.

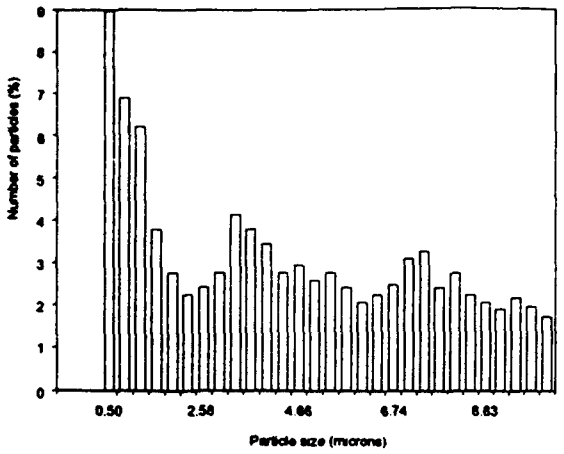

Fig. 3 Particle size distribution in normal burning of incense.

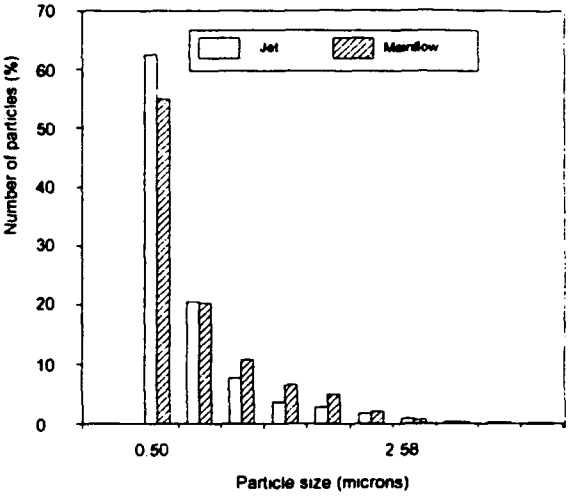

Fig. 4 Particle distributions in the jet and in the mainstream.

seeded. The second particle generator, used for the jet, was an incense burner modified as a cyclone. Normal burning of incense produces a wide range of particle sizes as shown in Figure 3. The air entered the generator tangential to the periphery and produced a cyclone effect to suppress all particles except the ones of smaller size. The particle size distribution of both seeding systems is shown in Figure 4. They were measured using a Phase Doppler Particle Analyzer (PDPA) from Aerometrics. The close similarity between both distributions indicates that the cyclone in the incense burner was working properly.

3 RESULTS

Measurements were performed in one half of the jet cross section at several positions downstream of the injection. Three different jet to mainflow density ratios (1.0, 1.5 & 2.0) and various mass flow ratios were considered. The characterization of the flow field within each measurement plane was obtained after composing the information taken from the two sets of measurements (from the lateral and downstream probe positions) as explained before. A total of 82 cross planes were surveyed, corresponding to different streamwise positions or different flow conditions. All these measurements were summarized in a graphical data base to facilitate the data analysis and allow easy comparisons. This graphical data base has been published earlier by the first

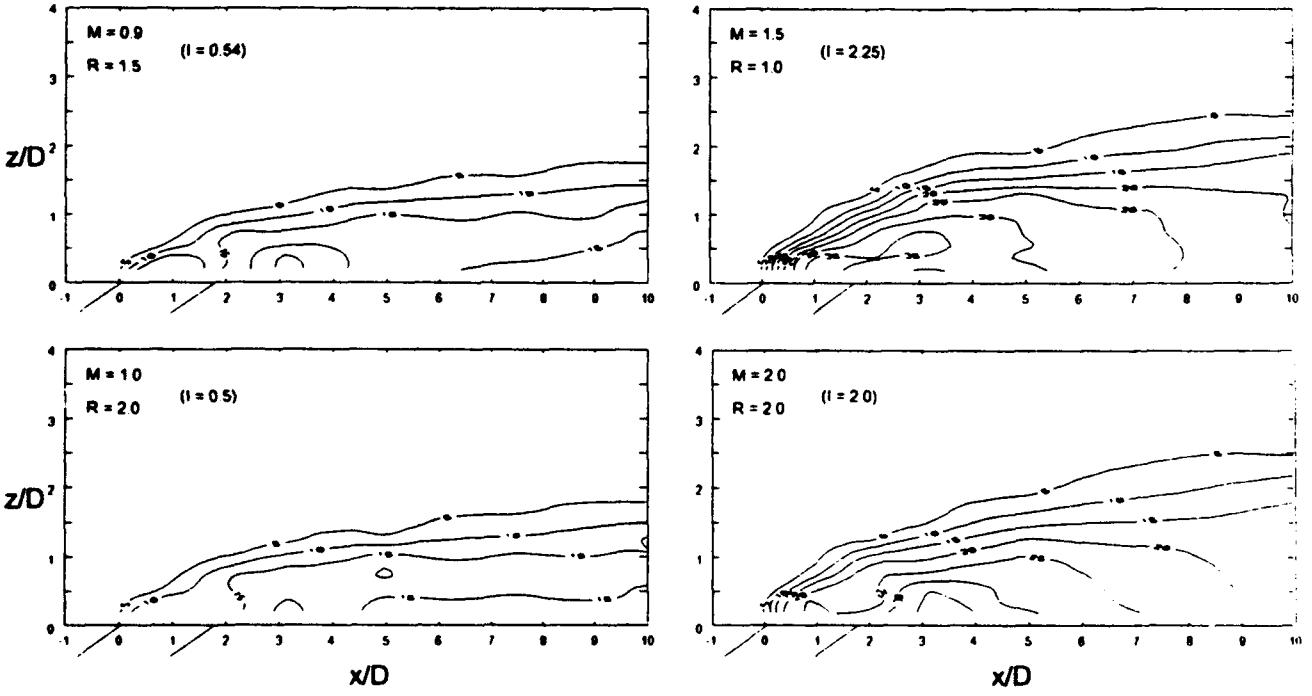

Fig. 5 Turbulence intensity along the meridional plane of jets with differnt coolant flow configurations.

measurements were taken along the jet meridional plane for different coolant flow conditions.

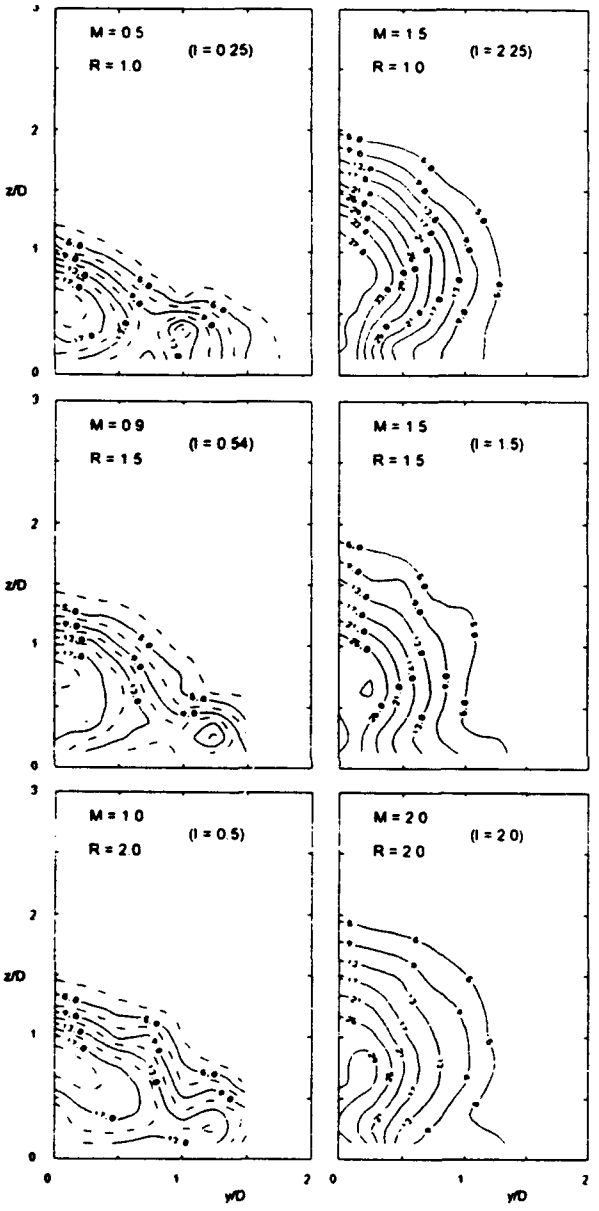

Fig. 6 Turbulence intensitfy in cross sections at 5 diameters downstream o the injection site.

The use of different density ratios allowed to distinguish between the mass flux ratio and the momentum ratio effects. Figure 5 represents the turbulence intensity along the jet meridional plane for four different flow conditions. The two cases in the upper part correspond with jets of mass flux ratios (M) equal to 2.0 and 1.5, and density ratios (R) equal to 2.0 and 1.0, respectively. The only flow parameter having similar values in both cases is the momentum flux ratio (I = 2.0 and I = 2.25 respectively). Despite the apparent differences in the flow regimes, the turbulence level patterns are quite similar. The two cases represented in the bottom of the figure correspond to mass flux ratios (M) equal to 1.0 and 0.9, and density ratios (R) equal to 2.0 and 1.5, respectively. The represented patterns are quite similar, the momentum flux ratio is again conserved in both cases (I = 0.5 and I = 0.54. respectively). Additional flow conditions were checked and similarities in the turbulence level distribution were always found when the momentum flux ratio value was conserved from one configuration to the other. It was therefore concluded that the momentum flux ratio is the parameter that correlates in the best way the jet penetration into the main stream.

The analysis of the measurement results in the cross planes indicates that the momentum flux ratio is again the parameter which provides the best correlation for the lateral spreading of turbulence. This can be verified in Figure 6 which shows isolines of turbulence intensity in a cross section located at five hole diameters downstream of the injection site for six different jet flow conditions. Only one half of the cross section is displayed, the vertical axis corresponds to the meridional plane of the jet. Two cases are considered for each of the three values of density ratio used in the present investigation (R = 1, 1.5, and 2). The density ratio (R), the mass flux ratio (M), and the corresponding momentum flux ratio (I) are quoted in each graph. There are three cases with a momentum flux ratio value lower than unity, and all three present a turbulent spot growing on the side of the jet itself. This turbulent spot is present in all cases characterized by a momentum flux ratio value lower than unity. The center of this turbulent spot appears at approximately y/D=1.3 and z/D=0.25, and is still identified 10 diameters downstream of the injection site as it has been shown by the authors (1993). This lateral spreading of turbulence is never observed to be present in configurations with momentum flux ratio values greater than unity. The preceding observations indicate that the high momentum jets break through the boundary layer and produce a large interaction with the free stream, while low momentum jets remain confined in the low levels of the boundary layer, producing a wide and spreaded interaction with this boundary layer. Figure 7 represents distributions of turbulence level at x/D=20 for two cases of single jets of air (R=1) with mass flux ratios (M) equal to 0.5 and 1.5 respectively. For the case of momentum flux ratio value lower than one (I=0.25), the turbulent spot present at x/D=5 has disappeared. Instead, a wide lateral spread of turbulence is present. The case of high momentum flux ratio (I=2.25) presents the perturbation zone that extends laterally till y/D=2.5. Outside this region the boundary layer remains laminar. The difference of maximum turbulence intensity between the two cases is less than 2% while for the same conditions at x/D=5 (Fig. 6) this difference is larger than 5%. This observation is consistent with the decay and increase in uniformity of turbulence intensity observed in the measurements in the z-x plane with increasing distance from the injection site

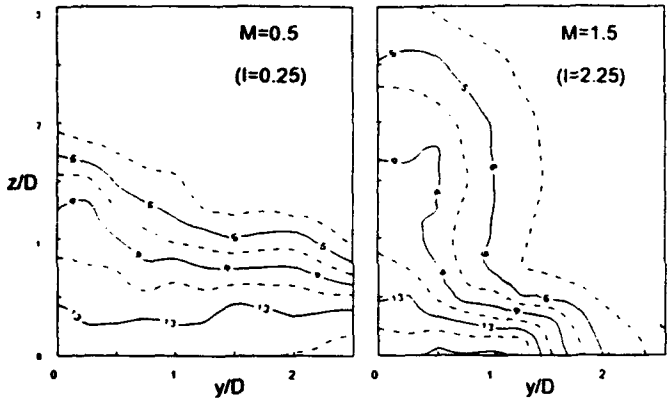

Fig. 7 Turbulence intensity in cross sections at 20 diameters of the injection site.

4 SUMMARY.

An experimental investigation on a subsonic slanted circular turbulent jet coming from a wall into a laminar cross flow of lower density has been presented in this paper. Measurements were taken with a two components fiber optic LDV system. Details about the implementation of this hardware and about the two particle seeding systems developed for this investigation have been also presented. Two sets of experimental results have been shown, the first one represents measurements taken along the jet meridional plane, and the second one represents measurements along the jet cross section. The analysis of the data indicates that the momentum flux ratio is the parameter that correlates in the best way the jet penetration into the cross flow. It has been found that for momentum flux ratio values lower than one the jet remains mainly inside of the boundary layer and induces a lateral spread of turbulence downstream of the injection location. On the contrary, when the momentum flux ratio value is larger than one, the jet breaks through the boundary layer and interacts with the main flow. In this latter case the boundary layer downstream the injection remains laminar except in a narrow region near the jet meridional plane.

ACKNOWLEDGEMENTS

The authors want to thank DANTEC Measurement Technology A/S for providing the Laser Doppler Anemometer used to perform the measurements for the present investigation.

REFERENCES.

Andreopoulos, J. & Rodi, W. 1984, Experimental Investigation of Jets in a Cross Flow, Journal of Fluid Mechanics, vol. 138, no 1, pp. 93-127.

Kelso, R. M., Delo, C. & Smits, A.J. 1993, Unsteady Wake Structures in Transverse Jets, in Computational and Experimental Assessment of Jets in Cross Flow, AGARD CP-534, ref. 4.

Lading, L. 1987, Spectrum Analysis of LDA Signals, Proc of an International Specialist Meeting on The use of Computers in Laser Velocimetry, Saint-louis, ISL-R 105/87, ref. 20.

López Peña, F. 1992, Aerodynamic Aspects of Film Cooling, Ph.D. thesis, Université Catholique de Louvain, Louvain la Neuve, Belgium.

López Peña, F. & Arts, T. 1993, On the Development of a Film Cooling Layer, in Heat Transfer and Cooling in Gas Turbines, AGARD CP-527, ref. 36.

Margason, R. J. 1993, Fifty Years of Jet in Cross Flow Research, in Computational and Experimental Assessment of Jets in Cross Flow, AGARD CP-534, ref. 1.

Pietrzyk, J. R., Bogard, D. G. & Crawford, M. E. 1989, Hydrodynamics Measurements of Jets in Crossflow for Gas Turbine Film Cooling Applications. ASME Journal of Turbomachinery, vol. 111, pp. 139-145.

Sinha, A. K., Bogard, D. G. & Crawford, M. E. 1990, Gas Turbine Film Cooling: Flowfield Due to a Second Row of Holes, ASME paper 90-GT-44.

NON-CIRCULAR TURBULENT JETS IN A CROSS FLOW

V. Sivadas*, B.S. Pani*, and K.A. Bütefisch**

* Dept.of Civil Engg.
IIT
Bombay, India

** SM - ES
DLR
Göttingen, Germany

SUMMARY

Experiments were conducted in a low-speed wind tunnel to understand the contrast between non-circular and circular turbulent jets in a cross-flow. The investigation involved flow conditions of incompressible momentum jets with exit Reynolds number in the range of 4500 to 9200. The study included the range of velocity ratios from 3.8 to 7.7 and is confined to the zone of established flow. The time-mean and statistical characteristics of the flow field were measured by a 3-component LDA. The study revealed that the flow field down stream of rectangular deflected jet was more asymmetric than a circular case and the tendency to acquire self-similarity of mean velocity profiles is relatively weak.

1. INTRODUCTION

Turbulent jets discharging from circular outlets at an angle to a moving stream are of practical significance and have received a reasonable amount of attention in the past Rajaratnam (1976). Examples of this flow can be found in waste disposal into water bodies and the atmosphere, V/STOL aircraft in transition flight, and turbomachinery. Most of the existing work on deflected jets was concerned with the interaction of a circular jet with a free stream, Keffer and Baines (1963). The jet issued either from an exit, set flush with a surface, or from the end of a pipe immersed in the stream. However, studies on non-circular jets were limited to either qualitative information about the associated vortices, Wu *et al* (1988), or deflected jet trajectories and the plate surface pressure distribution, pertinent to the V/STOL problem, Wu *et al* (1970).

The primary objective of the present study was to distinguish the exit geometry effect on the transverse jet development in the zone of established flow for a range of jet to free stream velocity ratios R. The characteristic properties studied are the similarity of mean velocity profiles and turbulence intensity distributions. The flow field being very complex, but quasi steady, the use of the LDA seems most appropriate for measurements.

The measured instantaneous velocity data in the cartesian system were converted into the curvilinear co-ordinates along the jet centre line by a matrix transformation. By this approach, the present study extracted the actual jet velocity field from this strongly three dimensional flow domain, in a direction orthogonal to the trajectory. The discharge coefficient of each of the nozzles in the range of exit jet velocities investigated were obtained from laser light sheet visualization coupled with image processing.

2. EXPERIMENTAL SETUP

The experimental studies were conducted in a low-speed wind tunnel of DLR-Göttingen. This tunnel is of a open-circuit blowing type. It had a rectangular test section of dimensions, 45 cm in length and 30 cm x 30 cm in cross-section. Specific features of this tunnel are its low free-stream turbulence level and the ease of access for high quality flow visualization.

Figure 1 shows the present experimental setup. Optical access for visualization of jet cross-sections and LDA measurements were provided through a plexiglass wall of the test section. However, in order to illuminate the entire flow field along the direction of the deflected jet trajectory, the light sheet apparatus was initially kept at the downstream end of the tunnel as shown in the above figure. Using this arrangement the deflected jet centre-line was obtained.

The jet stream was supplied with air flow from the compressed air system available in the laboratory. The static pressure and temperature of the flow in the settling chamber of the nozzle were continuously monitored by a pressure sensor and a PT-100 temperature probe. This way the conditions at the nozzle exit was set to obtain the desirable velocity ratio values, while keeping the tunnel flow fixed at 4.6 m/sec.

To minimize the tunnel boundary layer effect at the jet exit, the nozzles were flush mounted on a circular flat plate with a streamlined edge placed 2 cm above the test section bottom. A 10 mm diameter hole in the centre of this plate accepted different nozzle blocks which could fit flush with the plate surface. It was possible to rotate the plate and get different orientations of the nozzle with respect to the free stream flow direction, Figure 2. It may be noted that the two jet exit configurations chosen represent different ratios of jet perimeter to jet width with respect to the deflecting stream. Each of these nozzles possesses an equivalent physical area of 11.9 mm^2 at the outlet. Reynolds number for the respective jets were based on the corresponding

effective jet diameter, d_e, and the initial velocity at the exit port.

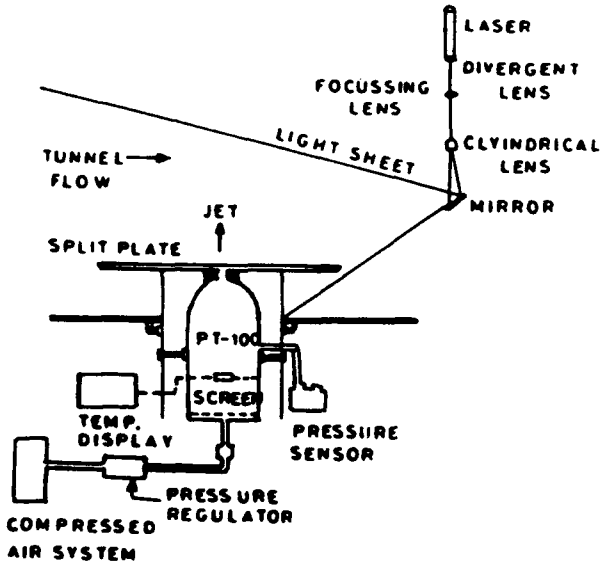

Fig. 1: Schematic diagram of experimental setup and laser light sheet arrangement

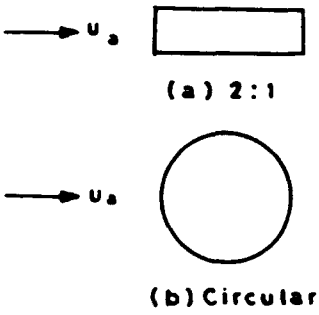

Fig. 2 : Nozzle outlet configuration

3. MEASUREMENT SYSTEM

3.1 Three Component Laser Doppler Anemometer

The present study utilised the 3-component LDA (Ar.ion laser, 4 W) system of DLR-Göttingen. Figure 3 shows schematically the optical arrangement of this dual beam LDA operated in back scatter, off-axis mode Bütefisch (1989). The three components were formed by the individual pairs of laser beam colours green, blue, and violet. The details of the LDA setup are as follows:

Beam-intersection angle, $2\varepsilon_{i=1,2,3} = 8^\circ$
Semi-angle between the two optical axis, $\Psi_i = 11^\circ$
Angle between the horizontal plane of the measuring platform and the measuring plane formed by one pair of beams are, $\eta_{green} = 90^\circ$, $\eta_{blue} = \eta_{violet} = 0^\circ$
Probe-volume diameter, $d_{pv} < 0.1$ mm
Probe-volume length, $l_{pv} = 0.5$ mm
Focal length of the transmitting lenses = 250 mm
Beam-spacing = 35 mm

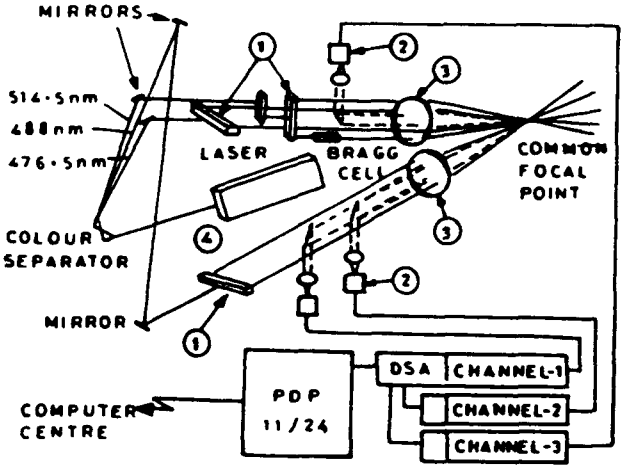

Fig. 3 : Optical arrangement of the three component laser doppler anemometer of the DLR

A Bragg-shift frequency of 40 MHz was applied to one beam of each component. The jet flow was seeded by olive oil particles produced by an aerosol generator attached to the jet flow system. The seeded mean particle diameter varies in the range of 0.8 to 3 μm. The Doppler shift frequency produced by laser light illuminating the solid particle moving with the fluid was measured by DSA-3000 series signal processor.

These frequency domain signal processors use high speed analog to digital converters (ADC) to record the signal. After removing the pedestal component of the Doppler burst, a burst detection scheme was utilised to locate the burst signal which is recorded and stored in memory. A Discrete Fourier Transform (DFT) was then applied to determine the frequency of the signal, provided the signal satisfied the preset signal to noise ratio criteria.In order to acquire reliable data, the correct values of the instrument parameters were set based on the initial estimate of the expected maximum Doppler frequency, ν_d, under the existing optical arrangement and flow conditions. Accordingly, the values for low-pass filter settings and the sampling frequencies were selected by keeping abreast with the criteria for avoiding aliasing and over sampling the signal.

The DSA measured frequency components correspond to the projections of the velocity vector $\vec{V}$ on to the respective axis of a non-orthogonal measuring plane formed by each pair of

laser beams. This had necessitated the transformation of velocity components from non-orthogonal system to orthogonal system with respect to the test section. After that, the orthogonal velocity field was again transformed into the curvilinear co-ordinate system, using the jet centre-line, Figure 4. This transformation was applied to preset number of individual bursts, eg., N=1000, at each measurement location. These operations were carried out by an algorithm presently developed, which also calculated the time-mean and statistical properties of the flow field.

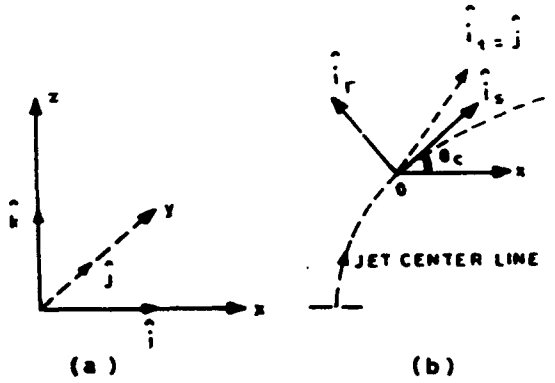

Fig. 4 :(a) Cartesian system
(b) Curvilinear system

4. RESULTS AND DISCUSSION

4.1 Axial Mean Jet Velocity

Figures 5 and 6 present the distribution of the axial component of mean jet excess-velocity along the lateral direction, η-axis, for the flow emanating from circular and rectangular nozzles of aspect ratio 2:1 respectively, deflected by the cross-stream. Each figure contains the velocity distribution measured at nine streamwise sections in the zone of established flow and three velocity ratios were created. It may be noted that the location of the sections along the trajectory was measured from the end of the flow establishment zone, z_o. The measured values are non-dimensionalised interms of the characteristic velocity scale, $(\bar{U}_m - U_a\cos\theta)$, which is the velocity excess at the jet centre, and a characteristic length, $\eta_{1/2}$, which is the jet width obtained from visualization.

From these results it is quite evident that, when the nozzle configuration changes from circular to non-circular ones, the velocity profiles do not seem to satisfy similarity. In other words, self preservation of the mean flow properties for non-circular deflected jets are practically not existing for a significant distance in contrast to the reasonable collapse of the measured data on to a single curve for the circular case. The possible explanations for this behaviour are as follows.

It was evident from Figure 7 that, the mass flux deficiency at the nozzle outlet is a function of exit jet Reynolds number and also the nozzle shape. In other words, the higher mass flux deficiency for a rectangular jet is the manifestation of the initial disturbances produced by the boundary layer and corners inside the nozzle. These disturbances affect the initial flow. So, it is expected that these initial disturbances, increasing with an increase in the exit jet velocity, adversely influence the similarity of the velocity profiles as they propagate down stream. In addition to this, the stronger bound vortex pair associated with a rectangular deflected jet will interact with the axial jet momentum and is also expected to adversely affect similarity. The latter conclusion was based on the present studies on deflected jet cross sections, using laser light sheet visualization coupled with image processing.

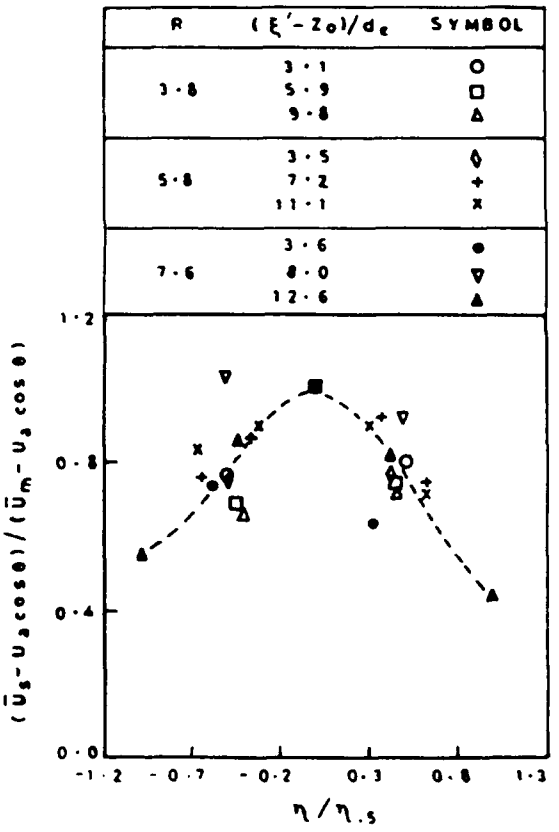

Fig. 5 : Lateral distribution of circular jet velocity

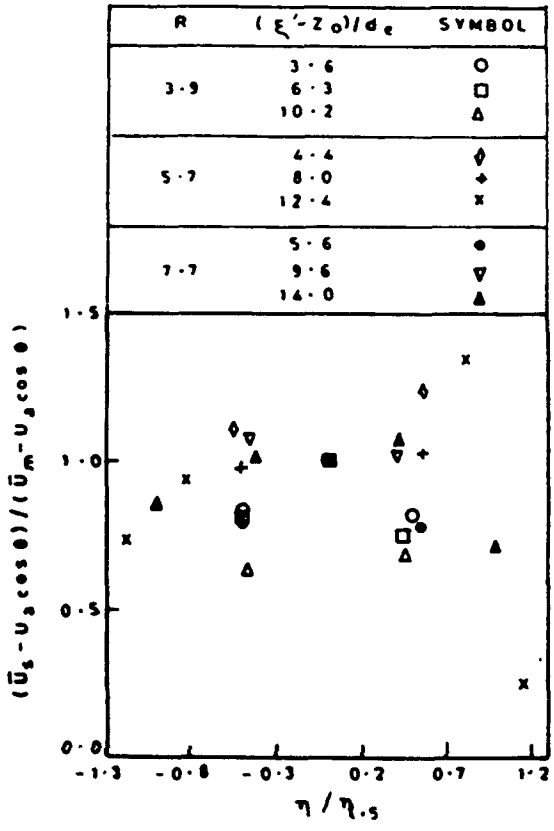

Fig.6 : Lateral distribution of (2:1) jet velocity

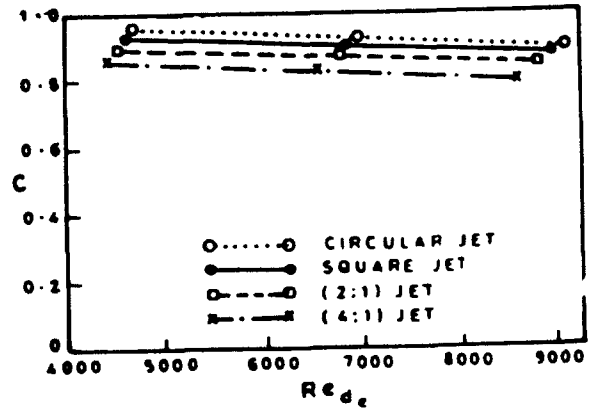

Fig.7 : Discharge coeff. of nozzles

4.2 Axial and Radial Components of Turbulence Intensity

Figures 8 and 9 show the axial component of turbulence intensity ($\hat{i}_s$ direction, Figure 4) distribution along the lateral directions, η-axis, for a deflected circular and a rectangular jet of aspect ratio 2:1 respectively. Each figure contains the measured data at three different sections in the zone of established flow for a specific velocity ratio of approximately 3.8. The measured values are non-dimensionalised in a similar way as was done for the corresponding mean velocity profiles. That is, the characteristic velocity excess at the jet centre, ($\bar{U}_m$-$U_a\cos\theta$), and the characteristic jet width, $\eta_{1/2}$ were used as the scales. In the same manner, the measured radial components of turbulence intensity ($\hat{i}_s$ direction, Figure 4) for the respective above cases were plotted in Figures 10 and 11.

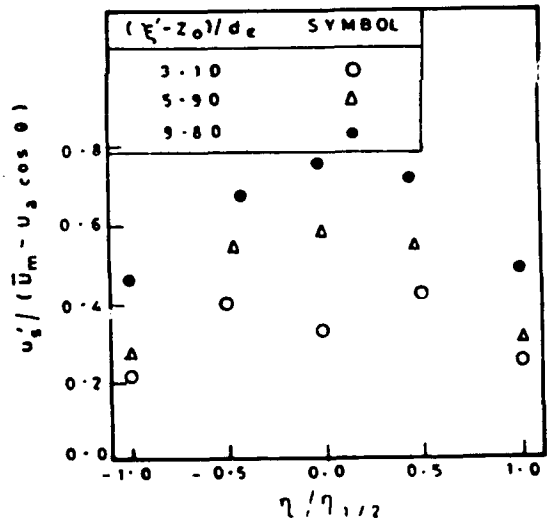

Fig. 8 : Axial turbulence intensity distribution of circular jet (R = 3·8)

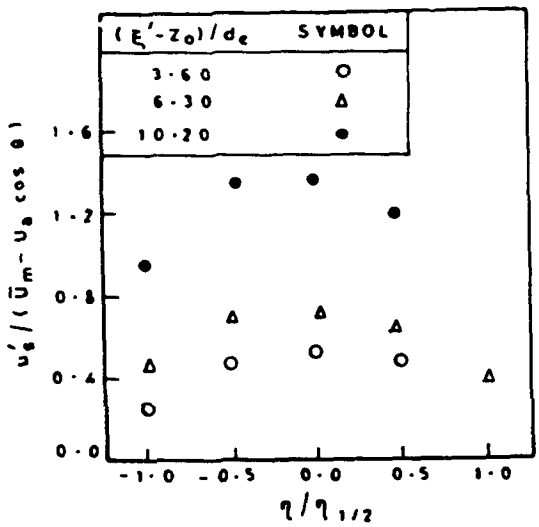

Fig. 9 : Axial turbulence intensity distribution of (2:1) jet (R = 3·9)

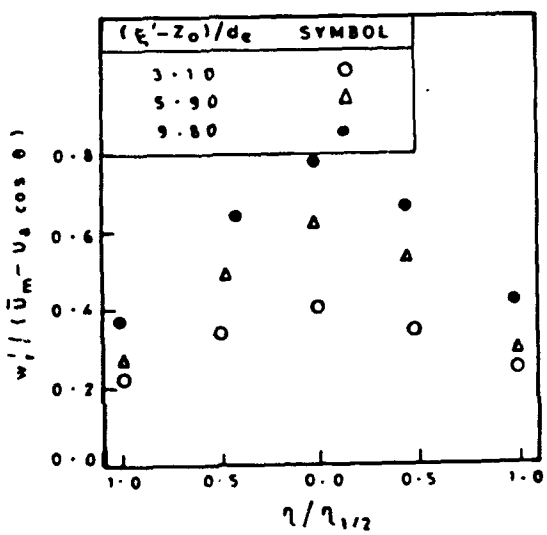

Fig. 10 : Radial turbulence intensity distribution of circular jet (R = 3·8)

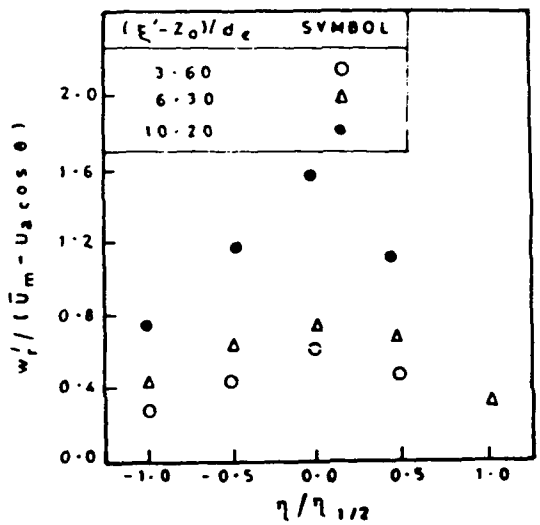

Fig. 11 : Radial turbulence intensity distribution of (2 : 1) jet (R = 3·9)

Table 1 : Comparison of turbulence intensity along jet axis

PRESENT EXPERIMENTAL DATA			KEFFER AND BAINES DATA		
R	ξ'/de	$u_s'/(U_j-U_a)$	R	ξ'/de	$u_s'/(U_j-U_a)$
	3·95	0·250		3·13	0·23
3·8	6·75	0·190	4·0	4·19	0·19
	10·85	0·110		6·83	0·10
				8·83	0·07
	5·5	0·228			
5·8	9·2	0·133		3·72	0·17
	—	—	6·0	5·72	0·10
				7·22	0·07
	6·1	0·195		9·22	0·07
7·6	10·5	0·110			
	15·1	0·088		4·2	0·15
			8·0	6·2	0·12
				7·7	0·10
				9·7	0·07

The results indicate that, the highest turbulence intensity is associated with the rectangular deflected jet of aspect ratio 2:1 compared to the circular case. This can be attributed to the low frequency events or large eddies carried by rectangular deflected jets forming an effective reservoir of turbulent kinetic energy for the generation and sustenance of high frequency fluctuations in the interacting flow field. The augmentation of turbulence level in the down-stream direction, for each of the cases studied, is caused by the enhanced shearing by the free stream on the jet as it propagates down stream. The similarity in the behaviour of the axial and radial components of turbulence intensities could have been caused by the strong entraining flow in the radial direction, characteristic of a bound vortex system associated with deflected jets. Also, it can be an indicator of a resulting isotropic flow field.

Table 1 compares the present turbulence intensity along the axis of circular deflected jet with Keffer and Baines (1963) measurements. The higher values of the present measurement can be attributed to the improved sensitivity of LDA to high frequency events compared to the hot-wire anemometer used in the earlier study, as well as the difference in the velocity ratios.

CONCLUSIONS

The measurements in the zone of established flow for deflected jets using 3-component LDA revealed the following:
1. The flow field down stream of non-circular deflected jets are asymmetric and the tendency to acquire self similarity in mean velocity profiles is relatively weak.
2. Distribution of the axial and radial components of turbulence intensity shows similar behaviour for each of the cases studied and the high turbulence level is associated with rectangular deflected jet.

ACKNOWLEDGEMENTS

We would like to thank Mr.K.H.Sauerland of Institute for Experimental Fluid Mechanics, DLR-Göttingen, for his kind assistance during the development of the LDA set-up.

NOTATIONS

d_e	effective jet diameter at the nozzle outlet
$\hat{i},\hat{j},\hat{k}$	unit vectors in the cartesian system
$\hat{i}_\xi,\hat{i}_\eta,\hat{i}_\zeta$	unit vectors in the curvilinear coordinate system
R	ratio of the jet exit velocity to that of the free stream
U_∞	free stream velocity
$\overline{U}_m$	maximum axial jet velocity
$\overline{U}_o$	mean jet velocity in the axial direction
u_o'	turbulence intensity in the axial direction
w_r'	turbulence intensity in the radial direction
x,y,z	cartesian coordinates
z_o	length of the potential core
ξ	distance measured along the jet axis
θ	angle of the deflected jet with free stream direction based on the jet axis
θ_c	angle of the deflected jet with free stream direction based on the jet centreline
η	locus of maximum velocity along lines of constant y in a plane perpendicular to the axial stream-line

REFERENCES

Bütefisch,K.A. 1989, 3-Component Laser Doppler Anemometry in Large Wind Tunnels, Prog.Aerospace Sci., Vol.26, pp. 79-113.

Keffer, J.F. & Baines, W.D. 1963, The Round Turbulent Jet in a Cross Wind, Journal of Fluid Mechanics, Vol. 15, pt.4, pp.481-496.

Rajaratnam, N. 1976, Turbulent Jets,, Elsevier, New York.

Wu, J.C., Mc Mahon, H.M., Mosher, D.K. & Wright, M.A. 1970, Experimental and Analytical Investigations of Jets Exhausting into a Deflecting Stream, J. Aircraft 7 (1), pp. 44-51.

Wu,J.M., Vakili,A.D. & Yu,F.M. 1988, Investigation of the Interacting Flow of Non-Symmetric Jets in Crossflow, AIAA Journal, Vol.26, No.8, pp. 940-947.

POWER SPECTRA OF THREE-DIMENSIONAL TURBULENT NONREACTING FLOW IN A DUCTED COMBUSTOR

Tong-Miin Liou Yi-Yung Wu Hsin-Li Lee

Department of Power Mechanical Engineering
National Tsing Hua University, Hsinchu, Taiwan 30043, ROC

ABSTRACT

The present work describes an experimental investigation of the flowfield and spectral characteristics of a three-dimensional isothermal turbulent flow in a chamber with one axial inlet and two side inlets by the use of laser-Doppler velocimetry and microphones. The momentum ratio of the axial inlet jet to side inlet jets was chosen to be 0.2 and the Reynolds number, based on the chamber bulk mean velocity and height was 5.9×10^4. The mean flow quantities were first measured to give an understanding of the mean turbulent flow structures resulting from jet expansion and impingement of multiple inlet jets in the present ducted flow. Subsequently, power spectrum measurements of velocity and pressure fluctuations were performed to investigate the oscillatory behavior of the multiple jet flows in the present combustor. The results show that the low frequency axial and transverse oscillations for the axial jet and the side jets, respectively, exist in the combustor. Moreover, the preferred mode of the axial jet and the oscillation of the impingement of the side-inlet flows upon the spanwise walls are found.

1. INTRODUCTION

The flowfield and spectral characteristics in a ducted chamber with one axial and dual side rectangular inlets are investigated experimentally in the present work using laser-Doppler velocimetry (LDV) and microphones. In practical applications, the simulated chamber is related to a solid-propellant ducted rocket (SDR) combustor. Under a sustaining operation of the SDR, the fuel-rich gas plume exhausted from a solid-propellant gas generator mixes and reacts with the side-inlet air flows. Flow impingement, recirculation, and oscillation in this type of flow field are closely related to the combustor performance. To achieve a high combustion efficiency, good mixing and flame holding in the combustors are required. Some important information on this topic has been reported by several researchers (Chuang et al., 1989; Hseih et al., 1989; Liou and Wu, 1993; Schadow and Chieze, 1981). Another aspect of the present flowfield with jet impingement is the flow oscillation. Oscillation of impingement flows occurs frequently in a widely variety of inner and outer flow configurations and provokes noises, structure loading and combustion instabilities (Clark, 1982; Rockwell and Naudascher, 1979; Rockwell, 1983). Occurrence of energetic flow and pressure oscillations in the investigated combustors will result in a serious reduction in the combustion performance if the coupling between the flow and combustor builds up (Dunlap and Brown, 1981; Byrne, 1983) or proper acoustical forcing is exerted (Schadow et al., 1987). However, relevant spectral analyses of the impingement flow field in the simulated SDR combustor are relatively sparse.

Based on the above brief survey, it is suggested that an improved understanding of the impingement of multiple jets in the ducted flow is needed in enhancing fluid mixing and avoiding combustion instabilities, and the pertinent spectral analyses in the literature are lacking. It is this fact motivating the present study in which the flow oscillation in a ducted combustor with dual side inlets and one axial inlet is examined by analyzing the LDV measured velocities and wall pressures power spectra of fluid.

2. EXPERIMENTAL SETUP AND CONDITIONS

The overall experimental system included the optical system, the signal processing system and the flow system. For the flow system, the side-inlet air streams were drawn into the test chamber through settling chambers, honeycombs and the screens, and 5:1 contraction by a 10-Hp turbo blower located at the downstream end. The axial jet was ejected from a 23:1 contraction by another 5-Hp turbo blower located upstream of the axial inlet. The air in the chamber then was exhausted through the square duct, a flow straightener, a rotameter, and a bellows, by the downstream 10-Hp turbo blower. In between the test duct and the blower there was a noise reduction chamber with the dimension of $100 \times 130 \times 80$ cm^3 to reduce the blower generated passage and mechanical vibration noise.

The schematic drawing of the configuration, coordinate system, and dimensions of the test model is shown in Fig. 1. The three-dimensional model consisted of a square cross-sectional combustor chamber (100 mm × 100 mm), two squares cross-sectional side-inlet ducts (50 mm × 50 mm) and a rectangular cross-sectional axial nozzle with an aspect ratio of 3:1 (6 mm × 18 mm). The two side-inlet ducts intersected the chamber walls at a right angle and were aligned carefully at the same streamwise position, while the single axial inlet was located at the head plate and directed along the chamber center axis. The rectangular cross-section of the axial inlet instead of a round or square one was utilized in the present work since mixing enhancement by using non-axisymmetric jets, such as the elliptic and rectangular jets, has been reported by many researchers (e.g. Ho and Gutmark, 1987; Lee and Baek, 1993). However, many of these works were made for free jets. One of the purposes of the present work is to study the development of the confined non-axisymmetric axial jet and the interaction between the axial and side jets.

A four-beam two-component laser-Doppler velocimetry set up in a backscatter configuration ,described in detail in the works of Liou and Wu (1993a) and Liou et al. (1990) was employed to measure the velocity in the combustor model. The probe volume dimensions, based on $1/e^2$ extent of light intensity, were approximately 0.06 mm by 0.65 mm and 0.13 mm × 3.6 mm for 480-mm and 1200-mm focal-length lenses, respectively. The saline particles with a nominal 1 μm were generated by the atomizers and introduced into the air streams to scatter light as the particles passed the probe volume.

Owing to the nature of the random arrival of seeding particles at the measurement volume, the power spectrum and the correlation of the LDV signals cannot be obtained directly by use of the conventional FFT algorithm, which is valid for signals with constant time intervals. There are several approaches to obtain the power spectrum of LDV signals (Tropea, 1987). In this paper, a sampled and held D/A converter circuit was employed and the converted analog output was processed by using a FFT analyzer to obtain the spectra. In this approach the high arrival rate of Doppler burst signals (or particle rate) is a crucial condition to acquire the bias-free spectral estimates. In order to avoid the step noise arising in the low arrival rate condition (Adrian and Yao, 1987), the required particle rate should not less than the reciprocal of the integral time scale. In the present experiment, the integral time scale is about 10^{-3} second. After examination of the measured spectra at various particle rates, it found that the levels of spectral peaks approached invariant as the particle rate was higher than 5,000 numbers/sec. Therefore, the adequate particle rates were controlled at about 10,000 numbers/sec during the measurements.

The wall pressure was measured using a Kulite microphone (MIC-190-140) with 1.8 mm active diameter and 100 KHz mechanical resonant frequency. The microphone was attached to pressure taps with 0.3 mm internal diameter. The signal obtained was amplified and properly filtered by a signal conditioner (CDV-230C, Kyowa). The power spectrum of the wall pressure analyses was conducted by a dual-channel FFT analyzer. At each measured position ensemble average of 256 spectra was made to reduce variations of the estimated spectra.

In the present investigation, the momentum ratio of axial jet to side inlet jets and the chamber bulk mean velocity were 0.2 and 9.3 m/s, respectively. Reynolds number, based on the combustor height and bulk mean velocity, was 5.9×10^4. More detailed inlet conditions for the axial and side inlets have been described in the previous work (Liou and Wu, 1993b).

3. RESULTS AND DISCUSSION

Mean Flow Patterns

Figure 2 shows the mean flow patterns in two vertical planes, $Z^*=0$ and $Z^*=-0.5$, and two horizontal planes, $Y^*=0$ and $Y^*=-0.5$ ($X^* \equiv X/H_c$, as $X>0$; $X^* \equiv X/L_d$, as $X \leq 0$, $Y^*=Y/H_c$, $Z^*=Z/H_c$), in terms of vector diagrams. In the central vertical plane ($Z^*=0$), Fig. 2(a), shows that for the present momentum ratio the central part of the high velocity axial jet penetrates through the side jets and the interaction of these jets forms a clockwise vortex at ($-7<X^*<0$, $-0.6<Y^*<-0.2$, $Z^*=0$) of the dome region ($-1<X^*<0$). In the quarter vertical plane ($Z^*=-0.5$, Fig. 2(b)) which cuts through the edge of the side-inlet port, the velocity vectors near the side-inlet port have larger axial components than those in the $Z^*=0$ plane. Figure 2(c) shows a clockwise vortex located in the dome region in the $Y^*=0$ plane and the strengths of the vortex become weaker in the $Y^*=-0.5$ plane (Fig. 2(d)). Also notice that the mean velocities in the dome region (Fig. 2) are generally very small, except for the axial jet, and therefore suitable for flame holding. On the basis of above description, the development of the axial jet and the impingement of the axial jet upon the side jets are two important features in the present three-dimensional ducted flowfield. In addition, the bimodal-shaped velocity histograms found in the impingement zone indicate the existence of the organized oscillating structures (Liou and Wu, 1993b). This dynamic behavior of the oscillation of the axial-inlet jet was further investigated by means of spectral methodology in the next section.

Spectral Characteristics

The velocity spectra for the axial and transverse fluctuations measured along the combustor central axis are depicted in Fig. 3(a) and Fig. 3(b), respectively. A very low frequency peak of 37.5 Hz is found in the axial velocity spectra, Fig. 3(a), from $X^*=-0.95$ to -0.87 and this peak

smears as $X^* \geq -0.83$. However, the peak of 37.5 Hz was not observed in the transverse velocity spectra, Fig. 3(b), at corresponding locations, indicating a low frequency axial oscillation near the axial inlet. On the other hand, for $X^* \geq -0.22$ a peak of 75 Hz appears in the transverse velocity spectra, Fig. 3(b), but not in the axial velocity spectra, Fig. 3(a). The transverse oscillation of 75 Hz is believed to be induced by the side inlet flows. In addition, for the transverse velocity spectra in the range of $-0.74 \leq X^* \leq -0.30$, a high frequency lobe located around 1 KHz, with a corresponding Strouhal number of $S_t = fD_f/U_f = 0.17$ ($D_f \equiv$ hydrodynamic diameter of the axial inlet port), can be observed. It is noted that the onset location of this high frequency lobe coincides with the location of potential core tip ($X^* = -0.76$). Therefore, the lobe tends to be related to the passage of coherent structures, i.e., the so-called preferred mode or jet column mode.

The wall pressure spectral measurements were also carried out at station $X^* = 0.25$, as shown in Fig. 4, in order to investigate the impingement of the deflected side-inlet flows after jet-to-jet collision upon the spanwise walls ($Z^* = \pm 1$). It is first noted that the shapes of spectra are quite symmetrical about $Y^* = 0$. In addition, a clear peak at about 80 Hz is detected at $Y^* = \pm 0.2 \sim \pm 0.5$ and tends to reflect the oscillation of spanwise deflection of the side-inlet flows.

The variations of peak frequency over the periphery of axial-inlet port at different streamwise stations are also examined and plotted in Fig. 5. Marks a, b, c, d, e, and f stand for the axial lines along various peripheral positions, respectively. For the axial velocity spectra, Fig. 5 depicts a peak of f = 37.5 Hz occurs only along line a and near the axial inlet port (empty circles). A peak of f=75 Hz also appears along lines c, d and e, but there are no peak frequencies observed along lines b and f. For the case of the transverse velocity spectra, a low frequency peak of about f = 75 Hz occurs along all the examined lines (a~f) and this oscillatory frequency is associated with the aforementioned bimodal velocity fluctuation histograms. In addition, high frequency peaks are also detected over the range of $-0.74 \leq X^* \leq -0.22$ and the peak frequencies decrease with increasing X^*. For $X^* \geq -0.22$ the high frequency lobe disappears and the peak of 75 Hz remains due to the side-inlet jet oscillation.

4. CONCLUSIONS

The flowfield in a three-dimensional simulated ducted combustor with multiple inlet jets investigated in the present work can be characterized by the dome recirculation, jet-jet impingement and flow developing regions from the measured mean flow patterns as well as by power spectra of velocity fluctuations, the 37.5 Hz axial oscillation associated with the axial jet and 75 Hz transverse oscillation associated with the side jets from the measured. The preferred mode of the axial jet with $S_t = 0.17$ is identified. In addition, the 80 Hz oscillation of the impingement of the side-inlet flows upon the spanwise walls is detected from the wall pressure measurements.

REFERENCES

Adrian, R. J., & Yao, C. S., 1987, *Power Spectra of Fluid Velocities Measured by Laser Doppler Velocimetry*, Experiments in Fluids, Vol. 5, pp. 17-28.

Byrne, R. W., 1983, *Longitudinal Pressure Oscillations in Ramjet Combustors*, AIAA paper 83-2018.

Chuang, C. L., Cherng, D. L., Hsieh, W. H., Settles, G. S., & Kuo, K. K., 1989, *Study of Flowfield Structure in a Simulated Solid-Propellant Ducted Rocket Motor*, AIAA paper 89-0011.

Clark, W. H., 1982, *Experimental Investigation of Pressure Oscillations in a Side Dump Ramjet combustor*, Journal of Spacecraft and Rockets, Vol. 19, No. 1, pp. 47-53.

Dunlap, R. & Brown, R. S., 1981, *Exploratory Experiments on Acoustic Oscillations Driven by Periodic Vortex Shedding*, AIAA Journal, Vol. 19, No. 3, pp. 408-409.

Ho, C. M., & Gutmark, E., 1987, *Vortex Introduction and Mass Entrainment in a Small-Aspect-Ratio Elliptic Jet*, Journal of Fluid Mechanics, Vol. 179, pp. 383-405.

Hseih, W. H., Chuang, C. L., Yang, A. S., Cherng, D. L., Yang, V., & Kuo, K. K., 1989, *Measurement of Flowfield in a Simulated Solid-Propellant Ducted Rocket Combustor Using Laser Doppler Velocimetry*, AIAA paper, 89-2789.

Lee, S. J., & Baek, S. J., 1993, *Near-Field Turbulent Structure of Elliptic Jets*, Ninth Symposium on "Turbulent Shear Flows", August 16-18.

Liou, T. M., Wu, S. M., & Hwang, Y. H., 1990, *Experimental and Theoretical Investigation of Turbulent Flow in a Side-Inlet Rectangular Combustor*, Journal of Propulsion and Power, Vol. 6, No. 2, pp. 131-138.

Liou, T. M., & Wu, Y. Y., 1993a, *Turbulent Flows in a Model SDR Combustor*, Journal of Fluids Engineering, Vol. 115, pp. 468-473.

Liou, T. M., & Wu, Y. Y., 1993b, *Experimental Study on Three-Dimensional Bounded Turbulent Jet Flows*, The Seventeenth Nation Conference on Theoretical and Applied Mechanics, Taipei, Taiwan, ROC, pp. 177-183.

Rockwell, D. & Naudascher, 1979, *Self-sustained Oscillations of Impinging Free Shear Layers*, Annual Review of Fluid Mechanics, Vol. 11, pp. 67-94.

Rockwell, D., 1983, *Oscillations of Impinging Shear Layers*, AIAA Journal, Vol. 21, No.5, pp. 645-664.

Schadow, K. C., & Chieze, D. J., 1981, *Water tunnel and Windowed Combustion as Tools for Ducted Rocket Development*, JANNAF Propulsion Meeting, CPIA-PUB-340, Vol. 2, pp. 101-115.

Schadow, K. C., Wilson, K. J., & Gutmark, E., 1987, *Characterization of Large-Scale Structures in a Forced Ducted Flow with Dump*, AIAA Journal, Vol. 25, No. 9, pp. 1164-1170.

Tropea, C., 1987, *Turbulence-Induced Spectral Bias in Laser Anemometry*, AIAA Journal, Vol. 25, No. 2, pp. 306-309.

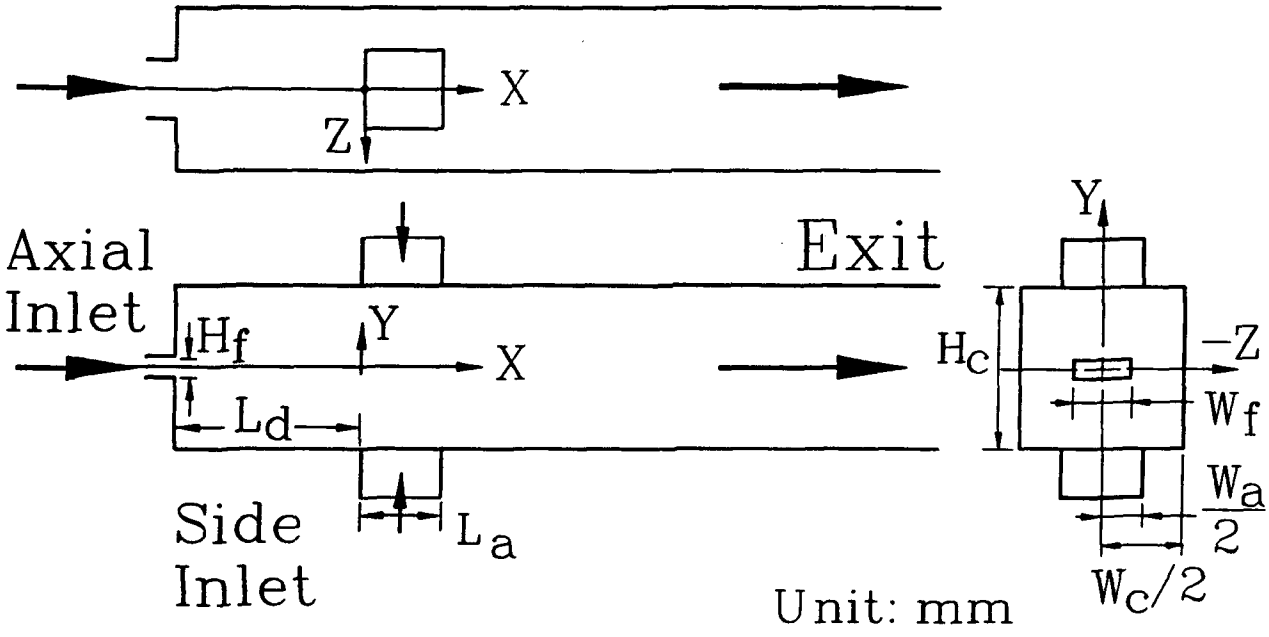

H_c	W_c	W_a	L_a	W_f	H_f	L_d
100	100	50	50	18	6	115

Fig. 1 Sketch of configuration, coordinate system, and dimensions of test model

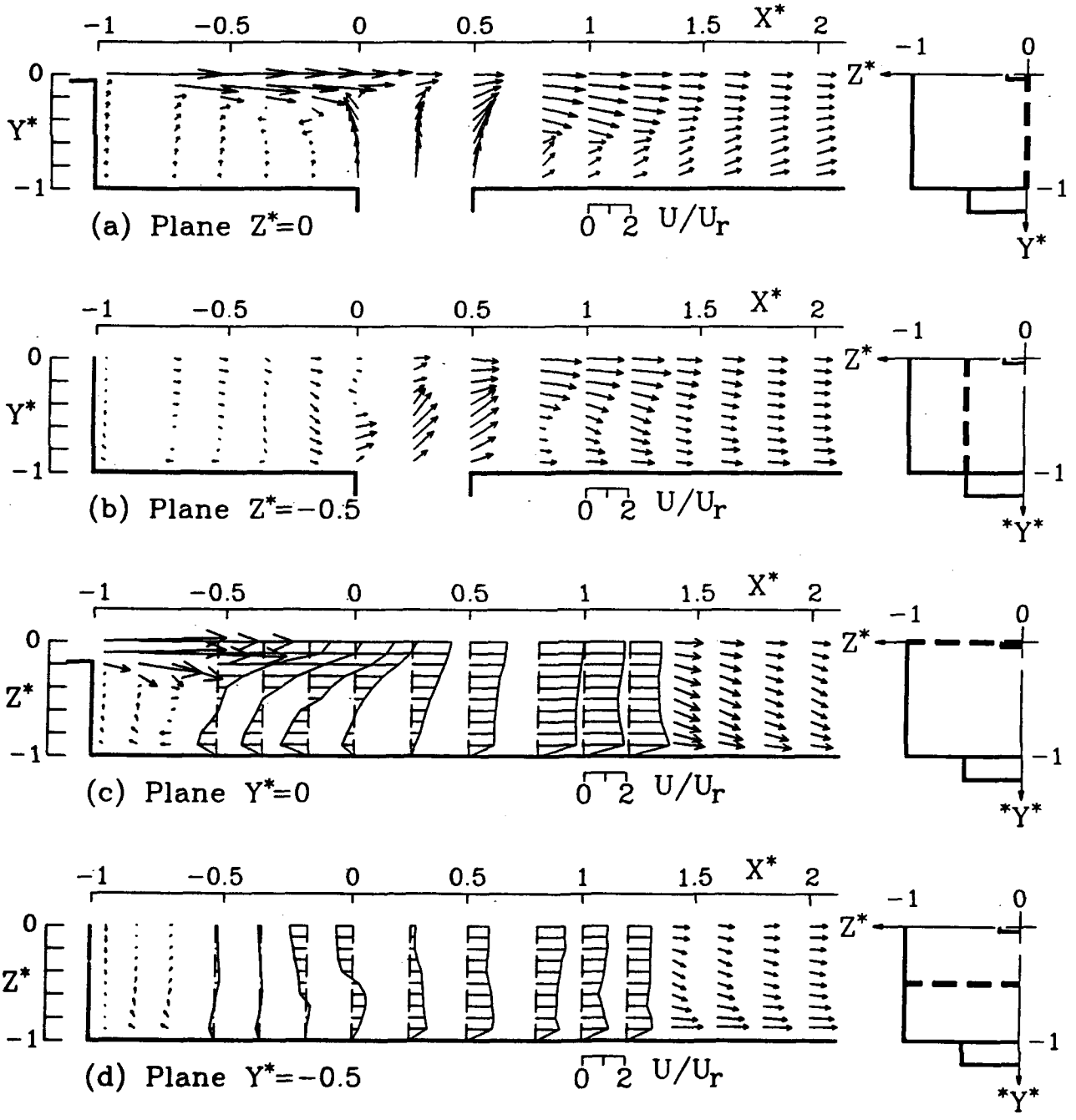

Fig. 2 Mean flow patterns for (a) Z^*=0, (b) Z^*=−0.5, (c) Y^*=0, and (d) Y^*=−0.5 planes

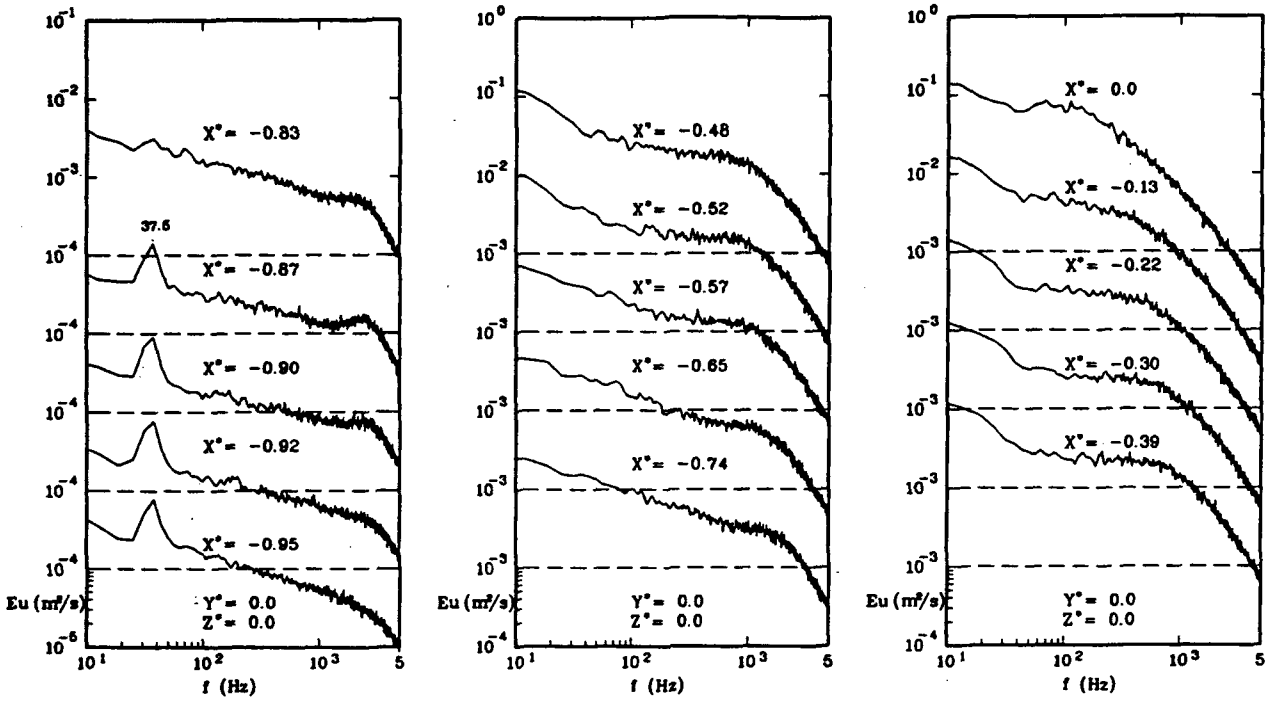

Fig. 3(a) Axial velocity spectra along combustor center axis

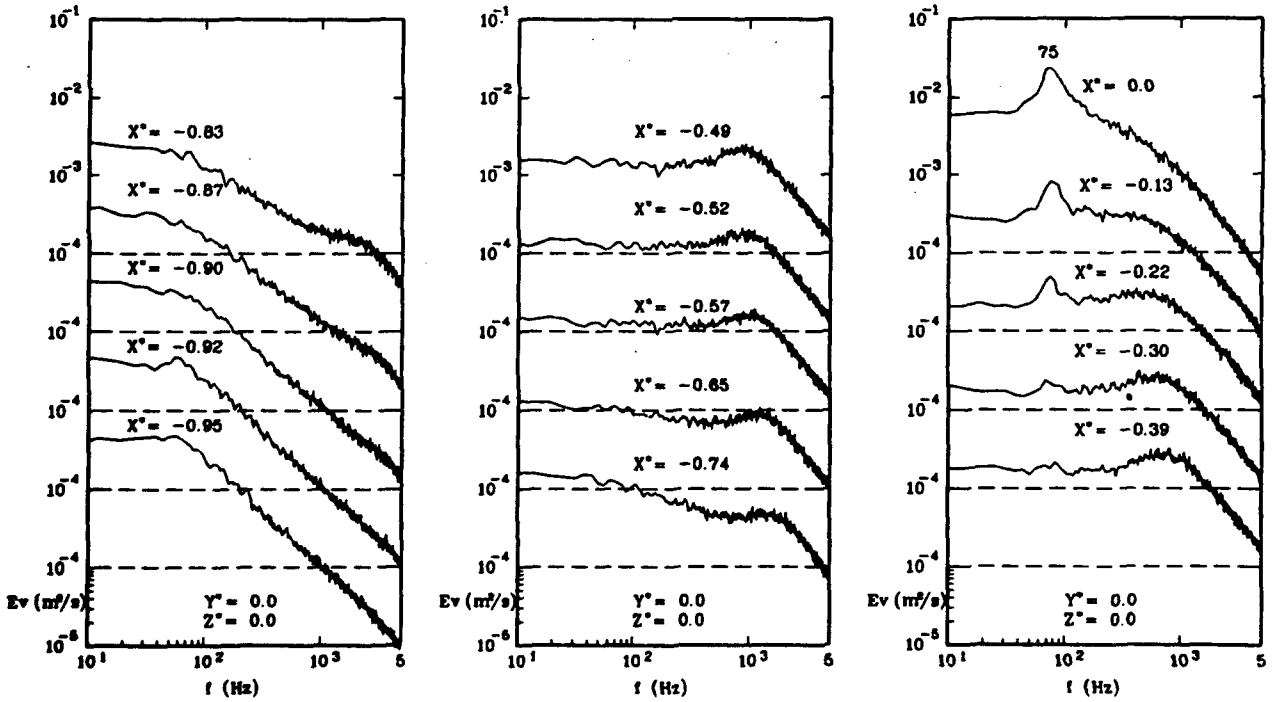

Fig. 3(b) Transverse velocity spectra along combustor center axis

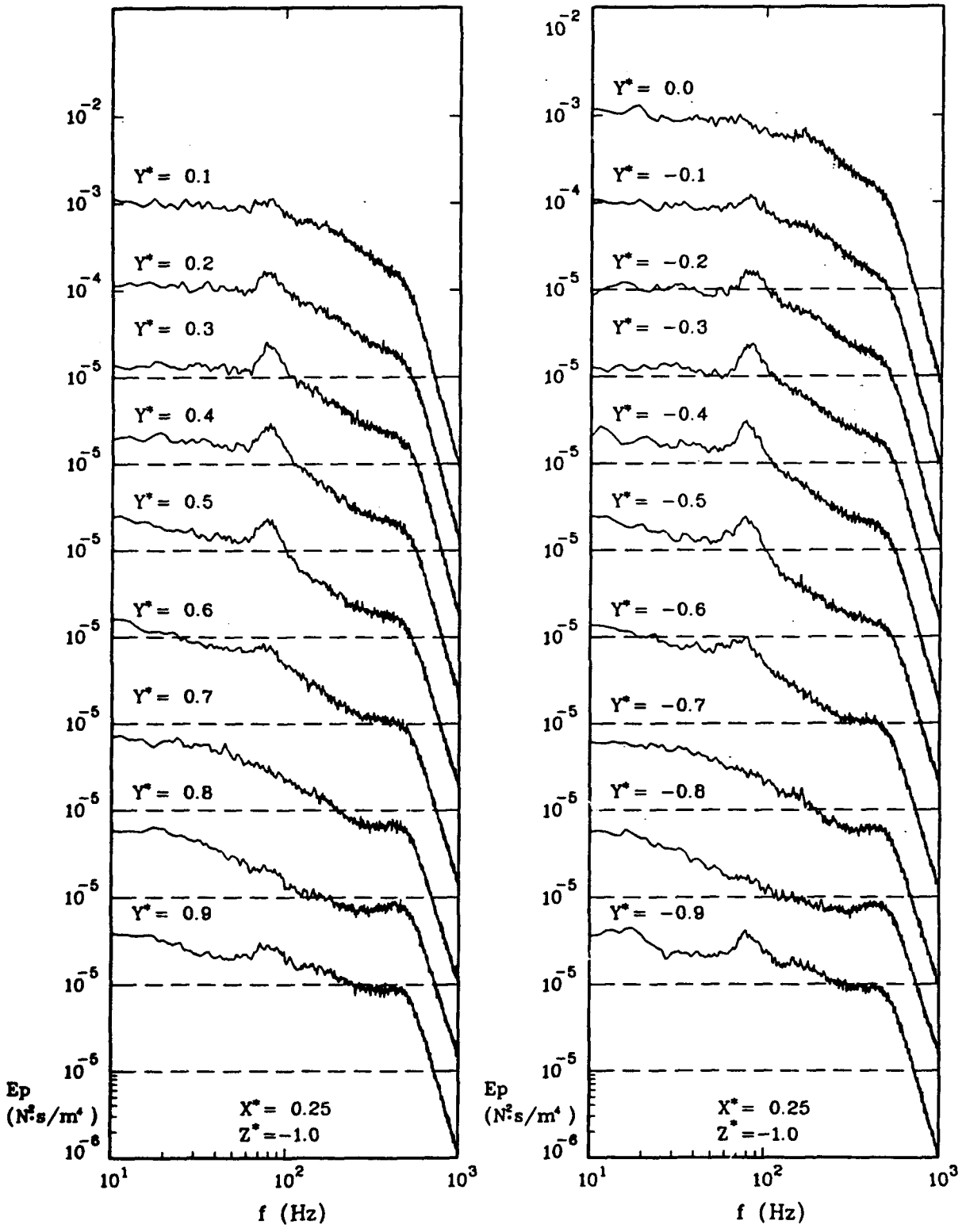

Fig. 4 Wall pressure spectra along line (X*=0.25, Z* = -1)

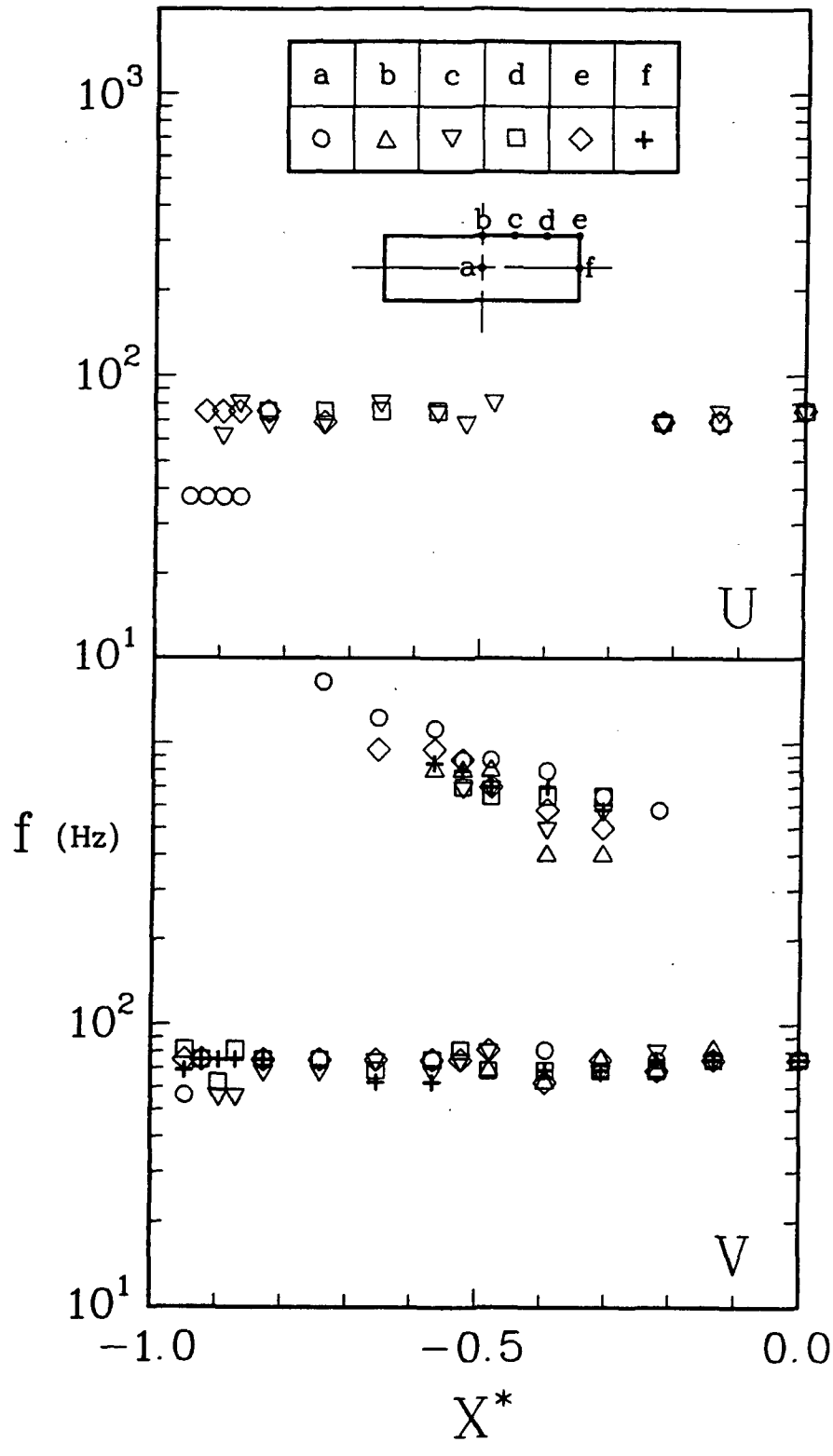

Fig. 5 Axial evolution of peak frequencies for (a) the axial and (b) transverse velocities at center and edge of axial inlet port

Session 8.
Data Processing I

QUANTIZATION OF DOPPLER SIGNALS: HOW MANY BITS ARE NEEDED?

Knud Andersen and Anders Høst-Madsen

Dantec Measurement Technology A/S
Tonsbakken 16-18, 2740 Skovlunde, Denmark.

ABSTRACT

In this paper we evaluate the effect of quantization of Doppler signals. We do this by calculating Cramér-Rao lower bounds for one bit quantization and by doing computer simulations. Both approaches show that there are serious problems with one bit quantization around certain critical frequencies. Contrasting, it is shown that 4 bit quantization performs nearly as good as no quantization. The conclusion is that 4 bits are adequate while fewer number of bits give unreliable results.

1. INTRODUCTION

Many aspects are crucial to obtain accurate and reliable LDA measurements. Good optics and lasers are necessary to obtain high quality Doppler signals; advanced accurate processing of the Doppler signal is needed to estimate the Doppler frequency with high precision; and, finally, the data analysis techniques applied to the measurements should give optimal and reliable results. Processing of the Doppler signal plays a pivotal role, since this determines the accuracy in any subsequent processing. This processing should use the information in the Doppler signals to the fullest extent, otherwise optimization in other links of the chain is wasted. In this paper we will consequently concentrate on this part of the LDA measurement.

The accurate determination of the Doppler frequency is dependent on a number of factors: burst detection and determination, filters, the processing method, windowing, interpolation etc. However, again we can point at one essential link in this chain: the sampling of the Doppler signal. The Doppler signal is a continuous signal, $s(t)$. In order to process this digitally, it must be sampled at certain instants to obtain $s(t_i)$. Further this value should be represented by a digital number. This is called quantization. Thus, the infinitely many possible states of the signal is reduced to a finite number of bits, and of course information of the signal is lost in this process. This information loss should be kept at a negligible minimum; once the information is lost, it is lost forever and can never be restored. Therefore, a proper sampling method is essential to Doppler processing.

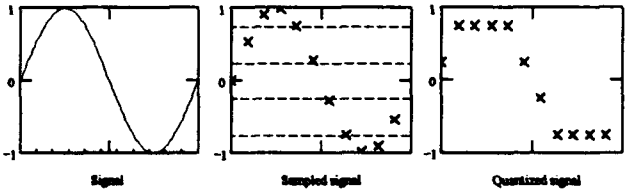

The contents of this paper is the determination of the requirements to the sampling in order to keep the information loss at a minimum.

The first parameter of the sampling process: when the signal should be sampled is readily determined by the well-known Shannon sampling theorem (alias the Nyquist criterion): the signal should be sampled at a frequency twice the maximal frequency in the Doppler signal. If this condition is fulfilled Shannon says that no information is lost in the sampling. Thus the information loss occurs in the quantization of the signal. In this paper we will investigate this information loss in the quantization and determine how this can be kept at a negligible minimum, answering the question: *Quantization of Doppler Signals: how many bits are needed?*

2. QUANTIZATION OF DOPPLER SIGNALS

In order to process the Doppler signal digitally it is converted to a digital value in an A/D-converter. This quantization can be done by a differing number of bits. The two extreme cases are 1 bit quantization and quantization by an infinite number of bits, corresponding to no quantization. For the number of bits converging towards infinity the effect of quantization will converge towards the optimal minimum of no quantization. In principle the more bits the better, but in a practical

implementation the number of bits has to be limited, and the question at issue is how low this number can be in order for the effects of quantization to be minimal.

It should be noted that we are discussing the quantization of the primary Doppler signal, not the resolution of the frequency output of an LDA processor. However, the number of bits in the quantization of the primary Doppler signal will limit the accuracy of the estimated Doppler frequency, thereby also limiting the number of *significant* bits in the estimated Doppler frequency. To output more bits than is significant considering the accuracy of the Doppler frequency makes little sense, and as we will see a low quantization will considerably limit the accuracy of the Doppler frequency.

One bit quantization (see Ibrahim et al. (1990)) is equivalent to determining the sign of the signal

$$s_{\text{one bit}}(t_i) = \begin{cases} +1 & s(t_i) \geq 0 \\ -1 & s(t_i) < 0 \end{cases}$$

From an immediate point of view, it might seem that one bit is too little to be useful. However, one bit quantization means determining the zero crossing of the signal, and to determine the frequency of the signal this is sufficient information, as known from the old counter principle, see also Ibrahim et al. (1990). However, it *will* limit the accuracy.

We will make a quantitative evaluation of one bit quantization, and compare this with no quantization and quantization with a limited number of bits. The accuracy of the Doppler signal is characterized by bias and variance. If the Doppler frequency is f then

$$\text{bias} = \overline{f_{estimated}} - f_{true}$$

$$\text{variance} = \overline{\left(f_{estimated} - \overline{f_{estimated}}\right)^2}$$

If the Doppler signal has bias, then measured mean values will be wrong, and normally one will try to keep bias at a minimum. The variance on the measurements will directly add to the turbulence intensity and also this should be limited.

We will calculate lower bounds for the variance of the estimated Doppler frequency. For no quantization this has been done in Rife and Boorstyn (1974) and in Lading and Edwards (1993) and it should be noticed that this bound does not apply to one bit quantization, in the sense that it gives too low bounds. We will calculate lower bounds that do directly apply to one bit quantization. Some work in this direction has previously been done in Ibrahim et al. (1990), but the bounds given in this reference are much too optimistic and do not give an impression of the problems with one bit quantization.

3. THE CRAMÉR-RAO BOUND

In the appendix we calculate the so called Cramér-Rao lower bound for one bit quantization. We will briefly discuss the significance of the Cramér-Rao lower bound. For a more complete discussion see, e.g. Kendal and Stuart (1993) and Papoulis (1988). If estimating a statistical quantity such as the Doppler frequency, this cannot be done with infinite accuracy, not even theoretically. There is a lower bound on the variance of the measurement, expressed in the Cramér-Rao inequality.

No *unbiased* estimator can do better than the Cramér-Rao (CR) bound. The CR bound thus plays the same role as Heisenberg's uncertainty relation in quantum mechanics or the speed of light in relativity theory. This does not mean that the CR bound can be reached. There might not exists any unbiased estimator that has as low variance as predicted by the CR bound. On the other hand, a biased estimator might have lower variance than the CR bound. An estimator that gives a constant value independently of the input will for example have zero variance but unlimited bias

The CR bound is an information theoretic criterion. This is important in the context of quantization. As mentioned in the introduction, quantization means information reduction and the CR bound is an evaluation of how this information reduction will manifest as variance on estimated value. If the reduced information is used optimally, the CR bound may be reached, but to repeat: it can never be surpassed.

4. CRAMÉR-RAO BOUNDS FOR DOPPLER SIGNALS

4.1 Doppler signal characteristics

To derive CR bounds for Doppler frequency estimation we will assume that the Doppler signal is a sinusoidal embedded in additive Gaussian white noise. This is only a partial truth. The noise in Doppler signals both consists of signal independent noise and Poisson noise due to the random arrival of photons (shot-noise), which is dependent on the amplitude of the signal. An investigation of the influence of this latter noise has been done in the papers Lading (1993) and Lading and Edwards (1993). To get the full picture both kinds of investigations have to be carried through. However, in the most difficult and critical measurement situations, the signal independent background noise will be dominating. Further, when taking into consideration the many different noise sources of the Doppler signal and using the central limit theorem, the assumption of additive Gaussian white noise seems very reasonable. Thus the Doppler signal can be expressed as

$$s(t) = b(t)\sin(\omega t + \theta) + n(t)$$

The factor $b(t)$ is the envelope of the signal. The exact form of the envelope will depend on the optical configuration, particle sizes etc. Two cases are of special interest. The envelope can be Gaussian due to the profile of the laser beams, or the envelope can be approximately rectangular (top-hat) due to apertures in the system or if only a part (i.e. the central part) of the burst is processed. We will consider both cases, but especially the latter. It can be proved that a rectangular envelope will give the best frequency estimation of all envelopes with a given power, so that a lower bound for a rectangular envelope will give a lower bound for any envelope.

4.2 Cramér-Rao bound for non-quantized sampling

The CR-bound for non-quantized sampling was found in Rife and Boorstyn (1974) for a rectangular envelope to be

$$\mathrm{var}[\hat{\omega}] \geq V_{CR,\text{non-quantized}} = \frac{12}{(SNR)^2 T^2 N(N^2-1)}$$

Where T is the sampling interval and N is the number of samples.

For arbitrary envelopes this expression can be easily generalized to (see also appendix)

$$\mathbf{I}_n = \left(\frac{b(t_n)}{\sigma}\right)^2 \begin{bmatrix} t_n^2 & t_n \\ t_n & 1 \end{bmatrix}$$
$$V_{CR,\text{non-quantized}} = \left(\sum_{n=0}^{N} \mathbf{I}_n\right)^{-1}_{11} \qquad (1)$$

where t_n are the sampling times and σ the noise amplitude. On the second line, the matrices should be summed, then the sum should be inverted as matrix; the lower bound for the variance on the signal frequency is then the element in row 1, column 1.

4.3 Cramér-Rao bound for one-bit quantization

In the appendix we have derived the CR-bound for one bit quantization, given by the expression

$$\mathbf{I}_n(\omega, t_n, \theta) = \frac{2}{\pi}\left(\frac{b}{\sigma}\right)^2 \begin{bmatrix} t_n^2 & t_n \\ t_n & 1 \end{bmatrix} \Pi(\omega, t_n, \theta)$$
$$V_{CR,\text{one-bit}}(\omega, \theta) = \left(\sum_{n=0}^{N} \mathbf{I}_n(\omega, t_n, \theta)\right)^{-1}_{11} \qquad (2)$$
$$V_{CR,\text{one-bit}}(\omega) = \frac{1}{2\pi}\int_0^{2\pi} V_{CR,\text{one-bit}}(\theta)\, d\theta$$

The second line of (2) expresses the CR bound for one bit quantization depending on both SNR (= b / σ) frequency ω and phase θ. Since the Doppler bursts have random phase with any value of the phase equally probable, we have averaged over the phase to derive at the SNR and frequency dependent CR bound on line 3, which is the expression we will use.

The function $\Pi(\omega, t_n, \theta)$ is given by the rather complicated expression

$$\Pi(\omega, t_n, \theta) = \frac{e^{-\left(\frac{b}{\sigma}\right)^2 \cos^2(\omega t_n + \theta)}}{1 - \mathrm{erf}\left(\frac{1}{\sqrt{2}}\frac{b}{\sigma}\cos(\omega t_n + \theta)\right)^2} \sin^2(\omega t_n + \theta)$$
$$+ \frac{e^{-\left(\frac{b}{\sigma}\right)^2 \sin^2(\omega t_n + \theta)}}{1 - \mathrm{erf}\left(\frac{1}{\sqrt{2}}\frac{b}{\sigma}\sin(\omega t_n + \theta)\right)^2} \cos^2(\omega t_n + \theta)$$

The first thing to notice about (2) is that it is similar to the CR bound for no quantization (1) except for the factors $2/\pi$ and $\Pi(\omega, t_n, \theta)$. Since it can be proven that $\Pi(\omega, t_n, \theta) \leq 1$ (se note in appendix) we arrive after some considerations to the conclusion

$$V_{CR,\text{one-bit}}(\omega) \geq \frac{\pi}{2} V_{CR,\text{non-quantized}}$$

or put in words

The variance for one-bit quantization always is at least 50 % higher than the variance for no quantization.

This statement, however, does not take into consideration the frequency dependency of the factor $\Pi(\omega, t_n, \theta)$, which gives a very remarkable behavior. Unfortunately (2) is so complicated that an analytical evaluation is impossible, and consequently one has to turn to a numerical calculation of it. Also this is tricky, but with care it is possible, and we have done so for a selection of frequencies and SNR in the results section below.

The CR bound will not be calculated for quantization of an arbitrary number of bits. Although this could be done in theory, the expressions would be so complicated that they would be without any interest. Instead we have done the evaluation of quantization for a higher number of bits by computer simulations.

It should be remembered that the CR bound calculated for one bit quantization is *independent of the signal processing method, it be FFT or correlation processing.*

5. COMPUTER SIMULATIONS

To relate the theoretical calculation of the CR bound in the previous section, we have also made computer simulations showing the effect of quantization. The computer simulations

have been done for a Doppler signal with rectangular envelope embedded in additive Gaussian white noise, quadrature mixed to give a complex signal. The processing has been done by a FFT analysis with 4 times zero padding followed by a peak search after Brent's method (see Press et al. (1992)). This is a very slow method which is not at all feasible for real-time implementation, but as the subject of this paper is quantization effects we have chosen this method to avoid the influence of other factors like interpolation.

For no quantization the FFT method (or rather Fourier method) is maximum likelihood, i.e. the (asymptotically) optimal method for frequency estimation (as proved in Rife and Boorstyn (1974). *For one-bit quantization the Fourier method is not maximum likelihood*, contrary to some belief (see, e.g. Ibrahim et al. (1990)). The maximum likelihood method for one-bit quantization can be derived by examining the likelihood function in the appendix. Thus, it is indeed possible that a better method than FFT can be found for one-bit quantization, but in this paper we will not proceed further in this direction.

The simulations will be done for one bit quantization and no quantization corresponding to the CR bounds calculated above, and in addition for 4 bit (complex) quantization, such as used by the DANTEC BSA.

6. RESULTS.

In this section we will present the results of the calculation of CR bounds for one-bit quantization, and the simulation results for no quantization, 4 bit quantization and 1 bit quantization, mainly in graphical form. All calculations and simulations show here are for 32 (complex) samples, which applies to a typical burst. The behavior for a larger number of samples is qualitatively identical but of course with different numbers. In all graphs frequency and standard deviations of frequencies are relative to sampling frequency (i.e., bandwidth). The numbers therefore easily can be scaled.

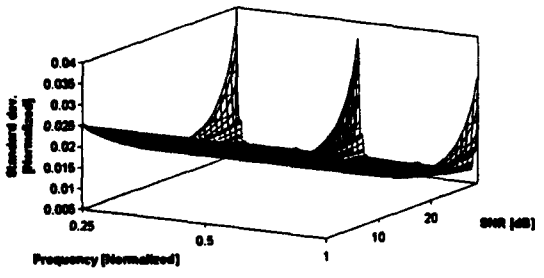

Figure 1. CR bound for one bit quantization; 32 complex samples. Standard deviation versus frequency and SNR.

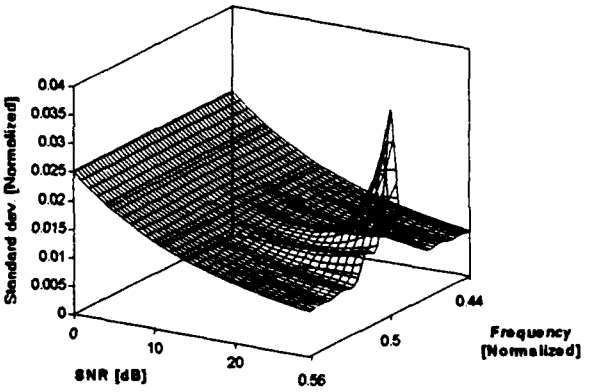

Figure 2. CR bound for one bit quantization; 32 complex samples. Standard deviation versus frequency and SNR around center frequency.

The CR bound for one-bit quantization depends on both frequency and SNR. Figure 1 with a closer detail in figure 2 shows this dependency in a 3D-plot. The remarkable feature is that at the frequencies that are a multiple of a quarter of the sampling frequency, $nf_s/4$, the variance does, as expected, decrease with increasing SNR, *until* it reaches a minimum, and then it increases dramatically. Thus, the paradoxical thing happens that adding noise to the measurements increases the accuracy. This is a strange, but to signal processing well-known, effect of quantization (see e.g. Bilinskis and Mikelsons (1992)). In the terms of the introduction one could say that there is a terrible waste of information around these frequencies.

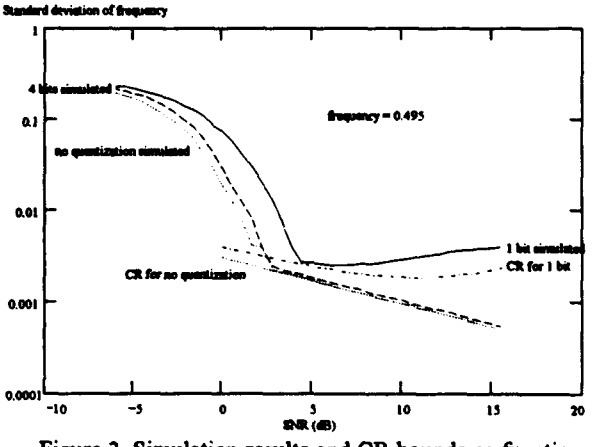

Figure 3. Simulation results and CR bounds as function of SNR.

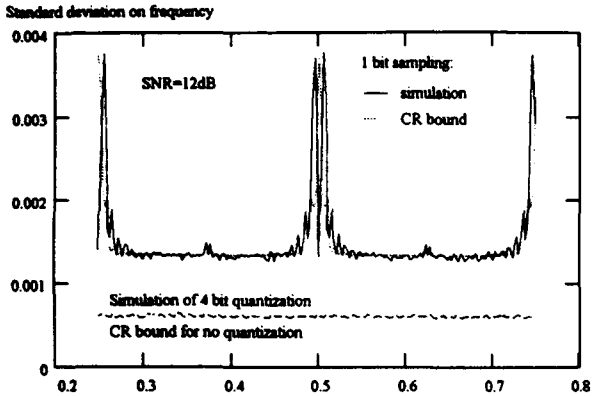

Figure 4. Simulation results and CR bounds as function of frequency. The CR bound for no quantization, the simulations results for no quantization and the simulation results for 4 bit quantization are indistinguishable.

In figure 3 and 4 we show the results of simulations. It is seen that there is a close agreement between the simulations and the CR bounds, and that 4 bit quantization is very close to non-quantized sampling. There is a disagreement between the CR bound and simulation for one-bit quantization just at the critical frequencies $nf_s/4$. Here the variance of the simulations are less than the CR bound. This seems to contradict that the CR bound is a lower bound, but one should bear in mind that this is only true for unbiased estimators, and FFT for one-bit quantization is *not unbiased*.

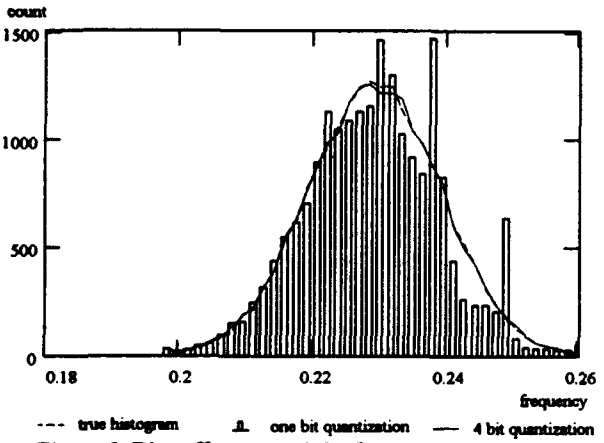

Figure 5. Bias effect around the frequencies $nf_s/4$.

We have investigated the question of bias further. In figure 5 we have input a range of frequencies distributed Gaussian as typically in turbulence. This was done for both one bit and 4 bit quantization, producing quite different results. The result for 4 bit quantization is almost indistinguishable from the input data. However, one bit quantization produces an histogram with a quite different form from the input. It is seen that he frequencies $nf_s/4$ acts as "black holes" that swallow every frequencies in their neighborhoods. Therefore the variance is low exactly at $nf_s/4$, lower than predicted by CR, but at the expense of bias.

Obviously, the behaviour of one bit quantization wil pose problems particularly when measuring turbulence. Here, an unwary user who is not aware of the problems around these critical frequencies may suddenly encounter some strange experimental results. Since one of the critical frequencies is 0, there will inevitably be problems when measuring reversing flows. The only way to avoid this is to stay within a frequency band of a quarter of the sampling bandwidth.

Finally figure 3 indicates that the threshold is higher for one-bit quantization than for no quantization with 4 bit quantization being identical to no quantization. This effect however has to be investigated further; we do not have any theoretical explanation for this.

From the computer simulations it appears that 4 bits quantization is adequate for an accurate determination of the Doppler frequency. However, to get the full benefit from the 4 bits, the signal need to be adjusted to the dynamic range. In the Dantec BSA an amplitude normalizing circuit in front of the analog to digital converter ensures that the dynamic range of the 4 bits is always used fully also when the Doppler signal amplitude varies over a large dynamic range. We have not made investigations for a fewer number of bits to see if 2 or 3 bits would also be adequate since we estimate that this normalization of the signal would be virtually impossible with the very limited dynamic range of 2 or 3 bits. Therefore, 2 or 3 bit quantization will in reality perform as badly as 1 bit quantization.

7. CONCLUSION.

We have investigated the influence of quantization on the estimation of the Doppler frequency. This has been done by calculating the Cramér-Rao lower bound for one-bit quantization, which gives a lower limit to the variance of the estimated Doppler frequency, and by computer simulations. Based on the investigations the following can be concluded:

- *The variance for one-bit quantization always is at least 50 % higher than the variance for no quantization.*
- *around the frequencies which are mulipla of one quarter of the sampling frequency the variance and bias for one bit quantization explodes.*
- *The variance and bias at these frequencies can seriously influence turbulence measurements*
- *The threshold (lower limit) SNR for one bit quantization is around 3 dB higher than for no quantization.*
- *Quantization with 4 bits gives an accuracy very close to no quantization without the problems around certain frequencies.*

It should be noticed that these are fundamental problems of one-bit quantization, not problems of a concrete implementation. Based on this, it can be recommended that the

following precautions be taken if one bit quantization is to give reliable results

- *The range of Doppler frequencies should be kept within one quarter of the sampling bandwidth for one bit quantization.*

The answer to the question posed is the title can now be answered: in general one bit is to little, while 2 or 3 bits are problematic due to adjustment problems. A quantization of 4 bits is adequate, and there is no gain in using a higher number of bits.

Finally it should kept in mind that once then quantization problem has been solved satisfactory many other factors of the signal processing are important in obtaining accurate LDA measurements.

APPENDIX: DERIVATION OF CR BOUND

Let the signal be given by

$$s(t) = b_{\mathbf{q}}(t)\cos(\omega t + \theta)$$

here $b_{\mathbf{q}}$ is the envelope of the signal, which depends on some parameters in the parameter vector $\mathbf{q}$ (such as signal amplitude and duration), which might be know or unknown. We will primarily concentrate on the case where $b_{\mathbf{q}}$ is constant, so that $\mathbf{q} = b_0$ and $b_{\mathbf{q}}(t) = b_0$, and in the derivations below we will not explicitly note the dependencies of b and accordingly write b for $b_{\mathbf{q}}(t)$.

We will assume that sampling is done on the complex signal, i.e., on the signal and its Hilbert transform, which may be obtained from the real signal by quadrature mixing. Thus, the samples (before quantization) can be written as

$$X_n = s(t_n) + W(t_n)$$
$$Y_n = \tilde{s}(t_n) + \tilde{W}(t_n)$$

where $\tilde{}$ denotes Hilbert transform and $\tilde{s}(t) = b\sin(\omega t + \theta)$. W is an additive noise contribution, which is assumed to be white Gaussian of zero mean and variance σ^2. Thus, the samples are uncorrelated, and the probability density function (pdf) of a single sample is given by

$$p(X_n;\mathbf{p}) = \frac{1}{\sqrt{2\pi}\sigma}\exp\left(-\frac{1}{2\sigma^2}(X_n - b\cos(\omega t_n + \theta))^2\right) \quad (3)$$

where we have explicitly noted the dependency of p on the parameter vector $\mathbf{p} = [\omega, \theta, \mathbf{q}]$. The pdf for Y_n is given equivalently. Since the noise is uncorrelated from sample till sample, the total probability distribution is give as a product:

$$p(\mathbf{X},\mathbf{Y};\mathbf{p}) = \prod_{i=1}^{N} p(X_i;\mathbf{p}) \prod_{i=1}^{N} p(Y_i;\mathbf{p})$$

From this expression we can calculate the CR bound for non-quantized sampling, as done in Rife and Boorstyn (1974).

One bit quantization corresponds to obtaining the sign of the samples. Thus we obtain a new series of samples, which can assume only the values +1 and -1,

$$x_n = \text{sign}(X_n)$$
$$y_n = \text{sign}(Y_n)$$

The pdf for x_n is found from (3)

$$p(x_n = -1;\mathbf{p}) = P(X_n < 0;\mathbf{p}) = \int_{-\infty}^{0} \frac{1}{\sqrt{2\pi}\sigma}\exp\left(-\frac{1}{2\sigma^2}(X_n - b\cos(\omega t_n + \theta))^2\right)dX_n$$
$$p(x_n = +1;\mathbf{p}) = P(X_n > 0;\mathbf{p}) = \int_{0}^{\infty} \frac{1}{\sqrt{2\pi}\sigma}\exp\left(-\frac{1}{2\sigma^2}(X_n - b\cos(\omega t_n + \theta))^2\right)dX_n$$

We can write this as the common expression

$$p_n^x(s) = p(x_n = s;\mathbf{p}) = \int_{0}^{\infty} \frac{1}{\sqrt{2\pi}\sigma}\exp\left(-\frac{1}{2\sigma^2}(X_n - sb\cos(\omega t_n + \theta))^2\right)dX_n$$

The elements of the Fisher matrix, due to the real component, are accordingly

$$\mathbf{I}_{ij}^x = \sum_{n=1}^{N}\sum_{s=\pm 1} \frac{1}{p_n(s)} \int_0^{\infty} \frac{1}{\sqrt{2\pi}\sigma}\exp(-k_n(x))\frac{\partial k_n}{\partial \varphi_i}(x)dx \int_0^{\infty} \frac{1}{\sqrt{2\pi}\sigma}\exp(-k_n(x))\frac{\partial k_n}{\partial \varphi_j}(x)dx$$

where $\varphi_1, \ldots$ are the unknown parameters to be estimated, and

$$k_n(x) = \frac{1}{2\sigma^2}(x - sb\cos(\omega t_n + \theta))^2$$

We find an equivalent expression for the Fisher matrix $\mathbf{I}_{ij}^y$ of the imaginary component of the signal, and the total Fisher matrix is

$$\mathbf{I}_{ij} = \mathbf{I}_{ij}^x + \mathbf{I}_{ij}^y$$

In general this is a rather complicated expression. To get a principal insight, we will therefore at first consider the simplified case where we assume that phase and amplitude of the signal is known. In this case there is only one unknown parameter to be estimated, the frequency ω, and the Fisher matrix is a scalar. After some calculation we find

$$I_n = \frac{2}{\pi}\left(\frac{b}{\sigma}\right)^2 t_n^2 \cdot \left(\frac{e^{-\left(\frac{b}{\sigma}\right)^2 \cos^2(\omega t_n + \theta)}}{1 - \mathrm{erf}\left(\frac{1}{\sqrt{2}}\frac{b}{\sigma}\cos(\omega t_n + \theta)\right)^2} \sin^2(\omega t_n + \theta) + \frac{e^{-\left(\frac{b}{\sigma}\right)^2 \sin^2(\omega t_n + \theta)}}{1 - \mathrm{erf}\left(\frac{1}{\sqrt{2}}\frac{b}{\sigma}\sin(\omega t_n + \theta)\right)^2} \cos^2(\omega t_n + \theta) \right)$$

$$V_{CR,\text{one bit}} = \frac{1}{\sum_{n=0}^{N} I_n}$$

The factor in the parenthesis is a periodic, highly oscillating function depending on both phase and frequency

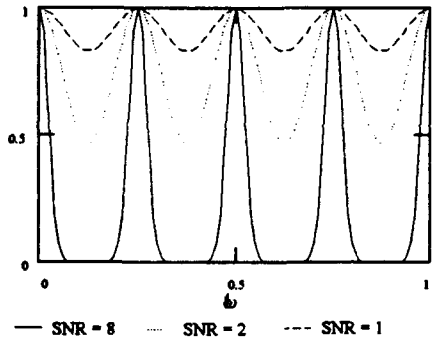

Figure 6. One bit factor

For non-quantized sampling the CR bound is in comparison (see Rife and Boorstyn (1974)):

$$I_n = \left(\frac{b}{\sigma}\right)^2 t_n^2$$

$$V_{CR,\text{non-quantized}} = \frac{1}{\sum_{n=0}^{N} I_n}$$

We can make the following evaluation of the CR bound for 1 bit quantization:

$$I_n \le \frac{2}{\pi}\left(\frac{b}{\sigma}\right)^2 t_n^2 \frac{1}{1 - \mathrm{erf}\left(\frac{1}{\sqrt{2}}\frac{b}{\sigma}\right)}$$

$$V_{CR,\text{one bit}} \ge \frac{\pi}{2}\left(1 - \mathrm{erf}\left(\frac{1}{\sqrt{2}}\frac{b}{\sigma}\right)\right) V_{CR,\text{non-quantized}}$$

This is not the best inequality, however. We are certain without doubt that the factor in the parenthesis is always ≤ 1 (see figure 6), although we have not made a rigorous mathematical proof of this. Therefore we can give the inequality

$$V_{CR,\text{one-bit}} \ge \frac{\pi}{2} V_{CR,\text{non-quantized}}$$

For both frequency and phase unknown, the CR bound can be found to

$$\mathbf{I}_n = \frac{2}{\pi}\left(\frac{b}{\sigma}\right)^2 \begin{bmatrix} t_n^2 & t_n \\ t_n & 1 \end{bmatrix} \cdot \left(\frac{e^{-\left(\frac{b}{\sigma}\right)^2 \cos^2(\omega t_n + \theta)}}{1 - \mathrm{erf}\left(\frac{1}{\sqrt{2}}\frac{b}{\sigma}\cos(\omega t_n + \theta)\right)^2} \sin^2(\omega t_n + \theta) + \frac{e^{-\left(\frac{b}{\sigma}\right)^2 \sin^2(\omega t_n + \theta)}}{1 - \mathrm{erf}\left(\frac{1}{\sqrt{2}}\frac{b}{\sigma}\sin(\omega t_n + \theta)\right)^2} \cos^2(\omega t_n + \theta) \right)$$

$$\mathbf{V}_{CR,\text{one bit}} = \left(\sum_{n=0}^{N} \mathbf{I}_n\right)^{-1}$$

and for non-quantized sampling the CR bound is (see Rife and Boorstyn (1974)):

$$\mathbf{I}_n = \left(\frac{b}{\sigma}\right)^2 \begin{bmatrix} t_n^2 & t_n \\ t_n & 1 \end{bmatrix}$$

$$\mathbf{V}_{CR,\text{non-quantized}} = \left(\sum_{n=0}^{N} \mathbf{I}_n\right)^{-1}$$

For both frequency, phase and amplitude unknown we get the somewhat more complex:

$$\mathbf{I}_n = \frac{2}{\pi}\frac{1}{\sigma^2}$$

$$\left(\begin{bmatrix} b^2 t_n^2 \sin^2(\omega t_n) & -\frac{1}{2} b t_n \sin(2\omega t_n) & b^2 t_n \sin^2(\omega t_n) \\ -\frac{1}{2} b t_n \sin(2\omega t_n) & \cos^2(\omega t_n) & -\frac{1}{2} b \sin(2\omega t_n) \\ b^2 t_n \sin^2(\omega t_n) & -\frac{1}{2} b \sin(2\omega t_n) & b^2 \sin^2(\omega t_n) \end{bmatrix} \frac{e^{-\left(\frac{b}{\sigma}\right)^2 \cos^2(\omega t_n)}}{1 - \mathrm{erf}\left(\frac{1}{\sqrt{2}} \frac{b}{\sigma} \cos(\omega t_n)\right)^2} + \right.$$

$$\left. \begin{bmatrix} b^2 t_n^2 \cos^2(\omega t_n) & \frac{1}{2} b t_n \sin(2\omega t_n) & b^2 t_n \cos^2(\omega t_n) \\ \frac{1}{2} b t_n \sin(2\omega t_n) & \sin^2(\omega t_n) & \frac{1}{2} b \sin(2\omega t_n) \\ b^2 t_n \cos^2(\omega t_n) & \frac{1}{2} b \sin(2\omega t_n) & b^2 \cos^2(\omega t_n) \end{bmatrix} \frac{e^{-\left(\frac{b}{\sigma}\right)^2 \sin^2(\omega t_n)}}{1 - \mathrm{erf}\left(\frac{1}{\sqrt{2}} \frac{b}{\sigma} \sin(\omega t_n)\right)^2} \right)$$

$$\mathbf{V}_{CR,\text{one bit}} = \left(\sum_{n=0}^{N} \mathbf{I}_n \right)^{-1}$$

Notice that in all these expressions the variance depends on both phase and frequency for the signal. For a given frequency, the phase of the Doppler burst will be random and any phase will be equally possible. Thus, to get the CR lower bound for a given phase, the variance should be averaged over all phases (a minor consideration will show that still gives a lower bound). Thus

$$\mathbf{V}_{CR,\text{non-quantized}}(\omega) = \int_0^{2\pi} \left(\sum_{n=0}^{N} \mathbf{I}_n \right)^{-1} d\theta \qquad (4)$$

since the integration is to be done after the matrix inversion, it is virtually impossible to arrive at an analytical expression. The evaluation of (4) must therefore be done numerical, which is also non-trivial due to the strange behavior of the one bit *factor* (figure 6).

REFERENCES

Bilinskis, I. and Mikelsons, A.: Randomized signal processing, Prentice Hall, London 1992.

Ibrahim, K. M., Werthimer, G. D. and Bachalo, W. D. : "Signal Processing Considerations for Laser Doppler and Phase Doppler Apllications", 5th International Symposium on Applications of Laser Techniques to Fluid Mechanics, Lisbon 1990, Springer-Verlag 1991, pp. 291-316.

Kendal, M. and Stuart, A.: "The advanced theory of statistics, vol. 2" London 1963.

Lading, L. and Edwards, R., "Laser velocimeters; lower limits to uncertainty", Applied Optics, vol. 32, No. 21, july 1993, pp. 3855-3866.

Lading, L.: "Signal processing for time resolved measurements," Summer School on optical diagnostics for flow processes, Risø, 1993.

Papoulis, A.: Probability, Random Variables and Stochastic Processes, McGraw-Hill, New York, 1988.

Press, H. et al.: Numerical receipies in C, Cambridge University Press, 1992.

Rife, D. and Boorstyn, R.: "Single-Tone Parameter Estimation from Discrete-Time Observations", IEEE Transactions on Information Theory, vol. IT-20, No. 5, Sep. 1974, pp. 591-598.

RUNNING FOURIER TRANSFORM AND MULTILINEAR TIME FREQUENCY REPRESENTATION IN THE ANALYSIS OF A DOPPLER SIGNAL

S. Camporeale* and A. Cenedese**

* Department of Mechanics of Fluids and Offshore Engineering
University of Reggio Calabria, Italy

** Department of Mechanics and Aeronautics,
"La Sapienza" University of Rome, Italy

ABSTRACT

The analysis of the Doppler signal is generally performed by algorithms that are able to provide only one frequency information for each burst. In this paper two different approaches are suggested in order to obtain information about velocity variations during the transit time:

-Running Fourier Transform;

-Multilinear Time Frequency Representation.

The two different approaches are tested by means a numerical simulation.

1. THE RUNNING FOURIER TRANSFORM

Running Fourier Transform (RFT) is a recursive algorithm able to continuously provide the Fourier Transform. Suppose to have a sequence consisting of $n+m$ samples, acquired at constant time intervals, Δt, of a real signal $x(t)$:

$$x_0, x_1, \ldots, x_{n-1}, x_n, \ldots, x_{n+m-1} \qquad (1)$$

the Discrete Fourier Transform of the first n data is given by:

$$X_{f,n-1} = \sum_{i=0}^{n-1} x_i \cdot exp(-j\,2\pi f \cdot i \cdot \Delta t / n) \qquad (2)$$

The Fourier transform over the sequence obtained by discarding x_0 and adding x_n , is obtained by the recursive formula:

$$X_{f,n} = exp(j\,2\pi f \cdot \Delta t / n) \cdot (X_{f,n-1} + x_n - x_0) \qquad (3)$$

This formula gives the Fourier Transform at selected frequencies because it is not required to perform the calculation for the whole spectrum. If the range of the selected frequency is limited, few calculations are required for the application of the method.

The RFT is used for a Doppler signal analysis, according to the following steps:

- a FFT is performed at the beginning of the burst;
- the presence of a peak in the power spectrum is recognised;
- at the next time step the spectrum is calculated only in a interval around the frequency peak;
- the measure is validated when the ratio between first and second peak is higher than a prefixed value.

No hypothesis are required on frequency variation. The number of points considered for the FFT does not affect the computational cost; nevertheless it must be selected carefully. A large number of points may reduce the accuracy because of the Doppler broadening produced by the variation of the frequency during the burst; whereas few samples may give poor accuracy because of aliasing.

To increase the resolution without increasing the number of the samples it is possible to apply the zero-padding technique modifying the relationship (3):

$$X_{f,n} = w \cdot (X_{f,n-1} + w^{-n} \cdot x_n - x_0) \qquad (4)$$

where:

$$w = exp\left[j\,2\pi f \cdot \Delta t / (n + n')\right] \qquad (5)$$

and n' is the number of zeros.

2. THE MULTILINEAR TIME FREQUENCY REPRESENTATION

Mulitilinear Time Frequency Representation (MTFR) is a method for the analysis of complex signal with

constant envelop; these methods have been proposed for applications such as sonar, radar, etc. (Barbarossa et al 1991, Barbarossa 1992, Barbarossa 1993, Peleg and Porat 1991).

A complex signal with constant envelop is given by:

$$x(t) = A\exp[j\phi(t)] \tag{6}$$

where A is a constant; the phase $\phi(t)$ is expanded in Taylor series:

$$\phi(t) = 2\pi \sum_{i=0}^{p} \frac{a_i}{i!} t^i \tag{7}$$

The r-th order kernel of $x(t)$ can be computed, according with the following recursive rule:

$$K_1(t) = x(t) \tag{8}$$

$$K_2(t,\tau_1) = K_1(t+\tau_1)\cdot K_1^*(t-\tau_1) \tag{9}$$

$$\vdots$$

$$K_r(t;\tau_1,\ldots,\tau_{r-1}) = K_{r-1}(t+\tau_{r-1};\tau_1,\ldots,\tau_{r-2})\cdot \cdot K_{r-1}^*(t-\tau_{r-1};\tau_1,\ldots,\tau_{r-2}) \quad \text{for} \quad r \geq 3 \tag{10}$$

where the star denotes the complex conjugate and $\tau_1, \tau_2, \ldots, \tau_r$ are time lags. *The r-th order MTFR of the signal is* defined as the Fourier transform of K_r:

$$MTFR_r(f,\tau_1,\ldots,\tau_{r-1}) = = \int_{-\infty}^{+\infty} K_r(t,\tau_1,\ldots,\tau_{r-1})\cdot\exp(-j2\pi f t)dt \tag{11}$$

It is possible to show that exists a relationship between the kernel and the coefficients of the Taylor expansion of the phase (Barbarossa 1993):

$$K_p(t;\tau_1,\ldots,\tau_{p-1}) = = A^{2^{p-1}} \exp\left[j2\pi 2^{p-1}\left(a_{p-1} + a_p t\right)\prod_{i=1}^{p-1}\tau_i \right] \tag{12}$$

The above relationship shows that K_p is a complex sinusoid whose frequency $\hat{f}$ depends only on the coefficient a_p and on the lags:

$$\hat{f} = 2^{p-1} a_p \prod_{i=1}^{p-1} \tau_i \tag{13}$$

The kernels with order higher than p are constant not depending on the lags. The p-th order coefficient a_p can be estimated from the frequency corresponding to the maximum in the power spectrum, assigned the lags. Once estimated the value $\hat{a}_p$, it is possible to remove the higher order term from the polynomial expression of the phase, multiplying $x(t)$ by:

$$\exp\left(-j\cdot 2\pi\cdot \hat{a}_p \cdot t^p / p!\right) \tag{14}$$

If the estimation is correct, the resulting signal has a phase given by a polynomial of $(p-1)$-th order. The method can be repeated in a recursive way until the estimation of the coefficient a_1.

If the signal is given over the interval $[0,T]$, the p-th order kernel is defined over the interval:

$$\left[\sum_{i=1}^{p-1}\tau_i \ , T - \sum_{i=1}^{p-1}\tau_i \right] \tag{15}$$

The method can be applied with arbitrary values of the lags, assumed that the interval defined by equation (15) is not empty. If the signal is sampled at constant time step Δt and n is the number of samples, the resolution of the frequency is given by $1/(n\,\Delta t)$. From equation (13) results that the resolution of a_p is given by:

$$\left(a_p\right)_{min} = \frac{1}{2^{p-1} n\,\Delta t \prod_{i=1}^{p-1}\tau_i} \tag{16}$$

The above expression shows that it is possible to increase the resolution of a_p using values of the lags as larger as possible.

The velocity is related to the phase by:

$$v(t) = \frac{\delta}{2\pi}\cdot\frac{d}{dt}\phi(t) = b_0 + b_1 t + \ldots + b_{p-1} t^{p-1} \tag{17}$$

where δ is the fringe space and:

$$b_{i-1} = \delta\cdot\frac{a_i}{(i-1)!} \tag{18}$$

The signal received by the photomultiplier in a LDA system presents variable envelope. If the envelope changes slowly so that the transit time is much longer than the time of a Doppler cycle, the properties of the MTFR are approximately verified.

To apply the MTFD time lags have to be defined in advance keeping in mind that:

- the best resolution of a_p is obtained with large time lags;
- the interval given by equation (15) must be not empty;

- increasing time lags the interval becomes shorter and the amplitude of the power spectrum of the kernel becomes smaller.

3. SIMULATION

A numerical simulation is performed in order to verify the capabilities of the two proposed methods to detect velocity variations of the particle that crosses the measurement volume in a LDA system (Cajani et al. 1992).

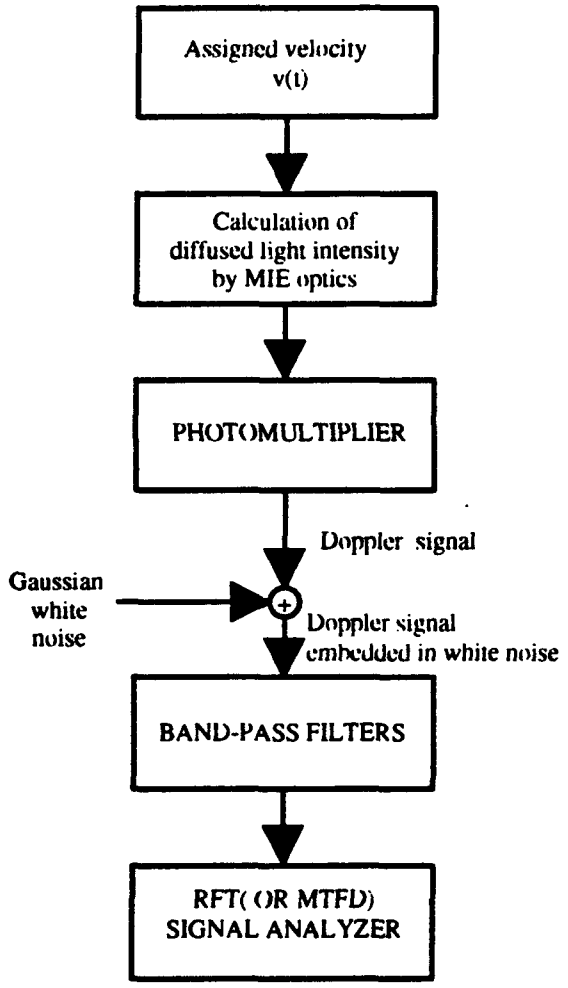

Fig.1 Overview of the LDA system simulator

The simulation is able to take into account all components of the measurement chain of a LDA system (fig.1). It is supposed that the velocity of the particle changes with a polynomial law as given in table 1.

Table 1- assigned coefficient for the velocity

b_0	$8.0 \cdot 10^{-2}$	m/s
b_1	5.0	m/s^2
b_2	$5.0 \cdot 10^{3}$	m/s^3
b_i per $i \geq 2$	0	

The Doppler signal received from the photomultiplier is calculated by means of the Mie optics. White Gaussian noise is added to the signal in order to verify the effectiveness of the proposed methods in presence of noise. The signal is then band-pass filtered in order to eliminate higher frequencies and the pedestal. The methods are compared in two test cases described in table 2.

Table 2- LDA system configuration

parameter	test case 1	test case 2	
laser beam diameter	120	120	10^{-6} m
laser beams angle	0.05	0.1	rad
wavelength	0.614	0.614	10^{-6} m
scattering angle	0.524	0.524	rad
photomultiplier distance	0.6	0.6	m
band filters	5-15	10-30	kHz
sampling rate	146.6	292.3	kHz

The signal received from the photomultiplier is shown in fig.2; the output of the filters in shown in fig. 3. The sampling frequency is selected about ten times higher than the maximum frequency of the signal.

Some parameters are need to be selected before using the RFT:

- number n of the points for the Fourier transform;
- the method to increase spectrum resolution, if needed;
- measurement validation criteria.

The frequency of the absolute maximum in the power spectrum, considered as Doppler frequency, is found using a polynomial interpolation. To validate the spectrum the two largest maxima are compared; if the ratio between them is greater than three, the measurement is validated. The factor three, was found a good criteria to have a low rate of false measurements.

RFT is applied to 300 samples corresponding to a time interval of $2 \cdot 10^{-3}$sec around the centre of the burst. The number of points considered in the FFT is 64 with a zero filling up to 128 samples. In fig.4. is shown the assigned law

and the results obtained by RFT: the method is able to reproduce the curve; the validation is about 30%.

The capability of the method has been verified in presence of noise; a test is carried out with 0 dB signal to noise ratio SNR before the filters (fig.5). The results are in good agreement with the assigned velocity variation law.

In order to use the MTFR the filtered signal is transformed in the complex form by a Hilbert filter that produces two outputs with a phase difference of $\pi/2$. The MTFR is applied the first to the signal without noise to 350 samples corresponding to a interval of $2.4 \cdot 10^{-3}$ sec around the centre of the burst. The lag are $\tau_1 = \tau_2 = 0.35 \cdot 10^{-3}$ s corresponding to 50 samples each one.

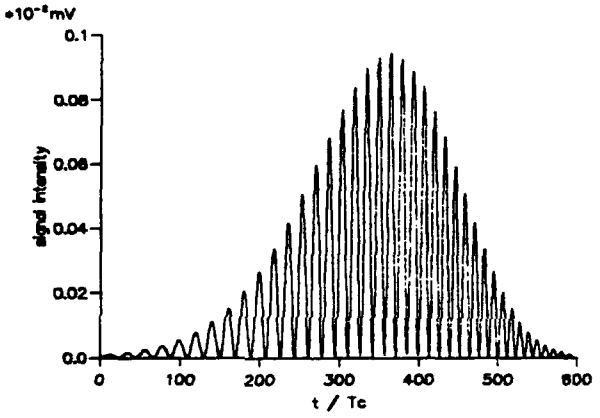

Fig.2 Doppler signal due to a particle that crosses the measurement volume with increasing velocity. No noise

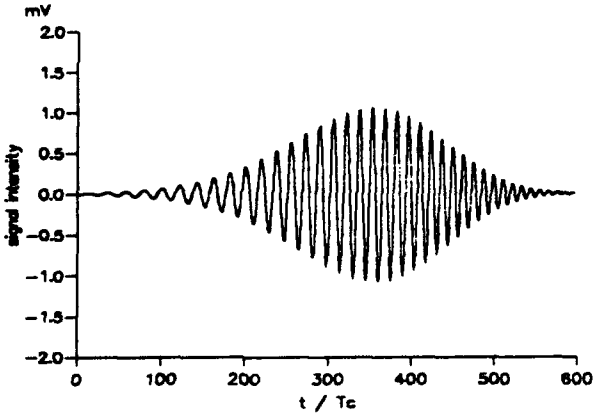

Fig.3 Filtered signal

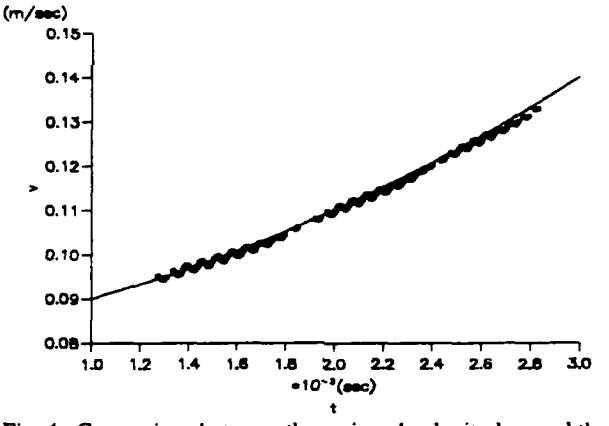

Fig. 4 Comparison between the assigned velocity law and the result obtained by RFT. No noise.

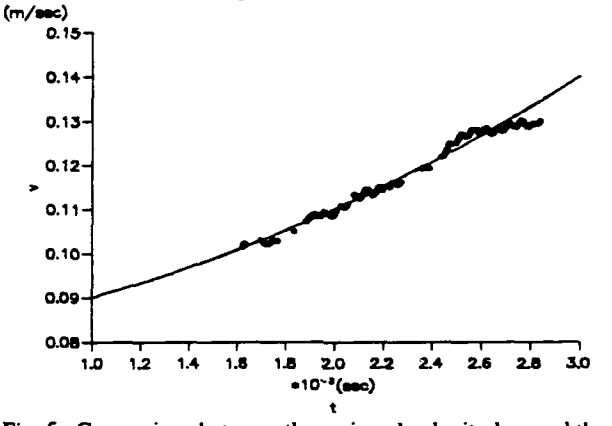

Fig. 5 Comparison between the assigned velocity law and the result obtained by RFT. SNR=0 dB

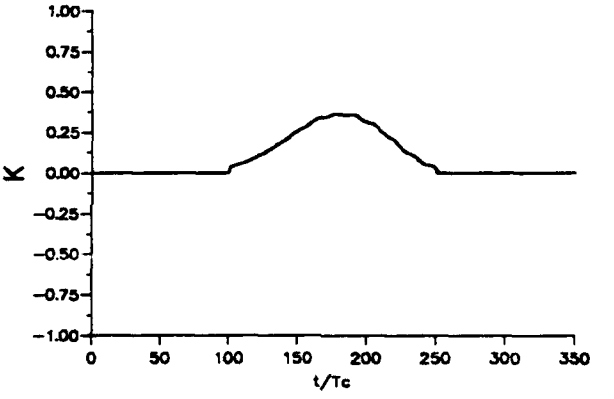

Fig. 6 3rd order kernel of the signal (test case 1)

In fig.6 is plotted the 3-rd order kernel of the signal; according to equation (15) the kernel is defined over 150 samples. The figure shows that the frequency of the kernel is low so that only half cycle is present. This problem depends on the relationship between the frequency of the kernel and the lags given by equation (16). Since the duration of the signal is

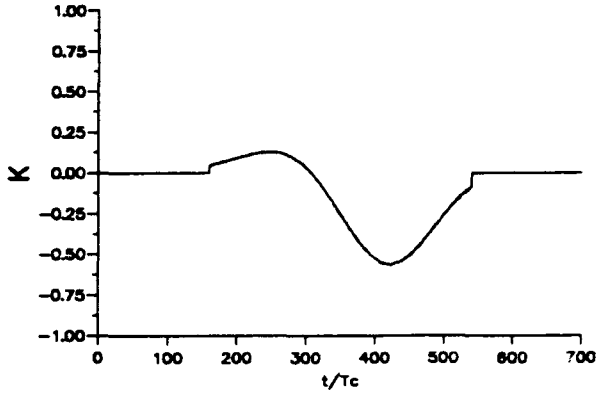

Fig. 9 3-rd order kernel. Test case 2. No noise.

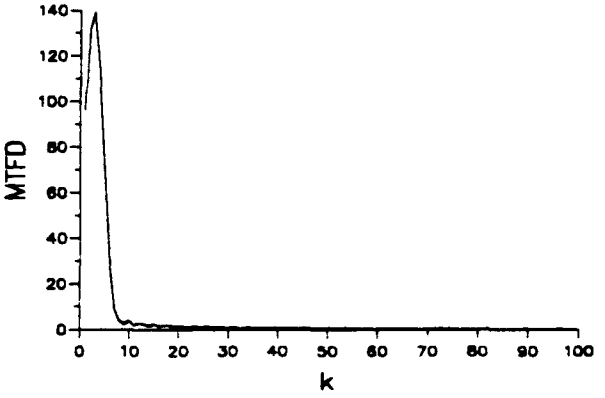

Fig. 12 Power spectrum of the 3-rd order kernel Test case 2. No noise.

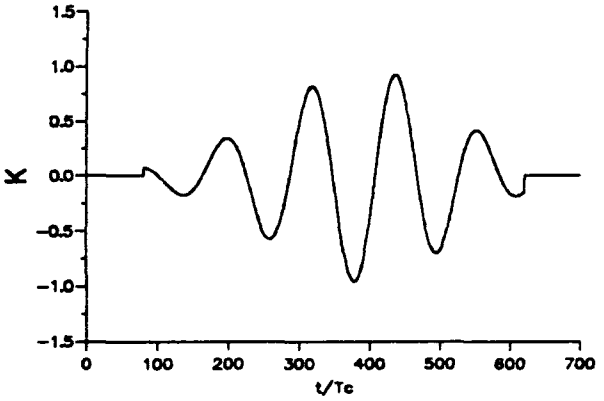

Fig. 10 2-order kernel. test case 2. No noise

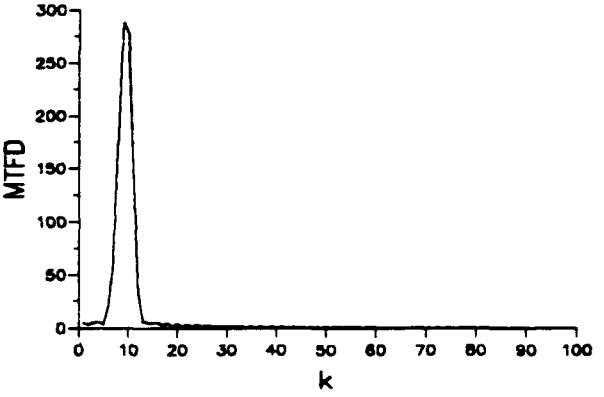

Fig. 13 Power spectrum of the 2-nd order kernel. Test case 2. No noise.

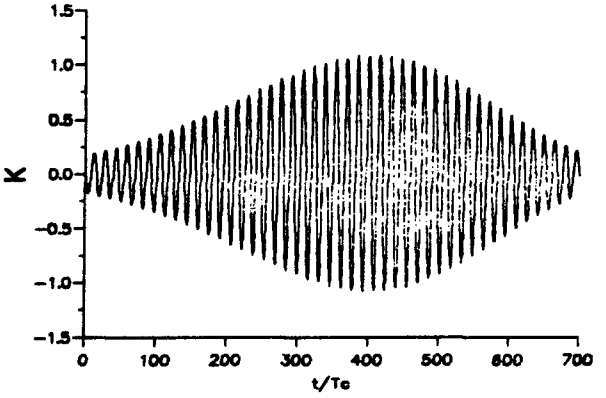

Fig.11 1-st order kernel. Test case 2. No noise.

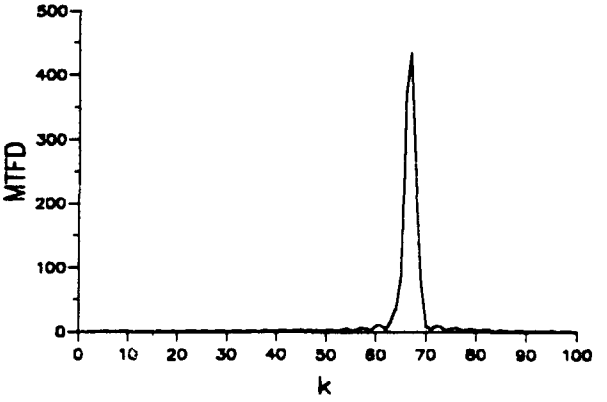

Fig. 14 Power spectrum of the 1-st order kernel. Test case 2. No noise.

limited also the lags must be limited and the frequency results very low. In this case the method is even applicable to detect the coefficient of the second order. In fig.7 and fig.8 are given the plots of kernel of 2-nd and 1-st order.

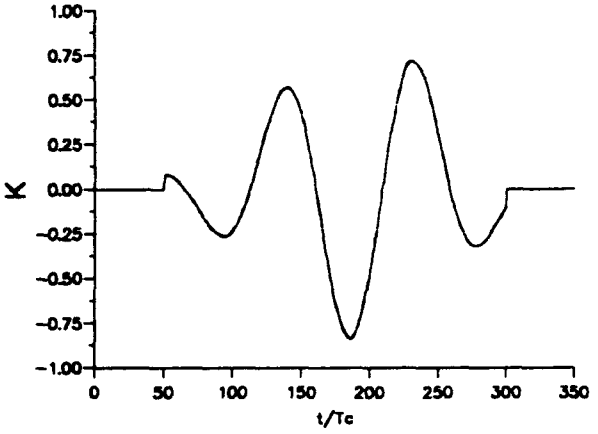

Fig. 7 2nd order kernel (test case 1)

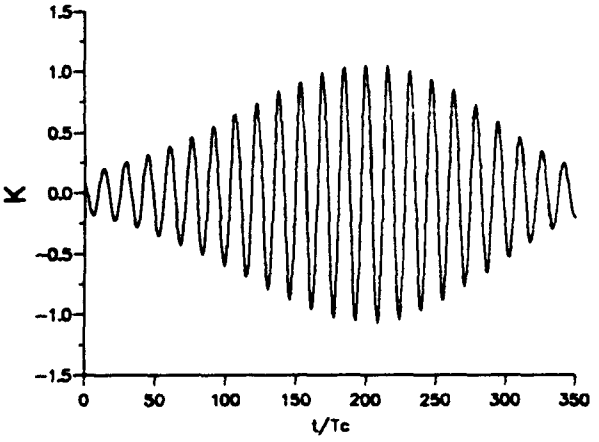

Fig 8 1-st order kernel (test case 1)

The 3-rd order kernel is plotted in fig.9. The kernel frequency is detected by FFT; the frequency resolution is increased by zero-filling up to 1024 samples (fig. 12). From the spectrum it is possible to detect the frequency corresponding to the peak and then calculate the coefficient a_3: in this way it is possible to calculate the coefficient given by equation (14) and then, according to the method described above, it is possible to obtain the 2-order kernel that evaluates the coefficient a_2. (fig. 10, 13). The fig shows that the kernel has envelope that varies similar to the envelop of the signal; the power spectrum is displayed in fig. 13; from this spectrum it is possible to detect $a2$. According to the same method it is elaborated the 1-st order kernel. This kernel presents a constant frequency that depends only from the 1-order coefficient of the phase (fig.11, 14). By equation (18) it is possible to elaborate the coefficients of the velocity and then compare the assigned law with the law estimated by MTFR (fig. 15).

In the second test case, increasing the angle between the laser beams, a double number of Doppler cycles is obtained. In this situation the 3-order coefficient of the phase of the signal can be detected more carefully.

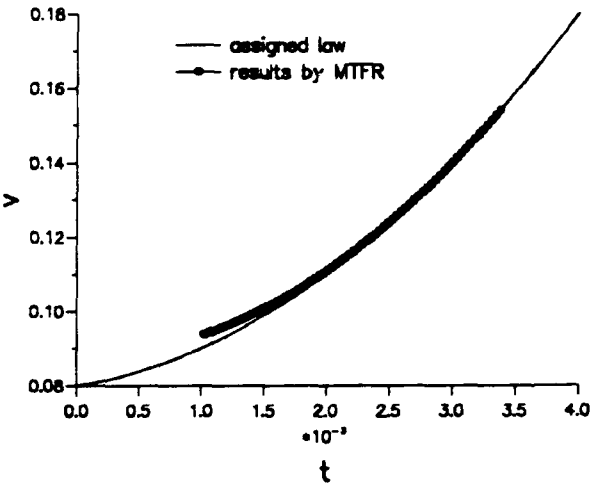

Fig. 15 Comparison between assigned velocity law and results obtained by MTFR

REFERENCES

Barbarossa, S. 1993. Detection and estimation of the instantaneous frequency of polynomial-phase signals by Multilinear Time Frequency representation. IEEE Workshop on Higher order statistics, Stanford Sierra Camp.

Barbarossa, S. 1992. Detection and imaging of moving objects with synthetic aperture radar (Part1.: Optimal detection and parameter estimation theory). IEE Proc.- F, Vol. 139, No. 1

Barbarossa, S., Gregori, C., Nicastro G. ,1991, On the use of Joint Time Frequency representation in SAR Signal Processing. European Transaction on Telecommunications, Vol.2, No6,

Cajani, F., Cenedese A., Di Felice, F. 1993, Numerical Simulation of an LDA system., Proc. of the Fifth Int. Conf. Laser Anemometry, Advances and Applications, pp703-710

Peleg S. Porat B., 1991, Estimation and classification of polynomial phase signals IEEE Trans. Information theory Vol 37 No2

CROSS SPECTRAL ANALYSIS USING LASER DOPPLER ANEMOMETRY

J.A.Fitzpatrick & C.McDonnell

Department of Mechanical Engineering
Trinity College, Dublin, Ireland

ABSTRACT

The use of laser Doppler measurements to calculate the spectrum of turbulence using a sample and hold technique is outlined and the extension of the procedure to enable the cross spectrum between the LDA measurements and equispaced data from conventional instruments is examined. The effect of the sample and hold process on the cross spectral properties is to introduce a drop in the coherence as a consequence of the step noise and a phase lag due to the low pass filter effect. The paper examines these errors and shows how they can be estimated when calculating the cross spectra between LDA and conventional data. The effect of mean sample rate on the coherence and phase is predictable and illustrated using a numerical simulation. The procedures are then used to examine the cross spectrum between LDA and hot wire measurements for turbulent flows with and without coherent eddy structures

1. INTRODUCTION

The fundamental understanding of problems such as flow induced vibration or noise, heat transfer in turbulent flows or noise generation in turbulent combusting flows requires measurement of the interaction of the various parameters. The experimental analysis of these systems involves quantifying the interaction of parameters either to validate a theoretical model or develop an empirical relationship to predict the system behaviour. The interdependence of two parameters is usually estimated from the cross spectrum or the cross covariance function and the various techniques for analysis have been detailed, for example, by Bendat & Piersol (1986). For data acquired from instrumentation where the output is a continuous function, the calculation of the spectra and cross spectra of the parameters of interest is straightforward and is readily determined directly using a hardware type spectrum analyser or by software analysis of digitised data. However, the data from most laser Doppler systems is usually digital data with intermittent spacing and the determination of the autospectrum of the LDA output and of its cross spectrum with measurements from other conventional instruments is not straightforward. The autospectrum of turbulence can be estimated from LDA signals using a number of different procedures. These are usually based on either time domain analysis such as the correlation slotting technique devised by Gaster & Roberts (1975) to obtain the autocorrelation function and hence the autospectrum or frequency domain procedures using a sample and hold procedure as described by Adrain & Yao (1987). The extension of the correlation slotting technique to the determination of cross correlation functions would be difficult whereas the sample and hold procedure with subsequent use of an FFT algorithm to estimate the spectrum lends itself to the efficient calculation of the cross spectrum. Two problems which arise as a consequence of the intermittent sampling are ensuring that the data to be analysed is compatible in time (i.e. the records are coincident) and in estimating the errors that arise from imposing a sample and hold type data acquisition procedure on the LDA data. The errors associated with the sample and hold process have been given in detail by Adrain & Yao (1987) and comprise of a step noise which is due to the sample and hold process and a low pass filter effect both of which are functions of the mean sample rate of data acquisition. A more recent paper by Lee & Sung (1994) has compared the errors in estimating the autospectrum of turbulence from LDA data using a number of different procedures.

In this paper, synthesised signals are used to illustrate how errors influence the determination of coherence and phase when calculating cross spectra between randomly sampled data and data sampled at equal intervals. Then, results from LDA and hot wire measurements in a grid generated turbulent flow and a vortex dominated flow are report.

2. SPECTRAL ANALYSIS

For the work reported in this paper, a sample and hold procedure was used to analyse the data from a counter processor. An advantage of using the sample and hold procedure is that spectral and coherence values are unaffected by bias due to particle statistics as shown by Tropea (1987). In addition, the sample and hold method allows the spectral analysis to be based on FFT type procedures with considerable reduction in computational effort as shown by McDonnell & Fitzpatrick (1992). For any process where x(t) is the input to

some dynamic system and y(t) is the output from or response of the system, the autospectra of x(t) & y(t) and the cross spectrum between x(t) & y(t) are defined by :

$$\begin{aligned} G_{xx}(f) &= E\langle X^*(f).X(f)\rangle \\ G_{yy}(f) &= E\langle Y^*(f).Y(f)\rangle \\ G_{xy}(f) &= E\langle X^*(f).Y(f)\rangle \end{aligned} \qquad (1)$$

where X(f) & Y(f) are the finite Fourier transforms of x(t) & y(t), * denotes a conjugate and E< > denotes an averaging or expectation operator. The autospectra give the distribution of the variance of each process as a function of frequency. The cross spectrum contains information on the relationship between the two processes and this is usually expressed in the form as a transfer function as :

$$H(f) = G_{xy}(f)/G_{xx}(f) \qquad (2)$$

This gives the magnitude and phase of the linear relationship between x(t) and y(t). For practical analysis, a normalised form of the cross spectrum termed the coherence function is used to determined the fractional power of the output which is linearly related to the input at every frequency. The coherence function $\gamma^2(f)$ is defined as :

$$\gamma_{xy}^2(f) = \frac{G_{xy}^*(f)G_{xy}(f)}{G_{xx}(f)G_{yy}(f)} \qquad (3)$$

and is bounded by 0 and 1. It is a frequency domain equivalent to the normalised cross covariance function. When a system is of the single input/output type, then for a linear system, the coherence function should be unity at all frequencies. If it is not, then the system is either non-linear or has been contaminated by measurement noise.

2.1 The Effect of Noise

In most practical cases, measurement noise can contaminate the analysis so that the system is as shown in figure 1.

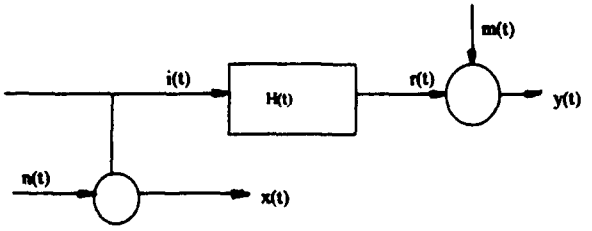

Figure 1

Here, n(t) & m(t) are noise added to the input, i(t) and output, r(t) respectively. If these noise contaminations are mutually uncorrelated and neither is correlated with either i(t) or r(t), then the contamination can be expressed in spectral form as :

$$\begin{aligned} G_{xx}(f) &= G_{ii}(f) + G_{nn}(f) \\ G_{yy}(f) &= G_{rr}(f) + G_{mm}(f) \\ G_{xy}(f) &= G_{ir}(f) \end{aligned} \qquad (4)$$

The coherence function between x(t) and y(t) is thus given by :

$$\gamma_{xy}^2(f) = \frac{G_{ir}^*(f)G_{ir}(f)}{\{G_{ii}(f)+G_{nn}(f)\}+\{G_{rr}(f)+G_{mm}(f)\}} \qquad (5)$$

as compared with the expression of equation (3). Clearly, the effect of noise at both the input and the output is to reduce the coherence function. If the noise contamination is known or measurable, then it is possible to predict its effect and to remove it from the auto and cross spectra so that noise free calculations can be performed.

2.2 Noise Arising from the Sample and Hold Process

The sample and hold process has been shown by Adrain & Yeo (1987) to contaminate the velocity measurements obtained by a laser Doppler system by adding a noise component (termed step noise) and by acting as a low pass filter. These are shown schematically in figure 2 where u(t) is the velocity, s(t) corresponds to the step noise and the low pass filter is represented by L(f).

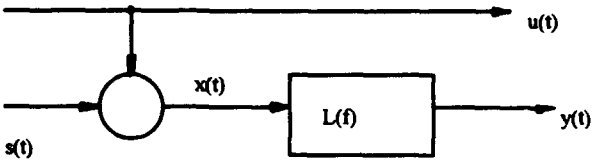

Figure 2

The above equations for noise etc. can now be written as :

$$\begin{aligned} G_{xx}(f) &= G_{uu}(f) + G_{ss}(f) \\ G_{yy}(f) &= |L(f)|^2 G_{xx}(f) \\ G_{xy}(f) &= L(f)G_{xx}(f) = G_{uy}(f) + G_{sy}(f) \end{aligned} \qquad (6)$$

Thus, the coherence function between u(t) and y(t) is:

$$\begin{aligned} \gamma_{uy}^2(f) &= \frac{G_{uy}^*(f)G_{uy}(f)}{G_{uu}(f)G_{yy}(f)} \\ &= \frac{1}{1+\{G_{ss}(f)/G_{uu}(f)\}} \end{aligned} \qquad (7)$$

The step noise will, therefore, result in a reduction of the coherence function and the low pass filter will cause phase distortion when the velocity data are to be used with other measurements to obtain information on interaction. The expresion for the step noise given by Adrain & Yeo (1987) is:

$$G_{ss}(f) = \frac{2\sigma_u^2}{f_m^3 T_\lambda^2} \tag{8}$$

where σ_u^2 is the variance of the velocity, f_m is the mean data rate and T_λ is the Taylor microscale. The effect of the step noise on coherence measurements can thus be estimated for typical spectra.

For example, for white noise with variance σ_u^2, the spectrum can be defined as:

$$G_{uu}(f) = \frac{\sigma_u^2}{\hat{f}}$$

and the Taylor microscale is:

$$T_\lambda = \sqrt{3} / \hat{f}$$

giving the signal to noise ratio as:

$$\frac{G_{uu}(f)}{G_{ss}(f)} = \frac{3}{2}\left(\frac{f_m}{\hat{f}}\right)^3 \tag{9}$$

For other spectra, the signal to noise ratio can also be determined. In all cases, the step noise is a constant so that its influence will be more evident at those frequencies where energy levels are low.

2.4 Numerical Simulations

To examine the error expressions derived in the previous section, a series of simulations using data with white noise and "pink noise" type spectra. Data sets with Gaussian characteristics and prescribed mean and variance were generated using an inverse Fourier transform procedure (Rice & Fitzpatrick, 1988). Two sets of data were used with time steps equivalent to 15 kHz, the first with a white noise type spectrum from 1 Hz to 1 kHz and the second a pink noise spectrum with a cut off at 1 kHz. Each data set was then sampled at equal time intervals and at different mean sample rates with a Poisson distribution to represent data from a counter type LDA processor. This was achieved by calculating the sample times using the algorithm

$$t_n = -\frac{1}{f_m}\ln(1-a_n) \tag{10}$$

where a_n is a random variable uniformly distributed between 0 and 1. For the comparison of uniformly and randomly sampled data, the latter was sampled at 3, 6, 8, 10 & 15 kHz, and the former at 4kHz.

The randomly sampled data was then resampled at equal time intervals equivalent to 4 kHz and the Fourier transforms of both data sets were computed using the FFT algorithm. Direct and cross spectra were evaluated for comparison as described in section 2. Figure 3(a) shows the autospectra for the white noise with various mean random sampling rates and it can be seen that little error is evident in the data. However, the coherence functions between the regularly and randomly sampled data are plotted in figure 3(b) and the effect of mean sample rate is significant and is as predicted from equations (7) and (9) with the exception of the lowest sample rate. The results for pink noise are shown in figure 4. The effect of mean sample rate on the autospectrum is to introduce errors at the higher frequencies where the ratio of signal to step noise is reduced. For the coherence functions, again the effect of mean sample rate is significant especially at the higher frequencies. Again, these effects are predictable from the analysis of the foregoing section.

Results for the effect of sample frequency on the phase between u(t) and y(t) showed that there was no phase distortion when the mean data rate was twice the maximum frequency. When the data rate was less than this, a positive phase was observed and when it was greater, a phase lag was obtained. These errors would influence the estimation of the transfer function between the LDA measurements and other data but, as the effects are predictable, they can easily be corrected.

3. EXPERIMENTS

A series of experiments were performed in which the measurements from an LDA system were directly compared with those from a hot wire in both a grid generated turbulent flow and vortex dominated flow. Autospectra and coherence functions and phase were determined for various flow and turbulence conditions.

3.1 Instrumentation & Analysis

A single channel laser Doppler system with a 32mW He-Ne laser was used operating in forward scatter with focal length of transmitting and receiving lenses of 350mm. The photomultiplier signal was processed using a TSI 1980B type counter interfaced to a 386-pc using a DMA board. The hot wire was a 55P14 miniature probe driven by a 55MO1 anemometer module with a 55D10 lineariser. The hot wire signal was interfaced to the pc using an A/ D board with a sample rate of 4kHz. The simultaneous sampling of the data was achieved by free running the A/D board until an interupt signal was recived from the counter. This signified a data ready condition and the LDA data was then transferred to the computer. The hot wire data was then stored using a backcount from the interupt signal to ensure the data was compatible. A series of tests in which the flow velocity was suddenly changed were performed to check the timing of the data acquisition arrangement. The LDA data was reconstructed with time intervals of ten times the mean data rate (~5kHz) and a Lanczos low pass filter was implemented

to avoid aliasing problems when performing the spectral calculations. Details of the procedure have been given by McDonnell & Fitzpatrick (1992). The auto and cross spectra were then calculated in the normal way and the coherence functions and phase determined from these.

3.2 Experimental Set-Up

A low turbulence wind tunnel with a working section of 127mm square was used for the experiments. For the grid generated tubulence, two sizes of mesh were used and the hot wire and the laser aligned together slightly off centre of the tunnel axis. Measurements were obtained at velocities of 5 m/s and 10 m/s with turbulence intensities of 5% and 15% for each velocity. For the vortex flow, a cylinder was mounted in the tunnel and measurements were taken close to the separating shear layer where coherent vortex action was expected. For this setup, a miniature microphone located on the surface of the cylinder was used to monitor the fluctuating pressure at the separation point. Cross spectral calculations of the microphone measurements and the LDA data were performed as described for the LDA-hot wire measurements and for the microphone-hot wire measurements, a spectrum analyser was used for the analysis.

3.3 Results

For the grid generated turbulence, the results for the autospectra from both hot wire and LDA data are shown in figures 5(a) and (b) for 10 m/s with turbulence levels of 5% and 15%. These show good agreement across the frequency range. However, the coherence function plotted in figures 5 (c) and (d) for each of these shows that the data is very poorly correlated expecially at the higher frequencies. The phases are shown in figures 5 (e) and (f) and, at low frequencies, these show a slight lag characteristic as expected as the hot wire is located somewhat behind the LDA. At higher frequencies, the lack of any coherence between the LDA and hot wire renders the phase data meaningless. Similar results were observed at 5 m/s.

For the vortex dominated flow, the results of the autospectra for the LDA and hot wire measurements are shown in figure 6(a). From the coherence between the LDA and the hot wire in figure 6(b) and the LDA and the microphone in figure 6(c), it is clear that they are correlated only at the vorticity frequency and elsewhere, noise is clearly dominant resulting in no coherence between the measurements. The coherence between the hot wire and the microphone is plotted in figure 6(d). This shows the same characteristics as the LDA results indicating that, in flows with coherent structures, there is little evidence of linear interdependence at other frequencies.

4. DISCUSSION & CONCLUSIONS

The effect of the sample and hold process on cross spectral calculations has been examined. This has been shown to reduce coherence function estimates by a factor dependent on the ratio of the mean sample frequency of the randomly sampled data and the normal cut-off frequency. As the step noise is constant, the ratio of signal to noise depends on the spectrum to be measured. The agreement between the theoretical estimates and the numerical simulations is, generally, very good. Thus, for broadband turbulent spectra, the step noise will greatly influence coherence measurements in the higher frequency range. In addition to the step noise, the low pass filter causes a phase lag which should be corrected when estimating transfer functions using LDA data.

For the experimental results, although the atuospectra for the LDA and hot wire measurements are generally in good agreement for the grid generated turbulence, the coherence between them is poor, especially at the higher frequencies where no correlation is evident at both turbulence levels. For the measurements in the vortex shedding region, the coherence is high only at the vortex shedding frequency. The microphone measurements show that this is the case regardless of whether a sample and hold process is used or not. These results show the poor linear and spatial correlation between measurements of turbulence especially at high frequency and have implications for the use of laser Doppler velocimetry for measurements of the spatial structure of turbulence.

REFERENCES

Adrain,R.J., Yao,C.S. 1987,Power spectra of fluid velocities measured by Laser Doppler velocimetry.Experiments in Fluids 5, 17-28.

Bendat,J.S., Piersol,A.G. 1986, Random Data: Analysis and Measurement Procedures, Wiley Interscience, New York.

Gaster,M., Roberts,J.B. 1975, Spectral analysis of randomly sampled signals, J.Inst.Math.Appl., 15, 195-216.

Lee,D.H., Sung,H.J. 1994, Assessment of turbulent spectral bias in laser Doppler velocimetry, Experiments in Fluids, 16, 223-235.

McDonnell,C., Fitzpatrick,J.A.1992, Spectral analysis of turbulent flows from LDA measurements, Proc. 6th Int.Symp. on Applications of Laser Techniques to Fluid Mechanics, Lisbon, paper 8.3.

Rice,H.J., Fitzpatrick,J.A.1988, A generalised technique for spectral analysis of non-linear systems, Mech. Systems & Signal Processing, 2, 195-207.

Tropea,C., 1987, Turbulence induced spectral bias in laser anemometry, AIAA Journal, 25, 306-309.

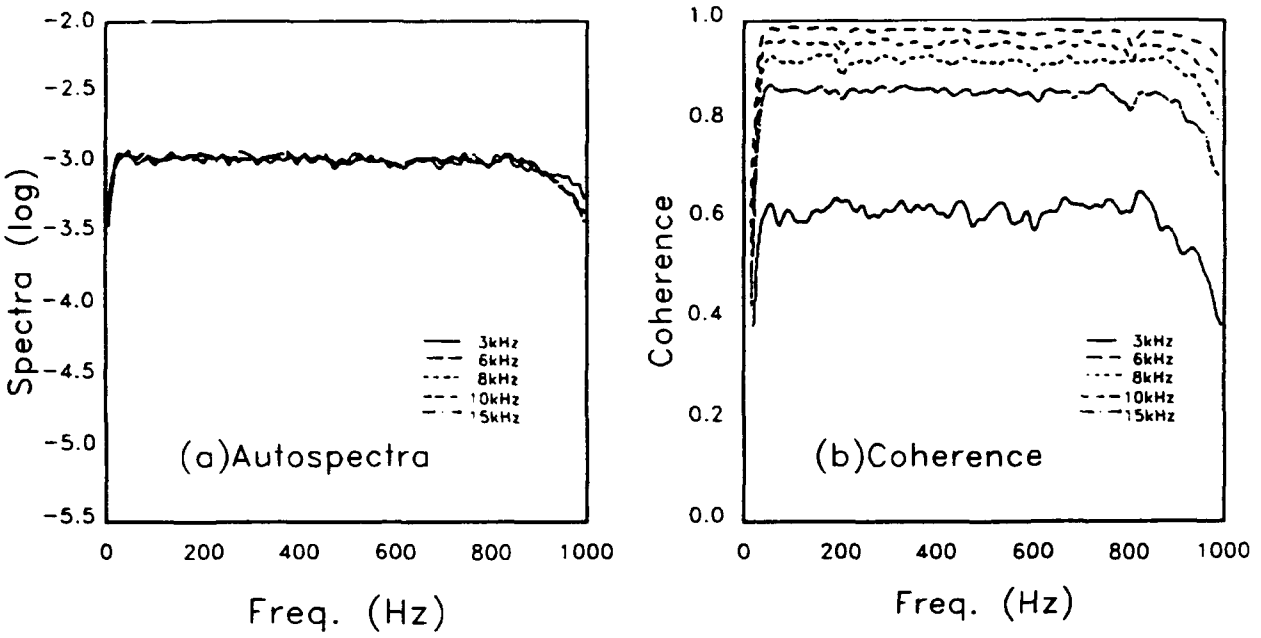

Figure 3: Results for white noise

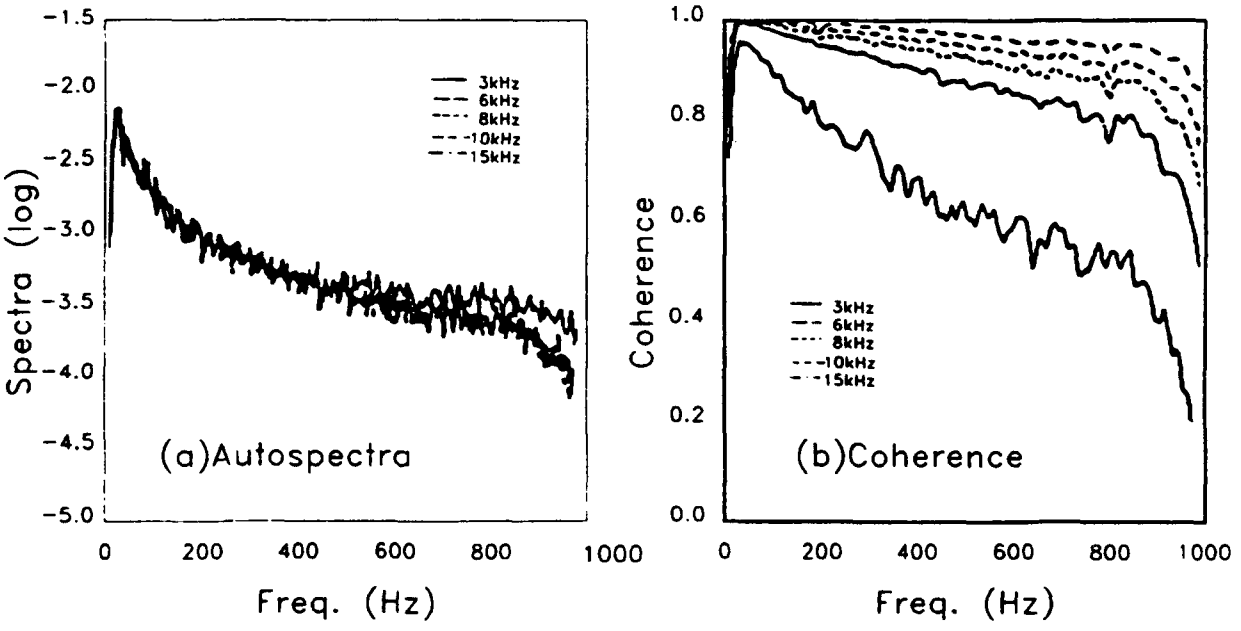

Figure 4: Results for "pink noise"

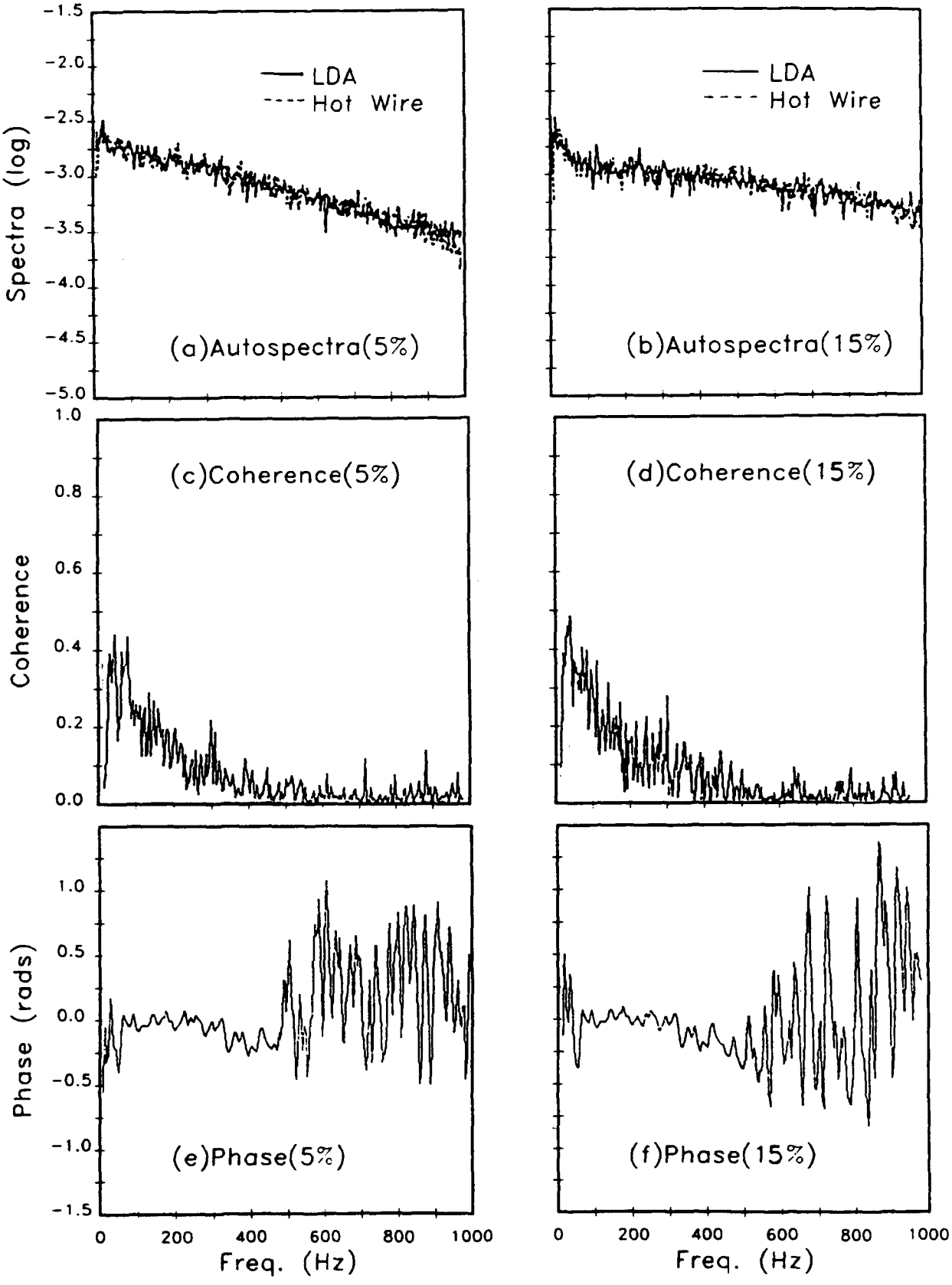

Figure 5: Results for grid generated turbulence

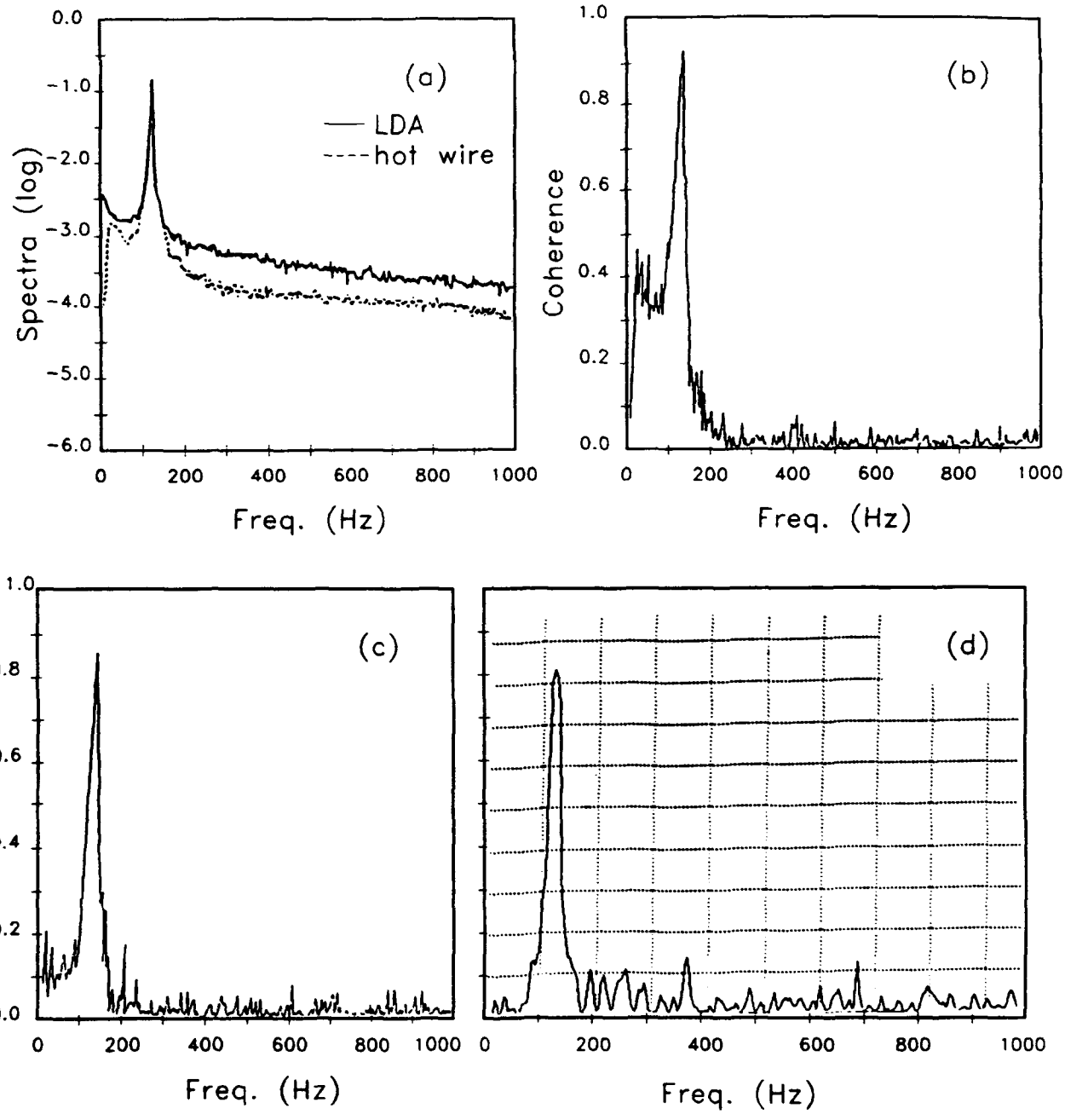

Figure 6: Results for vortex dominated flow
(a) autospectra
(b) coherence for LDA & hot wire
(c) coherence for LDA & microphone
(d) coherence for hot wire & microphone

Session 9.
Combustion III

Microscopic Structures in Turbulent Diffusion Flames by Laser Rayleigh Pyrometer

Tamio Ida
Kumano Technical College
2800 Arima-cho, Kumano, Mie 519-43 Japan

and

Kazutomo Ohtake
Toyohashi University of Technology,
1-1 Tempaku-cho, Toyohashi, Aichi 441 Japan

Abstract

Microscopic structures in turbulent diffusion flames are studied by time-resolved temperature distributions measured by a laser-sheet-illuminated Rayleigh scattering (LRS) method recorded by a high-speed VTR system, and one-point LRS measurement. The microscopic structures of temperature distribution are measured by analyzing the two-dimensional LRS pictures by image processing. Coaxial turbulent diffusion flames at moderate Reynolds numbers, which exhibit typical diffusion flame structures, are formed on laboratory-scale burners. It is found that the flame can be divided into four characteristic regions based on the distributions of macroscale temperature fluctuations. These four regions are visualized by the two-dimensional LRS images. The turbulent heat-transfer mechanisms in these four regions are discussed in terms of the two-dimensional LRS and the power spectral density of temperature fluctuations measured by one-point LRS. Clusters of temperature inhomogeneity are observed by the image analyses in Regions I and III. It is found that different structures of microscopic temperature inhomogeneity exist within Taylor's dissipation length scale defined by velocity fluctuations.

1. Introduction

Space- and time-resolved fundamental information, such as velocity, temperature and concentrations of chemical species, is quite essential for the detailed study of mixing, reaction and heat-transfer mechanisms in a turbulent diffusion flame. In the authors' previous studies, the turbulent diffusion flame structures were studied by time-resolved one-point LRS measurement. The turbulent time scale was obtained therein from the temperature fluctuations. It was determined that the flame could be divided into four regions based on the characteristics of time scale. The time-dependent phenomena have often been masked by the statistical analyses, and the spatial structures of turbulent diffusion flames are not yet fully understood.

Recently, new laser spectroscopy techniques have been adopted to measure the planar images of scalar quantities in the reacting flows by using a laser sheet as an incident light source(1)-(9). Such spatial information cannot yet explain the heat-transfer mechanisms occurring in the mixing process without additional information. Various methods such as fluorescence and Mie scattering have been used to measure the specie concentrations and instantaneous shapes of flame and/or fuel flow. With planar fluorescence spectroscopy it is slightly difficult to obtain qualitative information for the entire observation area since it is rather hard to excite all of the target molecules in the saturated condition(10). On the other hand the Mie scattering method is the easiest technique for obtaining the plane images(1)-(3). However, the difficulty in uniform introduction of fine particles into the flow remains a problem. An LRS can measure the time-resolved gas temperature in the reaction flow if the bulk scattering cross sections of the air, fuel and combustion gas mixture does not change very much before, during and after the combustion.

Fourguette et al. (4) presented a time-resolved two-dimensional LRS to map the instantaneous temperature of a non-premixed flame. They obtained important information for the large-scale struc

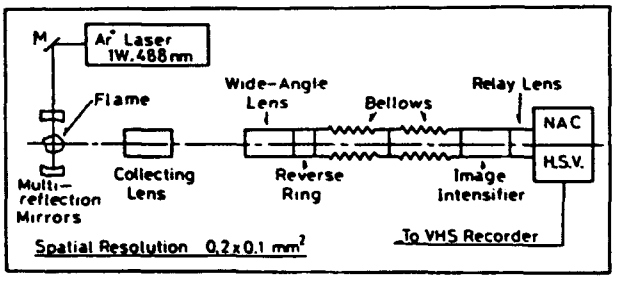

Fig. 1 Alignment of optical system.

tures in the turbulent mixing region between fuel flow and surrounding air. On the other hand, Gouldin(1) and Takeno and Murayama(2) attempted to predict the turbulent burning velocity and discuss the flame structures in premixed turbulent flames by fractal analyses applied to the images obtained by laser tomography. Some papers correlated the recorded signals of the phenomena occurring in the flame with the images taken simultaneously.

This study discusses in detail the microscopic structures of temperature inhomogeneity existing in the focused point, which corresponds to a minute volume, of incident laser light to measure the one-point local temperature by LRS thermometry. Typical microscopic structures were found to correspond to the mixing and reacting mechanisms in each region. Texture analyses were carried out to clarify the spatial and time-resolved mechanisms of turbulent combustion in the tested flames. The microscopic clusters of temperature inhomogeneity were found to exist within Taylor's dissipation length.

2. Experimental Apparatus

Figure 1 shows the alignment of the optical system. The LRS at the wavelength of 488 nm supplied from an Ar ion laser was adopted to measure the flame temperature. A pair of spherical multi-reflection mirrors reflected the laser light about ten times to intensify the incident light power at the focused point. This system could detect the temperature fluctuation up to 10kHz for one-point measurement. In order to measure the two-dimensional microscopic structure of temperature fluctuations in the focused point, the combination of a close-up lens and bellows system enlarged the local temperature distribution inside the area of 0.22x0.44 mm^2. The image intensifier was used to strengthen the power of the image of scattered light. A high-speed video camera (nac400) recorded the thus-enlarged and intensified LRS images. The area of one pixel was calibrated as 1.79 x 1.79μmm^2 by taking an image of a standard mesh.

The mixed gaseous fuel of 62.2%H_2+37.8%CH_4 was fed to the coaxial burner in which a fuel pipe of 2 μmm I.D.. was surrounded coaxially by an air pipe of 64mm I.D.. Burner Reynolds number was fixed at 5,000. The bulk Rayleigh scattering cross section of this fuel does not differ by more than 5% from those of air, fuel and burnt gas before, during and after combustion. The test section was fixed at x/D=25.

A pair of LDV systems was adopted to measure Taylor's dissipation length by two-point correlation of velocity fluctuations at 50 and 51.15mm above the burner tip, respectively. Talcum powder of 2μmm nominal diameter was used as the seeding particle for LDV measurement.

3. Image Analysis

The time-resolved VHS image was converted into an RGB plane of 512x512pixels. The LRS signal stored in the region of 125x250 pixels in the G-image plane was selected to be converted into the temperature signal. The irregularity of incident laser intensity in the measuring plane was corrected before conversion by the intensity pattern obtained at 300K. Flame luminosity always varies in the signal in Regions I and II; we must correct this effect. However, attention must be paid to the signal in Region III since there exist moments when the flame zone covers the entire area, and the air forms the large-scale roll-up eddies which entrain the surrounding air into the flame region. Figure 2 shows the probability density functions (PDF) of typical LRS signals in the cases where the flame region exists within the frame, for PDF of background at 300K and where flame luminosity appeared in the converted G-plane. The PDF of flame luminosity was almost constant for all these cases, and it was corrected before conversion. The lower limit of the time difference for the correspondence between the LDV signals at two measuring points was determined as 1.6kHz to obtain the velocity correlation. This value was selected as the aerodynamic following-up ability of seeded fine particles to the gas flow and was estimated as 5 kHz; the data pairs within an internal three times as long this characteristics time interval were used in the analysis.

4. Results and Discussion

The results obtained by cluster analysis, with different sizes of spatial filters, of the instantaneous two-dimensional LRS signals are discussed and the spatially averaged temperature in

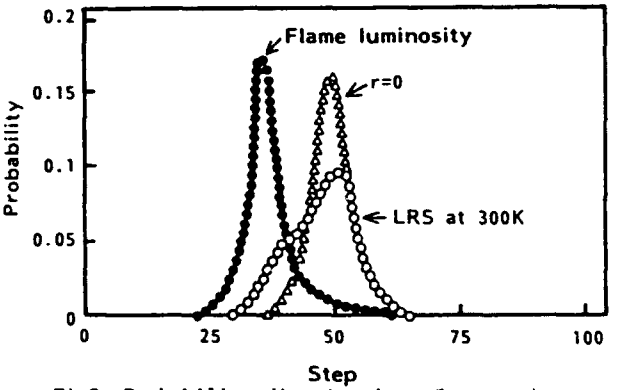

Fig2. Probability distribution of quanties included in raw data.

the measured area and that obtained by the one-point measuring method are compared.

4.1 Instantaneous two-dimensional temperature distribution

Figure 3 shows the instantaneous temperature distributions in the measured area with spatially by averaged temperature $\overline{[T]}$s at radial position r from the center line in the plane of x/D=25 at Re=5,000. These results can explain the characteristics of turbulent diffusion flame structures in the four regions discussed in the previous paper as follows(11)-(13). Region I corresponds to that of the fuel jet, and small areas of higher temperature are observed in lower and weakly fluctuating temperature fields. Region II is located between Regions I and III, and here the combustion takes place between the fuel and air, entrained from Region III, mixed by the turbulent motions. The measured area is almost always covered by the fluctuating high-temperature signals and high spatially averaged temperature results for almost all the frames. Region III entrains the surrounding air by large eddy motion and the typical entrainment behaviors appear between the fuel and air. There are instances at which cold air and fuel cover the measured area and high-temperature combustion gas exists under a homogeneous, coherent and weak turbulent condition. Similar behaviors as those in Region I are observed in this region. Region IV corresponds to the surrounding air flow and shows low and constant temperature distributions, however, occasionally gas at moderate temperatures diffuse into this region from Region III, and islands of cooled combustion gas are formed.

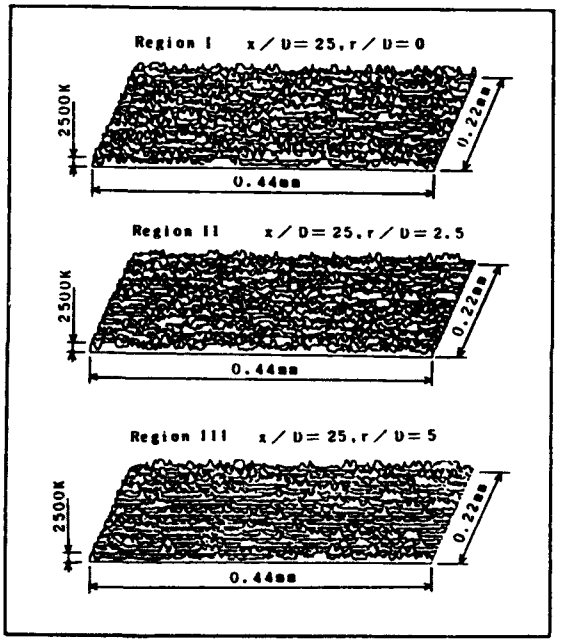

Fig. 3 Instantaneous temperature distributions in the measures area [0.22 x 0.44 mm^2].

Figure 4 shows the time-resolved spatially averaged temperature and PDF of temperature inside the measured area for thirty successive frames. Time mean temperature by one-point measurement is also shown for comparison. The difference between spatially averaged temperature and time mean temperature is not very marked in Region I and II. On the other hand, in Region III the spatially averaged temperature is from 300 to 800 K higher than the time mean temperature. One of the reasons for

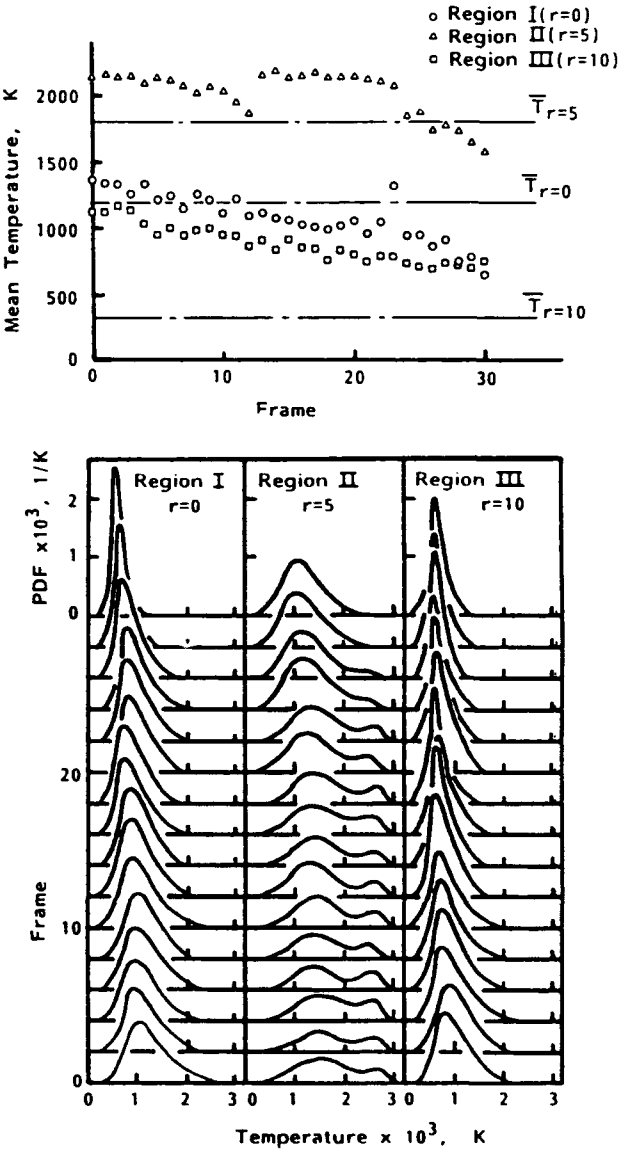

Fig. 4 Time history of spatially averaged temperature and probability density functions in three region.

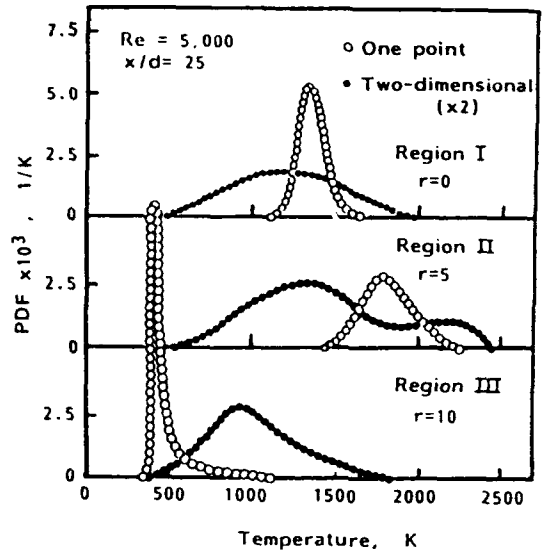

Fig. 5 Comparison of PDF between the instantaneous two-dimensional and one-point temperature measurement.

this difference might be considered as the influence of the flame luminosity, but the main reason is the fact that the series of frames containing high-temperature clusters have been selected.

The time histories of PDF in Regions I and III show that they cover a wider ranges of temperature, have shapes close to the Gaussian distribution and do not change markedly. In Region II PDF cover wide temperature range than in the other two regions, and is shaped bimodal distributions. These are in line with the results reported by Fourguette et al. (4) with their visualization experiment by the LRS method. This study clarifies that this kind of bimodal characteristic exists within the microscopic flame structures. In order to examine the flame structure in more detail, the results will be compared with those obtained by one-point measurement.

4.2Comparison between instantaneous temperature distribution by two-dimensional measurement and time-sequential temperature by one-point measurement

Figure 5 compares PDF obtained from the typical instantaneous two-dimensional temperature distribution with that from the 10,000 data points of one-point measurement (these data points correspond to those during 0.17s.). In Region I, PDF from one-point measurement shows Gaussian distribution near the middle of PDF from two-dimensional measurement. In Region II the former appears in a near-Gaussian distribution at the valley of bimodal distribution of the two-dimensional measurement.

From these results, it is found that Region I consists of microscopic inhomogeneous spatial temperature distribution which are formed by small islands of combustion gas separated from the flame region flowing into the cooler fuel flow and/or the separated small air chips flowing into the cooler fuel flow, and small combustion gas islands might be distributed. However, one-point measurement only produces the spatially averaged temperature by integrating the entire distribution over in the volume, hence it could not detect this micro-structure; it produces the time sequential temperature history shown in Fig. 4. Region II is the combustion region and produces the microscopic inhomogeneity by the interactions between aero-dynamic turbulence and chemical reactions.

4.3 Cluster analysis by spatial filter

A slight difference could be observed in the characteristic structures of Regions I and III from the spatial temperature distributions shown in Fig. 3. Cluster analysis was applied to the converted images to make their differences clearer. Different sizes of spatial filters with the same weight to every pixel were used to enhance the inhomogeneities in the images. Temperature was divided into two categories, one higher than 1,500 K which is dark, the other lower than 1,500 K shown by blank spaces. Typical examples for Regions I and III are shown in Fig. 6 in which the clusters become clearer with the larger-sized spatial filters. The cluster distributions do not change very much when the filter size becomes larger than 7x7. The difference between Regions I and III becomes clearer after this cluster analysis. In particular, in Region III the effect of filtering in cluster analysis begins to appear with the use of a relatively small 3x3 filter, and becomes marked at the filter size of 5x5. The results for Region II are almost completely dark, which shows the field is occupied by burnt gas and/or a burning zone; it is not shown here.

In order to discuss the above-mentioned microscopic flame structures, the one-dimensional power spectral density for each region is shown in Fig. 7. In Region I the turbulent thermal diffusion effect shown by the -5/3 power law is observed up to the higher-frequency region. This corresponds well to the fact that the microscopic high-temperature clusters diffuse into the fuel flow region due to the aerodynamic turbulent motions, as shown in Fig. 6. Contrary to this, in Region III the -5/3

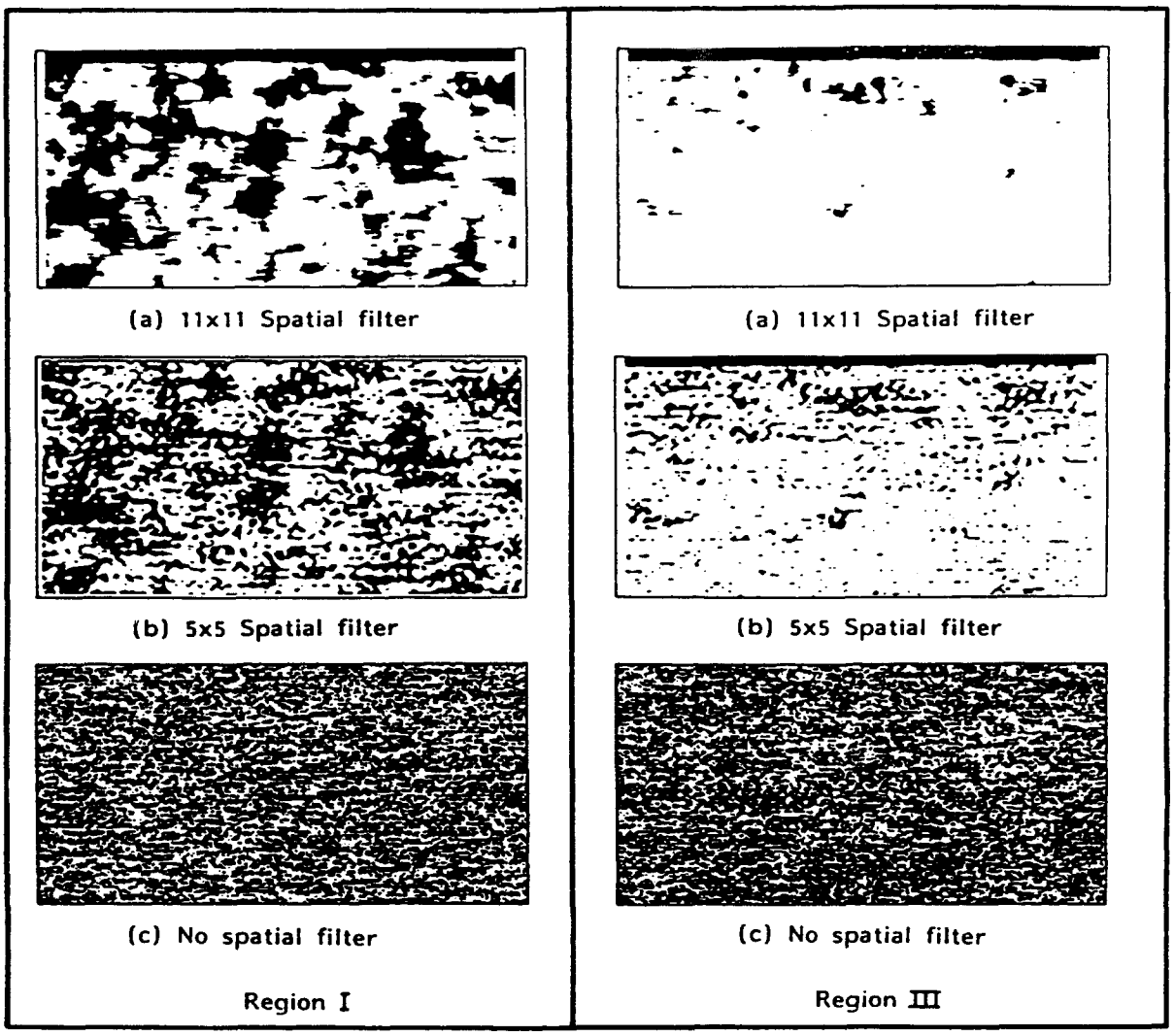

Fig. 6 The effect of spatial filter sizes on cluster analyses.

This is well understood from the Schlieren photog power law region is observed at lower frequency. raphy and two-dimensional laser tomography taken by the high-speed VTR system and presented in the previous paper(9) that this power law corresponds to the aerodynamic mixing due to rather large structures, and the finer cluster may indicate the -1 power law, showing the diffusion due to molecular-level mixing which exists at the regions of mild temperature gradient at the moderate-temperature range. As mentioned above, in Region II marked clustering could not be observed using the 3x3 spatial filter, but the clusters existing within the temperature range above 1,500 K might be aerodynamically diffused due to the turbulent mixing. The bulk gas flow speeds in Regions I and II are so high that the electric circuit could not record the density in the frequency region in which the -1 power law is observed. In Regions III and IV this could be recorded since the flow speed is lower than those in Regions I and II.

In order to observe the time history of variations of clusters the typical time sequence results in Regions I and III obtained with the 11x11 spatial filter are shown in Fig. 8. As seen in the results for Region I, the sizes of high-temperature clusters flowing from Region II are similar and distributed evenly within the area, and this may give the result of weak variation of temperature signals in one-point measurement. The changes of cluster sizes and their distributions in Region III are caused by the large-scale eddy motions of the surrounding air entrained from Region IV. Therefore, the patterns of cluster distributions change drastically from the range of flame regions to the air flow. The values of time mean temperature show the spatially averaged temperature over this two-dimensional area.

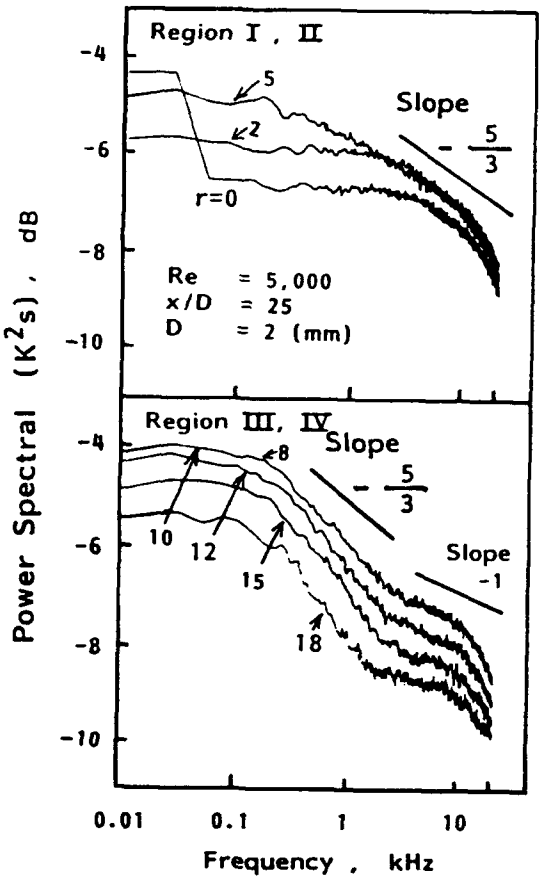

Fig. 7 One-dimensional power spectral density for each regioncalculated by one-point measurement.

5. Conclusions

1)A method for measuring instantaneous two-dimensional temperature distribution has been developed. Texture analyses corresponding to the four regions characterized by the tendencies of time scales of turbulence in the previous paper have been carried out. The existence of the clusters of combustion gas flowing into the fuel flow was clarified.

2)The variations in the characteristics of spatial temperature gradients could be observed by changing the size of spatial filters for the converted images. The results indicated that the spatial distributions and their relationships to temperature gradients are very important in explaining the various thermal diffusion effects in the turbulent diffusion flames.

3)The existence of microscopic inhomogeneities of temperature was examined using Taylor's dissipation length, the statistical quantity of velocity field. It was shown that the sizes of temperature inhomogeneities were around or order of this dissipation length.

Acknowledge

The authors would like to express their gratitude for partial funding through a Research Grand-in-Aid for Scientific Research on Priority Areas "Exploration of Combustion Mechanism" from the Ministry of Education, Science and Culture under Contract Number 02209102.

References

(1)Gouldin, F. C., Combust. Flame, Vol. 68, No. 3 (1987), p. 249.

(2)Takeno, T. and Murayama, M., Proc. 22nd Symp. (Int.) on Combust., (1988), p. 511.

(3)Gutmark, E., Hanson-Parr, D. M. and Schadow, K. C., Fractal Behavior of a Wrinkled Annular Diffusion Flame, Combust. Flame, Vol. 79 (1990), p. 7.

(4)Fourguette, D. C., Zurn, R. M. and Long, M. B., Two-Dimensional Rayleigh Thermometry in a Turbulent Nonpremixed Methane-Hydrogen Flame, Combust. Sci. and Tech., Vol. 44 (1986), p. 307.

(5)Miyawaki, K., et al., Proc. of 26th Combust. Symp. in Japan (1988), p. 22.

(6)Hanson, R. K., Combustion Diagnostics: Planar Imaging Techniques, 21th Symp. (Int.) on Combust., (1986), p. 1677.

(7)Mansour, M. S. and Bilger, R. W., Spatial-Averaging Effects in Raman/Rayleigh Measurements in a Turbulent Flame, Combust. and Flame, Vol. 82 (1990), p. 411.

(8)Namazian, M. and Kelly, J. T., Near-Field Instantaneous Flame and Fuel Concentration Structures, 22nd Symp. (Int.) on Combust., (1988), p. 627.

(9)Ohtake, K., Naruse, I., Horiuchi, K. and Tsuji, H., Structure of Turbulent Diffusion Flame by High-Speed Image Processing and Rayleigh Scattering, Trans. Jpn. Soc. Mech. Eng., (in Japanese), Vol. 57, No. 535, B(1991), p. 1135.

(10)Deguchi, Y., Yoshikawa, N. and Ohtake, K., Temperature and Concentration Measurement of OH by Three-Line Laser-Induced Fluorescence, Proc. 5th Int. Symp. Applicat. Laser Tech. Fluid Mech., (1990), p. 2. 3.

(11)Ida, T., Horiuchi, K. and Ohtake, K., Turbulent Diffusion Flame Structures and Their Similarities, Joint Int. Conference Australia/New Zealand and Japanese Sections, (1989), p. 48.

(12)Ida, T. and Ohtake, K., Experimental Study of Diffusion Flame Structures and Their Similarities, Trans. Jpn. Soc. Mech. Eng., (in Japanese), Vol. 56, No. 531, B(1990), p. 3514.

(13)Ohtake, T. and Ida, T., Proc. 5th Int. Symp. Applicat. Laser Tech. Fluid Mech., (1990), p. 31. 2.

(14)Townsend, A. A., The Structure of Turbulent Shear Flow, 2nd ed. (1980), p. 47, University of Cambridge.

TEMPERATURE MEASUREMENTS BY LASER RAYLEIGH SCATTERING IN COUNTERFLOW DIFFUSION FLAMES: A COMPARISON BETWEEN EXPERIMENTAL RESULTS AND THEORY

T. Croonenbroek, F. Aguerre, P. Versaevel, J.-P. Martin,
N. Darabiha and J.C. Rolon
Laboratoire d'Énergétique, Moléculaire et Macroscopique, Combustion
CNRS, École Centrale Paris
Grande Voie des Vignes
92295 Chatenay-Malabry Cedex, France

ABSTRACT

Non-intrusive, spatially resolved, Laser Rayleigh Scattering measurements in hydrogen-air and propane-air counter flow diffusion flames are reported. As the composition of the flame varies widely with progression of combustion, the difficulty consists in converting these measurements into temperature profiles. We demonstrate that with a simple interpolation procedure, Laser Rayleigh Scattering can be used to measure temperature to a good precision, though the effective Rayleigh cross section is a highly varying parameter in the flame. The experimental results are compared to temperature profiles obtained by theoretical calculations.

INTRODUCTION

Laser Rayleigh Scattering (LRS) is a well established non-intrusive diagnostic technique for analysis of mixing processes (Yip, 1986) and for temperature measurements in non-reactive gases (Miles, 1990). LRS has also been applied to flames. Müller-Dethleffs et al. (1978) investigated the effects of organic peroxides, traces of inhibitor on burning velocity and the effect of electrical fields on normal and inhibited flames. Several temperature measurements by LRS have also been performed on turbulent premixed flames (Gouldin, 1986) and non-premixed flames (Dibble, 1981; Fourgette, 1986; Stepowski, 1992).

As Rayleigh scattering is an elastic process which is not selective in the diffusing molecule, almost all authors supposed the scattering efficiency, expressed by the effective Rayleigh cross section (σ_{eff}), to be constant throught the reactive flow in order to deduce total number density and temperature from LRS measurements. Dibble and Hollenbach (1981) showed that this hypothesis is verified in premixed hydrocarbon flames within a precision of 10%. For investigations on turbulent diffusion flames, they proposed a special fuel mixture of 31% methane and 69% hydrogen (Dibble, 1981; Fourgette, 1986). In this special case, the mixture of CH_4 and H_2, the combustion products and air have approximately the same effective Rayleigh cross section. For general investigations on diffusion flames, this fuel composition is an important restriction as it does not correspond to commonly used fuel mixtures in practical applications.

Stepowski and Cabot (1992) tried to overcome this problem. They obtained single shot LRS profiles in the development zone of a turbulent diffusion flame of a diluted hydrogen jet issuing in a coflowing air stream. The effective Rayleigh scattering cross section at each laser shot was calculated as a function of mixture fraction and the temperature profiles by the use of an algorithm involving a strained flame library.

In this paper, we present a procedure to obtain the effective Rayleigh cross section and thus temperature profiles, which is based only on the imposed boundary conditions, the measured Rayleigh scattering signal and the properties of diffusion flames. This technique is applied to measurements on laminar hydrogen-air and propane-air counter flow diffusion flames.

Plane laminar strained flames are of great interest because they allow detailed understanding of combustion mechanisms and suitable test cases for the investigations of the interactions between aerodynamics, chemical kinetics and transport properties of combusting gases. Besides, these laminar strained flames are also important ingredients in the so called "flamelet models" (see review paper by Candel, 1994).

Counter flow flames are then well documented in the literature, and theoretical and experimental aspects of these flames have been studied by many authors. (Pandya and Weimberg (1964), Linan (1974), Giovangigli and Smooke (1987), Rolon et al (1986, 1988, 1991), Aguerre et al (1992), Dagusé et al (1992), Darabiha et al (1992, 1993), Lacas and Versaevel (1994), Magre et al (1994)). The counterflow diffusion flame constitutes a simple and practical test case to compare the LRS method proposed in this paper, with the available in the literature information.

Figure 1a shows an example of a counterflow propane-air diffusion flame by a laser sheet visualisation, and Figure 1b shows a flat hydrogen-air laminar couterflow diffusion flame.

Figure 1a. Laser tomogrphy of counterflow diffusion flame. The flame is formed by opposed jets of propane and air.

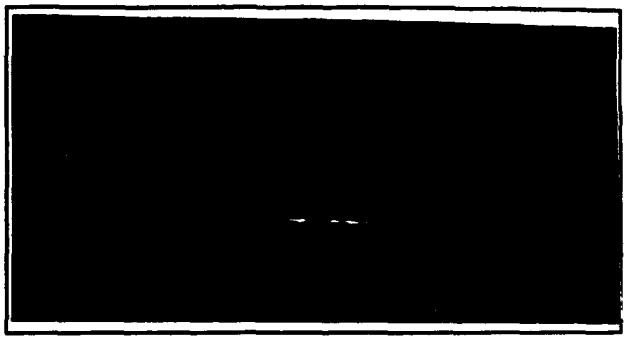

Figure 1b. Stabilised diffusion flame in the stagnation region of opposed jets of hydrogen and air.

THEORY OF RAYLEIGH SCATTERING

The cross section for Rayleigh scattering at 90° from the incident light is given by :

$$\sigma_i = \frac{4\pi^2}{\lambda^4}\left(\frac{\mu_i - 1}{N_0}\right)^2 \qquad (1)$$

it only depends on the index of refraction μ_i and the molecular number density N_0 at standard conditions, and the 4th power of the incident wavelength λ. However in flames, the effective Rayleigh cross section σ_{eff} is an average of the cross sections σ_i of the species weighted by their mole fractions χ_i:

$$\sigma_{eff} = \Sigma\, \chi_i\, \sigma_i \qquad (2)$$

The relative Rayleigh cross section of some major species in flames are listed in table 1 (Lide, 1992).

Molecule	relative Rayleigh cross section (σ_i/σ_{N2})
N_2	1,00
O_2	0.833
H_2	0.22
H_2O	0.716
C_3H_8	13.56
CO_2	2.29
CO	1.25
Air	0,965

Table 1

The intensity of scattered light I_s is proportional to the incident laser beam intensity I_0, the number density N and the effective Rayleigh cross section by:

$$I_s = C\, I_0\, N\, \sigma_{eff} \qquad (3)$$

where C is a constant which characterizes the experimental set-up. In the case of an isobar flame of pressure P, number density only depends on temperature through the ideal gas equation so that:

$$T = \frac{C\, I_0\, P\, A_0}{R}\,\frac{\sigma_{eff}}{I_s} = K\,\frac{\sigma_{eff}}{I_s} \qquad (4)$$

A_0 is Avogardo's number and R the universal gas constant. In the experiments K is a constant which is determined in calibration experiments on gas flows of known composition and temperature:

$$K = \left(\frac{T\, I_s}{\sigma_{eff}}\right)_{cal} \qquad (5)$$

Thus temperature in the flame can be derived as

$$T = \left(\frac{T\, I_{diff}}{\sigma_{eff}}\right)_{cal}\left(\frac{\sigma_{eff}}{I_{diff}}\right)_{flame} \qquad (6)$$

when the effective cross section in the flame is known as a function of space. This paper describes a new method to determine it in the fresh and burnt gases.

EXPERIMENTAL SET UP

Opposed-jet counter flow diffusion flames, employed in this study, are described in detail elsewhere(Rolon et al (1991, 1992), Lacas (1994) see in this Symposium). The burner configuration is shown in Figure 2 The flame is stabilized in the region of the stagnation plane established between two converging nozzles (see Figures 1a and 1b). Coflowing nitrogen is employed to eliminate air diffusion and dust particles from outside.

This flame is stable and established in a simple, well defined, axisymetric flow field (see Rolon et al (1992)). Mass flow rate and gas composition are controlled by sonic nozzles. A three stage filter was interposed in the air flow to avoid Mie scattering from particles.

The experimental set up is shown in figure 3. The beam of a power stabilized multiline argon ion laser, modulated by a mechanical chopper, is focused (D=0,13mm) on the axis of the flow.

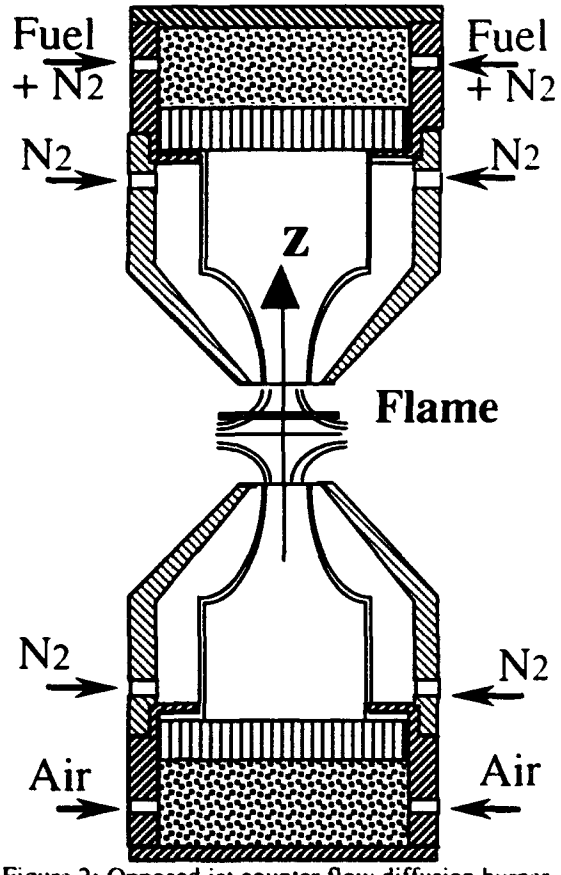

Figure 2: Opposed jet counter flow diffusion burner

The Rayleigh scattering signal is measured at 90°. The collection optics consists of two f/3,75 lenses (f=310mm) which image the measuring volume 1:1 on a pinhole (d = 0,5mm) placed in front of a photomultiplier tube. Thus the measuring volume is a cylinder of diameter 0,13mm and 0,5mm in length. Wavelength selection and rejection of background flame luminescence is achieved by a narrow bandwidth interference filter with a centerwavelength equal to 488nm placed between the pinhole and the photomultiplier tube. The output signal is processed by a lock-in-amplifier interfaced to a microcomputer.

As light scattered from surfaces (lenses, mirrors) is also modulated, it cannot be rejected by phase sensitive signal processing. Diaphragms and screens were placed in the experimental set up to prevent light scattered from these surfaces reaching the photomultiplier.

MEASUREMENTS OF RAYLEIGH SCATTERING

One of the more interesting simplifying conditions of opposet jet diffusion flames is that temperature andspecies concentration do not changes in the radial direction, and varie only along the axis, in the normal direction to the stagnation plane and to the flame surface.This situation facilitates not only the theoretical calculations,

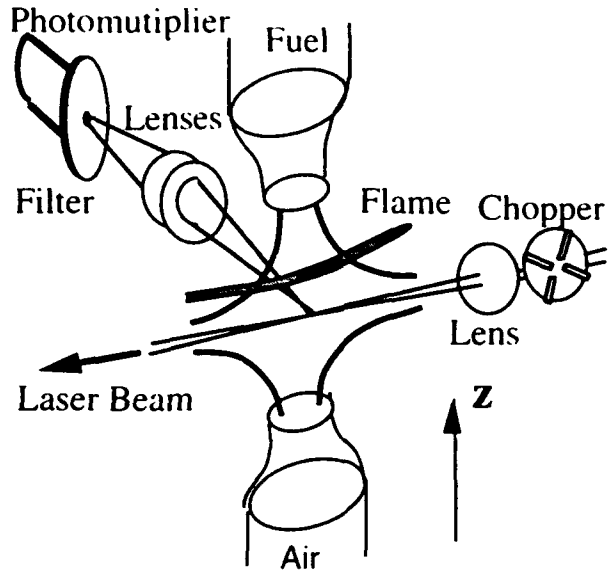

Figure 3: Experimental set-up

making possible one dimensional calculations with similarity solutions (see Darabiha and Candel (1992), Aguerre et al (1992)), but also the experiments with local measurements along the axis of velocity and density, (Rolon et al (1992)), temperature measurements by CARS (Magre et al (1994)) or OH concentration by LIF (Rolon et al (1992)). Following this, in our experiment, local LRS measurements have been performed along the axis of the flow.

A background signal caused by stray light can reduce the detection sensitivity; an uncorrected background of 2,5% of the Rayleigh signal at room temperature can cause the measured peak flame temperature to be reduced by 10%. Thus before each measurement, we verify that background is negligible. Calibration measurements are performed on an air jet. Its temperature is determined with a thermocouple to a precision of 1K. The standard deviation of the measured LRS intensities are typically 0,3% in calibration and flame measurements. To verify that the experimental settings deliver a correct Rayleigh signals , one may compare the ratio of the Rayleigh signals of fresh air and diluted fuel with the imposed equivalence ratio.

In figure 4, we show the Rayleigh scattering signal in the hydrogen-air flame (equivalence ratio Φ=1; global strain rate ε = 120 s^{-1}) along the axis of the flow. The origin is taken at the stagnation point. The intensity profile of the measured LRS signal allows 3 zones to be distinguished: air from -6mm to -1.8mm, the reaction zone from -1.8mm to 3.4mm and in nitrogen diluted fuel between 3.4mm and 6mm.

In figure 5 we show the Rayleigh scattering signal in the propane-air flame (equivalence ratio Φ=4.3; global strain rate ε = 51 s^{-1}). We also distinguish the different zones of fresh air, reaction process and fresh, in nitrogen diluted fuel. In this case the ratio between the Rayleigh

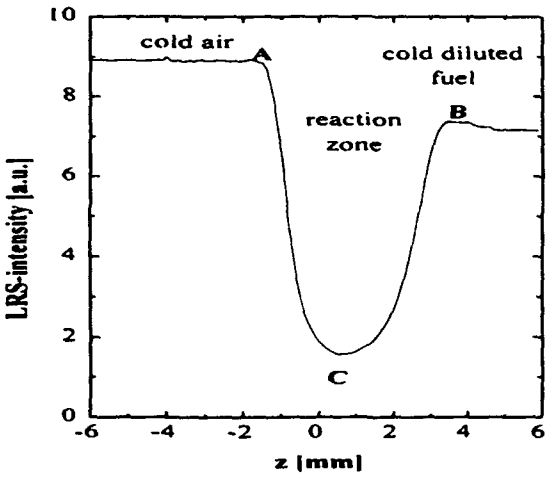

Figure 4: Rayleigh scattering signal along the axis of a counter flow hydrogen-air diffusion flame (equivalence ratio Φ=1; global strain rate $\varepsilon = 120\ s^{-1}$)

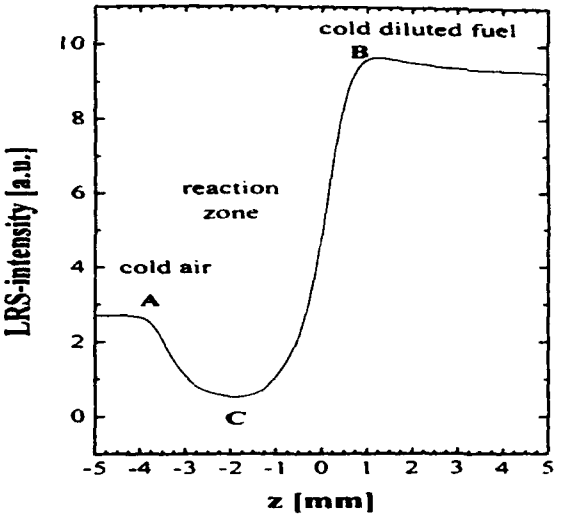

Figure 5: Rayleigh scattering signal along the axis of a counter flow propane-air diffusion flame (equivalence ratio Φ=4.3; global strain rate $\varepsilon = 51\ s^{-1}$)

cross section in fresh air and in fuel mixture ($\sigma_{fuel}/\sigma_{air}$ = 3.5) is more important than in the hydrogen - air flame ($\sigma_{fuel}/\sigma_{air}$ = 0.8) due to higher cross section of propane. Thus the LRS signal at the fuel side of the propane-air flame is more important than on the oxidizer side.

LRS TO TEMPERATURE CONVERSION

As discussed before, the local value of the effective Rayleigh cross section must be known to deduce temperature from LRS. In the fresh gases, the effective Rayleigh cross section is calculated from the composition of the injected gases using formula (2). It remains constant up to the reaction zone, point A on the air side and point B on the fuel side. In the reaction zone, between these two points the LRS signal goes through a minimum (point C) which corresponds to a maximum of temperature across the flame.

We can assume within a good approximation that at maximum temperature only the products of a stoichiometric combustion of the injected gases are present. Thus the effective Rayleigh cross section can be determined at the minimum of the Rayleigh scattering signal in the following way.

In the hydrogen-air flame the reaction can be described by:

$$0.585(29.8\%\ H_2 + 70.2\%\ N_2) + 0.415(21\%O_2 + 79\%\ N_2)$$

$$\Rightarrow 26.15\%H_2O + 73.85\%N_2$$

Injecting these mole fractions in formula (2) leads to the effective Rayleigh cross sections:

fuel: $\sigma_{eff} = 0.768$; air: $\sigma_{eff} = 0.965$
products: $\sigma_{eff} = 0.923$

In the propane-air flame:

$$0.18(19.1\%\ C_3H_8 + 80.9\%\ N_2) + 0.82(21\%O_2 + 79\%\ N_2)$$

$$\Rightarrow 8.85\%CO_2 + 11.8\%H_2O + 79.34\%N_2$$

fuel: $\sigma_{eff} = 3.399$; air: $\sigma_{eff} = 0.965$
products: $\sigma_{eff} = 1{,}073$

In propane-air diffusion flames, the assumption of a complete consummation of fuel and oxidizer at peak temperature is valid. However, the diffusivity of hydrogen is higher than that of nitrogen and the mole fractions of hydrogen and oxygen are not zero at peak temperature in hydrogen - air diffusion flames. We estimate that this phenomena causes an error on the peak temperature determination lower than 1%. Thus peak temperature can be measured to a good precision by LRS.

Knowing σ_{eff} in the fresh gases (point A,B) and at peak temperature (point C), we obtain the effective cross section σ_{eff} in the reaction zone by fitting through the known values at A,B and C. In figure 6 and 7 for hydrogen - air and propane - air flames respectively, we used linear (dotted lines) and error function (dashed lines) interpolation. The second fitting by error functions was used because reactants and products mole fractions in the reaction zone are defined in the analytical flame sheet approximation by error functions (Linan, 1974; Marathe, 1972).

The effective cross section σ_{eff} of both fitting procedures are compared to the theoretical effective cross

section (solid lines) calculated from the mole fractions of species participating in the Rayleigh signal. The mole fractions of these species were computed by standard laminar strained flame calculations taking into account complex chemistry and transport properties (Darabiha, 1992; Darabiha, 1989; Giovangili, 1987). These comparisons yield the following results:

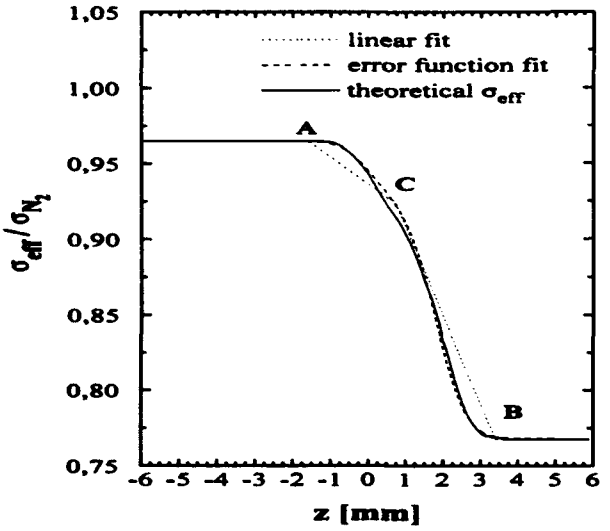

Figure 6: Fit of the effective Rayleigh cross section along the axis of a counter flow hydrogen-air diffusion flame (Φ=1; $\varepsilon = 120\ s^{-1}$).

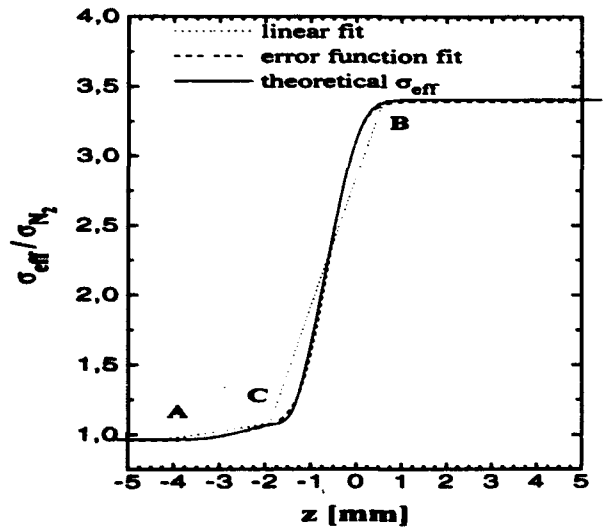

Figure 7: Fit of the effective Rayleigh cross section along the axis of a counter flow propane-air diffusion flame (Φ=4.3; $\varepsilon = 51\ s^{-1}$)

- In the hydrogen - air flame both fitting functions give an effective cross section in the reaction zone that do not differ more than 1% from the theoretical values (see figure 6). In this case both interpolations can deliver satisfactory results for LRS conversion into temperature.
- In the propane air flame a difference of σ_{eff} in the reaction zone was found using the two fitting functions. Using the linear interpolation, σ_{eff} is overestimated on the fuel side near the C point up to 25% and underestimated near the B point up to 20%. A linear fitting procedure for the effective cross section on the rich side of the propane - air diffusion flame is not appropriate. Anyway, using the error function fitting, a difference of at least 2.5% with respect to the theoretical calculated σ_{eff} was obtained (see figure 7).

RESULTS AND DISCUSSIONS

In figures 8 and 9 we show the temperature profiles for the hydrogen - air and the propane - air flames calculated from formula (6) and using the fitting procedures presented in the previous section. The experimental profiles are compared to theoretical ones.

In the case of the hydrogen - air diffusion flame (figure 8), the experimental temperature profiles obtained by the two fitting procedures and the theoretical calculated σ_{eff} using also the Rayleigh scattering signal overlap. The experimental and the calculated peak temperatures are in good agreement. At the flame front we found a systematic deviation between the measurement and theory. The deviations are explained by the limited spatial resolution of the optical system employed in this work. Another source of error could be the deviation of the laser beam by the density gradient but we demonstrated that it is small compared to the dimensions of the measuring volume so that it has negligible influence on the results.

In the propane - air flame, the determined temperture profiles converted from the LRS measurements through the two fitting procedures (linear and error function) show different behavior. On the rich side (z>-1.9mm) the linear fit shows a strong distortion of the profile and a displacement of the location of the temperature maximum ; on the contray the error function fit shows a very good agreement with the results of the modelling so that the shape and absolute value of the measured temperature profile coincident to the calculated one within the estimated error limits of measurement (estimated to 3%). On the lean side (z<-2mm) the two procedures give the same temperature profile and fit the predicted value within experimental error. This shows that the proposed new method for converting LRS measurements into temperature profile is better adapted to combustion cases than the previous linear fit.

The error limits of the experiments have been estimated as follows. The calibration measurements are performed with an uncertainty of 1K for T_{cal} and 0.3% for I_{cal}. In the measurements on flames, the same uncertainty was assumed for I_s. As the composition of air is well known, no uncertainty on σ_{cal} is taken. This leads to uncertainties of 1.5% in the case of the hydrogen-air

flame and of 3% for the propane-air flame on temperature in the reaction zone.

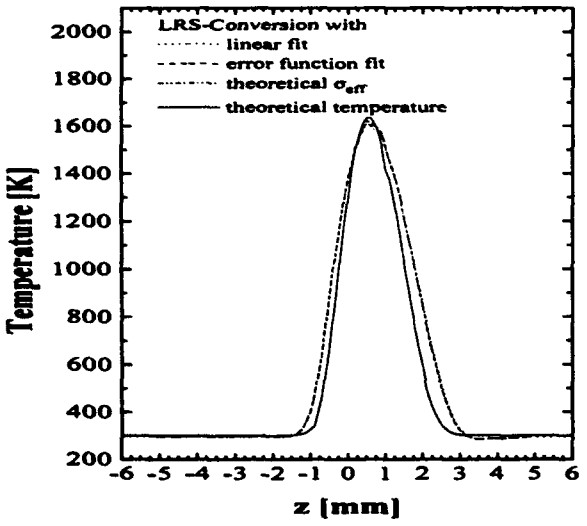

Figure 8: Experimental and theoretical temperature profiles along the axis of a counter flow hydrogen-air diffusion flame (Φ=1; $\varepsilon = 120\ s^{-1}$)

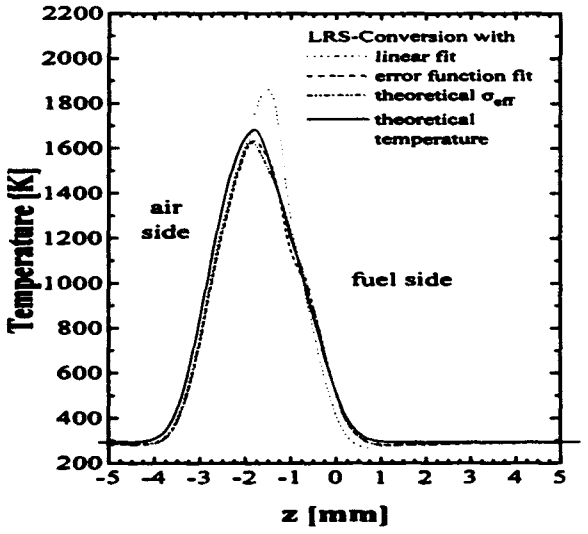

Figure 9: Experimental and theoretical temperature profiles along the axis of a counter flow propane-air diffusion flame (Φ=4.3; $\varepsilon = 51\ s^{-1}$)

CONCLUSION

In this work, we use a well established Rayleigh scattering method to measure temperature profiles in laminar diffusion flames. Up to now, in traditional experiments, laser Rayleigh scattering yield satisfactory results for only some limited flame cases (special fuel mixture , assumption of an overall equivalent cross sections). Nevertheless we show here, that Laser Rayleigh scattering may be extended to a wider domain of laminar diffusion flames by using a fitting procedure which leads to direct experimental definition of the effective cross section in the reaction zone of the flame.

We also compare these procedures to direct theoretical calculations, knowing the mole fraction distribution across the flame for molecules participating in the Rayleigh scattering process. Two test cases were studied in this work: the case of a hydrogen - air diffusion flame and the case of a propane - air diffusion flame.

In the case of the hydrogen - air diffusion flame, the measured peak temperatures is well predicted by theory. In both sides of the flame front, the measured temperature overestimates the theoretical values. We explain this discrepancy by a lack of spatial resolution because the flame front in such a flame is very thin. More precisely, the sensitivity of laser Rayleigh scattering to spatial resolution is very high. In the reaction zones where temperature and species concentration gradients are important, this sensitivity becomes critical. This spatial resolution may be considerably increased by using planar laser Rayleigh scattering associated to an intensified CCD camera, for which the spatial resolution is of the order of one pixel (20µm•20µm).

A better agreement between experiment and theory is achieved in the case of the propane air flame where the flame is thicker.

ACKNOWLEDGEMENTS

The authors wish to thank P. Scoufflaire et G. Coeur-Joly for their engaged technical assistance.

Financial Support was provided in part by the Joule Program of the Commission of the European Communities under Contract JOUE-0056C entitled "Development of Advanced Sensors".

REFERENCES

Aguerre, F., Darabiha, N., Rolon, J.C. and Candel, S., (1992). "Experimental and Numerical Study of Transient Laminar Counterflow Flames". Fizika Goreniya i Vzryva, 29, N°3, 61-66. © 1993 Plenum Publishing Corporation.

Candel, S. Veynante, D. Lacas, F. Darabiha, N. and Rolon, J.C. (1994) "Current Progress and Future trends in Turbulent Combustion". to be published in Comb. Sci. and Tech.

Dagusé, T., Soufiani, A., Darabiha, N., and Rolon, J.C. (1992). "Structure of Diffusion and Premixed Laminar Counterflow Diffusion Flames Including Molecular Radiative Transfer". Fizika Goreniya i Vzryva, 29, N°3, 55-60. © 1993 Plenum Publishing Corporation..

Darabiha, N. and Giovangili, V. (1989), "Vectorized Computation of Complex Chemistry Flames." Proc. of Int. Symp. on High Performance Computing, L. Delhaye and E. Gelenbe (Eds.) Elsevier Sci. Publ. B.V. 273-285

Darabiha, N. and Candel, S. (1992). "The Influence of the Temperature on Extinction and Ignition Limits of Strained Hydrogen-Air Diffusion Flames". Comb. Sci. and Tech., 86, 67-85.

Darabiha, N., Lacas, F., Rolon, J.C. and Candel, S. (1993) "Laminar Counterflow Spray Diffusion Flames: a Comparison between Expemental Results and Complex Chemistry". Combustion and Flame 95, 261-275.

Dibble, R. W., and Hollenbach, R. E. (1981). "Laser Rayleigh Thermometry in Turbulent Flames". 18th Symposium (Int.) on Combustion, 1489-1499. Pitsburg: The Combustion Institut.

Fourgette, D. C., Zurn, R. M., and Long, M. B. (1986). "Two-Dimensional Rayleigh Thermometry in a Turbulent Nonpremixed Methane-Hydrogrn Flame". Comb. Sci. and Tech., 44, 307-317.

Giovangili, V. and Smooke M. D. (1987). "Extinction of Strained Premixed Laminar Flames with Complex Chemistry". Comb. Sci. and Tech., 53, 23-49.

Gouldin, F. C., and Halthore, R. N. (1986). Experiments in Fluids, 4, 269-278.

Lacas, F., Darabiha, N., Versaevel, P., Rolon, J.C. and Candel, S. (1992). "Influence of Droplet Number Density on the Structure of Strained Laminar Spray Flames"., 24th Symposium (International) on Combustion, Sidney, Australia, July .

Lacas, F., Rolon, J.C. and Veynante, D. (1992). "Droplets Size and Velocity Measurements in a laminar Counterflow Spray Flame by Using Phase Doppler Anemometry". Joint Meeting of the French, Italian and Swedish Sections of the Combustion Institute. Capri, Italy, 21 - 22 September.

Lacas, F., and Versaevel, Ph., (1994) "Phase Doppler Velocimetry Measurements in Counterflow Spray Flame". 7th International Symposium on Application of Laser Techniques to Fluid Mechanics, Lisbonne, Portugal, 11-14 July.

Lide, D.R. Editor, (1992). Handbook of Chemistry and Physics, 72nd edition CRC Press.

Liñan, A. (1974). "The Asymptotic Structure of Counterflow Diffusion Flames for a Large Activation Energies. Acta Astronautics, 1, 1001-1009.

Magre, Ph., Aguerre, F., Collin, G., Versaevel, Ph., Lacas, F. and Rolon, J.C. (1994). "Temperature and Concentrations Measurements by CARS in a counterflow Laminar Diffusion Flame" Submited to Experiments in Fluids.

Marathe, A.G. and Jain, J.K. (1972). "Some Studies on Oposed-jet Diffusion Flames with General Lewis Numbers". Comb. Sci. and Tech., 6, 151.

Miles, R., and Lempert, W. (1990). "Two-Dimensional Measurement of Density, Velocity and Temperature in Turbulent High-Speed Air Flows by UV Rayleigh Scattering". App. Phys., B 51, 1-7.

Müller-Dethleffs, K., & Weinberg, F. J. (1978). "Burning Velocity Measurement Based on Laser Rayleigh Scattering". 17th Symposium (International) on Combustion. , 985-992. Pitsburg: The Combustion Institut.

Pandya, T.P. and Weimberg, F.J. (1964), "The Structure of Flat, Counterflow Diffusion Flames". Proc. Roy. Soc. A 279, 544-561.

Rolon, J.C., Martin, J.-P. and Durst, F. (1986). "Counter jet Stagnation Flows Yielding Flat Diffusion Flames". Third International Symposium on Application of Laser Aneometry to Fluid Mechanics, Lisbonne, Portugal., July 7-9.

Rolon, J.C., Veynante, D., Martin, J.-P., Jakob, G., Dornberger, E., and Durst, F. (1988). "Laser Doppler Velocimetry Measurements in Flat Counterflow Diffusion Flames." 4th International Symposium on Application of Laser Aneometry to Fluid Mechanics, Lisbonne, Portugal.

Rolon, J.C., Veynante, D., Martin, J.-P., Jakob, G., Dornberger, E., and Durst, F. (1991). "Laser Velocity and Density Measurement of Flat Counterflow Diffusion Flames." Aerothermodynamics in Combustors IUTAM Symposium Taipei, Taiwan. R.S.L. Lee-J.H. Whiteloaw-T.S. WUNG (Eds.) © Springer-Verlag Berlin Heidelberg 1992.

Rolon, J.C., Aguerre, F., Darabiha, N., Mac Manus, K. (1992). "H2-Air Laminar Counterflow Flames Analysis by Using Laser Doppler Anemometry and Planar Laser Induced Fluorescence". Joint Meeting of the French, Italian and Swedish Sections of the Combustion Institute. Capri, Italy, 21 - 22 September .

Stepowski, D., and Cabot, G. (1992). Comb. and Flame, 88, 296-308.

Yip, B. and M. B. Long (1986). "Instantaneous Planar Measurement of the Complete Three-dimensional Scalar Gradient in a Turbulent Jet". Opt. Lett. 11, 64-66.

VELOCITY AND TEMPERATURE CHARACTERISTICS OF JET DIFFUSION FLAMES IN MUTUAL INTERACTION

M. V. Heitor, A. L. N. Moreira and A. C. Pires
Instituto Superior Técnico
Technical University of Lisbon
Dept. of Mechanical Engineering
Av. Rovisco Pais, 1096 Lisboa Codex, PORTUGAL.

ABSTRACT

Turbulent transport in single and multiple jet flames in mutual interaction is studied through the analysis of 1 and 3 propane flames with a Reynolds number of 20400. The experiments included the combination of a laser velocimeter, operated in the backscatter mode, with digitally-compensated thermocouples and extend previously acquired knowledge on the analysis of flames in mutual interaction. Although the oxygen insufficiency is the controlling mechanism in the propagation of interacting flames, the present results quantify the extent to which turbulent transfer is altered in the interacting flame zone. The results show that turbulent mixing is affected as a consequence of changes in the mean flow characteristics, but the turbulent heat fluxes remain qualitatively unaltered at the level of flame interaction studied here, with single and multiple flames exhibiting zones of non-gradient turbulent heat transfer.

1. INTRODUCTION

Despite turbulent flames in mutual interaction are of great interest in a variety of pratical systems, there is still a poor understanding of the influence of the interaction mechanisms between the individual flames and the surrounding air flow on flame structure and propagation. Previous studies have considered full scale systems and report on the effects of operational parameters, such as load distribution and distance between burners on the flame length and pollutant emissions, Fricker et al. (1971), Payne (1977). Although they provide important information, a better knowledge of these effects on turbulent mixing and chemical kinetics is required and experiments at the laboratory-scale on simple geometries are crucial to provide this fundamental knowledge.

Previous laboratory experiments are sparsely reported in the literature and include the natural gas and town gas jet flames of Lenze et al. (1975) and the propane lifted flames of Mennon and Gollahalli (1985, 1988), where the interaction mainly arises from the lack of oxygen in the initial flame region with the consequent effects on the rates of combustion at downstream locations. Heitor et al. (1991) extended the analysis to lifted propane flames in the range $6.3 < Re \times 10^{3} < 37.3$ and $0.65 < Fr \times 10^{-3} < 23.4$ and reported results in the absence of upward entrainment of cold air in the flame zone. In general, the results have been limited to the flame length and time-averaged temperature and major species concentrations, suggesting that flame interaction is predominantly affected by oxygen deficiency with the degree of interaction dependent upon the upstream boundary conditions. However, it has also been recognized that the increased turbulent mixing rates and induced buoyancy levels which may occur in interacting flames, compete with the oxygen insufficiency and may alter the rates of combustion and, in general, the nature of the turbulent transport processes. This has not been considered in previous works and is the main objective of the work reported here. The analysis is based on measurements of mean and fluctuating velocity and temperature complemented by those of gas composition, together with measurements of the correlations associated with the turbulent transport of heat and momentum.

The following section describes the experimental arrangement, the flames investigated and the instrumentation used to obtain the results. The error sources associated with the measurement are considered and assessments of accuracy provided. The results are presented and discussed in secion 3 and the main findings and conclusions are summarized in section 4.

2. FLOW CONFIGURATION AND EXPERIMENTAL METHOD

2.1. THE BURNER CONFIGURATION

The experiments were conducted in jet flames formed on round nozzles with an exit diameter of D = 5mm and boundary conditions typical of a fully-developed pipe flow. A co-axial flow of H_2 was used to stabilize the flames and to attach them to the burners, in a way similar to that used by Godoy (1982). Commercial grade propane was used as jet fluid in the range 0.65 to 1.2g/s, resulting in single jet flames with Reynolds numbers in the range 20400 up to 37600 and Richardson numbers from 1.5×10^{-4} to 4.6×10^{-6}. The measurements reported here consider, however, arrangements up to 3 flames in line, with Re=20400 and a separation distance of 6 burner diameters. Analysis, which is not shown here for lack of space, proved that the results may be considered independent of the Reynolds number and showed time-averaged scalar characteristics in the single flames comparable to those reported by Godoy (1982).

2.2. THE EXPERIMENTAL TECHNIQUES

Velocity measurements were obtained with a dual-beam laser-Doppler velocimeter based on an argon-ion laser light source at 514.5nm, 2W, and operated in the backscatter mode, with sensitivity to the flow direction provided by a Bragg cell. The

frequency shift was set up to 5 MHz. The transmitting optics of the velocimeter comprised a 300 mm focal-length lens and the half angle between the beams was 2.39° the calculated dimensions of the measuring volume at e^{-2} intensity locations were 1.452 mm and 0.067 mm. The propane gas was seeded with submicron alumina particles making use of a range of cyclone generators. In addition, the entrained still air was also seeded by injecting seeded air below a plate located at the burner level in order to avoid the upward entrainment of cold air in the near burner flow. The light scattered by the particles was processed by a commercial frequency counter (DANTEC 55L96) interfaced with a 16-bit microcomputer, where all the velocity moments up to the third order were evaluated. The laser velocimeter was located on a three-dimensional traversing unit, allowing the positioning of the measuring control volume within ± 0.25 mm. The distributions of the Reynolds shear stress $\widetilde{u''v''}$ were obtained by traversing the control volume with the laser beams in the longitudinal and vertical planes and at ± 45°, as described by Durst et al. (1981).

Temperature measurements were obtained with butt-welded thermocouples made of Pt:Pt/13%Rh wires with 0.40mm, in diameter. The output of the thermocouples was differentially amplified (x100) and digitized by a 12-bit analogue-to-digital converter at sampling rates up to 30KHz. The noise level could be kept below 0.1% of full scale deflection, corresponding to a maximum temperature error of 2K. The thermal inertia of the fine-wire thermocouples gives rise to first-order damping of their frequency response, for which numeric compensation was performed. The process of compensation followed the recommendations of Heitor et al.(1985) and Ferrão and Heitor (1992). The time constant of the thermocouple was obtained from the Collis and Williams law, with the coefficients obtained at each point within the flame from the measured mean temperatures, velocities and gas species concentrations.

Major species concentrations of CO, CO_2, O_2, NO_x and unburned hydrocarbons were measured by gas sampling and subsequent on-line analysis, using an L-shaped, water cooled probe with an outer diameter of 6 mm and an orifice of 1.5 mm in diameter. The analysis was performed in a wet basis and the results were shown to be independent of the suction velocity.

Simultaneous time-resolved velocity-temperature measurements were made with a system similar to that described by Ferrão and Heitor (1992) implemented in a 16-bit, 80386 personal computer making use of digital and analog input/output boards for the temperature and the velocity signals, respectively. The thermocouple signals were continuously sampled through a DMA board and stored in a circular buffer memory. The occurrence of a velocity measurement was signaled by the data ready output of the LDV counter, which was hold until the transfer of a group of 12 temperature samples from the circular buffer to a separate storage area of the computer memory was performed, in order to allow the evaluation of the temperature derivatives. The data acquisition frequency could be set up to 100 KHz and, therefore, did not present a limitation to the joint measuring system which, on the other hand, was limited by the deterioration of the thermocouple as discussed in the following section. The population size varied with the measurement position, but was usually larger than 10000 samples for the measurements reported here.

The velocity and the temperature measurements conditioned by occurrence of the LDV signals correspond to Favre average quantities, as the measured gaseous species concentration. However, the unconditioned compensated temperatures correspond to unweighted values (e.g. Heitor and Moreira, 1993)

2.2. EXPERIMENTAL ACCURACY

The foregoing described the arrangement of the instrumentation which was used to characterize the flames analysed in this paper. This section presents the results of research made into the various aspects which potentially influence the simultaneous velocity-temperature results. The accuracy of the techniques used for the other time-averaged quantities reported has been analysed in the literature (eg. Heitor and Moreira, 1993) and are not reported here.

The results may be affected by three main sources of error, namely:

i) errors in the instantaneous compensated value of temperature;

ii) spatial separation of the measurement locations of velocity and temperature

iii) deterioration of the thermocouple bead;

iv) frequency resolution

The first type of error is mainly due to the inaccuracy in the evaluation of the thermocouple time constant, which is particularly influenced by the type of flame considered. Here, three different approaches were tested. First, the internal heating procedure reported by Ferrão and Heitor (1992) was used, which is based on the analysis of the time-averaged decay of the temperature of the thermocouple bead after the removal of a direct-current overheating pulse. The method was found to be unsuitable for the present experimental conditions due to a number of reasons, including:

- the highly intermittency of the flame front did not allow to keep the full wire at a constant temperature, thus precluding measurements out of the central flame zone;
- the catalytic activity on the thermocouple surface when the probe was located in fuel-rich regions of the flame close to the burner outlet;
- the soot accretion on the wire limits the exposure times of the probe and, therefore, perturbes the measuring process.

A second approach was considered based on the method of Strahle and Muthukrishmann (1976). This requires that the signals acquired by two different thermocouples were recorded simultaneously and analysed in the frequency domain; then, the real and imaginary parts of the cross-correlation functions of the signals were used to evaluate the time constants of each wire, as also described by Son et al. (1988). This method was also found unsuitable for the present experimental flame

conditions because the spatial separation between the two temperature measuring locations could not be controlled with the required precision and this strongly affects the results. In addition, the technique could not be used in the intermittent region of the flame, as also observed by Boyer and Queiroz (1991).

An alternative method to determine the time constant of the thermocouple wire, and that used throughout this work, consists in the evaluation of the heat transfer characteristics of the wire based on the law of Collis and Williams, as referred by Heitor et al. (1985), making use of the time-averaged flame properties at each measuring locations. The results have shown a monotonic increase of the time constant with the radial distance with values between 15 and 60 ms, as in the non-premixed flame of Ballantyne and Moss (1977). Their accuracy is likely to be affected by a systematic error up to about -5%, with the largest errors occurring in highly intermittent flame zones.

We now turn to the analysis of the influence of the spatial separation between the temperature and the velocity measurement locations, which represents the largest random error affecting the accuracy of the turbulent heat fluxes. This has also been addressed by Yanagi and Mimura (1981), Tanaka and Yanagi (1983), Heitor et al. (1985) and Ferrão and Heitor (1992) and occurs because the thermocouple junction must lie outside of the velocimeter measuring volume, but it is difficult to place, reliably, both measurement locations closer than 1 mm.

Figure 1 shows a typical result of an experimental analysis performed to quantify the effects of this source of inaccuracy, which was obtained by measuring the velocity-tempertaure correlations with the velocimeter fixed at x/D = 20 and r/D = 1.6 and for various positions of the thermocouple. The results show that the dependence of the velocity/temperature correlations on the spatial displacement between the two measuring points is comparable along the streamwise and spanwise directions, with errors reaching 25% of the maximum value if the displacement becomes larger than 1.5 mm.

Other errors may arise due to the deterioration of the thermocouple bead by seeding particle accretion, e.g., Ferrão and Heitor (1992). Analysis has shown that particle fluxes up to about 1000 Hz result in a change of the time constant smaller than 10% over 10 minutes of exposure, and this data rate was used in the present work to avoid any significant deterioration of the bead during the measurements.

Finally, it is important to mention that the accuracy of the compensation of the output of the thermocouple affects the results in terms of the highest frequency component which could be measured. The method used here comprised a least-square numerical derivative approach, as described by Savitzky and Golay (1976), and its accuracy was evaluated by comparing the frequency spectra of uncompensated and compensated signals. The results showed that the energy-containing frequencies of the flames analysed are negligible above around 1.5 KHz, which is smaller than the frequency response of the system. Compensation was, therefore, performed over 2 decades, which is acceptable as discussed by Ballantyne and Moss (1977).

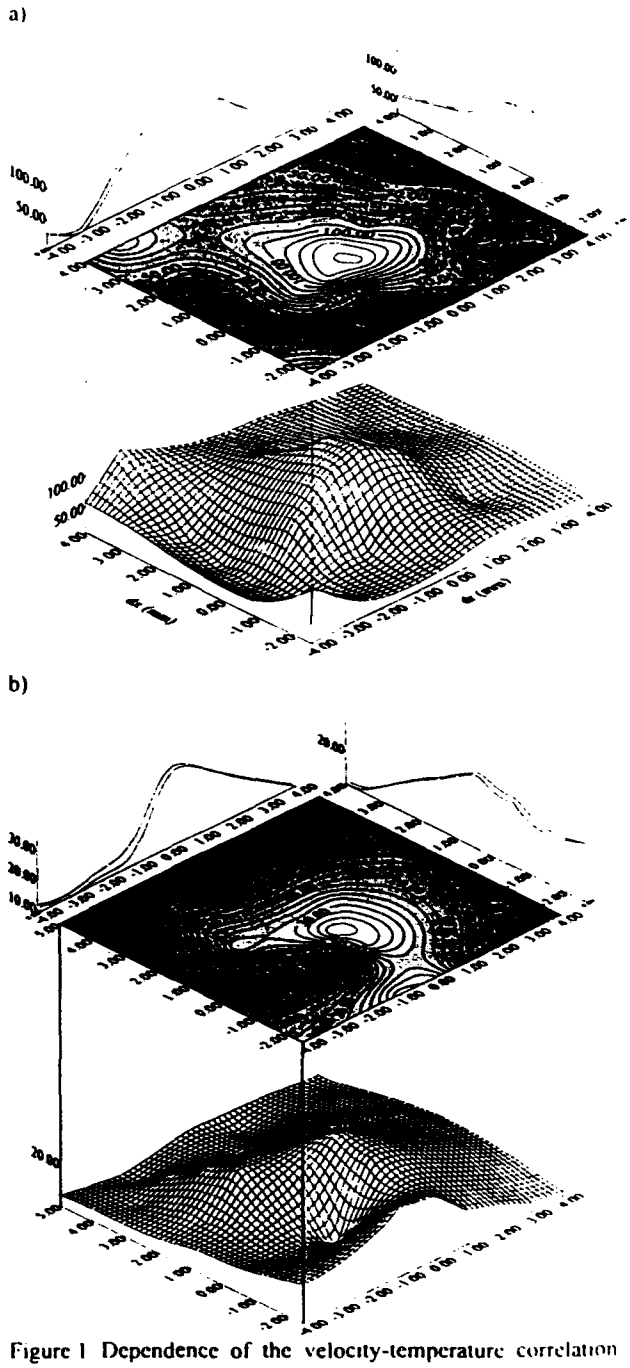

Figure 1 Dependence of the velocity-temperature correlation on the distance between the LDV control volume, at x/D = 20, r/D = 1.6, and the thermocouple
a) $\widetilde{u''t''}$
b) $\widetilde{v''t''}$

3 RESULTS AND DISCUSSION

The measurements of velocity, temperature, gas composition and turbulent heat flux obtained for single and multiple flames are presented in this section with the ultimate objective of

discussing the extent to which the interaction of flames may alter the typical transport processes of a single jet flame. The mean and turbulent velocity and temperature and the mean major gaseous species concentrations are analysed in a first part and, then, the results of the velocity-temperature correlations are presented and discussed.

3.1. THE MEAN AND TURBULENT FLOW FIELDS

Figure 2 shows radial distributions of the mean and turbulent velocity characteristics measured for the single flame from 10 to 40 diameters downstream of the burner exit. The results show the expected trends of a jet diffusion flame in still air: turbulence intensity is maximum in the shear layer where gradients of mean velocity are larger and where chemical reaction occurs. Probability density functions of velocity fluctuations (not shown here due to lack of space) were found to be nearly Gaussian, except near the outer edge of the jet, where the distributions are negatively skewed due to the entrainment of external air, as also observed by Driscoll et al. (1982).

Figure 3 shows the radial distributions of velocity characteristics measured in the multiple flames system by transversing the LDV control volume along a path perpendicular to the optical axis. The results showed that the flow is symmetric around the axis of the central flame and, here, only half profiles are presented, with the axis of the central flame located at r/D = 0 in figure 3, and the axis of the outer flame at r/D = 6. The central and the peripheral flames can be individualized up to x/D = 20, where both streams begin to merge. The width of the outer flame (defined as the radial distance between the points where the mean velocity is 5% of the centreline mean velocity) is about 20% larger than that of the central flame and comparison of these results with those of Fig. 2 shows that, at x/D = 20, the rate of spread of the central flame is decreased due to the proximity of the outer flames. Also, the locus of the minimum axial velocity in the region between the flames shows that the inner shear layer of the outer flow is deflected inwards. As a consequence, the interacting mixing zone established between the flames develops further downstream with an assimetric shape on the r-x plane, with larger radial gradients in the inner side and smaller gradients in the outer side.

The turbulent flow field (Figures 3b, c and d) is expected to vary in accordance with the changes observed in the mean flow. For example, the velocity fluctuations in the shear layer of the central flame are larger than those measured in the single flame, but smaller in the inner shear layer of the outer flame. Simultaneously, also the radial gradients of the normal stresses are increased, which alters turbulent diffusion further downstream. As a result, the normal stresses measured on the axis of the central flame at x/D= 30 are larger than those measured in the single flame, while those in the axis of the outer flames are smaller

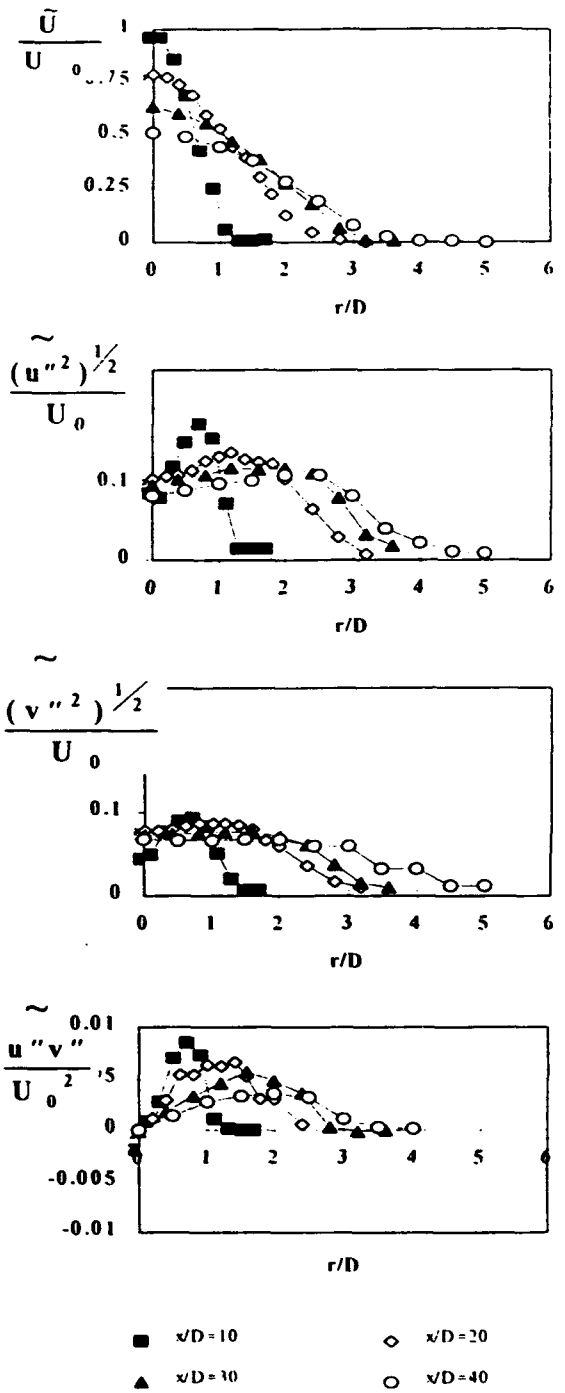

Figure 2 Radial distributions of the non-dimensional velocity characteristics in the single flame

a) Mean axial velocity, $\tilde{U}/U_0$

b) Axial velocity fluctuations, $(\widetilde{u''^2})^{1/2}/U_0$

c) Radial velocity fluctuations, $(\widetilde{v''^2})^{1/2}/U_0$

d) Turbulent shear stress, $\widetilde{u''v''}/U_0^2$

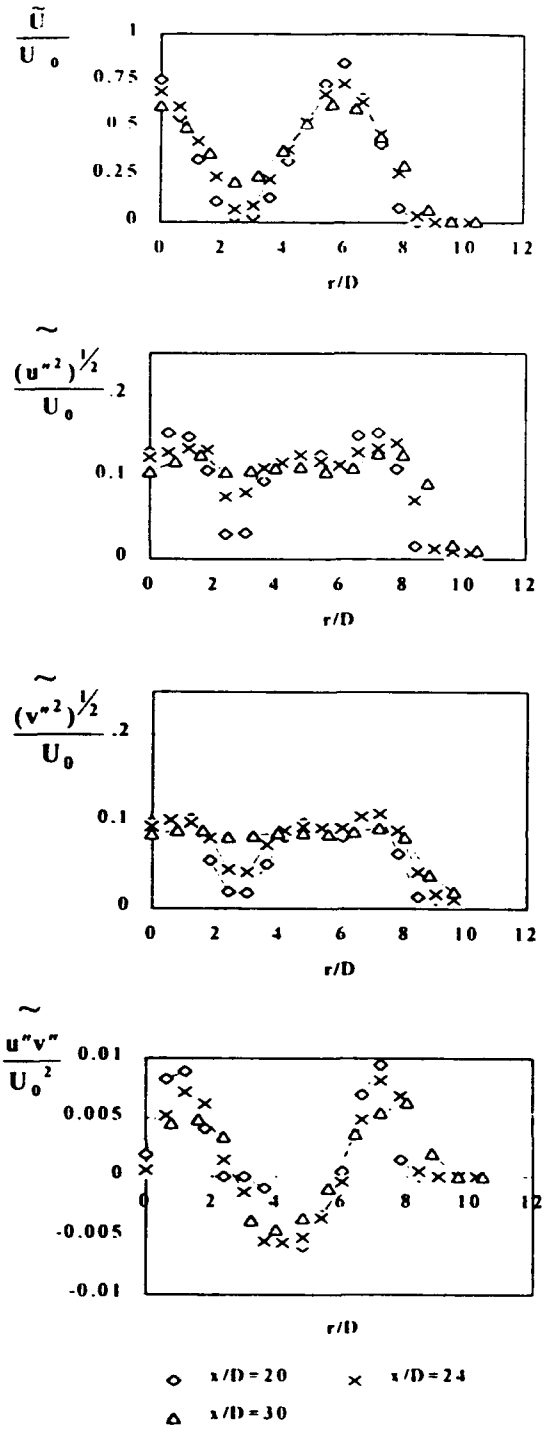

Figure 3 Radial distributions of the non-dimensional velocity characteristics in the multiple flames

a) Mean axial velocity, $\tilde{U}/U_o$

b) Axial velocity fluctuations, $(\widetilde{u''^2})^{1/2}/U_o$

c) Radial velocity fluctuations, $(\widetilde{v''^2})^{1/2}/U_o$

d) Turbulent shear stress, $\widetilde{u''v''}/U_o^2$

The above results suggest that the primarily aerodynamic effect of flames in mutual interaction is due to changes in the radial gradients of the mean flow, which in turn change the pattern of the shear stress $\widetilde{u''v''}$ and, consequently, the interaction of $\widetilde{u''v''}$ with $\delta U/\delta t$, which is expected to be the main mechanism associated with turbulent production. This mechanism first feeds energy into the axial velocity fluctuations, which is subsequently redistributed among the other components and, therefore, the velocity fluctuations in the radial direction are more affected than those in the axial direction, as observed in Figure 3 c). It must be noted that large radial velocity fluctuations were not measured in the upstream part of the interacting mixing layer, as observed in the multijet burner studied by Heitor and Moreira (1992), suggesting the unlikely influence of the axial gradients of mean velocity to turbulent production.

The analysis of the previous paragraphs suggest that the process of flame interaction may be important in practical systems where combustion is controlled, or strongly influenced, by the rates of turbulent mixing and, thus, by turbulent fluctuations. However, this process does not act isolated, since the presence of side flames also affects the entrainment of ambient air and, consequently, the amount of reactants available for mixing and combustion. Therefore, a better interpretation of the process requires the analysis of the temperature and gas composition fields. These are shown in Figures 4 and 5, respectively, in the form of radial distributions of mean and fluctuating temperatures and mean mixture fraction as calculated from the measured concentrations of stable species.

Figure 4a) shows that the maxima values of mean temperature in the single flame occur in the mixing region between the external ambient air and the fuel jet, where the local mixture fraction is close to the stoichiometric value (see Figure 4c) and velocity fluctuations are larger. Temperature fluctuations are larger along the outer edge of the flame and peak values are associated with very lean local mixture fractions, as a result of the concurrent processes of mixing and chemical reaction (e. g., Scheffer and Dibble, 1985).

In the multiple flames arrangement, the mixing layer between the central and the outer flames corresponds to a region lacking of oxygen. The minimum value of the mixture fraction moves outwards (Figure 5c), suggesting that the ambient air is preferential entrained into the outer flames, and resulting in an assimetric distribution of the mixture fraction with values in the axis of the central flame larger than those in the outer flames up to x/D = 30. While the lack of oxygen in the mixing layer does not significantly affect the temperature distributions at x/D = 20, the mean and the fluctuating temperatures further downstream are much smaller than those observed in the single flame.

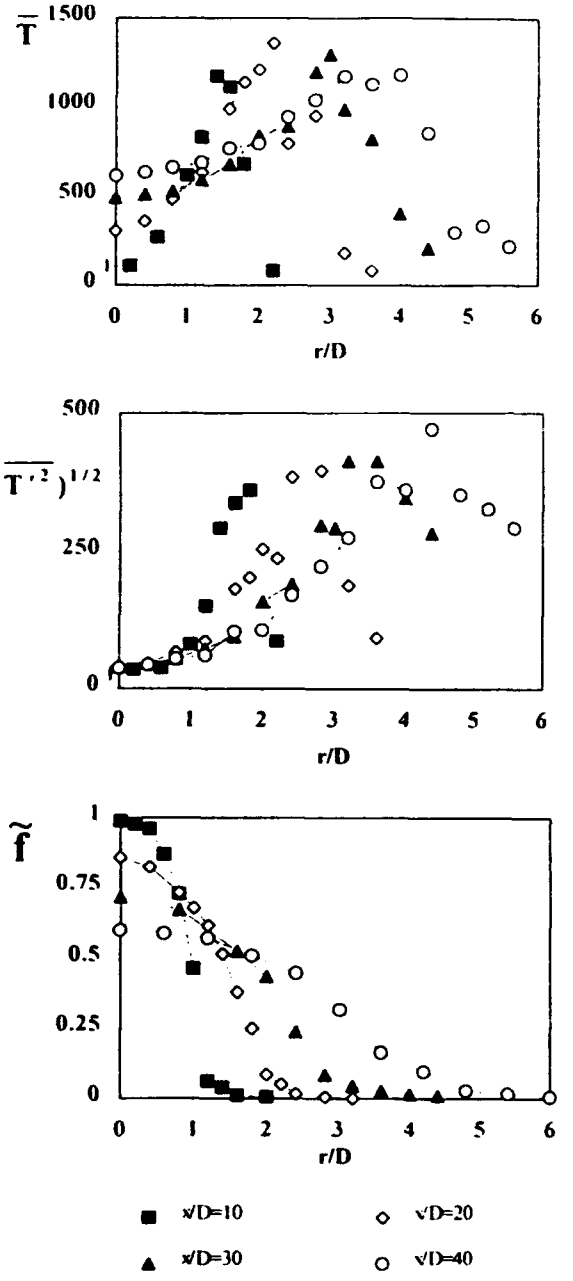

Figure 4 Radial distribution of temperature and mixture fraction in the single flame

a) Mean temperature, $\overline{T}$

b) Temperature fluctuations, $(\overline{T'^2})^{1/2}$

c) Mean mixture fraction, $\tilde{f}$

Measurements of spectral emitted radiation reported in a companion paper (e.g., Heitor et al. 1994) show that the lack of oxygen in the interacting mixing layer inhibits the free-radical reactions necessary for the formation of the final products of reaction further downstream. Although these reactions release a small amount of energy if they are not able to occur in the upstream part of the mixing layer, the decomposition reactions with high activation energy which should occur further downstream are inhibited, thus, contributing to a decrease of the final temperature of the combustion products. This, in turn, results in smaller rates of heat released by combustion, which mainly contributes to decrease the fluctuations of temperature in the interacting mixing layer, as observed by comparing Figures 4b) and 5b)

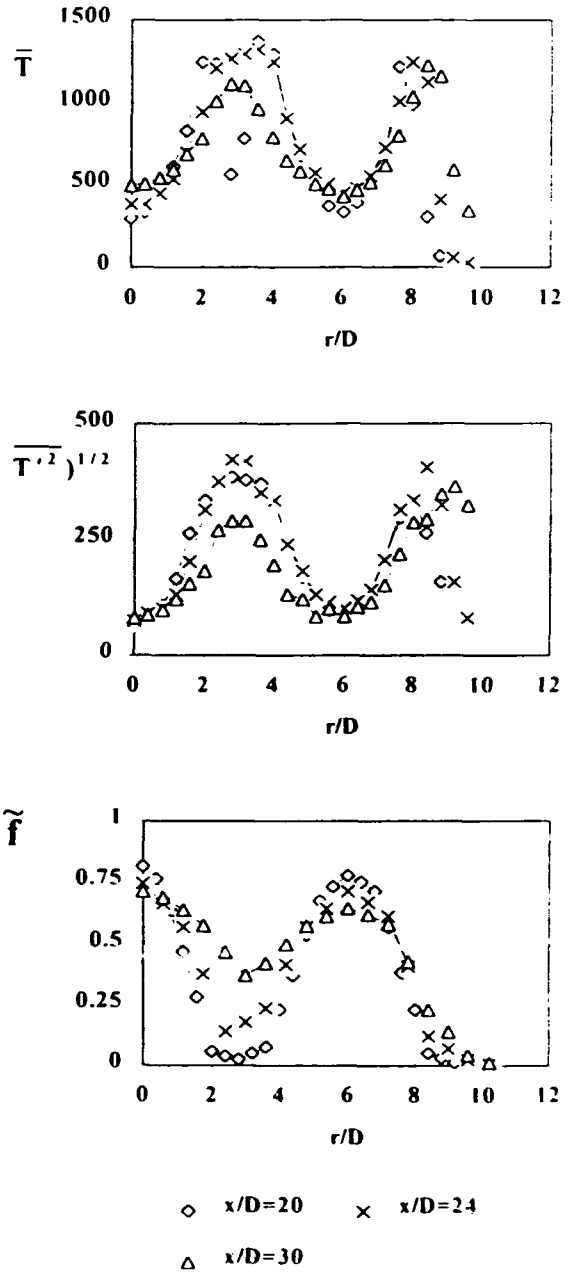

Figure 5 Radial distribution of temperature and mixture fraction in the multiple flames

a) Mean temperature, $\overline{T}$

b) Temperature fluctuations, $(\overline{T'^2})^{1/2}$

c) Mean mixture fraction, $\tilde{f}$

It must noted here that a subsequent effect of the rate of heat release would be to decrease the dilatation effects, which would contribute to increase the turbulent velocity fluctuations, as discussed Bilger (1989). The fact that $\widetilde{v''^2}$ is decreased in the shear layer of the jet diffusion flame due to the presence of a side flame, suggests that the shear-induced mechanisms dominate over the combustion-induced mechanisms of turbulence generation. Therefore, the turbulent flow field in the interacting flames is likely to be more influenced by aerodynamic effects, rather than by chemical effects due to the lack of entrained ambient air.

3.2. THE TURBULENT FLUXES

The main question adressed in the present paper is how the effects on the mixing patterns due to flame interaction influence turbulent transport and, thus, the structure and the mechanisms of flame propagation. To achieve these objectives, Figure 6 shows the measured vectors of turbulent heat flux, $\widetilde{u_i''t''}$, superimposed on the radial profiles of mean axial velocity and temperature. These quantities represent the turbulent heat transfer rate, and are responsible for the phenomenon of flame stabilization at the burner nozzle and for the downstream flame propagation. The results show that the turbulent heat fluxes tend to be restricted to the mixing layers where larger temperature gradient occur, and exhibit a large component directed along the isotherms. Table 1 shows that the magnitude of the measured values is comparable to that reported in the literature for other jet flames. In addition, the results follow similar qualitative trends for single and multiple flames, although the details are affected by the interacting process, as considered in the following paragraphs.

For the single flame, it should be noted that in the region of the shear layer where combustion occurs, $\widetilde{u''t''}$ is directed in the opposite direction of the axial gradient of mean temperature, $\partial\bar{T}/\partial x$, while $\widetilde{v''t''}$ changes from negative to positive close to the flame front, where $\partial\bar{T}/\partial r$ is still positive, so that non-gradient transport is likely to occur (see Figure 6a). This occurs only for a limited zone of the shear layer centered at x/D=10 and up to r/D=1. Otherwise, the assumption that heat is transported in the direction of the radial gradient is verified throughout all the flow. Similar observations of counter gradient diffusion of heat in the vicinity of the flame front has been reported in other jet diffusion flames (e. g., Yanagi and Mimura, 1981) and has been attributed to a the occurrence of wrinkle flame fronts (e. g., Bilger, 1989): the passage of a burned gas pocket through the measuring point gives rise to a positive velocity fluctuation in the radial direction due to thermal expansion and to a positive temperature fluctuation and, therefore, $\widetilde{v''t''} > 0$. It is worth mentioning that this interpretation is consistent with the shape of the probability density functions of temperature measured throughout this work, which exhibit flatness values far from a typical Gaussian distribution in random turbulence.
The turbulent heat flux distributions measured for the multiple flames, Figure 6b), show trends qualitatively similar to those analysed above for the single flame, with peak values occuring in regions of large gradients of mean temperature. Although the figures do not allow an accurate comparison of the variations in magnitude, it is worth noting that the peak value of $\widetilde{u''t''}$ in the mixing region at x/D = 20 is about 100% larger than that measured in the shear layer of the single flame. This difference is rapidly attenuated further downstream and, at x/D = 30, the peak values of $\widetilde{u''t''}$ are similar in the two experimental conditions used. Larger differences are observed in the radial component of the turbulent heat flux, $\widetilde{v''t''}$, which is significantly smaller than that measured in the single flame througout all the mixing region up to x/D = 30. While the initial increase of $\widetilde{u''t''}$ is consistent with the initial increase of the fluctuations of the axial velocity, the decrease of $\widetilde{v''t''}$ is associated with a comparatively larger decrease of the fluctuations of the radial velocity in the mixing layer, as discussed previously. Again, these results suggest that the aerodynamic effects on the turbulent transport of heat dominate over the chemical kinetic effects induced by the lack of oxygen in the mixing layer where the interaction between the flames occurs.

a)

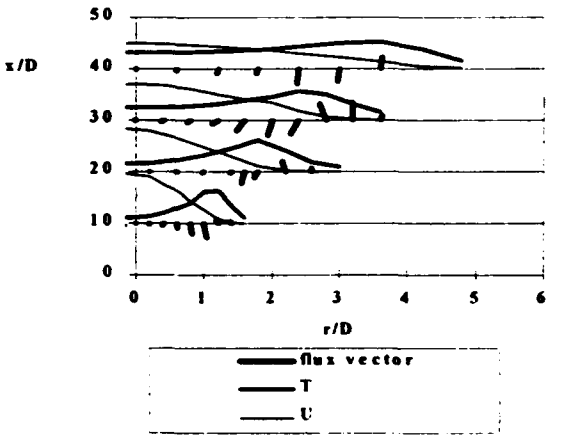

b)

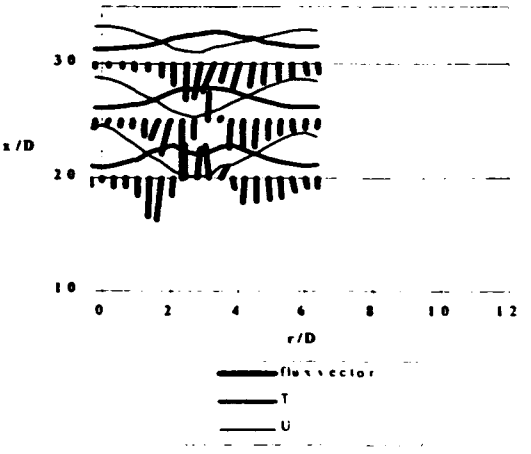

Figure 6 Radial distributions of the turbulent heat flux vectors.
a) Single flame.
b) Multiple flames.

Table 1 Summary of Velocity-temperature Correlation Measurements in Jet Flames

REFERENCE	FLAME CHARACTERISTICS	$\widetilde{u''t''}$ (C m/s)	$\widetilde{v''t''}$ (C m/s)	COMMENTS
Present work	Non-premixed jet flame D=5mm. Re=20400	-134 @ r/D=1.4 x/D=20. -40 @ r/D=0.0 x/D=10.	22 @ x/D=10. r/D=1.0 -25 @ x/D=20. r/D=1.8	Zones of non-gradient diffusion
Günther & Wittmer (1980)	Free jet non-premixed flame D=8mm. Re=37000	40 @ x/D=50 r/D=0.0		$R_{uv} < 0$ for $\partial T/\partial x > 0$ not explained
Yanagi & Mimura (1981), Tanaka & Yanagi (1983)	Open burner premixed flame D=8, 10mm. Re=3200	-30 @ x/D=2.5 r/D=35. (reaction zone)	30 @ x/D=2.5 r/D=4; (reaction zone)	Counter-gradient heat flux only within reaction and mixing zones
Stärner (1983)	H_2 non-premixed flame in co-flowing stream D=7.6mm. Re=11200		96 @ x/D=80;	Gradient diffusion of scalar characteristics over all the flame

Figures 7 and 8 show radial profiles of the correlation coefficients, R_{ut}, R_{vt} and R_{uv} calculated from the measurements obtained in the single and in the multiple flames, respectively, and are important to analyze the relative contribution of the turbulent velocity fluctuations to the transport of temperature.

For all the cases studied, R_{vt} is always smaller than R_{ut}, as observed in other jet diffusion flames (e g., Takagi et al., 1981, Yanagi and Mimura, 1981) and in strongly sheared recirculating diffusion flames (e g., Fernandes et al., 1993), suggesting that the turbulent motions are more efficient in transporting heat along the axial direction than along the radial direction. This is in accordance with the interpretation that the flame is represented by a wrinkled flame structure, in that the wrinkled shape of the instantaneous flame front affects more the radial transport of heat than that along the streamwise direction because the average flame region is nearly vertical.

The negative values of R_{ut} in the single flame occur in the rich side of the flame, while the positive values occur in the outer part of the flame where mixing with the ambient air occurs. In the interacting shear layer of the multiple flames, negative values of R_{ut} occur in the upstream region up to x/D = 24. However, the absolute peak values are larger in the multiple flames (around 0,5), as compared with those measured in the single flame (around 0,4). Similar trends, although with different magnitudes, are observed for the correlation coefficient R_{vt}, despite the observed decrease of $\widetilde{v''^2}$. This result suggest that, though the mechanisms of turbulent transport are similar, the contribution of the turbulent motions to the transport of heat is more efficient in the multiple flames than in the single flame. The correlation coefficient for the turbulent transport of momentum, R_{uv}, follows the trends of the shear stress $\widetilde{u''v''}$, with peak values around 0.5 in the single flame (Figure 7), in accordance with other measurements reported in jet diffusion flames (e g., Glass and Bilger, 1978, Starner and Bilger, 1980, 1989). The results obtained in the multiple flames (Figure 8) show a similar behavior suggesting that the interaction mechanisms do not give rise to extra mechanisms of production and transport of momentum.

4 CONCLUSIONS

Detailed velocity, temperature and major species concentration measurements are presented for burner-attached jet propane flames at Re=20400. The measurements encompass the analysis of single and 3 multiple flames in mutual interaction at

making use of thermocouple time-constants evaluated on the basis of the Collis and Williams law considering local flame properties. The largest error sources associated with the measurements are due to the spatial displacement between the two measuring zones, which may give rise to the underestimation of the velocity-temperature correlations by 25% of the maximum value if the displacement becomes larger than 1.5 mm.

The main question addressed is how the effects on the mixing patterns due to flame interaction influence the turbulent transport and the process of flame propagation. The results for the single flame show that the turbulent heat fluxes tend to be restricted to the mixing layer where large temperature gradients occur, and that they exhibit a larger component directed along the isotherms. Observations of non-gradient diffusion of heat in the vicinity of the flame front has been verified as already reported in others jet diffusion flames.

For the multiple flames, the results show qualitatively similar trends, with the process of turbulent flame propagation being unaltered at the level of flame interaction considered in this paper.

Analysis of the instantaneous velocity and temperature results shows that, in the multiple flames arrangement, the turbulent flow field appears to be more influenced by aerodynamic effects than by chemical effects due to the lack of entrained ambient air. The results further suggest that the interaction mechanisms do not give rise to extra mechanisms of production and transport of momentum.

ACKNOWLEDGEMENTS

The assistance of Mr. Carlos Carvalho in the preparation of this paper is gratefully appreciated. Financial support has been provided by the BRITE/EURAM programme of the DGXII of the European Commission, under the contract n° AER2-CT920035.

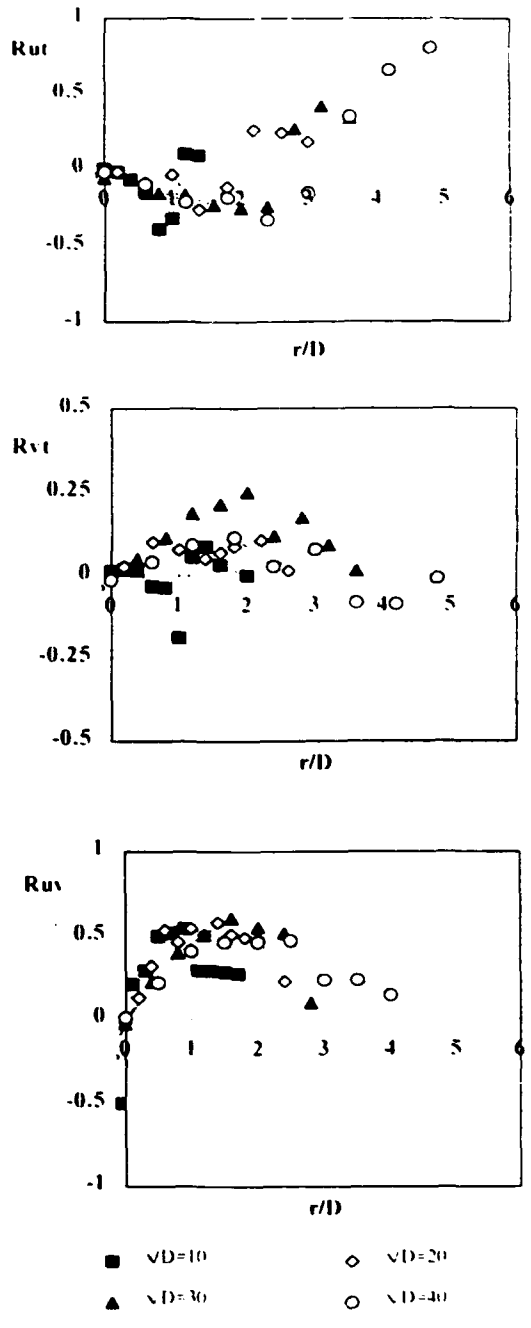

Figure 7 Radial distributions of the turbulent correlation coefficients in the single flame

a) $$R_{ut} = \frac{\overline{u\,t}}{\left(\overline{u^2}\right)^{1/2}\left(\overline{t^2}\right)^{1/2}}$$

b) $$R_{vt} = \frac{\overline{v\,t}}{\left(\overline{v^2}\right)^{1/2}\left(\overline{t^2}\right)^{1/2}}$$

c) $$R_{uv} = \frac{\overline{u\,v}}{\left(\overline{u^2}\right)^{1/2}\left(\overline{v^2}\right)^{1/2}}$$

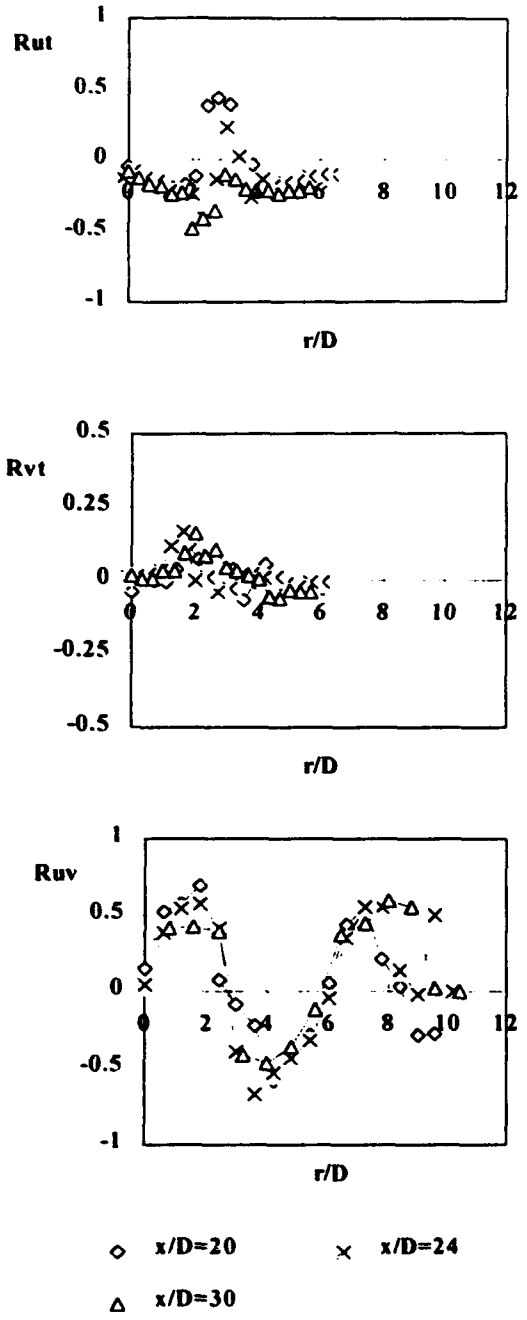

Figure 8 Radial distributions of the turbulent correlation coefficients in the multiple flames.

a) $$R_{ut} = \frac{\widetilde{u''t''}}{\left(\widetilde{u''^2}\right)^{1/2}\left(\widetilde{t''^2}\right)^{1/2}}$$

b) $$R_{vt} = \frac{\widetilde{v''t''}}{\left(\widetilde{v''^2}\right)^{1/2}\left(\widetilde{t''^2}\right)^{1/2}}$$

c) $$R_{uv} = \frac{\widetilde{u''v''}}{\left(\widetilde{u''^2}\right)^{1/2}\left(\widetilde{v''^2}\right)^{1/2}}$$

REFERENCES

Ballantyne, A. and Moss, J.B. (1977). "Fine Wire Thermocouples Measurements of Fluctuating Temperature". Comb. Sci. Tech., 17, pp. 63-72.

Bilger, R. W. (1989). "Turbulent Diffusion Flames", Ann. Rev. Fluid Mech., 21, pp. 101-135.

Boyer, L. M and Queiroz, M. (1991). "Temperature Dissipation Measurements in a Lifted Turbulent Diffusion Flame", Comb., Sci. and Tech., 79, pp. 1-34.

Driscoll, J. F., Scheffer, R. W. and Dibble, R. W. (1982). "Mass Fluxes ρ'u' and ρ'v' measured in turbulent non premixed flame", 19th Symposium (Intl.) on Combustion, The Combustion Institute, Pittsburg, pp. 477-485.

Durst, F., Melling, A and Whitelaw, J.H. (1981). Principles and Practice of Laser-Doppler Anemometry. Academic Press Inc., New York.

Fernandes, E. C., Ferrão, P., Heitor, M. V. and Moreira, A. L. N. (1994). "Velocity-Temperature Correlations in Recirculating Flames with and without Swirl", Exp. Thermal and Fluid Science, to appear.

Ferrão, P.M.C. and Heitor, M.V. (1992). "Simultaneous Measurements of Velocity and Scalar Characteristics for the Analysis of Turbulent Heat Transfer in Recirculating Flows", Proc. 6th Int. Symp. Appl. Laser Tech, to Fluid Mechanics, Lisbon, July 20-23.

Fricker, N., Van Heyden, L. and Michelfelder, S. (1971). "Investigations Into the Combustion of Natural Gas in Multiple Burner Systems", IFRF, Ijmuiden, Doc. N° F35/a/5.

Glass, M. and Bilger, R. W (1978). "The Turbulent Jet diffusion Flame in a Co-Flowing Stream - Some Velocity Measurements", Comb. Sci. and Tech., 18, pp. 165-177.

Godoy, S. (1982). "Turbulent Diffusion Flames", Ph.D. Thesis, Univ. of London.

Gunther, R. and Wittmer, V. (1981). "The Turbulent Reaction Field in a Concentric Diffusion Flame", 18th Symp. (Intl.) on Combustion, The Combustion Institute, Pittsburg, pp. 961-967.

Heitor, M. V., Moreira, A. L. N. and Pires, A.A.C. (1994). "Interaction of Multiple Jet Propane Flames", 25th Symp. (Int.) on Combustion, Irvine, California, USA, July 31-August 5.

Heitor, M. V. and Moreira, A. L. N (1992). "On the Analysis of Turbulent Transport Processes in Nonreacting Multijet Burner Flows", Exp. in Fluids, 13, pp. 179-189.

M.V. Heitor and A.L.N. Moreira (1993). "Thermocouples and Sampling Probes for Combustion Studies". Prog. Energy Combust. Sci., 19, pp. 259-278.

Heitor, M.V., Pires, A.C. and Simões, J.P. (1991). "The Thermal Characteristics of Turbulent Hydrocarbon Flames in Mutual Interaction", Proc. XI Brazilian Congress on Mechanical Engineering, São Paulo, Brasil, December 11-13.

Heitor, M.V., Taylor, A.M.K.P. and Whitelaw, J.H (1985)."Simultaneous Velocity and Temperature

Measurements in a Premixed Flame", Exp. in Fluids, 3, pp. 323.

Lenze, B., Milano, M.E. and Gunther, R. (1975). "The Mutual Influence of Multiple Jet Diffusion Flames", Comb. Sci. Tech., 11, pp. 1-8.

Mennon, R. and Gollahalli, S.R. (1985). "Multiple Jet Gas Flames in Still Air". In: Heat Transfer in Fire and Combustion Systems, ed. C.K. Lawn, L. Jaluria, W.W. Yuen, K. Miyasaka, HTD vol. 45, ASME, New York, pp. 127-133

Mennon, R. e Gollahalli, S.R. (1988). "Combustion Characteristics on Interacting Multiple Jets in Cross Flow", Comb., Sci. and Tech., 60, pp 375-389.

Payne, R. (1977). "Report on the Multiple Burner Trials - MJ3", IFRF, Ijmuiden, Doc. N° F35/a/11.

Savitzky, A. and Golay, M.J.E. (1976). "Smoothing and Differentiation of Data by Simplified Least Square Procedures", Anal. Chem., 36(8), pp 1627-1639.

Scheffer, R. W. and Dibble, R. W. (1985). "Simultaneous Measurements of Velocity and Density in a Turbulent Nonpremixed Flame", AIAA Journal, 23, No. 7, pp. 1070-1078.

Son, S.F., Queiroz, M. and Wood, C.G. (1988). "Digital Compensation of Thermocouple for Thermal Inertia Effects", Western States Section - The Combustion Institute, Fall Meeting.

Starner, S. H. (1983). "Joint Measurements of Radial Velocity and Scalars in a Turbulent Diffusion flame", Comb. Sci. and Tech., 30, pp. 145-169.

Starner, S. H. and Bilger, R. W. (1980). "LDA Measurements in a Turbulent Diffusion Flame with Axial Pressure Gradient", 18th Symp. (Intl.) on Combustion. The Combustion Institute, pp. 921-930.

Starner, S. H. and Bilger, R. W. (1989). "Further Velocity Measurements in a Turbulent Diffusion Flame with Moderate Swirl", Comb. Sci. and Tech., 63, pp. 257-274.

Strahle, W.C. and Muthukrishnan, M. (1976). "Thermocouple Time Constant Measurements bby Cross Power Spectra", AIAA J., 14(11), pp 1642-1644.

Takagi, T., Shin, H. D. and Ishio, A. (1981). "A Study on the Structure of Turbulent Diffusion Flame: Properties of Fluctuations of Velocity, Temperature and Ion Concentration", Comb. and Flame, 41, pp. 261-271.

Tanaka, H. and Yanagi, T. (1983). "Cross-Correlation of Velocity and Temperature in a Premixed Turbulent Flame", Comb. and Flame, 51, pp. 183-191.

Yanagi, T. and Mimura, Y. (1981). "Velocity-Temperature Correlation in Premixed Flame", 18th Symp. (Intl.) on Combustion, The Combustion Institut, Pittsburg, pp. 1031-1039.

FLUX MEASUREMENTS OF O_2, CO_2 AND NO IN OIL FURNACE

Yuji Ikeda, Nobuyuki Kawahara and Tsuyoshi Nakajima

Department of Mechanical Engineering
Kobe University

Rokkodai, Nada, Kobe 657 Japan

ABSTRACT

Velocity measurements in an industrial oil furnace with temperature and gas species were carried out by a developed Fiber LDV having high spatial resolution and high signal-to-noise ratio. The comparisons of gas concentrations and convective flux were performed in order to understand the reverse flow characteristics in the furnace. It was found that the gas concentration data is useful in the flame analysis but the convective flux is effective to understand the flow outer the flame region.

1. INTRODUCTION

Measurements of velocity, temperature, and gas concentration in a practical industrial furnace are currently challenging subjects in spite of the use of current advanced methods such as laser (Baker, 1973; Dugue, 1992). But, the difficulties in understanding of the physical phenomena in the industrial furnaces are not only depend on the difficulties of the measurement methods, but also the uncertainty of the measured data. For oil furnaces, the fuel spray is traveling, aggromated, collided, separated and evaporated (Edwards,1990). If temperature measurements by a thermocouple are carried out in such flows with fuel spray, the radiation problem, fuel stick problem occur which cause time delay in response (Williams,1985; Nakabe, 1975). It is still doubtful to use the laser technique to measure temperature in such complicated combusting flow fields (Eckbreth, 1987). In measuring gas species, the most common method is sampling method in which a resolution and an accuracy depend dramatically on the sucking speed and its direction, also freezing problems (Chigier, 1991). For velocity measurements, an advanced technique as laser Doppler velocimeter (LDV : Durst, 1976) can provide sufficient data, but there are same problems such as beam refraction at flame front (Hong, 1977), and low signal-to-noise ratio (SNR) due to other illuminated light.

Then, we opted for flux measurements (Heitor, 1993) in order to understand the physical phenomena in one parameter, and reduce the multiple uncertainties. Here, only convective flux of gas species are taken into account.

In order to acquire better velocity data having high spatial resolution, LDV probe was specially designed (Ikeda, 1990). Conventional LDV has long focal length so as to have large measurement volume, which can get the velocity data even with some beam refraction (Bonin, 1991; Ereaut, 1991), but has less SNR due to low light intensity. The strategy to obtain high data rate was on the basis of small measurement volume, with long focal length, which might have less probability to has two beams crossing but very high data rate at the crossing having high spatial resolution.

In this paper, the industrial furnace having A-type fuel oil was examined in order to measure velocity, temperature, and gas species with convective flux in axial direction. The purpose of this study is to show the effective usefulness of the convective flux to understand the combustion characteristics and demonstrate the role of the self-recirculating flow in the furnaces.

2. EXPERIMENTAL APPARATUS

2.1 Furnace

The test furnace used in this study is 0.103MW having an A-type fuel oil as shown in Fig. 1. The size of the furnace is 430 mm × 1440 mm having 7 separate blocks. Each block is made of annular structure having water cool to measure heat flux at each block. There are 7 optical windows of ϕ 150mm × t 15mm of BK-7 with anti-reflection coating. Each windows are double spaced to avoid the fogging.

The operational condition of the furnace is 0.103 MW, the fuel consumption is 9.45×10^{-3} (m^3/h) and an excess air ratio is λ=2. At the exit of the furnace, O_2=4.7%, CO_2=10.8%, CO=0%, and NO=58.4ppm. For designing the size of the optical windows, the required spatial resolution of measurement volume,

needed measurement range, and its focal length were taken into account, so that the size of the optical windows was determined.

2.2 Burner

The test burner is a gun-type burner as shown in Fig.2. An A-type fuel is pressurized up to 0.7 MPa and form hollow-corn spray at 60° . A buffle-plate mounted on the burner plays a role of flame holding. The slits at the buffle-plate are used to reassess the flame from the buffle-plate. Figure 3 is a direct picture of the flame. As seen in the picture, there are three main parts; one is the flame holding region near buffle plate, the second is the transparent region where the fuel droplets are evaporating, and the third part is the main combustion region having much luminescence as background noise. In our previous experiments under isothermal combustion, it was found that the droplets under 30μm are traveling and following to the reversing flow at the flame holding region, and over 50μm droplets were penetrating the reversing flows.

2.3 LDV Optics

In designing a LDV probes, four main problems were taken into account, that is, a beam "dancing" due to beam refraction at a flame surface, the decrease of probability of two beams crossing, the installation of the spatial filter to cut off background noise, and the light scattering at optical window which cause much background noise. Furthermore, the seeding particle problem is the indispensable matter. In this experiment, very light and uniform diameter particle (MSF; Ikeda, 1992) was added into combusting air.

In order to increase SNR, what we did was to make small measurement volume to increase light intensity so as to produce much light scattered from the measurement volume, and have large receiving aperture so as to collect much light scattered. These two parameters are combined into are parameter call SNR parameter (SNRP). To make small measurement volume can increase spatial resolution but decrease two beam crossing probability which causes low data rate. The measurement volume should be proper size to the velocity gradient region. In considering a visibility, a fringe spacing of 3.86μm was determined and the size of the measurement volume was determined to be 69.9 μm × 1030 μm at focal length of 500 mm. The schematic layout of the developed LDV probe is shown in Fig.4. The optimization of fringe spacing and the seeding diameter, SNRP, and spatial resolution were carried out.

The measurements were carried out by back-scattering mode and data rate of over 8 kHz was achieved near burner nozzle. Figure 5 shows a photograph of the measurement.

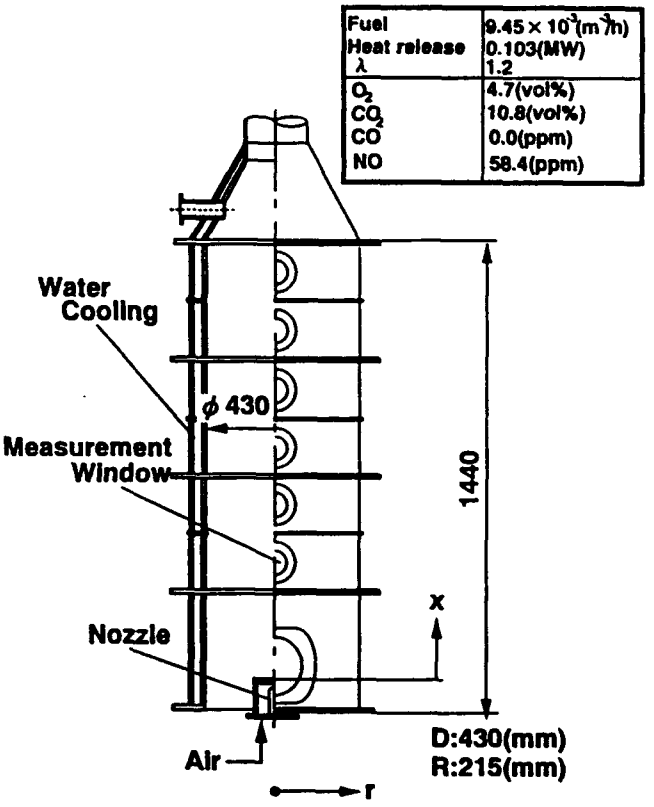

Fig.1 furnace

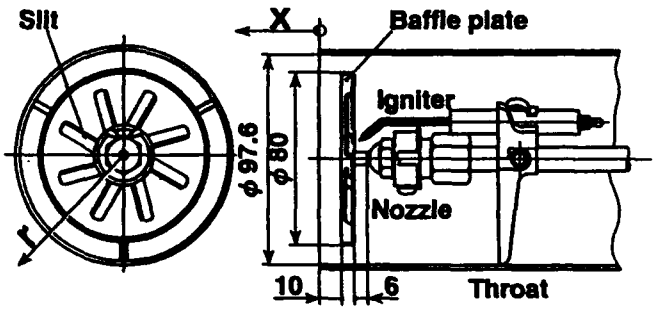

Fig.2 Burner features.

2.4 Temperature and Gas Species Measurements

For temperature measurements, a R-type thermocouple (Pt/Pt-Rh13%) was used. The wire diameter was 0.5mm and without sealing. A coating was done to avoid catalytic effect. In the temperature measurements, no corrections of radiation, heat conduction, droplet sticking were carried out.

In gas species measurements, a water cool sampling probe was used. The probe diameter was φ1.6 mm at the intake and φ10.0 mm at the main body. The sucking speed effect was taken into account so that a damp chamber was put in the gas flow line. For O_2 measurement, magnetic method (Shimazu) was used, CO_2 : (NDIR : Shimazu) , and NO : (chemiluminescence method : Shimazu).

Fig.3 Flame photograph

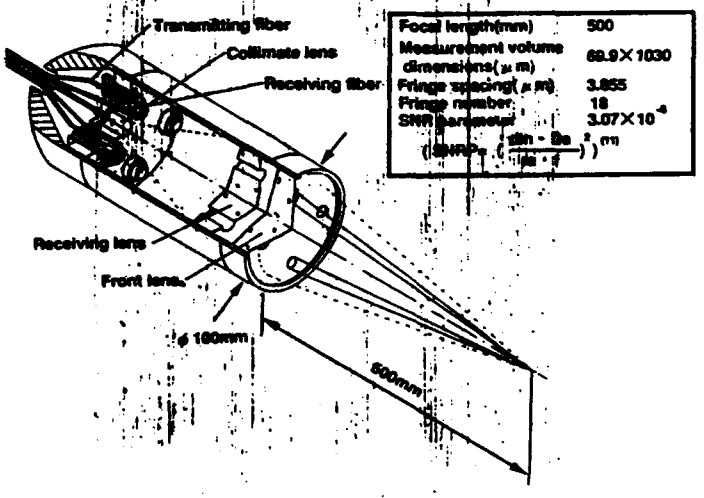

Fig.4 Schematic layout of the developed LDV probe

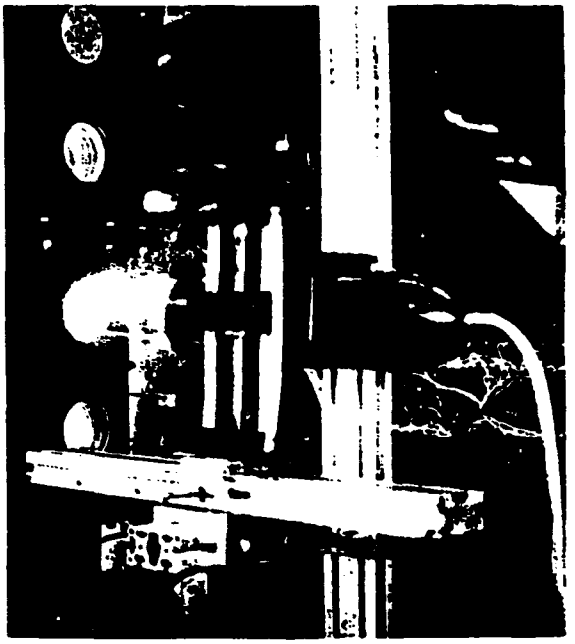

Fig.5 Velocity measurement photograph

2.5 Experimental Conditions

The pressure of the fuel was set up to 0.7 MPa and its flow rate was 9.45×10^{-3} (m^3/h) which translated to 0.103 MW. The fuel temperature was controlled by oil heater at 25℃. The air flow was controlled by a flow meter and an excess air ratio was λ=1.2. At the furnace exit, O_2=4.7 vol%, CO_2=10.8 vol%, NO=58.4 ppm (at O_2=0%), and CO=0 ppm. The NOx index was 2.97 g/kg Fuel.

3. MEASUREMENTS RESULTS AND DISCUSSION

3.1 Flow Field near Burner

Three components of velocity near the burner were measured by the LDV with BSA (Dantec). The mean velocity and its rms value at x/D=0.02 are shown in Fig. 6, where D is the diameter of the furnace of 430 mm. It is very difficult to identify the droplet velocity near the burner, because LDV measure the particle velocity which travels through the measurement volume. As shown in the previous study, the droplets under 30μm flues the reversing flow and over 50μm penetrated the reverse flow region as shown in Fig. 7. In Fig. 6 a broken line indicates the spray region which has 60° hollow-corn angle. It is found that there are two peaks in axial velocity profile, which means there are two reverse flows. The outer axial velocity peak is due to the flow passage between the buffle-plate and the burner throat, which is lower than that of area, but it is not possible to compare the velocity because the fuel

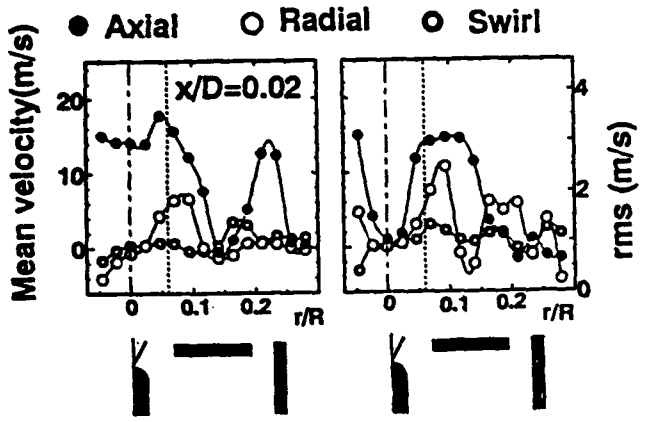

Fig.6 Three components of velocity near the burner.

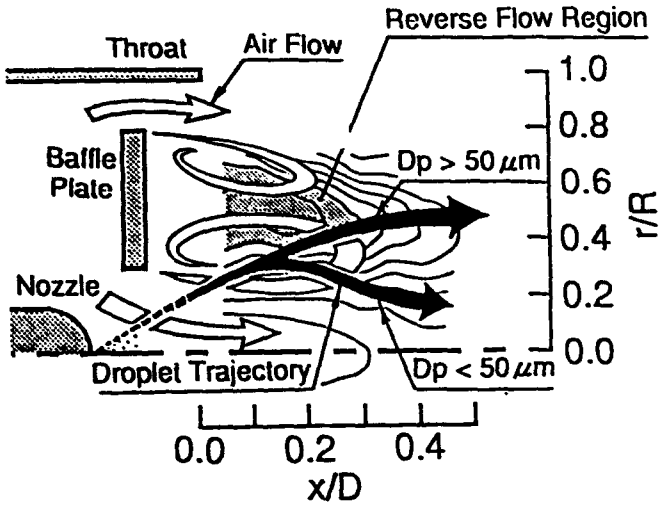

Fig.7 Spray structure.

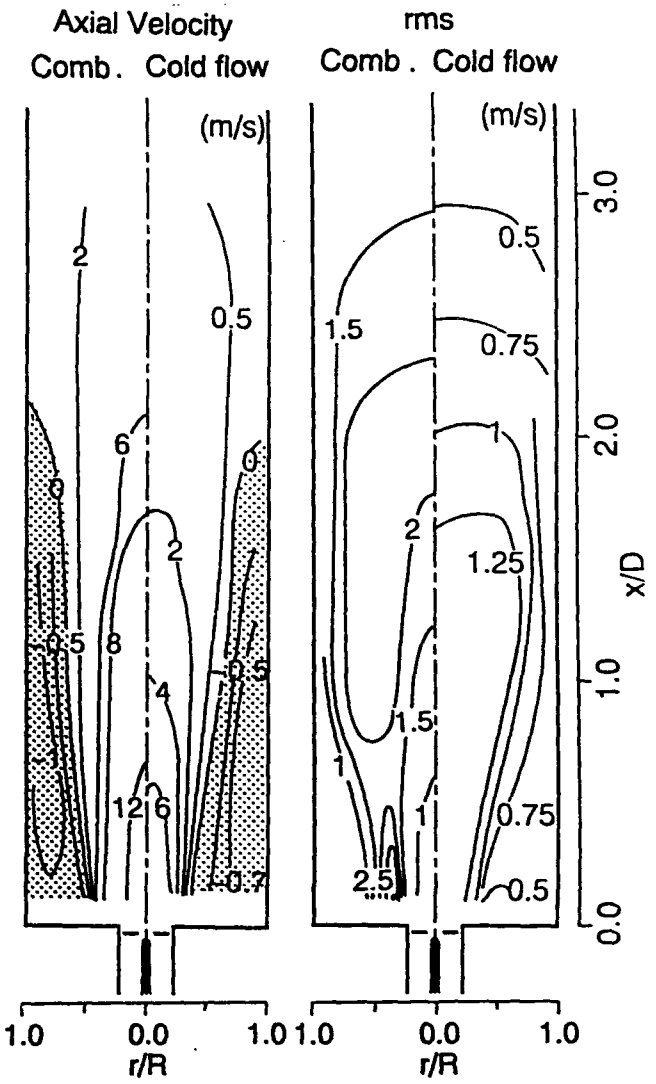

Fig 8 Flow field in the furnace.

droplet also traveling the inner reversing region. The maximum velocity yields at the spray region in the axial direction, but the maximum velocity in radial direction is slightly shifted outwards. Swirl velocity is observed in the outer reverse flow.

In rms values, maximum values in axial and radial direction were observed in the inner reverse flow regions, which was caused by the spray fuel penetration and its mixing with air in the reverse flow.

3.2 Flow Field in Furnace

First, the comparisons of flow in isothermal without fuel spray and in combustion were demonstrated as shown in Fig. 8. The hatching area shows the reverse flow region (u<0). The shape of axial velocity contours looks similar in both conditions, but the axial velocity in combustion near the burner was almost two times larger than that, which is due to volume expansion in combustion.

The shapes of axial rms values are different from each other. In combustion, the larger rms region is located just outer of the burner where the flame is formed and is the large velocity region.

The reverse flow region in combustion is shifted rather outer-ward than in isothermal condition, this is also due to the combustion effect. But the lengths of the reverse flow regions are almost the same in both conditions, and the maximum reverse flow velocity has less differences. The volume ratio of the reverse flows are 31%.in combus.'on and 34% in isothermal. This fact can provide a good understanding that the self-reverse flow area and its volume can predicted very well by isothermal flows.

3.3 Temperature and Gas Species Distributions

Figure 9 shows the distributions of O_2, CO_2 and NO concentrations together with velocity and the temperature. The flame holding region is at x/D=0.174

and main combustion region is at x/D=0.593 where much luminescence light yields, and the center part of furnace where the reverse flow region is over.

At x/D=0.174, the temperature distribution shows lower value at the center line where O_2 concentration is high and CO_2 concentration is low. This means that the mixing of fuel and air is not well done. At r/R=0.1 (r=21.5mm), O_2 is higher than that at the center line and CO_2 is increasing where NO concentration shows its maximum value. At this point the temperature shows its maximum value. Here, an active combustion process is carrying out, but no remarkable features can be seen in the velocity distribution. At r/R=0.25, O_2 value shows maximum and CO_2 decreases which is the opposite to those at r/R=0.1, where the temperature distribution starts to decrease. This radius [r/R=0.25] is the flame surface region. The reason of high O_2 value is due to air passage through the gap between the baffle plate and the burner throat. As shown in the direct picture of the flame, there is a transparent spray region where droplet evaporation takes place. The combusting air from this gap enhances the mixing of spray and air, but it takes sometime so that the flame is extended in the axial direction, where the O_2 values are high. At r/R>0.5, CO_2 value shows larger value than that in the flame region, this is due to residual combusted gas. It is needed to compare the inner high value region of CO_2 and the center residual CO_2 region by means of production rate or convective flux.

At x/D=0.593, the remarkable point is that the CO_2 concentration shows higher value in spite of no velocity. It is impossible to distinguish weather that is due to CO_2 production or residual CO_2. The same matter can be seen in NO distribution.

At x/D=2.302, the three gas species show almost constant values which means that combustion process was done perfectly.

As shown in this figure, we can understand the combustion characteristics separately such as velocity, temperature, and gas species concentration. But we can not find the understanding of NOx formation region and its production rate.

3.4 Reverse Flow Region

For understanding of the flows of O_2 and CO_2 in the reverse flows, the reverse flow ratio (reverse flow rate/total flow rate at each cross section area) are shown in Fig. 10. As shown in Fig. 8, the reverse flow region tail is at x/D≒2.0, so that the figure has the vertical axis up to x/D≒2.0. The maximum flow ratio is 37% at x/D=0.593, which is probably due to the corner reverse flows. The CO_2 reverse flow ratio shows its maximum at the same position as the flow rate, but the O_2 has the maximum near the burner up to 50%, which is due to incoming fresh air from the gap between the

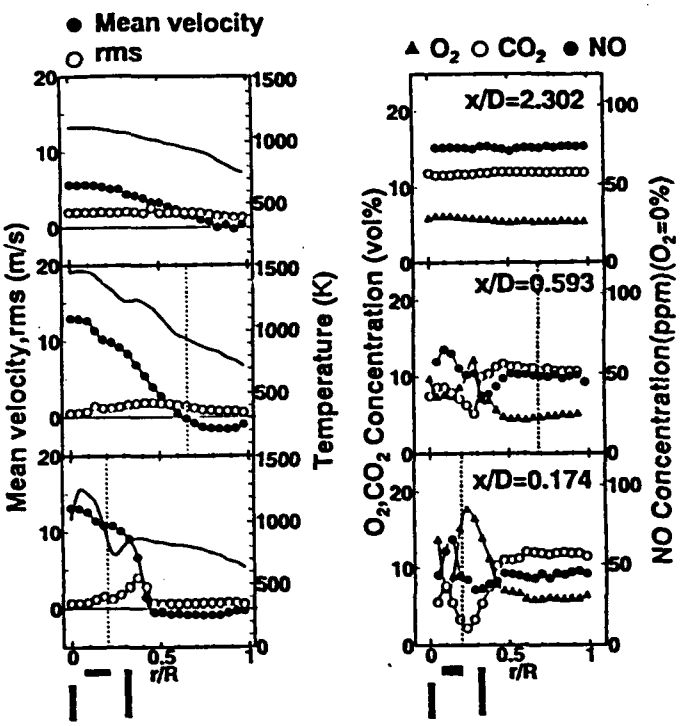

Fig 9 Distributions of O_2, CO_2 and NO together

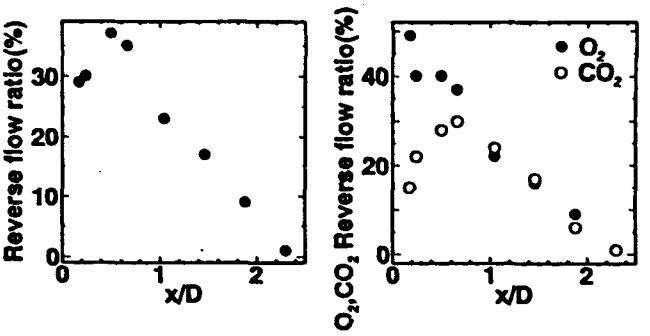

Fig. 10 Reverse flow ratio of O_2, CO_2. with velocity and temperature.

buffle plate and the burner throat, and the combustion process near the burner was not enough to consume O_2 so much.

The volume flow rates in consideration of temperature and concentration are shown in Fig.11. The volume flow at a certain circumstance was integrated and shown at each radius. At x/D=0.174, the incoming fresh air shows higher region, but its higher values decrease rapidly in axial direction due to combustion process. The reverse O_2 flow rate can be seen with this figure.

At x/D=0.244, the CO_2 flow rate shows very sharp distribution which is due to flame surface region. Also, it is found that no CO_2 production exists at the centerline.

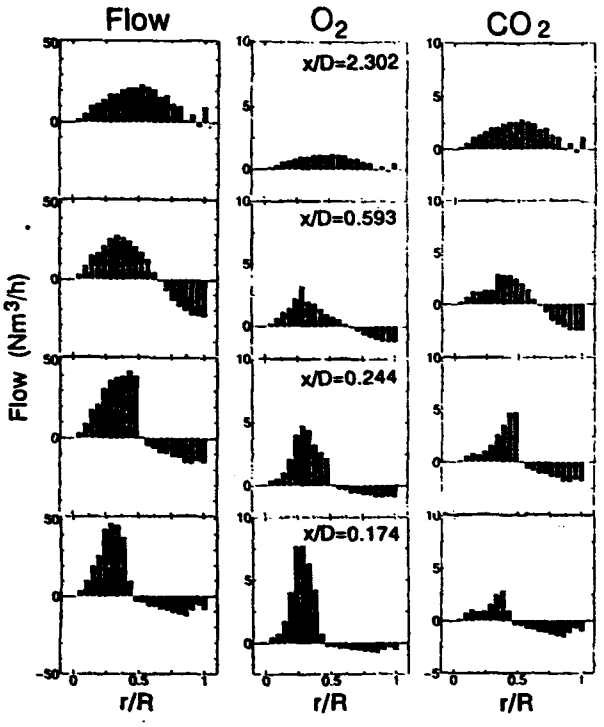

Fig 11 Volume flow in the furnace.

3.5 Flux

As explained in the above section, it is very difficult to demonstrate that the NO is produced very much in the region in which the NOx concentration shows its maximum value. For example, if NOx concentration is very low but the velocity is very high, the NOx production becomes high. So, we applied the convective flux concept to understand the combustion characteristics. The convective flux of each gas species means the gas mass per unit area per second, $kg/m^2/s$. In calculation of gas flux, a 10 mm grid is used. Figure 12 shows the comparisons of measured gas concentrations and axial convective flux at the three cross sections. The negative flux shows that the axial velocity is negative.

At x/D=0.174, the distributions of O_2, CO_2, and NO concentrations show the same tendency from the center line to r/R=0.4, where the flame surface exists, but large discrepancies come out at r/R>0.4. In case of O_2, the concentration shows almost 5%, this value is the same as that at the active combustion region at r/R=0.1. But in flux there is almost zero, which is due to zero velocity, that is only residual gas. The difference between the maximum and its minimum in concentration can not provide enough understanding of

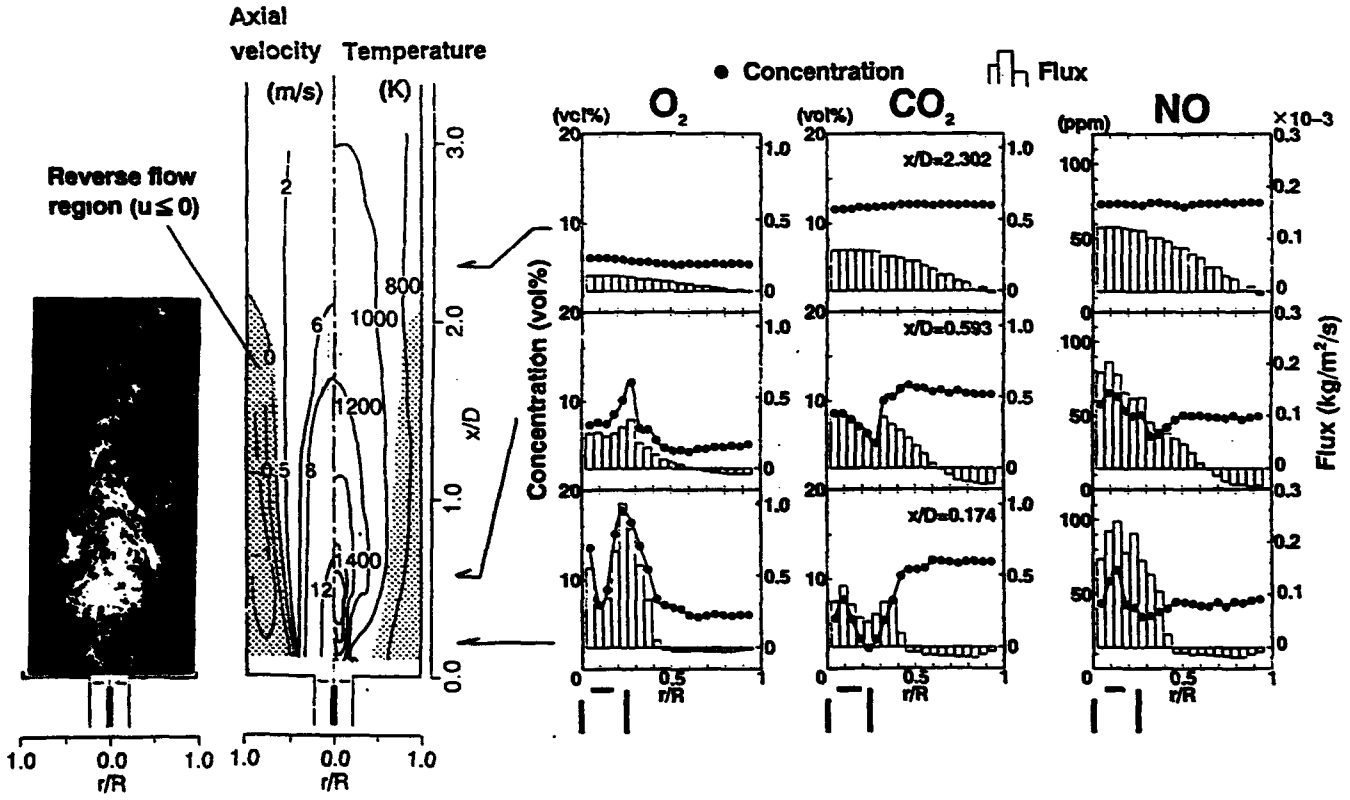

Fig 12 Comparisons of measured gas concentrations and axial convective flux.

the reverse flow region. In case of CO_2, the maximum value of 8% was seen in the flame but at r/R>0.4, the value exceeds the 8% and reaches to 10%.

But in flux, it is very clear that the inner flux is produced one but the outer one is due to the residual gas.

In case of NO, at r/R<0.4, a large amount of NO was produced in the flame region so as to be seen in the flux, but such understanding can not be obtained by the NO concentration.

At x/D=0.593, the remarkable discrepancies were observed especially at r/R>0.4. In the reverse flow region, the flux concept can provide the information of the reverse flow region very well. For NO at r/R>0.3 the higher values of NO concentration can be seen at outer region, this is due to the combination of residual gas and reversed gas.

As demonstrated in this figure, the implementation of convective flux is very effective to understand the combusting flow features, especially in the reverse flow and in the residual gas regions.

4 CONCLUSIONS

Measurements of velocity, temperature, and gas species concentration were carried out, and the results are summarized as follows:

(1) The axial velocity near the burner in combustion is almost two times higher than that in isothermal condition, but the negative velocity in the reverse flows in both conditions were almost the same -1.0 m/s.

(2) The length of the reverse flow regions were almost at x/D=2.0 in both conditions, and the reverse flow volumes were almost the same as 31% in combustion and 34% in isothermal.

(3) The convective flux concept can provide better understandings of combusted flows such as the reverse flow and the residual flows.

REFERENCES

Baker,R.J.,Bourke,P.J.,Whitelaw,J.H.,1973, Application of Laser Anemometry to the Measurement of Flow Properties in Industrial Burner Flames,14th Symp.(Int.) Comb.,pp 699-706

Bonin,M.P.,and Qeiroz,M.,1991,Local Particle Velocity,Size,and Concentration Measurements in a Industrial-Scale Purerized Coal-Fired Boiler,Comb. and Flame,85,pp121-133.

Chigier,N.,1991,Combustion Measurement,Hemisphere Publishing Corporation.

Dugue,J.,Weber,R.,1992,Laser Velocimetry in Semi-industrial Natural Gas,Oil and Coal Flames by means of a Water-cooled LDV Probe.,Proc. of 6th Int.Symp.on Appl. of Laser Anemometry in Fluid Mechanics.,22.3.1.

Durst,F., Melling,A.,Whitelaw,J.H.,1976, Principle and Practice of Laser-Doppler Anemometry, Academic Press.

Eckbreth,C.,1987,Laser Diagnostics for Combustion Temperature and Species,Abacus Press.

Edwards,C.F.,Rudoff,R.C.,1990,Structure of a Swirl-Stabilized Spray Flame by Imaging,Laser Doppler Velocimetry,and Phase Doppler Anemometry,23th Symp.(Int.) Comb.,pp1353-1359.

Ereaut,P.R.,Gover,M.P,1991,LDA Measurements of flame velocities at a 2000MWe Coal-fired Power Station,Journal of Institute of Energy,64,pp 135-142.

Heitor,M.V.,1993,Velocity,Size and Turbulent Flux Measurements by Laser Doppler Velocimetry, Instrumentation for Flows with Combustion,pp113-250.

Hong,N.S,Jones,A.R.,Weinberg,F.J.,1977, Doppler Velocimetry within Turbulent Phase Boundaries, Proc.R.Soc.Lond.A.,353,77-85.

Ikeda,Y.,Nishigaki,M.,Ippommatsu, M.,Hosokawa,S.,Nakajima,T., 1992,Optimum Seeding Particles for Successful LDV Measurements,6th International Symposium on Applications of Laser Techniques to Fluid Mechanics,32.2.5.

Ikeda,Y.,Nakajima,T.,Hosokawa,S., Matsumoto,R.,1990,A Compact fibre LDV with a Perforated Beam Expander,Meas. Sci.and Tech..1,pp 260-264

Nakabe,K.,Mizutani,Y.,Hirao,T.,Tanimura,S., 1988,Burning Characteristics of Premixed Sprays and Gas-Liquid Coburning Mixtures,Comb. and Flame, 74,pp39-51.

William,F.A.,1985,Combustion Theory 2nd Edition,The Benjamin/ Cummings Publishing Company,Inc.

Session 10.
Rotating Machines II

DEVELOPMENT OF AN ADVANCED LDA TECHNIQUE FOR THE DETERMINATION OF BOUNDARY LAYER PROFILES ON A ROTOR

Swales, C., Rickards, J., Lowson, M.V., Barrett, R.V.

Department of Aerospace Engineering, Bristol University
Bristol, U.K.

ABSTRACT

The structure of the boundary layer on a rotating body has to date only been determined in a qualitative manner and it is only the Laser Doppler Anemometer (LDA) which has been shown to offer a solution to this problem. It is the realisation of this potential, through a series of improvements to a Dantec 3D LDA, which is described for a model rotor operating in hover. The principal improvements to the system have been through operation of the system in the more stringent cross-coupled mode and through the development of a criterion, based on transit distance, by which erroneous data from the blade surface can be rejected. The blade height position is guaranteed through ensuring that only when light from a small alignment laser passes down a fibre-optic cable mounted within the leading edge is data accepted. A series of procedures to transform scatter plots of velocity against azimuthal position into three-dimensional boundary layer profiles have also been derived. These techniques and procedures, equally applicable to all rotating bodies, are described in detail and a series of results presented.

INTRODUCTION

Recent work at Bristol University has employed laser light sheet (Ref.1) and surface flow visualisation techniques to study the aerodynamics of rotor blades. Himmelskamp (Ref.2), among others, observed that significantly higher lift coefficients could be maintained near the hub of a rotating blade than on the same blade mounted statically. The postulate is that these higher lift coefficients are due to strong spanwise flows which are believed to exist within these regions. Some of the factors influencing these spanwise flows are shown in Fig.1. The results confirmed the existence of these strong spanwise flows but demonstrated the need for quantitative, rather than qualitative, results to enable the principal mechanisms to be fully understood.

The LDA is the only technique with the potential to realise such boundary layer velocity measurements (the hot-wire, though suitable for static blades, was unsuitable due to its intrusive nature). Initial evaluation of the department's three-component Dantec LDA further revealed this potential but it was also apparent that to enable such complex measurements to be performed, extensive improvements to the system would be required. An extensive literature search revealed that boundary layer measurements had not previously been obtained on rotor blades. In most circumstances the principal difficulty lay in the *'swamping'* of the Doppler burst, resulting from the passage of the seeding through the measurement volume, with the noise from the blade surface. It was with the intention of reducing this noise and hence obtain data within the boundary layer that this work was carried out.

EXPERIMENTAL PROCEDURE

The tests were performed within a large dedicated area and to further minimise any interference effects long focal-length lenses (1600mm) were employed. Both the optic heads, mounted on a fully

automated 3 axis Dantec traverse, were linked by fibre-optic cable to a 5 Watt argon-ion Spectra Physics laser. In addition each optic head could be rotated within its respective gimbal mount, which in turn could be swept and dipped relative to the traverse mount to provide the optimum optical configuration. Two pairs of beams (green and blue) are emitted from one head (referred to as the 2D head) and a third, violet, pair from the opposing (1D) head. As the optic heads were able to receive as well as transmit light, both the direct backscatter and simultaneous off-axis (cross-coupled) modes could be employed. Processing was performed by three Burst Spectrum Analysers (BSA) - a software suite comprised routines for automated data acquisition, data processing and graphical presentation.

The beams were aligned to a single point relative to the plane of rotation (Fig.2), and at a known height, and then with the LDA acquiring continuously a shaft encoder enabled the data to be sorted into azimuthal position (Fig.3). Three components of velocity were determined simultaneously and then translated into an orthogonal set of global U, V and W velocity components by a transformation matrix. The gaps in data corresponding to the passage of the two blades through the measurement volume, the large disturbance caused by the wake, and the undisturbed region between the passage of the blades can all clearly be noted. However no boundary layer data could be obtained.

Boundary layer studies on a flat plate mounted within the department's low turbulence wind-tunnel (Ref.3) had shown that data could be obtained significantly closer to the surface if the cross-coupled mode of light collection with its significantly smaller effective measurement volume was employed. However, when operating in the cross-coupled mode a sufficiently high data rate could only be guaranteed by the use of a pin-hole meter alignment technique, described in detail in Ref.3. The method uses the output of a light dependent resistor mounted behind a 20 micron diameter pin-hole to determine the peak intensity position across either a beam or a collection volume (created by passing light down the collection fibres) (Fig.4). The principal advantage of the technique is that it is not subject to the visual interpretation of the images of beams passing through an objective lens.

To further minimise the effects of noise caused by light reflected from the surface as it passes through the measurement volume, the optic heads were configured to minimise the grazing angles of the beams relative to the surface. In addition the blade was painted matt black.

The initial cross-coupled results showed that to achieve accurate data within the boundary layer both the data rate and the total acquisition time had to be consistently kept to a maximum. The former was achieved through accurate alignment, careful optimisation of the processor parameters, and through careful positioning of the seeding (atomised Ondina oil). Due to the contraction of the slipstream the optimum position was found to vary with given radial position, rotor speed and pitch angle.

Optimisation of the processor settings was necessary to achieve a balance between a high data rate and a low level of data '*swamping*' from the blade surface. To encompass the large range in velocities over the azimuth a large bandwidth span had to be set. However at any given azimuthal position this bandwidth is significantly larger than the velocity range and this, as previous evidence had shown, contributes to lower data and validity rates and with high attenuation levels can contribute to erroneous rms velocity. The photomultiplier high voltage and the processor gain had consequently to be set to the lowest possible values which resulted in a reduced data rate.

As only boundary layer information was required most of the data for a given test could be rejected. This was achieved by only having the BSAs enabled for a period of time corresponding to twice the passage of the blade through the measuring volume (Fig.5).

The inherently flexible nature of the rotor blades, the level of recirculation prevalent within the test area and the teetered hub all contributed to a significant blade height variation over the test period. Though not apparent from the scatter plots of velocity against azimuthal position, this problem would have manifested itself in elongated and hence inaccurate boundary layer profiles. The solution employed was to use a light dependent diode to enable the BSA when the blade was at the correct height. This was achieved by mounting a thin fibre-optic cable within the leading edge of the blade, enabling light to pass along the fibre-optic cable to be received by the diode when the blade was correctly positioned (Fig.2). A 5 mW helium-neon laser, mounted alongside the LDA, was used for this purpose. The resolution was further improved by mounting the tip end of the fibre-optic cable behind a pin-hole. The result is a vertical resolution of better than 0.005mm. At low rotational speeds and pitch angles the blade was at the required height for 80% of the revolutions, at the highest speeds and pitch angles this proportion could reduce to less than 5% - the requirement for longer acquisition times is apparent.

Even when operating in the cross-coupled mode, with low laser power, a matt-black blade surface and low attenuation levels, erroneous data was recorded due to reflections from the surface as it passed through the measurement volume. Extracting the data from the noise was only made possible through the use of a transit time rejection criterion. The concept of transit distance (or effective measurement volume size) was introduced and the value for data a significant distance from the influence of the blade surface determined. If, on approaching the surface, the transit distance for a given particle (transit time x particle velocity) exceeded this value it was rejected - evidence of the effectiveness of this technique is shown in Fig.6.

With these problems solved, a series of tests were configured. These comprised four rotational speeds (200, 400, 600 and 800 rpm), three pitch angles (1, 6 and 11 degrees) and two radial stations. With the constraints imposed as defined above, the technique was to record sufficient data at a particular height (15 minutes acquisition time per height) then traverse to a different height and repeat the exercise. To guarantee sufficient resolution, data had to be acquired at increments of 0.1mm and to provide boundary layer data over the whole of the upper surface of the blade 150 vertical positions were required. A total acquisition time of 37.5 hours per test.

DATA REDUCTION

The results produced were of velocity (U (chordwise), V (spanwise), and W (vertical)) against azimuthal position. Ultimately required were boundary layer profiles of velocities relative to the surface. The required procedures formed an intricate part of the data acquisition and are consequently described in detail (Fig.7a to Fig.7f)).

For a given traverse position the data file, exported from Burstware in ASCII format, was made up of three orthogonal components of velocity relative to the traverse. This data contained the erroneous data due to the reflections from the blade surface passing through the measurement volume. The first stage was consequently to remove the 'noise' by using the transit distance criterion described above. As with all the stages the procedure was to pass the data file through a Pascal program.

The data was then sorted into azimuthal position (obtained from knowledge of both the arrival time for each particle and the time between encoder pulses). The mean velocity for each component was then determined for each 0.1mm bin along this azimuthal window (Fig.7a). The bin size was chosen as a compromise between the required azimuthal resolution and the number of data points for an accurate statistical sample.

The ability to acquire measurements to within 0.005mm of the surface, and to distinguish genuine data from noise, has enabled the fore and aft positions of the blade surface to be determined on passing through the measuring volume. The procedure for the third stage is to process each file in turn noting the start and finish (fore and aft) positions of the gap in data corresponding to the blade and record these positions in terms of azimuthal angle (Fig.7b). These positions, for the whole range of traverse heights, are then combined into a single file, and when plotted should correspond to the known profile of the upper surface of the Gottingen 436 blade. Any discrepancy between these two profiles would result in careful analysis of both the data and the previous stages in processing. In most cases there was found to be excellent agreement between the two and this consequently gave confidence in the accuracy of the profiles.

Assuming the upper blade surface profile to have been correctly defined a combined file is then created to provide the orthogonal U, V and W mean velocity components at all heights and azimuthal positions relative to the blade surface. The position of each bin along the azimuth is then, from knowledge of the distance of the measurement volume from the centre of rotation, converted into cartesian coordinates (Fig.7c).

Each grid position is then determined relative to the trailing edge (defined as having coordinates 0,0). The surface position is defined by 'S' and any position corresponding to the blade passing through the measuring volume is defined by 'G'. At this stage the U and V velocities are converted from values relative to the LDA to values relative to the blade. As the measurement volume follows an arc (worse near the root due to the larger radius of curvature) rather than a pure chord-wise motion the data must be transformed. This is achieved by multiplying the data by a transformation matrix which takes into account the local angle between the chord of the blade and the path taken by the blade (Fig.7c).

The mean velocities are now relative to the surface. However convention states that the boundary layer profiles must be perpendicular to the surface, rather than in this case vertical. For a given chordwise position, the gradient between two neighbouring coordinate positions making up the surface profile was determined (Fig.7d). The equations for the perpendicular bisector to this tangent were then calculated. The U, V and W

velocity components have however been determined along orthogonal axes and not relative to the surface. Corresponding values, at intervals along these perpendiculars, had then to be determined by interpolating from the adjacent velocities along the chordwise direction (Fig.7e).

Finally these velocities were converted into values corresponding to a coordinate system aligned with the tangent of the blade surface at the chordwise position of interest (Fig.7f).

RESULTS AND THEIR DISCUSSION

This work was carried out with the intention of evaluating suitable techniques, rather than producing a full series of results. However evidence of the success of the results for a range of conditions is given in Figs.8 and 9.

Several characteristics are worthy of comment. Fig.8 shows an intermediate case (6° pitch, 600 rpm) with six boundary layer velocity profiles provided at equidistant positions along the chord. The first profile (x/c=0.16) is characteristic of a laminar boundary layer. The flow is nominally 2D, with a boundary layer thickness of 0.22mm. As the distance from the leading edge increases the adverse pressure gradient comes into effect with the slow moving air, nearest the surface, being the most strongly affected and becoming retarded.

As x/c reaches 0.5 the strong adverse pressure gradient results in a region of reversed flow which, for a 2D static wing, is indicative of a laminar separation bubble. This is due to the laminar boundary layer separating, undergoing transition and then due to its greater energy reattaching further downstream as a turbulent boundary. This appears to also apply to the case of a rotating blade. The familiar profile characteristic of a turbulent boundary layer can be noted for the most aft positions.

The results also help to quantify the extent of the spanwise flow. The strongest spanwise flows are noted within the separation bubble with values of up to 8% of the chordwise velocity. Within the turbulent boundary layer the spanwise flow again decreases. The hypothesis is consequently that significant spanwise velocities are only noted when the flow is separated and is able to be influenced by a combination of the spanwise pressure gradient, the centripetal forces, and the Coriolis effect (Fig.1). Though the separation bubble is notoriously difficult to seed even on static blades sufficient data was still acquired for an accurate mean velocity to be determined.

One further result is provided. Fig.9 shows the 1° pitch angle, 800 rpm case but this time near the tip. The profiles reveal that downstream of the characteristic separation bubble the flow reattaches as a turbulent boundary layer but then separates prior to the trailing edge. Of particular interest, however, is the spanwise component which, contrary to the previous results, does not show significant velocities within the separation bubble. Initial interpretation reveals that the small extent of spanwise flow within the separation bubble is due to the tip vortex inducing a flow in the opposing direction. Again this agrees with the flow visualisation results. Further analysis and interpretation is beyond the scope of this paper.

DISCUSSION OF ERRORS

The potential errors associated with these results are only briefly discussed and no quantitative assessment of them is given. The errors are fundamentally of three different forms and each is discussed individually - an appreciation of their combined effect is then given.

The conventional sources of error associated with LDAs, and particular those measuring three components simultaneously, are well known. Their effects on these results can however only be estimated. The principal reason is that contrary to other simpler tests no comparison with theoretical or experimental results can be made.

Velocity biasing caused by the large size of the measurement volume relative to the velocity gradient has been minimised through the operation of the system in the cross-coupled mode with low attenuation levels and with coincidence filtering. Due to the nature of the tests the level of biasing of this form which still exists cannot be ascertained. However, experience with boundary layer measurements on a flat plate has shown the effects of velocity biasing to be minor when operating in this mode.

As previously mentioned every effort has been made to maximise the number of samples within each azimuthal bin. For all the tests between 50 and 250 coincident samples were determined - a value satisfactory for a given mean.

The other potential forms of error associated with the LDA measurements, ie. through inaccurate calibration factors, component angles for the

transformation matrix etc. have been assumed to be small.

The errors associated with the rig are also small with the rotational speed of the rotor varying by only 0.1%. The nature of the data acquisition assumes the flow to be steady. Although the rotor site was such as to minimise the effects of recirculation it could not be entirely removed. The boundary layer flow consequently varied to some extent during each cycle and yet the data was recorded over a large number of revolutions. However, on analysis of the velocities within a given azimuthal bin, the rms quantity was not significant This indicated that the flow did not vary as much as had been believed. In addition as data was only recorded at one particular blade height, and the blade position is primarily affected by the recirculation, it was assumed that whenever data was recorded, the effects of recirculation were similar and consequently the boundary layer representative.

The third principal source of error lies in the extensive post-processing of this data from azimuthal variations of velocity into three component boundary layer velocity profiles relative to the surface. The technique of distinguishing between noise and data had been thoroughly tested and was found to be very accurate. A further test of the accuracy of the method was provide by comparison of the calculated coordinates of the blade with the actual coordinates. This source of error was consequently assumed to be minimal. In addition it gave confidence in the boundary layer data.

The anticipated errors in the determination of the mean velocities at each position within the grid surrounding the blade were also assumed to be small provided that the position of the measurement volume relative to the centre of rotation could be accurately determined. A larger potential source of error lay in the determination of the equations for the tangents and hence the perpendiculars to the surface. However the principal source of error was believed to be in the interpolation routine employed to determine the actual velocities along these perpendiculars. Future work would benefit from an improved interpolation routine.

In conclusion, it is accepted that there are several potential sources of error, most of which have not as yet been quantified. The trends shown by the boundary layer profiles are however genuine and the techniques and methods described can be assumed to be of significant use. The post-processing of the data would benefit the most from further improvement.

CONCLUSIONS

The ability to operate a three-component LDA in the cross-coupled mode through the development of an enhanced alignment technique has enabled unique 3D boundary layer velocity profiles to be determined for a model helicopter operating in hover at speeds of up to 1000 RPM. In addition data is only accepted within tight vertical constraints and a series of algorithms have been realised by which the genuine data is distinguished from the erroneous data caused by reflections from the blade surface and then converted into velocities relative to the blade.

The boundary layer profiles reveal data to within 0.005mm of the surface on blades rotating at speeds of up to 800rpm. Of particular interest are the strong spanwise flows noted within the laminar separation bubble as they confirm the results previously obtained by flow visualisation methods. However, significant errors cannot be discounted and consequently, though they show great potential, the results should be accepted as being only of a preliminary nature.

REFERENCES

(1) - Payne, F.M. "The Structure of Leading Edge Vortex Flows Including Vortex Breakdown". Ph.D. Thesis, University of Notre Dame, 1987.

(2) - Himmelskamp, H. "Profile Investigations on a Rotating Airscrew". Ph.D. Thesis, Gottingen, 1945.

(3) - Rickards, J., Swales, C., Brake, C.J., Barrett, R.V. "An Improved Alignment Technique Enabling Cross-Coupled Operation of a 3D LDA for Small Scale Flow Surveys". 5th International LDA Conference, Veldhoven, The Netherlands, 23-27th August 1993.

(4) - Barrett, R.V., Rickards, J., Swales, C., Brake, C.J. "Enhanced Performance of a Cross-Coupled 3D LDA for Small Scale Flow Surveys using Improved Alignment and Operational Procedures". Proceedings from ICIASF '93, International Congress on Instrumentation in Aerospace Simulation Facilities, Saint-Louis, Sept 1993.

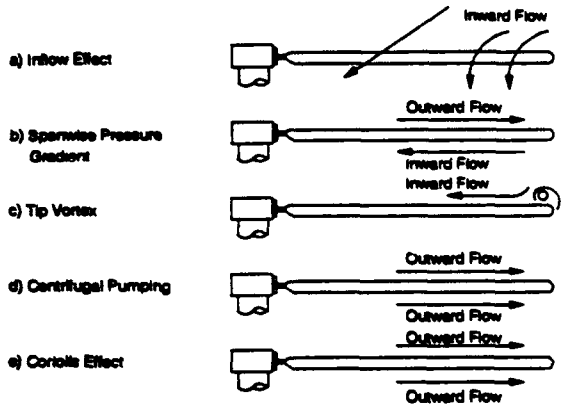

Fig.1 Principal Factors Affecting Rotor Flow

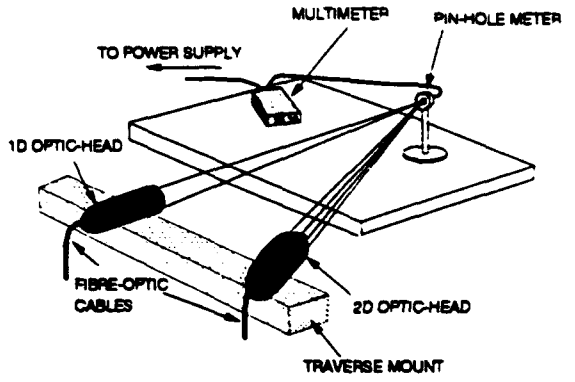

Fig.4 Principle Of Alignment Technique

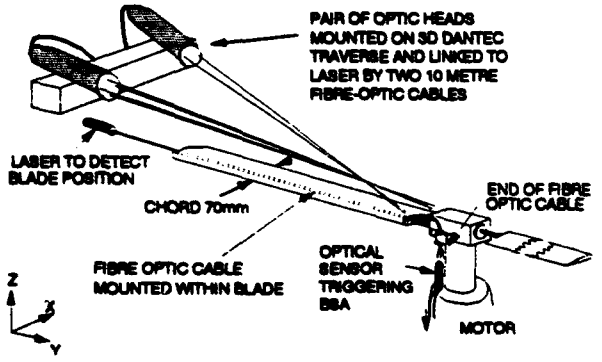

Fig.2 Schematic Of Rotor Rig

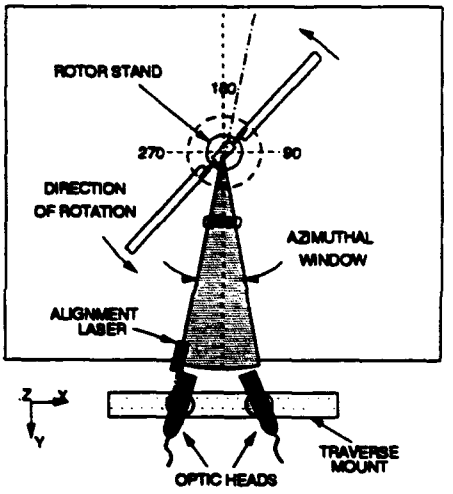

Fig.5 Azimuthal Window For Data Acquisition

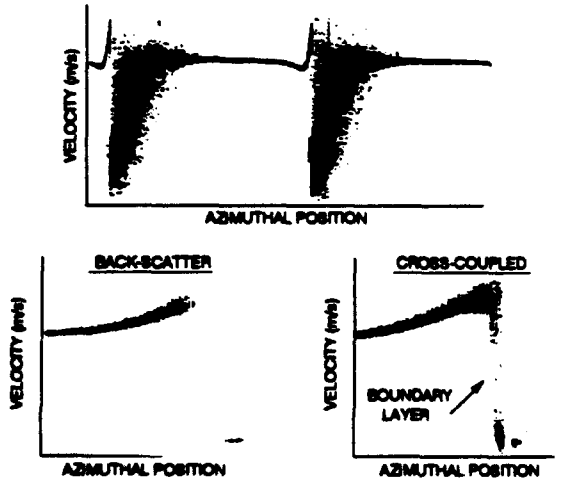

Fig.3 Azimuthal Velocity Distribution

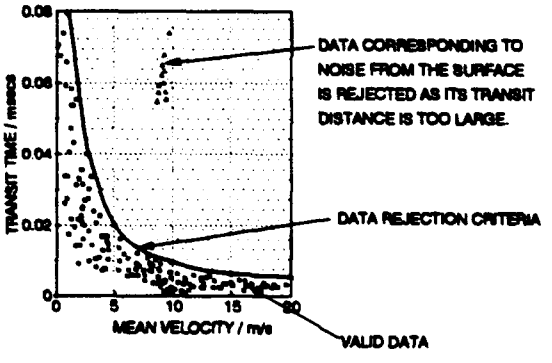

Fig.6 Data Rejection Criteria

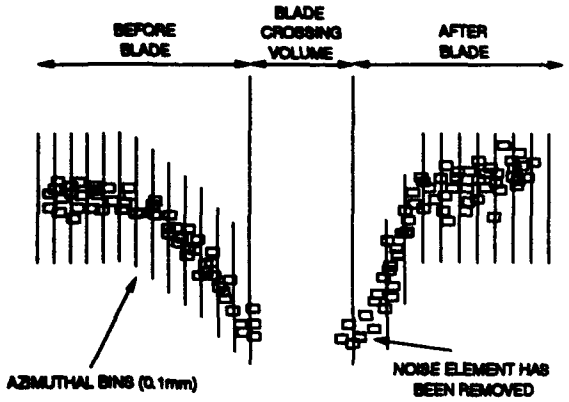

Fig.7a Sorting Of Data Into Azimuthal Bins

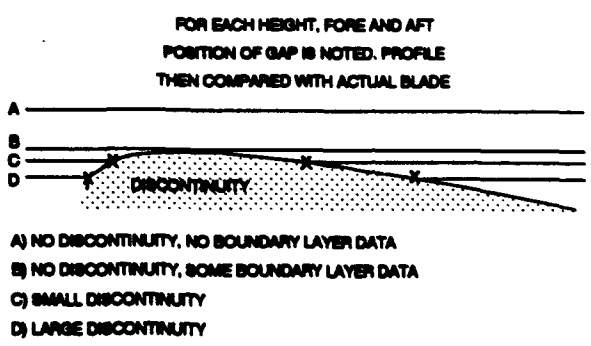

Fig.7b Determination Of Surface Profile

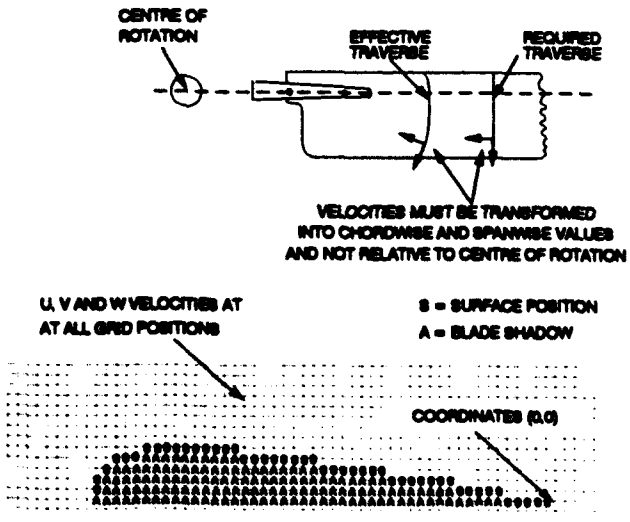

Fig.7c Creation Of Complete Traverse File

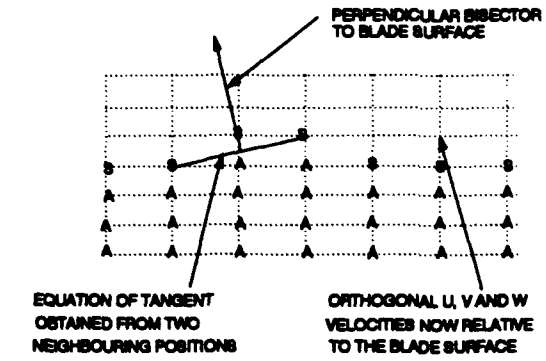

Fig.7d Equations For Perpendiculars to Surface

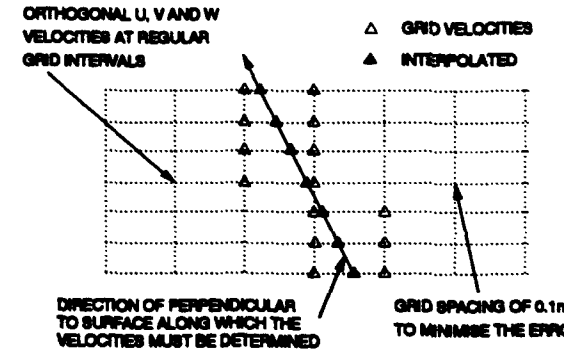

Fig.7e Interpolation Of Velocities

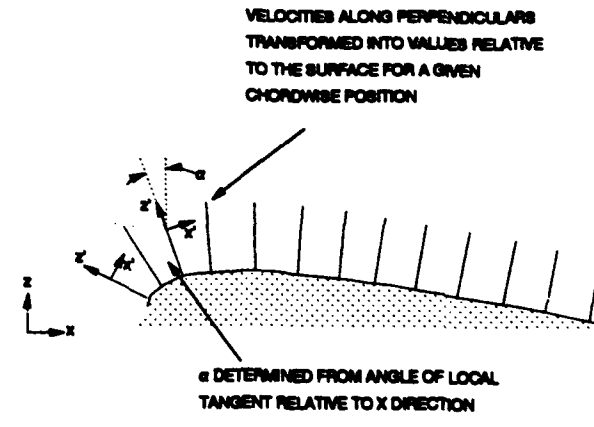

Fig.7f Determination Of Final Profiles

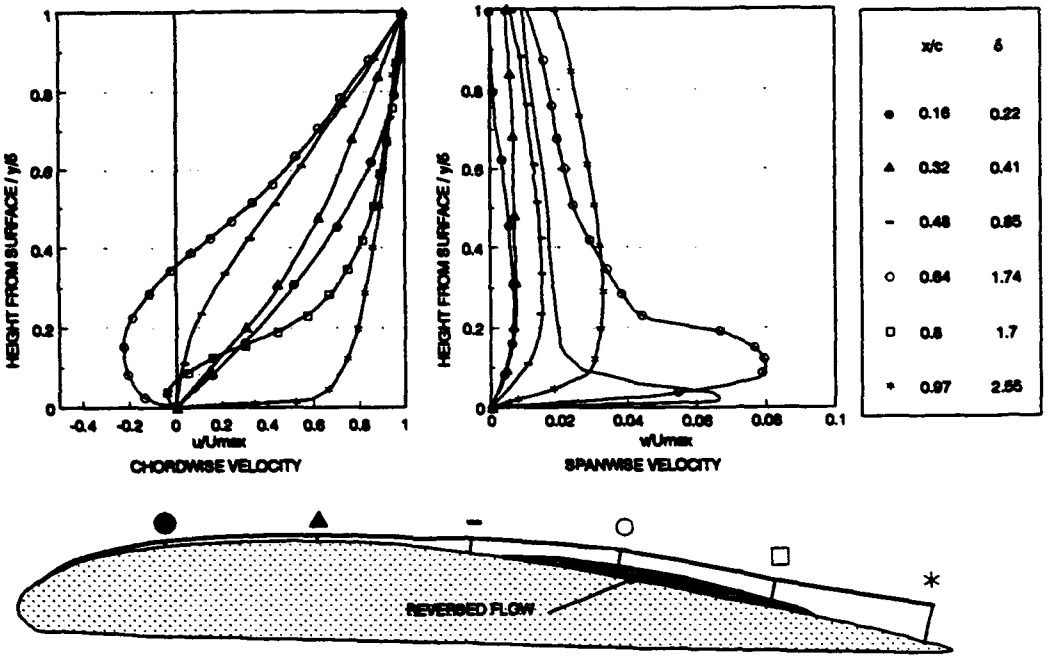

Fig.8 Example 3D Boundary Layer Velocity Profiles (Inboard, 600RPM ,6 Degrees)

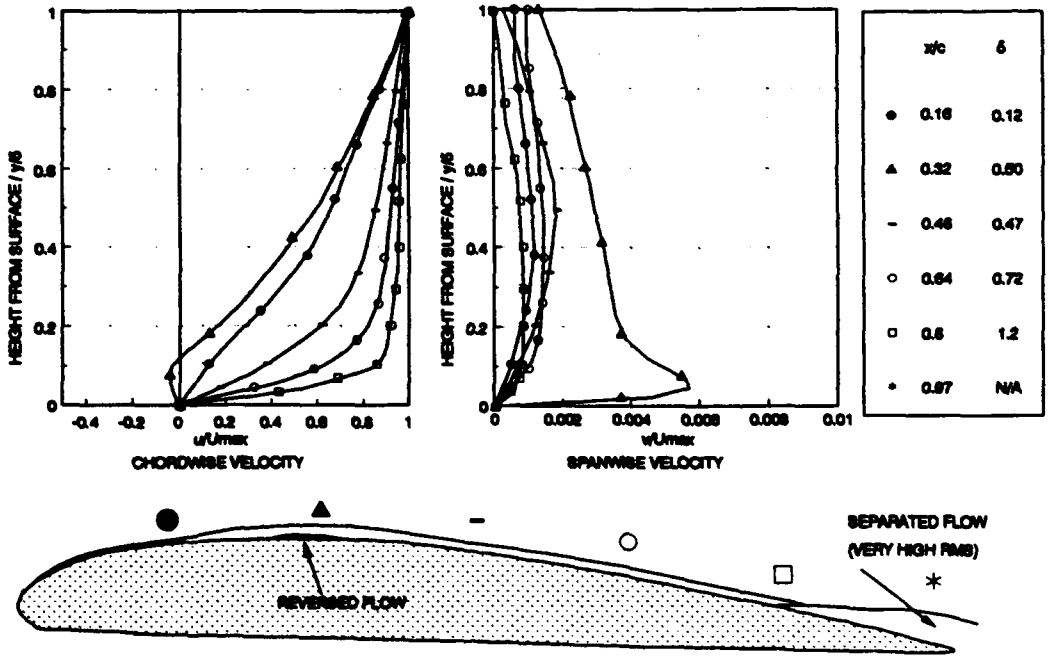

Fig.9 Example 3D Boundary Layer Velocity Profiles (Outboard, 800RPM,1 Degrees)

THE INTERACTION OF THE TRAILING VORTEX STREAMS FROM RUSHTON TURBINE BLADES

Rutherford K., Lee K. C. and Yianneskis M.

Centre for Heat Transfer and Fluid Flow Measurement,
King's College London, Strand, London, WC2R 2LS.

ABSTRACT

The trailing vortex structure and the impeller discharge flows generated in vessels stirred by both single and dual-Rushton turbines were investigated through angle-resolved and time-resolved laser-Doppler anemometry measurements in two tanks of diameter (T) 100 mm and 294 mm with impellers of diameter D = T/3. The effects of the trailing vortex structures on the turbulence levels in the vessel and the degree to which the impeller discharge flows interact in the dual-Rushton configuration are discussed. The results from the two vessels are compared to assess scale-up effects. The flow in the impeller streams was found to be anisotropic, and a cylindrical region was defined around the impeller disk of height 0.60D and radius 1.0D for the single impeller, while a similar region was defined around the centre of the vessel of height 1.2 D and radius 1.0 D for the dual-impeller combination, within which the periodicity of the flow generated by the impellers was contained. These findings have important implications for CFD prediction methods which at present are mostly based on the assumption of isotropic turbulence which may lead to erroneous predictions in the vicinity of the impellers. In addition, the main flow features were found to scale well between the two vessels. The results provide useful information for process design.

1. INTRODUCTION

The flow structure around Rushton turbine blades is very complex due to the formation of trailing vortices behind each blade, and consequently a number of studies have been concerned with this type of flow in vessels stirred by a single impeller [1 - 6]. Van't Riet and Smith [1 - 3] established that a trailing vortex, shown schematically in Figure 1, formed behind each impeller blade and maintained its identity for two to three blade lengths from the point of origin. They also reported that turbulence measurements made in the impeller stream with stationary probes were unreliable since most of the measured turbulence was due to the periodicity of the flow, attributable to the blade passages and associated trailing vortex structure. Yianneskis et al. [4], Calabrese and Stoots [5] and Yianneskis and Whitelaw [6] carried out detailed investigations in the impeller vicinity in vessels agitated by a single Rushton turbine, and documented the strong periodicity and anisotropy which exists in this region, and the associated trailing vortex structure.

Mahmoudi and Yianneskis [7], and Mahmoudi [8] investigated the effect of varying the impeller spacing in dual-Rushton turbine configurations and found that three stable and four unstable flow patterns were obtained, depending on the clearance of the lower impeller from the base of the mixing vessel (C1), the separation between the impellers (C2), and the submergence of the upper impeller (C3). Of the three stable flow patterns, merging flow, which occurred with a clearance C1 = 0.33T and separation C2 = 0.33T, was determined to be the most desirable since it produced the lowest mixing times and power consumption. This configuration was termed merging flow because the impeller streams were inclined towards each other and merged midway between the impellers.

In this investigation the trailing vortex structures with single-turbine and merging flow configurations are compared and the effect of vessel size is assessed.

2. EXPERIMENTAL CONFIGURATION AND TECHNIQUES

In the present study, a cylindrical Perspex mixing vessel of diameter T = 100 mm, with four 0.1 T wide baffles was used to acquire angle- and time-resolved LDA data for the single and dual-Rushton combinations. The cylinder was situated inside a water-filled Perspex trough in order to minimise refraction at the cylindrical surface and distilled water was used as the working fluid. A transparent Perspex base was incorporated in the vessel design to permit maximum optical access, and the vessel could be rotated about its axis to enable measurements to be performed in different planes. Angle-resolved LDA measurements were also performed in a T = 294 mm diameter vessel for the dual-Rushton configuration in order to establish scaling effects.

The impellers used were six-bladed Rushton turbines of diameter D = 0.33 T. A constant clearance C1 = 0.33 T was employed between the bottom of the mixing vessel and the lower impeller. A separation C2 = 0.33 T was used between the impellers for the double Rushton measurements in order to provide the merging flow pattern described in [7] and [8]. The liquid height in the tank was H = T.

The laser-Doppler anemometer made use of a 10 mW Helium-Neon laser and was operated in the dual-beam forward-scatter mode. The velocity components were measured with the beams entering either through the side of the tank or the cylinder base, and a rotating diffraction grating was used to implement a frequency shift on the two first order beams. The scattered light was collected with a photomultiplier, and the Doppler signals were processed by means of a frequency counter (TSI Model 1990) interfaced to a microcomputer. The impeller shaft was linked to an optical shaft encoder which

provided a train of 1999 pulses and a marker pulse per revolution. This permitted angle-resolved (a.r.) measurements to be performed over 1° of impeller revolution. For the purpose of these measurements the midpoint of one blade of the lower impeller was aligned with the shaft encoder marker pulse and the data were obtained over a specified 60° interval (between two neighbouring blades) during a number of impeller revolutions and the data were sorted into 1° bins. For the time-resolved measurements the frequency counter was set to measure all validated Doppler signals which arrived within a prescribed time interval (four impeller revolutions for the data presented).

The position of the measuring volume was determined for each measurement location using an iterative computer program and the optical system was mounted on a traversing table which allowed the measuring volume to be positioned in the stirred reactor with an accuracy of 0.05 mm. All of the measurements described were performed in the $\theta = 0°$ plane midway between two baffles.

The measurements were conducted at a Reynolds number of 40000, which corresponded to a constant impeller rotational speed of N = 2165 ± 10 r p m (V_{tip} = 3.77 m/s) for the T = 100 mm vessel, and N = 250 ± 0.5 r p m. (V_{tip} = 1.28 m/s) for the T = 294 mm vessel. The origin of the co-ordinate system used is the centre of the bottom of the vessel and all positions are described in terms of axial (z), radial (r), and tangential (θ) directions. The location of the measuring volume for the angle-resolved measurements is expressed in terms of polar co-ordinates r, ϕ with respect to the blades calculated from the r, θ co-ordinates. $\phi = 0°$ is located at the plane of the blade tip, and the impellers rotated in a clockwise direction as viewed from above the vessel.

A transparent Perspex lid was located above the liquid surface in the small vessel, at a height H = T, to prevent entrainment of air bubbles from the free surface of the liquid, and to permit measurements to be performed in forward scatter with the beams entering through the base of the vessel. Two mirrors were attached to the upper surface of the lid, and the space above the lid was filled with water to ensure that the mirrors were always submerged. This allowed the scattered light to be re-directed through 90° by the mirrors and collected using the photomultiplier. The effect of a lid on the flow in a stirred vessel has been previously investigated by Nouri and Whitelaw [9], who conducted comparisons between flows in vessels with and without lids. They concluded that the use of a lid only affects the flow in the immediate vicinity of the lid/free surface and that the flow velocities were almost identical elsewhere in the vessel.

3. RESULTS AND DISCUSSION

3.1 Single Rushton Turbine Results

The characteristic flow features in the T = 100 mm vessel operating with a single Rushton turbine can be seen from velocity vectors normalised by V_{tip} in the $\phi = 45°$ r - z plane plotted in Figure 2. The impeller discharge flow is directed towards the vessel wall with a slight upward inclination (around 2 - 3°) to the horizontal, in agreement with the previously reported results of Yianneskis et al. [4]. These authors also reported the formation of two well defined ring vortices which were almost symmetrical above and below the impeller disc, which are indicated in part by the vectors plotted in Figure 2.

3.2 Dual Rushton Turbine Results

Normalised velocity vectors in the $\phi = 45°$ r - z plane, for the dual-Rushton configuration are shown in Figure 3(a) for the region around the lower impeller in the T = 100 mm vessel. These results show a considerable change in the direction of the impeller discharge flow which is oriented at approximately 45° to the horizontal in comparison with the near-horizontal discharge flow of the single Rushton turbine shown in Figure 2. Consequently the centre of the trailing vortex is located at a higher elevation, z/T = 0.39, than with a single Rushton system. These effects are attributable to the influence of the additional impeller which prevents the formation of the two ring vortices per impeller typical of a single Rushton turbine system. Instead, with this impeller separation, the discharge streams are inclined at 45° towards one another, and merge midway between the impellers to form two very large ring vortices [7, 8]. As a result, the strong downward flow near the impeller tip due to the upper ring vortex above the impeller disc, which can be clearly identified in Figure 2 is not present in the dual-Rushton flow.

The structure of the trailing vortices and the inclination of the impeller discharge flow in the T = 100 mm vessel can also be assessed from the normalised contours of radial rms velocity (v'/V_{tip}) in the $\phi = 45°$ r - z plane shown in Figure 3(b). It can be seen that the regions of high rms velocity are located very close to the impeller blade tip, between r = 0.18 T and r = 0.21 T, and also that the levels decrease very quickly with increasing radial distance from the blade tip, and axial distance from the impeller mid - section. The net effect is that the main influence of the trailing vortex on the turbulence levels is found between the impeller blade tip and r = 0.32 T radially, and the impeller mid-section and z = 0.45 T axially.

Contours of normalised kinetic energy of turbulence (k/V_{tip}^2) in the z = 0.33 T r - θ plane are shown in Figure 4 and the trailing vortex structure is again indicated by the high value contours originating behind the leading blade at the lower edge of the figure, and dissipating while spreading radially outwards towards the trailing blade. The region of highest kinetic energy is located around r = 0.185 T, at a blade angle of approximately $\phi = 30°$. It can be seen that the outer edge of the region of high k extends to approximately r = 0.28 T, within two blade lengths of its origin. The remains of the trailing vortex from the preceding blade can also be seen in Figure 4 in the region between r = 0.19 T and 0.23 T, and from $\phi = 0°$ to $\phi = 11°$.

Typical traces of time-resolved radial velocity variations for the dual Rushton turbine configuration in the 100 mm diameter vessel are shown in Figure 5. Both Calabrese and Stoots [5], and Yianneskis and Whitelaw [6], showed that for single impeller systems a cyclic variation of the velocity is obtained with each blade passage in the vicinity of the trailing vortices. The expected six cycles per revolution can be clearly defined in Figure 5(a) for r = 0.17 T, z = 0.33 T, which is located 1 mm radially out from the impeller tip at the lower impeller disk elevation. Comparing this distribution with Figure 5(b) for r = 0.25 T, z = 0.41 T (9 mm radially out from the impeller tip and 7.66 mm above the impeller disk), the dissipation of the trailing vortices expected from the results of Figure 3(b) can be clearly seen. Although cyclic velocity fluctuations are still discernible in the velocity distributions, their magnitude has decreased significantly. Figure 5(c) shows the distribution obtained even

further from the impeller, at r = 0.30 T, z = 0.50 T, which is 20 mm from the vessel wall and midway between the two impellers. The trailing vortex structure has almost completely dissipated, and the turbulence is primarily random at this point.

3.3. Effect of Vessel Size

Characteristic r - z plane angle-resolved LDA results from the T = 294 mm diameter vessel are shown in Figure 6. These measurements were conducted with two Rushton impellers at the same r/T and z/T locations around the lower impeller as the corresponding measurements in the T = 100 mm diameter vessel. Studies in similar vessels have been conducted previously by van der Molen and van Maanen [10] in a vessel with a lid agitated by a single Rushton impeller. They reported an increase in dimensionless (normalised) velocity in the trailing vortex vicinity with increasing scale and concluded that geometric scaling of mixing equipment should be carried out very carefully. The effect of scale on the normalised rms velocities was not reported.

Normalised r - z plane velocity vectors are plotted in Figure 6 (a) for a blade angle ϕ = 45° behind the leading impeller blade. The results are very similar to those shown in Figure 3(a) for the T = 100 mm vessel, and both the trailing vortex circulation and the inclination of the strong impeller discharge flow at approximately 45° to the horizontal can be clearly identified. There is good agreement between both sets of results with the centre of the trailing vortex being located around z/T = 0.39 in both instances and the impeller stream is similar in both vessels. Differences in the direction of the impeller stream can be observed in the immediate vicinity of the blade. However, the flow fields are essentially similar for z/T > 0.425 and r/T > 0.25. The increase in normalised velocity with scale reported by van der Molen and van Maanen [10] is evident from Figure 6(a) since some of these vectors are slightly larger than those in Figure 3(a) for the T = 100 mm vessel.

R - z plane contours of normalised radial rms velocity (v'/V_{tip}), at the ϕ = 45° blade angle are shown in Figure 6(b). Comparison of this figure with the corresponding results obtained in the 100 mm vessel (Figure 3(b)) shows that the influence of the trailing vortices has dissipated significantly by r/T = 0.31 from the centre of the vessel and z/T = 0.12 above the lower impeller mid-section. There is some discrepancy between the locations of the regions of maximum rms velocity in the two vessels. The maximum value is found at a slightly higher elevation in the T = 294 mm vessel. However, in general the main flow features such as the trailing vortex structure and the bulk flow turbulence levels scale well between the two vessels. Therefore, these results could prove useful for the prediction of scaling effects in larger vessels.

These figures show that although the two impeller streams are directed towards each other due to the proximity of the impellers, the respective sets of trailing vortices from the upper and lower impellers do not actually interact with each other, since with this impeller separation, most of the turbulence associated with the vortex structure is dissipated within a region bounded by r = 0.31 T and z = 0.45 T. The present results support the findings of Lee and Yianneskis [11] who defined a cylindrical region of radius 1.0 D and height 1.2 D centred in the middle of the vessel, within which the majority of the effects of the flow periodicity due to the crossing of the individual impeller blades could be confined.

Inside this cylindrical region where the trailing vortex structure is dominant, comparison of all three turbulent velocity components have shown the flow to be anisotropic. This has important implications since many CFD prediction methods use turbulence models based on the assumption of isotropy across the entire velocity field. Hence, these methods may provide only an approximation of the flow structure in the impeller stream, and the corresponding predictions will be of reduced accuracy.

4. CONCLUDING REMARKS

The results quantify in detail the trailing vortex structure in single and dual-impeller mixing vessels and provide useful information to aid the understanding of the fluid mixing processes and to assess related CFD predictions.

The turbulence structure in the impeller streams has been shown to be anisotropic in the impeller discharge flow. Hence CFD models which use turbulence models based on the assumption of flow isotropy, such as the k-ε model, may result in erroneous predictions in these regions.

It has been shown that, although the impeller discharge streams interact with each other to form the merging flow pattern, there is no actual interaction between the trailing vortex structures since they have dissipated significantly by a distance of 0.12 T above and below the respective impeller mid-sections.

5. ACKNOWLEDGEMENT

Financial support from the S.E.R.C. under grant number GR/H80873 is gratefully acknowledged.

REFERENCES

1. Van't Riet K., & Smith J. M., 1973, The Behaviour of Gas - Liquid Mixtures Near Rushton Turbine Blades, Chem. Eng. Sci., vol. 28, pp 1031 - 1037.

2. Van't Riet K., & Smith J. M., 1975, The Trailing Vortex System Produced by Rushton Turbine Agitators, Chem. Eng. Sci., vol. 30, pp 1093 - 1105.

3. Van't Riet K., & Smith J. M., 1976, Real and Pseudo - Turbulence in the Discharge Stream From a Rushton Turbine, Chem. Eng. Sci., vol. 31, pp 407 - 412.

4. Yianneskis M., Popiolek Z., & Whitelaw J. H.,1987, An Experimental Study of the Steady and Unsteady Flow Characteristics of Stirred Reactors, J. Fluid Mech., vol. 175, pp 537 - 555.

5. Calabrese R. V. & Stoots C. M., 1989, Flow in the Impeller Region of a Stirred Tank. Chem. Eng. Prog., May 1989, pp 43 - 50.

6. Yianneskis M. & Whitelaw J. H, On the Structure of the Trailing Vortices Around Rushton Turbine Blades, Trans. I.Chem.E, vol. 71, Part A, September 1993, pp 543 - 550.

7. Mahmoudi S. M. & Yianneskis M., 1991, The Variation of Flow Pattern and Mixing Time with Impeller Spacing in Stirred Vessels with Two Rushton Impellers, Proc. 7th Eur.

Conf. on Mixing, Bruges, Belgium, 18 - 20 September 1991, pp. 17 - 24.

8. Mahmoudi S. M. S., 1994, Velocity and Mixing Characteristics of Stirred Vessels with Two Impellers, Ph.D. Thesis, University of London.

9. Nouri M. & Whitelaw J. H., 1990, Effect of Size and Confinement on the Flow Characteristics in Stirred Reactors, Proc. 5th Int. Symp. on App. Laser Tech. Fluid Mech., Lisbon, Portugal, Paper 23.2.

10. Van der Molen K. & van Maanen H. R. E., 1978, Laser Doppler Measurements of the Turbulent Flow in Stirred Vessels to Establish Scaling Rules, Chem. Eng. Sci., vol. 33, pp 1161 - 1168.

11. Lee K. C. & Yianneskis M., 1994, The Extent of Periodicity of the Flow in Vessels Stirred by Rushton Impellers, in Industrial Mixing Technology : Chemical and Biochemical Applications, ed. G. Tatterson, A.I.Chem.E.

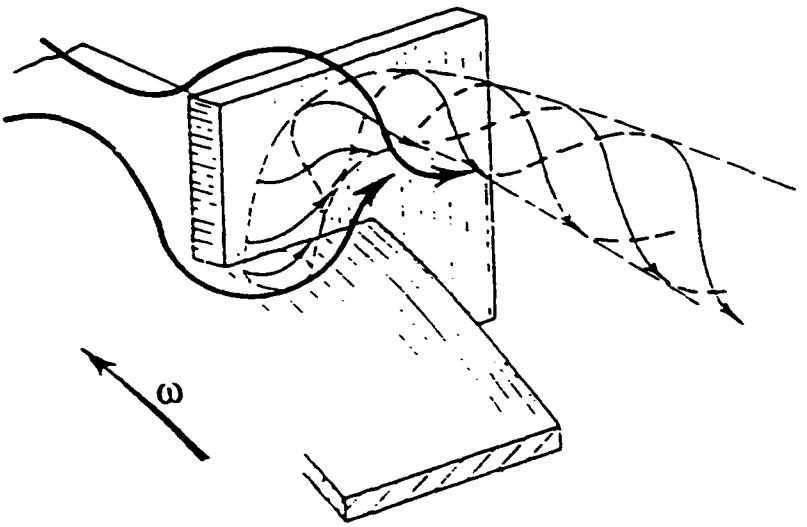

Figure 1. Three-dimensional representation of a trailing vortex.

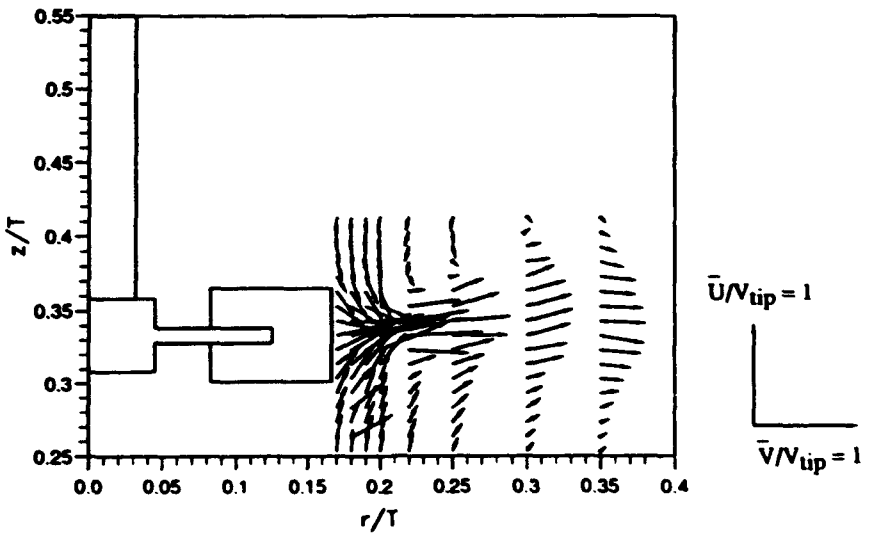

Figure 2. Normalised velocity vectors in the $\phi = 45°$ r - z plane for the single-Rushton impeller configuration in the T = 100 mm vessel.

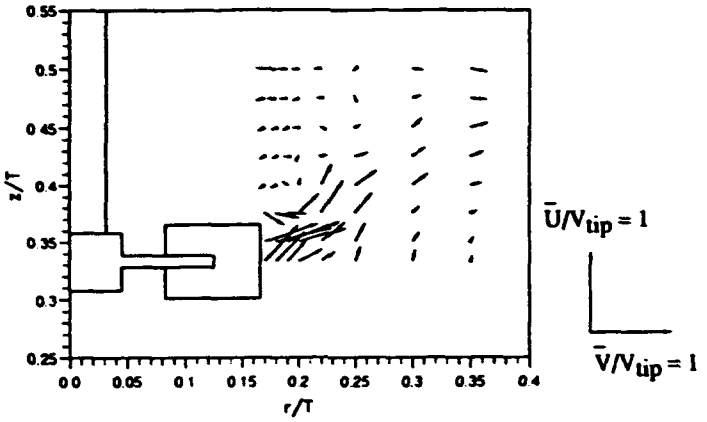

Figure 3(a) Normalised velocity vectors in the $\phi = 45°$ r - z plane for the dual-Rushton impeller configuration in the T = 100 mm vessel.

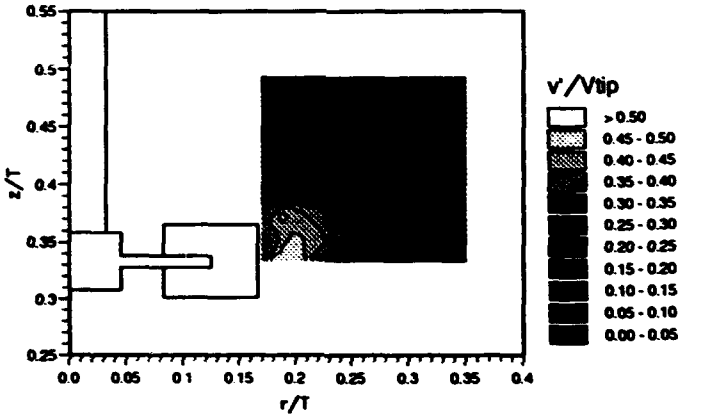

Figure 3(b) Contours of normalised radial rms velocity in the $\phi = 45°$ r - z plane for the dual-Rushton configuration in the T = 100 mm vessel.

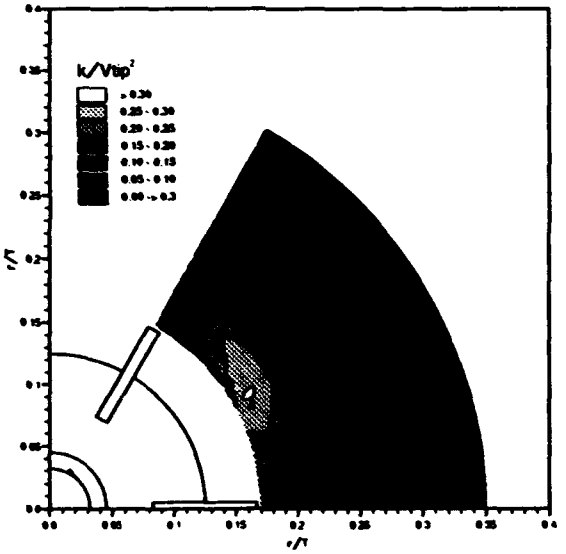

Figure 4. Contours of normalised kinetic energy of turbulence in the z = 0.33 T r - θ plane for the dual-Rushton impeller configuration in the T = 100 mm vessel.

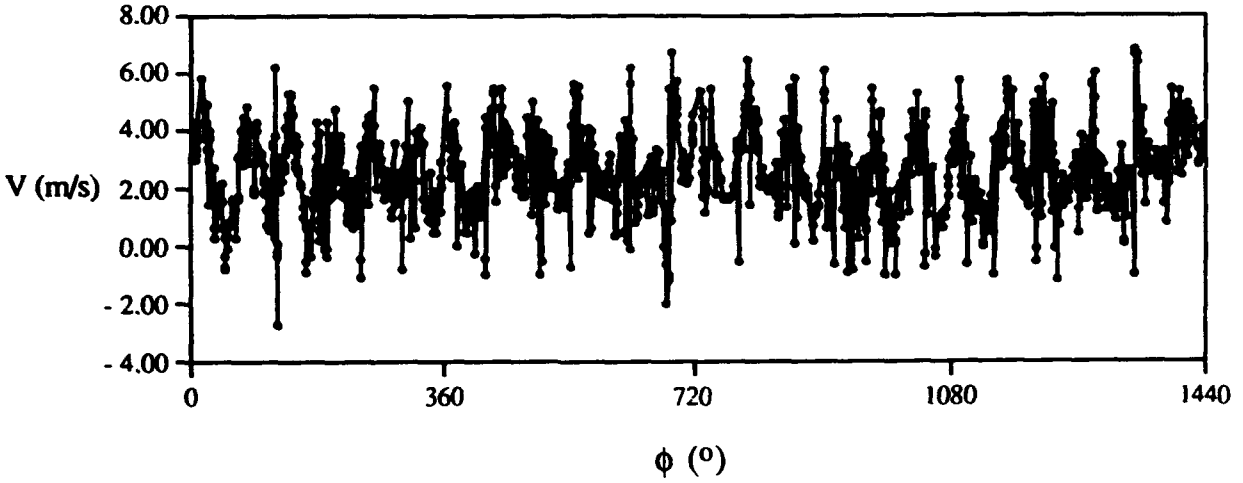

(a) r = 0.17 T, z = 0. 33 T

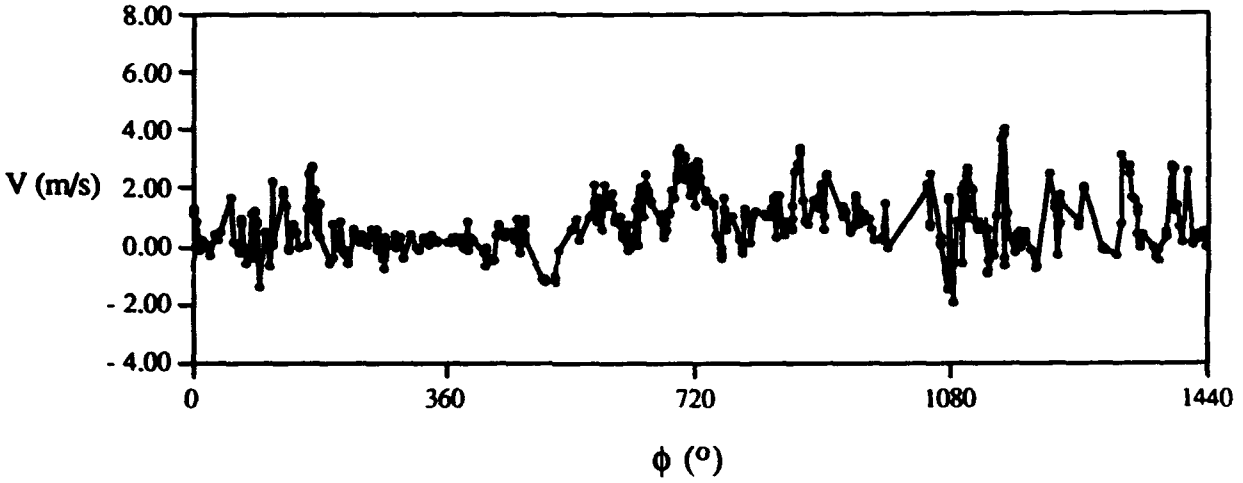

(b) r = 0.25 T, z = 0.41 T.

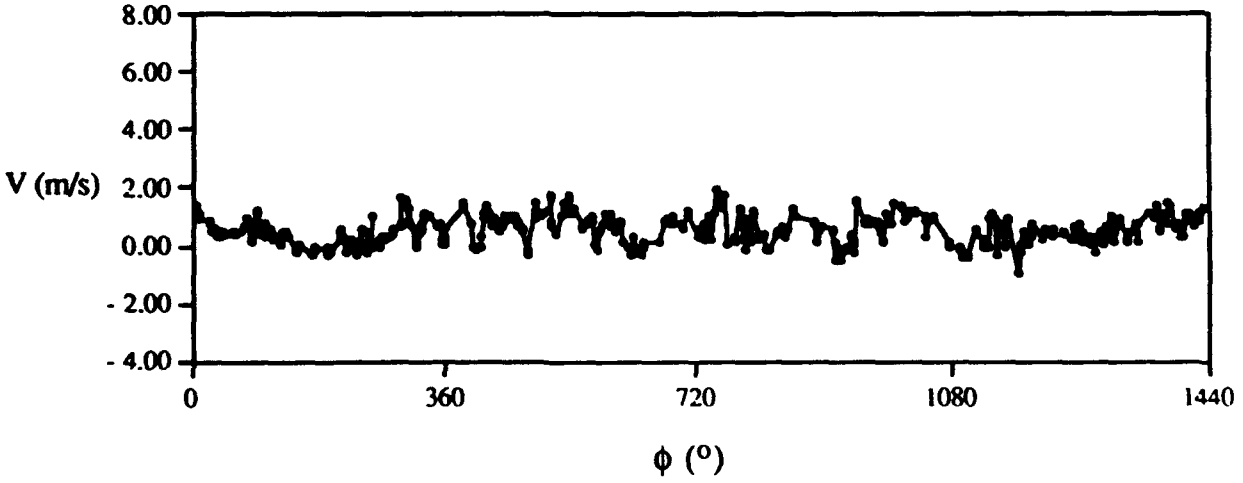

(c) r = 0.30 T, z = 0.50 T.

Figure 5. Time-resolved velocity distributions for the dual-Rushton impeller configuration in the T = 100 mm vessel.

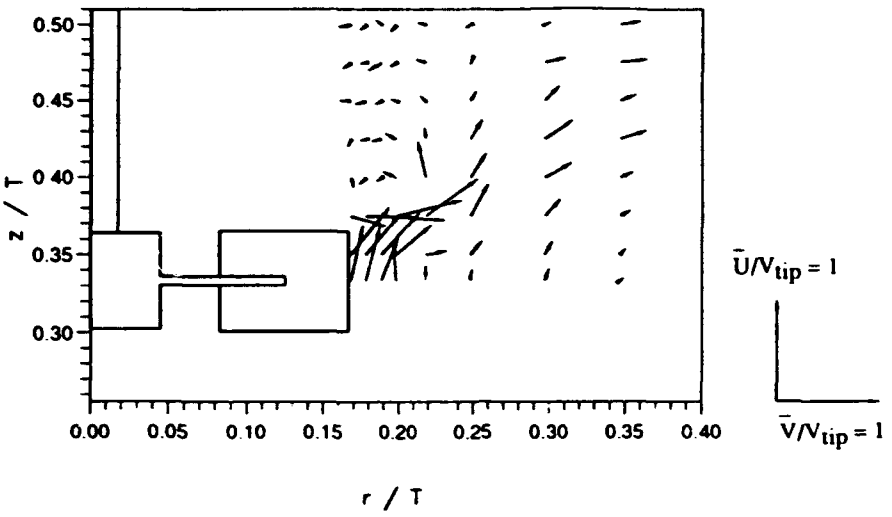

Figure 6(a) Normalised velocity vectors in the $\phi = 45°$ r - z plane for the dual-Rushton configuration in the T = 294 mm vessel.

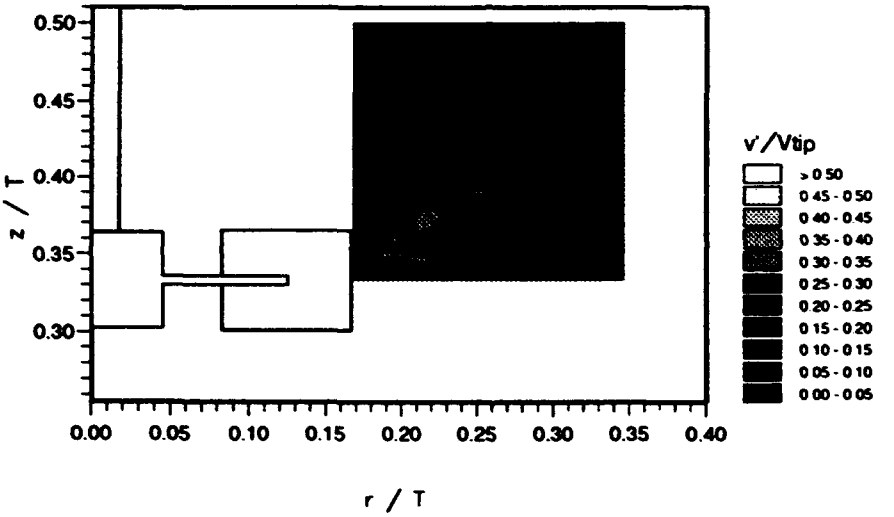

Figure 6(b) Contours of normalised radial rms velocity in the $\phi = 45°$ r - z plane for the dual-Rushton configuration in the T = 294 mm vessel.

L.D.A. MEASUREMENTS AROUND HOVERING ROTOR BLADES AND CORRELATION WITH LOCAL AND OVERALL AIRLOADS

E. BERTON, D. FAVIER, C. MARESCA and M. NSI MBA

Institut de Mécanique des Fluides, Université d'Aix-Marseille II, UM 34 du CNRS,
Les Souffleries de Luminy, 163 avenue de Luminy, 13009 Marseille, France.

ABSTRACT

The flowfield around hovering rotor blades with either rectangular or evolutive tip shapes is investigated in this paper. For different blade tip geometries the measurements concern local and overall aerodynamic data sets, including : the instantaneous velocity field around the blade and in its near wake and the global thrust and power coefficients. From such data sets the present paper is focused on deriving an original data post-processing method to correlate the L.V. flow measurements around the blade with the overall (C_T, C_Q) and local (C_L, C_D) airloads coefficients. This new method of determination of the overall and local airloads coefficients has been based on the Kutta and momentum equation (K.M.E.) applied to the velocity field (axial and tangential) measured along a close contour surrounding the blade section at a given blade radius. To check the capability of such a method the present paper offers a series of comparisons on overall and local aerodynamics coefficients deduced : from (C_T, C_Q) measurements performed by means of a rotative balance, and (C_L, C_D) coefficients obtained either in 2D steady flow conditions or from the K.M.E applied to the L.V. flow measurements performed around the blade.

INTRODUCTION

The prediction of the flowfield and the airloads repartition in the tip region of helicopter rotor blades play a major role for providing and evaluating improved rotor designs. Since the flow tip region experiences the largest amplitudes of variations in the bound circulation and the loading repartition, the adequate tip geometry modifications can lead to significant improvements in the overall rotor performances. However, the accurate prediction of the flowfield generated by sharp evolutive tip shapes still poses some problems to available numerical schemes, and requires additional research efforts using experimental investigations. This is the motivation of the present research.

1. METHODOLOGY

1.1 Rotor Model and Hovering Tests Conditions

The model-scale of rotor (diameter : 1.50 m) is set up on the hovering test rig installed in the testing hall of the IMFM S1-Luminy wind-tunnel. The rotor hub is mounted vertically by means of a supporting mast, so that the center of rotation is located 2.90 m above the ground. The model-rotor consists of a fully articuled rotor hub which can be equipped with interchangeable sets of blades (see Favier et al (1987)). Rotor geometry and hovering tests conditions are summarized in table 1.

Table 1 : Hovering Test Conditions

Test conditions	Rotor parameters
Diameter	1.50 m
Root cut out	0.22 R
Angular rotational freq.	143 rd/s
Rotational tip speed	107 m/s
Coning angle	2.5°
Number of blades	2 - 4
Airfoil section	(OA209)
Blade chord	0.05 m

As shown in Figure 1, the different sets of rotor blades tested are numbered from 4 to 7, and correspond to various combinations of blade twist, airfoil section and tip shape. All these different tip geometries are calculated so that the radii of the corresponding blade remain constant and equal to R = 0.75 m. The different tip geometries : swept, tapered, parabolic and rectangular (for rotors 4, 5, 6, 7) provide the same rotor solidity (σ = 0.08403 for b = 4).

1.2 Measurements Procedures

Several techniques (see Figure 2) suited for surveying the flow around the blades and the flow in the near and far wake regions, have been developed including X-hot wires anemometry, 2D-laser velocimeter and flow visualizations with image processing. Figure 2 also gives the fixed system coordinates (Oxyz) used for the flow velocity measurements. More detailed informations concerning these measurement techniques can be found in Maresca et al (1988), Nsi Mba et al (1988), only a short description is given here.

Overall thrust and torque coefficients (C_T, C_Q) are measured by a 6-components balance mounted on the rotor hub. The 3D wake velocity field is measured by two complementary techniques : a X-hot wires probe and a 2D

L.V. technique (back-scatter mode, Bragg cells for reversed flow).

Tip vortex paths (r, Z, ψ) are measured by means of a hot-wires technique which allows additionally the determination of the far wake position where the vortex instability is fully developed. However, in order to determine the tip vortex structure, its formation and its development very close to the blade tip, a flow visualization method has been used in connection with an image processing technique.

The velocity field around the blade is measured by means of the 2D L.V. technique providing the axial and tangential velocity components along a close contour surrounding the blade section and as a function of the blade azimuthal position (see Favier at al (1991) and Berton (1992)). A photograph of the model rotor installation is shown in Figure 3. Shown in the foreground is the IMFM hover test rig with the LV optics traversing device in the background. The overall and local airloads coefficients as well as the circulation distribution along the span are then deduced from the integration of these flow velocity measurements as described below.

1.3 The K.M.E. Method

The K.M.E. method stands here for the Kutta and momentum equation method. Application of the Kutta and Momentum Equation method in hover begins with the application of the momentum equation to the general control surface S surrounding the blade section at a given radial station r/R (see Berton et al (1993) and Silva et al (1993)) :

$$-\oint_S \vec{dF}_{ext}\,ds = \oint_S (\rho \vec{q}.\vec{n}).\vec{q}\,ds \qquad (1)$$

The contour S is divided into three contours, $S = \Sigma_a + \Sigma_w + \Sigma$, where Σ_a, Σ_w and Σ represent the contour enveloping the airfoil section, the near wake and the external contour around the blade section. Due to the non slip condition on the airfoil surface ($\vec{q}.\vec{n} = 0$), and the continuity of pressure across the wake sheet ($P_{wu} = P_{wl}$), the momentum equation can be written as :

$$-\oint_{\Sigma_a} dF_{ext}\,\vec{n}\,ds = \oint_{\Sigma} P.\vec{n}\,ds + \oint_{\Sigma} (\rho \vec{q}.\vec{n}).\vec{q}\,ds \qquad (2)$$

What remains is a line integral about the arbitrary contour Σ surrounding the blade section. As shown in Figure 4, selecting Σ as a rectangular box ABCD of length $2\pi/b$ (where b denotes the number of blades) obviates the need to include the vertical segments BC and DA of the line integral because of cancellation due to flow periodicity. Choosing this specific contour simplifies the momentum equation such that the horizontal force component dFy acting on the blade section can be expressed in terms of the axial and tangential velocity components along the upper and lower contour segments as follows:

$$-dF_y = \rho r \int_0^{2\pi/b} \left[W_l V_l - W_u V_u\right] d\psi \qquad (3)$$

while the application of the Kutta formula provides the vertical component dF_z as :

$$dF_z = \rho \Omega r^2 \int_0^{2\pi/b} \left[V_l - V_u\right] d\psi \qquad (4)$$

The Kutta equation formulation for dFz is more attractive than that derived from the momentum equation due to the lack of pressure terms. The above derivations show that the elementary forces (dF_y, dF_z) acting on the blade section can thus be deduced from the tangential and axial velocity components alone. The global thrust and power coefficients (C_T, C_Q) are derived by integrating the elementary forces (dF_y, dF_z) along the span as :

$$\Omega C = b \int_{R_0}^{R_1} dF_Y(\Omega r)\,dr \; ; \; C_Q = \frac{\Omega C}{\rho \pi R^2 Ve^3} \qquad (5)$$

$$T = b \int_{R_0}^{R_1} dF_z dr \; ; \; C_T = \frac{T}{\rho \pi R^2 Ve^2} \qquad (6)$$

Local incidence $\alpha = \theta - \theta i$ can also be determined from the streamlines computed from the measured velocity field in the immediate vicinity of the blade. The local section aerodynamic coefficients of lift and drag are then obtained by a simple transformation of the elementary forces (dF_y, dF_z) as :

$$dL = dFz \cos\theta i + dFy \sin\theta i$$

$$Cl = \frac{dL}{\frac{1}{2}\rho\left[(\Omega r - Vi)^2 + Wi^2\right].c} \qquad (7)$$

$$dD = dFy \cos\theta i - dFz \sin\theta i$$

$$Cd = \frac{dD}{\frac{1}{2}\rho\left[(\Omega r - Vi)^2 + Wi^2\right].c} \qquad (8)$$

2. RESULTS

In the present experimental investigation, both overall and local aerodynamic quantities of the flowfield through the hovering rotor have been measured on configurations of rotors 4, 5, 6, 7, for collective pitch angles θ, and number of blades b, varying in the following ranges : $6° \leq \theta \leq 10°$; $2 \leq b \leq 4$.

For the purpose of the present paper, the following experimental results will be only focused on the analysis of the tip shape influence as deduced from measurements performed on the two rotors 4 and 7 (see Figure 1). Both rotors are considered at the same set of operating parameters : b=4 or 2, θ = 10°, ΩR = 107 m/s, and the blades only differ

by the tip geometry, which is rectangular on rotor 7 and swept on rotor 4. Both rotors have also very close thrust coefficient : C_T = 0.00797 for Rotor 4, and C_T = 0.00766 for Rotor 7, in a four-bladed configuration.

2.1. Axial and Tangential Velocity Field Around the Blade

As previously mentionned, the tangential velocity field around the blade is determined by means of velocimetry laser measurements performed at two fixed points (u and l) on the upper and lower side of the blade section. In order to validate the L.V. measurement method and to determine the adequate dimension Z_Σ of the contour surrounding the blade airfoil section, an optimization of the contour thickness has been firstly performed. Different contour thicknesses corresponding to different distances varying from Z = -10 mm to Z = 0 on the upper side, and from Z = 0 to Z = 10 mm on the lower side, have been define, as shown in Figure 5. Along these Z_Σ-lines the axial and tangential velocity components have been measured as a function of ψ and thus as a function of the distances Z_Σ to the blade.

Figures 6 and 7 show an example of the $W_u = W_u(\psi)$ and $W_l = W_l(\psi)$ axial velocity component obtained as a function of Z_Σ on the upper side ($Z_\Sigma \leq 0$ in Figure 5) and on the lower side ($Z_\Sigma \geq 0$ in the Figure 5). The velocity profiles indicated an increase in the amplitude as the distance Z_Σ to the blade decreases.

In order to deduce the local aerodynamic incidence, α, the velocity field must be mapped in sufficient detail to compute the streamlines around the blade section. An example of the flowfield scannerized by the L.V. technique is provided by Figure 8 which shows a composite of the axial and tangential velocity measurements made at r/R = .75. From such instantaneous flow scanning around different spanwise stations, the streamlines and the local aerodynamic incidence are obtained as exemplified in Figure 9.

When integrating the W and V velocity profiles, the (dF_y, dF_z) forces deduced from equations (3) and (4) are plotted versus Z_Σ in Figure 10. The results in Figure 10 indicate that the dimension of the contour of integration has to be selected so that $|Z_\Sigma| \leq 25$ mm (i.e. nearly half a chord), to get consistent values on the elementary forces dF_y and dF_z. Thus a contour thickness of $|Z_\Sigma|$ = 15mm has been selected for all the present tests.

2.2. Local Airloads and Integrated Global Performance

Using such an optimal contour thickness the L.V. measurements have been performed all along the blade span, and Figure 11 gives the evolution of the elementary force dFy plotted versus the blade span as deduced from the integration of the velocity profiles (equations (3) and (5)). The results indicate that the C_Q coefficient value deduced from the 6-components balance is very close to those deduced from the L-V flow measurements and from the application of the K.M.E. method. In the same way similar results and conclusions are also obtained in Figure 11 concerning the C_T coefficient (equations (4) and (6)). In this case the difference between the thrust coefficient deduced from the K.M.E. method and the thrust coefficient obtained by means of the 6-components balance is less than 1%.

Figure 12 illustrates another application of the K.M.E. method on the swept rotor 4. In this case, the power coefficient deduced from the momentum equation is equal to 0.000707 and the power coefficient measured by the balance is 0.000720. The difference between the two values is also less than 2%. Note also a difference less than 1% between the thrust coefficient deduced from the K.M.E. method and the thrust coefficient obtained by means of the 6-components balance.

A last example of the capability of the measurement method is given in Figure 13, concerning the rotor 7 at b = 4 and θ = 10°. The Figure gives a comparison between the OA209 coefficients 2D-table and the lift and drag coefficients (C_L and C_D) as deduced from the application of the K.M.E. and from the determination of the the streamlines and from the corresponding local aerodynamic incidence (equations (8) and (9)). The distributions of the lift and drag coefficients deduced from the two determination procedures are shown to be in good agreement along the blade span r/R.

CONCLUSIONS

In the present study, an experimental approach has been derived to investigate the fine structure of the flowfield around hovering rotor blades. An original method to correlate the flow measurement around the blade with the overall and local airloads coefficients has been also presented in this paper.

This new method of determination of the overall and local airloads coefficients has been based on the Kutta and momentum equation applied to the velocity field measured along a close contour surrounding the blade section at a given blade radius.

The capability of such a method has been checked from a series of comparisons on overall and local aerodynamics coefficients deduced : either from (C_T, C_Q) measurements performed by means of a rotative balance, and (C_L, C_D) coefficients obtained in 2D steady flow conditions, or from the K.M.E method applied to the flow measurements performed around the blade.

ACKNOWLEGMENTS

The authors wish to thank the support provided by the "Direction des Recherches Etudes et Techniques" under Grants 90/169 and 92/061.

NOMENCLATURE

b	number of blades (b=2 ou 4)
c	constant blade chord, (c=0.05 m)
C_T	rotor thrust coefficient
C_Q	rotor power coefficient
Γ	blade circulation along the span, (m^2/s)
Oxyz	reference system defined in Fig. 2
θ	collective pitch angle at r/R=0.75, (deg)

θ_v	blade twist law, (deg)
r	radial distance from rotation axis, (m)
R	rotor blade radius, (R=0.75 m)
Ro	root cut out, (Ro=0.22R)
σ	rotor solidity (σ=bc/πR)
T,Q	rotor thrust and torque, (N, N.m)
u, l	upper and lower side of the blade sections
V,W	tangential and axial velocities
V_e	rotational tip speed, (V_e=ωR=107 m/s)
ω, Ω	angular frequency, (ω=143 rad/s)
ψ, ψ_p	blade azimuth, (deg)

REFERENCES

Berton, E. 1992, Contribution à l'Etude de l'Ecoulement Induit Autour et dans le Sillage de Surfaces Portantes en Rotation. Application au Rotor d'Hélicoptère en Vol Stationnaire., Thèse de Doctorat, Université d'Aix-Marseille II, I.M.2., I.M.F.M., Marseille.

Berton, E. 1993, Favier, D., Maresca, C. & Nsi Mba, M. : Détermination des charges aérodynamiques d'un rotor en vol stationnaire par vélocimétrie laser, Proceedings du 11ème Congrès Français de Mécanique, Lille - Villeneuve d'Asq, Vol. 2, pp. 365-368.

Favier, D., Nsi Mba, M., Barbi, C. & Maresca, C. 1987, A Free Wake Analysis for Hovering Rotors and Advancing Propellers, VERTICA, Vol. 11, n°3, pp. 493-511.

Favier, D., Maresca, C., Berton, E. & Plantin de Hugues, P. 1991, Investigation of the Tip Shape Influence on the Flowfield Around Hovering Rotor Blades, A.I.A.A., 22nd Fluid Dynamics, Plasma Dynamics and Laser Conference, Honolulu.

Maresca, C., Favier, D., Nsi Mba, M. & Barbi, C. 1988, Validation à l'Aide d'Essais en Soufflerie de Codes de Calcul du Champ Aérodynamique de Rotors et d'Hélices dans des Conditions de Vol Variées, AGARD-FDP on Validation of Comutational Fluid Dynamics, AGARD CP 347, Lisbon, Paper n° 29.

Nsi Mba, M., Favier, D., Maresca, C. & Crespi, P. 1988, Helicopter Rotor Wake Investigation Using a Laser Doppler Velocimeter Technique, ISALA, Proceedings of 4th International Symposium on Application of L.D.A. to Fluid Mechanics, Lisbon.

Silva, M., Favier, D., Ramos, J., Nsi Mba, M. & Berton, E. 1993, An Experimental Investigation of the Drag Mechanisms of a Helicopter Rotor in Hovering Flight, Proceedings of 19th European Rotorcraft, Cernobbio, Paper n° 18.

Rotor Number	Twist	Planform	Airfoil
4	-8,3°		OA209
5	-8,3°		OA209
6	-8,3°		OA209
7	-8,3°		OA209

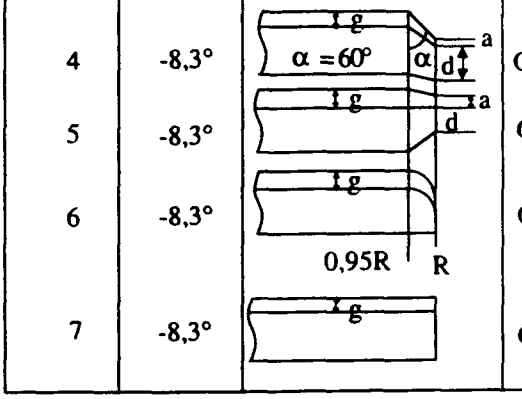

$\frac{a}{c} = 0.15$
$\frac{g}{c} = 0.25$
$\frac{d}{c} = 0.6$

Fig. 1. Rotor blades definition.

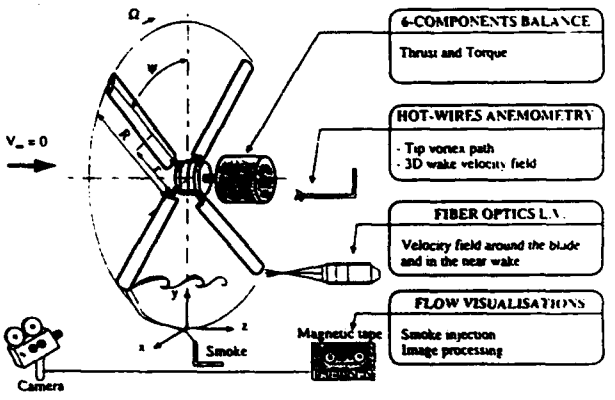

Fig. 2. Measurement techniques.

Fig. 3. Laser velocimetry system.

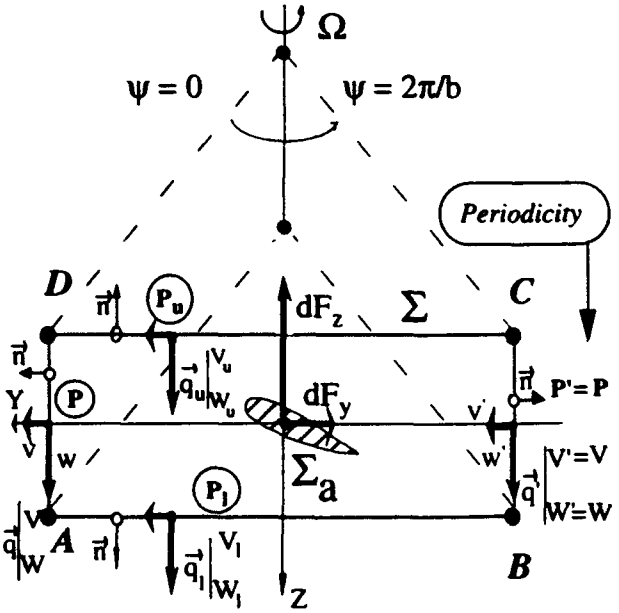

Fig. 4. Specific Σ-contour, 2π/b-length.

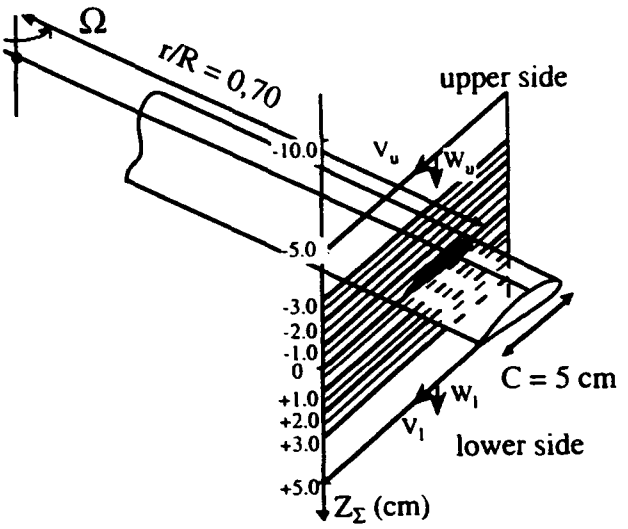

Fig. 5. Selection of the contour thickness Z_Σ.

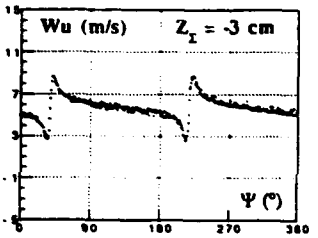

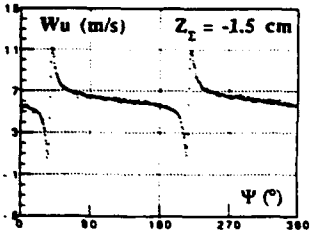

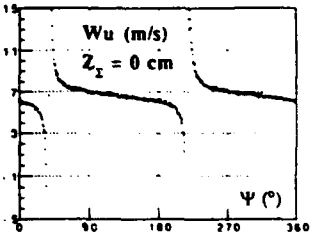

Fig. 6. Upper side axial velocity as a function of Z_Σ (rotor 7, b = 2, θ = 10°, r/R = 0.70).

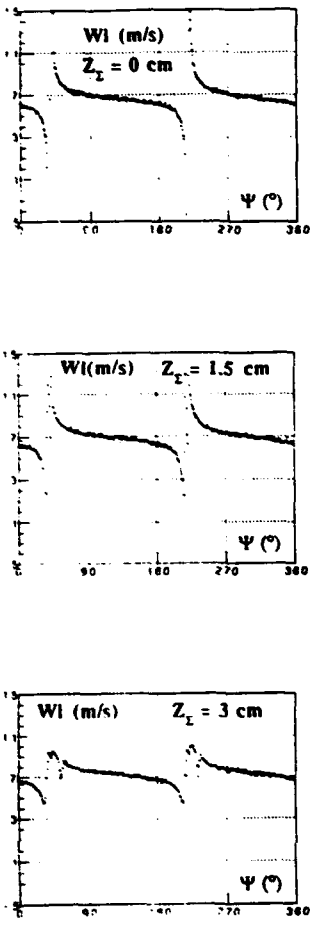

Fig. 7. Lower side axial velocity as a function of Z_Σ (rotor 7, b = 2, θ = 10°, r/R = 0.70).

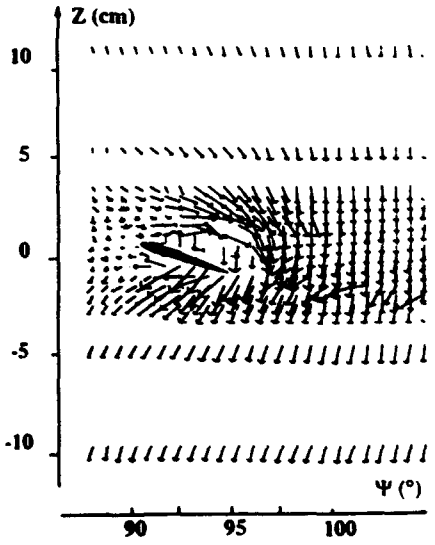

Fig. 8. Induced velocity field, r/R = 0.75 (rotor 7, b = 4, θ = 10°).

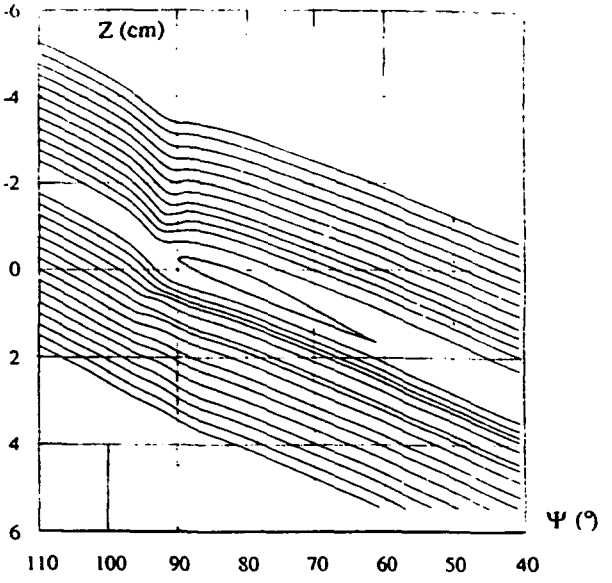

Fig. 9. Streamlines around the blade section (rotor 7, b = 4, θ = 10°, r/R = 0.75).

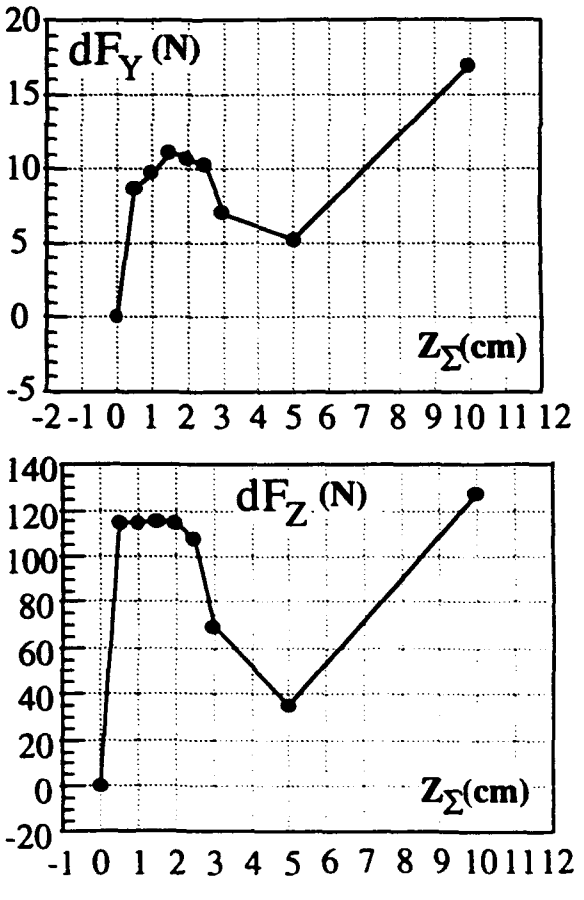

Fig. 10. Influence of the integrating contour Z_Σ (rotor 7, b = 2, θ = 10°, r/R = 0.70).

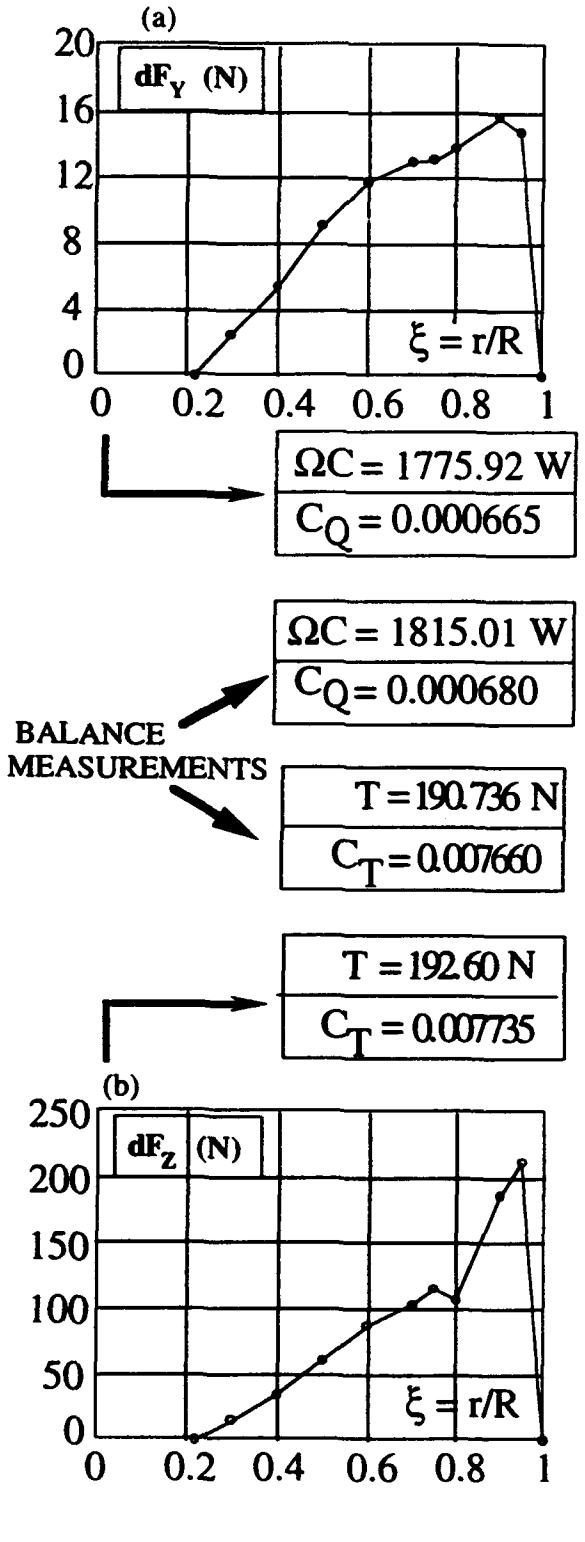

Fig. 11. Blade span evolution of the elementary forces (rotor 7, b = 4, θ = 10°).

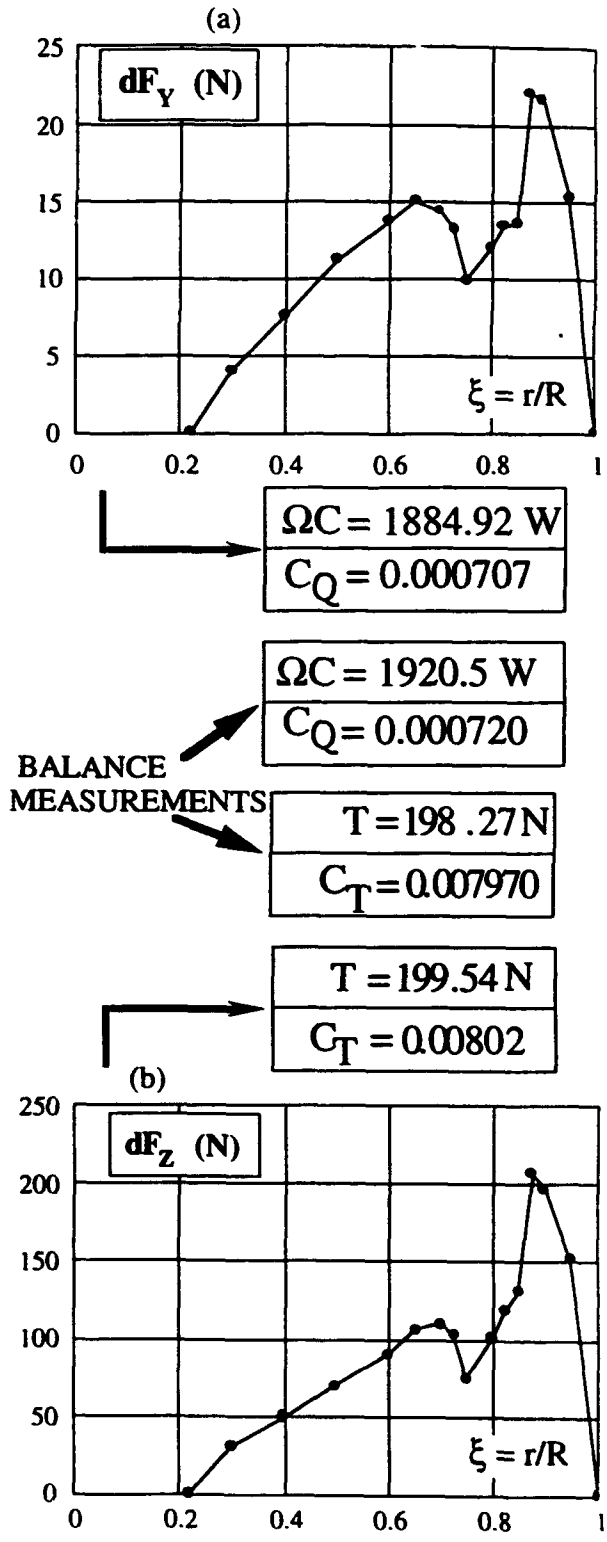

Fig. 12. Blade span evolution of the elementary forces (rotor 4, b = 4, θ = 10°).

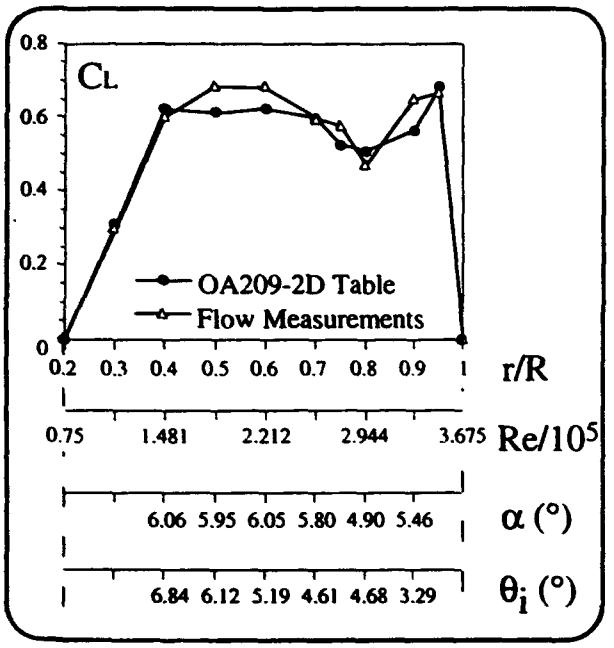

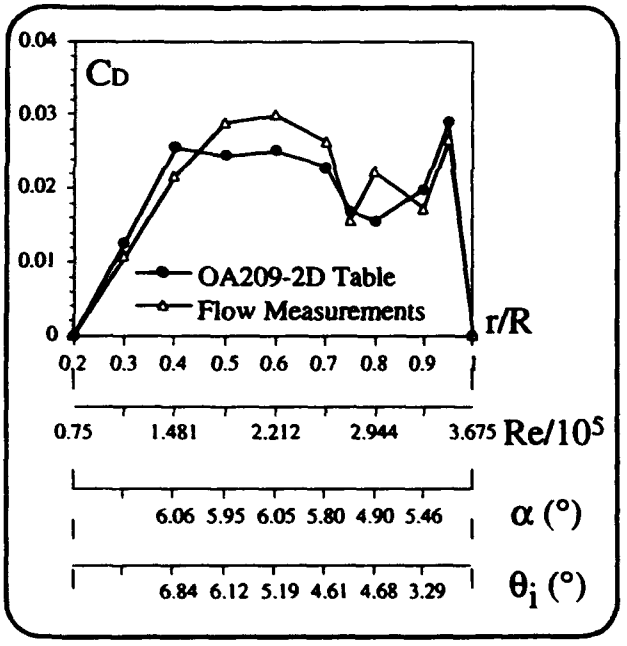

Fig. 13. Comparison on (CL, CD) deduced from L.V. measurement and OA209 2D-table (rotor 7, b = 4, θ = 10°).

LASER SHEET VELOCIMETRY MEASUREMENTS OF ROTOR CRAFT BLADE- VORTEX INTERACTION.

M B Horner*, J N Stewart+, R A McD Galbraith,* I Grant+, F N Coton* and G H Smith+.

*University of Glasgow, Glasgow, Scotland.
+Heriot-Watt University, Edinburgh, Scotland

ABSTRACT.

An experimental blade-vortex interaction (BVI) study was conducted using particle image velocimetry in the PTV mode. The vortex was generated by a double aerofoil spoiler and interacted with a spinning rotor in a wind tunnel. Results show the effectiveness of PIV in both measurement and visualisation of complex flows.

1 INTRODUCTION

The passage of a trailing tip vortex through a moving rotorcraft blade leads to significant noise and vibration in rotor craft (Scheimanand Ludi (1963), Brotherhood and Riley (1978), Schmitz et al (1978)). The need to reduce these undesirable effects requires that the rotorcraft designer has a clear understanding of the fluid dynamics underlying the phenomenon of blade-vortex interaction. Experimental studies by Surendraiah (1969) established a methodology where an upstream wing tip was used to generate a vortex that interacted with a downstream rotor. This work, and other studies reviewed by the authors elsewhere (Horner et al (1993), (1994)), demonstrates many of the gross features of the blade-vortex interaction, including the development and collapse of a large leading edge suction peak, and the associated build up and reversal of the normal force.

Previous experimental BVI studies have yielded detailed and informative pictures of the blade performance in terms of pressure distributions. The centrally important convective disturbance and development and collapse of the large leading edge suction peak, produced by the passage of the trailing tip vortex has, until the present work, remained a feature identified in time domain pressure records.

The objective of the present study was to provide flow field information to complement the existing database of pressure measurements. Earlier studies (Ziada (1992)) used both hydrogen bubble and dye injection methods to observe the BVI effect. The formation of secondary vortices and the convective trajectories of the vortices were observed. The significance of this work was limited, however, by the low Reynolds numbers and the lack of a trailing edge on the blade.

2 EXPERIMENTAL METHODS.

In the present study, the effects of the passage of the vortex were examined in an experimental set-up similar to that developed by Surendraiah (Figure 1). An upstream vortex generator produced a vortex which interacted with a downstream rotor. Flow visualisation information and velocimetry data were obtained during interactions through the use of particle image velocimetry. The data was obtained under the same conditions as in previous studies by the authors in which surface pressure data were recorded (Horner et al (1991)). This allowed a direct comparison of the two data sets, and for validation of the flow inferences made from the surface pressure measurements.

The experiments described here were conducted in a collaborative study between the University of Glasgow and Heriot-Watt University. The tests were carried out in the "Handley-Page" wind tunnel (UG) using Heriot-Watt PIV facilities. The development and application of the PIV method in engineering applications is well described by the authors and elsewhere (Grant (1994), Grant and Smith (1988)).

The aluminium rotor blade had a NACA 0015 aerofoil section, with a 0.149 m chord and a 0.9426 m radius. The vortex generator comprised of two adjoining NACA 0015 aerofoil sections spanning the height of the test section 2.1 rotor radii upstream of the rotor hub. During the test sequence conducted in the 1.61 x 2.13 m octagonal test section, the tunnel speed was 47.0 m/s while that of the rotor tip was 59.25 m/s. The vortex strength was controlled by setting the two sections of the vortex generator at equal but opposite incidence. The horizontal position of the vortex generator (Zv) was altered to control the angle of intersection between the interaction vortex and the blade, resulting in either a nominally parallel or oblique BVI. The vertical position of the aerofoil junction on the vortex generator (Yv) was varied to allow an examination of interactions for different blade-vortex separation heights.

Particle Image Velocimetry data was collected in one of two planes oriented perpendicularly to the tunnel free stream, one plane at 0.78 rotor radii upstream of the rotor hub, and the second at 0.94 rotor radii.

Flows were examined in nine different combinations of interaction geometry and measurement position, so allowing a comparison of data collected during parallel and oblique interactions, near the tip, inboard and for several different interaction heights.

Particle Image Velocimetry data was collected in the measurement plane by photographing the seeding particles, illuminated by a pulsed sheet of laser light. A 35 mm camera (Nikon F801) was mounted below the rotor hub, facing upstream. Images were collected on Kodak Recording Film 2475 using a 55 mm flat field lens. The camera mount was constructed of 49 mm box section mild steel, attached directly to the floor of the wind tunnel bay, thus isolated from the vibration of the tunnel and rotor system. A faring covering the camera mount and the lower half of the rotor shaft was also employed to shield the camera mount from any aerodynamic buffeting. An accelerometer attached to the top of the camera mount indicated that errors in velocity measurement due to camera vibration were less than 0.3% of full span.

A Lumonics HLS4 ruby laser was used to produce a light sheet using a suitable lens configuration. The laser was triple pulsed to give three images of each seed particle on the photographic film, thus allowing later calculation of local velocities in the vicinity of each particle. Laser pulses were typically separated by 60 to 80 ms, with each individual pulse having an energy of approximately 1.5 J. If required, directional ambiguity was addressed in a select number of tests by setting the first inter-pulse interval longer than the second. This procedure results in unequally spaced 3 spot patterns which could be used to derive flow direction.

Image processing was carried out in the Fluid Loading and Instrumentation Centre at Heriot-Watt University in Edinburgh. The images were analysed using statistical windowing procedures suitable for low image density PTV type images (Grant and Liu (1989)). In the present tests correction for the apparent in-plane motion due to the through plane motion of the particles was made.

12 or more images were recorded of each azimuthal position and relative positions of the blade and vortex in each of the twelve images were then determined. The most suitable or representative of the set was then chosen for processing. Under some conditions the interaction vortex passed above the aerofoil and so out of the camera's view. In these cases a second camera, mounted above the rotor hub, and operating simultaneously with the lower camera, was used. Data from the upper camera simply documented the overhead position of the vortex as an aid in selecting the lower camera image representative of flows beneath the blade. The upper camera was not used for collecting velocimetry data.

3 RESULTS

Flow field velocimetry data were collected about the aerofoil during interaction with a free vortex. These data documented many of the flow features observed in the previous studies discussed above. In addition, however, the velocimetry data quantified the spatial flow direction and magnitude together with an assessment of the temporal flow development. The data does not include the component associated with blade movement.

The lack of data in the vortex core is a consequence of the gradual evacuation of the seeding particles due to the strong radial accelerations. Typical circumferential velocities of the vortex range from 25 $m.s^{-1}$ close to the core down to 6 $m.s^{-1}$ in the near field.

Figures 2a to 2f present PIV data collected during a blade-vortex interaction. During this interaction the vortex was nominally positioned 0.2 chords below the tunnel centre line, resulting in a parallel interaction. The velocity measurements are presented in the tunnel frame of reference, with the blade moving from left to right at approximately 47 m/s. The origin of the co-ordinate system is the blade leading edge. Fig. 2a depicts the flows pattern as the rotor reaches the 168 azimuth and the vortex 0.6 chords ahead of the blade's leading edge. It is clear that the advancing blade is entering a region of strong upwash in which the combination of this and the blade forward motion produce a leading edge incidence approaching 18°.

In Figure 2b the rotor has reached the 172° azimuth, and the vortex is only 0.3 chords ahead of the aerofoil producing an incidence greater than 30 . Notice the "arched" appearance of the flow on the upper surface. At 176° azimuth (Fig. 2c) the leading edge is just above the vortex core, and the incidence is now dropping rapidly below zero.

Fig 2d characterises flows generated as the rotor passes through an azimuth of 181° . In this image the vortex is evident below the mid chord and the leading edge is now past the region of strongest vortex-induced downwash. Pressure data, taken under the same conditions as the PIV data of Fig. 2d is included in Fig. 3 for comparison. This data was collected in previous investigations in the University of Glasgow BVI facility that utilised pressure instrumentation to provide time dependent pressure profiles about the rotor blade at a variety of spanwise positions . Across the chord the lower surface pressure is less than that of the upper surface, but the pressures measured in regions directly above the vortex are evidently enhanced slightly, presumably due to the flow retardation effected by the vortex in this area.

At an azimuth of 187° (Fig. 2e) the vortex is below the trailing edge and finally, in Fig. 2f the blade leaves a distorted vortex behind in the wake. In this last figure an area of vorticity is evident aft and slightly above the interaction vortex. Similar vortical structures are evident in many PIV data collected in the distant wake and they appear to drift towards

the right with increasing azimuth. This additional vortex element may originate as a tip vortex or shed vorticity from the earlier interaction.

Figure 4 presents data from a "head-on" parallel interaction in which Yv/c=0.0 and Zv/c=0.0. These data illustrate the rotor blade at 187° azimuth as it cuts through the interaction vortex. The upper vortex fragment is just above the trailing edge, and is accompanied by a small secondary vortex that is positioned below and just aft of the primary fragment. This secondary vortex was generated as the interaction vortex approached the leading edge, and preceded the upper vortex fragment in its traverse of the upper surface. The initiation of such a secondary vortex is consistent with the results of previous studies. The lower surface vortex fragment has been deformed and stretched to such an extent that its vorticity is spread from the leading to the trailing edge of the aerofoil.

4 DISCUSSION

A preliminary set of results from a blade-vortex interaction investigation has been presented. Baseline vortex flows have been captured utilizing particle image velocimetry so documenting this evolution. Both the deformation and division of the interaction vortex has been observed.

Typical unprocessed PIV data are presented in Figures 2a to 2f and Fig 5 . Figure 5 captures the motion of the seeding particles during a parallel interaction in which the interaction vortex was positioned 0.2 chord lengths below the rotor blade. In this case, seed particles and the rotor blade have been illuminated by a triple pulse of the laser sheet.

The isolated interaction vortex velocity distribution is given in Fig. 6 and corresponds to the data of Fig. 5. In Fig. 6a all of the velocity data from Fig. 5 are plotted, giving an overview of the vortex which has a peak in tangential velocity near a radius of 25 mm, indicating a vortex core with a radius 17% of the chord length of the blade. Beyond the 25 mm radius the tangential velocity is seen to decrease. The obvious scatter is indicative of the variation in the tangential velocities recorded at any given radial station. It is not clear, however, whether this reflects any large scale asymmetry in the vortex or simply significant turbulence in the observed flows.

Figure 6b presents a subset of these data in that it shows the velocity distributions taken from those points of Fig. 5 that lie within 10 mm of a line emanating straight to the right of the vortex centre, effectively simulating a traverse of the vortex velocity field. In this form the data is less scattered, but still shows considerable variation, suggesting that much of the scatter of Fig. 6a is due to turbulent fluctuations in the velocity of vortex flows.

Figure 6b also compares the data from this "traverse" with that expected for an ideal potential flow vortex with a circulation of 5 m^2/s. This comparison highlights the deviation of the experimental data from the expected "$1/r$" curve. It would appear that the vorticity about the vortex centre spills over into regions outside the vortex "core", so that the total circulation is still increasing with radius out to 50 or 60 mm.

As indicated in Fig. 2d, previous investigations in the University of Glasgow BVI facility have utilized pressure instrumentation to provide pressure profiles measured about the rotor blade. Such pressure data were also integrated about the blade chord to document force and moment histories. An example of these is presented in Fig. 7. The upper plot is the normal force data, the middle plot is moment data, and the lower plot is the tangential force data. The data in these plots were collected under the same conditions as the data of Fig. 2: Yv/c = -0.2, Zv/c = 0.0, vortex generator sections at an incidence of 12.5 , and data collected at the 78.5% span location.

Six timing lines have been added to indicate the position of the corresponding data presented in Fig. 2. The first line, near Xv/c = -0.55, corresponding to Fig. 2a, indicates that the flow is causing a near maximum value in Cn, presumably due to the increased effective blade incidence. The moment coefficient maintains a steady value of about 0.02, whilst the thrust is rising, reflecting the large velocities about the blade leading edge.

When the interaction has progressed as far as the second timing line (Fig. 2b) the normal force has passed its maximum and is falling. Figure 2b suggests that, although the incidence is still increasing, the velocities about the blade leading edge have dropped, reflecting the local increased upwind component of the vortex induced velocities. The moment remains positive, but exhibits a dip as the vortex lends larger velocities below the blade leading edge than those above. The forward force has passed its peak, but the high lower surface velocities still result in strong forward forces.

The third timing line, near Xv/c = 0.12 corresponds with the data of Fig . 2c, which indicates that the effective incidence has fallen through zero, and the upper surface flows have slowed more than those of the lower surface. The result is a negative and declining value of Cn. The moment has risen slightly, as the lower surface flows in the aft portion of the aerofoil outpace their upper surface counterparts. Ct is almost zero as leading edge flows stagnate under the upstream influence of the vortex.

The fourth timing line, near Xv/c = 0.6, corresponds with the data in Fi g. 2d, in which the vortex is situated below the mid chord. The angle of attack is negative, and a strong shear is evident across the wake. Cn has reached its minimum value, indicating that despite the evident retardation of lower surface flows the negative incidence is producing a strong region of suction at the leading edge. This effect is also evident in the Cm history, which is at this point beginning a substantial drop towards negative values, as the stagnating vortex flows convect farther aft. Ct starts to recover from the dip at the previous timing line, as leading edge escapes from the influence of the vortex, and the corresponding reductions in velocities past the leading edge.

The fifth timing line, near Xv/c = 1.1, corresponds with Fig. 2e, in which the vortex is evident below the trailing edge, where it results in strong flow retardation. The result is obvious in the Cm curve, where a large drop in Cm to a minimum value follows from the higher pressures under the trailing edge, associated with the flow retardation. Cn exhibits a brief surge at this point, presumably reflecting the gradual lessening of vortex influence on leading edge incidence, and the higher pressures on the aft lower surface. The reduction in velocities in the aft portions of the aerofoil also push the thrust force back towards a local maximum.

The sixth and final timing line, near Xv/c = 1.6, corresponds with Fig. 2e, in which the vortex is well aft of the trailing edge, and the influence of all vortex flows is lessening. This is reflected in the convergence of all integrated coefficients towards zero.

5 CONCLUSIONS.

The particle image velocimetry data collected in this study was found to correspond well with the pressure data collected in earlier investigations. Maxima and minima in all the integrated force and moment histories have been explained in terms of the PIV images reduced to velocity field data.

Vortex flows, both before and during interactions have been examined. Vorticity was evident further outside of the nominal vortex core than was previously anticipated. During interactions in which the vortex passed below the blade, the deformation of the vortex was found small until the vortex passed the trailing edge. During head-on interaction the blade was found to split the vortex into two fragments. The lower fragment was seen to distort and spread across the lower aerofoil surface, while the upper fragment was only slightly distorted. A secondary vortex was found to form on the downstream edge of the upper vortex fragment.

Particle image velocimetry was found to provide an excellent method to document the complicated temporal and spatial evolution of flows generated during blade-vortex interaction.

6 ACKNOWLEDGMENTS.

The authors would like to acknowledge the support of the British Ministry of Defence, the Defence Research Agency (formerly RAE) and the Department of Industry. The help of Westland Helicopters, in particular T. Beddoes, during the design and execution of the experiment was appreciated. The authors would also like to thank Dr. M. Luttges and Dr. M. Robinson of the Dept. of Aerospace Engineering Sciences of the University of Colorado, Boulder, for their support.

REFERENCES.

Brotherhood, P., and Riley, M.J.: 1978, Flight Experiments on Aerodynamic Features Affecting Helicopter Blade Design, Vertica, Vol. 2 , pp. 27-42, 1978.

Grant I (Editor): 1994, Selected Papers on PIV; SPIE Milestone Volume MS99,1994.

Grant, I and Liu, A: 1989, Method for the Efficient Incoherent Analysis of Particle Image Velocimetry Images", Applied Optics, 28, 10, May 1989 reprinted in Selected Papers on PIV; SPIE Milestone Volume MS99, Editor Ian Grant, May 1994.

Grant, I and Smith, G H: 1988, Modern developments in particle image velocimetry, Journal of Optics and Lasers in Engineering, 9, pp 245-264, 1988, reprinted in Selected Papers on PIV; SPIE Milestone Volume MS99, Editor Ian Grant, May 1994.

Horner, M B, Galbraith, R A McD, Coton, F, Grant I and Stewart, J N: 1994, Examination of vortex deformation during blade-vortex interaction utilising particle image velocimetry, Proc 19th Congress of the International Council of the Aeonautical Sciences, Anaheim, California, USA September, 1994.

Horner, M.H., Saliveros, E., and Galbraith, R.A.McD.: 1991, An Examination of Vortex Convection Effects During Blade-Vortex Interaction, AHS/RAeS Technical Specialists Meeting on Rotorcraft Acoustics and Rotor Fluid Dynamics, Philadelphia, U.S.A., October, 1991.

Horner M, Stewart J N, Galbraith R A McD, Grant, I ,Coton F N, Smith G H: 1993, Preliminary results from a particle image velocimetry study of blade-vortex interaction, Proc 19th European Rotorcraft Forum and 11th EHA, Como, Italy, September 14-16, 1993

Scheiman, J. and Ludi, L.H.: 1963, Qualitative Evaluation of Effect of Helicopter Rotor-Blade Tip Vortex on Blade Airloads, NASA TN D-1637, May, 1963.

Schmitz, F.H., Boxwell, D.A., Lewy, S., and Dahan, C.: 1978, Model- to Full-Scale Comparisons of Helicopter Blade-Vortex Interaction Noise, 38th Annual National Forum of the American Helicopter Society, Anaheim, Calif., May, 1978.

Surendraiah, M: 1969, An Experimental Study of Rotor Blade-Vortex Interaction, M.S. Thesis, The Pennsylvania State University, December, 1969.

Ziada S and Rockwell D: 1992, Vortex -Leading Edge Interactions, J Fluid Mec, 118, pp 79-107, 1992.

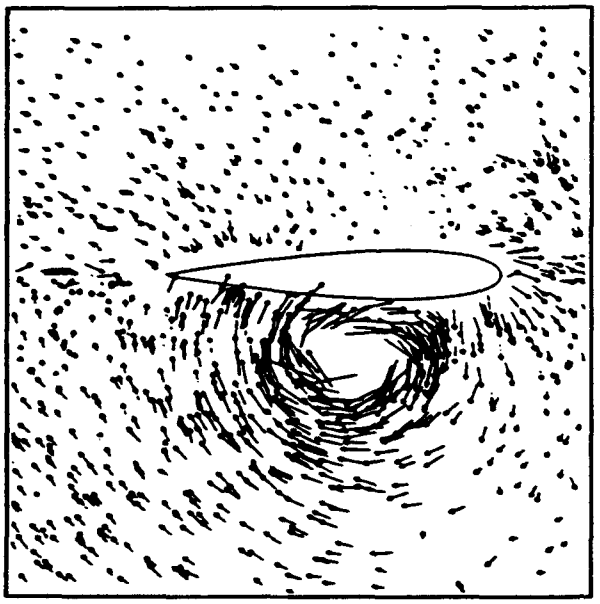

Figure 2d. Ψ=181°

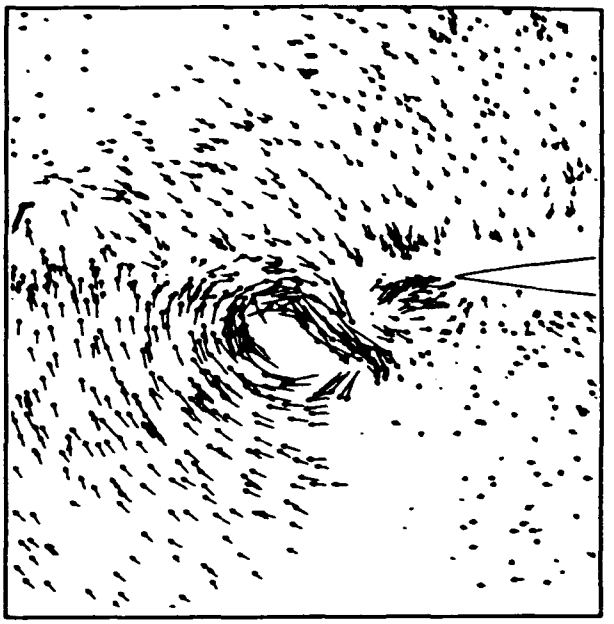

Figure 2f Ψ=193°

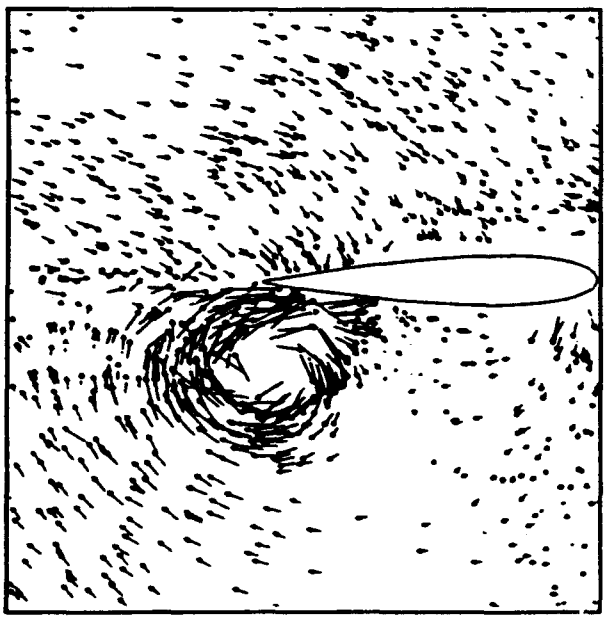

Figure 2e. Ψ=187°

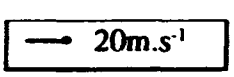

Figures 2. PIV Data Showing Parallel BVI.

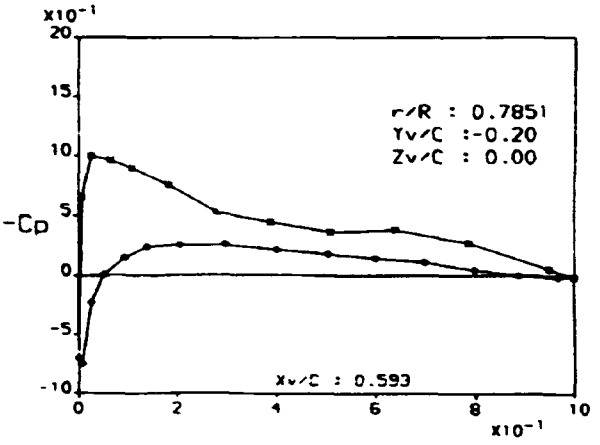

Figure 3. Pressure Data Corresponding to Fig 2d.

FIGURES

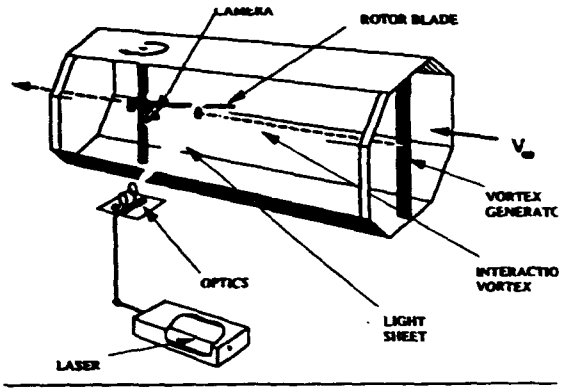

Figure 1. The Experimental Set Up.

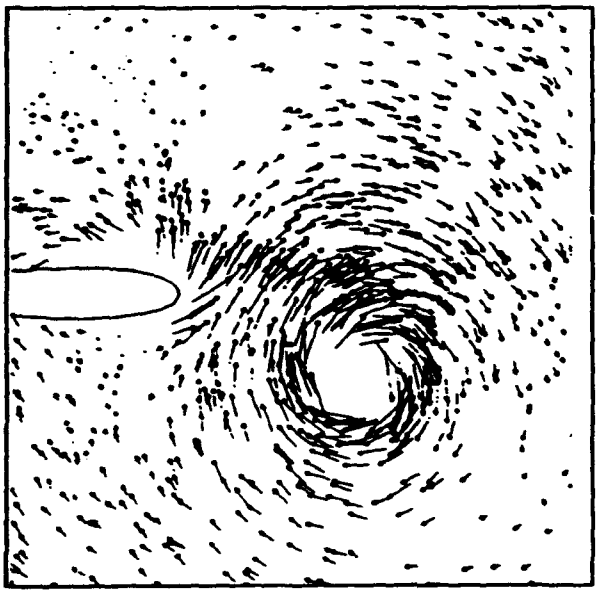

Figure 2a. Ψ=168°

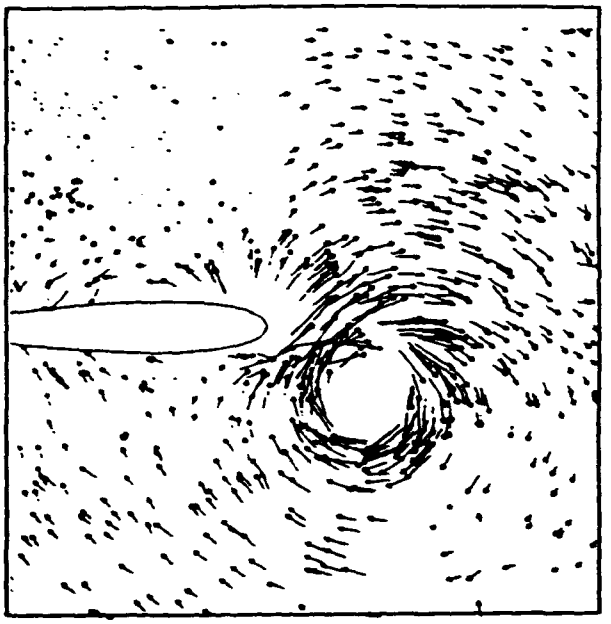

Figure 2b. Ψ=172°

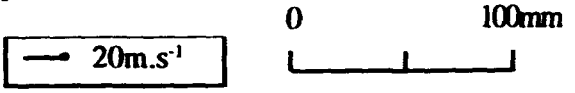

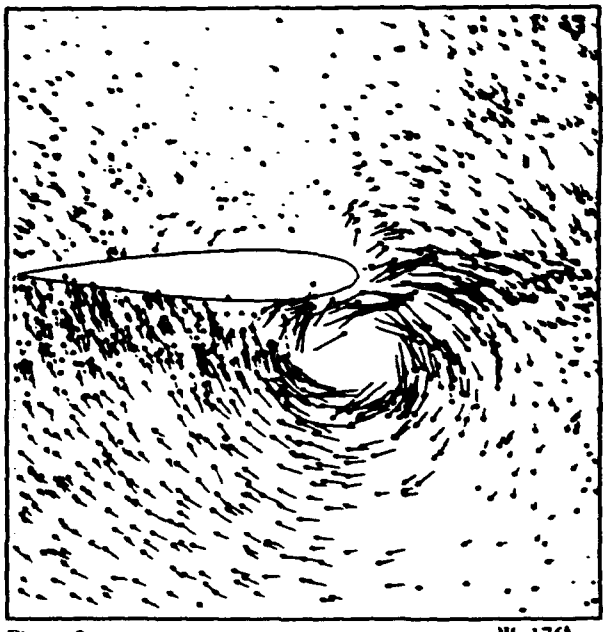

Figure 2c. Ψ=176°

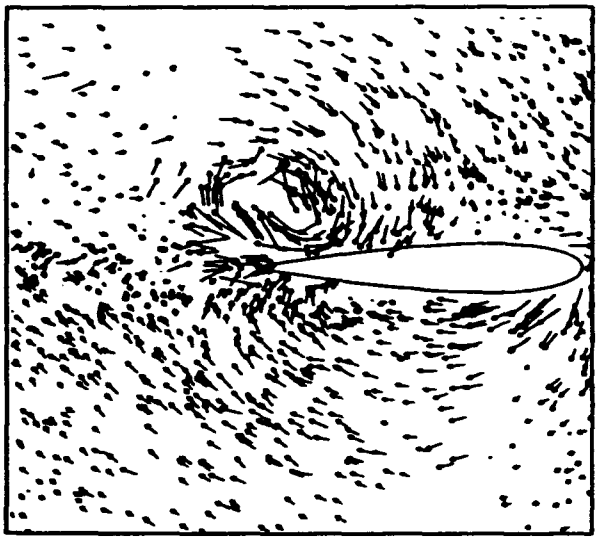

Figure 4. PIV Data Showing Head on Parallel BVI Interaction.

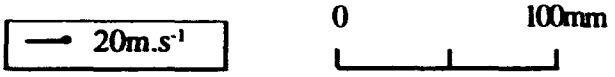

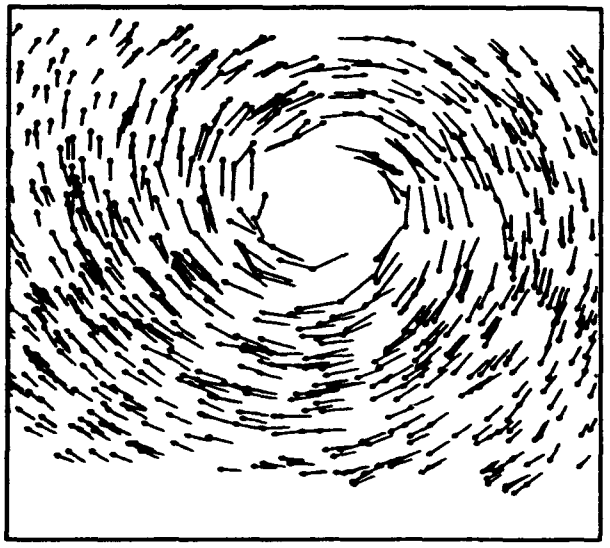

Figure 5. PIV Data Showing Baseline Vortex Flow.

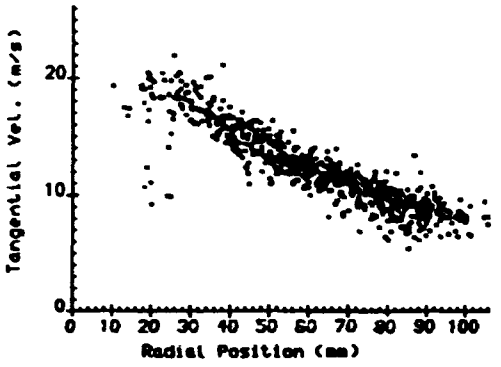

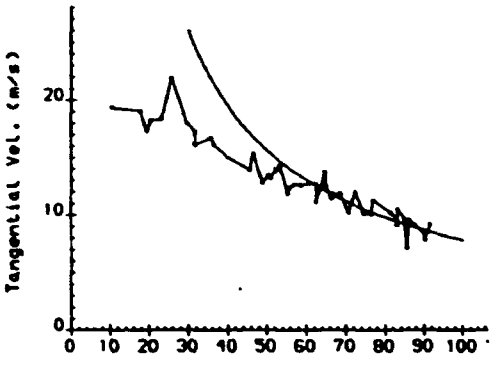

Figure 6. Tangential Velocity Data Derived From Figure 5.

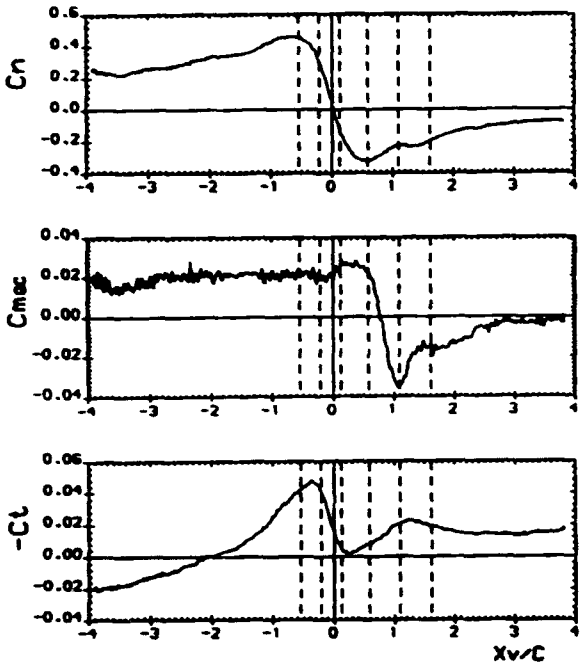

Figure 8.. Pressure Data Corresponding to Fig. 2d

APPENDIX.

Symbols Used in Figures and Text

c	blade chord length
Cmqc	quarter chord moment coefficient
Cn	normal force coefficient
Ct	tangential force coefficient
r	radial position of pressure sensor
R	blade radius
Xv	horizontal distance between the leading edge, at the measurement position, and the vortex centre, measured perpendicular to the vortex core
Yv	vertical displacement of the vortex generator junction above the rotor disk
Zv	lateral displacement of the vortex generator from the tunnel centre line
δ	vortex generator section incidence
Γ	vortex circulation
Ψ	blade azimuth angle

MEASUREMENTS OF THE FLOW AROUND WIND TURBINE ROTORS BY PARTICLE IMAGE VELOCIMETRY.

I Grant, G H Smith, D Infield *, X Wang, Y Zhao, S Fu
Fluid Loading and Instrumentation Centre, Heriot-Watt University, Edinburgh EH14 4AS UK
*CREST Loughborough University, UK.

ABSTRACT.

The aerodynamic characteristics of an operational wind turbine are complex (Hansen and Butterfield (1993)). A description is given of the flow conditions generated by the interaction of the wind with the spinning rotor blades.

Experiments are described in which PIV (in Particle Tracking Mode) was used to obtain instantaneous flow field measurements around wind turbine blades. Wake measurements have also being obtained. Phase sampled data was obtained by synchronising the pulsed laser trigger/camera trigger point with the rotor rotation angle. The estimation of derived quantities, such as angle of attack and circulation, is discussed.

The paper describes the procedures and techniques being adopted in the outdoor application of particle image velocimetry. The measurement of the aerodynamic characteristics of an operation horizontal axis wind turbine in field (out-of-doors) conditions is described. The procedures for the safe and effective deployment of a pulsed Nd: YAG laser and its control by computer on site are discussed.

Field PIV images and measurements are presented showing the approaching flow field near a 17m diameter horizontal axis wind turbine. The measurements were obtained between 8 and 10 m from the ground. The methods adopted for the derivation of the angle of attack from the field images are described.

Laboratory measurements of angle of attack on a small wind turbine are presented. Wake data obtained from this turbine is also presented

1. BACKGROUND.

Future developments in the understanding and computation of wind turbine aerodynamics require the assembly of an extensive data base of fundamental measurements. The data base is required to give a quantitative description of the flow field around wind turbines under operating conditions. Although established point measurement techniques such as hot-wire anemometry and LDA have much to offer (Vermeer (1992)), their application to complex flow fields is laborious. A major role is therefore seen for the whole field technique, Particle Image Velocimetry.

The Reynolds number dependence of the flow over a turbine blade is a critical consideration in any experimental study. Model experiments, for instance hydraulic studies for flow visualisation purposes, may be poorly conditioned since the aerofoil blades will be almost always be permanently stalled with gross separations occurring on the blades. Important scale effects result from this which can invalidate extrapolation of model results to full scale conditions. Under these model conditions, the blade profile, fundamental in defining performance, will have little or no effect on the vorticity transport into the wake.

The unsteady nature of wind conditions in the field is a second prototype feature, often neglected in model studies, which has important implications in defining performance. This is because dynamic inflow, produced by such an unsteady environment, is fundamental in establishing turbine loading around the equivalent rotor disk.

For these reasons the present study was phased to allow establishment of experimental methods in wind tunnel studies followed by prototype studies under field conditions on operational rotors.

2. THE HORIZONTAL AXIS WIND TURBINE.

The horizontal axis wind turbine is the most popular configuration for wind energy utilisation. The energy is extracted from the wind as it passes through the surface swept out by the spinning rotor. This surface is commonly considered as an *actuator disk*. The air velocity is changed from its free stream value as it passes through the actuator disk by an amount given by the *axial flow induction factor*. Most turbines use blades of aerofoil section since this is the most efficient way to develop the lift force, a component of which is then converted to useful axial torque.

The *tip speed ratio* is used to define the operating conditions of the turbine. This is obtained from the ratio of the tangential speed of the blade tips to the undisturbed wind speed. The tip speed ratio directly effects the angle of attack and, through the induction factor, the overall performance of the turbine.

The turbine blades are aerofoil in shape and the general aerodynamic principles apply to this complex rotational case The foil shape leads to a variation in the vorticity between the upper and lower surfaces of the blade and a net circulation

around it. The consequential lift forces on the blades cause the turbine to rotate. The angle of attack, or the angle between the approaching wind and the aerofoil central chord line determines the circulation, and hence, the lift force.

A commonly adopted strategy for turbine control is stall regulation. For a fixed rotor speed an increase in the wind speed causes a decrease in the tip speed ratio. As the tip speed ratio decreases the relative angle of attack increases and flow separation accompanied by stall inhibits any further increase in rotor torque. Using the flow characteristics of the aerofoil in this way is a particularly reliable and efficient way to limit the electrical output of a wind turbine.

The flow around the tip, of a typical turbine blade, from the underside is caused by the pressure difference. Vorticity is shed from the tip and rolls up into a vortex tube. The rotation of the turbine means that each tube from a blade is wound into the form of a helix as it convects downstream.

The circulation along the turbine blade reaches a maximum at approximately 80% of the blade length measured from the hub. The circulation of the shed vortex tube is approximately equal to the maximum value measured on the blade. This in turn can be related to the aerodynamic forces on the blades.

From this brief description of the aerodynamics of the turbine it can be seen that flow field measurements are essential to any description of performance or loading. The complexity of the problem means that scale model tests are difficult. The simultaneous requirements of scaling tip speed ratio and Reynolds number are difficult to achieve in such a manner that energy is extracted and the flow correctly modelled. Model tests are thus of limited usefulness. The present investigation thus had as its principal purpose the measurement of salient flow features on operational wind turbines of various sizes

3. PARTICLE IMAGE VELOCIMETRY (PIV).

Particle Image Velocimetry is a branch of the discipline of Pulsed Laser Velocimetry. When low flow seeding densities are used, most convenient for large scale and outdoor experimentation, it may be referred to, descriptively, as Particle Tracking Velocimetry. For simplicity the technique is referred to as PIV throughout the paper.

PIV is a flow field measurement method well suited to measurement of transient or unsteady flows of the type encountered near wind turbines by following the motion of moving, "seed', flow following particles introduced into the flow. Velocities are calculated from the displacement between successive images of individual particles as they translate with the flow (Grant (1994), Adrian (1984), Pickering (1984), Grant and Smith (1988)). This was an ideal method for measuring the complex aerodynamics of the turbine rotor where the parallel visualisation capability of the method proved invaluable.

A high intensity, multiply-pulsed, laser light-sheet was used to illuminate the particles. A photograph was taken of the region of interest with an exposure time which resulted in a transparency containing multiple images of the seeding particles. From the optical magnification of the camera optics, the time between successive light pulses and the measured displacement on the photographic image, the particle and hence the fluid velocity was calculated.

3.1 Laser Illumination.

The choice of the light source was influenced by several factors, the most important being the requirement for high intensity illumination and a light pulse length and rate compatible with the fluid velocity. In aerodynamic studies this generally results in a pulsed laser source being chosen. The ease with which the light sheet can be formed and manipulated was also relevant. Portability was also a requirement since the work program was to be extended to field measurements when sufficient experience had been obtained in wind tunnel tests.

These constraints lead to the choice of a frequency doubled Yag laser with a wavelength of 532 nm (green) with an output energy of about 135 mJ. The very short pulse width of about 6 ns resulted in very sharp particle images. For example, a 60 micron seed particle moving at 10 m/s travelled less than 0.1% of its diameter during the pulse. In Q- switched mode two pulses were produced within the pulse envelope. The energy associated with each pulse was less than for single pulse. The light energy from the laser is a maximum at a pulse repetition rate of approximately 10 Hz. Single trigger application resulted in significant loss of energy. These considerations were taken into account when designing the experiments.

3.2 Image Recording and Analysis.

The image was photographed on 35 mm film using a standard single lens reflex camera. For the wind tunnel work a Nikon 105 mm macro lens at an approximate magnification of 0.25 was used. Kodak T Max film was used for the wind tunnel experiments, developed in T Max developer at a dilution of 1:4 for 15 minutes. For outdoor work, Ilford HP5 film (400 ASA) was generally used with the Yag laser, being a good compromise between grain size (and hence resolution) and sensitivity. A shutter speed was selected to encompass the pulse separation time.

The low seeding and image densities used in the studies meant that particle tracking techniques were particularly effective in the analysis of the images. The analysis of the photographic images was conducted automatically using a PC based image scanning and analysis system.

The software used the statistical approaches, described by Grant and Liu (1989), (1990), which allowed the efficient calculation of flow velocities. In regions of higher seeding density correlation algorithms were available. Software to allow the averaging and interpolation of flow fields and the calculation of derived quantities such as vorticity and circulation was also available.

In regions of high turbulence or where flow direction was uncertain computer control of the laser allowed intensity control of the laser Q- switch circuitry enabling "tagged" images to be obtained (Grant et al (1994)). The direction was then automatically extracted using customised software (Grant and Liu (1990)).

4. WIND TUNNEL EXPERIMENTAL ARRANGEMENT.

Experimental work has been undertaken at Heriot-Watt in a closed-return wind-tunnel, some results from which were previously presented elsewhere (Smith et al (1991)) . The working section of the tunnel was removed and the wind turbine placed in the open working section to minimise blockage effects.

4.1 Wind Turbine.

Two small commercial wind turbines manufactured by Marlec were used in this part of the study. Both had an overall rotor diameter was 0.9 m with a hub diameter of 0.24 m. The turbines were supplied with six moulded synthetic blades, although tests were also undertaken with three blades. The blades of the first rotor had non-tapered blades, each having a simple cambered profile. The second model had approximate NACA section blades.

The turbines were designed for battery charging at up to about 50 Watts. For experimental purposes the wind vane of the turbine was removed and the rotor locked in the upwind position. The generator was electrically loaded by a 12 volt battery with solid state by-pass to prevent overcharging. An optical trigger was fitted to the rotor hub. This enabled rotation rate to be measured, and was also used for triggering of the laser and the camera.

4.2 Experimental Geometry.

The Yag laser was located on the wind tunnel roof with the beam being projected down into the working section. Suitable optical arrangements were used to produce a fan shaped light sheet of approximate thickness 1cm. Figure 1 shows the wind generator and laser in the wind tunnel.

The flow around an individual blade was examined by positioning the laser sheet to intercept a horizontal blade at the selected blade radius. The laser sheet was positioned on the rotor centre-line for study of the near wake region. This is shown together with the blade numbering in Figures 1 and 2.

4.3 Flow Seeding.

Flow volume rates and hence seeding requirements were much higher than for hydrodynamic work. In addition, the flow field covering a relatively large area was to be investigated. At a typical wind speed of 10 $m.s^{-1}$ about 14.4 m^3 of air passed through the working section each second. Seeding was introduced to the tunnel downstream of the turbine, causing no disturbance to the flow incident on the rotor. This was a clear advantage of a recirculating tunnel. After some use the tunnel accumulated enough seeding to seed the flow automatically. Seeding particles of polycrystalline form, with a mean diameter of about 30 microns, were used. These particles were found to have high scattering efficiencies.

4.4 Laser Control.

The signal from the optical switch on the hub of the wind turbine was used to trigger the laser. The rotational speed of the turbine was found to be close to 10 Hz which allowed the laser to operate efficiently. A variable delay was used so that the blade phase position during the pulse could be adjusted. Each time the laser was triggered a Q-switch produced a double pulse within the intensity envelope (Grant et al (1994)).

5. RESULTS FROM WIND TUNNEL WORK.

5.1 Flow Around an Individual Blade.

Using the synchronising electronics, described above, photographic images were obtained with the blade instantaneously in the horizontal position. Particle pairs were identifiable. As flow conditions in the tunnel were steady, flow fields calculated from a number of images can be ensemble averaged. Ten images have been averaged in this way to give Figure 3. The length of the vector gives the magnitude of the in-plane component. The disturbance caused by the blade is visible but it was more informative to transform the frame of reference to either that of the blade or that of the fluid.

From the measured blade rotation rate, and radial position the local blade velocity was calculated. Changing co-ordinates accordingly, the flow that would be seen by an observer in the frame of reference of the blade was produced as shown in Figure 4a. The angle of attack of the wind to the blade can be derived from this representation.

Alternatively by transforming to the frame of reference of the fluid by removing the mean measured flow velocity at the rotor disc, the circulation around the blade becomes apparent, Figure 4b.

Contour integration provides the numerical value of the blade bound circulation. This has been calculated at a number of blade stations and the results are plotted in Figure 5. Some inconsistency was evident. This arose because data was collected from arbitrary blades at that stage of the experimental work. Since then significant variations between the performance of different blades have been identified. This matter is discussed in more detail in relation to tip vortices in the next sub-section.

5.2 Investigation of the near wake.

Photographic images recording a section through the near wake were obtained. From the calculated velocity field vorticity contours were produced as shown in Figure 6 with the structure of tip vortices highlighted. Contour integration around individual tip vortices gave the circulation. This has been calculated for a series of concentric paths so as to give the dependence on the distance from the vortex core. Results, normalised by the maximum measured blade bound circulation, for all six blades, with the vortex in position 1 as given by Figure 6, are shown in Figure 7. It is clear that the tip vortex from blade 3, and to a lesser extent blade 5, is weaker than for the other blades. If the vortex from blade three is examined at different positions (ages) it appears, see Figure 8, that the problem could be associated with an abnormally long role up process.

6 FIELD APPLICATION TO FULL SIZE ROTORS

6.1 Safety Considerations.

The experiment required that the laser, a class IV, be directed into the air in an expanding sheet. In the first stage the beam propagated freely into the sky with no obstruction. In the later stages of the experiment it impinged upon the rotating blade of a small wind turbine set at a heights between 7m and 15m above ground level. The region was seeded by small, 50-100 micron sized particles, injected some 10 -15 m upstream.

The guidance at ground level, of the unexpanded beam, used a customised containment arrangement with suitable interlocks. The laser sheet left the containment system through a slot in the roof, at a height of approximately 2 m above ground level expanding as it propagated. No viewing directly along the line of the beam was possible.

Calculations of the Maximum Permissible Exposure (MPE) were made using BS4803 table 3. Nominal Ocular Hazard Distance was then calculated . This was the distance beyond which viewing of the beam was non-hazardous.

The first field measurements of flow around full size turbine were undertaken at a field station near Edinburgh, Scotland . These tests established that seeded ambient air flow, at a height of about 10 m could be successfully imaged. The seeding particles were introduced and dispersed into the flow at the appropriate height by a powder transport apparatus. Great care was needed to ensure focused images and adequate illumination levels.

More recent work outdoors at RAL, Didcot (England) has provided images of flow around the blade of a larger , Wind Harvester, turbine rotor in motion. The turbine had a hub height of 15.5 m above the ground and a rotor diameter of 17 m. A laser and camera arrangement was been devised to produce images at 80% of the radius. Figure 9 presents the measurements obtained from one of these early images.

An optical switch was fitted to the rotor for triggering purposes. The laser triggering was more complex than in the wind tunnel tests as the blade passing frequency was not compatible with high laser pulse energy. A repetition rate of about 10 Hz was required and a designated double pulse must be timed to coincide with the required blade position. In these circumstances the camera also required to be automatically triggered. A PC based control system has been developed for these purposes (Grant and Liu (1989), (1990)).

In the field the TMAX 3200 or 400 was used giving a good compromise between speed and resolution. The camera was sited on the ground some 13m from the illuminated flow sheet. Using a 300 mm Nikon lens it was possible to obtain an image corresponding to a flow region of approximately 1 square metre around the turbine blade. In order to obtain satisfactory images the development of the film was 'pushed' to 1 or 2 minutes beyond the recommended, giving a development time of 13-15 minutes in general.

7. CONCLUSIONS AND POTENTIAL FUTURE WORK.

The application of PIV to wind-tunnel and field measurements of wind turbine aerodynamics has been described and demonstrated. The results presented so far show that the technique can provide a valuable insight into the aerodynamic properties of the blades and that derived quantities, such as vorticity and circulation, can be obtained allowing a more comprehensive understanding of the wind and turbine interaction.

Further refinements in technique are being developed to give detailed information on the tip vortex roll up process and flow separation from the blade at high angles of attack.

REFERENCES.

Adrian, R J: 1984, Scattering particles characteristics and their effect on pulsed laser measurements of fluid flow: speckle velocimetry vs particle image velocimetry. Applied Optics, Vol 23, page 1690, June 1,1984. *

Grant I (Editor): 1994, Selected Papers in PIV, SPIE Milestone Volume on Particle Image Velocimetry, May 1994.

Grant I and Liu A :1989, Method for the efficient incoherent analysis of Particle Image Velocimetry images, Applied Optics, 28, 10, May 1989. *

Grant I and Liu A: 1990, Directional ambiguity resolution in particle image velocimetry by pulse tagging, Experiments in Fluids, Vol 10, pp 71-76, 1990. *

Grant I and Smith G H: 1988, Modern developments in Particle Image Velocimetry. Optics and Lasers in Engineering, 9 pp 245-64 (1988). *

Grant I, Wang X and Aroussi A: 1994, Data capture and illumination control in computer based systems for flow diagnostics, Proc Second International Conference on Fluid Dynamic Measurements and its Applications, Beijing, October 1994.

Hansen A C and Butterfield C P: 1993, Aerodynamics of horizontal-axis wind turbines, Annu Rev of Fluid Mechanics, 25, 115-49, 1993.

Pickering C J D, Halliwell N A: 1984, Speckle photography in two phase flows: signal recovery with two step processing. Applied Optics, 23, 1128-29, 1984. *

Smith G H, Grant I, Liu A, Infield D and Eich T: 1991, The wind tunnel application of Particle Image Velocimetry to the measurement of flow over a wind turbine. Wind Engineering, Vol 15, No 6 (1991).

Vermeer N-J: 1992, Local circulation on rotating wind turbine blades from velocity measurements in the wake of a model rotor. Proc. BWEA 14, MEP (1992).

Papers marked with an "* " are reprinted in "Selected Papers in PIV",, SPIE Milestone Volume on Particle Image Velocimetry, Editor I Grant, 1994

FIGURES

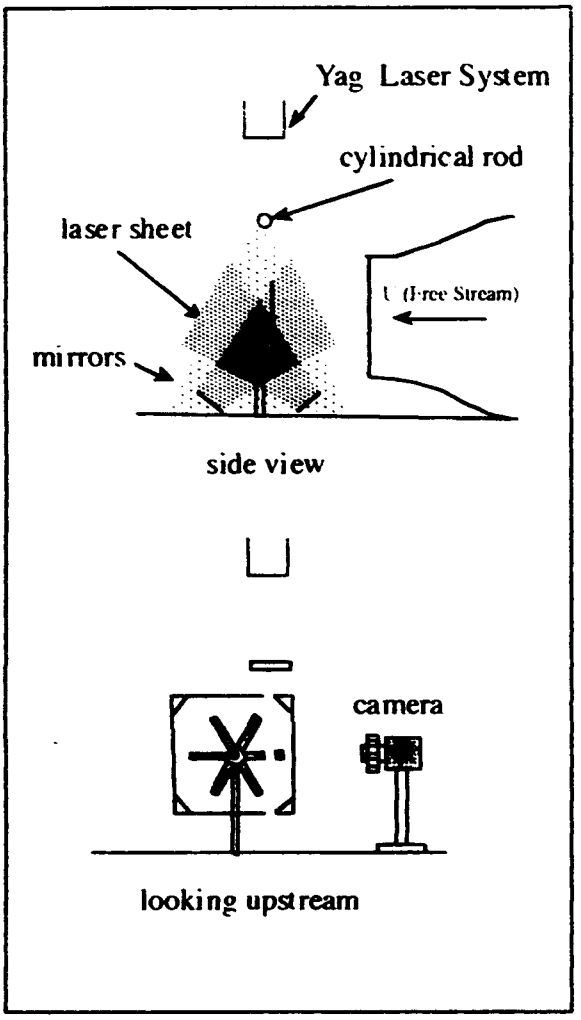

Figure 1 The Wind Turbine in the Wind Tunnel

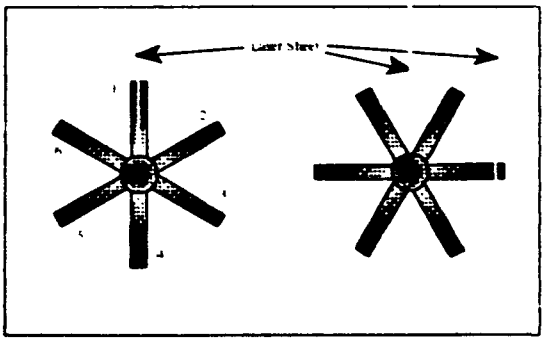

Figure 2 Laser Sheet Positioning

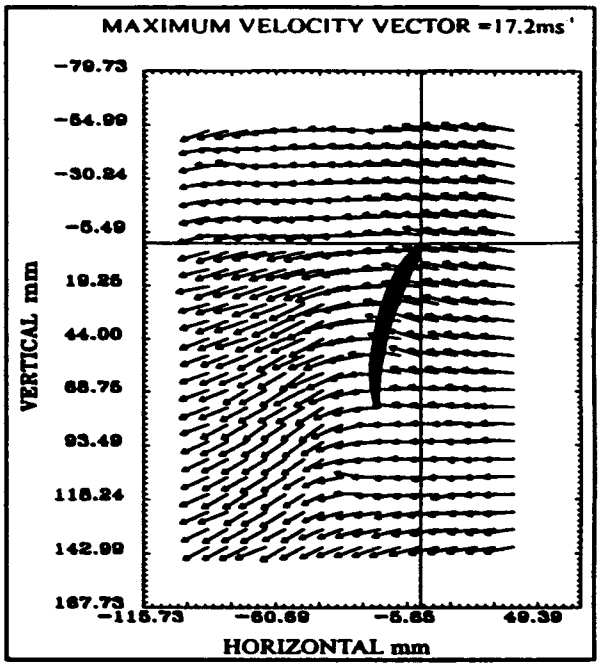

Figure 3. Typical Flow Measurements Around a Turbine Blade While in Motion.

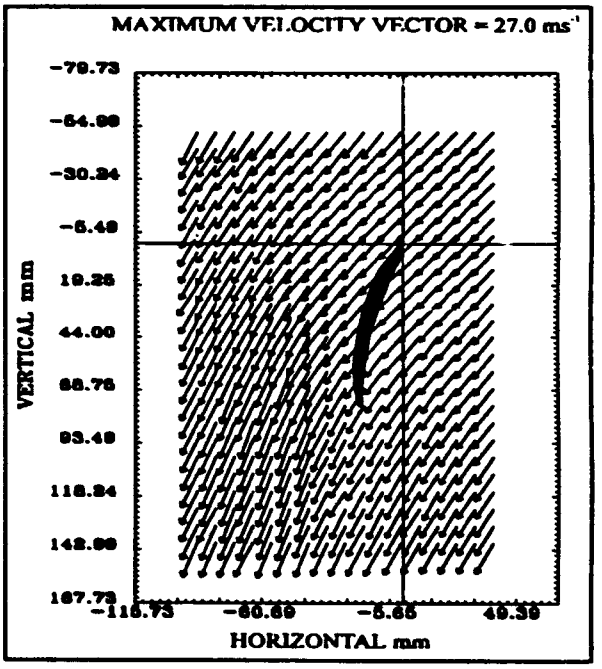

Figure 4a. Typical Flow Measurements Around a Turbine Blade While in Motion Seen From the Frame of Reference of the Blade.

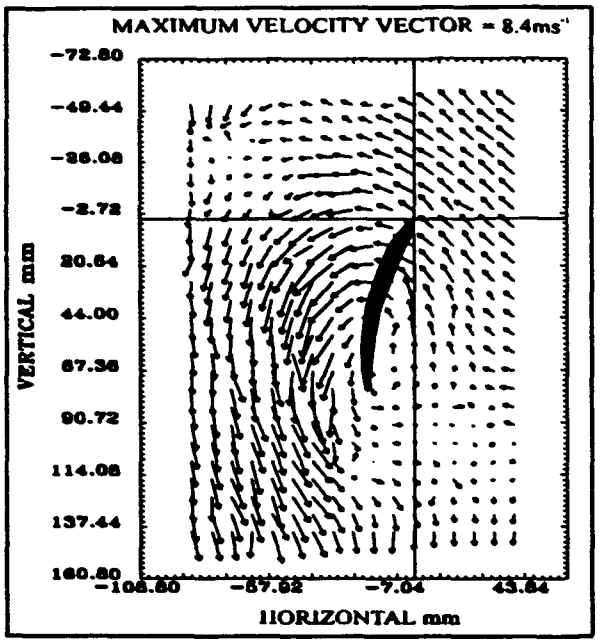

Figure 4b. Typical Flow Measurements Around a Turbine Blade While in Motion Seen From the Frame of Reference of the FreeStream Flow.

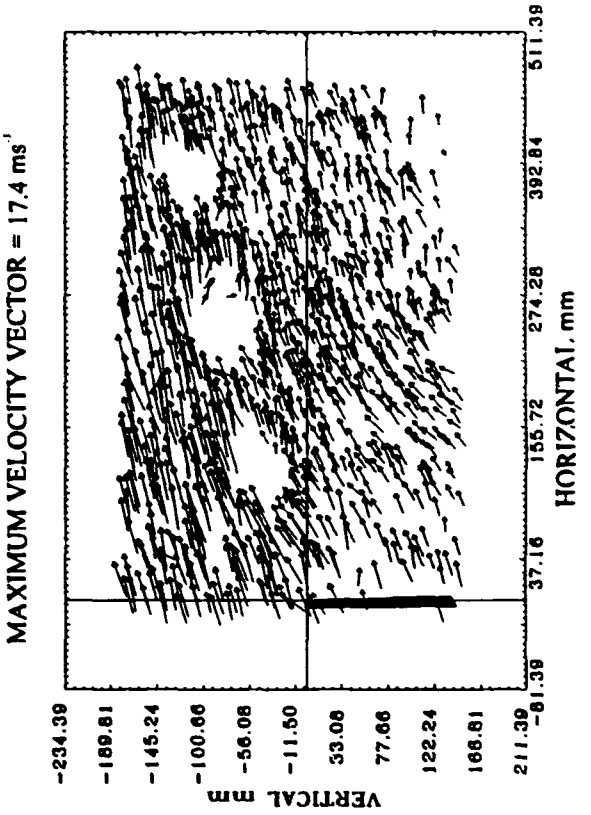

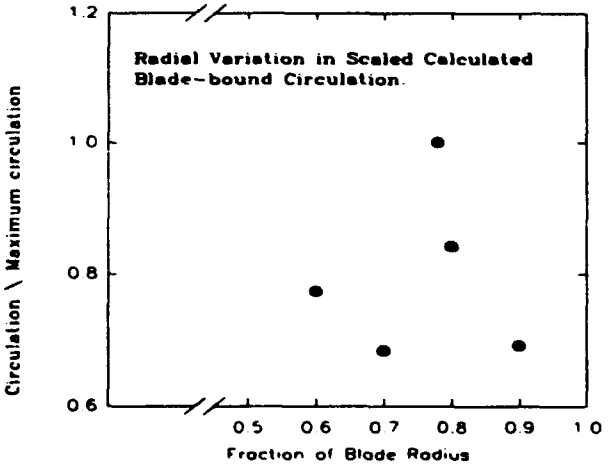

Figure 5. Variation of Normalised Circulation Along the Blade.

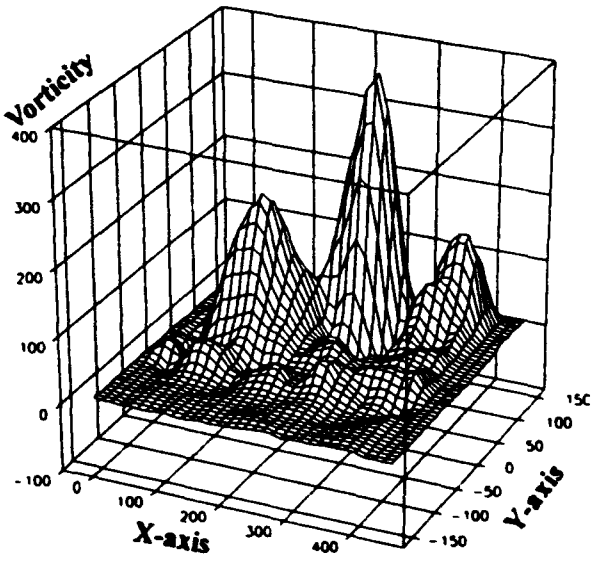

Figure 6. Calculated Vorticity Contours for the Near Wake (Typical wake image shown abonve for reference).

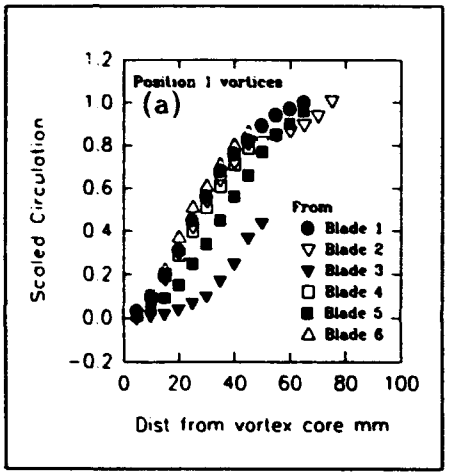

Figure 7. Tip Vortex Circulation in the First Position.

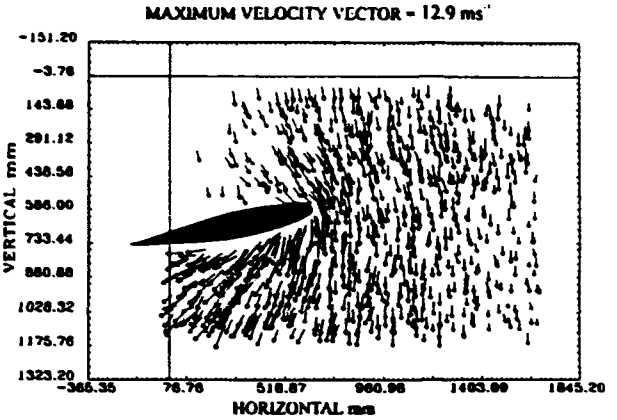

Figure 9. Typical Flow Field Measured Around a Full Scale Turbine Blade at 0.8 Blade Radius.

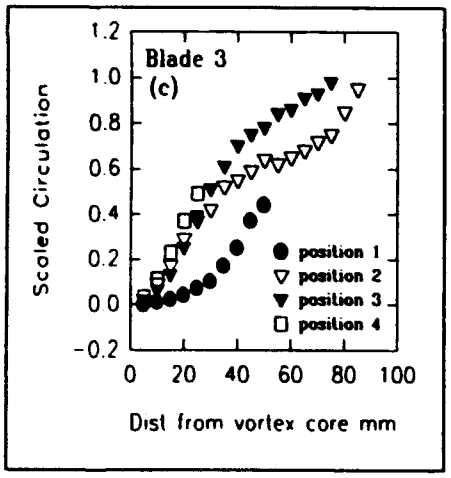

Figure 8. Tip Vortex Circulation at Different Development Times.

Session 11.
Data Processing II

A NEW METHOD FOR ESTIMATION OF TURBULENCE SPECTRA FOR LASER DOPPLER ANEMOMETRY

Anders Høst-Madsen

Dantec Measurement Technology A/S
Tonsbakken 16-18, 2740 Skovlunde, Denmark.

ABSTRACT

We introduce a new method for spectral estimation by LDA measurements and verify this by computer simulations and measurements.

0 INTRODUCTION

In Laser Doppler Anemometry there are two major problems faced when making a statistical analysis of the measurement data: velocity bias and the random arrival of the particles to the measurement volume. While velocity bias is the predominant problem for simple statistical values, such as mean and rms values, the random sampling seems to be the main problem for statistical quantities that depend on the timing of events, such as spectrum and correlation functions (see also [20]). In this paper we will deal with methods to overcome this problem.

The first to consider random sampling were Shapiro & Silverman [15], who proved that sampling after a Poisson process is free of aliasing. Further theoretical work in this direction was done by Beutler [4,5] and Masry [11,12]. The methods given to find the spectrum was however unfeasible for practical calculation, and Gaster & Roberts et al developed the so-called direct method in a series of papers [7,8,13,2]. In practice the so-called sample & hold method was also much used, and a theoretical analysis of this method was done by Adrian & Yao [1]. In LDA context different methods have been investigated in the papers [19] and [22].

This paper is the first step towards a more general investigation of practical methods for spectral estimation by random sampling. The direction we believe will be fruitful is spectral estimation through interpolation: we interpolate between samples, and derive a new time series by sampling this interpolated process equidistantly. The spectrum of the interpolated process of course is not identical to the spectrum of the original process, there is a bias. To use a method, this bias should be known, and if it is not negligible, it should be possible to compensate for it. In section 1 we arrive at expressions for the bias of the most basic interpolation: the interpolation where we use only the immediate preceding sample for interpolation. Even for this, the bias has a rather complicated form. But for a special case, the exponential interpolator, which was introdued in [19], we are able to fully calculate the bias, and we show how this can be compensated for. This compensation has previously partially been used by Boyer and Searby [6] for sample & hold. The exponential interpolator introduced here encompasses most of the estimators previously used as special cases.

The motivation for developing new spectral estimators is that random sampling adds variance to the spectrum, but the amount depends on the spectral estimator used (see also [19]). Thus, the quest is to develop an (unbiased) estimator with as low variance as possible. An interesting question, which we will not answer here, is if there is a lower limit for this added variance. Here we investigate different estimators with respect to variance, and show that in all most all cases the estimator introduced here has the least variance.

The theoretical developments are finally supplemented with computer simulations and comparisons with hot wire measurements showing the viability of the methods in practice and the limits of the methods.

1 GENERAL SPECTRAL ESTIMATION.

In the following we let $X(t)$ denote a stationary, Gaussian stochastic process as might be assumed for a turbulent process. For simplicity we assume that $X(t)$ has zero mean and finite energy. The autocorrelation function of $X(t)$ is defined as

$$R(\tau) = E\left[X(t).X(t+\tau)\right]$$

The (power)spectrum of X is defined as the Fourier transform of the autocorrelation,

$$S(\omega) = \mathrm{F}\{R\} = \int_{-\infty}^{\infty} R(\tau) e^{-i\omega\tau} d\tau$$

We assume that $\tau R(\tau)$ is absolutely integrable, so that the spectrum can also be found directly from $X(t)$ by (see [18])

$$\hat{S}_T(\omega) = \frac{1}{2T}\left|\int_{-T}^{T} X(t) e^{-i\omega t} dt\right|^2$$

$$S(\omega) = \lim_{T\to\infty} E\left[\hat{S}_T(\omega)\right]$$

The variance on the spectral estimator $\hat{S}_T(\omega)$ is (see, e.g., [3]) (1)

$$\lim_{T\to\infty} V\left[\hat{S}_T(\omega)\right] = S^2(\omega) \qquad (2)$$

2 SPECTRAL ESTIMATION BY INTERPOLATION

2.1 General interpolation

We sample $X(t)$ when a particle passes through the measurement volume, i.e. at times $\{\tau_n | n = \ldots,-2,-1,0,1,2,\ldots\}$. The times τ_n are the outcome of a stationary point process, which we will assume independent of $X(t)$. This assumption is true at moderate turbulence intensities. We assume that $\tau_n = \tau_{n-1} + \gamma_n$ with the γ_n independent random variables with identical probability density $\rho(t)$ (as in [15]). Typically for LDA the process will be a Poisson process. The task is to estimate the power spectrum from the set $\{(X(\tau_n), \tau_n) | n = \ldots,-2,-1,0,1,2,\ldots\}$. Our method to pursue this task is through *linear interpolation* or linear estimation. Thus, we define a new stochastic process $X'(t)$ by

$$X'(t) = \alpha(t - t^-) X(t^-)$$

Where we of course may assume $\alpha(t) = 0$ for $t < 0$. We will denote the spectrum of $X'(t)$ by $S'(\omega)$.

For the general interpolation we get (for a proof see [19]

THEOREM 1 For the general one-point interpolation, the spectrum is given by

$$\begin{aligned} S'(\omega) &= S(\omega)\left|\mathrm{F}\{\rho\alpha\}(\omega)\right|^2 \\ &+ \mathrm{Im}\left(\mathrm{H}\{S\,\mathrm{F}\{\rho\alpha\}\}\,\mathrm{F}\{\rho\alpha\}^*\right)(\omega) \\ &+ 2R(0)\left(\mathrm{Re}\left\{\mathrm{F}\{\rho\alpha\}\,\mathrm{F}\{\alpha\}^*\right\}(\omega) + \mathrm{Im}\mathrm{H}\left\{\mathrm{F}\{\rho\alpha\}\,\mathrm{F}\{\alpha\}^*\right\}(\omega)\right) \end{aligned}$$

where H is the Hilbert transform,

$$\mathrm{H}\{f\}(\omega) = -\frac{1}{\pi}\int_{-\infty}^{\infty} \frac{f(s)}{\omega - s} ds$$

Thus the general form of the spectrum is

$$S'(\omega) = S(\omega)k(\omega) + R(0)g(\omega) + T\{S\}(\omega)$$

The last term is due to the Hilbert-transform term of theorem 1. This will in general have a complicated dependence on S so that it is difficult, if not impossible, to find S from S'. It is also impossible in general to find the extra variance on the estimate of S' from theorem 1, so is remains open, which is the optimal one-point interpolator. However, we can get a guideline from prediction theory. The optimal linear estimation of $X(t+\lambda)$ from $X(t)$ in terms of mean square error in the time-domain is $X(t)R(\lambda)/R(0)$ (see e.g. [18], example 11-1), where R is the correlation function of X. Thus, it is *reasonable to assume that* $\alpha(t) = R(t)/R(0)$ will give the least interpolation error, and our calculations below on a specific process makes probable the correctness of this assumption. There are, however, two obstacles to using $\alpha(t) = R(t)/R(0)$: firstly, we do not know R in advance (it is actually R that we want to estimate), and secondly, as stated above, it is virtually impossible to find S from S' for a general R. We will therefore proceed otherwise.

2.2 Single Exponential Interpolation.

Even when $\mathrm{F}\{\alpha\}$ is a rational function, the expression for $S'(\omega)$ is extremely complicated (see [19]). However, in the case where $\mathrm{F}\{\alpha\}$ has a single root, i.e. α is an exponentially decaying function, we get immediately from theorem 2

THEOREM 3 Let

$$X'(t) = e^{-b(t-t^-)} X(t^-)$$

Then

$$S'(\omega)=\left(S(\omega)+2R(0)\frac{\nu+b}{(\nu+2b)\nu}-2R_{\nu+b}(0)\frac{1}{\nu+b}\right)\frac{\nu^2}{(\nu+b)^2+\omega^2} \quad (3)$$

with

$$R_{\nu+b}(0)=\frac{1}{2\pi}\int_{-\infty}^{\infty}S(t)\frac{(\nu+b)^2}{(\nu+b)^2+t^2}dt$$

We will claim that really this is the only practically feasible one-point interpolation, practically meaning that we should be able to find $S(\omega)$ from $S'(\omega)$. And this is indeed possible for exponential interpolation. We have

$$S(\omega)=\left(\left(1+\frac{b}{\nu}\right)^2+\left(\frac{\omega}{\nu}\right)^2\right)S'(\omega)-\left(2R(0)\frac{\nu+b}{(\nu+2b)\nu}-2R_{\nu+b}(0)\frac{1}{\nu+b}\right) \quad (4)$$

While we can easily find (an estimate for) $R(0)$, we cannot in general find $R_{\nu+b}(0)$, which is the spectrum of the process $X(t)$ low-pass filtered. However, notice that

$$\mathcal{F}^{-1}\left\{\left(\left(1+\frac{b}{\nu}\right)^2+\left(\frac{\omega}{\nu}\right)^2\right)S'(\omega)\right\}(\tau)$$
$$=R(\tau)+\delta(\tau)\cdot\left(\left(1+\frac{b}{\nu}\right)^2+\left(\frac{\omega}{\nu}\right)^2\right)\left(2R(0)\frac{\nu+b}{(\nu+2b)\nu}-2R_{\nu+b}(0)\frac{1}{\nu+b}\right)$$

So, to find $S(\omega)$, we divide out the mulitiplicative factor, take the inverse Fourier transform, "remove" the δ-pulse, and take the Fourier transform.

There are to special cases of exponential interpolation worth separate consideration. For $b = 0$ we get the well-know sample & hold interpolation, and for this the spectral estimate is from (3)

$$S'(\omega)=\left(S(\omega)+\frac{2}{\nu}(R(0)-R_\nu(0))\right)\frac{\nu^2}{\nu^2+\omega^2}$$

an expression which, after some calculation, is seen to be equivalent to the expression found in [1].

The other special case is to let b tend to infinity while at the same time scaling with b, so that the interpolated process approaches a train of δ-pulses. We hereby get the so-called direct method [8], and for this (3) gives

$$S'(\omega)=\nu^2\left(S(\omega)+\frac{R(0)}{\nu}\right)$$

in accordance with [8]

2.3 Autocorrelation estimates.

To complete the discussion, we will mention that the autocorrelation $R'(0)$ of the exponentially interpolated process is given by (see [19])

$$R'(0)=\frac{\nu}{\nu+2b}R(0)$$

3 THEORETICAL EVALUATION OF PERFORMANCE

In this section we will make a theoretical comparison of spectral estimation by the method of exponential interpolation, sample and hold and the direct method. Since these are all variations of exponential interpolation, this amount to evaluating exponential interpolation for different values of the decay. We will call the added standard deviation on S' due to interpolation for the *interpolation error*.The interpolation error for exponential interpolation was found in [19] to be

$$e_b=2R(0)\frac{\nu+b}{(\nu+2b)\nu}-2R_{\nu+b}(0)\frac{1}{\nu+b}$$

For the special cases of sample and hold and the direct method, the interpolation errors are (5)

$$e_{SH}=\frac{2}{\nu}(R(0)-R_\nu(0))$$

$$e_{dir}=\frac{R(0)}{\nu}$$

We can immediately make the following estimations

$$\frac{e_0(\nu)}{e_{dir}(\nu)},\frac{e_{SH}(\nu)}{e_{dir}(\nu)}\le 2$$
$$\frac{e_b(\nu)}{e_{dir}(\nu)},\frac{e_{SH}(\nu)}{e_{dir}(\nu)}\to 2 \text{ for } \nu\to 0$$
$$\frac{e_b(\nu)}{e_{dir}(\nu)},\frac{e_{SH}(\nu)}{e_{dir}(\nu)}\to 0 \text{ for } \nu\to\infty$$

So, for "low" data rates the direct method performs a little better, whereas for "high" data rates the exponential interpolation and sample and hold performs much better.

To quantify the terms "high" and "low" we will compare the methods for spectrum that is close to a typical turbulence spectrum, a first order spectrum, i.e.,

$$S(\omega)=\frac{a^2}{a^2+\omega^2}$$

The total power of the first order spectrum is

$$R(0)=\frac{1}{2}a$$

and the interpolation error is

$$e_b(\nu)=a\left(\frac{\nu+b}{(\nu+2b)\nu}-\frac{1}{a+(\nu+b)}\right)$$

The choice of b giving the least interpolation error is

$$b=a$$

Thus, the optimal interpolation function (among the exponential ones) is $\alpha(t)=R(t)/R(0)$, in accordance with our previous prediction.

Method	Interpolation error
Sample & Hold, $b=0$	$\frac{1}{\nu}\frac{a^2}{a+\nu}$
Optimal decay, $b=a$	$\frac{1}{\nu}\frac{a^2}{2a+\nu}$
Direct method, $b=\infty$	$\frac{a}{2\nu}$

Table 1: Interpolation error of different estimators for first order spectrum.

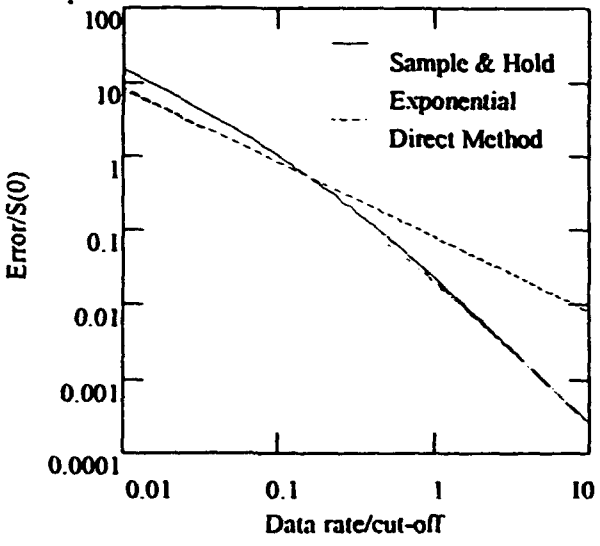

Figure 1: Standard deviation versus datarate for different methods. First order spectrum without added noise.

Table 1 gives the interpolation error for the three spectral estimators and it is plotted in figure 1.

We see that already for $a=\nu$ the sample & hold method becomes better than the direct method. And for $\nu<a$ spectral estimation does not really give any meaning, since the variance on the spectrum is greater than $S(0)$! We see that in all cases, the exponential interpolation is best.

If we add noise to the system, the results change somewhat. We consider band limited white noise of power $\frac{1}{2}\sigma$ and let the band limit tend to infinity. Asymptotically we then have $R(0)=\frac{1}{2}\sigma$ while $R_{\nu+b}(0)=0$ so that the interpolation error of the first order system plus noise is

$$e_b(\nu)=\frac{(a+\sigma)(\nu+b)}{(\nu+2b)\nu}-\frac{a}{a+(\nu+b)}$$

For this system the optimal choice of b will depend in a complicated manner on a and σ, but we suggest to put

$$b=a+\sigma$$

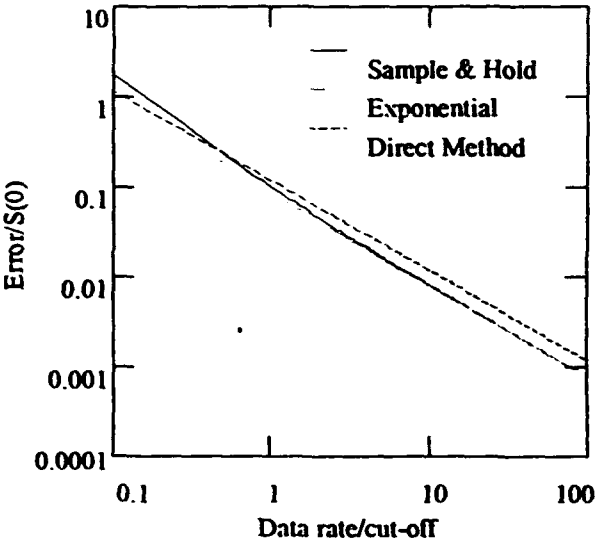

Figure 2: Standard deviation versus datarate for different methods. First order spectrum with added noise with S/N = 2.

by the argument found below. Formulas similar to the above table can be calculated, and the plot looks like in figure 2. We observe that for a signal to noise ratio of 2 (where the signal to noise is a/σ) the exponential interpolation with the suggested decay will perform best for all data rates. For a signal to noise of 0.5, the direct method will perform better. However, at S/N of 0.5 is very low to do spectral estimation. In case of very broad band noise, a filter should be used to filter out the high frequency noise prior to spectral estimation.

Based on these experiences, we can predict the relative performance of the exponential interpolator for other types of spectra. The general rule is that the more "low" frequency ($< \nu/2\pi$) power the process has, the better the exponential interpolator will perform. So, If the decay of the spectrum is

steeper than -2, the exponential interpolator becomes even better, if there are low frequency harmonics, the exponential interpolator will perform better and so on.

Shapiro and Silverman proved that Poisson sampling is free of aliasing so that it is theoretically possible to make spectral measurements at arbitrary high frequencies for a given data rate, ignoring the Nyquist criterion. How far is it possible to go in practice? The statistical error on the spectrum is the value of the spectrum itself plus the interpolation error. We define the *limit frequency* f_{limit} as the frequency where the interpolation error reaches the value of the spectrum. For the first order spectrum from above and exponential interpolation with optimal value of the decay we find (with $\alpha = \nu/a$)

$$f_{limit} = \frac{1}{2\pi}\nu\frac{\sqrt{\alpha^2+2\alpha-1}}{\alpha} \approx \frac{1}{2\pi}\nu$$

Which is even lower than the Nyquist frequency! Of course we can surpasse the limit frequency by block averaging. The error on the spectrum is reduced by a factor $\sqrt{N}$ where N is the number of blocks. Suppose that we modestly want to measure up till the "Nyquist frequency", $\nu/2$. At this frequency the interpolation error is about 10 times the value of the spectrum itself. If we want to reduce this error to the same order as the spectrum itself we need to average over 100 blocks, i.e., we need 100 times the data needed for equidistant sampling! If we want to have a total error of less than, i.e., 10 % we need to average over 10000 blocks!

Conclusion? Random sampling is not an advantage, it is an evil!

4 ALIASING

We have seen that the exponential method exceed the direct method in terms of interpolation error. The exponential method and sample and hold also have another advantage: we can resample the interpolated signal equidistantly and use FFT on this time series, thereby obtaining an enormously gain in speed. Doing this, one should be aware of aliasing. The resampling frequency should of course be so chosen that the process itself is not aliased, but the interpolation error will in all circumstances be aliased. Thus formula (3) should be replaced by

$$S'(\omega) = S(\omega)\frac{\nu^2}{(\nu+b)^2+\omega^2} + \left(2R(0)\frac{\nu+b}{(\nu+2b)\nu} - 2R_{\nu+b}(0)\frac{1}{\nu+b}\right)G(\omega) \quad (6)$$

where, as is well-know, G is given by

$$G(\omega) = \frac{\nu^2\Delta t}{2(\nu+b)}\frac{\sinh\left((\nu+b)\Delta t\right)}{\cosh\left((\nu+b)\Delta t\right)-\cos(\omega\Delta t)}$$

where Δt is the resampling interval.

We still may find $S(\omega)$ from $S'(\omega)$ like in (4):

$$F^{-1}\left\{\left(\left(1+\frac{b}{\nu}\right)^2+\left(\frac{\omega}{\nu}\right)^2\right)S'(\omega)\right\}(\tau)$$
$$= R(\tau) + F^{-1}\{G\}(\tau)\cdot\left(\left(1+\frac{b}{\nu}\right)^2+\left(\frac{\omega}{\nu}\right)^2\right)\left(2R(0)\frac{\nu+b}{(\nu+2b)\nu} - 2R_{\nu+b}(0)\frac{1}{\nu+b}\right)$$

If we know $R(0)$ and $F^{-1}\{G\}$ (which can be calculated analytically in the discrete version) we can then bias correct without knowing the factor on $F^{-1}\{G\}$.

Note however that the interpolation error will no longer be given by (5), but the aliased version of it found from (6). This increase in error on the spectral estimate can be avoided by oversampling, e.g., by a factor 2.

In respect to aliasing, random sampling has a clear advantage. If we use the direct method, we totally avoid aliasing. If we use exponential interpolation followed by resampling, we do not avoid aliasing completely, but exponential interpolation induces a low pass filter on the process (see (3)), thereby reducing the problem of aliasing considerable.

5 PRACTICAL USE OF METHODS

To use the method of exponential interpolation we need to know the right choice of the decay parameter b in advance. For general spectra it is difficult to find this optimum, and we suggest to put

$$b = \frac{R(0)}{\int_0^\infty R(\tau)d\tau} = \frac{R(0)}{\frac{1}{2}S(0)} = \frac{2E\left[X(t)^2\right]}{\lim_{T\to\infty} E\left[\frac{1}{2T}\left|\int_{-T}^{T} X(t)dt\right|^2\right]} \quad (7)$$

This inverse of this, $1/b$, is known as the integral time scale of the process. Note that it can easily be calculated from data without pre knowledge of the spectrum or autocorrelation. In the two theoretical examples this will give the suggested and (in one case) optimal decays.

5.1 Windows

To chose a proper window for spectral estimation is a science in itself. Or maybe it is not science, but rather metaphysics. Some people advocate one type of window, other people another type. The optimal window will depend on the concrete spectrum to be estimated.

Windows can be applied at three points in the estimation: on the original time series, on the interpolated time series and on the autocorrelation function. We suggest to use windowing of the autocorrelation since the other kinds of

windowing will give a complicated bias due to "interference" with the interpolation process. Thus, it is recommended to use rather long blocks and then obtain the required reduction in variance by an autocorrelation window. If too short blocks are used, the bias will be large and the above method will give strange results, as the computer simulations below show.

The reason to use a window is to extract as much information out of the noisy spectrum as possible, while at the same time keeping the bias low. The window acts as a low pass filter on the spectrum. By choosing a narrow window more noise will be filtered out from the spectrum, but also the bias will increase. To reach a reasonable balance between noise and bias, some experimentation is needed.

6 SIMULATIONS AND MEASUREMENTS

The formulas for variance calculated above are asymptotic formulas. To verify the valuations of the methods also for finite records, we have simulated first order spectra with and without added noise. The results can be seen in figure 3 - 6. All simulations were done using $\nu = 1$, and 1 million samples. The spectral estimation was done using the procedure outlined above with an oversampling factor of 2 and multiplicative and additive corrections. For sample and hold the decay was put to zero and for exponential interpolation, the decay was calculated from (7). In all figures, the solid line is the theoretical spectrum.

Figure 3 shows the result for a cutoff-frequency of 0.01 ($\alpha = 100/2\pi$).

Figure 4 shows the result for a cutoff-frequency of 0.2 ($\alpha = 5/2\pi$). It is noticeable that although the error is large we are still able to determine the decay of -2 of the spectrum. If we had not done the additive correction, the result would have looked like the top curve in the figure. Thus, the correction incorporated in our method is essential to obtain unbiased results, and with this correction it is possible to do spectral estimation with rather low data rates.

Figure 5 shows the variance in the estimated spectrum by respectively ordinary sample and hold and exponential interpolation. The increase in the calculated error over the theoretical error at high frequencies is due to aliasing.

Figure 6 shows what happens if one uses too short blocks. The expected spectrum is identical to the spectrum of figure 3, but in this calculation we have used only 200000 samples with still 1000 blocks and ordinary sample and hold. We notice that there is a strong bias. Actually, the estimated spectrum dips consequently below zero above a certain frequency (as opposed to the other cases presented, where variance can make the spectrum occasionally negative). This confirms our recommendation: one should use relatively long blocks and subsequent autocorrelation windows, since then bias is predictable (it is a convolution).

Figure 7-8 show comparisons between LDA and CTA measurements on a nozzle. More information on the measurements can be found in [21]. In figure 7 the spectral analysis for LDA was done by ordinary sample and hold. One observes that this completely obscures the change in decay. When the spectral estimation is done by the method discussed in this paper, as in figure 8, the spectrum for LDA follows closely the spectrum for CTA, until it reaches a noise bottom. This is not a proof that the spectrum measured by LDA is unbiased, but it is a strong indication.

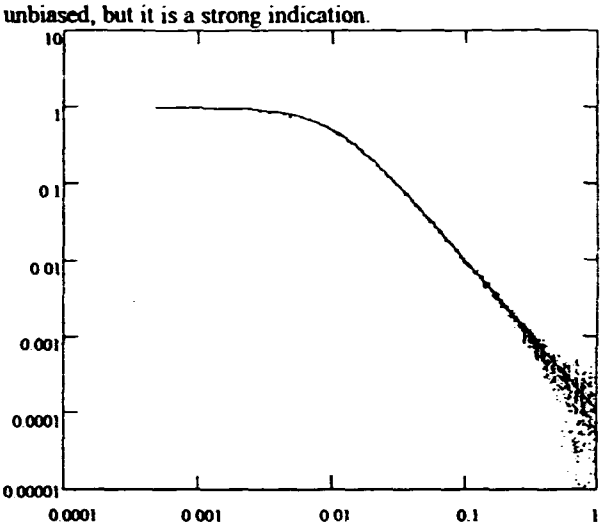

Figure 3: *Exponential* estimation of first order spectrum with cutoff frequency 0.01. The data rate is 1, 1000000 samples are evaluated divided into 1000 blocks.

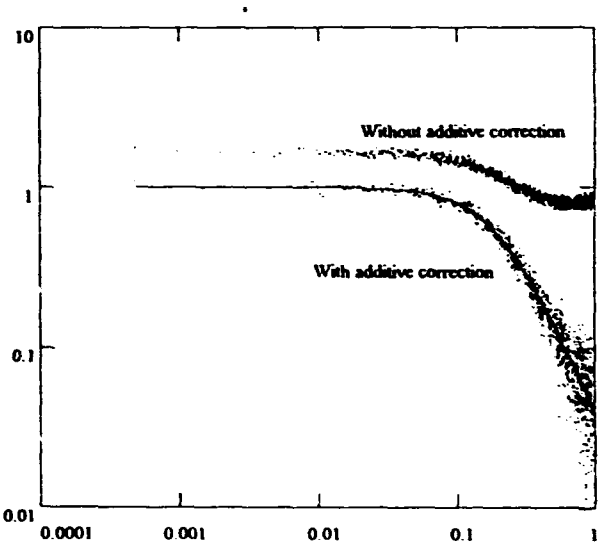

Figure 4: *Exponential* estimation of first order spectrum with cutoff frequency 0.2. The data rate is 1, 1000000 samples are evaluated divided into 1000 blocks.

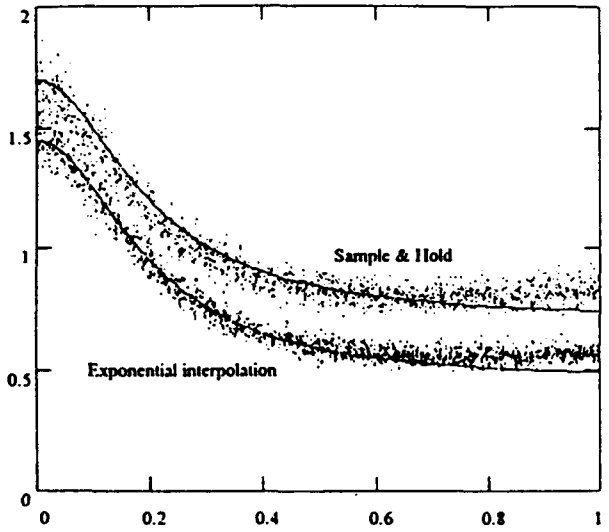

Figure 5: Standard deviation of spectral estimators. Both are evaluated on a first order spectrum with cutoff frequency 0.2. The data rate is 1, 1000000 samples are evaluated divided into 1000 blocks.

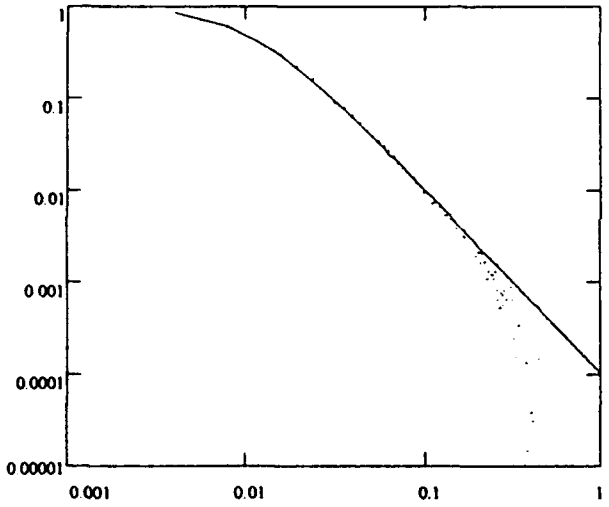

Figure 6: Bias due to too short blocks. *Sample and hold* estimation of first order spectrum with cutoff frequency 0.01. The data rate is 1, 200000 samples are evaluated divided into 1000 blocks.

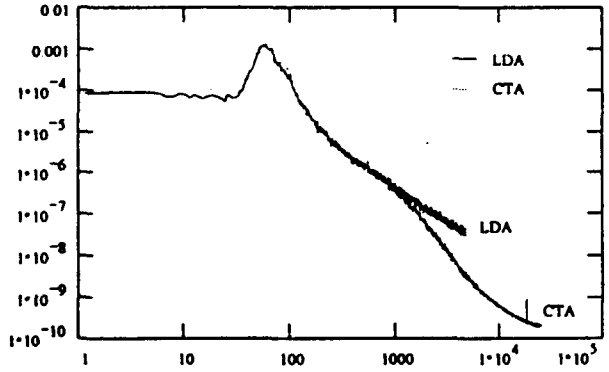

Figure 7: Measurements on nozzle. Spectral estimation for LDA done by ordinary sample and hold without any bias correction.

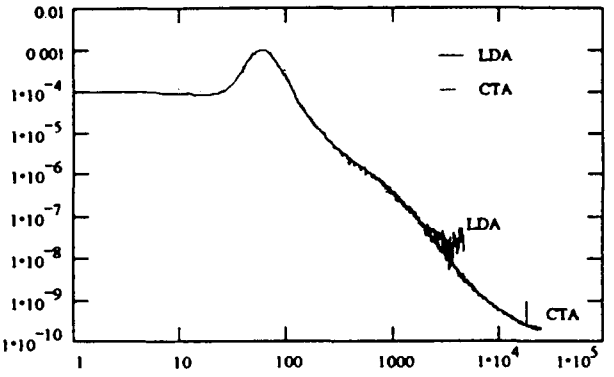

Figure 8: Measurements on nozzle. Spectral estimation for LDA done by exponential interpolation with bias correction and using a Papoulis window on the correlation function.

7 CONCLUSION

We have introduced a new spectral estimator for turbulence measurements: the exponential estimator. We have theoretically shown that this is *unbiased* and this has further been verified by computer simulations and measurements by CTA Therefore, we will claim that the method gives the correct spectrum, at least a low turbulence. What is still needed is to verify the method with respect to velocity bias, i.e. at high turbulence intensity. However, since sample and hold is equivalent to arrival time correction, we may expect that velocity bias will have little influence. This is also confirmed by recent simulations in [20].

REFERENCES

[1] Adrian, R.J. and Yao, C.S.: *Power spectra of fluid velocities measured by laser Doppler velocimetry*, Exp. in Fluids 5, 17-28 (1987).

[2] Ajamani, D.B.S. and Roberts, J.B.: *Improved Spectral Estimation for Irregularly Spaced Data Using Digital Filters*, Mechanical Systems and Signal Processing 4(1), 77-94 (1990).

[3] Bendat , J.S. and Piersol, A.G.: *Random Data, Analysis and Measurement Procedures*, 2nd Edition, John Wiley & Sons, Inc., New York, 1986.

[4] Beutler, F.J.: *Alias-Free Randomly Timed Sampling of Stochastic Processes*, IEEE Trans. Info. Theo., vol IT-16, no. 2, March 1970.

[5] Beutler, J.B.: *Recovery of Randomly Sampled Signals by Simple Interpolators*, Information and Control 26, 312-340 (1974).

[6] Boyer, L. and Searby, G.: Random sampling: Distortion and reconstruction of velocity spectra from fast Fourier-transform analysis of the analog signal of a laser Doppler processor, J. Appl. Phys. 60(8), 15 October 1986.

[7] Gaster, M. and Roberts, J.B.: *Spectral Analysis of Randomly Sampled Signals*, J. Inst. Maths Applics (1975) 15, 195-216.

[8] Gaster, M. and Roberts, J.B.: *The spectral analysis of randomly sampled records by a direct transform*, Proc. R. Soc. Lond. A 154, 27-58 (1977).

[9] Marquardt, D.W. and Acuff, S.K.: *Direct quadratic spectrum estimation with irregularly spaced data* Symposium on Time Series Analysis of Irregularly Observed Data, College Station, TX, 1983, p. 211-223 (Springer-Verlag).

[10] Marvasti, F.A.: *A unified approach to zero-crossings and non-uniform sampling*, Nonuniform, P.O. Box 1505, Oak Park, IL 60304.

[11] Masry, E. and Lui, M.-C.C.: *A consistent estimate of the spectrum by random sampling of the time series*, SIAM J. Appl. Math., vol. 28, no. 4, June 1975.

[12] Masry, E.: *Spectral and Probability Denstity Estimation From Irregularly Observed Data*, Symposium on Time Series Analysis of Irregularly Observed Data, College Station, TX, 1983, p. 224-250 (Springer-Verlag).

[13] Roberts, J.B. and Gaster, M.: *On the estimation of spectra from randomly sampled signals: a method of reducing variability*, Proc. R. Soc. Lond. A 371, 235-258 (1980).

[14] Schürmann, B.: Zur Ermittlung von Frequenzgängen auf der Basis zufällig abgetasteter stochastischer Signale, Automatisierungstechnik at, 35, 1987.

[15] Shapiro, H.S. and Silverman, R.A.: *Alias-free Sampling of Random Noise*, J. Soc. Indust. Appl. Math., Vol. 8, No.2, June 1960.

[16] Veynante, D. and Candel, S.M.: Application of nonlinear spectral analysis and signal reconstruction to laser Doppler velocimetry, Exp. in Fluids 6, 534-540 (1988).

[17] Veynante, D. and Candel, S.M.: A promising approach in Laser Doppler Velocimetry Data Processing: Signal reconstruction and Nonlinear Spectral Analysis, Signal Processing 14, 295-300 (1988).

[18] Papoulis, A.: *Probability, Random Variables and Stochastic Processes*, McGraw-Hill, New York, 1965.

[19] Host-Madsen, Anders and Caspersen, Christian: "Spectral estimation by interpolation," Signal Processing, to appear.

[20] Lee, Do Hwan and Sung, Hyung Jin: "Assessment of turbulent spectral bias in laser Doppler velocimetry," Experiments in Fluids 16, 223-235 (1994).

[21] Host-Madsen, A. and Caspersen, C.: "The Limitations in High Frequency Turbulence Spectrum Estimation Using the Laser Doppler Anemometer," accepted for seventh international symposium on applications of laser techniques to fluid mechanics.

[22] Tropea, C.: Turbulence-induced spectral bias in laser anemometry, AIAA J. 25, 306-309 (1987).

The Limitations in High Frequency Turbulence Spectrum Estimation using the Laser Doppler Anemometer

by

Anders Høst-Madsen and Chr. Caspersen

Dantec Measurement Technology

Abstract

Over the past decade, there has been very little interest in using the laser Doppler Anemometer to measure turbulent spectra. One reason for this is the requirement to instrumentation, amount of data and the requirement to low noiselevel in the results. Furthermore the work that was started in the seventies by Gaster and Roberts and by Buchhave et al. was never followed up to a level of practical implementation. The fact that the random sampling was difficult to unify with the upcoming stream of Fourier processing methods set a stop to the further development of method and algorithms for dealing with this subject.

However with the present state of the art in optics, signal processing and data handling facilities, it is time to renew the interest in this field, as a large number of applications are of interest both in pure fluid mechanics and also in a number of industries. This paper is trying to answer the question of the requirements to the equipment for this type of measurements and also to set some limitations in how far, it is possible to come in terms of spectral resolution and frequency.

The research is focussed on the high frequency end of the measured spectrum. The limitation in frequency is analyzed and supported by measurements. The influence from the size of the measurement volume is investigated by using off-axis observation angles in order to maximize the spatial resolution of the measurement, while maintaining the signal to noise ratio.

Most of the work until now in estimation of turbulence spectra has been done with hot-wires, so it makes sense to do a comparison with hot-wires to a certain extend, as the hot-wire also has it's own limitations These limitation are however well-known and they are reported extensively in the literature. As the hot-wire is most suitable for lower turbulence intensities, these comparisons are performed in a well developed turbulence, with a degree of turbulence below 10%.

The conclusion of the paper will give a framework for the requirements to spectral estimation and an overview of the limitations that can be expected.

Introduction

In order to get an overview of the parameters influencing the quality of the spectrum, it is reasonable to divide these parameters into three different groups. The first group is related to the parameters influencing the signals received from the optical system and transmitted to the signal processor. This group will include laser noise, optical misalignment and particle interaction. The second group is related to the signal processing, both in terms of processing principles and efficiency of the realization of the principle. Finally the third group is related to the data-processing, as a number of different methods can be applied.

After an estimation of the influence of these parameters an experiment is performed, where the parameters can be verified.

The experiment is set up in a jet where the degree of turbulence can be adjusted by changing the axial position of the measurement point in the centerline of the jet. In this way it is also possible to select the scale of the turbulence. The flow is very low turbulent and very well conditioned before it comes to the outlet nozzle grid. A series of measurements are performed with a hot-wire in the centerline of the jet, both close to the nozzle and at a number of locations downstream. At the same locations a laser Doppler Anemometer is positioned in order to compare the measured turbulence intensities and the spectra by the two measurement principles. In order to understand the results a number of contributions to the variance of the LDA data are estimated, both from theory and from experimental verifications. The experimental parameters are evaluated in order to find the best possible selection of optical and processing parameters.

Laser noise

In this work an air cooled Ar-Ion laser is used. This can under certain circumstances cause problems. The mechanical vibrations from the blowers can in a traditional optical system contribute to a movement of the measurement volume and in this way cause an artificial contribution to the variance. This effect is eliminated by using an optical fibre between the measurement probe and the laser. The mechanical vibration from the blowers can also cause instabilities in the cavity of the laser

,and in this way cause additional noise in the signal. In this work we found no evidence for the existence of such effects.

The variance generated by imperfect alignment of the optics.

If a slight misalignment takes place, it can result in a signif cant variance of the data due to a varying distance between the fringes in the direction of the measurement volume. This fact has been verified by several authors, the latest and most thorough investigation has been performed by Miles and Witze in ref. 1. What is interesting is, that there in many situations is a maximum of the variance at a relatively small misalignment, while larger misalignments are causing less variance. In fig. 1 a typical relation between relative misalignment and error, which will correspond to variance, is shown. One method to reduce the variance from the misalignment effect is to reduce the observation length of the measurement volume by using off-axis reception, and specifically using a spatially limited reception volume. However this will reduce the data-rate, as only particles passing the common volume will contribute to the signal. The influence from this will be discussed later. An estimation of the effect depends on many parameters. Only one example is given in fig. 1

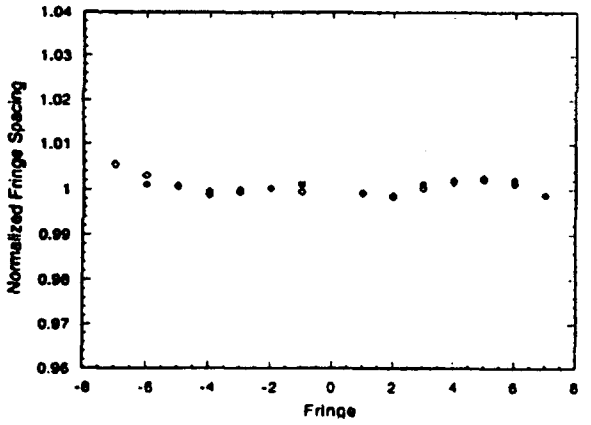

fig. 1 Variation in the fringespacing at z=0

Particle interaction

There has recently been done some work by Ruck ref. 2, pointing at the fact, that particles in the beams outside the measurement volume will cause optical distortions of the fringepattern in the measurement volume, and in this way increase the variance of the data. It is however more likely, that these effects will cause problems for the signal processor and result in rejected signals, rather than giving validated data with an increased variance. As concluded in ref. 2 the distortion effect is reduced when the number of fringes used in the determination of the Doppler frequency is increased. The effect is minimized by a low concentration of particles, which on the other hand is a disadvantage in the further processing schemes. The effect can not be completely disregarded, but it is difficult to quantify.

The signal to noise ratio

Although a significant number of factors are influencing the signal to noise ratio, and as will be shown later will influence the final limitation for the generation of a spectrum, it is important to point out, that the very fundamental parameters like particle size. laser power, intensity in the measuring volume and the receiver aperture always should be optimized in order to have the best possible signal to noise ratio.

In this experiment it is possible to optimize the parameters to an extent, which normally will be prevented by practical considerations.

The processing methods

Although a significant number of processing methods are available, there are some basic limitations to the uncertainty of the individual realizations. If the processing method is based upon a spectrum analysis of the burst, the lowest relative uncertainty on the individual realization is determined from ref.3 as

$$\frac{\delta u_i}{u_i} = \frac{1}{T_m N_m}\left[\frac{1}{B}\left(\frac{n'}{s}\right)^2\right] \quad (1)$$

where T_m = The transit time
B = The bandwidth
N_m = The number of fringes
$\left(\frac{n'}{s}\right)$ = The inverse signal to noise ratio

From this equation it is clear, that the signal to noise ratio must be held at the highest possible level. On the other hand it is also clear, that even a moderate number of fringes combined with reasonable transit time will result in a very low inherent variance on the data. An other interesting fact is the bandwidth independence in the parenthesis. The ideal spectrum analysis processor will be independent of the bandwidth. This statement will not hold in the realized process as proved by the experiments.

The processing methods

In order to compare two different realizations of processors, a Dantec Burst Spectrum Analyzer and a Dantec Flow Velocity Analyzer are compared, when they measure on the same signal. The basic processing methods for the two processors are given in fig. 2 and 3. The Burst Spectrum Analyzer is sampling the signal with a 4-bit resolution and performing a complex FFT on the signal, while the Flow Velocity Analyzer is working according to the Cross Covariance principle. The two processors are described in ref. 4 and ref. 5 in more details. Besides the difference in measuring principle, the two processors are also different in operation. While it is possible to optimize the BSA on a number of parameters, the optimization of the FVA is relatively limited. Only the range and the validation level can be adjusted.

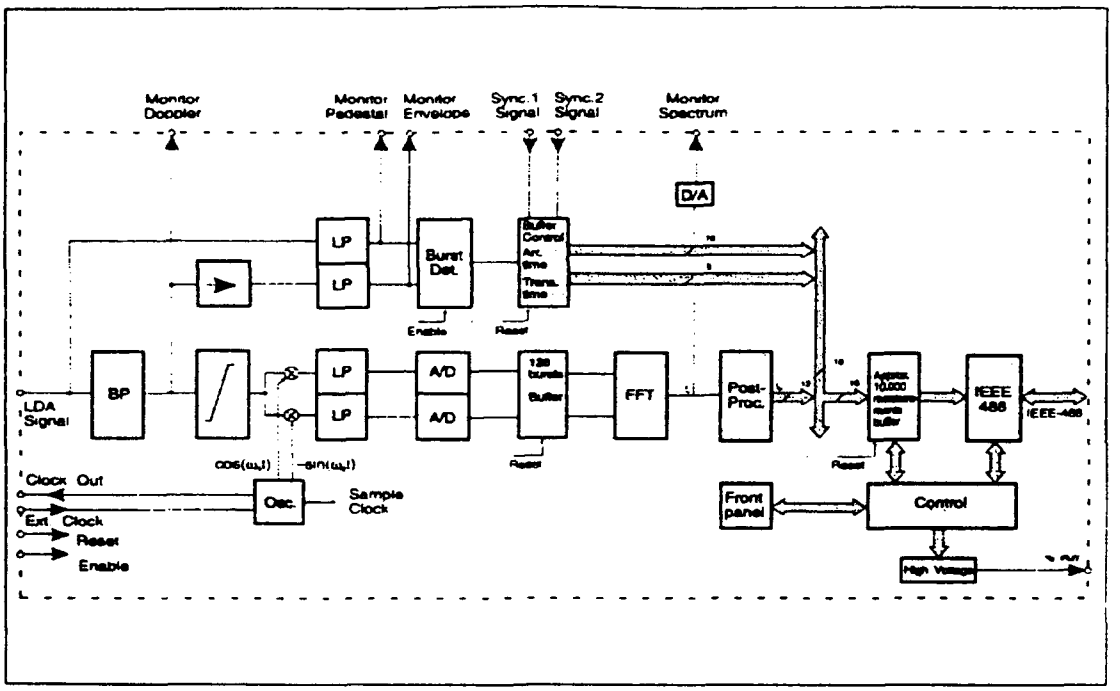

fig. 2 The principle operation of the BSA

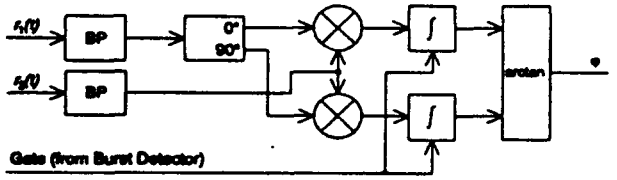

fig. 3 The principle operation of the FVA

The theoretical limitations in the accuracy of the results based upon the resolution of the processor

One issue that has caused great concern is the resolution on the output of the processors. This is a bit strange as it will be proved to have only a insignificant influence on the results from the process, independently if the output is used to form ordinary statistical informations like mean values and RMS values, or it is used to generate turbulence spectra. A much more significant factor is the accuracy the processor is able to provide. The influence of the quantization on the output can easily be estimated from ref. 6

$$\sigma^2 = \frac{\Delta^2}{12} = \frac{2^{-2b}}{12} \qquad (2)$$

where σ^2 is the noisepower
and b is the number of bits
A little more elaboration will give

$$SNR = 6b - 1.24dB \qquad (3)$$

A 50 dB SNR will consequently require between 8 and 9 bits

This result is indicating the very limited value in adding bits to the output of a processor. It will only make sense if the processor itself has an extremely high accuracy. In most applications the high resolution on the output will therefore have an insignificant improvement on the results.

The influence of limited resolution on the generation of turbulence spectra

The somewhat surprising result did lead to a recalculation on a recorded data file, where the bits were removed one after the other. The results are given in the fig. 4a - 4d. Also here is a clear indication, that the limitation in the spectrum does not relate to the limited resolution, until the resolution decreases to 4 bits. With 4 bits the maximum span that can be obtained is according to eq. 3: SNR = 22.76 dB. According to fig. 4a - 4d this is also what can be obtained as the ratio between the signal and the noise level. For any higher resolution than 4 bits on the output, the resolution has no influence on the noiselevel.

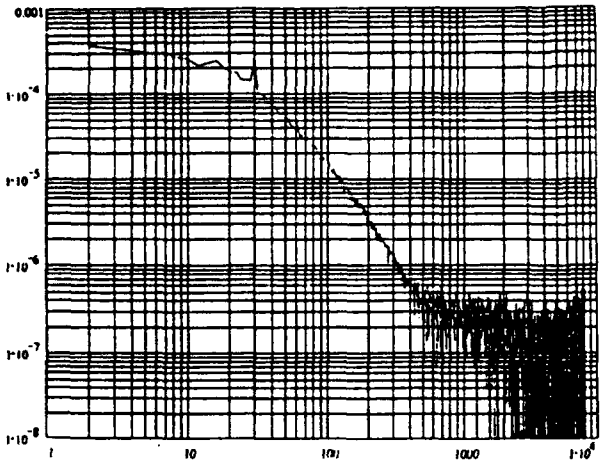

fig. 4a Turbulence spectrum with 12 bits resolution

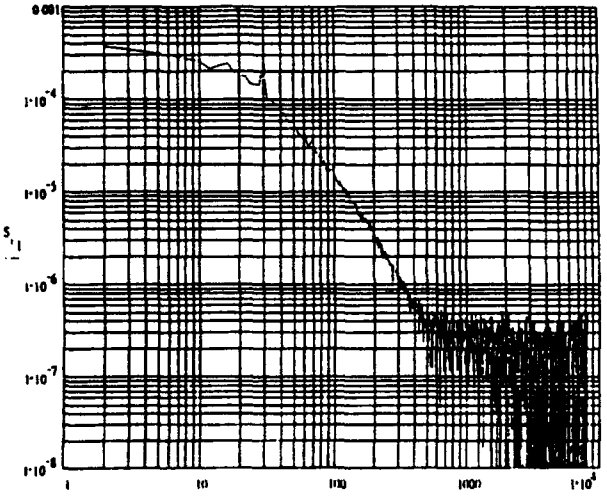

fig. 4b Turbulence spectrum with 8 bits resolution

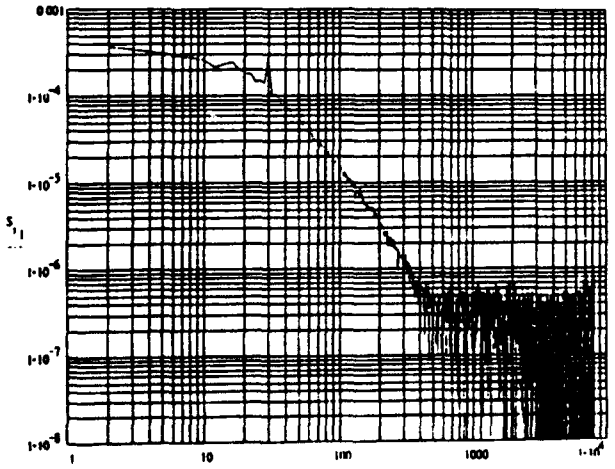

fig. 4c Turbulence spectrum with 6 bits resolution

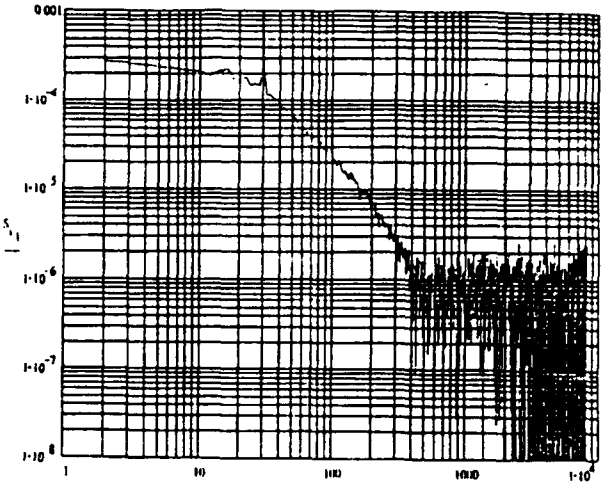

fig. 4d Turbulence spectrum with 4 bits resolution

The experimental set-up

The generation of a Low Turbulence Jet

A low turbulent jet is used to generate a variable degree of turbulence along the axis. The nozzle is shown in fig. 5. The degree of turbulence at the exit of the nozzle is measured by a hot-wire system to 0.4%. The low turbulence is achieved by using a large settling chamber with absorbing walls. This is combined with a strong contraction and a configuration of flowstraightners and grids in order to minimize the turbulence.

The nozzle is running at an extremely constant velocity at around 5 m/sec. There is no facility to vary the velocity

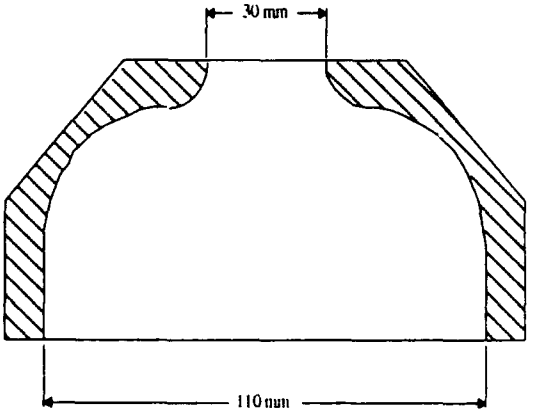

fig. 5

The seeding system

The seeding system is a smokegenerator "Fog 2001" from Dantec-Invent. The generator is positioned at the intake to the ventilators in the box. Using this seeding generator, it is possible to adjust to any degree of seeding density required. As it will be discussed later, the maximum possible data-rate is far

below what is achievable from the seeding generator itself and only determined by the transit time. Due to possible contamination of the hot-wire probe, the seeding is switched off, when hot-wire measurements are done, and the hot-wire is removed, when the LDA is used. It is assumed, that the seeding has no influence on the level or development of the turbulence.

The Hot-Wire System

The Hot-Wire system is the Dantec StreamLine System. It is used with a Dantec P01 probe. This probe is not the most ideal probe as it is relatively long (3 mm) however the active area is only 1.25 mm. The probe is positioned so it is at exactly the same position as the receiving measuring volume. This is easily checked using the large aperture receiver described in the section on the LDA system. It is possible to see the image of the wire on the pin-hole plate and adjust both the transverse position and the distance by using the focus adjustment. The bridge is the standard 1:20 bridge combined with a signal conditioner and and A/D converter to the PC. The probe is calibrated by the automatic Dantec calibration system in the range 0 - 10 m/sec.

According to specifications it can be expected that the hot-wire system is able to measure a degree of turbulence lower than 0.3%. This will be sufficient for this application

The LDA System

An LDA System is established to measure the vertical component of the flow. It consists of a 85 mm diameter 41X820 Dantec FiberFlow Probe mounted with a 55X29 Beamtranslator and a 55X12 Beamexpander. The probe is able to measure two components of the flow, but only one component is used. The probe is receiving the laser light from a 60X41 Transmitter Box. The focal length is selected to 310 mm and the beamseparation to 64 mm. This will give a calibration factor of 2.504 m/sec/MHz. The laser is an aircooled Ar-Ion laser running at 100 mW. Due to the low laser power, the set-up has facilities to measure in both forward and back scatter. In the forward scatter set-up a receiving system normally used in Particle Dynamic Analyzer is used in order to obtain a large receiving aperture. As the purpose of this work is to find the limitation of the system, the forward scatter configuration has advantages in terms of a better signal quality and therefore less added noise to the signals.

Limitation on data-rate

In the spectral measurements with the LDA, there is a strong demand to have the highest possible data-rate. As it will be shown later in this paper, it is realistic to measure turbulence spectra up to 1/5 of the average data-rate. Several things can be done to increase the data-rate. The most natural thing to do is to increase the seeding density. However, the seeding density can not be increased infinitely. Sometimes there is a natural limitation to the seeding density imposed by the constraints on the measurement set-up. It is not always possible to add seeding. Even if the seeding density can be increased, there is a fundamental limit to the data-rate imposed by the measurement volume size. When there are two or more particles in the measurement volume at the same time, this will usually not give a valid burst. A simple argument therefore shows that

$$D_{max} = 1/\Delta t \approx u/\Delta x$$

where Δt is the transit time, u the velocity and Δx the dimension of the measurement volume in the x direction. This gives however a too optimistic estimate, since the particles usually do not arrive equidistantly.

If we suppose that the seeding is uniform, the particles will arrive after a Poisson process. The probability to have exactly one particle in the measurement volume is given by

$$P_1(1) = \lambda\Delta t e^{-\lambda\Delta t}$$

where λ is the seeding rate (the number of particles passing through the measurement volume per unit time). If we assume that a burst is only valid, when there is exactly one particle in the measurement volume, the valid data-rate is therefore

$$D_{valid}(\lambda) = \lambda^2 \Delta t e^{-\lambda\Delta t}$$

This is maximum for

$$\lambda = 2/\Delta t$$

giving a maximum data-rate of

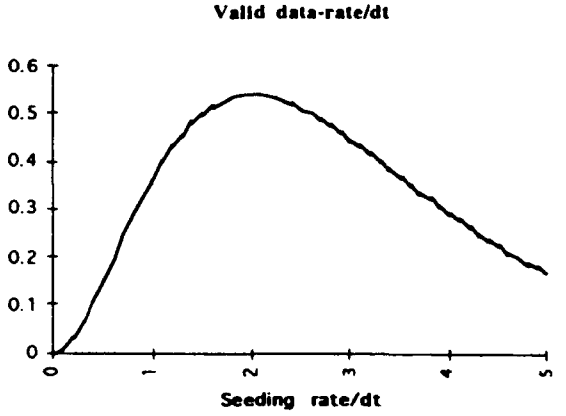

fig. 6

$D_{max} = 4e^{-2} / \Delta t \approx 0.5 / \Delta t \approx 0.5\ u / \Delta x$

The figur 6 shows the validation percentage (the number of bursts when only one particle is in the measurement volume at a time) and the valid data-rate.

In our experiment the Damtec/Invent Fog 2001 seeding generator was used. With this seeding generator, it is possible to vary the seeding rate to any level, adding more seeding, did not increase the data-rate. The maximum data-rate we we able to obtain was around 13 - 15 kHz. The average transit time was around 0.03 ms. Inserting this value into the above formula we get a maximum data-rate of:

$$D_{max} = 0.54 / \Delta t = 18kHz$$

which is in very good agreement with the prediction.

The Turbulence Spectrum

The spectrum is measured by the Hot-Wire system at a distance of 2 diameters over the nozzle. At this position, the turbulence has developed quite well, and it is possible to detect the structure. The spectrum is in fig. 7. Even here, the spectrum is dominated by the generating frequency on 100 Hz. The decay has a slope of 1.89 until a frequency at 1100 Hz where the slope increases to 3.4. The spectrum is only valid to 8 kHz, where noise is taking over. The peak at 14 kHz is electronic noise.

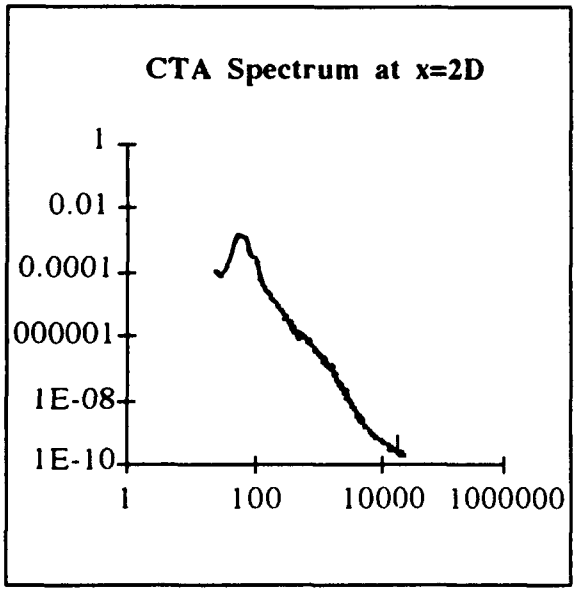

fig. 7

Measurement of turbulence level and measurement of turbulence spectra using the FVA

In the region close to the outlet, the flow is entirely dominated by the fundamental frequency from the outlet, and it is not possible to receive information on the spectrum, neither from the CTA nor from the FVA. There are a number of peaks existing both in the spectrum from the CTA, and from the spectrum from the FVA. The peaks can not be related to any well defined frequency in the system, so at the present time, we have no explanation for these peaks.

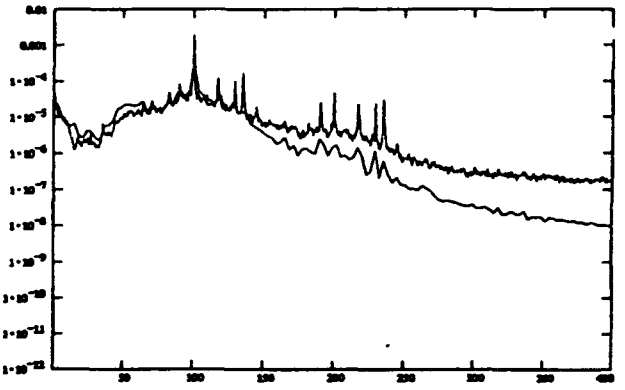

fig. 8

In order to evaluate to which limitation, it is possible to get reliable information from the spectrum all the remaining measurement were made at a height of 2 diameters above the nozzle. As a reference all the measurements are compared to the CTA measurements. In the processing a number of parameters can be changed for evaluation of the effect from different processing schemes.

If a 2 times oversampling is used, the minimum bias window and no noise correction is applied the result is shown in fig. 9. Both the variance and the noise is dominating at a relatively high level, in this case 10^{-7}.

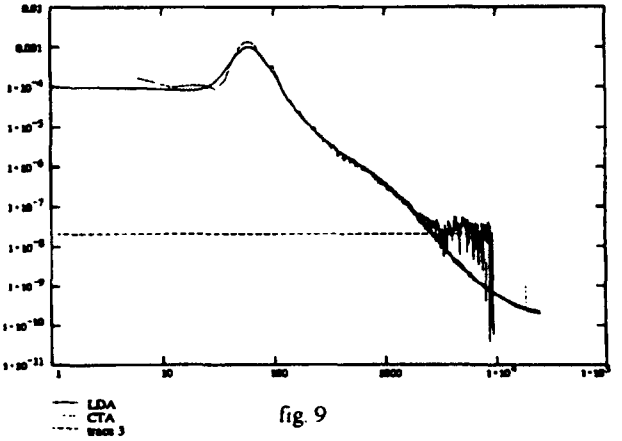

fig. 9

If 4 times oversampling is used and a minimum bias window is applied with a width of 0.125 and no noisecorrection is applied the result is shown in fig. 10. The variance is now suppressed significantly and the noiselevel is now close to 10^{-8}. In relation to the maximum achievable data-rate at 13 - 14 kHz the spectrum is now coming to 3 kHz, very well according to the previous statements.

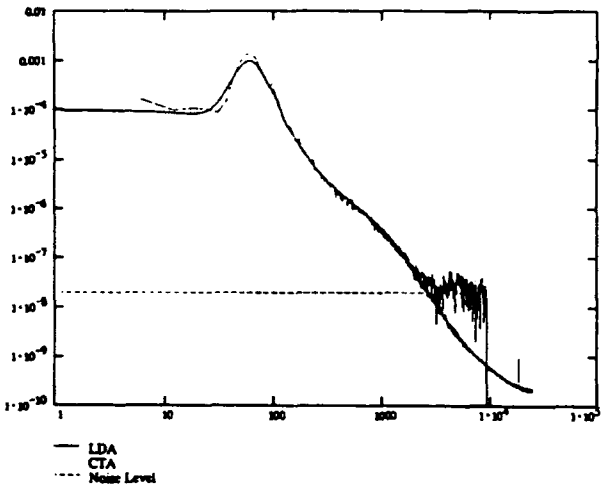

fig. 10

If 4 times oversampling is used and a minimum bias window and noisecorrection is applied, the best result is obtained. This is given in fig. 11

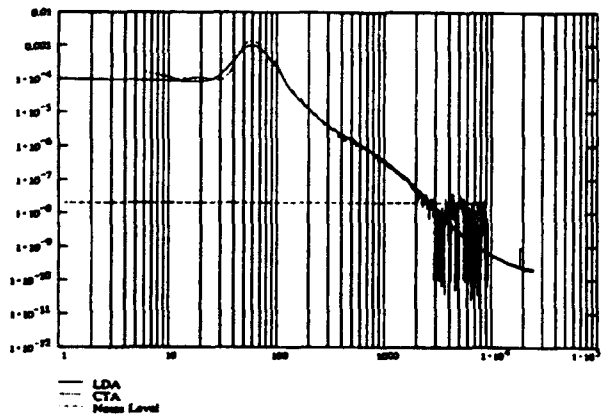

fig. 11

The limitations to the estimation of the spectrum

If the best possible choice is taken in terms of oversampling, windowing and noisecorrection, and the number of samples are limited to app. 1 mill. samples, the best spectrum in terms of low variance and low noise is displayed in fig. 11. In this figure, it is displayed with the CTA spectrum measured at the same position. If a higher frequency should be measured, it will be necessary to reduce the probevolume further. This will however lead to other limiting factors.

Using the information for the highest possible data-rate and the 5 times oversampling mentioned in the "Limitation on data-rate section", it can be concluded, that the maximum frequency, that can be obtained will be:

$$f_{max}=(1/5)(1/2)(u_x/\Delta x)$$

where u_x is the mean velocity and Δx is the $1/e^2$ dimension of the measurement volume in the x direction. In the present experiment u_x is 5 m/sec and Δx is 150 μ. The predicted maximum frequency will be 3 kHz, which is also seen from fig. 11.

Summery and Conclusion

The maximum frequency, that can be determined in a spectrum based upon LDA measurements, is found from theory and verified experimentally. A number of the limiting factor in estimation of spectra are described. The following can be concluded:

1. It is possible to make reliable spectra with LDA, which will follow those obtained by CTA to a large extent, only limited by the data-rate and the practically obtainable SNR

2. It is important to have a good SNR

3. The arrival time registration is important.

4. Improved resolution on the processor does not improve the spectrum. The quantization noise is normally far below the inherent noise in the signal.

5. There is a maximum data-rate for a given transit time, that can not be surpassed, additional seeding will decrease the data-rate.

6. By proper processing, it is possible to suppress the noiselevel by almost one decade.

References

1.

Fringe field quantification in an LDV probe volume by use of a magnified image

P. C. Miles, P. O. Witze

Experiments in Fluids 16, 330 - 335

Springer Verlag 1994

2

Limited accuracy of turbulence measurements in laser Doppler anemometry

B. Ruck, B. Pavlowski

Proceedings from the Fifth International Conference on Laser Anemometry

23 - 27 August 1993

Koningshof, Veldhoven, The Netherlands

3.

Three-component LDA Measurements

P. Buchhave

DISA Information No. 29

January 1984

4.

Spectrum Analysis of LDA Signals

L. Lading

Proceedings of an International Specialists Meeting on

The Use of Computers in Laser Velocimetry

ISL May 18-20 1987

5.

Burst Detection in Phase/Frequency Processors

Knud Andersen and Lars Lading

Proceedings from the Fourth International Conference on Laser Anemometry, Advances and Applications

Cleveland, Ohio

August 5 - 9, 1991

6.

Digital Signal Processing

Alan V. Oppenheim and Ronald W. Shafer

Prentice-Hall Inc. New Jersey

1975

THREE-DIMENSIONAL ASSESSMENT OF SPECTRAL BIAS IN LDV

Do Hwan LEE and Hyung Jin SUNG

Department of Mechanical Engineering
Korea Advanced Institute of Science and Technology
373-1 Kusong-dong Yusong-gu Taejon 305-701 Korea

ABSTRACT

A three-dimensional evaluation is made of the spectral bias in the use of a laser Doppler velocimeter (LDV). An improved version of autoregressive vector model is proposed. The particle arrival time statistics are modeled as a doubly stochastic Poisson process. Four well-known spectral algorithms, which are the sample and holds interpolation method (SH), the nonuniform Shannon reconstruction technique (SR), the direct transform method (RG), and the transit time weighting method (TW), are compared with the theoretical spectra for various sampling and flow conditions. Assessment is made of these processing algorithms over a broad range of data densities ($0.05 \le d.d. \le 5$) and turbulence levels (t.i.=0.3, 1.0). The influences of the ratio of the minimum number of zero-crossings to the maximum fringe number (Q), and the frequency shifting on spectral distortion are also examined.

1. INTRODUCTION

The power spectral analysis of fluid velocity by laser Doppler velocimeter (LDV) is crucial to the understanding of dynamic characteristics in turbulent fields. Most of the experimental works estimating the power spectra have been made with the conventional thermal probes. However, due to their limitation in tracking high turbulent fluctuations and the hostility to discriminating the flow directions, they are not well-suited for the measurement of recirculating flows with high turbulence intensity. In spite of the adequacy of LDV to the aforestated flow situations, relatively scarce studies have been reported concerning the power spectral estimations with LDV. One reason of these rarities is that the probabilistic nature of sampling times in a burst type LDV is conditional Poisson depending on the system parameters and velocity fields. Since Gaster and Roberts (1977) have devised the direct estimator based on random sampling times, which is basically independent of the velocity field, the attention of recent studies has been gradually moved to the precise evaluations of spectra including the effect of sampling conditions and flow conditions on sampling times (Buchhave et al. 1979; Tropea 1987, Adrian & Yao 1987; Veynante & Candel 1988; Lee & Sung 1994). As the probability of sampling times invokes significant implicit nonlinearities into the sample function density of flow field, the theoretical approach to spectral estimation is highly subjected to restriction. Furthermore, the experimental verification of the variability and the spectral bias is also limited without a confident measurement system or estimation technique, especially in a three-dimensional high turbulent flow field. Systematic assessment of statistical estimators through numerical simulations containing the various sources causing the sampling bias is, therefore, an attractive route to clarify the errors and the confidence limit of estimators.

In order to analyze the spectral information properly obtained from applicable turbulent fields with LDV, a reliable spectral estimator appropriate to the flow condition should be, of course, selected at first. The main purpose of this paper is to examine available ranges of various spectral estimators and to enlarge the comprehension of the spectral bias induced by essential turbulent quantities and sampling parameters. For the systematic evaluation of several spectral estimators, numerical comparisons are made with the known spectra, which is obtained from the analytical derivations from the given autoregressive model (Tropea 1987; Lee & Sung 1994). Variations of sampling parameters pertaining the bias in LDV are selected over a wide range, such as the data density ($d.d. = \lambda_m T_\lambda$), the relative velocity magnitude by frequency shifting ($R = u_s / U$) and the ratio of the minimum number of zero-crossings N_c to the maximum fringe number N_f ($Q = N_c / N_f$), assuming a counter type signal processor. Furthermore, the influence of turbulent quantities on spectral bias, i.e., the turbulent intensity ($t.i. = \sigma_u / U$) and the Reynolds shear stress coefficients ($R_{uw} = \langle u_i w_i \rangle / (\sigma_u \sigma_w)$, $R_{vw} = \langle v_i w_i \rangle / (\sigma_v \sigma_w)$ and $R_{uv} = \langle v_i w_i \rangle / (\sigma_v \sigma_w)$), is also systematically scrutinized.

Statistics of the particle arrival times with bias are

generally modeled as a doubly stochastic Poisson process which is a conditional Poisson process with the temporal expected rate parameter depending on the velocity fields and various sampling conditions, which include the type of signal processor and the optical parameters (McDougall 1980). An autoregressive vector model with specified second-order moments, is adopted to construct a primary velocity field (Buchhave et al. 1990; Fuchs et al. 1992). It is then utilized to construct an Poisson process conditional on the invertible mean-value function of velocity fields and sampling parameters by the time-axis transformation (Snyder 1975).

As indicated by Fuchs et al. (1992), if the experiment is performed in high turbulent flow fields, e.g., the recirculating flow behind a backward-facing step, the instantaneous data rate is influenced not only by the velocity component u_i to be measured but also by other subsidiary components, i.e., the transverse component v_i and spanwise component w_i. These subsidiary components cause the substantial nonlinear change of the correlation between the sampling process and the velocity field, and then, they yield statistical bias in a nonlinear fashion. This aspect strongly calls for the three-dimensional treatment, in which the problem of three-dimensional spectral bias is also accompanied concurruntly. In order to resolve this spectral bias, the generation process of a three-dimensional autoregressive model should be preceded. It is notable that two recent studies have been attempted to develop the generation procedures from three-dimensional turbulent flow fields with the prescribed statistical parameters for evaluating the statistical bias (Buchhave et al. 1990; Fuchs et al. 1992). However, it is revealed that the model of Buchhave et al. (1990) did not consider the dependency of spanwise component w_i on other velocity components, i.e., u_i and v_i. Furthermore, these previous models were not adequate for a qualitative comparison between the spectral results from one-dimensional velocity field and those from three-dimensional velocity field unless the autoregressive parameters are fixed at certain values. In the present study, a promising three-dimensional generation process is developed. The present model improves these prior drawbacks and the detailed generation procedure will be recapitulated in section 2.

With a view toward extending the preceding two-dimensional approach (Lee & Sung 1994), this paper presents a full three-dimensional assessment of spectral bias in LDV. Toward this end, four well-known processing algorithms for spectral estimation are evaluated from nonuniformly spaced samples. The first is known as the direct transform of Roberts and Gaster (1980). This approach is based on the random sampling instants and the assumption of arrival process which is independent of the velocity field. Hereafter, this method is designated by RG. In order to verify the capabilities of the transit time weighting method (hereafter referred to as TW) of Buchhave (1979) for the case of low data density and high turbulent intensity, TW is evaluated. In the present spectral estimation, the transit time simulator developed by Buchhave et al. (1990) is employed, where the values of transit time are utilized in the spectral estimation. In the third, the random sampling sequences are periodically resampled by the sample and hold interpolation, and the resulting time series is applied to a conventional periodogram to obtain a power spectral density function (denoted by SH). The last is the nonuniform Shannon reconstruction algorithm (SR) for randomly sampled data, and the way of obtaining power spectra is similar to the above-stated SH. (Veynante & Candel 1988). Details regarding the aforestated construction algorithms are well compiled in Lee and Sung (1994).

2. THREE-DIMENSIONAL VELOCITY FIELD

The present section describes the three-dimensional generation procedure of velocity field using a first order autoregressive vector model (ARV). As in the two-dimensional generation process by Lee and Sung (1994), the first order ARV can be specified by three autoregressive parameters:

$$\begin{aligned} u_t &= \phi_{11} u_{t-1} + a^*_{ut}, \\ v_t &= \phi_{22} v_{t-1} + a^*_{vt}, \\ w_t &= \phi_{22} w_{t-1} + a^*_{wt}, \end{aligned} \tag{1}$$

where a^*_{ut}, a^*_{vt} and a^*_{wt} are mutually correlated random numbers with Gaussian probability distribution. The uncorrelated random numbers a_{ut}, a_{vt} and a_{wt} can be extracted from the correlated random number vector a^*_t by using a symmetric transformation matrix Θ:

$$\begin{aligned} u_t &= \phi_{11} u_{t-1} + \theta_{11} a_{ut} + \theta_{12} a_{vt} + \theta_{13} a_{wt}, \\ v_t &= \phi_{22} v_{t-1} + \theta_{12} a_{ut} + \theta_{22} a_{vt} + \theta_{23} a_{wt} \\ w_t &= \phi_{33} w_{t-1} + \theta_{13} a_{ut} + \theta_{23} a_{vt} + \theta_{33} a_{wt}. \end{aligned} \tag{2}$$

In order to determine Θ from the statistical moments, the components of vector a_t should be prescribed to have unit variance and zero mean. By forming the expected values of products of velocity samples, the following relations can be derived for the transformation variables of Θ based on the preadjusted Reynolds stress coefficients and the corresponding autoregressive parameters:

$$\begin{aligned} (1-\phi_{11}^2)\sigma_u^2 &= \theta_{11}^2 + \theta_{12}^2 + \theta_{13}^2, \\ (1-\phi_{22}^2)\sigma_v^2 &= \theta_{12}^2 + \theta_{22}^2 + \theta_{23}^2, \\ (1-\phi_{33}^2)\sigma_w^2 &= \theta_{13}^2 + \theta_{23}^2 + \theta_{33}^2, \\ -(1-\phi_{11}\phi_{22})R_{uv}\sigma_u\sigma_v &= \theta_{11}\theta_{12} + \theta_{12}\theta_{22} + \theta_{13}\theta_{23}, \\ -(1-\phi_{11}\phi_{33})R_{uw}\sigma_u\sigma_w &= \theta_{11}\theta_{13} + \theta_{12}\theta_{23} + \theta_{13}\theta_{33}, \end{aligned} \tag{3}$$

$$-(1-\phi_{22}\phi_{33})R_{vw}\sigma_v\sigma_w=\theta_{12}\theta_{13}+\theta_{22}\theta_{23}+\theta_{23}\theta_{33},$$

where the Reynolds stress coefficients are denoted as,

$$R_{uv}=-\frac{<u_tv_t>}{\sigma_u\sigma_v},\ R_{uw}=-\frac{<u_tw_t>}{\sigma_u\sigma_w},\ \text{and}\ R_{vw}=-\frac{<v_tw_t>}{\sigma_v\sigma_w}.$$

The matrix Θ is obtained by solving Eq. (3) iteratively. Note that, since the left hand side of Eq. (3) may not guarantee nonnegative definite in matrix form, it is hard to decompose the right hand side into two triangular matrices as the case in a two-dimensional field (Lee & Sung 1994). The covariance functions are rearranged as one following equation by taking product of "t"-th sample and "t-k"-th sample:

$$\Gamma_{\alpha\beta}(k)=\Gamma_{\alpha\beta}\phi_{\beta\beta}^{k}, \tag{4}$$

where $\Gamma_{\alpha\beta}$ denotes $<\alpha_t\beta_t>$.

The expected spectra can be calculated after some algebraic manipulations with the aid of Z-transformation and matrix techniques as follows:

$$E_{uu}(f)=\frac{2(1-\phi_{11}^2)\sigma_u^2}{1+\phi_{11}^2-2\phi_{11}\cos 2\pi f},$$

$$E_{vv}(f)=\frac{2(1-\phi_{22}^2)\sigma_v^2}{1+\phi_{22}^2-2\phi_{22}\cos 2\pi f},$$

$$E_{ww}(f)=\frac{2(1-\phi_{33}^2)\sigma_w^2}{1+\phi_{33}^2-2\phi_{33}\cos 2\pi f}, \tag{5}$$

$$\begin{aligned}E_{uv}(f)=\{&-2(1-\phi_{11}\phi_{22})R_{uv}\sigma_u\sigma_v[1+\phi_{11}\phi_{22}-(\phi_{11}+\phi_{22})\cos 2\pi f\\&+i(\phi_{11}-\phi_{22})\sin 2\pi f]\}/\{(1+\phi_{11}\phi_{22})^2+\phi_{11}^2+\phi_{22}^2\\&-2(1+\phi_{11}\phi_{22})(\phi_{11}+\phi_{22})\cos 2\pi f+2\phi_{11}\phi_{22}\cos 4\pi f\}\end{aligned}$$

$$\begin{aligned}E_{uw}(f)=\{&-2(1-\phi_{11}\phi_{33})R_{uw}\sigma_u\sigma_w[1+\phi_{11}\phi_{33}-(\phi_{11}+\phi_{33})\cos 2\pi f\\&+i(\phi_{11}-\phi_{33})\sin 2\pi f]\}/\{(1+\phi_{11}\phi_{33})^2+\phi_{11}^2+\phi_{33}^2\\&-2(1+\phi_{11}\phi_{33})(\phi_{11}+\phi_{33})\cos 2\pi f+2\phi_{11}\phi_{33}\cos 4\pi f\}\end{aligned}$$

$$\begin{aligned}E_{vw}(f)=\{&-2(1-\phi_{22}\phi_{33})R_{vw}\sigma_v\sigma_w[1+\phi_{22}\phi_{33}-(\phi_{22}+\phi_{33})\cos 2\pi f\\&+i(\phi_{22}-\phi_{33})\sin 2\pi f]\}/\{(1+\phi_{22}\phi_{33})^2+\phi_{22}^2+\phi_{33}^2\\&-2(1+\phi_{22}\phi_{33})(\phi_{22}+\phi_{33})\cos 2\pi f+2\phi_{22}\phi_{33}\cos 4\pi f\}\end{aligned}$$

$$E_{vu}(f)=E_{uv}(-f),\ E_{wu}(f)=E_{uw}(-f),\ E_{wv}(f)=E_{vw}(-f).$$

In the above, in order to simulate the given flow conditions, the mean velocity vector, the r.m.s. vector and the Reynolds stress coefficients should be prescribed. The transformation matrix Θ in Eq. (3) is obtained by an iterative method or an optimal solution procedure.

3. GENERATION OF CONDITIONAL POISSON SAMPLING PROCESS

In LDV measurements, the conditional mean occurrence rate at which the particles pass through the measuring volume is known as (Buchhave et al. 1979; McDougall 1980)

$$\lambda_t=C|\vec{V}_t|A(\vec{V}_t) \tag{6}$$

where A is the cross-sectional area of the measuring volume in the plane normal to the velocity vector $\vec{V}_t$ and C is the mean concentration of particles. However, Eq. (6) is constructed on the assumption that the particles are uniformly distributed in space, i.e., a constant value of C, and the velocity gradient is not seriously changed in the vicinity of the measuring volume. If we look into the probe volume, it is approximated by an ellipsoid, which is enclosed by $1/e^2$ boundary of the modulation depth of the fringe pattern existing in the intersection region of laser beams. Furthermore, the condition for a signal measurement assuming the use of a counter type signal processor makes the precise derivation of λ_t (McDougall 1980):

$$\lambda_t=\begin{cases}\dfrac{C\pi N_f^2d_f^2}{4}\cos(\theta/2)\cot(\theta/2)\\ \cdot\sqrt{(u_t^2+v_t^2\sec^2(\theta/2)+w_t^2\tan^2(\theta/2)}\cdot\chi, & \chi\geq 0,\\ 0, & \chi<0.\end{cases} \tag{7}$$

where $\chi=[1-\dfrac{Q^2}{(u_t^2+u_s)^2}(u_t^2+v_t^2\sec^2(\theta/2)+w_t^2\tan^2(\theta/2))]$.

N_f, d_f and θ denote respectively the number of fringe plane intervals, the fringe spacing and the angle between the laser beams. The parameter Q is defined as the ratio of the minimum number of zero-crossings N_e to the maximum fringe number N_f. u_s is the velocity magnitude by frequency shifting. If we use other types of signal processors, Eq. (7) can be slightly modified according to the knowledge of their characteristics. Once a primary velocity field is made, a Poisson sampling process with λ_t in Eq. (7) is generated subsequently by a nonlinear arrangement of time axis of a homogeneous Poisson process with unit intensity (Lee & Sung 1994).

In an effort to examine the relation between the mean sampling rate and the effective bandwidth pertaining the significant spectral contents contained in flow, it is common practice to define a non-dimensional data density. If the Taylor micro time scale is used as a flow characteristic time scales of second order moments, which is defined by

$T_\lambda = \sigma_u / \sqrt{<(du/dt)^2>}$, the data density (d.d.) is a measure of mean number of sampling during the periods of one standard deviation change of the random velocity u(t):

$$d.d. = \lambda_m T_\lambda \tag{8}$$

where λ_m is the mean sampling rate or the average intensity of sampling process. Three regions of data density are defined in this paper, as were classification by Edwards (1987); i.e.,

$$\begin{array}{ll} d.d. > 5, & \text{for high data density,} \\ 5 \geq d.d. \geq 0.05, & \text{for intermediate data density,} \\ 0.05 \geq d.d., & \text{for low data density.} \end{array} \tag{9}$$

4. RESULTS AND DISCUSSION

For a quantitative measurement of spectral bias by means of the present stochastic simulations, a large number of secondary samples and consequent averages are required to reduce the statistical variability to an acceptable level. In these respects, secondary samples of 200,000 are generated in this study. The short block with fixed length of 1,024 normalized times is used for averaging operations, which renders final spectra to be adequate for the study of spectral bias. However, as is well-known, in the first two processing methods (RG and TW) based on random sample times, a satisfactory alleviation of high frequency variability is generally difficult. Two values of turbulent intensity, based on the streamwise components, are typically chosen as the low and high turbulence flow, i.e., t.i.=0.3 and 1.0, respectively. In the present three-dimensional calculation, the unit mean is assigned to all components of velocity. The r.m.s. values of lateral components (v_t and w_t) take an equal value of the streamwise component (u_t). Standard values of several optical variables, i.e., the laser beam half-angle (θ), the number of fixed fringes along the center of measuring volume (N_f), and the fringe spacing (d_f) are specified on the present calculation; $\theta = 11.04^\circ$, $N_f = 55.93$ fringes and $d_f = 3.29 \times 10^{-4}$ m, respectively, where these are from the commercially used LDV system with He-Ne laser.

The computed spectra obtained from the present three-dimensional flow field are shown in Fig. 1 with the expected spectrum for d.d.=0.05 and t.i.=1.0, which simulates an ideal processor (Q=0.0). It should be noted that the large variation at high frequencies owing to variability has been trimmed. Thus, the plotted signal lines contain high variations at high frequencies. The known expected spectrum is represented by the thick solid line. Among the results, RG and TW produce qualitatively agreeable results with the expected value at low frequencies. However, the estimated spectra from these methods are not guaranteed to be nonnegative, which generally causes the negative values at high frequencies like the Blackman-Tukey method. Furthermore, since the transit time

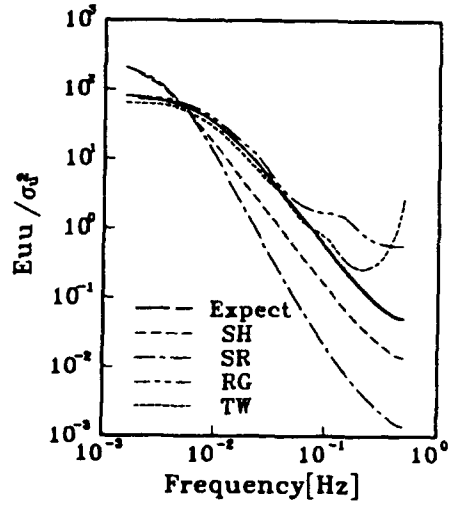

Fig. 1 Comparison of the computed power spectra for d.d.=0.05 and t.i.=1.0; $R_{uv} = 0.0$, $R_{uw} = 0.0$, $R_{vw} = 0.0$, R=0.0, and Q=0.0

in the transit time weighting method (TW) behaves as another sample function of the stochastic process, the spectral variability is accelerated due to the variability induced by random sampling times. As a result, the increased variability of TW leads to the reduction of analyzable frequency support rather than RG. The first negative values of TW are observed almost earlier than RG. As compared with the previous results obtained from one- or two-dimensional flow fields (Lee & Sung 1994), it can be observed that the spectral bias in RG is slightly decreased in the present three-dimensional field. As addressed by previous authors (Tropea 1987; Lee & Sung 1994), however, it is seen that the results of SH and SR are affected mainly by data densities rather than turbulent quantities.

When the data density is high enough (d.d.=5.0), while the turbulent intensity remains unchanged (t.i.=1.0), the spectra from four processing algorithms are represented in Fig. 2. Two resampling methods (SH and SR) and TW give allowable results in the low frequency region ($f \leq 0.1$). A global inspection of Figs. 1 and 2 reveals that the use of TW is quite reasonable for qualitative spectral analysis in high turbulent flow. However, TW has the following problems, i.e., the difficulties are encountered in the exact measurement of the transit time experimentally. Note that Buchhave et al. (1990) dealt with this topic through the simulation as well as experiment. It is shown, however, that the experiment was not well consistent with the simulation.

Consider now the dependence of spectral estimates on the factor Q, which is the ratio of the minimum number of zero-crossings to the maximum fringe number. In this calculation, we employ the count-mode in which the only one measurement is validated per burst, if zero-crossings exceed a fixed number

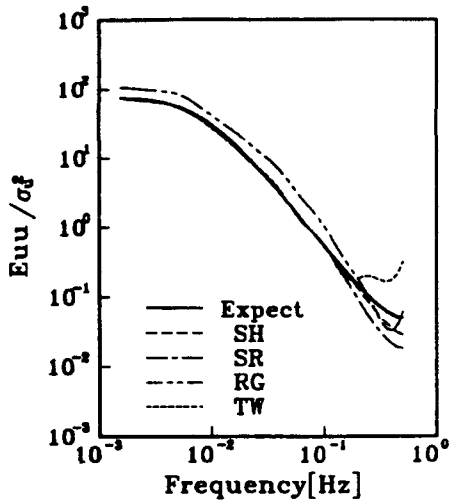

Fig. 2 Comparison of the computed power spectra for d.d.=5.0 and t.i.=1.0; $R_{uv}=0.0$, $R_{uw}=0.0$, $R_{vw}=0.0$, R=0.0, and Q=0.0

N_e. In order to disclose the effect of Q clearly, a large value of Q is chosen (Q=0.57). As shown in Fig. 3, the large spectral bias is displayed for the random sampling techniques (RG and TW). While the two resampling methods (SH and SR) produce relatively allowable results, it is seen that the transit time weighting over sampling bias is substantial. For the spectra predicted by SH and SR in comparison with Fig. 2, the overprediction at low frequencies and slight attenuation at high frequencies are displayed. As apparently seen in Eq. (7), Q

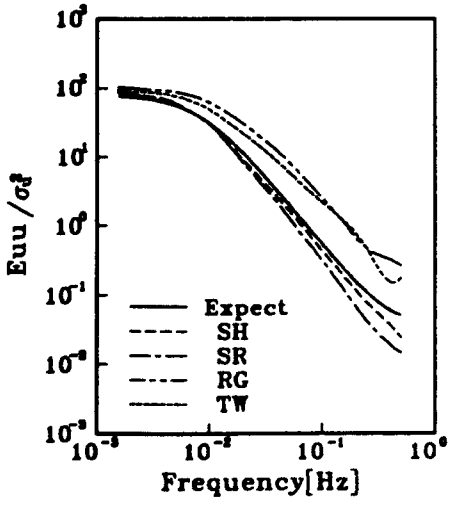

Fig. 3 Comparison of the computed power spectra for Q=0.57; d.d.=5.0, t.i.=1.0, $R_{uv}=0.0$, $R_{uw}=0.0$, $R_{vw}=0.0$, and R=0.0

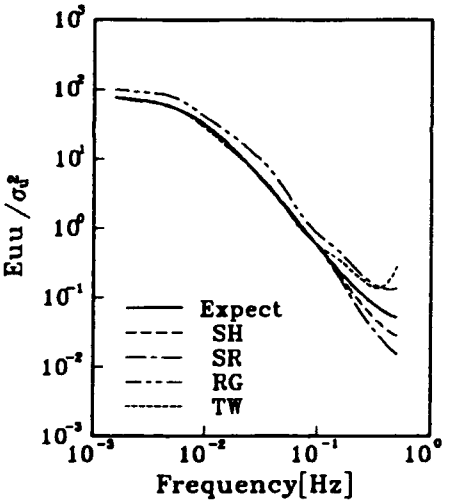

Fig. 4 Comparison of the computed power spectra for Q=0.57 and R=5.0; d.d.=5.0, t.i.=1.0, $R_{uv}=0.0$, $R_{uw}=0.0$, $R_{vw}=0.0$

acts as a strong function of changing the instantaneous sampling rate λ_t. It is also observed that a finite value of Q enhances significantly the sampling bias, and finally it leads to an unfavorable spectral distortion.

Inspection of spectral bias is extended to the effectiveness of frequency shifting in Fig. 4. Here, the required zero-crossing for a measurement is the same as in Fig. 3. Spectral bias caused by the finite value of Q is profoundly reduced with frequency shifting (R=5.0). Since most of realistic burst type processors have the validation circuits, like a part of Q in the present study, an appropriate frequency shift is required for the consideration of the quantization error, where the determination of Doppler frequency and transit times are closely related to the amount of frequency shift.

Since the spectral components at high frequencies in logarithmic scales are smaller than those at low frequencies in an absolute sense, the quantification of averaged overall error is inevitable to analyze the spectral error effectively. In the present study, the following averaged error base is proposed:

$$e = \frac{1}{\sqrt{N}} \left\| (E_{uu} - \hat{E}_{uu}) / E_{uu} \right\| \qquad (10)$$

where E_{uu} is the expected spectrum and $\hat{E}_{uu}$ is the estimated spectrum. N denotes the number of spectral components to be compared and the norm is defined as $\|E_{uu}\|^2 = \sum_{i=1}^{N} E_{uu}^2(f_i)$. Since negative values are always happened in spectra obtained from the random sampling methods, it is generally difficult to

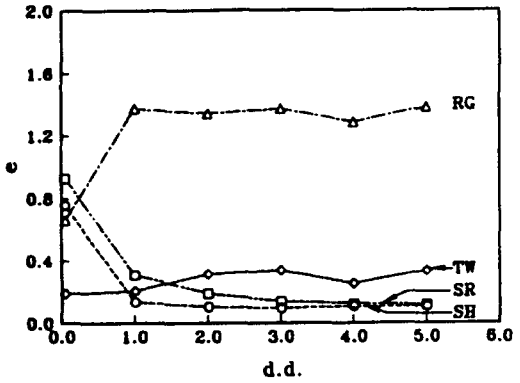

Fig. 5 Comparison of the averaged overall spectral errors for one-dimensional turbulence; t.i.=1.0, R=0.0, and Q=0.0

compare the spectral errors from the random sampling methods with those from the resampling techniques directly. Therefore, the present error calculations are subjected to the range $f \leq 0.1$ for $d.d. > 0.05$ and $f \leq 0.05$ for $d.d. \leq 0.05$. These ranges are appropriate for a confident error estimation in the low frequency region. However, these are not sufficient for the study of high frequency attenuation, which is shown in the resampling spectra.

The averaged overall spectral errors for one-and three-dimensional simulation results are shown in Figs. 5-6. Comparison of Figs. 5 and 6 (b) reveals that spectral errors produced by RG postulating the homogeneous Poisson process in sampling times are discernibly reduced for the case of three-dimensional flow. Since the integration of spectral components provides the r.m.s. value, the aforestated eminent result may be at first glance inconsistent with the r.m.s. estimates using the unweighted method by Buchhave et al. (1990). It means that larger positive bias is detected in their results for the case of three-dimensional flow (t.i.=1.0). As is well known in turbulent flows, most of energies are concentrated in large scales, i.e., low frequency ranges. For one-dimensional case, large spectral distortion of RG is distributed in high frequencies, whereas the spectral bias of RG for three-dimensional case is relatively small in high frequencies. It implies that the spectral energy for one-dimensional case, which contains smaller energy in low frequency region than the three-dimensional flow, increases rapidly with frequencies rather than that of three-dimensional case. Consequently, the averaged overall spectral error of three-dimensional case is smaller than that of one-dimensional case in an absolute sense. The spectral error by TW is attributed mainly to the variability rather than the spectral bias. Based on the spectral error produced by SH for d.d.=1, over which SH gives agreeable results as previously mentioned by Lee and Sung (1994), the TW estimation is marginally acceptable for low data densities. In order to estimate the spectra quantitatively by TW, an appropriate smoothing

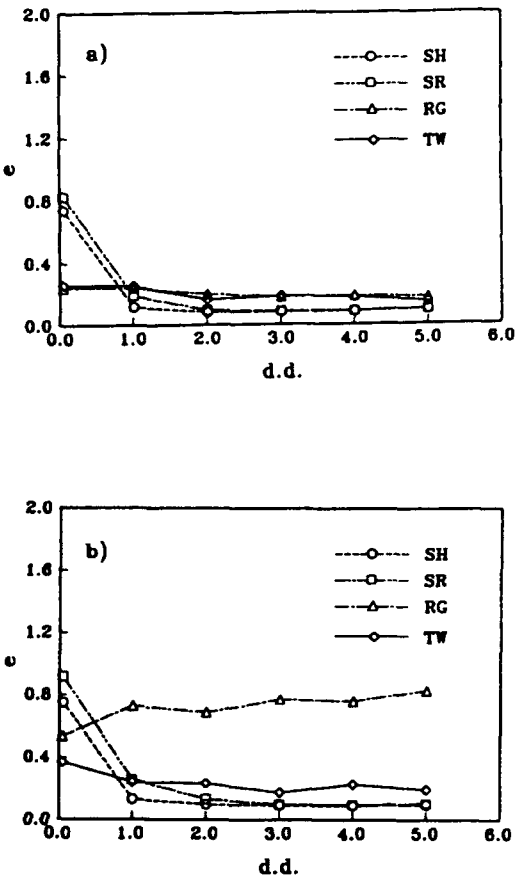

Fig. 6 Comparison of the averaged overall spectral errors for three-dimensional turbulence; $R_{uv} = 0.0$, $R_{uw} = 0.0$, $R_{vw} = 0.0$, R=0.0, and Q=0.0: a) t.i.=0.3; b) t.i.=1.0

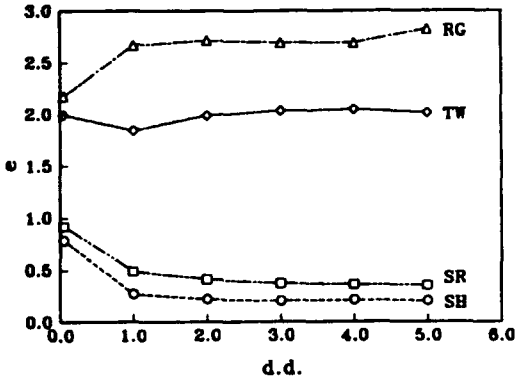

Fig. 7 Comparison of the averaged overall spectral errors for three-dimensional turbulence; t.i.=1.0, $R_{uv} = 0.0$, $R_{uw} = 0.0$, $R_{vw} = 0.0$, R=0.0, and Q=0.57

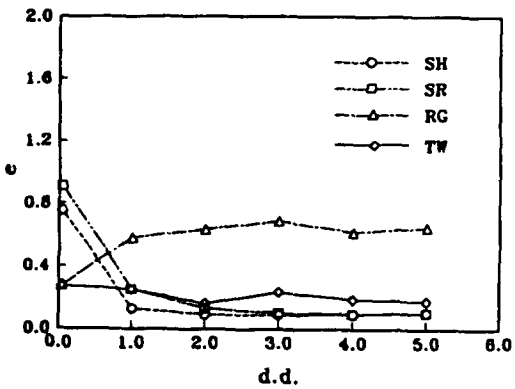

Fig. 8 Comparison of the averaged overall spectral errors for three-dimensional turbulence; t.i.=1.0, $R_{uv}=0.0$, $R_{uw}=0.0$, $R_{vw}=0.0$, R=5.0, and Q=0.57

operation, such as a frequency window, should be developed. For d.d.≥1, the spectra by resampling techniques (SH and SR) present relatively good estimates. In Fig. 6 (a) and (b), the spectral bias of TW is slightly changed with the variations of turbulent intensity. It is thought that the stability of TW is decreased as the turbulence intensity increases.

Figures 7 and 8 summarize the discussion on the finite value of Q and the usefulness of frequency shifting (R) quantitatively. It is shown that the random sampling methods (RG and TW) are influenced by the finite value of Q than the resampling methods (SR and SH).

5. CONCLUSION

In order to resolve the spectral bias in three-dimensional turbulent flow fields, a promising three-dimensional generation process was developed. The present model is adequate for qualitative and quantitative comparisons between the spectral results from one-dimensional velocity field and those from three-dimensional velocity field. Four spectral processing algorithms, i.e., SH, SR, RG and TW, respectively, were assessed numerically to estimate the spectral bias over wide range of data densities ($0.05 \le d.d. \le 5$) and turbulence levels (t.i.=0.3, 1.0). Furthermore, the influence of turbulent quantities and system parameters (Q and R) on spectral bias was also scrutinized. The spectral errors produced by RG from the three-dimensional flow are reduced rather than those from the one-dimensional flow. It reflects mainly the fact that the spectral error from the one-dimensional flow increases rapidly with frequencies rather than the case of three-dimensional flow. The TW estimation is marginally acceptable flow for low data density. For d.d.≥1.0, the spectra from the resampling techniques (SH and SR) present relatively good estimates rather than the random sampling methods.

REFERENCES

Adrian, R.J. & Yao, C.S. 1987, Power Spectra of Fluid Velocities Measured by Laser Doppler Velocimeter, Exp. Fluids, vol. 5, pp. 17-28.

Buchhave, P. 1979, The Measurement of Turbulence with the Burst-type Laser Doppler Anemometer-Errors and Correction Methods, Ph.D. Dissertation, State Univ. New York at Buffalo.

Buchhave, P., George, W.K.Jr. & Lumley, J.L. 1979, The Measurement of Turbulence with the Laser-Doppler Anemometer, Ann. Rev. Fluid Mech., vol. 11, pp. 443-503.

Buchhave, P., von Benzon, H.-H. & Rasmussen, C.N. 1990, LDA Bias: Comparison of Measurement Errors from Simulated and Measured Data, Proc. of the Fifth Int. Symp. on Appl. of Laser Anem. to Fluid Mech. Lisbon, paper 29.3.

Edwards, R.V. 1987, Report of the Special Panel on Statistical Particle Bias Problems in Laser Anemometry, J. Fluids Eng., vol. 109, pp. 89-93.

Gaster, M. & Roberts, J.B. 1977, The Spectral Analysis of Randomly Sampled Records by a Direct Transform, Proc. R. Soc. Lond., Ser. A, vol. 354, pp. 27-58.

Lee, D.H. & Sung, H.J. 1994, Assessment of Turbulent Spectral Bias in Laser Doppler Velocimeter, Exp. Fluids, vol. 16, pp. 223-235.

McDougall, T.J. 1980, Bias Correction for Individual Realisation LDA Measurements, J. Phys. E. Sci. Instrum., vol. 13, pp. 53-60.

Roberts, J.B. & Gaster, M. 1980, On the Estimation of Spectra from Randomly Sampled Signals: A Method of Reducing Variability, Proc. R. Soc. Lond., Ser. A, vol. 371, pp. 235-258.

Snyder, D.L. 1975, Random Point Processes, John Wiley & Sons, New York.

Tropea, C. 1987, Turbulence-induced Spectral Bias in Laser Anemometry, AIAA J., vol. 25, pp. 306-309.

Fuchs, W., Albrecht, H., Nobach, H., Tropea, C., & Graham, L.J.W. 1992, Simulation and Experimental Verification of Statistical Bias in Laser Doppler Anemometry Including Non-homogeneous Particle Density, Proc. of the Sixth Int. Symp. on Appl. of Laser Anem. to Fluid Mech. Lisbon, pp. 8.2.1-8.2.6.

Veynante, D. & Candel, S.M. 1988, A Promising Approach in Laser Doppler Velocimetry Data Processing: Signal Reconstruction and Nonlinear Spectral Analysis, Signal Process., vol. 14, pp. 295-300.

ESTIMATION OF SPECTRAL POWER DENSITY OF TURBULENCE FOR FLOW FIELD IN A DEFIBRATOR

Pentti Saarenrinne[+], Heimo Ihalainen[*], Sakari Soini[+], Sirpa Vienola[+] and Reijo Karvinen[+]

[+]Thermal Engineering, [*]Measurement Technology
Tampere University of Technology

ABSTRACT

The defibrator is an important process component of the paper mill. The understanding of the pulsatile flow field in the defibrator is crucial to the quality of the pulp suspension. This study concentrates on the frequency analysis of the time series of the flow fields measured by a Laser Doppler Anemometer (LDA). To achieve results we had to apply several spectrum estimation techniques and develop a LDA data simulator. The used methods were capable to analyse the frequency content of the flow up to ~1 kHz. The results were very informative for pulsative flow but highest turbulence frequencies were not resolved.

1. INTRODUCTION

A defibrator is a machine used in a paper mill to break up fibre bundles still existing in the pulp after the pulper. At this phase pulp exists as ~1 % fiber-water suspension with some fiber bundles. By defibering one means to fiberize a mixture of recycled waste paper-, thermo-mechanical- and chemical pulp, so that fibers get separated with as few grinding as possible. This device creates a powerful circulating flow field in and between the blades of rotor and stator (figure 1). The aim of this study is to get information from defibration process, what factors influence on the releasing of fibre bundles and how to improve the releasing process?

In order to break up the fiber bundles and flocs a pulsatile flow field is needed. If one wants to evaluate different parameter and construction combinations influence on flow field properties, a spectrum of flow variation is needed.

To assest the effectivity of different constructions and drive parameters, several tests were performed with pure water without fibers. Measurements were carried out in industrial enviroment with a real defibrator.

For comparison of the different spectral estimation methods one can use either real data measured from a well known flow situation Rajan and Munukutla (1992) or simulated data generated by a mathematical model of the LDA. One can model actual measured data and find variable parameters to change the properties of data Tropea (1987) or one can simulate the actual LDA measurement process Lee and Sung (1994). In this study artificially generated data sets have been constructed by simulating the measurement process.

Only few comparison studies about spectral estimation exist in the literature. They are considering data approximation, direct transform or periodogram method, correlation based or correlogram method and autoregressive method. Periodogram methods and correlogram methods are compared in a study of Bell (1983). He concluded that a slotted correlogram method is suitable for LDA spectrum calculations. In another study it was concluded that direct transformation method is appropriate method (Gaster and Roberts 1980). Periodogram method, correlogram method and autoregressive method was compared in Rajan and Munukutla (1992). In a recent paper Lee and Sung (1994) spectral estimates were evaluated by using direct transform and with three different data approximation methods. Sample and hold resampling, nonuniform Shannon reconstruction algorithm and projection onto convex sets, for data approximation and a periodogram method for spectrum calculation.

To facilitate a proper choice of appropriate spectral analysis method for the problem on hand, a comparative study of basic spectral analysis methods was made. The spectrum estimation methods were evaluated using simulated LDA data. The correlogram method were found to be best choice for the defibrator analysis.

The organization of this paper is as follows. Chapter 2 provides a description of the defibrator and measurement system. The developed LDA-data simulator is presented in chapter 3. Discussion about the spectrum estimates and their evaluation is in chapter 4. The application results of the chosen spectrum estimate are presented in chapter 5. Finally, some results are summarized in chapter 6.

2. THE DEFIBRATOR AND THE MEASUREMENTS

The measured defibrator was composed of a stationary stator and of a conical rotor which is rotating inside the stator (figure 1). Both the stator and the rotor have five blade zones. Every blade zone has a different number of blades. The blades of the stator are not parallel with the ones of the rotor and the axial inclination of the blades is different at every zone. The distance between the end faces of the stator and rotor blades is called the cutting clearance (Figure 2). and it can be adjusted. The blade clearance means the average distance between the blade edges and it can not be changed. The measurements were made through a window at second zone.

The pulp is pumped from a zone to the next one through the gap between the stator and the rotor. Most of the flow takes place in the blade channels of the rotor and the stator. The channel flow is rotational, periodic and pulsatile.

Instead of pulp, water with TiO_2 particles was circulated in the defibrator. A Laser Doppler anemometer was applied to measure axial and peripherical velocities

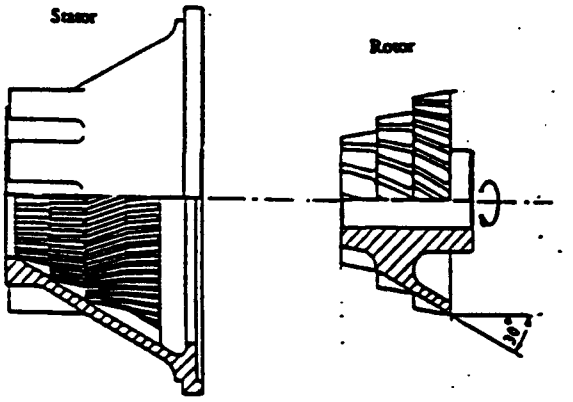

Fig. 1 The rotor and the stator of a defibrator.

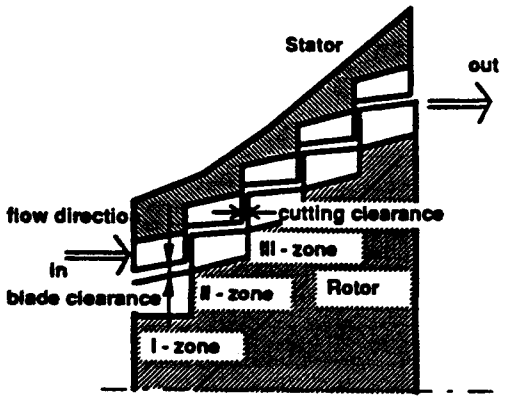

Fig. 2 The axial cross-section of a defibrator.

between the blades of the defibrator. It was not possible to measure the radial velocity. The main propagation direction of the flow was the axial direction. The measurement point was located in the middle of the stator channel in the second zone. During the measurements different process parameters (cutting clearance, rotational speed and blade clearance) were varied.

The laser beam reflections from the end faces of the rotor blades caused the main practical problem of the measurement. Several attempts, eg. painting the blades black, were made to solve the problem. Unfortunately, even though the situation improved, quite a lot reflections still remained.

For practical reasons only 10000 ... 16000 samples long data series were collected. The highest data-rate achieved was 2800 samples per second.

3. THE SIMULATED LDA DATA

To simulate the LDA-data a doubly stochastic Poisson process has to be generated. One method to do this is to model the data with a so called "conveyor belt" model (Tropea 1987). Uniformly distributed particles are spread in a tube (or in the one dimensional case on a conveyor-belt). The tube is then fed with variable speed and direction through the probe volume. So the arrival rate of the particles is proportional to the volume flow across the measurement volume and the arrival time distribution will be a Poisson distribution weighted by the velocity vector (Buchhave 1979).

$$P_M(n,T) = \int \frac{u^n}{n!} e^{-u} P(u)\,du$$

The measurement volume of a LDA with a sufficient frequency shift can be approximated to be an ellipsoid (Mc Dougall 1980)

$$\left(\frac{x}{a}\right)^2 + \left(\frac{y}{b}\right)^2 + \left(\frac{z}{c}\right)^2 = 1$$

where $a=b/\cos(\varphi/2)$ and $c=b/\sin(\varphi/2)$. In our case we used the dimensions of the DANTEC 60X11 fiber optical probe with a f=160mm front lens.

The volume flow V_f through the measurement volume is

$$V_f = |V| S(V)$$

$|V|$ is the magnitude of the instantaneous velocity and S(V) is the area of the measurement volume projected on the normal plane of the velocity vector V, and the mean number of measurements per second λ is

$$\lambda = C|V|S(V)$$

where C is the particle number density per unit volume. Because the area S(V) depends on the velocity direction, the arrival events are modulated both with velocity magnitude and direction. The arrival times can be calculated by integrating the volume flow into the measurement volume and solving for the times when particles enter the measurement volume.

$$V_n = \int_0^{t_n} VS(V)\,dt$$

The particles arriving to the measurement volume are distributed uniformly on the area of the measurement volume cross section to the normal of the instantaneous velocity vector. The residence time of a particle (the time the particle stays inside the measurement volume) is calculated by assuming that the velocity of the particle remains constant during the travel across the measurement volume. Therefore the residence time is a function of the velocity vector and the random place on the cross section of the measurement volume. And the smallest scale resolved is of the order of the size of the measurement volume.

The particles present simultaneously in the measurement volume are rejected.

The essential features, the arrival and residence times, of the LDA-simulator are expected to be close enough of those of a real LDA. This kind of simulation can be used when the purpose is to compare different spectral estimation methods for given 3D velocity field.

The performance of the simulation model was checked to give a correct average for velocity when the residence time weighting was used.

The u, v and w velocities were calculated by a autoregressive model

$$u(t) = a_{u1}u(t-1) + a_{u2}u(t-2) + \varepsilon_u(t) + b_{u1}\varepsilon_u(t-1) + \mu_u$$
$$v(t) = av(t-1) + \varepsilon_v(t)$$
$$w(t) = aw(t-1) + \varepsilon_w(t)$$

where a_{u1}=0.95, a_{u2}=-0.9025, b_{u1}=0.95 and a=0.95, are autoregressive parameters and ε_u, ε_v and ε_w are white Gaussian processes. The mean velocity in x-direction is μ_u. The mean of the velocities v and w is zero and the correlation coefficients between these velocities and between the u velocity are zeros. The standard deviations of ε_v and ε_w are adjusted so, that the standard deviations of the velocities v and w are 0.8 times the standard deviation of the velocity u.

4. SPECTRAL ANALYSIS OF THE LDA SIGNALS

The basic difficulty with LDA signal at medium and low data rates is the non-even and velocity correlated nature of the sampling of the signal. Special methods for spectral analysis of Poisson-sampled signals have been developed (Gaster and Roberts 1975, Gaster and Roberts 1977, Roberts and Gaster 1980, Adrian and Yao 1987), examined (Roberts et al. 1980, Bell 1983, Lee and Sung 1994) and applied to measured data. The present application for defibrator analysis was however quite a challence.

The signal seems to be mostly random although some deterministic components generated by the rotating blades were present. The LDA signal has quite a lot of velocity correlated bias because of the high variability $\sigma_u/\mu_u \approx 100$ % (σ_u is the standard deviation of the velocity and μ_u is the mean velocity in the measurement direction). The interesting frequency range of the dissipation of the turbulence and also harmonic components of the blade frequency at 600 Hz were quite high as compared to the mean sampling rate (~1 ... 2 kHz) achieved.

The main methods available for spectral analysis can be divided into three main classes: 1) even-interval approximations of the signal itself, 2) correlation function based methods and 3) direct Fourier transform approach. All of these were tried but most of our attention was directed to the correlation based methods that we believe to be most effective for this signal.

We applied basically three types of the even interval approximations. The sample and hold approximation (Adrian and Yao 1987) removes the velocity correlated bias. It can be seen to weight more the samples that are followed by long intervals by keeping their values for longer time. It is actually doing post-interval weighting of the signal. The interval weighting can be achieved by sample and hold into reverse direction in time. The method did not give good results in this case because the data density achieved $d_d \approx 0.5$ was so low

$$d_d = \frac{\lambda}{2p f_{rms}}, \text{ where } f_{rms} = \frac{\sqrt{\int_0^\infty f^2 S_u(f) df}}{\sqrt{\int_0^\infty S_u(f) df}}$$

as derived by (Lee and Sung 1994). Here λ is the mean sampling rate. Also the approach of Taylor microscale (Aronson and Löfdahl 1993) can be applied. The computed spectrum contained much extra power at low frequencies as predicted by (Adrian and Yao 1987). The linear interpolation between samples resulted into same kind of result.

The third even interval approximation studied was motivated by bias removal with residence time weighting. We formed an even interval signal from pulses that look like the analog signal of burst type velocity measurement. The signal stays at measured velocity the length of the residence time at each sampling point. Elsewhere the signal remains zero. To reach pulsewidths of several sampling intervals we multiplied the measured residence times by a factor $c \approx 1000$. From this even interval sampled signal we computed the autocorrelation function by a method that discards the zeros between samples (Priestley 1981). The resulting spectrum depended of the used c factor transforming towards something similar that sample and hold spectrum when c values are high .

The direct Fourier transform methods we applied are developed by Roberts and Gaster (1980). The basic method is to apply direct Fourier transform to short windowed periods of measured data and average the results. With this method the variance induced white part of the spectrum must be subtracted from the result.

$$\hat{S}(f) = \hat{P}(f) - \hat{Q} \qquad \text{where}$$

$$\hat{P}(f) = \frac{2}{\lambda^2 T}\left|\sum_j w(t_j)x(t_j)e^{i2\pi f t_j}\right|^2 \qquad \text{and}$$

$$\hat{Q} = \frac{2}{\lambda^2 T^2}\sum_j w^2(t_j)x^2(t_j)$$

Here w is the weighting window (Hanning) and x the time series to be transformed. Roberts and Gaster (1980) have also given the asymptotic variance formula for the estimator

$$\text{var}\left\{\hat{S}(f)\right\} \to \left[S(f) + \frac{r(0)}{\lambda}\right]^2 \quad \text{as } T_s \to \infty$$

Here $r(0)$ is the autocorrelation function value at zero delay and T_s is the segment length. For N independent segments averaged the variance is multiplied by $1/N$. They have also suggested a scheme with removal of the mean and some of the largest single frequency components at each segment. This diminishes the variance induced by the mean square of the signal itself. Hoesel and Rodi (1977) give a bias correction method by weighting with residence times

$$x(t_j) = \frac{t_r(t_j)}{\sqrt{\sum t\,(t_j)\,t\,(t_k)}}u(t_j)$$

Here $t_r(t_j)$ is the residence time at sample point t_j. The computed estimates seemed to have much bigger variance than estimated by the variance formula. The reason was the residence time weighting that introduced much white noise to the signal by multiplying it by a quite wide band signal formed by the residence time values. It seems that smoother weighting factors than the residence times should be applied. We did not yet apply the variable bandwidth method where spectrum at higher frequencies is calculated from shorter segments to increase the number of the segments N.

Our main effort was directed to correlation function based methods. We see some good reasons to this approach: 1) The 'slotted' correlation function approach (Gaster and Roberts 1975, Bell 1983) is quite fast to compute, 2) The achieved correlation function itself is also interesting, 3) The correlation

function can be applied to either Fourier-type or parametric spectral estimates, 4) The method seems to provide a basis for some improvements. Gaster & Roberts (1975) have given a similar varance formula for the correlation method.

$$\mathrm{var}\left\{\hat{S}(f)\right\} \to \frac{3}{4}\frac{\tau_{max}}{T}\left[S(f)+\frac{r(0)}{\lambda}\right]^2 \quad as\ T \to \infty$$

With the basic 'slotted' method the correlation function is computed from the measured data using the actual sampling time points

$$r(k\Delta\tau)=\frac{\sum w(i,j)x(t_i)x(t_j)}{\sum w(i,j)}$$

Here $k\Delta\tau$ is the centerpoint of the k th bin where the correlation function is cumulated, $w(i,j)$ is the applied weight for the product $x(t_i)x(t_j)$. The product $x(t_i)x(t_j)$ is summed to the bin where $\left|(t_j-t_i)-k\Delta\tau\right| \le 0.5\Delta\tau$. In the basic method the weigths $w(i,j)=w(i)w(j)$ are the products of the weigths of the samples eg. residence time t_r or $\sqrt{t_r}$. Also the sum $w(i,j)=w(i)+w(j)$ or more complicated formula can be applied. The average number of products per bin is $(T-\tau)\lambda^2\Delta\tau$ when the time intervals are Poisson distributed. When the autocorrelation function is computed this way an error of small time shifts is introduced. Bell [Be83] has evaluated it as

$$\hat{r}_{xx}(k\Delta\tau) \equiv r_{xx}(k\Delta\tau)+\Delta t\, r_{\dot{x}\dot{x}}(k\Delta\tau)$$

where Δt is the rounding error made. It can also be evaluated as $\hat{r}_{xx}(k\Delta\tau) \equiv r_{xx}(k\Delta\tau)+\Delta t \frac{dr_{xx}}{dt}(k\Delta\tau)$ and the estimated autocorrelation function can be recursively corrected based on the formerly computed estimate (see Fig 3).

This gives better estimates of the autocorrelation function at exactly the points $k\Delta\tau$ instead of giving the integral of the area under the slot. Bell has approximated this error to be significant (Bell 1983).The error seems to be large at the small τ values where the distribution of the time lag values is not even.

The second improvement to the basic method is to compute the autocorrelation function 'half step shifted'. Instead of $\left|(t_j-t_i)-k\Delta\tau\right| \le 0.5\Delta\tau$ we form the bin as $\left|(t_j-t_i)-(k+0.5)\Delta\tau\right| < 0.5\Delta\tau$. This leaves out the white noise variance located at $\left|t_j-t_i\right|=0$ when $i=j$. This is more according to the original Gaster & Roberts (1975) formula. The $0.5\Delta\tau$ shift is easily taken into account at the FFT phase.

The third applied improvement takes the approach of minimal approximation. In this method we do not cumulate all $x(t_i)x(t_j)$ products that fall into the bin at $k\Delta\tau$ but only the nearest one. Eg. for t_i we compute and cumulate only the product $x(t_i)x(t_j)$ for which t_j-t_i falls nearest to $k\Delta\tau$ (see Fig 4).

The slot width can even be made smaller to gather less products. This approaches the controlled LDA measurements at high data rates.

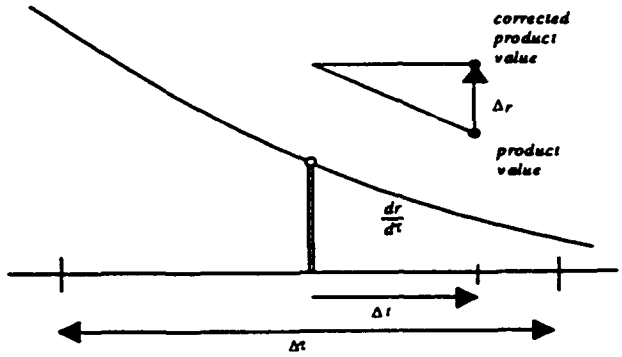

Fig. 3 Correcting the autocorrelation function estimate by adding small increnment to every lagged product based on former estimate of r.

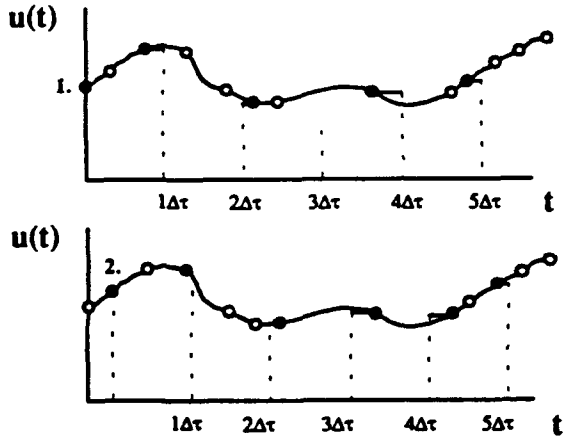

Fig 4. Minimal approximation method. The selection of the products $x(t_i)x(t_j)$ fullfilling the conditions set is illustrated for the first two samples (marked black).

We have also tried the mean removal procedure of Roberts and Gaster (1980) to improve the basic correlation method. This can be applied as a filter to the data before the correlation function computation. For our data no noticeable correction was achieved.

We have not yet fully examined the statistics and the practical properties of the developed methods, but the work is continuing. Our goal is to use the developed simulator as a tool to test the properties of the computational methods by signals with spectra similar to the measured ones.

5. RESULTS FOR THE DEFIBRATOR

The spectra were estimated with the slotted correlogram method and weigthed by the sum of the residence times. The calculated axial velocity spectra are shown in the linear scale in the figure 5 and in the logarithmic scale in the figure 6. It can be seen (figure 5) that there is two clear peaks in the spectrum when the relative cutting clearance is 1. One peak is at 600 Hz and the other is at 40 Hz. When the relative cutting clearance is increased (cases 4 and 6) the peak at 600 Hz is decaying and the peak at 40 Hz is sligthly increasing.

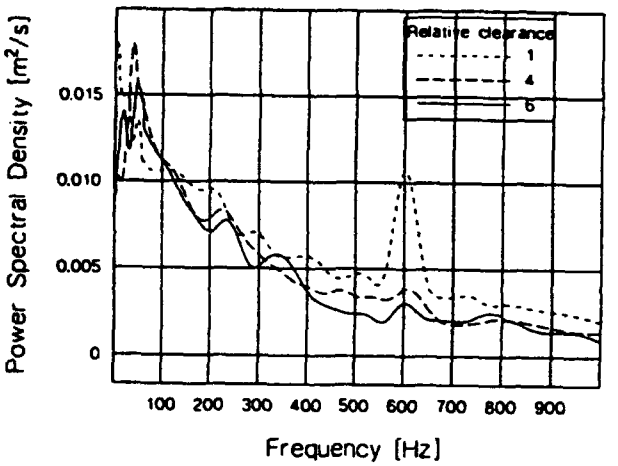

Fig. 5 Linear scale axial velocity spectra for different relative clearance.

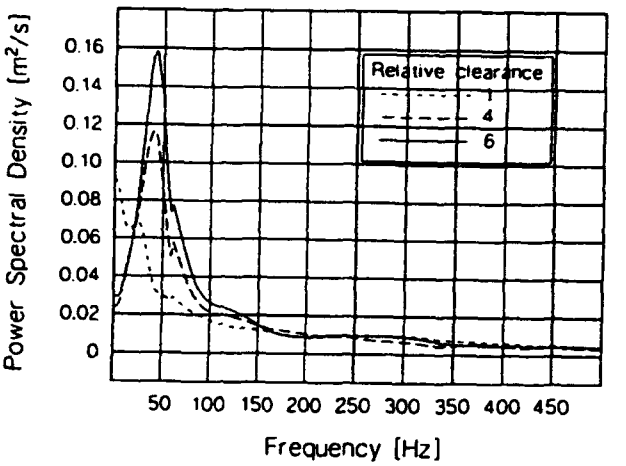

Fig. 7 Linear scale tangential velocity spectra for different relative clearance.

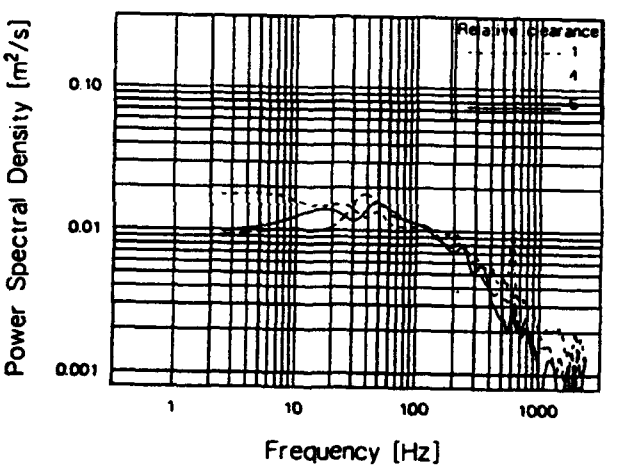

Fig. 6 Logarhitmic scale axial velocity spectra for different relative clearance.

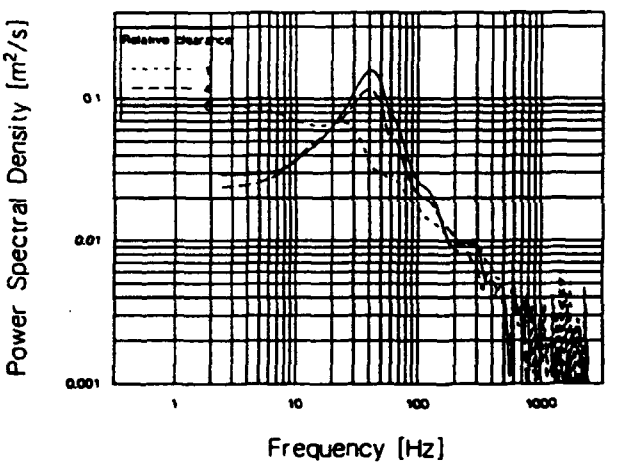

Fig. 8 Logarhitmic scale tangential velocity spectra for different relative clearance.

The kinetic energy of the turbulence decreases from about 200 Hz (figure 6), excluding the peak at 600 Hz. There exist no clear inertial subrange in the calculated spectra. The kinetic energy of the turbulence is practically zero above the frequency 900 Hz.

In the figures 7 and 8 are shown the spectra for the tangential velocity in the linear and logarithimic scale. The kinetic energy of the flow is highest at the wide peak around the frequency 40 Hz in every case. The energy is highest at the largest relative cutting clearance. There exist practically no kinetic energy above the frequency 350 Hz. From figure 8, can be seen that there is no other peaks and the kinetic energy is clearly decaying after the 40 Hz peak.

The areas under the curves (the kinetic energies) is about the same order in figures 5 and 7 and the kinetic energy is moved to the higher frequencies when the cutting clearance is decreased. By using the Taylor hypothesis one can estimate that the eddy size calculated from the axial mean fluctuating velocity is order of few millimeters at 600 Hz, which is of the same order with the characteristic length of the fiber bundles. The length scale calculated from the tangential mean fluctuating velocity is one order higher than the axial one.

A similar phenomena is also recognised in the test runs with a real pulp suspension. The quality of the processed pulp is better when the cutting clearance is small.

6. CONCLUSIONS

The studied methods for spectral analysis were even-interval approximations of the signal, correlation function based methods and direct Fourier transform methods. All of these were tried but according to our tests, the correlation based methods were the most effective for this signal.

The calculated spectra give a good insight to the behaviour of the flow field inside a defibrator. The achieved

result of the flow behaviour confirms and gives an explanation for the in practice recognised phenomena of the influence on the cutting clearance to the fiber bundle break up. The explanation is, that the kinetic energy is transferred to the higher frequencies when the cutting clearance is reduced, because of the increased pulsating of the axial velocity. It can be said, that even the limited bandwidth spetra are valuable for the development of the defibrator construction.

ACKNOWLEDGEMENTS

The measurements was conducted under a research contract with Sunds Defibrator Jylhä Oy. Also the authors are grateful for the free computer time and use of the latest version of the MATLAB-program provided by Automation Experts Oy.

REFERENCES

Adrian, R.J. and Yao, C.S., 1987, Power spectra of fluid velocities measured by laser Doppler velocimetry, Experiments in Fluids, vol. 5, pp. 17-28.

Aronson, D. and Löfdahl, L., 1993, The Plane Wake of a Cylinder: Measurements and Inferences on Turbulence Modeling, Experiments in Fluids, vol 15.

Bell, W.A., 1983, Spectral Analysis Algorithms for the Laser Velocimeter: A Comparative Study, AIAA J., vol. 21, no. 5, pp.714-719.

Buchhave, P., 1979, The Measurement of Turbulence with the Burst-type Laser Doppler Anemometer -Errors and Correction Methods, Ph.D. thesis, State University of New York at Buffalo.

Gaster, M. and Roberts, J.B., 1975, Spectral Analysis of Randomly Sampled Signals, J. Inst. Maths. Applics, vol 15, pp. 195-216.

Gaster, M. and Roberts, J.B., The spectral analysis of randomly sampled records by a direct transform, Proc. R. Soc. Lond. A. 354, pp. 27-58.

Hoesel, W. and Rodi, W., 1977, New biasing elimination method for laser-Doppler velocimeter counter processing, Rev. Sci. Instrum., vol 48, no. 7, pp. 910-919.

Lee, D.W. and Sung, H.J., 1994, Assessment of turbulent spectral bias in laser Doppler velocimetry, Experiments in Fluids, vol 16, pp. 223-235.

McDougall, T.J., 1980, Bias correction for individual realisation LDA mesuarements. J.Phys.E.Sci.Instrum., Vol.13 pp. 53-60

Tropea, C., 1987, Turbulence-Induced Spectral Bias in Laser Anemometry, AIAA J., vol. 25, no.2 pp. 306-309.

Priestley, M.B., 1981, Spectral Analysis and Time Series I & II, Academic Press.

Rajan, P.K. and Munukutla, S.S., 1992, A comparative study of three techniques for estimation of turbulence energy spectrum, Experiments in Fluids, vol 12, pp. 422-424.

Roberts, J.B., Downie, J. and Gaster, M., 1980, Spectral analysis of signals from a laser Doppler anemometer operating in the burst mode, J. of Physics E: Scientific Instruments, vol 13, pp. 977-981.

Roberts, J.B. and Gaster, M., 1980, On the estimation of spectra from randomly sampled signals: a method of reducing variability, Proc. R. Soc. Lond. A 371, pp. 235-258.

Session 12.
Combustion IV

LAMINAR SPRAY FLAME OSCILLATION

Yeshayahou Levy and Boris Golovanevsky
Faculty of Aerospace Engineering
Technion - Israel Institute of Technology
Haifa 32000, Israel.

Abstract

A spray combustor, with low velocities in the laminar range, exhibits a unique operating model where large amplitude, self-induced oscillations of the flame shape occur. Several coupled aero-thermodynamics mechanisms are resposible for the triggering of the flame oscillation. The phenomenon, previously described by the first author was only qualitatively analyzed. A parametric study is described directed to investigate the various coupled mechanisms. Two main parameters were changed during the present work, namely the fuel flow rate and momentum of the coflowing streams. The flow was monitored using a PDA system together with a computerized video camera. The results show an increase in the frequency of the flame oscillations with fuel flow rate and a decrease in oscillation frequencies with an increase in the momentum of the coflowing jets. Both effects indicates the significance of gravity.

Introduction

The equivalent of the Burke and Schumann [1] flame, while using liquid fuel in the form of liquid droplets, was the topic of several recent studies, most of which were theoretical [2-5] and one, by the first author [6] which was experimental. This unique experimental work indicated that gravity, a phenomenon neglected by all theoretical studies, may have a most significant effect on the behavior of the laminar spray flame. It showed clearly that the flame naturally obtained an oscillatory motion under most operating conditions. It practically oscillates from very low flow velocities until relatively high flow rates are obtained, where it can no longer be considered as a laminar flow. It was assumed that gravity causes the heavier central fuel stream to loose its momentum and collapse into a mushroom shape. Thereafter it accelerate vertically by the buoyancy force generated through heat transfer from the flame. This cycle, which is explained in more detail in [6] is repeated periodically. It was not predicted by any of the theoretical work, probably due to the negligence of gravity.

Flame oscillations in a gaseous flame were reported in the literature. However, these are much smaller in amplitude and much higher in frequency. Various observations of a Burke-Schumann type flame revealed the phenomenon of the flame tip flickering at frequencies of about 10-20 Hz. This effect, which was observed experimentally [7-11] and also predicted numerically [12,13], is the direct result of gravity induced buoyant forces on the flow of the reaction products, of aerodynamic instabilities in the jet itself and of heat release effects. Ellzey, et al. [13] presented predictions both considering and neglecting gravity. They showed that neglecting gravity gave a steady flow field but including gravity caused large structures to form that were convected downstream at frequencies on the order of 15-20 Hz.

An interesting experimental configuration is that of a combustor operating in a horizontal direction as if it is unaffected by gravity. This case is explained in more detail in the paper. The present study is directed to investigate the governing parameters that affect the oscillatory motion, mainly the amplitude and frequency. The fact that the oscillatory motion is affected by a relatively large number of aerothermodynamics phenomena had led to a parametric study, where each time only one parameter is changed. In the present work the equivalence ratio and the momentum of the co-flowing streams were changed between the maximum possible limits. Future work will include geometrical configurations as well.

The experiment

A schematic drawing of the combustor is illustrated in Fig. 1. The combustor consisted of two coaxial quartz tubes. The outer tube had an I.D. of 71 mm with a wall thickness of 2 mm and the inner one had an I.D. of 12.90 mm and an O.D. of 14.80 mm. The length (height) of the outer tube was 30 cm. Tests with different length tubes or even without the outer tube, were performed to eliminate the possibility that the dominant phenomena originates from acoustic coupling, and it has shown negligible differences in behavior. As illustrated in Fig. 1, the combustion air entered through four radial entrance holes and passed through a series of fine-mesh screens and flow straighteners. The upstream length from the screens to the combustor (the tip of the center tube) was about 25 cm and the total length of the center tube (from the atomizer to the tip) was about 50 cm.

Heptane fuel was introduced into the combustor through the center tube in the form of fine droplets. A slightly modified Sonotek ultrasonic nozzle # 8700-60 MS was used to generate the droplets. As shown in Fig. 2, the droplets were injected towards a narrow critical spray. The droplets were then carried upwards by a nitrogen gas stream. The nitrogen was injected through a tube which surrounds the "horn" of the ultrasonic atomizer. As the droplets traveled upwards through the 50 cm tube, they partially vaporized and interacted with each other, causing a subsequent change in their size and momentum. The flow of nitrogen was always adjusted to have an equale average velocity value as that of the air. The properties of the droplets were measured at the exit of the central tube. Typical size distribution at the center of the inner tube is shown in Fig. 3a. Figure 3b shows the total velocity histogram and Fig 3c demonstrates the size velocity correlation. It can be seen that velocity histogram has a nearly Gaussian distribution which extends to near zero negative values. As can be seen from Fig 3c, that part of the histogram is mainly originated from the large droplets which are too heavy to be carried upwards by the nitrogen. The small droplets (less than about 10 microns) can be used to represent the carrier gas velocity. Experimental uncertainty in measurements for drop size is estimated at ±6.5%

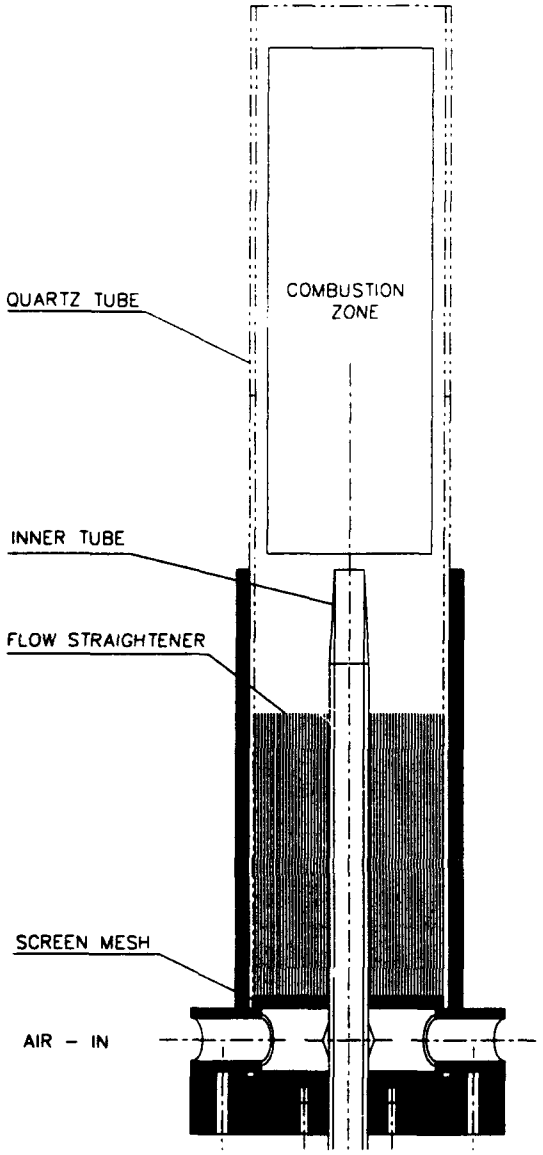

Figure 1. Schematic drawing of the combustor.

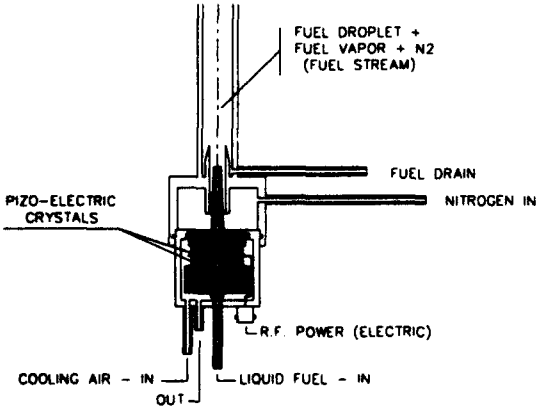

Figure 2. Schematic drawing of the ultrasonic atomizer.

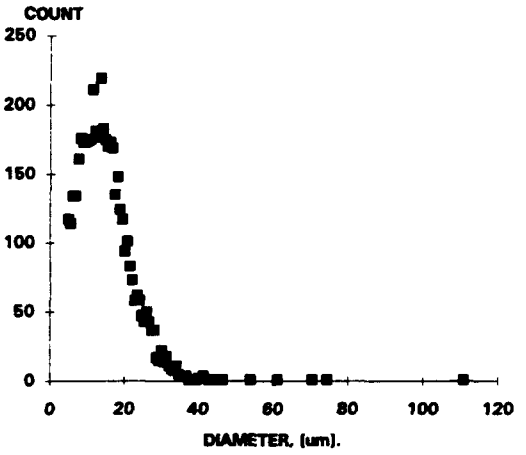

a. size distribution.

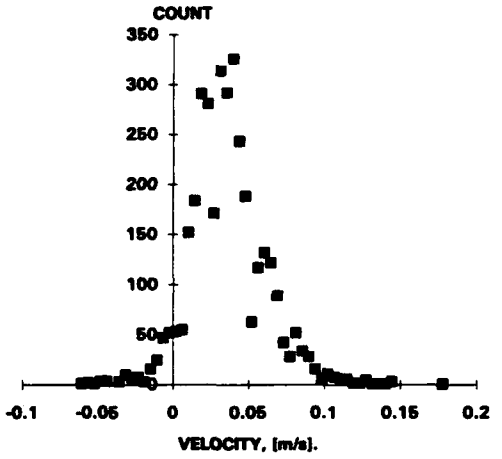

b. velocity histogram.

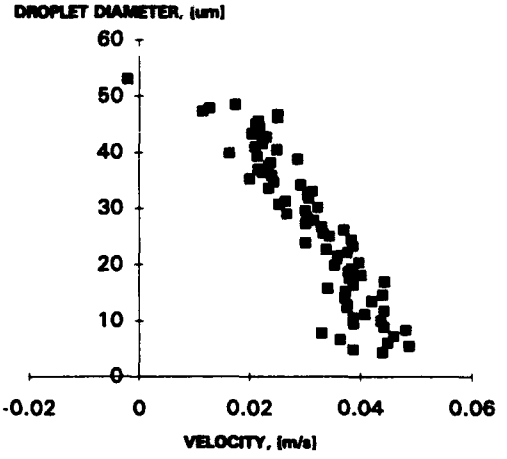

c. size - velocity correlation

Figure 3. Droplets characteristics at the exit of the center tuber, h=0 mm (entrance to the combustor).

and ± 0.5% for velocity [6]. The relatively low velocity of the carrier gas near the wall of the inner tube was not sufficient to carry the larger drops. This caused them to descend and come into contact with the tube wall forming a liquid film that flowed downward. The number of droplets that hit the wall and the resulting fuel flow in the downward direction was significant, especially in the lower parts of the center tube. A drain was incorporated in the combustor configuration at the bottom of the center tube (see figure 2) for continuous removal of the liquid film. The measurement of the actual fuel flow rate to the combustion zone always considered the drained amount. Due to the high turbulence within the inner tube, caused by the interaction between ascending droplets and the descending heavier droplets, fluctuation in the drained amount was detected and hence also in the net fuel flow, see Fig.4.

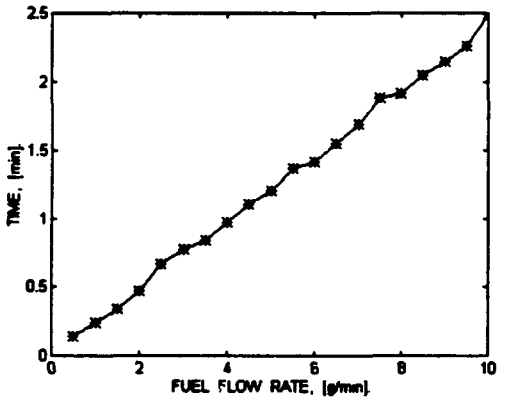

Figure 4. Variation of net fuel flow with time.

Experimental measurements were obtained using two techniques: Phase Doppler Anemometer (PDA) which simultaneously measured the size and velocity of individual droplets, and a CCD camera alternatively coupled with laser light-sheet illumination for large scale observations of the two-phase flow and flame. The frequency of flame oscillation was measured using the FFT routine over the instantaneous gas velocity (PDA) results in the combustion zone during several flame cycles. A special case where the combustor was mounted horizontally was also investigated. This test was performed in an attempt to isolate the effect of gravity on the flame. However, due to accumulation of droplets on the inner tube walls and the necessity for drainage, a small inclination angle (2°) was allowed. The special alignment of the combustor in this case disabled the possibility for PDA measurements and only video photography was obtained.

Results and Discussion

The oscillatory motion analyzed in the present study is different from the conventional flame flickering commonly reported in the literature. In the present study the entire volume of the flame is affected in an expansion-contraction type modulation whereas the reported gaseous flame flickering affected the flow of reaction products only at a distance downstream of the nozzle. Operating the combustor in a horizontal orientation changed the behavior of the flame significantly. The primary goal, which was to eliminate or minimize the effect of gravity, was only partially achieved. The initial part of the flame obtained a constant behavior with a steady flame. However further downstream the flame, which was horizontal at the beginning, obtained a vertical direction (due to buoyancy). In conditions, where fuel evaporation was completed before the vertical part of the flame, the flame remained almost stable. In cases where droplets existed even at the region where the flame obtained a vertical direction (higher flow momentum), periodic oscillations were observed only in the vertical portion of the flame. As indicated, this part of the experiment was only recorded by a CCD camera (which will be presented at the symposium) and therefore no quantitative data is given in the paper. It seems that this experiment strengthens the hypothesis that oscillations are induced by gravity (as only the vertical portion oscillates). However, it cannot yet be considered as conclusive.

A major part of the experimental effort was directed to study the influence of fuel to air ratio on the flame behavior. The combustor was operated during constant air and nitrogen flow rates while altering only the liquid fuel flow rate to the ultrasonic nozzle. This arrangement enables to maintain constant velocity of the fuel stream while changing the mass flow rate of the fuel. Hence it allows to isolate the effect of fuel flow and heat release on the flame behavior. Several similar sets of tests were performed, while each set was carried out with different air (and nitrogen) velocity. Results are given in Figs. 5-10.

Figure 5 shows a typical result of an FFT performed on the instantaneous velocity fluctuations. A domination amplitude in the frequency spectra is clearly observed at the value of the oscillation. Figure 6 shows size histogram and velocity histogram of the flow at 3mm above the nozzle. A double peak is seen, typical in oscillation flows. The histogram is distributed around the zero value with relative large negative velocity values. This could indicate that the measurements were performed within the core of the vortex that is responsible for the descent of the flame within the oscillation cycle of the flame. Figure 7 illustrates the variation of oscillating frequency with height for a typical operating condition. It shows that the frequency remains almost constant along the flame. This indicates that the whole of the flame is oscillating as a common element and that the effect is of macro-scale. The figure also shows that the frequency is reduced to zero, hence no oscillations, close to the fuel nozzle tip. This indicates that the oscillations are not driven by the fuel or air supply lines but rather are self induced at some distance downstream of the combustor (the zero frequency value at higher levvels, above 12 mm are due to insufficient measurement data). Even though the flame oscillates, the average velocity along the center line increases rapidly with height (a factor of 10 within 15 mm).This is mainly due to the heat addition from the chemical reaction and the associated expansion of reaction products and due to entrainment from the surrounding air. Meanwhile the average diameter of the fuel droplets is decreased by a factor of 4 (from 22 microns to about 5 microns over a distance of about 7 mm), see figure 9. An apparent bias effect on the measurements of the

mean size of the droplets indicated that the size of the droplets increases after a certain distance. This effect is typically caused by the fact that most of the small droplets evaporate and disappear, leaving only the big ones, hence mathematically indicating an increase in the mean size.

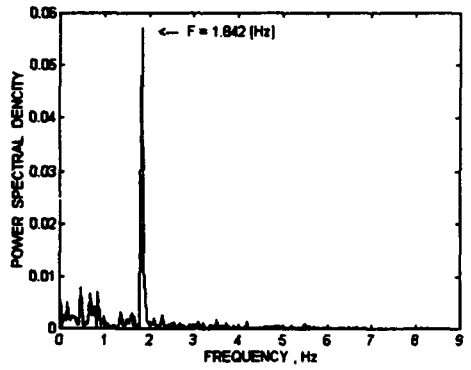

Figure 5. A typical frequency spectral density of the velocity oscillations.

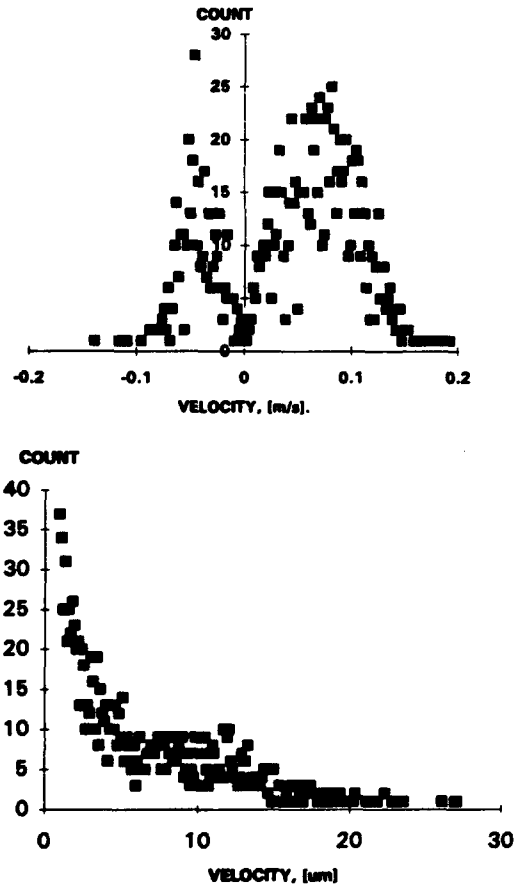

Figure 6. Velocity and size histogram at 3 mm downstream of the fuel nozzle.

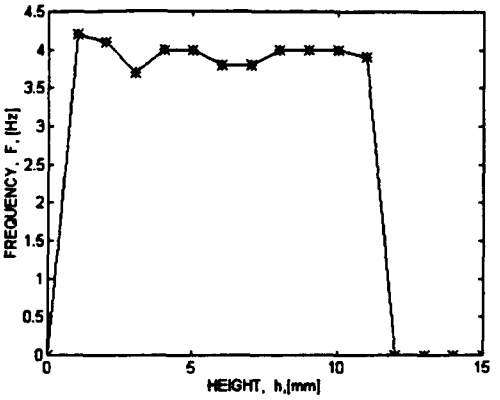

Figure 7. Variation of the oscillation frequency with height along the combustor center line.

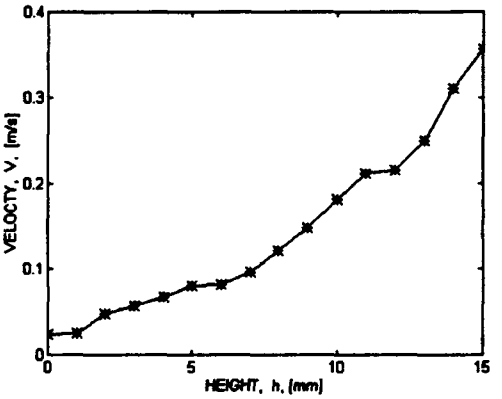

Figure 8. Variation of average velocity along the centerline of the combustor.

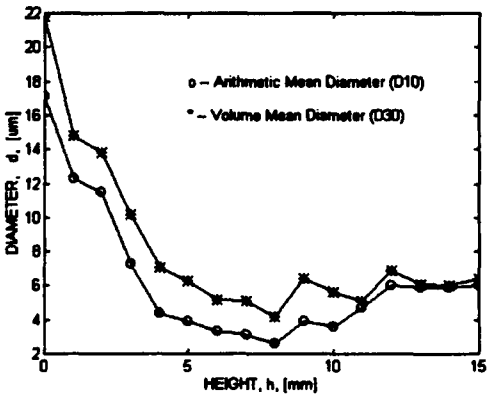

Figure 9. The change in average fuel droplet diameter along the centerline of the combustor.

Figure 10 summarizes numerous experimental results during which parametric study of two major parameters was performed. The combustor was operated from the lowest possible air flow to the maximum practical one. The nitrogen flow in the central tube was always adjusted to maintain equal average velocity as that of the air. It is clearly seen from the figure 10 that increasing the fuel flow rate (and the fuel to air

ratio) increases monotonically and significantly the frequency of oscillations. This phenomenon occurs independently of the air and fuel stream velocities. The changes in frequencies is sometimes by more than a factor of 2 in the investigated range. The reason for the latter is probably the higher associated heat release which increases buoyancy that accelerate faster the elevation of the flame and its separation from the fuel stream. The fuel stream which is even heavier, due to the higher portion of fuel, collapse faster and disengages itself earlier from the heat source. The flame consequently reduces in size and is pulled downwards by the center part of the vortex generated at the wake of the central fuel stream [6]. Hence all the process occurs
faster.

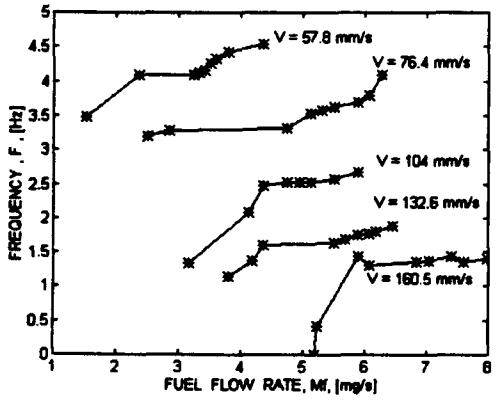

Figure 10. Variation of flame oscillation frequency with fuel flow rate and average velocity (air and nitrogen).

The momentum of the flow seems to have an opposite and more significant effect. The higher the air (and fuel stream) velocities, the slower the frequencies of oscillations. This phenomenon was investigated over a large range of velocities and was found to exist monotonically over the whole operating range. The reason for the latter is probably the fact that higher surrounding air flows reduce and delay the collapse of the fuel stream into the mushroom shape, hence it maintains a higher vertical level. Consequently, it separates less from the flame, reducing the driving force for the oscillations.

Conclusions

The recent experimental results strengthen the hypothesis that the naturally occurring oscillations are primarily induced by gravity. The horizontal combustion experiment indicated that the initial (small) zone, where the flame was still horizontal and uninfluenced by gravity, did not oscillate. In the vertical (normal) configuration, the increase of heat release has led to speeding the frequency of oscillations where as increasing the momentum of the flows decreased the speed of oscillations. Both effects are directly linked to gravity further highlighting the necessity to incorporate gravity effects in the numerical modeling.

References

1. Burke, S.P., and Schumann, T.E.W. *Ind. Eng. Chem.* 20:998-1004 (1928).

2. Greenberg, J.B. *Combust. Sci. Technol.* 75:13-30 (1991).

3. Greenberg, J.B. *Combust. Flame* 77:229-240 (1989).

4. Greenberg, J.B., and Cohen, R. *Atomiz. Sprays* 2:275-293 (1192).

5. Greenberg, J.B., and Cohen, R., Winter Annual Meeting of ASME on Heat and Mass Transfer in Spray Systems, Atlanta, Georgia, HTD - Vol. 187, 1991, p. 11.

6. Levy, Y. and Bulzan, D., "On the Oscillation of Combustion of a Laminar Spray", accepted for publication in *Combust. Flame* (1994)

7. Durao, D.F.G., and Whitelaw, J.H. *Proc. R. Soc. A.* 338:479-501 (1974).

8. Toong, T.Y., Salant, R.F., Stopford, J.M., and Anderson, G.Y. *Tenth Symposium (International) on Combustion*, The Combustion Institute, Pittsburgh, 1965, p. 1301.

9. Kimura, I. *Tenth Symposium (International) on Combustion*, The Combustion Institute, Pittsburgh, 1965, p. 1295.

10. Ballantyne, A., and Bray, K.N.C. *Sixteenth Symposium (International) on Combustion*, The Combustion Institute Pittsburgh, 1976, p. 777.

11. Chen, L.D., Seaba, J.P., Roqumore, W.M., and Goss, L.P. *Twenty-Second Symposium (International) on Combustion*, The Combustion Institute, Pittsburgh, 1988, p. 677.

12. Davis, R.W., Moore, E.F., Roqumore, W.M., and Chen, L.D. *Combust. Flame* 83:263-270 (1991).

13. Ellzey, J.L., Laskey, K.J., and Oran, E.S. *Combust. Flame* 84:249-264 (1991).

PHASE DOPPLER VELOCIMETRY MEASUREMENTS IN COUNTERFLOW SPRAY FLAMES

F. Lacas and P. Versaevel

Laboratoire EM2C du CNRS et de l'ECP
Grande Voie des Vignes, 92295 Chatenay Malabry - France

ABSTRACT

The present work is concerned with an application of Phase Doppler Velocimetry to counterflow spray flames. Laminar counterflow flames are of great interest in the study of flame structure, due to their stability. We are presenting here a setup where the use of a droplet spray as fuel has been made possible. Thank to PDA, simultaneous measurements of velocity, droplets size and number density have been pursued on such a configuration. From these quantities we were able to compute the trajectories of the droplets and drag coefficients.

1. INTRODUCTION

In many practicle applications dealing with energy production and transformation, it is more convenient to store and burn liquid fuel. This is the case in Diesel or rocket engines, turbojets, and furnaces. In all these configurations, the interaction between the flame and the spray is a leading phenomenum. In order to study the combustion of sprays, we have build in our laboratory an experimental setup to produce counterflow diffusion flames using liquid droplets cloud as fuel. The size and velocity field of the droplets was studied in the flame using Phase Doppler Velocimetry.

In the first section we briefly describe the experimental setup and the Phase Doppler Velocimetry system used. In the second section we present the velocity, size and droplets density number measured in the counterflow flame experiment. In the last part, the experimental datas are processed to obtain more global parameters such as gas velocity field and drag coefficients.

2. EXPERIMENTAL SETUP

The counterflow laminar diffusion flame is a very convenient geometry for combustion studies (see Tsuji [1982]). It makes possible the production of a very steady laminar flame without interaction with the surounding structure or the burners and with a very good optical access to the flame. This is achieved with two axisymetrical converging nozzles. The upper burner is feeded with air and the lower burner is feeded with a mixture of nitrogen, gaseous fuel and liquid fuel droplets. The main flow is surrounded with a coaxial nitrogen screen to prevent reaction with ambient air. The gaseous flow rates are controlled using sonic nozzles. The burners are fixed on a moving berth which enables exploration along radial (Or) and axial coordinates (Oz). A schematic view of the burner is presented on figure 1.

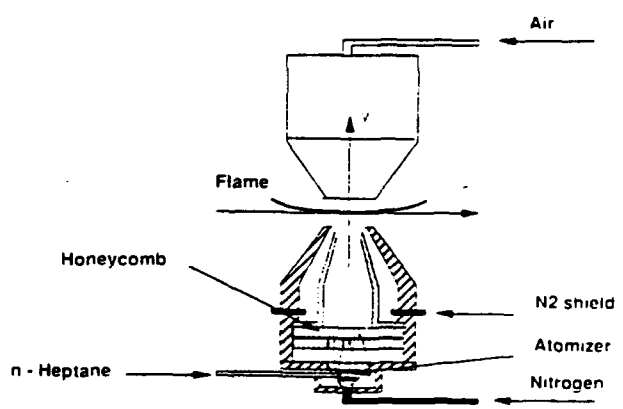

Fig 1: Schematic view of the burner and of the flame.

The droplets spray is produced using an ultrasonic atomizer, which gives low droplets size dispertion and initial velocity . Liquid heptane is used as fuel. It is feeded to the atomizer from a pressurized vessel through a liquid mass flow rate controller, so that the liquid flow rate is measured during the experiment. A more complete description of the experimental setup and atomization system may be found in Darabiha et al. [1993].

Measurements of droplets size, velocity and number per unit volume were performed using Phase Doppler Velocimetry. This technique is an extension of Laser Doppler Velocimetry (see Durst [1975]). The light from a laser (HeNe) is separated into two beams which are separately focused by a converging lens. Interference fringes appear in the intersection volume of the two beams. The light scattered by a particle crossing this volume features a periodic signal having a frequency proportional to the particle velocity and to the inverse of the distance between two fringes. This distance is a constant depending on the geometry of the set-up and on the wavelength of the laser. If one now observes the scattered light from two different angles, one detects a phase shift between the two signals, which is proportional to the droplets diameter. It is thus possible to measure droplets size and velocity simultaneously. The data acquisition rate and the velocity also makes possible to know the number of droplets per unit volume.

In our set up, the laser beam intersection angle is θ=9°30', the scattering angle is φ=64° and the collection angle is ψ=4°40' (see Figure 2 for the definition of these angles). A 500 kHz phase shift was used. The laser was a HeNe laser with a wavelength of 632 nm. The data were stored on a digital osciloscope and transfered through a GPIB bus to a PC486 type computer where data processing takes place (see Veynante [1992]). The quite slow data acquisition and processing rate was not a problem in our case, because we are studying laminar steady flows.

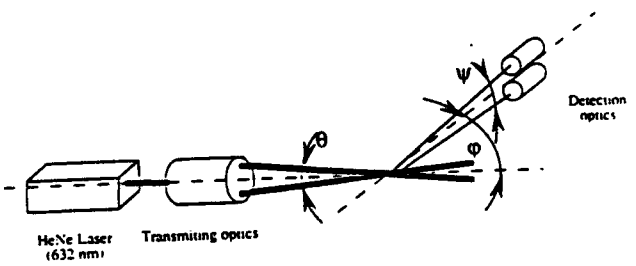

Fig 2: Schematic view of the Phase Doppler Velocimetry system.

3. VELOCITY, SIZE AND DROPLETS NUMBER DENSITY

The first series of measurements were performed in the counterflow of air on one side and a mixture of heptane droplets and nitrogen on the other side, but without combustion. The purpose was to test the possibilities of our Phase Doppler Velocimetry setup on one hand, and to check the quality of the two phase flow at the outlet of the lower burner on the other hand.

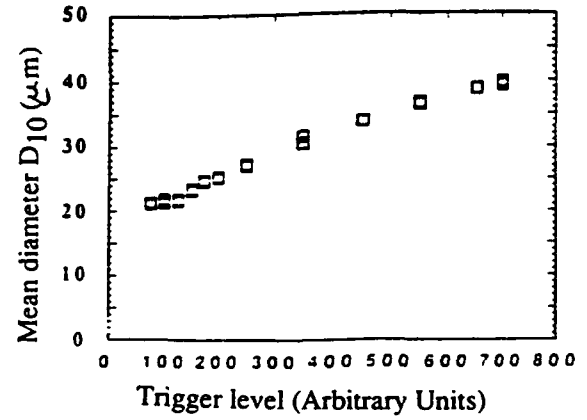

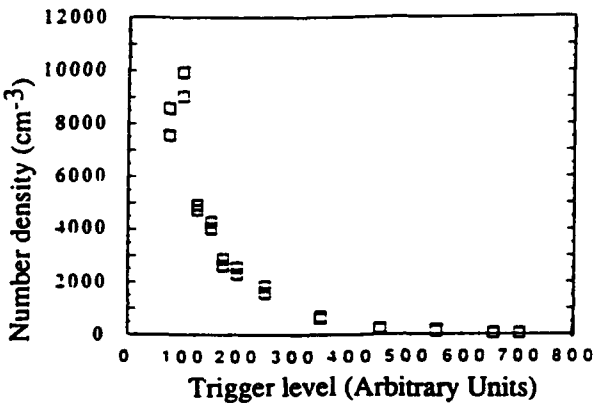

Fig 3: Influence of trigger level on measured droplets size (a) and droplets number density (b) at the outlet of the burner.

We have plotted on figure 3a and 3b the droplets mean diameter D_{10} and the droplets density number as a function of the trigger level of the detection of the PDA system. The fact that the diameter depends on the trigger level is not surprising: if the trigger level is to high, the smallest droplets are not detected and the size distribution is modified. The effect may also be seen on the droplets density number : the higher the trigger level is, the less droplets are detected. This effect is to be compared to the well known "bias effect". This shows that the trigger level has to be chosen very carefully when using PDA system. The optimization of the validation rate is in this case very important.

Figure 4a displays the velocity of the droplets at the outlet of the burner measured with the PDA system as a function of the gaz velocity computed from the measured gaseous flow

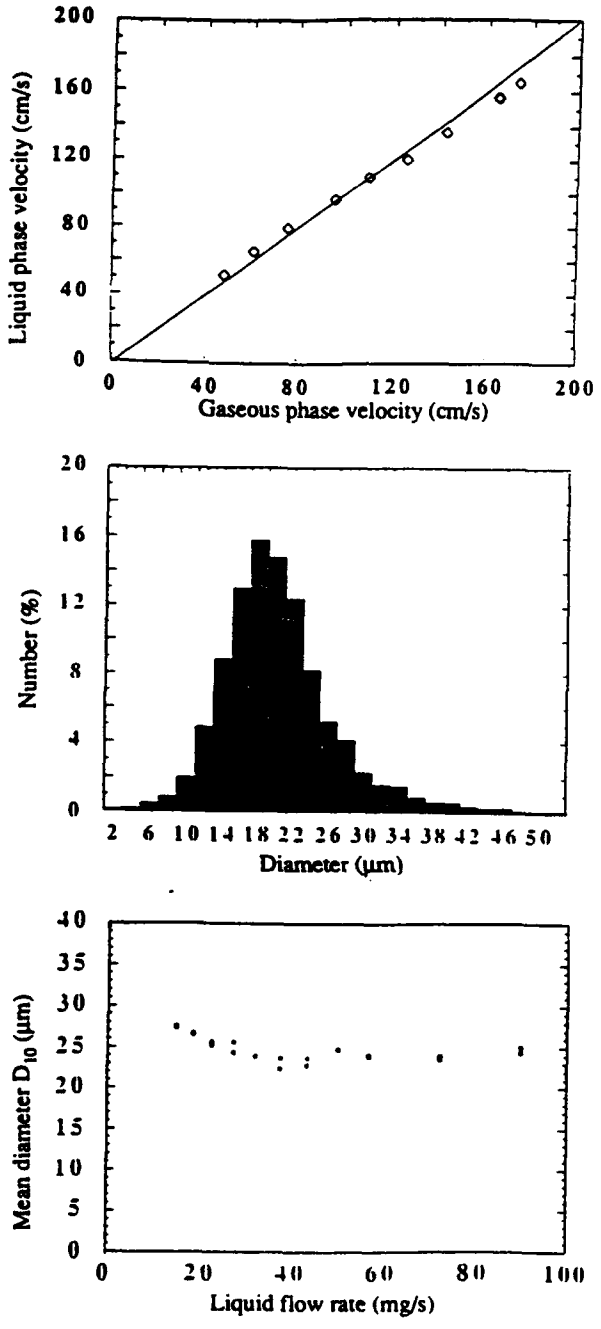

Fig 4: (a) droplets velocity measured from PDA as a function of gaz velocity measured from flow rate control system. (b) droplets size distribution at the outlet of the burner. (c) Influence of liquid flow rate on droplets mean diameter.

rates . One can see that this curve is linear with a unity slope. This shows the good correlation between these two measurements. It also shows that the droplets and the gaz have the same velocity at the outlet of the burner. We have plotted on figure 4b the droplets size distribution at the same place. One can see that the size dispersion is rather weak, which was one of the goal aimed at when using ultrasonic atomization. And as shown on figure 4c, the droplets mean diameter is independent of the liquid flow rate, which was another design parameter of this system.

We have plotted on figure 5 the mean diameter D_{10} and the mean droplets velocity as a function of position along the axis in the cold counterflow. One can see that the diameter remains constant in the flow far from the steady plane. This means that no evaporation takes place after the outlet of the burner and that the two phases are in thermodynamic equilibrium. The mean droplets size is increasing near the steady plane (z=15mm). This is not due to condensation but this is a statisctical effect: the larger the droplets are, the more inertia they have and the later they follow the gasous flow. So that only the bigger droplets are crossing the steady plane and the mean size is increased. The droplets mean velocity profile shows a smooth decrease that may be compared to the case of pure gaseous counterflows. (see Rolon et al. [1991]).

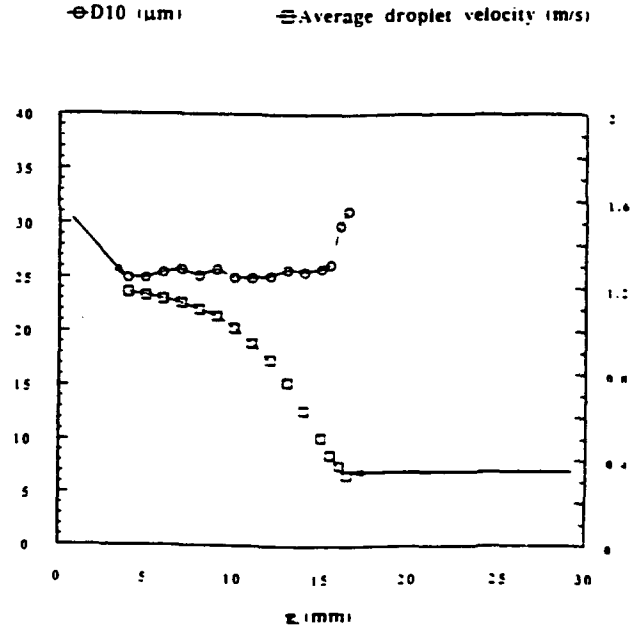

Fig 5: Mean droplets size and average droplets velocity along Oz axis in the cold counterflow (the distance between the two burners is 30mm).

The same kind of experiments were performed in the burning flow. Figure 6 presents profiles of mean diameter D_{10} , droplets number density and mean velocity. The global behaviour is the same as for the non reactive case. The mean diameter D_{10} remains constant in the main flow, and increases near the flame zone for the same statistical effect. The droplets number density exhibits a maximum in the same zone due to the fact that the liquid phase flow is limited by the

counterflow and this leads to accumulation of droplets near the flame. Droplets number density then strongly decreases to zero after the flame front. The velocity profile is also typical from counterflows. A small increase in the droplets velocity can be observed after the flame front. This behaviour is due to burnt gases expansion and is also observed in pure gaseous flames (see Rolon et al. [1991]). The same profiles have been measured for various values of the flow velocity at the outlet of the burner. The same general trend is observed.

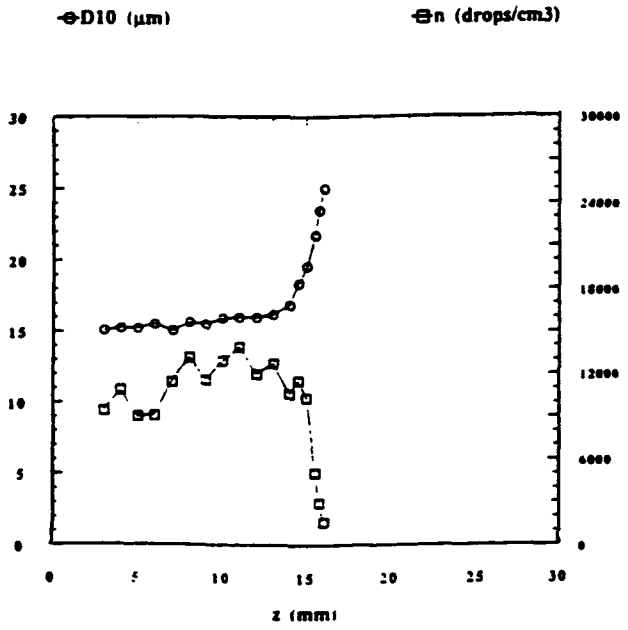

Fig 6: Mean droplets size, number density and average droplets velocity along Oz axis in the burning counterflow (the distance between the two burners is 30mm).

4. VELOCITY/SIZE CORRELATION

One of the main advantages of Phase Doppler Velocimetry measurement is that velocity and size of the droplets are measured simultaneously. So that velocity / size correlations are available. We have plotted on figure 7 such correlations for the cold and burning cases and for various values of the axial position z. We can see that in both cases the droplets velocity at the outlet of the burner (z=6mm and z=3mm) does not depend of the size: all the droplets are going at the same velocity. Then, when the distance with the burner increases, the smallest droplets velocity is decreasing faster than the largest ones. This is due to the fact that the mass of the larger droplets is considerably bigger than the one of the smallest

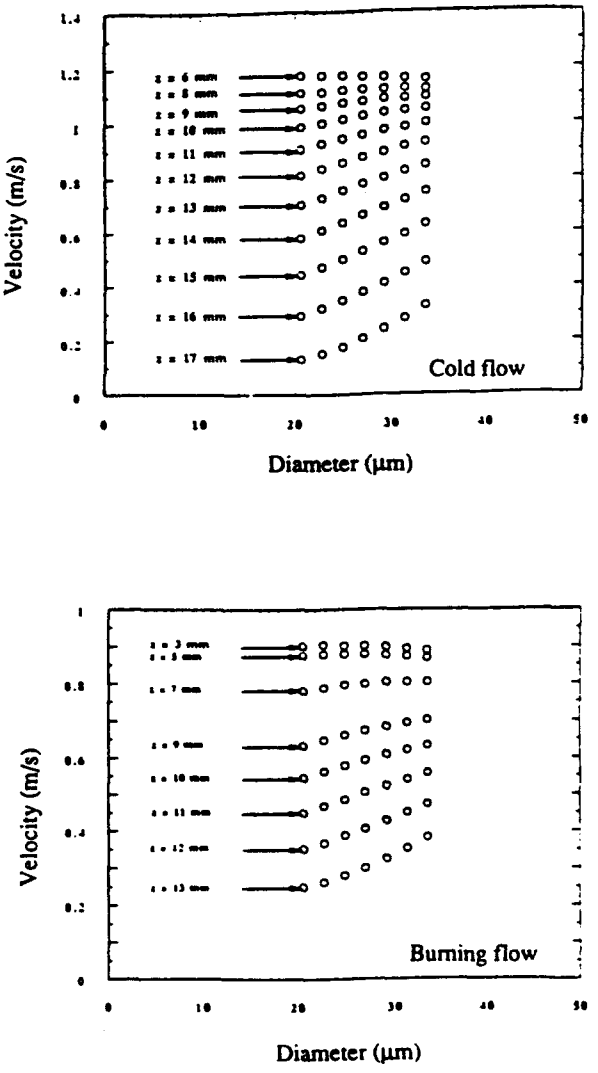

Fig 7: Measured velocity for each diameter class for the cold flow (top) and for the burning flow (bottom).

one (the mass is proportionnal to d^3). And so is their inertia. The small droplets are following the gaz motion better than the big ones. One can also notice that in the burning case, the droplets are disappearing before the stagnation plane.

In a simple flow pattern such as laminar counterflow, it is possible to process these data to obtain the drag coefficient of the droplets. Such measurements of the drag coefficient from Phase Doppler Anemometry data have already been performed by Bachalo [1994], but in different configurations. Let us assume that the size distribution may be splitted into M classes $(D_i)_{i=1,M}$. A drop is part of class D_i if its diameter is included between $D_i+\delta/2$ and $D_i-\delta/2$. If δ is small enough, all droplets of class D_i have the same velocity V_i For a drop of class D_i, the motion equation is then:

$$m_i \frac{\partial V_i}{\partial t} = - m_i g + C_d \frac{1}{2} \rho \left(V_g - V_i\right)^2 \frac{\pi D_i^2}{4} \qquad (1)$$

where m_i is the mass of one drop of class D_i, g is the gravity, V_g is the gaz velocity and C_d is the drag coefficient. Let us now assume that the drag law may be written, following Stokes:

$$C_d = \alpha \frac{23}{Re} \qquad (2)$$

where α is a constant. α=1. stands for the classical Stokes law. For a given axial position z in the flow, if α is considered constant, one can compute from the motion equation a value $(V_g)_i$ of the gaz velocity for each class of droplets D_i. The value of α is then the one that minimize the standard deviation of $(V_g)_i$ for i=1,M, i.e. for all classes. We have then both the gaz velocity and drag coefficient. Typical values of α measured are $0.5<\alpha<0.6$. This drag coefficient lower than the Stokes law may be explained by the interaction between droplets.

We have plotted on Figure 8 The ratio of the drag coefficient measured in the flame using the technique described above to the one given by the Stokes Law, versus the axial coordinate (z). This experimental case coresponds to an initial velocity of the gas and the droplets of 0.9 m/s at the outlet of the burner. The mean values of the drag coefficient is, as already noticed lower than the one of the classical Stokes Law. One can also notice an important decrease of the drag coefficient through the flame. This behaviour may be explained by several causes. First of all, strong variations of the thermodynamical and transport properties take place in the flame front. These variation may change the drag forces. The evaporation is very fast, and the evaporation front is very thin (see also Fig. 6). In the vicinity of the evaporation front, the gaseous flow rate coming out of the droplets is very high, and the Stefan flow may be very important and change the condition of the flow around the droplets. So that the drag cannot any more be interpreted as the Stokes drag.

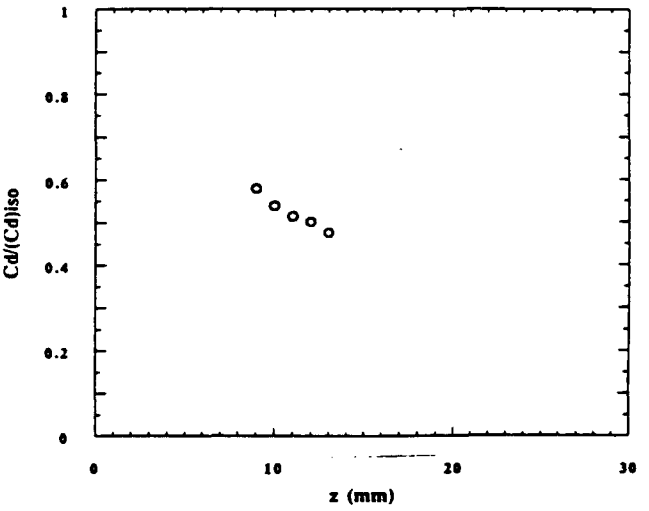

Fig. 8: Ratio of the measured drag coefficient to the Stokes law as a function of the axial coordinate (z)

This behaviour may be important in two phase flames, where for instance a flame front is propagating in a spray. In that case the trajectory of the droplets may be strongly affected by the changes in the drag force, due to the same variations of the drag coefficient we have measured.

5. CONCLUSION

Phase Doppler Velocimetry is a very interesting technique for the study of reactive laminar flows. A great care has to be taken of data processing parameters. But important informations may be collected on size, velocity and number density of the droplets in a burning flow. The first interesting topic is to check the quality of the experimental setup in term of spray flow rate, velocity and homogeneity.

Measurements of Droplets size, velocity and number density is also possible in the vicinity of a counterflow laminar flame. These quantities are of great importance in the understanding of flame spray interaction. Counterflow laminar flame is a good configuration to study this phenomenum. Its simplicity makes possible further data processing to compute drag coefficients and gaz velocity. Interesting phenomena have been noticed. In our case, the droplets vaporization is very fast and very well localised in space. This behaviour may be of special interest for the modelling of spray flames. The drag

coefficient may encounter important variation in the same area. These variation may cause changes in the droplets trajectories, especially if an important velocity gap exists between the two phases. This may also be important to take into account in turbulent spray flames, were velocity fluctuations may induce trajectories changes.

The work on this topic is now undergoing, and further measurements will be pursued to study the influence of pressure on spray flame interaction. A special care is now taken of the way all these phenomena may be taken into account in modelisations.

ACKNOWLEDGEMENTS

This work was funded by the Groupe de Recherches sur les Moteurs Fusées CNRS/CNES/SEP. Société Européenne de Propulsion is gratefully acknowledged for having supported the second author during his work.

REFERENCES

Bachalo, W.D., 1994, The Phase Doppler Method: Analysis, Performance Evaluations, and Applications, Part. Part. Syst. Charact, 11, pp73-83

Darabiha N., Lacas F., Rolon J.C., Candel S., 1993, Laminar Counterflow Spray Diffusion flames: A Comparison Between Experimental Results and Complex Chemistry Calculations, Comb. and Flame, 95:251-275

Durst F., Zaré M., 1975, Laser Doppler Measurements in Two Phase Flows, Proc. of the LDA Symp., Copenhagen

Rolon J.C., Veynante D., Martin J.P. and Durst F., 1991, Counterjet Stagnation Flow, Exp. Fluids, 11:313-324

Tsuji H., 1982, The Influence of Laminar Transport and Chemical Kinetics on the Time Mean Reaction Rate in a Turbulent Flame, Prog in Eng. Comb. Sci., 8:93

Veynante D., Lacas F., 1992, Moder Spectral Analysis for LDV and PDA Data Processing, Proc. of the 6th LDA Symp., Lisbon

Structure of Spark-Ignited Spherical Flames Propagating in a Droplet Cloud

Fumiteru AKAMATSU, Kazuyoshi NAKABE, Masashi KATSUKI,
Yukio MIZUTANI and Toshikatsu TABATA

Department of Mechanical Engineering, Osaka University
2-1 Yamada-oka, Suita, Osaka 565, Japan

ABSTRACT

A droplet cloud of liquid fuel produced by an ultrasonic atomizer was ignited by a spark, and the flame ball propagating outwards was observed in detail in order to elucidate the mechanism of flame propagation and complicated group combustion behaviors of spray flames. For that purpose, the instantaneous images of droplet clusters, OH-radical chemiluminescence and C_2-band flame luminosity were taken simultaneously, and the light emission signals in OH- and CH-bands, Mie-scattering signal from droplets, and the size and velocity of droplets were monitored simultaneously in time series. It was found that a nonluminous flame propagated ahead of the luminous flame, and that droplets disappeared in the luminous flame zone due to their rapid evaporation, and that a number of small-scaled droplet clusters were burning in diffusion combustion mode associated with solid-body emissions inside a flame ball.

1. INTRODUCTION

The combustion of a single droplet or a droplet array has been investigated so far by numerous researchers (for example, Williams, 1973; Law, 1982). However, detailed structure and propagation mechanism of a flame propagating through a droplet cloud has not been discussed extensively yet. A spray flame is thought to be composed of a number of flamelets where droplets and fuel vapor burn in a complicated manner interacting with each other (Faeth, 1977; Chigier, 1981; Nakabe et al., 1991). Apparently, random and discontinuous flame propagation occurs in a liquid fuel spray as far as one observes luminous spray flames by conventional high-speed direct photography (Mizutani and Nishimoto, 1972; Nakabe et al., 1988). This fact implies that the spray burns in a complicated group combustion mode (Suzuki and Chiu, 1971; Chiu and Liu, 1977; Chiu et al., 1982) being divided into many clusters and subclusters corresponding to the number density distribution of droplets. Since the conventional high-speed photography cannot visualize nonluminous flames which are supposed to play an important role in the flame propagation process, the planar laser-induced fluorescence (PLIF) (Allen and Hanson, 1986) or chemiluminescence of OH-radicals should be observed to elucidate the actual flame propagation mechanism in a spray. The simultaneous visualization of luminous and nonluminous flames along with unburned droplets is also very useful for understanding of the detailed spray flame behavior.

In the previous study (Mizutani et al., 1993), we observed a flame ball ignited by a spark, propagating through a droplet suspension, freely falling and entraining surrounding air, in order to observe in detail the flame propagation mechanism and flame structure of droplet clusters burning in sprays under the minimal influences of atomization process and fluid motion. Firstly, the characteristics of the droplet suspension were examined for the non-burning case by the simultaneous measurement of the velocity and diameter of droplets with three laser beams, two He-Ne laser beams and one Ar^+ laser beams crossing at one point with each other. Secondly, the behavior of the growing flame ball was examined by comparing the local light emission signals of OH- and C_2-radical bands with the processed images of the flame ball obtained by a high-sensitivity CCD camera and a high-speed camera.

In the present study, a pair of short-exposure images of OH-radical chemiluminescence and either of flame luminosity in the C_2-radical emission band or of Mie-scattering by droplet clusters were taken simultaneously to clarify the spacial relation between the nonluminous and luminous flame and unburned droplet clusters. Furthermore, this observation was compared with local continuous measurements, where the size and velocity of droplets, signals of the light emissions in OH- and CH-radical bands and Mie-scattering signal from droplets were monitored simultaneously. It was found that a nonluminous flame first propagated continuously through a coexisting region of small droplets and gas-phase mixture and that a number of small-scaled droplet clusters burned randomly associated with discontinuous luminous flames behind the nonluminous flame front.

2. EXPERIMENTAL APPARATUS

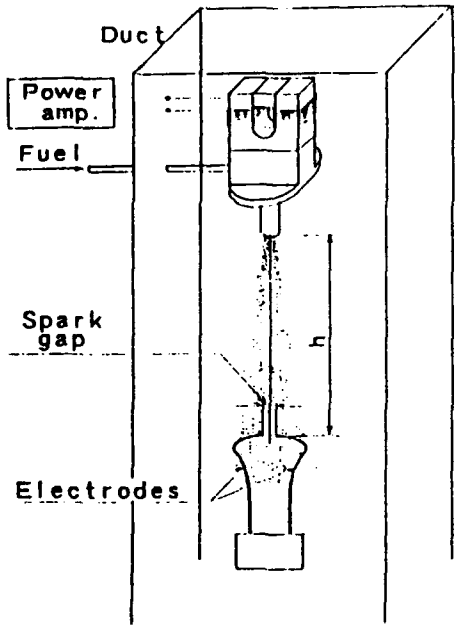

Fig. 1 Experimental apparatus

Figure 1 shows a schematic illustration of the experimental apparatus. An ultrasonic atomizer of ferrite magnetostriction type (resonance frequency=18.5 kHz) was installed at the top center of a vertical square duct (280mm X280mmX1325mm) for shielding the spray from environmental disturbances. A spark gap, 4.0 mm wide, was located 400 mm below the atomizer tip. A liquid fuel (kerosene) was fed to the atomizer by a microsyringe pump. The freely falling droplet suspension was ignited by an intermittent electric spark. A pulse-delay-generator (Stanford Research Systems, WC Model DG535) was used to control the triggering timing of each instrument and device.

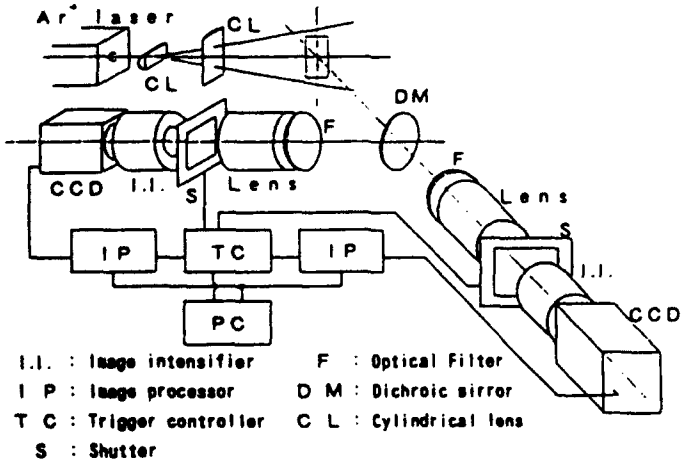

Fig. 2 Optical image processing system

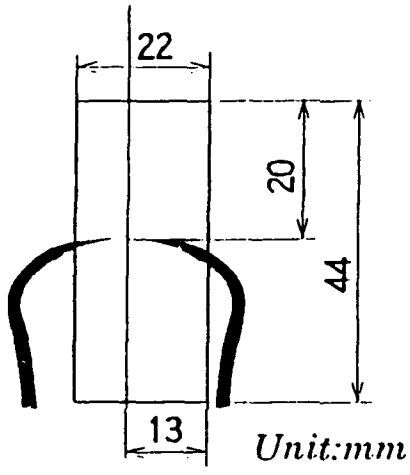

Fig. 3 Imaging region

Preliminary observation by a high-speed video recorder (Nac, HSV-1000) demonstrated a ignition delay of several milliseconds, almost spherically propagating flame ball for several tens of millisecond and the final deformation of flame ball due to buoyancy. Therefore, the observations were confined in the period of spherical flame propagation. Throughout the present experiment, the fuel injection rate was kept 4.44 cm^3/min and the discharge duration time was 20 ms.

The optical and image processing system used to obtain various simultaneous flame images is shown in Figure 2. The planar beam of an Ar^+ laser tailored by a cylindrical lens illuminated a vertical plane involving the central axis of the apparatus. The thickness of the laser sheet was approximately 1.5 millimeters. The light, perpendicularly scattered by the droplets in the rectangular area (indicated in Fig.2) and passed through a dichroic mirror (DM) and an interference filter (F) (transmission peak wavelength of 514.5 nm), was focused by a UV Nikkor lens onto the photocathode of an image intensifier (I.I.). On the other hand, OH- chemiluminescence, emitted in the same direction, reflected by the dichroic mirror and filtered by another interference filter (transmission peak wavelength of 308.5 nm), was focused on the photocathode of another image intensifier. In order to obtain the OH-chemiluminescence image and the spectral luminosity image of a flame in the C_2-radical band simultaneously, the laser was turned off and the optical interference filter in the droplet image path was replaced with the one for C_2-band. This system consisted of a pair of image processors (IP) and mechanical focal plane shutters (S), both of which were controlled by the trigger controller (TC) connected to the personal computer (PC). Image data were transferred to the computer and stored in floppy disks. The ordinary exposure were set at 1/250 (4 ms). A rectangular area for visualization are indicated in Fig.3.

Figure 4 shows the optical system for local continuous monitoring of droplet velocity and diameter. Mie-scattering signals from droplets and the light emission signals in OH-

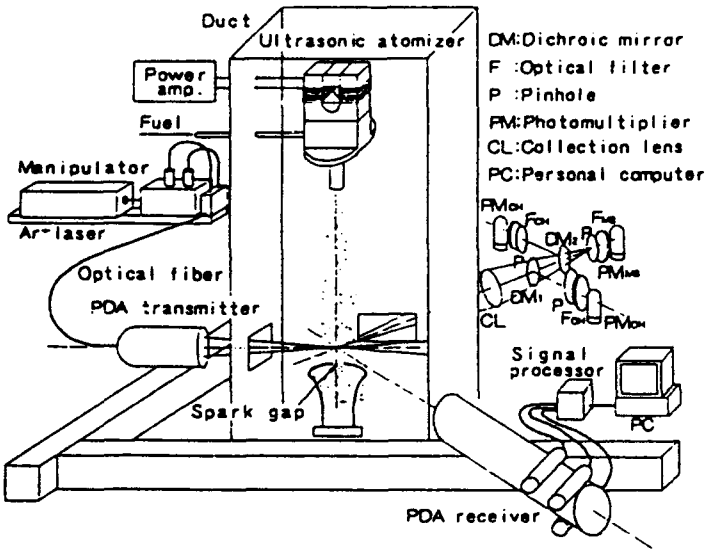

Fig. 4 Optical system for local continuous monitoring

and CH-radical bands. The monitoring location was chosen at 25 mm directly above the spark gap, where the flame propagated upward steadily. The light source for Mie-scattering and PDA transmitter was an Ar^+ laser (Spectra Physics, Stable 2016, wave length=514.5 nm). The light emissions in OH- and CH-radical bands and Mie-scattering from droplets were detected in the direction perpendicular to the axis of the PDA transmitter using dichroic mirrors (DM), optical interference filters (F) and photomultipliers (PM).

The size and velocity of droplets were also measured simultaneously using a PDA receiver (Dantec, Model 57X10) and a signal processor (Dantec, Model 58N10). Scattering angle was set at 70.3 degrees. This detection angle was selected so as for the first order refracted light to be dominant and the measured values by PDA not to be sensitive to the refractive index changes of droplets (Pitcher et al., 1990). The specification of the PDA system is shown in Table 1.

Table 1 Specification of PDA system

Probe:	Focal length	500	mm
	Spot diameter	244.8	μm
	Fringe spacing	5.0	μm
	Fringe number	49	
Range:	Maximum diameter	190	μm
	Maximum velocity	1.5	m/s
	Minimum velocity	-0.5	m/s
Focal length of receiving optics		310	mm
Wavelength of laser beam		514.5	nm
Bandwidth of signal processor		0.4	MHz
Frequency shift		40	MHz

The Mie-scattered light corresponds to the number density of droplets or the passage of droplet clusters. The OH-band luminosity indicates the existence of combustion reaction in case of spray flames because relatively low temperatures (less than 2000 K) prevail in the whole flame. On the other hand, the light emission in CH- and C_2-band are biased by the continuous spectrum of solid-body emission, so that they correspond to each radical emission overlapped by the solid-body emission from soot particles (Mizutani et al., 1989). For luminous spray flames, the sensitivity of the detectors for CH- and C_2-band emissions should be lowered by an order of magnitude as compared with the OH-band detector.

3. RESULTS AND DISCUSSIONS

3.1 Image Processing

Figures 5 (a) and 5 (b) show typical simultaneous images in OH- and C_2-band, respectively, at 35 ms after the electrical discharge. As mentioned previously, in the case of luminous flame like a spray flame, the light emission in C_2-band is biased by the continuous solid-body light emission. Because its intensity is much stronger than that of OH-band, the sensitivity of the I.I. in C_2-band must be lowered by an order of magnitude than that in OH-band. Therefore, the region where an intense OH-band emission and a weak C_2-band emission coexist is thought to be the nonluminous flame region. On the other hand, the region where both OH- and C_2-band images are strong is thought to be the luminous flame region accompanied with intense solid-body light emissions from soot. Furthermore, the region of intense C_2-band emission not synchronized with OH chemiluminescence is regarded as the high temperature burnt gas region. It is noticed from these images that the flame first propagates spherically, although the flame eventually drifts upward due to buoyancy effect as mentioned above.

The comparison between the images in OH-band and C_2-band reveals that the region of intense OH-band emissions associated with weak C_2-band emissions is located in the upper portion of the flame ball, whereas the intense C_2-band emission region is confined in the inner (lower) portion of OH image; i.e. the nonluminous flame region is followed by the luminous flame region. The bright dots of C_2-band emission are regarded as small-scaled droplet subclusters buried in a nonluminous flame.

Figures 6 (a) and 6 (b) show typical images of OH-band emission and Mie-scattering from droplets, respectively, simultaneously taken at 35 ms after the electrical discharge. The thin white streaks in Fig.6 (b) are droplet clusters illuminated by the Argon-ion laser sheet. Because an intense flame luminescence can pass through the optical interference filter for Mie-scattering (F_{MS}) (transmission peak wavelength

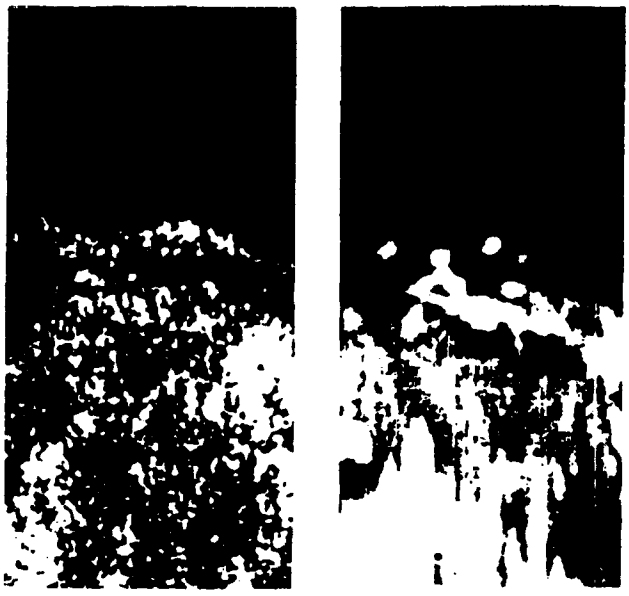

(a) OH-band image (b) C_2-band image

Fig. 5 Short-exposure images of OH-chemiluminescence and flame luminosity in C_2-band

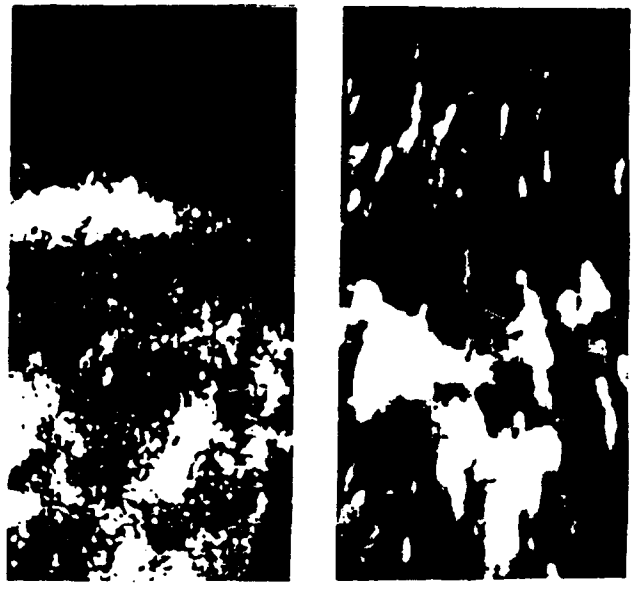

(a) OH-band image (b) Mie-scattering image

Fig. 6 Short-exposure images of OH-chemiluminescence and droplet distribution

of 514.5 nm), both Mie-scattering image and flame luminescence image are superimposed in Fig.6 (b) but they are distinguishable from each other since the luminous flame images are blotted ones different from streaks.

By comparing these two images, it is found that the intense OH emission appears in the outer layer of the flame ball and that the luminous flame is located inside the flame ball. Furthermore, in the outer region of the flame ball, there are clear streaks of droplet clusters regardless of the existence of OH emission. Consequently, it is considered that a nonluminous flame is propagating continuously through the region of small droplets and gas-phase mixture and the remaining droplet clusters penetrate into the nonluminous flame. A number of droplet clusters are ignited randomly behind the nonluminous flame and burn associated with luminous flames.

3.2 Local Continuous Monitoring

Although two-dimensional information can be derived from flame images, temporal transition is ambiguous. So, let us here compare the above results with the signals monitored at a point continuously. The monitoring location was chosen at 20 mm above the center of the spark gap where the flame propagated upward steadily as mentioned previously. The reason why we adopted light emission in CH-band instead of that in C_2-band during the local continuous monitoring is that it is difficult to detect simultaneously both C_2-band light emission and Mie-scattering because their bands are so close to each other. The C_2-band is located on the longer wave length side of the CH-band, so the C_2-band is more biased by continuous solid-body light emission than CH-band. But, we have confirmed in the preliminary experiment that flame luminosity both in CH- and C_2-bands show almost same tendency.

Figure 7 shows the five simultaneous signals at a local point; that is, OH emission (I_{OH}), CH-band emission (I_{CH}), Mie-scattering from droplets (I_{MS}), droplet velocity (V_h) and droplet diameter (D). The abscissa is the time after

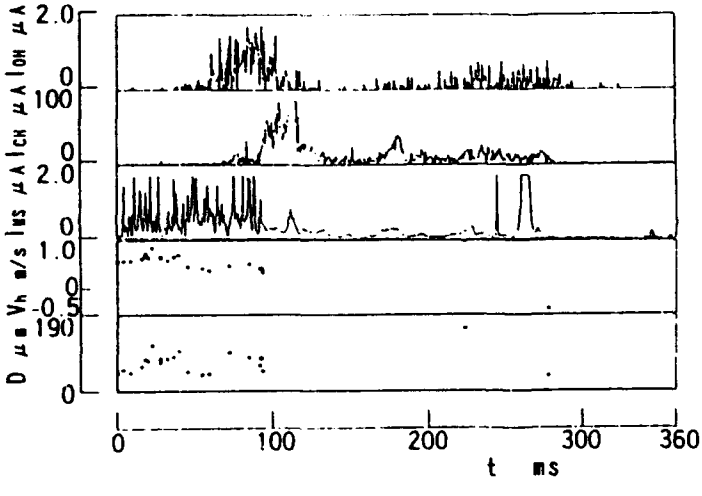

Fig. 7 5 simultaneous signals at 20 mm above spark gap

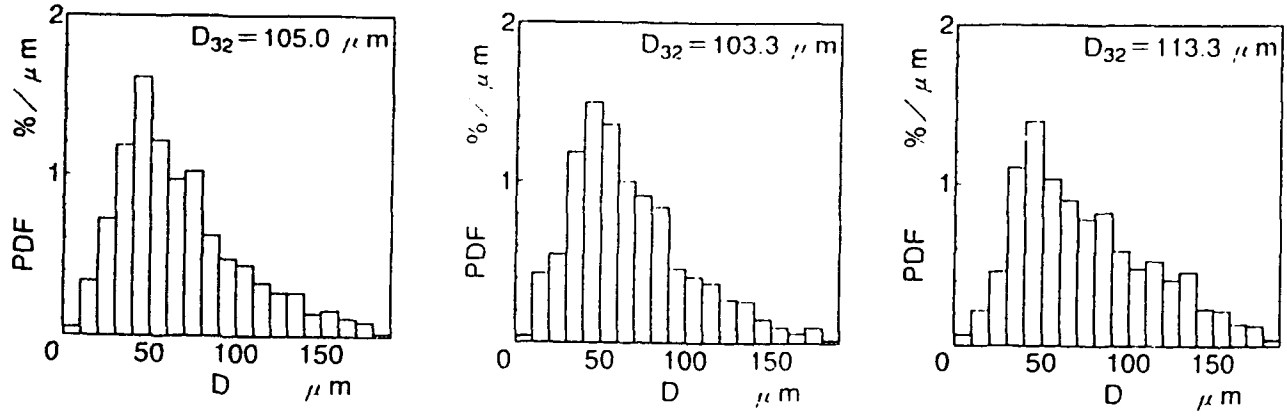

(a) Cold flow (b) Before flame arrival (c) After flame arrival

Fig. 8 Size distribution of droplets

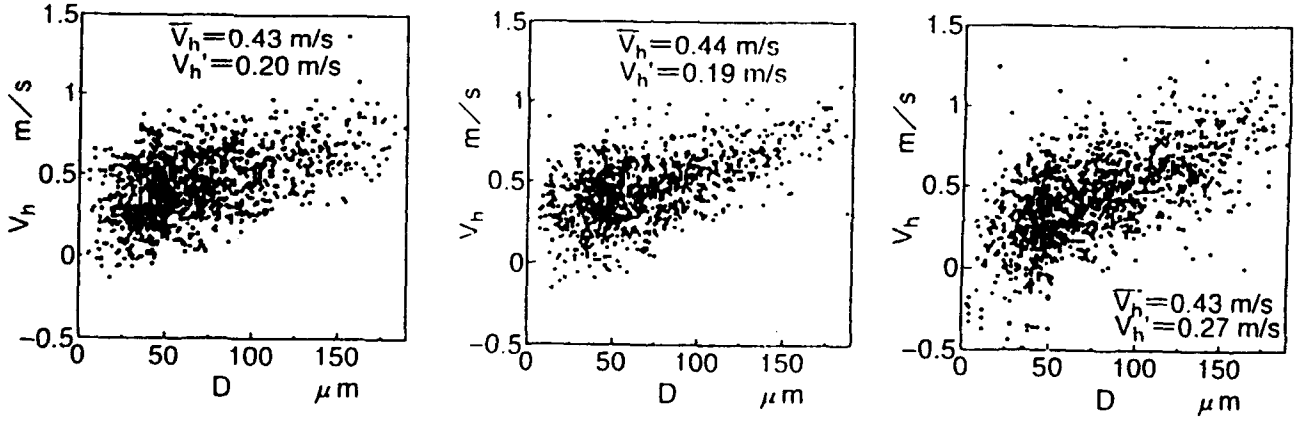

(a) Cold flow (b) Before flame arrival (c) After flame arrival

Fig. 9 Correlation between size and velocity of droplets

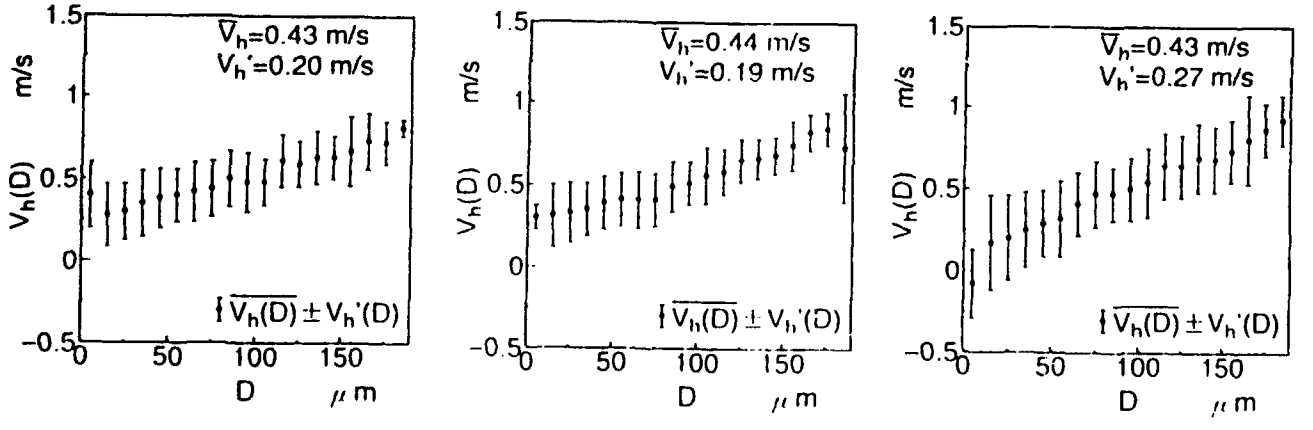

(a) Cold flow (b) Before flame arrival (c) After flame arrival

Fig. 10 Mean velocity and its fluctuation of droplets

spark initiation in milliseconds. Since we know that the flame propagates upward steadily at this point, these time series signals represent the structure of the upper portion of the flame ball. The droplet number density under the cold condition was estimated about 15 particles/mm^3 by the calibration method by Saffman (1987).

The comparison between the signals in OH-band and CH-bands reveals that both of them appears at the same time, if the fact is considered that the scale of I_{CH} signal is fifty times larger than that of I_{OH}. The CH-band emission synchronizes with OH chemiluminescence, so that the former seems to be CH radical chemiluminescence. We have checked this by using of the common scale for the signal intensities. Thus, nonluminous flames (I_{OH} signal) begin to appear at around 50 ms after electrical discharge, followed by luminous diffusion flames accompanied with solid-body light emission from soot (I_{CH} signal) with a delay of several tens of milliseconds. It well corresponds to the images in Figs. 5 and 6.

The Mie-scattering signal I_{MS} gives us the information on the behavior of droplet clusters during the flame passage through the optical control volume. Droplets randomly fall through the control volume until the luminous flame front arrives there. Only few droplets, on the other hand, are detected after the luminous flame region appears, since the population density of droplets rapidly decreases due to the thermal expansion, evaporation and combustion reaction.

Thus, we arrive the same conclusions as already derived from the image processing that a nonluminous flame is propagating continuously through the region of small droplets and gas-phase mixture and that remaining droplet clusters are swallowed into the nonluminous flame and then a number of droplet clusters associated with solid-body emissions appear randomly and discontinuously behind the nonluminous flame front.

3.3 Conditional Sampling of PDA data

Figures 8, 9 and 10 show the size distribution of droplets, the correlation between diameter D and axial velocity of droplets V_h and mean axial velocity and its fluctuation of droplets in every diameter range of 5 μm, respectively. A solid circle, ● in Fig. 10, indicates the average velocity, and the line segments correspond to ± root-mean-square (rms) value of velocity fluctuation. Sub-indices (a), (b) and (c) in Figs. 8, 9 and 10 denote the cold flow, before flame arrival and after flame arrival, respectively. The data in (b) and (c) were obtained in the way that the data of droplet size before and after the OH signal riseup were accumulated separately through several hundreds of runs.

The patterns in (a) and (b) considerably resemble each other, which suggests that the behavior of droplets is not affected by the flame until the flame arrival. Let us here compare the patterns in (a) and (b) with that in (c) in order to examine the droplet behavior behind the nonluminous flame front. The size distribution patterns in Fig. 8 does not change considerably between (a), (b) and (c) except for the slight increase of fraction of droplets over 80 μm. The average velocity in Figs. 9 and 10 does not change much, but the width of fluctuation is expanded after the flame arrival in every size class. This fact suggests that droplets are affected by the thermal expansion after the flame passage.

4. CONCLUSIONS

A droplet suspension, freely falling and entraining surrounding air, was spark-ignited and the flame propagation mechanism and flame structure were observed in detail. A pair of short-exposure images of OH-radical chemiluminescence and either droplet distribution pattern or flame luminosity pattern in the C_2-radical emission band were taken simultaneously to observe the spacial relation between nonluminous and luminous flame regions and droplet clusters distribution. These data were compared with local continuous measurements, where droplet velocity and diameter, signals of the light emissions in OH- and CH-radical bands and Mie-scattering signal from droplets were monitored simultaneously. The results were summarized as follows;

(1) A nonluminous flame first propagates continuously through a region of small droplets and gas-phase mixture.

(2) Remaining droplet clusters are swallowed into the nonluminous flame and then a number of droplet clusters associated with luminous flames appear randomly and discontinuously behind the nonluminous flame front.

ACKNOWLEDGEMENT

The authors wish to express their gratitude to professor K. Nakajima and associate professor Y. Ikeda and Mr. N. Kawahara of Kobe university for their instruction and help in designing the PDA system, and Mr. T. Osaki of osaka university for their cooperation in experiments. The authors also appreciate that Nac Co. Ltd. allowed us to use their high-speed video system.

REFERENCES

Allen, M.G. and Hanson, R.K. 1986, Digital Imaging of Species Concentration Fields in Spray Flames, Proc. 21st Symp. (Int.) on Combustion, pp.1755-1762.

Allen, M.G. and Hanson, R.K. 1986, Planar Laser-induced-fluorescence Monitoring of OH in spray flame, Optical Engineering, vol.25, pp.1309-1311.

Chigier, N. 1981, Energy, Combustion and Environment, pp.248, McGraw-Hill, New York.

Chiu, H.H., Kim, H.Y. and Croke, E.J. 1982, Internal Group Combustion of Liquid Droplets, Proc. 19th Symp. (Int.) on Combustion, pp.971-980.

Chiu, H.H. and Liu, T.M. 1977, Group Combustion of Liquid Droplets, Combust. Sci. Technol., vol.17, pp.127-142.

Faeth, G.M. 1977, Current Status of Droplet and Liquid Combustion, Prog. Energy Combust. Sci., vol.3, no.4, pp.191-224.

Law, C.K. 1982, Recent Advances in Droplet Vaporization and Combustion, Prog. Energy Combust. Sci., vol.8, no.3, pp.171-201.

Mizutani, Y., Nakabe, K., Fuchihata, M., Akamatsu, F., Zaizen, M. and El-Emam, S.H. 1993, Spark-Ignited Spherical Flames Propagating in a Suspended Droplet Cloud, Atomization and Sprays, vol.3, pp.125-135.

Mizutani, Y., Nakabe, K., Matsumoto, Y., Saeki, T. and Matsui, T. 1989, Processing of Luminescent Radical Images for Flame Diagnostics, JSME International Journal, Series II, vol.32, pp.455-463.

Mizutani, Y. and Nishimoto, T. 1972, Turbulent Flame Velocities in Premixed Sprays: Part I. Experimental Study, Combust. Sci. and Technol., vol.6, pp.1-10.

Nakabe, K., Mizutani, Y., Hirao, T. and Fujioka, H. 1991, An Experimental Study on Detailed Flame Structure of Liquid Fuel Sprays With and Without Gaseous Fuel, Combust. Flame, vol.84, no.1, pp.3-14.

Nakabe, K., Mizutani, Y., Hirao, T. and Tanimura, S. 1988, Burning Characteristics of Premixed Sprays and Gas-Liquid Coburning Mixtures, Combustion and Flame, vol.74, p.39-51.

Pitcher, G., Wigley, G. and Saffman, M. 1990, Sensitivity of Dropsize Measurement by Phase Doppler Anemometry to Refractive Index Changes in Combusting Fuel Sprays, Applications of Laser Techniques to Fluid Mechanics 5th Int. Symp., Lisbon, pp.227-247, Springer-Verlag.

Saffman, M. 1987, Automatic Calibration of LDA Measurement Volume Size, Applied Optics, vol.26, pp.2592-2597.

Suzuki, T. and Chiu, H.H. 1971, Multi-Droplet Combustion of Liquid Propellants, Proc. 9th Int. Symp. on Space Technology and Science, pp.145-154.

Williams, A. 1973, Combustion of Droplets of Liquid Fuels: A Review, Combust. Flame, vol.21, pp.1-31.

SIMULTANEOUS IN-SITU MEASUREMENTS OF SOOT PARTICLE SIZE AND OF ITS TEMPERATURE DEPENDENT OPTICAL CONSTANT FOR THE DIAGNOSTICS OF SOOTING FLAMES

B. Mandel and B. Ineichen

I.C. Engines and Combustion Technology Laboratory
Swiss Federal Institute of Technology
Zurich
Switzerland

ABSTRACT

On the way to understand the soot origin mechanisms in diffusion flames it is necessary to determine the time dependent size of soot particles *in-situ*. The combination of laser light scatter and transmission methods on the experimental side and the G. Mie´s theory on the theoretical side has been used to investigate the behavior of soot particle diameter, number and density in steady and non-steady flames. Accurately determination of the *temperature dependent optical constant of soot particles* in flames is a substantial part of the diameter measurement.

The linked usage of two different methods, one called *opto-acoustic laser beam deflection technique* for determination of the soot particle temperature, and a *light scattering/polarization extinction ratio method* to measure the refractive index, size and shape, was investigated.

The scattering/polarization extinction ratio method, together with a diffraction pitch factor method to consider the influence of non-spherical particles, determines the refractive index, size and shape of soot particles in diffusion flame.

To consider the temperature impact onto the refractive index measurement, the opto-acoustic laser beam deflection method, based on the relation between temperature and acoustic wave velocity, was examined.

1. INTRODUCTION

The techniques used for particle size measurements in a flame system can be divided into two categories: *ex situ* and *in situ*. Extracting the particles from the flame by a mechanical probe or a water-cooled plate introduces other sizing techniques, such as electron microscopy. These *ex situ* techniques have been criticized because the flame is disturbed during sampling, and therefore the morphology of the extracted particles can be different from that of the primary particles in the flame.

For *in situ* particle size measurements optical techniques are used with the advantages of non-intrusion of the flame and real-time analysis. Soot particle sizing in flames (Erickson et.a. (1964), D´Alessio et. a. (1972), D´Alessio et. a. (1975)) utilizes the average scattered light intensity as a function of the wavelength and scattering direction.

The methods based on G. Mie´s light scatter theory have made it possible to measure with some accuracy the diameter, number and density of soot particles in steady and non-steady diffusion flames. However, the optical constant of soot particles is an uncertain element in determining their diameter. A soot particle is an absorptive substance, its chemical composition is unclear, it changes in lifetime, and moreover its optical constant differs with the temperature of the soot particle. It is very difficult to determine accurately the complex *temperature dependent refractive index* (the optical constant). The temperature measurement of soot particles is an important foundation of the determination of the refractive index.

The existence of spherical particles is a strong requirement for the use of the Mie theory (Mie (1908)) to reduce the data. In combustion systems the particles depart after their formation from sphericity because of coalescence and subsequent agglomeration into non-spherical aggregates. This has been pointed out by several investigators (Jones (1972), Lee and Tien (1983), Drolen and Tien(1986), Drolen and Tien(1987)). The aggregates may have various shapes such as clusters, straight chains and / or random structures. The knowledge of the number of primary particles that constitute the agglomerate, their largest dimension, as well as the refractive indices and the size of the primary particle represent the first step for a detailed characterization of a given agglomerate. In addition, since in general the aggregates are elongated structures with different largest dimensions, their aspect ration distribution needs to be determined, and when their total mass is required the number density must also be known.

2. CHARACTERIZATION OF SOOT PARTICLES

2.1. Determination of the Refractive Index

With reference to Figure 1, let us consider a beam of light passing through a cloud of spherical particles. The scattering plane is defined as the plane containing the incident light beam and the line of sight to the detector. The measured scattered light P_s is related to the properties of the particles and the parameters of the optical system by the expression

$$P_{s,p} = I_{s,p}\,\Delta\Omega\,\Delta V\,K_{s,p}\,\eta_{opt}\,\tau_\lambda \qquad (1)$$

where $I_{s,p}$ is the incident energy flux, $\Delta\Omega$ the solid angle aperture of the collection optics, ΔV is the scattering volume and η_{opt} accounts for the efficiency of the optical and electronic components comprising the detection system. The subscripts s and p denote the polarization state (vertical or horizontal) of the incident and scattered beams, respectively. The parameter $K_{s,p}$ ($cm^{-1}sr^{-1}$) denotes a differential scattering coefficient and is defined as the energy scattered per unit time and per unit volume into a unit solid angle about a direction Θ. Since the scattering intensity is attenuated as the light travels between the scattering volume and the detector, the factor τ_λ is introduced to account for this attenuation.

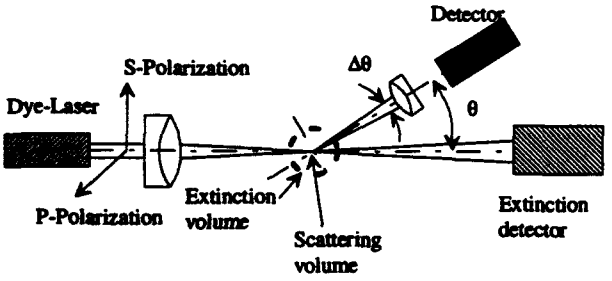

Fig. 1. Experimental setup for the scattering measurement of soot particles

The mean scattering coefficient for a size distribution of particles is given by

$$K_{s,p} = N\overline{D}_{s,p} \qquad (2)$$

where N (cm^{-3}) is the particle number density and $D_{s,p}$ (cm^2sr^{-1}) is the mean scattering cross-section for all spheres in the scattering volume given by

$$\overline{D}_{s,p} = \int_0^\infty D_{s,p}P(r)dr \qquad (3)$$

The differential scattering cross-section for a single homogeneous spherical particle of radius r is given by the expression

$$D_{s,p} = \frac{\lambda^2}{4\pi^2} i_{s,p} \qquad (4)$$

where $i_{s,p}$ are the Mie scattering amplitude functions (Bohren and Huffman (1983), Van de Hulst (1957), Kerker (1969))

$$i_{ss} = \left|\sum_{v=1}^{\infty} \frac{2v+1}{v(v+1)}\left(a_v\pi_v + b_v\tau_v\right)\right|^2 \qquad (5)$$

$$i_{pp} = \left|\sum_{n=1}^{\infty} \frac{2n+1}{n(n+1)}\left(a_v\pi_v + b_v\tau_v\right)\right|^2 \qquad (6)$$

The functions a_v and b_v are the electric and magnetic multipole coefficients of the scattered light expressed in terms of the size parameter $x = 2\pi r/\lambda$ and complex refractive index $n = m - ik$. The functions π_v and τ_v are expressed in terms of the associated Legendre polynomials and depend only on the scattering angle Θ. The function P(r) represents the size distribution of the particles and for the flame soot is usually taken to be the zero order log normal distribution function (Kerker (1957)). For a distribution of sizes with average particle radius r_0 and geometry width σ, P(r) may be expressed as

$$P(r) = \frac{exp\left(-ln^2(\sigma/2)\right)}{\sqrt{2\pi}r_0 \ln\sigma} exp\left[-\frac{ln^2(r/r_0)}{2ln^2\sigma}\right] \qquad (7)$$

As mentioned earlier the angular and size parameter dependencies of the scattering cross section in combination with the extinction cross section and an experimentally determined refractive index can yield the particle size and particle size distribution. However, it is essential to determine not only the soot particle temperature but also the temperature dependent refractive index of the soot particles as a first step in particle size measurement.

2.2. Measurement of the Soot Particle Temperature

The strong impact of soot particle temperature on the refractive index requires an exactly determination of the flame temperature close to a particle.

This experimental technique is based on the thermodynamic dependence of the acoustic wave velocity from the temperature T (Eq. 8). The change into Eq. 9 shows the implementation: The measurement of the acoustic wave velocity a, linked with a calculation of the thermodynamic parameters of the gas at the measurement volume, leads to the determination of the temperature T at this point in the flame.

$$a = \sqrt{\kappa RT} \qquad (8)$$

$$T = a^2 \frac{M}{R\left(1 + R/c_v\right)} \qquad (9)$$

The measurement of the acoustic wave velocity was realized by deflection of two parallel HeNe laser beams based

on the change of the local refractive index in the flame. The propagation of a spherical acoustic wave through the flame produces this change of the refractive index and, furthermore, the deflection (Figure 4).

Computation of the thermodynamic parameters like specific heat c_v and molecular weight M requires an information about the local consistence of the flame at the measurement point. This will be discussed in more detail in Section "Modeling".

3. EXPERIMENTAL SETUP

3.1. Soot Particle Detection by Light Scattering Techniques

The experimental methods in determining the refractive index can be divided to the *light scattering method* and the *transmission law method.*

The *light scattering method* is an application of the polarization ratio method. The refractive index is measured by determining the polarization ratio between two polarized light components vertical and horizontal to the incident light at a position where the incident light is at an angle of 120° (the scattering angle: $\theta = 60°$) to the scattered light from the measured object and as an function of at least two different laser wavelengths with the absorption factor kept constant.

The *transmission law method* estimates the refractive index by measuring how much light is reduced, (the attenuation factors of the light at two specific wavelengths λ_1 and λ_2) after it has passed through the measured object, then determining the specific ratio

$$\frac{ln\,\tau_{R,\lambda_1}}{ln\,\tau_{R,\lambda_2}} \qquad (10)$$

of the logarithmic decrements of the wavelengths determined through the monochromator and the CCD camera. Since arbitrary incident light passes through e.g. the flame, the specific ratio between the logarithmic values of the two attenuation factors is equal to their attenuation coefficient ratio

$$\frac{Q_{ext,\lambda_1}}{Q_{ext,\lambda_2}} \qquad (11)$$

Here the particle diameter changes when the refractive index changes relative to the attenuation coefficient ratio. In this way we obtain the particle diameter and the refractive index common to the measured values of both the polarization ratio and the attenuation coefficient factor ratio.

The experimental setup is illustrated in Figure 2. The output of a Nd:YAG frequency-doubled pumped broad band dye laser is polarized at 45° and is focused to a width of approximately 400 µm into the slit burner. The polarization components had a 100:1 extinction ratio. Pulse energy and pulse width were approximately 15 mJ at 10 ns.

The wavelength dependence on the form factor determined by measurement of the scattered light under two angles is shown in Figure 3. This is an agreement with the theory described above.

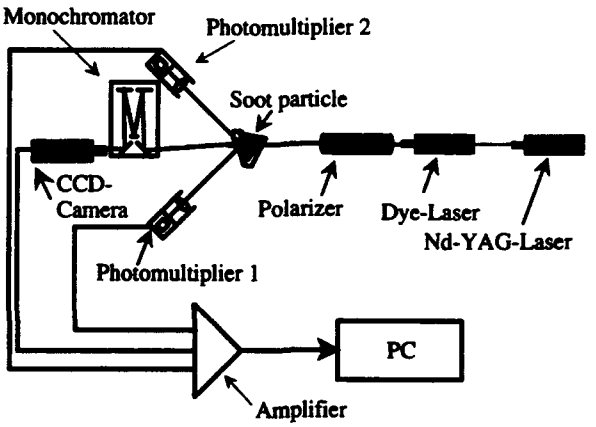

Fig. 2. Experimental setup for soot particle characterization

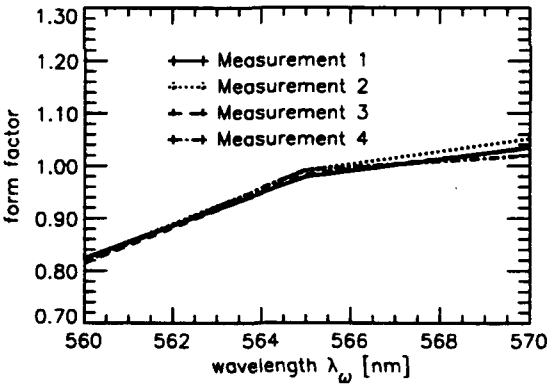

Fig. 3. Intensity ratio under two angles for different wavelengths, scattered at a diffusor

Single-shot scattered intensity of the focused dye laser was acquired by use of photomultipliers. Required for polarization ratio and extinction measurements, but this enables normalization of the scattered intensity measurement by the laser energy for each single-shot. Furthermore this provides a useful check on the alignment of the soot particle stream and the laser illumination focus, because the same scattered intensity after normalization by the laser illumination should result. Single-shot spectral-intensity profiles will be monitored with a spectrograph system.

A typical spectrum showed, that shot-to-shot variations in the spectral profile will not affect the accuracy of the measurement (the magnitude of residual oscillation did not

change appreciably). A small fraction of the energy from the 532 nm pump beam split off and focused into the slit burner. This focus with a width of approximately 150 µm is aligned collinearly with the propagation axis of the focused broad band dye laser beam. The 532 nm focus serves as a conditional sample volume that indicates whether particles were in the larger focus volume of the broad band laser beam. This is necessary, because the illumination intensity will presumably cancel out in the polarization ratio. However, the position of the soot particle within the focus not only affects the intensity of the scattered light but also influences the polarization ratio by changing the relative contributions of the different scattering mechanisms. To our knowledge particle position is an important effect that limits practical application of the technique to particle sizes smaller than the beam waist width.

3.2. Temperature Measurement by Opto-acoustic Laser beam Deflection

To determine the acoustic wave velocity in the flame close to a particle, two parallel HeNe laser beams were focused in the flame using long focal-length lenses (f = 500 mm). The position of the beam waist diameter (less than 1 mm) defines the measurement plane.

For the detection of the deflection two position-sensitive detectors, each having four quadrants, were used. The accurate setup of the diodes guarantees the detection of only one direction of deflection, parallel to the plane of the two HeNe laser beams (Ineichen et. a. (1992), Ineichen, Mandel (1993)).

A frequency-doubled Nd:YAG laser pulse (532 nm), focused onto a target, produces the spherical acoustic wave by local heating of the gas. The propagation of the acoustic wave through the flame changes the refractive index of the gas. The deflection signals of the two parallel HeNe laser beams are compared to determine the transit time of the acoustic wave through the flame (Figure 4).

4. MEASUREMENT

The first part of out experiment belongs to the determination of the temperature in the flame very close to the particle. Under the assumption that the radiation of the soot particles produces a negligible drop in temperature relative to that of the surrounding gas, the temperature of the soot particles is determined by the following results.

4.1. Critical Parameters of the Temperature Measurement

The target used for the acoustic wave source should be placed inside the measurement plane defined by the two parallel HeNe laser beams. A target outside of this plane would results in a deflection that contains a component outside of the main deflection plane. The distance between the two HeNe probe beams was carefully adjusted to a value of s = 4 mm with an accuracy of Δs = +/- 0.02 mm using a diffraction technique.

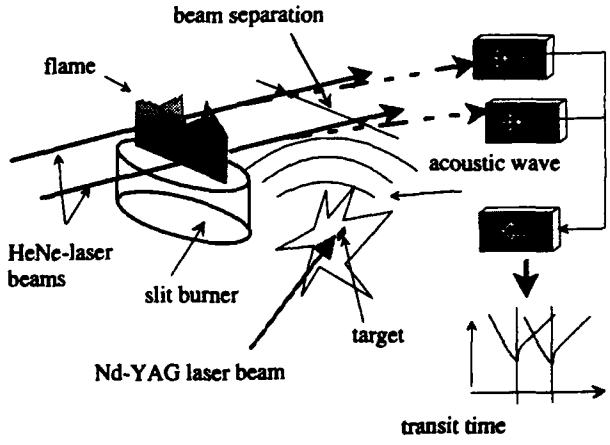

Fig. 4 Experimental setup for the temperature determination of soot particles in a flame

4.2. Measured Profiles

For this study a slit burner (acetylene-air-flame, dimensions of the slit: 1 mm x 50 mm) with a pre-mixed equivalence ratio of λ = 0.7 was used. This burner produces a rather

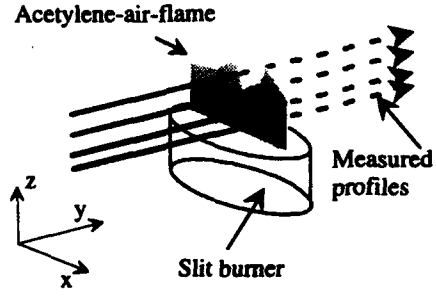

Fig. 5 Traces of the measured profiles

2-dimensional flame. Figure 5 shows the position of the measured profiles. Each profile consists of approximately 15 measurement points along the y-axis; 5 measurements were made at each point. Figure 6 shows typical deflection signals with a statistical deviation less than 1% by measuring the transit time in the flame. The exact y-position of the profiles is defined by the focal plane of the two HeNe laser beams.

5. MODELING

The determination of the temperature inside the flame based on acoustic wave velocity measurements demands the

calculation of the thermodynamic parameters of the gas at the measurement volume. Furthermore, an acetylene-air-flame burning in an environment of air, produces a diffusional stream of air into the flame changing the local equivalence ration. The model described in this section considers this diffusion.

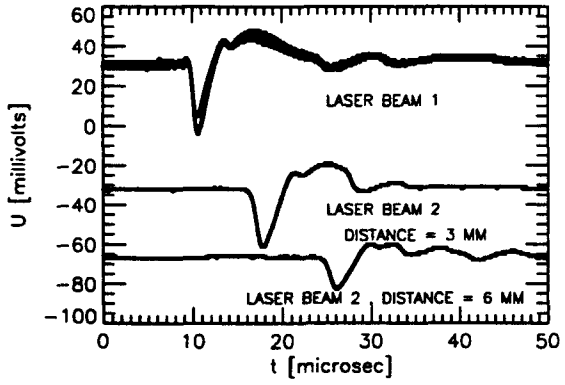

Fig. 6 Multiple deflection signals at the same measurement volume

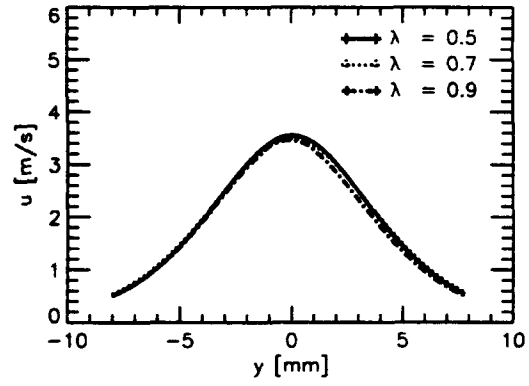

Fig. 7 Local computed velocity profiles for different premixed flames, at 45 mm above the burner exit plane

The computation of the local jet velocity in the flame is based on the continuity equations for the fuel mass and on the momentum continuity equation (Ineichen et. a. (1992), Kee et. a. (1992), Ineichen, Mandel (1993)). The consideration of the boundary conditions ($u_{-\infty}=0$) gives a similarity between the local jet velocity and the local fuel mass concentration. (Figure 7 and Figure 8).

Furthermore, the calculation of the ratio of the given species C, CO, CO_2, H_2O H_2, and OH in the burned region of the flame, based on the known local equivalence ratio λ, was made under the use of the CHEMKIN code (Kee et. a. (1992)).

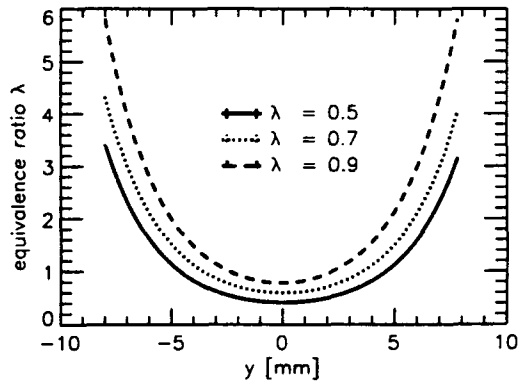

Fig. 8 Local computed equivalence ratios λ for different premixed flames, at 45 mm above the burner exit plane

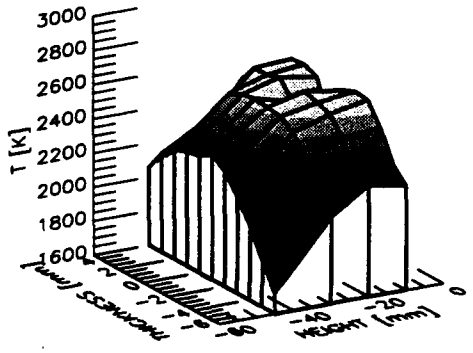

Fig. 9 Temperature profiles in different heights above the burner exit plane for a global equivalence ratio of $\lambda_{global} = 0.7$

6. RESULTS

6.1. Measurement of the Local Particle Temperature in the Flame

In a first step some profiles in a flame with a pre-mixed equivalence ratio of λ = 0.7 were made in different heights above the burner head. The model described in the section above was used to determine the local equivalence ratio in the flame considering the temperature dependent consistence of the flame. The measured profiles are shown in Figure 9.

In the center of the flame, belonging to the parameter "thickness" = 0, a typical temperature decrease is shown, corresponding to the predictions of the model. Figure 10 compares the predictions of the model and the experimental

results. A final comparison, Figure 11, was made with the same flame under the same conditions with holographical interferometry.

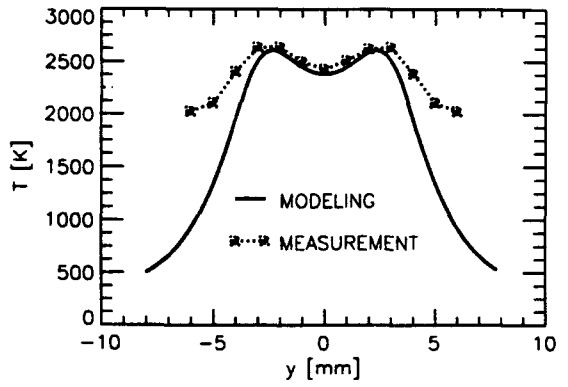

Fig. 10 Temperature profiles for a global equivalence ratio of $\lambda_{global} = 0.7$ at a height of h = 20 mm. Comparison of model predictions and experimental results

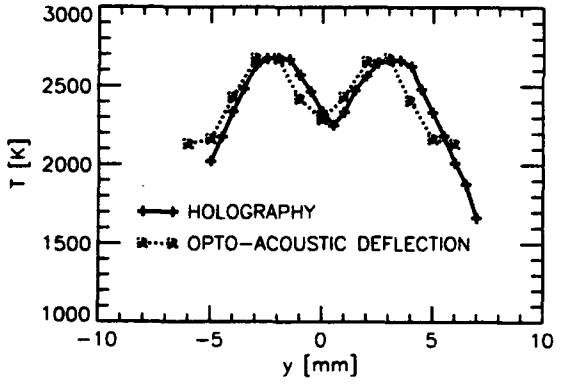

Fig. 11 Temperature profiles for a global equivalence ratio of $\lambda_{global} = 0.7$ at a height of h = 20 mm. Comparison of holography and laser beam deflection method

ACKNOWLEDGMENTS

The authors wish to thank Prof. M. K. Eberle for his encouragement and K. Boulouchos for his excellent discussion. P. Obrecht, Obrecht Engineering, wrote the computer program on the IBM PC for experimental process control, data acquisition and data evolution. Special thanks to T. Steiner for his help on modeling. For the technical support we wish to thank P. Eberli, S. Nguyen-Chi and A. Schmid.

Financial support for the current work was provided by the Swiss Federal Office of Energy (BEW), Grant Nr. EF-FOS (89)004.

REFERENCES

Bohren, C.F. and Huffman, D.R., 1983, Absorption and scattering of Light by Small Particles, John Wiley, New York.

D'Alessio, A., Di Lorenzo, A., Beretta, F. and Venitozzi, C., 1972, Optical and chemical investigators on fuel-rich methane-oxygen premixed flames at atmospheric pressure, 14th Symp. (Int.) on Combust. p. 941.

D'Alessio, A., Di Lorenzo, A., Sarofim, A.F., Beretta, F., Masi, S. and Venitozzi, C., 1975, Soot formation in methane-oxygen flames, 15th Symp. (Int.) on Combust. p. 1427.

Drolen, B.L. and Tien, C.L., 1986, Absorption and scattering of agglomerated soot in flames, Easter Section: Fall tech. Meet., The Combustion Institute .

Drolen, B.L. and Tien, C.L., 1987, Absorbtion and scattering of agglomerated soot particulate, J. Quant, Specttrosc. Radiat. Transfer 37, 433.

Erickson, W.D., Williams, D.C. and Hottel, H.C. 1964, Light scattering measurements on soot in a benzene-air flame, Combust. Flame 8, 127.

Ineichen, B. , Mandel, B. and Steiner, T. , 1992, Soot particle detection and characterization in a diffusion flame, 2nd Workshop on: Fluid mechanics, combustion emissions and Reliability in Reciprocating Engines, Capri, September 1992

Ineichen, B. Mandel, B., 1993, Soot Diagnostics based on simultaneous Measurements of Soot Particle Size and of its Temperature Dependent Optical Constant in Flames, 3rd International Symposium on Special Topics In Chemical Propulsion: Non-Intrusive Combustion Diagnostics, Scheveningen, May, 1993

Ineichen, B., Mandel, B., 1994, Combination of Deflection, Scattering/Extinction and Diffraction Measurements for the Analysis of Soot Particle Temperature, Size and Shape, COMODIA 1994, Yokohama, Japan, July 1994

Jones, A.R., 1972, Scattering and emission of radiation by clouds of elongated particles, J. Phys. D: Appl. Phys. D: Appl. Phys. 5, LI.

Kee, R. J., Miller, J. A. and Rupley, F. M., 1992, CHEMKIN II: A Fortran Chemical Package for the Analysis for Gas Phase Chemical Kinetics, Sandia Report: SAND-8009. UC-706, New Mexico and California

Kerker, M.K, 1969, The Scattering of Light and Other Electromagnetic Radiation, Academic Press, New York .

Lee, S.C. and Tien, C.L., 1983, Effect of soot shape on soot radiation, J. Quant. spectrosc. Radiat. Transfer 29 (3), 259.

Mie, G., 1908, Beitrage zue Optik trüber Medien speziell kolloidaler Metallosungen, Ann. Phys. 25, 377.

Thomann H. , 1986, Strömungslehre I + II, Manuscript zur Vorlesung Strömungslehre, ETHZ

Van de Hulst, H.C., 1957, Light Scattering by Small Particles, John Wiley, New York.

TWO-DIMENSIONAL MIE SCATTERING TECHNIQUE FOR SPRAY DIAGNOSTICS UNDER RUNNING ENGINE CONDITIONS

K.-U. Münch and A. Leipertz

Lehrstuhl für Technische Thermodynamik
Universität Erlangen-Nürnberg; 91058 Erlangen, Germany

ABSTRACT

A two-dimensional Mie scattering technique was applied for spray diagnostics inside a real direct injection Diesel engine. The engine was provided and driven by Volkswagen and was modified to allow an optical access to the piston bowl. The light sheet was positioned slightly below the five hole nozzle. Therefore the liquid fuel distribution of each individual spray jet inside the light sheet plane could be determined by the detection of the scattered light from droplets. The measurements were performed with an intensified CCD camera. The temporal resolution corresponded to the shutter time of 100 ns. The spatial resolution was sufficient to determine the shape of the liquid fuel distributions and their position inside the light sheet plane. The spray penetration process inside the engine could be investigated under running engine conditions and compared to empirical and theoretical results from literature.

1. EXPERIMENTAL SETUP

The measurements were performed inside a transparent four cylinder 1.9 l direct injection (DI) Diesel engine which was provided and driven by VOLKSWAGEN. The optical access was achieved by windows inside the piston and cylinder walls. A schematic of the setup is given in Figure 1. In order to generate a light sheet inside the piston bowl an Ar-Ion-Laser was used. The irradiation power was adjusted to 7 W at a wavelength of 488 nm. By means of an irradiation optics the laser beam was formed to a thin light sheet with thickness of approximately 200 microns and focused into the measurement volume. The light sheet was positioned 5 mm below the five hole nozzle. Perpendicular to the light sheet plane the scattered light was detected by an intensified CCD camera. The temporal resolution of the measurement system corresponded to the camera shutter time of 100 ns. The spatial resolution was 0.1 mm x 0.1 mm. Due to constructive reasons not the whole area of the piston bowl could be detected. The limited observation area is indicated in Figure 2.

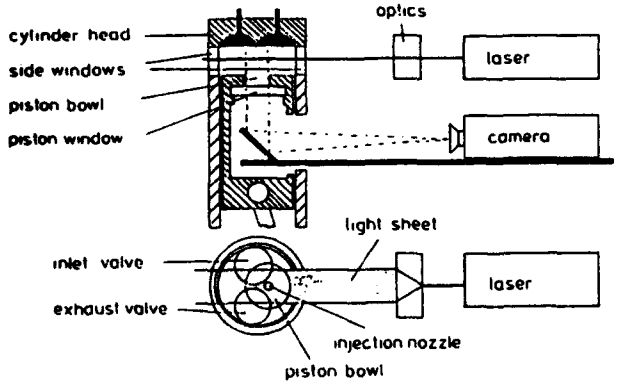

Fig. 1 Schematic of the experimental setup

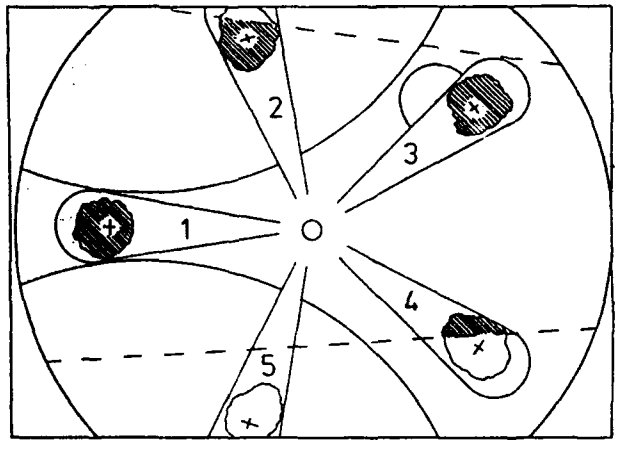

Fig. 2 Light sheet area inside the measurement field of the camera

In order to suppress the flame luminosity during the combustion process an interference filter was applied in front of the detection optics. The image intensifier operated as a fast shutter without setting the gain option in order to retain the whole dynamic range.

2. EVALUATION PROCEDURE AND MEASUREMENT RESULTS

The Mie scattered signal detected from the camera system contains three signal portions which have to be separated. Figure 3 presents the measured intensities along a line from the orifice of the nozzle to the spray tip.

The strongest signal portion was detected from the light sheet signal generated by droplets staying inside the light sheet during the exposure time. The other signal portions occur due to multiple scattering, diffuse illumination of the piston bowl, reflections on engine components and sensor noise denoted as integral scattering and background signal in Figure 3. The integral scattering signal can be exploited to determine the spray parameters like the spray tip penetration and the cone angle.

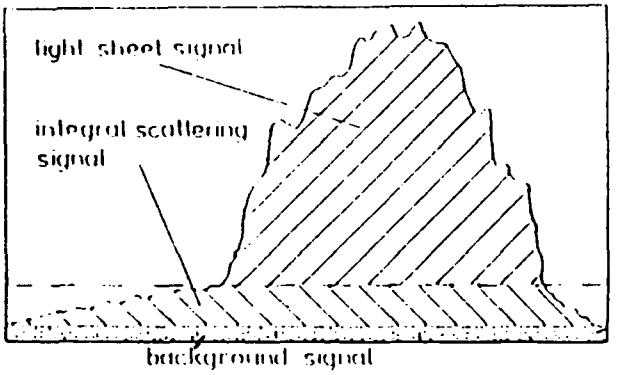

Fig. 3 Intensity profile along a line inside a measured liquid fuel distribution

To distinguish the light sheet signal from the other signal portions a steep intensity gradient at the edges of the liquid fuel distributions can be used. The intensity gradient of the increasing intensities can certainly be recognized. In order to distinguish between the signal portion tangents can be applied to the light sheet signal and the integral scattering signal providing a point of intersection which can be used to define an intensity threshold. By means of this threshold a binary liquid fuel distribution can be calculated from the measured intensity distribution, see Münch and Leipertz (1992).

The measurements show, that strong cycle fluctuations occur at the same injection time in successive cycles. Figure 4 presents as an example four different measurements for the same crank angle position. The black areas inside the bright ranges of the spray jets correspond to the determined binary liquid fuel distributions of the individual jets.

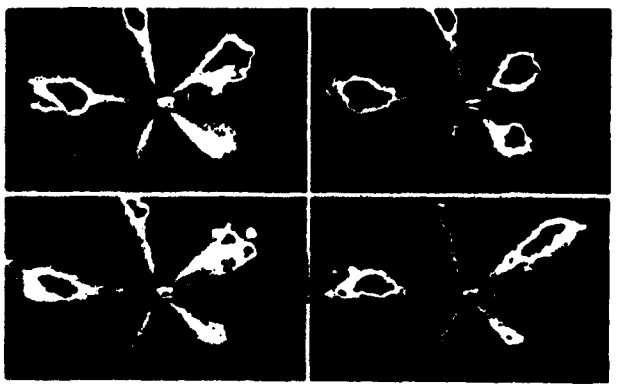

Fig. 4 Fluctuations of the liquid fuel distributions inside the light sheet plane (black areas) in successive cycles

The strong fluctuating behaviour can be expressed by a frequency distribution of the local appearance of liquid fuel inside the light sheet. The binary liquid fuel distributions of a certain injection time can be superposed by image processing in order to achieve statistical information. Subsequently the result can be normalized by the number of distributions taken into account to obtain probability values between 0 and 1. Figure 5 presents a calculated Appearance Frequency Distribution (AFD) for a certain injection time at top dead center.

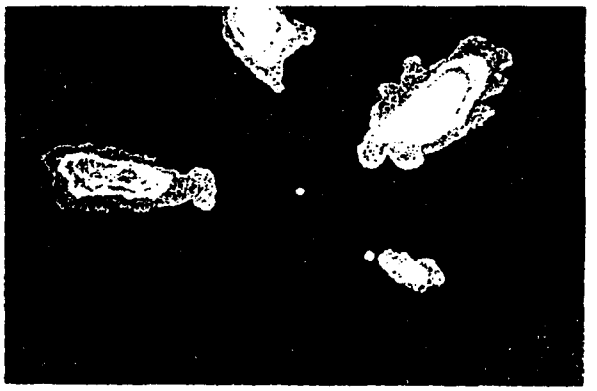

Fig. 5 Calculated appearance frequency distribution of the liquid fuel at TDC

The probability values increase from dark to bright colours. The whole injection process can be described with AFDs by scanning the injection process in successive time steps. The experimental effort for such a description is very high, but it provides valuable information of the spray penetration process and the results can be compared with numerical calculations.

From the ADFs of each jet also the centers of gravity were determined. They define the points of intersection between the jet axis and the light sheet plane. A comparison of these points with the points of intersection given from the geometry of the nozzle holes has indicated that deviations in the direction of the spray penetration occur in dependence of the injection time and the engine operating point under investigation. It has been pointed out by Münch and Leipertz (1993 and 1994) that these deviations cannot be determined with conventional imaging techniques integrating the detected signal over the path of observation.

The already described integral scattering signal can be easily distinguished from the light sheet signal (see Figure 3) and can be used for the investigation of the spray penetration process in observation direction comparable to investigations with the often used shadowgraphy technique. Figure 6 shows the measurement results of the spray tip penetration in comparison to calculated curves from empirical and theoretical equations by Wakuri *et al* (1960), Taylor and Walsham (1970), Dent (1971), Lustgarten(1974), Fujimoto *et al* (1981), Hiroyasu and Arai (1990), and Yule *et al* (1991).

In comparison to the calculated curves smaller values of the spray tip penetration were measured inside the engine for

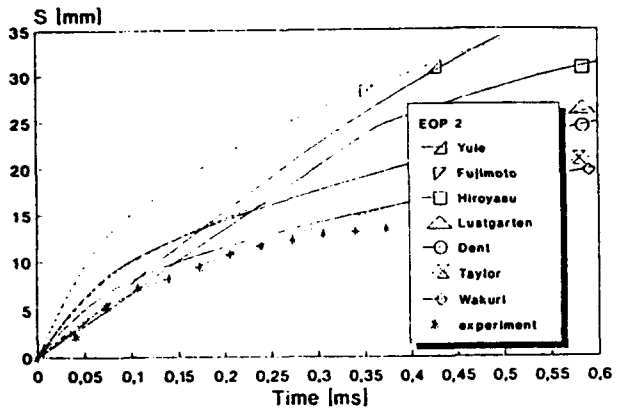

Fig. 6 Spray tip penetration in dependence of the injection time for a transient injection process

the considered engine operation point. It can be demonstrated, that most of the theoretical and empirical equations were derived for another range of engine speed and that therefore no good agreement to our mesurements could be expected. Agreement was found for the equations of Taylor and Walsham (1970) and of Wakuri *et al* (1960).

Taylor and Walsham (1970) employed both conventional and schlieren photography for tracking the penetration of single injections of fuel into quiescent nitrogen at high pressure. The experimental conditions were matched to medium speed Diesel engines with a bore of approximately 200 mm, being one order of magnitude larger than in small high speed Diesel engines. Thus the good agreement seems to be more accidental in view of our conditions. The equation by Wakuri *et al* (1960) needs the experimentally determined cone angles of the jets as the most relevant input parameter. Here, agreement with the experiment is much more probable, but it also gives an indication for the internal coincidence of our measurements and thus for the measurement technique applied.

The comparison of the applied Mie light sheet technique and shadowgraphy measurements provides in general good agreement between the achieved spray tip penetration measurements. Cone angle measurements with both techniques deviate from each other. The cone angles measured by the shadowgraphy technique were larger than the determined cone angles from the Mie scattering experiments under the same engine conditions. Reasons for this behaviour may be found in the different basic principles of both techniques. The scattering cross section of the Mie signal decreases rapidly with decreasing droplet diameter. It might be possible, that the very small droplets at the edges of the spray cannot be detected appropriately due to their small cross sections. On the other hand it may also be possible, that the evaporating fuel vapor close to the spray edges are detected as a real signal contribution by the shadowgraphy technique thus not giving information on the liquid part. More detailed investigations seem to be necessary to clarify this problem, which surely must be found in the measurement techniques.

ACKNOWLEDGEMENTS

Research was funded by the Commission of the European Communities within the frame of the JOULE Programme, by the Swedish National Bord for Industrial and Technical Development (NUTEC), and by the Joint Research Commitee of European Automobile Manufactures (Fiat, Peugeot SA, Renault, Volkswagen and Volvo) within the IDEA Programme.

REFERENCES

Dent, J.C. 1971 A Basis for the Comparison of Various Experimental Methods for Studying Spray Penetration, SAE Paper 710571.

Fujimoto, H. & Sugihara, H. & Tanabe, H. & Sato, G.T. 1981 Investigation on Combustion in Medium-Speed Marine Diesel Engines Using Model Chambers, Proc. CIMAC-Congress, Helsinki.

Hiroyasu, H. & Arai, A. 1990 Structures of Fuel Sprays in Diesel Engines, SAE Paper No. 900475.

Lustgarten, G. 1974 Modelluntersuchung zur Gemischbildung und Verbrennung im Dieselmotor, MTZ, Motortechnische Zeitschrift, vol. 35, no. 9, p. 421.

Münch, K.-U. & Leipertz, A. 1992, Investigation of Spray Penetration and Fuel Distribution inside the Piston Bowl of a 1.9 l DI Diesel Engine Using Two-Dimensional Mie Scattering, SAE Paper No. 922204.

Münch, K.-U. & Leipertz, A. 1993, Two-Dimensional Mie Scattering Technique for the Investigation of Spray Structures and Penetration Process under Engine Conditions, Proc. Euromech 309, Optical Flow Diagnostics, Göttingen.

Münch, K.-U. & Leipertz, A. 1994, Laser Mie Scattering for the Characterization of Diesel Engine Processes in Non-Intrusive Combustion Diagnostics, Editor: K. K. Kuo, Bergell House (in press).

Taylor, D.H.C. & Walsham, B.E. 1970 Combustion Process in a Medium-Speed Diesel Engine, Proc. Institution of Mechanical Engineers, part 3J, vol. 184, pp. 67-76.

Wakuri, Y. & Fuji, M. & Amitani, T. & Tsuneya, R. 1960 Studies on the Penetration of Fuel Spray in a Diesel Engine, Bulletin of J.S.M.E., vol. 3, no. 9, p. 129.

Yule, A.J. & Filipovic, I. & Mirza, M.R. 1991 On the Break-Up Times and Length of Diesel Sprays, Editor: Balachandran, Guilford, Surry, Proc. Sprays and Aerosols '91, 126.

Session 13.
Separated Flows

THE TURBULENT FLOW IN A CHANNEL WITH LARGE-AMPLITUDE WAVY SURFACES

G.P. Almeida, D.F.G. Durão and M.V. Heitor

Technical University of Lisbon
Instituto Superior Técnico
Dept. of Mechanical Engineering
Av. Rovisco Pais
1096 Lisboa Codex, PORTUGAL

ABSTRACT

Laser-Doppler measurements of velocity characteristics are presented for the turbulent channel flow established between two wavy surfaces (top and bottom) with an amplitude-to-wavelength ratio of $h/\lambda = 0.22$ and mounted downstream of a fully-developed channel flow for Reynolds numbers up to 3.6×10^5. The study involves analysis of the flow for two different channel heights, namely $H_2/h = 2.55$ and 3.55, with the latter being associated with the occurrence of flow recirculation in the lee of the concave surfaces. The results reveal a flow structure qualitatively similar to that found in other turbulent curved flows and include analysis of the turbulent stresses in order to identify the effect of extra rates of strain on the mean flow. Their implications for the calculation of recirculating and non-recirculating turbulent flows over curved boundaries using turbulence models are discussed through analysis of the terms in the conservation equation of turbulent kinetic energy.

1. INTRODUCTION

Turbulent flows distorted by imposed boundaries, namely those under the influence of longitudinal streamline curvature, experiences large positive and negative pressure gradients and have been the subject of intensive experimental research in the last two decades, with the common aim of improving knowledge of the effect of extra strain rates (i.e., rates of strain additional to simple shearing) on the behaviour of turbulent flows.

It should be noted that it has been recognized for many years (e.g. Bradshaw, 1973; Bradshaw and Johnston, 1988) that a small amount of streamline curvature can have a significant effect on the behaviour of a turbulent flow. The magnitude of this effect is obviously dependent upon the ratio of the shear layer thickness, δ, to the ratio of curvature, R, of the imposed boundaries and, for example, Baskaran et al (1987) have shown that the flow may separate in the lee of curved surfaces for $\delta/R < 1$ due to strong adverse pressure gradients. In general, analysis has been focused on flows over a curved surface free of the influence of additional shear or of other flow boundaries (Buckles et al, 1984; Patel et al, 1990).

The presence of an additional interacting shear layer may alter the pressure distribution along the flow and, consequently, minimize the effect of δ/R mentioned above. This paper is aimed to quantify this phenomena, in that the flow established between two parallel and out-of-phase curved surfaces is studied for different interacting levels of the shear layers formed in the vicinity of each surface.

The work follows that of Almeida et al (1993) for the channel flow over a large amplitude wavy surface (i.e., the bottom wall) and is centered on obtaining a basic understanding of the conditions for which a recirculating zone is formed in the wake of the surfaces. The previous flow field has been strained by a geometrically-similar wavy surface, so that it resembles the flow in a wavy channel.

The next section describes the experimental method, gives details of the flow configuration, of the laser-Doppler velocimeter and of the errors incurred in the measurements. Section 3 presents the mean and fluctuating velocity characteristics of the flow between wavy surfaces, and discusses the results in terms of their contribution to improve knowledge of complex flows. The last section summarizes the main findings and conclusions.

2. EXPERIMENTAL CONFIGURATION AND PROCEDURES

The experiments were conducted in the long horizontal water tunnel made of perspex, 0.170 m in depth, 0.2 m in width and 7 m in length, of Durão et al (1989). The facility has a recirculating system whereby the water is drawn from a constant-head discharge tank and pumped

into a pressurized tank. The water is then passed through straightners and screens upstream of the duct inlet, which assures the uniformity of the flow.

The curved surfaces were made of plastic and its shape is that of the plane of symmetry of the 3-D hills used by Hunt and Snyder (1980) which, ideally, is the inverse of a fourth order polynomial. The height and radius of the base of the wavy surfaces are respectively equal to h= 29 mm and R= 67 mm (figure 1):

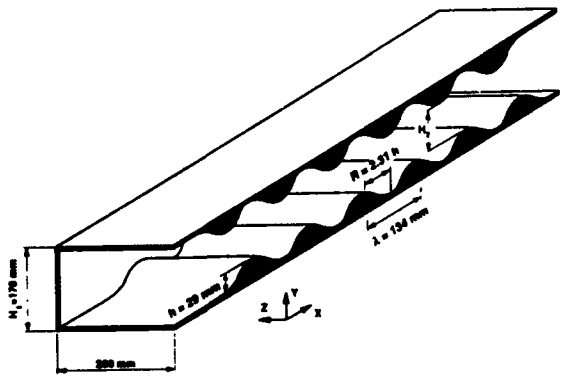

Figure 1. Schematic diagram of the flow configuration.

their wavelength is λ= 134 mm= 2R. The measurements reported here were obtained for two different channel heights, namely for H_2/h= 2.55 and 3.55. The origin of the horizontal, x, and vertical, y, coordinates is taken on the top of the bottom surface, and the results are presented in terms of a dimensionless channel height.

The measuring section was located about 6 m downstream of the tunnel inlet, where laser-Doppler measurements obtained in the absence of any perturbation, and along several vertical profiles, have identified a fully developed channel flow, which has been analyzed in detail by Almeida et al (1990). The upstream mean reference velocities for the two flow conditions studied were respectively equal to $\langle U_0 \rangle$= 1.487 and 1.340 m/s, with the centerline turbulence intensity of 3%: the friction factor is C_f=0.0035 and the wall friction velocities were U_τ = 0.13 and 0.10 m/s for H_2/h= 2.55 and 3.55 respectively. The Reynolds number of the flow for these two conditions, based on the mean reference velocity in the wavy channel, <U>, and its hydraulic diameter, was kept constant at 3.6×10^5.

Velocity was measured by a laser-Doppler velocimeter operated in the dual-beam, forward-scatter mode with sensitivity to the flow direction provided by light-frequency shifting from acousto-optic modulation (Bragg cells). The resulting frequency shift was normally set at 2 MHz. The principal characteristics of the laser-Doppler velocimeter, and in particular those of the transmitting optics, are summarized in Table 1.

Table 1 - Principal characteristics of the laser-Doppler velocimeter

• Argon-Ion laser (1W, nominal); wavelength	514.5 nm
• local length of focusing lens	310 mm
• laser beam diameter, at e^{-2} intensity	1.5 mm
• measured half-angle of beam intersection (in air)	4.85°
• calculated half-angle of beam intersection (in water)	3.64°
• calculated dimensions of measuring volume, at e^{-2} intensity, (major and minor axis of ellipsoid in water)	1.107; 0.136 mm
• velocimeter transfer constant	0.315 MHz/(ms^{-1})

The light scattered by naturally-occurring centers in the water was collected by a lens (focal length of 200 mm) and focused onto the pinhole aperture (0.3 mm) of a photomultiplier (OEI, type LD-0-810) with a magnification of 1.0. The output of the multiplier was band-pass filtered and the resulting signal processed by a purpose-built frequency counter operated in the single-measurement-per-burst mode with fixed cycles (N=8) validated in the time domain within 1%. The validated data were transferred to a laboratory 8-bit minicomputer, where the time-averaged moments of velocity were evaluated.

The complete LDV system was mounted on a three-dimensional traversing unit, allowing the positioning of the laser-velocimeter control volume within ± 0.25 mm. Spectral analysis of the LDV velocity signals was carried out by sampling and holding the velocity at each new Doppler burst until another valid signal arrives. A high mean sampling frequency up to 2 KHz was used, suggesting that structures of the order of 1.0 mm and above can be resolved. This is at least one order of magnitude smaller than important length scales in the duct, which implies that the energy containing motions are resolved by the counter. It should be pointed out that in the present study we are particularly interested in the low range of the spectrum and that the power spectral density could be accurately reconstructed up to about 300

Hz. Sample results are presented in figure 2 for a typical point of the shear layer for flow conditions associated with the separation of the flow in the lee of the concave surfaces and show the absence of discrete flow oscillations.

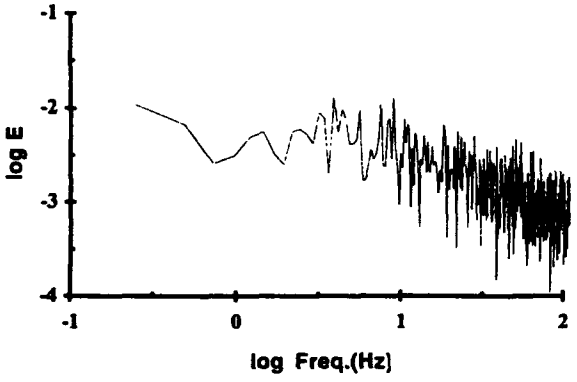

Figure 2. Power spectral density of a measured signal in a typical point of the shear layer for the wavy channel with H_2/h=3.55

Detailed laser-Doppler measurements of the flow were obtained along fourteen vertical profiles in the central plane of the duct, namely at x/h = -1.034; -0.69; 0.0; 0.345; 1.034; 1.379; 1.724; 2.310; 2.586; 3.276; 3.793; 4.138; 4.621 and 4.966. The measurements were performed with the laser beams in the horizontal and vertical plane and at 45° to allow the determination of the horizontal, $\overline{U}$ and vertical , $\overline{V}$, mean and turbulent velocities and of the distribution of the Reynolds shear stress, $\overline{u'v'}$, Durst et al (1981). The measuring volume was located up to 1 mm from the surfaces with the transmitting optics inclined half-angle of the beam intersection and with the scattered light collected off-axis.

The errors incurred in the measurements have been discussed in detail elsewhere, and only the major sources are summarized here. Non-turbulent Doppler broadening errors due to gradients of mean velocity across the measuring volume, Durst et al (1981), may essentially affect the variance of the velocity fluctuations, but for the present experimental conditions are at least five orders of magnitude smaller than the values of the variances and, therefore, sufficiently small for their effect to be neglected. In the experiments the number of individual velocity values used to form the averages was always above 10 000 and, therefore, the largest statistical (random) errors were of 0.5 and 3% respectively for the mean and variance values, for a 95% confidence interval, Yanta and Smith (1978). Systematic errors incurred in the measurements of Reynolds shear stress can arise from lack of accuracy in the orientation angle of the normal to the anemometer fringe pattern, Melling and Whitelaw (1976), and can be particularly large in the vicinity of the zones characterized by zero shear stresses. For the present experimental conditions the largest errors are expected to be smaller than 2%.

3. EXPERIMENTAL RESULTS AND DISCUSSION

This section presents the detailed laser-Doppler measurements of the flow between the wavy surfaces described before. The results include the comparison of the flow for two different channel heights, namely H_2/h= 2.55 and 3.55, which allow to analyze the conditions for which a recirculating zone is established in the wake of the concave surfaces.

3.1. The Mean Flow

Some of the salient features of the two flows considered are summarized conveniently by the vectorial distribution presented in figure 3, which quantify the mean flow along the central plane of symmetry.

The measurements have been preceded by a detailed analysis along the traverse direction of the measuring cross-section, which confirmed that the results presented here are free of any 3-D effects, in that the flow in the centre of the channel can be considered as two-dimensional.

The results reveal a considerably thin boundary layer along the upstream part of the concave surfaces, which accelerates strongly as it approaches the top zone with an increased deflection of the mean flow for the narrower channel. The two cases studied exhibit similar flow patterns, with the deflection of the mean flow over the curved surface being affected by the level of flow confinement. For H_2/h = 2.55 the flow does not separate in the valley zones and the mean horizontal velocity above the top of the concave surfaces is increased by $\overline{U} / < U > = 1.71$. On the other hand, for the larger channel height the deflection of the mean on the top of the surfaces is comparatively smaller with $\overline{U} / < U > = 1.61$, and flow separation occurs between $x/\lambda = 0.22$ and $x/\lambda = 0.56$ in a way qualitatively similar to that found by Almeida et al. (1993).

Following the analysis of Buckles et al. (1984), the flow for H_2/h = 3.55 separates in a region of unfavourable

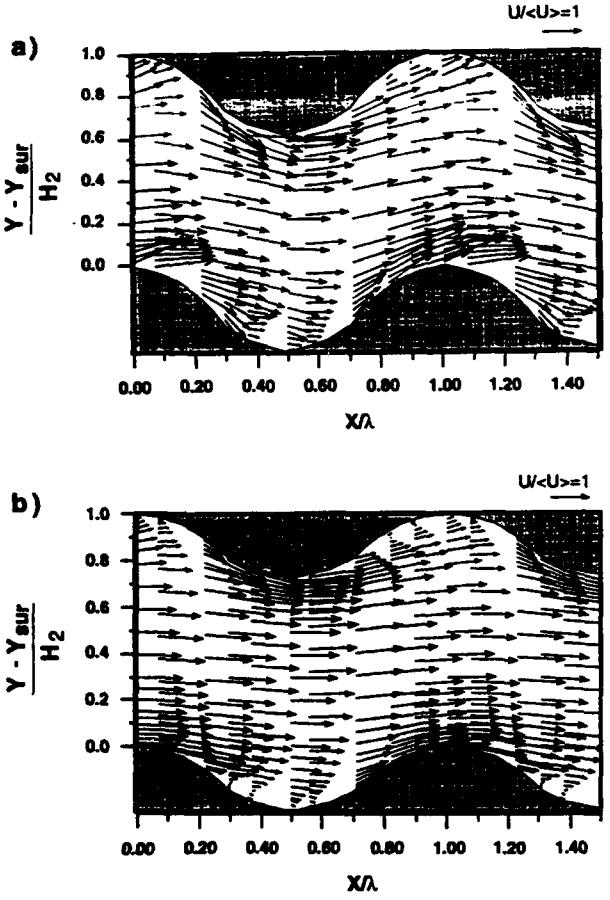

Figure 3. Vectorial distribution of the mean flow.

a) H_2/h= 2.55
b) H_2/h= 3.55

pressure gradient and reattachs upstream of the pressure maximum at an oblique angle. The extent of the flow reversal zone is comparatively smaller than those found for the flow over wavy surfaces by Almeida et al. (1993) and Buckler et al. (1984), respectively, between $0.16<x/\lambda<0.76$ and $0.14<x/l<0.69$, which is explained by the level streamline curvature experienced by those flows. For comparison, typical flows over sharp obstacles (eg. Durst and Rastogi, 1980) separate for considerably larger zones, as the transfer of momentum across the shear layer is different from that found here. The maximum measured values of the reverse velocity is equal to $\overline{U}/<U>=-0.29$ and, again, this compares with the values of $\overline{U}/<U>=-0.33$ of Almeida et al. (1993).

3.2 The Turbulent Flow

The previous paragraphs have considered the mean flow over the 2-D wavy surfaces. We now turn to the analysis of the turbulent flow, which is quantified by the distributions of the contours of normal and shear stresses of Figures 4 and 5, although the present results do not convey any information on the turbulent levels along the transversal direction. The results indicate a region of high velocity fluctuations along the shear layer downstream of the top of each wavy surface, in a way qualitatively similar to that found in other turbulent curved flows. Peak values of normal stresses occur in the zones characterized by the highest mean velocity gradients and are associated with near-Gaussian velocity probability density functions, typical of the absence of discrete frequency oscillations.

The turbulent flow in the two conditions studied is anisotropic with values of $\overline{u'^2}$ consistently higher than those of $\overline{v'^2}$. In the freestream, the levels of turbulence anisotropy reach those of the undisturbed flow, with vertical velocity fluctuations half of those in the longitudinal direction.

The distribution of the shear stress, $\overline{u'v'}$, quantify the turbulent diffusion along the shear layer and is consistent with the direction of the mean flow. The maximum values occur along those of the normal stresses and are similar to those found over the wavy channels of Buckler et al. (1984) and Almeida et al. (1993).

In agreement with other flows over curved boundaries, the turbulent kinetic energy increases with the distance from the top of the concave surface up to the upward tilting of the flow at the upstream face of the following wave. This is because downstream of the top of the curved surfaces the overall effect of positive shear strain is to increase turbulence intensity by the destabilizing effect of streamline curvature, while along the approaching faces of the waves the opposite signs of the shear strains suppresses turbulence by stabilizing curvature effects, (see Bradshaw, 1973). This explains the attenuation of the Reynolds stresses in the case of H_2/h= 2.55 compared with the values found for the recirculating flow associated with the flow in the channel for H_2/h= 3.55.

3.3. Discussion

The analysis of the previous sections was based upon results presented in laboratory coordinates, but this does not affect the main conclusions of the work as noted by Almeida et. al. (1993). The results have identified that the shear layers formed in the downstream part of the concave surfaces are zones of intense velocity fluctuations, with increased values for the recirculating flow found in the case of the largest channel height. The aim of this discussion is to analyze the implications of the results presented above for the calculation of

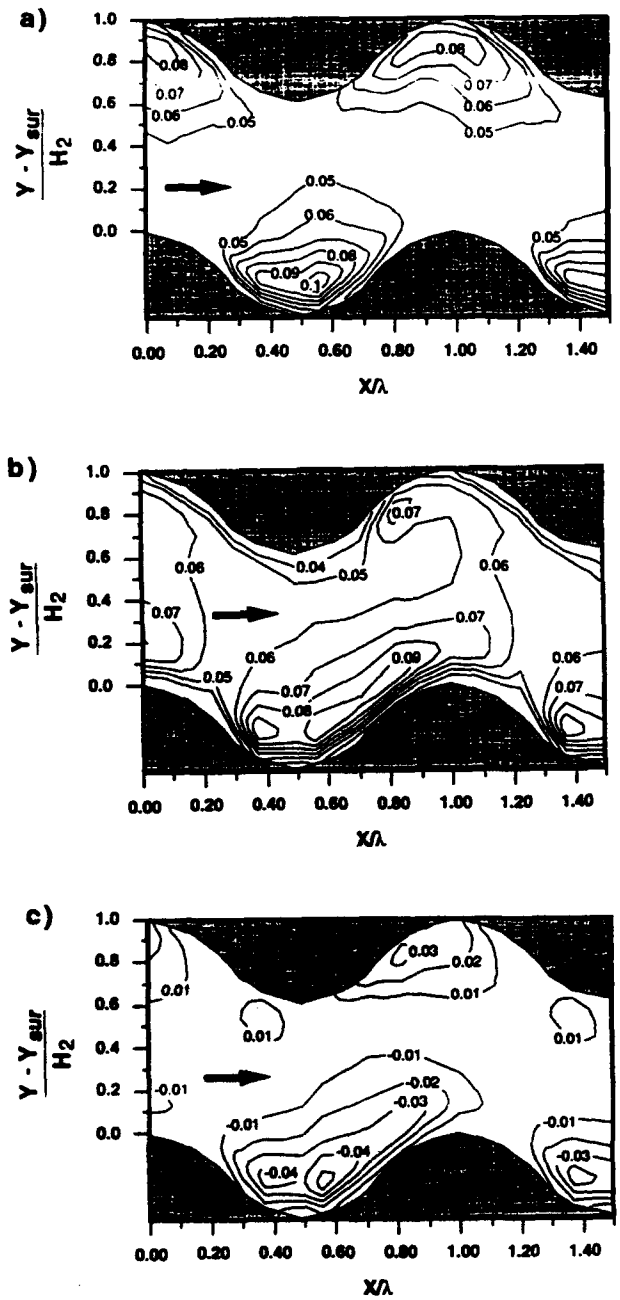

Figure 4. Measured contours of Reynolds stresses for H_2/h= 2.55. Re= 3.6 x 10^5.

a) Variance of velocity fluctuations along the streamlines, $\overline{u'^2} / \langle U \rangle^2$

b) Variance of velocity fluctuations normal to streamlines, $\overline{v'^2} / \langle U \rangle^2$

c) Reynolds shear stress, $\overline{u'v'} / \langle U \rangle^2$

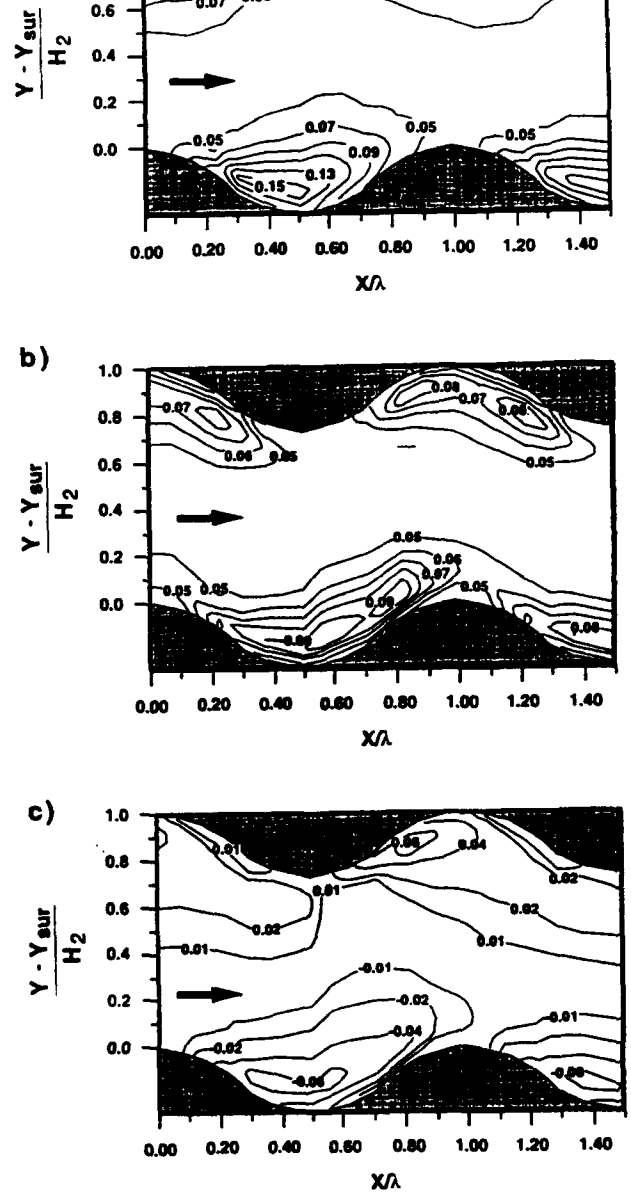

Figure 5. Measured contours of Reynolds stresses for H_2/h= 3.55. Re= 3.6 x 10^5.

a) Variance of velocity fluctuations along the streamlines, $\overline{u'^2} / \langle U \rangle^2$

b) Variance of velocity fluctuations normal to streamlines, $\overline{v'^2} / \langle U \rangle^2$

c) Reynolds shear stress, $\overline{u'v'} / \langle U \rangle^2$

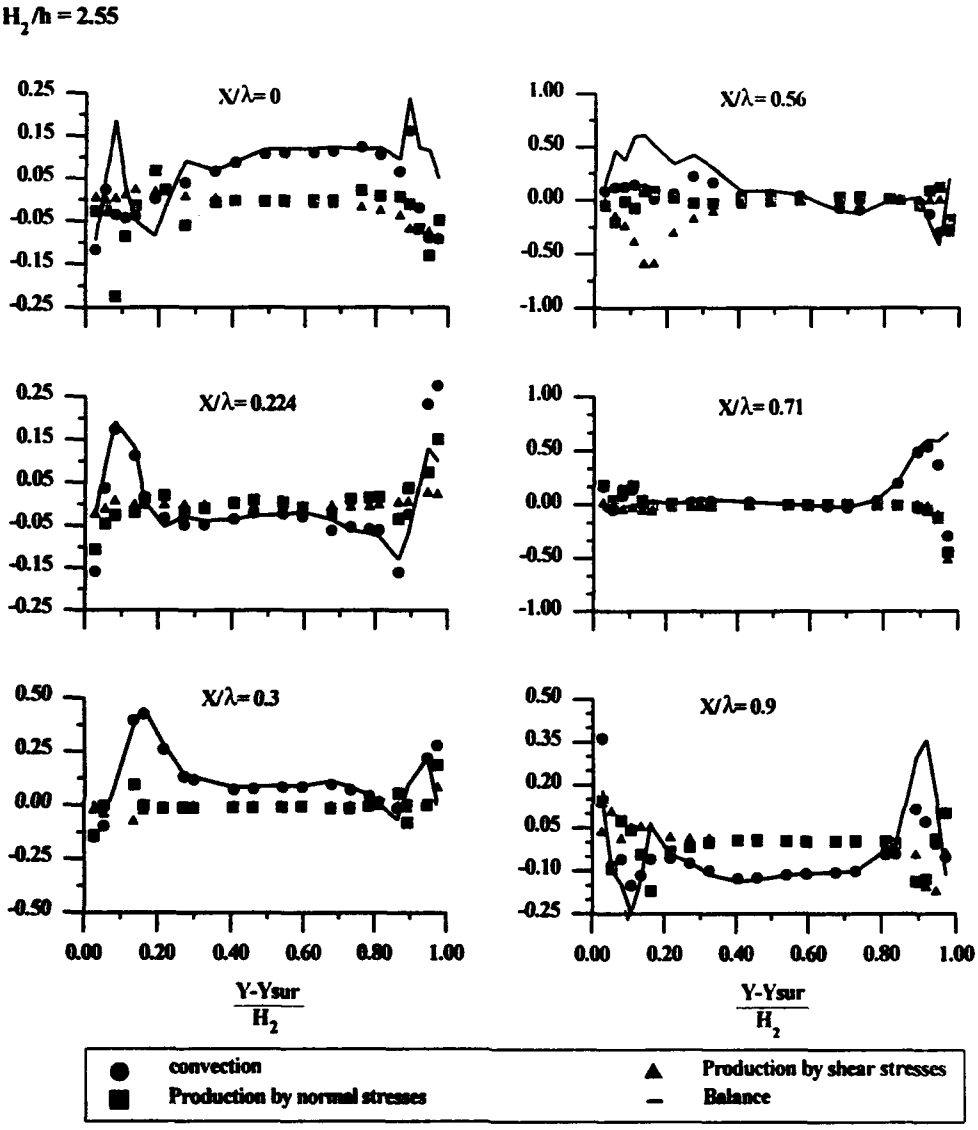

Figure 6. Budgets of turbulent kinetic energy for $H_2/h = 2.55$. $Re = 3.6 \times 10^5$.

recirculating flows between imposed curved boundaries. The approaches used here consist in the analysis of the convection and production terms in the conservation equation of the turbulent kinetic energy, k, which in a rectangular coordinate system for stationary, incompressible, isothermal and a two-dimensional flow (Rody, 1970), is given by:

$$\underbrace{U\frac{\partial K}{\partial x} + V\frac{\partial K}{\partial y}}_{1} = \underbrace{-\overline{u'^2}\frac{\partial \bar{U}}{\partial x} - \overline{v'^2}\frac{\partial \bar{V}}{\partial y}}_{2} \underbrace{- \overline{u'v'}\left(\frac{\partial \bar{U}}{\partial y} + \frac{\partial \bar{V}}{\partial x}\right)}_{3}$$

$$\underbrace{-\frac{\partial}{\partial x}\left(\overline{K'u'} + \frac{\overline{p'u'}}{\rho}\right) - \frac{\partial}{\partial y}\left(\overline{K'v'} + \frac{\overline{p'v'}}{\rho}\right) - \frac{\partial}{\partial z}\left(\overline{K'w'} + \frac{\overline{p'w'}}{\rho}\right)}_{4} \underbrace{-\epsilon}_{5}$$

The terms 1, 2, 3, 4 and 5 represents, respectively, the convection, the turbulent production by the interaction of normal and shear stresses and the diffusion and dissipation terms, which are represented in figures 6 and 7 respectively for $H_2/h = 2.55$ and 3.55, in a way that

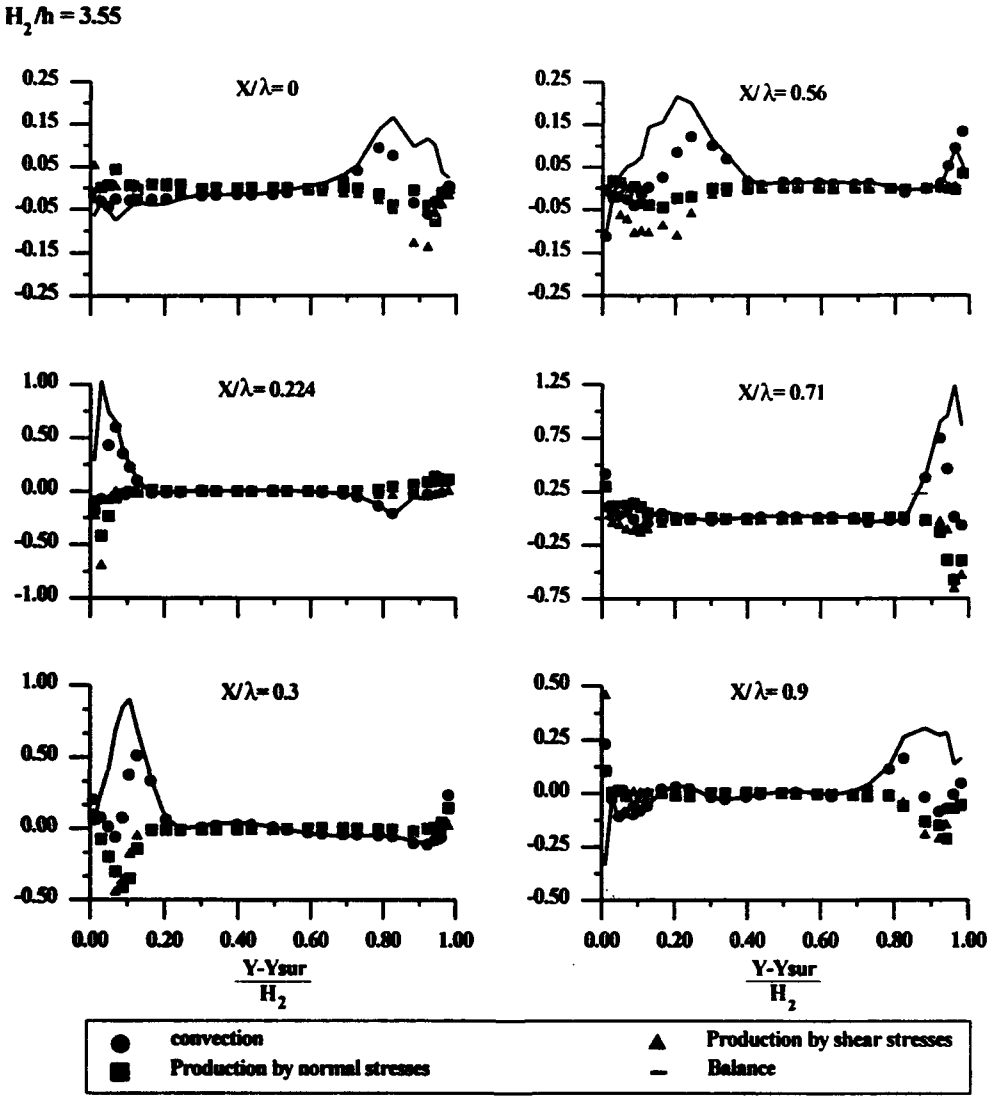

Figure 7. Budgets of turbulent kinetic energy for H_2/h= 3.55. Re= 3.6 x 10^5.

negative convection represents a gain of turbulent kinetic energy. At the top of each bottom concave surface and downstream of this zone up to x/λ=0.3, turbulence production by normal stresses is the largest term, which is balanced by convection and diffusion. This is also shown in the vicinity of the top surface for x/λ=0.7 and is associated with the occurrence of flow separation for H_2/h= 3.55. The observation accounts for the large turbulence anisotropy in these zones since, although production of $\overline{v'^2}$ represents a gain, production of $\overline{u'^2}$ is $-2\,\overline{u'^2}\frac{\partial \overline{U}}{\partial x}$, which is a negative quantity, and represents a loss of turbulent energy.

The results also quantify the large rate of production of turbulent kinetic energy by the interaction between shear stresses and strains in the "valley" zone. Further downstream, with the approach of the top of the concave surfaces, convection is the largest term and is balanced by turbulent diffusion.

A remarkable observation is that the occurrence of zones dominated by the intreaction of normal stresses and strains is not strictly associated with the separation of the flow and occurs for the two cases studied. This is important in that it is necessary to calculate the individual normal stresses adequately (using an appropriate turbulence model) if the correct turbulent kinetic energy is to be obtained.

Finally, figure 8 identifies the locus of the maximum velocity fluctuations for the two conditions studied and shows that the wall boundary layer formed at the rising surface of the wavy surfaces remains quite thin up to the top of the concave surfaces. Then it spreads as it approachs the wake region, where it becomes a free shear layer detached from the surface similar to that analyzed by Buckles et al (1984). The rate of spread, define as the ratio of distance between the shoulder of the shear layer and the distance along the locus of the maximum intensity, is about 0.164 for H_2/h= 3.55 mm on the upper side of the shear layer and, therefore, similar to the value of 0.18 usually considered for plane shear layers with zero velocity on the low-speed side. This value increases for H_2/h= 2.55, and although the results show that there is not a complete interaction between the top and bottom shear layers for the two flow conditions studied, analysis of the differences between the present spread rates and those typical of plane free shear layers suggests that the shear layers reported here cannot be modelled entirely as unbound layers. Direct comparisons of growth rates are subject to uncertainty because of their dependence upon the boundary conditions, but the previous analysis agrees with that of Castro and Hague (1987) and is important to establish a suitable model to predict flows along curved surfaces.

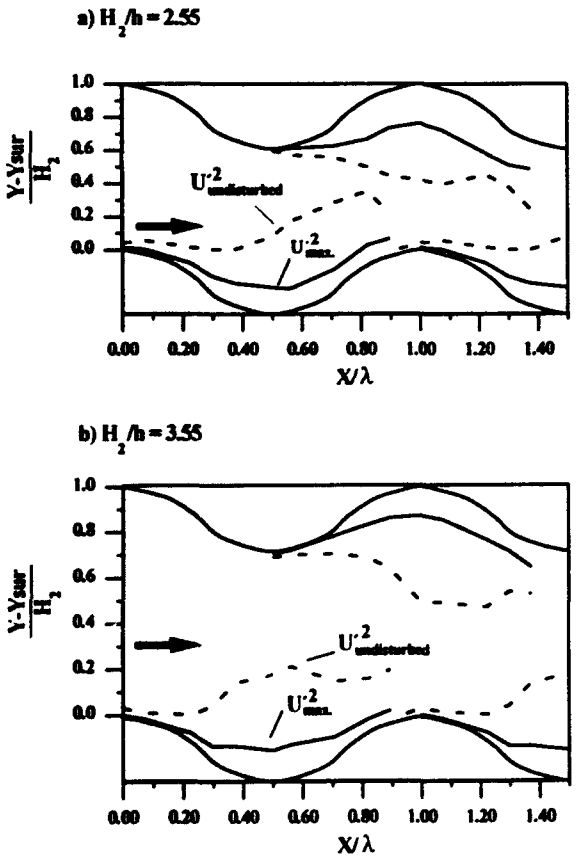

Figure 8. Map of the shear layer.

a) H_2/h= 2.55
a) H_2/h= 3.55

4. CONCLUSIONS

Laser-Doppler measurements of the flow field established between large-amplitude wavy surfaces mounted in a water channel in a region of fully developed channel flow for a Reynolds number up to 3.6×10^5, have provided detailed information about the turbulent structure formed in the lee side of the obstacles. The study includes comparison of the flow in a wavy channel for two different channel heights and provides a set of benchmark data for the evaluation, in turbulent flows over curved boundaries, of numerical solutions of the equation of motion which use turbulence models.

The results reveal a flow structure qualitatively similar to that found in other turbulent curved flows and include the analysis of the recirculating flow formed in the wake of the concave surfaces for one flow condition. In general, a thin boundary layer is established on the rising surface of the curved surfaces and accelerates up to their top. The curvature of the flow imposes mean velocity effects on the turbulent flow, resulting in the establishment of a zone of high intensity velocity fluctuations along the shear layer downstream of the top of each wavy surface. This is rapidly suppressed with the approach of the following concave surface, in a way that suggests that the response of the turbulent boundary layer to convex curvature is faster than that relative to concave curvature. The evidence suggests that the calculation of turbulent flows over curved boundaries of the type considered here must be found from a modeled transport equation rather than from a turbulent -viscosity hypothesis.

ACKNOWLEDGMENTS

The measuring section was made at the workshop of the Applied Thermodynamics Section of the Department of Mechanical Engineering of the Instituto Superior Técnico. The assistance of Messrs Carlos Carvalho and

Jorge Coelho in typing the manuscript and preparing the figures is gratefully appreciated.

REFERENCES

Almeida, G.P., Durão, D.F.G., Heitor, M.V. and Simões J.P. (1990). Laser-Doppler Measurements of Fully-Developed Turbulent Channel Flow. Proc. 5th Intl. Symp. on Appl of Laser Tech. to Fluid Mech. Lisbon 9-12 .

Almeida, G.P., Durão, D.F.G. and Heitor, M.V. (1993). Wake Flows Behind Two-dimensional Model Hills. Exp. Thermal Fluid Sci. , 7, pp. 87-101.

Barlow, R.S. and Johnston, J.P. (1988). Structure of a Turbulent Boundary Layer on a Concave Surface. J. Fluid Mech., 191, pp. 137-176.

Baskaran, V., Smits, A.J. and Joubert, P.N. (1987). A Turbulent Flow Over a Curved Hill: Part 1 - Growth of an Internal Boundary Layer. J.F. Mech., 182, pp. 47-83.

Bradshaw, P. (1973). Effects of Streamline Curvature on Turbulent Flow, Agardograph 169.

Buckles, J.J., Hanratty, T.J. and Adrian, R.J. (1984). Separated Turbulent Flow Over a Small Amplitude Wave, in: Laser Anemometry in Fluid Mechanics II, Editors, R.J. Adrian et al., LADOAN - IST-Lisbon, pp. 347-358.

Buckles, J.J., Hanratty, T.J. and Adrian, R.J. (1984). Turbulent Flow Over Large-Amplitude Wavy Surfaces, J. Fluid Mech., 140, pp. 27-44.

Castro, I.P. and Hague, A. (1987). The Structure of a Trubulent Shear Layer Bounding a Separation Region. J. Fluid Mech., 179, pp. 439-468.

Durão, D.F.G, Heitor, M.V. and Pereira J.C.F. (1989). A Laser Anemometry Study of Separated Flow over a Model Three-Dimensional Hill, in: Applications of Laser Anemometry to Fluid Mechanics" ed. Adrian et al, Springer-Verlag; pp. 93-118.

Durst, F., Rastogi, A.K. (1980). Turbulent Flow Over Two-Dimensional Fences, in: Turb. Shear Flows 2, Springer-Verlag, pp. 218-231.

Durst, F., Melling, A. and Whitelaw, J.H. (1981). Principles and Practice of Laser-Doppler Anemometry, 2nd. ed., Academic Press, New York.

Hunt, J.C.R. and Snyder, W.H. (1980). Experiments on Stably and Neutrally Stratified Flow Over a Model Three-Dimensional Hill. J. Fluid Mech., 96, pp. 671-704.

Melling and Whitelaw, J.H. (1976). Turbulent Flow in a Rectangular Duct, J. Fluid Mech., 78, pp. 283-315.

Patel, V.C., Chon, J.T. and Yoon, J.Y. (1991). Turbulent Flow in a Channel With a Wavy Wall. J. Fluids Engn., 113, pp. 579-586.

Rody, W. (1970). Basic Equations for Turbulent Flow in Cartesian and Cylindrical Coordinates, Imp. College of Science and Tech. London.

Yanta, W.J., Smith, R.A. (1978). Measurements of Turbulent-Transport Properties With a Laser-Doppler Velocimeter. AIAA paper 73-169, 11th Aerospace Science Meeting, Washington.

AN EXPERIMENTAL STUDY OF THE UPSTREAM OF A CIRCULAR CYLINDER

Hani Nigim* and Cameron Tropea++

*Department of Mechanical Engineering
Birzeit University, West Bank, Palestine

++Lehrstuhl für Strömungsmechanik
Universität Erlangen-Nürnberg, Germany

ABSTRACT

The structure of a fully developed turbulent flow in the plane of symmetry upstream of a vertically mounted circular cylinder is being described. The Reynolds numbers for this study, based on the channel height and the channel bulk mean velocity are 10000 and 40000 respectively. Detailed of time averaged mean flow properties, turbulence intensities and Reynolds stresses were obtained using a mobile fiber-optic laser Doppler anemometer (DFLDA). Pressures were measured on the channel floor with surface static pressure taps. The main flow characteristic upstream is a system of vortices which are shaded quasi-periodically. The shedding of these vortices are associated with bimodal velocity distributions as well as large contributions to the Reynolds shear stress.

1. INTRODUCTION

The flow field of a fluid approaching a three-dimensional body mounted vertically on a wall is not only complicated but also an important problem in many engineering applications, e.g. in the flow field in turbo-machinery, junction of aeroplane wings, and around the base of bridge piers. The complication of such flow is resulting from the secondary flows caused by both skewing and blockage effects that arise due to the interaction between the two-dimensional approaching flow and the adverse pressure gradient set up by the upright wall mounted body. This is essentially a three-dimensional separated flow and the developed vortex system is generally referred to as a horseshoe vortex.

The phenomenon of the horseshoe vortex is well known and a vast amount of experimental work concerning this phenomenon has been reported by many investigators. Baker (1979,1980) studied the separation of laminar and turbulent boundary layers formed around the base of a cylinder. The presence of multiple vortices was observed from the photographs of smoke- and oil-flow visualizations. A "four vortex" model was developed to correlate these observations. Eckerle and Langston (1987) reported pressure probe measurements in the front of a cylinder. They demonstrated that the four-vortex model is not clear for turbulent boundary layers. Merati *et al* (1991) used hot-wire probes to make interior measurements in the vortex formation region. Their results gave similar indication as those obtained by Eckerle and Langston (1987).

Typically, with three-dimensional separated flow situations, very large velocity fluctuations occur. This include complete flow reversals, and the question of probes may interfere with the flow field can be raised. Pierce and Tee(1990) as well as Eckerle and Awad (1991) used LDA to examine such separated flow field. They reported LDA velocity field measurements in a turbulent junction vortex. Devenport and Simpson (1990) examined the Turbulent flow near the nose of a wing-body junction. They showed that the flow in the plane of symmetry immediately upstream of the junction is characterized by large scale, low-frequency unsteadiness.

While the three-dimensional separation of a boundary layer approaching an obstacle is well documented , very little data has been published on the separation of a fully developed channel flow. Larousse *et al* (1990) investigated the flow field around surface-mounted prismatic obstacles using two-component LDA to gain detailed information about the time -averaged and time-resolved turbulence parameters. Their data reveals a distinct unsteadiness of the upstream flow and very high values of the Reynolds shear stress.

Generally, in most studies the scale of the experiment was too small for accurate and detailed measurements. In this paper the experimental data of the flow upstream of the intersection of a circular cylinder mounted vertically on the

floor of a fully developed channel flow is presented and the results are discussed. The Reynolds numbers for this study, based on the channel height and the channel bulk mean velocity are 10000 and 40000. Detailed of time averaged mean flow properties, turbulence intensities and Reynolds stresses were obtained.

2. EXPERIMENTAL APPARATUS AND INSTRUMENTATION

The experimental measurements were made in an open, blower-type air channel in the Lehrstuhl für Strömungsmechanik at the Universität Erlangen-Nürnberg, Germany. The test section of the channel which made of plexiglass, has a rectangular cross-section of 600 mm wide by 50 mm height and 3900 mm length. The boundary layer was tripped at the inlet of the air channel to avoid any unsteadiness or uneveness in the flow that may result from natural transition, also to obtain a fully-developed flow conditions well ahead of the obstacle. Air from the blower is supplied to the test section after first passing through a fixed-setting damper, a section of honeycomb to remove the mean swirl of the flow and several screens to remove much of the turbulence intensity. Further details can be found in Larousse *et al* (1991).

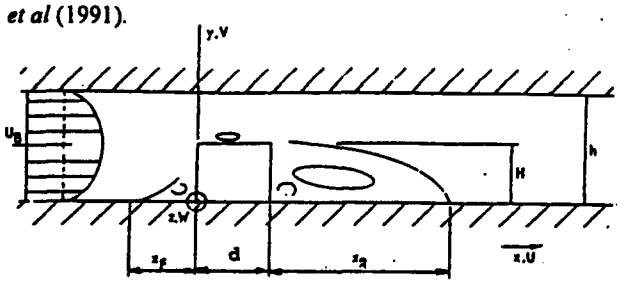

Fig.1 Sketch of the cylinder geometry in a channal

The experimental setup consisted of a cylinder of 25 mm diameter by 25 mm height mounted vertically inside the test section. Because of the simplicity of the cylinder geometry, the approaching fully-developed flow separated symmetrically on each side of the cylinder. Therefore, here, the data were reported for, only, the plane of symmetry upstream of the obstacle. Figure 1 illustrates the channel and the cylinder that have been used.

Pressure taps of 1.0 mm diameter were provided on the channel floor in order to carry out static pressure measurements. These measurements were conducted using Betz water manometer with a measuring range of ± 0.05 mm. The static pressure coefficient C_p was based upon the channel bulk velocity U_B, and the atmospheric pressure.

In order to avoid uncertainty due to the probe interfere with the flow field a mobile fiber-optic laser Doppler anemometer (DFLDA) was used. This type of anemometers has been implemented for the first time with such experimental set up. The DFLDA system is portable and mobile measurement system with low power consumption, easy handling and high signal quality. The laser source is a 100-mW single-stripe, monomode laser diode operating at 828 nm and packaged with a temperature regulator ($\pm 0.1^{\circ}$) and correction optics for astigmatism and for achieving a circular beam profile. It is working in back-scatter mode with sensitivity to flow direction provided by a double Bragg cell arrangement for achieving frequency shift of up to 10 MHz. The output of the system is 94 mW and the beam is nearly circular with a diameter of 5.6 mm. The complete details of the DFLDA system is given in Stieglmeier and Tropea (1991); the optical system is illustrated schematically in Figure 2.

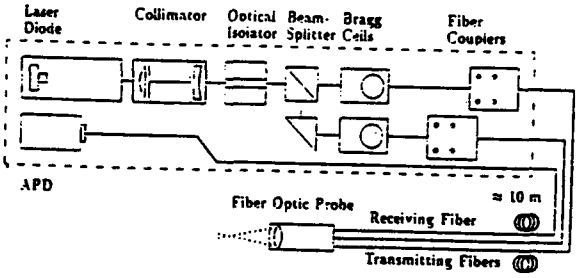

Fig. 2 Block diagram of DFLDA optical system

To perform velocity measurements in the separated flow upstream the cylinder/floor junction, the 25 mm probe was mounted on an 2-D traversing system which was located on top of the test section. The traversing, mounting and rotation of the probe allowed measurement of, U, U-W components, including Reynolds shear stresses. Data were acquired with a computer controlled data acquisition system via a counter-processor (TSI, Inc., 1980). Data of ensemble sizes of 1000 or more were typical. Several seeding materials were tried. The ultimate choice of seed was atomized from a solution made up of 25 percent di-ethylglycol and 75 percent water (by volume). The seed was generated by a medical nebulizer. Six nebulizers were introduced upstream of the channel inlet in the setting chamber of the blower.

3. RESULTS AND DISCUSSION

The experimental data of the flow upstream of the intersection of a circular cylinder mounted vertically on the floor of a fully developed channel flow is presented and the results are discussed. The measurements were obtained using a DLFDA probe. The Reynolds numbers, R_h, for this study, based on the channel height, h, and the channel bulk mean velocity, U_B, are 10000 and 40000. These Reynolds numbers were obtained at U_B = 3 m/s and 12 m/s respectively.

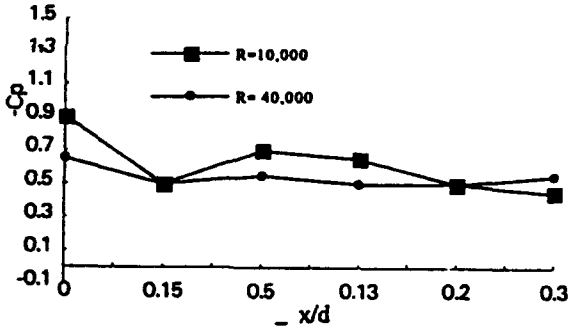

Fig. 3 Cp vs x/d upstream of the cylinder

Floor static pressure measured in the plane of symmetry are shown in Figure 3 for the two Reynolds numbers tested. The static pressure is highest next to the cylinder leading edge, which indicates the stagnation of the approaching flow at the cylinder/floor junction. Figure 3 shows that, as x/d increases from the cylinder the coefficient C_p drops rapidly which is associated with the reverse flow accelerating away from the cylinder leading edge toward the saddle point region. The trends shown by the pressure data are similar to the results reported in Eckerle and Awad (1991).

Velocity distribution in the plane of symmetry were obtained from x/d =1.0 to the cylinder leading edge between y/d ≈ 0.0 to 0.3. Figures 4a and 4b show the normalized streamwise velocity U/U_B, for Reynolds numbers, based on the height of the channel, 10000 and 40000 respectively. It appears that the reverse flow regions are not symmetric; for the Reynolds number, R_h= 10000, the region of reverse velocity flow is 40% greater than that region observed when the Reynolds number is 40000. The main feature of the figure is the presence of a single relatively large vortex structure. It was noted that the flow in the cylinder floor corner was allusive and agreeable with the presence of a small, counter rotating corner vortex.

Figure 5 shows bimodal (double-peaked) probability-density functions (p.d.f.s) of the streamwise velocity, U, which were measured during the traverse performed with the high Reynolds number, R_h= 40000. This phenomenal is associated with the very large turbulent stresses. The bimodal were observed in the range x/d ≈ -0.18 to -0.4 and correspond to the reverse velocity measured between x/d ≈ 0.0 to -0.25. The bimodal b.d.f.s also occur in the W- and (U-W)-components but over slightly different regions (Figure 6).

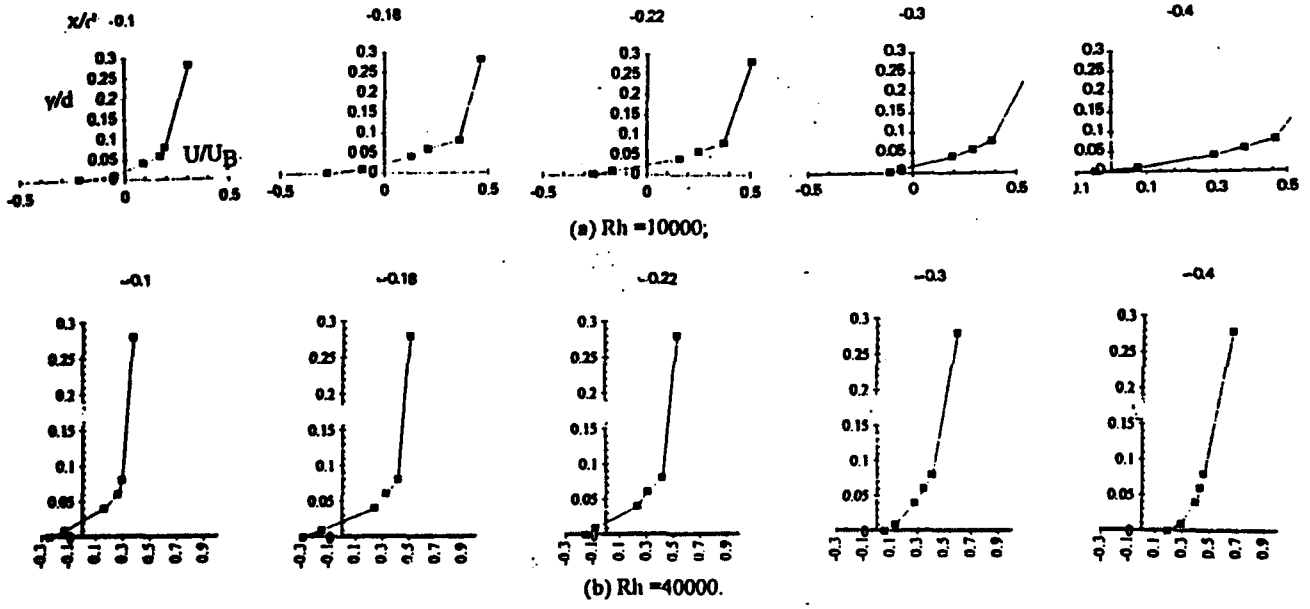

Fig. 4 Streamwise velocity distributions upstream of a cylinder; (a) Rh =10000; (b) Rh =40000.

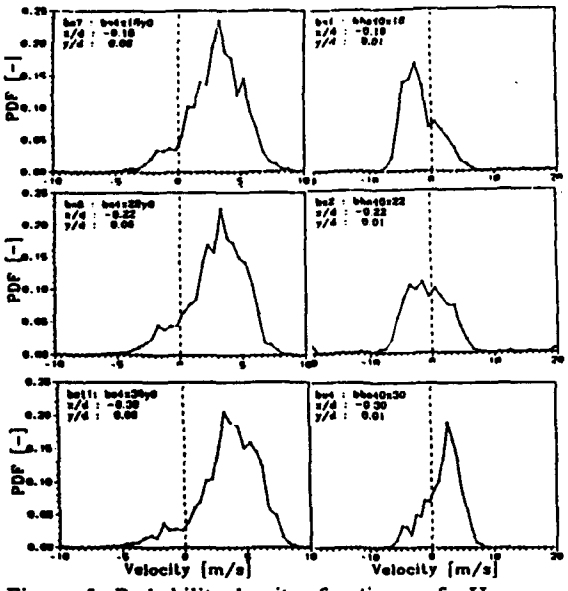

Fig. 5 Probability-density functions of U-component fluctuations.

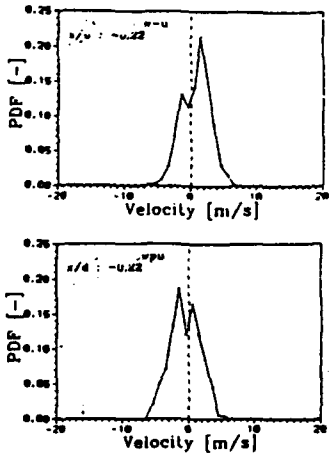

Fig. 6 Probability-density functions of uw-component fluctuations.

However, when the measurements where made at R_h= 10000, no bimodal regions were detected. Probably no previous work has conclusively demonstrated the presence of bimodal velocity probability-density functions in a fully developed channel flow circular cylinder/ floor junction.

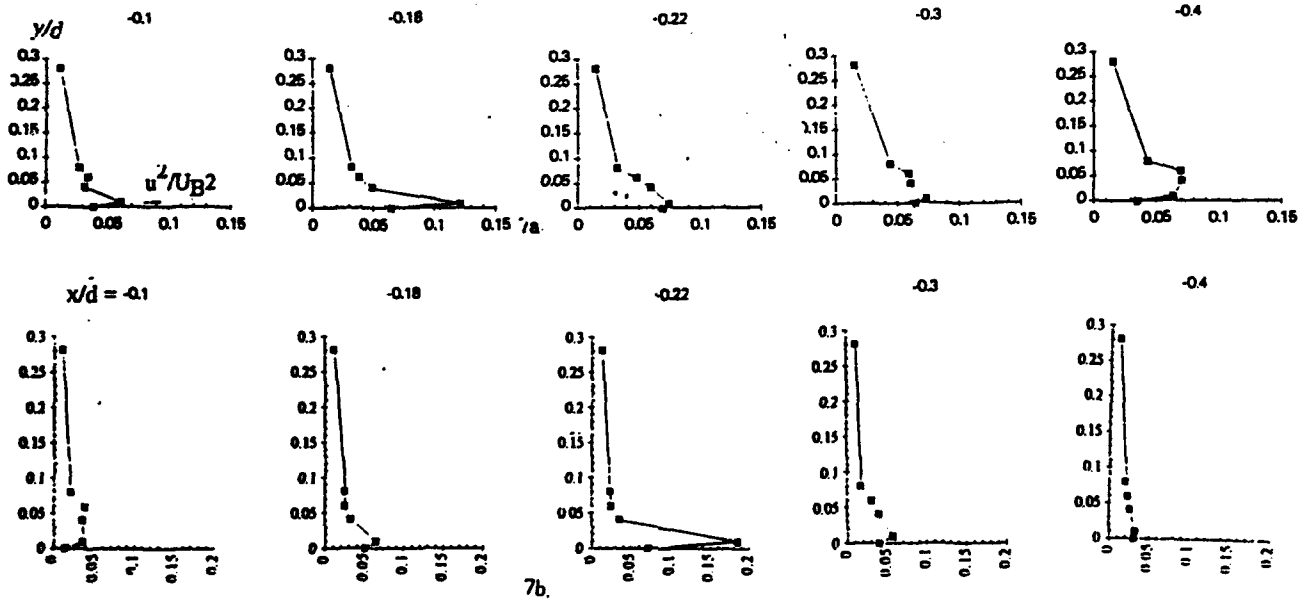

Fig. 7 Profiles of the turbulence intensities;
(a) Rh =10000; (b) Rh =40000.

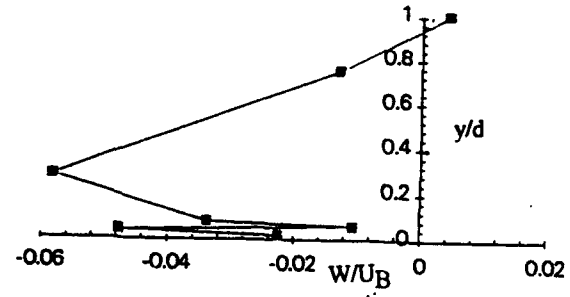

8a

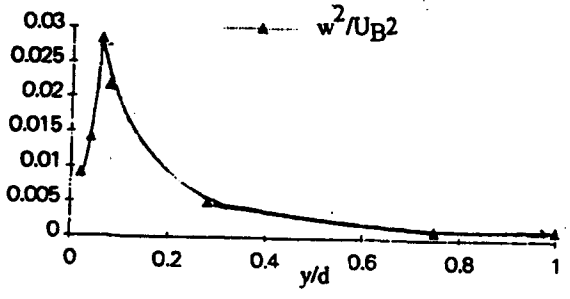

8b

Fig. 8 Spanwise velocity measurements, at Rh = 40000; (a) mean velocity; (b) rms velocity.

Turbulence intensities, u^2/U_B2, for R_h = 10000 and 40000 are presented in figure 7a and 7b. It was observed that the fluctuating velocities peaked in the bimodal region and only a small peak was measured with no bimodal presence. In the bimodal region the measured values of turbulence intensities are many times larger than those normally obtained in turbulent separated flows. Above the junction main vortex (y/d≥ 0.15) the turbulence intensities fall with distance downstream, perhaps as a result of the distortion of the flow structures in the junction region.

As a reference for data measured in the bimodal and reverse flow regions, spanwise mean and rms velocities as well as Reynolds stresses (W, w, uw respectively) were measured in the plane of symmetry at x/d = -0.22 and R_h =40000. The normalized data of the sanpwise and rms velocities, W/U_B and w^2/U_B2 are presented in Figures 8a and 8b respectively. These figures reveal an interesting three-dimensional effect which is, partially, due to the removal of fluid from the plane of symmetry by the secondary flow acting on either side of the cylinder/floor junction. Close to the junction w^2 remains approximately constant at its peak value becoming equal to, if not exceeding, u^2 very close to floor; in two-dimensional separated flows w^2 remains a small fraction of u^2.

Reynolds shear stresses, uw, are presented in Figure 9 for R_h =40000. Also, the high values of Reynolds shear stress, uw, in the region of measured bimodal velocity distributions suggesting that this production is associated with large-scale unsteadiness.

The vortex pattern deduced from the experimental data suggested that a two-vortex flow model is existing, which is in good agreement with the recently published data by Eckerle and Langsten (1987), Pierce and Tree (1990) and Eckerle and Awad (1991). This vortex pattern, however, is in contrast to the four-vortex modal reported in the most earlier publications for low speed turbulent junction vortex flows, and mainly based on surface flow visualizations (Baker (1980); also see the reproduction of the well known photograph by Sutton in Thwaites (1960)). Evidently, the fully developed turbulent flows generate enough turbulence stresses to prevent the formation of multiple vortices. Although, further experimental work, using laser-sheet flow visualization as described by Martinuzzi (1992), is needed to check the existence of any extra vortices which may form away from the cylinder/floor junction.

In addition, the present data shows a substantial quasi-periodic unsteadiness within the vortex system. Similar observations were reported by Devenport and Simpson (1990) , Larousse *et al* (1991) and Olcman and Simpson (1994). However such phenomenon was observed with data obtained at high Reynolds number (R_h = 40000) only. This is in turn was associated with the size of separation region upstream of the cylinder stagnation; the larger the size of the separation region the more space exist for a steady junction vortex to be developed.

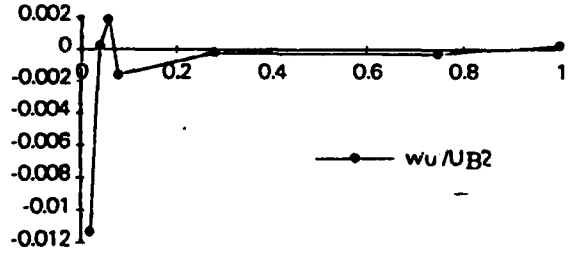

Fig. 9 Reynolds shear stress uw, at Rh =40000.

4. CONCLUSIONS

The flow field upstream of a circular cylinder has been investigated experimentally in a fully developed turbulent channel flow. The measured pressure distributions showed little variation with Reynolds numbers. A single junction saddle point was observed while a multivortex model was not present. Analysis of the experimental data reveals that in the vicinity of the wall-cylinder junction vortex a distinct unsteadiness of the upstream flow field and the turbulent stresses become very large. This unsteadiness is bimodal in nature, with streamwise mean velocities near the wall alternating between large negative values and near-zero values. In addition, a relatively weak, counter-rotating recirculation pattern exists near the wall upstream of the primary recirculation.

ACKNOWLEDGMENTS

The authors wish to acknowledge the Deutscher Akademischer Austauschdienst (DAAD) and the Lehrstuhl für Strömungsmechanik at the Universität Erlangen-Nürnberg, for the support of this work. The first author would like to thank Dr. Kh. Al-Jamal for preparing the illustration figures.

REFERENCES

Baker, C.J. 1979, The Laminar Horseshoe Vortex, J. Fluid Mech., vol. 95, pp. 347-387.

Baker, C.J. 1980, The Turbulent Horseshoe Vortex, J. of Wind Engineering and Industrial Aerodynamics, vol. 6, pp. 9-23.

Devenport, W.J. & Simpson, R.L. 1990, Time-Dependent and Time-Averaged Turbulence Structure Near the Nose of a Wing-Body Junction, J. Fluid Mech., vol. 210, pp. 23-55.

Eckerle, W.A. & Langston, L.S. 1987, Horseshoe Vortex Formation Around a Cylinder, J. of Fluids Engineering, Trans. of the ASME, vol. 109, pp. 278-285.

Eckerle, W.A. & Awad, J.K. 1991, Effect of Freestream Velocity on the Three-Dimensional Separated Flow Region on Front of a Cylinder, J. Fluids Engineering, Trans. of the ASME, vol. 113, pp.37-44.

Larousse, A., Martinuzzi, R. & Tropea, C. 1991, Flow Around Surface-Mounted, Three-Dimensional Obstacles, Proc. 8th Symposium on Turb. Shear Flows, Munich, FRG.

Matinuzzi, R. 1992, Experimentelle Unersuchung der Umstromung Wandgebundener, Rechteckiger, Prismatischer, Hindernisse, Ph.D. thesis, University of Erlangen-Nürnberg, Erlangen, Gremany.

Merati, P., McMahon, H.M. & Yoo, K.M. 1991, Experimental Investigation of a Turbulent Flow in the Vicinity of an Appendage Mounted on a Flat Plate, J. Fluids Engineering, Trans. of the ASME, vol. 113, pp. 635-642.

Ölçmen, S.M. & Simpson, R.L. 1994, Influence of Wing Shapes on Surface Fluctuations at Wing-Body Junctions, AIAA Journal, vol. 32, No. 1, pp. 6-15.

Pierce, F.J. & Tree, I.K. 1990, The Mean Flow Structure on the Symmetry Plane of a Turbulent Junction Vortex, J. Fluids Engineering, Trans. of the ASME, vol. 112, pp. 16-22.

Stieglmeier, M. & Tropea, C. 1992, Mobile Fiber-Optic Laser Doppler Anemometer, Applied Optics, vol. 31, No. 21, pp. 4096-4105.

Thwaites, B. 1960, Incompressible Aerodynamics, Oxford University Press.

FLOW STRUCTURE NEAR THE FRONT EDGE OF AN ICE COVER

J. G. Eriksson and R. I. Karlsson*)
Vattenfall Utveckling AB, S-810 70 Älvkarleby, Sweden

*) also the Royal Institute of Technology, Department of Mechanics/Hydromechanics, S-100 44, Stockholm, Sweden

ABSTRACT

Simultaneous 2-D LDV measurements have been made in a laboratory flume simulating the flow field immediately upstream of and beneath the front edge of an ice cover on a river. Mean velocities, turbulence intensities, and the turbulent shear stress were determined. A comparison with hot-wire data after reattachment shows that LDV data generally give higher turbulence levels, which is ascribed to the inability of the hot-wire technique to cope with the high local turbulence intensities and instantaneous flow reversals present in this flow.

A separation bubble occurs beneath the ice cover, and the flow field inside and outside of the separation bubble is mapped in detail. The mean dividing streamline is determined, and a size/time-duration map of the separation bubble is constructed from the velocity-vector and -angle histograms. The results clearly verify the unsteady nature of the separated flow region.

1. INTRODUCTION

The problems of ice formation, frazil ice transport and growth of the ice cover in rivers are important factors for optimal use of water power during wintertime. Except in streams with low velocities, the first ice cover to form is drift ice that accumulates under the action of hydrodynamic forces (Ashton, 1986). Under certain circumstances an ice cover is formed with the front edge perpendicular to the mean flow direction. Such a simplified flow case in which the ice cover is a rectangular block with sharp edges is studied in the present work. Of course a real ice cover has a rounded edge: the sharp edge in the experiment was chosen in order to obtain a geometrically fixed separation point.

The primary aim of the work was to provide a comprehensive set of experimental data for comparisons with numerical computations, with the further aim of being able to calculate the paths of frazil ice particles convected with the flow.

The sharp edge of the ice cover creates a separation region beneath the ice cover, and the properties of the flow within and outside this region are studied in detail. Basically the geometry is that of a forward-facing blunt plate, studied by e.g. Cherry et al. (1984), and Kiya & Sasaki (1983, 1985), with the added complexity of the free surface. These authors made extensive pressure measurements in the separation region and used hot-wire anemometry (standard or split-film probes) for the velocity measurements. An intermittency measure was used together with the split-film probe data by Kiya & Sasaki to obtain limited velocity information in the separation region. The flow reversal and the large velocity fluctuations does however make hot-wire anemometry unsuitable for this flow case. An alternative technique is pulsed-wire anemometry (Castro & Dianat, 1990), which was successfully used by Castro & Haque (1987) in a separated flow. We, however, chose to use the LDV technique, since it is extremely well suited for obtaining accurate mean velocity and turbulence data in separated flows. Besides presenting new mean velocity and turbulence data in- and outside the separation bubble, some interesting general observations concerning the flow structure in separated regions have been made and will be presented in the paper.

2. EXPERIMENTAL APPARATUS

2.1 Test facility

The experiments were performed in a 1 m wide laboratory flume with a free-stream velocity U_0 of 0.6 m/s, see Fig. 1. Separate roughness elements and roughness in the form of a grating with a height of 25 mm on the floor of the flume were used to enhance the boundary-layer growth, so that the boundary-layer thickness corresponded to the water depth 0.535 m after a development length of 13.2 m. Here the ice cover (in the form of a sharp-edged wooden block) was situated and fixed relative to the flume. The wetted height of the ice cover was 55 mm. The Reynolds number of the boundary layer, based on the streamwise length, was about $7.9 \cdot 10^6$. The corresponding Reynolds number based on the wetted height of the blunt plate and the free-stream velocity was 33 000.

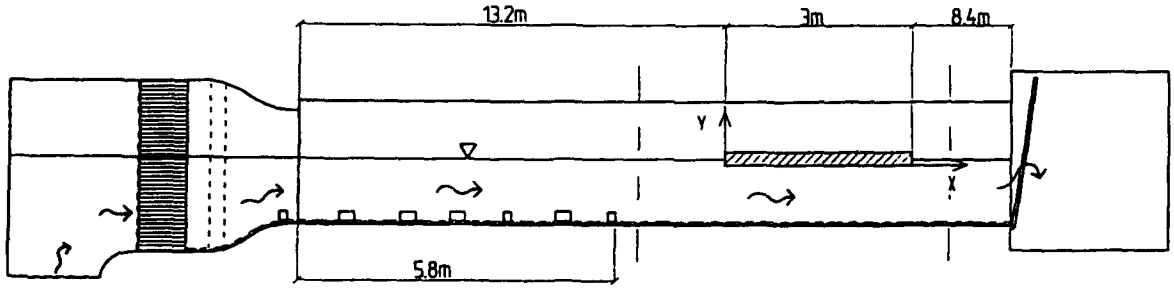

Fig. 1. Experimental facility: laboratory flume with simulated ice cover.

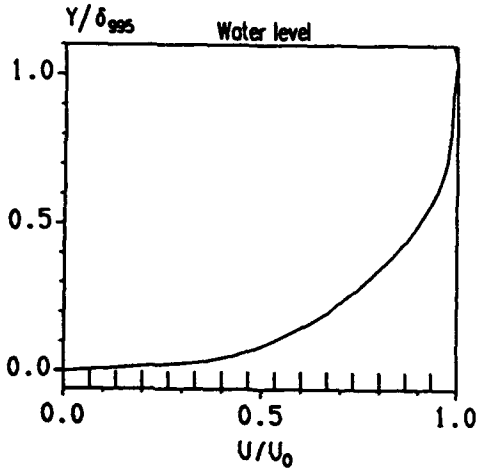

Fig. 2. Mean velocity profile through the boundary layer 0.5 m upstream of the ice cover. (Note that the origin of y here is at the crest of the roughness elements)

2.2 Flow qualification

Pitot-static tube measurements and flow visualization by means of dye were used to check that the floor boundary layer had reached the free surface at the position of the ice cover. A mean velocity profile taken 0.5 m upstream of the ice cover is shown in Fig. 2. One can note that the maximum mean velocity occurs just beneath the water surface, which is typical for open-channel flows with limited width. The friction factor C_f was determined for this profile by the method of Perry and Joubert (1963), which gave C_f=0.0079. Although this method, as well as the experimental data, has limited accuracy, the value obtained is consistent with the measured head loss.

The limited width (1 m) of the flume gives a non-negligible effect of the side-wall boundary layers on the flow. Calculations (Karlsson, 1985) of the boundary-layer growth in the flume shows that the displacement thickness after 13 m of development length is about 0.025 m and the physical boundary-layer thickness is less than 0.25 m.

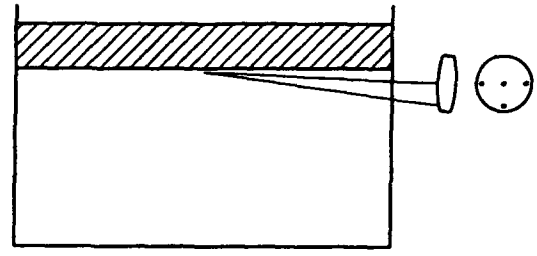

Fig. 3. Cross section of the flume with the ice cover, showing the optical set-up.

Flow visualizations of the side-wall boundary layers confirmed these figures. Thus, there exists a region about 0.5 m wide at the center of the channel where the flow is closely two-dimensional. This gives an aspect ratio of about 10 based on the wetted height of the ice cover and about 12 based on the depth of the separation bubble, which is generally considered sufficient (Kiya & Sasaki, 1983) to assure a reasonably uniform separation bubble in the spanwise direction. With the relatively small growth rate of the side-wall boundary layers at the position of the ice cover, it is reasonable to assume that the changes in the flow over the axial distance (0.74 m) studied in detail in the paper is caused by the ice cover only and not by the side-wall boundary layers. Therefore, all LDV measurements were performed on the centreline of the flume.

2.3 Instrumentation

A two-component TSI LDV system was used for the measurements. The focusing lens had a focal distance of 750 mm. The total beam expansion ratio was 8.5. A central-lower beam arrangement, as shown in Fig. 3, was used in order to simplify measurements of the vertical component under the ice cover. With the optical set-up used, the resulting measuring volume sizes are (0.75 * 0.05) mm for the horizontal component (λ = 488 nm) and (1.5 * 0.05) mm for the vertical component (λ = 514.5 nm).

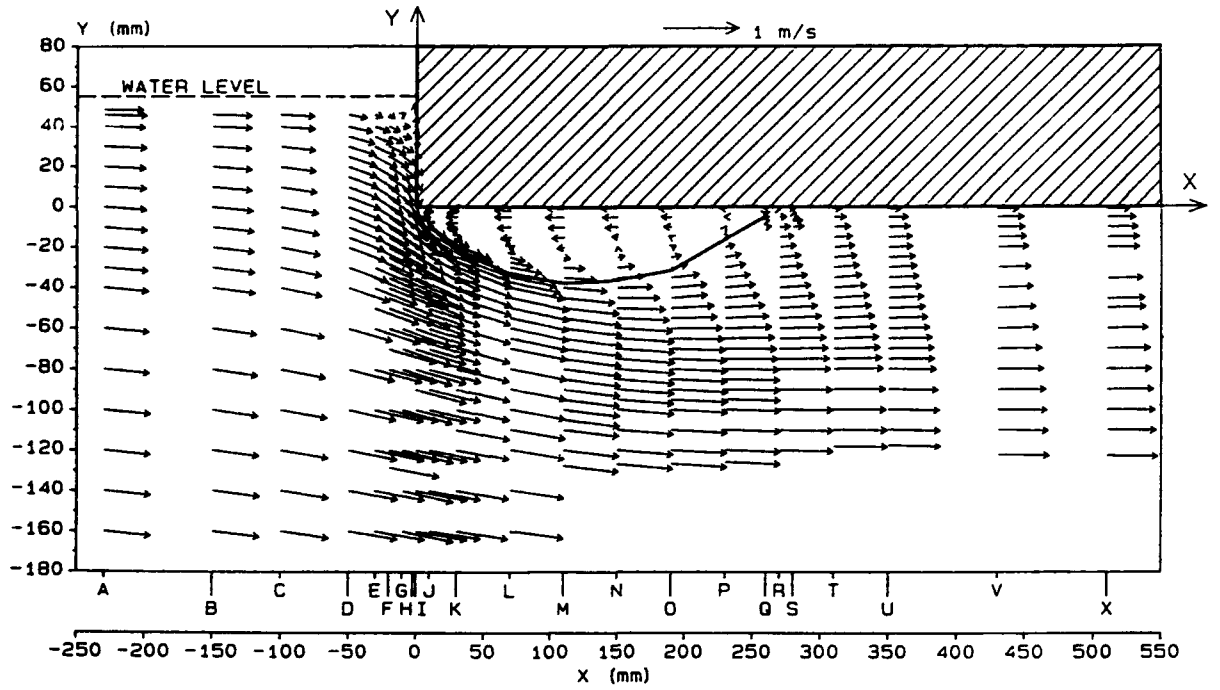

Fig. 4. **Mean velocity field in the x-y plane. Note the double scale in the streamwise direction: the lower scale (in mm) gives the x-coordinate and the upper scale A-X, used in subsequent figures, defines the position of the measured profiles. Solid line ⇔ mean dividing streamline.**

The corresponding fringe spacings were 3.0 μm and 5.9 μm, respectively. TSI 1980 counters were used as signal processors. Standard TSI software was used for all statistical evaluation. Mean velocities, turbulence intensities, the turbulent shear stress $\overline{uv}$, and higher order moments were evaluated from the data.

It should be noted that the central-lower beam arrangement used causes a non-orthogonality in the experimental set-up, with the consequence that the measured vertical velocities will be influenced by the spanwise velocity component. This was thoroughly treated by Karlsson et al (1993), who performed an analysis of the influence on the measured quantities for a 2-D flow (zero mean spanwise velocity). They concluded that for a tilt angle of the order of 3°, which is what we have here, the influence can safely be neglected except for (near-wall) regions where $(w')^2$ is significantly larger than $(v')^2$, where there is an increase in the measured v'.

2.4 Measurement positions

Measurements were made in 21 streamwise positions (A-X in Fig. 4), with the first profile 230 mm upstream of the front edge of the ice cover and the last profile 510 mm downstream of the front edge. In total, about 500 data points were acquired. The measurements beneath the ice cover started about 1 mm from the surface. The maximum depth at which measurements could be taken was limited by the traversing system.

2.5 Experimental methodology

The velocity measurements were made in coincidence mode, permitting multiple measurements per burst. The number of samples in each point was 20 480 and the measurement times were typically 10 minutes per data point. Very close to the ice cover, however, the number of samples were 10 240 and the measurement times were considerably longer. Silicon carbide particles with a mean diameter of 1.5 μm were used as seeding particles. Frequency shift was used for all measurements in order to avoid directional bias and to resolve the flow field in the separated region beneath the ice cover.

When taking measurements close to the upstream end of the ice cover, at axial positions F, G and H in figure 4, the optical axis of the LDV-system was tilted approximately 5° relative to the y-z plane. This results in a further non-orthogonality, meaning that the measured horizontal velocities will be influenced by the spanwise component. Performing an analysis similar to that of Karlsson et al (1993), one finds that the influence on U and $\overline{uv}$ is negligible. The influence on u' is significant only

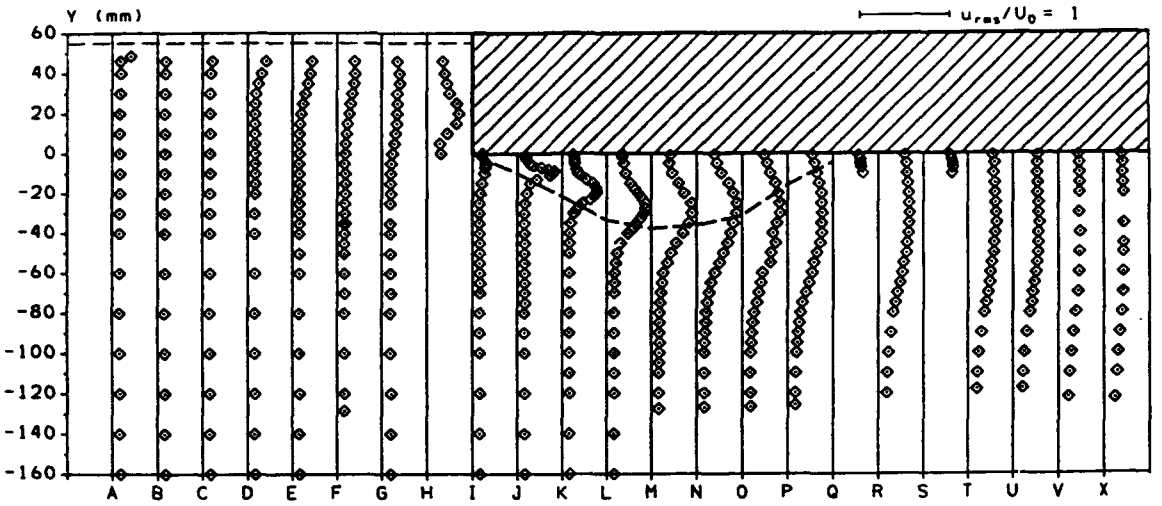

Fig. 5. Turbulence intensity u'/U_0. (Note that the horizontal coordinate is not to scale, see Fig.4). Broken line ⇔ mean dividing streamline.

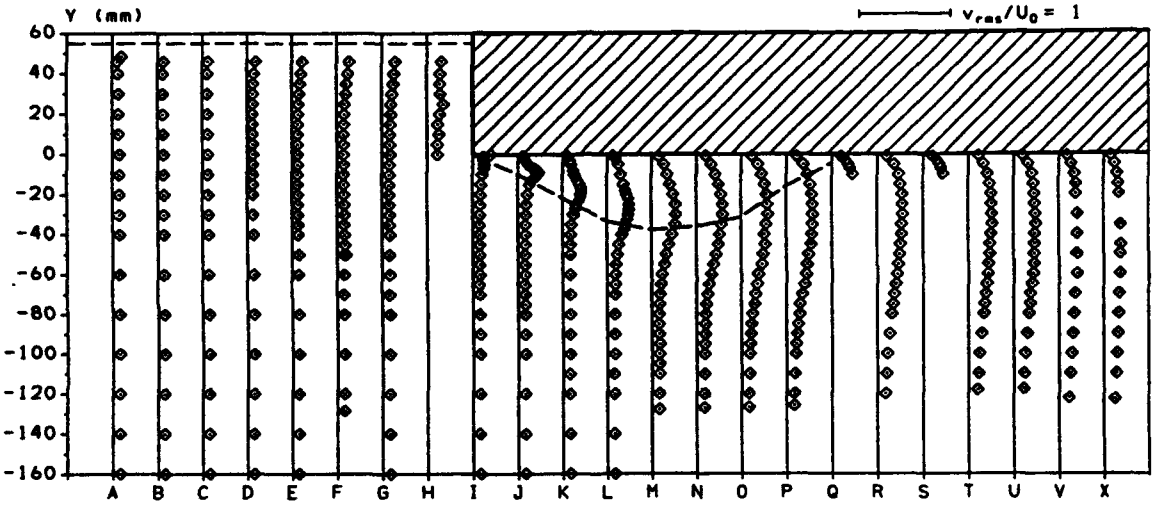

Fig. 6. Turbulence intensity v'/U_0. (Note that the horizontal coordinate is not to scale, see Fig.4). Broken line ⇔ mean dividing streamline.

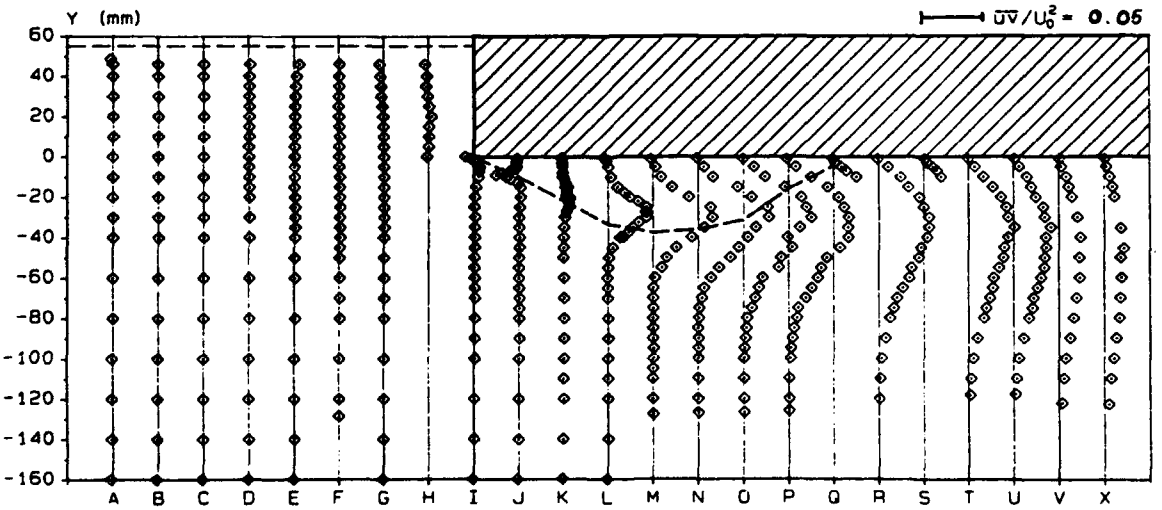

Fig. 7. Normalised shear stress distribution $\overline{uv}/U_0^2$. (Note that the horizontal coordinate is not to scale, see Fig.4). Broken line ⇔ mean dividing streamline.

when $(w')^2$ is significantly larger than $(u')^2$. Close enough to the upstream end of the ice cover, this will certainly be the case. Comparing measured values of u′ and v′ at the axial position H, we find that those are of the same order. Assuming that v′ ~ w′, we conclude that we are nowhere close enough to the upstream wall to have a noticeable influence on u′.

3. RESULTS

3.1 Mean flow and turbulence characteristics

The mean velocity field is presented in the form of a vector plot in Fig. 4. The mean dividing streamline (see section 3.3) is included in the figure in order to simplify the interpretation of results.

As can be seen from Fig. 4, a flow separation occurs beneath the ice cover. The separation starts at the sharp front edge of the ice cover (x = 0 mm, y = 0 mm) and extends to x ≈ 275 mm, which gives a separation length of about 5 times the displacement (55 mm) of the water surface. It can be noted that this is considerably shorter than the corresponding length for a rearward facing step. (Or using a different terminology, the separation length for the single-step contraction under investigation here is considerably shorter than that for a single-step expansion.) For a rearward facing step, the flow usually reattaches at about 7 step heights, cf. Stevenson et al (1984).

Maximum negative mean velocity in the recirculation zone is about 0.25 m/s, which is about 1/3 of the maximum velocity outside the separation bubble, and the maximum height of the mean dividing streamline over the surface is about 38 mm.

The turbulence intensities u'/U_0, v'/U_0 are shown in Fig. 5 and 6, respectively. The data are made dimensionless with the undisturbed mean velocity upstream of the ice cover. Note that the horizontal distances are not to scale. It is observed that the peak intensities lie within the recirculation zone in the upstream part of the region and outside the recirculation zone further downstream. The shear-stress distribution (Fig. 7) shows the same trend. The peak value is about 45 % for the longitudinal turbulence intensity and 30 % for the normal turbulence intensity. To compare these values by those found by Stevenson et al (1984) for a single-step expansion, we have also normalized u′ for both flows by a bulk velocity based on dimensions after the area change. It is interesting to note that using this scaling, the observed peak longitudinal turbulence intensity is the same for both flows, namely 40%.

The shear stress distribution $\overline{uv}/U_0^2$ for the whole region studied is shown in Fig. 7. (Note that V is positive upwards). Far upstream of the ice cover the shear stress is close to zero and becomes negative (as it should) for larger depths. Just downstream of the front edge (x = 10 mm), the shear stress exhibits a negative peak which disappears further downstream and is replaced by a large positive peak outside of the recirculation zone. The highest peak value is about 0.058 at position N. After reattachment the peak gradually decreases in magnitude, and the flow relaxes towards a more "normal" turbulent boundary layer flow.

The negative peak in the shear stress distribution at position J, 10 mm downstream of the front edge of the ice cover, is caused by the unsteadiness of the instantaneous dividing streamline. The peak is situated 8 mm from the surface, just outside of the mean dividing streamline. When this point is outside of the instantaneous dividing streamline, there is a drastic increase of the (positive) u-velocity and the negative v-velocity decreases further, thus giving a negative shear stress contribution which is larger than the positive contribution emanating from the situation when the instantaneous dividing streamline is situated outside of the point. An inspection of the velocity- and angle histograms also shows that the u-velocity histogram is strongly skewed towards positive velocity fluctuations. Thus, the large negative contributions to the shear stress dominate over the small positive contributions, which together gives a negative shear-stress peak.

The positive peak is easily interpreted as an upward transport of u-momentum, by the vertical turbulent fluctuations. In this area, fluid transported upwards, i.e. emanating at positions having more or less free-stream conditions, carries an excess of u-momentum. During this movement, the v-fluctuation is positive, which gives a positive shear stress. Similarly, fluid transported downwards, coming from the wall region, has a u-momentum deficit. The net effect is an upward transport of u-momentum and a positive peak in the shear stress.

3.2 Flow conditions upstream of the ice cover

The LDV-measurements start at position A, x = -230 mm. Here, the axial mean velocity is slightly lower than the free-stream velocity from y ≈ -60 mm and upwards. The vertical mean velocity is negative for the whole profile. Taken together, this shows that the influence of the ice cover is felt at the current position. The turbulence intensities are about 8%, the longitudinal turbulence intensity a little higher, the normal turbulence intensity a little lower. Close to the water surface, a slight increase in u′ and a clearly visible decrease in v′ is found.

When the ice cover is approached, the upper part of the flow is deflected and its velocity reduced. From y = 0 and upwards, the turbulence intensities increase in magnitude. Close to the front edge and just below the free surface, a vortex with its axis horizontal and normal to the x-y-plane is found.

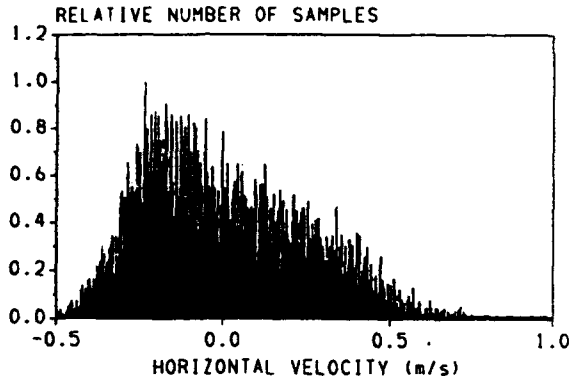

Fig. 8a. Histogram of the instantaneous horizontal velocity, U, at x = 150 mm, y = - 20 mm.

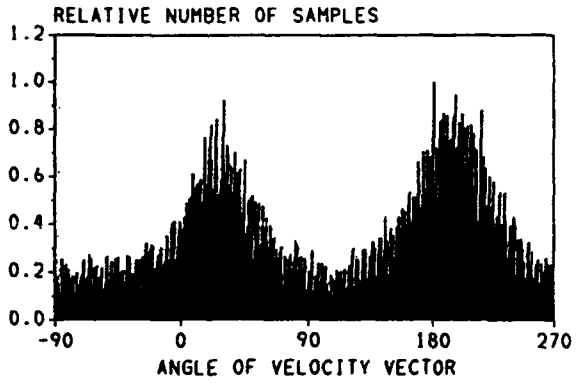

Fig. 8b. Histogram of the directional angle for the instantaneous velocity vector at x = 150 mm, y = - 20 mm. 0° corresponds to U >0, V = 0, 180° corresponds to U < 0, V = 0.

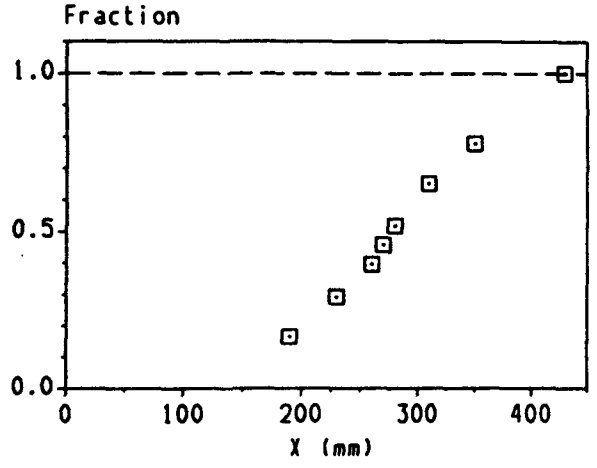

Fig. 9. Fraction of samples having positive horizontal velocity versus distance from front edge of ice cover. y = -1 mm.

3.3 Flow structure in the separation region

An interesting observation regarding the flow in the separation region is that the instantaneous flow field is identical to the mean flow field for only a small fraction of the total time. This is exemplified by the horizontal velocity and total velocity vector angle histograms in Fig. 8a-b, taken on a radial position very close to where the axial flow reverses. A mean velocity vector constructed from the mean component velocities has, naturally, an almost vertical direction. The angle of this mean velocity vector is ~ 100°, using the definitions given in figure 8. This can be compared to the instantaneous values shown in the histograms. The horizontal velocities are distributed over a broad range of values, whereas a bimodal distribution can be clearly seen in the angle histogram. The maxima in the angle histogram are situated at ~ 25° and 195°, with the angle of the mean velocity vector at a minimum almost right between the peaks. This shows that the position in question most of the time is either well inside or well outside the position of instantaneous flow reversal.

The reattachment point has been determined as the horizontal position where a data point taken close to the ice cover, vertical distance ~1 mm, contains 50% samples with positive horizontal velocities and 50% samples with negative horizontal velocities. Fig. 9 shows a plot of the fraction of samples with positive horizontal velocities as a function of the distance from the front edge of the ice cover. From this plot the reattachment position is determined as x ~ 275 mm, being equivalent to 5 times the wetted height of the ice cover. The data points taken close to this position shows the same bimodal distribution in the angle histogram as was seen in Fig. 8b, meaning that the instantaneous flow separation region most of the time is either longer than or shorter than the time-averaged flow separation region. The histograms contain samples with negative horizontal velocities until the position x = 430 mm is reached. The maximum instantaneous length of the recirculation zone is estimated to be slightly shorter than this, say 7.5 wetted heights. None of the histograms from the data points taken close to ice cover are free from samples with positive velocities. A physical interpretation of this observation is that the separation bubble now and then is totally "blown away" by the external flow field.

In Fig. 10, the size of the separation bubble is sketched. Several different measures are used. These measures are: mean dividing streamline, zero horizontal mean velocity, 50% of the samples having positive velocities, 25% of the samples having positive velocities and 75% of the samples having positive velocities. The size according to the zero horizontal mean velocity criterion and the 50% samples having positive velocities criterion is almost identical. The position for the 25% and 75% curves differs considerably from the 50% curve. For the more

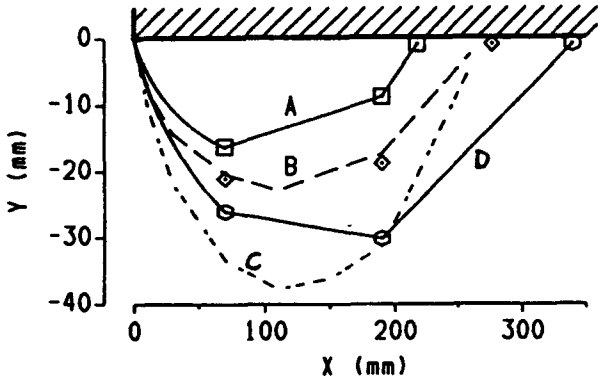

Fig. 10. Size of separation bubble defined as:
A: 25% probability for positive horizontal velocity
B: zero mean axial velocity =
50% probability for positive horizontal velocity
C: mean dividing streamline
D: 75% probability for positive horizontal velocity

downstream position shown, the vertical positions for the 75% and 25% positive samples curves differs by ± 50% from the position for the 50% positive samples curve. (The 75% positive samples position almost coincides with the mean dividing stream line.) For the more upstream position, this difference is about ± 25%. It is obvious that negative velocities prevail for a considerable fraction of time at positions quite far outside the line of zero mean axial velocity, and, for the downstream part of the separation region, even for positions on and outside the mean dividing streamline.

In the foregoing, we have mainly discussed in terms of fraction of samples instead of fraction of time, although we, when determining the position of the reattachment point, implicitly assumed that 50% of the samples having positive horizontal velocity is eqivalent to the horizontal velocity being positive 50% of the time. It is not generally possible to assume such a simple equivalence, due to the fact that the probability of taking a sample is not independent of the flow velocity. If the true probability density function of the variable in question is symmetrical around zero, this is no problem since then the higher probability for high-velocity samples will increase the probabilities for positive and negative velocity samples equally much. If, on the other hand, the pdf is displaced relative to zero velocity, there will be unproportionally many samples having the sign of the direction of displacement. Therefore, the 50% positive samples - position is probably a good representation of the "positive velocity 50% of the time" - position, whereas for the 75% positive samples - position, the time fraction having positive velocities is probably somewhat smaller. (And for the 25% positive samples - position, the time fraction is probably somewhat larger.) Nevertheless, we think that it is possible, with a reasonable degree of accuracy, to interpret the "fraction of samples-curves" in figure 10 as a size/time-duration map.

3.4 Flow structure in the reattachment and recovery regions

The profile at x=310 mm (position T), just downstream of the mean reattachment point, has been chosen for some comparisons with the data of Kiya & Sasaki (1983), who present results on turbulence intensities and turbulent shear stress at the reattachment point. The peak longitudinal turbulence intensity is about 25 % in their measurements, whereas we have about 35 %. The normal turbulence intensity is about 25 % lower and the turbulent shear stress is 35 % lower in the measurements of Kiya & Sasaki compared to our data. Thus, there is a systematic difference in results between hot-wire and LDV measurements. This difference must be ascribed to the inability of the hot-wire to cope with large local turbulence intensities and instantaneous flow reversals (rectification effects), which is typical for this flow (Hussein et al., 1994).

The flow in the two most downstream positions, x=430 mm (position V), x=510 mm (position X), is recovering from the flow separation, and a "normal" turbulent boundary layer is forming. This process is by no means finished, as can be anticipated from the high excess values of the turbulent shear stress and the turbulence intensities in position X compared to a fully developed turbulent boundary layer (Karlsson & Johansson, 1988).

4. SUMMARY AND CONCLUSIONS

An experimental study of the flow structure near the front edge of a simulated ice cover in a river has been performed using LDV. This geometry is basically that of a forward-facing blunt plate, and therefore also of a more general fluid mechanical interest.

The sharp front edge of the ice cover creates a separation region beneath the ice cover, and the properties of the flow within and outside this region have been studied in detail. Data for mean velocities, turbulence intensities and the turbulent shear stress have been presented.

- The mean reattachment position was found to be at ~ 5 wetted heights of the ice cover. The maximum instantaneous length of the recirculation zone is estimated to ~ 7.5 wetted heights.
- No data points taken in the recirculation zone contained only samples with negative horizontal velocities. Our interpretation is that the separation bubble now and then is totally "blown away" by the external flow field.

That is, the minimum instantaneous length of the recirculation zone is zero.

- A size/time-duration map of the separation bubble has been constructed using total velocity vector angle histograms. The large variation in size of the separation bubble, as indicated by the 25% and 75% time-duration lines, clearly verifies the unsteady nature of the flow.
- Comparisons (made in the reattachment region) with HWA data shows that the latter gives consistently lower values for the turbulence quantities. This is due to the inablility of the HWA-technique to cope with the high local turbulence intensities and the instantaneous flow reversals which appear in the flow.

REFERENCES

Ashton, G. 1986, River and Ice Engineering, Water Resources Publications.

Castro, I.P. & Dianat, M. 1990, Pulsed wire anemometry near walls, Experiments in Fluids 8, pp. 343-352.

Castro, I.P. & Haque, A. 1987, The structure of a turbulent shear layer bounding a separation region, Journal of Fluid Mechanics, vol.179, pp. 439-468.

Cherry, N.J., Hillier, R. & Latour, M.E.M.P. 1984, Unsteady measurements in a separating and reattaching flow, Journal of Fluid Mechanics, vol. 144, pp. 13-46.

Hussein, H.J., Capp, S.P. & George, W.K. 1994, Velocity measurements in a high-Reynolds-number, momentum-conserving, axisymmetric, turbulent jet. Journal of Fluid Mechanics, vol. 258, pp. 31-75.

Karlsson, R.I. 1985, Boundary Layer in a Flume, Report UL-FUD-B-85:3, Vattenfall, Älvkarleby Laboratory. (In Swedish).

Karlsson, R.I., Eriksson, J. & Persson J. 1993, LDV Measurements in a Plane Wall Jet in a Large Enclosure, in Laser Techniques and Applications in Fluid Mechanics, Eds. R.J. Adrian et al, Springer Verlag, Berlin Heidelberg.

Karlsson, R.I. & Johansson, T.G. 1988, LDV Measurements of Higher Order Moments of Velocity Fluctuations in a Turbulent Boundary Layer, in Laser Anemometry in Fluid Mechanics, Eds. R.J.Adrian et al, Ladoan, Lisbon.

Kiya, M. & Sasaki, K. 1983, Structure of a turbulent separation bubble, Journal of Fluid Mechanics, vol. 137, pp. 83-113.

Kiya, M. & Sasaki, K. 1985, Structure of large-scale vortices and unsteady reverse flow in the reattaching zone of a turbulent separation bubble. Journal of Fluid Mechanics, vol.154, pp. 463-491.

Perry, A.E. & Joubert, P.N. 1963, Rough-wall boundary layers in adverse pressure gradients, Journal of Fluid Mechanics, vol.17, pp. 193-211.

Stevenson, W.H., Thompson, H.D. & Craig, R. R. 1984, Laser Velocimeter Measurements in Highly Recirculating Flows, Journal of Fluids Engineering, vol. 106, pp. 173-180.

TURBULENT SHEAR FLOW OVER THE REPEATED TWO-DIMENSIONAL SQUARE RIBS ON GROUND PLANE

Shiki Okamoto, Kazumi Tsunoda, Tomohide Katsumata,
Daichi Suzuki and Nobuaki Abe

Department of Mechanical Engineering,
Shibaura Institute of Technology, Tokyo, Japan

ABSTRACT

This paper describes the detailed study of the flow structure over the repeated two-dimensional square ribs, of side length D, placed at a pitch S on a ground plane for various values of S/D, and the optimum value of S/D to augment the turbulence intensity near the ground plane. The pitch between the centers of two adjoining square ribs was varied at S/D = 2, 3, 4, 5, 7, 9, 11, 13 and 17. The time-mean velocity and turbulence intensity were measured by Laser Doppler Velocimeter. The static pressure was measured by the Pitot and static pressure tubes. As a result, it is concluded that the pitch ratio S/D =9 is optimum to augment the turbulence intensity, when the two-dimensional square ribs are aligned on the wall as a turbulence promoter.

1. INTRODUCTION

The flow over rough walls has been hitherto investigated in relation to the drag of a rough wall as well as early establishment of a turbulent boundary layer which augments the heat transfer. Nikuradse(1933) studied first the turbulent flow in pipes roughened by sand, and Schlichting(1936) investigated the resistance of a wall with repeated roughness elements. Perry et al(1969) studied the turbulent boundary layer that develops over a rough wall and proposed to divide them into two types: "d-type" , independent of the size of roughness element for a value of $S/D \leq 4$, (where S is the pitch between adjoining roughness elements and D is the height of the roughness element) and "k-type" which is dependent on the roughness size for $S/D > 4$. Antonia and Luxton(1971) studied the "k-type" and Osaka et al(1984) investigated the "d-type" boundary layer.

In connection with the problem of augmenting the heat transfer, Nunner(1956) measured the heat transfer and the pressure loss in the pipe where the inner wall was roughened by wires of various sizes. Webb et al(1971) studied the relation between the heat transfer and the resistance of tubes roughened by the repeated ribs for the cases of $10 < S/D < 40$, and Berger and Hau(1979) measured the mass and heat transfer in pipes roughened with the repeated square ribs for cases of $3 < S/D < 10$. Rao and Picot(1970), and Edwards and Sheriff(1961) studied the heat transfer on the inner tube of an annulus and the ground plane in the test section of a wind tunnel using wires as promoters for various values of S/D. Optimum values of S/D to augment the heat transfer were given at $S/D = 7$ by Rao and Picot(1970), and S/D = 10 by Edwards and Sheriff(1961), and Han et al(1978).

In the references mentioned so far no information is presented on the detailed flow structure. This was undertaken by Hijikata et al(1984) and Mori et al(1985) who studied the flow between adjoining ribs among repeated two-dimensional ribs on the ground plane for the single case of $S/D = 15$. Ichimiya et al(1983) measured the flow over repeated ribs on the lower insulated wall of the duct whose upper wall was heated for cases of S/D = 5, 7 and 15. However, these studies were performed for limited cases of S/D and did not, as a consequence, describe the variation of flow properties with the pitch ratio S/D. Okamoto et al(1993) reported the detailed study of the flow properties above the repeated two-dimensional square ribs on the ground plane for various values of S/D and the optimum value of S/D to augment turbulence of the free stream.

The present paper describes the experimental study of the flow structure around the repeated two-dimensional square ribs on the ground plane and especially in the groove between two adjoining square ribs, for various values of S/D.

2. EXPERIMENTAL APPARATUS AND MEASUREMENT PROCEDURES

The experiment was carried out in a circuit type wind tunnel having a 200mm × 200mm working section of 2000mm length. A half-ogival forebody of 100mm length was placed on the leading-edge portion of the ground plate(as shown in Figure 1). Two-dimensional square ribs with side length D = 10mm were aligned at regular pitch, S, on the lower wall of the test section and were varied to provide S/D = 2, 3, 4, 5, 7, 9, 11, 13 and 17. The trough thus created between two square ribs will be referred to as a groove. The time-mean velocity and turbulence intensity were measured by Laser Doppler Velocimeter. The Laser Doppler Velocimeter used in this experiment is as follows (forward scattering dual beams mode, 2 colors 4 beams, power: 4 watts argon-ion, operating power: 300mW, wavelength: green 514.5nm,

blue 488nm, beam spacing: 50mm, focal distance: 250mm, measurement region: diameter 0.08mm, length 0.82mm). The smoke of the joss stick was used for seeding the air flow. Auto-correlation was obtained using an F.F.T. Analyzer connected to a hot wire anemometer. The static pressure was measured by Pitot and static pressure tubes. The previous work by Okamoto et al(1993) describes the flow structure over the two-dimensional square ribs on the ground plane by using Pitot-tube and hot wire, and the flow pattern in the groove between two adjoining square ribs by a three hole cylindrical yawmeter. Use of the anemometer in the recirculation zone was avoided by restricting measurements above the top of the ribs. Therefore the present work is focused on investigating the flow structure in the groove between two-adjoining square ribs on the ground plane. Measurements were made at 7 axial locations corresponding to the centers of the groove and 5 locations in the groove between two adjoining square ribs for a free stream velocity of $U_\infty = 6 \sim 18$m/s corresponding to $Re = U_\infty D/\nu = 3750 \sim 11250$.

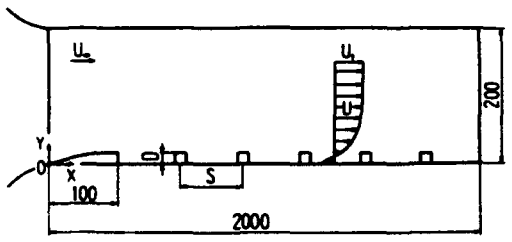

Fig.1 Apparatus and nomenclature

3. EXPERIMENTAL RESULTS AND DISCUSSIONS

3.1 Velocity Profiles in Shear Layer around the Repeated Square Ribs

Figure 2 shows the distribution of the velocity in the section at the center of grooves between two adjoining square ribs for the case of $S/D = 9$, $D/h = 0.1$ and $Re = 7500$. It can be seen from this figure that the turbulent shear layer is developed in the downstream distance and the velocity profiles tend to be similar in the region of $X/D \geq 86$. Figure 3 and 4 show the variation of the velocity profile in a section at the groove center in the similar profile region, near $X/D \approx 104$ for $D/h = 0.1$ and 0.3 with pitch ratio S/D respectively. The difference between the velocity profiles for the various values of S/D is concentrated in the region of $Y/D \leq 1$, namely in the groove between two-adjoining square ribs. The velocity profiles are almost similar in the region of $Y/D \geq 1$ outside the groove for the various values of S/D except $S/D = 3$ and 5 at $D/h = 0.1$ as shown in Fig.3. However for the case of $D/h = 0.3$, the velocity profiles become similar in the region of $Y/D \geq 1$ independent of values of S/D, as shown in Fig.4.

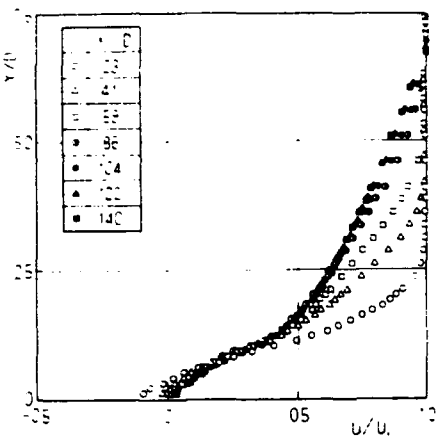

Fig.2 Velocity profile in shear layer for $S/D = 9$ ($D/h = 0.1, Re = 7500$)

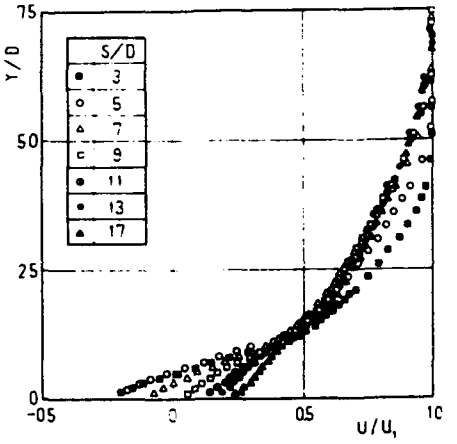

Fig.3 Velocity profile in shear layer in region of similarity ($D/h = 0.1, X/D \approx 104, Re = 7500$)

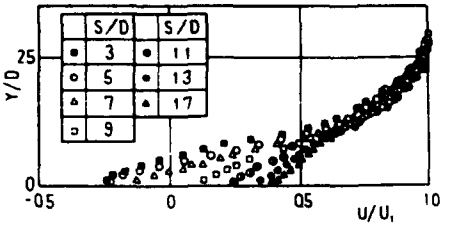

Fig.4 Velocity profile in shear layer in region of similarity ($D/h = 0.3, X/D \approx 104, Re = 7500$)

3.2 Turbulence Intensity in the Shear Layer around the Repeated Square Ribs

The turbulent shear layer is developed over the square ribs along the downstream distance. It can be assumed that the mixing phenomenon in the shear layer becomes strong

due to the existence of square ribs. Figure 5 shows the X-component of turbulence intensity in the shear layer at the groove centers for the case of $S/D = 9$, $D/h = 0.1$. The turbulence intensity in the shear layer decays with an increase in the downstream distance, and moreover tends to achieve the self-preserving profiles, like the velocity profiles at the same position. In order to examine the variation in the turbulence intensity with the pitch ratio S/D, profiles of turbulence intensity were measured at the position near $X/D = 104$ at the groove centers. Figure 6 and 7 show the variation of turbulence intensity in the shear layer at the positions in $D/h = 0.1$ and 0.3 with pitch ratio S/D. It can be seen from these figures that the turbulence intensity increases for $S/D \leq 9$ and decreases for $S/D > 9$ as the values of S/D increases. Figure 8 shows the variation of turbulence intensity at $Y/D = 1$ in the groove center near $X/D = 104$ for the case of $D/h = 0.1$ to 0.4, with the pitch ratio S/D,

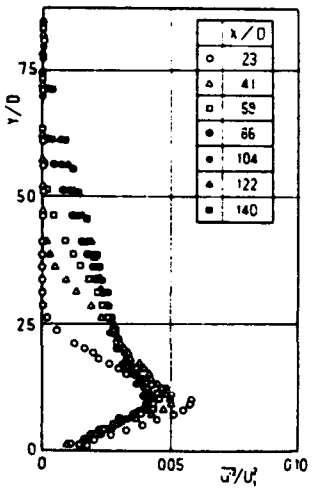

Fig.5 X-component of turbulence intensity in shear layer for $S/D = 9$ ($D/h = 0.1, Re = 7500$)

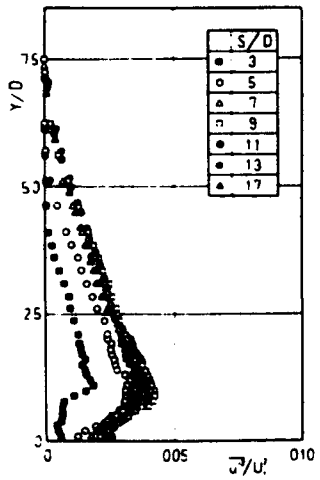

Fig.6 X-component of turbulence intensity in shear layer for various values of S/D ($D/h = 0.1, X/D \approx 104, Re = 7500$)

in order to establish the optimum pitch ratio to augment the turbulence intensity as a turbulence promoter. It can be seen from this figure that the turbulence intensity attains the maximum at $S/D = 9$ independent of values of D/h, and the turbulence intensity increases at the constant value of S/D as the value of D/h increases. Moreover the effect of the Reynolds number on the optimum pitch ratio S/D seems to be few study since Rao and Picot(1970) reported that the optimum pitch ratio was almost the same in the range of $Re = 6 \times 10^4 \sim 1.2 \times 10^5$. Figure 9 shows the variation of turbulence intensity at $Y/D = 1$ in the groove center near $X/D = 104$ for the case of $Re = 3750, 7500$ and 11250,

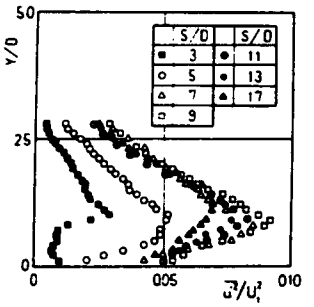

Fig.7 X-component of turbulence intensity in shear layer for various values of S/D ($D/h = 0.3, X/D \approx 104, Re = 7500$)

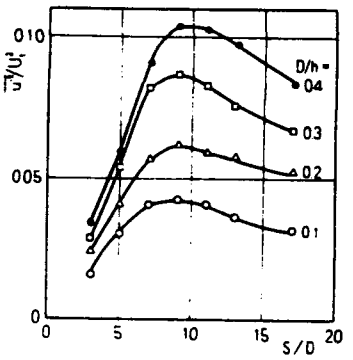

Fig.8 Variation of X-component of turbulence intensity at groove center with S/D ($X/D \approx 104, Y/D = 1, Re = 7500$)

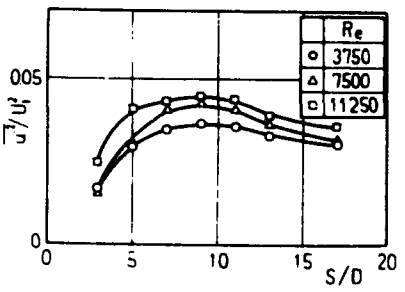

Fig.9 Variation of X-component of turbulence intensity at groove center with S/D ($D/h = 0.1, X/D \approx 104, Y/D = 1$)

in order to investigate the effect of Reynolds number on the optimum pitch ratio to augment the turbulence intensity. It is found from this figure that the optimum pitch ratio is a constant $S/D = 9$ in the range of Reynolds number for the present experiment. It therefore appears that the effect of the Reynolds number may be insignificant. Hence, when the two-dimensional square ribs are aligned on the wall as a turbulence promoter, the pitch ratio $S/D = 9$ is optimum to augment the turbulence intensity.

3.3 Flow Pattern and Turbulent Eddies in the Groove

As described in Section 3.2, when the two-dimensional square ribs are aligned on the wall as a turbulence promoter, the turbulence intensity attains the maximum at $S/D = 9$, which means that the mixing phenomenon is more active for the pitch ratio $S/D = 9$ than that for other values of S/D. Flow visualization are presented first in order to provide a qualitative picture of the flow field. Flow visualization was performed in a water channel with flow corresponding to $Re \approx 2000$. Figure 10 shows photographs of the flow and vortices generated behind a rib for the cases of $S/D = 2, 5, 9$ and 11. A small stable vortex exists in the groove for $S/D = 2$ and for $S/D = 5$ a larger stable vortex occupies the entire groove, without reattachment of the separation streamline on the floor of the groove. For $S/D = 9$ and 11, in contrast, this streamline reattaches to the floor of the groove at about $4D$. This result was confirmed in the wind tunnel, at the Reynolds number used later. Figure 11 shows the velocity profile in the groove between two adjoining square ribs for the case of $S/D = 5, 9$ and 13 in order to investigate the features of the flow in the groove between two square ribs. It is seen from Fig.11(a) that the backflow occupied the area near the floor in the groove for $S/D = 5$. In contrast , there is a backflow near the floor in the region of $\overline{X}/D < 4.5$ behind the upstream square ribs and favorable flow in the region of $4.5 \leq \overline{X}/D \leq 7.5$ for $S/D = 9$ as shown in Fig.11(b). For the case of $S/D = 13$, it can be seen from Fig.11(c) that there is backflow in the region of $\overline{X}/D \leq 4.3$ behind the upstream square rib and favorable flow in the region of $4.3 < \overline{X}/D \leq 10.8$. Hence, the free streamline left from the edge of the upstream square rib encloses the recirculation region and reattaches to the ground plane at $\overline{X}/D \approx 4$ as shown in Fig.11(b) and 11(c).

The length of the recirculation region, namely, the distance from the rib center to the reattachment point for the pitch ratio S/D, is shown in Fig.12. The abscissa D/S is selected to simultaneously show the result for the case of the single rib. The existing experimental results are denoted in this figure for the sake of comparison. Mantle(1966) reported that the free streamline left from the edge of the upstream square ribs does not reattach in the groove for the case of $S/D < 6.6$, but reattaches at $\overline{X_r}/D = 4$ for the case of $6.6 \leq S/D \leq 12$ and at $\overline{X_r}/D = 8.5$ for the case of infinite pitch ratio, namely, the case of a single rib. Mori et al(1985) showed $\overline{X_r}/D = 4.5$ for the case of $S/D = 15$. Their results and the present results are plotted on a single curve in Fig.12. Therefore the present result is consistent with the results of Mantle(1966) and Mori et al(1985). Okamoto(1979) previously reported the shear flow behind a flat plate normal to a plane boundary and pointed out that the turbulence intensity is largest immediately behind the reattachment point and decreases gradually in the downstream flow. Figure 13 shows the turbulence intensity in the groove between two adjoining square ribs for the case of $S/D = 5, 9$ and 13. The turbulence intensity has almost the same low value in the groove as for the case of $S/D = 5$. However for the case of $S/D = 9$ and 13, the turbulence intensity attains a maximum near the reattachment point. For the case of $S/D = 5$, the square ribs are close together and stable vortices arise in the groove and hence, the recirculation region occupies

(a) $S/D = 2$

(b) $S/D = 5$

(c) $S/D = 9$

(d) $S/D = 11$

Fig.10 Photographs of vortices

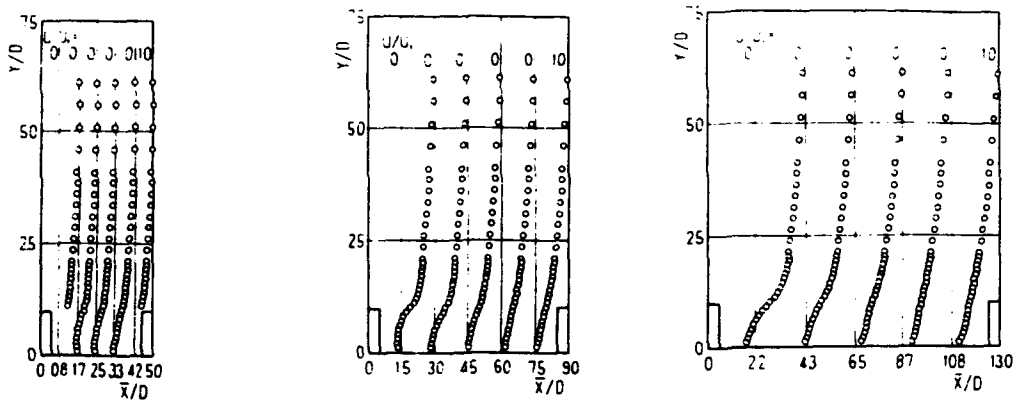

(a) $S/D = 5$ (b) $S/D = 9$ (c) $S/D = 13$

Fig.11 Velocity profile in the groove between two adjoining square ribs
($D/h = 0.1, Re = 7500$)

the entire groove between the square ribs without reattachment, because the length of the recirculation region is nearly $4D$(see Fig.10(b)). Hence the turbulence intensity becomes low as compared with those of $S/D = 9$ and 13. On the other hand, for the case of $S/D > 5$, there is a recirculation region behind the upstream square ribs, and the reattached flow goes downstream from the reattachment point(see Fig.10(c) and 10(d)). The reattachment point which corresponds to the position of the maximum turbulence intensity near the ground plane is near the midpoint of the groove for the case of $S/D = 9$. Furthermore, for the case of $S/D = 13$, the turbulence intensity decreases as compared with that for $S/D = 9$. The distance from the reattachment point to the next downstream square rib is longer for the case of $S/D = 13$ than for $S/D = 9$. Hence, the turbulence intensity decays with an increase in the distance downstream behind the recirculation region, so that it becomes larger for $S/D = 9$ than for $S/D = 13$.

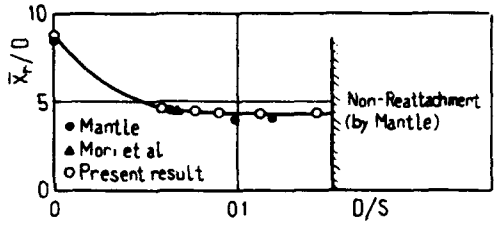

Fig.12 Reattachment point

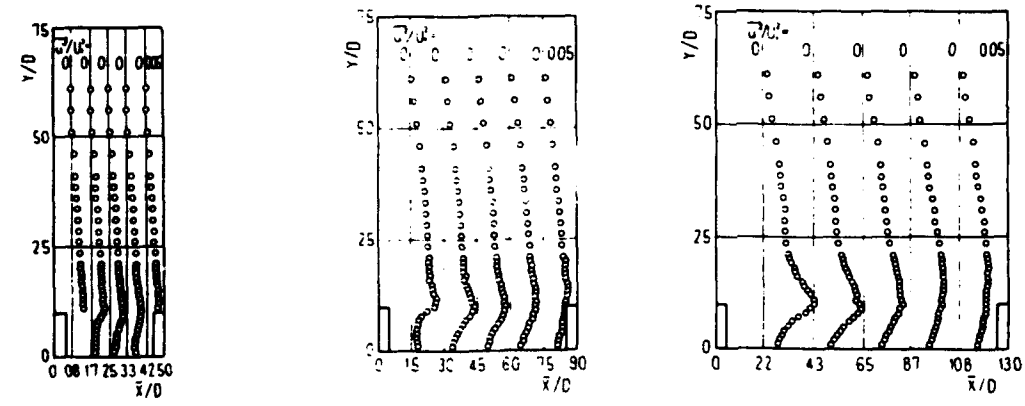

(a) $S/D = 5$ (b) $S/D = 9$ (c) $S/D = 13$

Fig.13 Turbulence intensity in the groove between two adjoining square ribs
($D/h = 0.1, Re = 7500$)

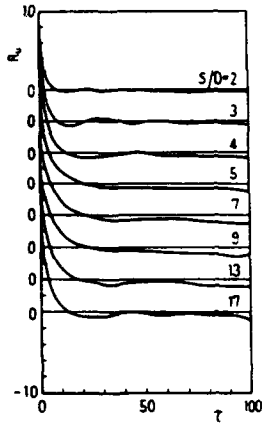

Fig.14 Auto-correlation at $Y/D = 1.5$ above groove center

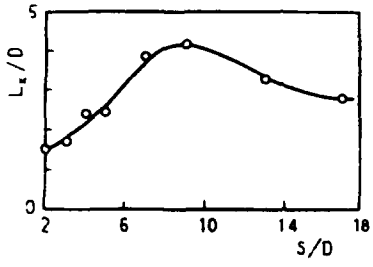

Fig.15 Integral scale at $Y/D = 1.5$ above groove center

This phenomenon can be explained from the feature of the turbulent eddies in the flow above the groove between two ribs. The auto-correlation of the X-component of fluctuation velocity was measured in order to investigate the structure of large-scale turbulence. Figure 14 shows the auto-correlation coefficient of u' in the shear layer at $Y/D = 1.5$ at the groove center near $X/D = 122$. There is no large negative correlation in the curves due to the existence of the periodical vortex shedding. The time delay of the first zero correlation increases in the range of $S/D \leq 9$ and decreases in the range of $S/D > 9$ as the value of S/D increases. The time delay of the first zero correlation attains the maximum at $S/D = 9$. The time delay which first becomes the zero correlation lengthens with an increase in the value of S/D for $S/D \leq 9$, which shows that the correlation vanishes slowly and that the decay of a large eddy is slow. The average scale of the large turbulent eddy is predicted to be the largest for $S/D = 9$.

The integral, which identifies the average scale of the large eddy, is obtained by integrating the auto-correlation function

$$L_X = U \int_0^\infty Ru(\tau)d\tau$$

where the convection velocity is estimated by the local time-mean velocity according to Taylor's hypothesis. Figure 15 shows the integral scale in the shear layer at $Y/D = 1.5$ at the groove center. The integral scale becomes largest at $S/D = 9$, which means that the average scale of the large eddy is maximum.

3.4 Pressure Distribution in Shear Layer over the Repeated Square Ribs

When the repeated square ribs on the ground plane are utilized as the technique of augmenting turbulence, the pressure loss due to the square ribs is the practically important problem. The pressure distribution on the floor in the groove between two adjoining square ribs was investigated. Figure 16 shows the pressure distribution on the floor in the groove for the case of $S/D = 9$, 13 and 17. The pressure distribution becomes negative due to the existence of the vortices behind the upstream rib for the case of $S/D = 9$

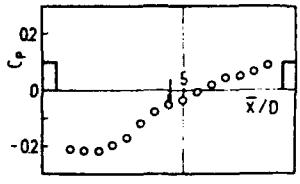

(a) $S/D = 9$

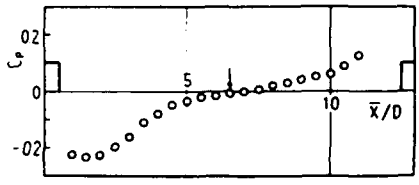

(b) $S/D = 13$

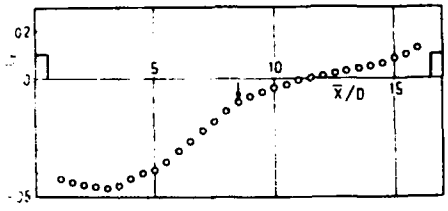

(c) $S/D = 17$

Fig.16 Surface pressure distribution on ground plane in the groove between two adjoining square ribs

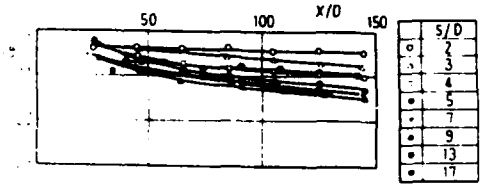

Fig.17 Pressure distribution at $Y/D = 1.5$ above groove centers

and then has gradually a high value with an increase in the downstream distance as shown in Fig.16(a). However for the case of $S/D = 13$ and 17, the pressure distribution which is low behind the upstream square rib in similar manner of the pressure distribution on the ground plane behind the flat plate normal to the free stream, and increases again in front of the downstream square rib. Therefore it seems that the pressure at the groove center is close to the average value among the pressure variation in the groove between two adjoining square ribs. Figure 17 shows the pressure distribution at $Y/D = 2.5$ at the groove centers. The pressure is reduced with an increase in the downstream distance independently of S/D. It is found that the pressure decreases in the range of $S/D \leq 9$ as the value of S/D increases, and the loss is largest at $S/D = 9$. Furthermore the pressure loss for $S/D = 13$ and 17 become slightly smaller than that for $S/D = 9$. Hence, when the optimum pitch ratio, $S/D = 9$ of the repeated square ribs is used as a promoter, the pressure loss is maximum.

4. CONCLUSIONS

This paper presented the flow structure over the repeated two-dimensional square ribs, of side length D, placed at a pitch S on a ground plane to find the value of S/D which most augments the turbulence of the free stream. The results of the present study are summarized as follows:

(1) The velocity profiles tend to be similar at the groove center with an increase in the downstream distance. The difference between the velocity profiles for the various values of S/D is concentrated in the region of $Y/D \leq 1$, namely in the groove between two adjoining square ribs.

(2) The turbulence intensity in the shear layer decays with an increase in the downstream distance, and moreover tends to achieve the self-preserving profile. The turbulence intensity attains the maximum at $S/D = 9$. Therefore the optimum value of S/D to augment turbulence of the free stream is $S/D = 9$, when the two-dimensional square ribs are aligned on the wall as a turbulence promoter.

(3) The turbulence intensity in the shear layer increases as the value of D/h increases. The optimum pitch ratio $S/D = 9$ is independent of values of D/h.

(4) The effect of the Reynolds number on the optimum pitch ratio may be insignificant.

(5) The turbulence intensity is largest immediately downstream of the reattachment point and decreases gradually to the next rib. Hence for the case of $S/D \leq 5$, the turbulence intensity becomes relatively low due to non-reattachment. Moreover, the distance from the reattachment point to the next square rib is longer for $S/D = 13$ than for $S/D = 9$ so that the turbulence intensity decays in the flow downstream of the recirculation region.

(6) The average scale of the large eddy, deduced from the integral scale, is largest at $S/D = 9$.

(7) When the optimum pitch ratio $S/D = 9$ of the repeated square ribs is used as the promoter, the pressure loss attains its maximum.

NOMENCLATURE

Cp	:	pressure coefficient = $(P - P_\infty)/(\rho U_\infty^2/2)$
D	:	side length of square section of two-dimensional ribs
h	:	height of test section of wind tunnel
L_X	:	integral scale in X-direction
P	:	static pressure
P_∞	:	static pressure in free stream
Re	:	Reynolds number = $U_\infty D/\nu$
Ru	:	auto-correlation coefficient of u'
S	:	Pitch between the centers of two adjoining square ribs
U	:	time-mean velocity
U_1	:	velocity at outer edge of shear layer
U_∞	:	velocity in free stream
u'	:	X-component of fluctuation velocity
X, Y, Z	:	co-ordinates with origin at the center of the leading edge of the ground plane(see Fig.1). X is chosen along the ground plane, Y and Z for the vertical and horizontal directions respectively.
$\overline{X}$	:	distance in X-direction from the center of the rib
$\overline{X_r}$	:	distance from the center of square rib to the reattachment point
ν	:	kinematic viscosity of air
ρ	:	density of air

REFERENCES

Antonia,R.A. & Luxton,R.E. 1971, The response of a turbulent boundary layer to an upstanding step change in surface roughness, Transactions of the ASME, Ser.D 93-1, pp.22-34.

Berger,F.P. & Hau,K.-F.,F.-L. 1979, Local mass / heat transfer distribution on surfaces roughened with small square ribs, International Journal of Heat Mass Transfer, vol.22, pp.1645-1656.

Edwards,F.J. & Sheriff,N. 1961, The heat transfer and friction characteristic for forced convection air flow over a particular type of rough surface, International Development in Heat Transfer, Part II, pp.415-425.

Han,J.C.,Glicksman,L.R. & Rohsenow,W.M. 1978, An investigation of heat transfer and friction for rib-roughened surfaces, International Journal of Heat Mass Transfer, vol.21, pp.1143-1156.

Hijikata,K.,Mori,Y. & Ishiguro,H. 1984, Turbulence structure and heat transfer of pipe flow with cascade smooth turbulence surface promoters, Transactions of the JSME, 50-458B, pp.2555-2562.

Ichimiya,K.,Yokoyama,M. & Shimomura,R. 1983, Effects of several roughness elements for the heat transfer from a smooth heated wall, Proceedings of ASME / JSME Thermal Engineering Joint Conference, vol.1, pp.359-364.

Mantle,P.L. 1966, A new type of roughened heat transfer surface selected by flow visualization techniques, Proceeding of 3rd International Heat Transfer Conference, vol.1, pp.45-55.

Mori,Y,Hijikata,K. & Ishiguro,H. 1985, Fundamental study of heat transfer augmentation by smooth turbulence surface promoters, Transactions of the JSME, 51-461B, pp.160-168.

Nikuradse,J. 1933, Stromüngsgesetze in rauhen Rohren, VDI-Forschungsheft, 361.

Nunner,W. 1956, Wärmeübergang und Druckabfall in rauhen Rohren, VDI-Forschungsheft, 455 pp.1-38.

Okamoto,S. 1979, Shear layer behind two-dimensional flat plate normal to plane boundary, Theoretical and Applied Mechanics, 27, pp.563-570.

Okamoto,S., Nakaso,K. & Kawai,I. 1993, Effect of rows of two-dimensional square ribs on flow property along plane wall, JSME International Journal, Ser.B, 36-1, pp.121-129.

Osaka,H.,Nakamura,I. & Kageyama,Y. 1984, Time averaged quantities of a turbulent boundary layer over a d-type rough surface, Transactions of the JSME, 50-458B, pp.2299-2306.

Perry,A.E.,Schofield,W.H. & Joubert,P.N. 1969, Rough wall turbulent boundary layers, Journal of Fluid Mechanics, 37-2. pp.383-413.

Rao,C.K. & Picot,J.J.C. 1970, The effect of turbulence promoters on heat and momentum transfer for air flow in an annulus, Proceedings of 4th International Heat Transfer Conference, F.C.4.8, pp.1-12.

Schlichting,H. 1936, Experimentelle Untersuchung zum Rauhigkeitsproblem, Ingenieur-Archiv, 7, pp.1-34.

Webb,R.L.,Eckert,E.R.G. & Goldstein,R.J. 1971, Heat tansfer and friction in tubes with repeated-rib roughness, International Journal of Heat Mass Transfer, 14, pp.601 - 617.

INVESTIGATIONS OF FLOW-FIELD FOR SUDDEN-EXPANSION PIPE WITH TRANSVERSE SIDE-FLOWS

A.B. Wang, S.P. Jow and C.C. Lin

Institute of Applied Mechanics,
National Taiwan University,
Taipei 10764, Taiwan, Republic of China

ABSTRACT

A new constructure, combining the side-flow and sudden-expansion pipe, to enhance the mixing phenomena in pipe was designed and investigated in this paper. This construction produces a fixed separated shear layer from pipe sudden-expansion on the one hand and the adjustable lateral shear layer(s) from the transverse of side-flow(s) downstream of the sudden-expansion plane on the other hand. Three basic types of arrangement for the transverse side-flow(s), together with different side-flow intensities (defined as volume-flow ratio of the side-flow to main flow), relative intensity ratio and injection angles of two side-flows, were tested to analyse their influences on the flow. Experiments, measured using LDA, are concentrated on the effects of weak side-flow intensities and the optimal design. Results show that this new constructure, especially using a single side-flow injection, is recommended to improve the mixing phenomena. There is a critical injection intensity for such a flow. The mechanism of side-flow injection is to cause a momentum transfer away from the jet-plane of side-flow. The results offer not only a useful guide-line for the flow control design, but also a good bench mark for testing the numerical modelling. This design has the benefits of simple, low cost and high flexibility.

INTRODUCTION

Performance of mixing of different fluid flows determines the efficiency of many chemical reactions, heat transfer operations and combustion processes in industry. Many successful examples show that effective use of turbulence may dramatically enhance mixing (e.g. Schetz(1980), Oldshue(1986), Forney(1986)). They reduce reaction time and eliminate excessive corrosion in reactor or increase the efficiency of the heat transfer and combustion process, thus significantly reduce the cost.

By careful analyzing many high-efficient mixers, it was found that the turbulence generated by the flow separation caused by the baffles, stirrers or many other complex geometries is the main mechanism for the process of mixing enhancement in such mixers. However, they introduce the problem of high cost, maintenance of moving parts and very often also high pressure drop. From these considerations, a back-facing sudden-expansion nozzle-block (with expansion ratio 1.67) combined with the side-flow(s) configuration, as shown in Fig.1, was designed and investigated in this paper. This construction basically produces a separated shear-layer from sudden-expansion of pipe in the streamwise direction on the one hand and also the shear layer(s) of side-flow(s) from the lateral pipe-wall just downstream of the sudden-expansion plane on the other hand. The interactions of shear layers caused by this construction were used to generate high turbulence in order to enchance mixing.

Highly turbulent three-dimensional flow field produced by three basic arrangements of side-flows, which were combination of positive (injection) and/or 'negative' (suction) side-flow(s), defined as case 1, case 2 and case 3 shown in Fig. 1, were experimentally investigated. The results were compared to the case without side-flows (denoted as case 0) to evaluate effects of the present design. To optimize the design of injection, the effects of the influential parameters including side-flow arrangement (case 1 to case 3), side-flow intensity (q/Q, defined as volumetric flow ratio of the side-flow to main stream), the injection an-

gle (α, defined as the angle between two separate side-flow) and the relative intensity ratio of two side-jets were studied and concluded in this paper. The results offer not only a good guide-line for the design of a mixing-enhancer but also a data-base for the numerical modelling of highly turbulent complex flows.

EXPERIMENTAL DESCRIPTIONS

The experiments were performed in a closed-circuit pipe system at flow-control lab. of the institute of applied mechanics, Taiwan University. The working fluid was water. The test-section comprised a 1 m long, 50 mm diameter (D) glass pipe and a nozzle-block which was located axisymmetrically at the beginning of test-section to form the sudden-expansion geometry. The test-section was immersed in a plane-wall glass trough filled with water to minimize the refraction and reflection of the laser-beams caused by the circular pipe-wall. The Reynolds number of the main flow, based on the nozzle-exit diameter and average mean velocity at the nozzle exit, was remained as 15,200. Side-flow was conducted into the test-section after the pipe sudden-expansion by connecting with the junctions of the nozzle-block. Independent reliable pump(s) and flowmeter(s) were used for the side-flow system.

Different tracer-techniques were used to visualize the flow-field to get an overview of the flow-field. Measurements of the axial mean velocity components and their turbulent fluctuations were obtained with a dual beam laser-Doppler anemometer operated in the forward scattering mode. The size of the measuring control volume was approximately $\phi 90\mu m \times 0.43mm$. The TSI-counter 1980B was used for the signal processing. Mean velocity and r.m.s.-values of velocity fluctuations were calculated from around 3,000 to 30,000 samples, depending on the locations of measurements. Each measurement was repeated at least three times. Detailed descriptions could be found in Jow (1994).

RESULTS AND DISCUSSIONS

1. Flow properties along the centerline

Fig. 2 (a) shows the distributions of the axial mean velocity along the centerline under the case 1 arrangement. Data of four different side-flow intensities (q/Q) are compared in the figure. It shows that the axial mean velocity along the center axis drops very quickly to its "asymptotic final value" when the side flow was used. Increasing the value of q/Q enhances this trend. The dimensionless axial mean velocity along the centerline reaches the final value (about 0.4) at around 20 H for the $q/Q = 2.78\%$ rather than 30 H for the case without side-flow ($q/Q = 0$). Fig. 2 (b) is the corresponding axial r.m.s.-velocity for the same conditions. By the case 0 (without adding side-flow), the $\sqrt{\overline{u^2}}/U_0$ along the center axis increases in the downstream direction and reaches its maximum value 0.144 at about 18 H, where the free shear layers from the exit of the nozzle interact together, and then asymptotically decreases to the final value. However, by the case $q/Q = 2.78\%$, the $\sqrt{\overline{u^2}}/U_0$ reaches 0.262 (about double value of the case 0) at $x/H = 4.5$. Similar phenomenon can be found for the other arrangements (case 2 and case 3, but not shown here) except somewhat different 'approaching rate' toward the end value of the mean and r.m.s. velocities.

Distributions of $\sqrt{\overline{u^2}}/U_0$ in the normal plane for different side-flow arrangements at x/H=4.2 are plotted in Fig. 3. Almost all the data of $\sqrt{\overline{u^2}}/U_0$ for three cases with side-flow(s) locate within the region with the values of $0.21 \pm 0.05\ U_0$, which is about a factor 10 higher than that of the case 0 (about $0.02\ U_0$) in the center region of the flow. It is worthy noting here that the value of 0.21 for $\sqrt{\overline{u^2}}/U_0$ was concluded as the 'general' maximum value in the whole flow-field for the flows after axisymmetric sudden-expansion pipe by comparisons of different investigations (Wang & Durst (1993)). From results of Fig. 2 and Fig. 3, this means that side-flow(s) may effectively increase turbulent fluctuations of the flow in order to enhance mixing.

2. Velocity-field in the normal plane

Left hand side (LHS) of Fig. 4 shows the flow field of the axial mean velocity in the normal plane for (a) case 0 (without side-flow), (b) case 1, (c) case 2, (d) case 3 and (e) case 3' (with double side-flow intensity of case 3). The effect of the side-flow causes the decreasing of velocity in the center part of the flow field and the increasing of velocity near the pipe wall. No reverse flow is found in the normal plane within the measured region ($x/H \geq 4.2$) for all the cases with side-

flows.

Comparisons of the flow fields between case 1 and case 2 in the LHS of Fig. 4, it reveals that they both display quite similar distributions in the streamwise direction, although case 1 and case 2 represent quite different control type of the side-flows. Further comparing these two sets of data with (d) case 3 in Fig. 4, it is surprisingly found that all the three cases show roughly similar distributions of the flow field for each corresponding cross-sections. However, the case 3 in (d) is the arrangement with only single q injection, but both case 1 and case 2, as shown in (b) and (c) of Fig. 4 respectively, have double value of side-flows ($2q$) from the opposite walls. This reveals that, the 'extra suction' in case 1 or the 'extra injection' in case 2 does not play an important role for the flow development of axial mean velocity in the normal plane.

The effect of side-flow intensity can be shown by comparing the results of single injection cases of (d) and (e) in the LHS of Fig. 4. There exists a reverse flow region in the center part of the case 3' for $x/H < 6$, however, none is found for the case 3. This means that the injection of side-flow with only $2q/Q$ (=5.56%) is strong enough to penetrate the main stream.

It is important to note about (c) case 2 and (e) case 3' in Fig. 4 that although the case 2 has the same value of total injection of side-flow as the case 3', however the flow-field of case 3' in the normal plane has changed much more significant than that of the case 2. This means that the magnitude of side-flow intensity from a single side-flow, but not the total amount of the injection, dominates the changing of the flow field in the normal plane.

3. Velocity field in the jet-plane

Right hand side (RHS) of Fig. 4 shows the flow field of the axial mean velocity in the jet-plane. Flow fields of (b), (d) and (e) display the skewed velocity profiles due to the asymmetric injection of side-flows. It reveals again the similar distributions for the case 1 and case 3. Increase of the intensity of side-flow pushes the axis of the main flow (defined as the connection line of the positions where the maximum axial mean velocity of each cross-section locates) closer towards the opposite wall. Comparing the maximal mean velocity at the section x/H=4.2, it is found that the case 2 has the minimum value (about 0.78 U_0) than the other cases (about 1 U_0). Also, it is found that the higher the injection flow-rate, the less the mass-flux remains in the jet-plane. From the physical viewpoint, this means that the higher the injection of side-flow, the more mass flux is transfered from the jet-plane to the other planes.

4. Effects of injection angle

Fig. 5 shows the axial mean velocity along the centerline for different injection angle by dual injections with equal side-flow intensity (q_1/Q=q_2/Q=q/Q=2.78% for each). The data of case 3 with single injection intensity q/Q=2.78%, shown as solid line in the figure, is also displayed for the purpose of comparison. It is important to note here that the axial mean velocities along the centerline are relatively insensitive to the variations of injection angle except for the case of α=0, which is basically the case of case 3' metioned above. This result clearly reveal again that the side-flow intensity is the dominate factor for the side-flow injection, but not the total amount of the side-flows. By changing the q_1/q_2 ratio for different injection angle (results are not shown here dute to the limiting space), we may get the same conclusion as above.

5. Effects of side-flow intensity

Fig. 6 shows the axial mean velocity along the centerline for different side-flow intensities by case 3 arrangement. For the injection intensity less than 1%, the injection has almost no effect on the axial mean velocities in the centerline region. However, when the intensity increases but less than 3%, the centerline velocity decreases monotonically very quickly to its final value ($\sim$0.4 U_0) at about x/H $\sim$10. This is evidently shorter than that of case 1 (x/H $\sim$20) and of case 0 (x/H $\sim$30). If the intensity increases further, the velocity decreases still quicker and forms a minimum value before it increases to approach the final value. The minimum value of U/U_0 decreases and its corresponding position shifts towards upstream for the further increase of injection intensity. It is found that, as the q/Q> 4.17%, the flow has a reverse velocity in the centerline region. As shown in the previous figures, if the side-flow penetrate the main stream in the center region of the pipe, the flow has quite different character than the cases without penetration. That is to say that the injection intensity $q/Q\approx$4.2% could be considered as the critical injection intensity for the construction of case 3. The critical velocity ratio (defined as the bulk velocity of side-flow to the bulk velocity

of main stream) for this case is about 1.3.

6. Flow structure of the flow-field by a single jet injection

To get a better overview of the flow in such a three dimensional complex structure, as a example, a superposition of the mean velocity distributions in the jet-plane, normal plane and 45°-plane for the case 3 is displayed in Fig. 7. Although the flow is quite three-dimensional in the near field, however both the mean and turbulent velocities of the flow are approximalely symmetric again at x=52H.

It could also be found from Fig. 7 that the axial mean velocity on the jet-plane has almost the lowest values in each cross-section over the whole range than those on the other planes. This seems to say that the mechanism of injecting a side-flow is to transfer momentum away from the jet-plane. It is worthy noting here that almost all values of the axial mean velocity located on the normal plane are the largest for each corresponding r/R-position in this case.

Fig. 8 is the distributions of iso-U/U_0 and iso-$\sqrt{u^2}/U_0$ lines, which were interpolated from the experimental data by the commercial Surfer-program. It reveals clearly that the side-flow of case 3 causes larger strong turbulence region, where values of $\sqrt{u^2}/U_0$ are higher than 0.2. Although there are some small ambiguous structures located near the pipe wall, and are believed to be from the interpolation process. However, it clearly shows again that the interaction of the designed shear layers generate highly turbulent flow and is able to enhance mixing phenomena.

CONCLUSIONS

The main findings of the present investigations are:

- The sudden-expansion geometry combined with the side-flow injection/suction in pipe produce highly turbulent flow. This construction could be used to improve the mixing in pipe-line system.
- The side-flow intensity is a critical parameter for the injection control of pipe than the other influential parameters, such as the arrangement of injection and suction, injection angle, relative side-flow intensity etc.
- The mechanism of injection a side-flow is to cause a momentum transfer away from the jet-plane.
- Increasing the intensity of a single side-injection larger than 4.2%, (or velocity ratio $\geq$ 1.3), the side-flow penetrates the main stream and form a reverse flow in the center-line region. This value could be considered as the critical injection intensity.
- It is recommended to use single side-flow injection instead of using many side-flows with the same total amount of side-flow injection.

ACKNOWLEDGEMENT

This work was supported by Natonal Science Council, Taiwan, Republic of China under grant number NSC 81-0401-E002-570 and NSC 83-0401-E-002-135.

REFERENCES

Forney, L.J., 1986, "Jet Injection for Optimum Pipeline Mixing," Encyclopedia of Fluid Mechanics, Vol.2, Dynamics of Single- Fluid Flows and Mixing, Gulf Publishing Company, Houston, Texas, pp.661-690.

Forney, L.J., Lee, H.C., 1982, "Optimum Dimensions for Pipeline Mixing at a T-Junction," AIChE Journal, Vol.28, No.6, pp.980-987.

Jow, S.P., 1994, "Investigations of flow-field of sudden-expansion pipe with transverse side-flows", M.S. thesis, Institute of applied mechanics, Taiwan University, Taiwan (in chinese).

Oldshue, J.Y., 1986, "Industrial mixing Equipment," Encyclopedia of Fluid Mechanics, Vol. 2, Dynamics of Single- Fluid Flows and Mixing, Gulf Publishing Company, Houston, Texas, pp. 803-850.

Wang, A.B., Durst, F., 1993, "Selection of Velocity Scale and Effects of Reynolds Number on Axisymmetric sudden-Expansion Flows," Transactions of Aeronautical and Astronautical Society of the Republic of China, Vol. 25, No. 2, pp. 121-127.

Schetz, J.A., 1980, "Injection and Mixing in Turbulent Flow," Vol. 68, Progress in astronautics and Aeronautics New-York, New-york.

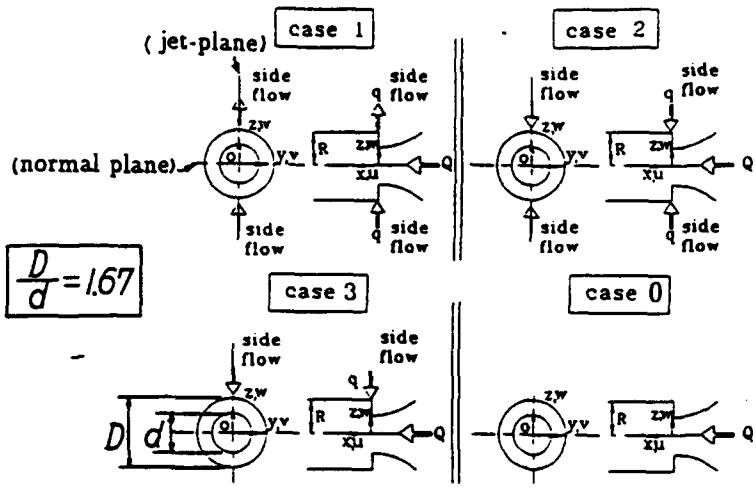

Figure 1: Nomenclature and coordinates

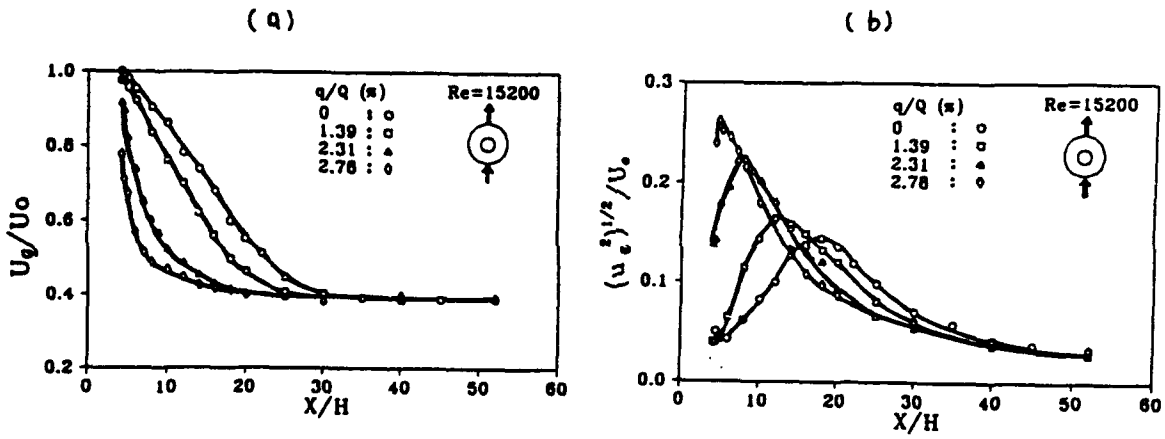

Figure 2: Distributions of axial (a) mean and (b) r.m.s.-velocity along the centerline (case 1)

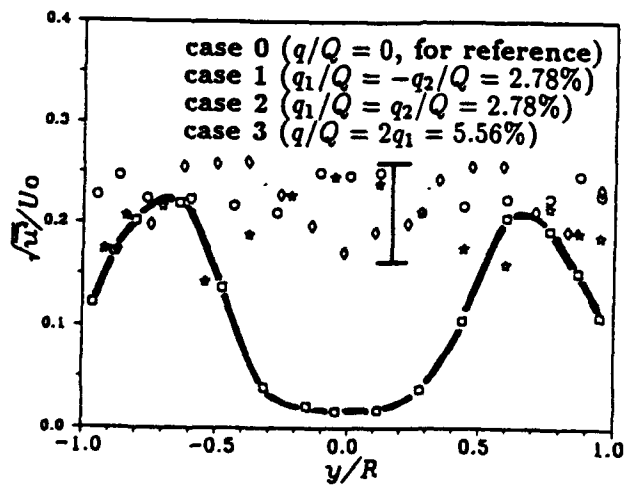

Figure 3: Distributions of axial r.m.s.-velocity in the normal plane at X/H=4.2 for different side-flow arrangements

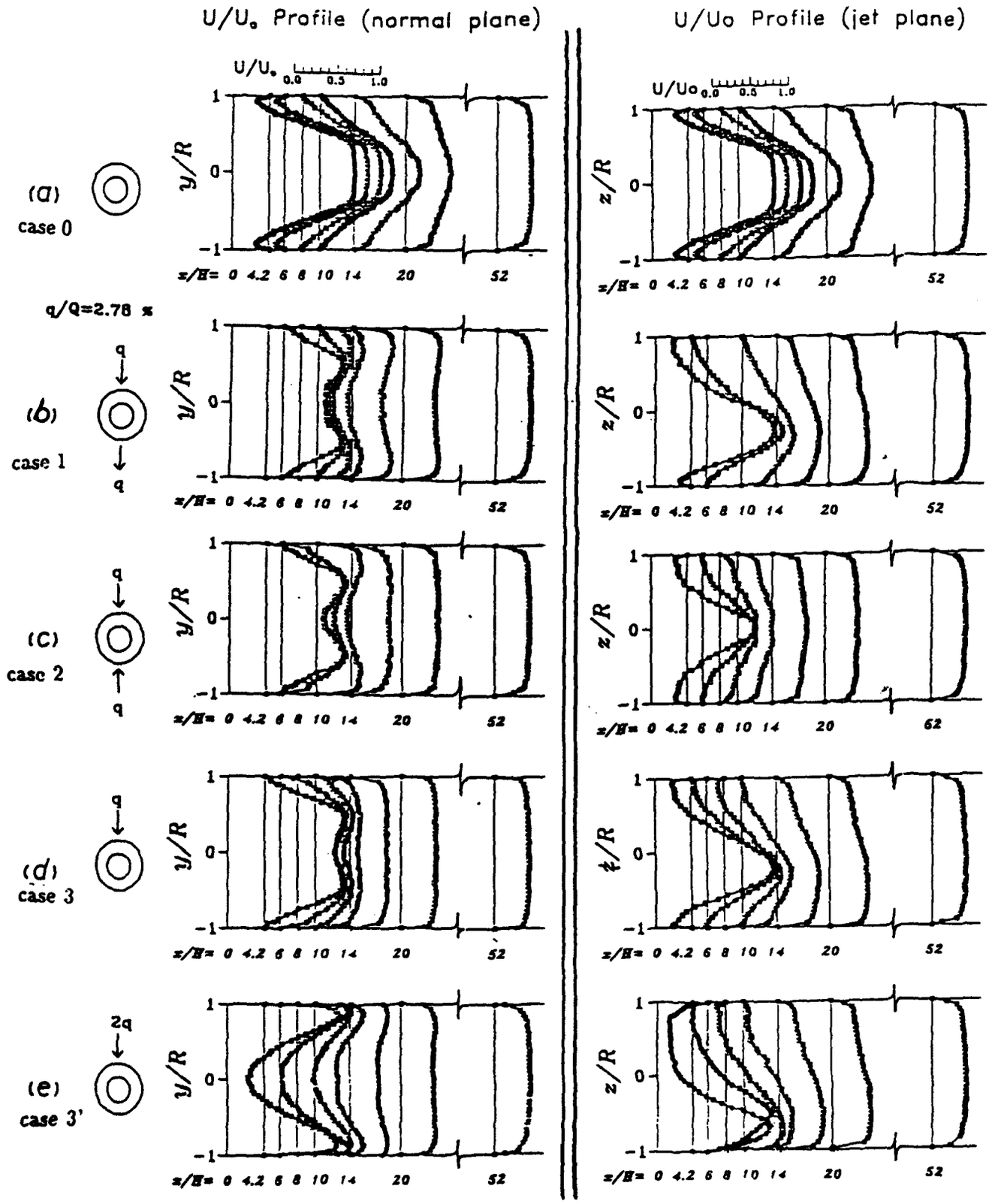

Figure 4: U/U_0 profiles in the normal (LHS) and jet plane (RHS)

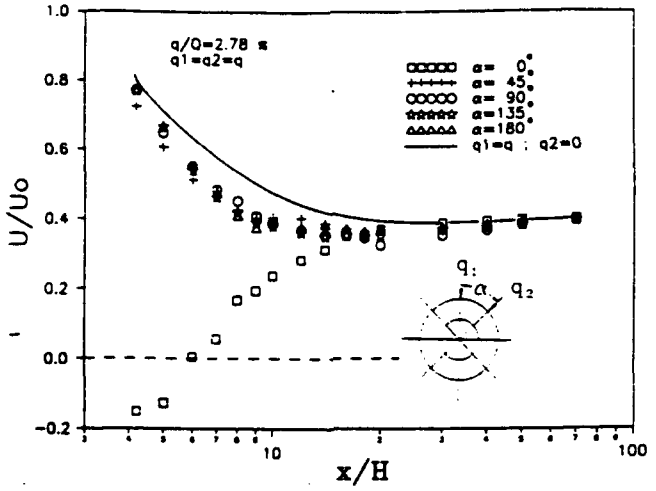

Figure 5: Distributions of axial mean velocity along the centerline for different injection angle

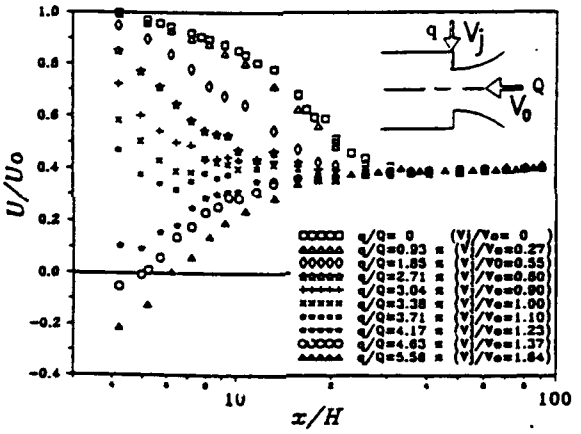

Figure 6: Distributions of axial mean velocity along the centerline for different injection intensities (case 3)

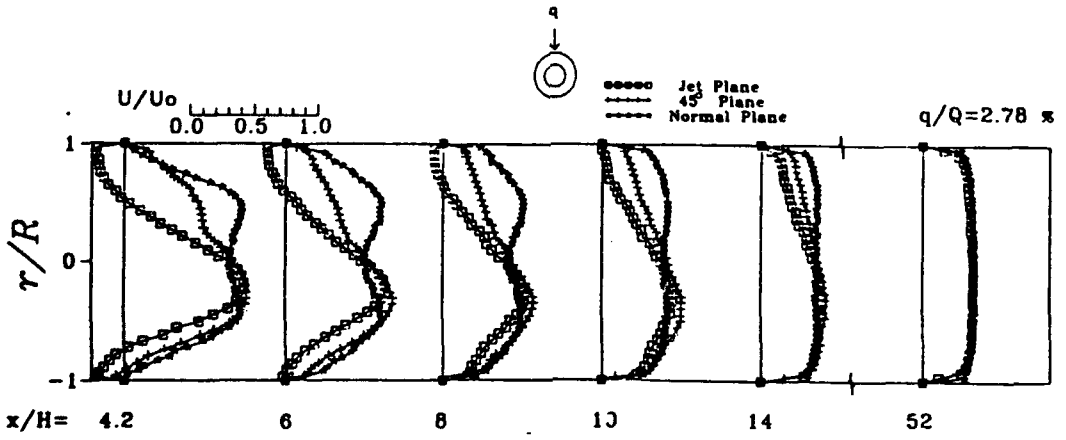

Figure 7: Axial mean and r.m.s.-velocity profiles in three different planes for case 3

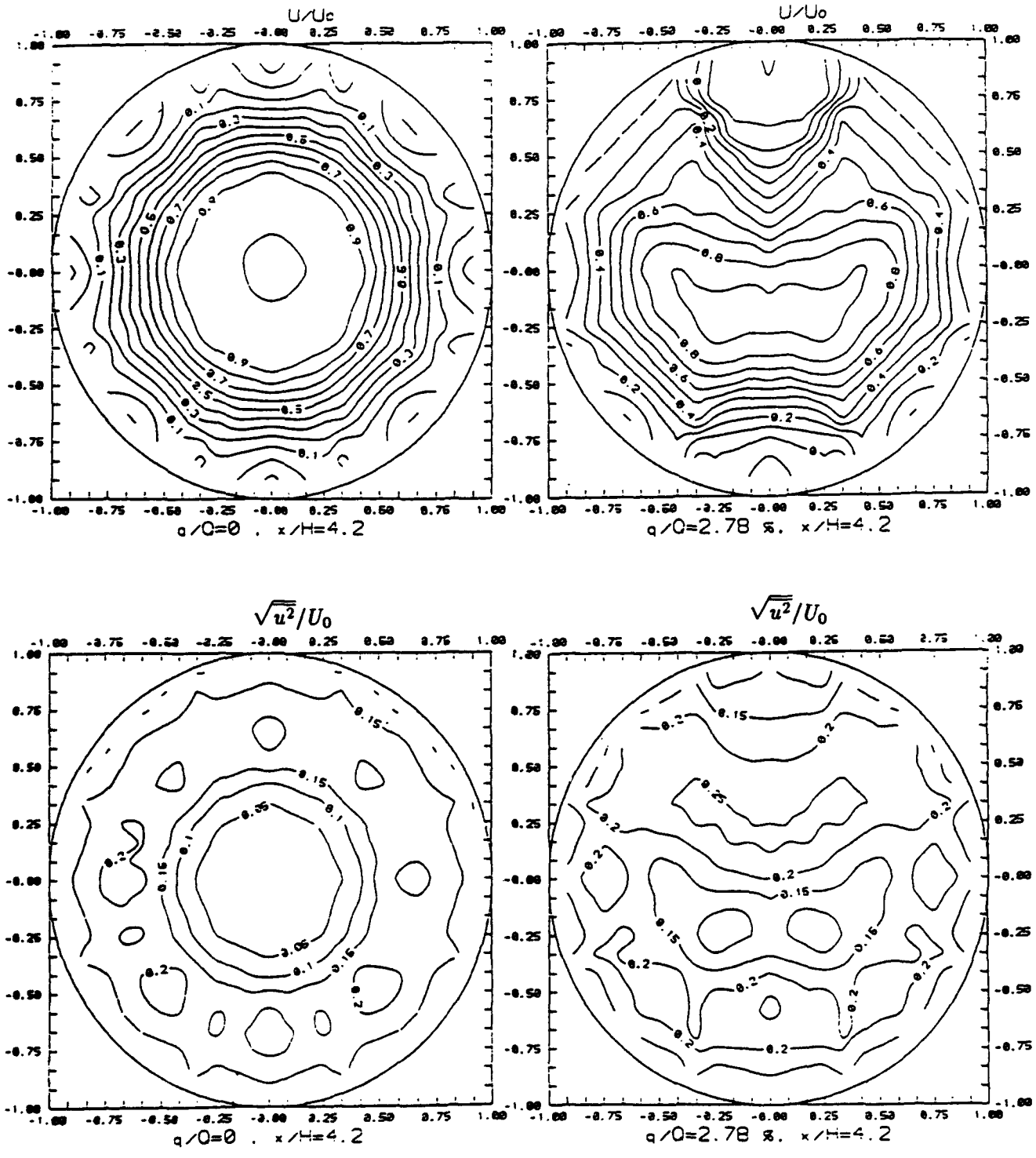

Figure 8: Constant axial mean and r.m.s.-contours at x/H=4.2 for case 0 (LHS) and case 3 (RHS)

Session 14.
Optics I

DIRECTION SENSITIVE LDA USING A SINGLE HIGH-FREQUENCY PULSED LASER DIODE AND A SINGLE PHOTODETECTOR

H. Wang, H. Müller, V. Strunck and D. Dopheide

Physikalisch-Technische Bundesanstalt (PTB)
Laboratory for Fluid Flow Measuring Techniques
Bundesallee 100, D-38116 Braunschweig
Federal Republic of Germany

ABSTRACT

Conventional directional LDAs are based on the frequency shifting technique. In this paper a technique has been proposed for the realization of a direction sensitive HF-pulsed LDA on the basis of switch demultiplexing and quadrature signal processing. This technique allows one to take advantage of HF-pulsed LDAs and to use only one high-frequency pulsed laser diode and one detector for directional flow velocity measurements without frequency shifting. The first experimental verification of this technique has been made. Improvements to the experimental set-up and practical miniaturized realizations of a directional HF-pulsed LDA using light fibres and integrated optical devices are described.

1. INTRODUCTION

It has been reported that high-frequency pulsed laser diode LDAs (HF-pulsed LDA) can be realized by using only one detector, one data processing chain and laser diodes at an identical wavelength for simultaneous multi-component flow velocity measurements (Dopheide et al, 1990). In addition to this, the single pulse emitted from the HF-pulsed laser diodes has a high peak power, giving a better signal-to-noise ratio (SNR). Experimental investigations on these systems have been described in detail by Dopheide et al. (1993) and by Wang et al. (1994a). At present, the HF-pulsed multi-component LDAs need more than one laser diode and are not capable of discriminating the direction of velocity components.

Frequency shifting is generally the most convenient method used in realizations of direction sensitive LDAs. In principle, this can also be applied in HF-pulsed LDAs for direction discrimination. A technique for the realization of a directional LDA without frequency shifting has been described by Köhler et al (1993), but, two detectors and a variable attenuator are required.

Since the peak power of laser diodes can be enhanced by the high-frequency pulsing technique, it becomes possible to divide the output beam of the HF-pulsed laser diode into several beams to realize:

1) a multi-component LDA as described by Wang et al (1994b);
2) a directional HF-pulsed LDA.

In this case, only a single laser diode is required to measure more than one component of a directional flow velocity simultaneously.

This paper describes the technique used to realize such a direction sensitive system with a single laser diode and a single photodetector and without frequency shifting. The first experimental results are reported. Improvements made to the experimental set-up and practical realizations of this technique, for example, miniaturized directional LDAs, using fibre optics and integrated optical devices are also outlined.

2. METHOD

2.1 Experimental set-up

As shown in Fig. 1, the PTB's two-dimensional HF-pulsed LDA has been modified to consist of a single laser diode (Dopheide et al, 1990 & 1993; Wang et al, 1994b). The two equidistant fringe patterns are parallel in the measuring volume instead of being placed orthogonally like the fringe patterns used for multi-component measurements.

As shown in Fig. 2, the fringe patterns do not coincide exactly but are locally shifted relatively to each other in the direction parallel to the flow direction. A particle flying through the measuring volume now results in two individual Doppler signals whose phase difference indicates the direction of the flow velocity. In order to use the quadrature signal processing technique described by Czarske et al (1993), the two equidistant fringe systems are locally shifted relatively to each other by a quarter fringe spacing. The experimental realization of such an arrangement will be discussed later in more detail.

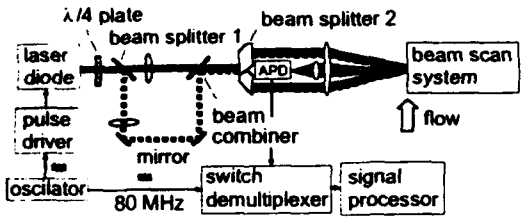

Fig. 1 Set-up of the direction sensitive HF-pulsed LDA with only one laser diode and one photodetector. One 80 MHz electrical pulse train is applied to the laser diode driver to trigger the laser diode, giving the first laser pulse train at 80 MHz (black line, main beam). By means of the beam splitter and mirrors, a second laser pulse train which is phase-delayed to the first one is obtained (dashed black line, by-pass beam). The phase difference between the first and the second laser pulse train can be optimized by adjusting the mirrors, so that two 80 MHz pulse trains are observed in sequence in the measuring volume. The switch demultiplexer is explained in Fig. 3.

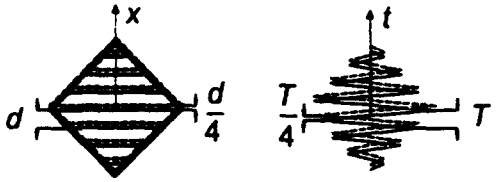

Fig. 2 Cross sections of successive fringe patterns in the measuring volume and the generation of a quadrature signal pair by two equidistant fringe systems locally shifted relatively to each other by a quarter fringe spacing d. Such an arrangement allows the quadrature signal processing technique to be used (see Fig. 4).

2.2 Switch demultiplexing

The scattered light is collected on an APD using a lens. The pulse signals from the amplifier are connected to a switch demultiplexer which converts the pulse signals modulated by the Doppler signals into two standard Doppler signals for the laser pulse trains 1 and 2. By optimizing the phase shift of these two reference signals through the delay, either channel 1 or channel 2 can be switched on and off, thus separating the Doppler signal of every component. The separated Doppler signals can be processed using a conventional LDA signal processor (see Fig. 3, Wang et al . 1994a).

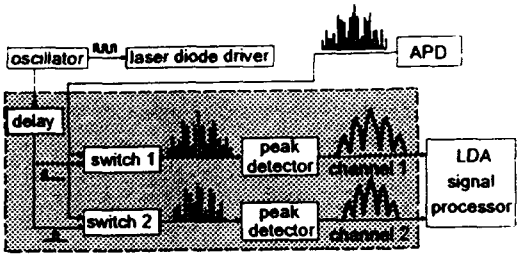

Fig. 3 Working principle of a switch demultiplexer. The received electrical pulse trains are switched into channels 1 and 2 synchronously by two reference signals at 80 MHz. The peak detector is optimized at the peak of the signal pulses at 80 MHz (coherent sampling) which converts the burst signal behind the switch into the standard Doppler signals. This allows the conventional LDA signal processor to be used for signal processing in HF-pulsed LDAs.

2.3 Quadrature signal processing

If the conditions in Fig. 2 are satisfied, the Doppler signals after switch demultiplexing are actually a quadrature signal pair and can be processed using the quadrature signal processing technique (Czarske et al, 1993, Müller et al 1994). In such a case, the two Doppler signals have a 90° phase difference and the same amplitude $A(t)$:

$$a_1 = A(t)\sin \Phi(t) \quad (1)$$

$$a_2 = A(t)\cos \Phi(t) \quad (2)$$

The phase angle $\Phi(t)$ is given by the quotient of signals a_1 and a_2 and becomes independent of the amplitude $A(t)$:

$$\Phi(t) = \arctan(a_1/a_2) \quad (3)$$

Based on the measured time series of phase angle values during a burst, an estimation of the Doppler frequency can be made by using the least-squares method. A linear regression by

$$\Phi(t) = \Phi_0 + 2\pi f_D t \quad (4)$$

allows a direction analysis of the averaged tracer particle velocity in the measuring volume. This velocity is proportional to the center frequency f_D in Eq. (4).

The pair of quadrature signals can be considered as the real part and the imaginary part of a complex rotating vector where the rotation describes the time dependence of the phase angle $\Phi(t)$. As shown in Fig. 4, the rotation direction gives the sign of the flow velocity and the rotation number is equal to the fringe number in the measuring volume.

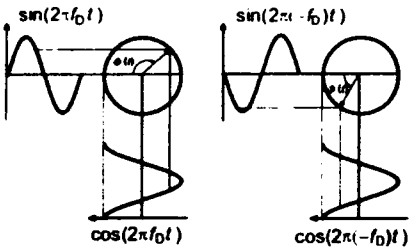

Fig. 4 Phase angle measurement by a quadrature signal pair. The signal pair $\sin(2\pi f_D t)$ and $\cos(2\pi f_D t)$ curve in the left hand shows one direction, while the signal pair $\sin(2\pi(-f_D)t)$ and $\cos(2\pi(-f_D)t)$ in the right hand represents the opposition direction.

3. RESULTS

Referring to Fig. 1, the direction sensitive HF-pulsed LDA consists of practically two dual-beam LDAs which have two similar fringe systems. These two fringe systems are relevant to the main and by-pass beams, and are illuminated alternatively because of the optical path length difference between the main and by-pass beams. During experiments, an optical path length of about 1.5 m is used due to the pulse frequency of 80 MHz. In such a case, the main and by-pass beams become two conjugate pulse trains and allow the switch demultiplexing technique to be used (Wang et al, 1994a). A shorter optical path length is required if a higher pulse frequency is used. For example, an optical path length difference of about 0.3 m is required if a pulse frequency of 1 GHz is used.

In principle, the main and by-pass beams have the same beam diameter in the measuring volume if the diode laser output is collimated to have a very small divergence. During experiments, however, divergent laser beams have been obtained due to the limitation of the experimental conditions. The main and by-pass beams have therefore different shapes in the measuring volume due to their different optical path lengths, resulting in two different Doppler signals (Fig. 5). This makes the use of the quadrature signal processing technique impossible, but, the direction and the magnitude of the flow velocity can be easily determined.

In order to show the influence of optical path length differences between main and by-pass beams on the shape of fringe patterns, experiments have been done after the optical path length difference is reduced from 1.5 m to 0.3 m. As shown in Fig. 6, such main and by-pass beams allow two similar fringe pattern (i.e. two similar Doppler signals) to be obtained and the quadrature signal processing technique to be used.

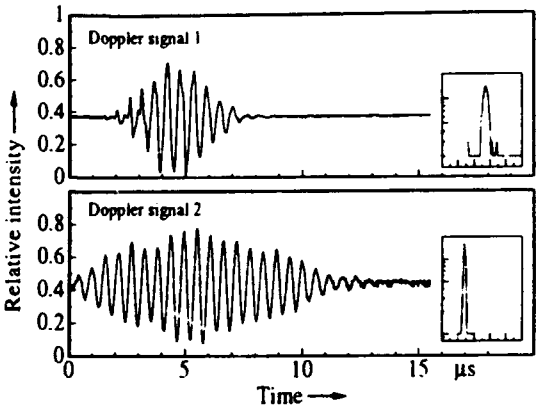

Fig. 5 The Doppler signals after switch demultiplexing. The sign of the flow velocity is determined by the sign of the phase difference between the Doppler signals 1 and 2 and its magnitude by the power spectrum of either of the two Doppler signals. An inverse flow direction will result in an opposite phase difference. In order to obtain better SNR, the forward scattering has been detected.

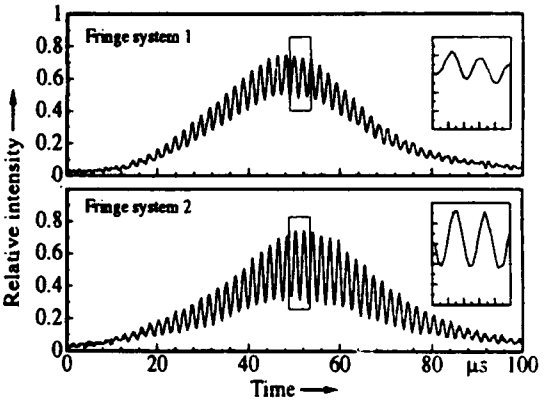

Fig. 6 Fringe patterns measured in the measuring volume when the optical path length between the main and by-pass beams for the fringe systems 1 and 2 is reduced to about 0.3 m. The laser beam of fringe system 1 is blocked when fringe system 2 is measured, and vice versa. The phase shift is obvious if the parts of enlarged fringe patters shown in the insets are compared.

4. IMPROVEMENT OF THE EXPERIMENTAL SET-UP USING LIGHT FIBRES

Referring to Fig. 7, the mirrors and beam splitters are replaced by light fibres in order to produce the optical path length difference between the diode laser beams. The HF-

AD-A285 647 INTERNATIONAL SYMPOSIUM ON APPLICATIONS OF LASER TECHNIQUES TO FLUID MECH..(U) TECHNICAL UNIV OF LISBON (PORTUGAL) 14 JUL 94 R/D-7414-AN-02 N68171-94-M-6048

5/7

UNCLASSIFIED

NL

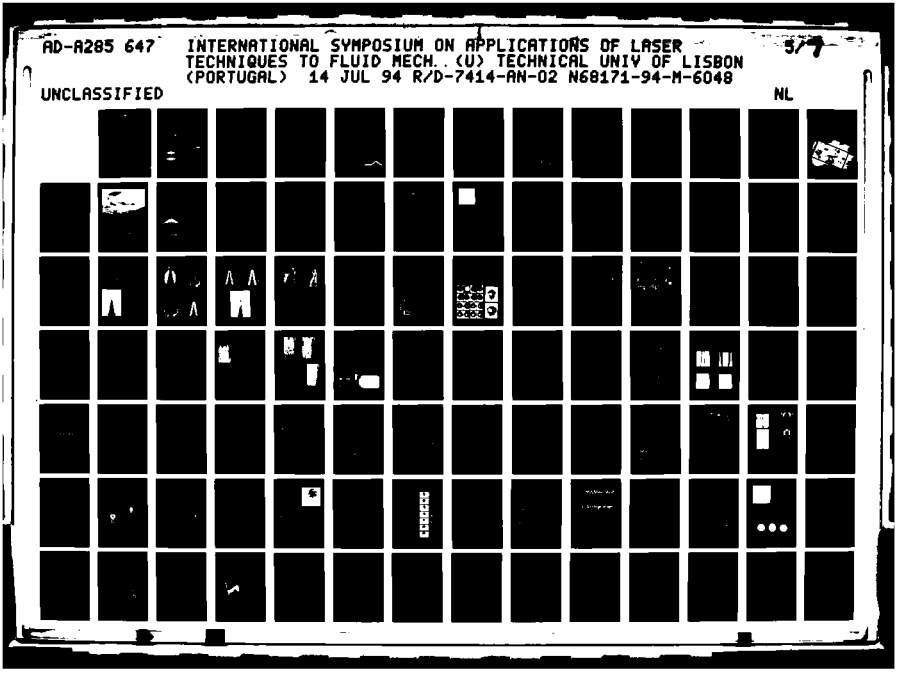

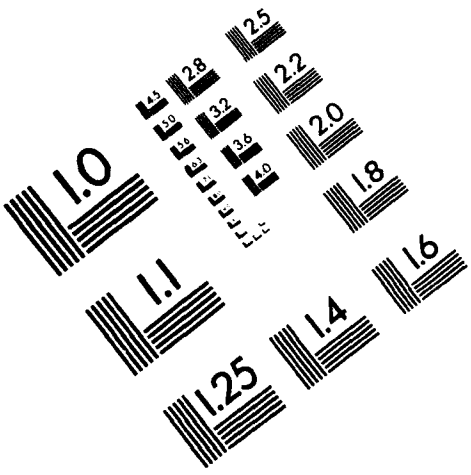

Association for Information and Image Management
1100 Wayne Avenue, Suite 1100
Silver Spring, Maryland 20910
301/587-8202

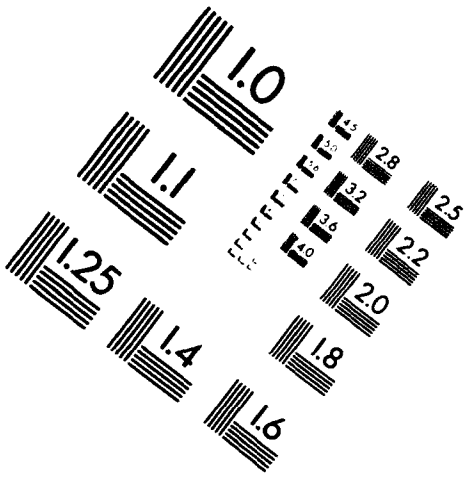

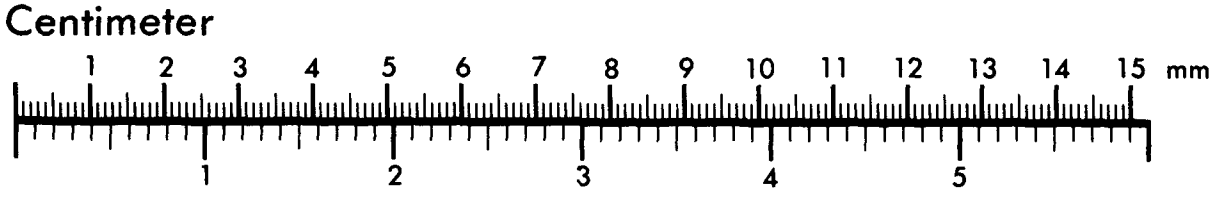

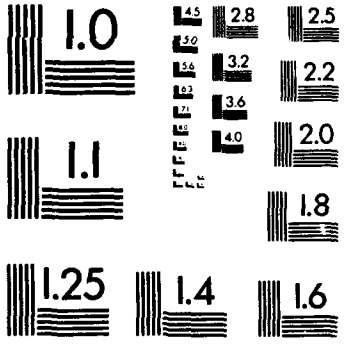

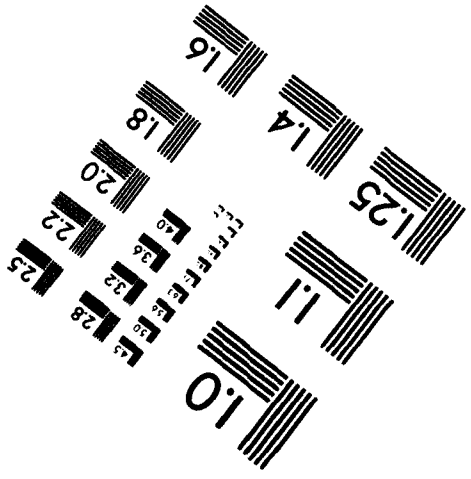

MANUFACTURED TO AIIM STANDARDS
BY APPLIED IMAGE, INC.

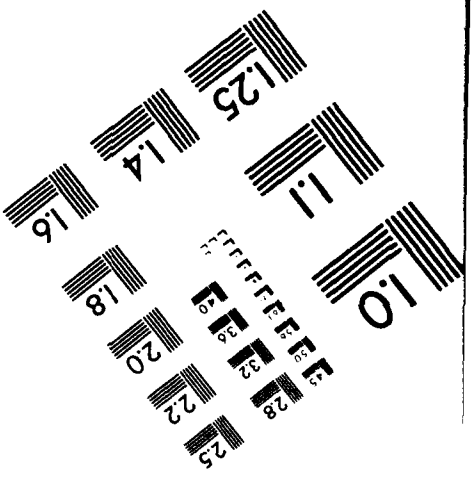

pulsed laser beam is coupled into the light fibre, which in turn is split into two light fibres of different lengths. The short light fibre is used to obtain one dual-beam LDA, while the other long light fibre produces the second fringe system. The time difference between these two parallel fringe patterns can be controlled by the length of the light fibres. In such a case, the two similar equidistant fringe systems can be generated by adjusting collimators to ensure that the fringe patterns have the same properties and allow the quadrature signal processing technique to be used.

Fig. 8 shows the Doppler signals obtained using the set-up in Fig. 7. It is obvious that these Doppler signals form a quadrature signal pair and can be processed using the quadrature signal processing technique described in section 2.3.

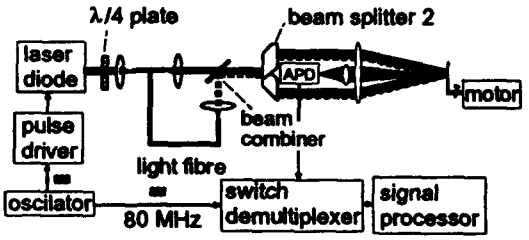

Fig. 7 Set-up of the direction sensitive HF-pulsed LDA with only one laser diode and light fibres. The fine adjustment of the collimators allows the two equidistant fringe systems to be shifted locally relatively to each other by a quarter fringe spacing and the quadrature signal processing technique to be used.

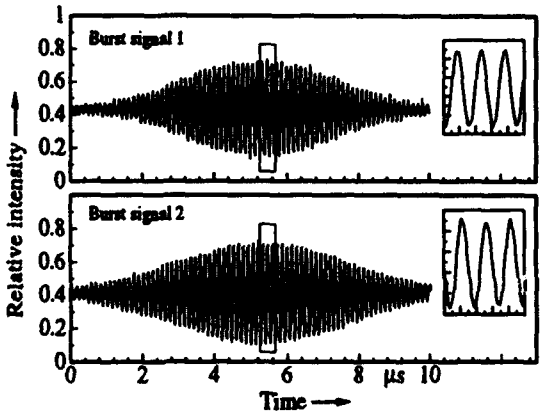

Fig. 8 Quadrature signal pair obtained after switch demultiplexing in Fig. 7. The insets show parts of the enlarged burst signal. In order to obtain better SNR, the forward scattering of a rotating light fibre has been measured.

It should be pointed out that:

1) Referring to Fig. 7, there is a coupling loss of more than 50% if a conventional beam combiner is used. The use of beam-splitting and beam-combining polarizers, and of polarization maintaining light fibres, supplies also two orthogonal linearly polarized beams in the measuring volume, reduces a coupling loss and gives a better SNR
2) As an alternative to the polarization optics described above, the experimental set-up in Fig. 7 can be further improved if, instead of the beam splitter, a mirror is used. As seen in Fig. 9, the use of the mirror can reduce the coupling loss such as occurs with the set-up in Fig. 7. Such an arrangement can also be applied to the experimental set-up in Fig. 1 to reduce the coupling loss and to enhance the SNR.
3) The use of pigtailed laser diodes would be an advantage to reduce the requirements for adjustments to the optical system in Figs. 7 and 9.
4) Difficulties have been met in keeping the stability of two equidistant fringe systems in the set-up shown in Figs. 1 and 7. Better results have been obtained if short optical path length difference is used. It is hoped that such instabilities can be reduced using integrated optics.

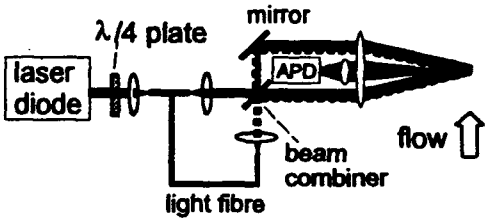

Fig. 9 Set-up of the direction sensitive HF-pulsed LDA with only one laser diode and light fibres. Instead of the beam splitter, a mirror is used to reduce the coupling loss and enhance the SNR. The integration of the mirrors and light fibres would ensure the stability of the shifted fringe systems.

As described by Wang et al (1994b) and Stieglmeier et al (1993), the cw laser can be used as the light source in HF-pulsed LDAs if an optical amplitude modulator is applied. When a control voltage is applied onto the central plate of a hybrid Mach-Zehnder modulator (Fig. 10), an incoming cw light beam can be modulated up to 20 GHz and used as an HF-pulsed laser source for the realization of LDAs.

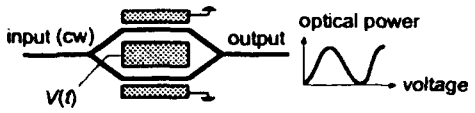

Fig. 10 Mach-Zehnder modulator described by Power. When a voltage $V(t)$ is applied to the central electrode, the cw light input is modulated to the high-frequency pulse output in accordance with the electro-optical effect (Powell, 1993).

5. DISCUSSION

It has been experimentally verified that only one HF-pulsed laser diode and one detector are required to measure directional flow velocities. Consequently, only one temperature stabilization, one current stabilization and one pulse driver are required for the direction sensitive HF-pulsed LDA.

Such a LDA can also be realized by using light fibres and integrated optical devices for the miniaturized design of directional HF-pulsed LDAs without frequency shifting. The use of the quadrature signal processing technique for example, the miniaturized signal processor developed by von Wnuck et al (1994), would simplify data processing and improve the function of the direction sensitive HF-pulsed LDA.

REFERENCES

Czarske, J.; Hock, F. & Müller, H. 1993: Quadrature demodulation - a new LDV-burst signal frequency estimator, Proc. of the 5th International Conference, Laser Anemometry - Advances and Applications, 23 - 27 August 1993, Konigshof, Veldhoven, The Netherlands, SPIE Vol. 2052, pp. 79-86.

Dopheide, D.; Strunck, V. & Pfeifer, H. J. 1990, Miniaturized multi-component laser Doppler anemometers using high-frequency pulsed laser diodes and new electronic signal acquisition systems, Experiments in Fluids, Vol. 9, pp. 309-316.

Dopheide, D.; Rinker, M. & Strunck, V. 1993, High-frequency pulsed laser diode application in multi-component laser Doppler anemometry, Optics and Lasers in Engineering, Vol. 18, pp. 135-145.

Köhler, R.; Stetter, M. & Schroff, G. 1993, Laserrdoppler-Richtungserkennung - ohne Braggzellen, ganz anders, Tagungsband 2. Workshop Lasermethoden in der Strömungsmesstechnik: Aktueller Stand und neue Anwendungen (Herausgeber: Dopheide, D.; Leder, A.; Ruck, B., Verlag Shaker, Aachen 1993), 14 - 16 Semptember 1993, (PTB) Braunschweig, Germany, Paper 1.

Müller H.; Czarske, J.; Kramer, R.; Többen, H.; Arndt, V.; Wang, H. & Dopheide, D. 1994, Heterodyning and quadrature signal generation: Advantageous techniques for applying new frequency shift mechanisms in the laser Doppler velocimeter, paper published in the proceedings.

Powell, M. A. 1993, An ally for high speed and the long haul: Integrated optical modulator applications in communication systems, Photonics Spectra, Special CLEO issue, pp. 102-108.

Stieglmeier, M.; Theis, F.; Tropea, C.; Weber, H. & Rasch, A. 1993, Zwei Komponenten LDA mit integriert-optischem X-Schalter und kohärenter Abtastung, Tagungsband 2. Workshop Lasermethoden in der Strömungsmesstechnik: Aktueller Stand und neue Anwendungen (Herausgeber: Dopheide, D.; Leder, A.; Ruck, B., Verlag Shaker, Aachen 1993), 14 - 16 Semptember 1993, (PTB) Braunschweig, Germany, Paper 6.

von Wnuck, J.; Strunck, V. & Dopheide, D. 1994, Universelle Miniatur-Signalauswertung für die Laser Doppler Anemometrie, PTB Bericht No. PTB-MA-32, Braunschweig, January 1994.

Wang, H.; Dopheide, D.; Müller, H. & Strunck, V. 1994a, Optimized signal separation in a high-frequency pulsed laser diode Doppler anemometer for multi-component measurements, PTB Mitteilungen, Vol. 104, pp. 83-88.

Wang, H.; Strunck, V.; Müller, H. & Dopheide, D. 1994b, New technique for multi-component flow velocity measurements using only one laser diode and integrated optical devices, Paper presented at The Conference on Lasers and Electro-Optics (CLEO® '94), May 8-13, 1994, Anaheim, USA.

BRILLOUIN FREQUENCY SHIFT LDA

H. Többen, H. Müller and D. Dopheide

Laboratory for Fluid Flow Measuring Techniques
Physikalisch Technische Bundesanstalt
38116 Braunschweig, Germany

ABSTRACT

In the laser Doppler anemometry frequency shift techniques are used to determine the magnitude and sign of fluid velocities. These techniques require two coherent light beams with slightly different frequencies. Using stimulated Brillouin scattering as frequency shift mechanism, an adjustment-insensitive fibre optical system has been realised as a noval laser Doppler anemometer for directional velocity measurements.

INTRODUCTION

In fibre optical communication systems the output powers of the laser sources are limited in the lower mW-range. The emergence of stimulated Brillouin scattering restricts the signal transmission in single-mode fibres up to a distinct signal power level. Using pump powers above this threshold, the emergence of SBS can be used for other applications like the generation of a frequency shift in a direction sensitive laser Doppler anemometer (LDA), which will be presented.

SBS can be described as a coupled three-wave interaction involving the incident pump wave, the generated acoustic wave, and the scattered Stokes light wave. The pump wave creates a pressure or acoustic wave in the fibre due to electrostriction, and the resultant variation in density changes the optical susceptibility. Thus the pump-induced index grating moves to the fibre end, away from the incoupling side, and scatters the pump light. This scattering mechanism is called Brillouin-scattering. As a result of the conservation of energy, the Bragg-condition and the guiding nature of the fibre, the pump light is scattered in the backward direction and is simultaneously downshifted in frequency by an amount equal to the frequency of the acoustic wave as described by Agrawal (1986).

A principle set-up producing Stokes light with only fibre optical components is shown in figure 1. The pump laser power P is launched into port 1 of a fused fibre coupler. Using an ideal 3 dB coupler and ideal connections without losses, 50% of the pump power is transmitted to port 2 and is launched into the fibre coil. The launched pump power can be simply measured at port 3. At the end of the fibre coil the pump power, P_T, which is transmitted through the fibre coil, is measurable. The Stokes light wave S, which is generated in the fibre coil and propagates

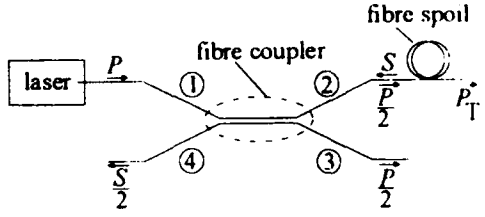

Figure 1 Principle set-up for the generation of Stokes light with only fibre optical components

in the backward direction, will be transmitted through the fibre coupler to port 4 and port 1. An optical isolator in front of the laser source prevents the incoupling of Stokes light into the laser resonator and ensures stable laser radiation. At last, half of the frequency shifted Stokes light, which is transmitted to port 4, is usable.

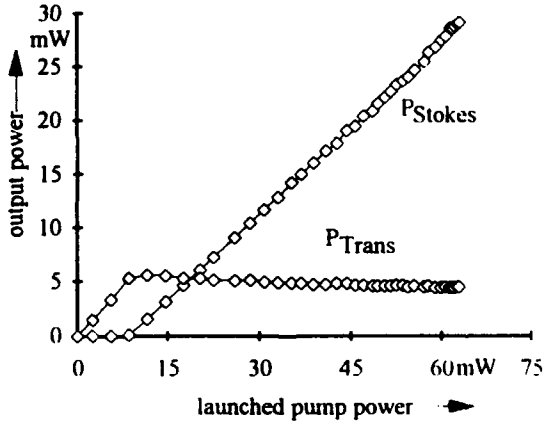

Figure 2 Stokes light power P_{Stokes} and transmitted pump power P_{Trans} measured with the set-up shown in fig. 1

A typical input-output characteristic measured with the set-up presented in figure 1 is shown in figure 2. Above a distinct input power level, Brillouin scattering changes from the spontaneous to the stimulated condition with saturated

transmitted power P_{Trans} and a linear increase of the backward scattered Stokes light power P_{Stokes} with increasing pump power. The behaviour shown in the Stokes light power characteristic looks like a typical laser characteristic well known from laser diodes, for example. It must be mentioned, that the presented Stokes light power values in figure 2 are the power values measured at port 4 and not the calculated values generated in the fibre coil.

The threshold primarily depends on the fibre parameters and the line width of the pump source. Aoki *et al* (1988) have shown a simple equation for estimating the threshold level. Assuming a Lorentzian profile for both the laser spectrum and the Brillouin gain curve, the SBS threshold power P_{th} can be calculated for the continuous wave mode condition with

$$P_{th} = 21\frac{A_E K}{g_B L_E}\frac{\Delta\nu_P + \Delta\nu_B}{\Delta\nu_B} \qquad (1)$$

where L_E is the effective interaction length which considers the attenuation of pump power due to the fibre loss. Particularly in long fibres, to the end of the fibre the reduction of pump power results in a decrease of the generated Stokes light power. This behaviour takes the effective interaction length into account which can be calculated from

$$L_E = \frac{1-\exp(-\alpha l)}{\alpha} \qquad (2)$$

A_E is the effective core area of the fibre calculated with the mode field diameter of the fundamental mode in a single-mode fibre. α is the linear absorption coefficient, l is the length of the fibre, K is the polarization factor ($1 \le K \le 2$; $K = 2$ for complete polarisation scrambling), g_B is the peak Brillouin gain coefficient, $\Delta\nu_B$ is the spontaneous Brillouin bandwidth and $\Delta\nu_P$ is the laser linewidth.

A typical standard telecommunication fibre with a core diameter of 8 µm has at a wavelength of 1.3 µm a mode field diameter of approximately 9 µm. The attenuation coefficient at this wavelength is typical 0.34 dB/km, which results in a linear absorption coefficient of $\alpha = 7.8\cdot10^{-5}$ m^{-1}. The spontaneous Brillouin bandwidth has been considered by Cotter (1983) to be approximately 20 MHz in a single-mode fibre at a pump wavelength of 1.3 µm. The Brillouin peak gain coefficient was determined to be $4.5\cdot10^{-11}$ m/W calculated by Stolen (1979). Thus, for generating Stokes light with low SBS threshold powers it is necessary to use a long and low loss single-mode fibre which is pumped by a laser with small line widths.

The frequency shift or rather the frequency of the acoustic wave f_A can be estimated from

$$f_A = \frac{2\,\nu_A\,n_{eff}}{\lambda_P} \qquad (3)$$

where $\nu_A = 5960$ m/s is the velocity of the acoustic wave in fused silica, as presented by Cotter (1983), n_{eff} is the effective refractive index of the fibre and λ_P is the vacuum wavelength of the pump laser beam. Applying typical

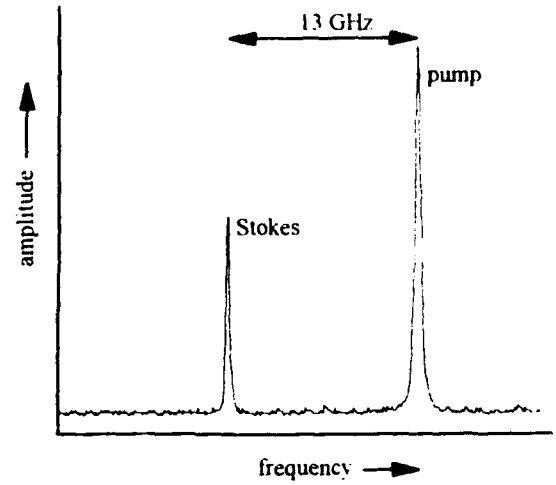

Figure 3 Typical Fabry-Perot spectrum of the emission line of the pump laser and the Stokes line generated in a single-mode fibre at a laser wavelength of 1.3 µm

communication single-mode fibres at 1.3 µm pump wavelength. f_A lies in the range of 13 GHz as shown in figure 3.

For a reduction of the frequency shift out of the GHz-range into the cost-saving MHz-range, the beat signal of two Stokes waves was used. The Stokes waves were generated in two single-mode fibres with different refractive indices. Both fibres were pumped simultaneously by the same pump source. Figure 4 shows the beat signal of the Stokes lines generated in a fibre with a SiO_2-GeO_2 core with $n = 1.463$ and a second fibre with a SiO_2 core and $n = 1.451$. In the plotted figure the beat frequency, which has been used as shift frequency, lies at 257 MHz. It must be pointed out that the peak position of the beat signal fluctuated stochastically in the range 250 MHz to 265 MHz where spontaneous Brillouin scattering is also detected. This fluctuation does not appear to be a problem for the evaluation of the Doppler shift frequency by using mixing techniques as presented by Müller (1993).

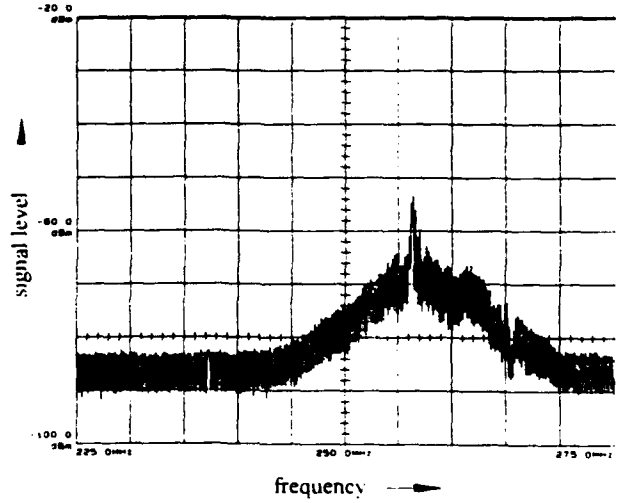

Figure 4 Beat signal of two Stokes waves which is used as shift frequency for direction-sensitive Brillouin-LDA

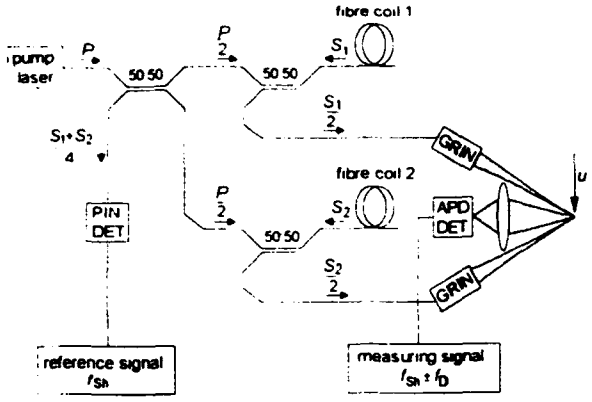

Figure 5 Experimental set-up of the Brillouin frequency shift LDA exclusively based on fibre optical components

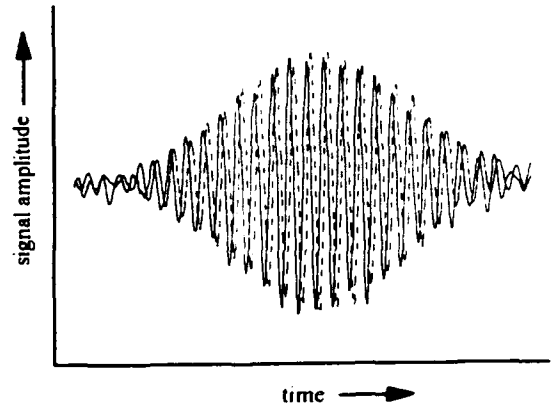

Figure 6 Quadrature burst signal pair included the velocity and the flow direction of tracer particles

EXPERIMENTAL

The experimental set-up of the noval Brillouin frequency shift velocimeter is shown schematically in figure 5. A pigtailed 1.32µm Nd:YAG laser with a non-planar ring oscillator design, 5 kHz linewidth and 150 mW fibre output power, P, was used as pump source. Via 3 dB fibre couplers nearly a quarter of the pump power was launched into fibre coil 1 (n = 1.463, l = 6.4 km) and fibre coil 2 (n = 1.451, l = 6 km). Again via the fibre couplers, nearly 20 mW of the Stokes-light, S_1 and S_2, was focused into the measuring volume by pigtailed gradient index (GRIN) lenses.

The measured signal of the scattered light from tracer particles passing through the measuring volume is detected by an APD photo diode and consists of the beat frequency of the two Brillouin waves f_{Sh}, as shift frequency, and the Doppler frequency f_D, which is proportional to the velocity of the particles. The frequency of the measuring signal is higher or lower than the shift frequency according to the sign of the velocity u of the particles passing through the measuring volume.

Because the beat frequency of the Brillouin waves fluctuates over a range of 15 MHz, as mentioned briefly in figure 4, it is not possible to determine exactly the frequency part of the Doppler signal included in the measuring signal. An elegant method of eliminating the shift frequency fluctuations is the correlation of the measuring signal with a reference signal generated by the beat signal of the two Brillouin waves and detected by a PIN photo diode.

To retain the directional information when eliminating the shift frequency with all its fluctuations by the mixer stage, the measuring signal has to be mixed with a quadrature reference signal pair. This signal pair can be produced by a phase shifter which generates from the reference signal a signal pair with a phase relationship of 0° and 90° corresponding to the input signal, as reported by Müller (1993), (1994).

The resulting burst signal pair behind the correlator unit, is directly given the Doppler frequency in the base band containing the information about the velocity of the tracer particles. Figure 6 shows a typical burst signal pair measured with the set-up presented in figure 5. The phase relationship of these quadrature burst signals, +90° and -90°, corresponds to the velocity direction. In the figure presented, the burst printed with the dotted line follows the burst with continuous line. A change of the flow direction is indicated by a change in the temporal order of the burst signals. Therefore, quadrature mixing technique allows simple evaluation of flow velocities and flow directions with the Brillouin frequency shift LDA independently of frequency shift fluctuations of the Brillouin waves.

CONCLUSION

A new method exclusively based on fibre optical components was presented as a frequency shift mechanism for directional velocity measurements. Stimulated Brillouin scattering occurring in two different single-mode fibres was used for the development of a noval anemometer. The influence of Brillouin wave linewidths and frequency shift fluctuations on the measuring signal have been eliminated by correlating the measuring signal with the beat signal of the Brillouin waves. Employing quadrature demodulation techniques, the amount and sign of velocities can be precisely determined.

REFERENCES

Agrawal, G.P. 1989, Stimulated Brillouin Scattering, in Nonlinear Fiber Optics, Academic Press, Boston-London-Toronto, pp. 263-288

Aoki, Y., Tajima, K. & Mito, I., 1988, Input power limits of single-mode optical fibres due to stimulated Brillouin scattering in optical communication systems, J. of Lightwave Technology, Vol. 6, No. 5, pp. 710-719

Cotter, D. 1983, Stimulated Brillouin Scattering in Monomode Optical Fiber, J. of Optical Communications, Vol. 4, No. 1, pp 10-19

Müller, H. & Dopheide D. 1993, Direction sensitive Laser Doppler Velocimeter using the optical frequency shift of two stabilized laser diodes, SPIE Vol. 2052, Laser Anemometry Advances and Applications, pp. 323-330

Müller, H., Czarske, J. Kramer, R., Többen, H., Arndt, V., Wang, H. & Dopheide, D. 1994, Heterodyning and quadrature signal generation: advantageous techniques for applying new frequency shift mechanisms in the laser Doppler velocimetry, Proc. of 7th Int. Sym. on Applications of Laser Techniques to fluid Mechanics, Lisbon

Stolen, R.H. 1979, Nonlinear properties of optical fibres, in Optical Fibre Telecommunications, Academic Press, New York, pp 125-150

LDV-SYSTEM WITH FREQUENCY SHIFT USING TWO MODES OF A ND:YAG MICRO CRYSTAL LASER

R. Kramer, H. Müller, D. Dopheide, J. Czarske*, N. P. Schmitt**

Physikalisch-Technische Bundesanstalt (PTB)
Laboratory for Fluid Flow Measuring Techniques
Bundesallee 100, D-38116 Braunschweig

*Universität Hannover, Institut für Meßtechnik im Maschinenbau
Nienburger Str. 17, D-30167 Hannover

**Daimler Benz AG, Forschung und Technik
Postfach 80 04 65, D-81663 München

ABSTRACT

The paper presents a novel shift technique without using additional optoelectronic components for the generation of a difference frequency between the two LDV beams focused into the measuring volume. The technique utilises the frequency difference of two orthogonal polarised modes of a diode pumped micro crystal laser which are separated into two laser beams as frequency shift. The optical frequency difference of the two modes can be tuned via the crystal temperature and lies in the range of up to 100 MHz. Detecting the difference frequency (beat signal) of the two laser modes and the signal frequency simultaneously the Doppler frequency can be evaluated independently of frequency shift fluctuations. For the signal processing FFT as well as mixing techniques can be employed. Using mixing techniques it is possible to eliminate the frequency shift with all its fluctuations but retaining the directional information in a quadrature signal pair.

1. INTRODUCTION

LDV systems with frequency shift usually are realised with Bragg cells or rotating gratings. Alternative techniques have been demonstrated using two frequency adjustable single mode laser sources for the generation of the LDV beam pair as reported by Müller *et al* (1993). The application of two single mode diode lasers as sources of the two intersecting beams of a LDV system requires mixing techniques to eliminate the influence of the laser diode line width of up to 100 MHz to the signals for the realisation of direction sensitive LDV as shown by Müller and Dopheide (1993). In contrast to the techniques which have been presented up to now, the use of Nd:YAG micro crystal lasers allows to utilize a frequency shift which is generated in the laser resonator itself without employing additional optoelectronical components.

Due to the optical frequency difference of the two orthogonally polarized states of a single lasing mode in the laser crystal, two frequency shifted LDV beams can easily be generated by the use of polarizing beam splitters. Thus it will be possible to realize very compact low cost directional LDV systems.

2. PROPERTIES OF ND:YAG-MICRO CRYSTAL LASERS

Micro crystal lasers can be specified such that the resonator length is as short (0.3 mm up to 0.8 mm) that only one lasing mode can be amplified inside the gain bandwidth of the lasing medium (see fig 1).

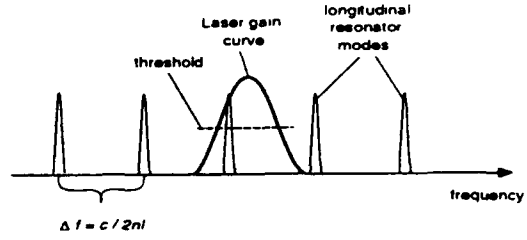

Fig. 1 The micro crystal laser concept

Furthermore the line width of such lasers are below 10 kHz and they are tuneable in wavelength by changing the temperature of the crystals. Schmitt *et al* (1993) reported that the tuning range without mode hops is more than 130 GHz.

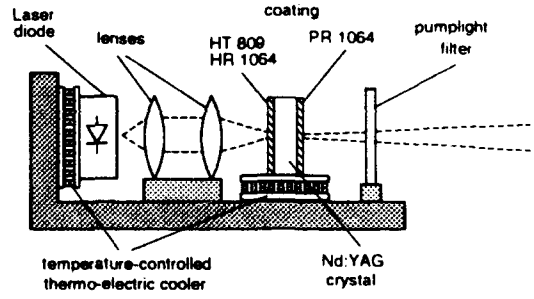

Fig. 2 Nd:YAG-micro crystal laser arrangement

A laser diode array emitting 250 mW at a wavelength of 809 nm is used for pumping the laser (Fig. 2). The output power in a single line mode can be more than 20 mW.

It is assumed that caused by the crystal growing and the production process of the small crystal pieces stress is induced into the crystals. Consequently the crystals are local birefringent so that it is possible to realize a single line emission of the micro crystal lasers in two orthogonal polarized modes as shown by Schmitt *et al* (1994). The frequency separation of the two modes depends from the adjustment of the crystals because the amount of birefringence is local different. Depending on the adjustment of the pump laser diode and laser crystal the frequency difference can be tuned in the range up to 100 MHz by altering the temperature of the Nd:YAG crystal (see Fig. 3).

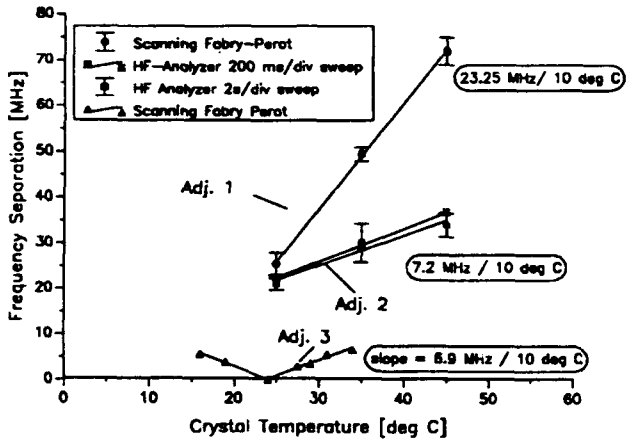

Fig. 3 Difference frequency of the two modes for several adjustments

Figure 3 shows that the tuning slope as well as the difference frequency offset varies with the adjustment. The difference frequency was measured by a scanning Fabry perot cavity as well as by observing the beat frequency between the modes with an rf analyser. Depending on the adjustment (adj. 3 in Fig. 3) the modes also can be degenerated (frequency difference equal to zero) at one temperature (see Fig. 4).

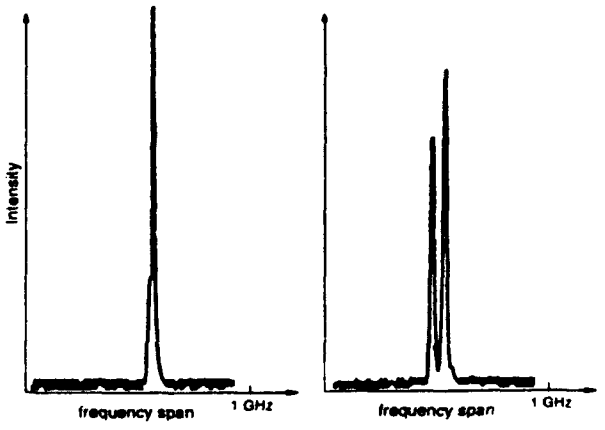

Fig. 4 Fabry-Perot spectra of a micro-crystal laser for one adjustment and different temperatures

The polarization of the two laser modes is in general far or less elliptical which depends also from the adjustment of micro crystal laser and the crystal temperature.

Using appropriate adjustments and working temperatures it is however possible to generate a single line emission with two orthogonally polarized modes whose frequency difference can be used as frequency shift for a novel directional Laser Doppler Velocimeter.

3. EXPERIMENTAL SET-UP

A set-up of a LDV system based on a micro crystal laser is shown in Fig. 5. A quarter wave plate in the output beam of the micro crystal laser generates two almost linear polarized orthogonal light waves which are separated and splitted by a Wollaston prism into two frequency shifted orthogonal polarized laser beams. Behind the first lens the laser beams are parallel. A half wave plate is inserted into one beam path to provide the same polarization for the two beams being focused into the measuring volume by a second lens.

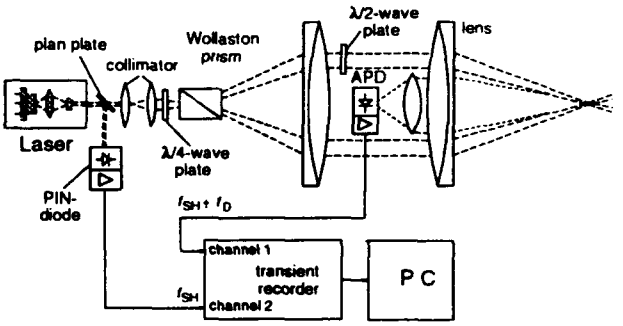

Fig. 5 Set-up of the realized LDA system using a two channel transient recorder for signal processing

The scattered light of particles passing through the measuring volume is detected in backward direction and focused onto an avalanche photo diode (APD) which generates the measuring signal. The measuring signal is given by the carrier frequency which is identical to the frequency shift and the Doppler frequency determined by the particle velocity to be measured. To avoid an influence of shift frequency fluctuations on the evaluation of the Doppler frequency a reference signal has to be detected simultaneously. Therefore a plan plate is inserted into the output beam of the micro crystal laser which reflects a fractional part of the micro crystal laser output beam onto a PIN photo detector, where the two orthogonal laser modes are superimposed to generate a beat signal.

The small linewidth of the beat signal allows to employ a two channel transient recorder for the signal evaluation in the signal processing chain. The measuring signal (burst signal) and the reference signal (beat signal) are detected simultaneously and FFT procedures are used to calculate the Doppler frequency. Fig. 6 shows the unfiltered signals sampled with a two channel transient recorder.

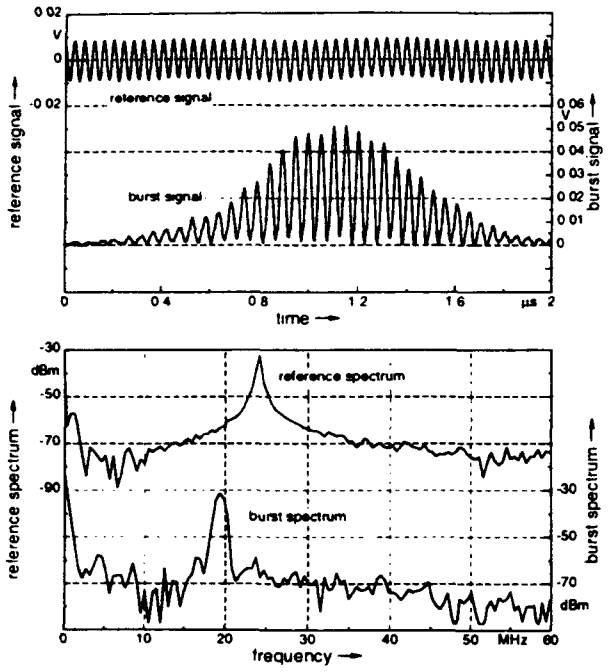

a)

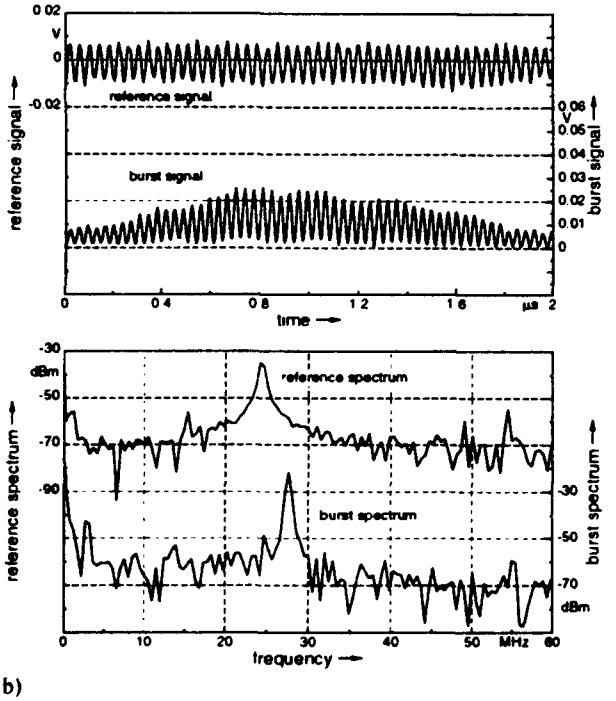

b)

Fig. 6 Unfiltered reference and measuring signal of the realized LDV system in the time and in the frequency domain, represented for different velocity directions
a) the tracer particle has the same direction as the moving fringe system, the burst frequency is lower than the reference frequency
b) the velocity of the particle is opposite to movement of the tracer particle, the burst frequency is higher than the reference frequency.

The signal spectra calculated with a FFT algorithm show peaks with a small line width which exceed the noise floor more than 20 dB. The shift frequency was 22 MHz.

Furthermore the simultaneous detection of a measuring signal (APD detector) and a reference signal (PIN detector) allows to employ mixing techniques for the correlation of the measuring signal with the reference signal to eliminate the influence of shift frequency fluctuations onto the evaluation of the measuring information. By mixing the measuring signal with a reference signal the carrier frequency which is given by the frequency shift can be eliminated with all its fluctuations. In order to retain the directional information when eliminating the shift frequency, the measuring signal has to be mixed down with a reference quadrature signal pair. The phase relationship of the resulting sine/cosine signal pair in the base band contains the information of the velocity direction.

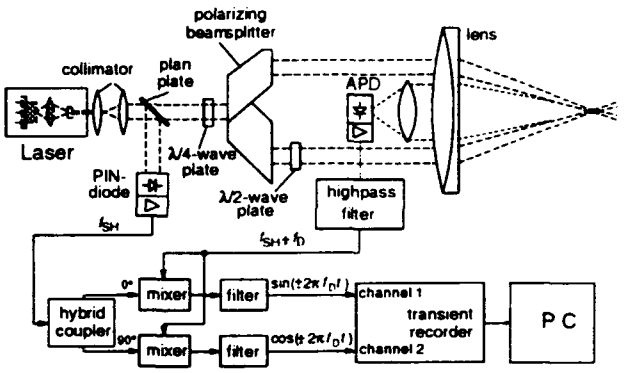

Fig. 7 Block diagram of a micro-crystal laser Doppler Velocimeter using mixing techniques for the signal evaluation

Fig. 7 shows the complete block diagram of a micro-crystal laser Doppler Velocimeter employing mixing techniques for the signal evaluation. The only difference in the optical set-up shown in Fig. 5 is the application of a conventional polarizing LDA beam splitter instead of a Wollaston prism. The high pass filter in the measuring signal path provides the possibility to eliminate the influence of an optical cross talking caused by an incomplete separation of the orthogonal polarized laser modes differing in their emission frequencies.

Fig. 8 represents intervals of two typical burst signal pairs behind the mixer unit detected for different flow directions. The signal pairs are drawn as x-y plot as well as signal-time plot. In the x-y plot a rotating phaser given by the quadrature burst signal pair describes a spiral with a rotating direction depending on the sign of the velocity to be measured. The phase relationship in the quadrature signal pair, especially the temporal order of which channel leads the other, gives the directional information.

Due to the small line width of the resulting carrier frequency signal the mixing technique has not necessary to be used. The advantages of generating and evaluating quadrature signal pairs in the base band by eliminating the carrier frequency in the measuring signal are discussed by Müller *et al* (1994), especially for measuring signals having instable carrier frequency with high band widths.

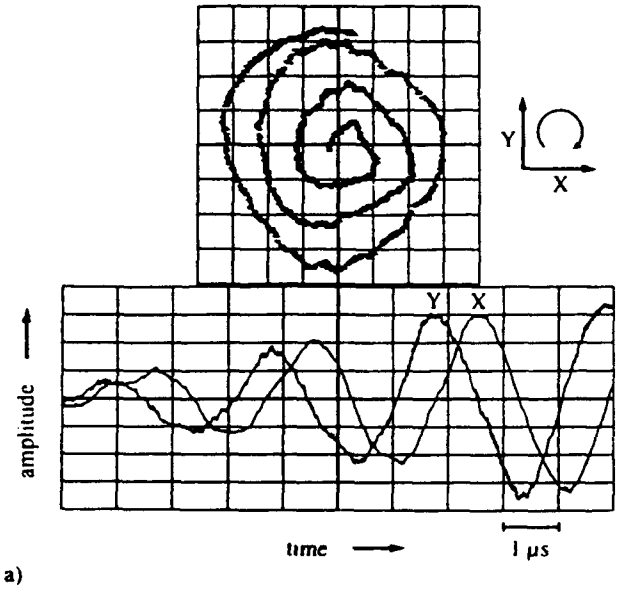

a)

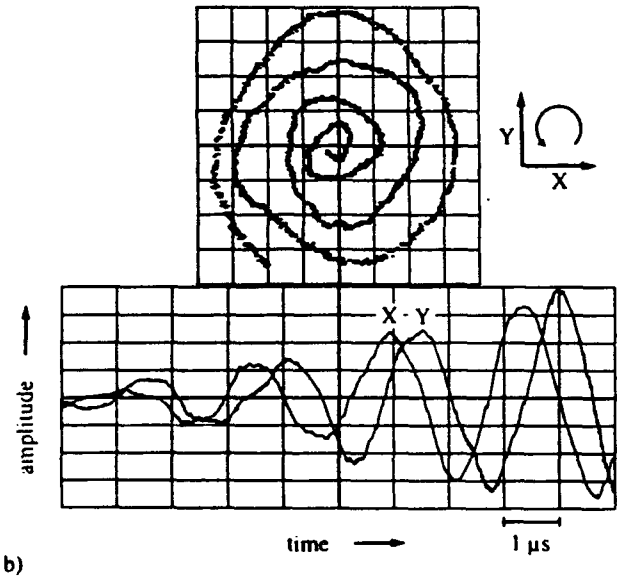

b)

Fig. 8 Intervals of two signal bursts corresponding to opposite velocity directions of tracer particles a) and b).

CONCLUSION

The described LDV system based on a Nd:YAG micro crystal laser allows to realise direction sensitive flow measurements. Using two separated laser modes with suitable frequency distance no additional components for the shift frequency generation are required. The output power of up to 25 mW is interesting for many applications especially for the detection of the scattered light in forward direction. Signal processing based on transient recorders as well as mixing techniques are applicable to realise a direction sensitive LDV system.

REFERENCES

Müller , H., Kramer, R., Dopheide, D. 1993, Neue Verfahren zur Erzeugung einer Frequenzshift in der Doppler-Anemometrie mit abstimmbaren Festkörperlasern, PTB Mitteilungen, vol. 103, no.1, .pp. 3 - 17

Müller, H., Dopheide, D. 1993, Direction sensitive Doppler Velocimeter using the optical frequency shift of two stabilized laser diodes, Proceedings of Fifth International Conference Laser Anemometry - Advances and Applications, Koningshof, Veldhoven 23.-27. 8.1993 SPIE, vol. 2052 ,pp. 323 - 330

Schmitt, N. P.; Peuser, P.; Heinemann, S.; Mehnert, A. 1993, A model describing the single and multiple line spectra of tuneable microcrystal lasers, Optical and Quantum Electronics, vol. 25, pp. 527 - 544

Schmitt, N. P., Heinemann, S., Mehnert, A., Peuser, P. 1994, Abstimmbare Mikrokristall-Laser, in Laser in Engineering, ed. W. Waiderlich, pp. 8-12, Springer, Berlin

Müller, H., Czarske, J., Kramer, R., Többen, H., Arndt, V., Wang, H., Dopheide, D. 1994, Heterodyning and Quadrature Signal Generation: Advantageous Techniques for Applying New Frequency Shift Mechanisms in the Laser Doppler Velocimetry, Proc. 7th Int. Symposium on Application of Laser Techniques to Fluid Mechanics, Lisbon

THE REALIZATION OF A CONTINUOUSLY TUNEABLE OPTICAL FREQUENCY SHIFT LDV-SYSTEM AT GREEN WAVELENGTH FOR HIGHLY TURBULENT FLOWS USING DIODE PUMPED ND:YAG LASERS AND MONOLITHIC RING FREQUENCY DOUBLERS

R. Kramer, H. Müller, D. Dopheide

Physikalisch-Technische Bundesanstalt (PTB)
Laboratory for Fluid Flow Measuring Techniques
Bundesallee 100, D-38116 Braunschweig

ABSTRACT

In contrast to LDV systems based on established techniques for the generation of a frequency shift between the LDV beams being focused into the measuring volume the presented LDV system employs two tunable frequency doubled Nd:YAG ring lasers, one for each LDV beam. The shift frequency is continuously adjustable in an extremely wide range up to some hundred MHz according to the requirements of the flow and the signal processing. An output power of more than 100 mW in both laser beams allows the detection of small particles. Furthermore, the visibility of the laser beams (λ = 532 nm) is useful for the aligning and positioning of the LDV system.

1. INTRODUCTION

LDV measurements in high turbulent flows as well as in flows with high velocity gradients require shift techniques for the discrimination of the flow direction. Well known are LDV systems based on Ar^+-ion lasers incorporating bragg cells or rotating gratings to realize a frequency shift. These techniques are reviewed by Durst *et al* (1987).

The application of two superposed 300 mW Nd:YAG ring laser beams at 1064 nm reported by Müller *et al* (1993) allows to realize LDV systems with an adjustable frequency shift by tuning the emission frequency of one laser. By the use of two lasers the light intensity in the measuring volume can be doubled and the signal to noise ratio increases.

To overcome the disadvantages of using infrared light at a wavelength of 1064 nm emitted by Nd:YAG ring lasers, monolithic ring frequency doublers are applied. The frequency doubled laser light of 532 nm allows (in comparison to infrared light at 1064 nm)

- the use of photo detectors with a higher quantum efficiency and a low thermal noise,
- to measure in water flows over long working distances (the absorption coefficient in water is small at 532 nm) and
- an easy alignment and positioning of the LDV system.

Furthermore, the small dimensions of solid state lasers and the low power consumption are advantageous in comparison with Ar^+-ion lasers.

2. FREQUENCY DOUBLED ND:YAG RING LASERS

2.1. 1064 nm - Nd:YAG ring lasers

The frequency doubled lasers are based on tuneable Nd:YAG ring lasers which are designed as monolithic blocks of a Nd:YAG crystal with four reflecting facets (Fig. 1). The dielectric coated front facet serves as output mirror of the laser. The three other facets have total internal reflection faces. Caused by an applied magnetic field the crystal acts as a Faraday rotator. In addition with the non planar beam path in the resonator and the polarization sensitive front facet coating an internal optical isolator is realized. In this way the effects of spatial hole burning are eliminated and very small line widths are achieved as reported first by Kane and Byer (1985). The lasers operate in a TEM_{00} spatial mode with an oval beam and in a single longitudinal mode with a linewidth below 10 kHz. In contrast to laser diodes they are insensitive to optical feedback.

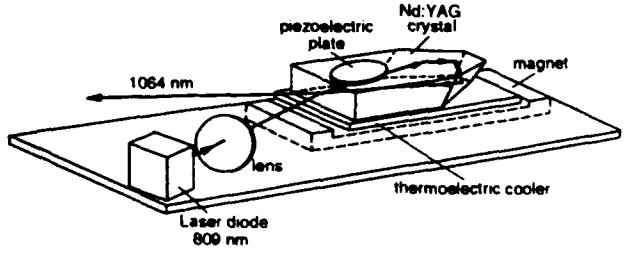

Fig. 1 Nd:YAG ring laser

In the set-up shown in Fig. 1 the ring resonator is pumped by a GaAlAs laser diodes array with an output power of 1 W. By matching the emitted wavelength of the laser diode to the

Nd:YAG absorption band at 809 nm the output power of the ring lasers reaches 300 mW. The output power can be increased up to 1.1 W by applying two pump diodes as reported by Freitag *et al* (1993). As shown in Fig. 2 and Fig. 3 the beams of the two pump diodes are combined by a polarizing beamsplitter.

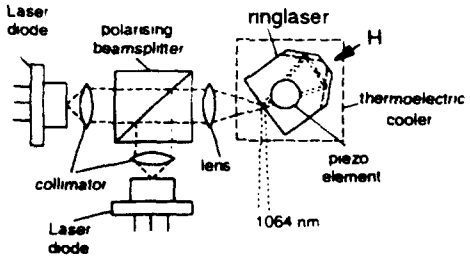

Fig. 2 Nd:YAG ring laser pumped with two Laser diode arrays

The temperature of the Nd:YAG crystal is controlled by a thermoelectric cooler and allows a slow tuning of the emission wavelength with a tuning coefficient of - 3 GHz/K.

Fig. 4 shows the mode chart of a ring laser. The tuning ranges without mode hopping are about 10 GHz in a total range of more than 50 GHz.

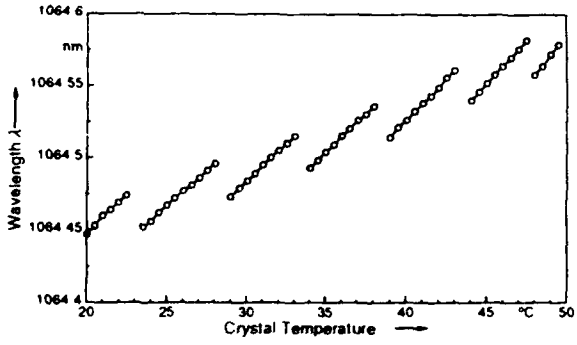

Fig. 4 Mode chart of a Nd:YAG ring laser

To realize a fast frequency tuning a piezoelectric element is bounded to the upper face of the monolithic resonator which exerts a force on the crystal face that slightly changes the

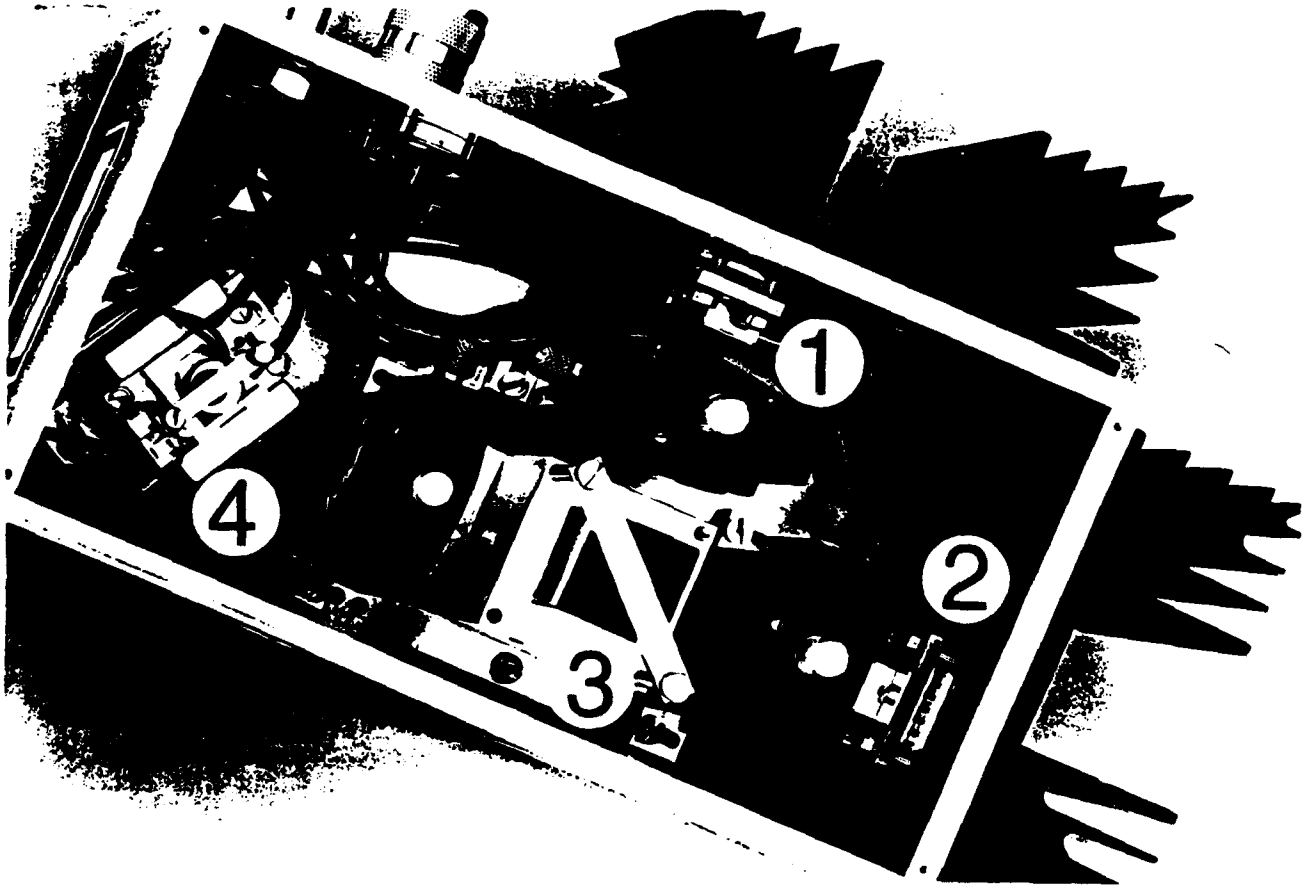

Fig. 3 Photograph of a Nd:YAG ring laser with a output power up to 0.7 W with two 1 W pump diodes (manufactured by the Laserzentrum Hannover)
1, 2 - Laser diodes on thermoelectric coolers 3 - polarizing beamsplitter 4 - Nd:YAG ring crystal

dimension of the resonator as well as the refractive index of the crystal . The tuning coefficient is approximately 2 MHz/V in a range of ± 50 V. The modulation bandwidth which is limited by the mechanical properties of the system, i.e. the piezoelectric element and the crystal, surpasses more than 100 kHz.

In order to reduce relaxation oscillations as well as noise, a feed back circuit is implemented which controls the current of the pump diode. In this manner the rms noise value of the output beam is reduced to less than 0.05 % in the range up to 1 MHz and is small in comparison with gas lasers.

2. 2 Set-up of the frequency doubled Nd:YAG ring laser

As shown in Fig. 5 a monolithic ring resonator with triangular beam path doubles the frequency of the ring laser. The front facet is curved polished and coated to get a reflection of 98.5 % at 1064 *nm* for the polarization of the incident laser beam. The phase matching of the magnesium-oxide-doped lithium niobate ($MgO:LiNbO_3$) crystal for second harmonic generation is realised for one of the longer parts of the optical beam path by an adequate crystal cut and a small oven which stabilizes the crystal temperature at 107 °C. To achieve a high conversion efficiency a coincidence of the laser frequency with one of the mode frequencies of the doubler resonator is necessary. To avoid photo refractive damage of the doubler crystal a control unit is implemented to match the ring laser frequency to a resonance of the doubler cavity without an electro-optically tuning of the doubler crystal. To achieve a frequency locking firstly the temperature of the ring laser is changed periodically in a range of ± 2.5 K around a chosen start temperature T_K (see Fig. 6) by the control unit. If the ring laser frequency is identical to the resonance frequency of the doubler the conversion efficiency increases and a fast control loop which acts on the piezoelectrical tuning input of the ring laser allows an optimal conversion as reported by Gerstenberger *et al* (1991).

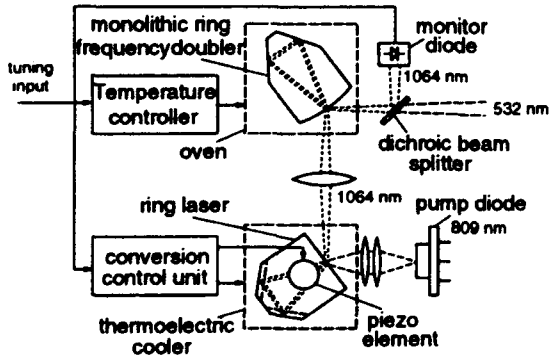

Fig. 5 Schematic of a frequency doubled Nd:YAG-lasers

It is possible to achieve from a 300 mW Nd:YAG ring laser more than 100 mW green light in a oval TEM_{00} mode and a line width of 50 kHz (1 ms). A slowly frequency tuning of the green laser up to 1 MHz/s is possible by altering the temperature of the doubler crystal.

Fig. 6 shows the mode charts of two frequency doubled ring lasers. By changing the start temperature T_K of the control unit as specified in Fig. 6 three different resonator modes of the doubler can be used. Since the phase matching of the crystal depends on the temperature the tuning ranges are limited by the decreasing conversion efficiency. The half power width (FWHM) is about 12 GHz. Due to mechanical differences of the two doubler crystals the tuning ranges do not overlap exactly.

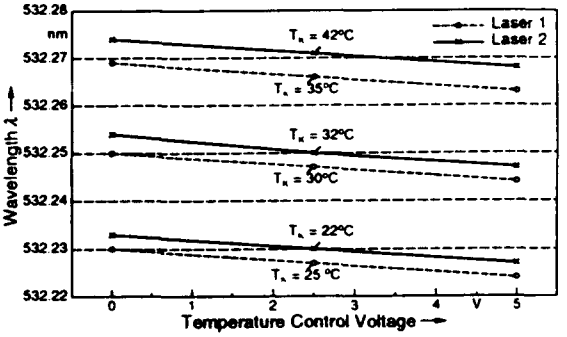

Fig. 6 Mode charts of the used frequency doubled Nd:YAG lasers

To achieve large temperature intervals for heterodyne experiments, the manufacture of doubler crystals demands a high precision.

3. REALISATION OF A LDV SYSTEM

The experimental set-up of a LDV with adjustable shift frequency is illustrated in Fig. 8. Two 100 mW lasers at 532 nm are used for the LDV. The shift frequency f_{SH} of the LDV is given by the difference of the emission frequencies f_1 and f_2 of the laser beams

$$f_{SH} = f_1 - f_2 \qquad (1).$$

The detection of the reference signal which is necessary for the signal evaluation and the shift frequency stabilization is carried out by the superposition of small fractions of both laser beams on a PIN diode. To achieve a beam diameter of about 60 µm in the measuring volume the output beams of both lasers are matched with two collimators. The chosen beam distance is 65 mm and the focal lengths of the front lens amounts to 310 mm. A Si-avalanche photo diode (APD) detects the scattered light of the particles passing the measuring volume. Fig. 7 shows a photograph of the optical set-up (including both lasers). The dimensions of the optical head are (460 x 245 x 150) mm^3.

The calculation of the signed Doppler frequency follows by the equation:

$$f_S = f_{SH} \pm f_D \qquad (2).$$

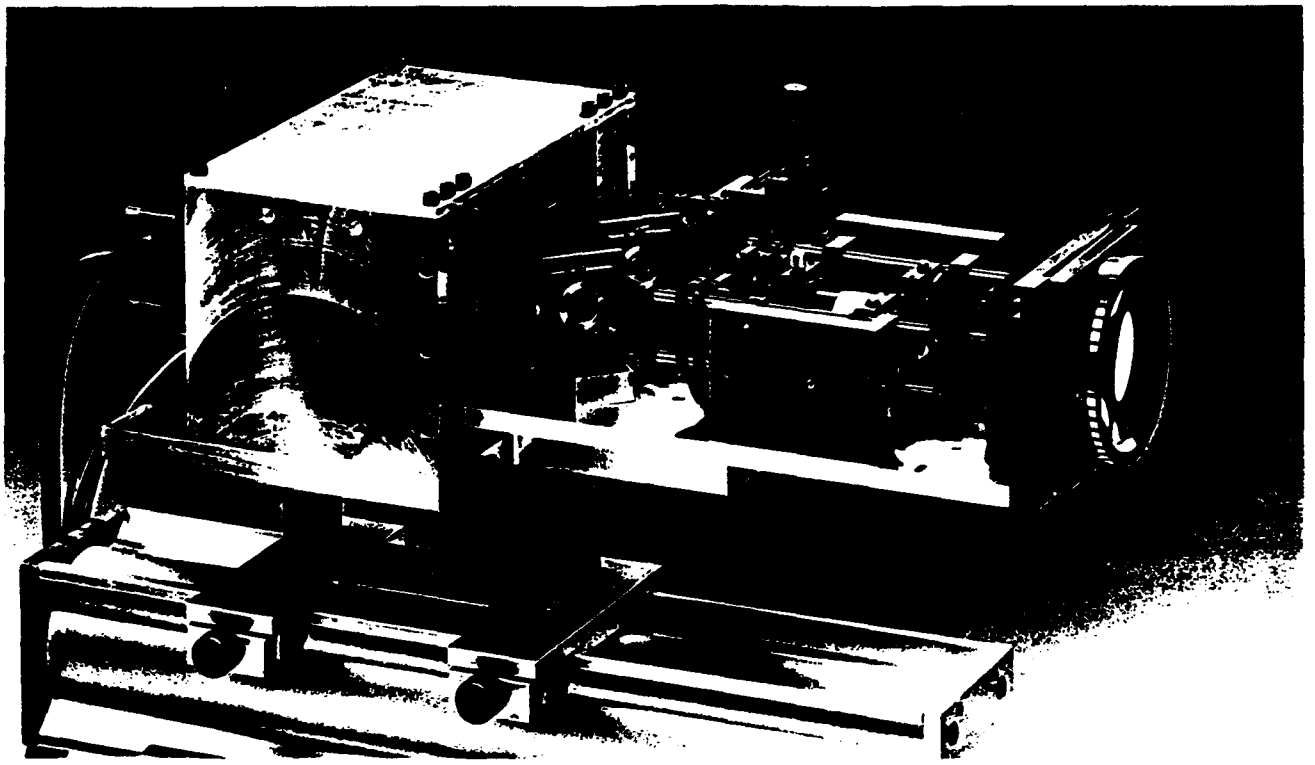

Fig. 7 Photograph of the realized system

In order to eliminate shift frequency fluctuations, caused by drift influences of the lasers, the LDV burst signals f_S and the reference signal f_{SH} have to be detected simultaneously by a two channel transient recorder. Applying FFT procedures to both signals, the shift frequency as well as the signal frequency can be evaluated. Furthermore the two channel signal recording in the time domain allows an elimination of the influence of the laser line width on the evaluation of Doppler frequencies by digital correlation techniques. This is necessary for precise measurements of Doppler frequencies in a range below the bandwidth of the reference signal.

Caused by environmental influences like mechanical vibrations and temperature changes the emission frequency of the lasers drifts up to 1 MHz/s. To maintain the desired shift frequency a software control loop is employed. By using the evaluated reference signal frequency an error signal is calculated and fed back to the tuning input of one laser by a D/A - converter. Because of the slow tuning coefficient of the laser emission frequency, the shift frequency deviations of the control loop are in the range of some hundred kHz. To guarantee an exact determination of the Doppler frequency the lower limit of the shift frequency must be approximately two times the highest estimated Doppler frequency independently of temporary shift frequency deviations. Therefore the lower limit of the shift frequency range of the LDV-system is about 1 MHz.

Furthermore, the large control deviations require unconditionally a second signal processing channel for the measurement of the reference frequency simultaneously to the bursts. This is disadvantageous in comparison to the application of ring lasers at 1064 nm for LDV systems presented by Dopheide and Kramer (1993) which allow the application of a one channel signal processing unit for the burst signal evaluation by using a PLL for the shift frequency stabilisation .

The upper limit of the shift frequency is given by the bandwidth of the photo diodes and the applied transient recorders. Measurements were carried out with shift frequencies up to 200 MHz.

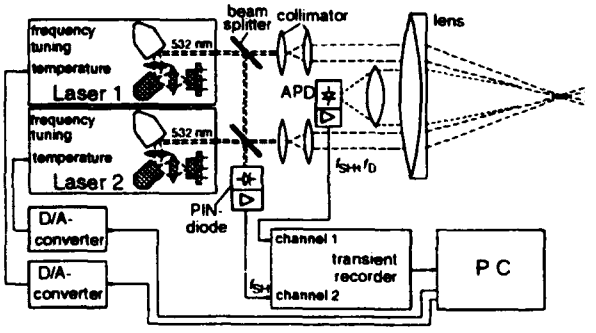

Fig. 8 Schematic of the realized LDA system using a two channel transient recorder for signal processing

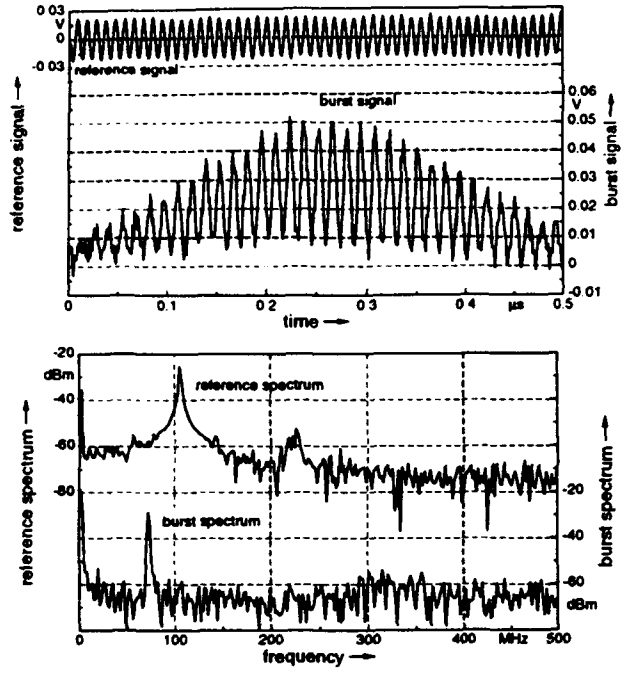

a)

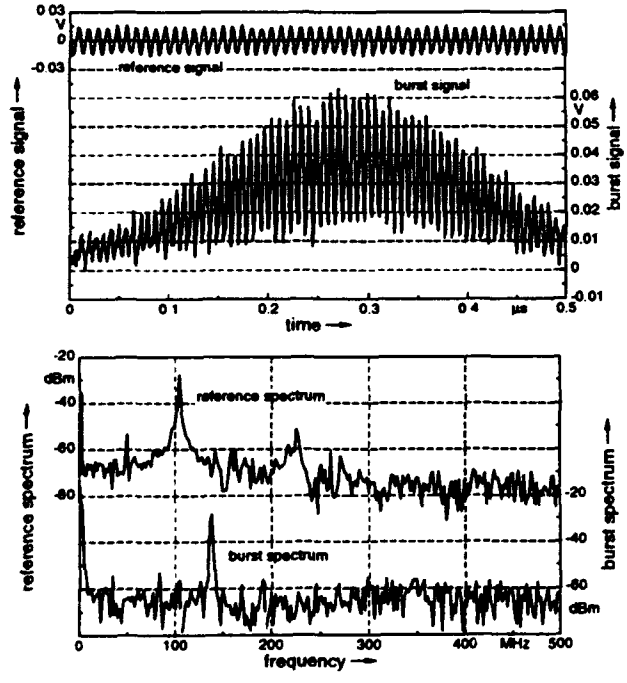

b)

Fig. 9 LDV burst and reference signal in the time and frequency domain
a) Particle flow direction is in the direction of moving fringe system
b) Particle flow direction is opposite to the direction of the of moving fringe system

Fig. 9 shows typical unfiltered burst signals measured in an air jet and the simultaneously recorded reference signals. A TSI 9302 atomiser with a cyclone to achieve particle diameters in the range of 1 µm was used as particle generator. Although the power of both beams was attenuated to 5 mW, the signal peaks exceed the noise level more than 30 dB.

The calculated signal power at a laser wavelength of 532 nm as well as at 1064 nm is plotted in Fig. 10 for the realized optical arrangement. For the interesting particle diameters below 1 µm the signal power shows large fluctuations for both wavelengths, however the signal power at 532 nm is predominant more than 5 times higher as the signal power at 1064 nm.

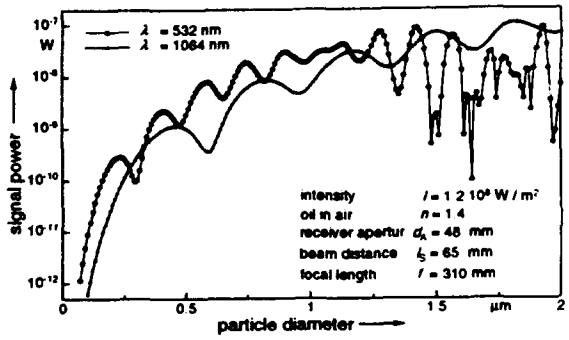

Fig. 10 Calculated light power scattered by oil particles in air flow versus particle diameter

For the comparison of the light power scattered at different wavelength the spectral properties, especially the quantum efficiency, of the photo diodes used for the signal detection have to be considered. While the quantum efficiency of infrared enhanced Si-diodes at 1064 nm is up to 40 %, the quantum efficiency at 532 nm reaches 75 %. Therefore, the system based on frequency doubled Nd:YAG ring lasers delivers for particles with a diameter below 1 µm a better signal to noise ratio than a system with up to more than 5 times higher output power at 1064 nm.

CONCLUSIONS

The high output power of more than 100 mW of both lasers at a wavelength of 532 nm, as well as the low intensity noise of the lasers, allows to achieve high SNR values. In combination with the adjustable frequency shift, the system is suitable for measuring high turbulent flows seeded with small particles.

The applied signal processing is based on a two channel transient recorder which samples the burst signals and the reference signals simultaneously. The small dimensions and the low power consumption of the lasers are advantageous for the application of the developed LDV system.

REFERENCES

Durst, F.; Melling, A., Whitelaw, J.H. 1987, Theorie und Praxis der Laser-Doppler-Anemometrie, G. Braun Verlag, Karlsruhe

Müller, H.; Kramer, R., Dopheide, D. 1993, Neue Verfahren zur Erzeugung einer Frequenzshift in der Doppler-Anemometrie mit abstimmbaren Festkörperlasern, PTB Mitteilungen, vol. 103, no. 1, pp. 3-17

Kane, T.J., Byer, R. L. 1985, Monolithic, unidirectional single-mode Nd:YAG ring laser, Optics Letters, vol. 10, pp. 65-67

Gerstenberger, D. C., Tye, G. E., Wallace, R. W. 1991, Efficient second-harmonic conversion of cw single-frequency Nd:YAG laser light by frequency locking to a monolithic ring frequency doubler, Optics Letters, vol. 16, pp. 992-994

Freitag, I., Rottengatter, P., Tünnermann, A., Schmidt, H. 1993, Frequenzabstimmbare, diodengepumpte Miniatur-Ringlaser, Laser und Optoelektronik, vol. 25, no. 5, pp.70-75

Dopheide, D., Kramer, R. 1993, Realisierung eines Laser-Doppler-Anemometers mit kontinuierlich variierbarer Frequenzshift durch den Einsatz abstimmbarer Nd:YAG-Ringlaser, Proceedings 6. Internationale Fachmesse mit Kongreß für Sensorik & Systemtechnik (Sensor 93), Nürnberg, vol. 2, pp. 65-72

OPTICAL-FIBRE-BUNDLE BEAM DELIVERY SYSTEM FOR PULSED LASER PIV ILLUMINATION

D.J. Anderson†‡§, J. D. C. Jones†, W. J. Easson‡ &
C. A. Greated§

† Department of Physics, Heriot-Watt University, Edinburgh EH14 4AS
‡ Department of Mechanical Engineering, The University of Edinburgh, Edinburgh EH9 3JL
§ Department of Physics and Astronomy, The University of Edinburgh, Edinburgh EH9 3JZ

ABSTRACT

We demonstrate the design and implementation of a fibre-optic-bundle (FOB) beam delivery system for particle image velocimetry (PIV) applications. The system is designed for the transmission of high peak power pulses from a Q-switched and frequency doubled Nd:YAG laser; it is thus suitable for illuminating high speed fluid flows. A fibre bundle offers advantages over a single fibre in beam delivery systems for light sheet formation. The damage-limit-maximum power that can be transmitted is greater for the bundle than for any of its component fibres, and the quality of the derived light sheet is higher than that obtainable from a single large core fibre of power handling capacity equivalent to that of the bundle. The beam delivery system was demonstrated in PIV measurements on a premixed propane-air flame.

1. INTRODUCTION

Particle image velocimetry (PIV) has been developed in recent years as a technique to provide two-dimensional velocity measurements in a fluid flow. The use of an optical fibre delivery system minimises the free space laser transmission, improving safety and reducing the possibility of stray light reflections which could compromise image quality. In addition the fibre delivery system eases the problem of optical access, allowing PIV to be used in test rigs where it would not be possible with a bulk optic delivery system. Pulsed lasers, such as the frequency doubled Q-switched Nd:YAG, are essential for illuminating high velocity air flows as reported by Kompenhans and Hocker (1988). Such lasers can deliver high energy pulses (~ 150 mJ) in a few nanoseconds, and while the average output power of such a laser may be less than the average power output of a continuous wave (CW) laser, the peak power is considerably higher. Thus there exists a requirement for optical fibre delivery systems for PIV capable of delivering peak powers which are orders of magnitude greater than those found in, for example, LDA delivery systems.

In this paper we show that when a single fibre is used in the beam delivery system, then a compromise exists between the maximum transmittable power and the quality of the output beam. We further show that the compromise may be significantly improved by using a bundle of fibres rather than a single fibre, and demonstrate that a FOB delivery system may be used for PIV applications requiring pulsed laser illumination. By considering the optical damage threshold of the FOB, we determine the maximum energy from a Q-switched and frequency doubled Nd:YAG laser which may be transmitted through the bundle. By characterising the output beam from the FOB, we demonstrate the formation of a light sheet suitable for PIV applications.

PIV measurements have been demonstrated on combusting flows by Armstrong et al (1992) using conventional beam delivery optics; however in these studies we describe a PIV experimental set-up incorporating a FOB delivery system which was used to obtain PIV images of a laboratory-based propane-air flame seeded with 3 μm Al_2O_3 particles.

2. DESIGN OF FIBRE OPTIC BUNDLE BEAM DELIVERY SYSTEM

A single-mode step-index fibre suitable for use with visible light has a core diameter of about 3 μm and has been used to transmit at least 500 mW from a CW argon ion laser as reported by Jackson et al (1984). However, to transmit the high peak powers present in Q-switched lasers, in the order of 3 MW in the present experiments, we must consider using large core multimode step-index fibres with core diameters

ranging typically from 200 to 1000 μm as described by Allison et al (1985). Previous research by Anderson et al (1994) has successfully used single multimode optical fibres to deliver high peak power laser radiation for PIV sheet illumination; however, systems based upon single multimode optical fibres are limited by the maximum power transmitted and the relatively poor beam quality at the fibre output.

The laser-induced-damage threshold (LIDT) of multimode fibres increases as the core diameter of the fibre is increased as reported by Anderson et al (1994). The output beam quality from a step-index multimode fibre is given approximately by the product of the output beam numerical aperture and the fibre core diameter after Su et al (1992). For the transmission of a high power beam, a sufficiently large fibre core diameter must be specified to avoid damage. Thus, the output beam quality is generally much lower than that of the input laser beam. Hence, the poor beam quality at the output of a large core multimode fibre prevents the formation of a well collimated and "thin" light sheet as required for PIV illumination. In one practical example, a step-index optical fibre with a core diameter of 600 μm, Anderson et al (1994), resulted in an output beam quality of ~ 72 mm mrad, which when imaged into a light sheet 2 mm thick remained collimated over a relatively short distance of 22 mm. Hence, the choice of optical fibre for laser beam delivery must therefore be a compromise between output beam quality and peak power transmitted.

To improve the compromise between output beam quality and peak power transmitted we have investigated the use of a fibre-optic-bundle. The maximum power transmission of the bundle will scale with the number of component fibres used in its construction; because the fibres are arranged into a line at the bundle output end then the beam quality depends only upon the core diameter of the individual fibres.

An additional concern, when using large core multimode optical fibres, is that the output beam profile may show considerable small scale intensity variations, or speckle, arising from interference between the many guided modes of the fibre. Ideally, variations in the light sheet intensity must be such that all the particle image pairs can be analysed. That is, even in those regions of the sheet where the power density is at its lowest there must be adequate illumination to produce satisfactory images on the photographic film. The resulting image intensity of the particle seeding on the photographic film should meet the detectability criterion discussed in Adrian and Yao (1985), i.e. that 45 % of a Gaussian image spot should exceed the gross fog level of the film.

2.1. Construction of Fibre Optic Bundle

The fibre-optic bundle was constructed using nineteen fused silica step-index fibres (Manufactured by CeramOptec) with core and cladding diameters of 200 and 220 μm respectively; the fibre core material was pure fused silica with a doped cladding and the fibres were coated with an acrylate buffer. At the input, the individual fibres were bound together mechanically into a round bundle. Adhesives were not used because they would not be able to withstand the high peak laser powers present at the launch. The first step in the construction of the fibre bundle was to cut the nineteen individual fibres into 5 m lengths, then the input faces of the fibres were cleaved to avoid excess scattering and absorption of the laser radiation. Both the fibre bundle and the cleaver were clamped to an optical table, allowing all of the fibres to be cleaved with equal lengths to an accuracy of ± 0.5 mm at the input. The fibres were then guided into a tapered pyrex capillary tube to mechanically hold the fibres into a circular bundle; the internal diameter of the pyrex capillary at the output was approximately 1.2 mm.

At the output of the bundle, the fibres were arranged without correlation between positions at the input and output ends in a line ~ 4.2 mm long. The fibres were placed in a channel machined from an aluminium block and were secured in place using UV curing glue and a rubber clamp. The fibres were carefully polished, using a special polishing rig, with various grades of abrasive paper down to a minimum abrasive grit size of 0.3 μm; this ensured that the output facets were accurately aligned. The complete fibre bundle assembly was sheathed in polythene tubing to protect the bundle from mechanical damage.

2.2. Launch Optics for the FOB

A single plano-convex lens with a focal length of 400 mm was used to launch light into the fibre bundle, see figure 1; the lens was chosen to ensure that the numerical aperture of the input beam (12.5 mrad) was less than the numerical aperture acceptance angle of the individual fibres (220 mrad). To match the outer diameter of the bundle, ~ 1.1 mm, to the beam diameter, the input face of the fibre bundle was positioned upstream of the lens focus at a distance of 325 mm from the lens resulting in a beam diameter of ~ 1.4 mm at the input of the FOB to give a reasonably uniform illumination.

The launch efficiency depended upon the packing density of the fibres at the input and the size of the laser beam relative to the bundle diameter. The maximum launch efficiency achieved was 31 %.

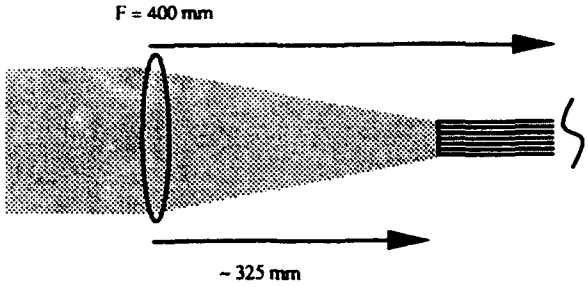

Fig. 1 Launch optics for the fibre optic bundle.

2.3. Laser Induced Damage Threshold

The laser used in the experiments described in this paper is typical of those used for air flow measurements using PIV. The laser was a Spectra-Physics GCR12, which is a frequency doubled Nd:YAG giving an output with a wavelength of 532 nm, a pulse duration of 6 ns at a repetition frequency of 10 Hz and pulse energy up to 150 mJ. In previous studies reported by Anderson et al (1994) the laser induced damage threshold (LIDT) of three step-index fused silica fibres was determined for fibres with core diameters of 400, 600 and 1000 μm, using the above mentioned laser, as 7, 9 and 14 mJ. In addition the LIDT for the optical fibre used in the construction of the bundle, i.e. 200 μm core diameter step index fibre, was found to be ~ 1.5 mJ. In these previous experiments using individual fibres and also for the FOB, the LIDT was taken as the transmitted power level achieved before there was a catastrophic drop in the transmitted power; 600 Q-switched laser pulses were used at each power level in each damage test. All the observed fibre damage was internal, occurring within ~ 40 mm of the input fibre facets, generally at the core cladding interface. The launch optics for the LIDT tests of the fibre bundle were as described in section 2.2 . The LIDT for the bundle was measured as 21 mJ. There is evidence reported by Merkle et al (1984) of accumulative damage occurring in optical materials at power levels lower than the LIDT, and hence it is recommended that for prolonged operation power levels significantly below the LIDT level are used.

2.4. Light Sheet Characteristics

A single cylindrical lens with a focal length of 75 mm was used to form the light sheet for PIV illumination, see figure 2. The light from the fibre array was allowed to expand freely in one dimension, with an angle θ of 104 mrad, whilst the cylindrical lens focused the sheet in the other dimension. With the lens positioned 92 mm from the fibre array, then the light sheet waist was formed at a working distance of 460 mm from the lens. The width of the light sheet at the waist position, t_w, was 1.3 mm.

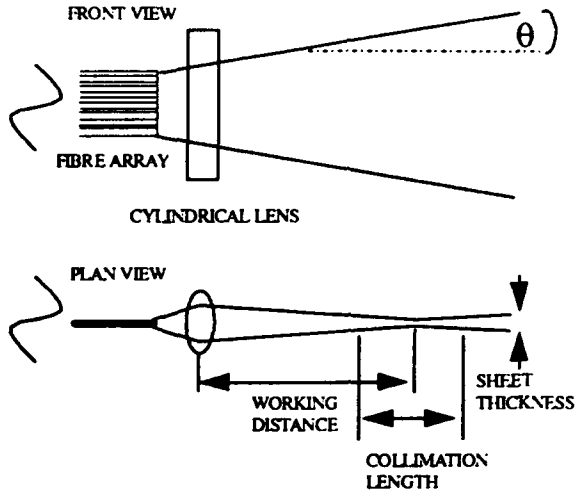

Fig. 2 Output optics for light sheet formation.

The sheet thickness, as measured at the $1/e^2$ intensity points, is displayed in figure 3 as a function of the working distance from the cylindrical lens. The collimated distance, i.e. the distance over which the sheet thickness is less than $\sqrt{2} \times t_w$, is 105 mm, see figure 3. Using the beam waist t_w and the far-field divergence angle α (18.2 mrad) as shown in figure 3, then the beam quality of the light sheet is approximately 24 mm mrad.

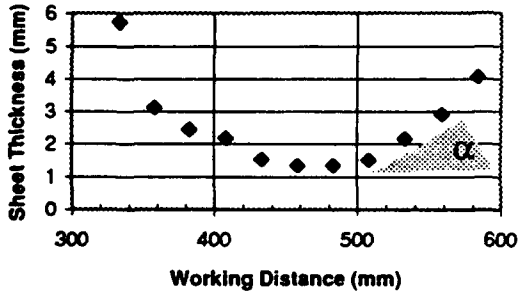

Fig. 3. Light sheet thickness as a function of working distance.

With many modes guided at the output of each of the multimode fibres, interference will lead to the formation of speckles in the far-field intensity distribution. In addition there will be interference between the modes from the fibres in the array. As an illustration, figure 4 shows the far-field intensity distribution at the output of a 100 μm diameter core step-index fibre which clearly demonstrates the presence of speckles.

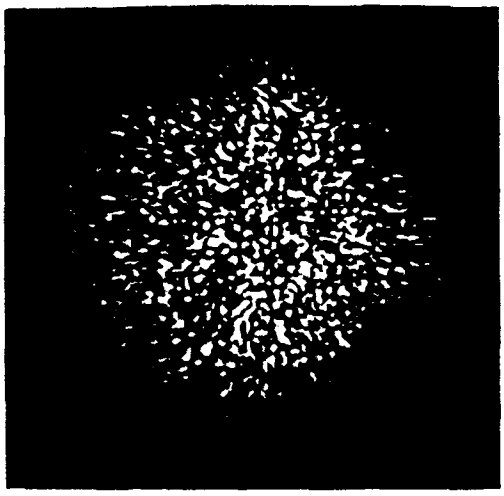

Fig. 4. Typical far-field intensity distribution at the output of a 100 μm diameter core fibre.

The visibility, V, of small scale, speckle-induced intensity variations in a region of the fibre far field can be defined as

$$V = \pm \frac{(I_{max} - I_{min})}{2I_{av}} \qquad (1)$$

Where I_{max}, I_{min} and I_{av} are the maximum, minimum and average intensity values recorded in the intensity distribution of the fibre far-field, respectively.

A CID (Charge Injection Device) camera was used to capture images of the output beam profile of the fibre. Measurements were made of both the full output beam and of the central region of the expanded beam. The speckles in the light sheet formed with the fibre bundle had a visibility of 15 %; however, even with the speckle induced intensity variations in the light sheet it is still possible to obtain PIV images of sufficient quality to create a 2-dimensional velocity vector map, as illustrated in section 4.1.

3. BURNER AND FLOW SEEDING

The burner design used in these studies was based upon a torch used for glass blowing which had been modified to give an outlet nozzle diameter of 9 mm. Propane (commercial grade) and compressed air were mixed before entering the nozzle. The air flow is seeded prior to mixing with the propane. Aluminium oxide powder has been used by various researchers, such as Kennedy (1982) and Witze & Baritaud (1986), for seeding combusting flows; in the present experiments the Al_2O_3 seed used had a mean size of 3 μm and was introduced to the air flow using a cyclone aerosol generator as described by Glass and Kennedy (1977).

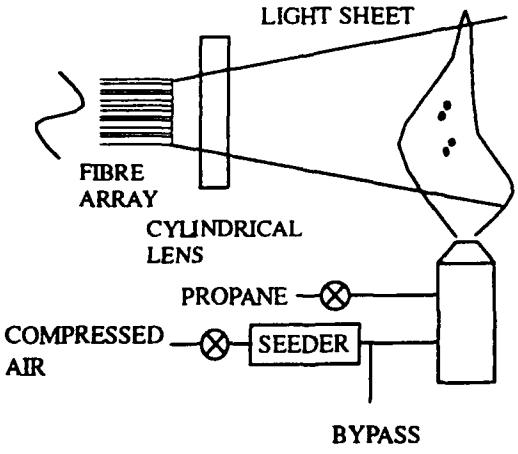

Fig. 5 Experimental arrangement.

4. PIV IMAGE RECORDING

The dimensions of the light sheet used for illumination of the propane flame are identical to those described in section 2.4. The laser was operated in double-pulsed mode; the pulse interval was set to 100 μs. The energy of each pulse was measured at the output of the fibre bundle to be 12 mJ .

A Nikon camera and a 55 mm MicroNikkor lens were used to image the particle-laden flow-field onto the 35 mm film. The magnification from the light sheet to the film was set as 1/3. In order to remove the flame luminosity, an interference filter (bandpass wavelength of 532 nm and 10 nm bandwidth) was attached to the front of the lens. Kodak Tmax film with an ASA rating of 400 was used; the aperture of the lens was set at *f*/2.8, and the camera shutter timings were synchronised with the pulse output of the laser.

4.1. PIV Analysis

The PIV photographic images were analysed using the Young's fringe technique, Robinson and Reid (1993), to give a two-dimensional velocity vector map of the flow. Figure 6 shows a typical uninterpolated velocity vector map of the propane flame; the mean velocity component in the vertical direction was measured as 3.1 m s^{-1}. The analysis software was used to subtract a velocity of 2.5 m s^{-1} from the vertical velocity vector components; the resulting vector map shown in figure 7 reveals the changing nature of the flame flow field.

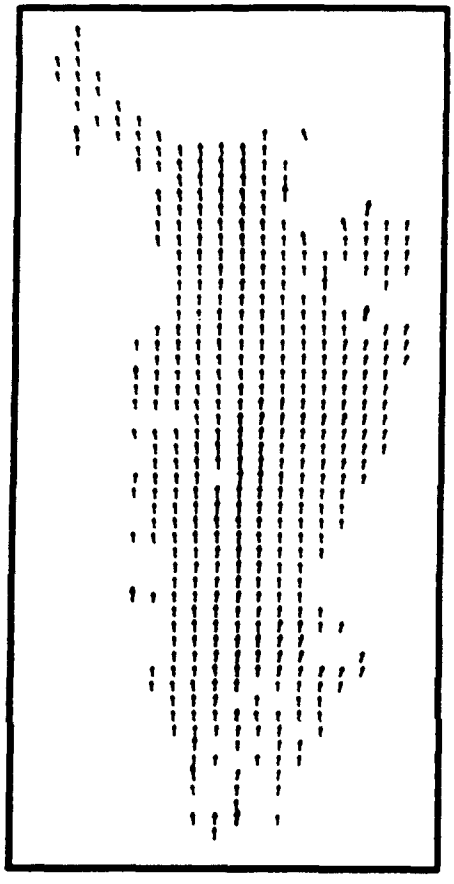

Vertical node separation = 1.5 mm
Horizontal node separation = 1.5 mm

Fig. 6 Uninterpolated velocity vector map of the propane flame.

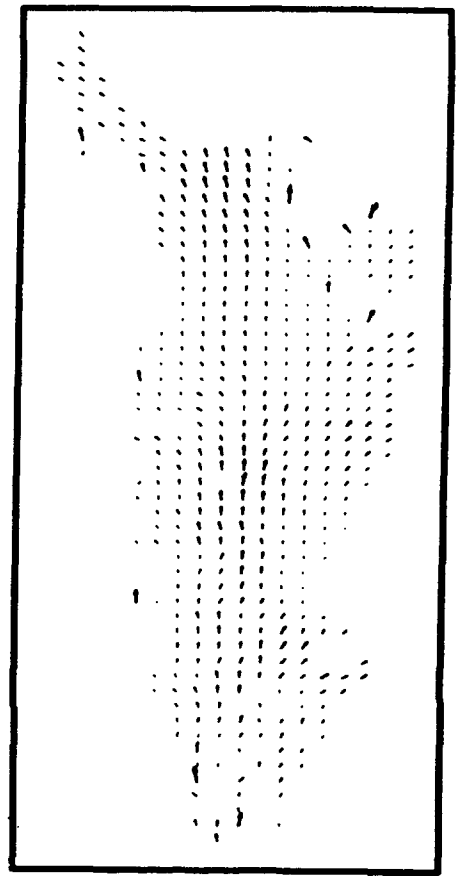

Vertical node separation = 1.5 mm
Horizontal node separation = 1.5 mm

Fig. 7 Velocity vector map of the propane flame. A velocity of 2.5 m s^{-1} has been subtracted from the velocity vectors in the vertical direction.

5. SUMMARY

This paper has demonstrated the use of a fibre-optic-bundle beam delivery system suitable for PIV applications that require light sheet illumination from high peak-power pulsed lasers. The maximum power capable of being transmitted by a fibre bundle is greater than that for any of its component fibres, and the quality of the derived light sheet is superior to that obtainable from a single large core fibre of power handling capacity equivalent to that of the bundle. A fibre-optic-bundle beam delivery system has been used to obtain PIV measurements on a premixed propane-air flame.

ACKNOWLEDGEMENTS

The authors acknowledge the financial support of both the Science and Engineering Research Council (UK.) and Rolls-Royce plc.

REFERENCES

Adrian, R.J. & Yac, C-S., 1985, Pulsed Laser Technique: Application to Liquid and Gaseous Flows and the Scattering Power of Seed Materials, Appl. Opt., vol. 24, pp.44-52.

Allison, S.W., Gillies, D.W., Magnuson, D.W. & Pagano, T. S., 1985, Pulsed Laser Damage to Optical Fibres, Appl. Opt., vol. 24, pp. 3140-3145.

Anderson, D.J., Morgan, R.D., McCluskey, D.R., Jones, J.D.C., Easson, W.J. & Greated, C.A., 1994, Optical Fibre Delivery System for Pulsed Laser PIV Illumination, J. Meas. Sci. Technol., In Press.

Armstrong, N., Bray, K., Shand, A., & Ereaut, P., 1992, PIV Applied to Premixed Turbulent Flames, I. Mech. E. Proc. of Optical Methods and Data Processing in Heat and Fluid Flow, City University, pp.83-87.

Glass, M. & Kennedy, I.M., 1977, An Improved Seeding Method for High Temperature Laser Doppler Velocimetry, Combustion and Flame, vol. 19, pp. 333-335.

Jackson, D.A, Jones J.D.C. & Chan R.K.Y., 1984, A High-Power Fibre Optic Laser Doppler Velocimeter J Phy E: Sci. Instrum, vol. 17, pp.977-980.

Kennedy, I.M., 1982, Flames with Refactory Oxide Particles, Combustion Science and Technology, vol. 27, pp. 247-252.

Kompenhans, J. & Hocker, R. 1988, Application of PIV to High Speed Flows, von Karmen Institute Lecture Series, 1988-06.

Merkle, L.D., Koumvakalis, N. & Bass, M., 1984, Laser-Induced Bulk Damage in SiO_2 at 1.064, 0.532, and 0.355 μm J. Appl. Phys., vol. 55, pp. 772-775.

Robinson D.W. and Reid G.T., 1993, Interferogram Analysis: Digital Fringe Pattern Measurement Technique, *IOP Publishing*, ISBN 0-7503-0197

Su, D., Boechat, A.A.P. & Jones, J.D.C., 1992, Beam Delivery by Large Core Fibres: Effect of Launching Conditions on Near Field Output Profile Appl. Opt. vol. 31, pp.5816-5821.

Witze, P.O. & Baritaud, T.A., 1986, Particle Seeding for Mie Scattering Measurements in Combusting Flows, Proceed. Laser Anemometry in Fluid Dynamics, Lisbon, pp.489-502.

Session 15.
Combustion V

Instantaneous Velocity Measurements in Laminar and Turbulent Premixed Flames Using On-Line PIV

M. G. Mungal, *Mechanical Engineering Department, Stanford University, Stanford, CA 94305*

L. M. Lourenco & A. Krothapalli, *Department of Mechanical Engineering, Florida A&M University and Florida State University, Tallahassee, FL 32316*

ABSTRACT

Particle Image Velocimetry (PIV) is used to measure the instantaneous velocity field in laminar and turbulent premixed flames formed at the exit of a round Bunsen burner. The seeding levels were adjusted to provide data in both the unburned as well as burned gases. The PIV system employs a double-pulsed laser with a solid state sensor as the recording device. Customized image acquisition is used to quickly process the data, thus rapidly providing the velocity field. Two-dimensional, instantaneous velocity fields are measured in a steady laminar flame and captures the sudden change in flow speed at the flame sides as well as the high speeds sustainable at the flame tip. A wake profile downstream of the flame cone is revealed. Turbulent flame tips show similar phenomena occurring instantaneously on convoluted flame shapes. Vorticity and strain rates are possible with these datasets and are also reported, with the strain rate seen to be providing a close approximation to the instantaneous flame shape.

INTRODUCTION

Particle Image Velocimetry (PIV), from its early beginnings in the seventies (Dudderar & Simpkins 1977, Grousson & Mallick 1977, Meynart 1977) is now becoming the technique of choice for the measurement of fluid velocity in a planar region (Pickering & Halliwell 1984, Adrian 1984, Lourenco et al. 1989, Goss et al. 1991, Adrian 1991, Willert & Gharib 1991, Dong et al. 1992, Molezzi & Dutton 1993). The technique uses planar laser sheet illumination and multiple exposures of fine particles seeded into a flow; an image is captured on film or a CCD array for subsequent analysis. Interrogation of these images over small regions via correlation techniques yields the local velocity averaged over the interrogation region. While the approach has been mostly applied to non-reacting flows, there have been some attempts to apply the technique to both premixed as well as non-premixed flames. Reuss et al. (1989) studied laminar Bunsen flames while Reuss et al. (1989) investigated IC engine combustion. In both of these studies, velocities were reported in only the cold flow, ahead of the flame, owing to the reduced density of seed in the post-flame gases. Both studies also used film as the recording medium. Thus, film development and the subsequent processing and analysis represent a relatively long step in the conversion to velocity. These pioneering studies however do demonstrate that PIV is a viable technique in combustion studies.

Additional studies involving reacting flows have been performed on the near-field of jet diffusion flames (Post et al. 1991) and combusting, premixed vortex rings (Driscoll et al. 1993). Both of these studies used the same two-color approach with color film as the recording medium. A hybrid vector finding algorithm that combines elements of PIV with that of particle tracking (see Adrian 1991) is used. The seeding density was relatively low, and as such, the velocity field is obtained at only discrete particle-pair locations in the flow with interpolation used to fill in the velocity field.

In the present work, we extend the earlier reacting PIV studies in two ways: first, we use the technique of "On-line PIV" (Lourenco et al. 1994), whereby the film camera is replaced by a high resolution CCD array and customized data acquisition, thus eliminating the wet step; this leads to immediate turnaround and analysis of data. Second, we utilize a sufficiently high particle seeding density that allows velocity data to be obtained simultaneously in both the (cold) pre-flame and (hot) post-flame gases. Given the volume expansion associated with the combustion process, and the strict seeding requirements of PIV, this represents a challenge to the application of PIV in reacting flows. In fact, it is fair to say that it is the on-line feature of the present arrangement that allowed us to achieve the proper seeding density, in reasonable time, thus allowing good data in both the pre- and post-flame regions of the flow.

The work is described below in three stages. First PIV is applied to a cold, non-reacting jet at high seeding density. Next, it is applied to a laminar Bunsen flame to demonstrate several features of the technique in acquiring velocity data throughout the field of interest. Finally, the technique is applied to the tip region of a turbulent premixed flame which is inherently unsteady owing to the high flow speed used. We begin by first describing the experimental setup and details relevant to the PIV approach.

EXPERIMENTAL DETAILS

Flame Facility

Premixed flames were produced using the arrangement shown in Fig. 1. Commercial grade propane is supplied from a tank, pressure regulated and metered using a standard rotameter. House air is similarly metered before entering a seeder containing alumina powder (0.3 micron diameter). Multiple feed holes into the seeder and use of steel wool at the seeder exit were used to produce good seeding characteristics. Both streams are mixed at a tee using an ejector design to promote steady mixing. The gas mixture then proceeds horizontally to complete mixing before turning into a vertical 1.1 cm ID tube of length 46 cm. Before entrance to the tube, a honeycomb and two stations of fine mesh screen are used to remove the effects of the turning elbow. For laminar

conditions, air was flowed at 7160 sccm while propane was flowed at 223 sccm. This yields an average flow speed of 127 cm/s at the tube exit, with a tube Reynolds number of 940. Under these conditions, the equivalence ratio was ϕ = 1.35. Yu et al. (1986) give an unstretched laminar flame speed of 31.5 cm/s for this condition. The temperature in the post-flame gases (Mizomoto et al. 1984) would vary from 1600^{o}C at the tip to 1800^{o}C at the largest flame radius, consistent with a Lewis number less than unity for this gas mixture. For turbulent conditions, the flow speeds were increased; the corresponding conditions were: average flow speed = 243 cm/s, Re = 1800 and ϕ = 1.34, with a laminar flame speed of 32 cm/s.

For these experiments, we found that a small amount of vibration applied to the seeder was sufficient to generate the required seeding densities. The ability to immediately view the data and process into velocity allowed us to quickly determine an optimal seeding density which allow simultaneously valid data in both the cold and hot regions of the flow; overseeding led to invalid data in the cold regions, while underseeding led to sparse data in the post-flame regions. The determination of proper seeding, which is crucial to the success of this application of PIV as will be seen later, takes only a few minutes with on-line operation. With film operation, the process would be considerably more difficult before optimal and repeatable conditions could be found. We found that the system described here produced sufficiently uniform seed for good and repeatable results. Accumulation of larger seed particles was observed in the horizontal portions of the flow train; thus it was necessary to disassemble and clean the system after every few hours of operation. Finally, we found it necessary to surround the flame by a 15 mesh per inch screen enclosure to avoid draughts due to the room ventilation and exhaust system.

PIV System

The PIV system utilized in this study is shown is described in Lourenco et al. (1994). It consists of a double-pulsed Nd:Yag laser (Lumonics Model HY400) as the light source with appropriate sheet forming optics. The camera (Kodak Videk Megaplus) utilizes a CCD array of 1320 x 1035 pixels. Each pixel is 6.8 x 6.8 micron in size with 100% fill factor. The imaging lens was a standard Nikon lens using f/11 optics for most of the results shown here. The data acquisition occurs on customized A/D boards on a 486-type PC platform. Customized software on an array processor is used to speed up the data reduction process. Since there was no velocity ambiguity (due to flow reversal) in these results, no image shifting (Adrian 1986, Lourenco et al. 1986, Landreth & Adrian 1988, Lourenco 1993) was used. Since image shifting has the additional, beneficial effect of resolving low velocity regions, the results shown below will have this limitation; however as will be seen, this is of little consequence for the present arrangement.

The processing software used to convert the data to velocity vectors involves subdividing the image into subregions of (n x n) pixels. In each subregion an autocorrelation technique is used to identify the average particle displacement within the subregion, corresponding to the local fluid velocity. The present system performs this operation in about 20 msec for each velocity vector. For the results shown below, a subregion box size of 56 x 56 pixels was generally used corresponding to a physical dimension of 1.2 x 1.2 mm. This box size was determined mostly by the requirement for a minimum of 5 particle pairs in the post-flame gases. While smaller box sizes were possible in the pre-flame gases (owing to the higher seed density), we did not change the box size there simply as a matter of convenience. The implementation of the technique is described in greater detail in Lourenco et al. (1994), where the accuracy of the technique is shown to be of the order of +/- 1 to 2% full scale.

RESULTS & DISCUSSION

Figure 2 shows sketches of the flow patterns believed to be occurring at the side and tip of a laminar flame. For the side, the normal component of flow velocity is equal to the laminar flame speed and is increased due to volume expansion, while the tangential component remains unchanged; this classical picture is described in most combustion texts, e.g. Lewis & von Elbe (1961). At the tip however the flow pattern is quite different as lateral streamtube divergence occurs. Echekki & Mungal (1990) have shown experimentally the flow speed can be up to an order of magnitude higher than the laminar flame speed at the tip. The mechanism for the increased flame speed involves heat convergence and reactant leakage at the flame tip. It is also shown that increasing tip speed requires a decreasing flame radius of curvature. Poinsot et al. (1992) have performed numerical simulations which confirm the experimental findings of Echekki & Mungal (1990) at the flame tip. These characteristic features sketched here will be used to interpret the results to be presented later.

Cold Flow

Cold flow images of the non-reacting, laminar jet were first obtained at a range of seeding densities, but are not shown here for brevity. A high seeding density is required so that valid data would be obtained at "typical" seeding densities in the hot, expanded post-flame gases under reacting conditions. It is also required that the cross-correlation algorithm would not fail in the cold premixture, thus yielding simultaneously valid data in both the unburned and burned gases. We do note however, that use of lower, more typical, seed densities produced essentially the same results in the non-reacting cases.

Laminar Flames

Figure 3 shows an image of a laminar premixed Bunsen flame at Re = 940, taken with a pulsewidth separation of 60 μsec. Immediately apparent is the strong volume expansion associated with the presence of the flame. The heavier seeding level marks the region of the flow up to the preheat region of the flame, before significant flow turning occurs. Figure 4 shows velocity vectors along select lines in the flow; these vectors were all computed over a box size of 56 x 56 pixels (1.2 x 1.2 mm). The initial velocity profile shows the parabolic shape expected for this Reynolds number. As we proceed towards the flame tip, the lower velocity portions of the approach flow have been consumed by the flame leading to a considerably more top-hat velocity profile. Corroborating evidence for this can be seen by carefully examining the results of Reuss et al. (1989), where data for the cold regions of a Bunsen flame at similar conditions are presented. The post flame gases show the profound effects of the expansion associated with heat release, with velocity magnitudes easily exceeding the maximum incoming speeds.

The velocity vectors at the sides of the flame show the strong turning associated with conservation of the tangential component and increase of the normal component consistent with the volume expansion, Fig. 2(a). As noted by several authors (see for example, Law 1988), the normal component of velocity at the flame side for this round configuration is not the laminar flame speed as the flame is negatively stretched; thus the flame angle must adjust to both the changes in the incoming velocity profile as well as the effects

of stretch. The expansion effect of the flow is seen to be essentially similar along the sides, until the tip region of the flame where streamtube expansion becomes the dominant effect, Fig. 2(b). The profile furthest past the flame tip shows that the post-flame gases evolves into a slight wake-like profile with a velocity minimum on the flame centerline, even though the incoming profile is jet-like with a central maximum. This post-flame wake was observed for all laminar flames which we examined at similar conditions, and must be characteristic of the overall flame evolution. Poinsot et al. (1992) show that a low pressure region exists immediately downstream of the flame tip and serves to curve the post-flame gases back towards the centerline. Such a pressure distribution is consistent with the formation of a wake-like region downstream. Poinsot (private communication) has noted that the two-dimensional flame computation described in Poinsot et al. (1992) also shows a moderate wake profile in the post flame gases; since buoyancy is not included in the computation we can conclude that the phenomena reported here are therefore associated with the nature of premixed combustion and not with buoyancy effects per se. To our knowledge, the far wake has not been shown before experimentally.

The centerline velocity for this flow has been compared to the corresponding non-reacting case. The cold flow shows an essentially non-decaying value consistent with a potential core. The flame on the other hand shows an increase of 15% in the tip vicinity with a subsequent decay to about 75% past the flame tip. Comparable results have been found by Echekki & Mungal (1990) who used particle tracking in a two-dimensional Bunsen flame and by Poinsot et al. (1992) in a two-dimensional computation. Somewhat different results have been reported by Wagner & Ferguson (1985), who performed LDV measurements in a round bunsen flame; they report a gradual decay in the potential region, followed by the sudden rise and subsequent decay at the tip. Wagner & Ferguson conclude that the presence of the flame affects the entire flowfield, while the present results suggest that the region of influence extends only to the preheat zone. The main difference between the two experiments lie in the measurement techniques: LDV for Wagner & Ferguson, PIV for the present studies. It is unclear at present why the results are not in closer agreement.

Several PIV images of laminar flames were acquired. By adjustment of the exposure of the camera system it was possible to capture both the PIV image as well as the feint image of the blue flame, just visible outside of the heavier seeding core. The distance between the heavier seeding and the flame image is indicative of the preheat zone thickness. This zone is measured to be relatively constant at the flame sides and equal to 0.3 mm, but of much larger extent at the flame tip, 1.4 mm, where the merging of the zones leads to velocity changes well before the visible flame. Similar results are found in the results of Echekki & Mungal (1990) and the numerical results of Poinsot et al. (1992) where the effects of heat focussing on the central streamtube is discussed, leading to a much larger preheat zone and diffusion of reactants at the flame tip. These observations suggest that the heavier seeding density regions must be regarded with some caution as they mark the boundary of the preheat zone and not the location of maximum reaction rate (the blue flame). Further caution is required in the highly curved, concave portions of the flame (e.g the tip) where the dense seeding would not be a good approximation to the local flame radius of curvature.

The velocity field on a grid of 60 x 40 points is shown in Fig. 5 using a 56 x 56 (1.2 x 1.2 mm) box. The purpose here is to illustrate the type of data possible with the On-line PIV system at the seeding levels used. These data have been interpolated and used to extract the vorticity and strain fields seen in Figs. 6-8. The vorticity is defined as $\omega_z = \partial v/\partial x - \partial u/\partial y$ with the strain rate defined as $S_{xx} = \partial u/\partial x$, $S_{yy} = \partial v/\partial y$, $S_{xy} = (\partial u/\partial y + \partial v/\partial x)/2$. The strain rates are seen to be highest at the flame surface and preheat zone, and indeed serve as a good marker of the flame location. S_{xy} is seen to be the best marker of the flame location among the three strain rates shown. Poinsot (private communication) has noted that the dilatation $\nabla \cdot u = \partial u/\partial x + \partial v/\partial y$ should be the best marker of the flame zone, as it is directly related to the change in density; however the plots show that S_{xy} is an equally good indicator. This finding is somewhat different from the results of Driscoll et al. (1993) for a combusting vortex ring where the correspondence between the flame position and strain is not as close. We do however note that the seeding and hence data density of Driscoll et al. is relatively light compared to the present studies, so that the required interpolation tends to smooth the original data which may lead to more diffuse strain rate contours.

The vorticity, Fig. 6 shows some interesting results. The positive and negative vorticity associated with the post-flame wake are revealed, as is the vorticity associated with the incoming flow. Of most interest however is the accumulation of vorticity in the region just past the flame tip. Poinsot (private communication) notes that a similar accumulation is also found in the numerical simulations (associated with the local low pressure region just past the tip), thus lending credence to the present findings. A limitation of the present approach is also revealed in the vorticity and, to a lesser extent, the strain plots. Namely, the interrogation box is larger than the preheat zone and sometimes overlaps the flame zone at an inclined angle. The velocity field is thus averaged within the box leading effectively to a resolution error which is reflected in the vorticity and strain field. We do not believe that the small-scale variations at the flame sides are real; however it would require an adjustable box size and orientation to overcome this problem in future.

Turbulent Flames

To illustrate the further capability of PIV in the study of transient flame phenomena, some images of turbulent flames were acquired. For the examples reported here, the flow speed was increased to the point where the flame tip was oscillatory, and the flame was on the verge of blowout with any further increase in speed. This corresponded to a mean flow speed of 243 cm/s at $\phi = 1.34$. In this case the sides of the flame adjusted their angle to the incoming flow, Fig. 2(a), resulting in a tip now located about 2.5 cm above the burner lip; this region was imaged by translating the burner relative to the optical setup. One example of a turbulent tip is shown in Fig. 9; a 760 x 640 pixel (17.3 x 14.6 mm) region is highlighted for later use in extracting the velocity. Figure 10 shows the corresponding set of 40 x 30 velocity vectors which were extracted on a regular grid using a 56 x 56 pixel (1.2 x 1.2 mm) box. This image (and others not shown) suggest that similar phenomena are occurring instantaneously on the turbulent tips as was seen in the steady, laminar flame tips. For example, the sudden change in velocity is seen on the flame sides, while the tip allows a considerably higher velocity associated with the volume expansion phenomenon; the mechanism of a reduced radius of curvature (Echekki & Mungal, 1992) leading to higher tip speeds appears to be at work in the turbulent tip. We do note that since the turbulent tip is highly unsteady, the velocity may appear to penetrate planar portions of the flame at speeds exceeding the laminar flame speed; however this is not the case as the velocity of the flame itself is not known. The strain rate, Fig. 10, again shows good correspondence with the instantaneous flame shape.

CONCLUSIONS

This work has demonstrated the applicability of On-line PIV to the study of laminar and turbulent premixed flames. The technique, with judicious seeding, is able to reveal several details about the flow into and out of premixed flames. The present results agree with previous studies which performed measurements at the flame side and tip using particle tracking and continue to show the high speeds sustainable at the flame tip. Our results show that the potential core is largely unaffected by the presence of the flame while the region of influence is primarily the preheat zone; this observation is different from LDV measurements on a similar burner. New findings are: the velocity profile becomes wake-like past the flame tip, a vorticity concentration occurs just past the flame tip and that the strain and dilatation serve as good flame zone markers; these results have now been observed in numerical simulations. The present measurements can be near instantaneous, occurring within a few tens of microseconds. The technique reveals planar velocity measurements as well as quantitative information on the location of the flame surface through the change in seeding density. The vorticity and strain are determined to within the accuracy of the measurement subregion. In principle, we see no reason why this approach cannot be used in non-premixed flames with equal success; our own preliminary efforts have already led to promising results.

ACKNOWLEDGEMENTS

We are grateful for the help of S. P. Gogenini and T. Ding in data reduction and processing, and T. Poinsot in discussion of numerical flame results.

REFERENCES

Adrian, R. J. (1984) Scattering particle characteristics and their effect on pulsed laser measurements of fluid flow: speckle velocimetry vs. particle image velocimetry. Appl. Opt. **23**, 1690.

Adrian, R. J. (1986) Image shifting technique to resolve directional ambiguity in double-pulsed velocimetry. Appl. Opt. **25** (21), 3855.

Adrian, R. J. (1991) Particle-imaging techniques for experimental fluid mechanics. Ann. Rev. Fluid Mech **23**, 261.

Dong, R., Chu, S. and Katz, J. (1992) Quantitative visualization of the flow within the volute of a centrifugal pump. Part A: technique. Jr. Fluids Eng. **114**, Trans. ASME, September 1992, 390.

Driscoll, J. F., Sutkus, D. J., Roberts, W. L., Post, M. E. and Goss, L. P. (1993) The strain exerted by a vortex on a flame - determined from velocity field images. AIAA-93-0362, 31st Aerospace Sciences Meeting, Reno, NV, January 1993.

Dudderar, T. D. and Simpkins, P. G. (1977) Laser speckle photography in a fluid medium. Nature **270**, 45.

Echekki, T. and Mungal, M. G. (1990) Flame speed measurements at the tip of a slot burner: effects of flame curvature and hydrodynamic stretch. Twenty-Third Symp. (Int.) on Comb., The Combustion Institute, 455.

Goss, L. P., Post, M. E., Trump, D. D. and Sarkar, B. (1991) Two color particle imaging velocimetry. J. Laser Applic., Winter 1991, 36.

Grousson, R. and Mallick, S. (1977) Study of flow pattern in a fluid by scattered laser light. Appl. Opt. **16**, 2334.

Landreth, C. C. and Adrain, R. J. (1988) Electro-optical image shifting for particle image velocimetry. Appl. Opt. **27** (20), 4216.

Law, C. K. (1988) Dynamics of stretched flames. Twenty Second Symp. (Int.) on Comb., The Combustion Institute, 1381.

Lewis, B. and von Elbe, G. (1961) Combustion, Flames and Explosion of Gases. Second Edition, Academic Press.

Lourenco, L. M. (1993) A velocity bias technique for PIV measurements of high speed flows. Appl. Opt. **32**, 12.

Lourenco, L. M., Gogineni, S. P. and LaSalle, R. T. (1994) "On-line PIV": an integrated approach. To appear Appl. Opt.

Lourenco, L. M., Krothapalli, A., Buchlin, J. M. and Reithmuller, M. L. (1986) A non-invasive technique for the measurement of unsteady velocity and vorticity fields. AGARD CP-413, Aerodynamic and Related Hydrodynamic Studies Using Water Related Facilities. 23-1.

Lourenco, L. M., Krothapalli, A. and Smith, C. A. (1989) Particle image velocimetry. Advances in Fluid Mechanics Measurements, M. Gad-el-Hak, Ed. (Springer-Verlag, Berlin) 127.

Meynart, R. (1977) Flow velocity measurement by a speckle method. Second European Congress on Optics Applied to Metrology, SPIE **210**, 25.

Mizomoto, M., Asaka, Y., Ikai, S. and Law, C. K. (1984) Effects of preferential diffusion on the burning intensity of curved flames. Twentieth Symp. (Int.) on Comb., The Combustion Institute, 1933.

Molezzi, M. J. and Dutton, J. C. (1993) Application of particle image velocimetry in high-speed separated flows. AIAA Jr. **31** (3), 438.

Pickering, C. J. D. and Halliwell, N. A. (1984) Speckle photography in fluid flows: signal recovery with two step processing. Appl. Opt. **23**, 1128.

Poinsot, T., Echekki, T. and Mungal, M. G. (1992) A study of the laminar flame tip and implications for premixed turbulent combustion. Comb. Sci. and Tech. **81**, 45.

Post, M. E., Goss, L. P. and Brainard, L. F. (1991) Two-color particle-imaging velocimetry in a diffusion flame. 1991 Spring Technical Meeting, Central States Section of the Combustion Institute, Nashville, TN.

Reuss, D. L., Adrian, R. J., Landreth, C. C., French, D. T. and Fansler, T. D. (1989) Instantaneous planar measurements of velocity and large-scale vorticity and strain rate in an engine using particle-image velocimetry. SAE Tech. Paper No. 890616. Soc. Automot. Eng., Detroit.

Reuss, D. L., Adrian, R. J. and Landreth, C. C. (1989) Two-dimensional velocity measurements in a laminar flame using particle image velocimetry. Comb. Sci. and Tech. **67**, 73.

Wagner, T. C. and Ferguson, C. R. (1985) Bunsen flame hydrodynamics. Comb. and Flame **59**, 267.

Willert, C. E. and Gharib, M. (1991) Digital particle image velocimetry. Expts. Fluids **10**, 181.

Yu, G., Law, C. K. and Wu, C. K. (1986) Laminar flame speeds of hydrocarbon + air mixtures with hydrogen addition. Comb. and Flame **63**, 339.

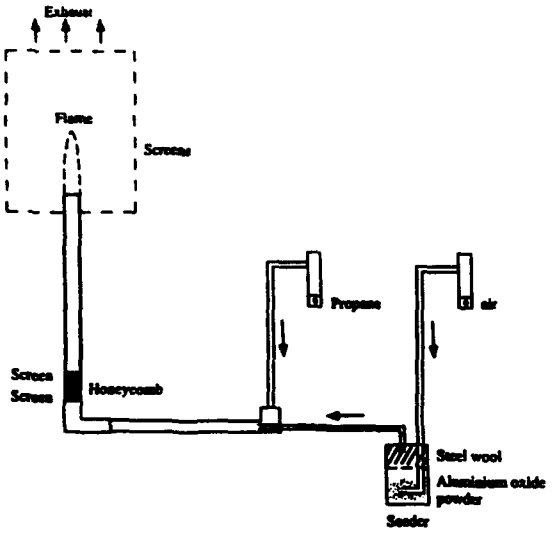

Fig. 1. Experimental arrangement for premixed flames.

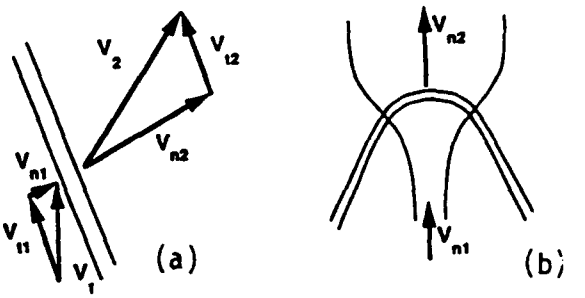

Fig. 2. Flow path at flame (a) side, (b) tip.

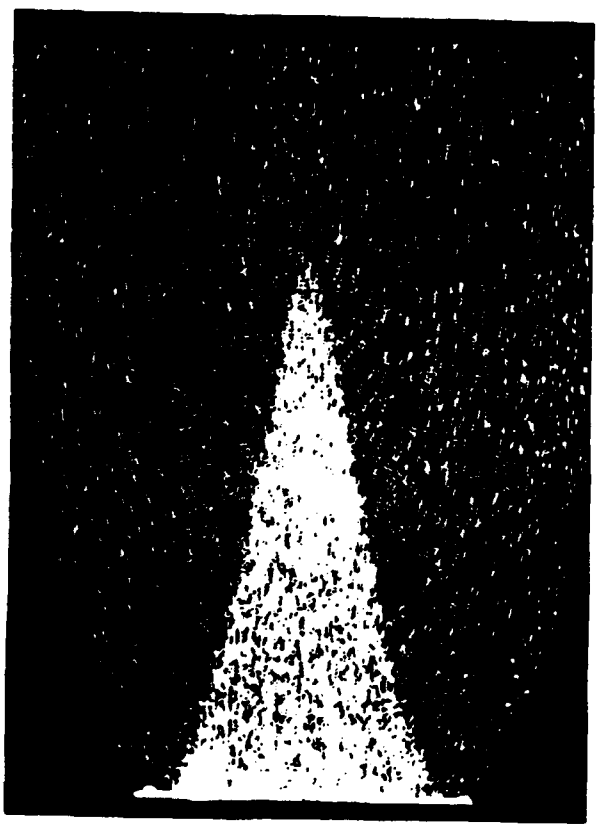

Fig. 3. PIV image of steady Bunsen flame. Re = 940.

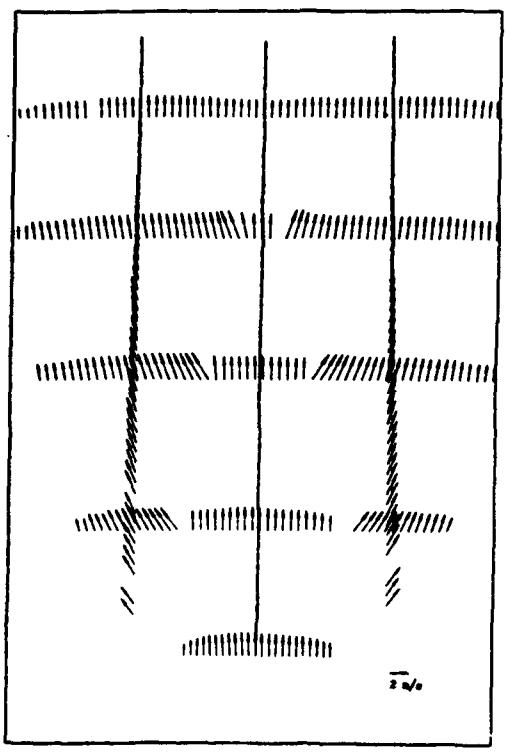

Fig. 4. Velocity vectors at select locations of Fig. 3, illustrating flow development.

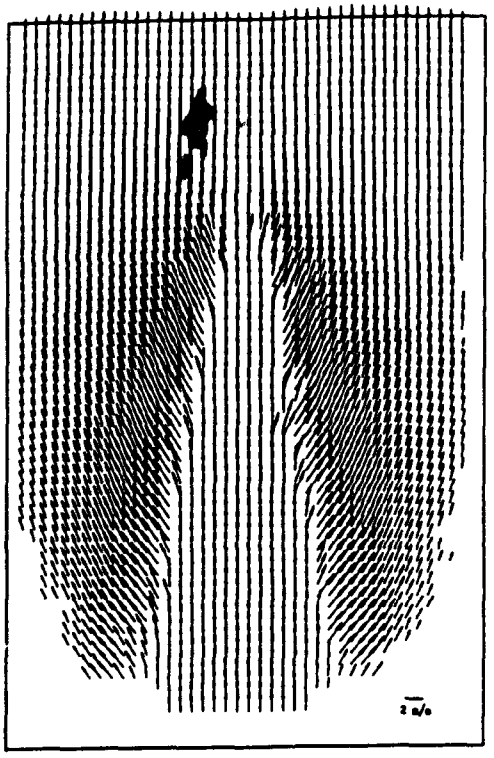

Fig. 5. Velocity vectors on 60 x 40 grid for steady Bunsen flame. Re = 940.

Fig. 6. Vorticity computed from Fig. 5.

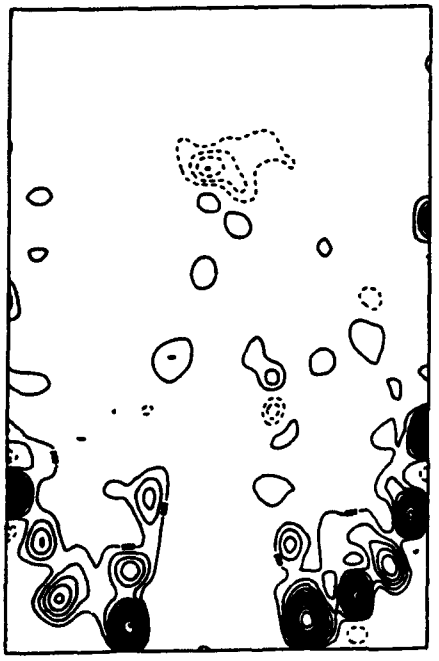

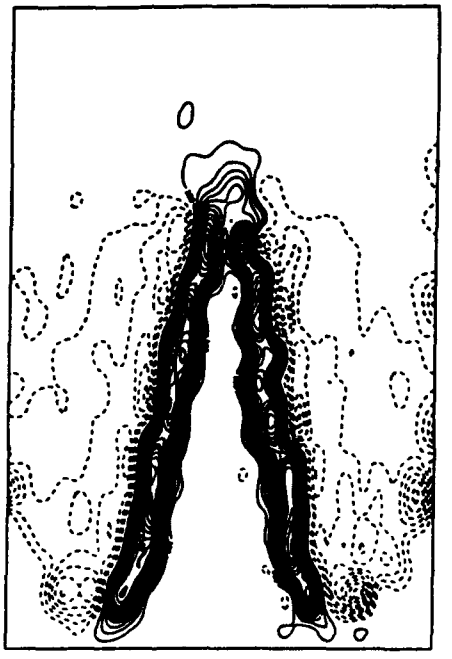

Fig. 7. Strain rates, S_{xx} (left), S_{yy} (right) computed from Fig. 5.

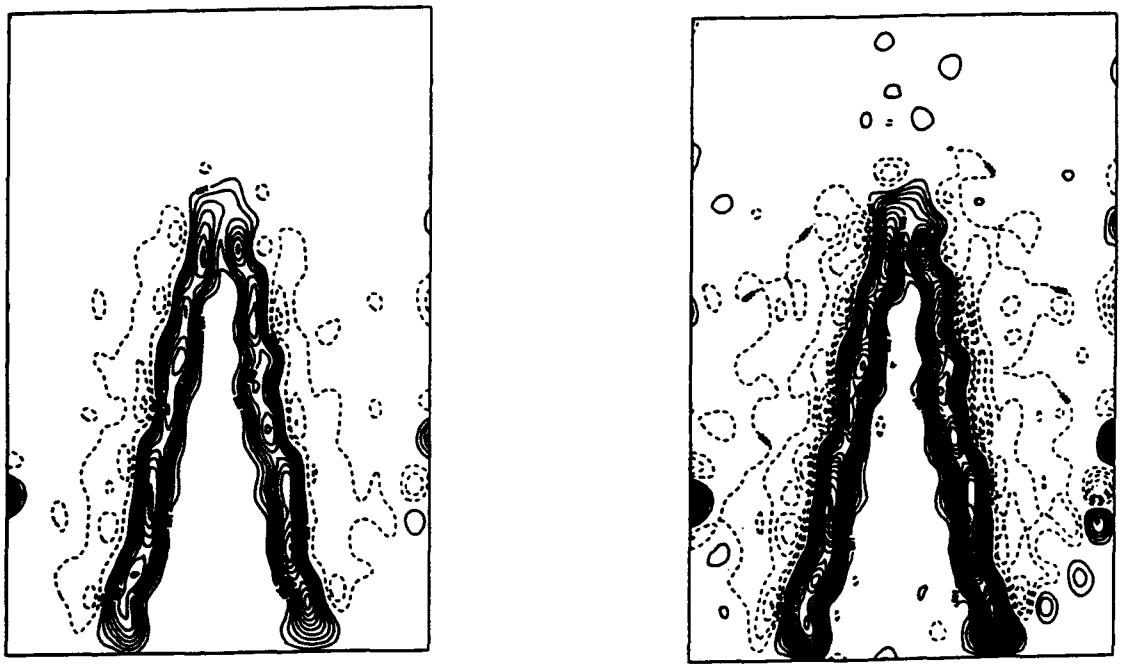

Fig. 8. Strain rate, S_{xy} (left), and dilatation (right) computed from Fig. 5.

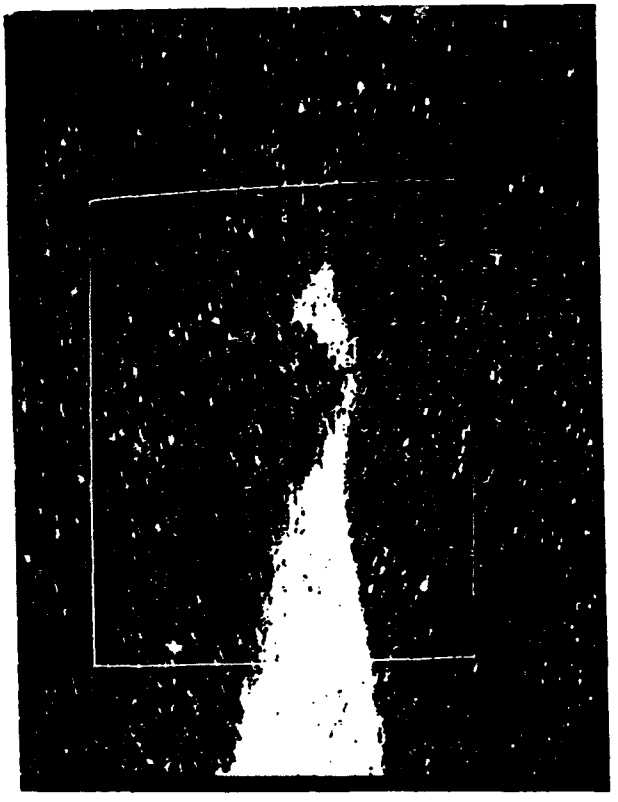

Fig. 9. PIV image of turbulent flame tip. Re = 1800.

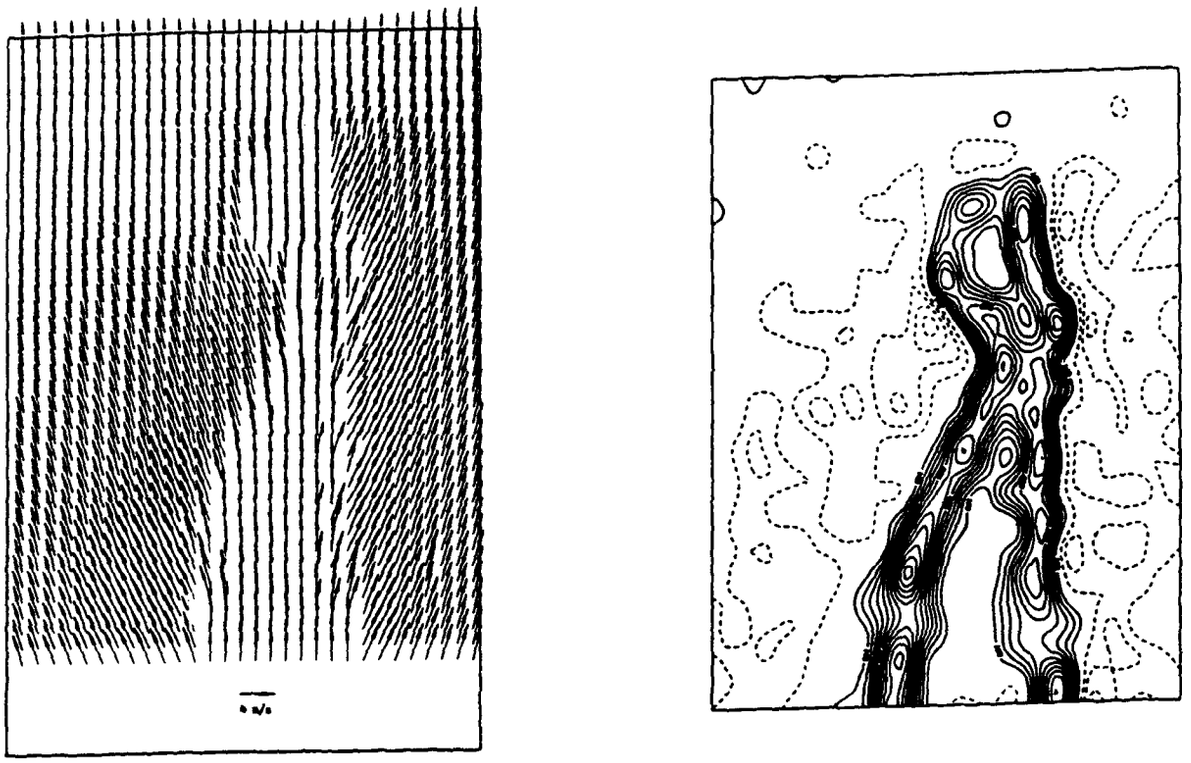

Fig. 10. Velocity vectors and strain rate corresponding to Fig. 9.

SIMULTAENOUS 2D MEASUREMENTS OF FLAME FRONT PROPAGATION BY HIGH SPEED TOMOGRAPHY AND VELOCITY FIELD BY CROSS CORRELATION

B. Lecordier - M. Mouqallid - M. Trinité
URA CNRS 230 CORIA
Université de Rouen
76821 Mont-Saint-Aignan Cedex (FRANCE)

Abstract

Premixed flame propagation has been studied in a simulated engine. A premixed flame is ignited in a constant volume chamber with different characteristics of turbulence. High speed laser tomography is used to visualize the flame propagation. To extract quantitative informations from laser tomography records (flame front location), a high resolution film acquisition device has been employed. In addition, cross-correlation Particle Image Velocimetry (PIV) technique has been developed to perform velocity field in fresh gases from two successive tomography images. Next an adaptative grid constructed from the flame front coordinate has allowed to obtain a local burning velocity.

1. Introduction

In engine cylinders, the turbulence is highly unsteady and the life time of the propagation is only of few milliseconds. In an aerodynamical point of view, the flame propagation is different at each cycle of combustion. These cycle to cycle variations are principally introduced by large eddies which are different from one cycle to another. Thus to define the characteristics of the turbulence, Hall. and Bracco (1986) had shown that cycle-resolved studies are necessary in order to dissociated the cycle to cycle velocity fluctuations from fluctuations found in each individual cycle. Actually, a large number of studies have been realized with one point time resolved velocity measurement (LDV). In order to contribute to increase of knowledge of interactions between the turbulence and the combustion, two or three dimensional time resolved diagnostics are necessary.

Up to now, the laser tomography has been extensively developed for many combustion studies. It allows to visualize and characterize the reaction zone thanks to different parameters such the fractal dimension or the local curvature. These parameters affords informations on influence of the turbulence on the combustion but any on the influence of the flame propagation on the turbulence. Nowadays, the Particle Image Velocimetry is in full expansion. This technics permits to obtain a quantitative flow mapping and it used the same principle of seeding that the flow visualizations. The combination of the PIV method and the laser tomography seems really suited to to study the interactions between the combustion and the turbulence.

The PIV method is based on two investigation methods. When the successive flow exposures are stored on the same physical support, the auto-correlation is performed. The second approach consists in recording successive and separated images of the flow, and applying cross-correlation to them. An advantage of the cross-correlation PIV method is its capability to determine a velocity field from a large range of seeding concentration and thus it can be directly used from laser tomography records

Our objective is to developed high speed tomography with a copper vapor laser. With this technic, the evolution of flame front parameters such as flame surface, fractal length and radii of curvature, can be studied. In addition cross-correlation PIV method can be used from two successive laser tomography records to measure detailed velocity vectors in the neighborhood of the flame front. Next an adaptative grid is realized to measure the local burning velocity. These simultaneous measurements of the flame front location and fresh gases velocity field close to the reaction zone permit to increase the knowledge on the process of interactions between the reaction zone and the turbulence.

2. Experimental facilities and High speed tomography.

A schematic diagram of experimental setup is shown on the figure 1. The combustion device presented by Floch et a.(1989) is composed of two main parts : a combustion chamber of 60 x 60 mm square cross section and 100 mm length, and an axisymmetrical, pneumatic driven, single shot piston mounted in a cylinder. Both parts are connected by means of interchangeable perfored blocks. Initial turbulence is generated in the combustion chamber by interaction of the jets due to the piston movement towards its top dead center. Energy and scales of turbulence can be modified by varying number and diameter of holes in the interchangeable turbulence generator, by adjusting the piston velocity or by igniting the mixture at different time after the piston arrival.

The chamber is initially filled by a propane-air mixture. The piston is then activated and locked on the inlet surface of the flow generator by means of an electronically controlled two stages compressed air supply on its rear face. The compression occurs in 90 ms and produce a compression ratio of 2.54. Optical access are provided by three rectangular quartz windows. A detailed view of the combustion chamber is shown in figure 1. The axis of the piston is monitored by an electronical sequencer. The output of which provided variable trigger pulses to control the timing of the ignition, cameras and laser pulses. The reproducibility of the piston motion is analyzed in real time by means of an opto-electronic position transducer installed on the piston rod.

Up to now, the reactant is seeded with silicone oil droplets generated by a blast atomizer. These particles are

evaporated at the flame front. Thus, oil droplets enable velocity measurements by LDV or PIV method only in the reactant mixture and they allow to obtain the location of instantaneous flame front. Refractory particles (ex : zirconium dioxide particles) can be used to simultaneous measurements of velocity in both reactant and product flow. With these particles mixed with oil droplets Armstrong et a. (1992) had shown that flame location can be indicated by the differing densities between reactant and product gaseous mixture. The mixture is spark ignited and can take place at two locations in the chamber. The spark can occur either at the center of the chamber using thin tantalum wire electrodes (d = 0.3 mm) or at the center of the chamber wall opposite to turbulence generator to simulate a wall ignition.

In our study, the laser tomography (LST) is used. This method is based on the visualization of a flow by illuminating micronic seeding particles within the flow with a laser sheet. For the most part in combustion studies, silicon oil droplets which evaporate at the flame are used. Thus, the instantaneous flame is differentiate on the LST records by the boundary between light (cold reactant) and dark (hot product) regions. To illuminate the flowfield an Oxford copper vapor laser (45 Watts) is used. It delivers 6.5 mJ per pulse with 100 ns pulse width at adjustable repetition rates up to 10000 Hz. The laser can also operated in the burst mode down to single pulse operation. The laser beam is focused with spherical and cylindrical lenses and directed to produce a 0.6 mm thick laser light sheet across the mid plane of the combustion chamber.

To obtain a time following of the flame propagation, high speed Cordin camera model 351, able to take up to 35000 frames per second has been used. The film used to record the LST is Ilford HP5 Plus (400 ASA). This device associated with the copper vapor laser allows cycle resolved studies presented by Hall and Bracco (1986). A typical photographic record of a propagating flame is shown on the figure 2.

To extract quantitative informations of photographic records, a high resolution film acquisition device has been used. A film scanner Kodak RFS 2035 connect with Macintosh computer (Quadra 950) digitizes each film picture. Its area array sensor provides six millions pixels per scan. Each frames (24mm*36mm format) is digitized in a 3072*2048 pixels either 24 bit (16 millions of colors) or 8 bit (256 grey scales). This device is able to conserve the high photographic film resolution and thus provides a powerful digitization film process to perform cross-correlation PIV algorithm from two successive images

The instantaneous flame sheet on the tomography record is shown to be the boundary between burned and unburned regions (Figure 2). In order to separate the two regions, a threshold algorithm is applied.

The LST pictures have a very good contrast between the burned and unburned regions. By using a simple thresholding procedure each picture is reduced to a bipolar image containing dark and bright areas representing burned and

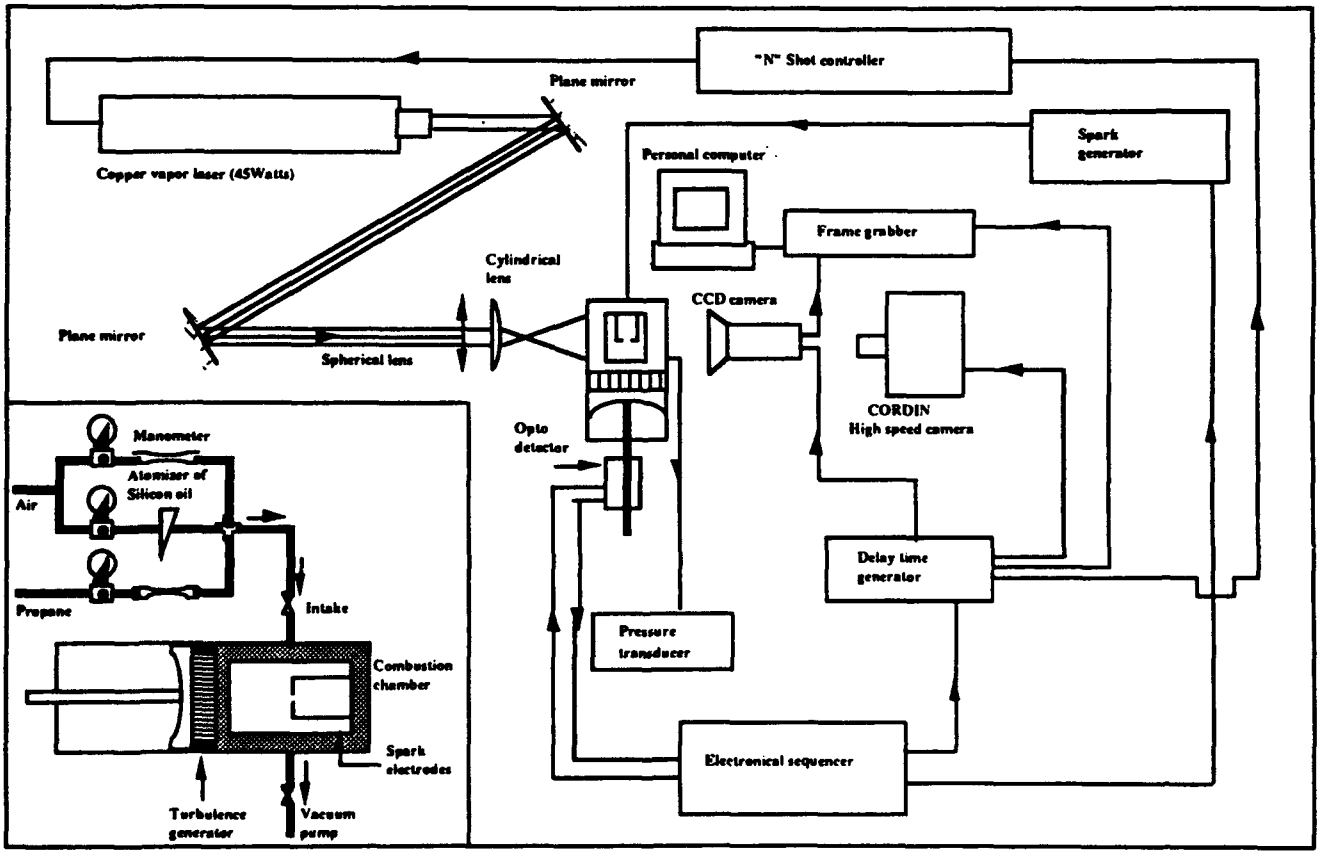

Figure 1 - Schematic of experimental setup

unburned states respectively. The burned gas "area" on the record is computed automatically by summing the number of pixels that have intensity values above a chosen threshold. This area is used to define an equivalent flame radius which can be linked to the mass fraction of burned gases.

The flame front coordinates are detected by simple intensity thresholding followed by an edge detection algorithm. An example of flame fronts for both laminar and turbulent flame are shown in figure 3. Next, each two dimensional flame contour is analyzed to characterize the influence of the turbulence on the shape of the reaction zone. All the treatments, such as fractal analyze, local radius of curvature or mean flame radius, used to characterize the flame front are presented by Mouqallid et a. (1994). The efficiency of the high speed tomography is the possibility to have a time evolution of all the flame front properties.

The purpose of this paper is not to describe the flame properties but it is to show the capability of the high speed tomography to simultaneously obtain the flame front location and the fresh gas velocity. The flame front properties will be exposed in other paper

3. Cross-correlation PIV method.

Up to now, the cross correlation PIV method has not been extensively developed. The lack of separate images in experimental research and the experimental difficulty to obtain two separate images in high speed flows has limited this technic to studies of relatively slow flows (ex : water flows). Nowadays, some acquisition devices permit to acquired two or more successive images with very short time delay and in the future, they will become more and more democratic. As an example, an original storage method on two half frames of a CCD camera has been developed by Lecordier et a.(1994). The time delay between the two flow exposures can be decrease to 10 µs and thus permits to study high speed flow.

The use of the cross-correlation PIV algorithm affords significant advantages in comparison with auto-correlation. A presentation of these two methods has been realized by Gray (1992) and a comparison has been made by Keane and Adrian(1993) . The most significant advantage of the cross-correlation is the measurement of a large range of velocities on the same flow which automatically includes zero and reverse velocities without have recourse to an external "image shifter", "image labelling" or other. In addition Rouland et a. (1994) has shown that the cross-correlation can be used from high density of seeding particle whereas the auto-correlation

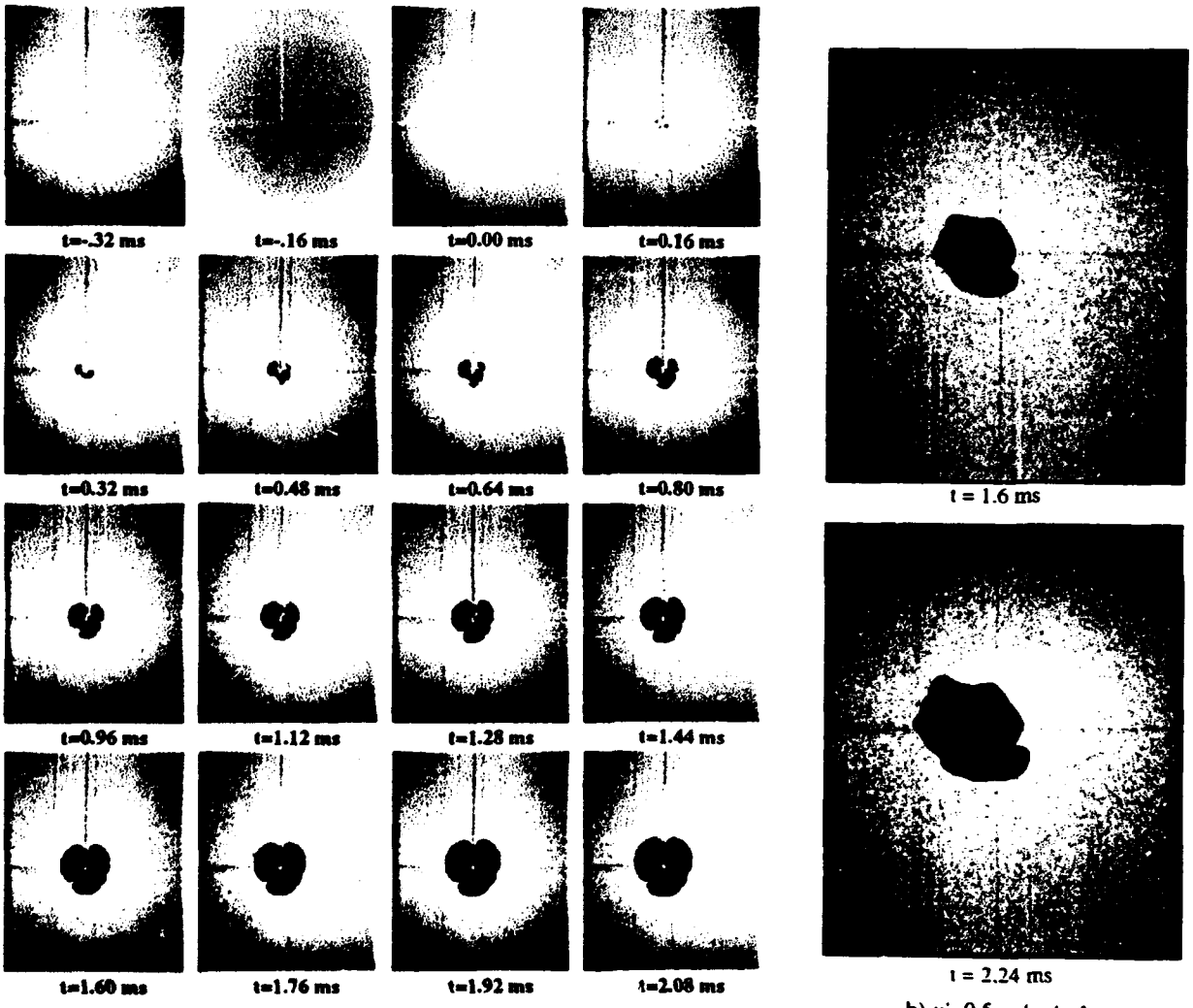

a) u'= 0.1 m/s, ϕ=1.

b) u'=0.5 m/s, ϕ=1.

Figure 2 - Example of laser tomography records.

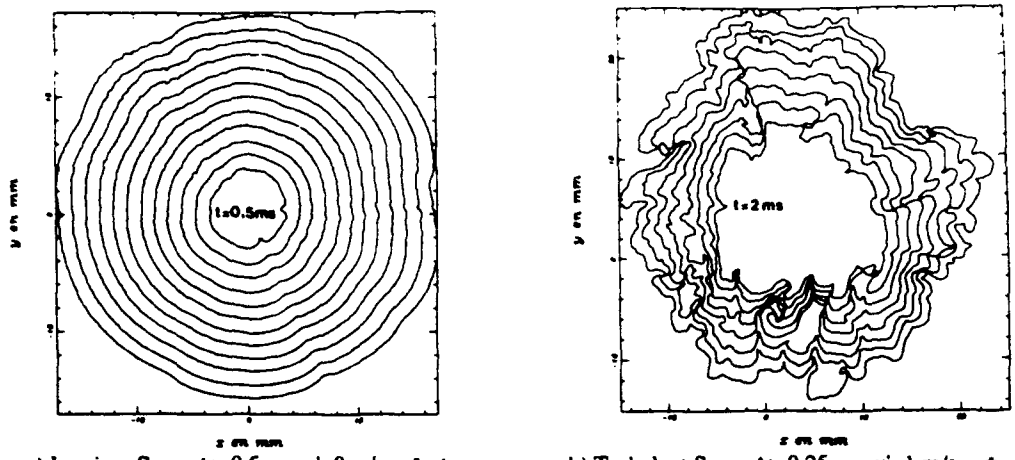

a) Laminar flame Δt=0.5 ms, u'=0 m/s, Φ=1 b) Turbulent flame Δt=0.25 ms, u'=1 m/s, Φ=1.1

Figure 3 - Time evolution of laminar and turbulent flame fronts

with the same concentration of seeding is not applicable. Thus for a same seeding concentration and the same spatial resolution of acquisition device, the cross-correlation provides a larger investigation area than the auto-correlation.

Actually the determination of the velocity field is principally realized from numeric correlations, using Fast Fourier Transform. This choose is due to important developments of computers which now compute a velocity field in a reasonable time. In few cases, the treatment can be considered as a pseudo real-time processing. The massive use of numeric pictures (High resolution film scanner, frame grabber, numeric video...) and the convenience of "on-line" capture of PIV images associated to pseudo real-time processing have also contributed to full expansion of numeric treatments. But initially, an optical treatment of photographic images was the one mean to resolve the spatial scales of flows. Now, the difference between optical and numeric treatments is less important, thanks to the increase of the spatial resolution of numeric acquisition devices. In addition, numeric methods presented by Willert and Gharib (1991) to measure the particle displacement to sub-pixel accuracy permit to increase the range of velocity determined from numeric correlations.

4. Necessity of short particles displacements to study the turbulent flows.

The most important problem to study turbulent flows is the 3 dimensional effects which introduce out-off pattern motions and thus decrease the correlation between the two particle images. To reduce these 3D effects of flows, the maximum particle displacement should not be greater than the thickness of the laser sheet. Thus, experimentally it is necessary to store the successive flow exposures with very short time delay and work on low displacements. In addition, to have a good correlation, the maximum of particle displacement should be included in ±N/4 pixels on the acquisition device, where N is the size of the correlation window.

One of advantages of the cross-correlation PIV method is the possibility to obtain very low particle displacement including zero displacement. This is due to the absence of the central peak. The effect on the very low displacement of the self-correlation peak for the auto-correlation treatment is shown by Rouland et a.(1994). The self-correlation peak introduce a dead zone of around five square pixels which doesn't permit to measure particle displacement lower than around five pixels. Thus, the cross-correlation PIV method is more appropriate to study low displacement and therefore the studies of turbulent flows.

Nevertheless, when the correlation is numeric, the decreasing of the maximum particle displacement reduce the range of velocity components (u,v) and it produces discretization effects on the velocity field. The figure 4-a shows an experimental velocity field with velocities included between ±2 pixels. The discrete values of velocity components are significant and the velocity field is not clearly resolved. The areas without vector represent a zero particle displacement. The cross-correlation treatment of the two particle images is realized with window size of 64 pixels. The figure 4-b presents the same velocity field computed with an interpolation of the correlation peak to obtain the particle displacement with a sub-pixel accuracy. A two dimensional gaussian curve is used to interpolate the correlation peak. This velocity field is shown without smooth or extraction of spurious vectors. In this case, the velocity range included between ±2 pixels is resolved and the discretization effect on the velocity components are not observable. In addition, we can notice that the sub-pixel method doesn't introduce a modification of velocity field in its whole as the smooth but increase the accuracy of each individual vector.

To conclude this part, we can say that the cross-correlation PIV method affords significant advantages to study turbulent flows thanks to the possibility to determined low particles displacement. Afterwards, all the velocity field presented will be obtained by cross-correlation algorithm of two successive tomography visualizations and the particle displacement will be determined with sub-pixel accuracy.

5. Application of cross-correlation PIV

The first case studied is a laminar premixed flame propagation in a propane-air mixture with an equivalent ratio equal to unity. The initial turbulence in the chamber is weak (≈ 0.1 m/s) and the mixture is seeded with fine oil droplets. The laser tomography images are recorded with a high speed camera. The repetitive rate of frames recording is 6250 hz (laser frequency) and thus the time between two successive

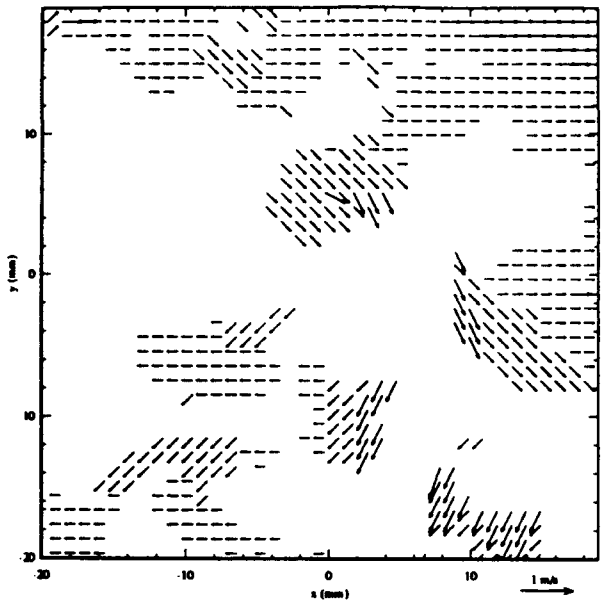

Figure 4-a without sub-pixel

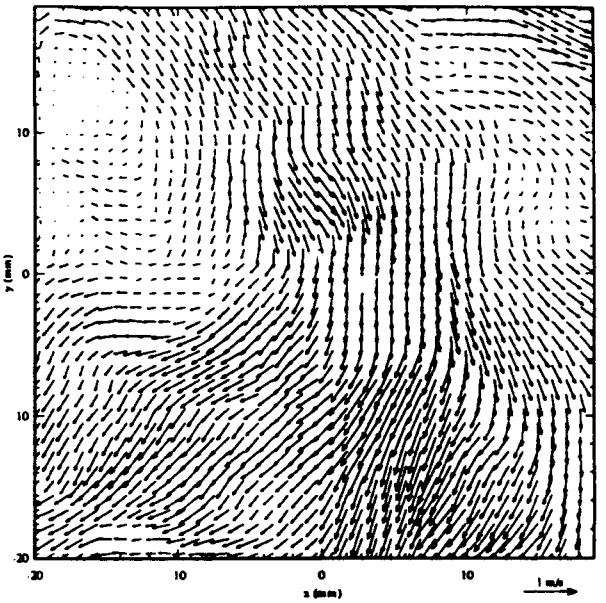

Figure 4-b : with sub-pixel interpolation

Figure 4 - Two same velocity field computed with and without sub-pixel interpolation

acquisitions is 160 µs. To computed the velocity field and the flame front location, a part of each flame picture is digitized in a 1440*1740 pixels and analyzed on a workstation (SUN).

The figure 2 illustrates the type of images which can be recorded from the flowfield within the combustion chamber during one cycle of combustion. The zero time reference corresponds to the spark. On these pictures, the flame front exhibits weak wrinkled patterns principally introduce after the spark in the early stage of the flame. After the flame front structures stay similar. The Time evolution of this flame and its velocity field are shown in the figure 5. The velocity field, as for it, is computed with a cross-correlation PIV method and each vector is obtained with the sub-pixel accuracy. The window size of treatment is 64*64 pixels. The figure 5 serves to illustrate the efficiency of the cross-correlation PIV method used to determined the velocity field. The time evolution as well as the spatial distribution of the velocity vectors are simultaneous obtained. All the results are represented without smooth or extraction of invalid data. Only a validation criterion is used during velocity computation. It consists in locating the highest peak in the correlation window, in assuming this peak corresponds to the correlation peak, compares it to the second tallest peak (maximum noise of correlation). If the ratio of the tallest peak to the second tallest peak is less than 1.05, the velocity vector computed is not retained. In the figure 5, we can noticed that this validation criterion only affects a small number of vectors. Added to that, the majority of velocity vectors are determined with a signal/noise ratio higher than 1.2.

The second study is a case of premixed flame propagation in the combustion chamber with a larger turbulence intensity than the previous case. The equivalent ratio is equal to unity and the velocity fluctuations are of order of 0.5 m/s. Contrary to the previous case, all the flame pictures are not exposed in this paper (Figure 2-b) but the principle of recording and treatment to obtain the time evolution of the velocity field and the flame front location is similar.

In the framework of our study, it seems that the turbulent velocity field is well resolved in spite of a large window of analyze (64*64 pixels ≈ 1.8 mm*1.8 mm). To illustrate our point of view, the figure 6 shows two turbulent velocity fields corresponding to flame pictures exposed figure 2-b. The treatment is realized with 64*64 window size. The velocity field seems well resolved. Nevertheless, an treatment with 32*32 window size will be better to appreciate the strong velocity gradients. The limitation of 32*32 treatment is the decreasing of the noise/signal ratio when the velocity is large. To solve this limitation, the velocity field can be computed with 64*64 window size to estimate the first velocity field without determinate the strong velocity gradients. Next, the velocity field is compute a second time with 32*32 pixel windows. But to increase the correlation, the two windows, corresponding to the first and the second exposure, are spatially shifted of velocity vector previously obtained (64*64 pixels).

To conclude this part,we want focus your attention on the capability of the cross-correlation PIV method to obtain a velocity field with high particle concentration and thus it allows to simultaneous measure the flame front location and the fresh gas velocity. Nevertheless, the figures 5 and 6 indicates that the fresh gases velocity near to the flame front are not measured. This problem is due to the large difference of intensity between the reactant and product which is a disruptive factor for the correlation. To remedy to this problem, we present a new approach of the PIV based on an adaptative grid.

6. Principle of an adaptative grid.

All the velocity field previously presented (Figure 5 and 6) had been computed from a regular mesh (Figure 7). This technic are not suited to resolve the velocity field close to the

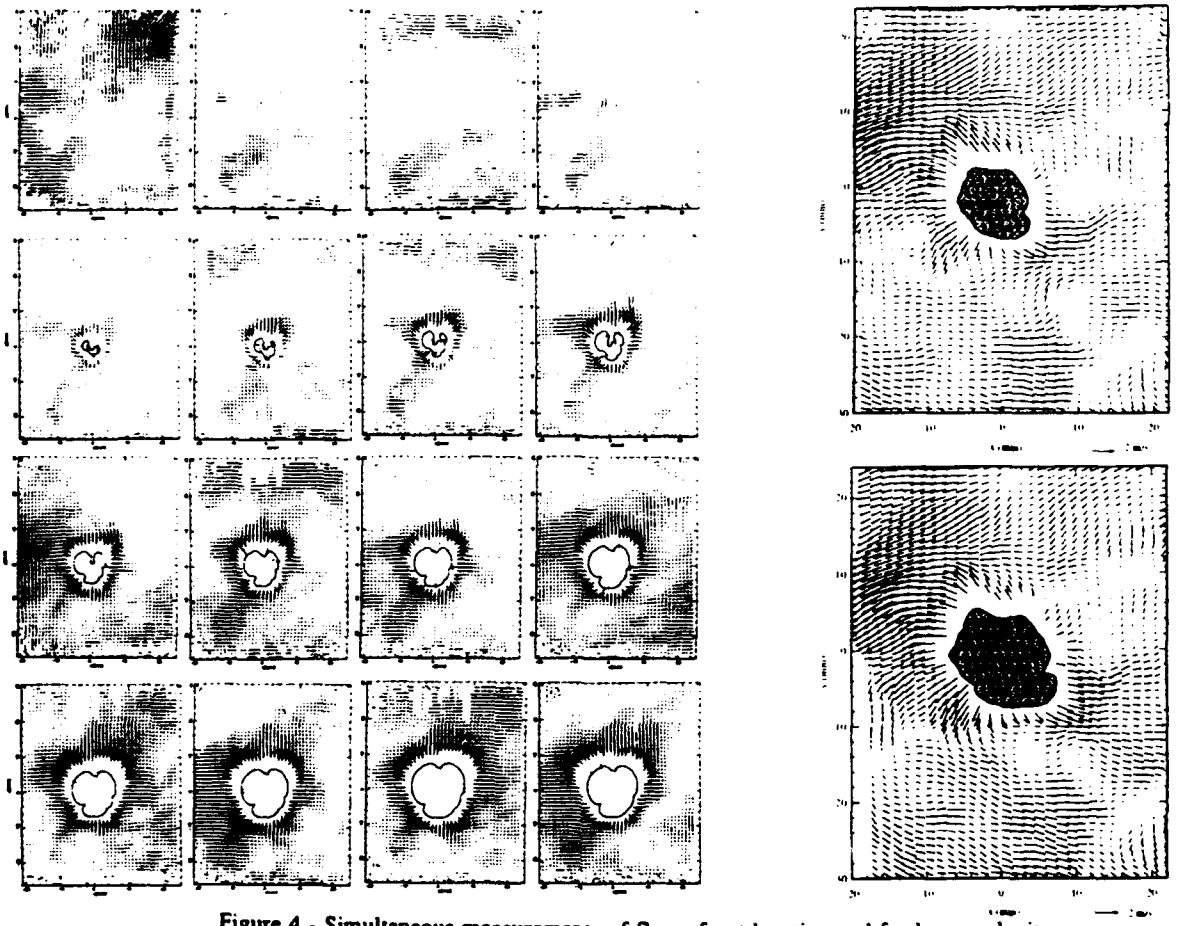

Figure 4 - Simultaneous measurements of flame front location and fresh gas velocity

reaction zone. Up to now, the seeding particles are burned in the reaction zone and thus the flame pictures exhibit an important difference of intensity between the burned and unburned regions. When a window of analyze contains this threshold, the correlation is disrupted and thus the velocity vector can not be retained. This problem explains why on the all velocity fields previously presented, the instantaneous velocity near to the reaction zone are not determined. In these conditions, it seems difficult to characterize the interaction between the combustion and the velocity field.

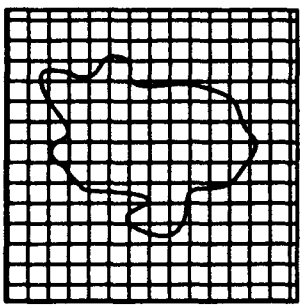

Figure 7 - Principle of regular mesh.

To resolve the velocity field close to the flame front, we have used an adaptative grid constructed with the directions perpendicular to the flame front. Figure 8 illustrates the principle of this adaptative grid. Each window of analyses is placed on the two successive flame fronts and their are oriented with its normal direction. The correlation of these two windows gives the fresh gases velocity in front of the reaction zone. From this adaptative grid, the flame speed (U_f) and the normal and tangential components of the fresh gases velocity (U_{gt},U_{gn}) in the flame front coordinate system (τ,v) are obtained. Thus, the difference $U_c=U_f-U_{gn}$ gives the burning velocity.

In the first place, to realize a validation of all the velocities computed from this adaptative grid, synthetic images have been used. Two synthetic images are created to obtain a vortex velocity field. The contour used to perform

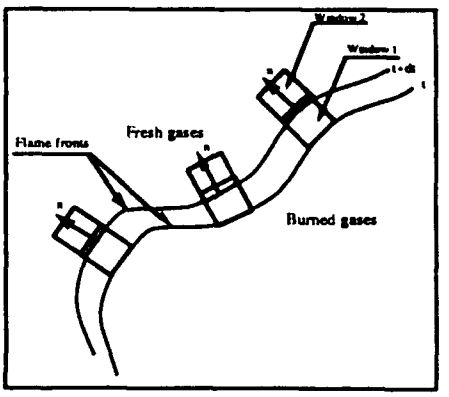

Figure 8 - Principle of adaptative grid.

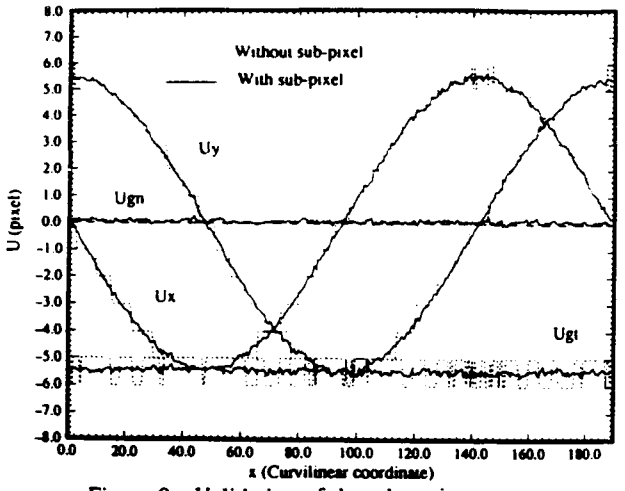

Figure 9 - Validation of the adaptative grid from synthetic particle images.

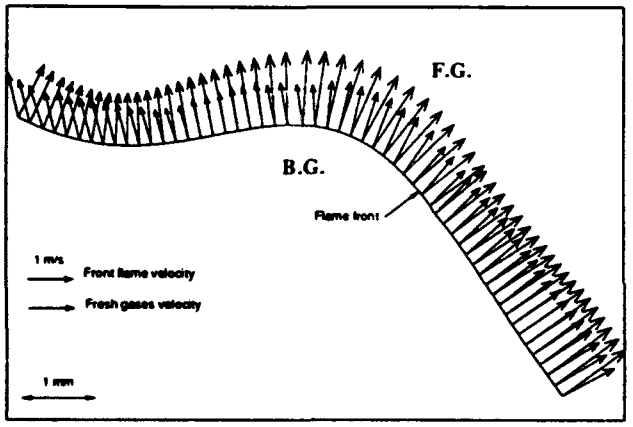

Figure 10-Example of the adaptative grid on a part of a turbulent flame front (u'=0.5 m/s, ϕ=1, P=2.3 bar)

the adaptative grid computation is a circle centered on the vortex center. The analyze windows go round the circle and thus the normal component should be equal to zero whereas that tangential component should be constant. The figure 9 shows the variation of these two components (U_{gt},U_{gn}) all around the circle. This plot shows that the normal component is equal to zero and that the tangential component is constant. The behavior of these two components validates the measurements of the velocities in a no regular mesh.

In addition, the velocities computed without sub-pixel interpolation have been superimposed on the plot (dash-lines). These velocities show the discretization effects of numeric correlations. The draw of the components (U_x,U_y) obtained from (U_{gt},U_{gn}) exhibits the efficiency of the sub-pixel interpolation. The component variation (U_x,U_y) should be sinusoidale. This variation is not resolved without sub-pixel interpolation. The continuous curves are obtained without smooth but only by a increasing of the accuracy of each individual vector thanks to the correlation peak interpolation.

7. Results

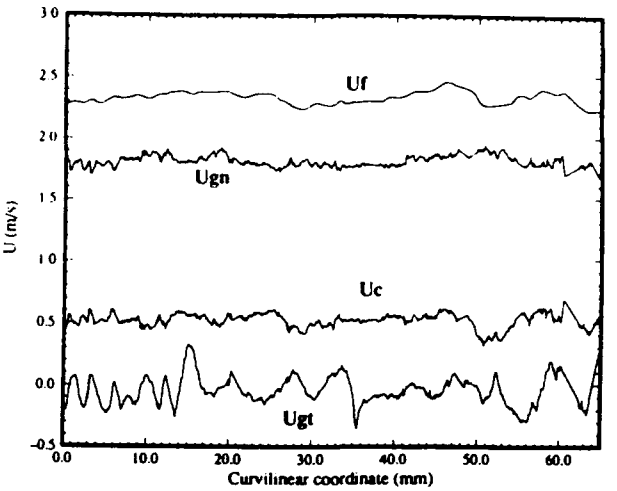

Figure 11 - Velocities versus curvilinear coordinate

The adaptative mesh has been used from flame tomography visualizations presented figure 2-b. The figure 10 shows a treatment on a part of turbulent flame front. The longer vector perpendicular to the flame front represents the flame front velocity. The other vector is the fresh gases velocity. On this plot, we can noticed that when the flame front is flat, the fresh gases velocities is brought into alignment with the flame front velocity. On the other hand, as soon as, the radius of curvature of the flame front decreases, the tangential components of fresh gases velocity modified this alignment. Thus it appears that this approach to study the interaction between the reaction zone and the turbulence is very promising.

From this adaptative grid, at any point of the flame front, we can computed the tangential and normal velocity of fresh gases. The figure 11 shows the evolution of all these velocities in a case of a laminar propagation, versus a curvilinear coordinates of the flame front. On this plot, we can see that all the velocities are about constant and that the tangential velocity is approximately equal to 0. From these velocities computed all around the flame front, we can deduce mean velocities. An example of time evolution of these mean velocities obtained in a laminar propagation is shown figure 12. On this plot, we can noticed that the tangential component of fresh gas is negligible and that the flame front speed is constant. On the other hand, the burning velocity decreases. This indicates that the PIV method based on an adaptative grid allows to estimate the effects of the local curvature modifications of the reaction zone on the burning velocity. For this case, the decreasing of burning velocity is due to the increasing of local radius of curvature of the reaction zone during the propagation.

The tangential and normal velocities of the flame front afford significant knowledges on the process of interaction between the reaction zone and the turbulent field. In the future, we hope computed new flame characteristics such as the strain rate or the burning velocity.

8. Conclusions

Compared to auto-correlation, cross-correlation is more appropriate to study turbulent flows. The ability to measure

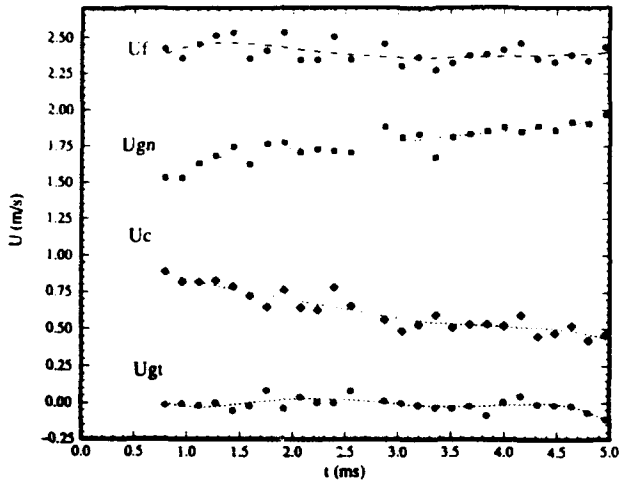

Figure 12 - Evolution of mean velocities

reverse flows and short particle displacements including the zero velocity permit to work on short displacements to limit the 3-dimensional effects such as displacement fluctuations or out-off motions. And the decreasing of number of velocity values computed from numeric correlations is counterbalanced by the determination of particle displacement with the sub-pixel accuracy.

The capability of the cross correlation PIV method to provides a velocity field from high density particles images has been presented. Therefore it can be used from laser tomography records of turbulent flame to simultaneously obtain the flame front location and the fresh gas velocity. The good knowledge of the turbulence properties with a sufficient accuracy will allow to compare our experimental study to numeric simulations realized with the same initial conditions (example DNS).

In addition, the use of an adaptative grid to perform PIV algorithm permits us to measure the velocity field close to the reaction zone in the flame front coordinate system and thus to deduce the local burning velocity and its evolution during the flame propagation. This approach seems very promising to study the interactions between a flame front and a turbulent field. We think also that this principle of adaptative grid can also be used to boundary layers studies.

References

(Symposium proceedings)
N. W. H. Amstrong, A.M. Shand, K.N.C. Bray, P.R. Ereaut, PIV applied to premixed turbulent flames, Optical Methods and Data Processing in Heat and Fluid Flow (2-3 April 1992 City University LONDON))

(Symposium proceedings)
A. Floch,M. Trinité,F. Fissow,T. Kageyama,CH. Know, A. Pocheau, "Flame propagation behavior in a variable hydrodynamic constant volume combustion chamber". 12th International Colloquium on Dynamics of Explosions and Reactive Systems, Ann Arbor, 1989.

(Symposium proceedings)C. Gray (1992). The evolution of particle image velocimetry (Optical Methods and Data Processing in Heat and Fluid Flow (2-3 April 1992 City University LONDON))

(Journal article)
M.J. Hall. and F.V. Bracco, "a cycle-resolved velocity and turbulence measurements near the cylinder wall of a firing S.I. engine" SAE Report 86, 1530 (1986)

(Journal article)
R.D. Keane and R.J. Adrian, Theory and simulation of Particle Image Velocimetry, Laser Anemometry advances and applications, 1993, 2052, 477-492.

(Journal article)
B. Lecordier, M. Mouqallid, S. Vottier.,E. Rouland,D. Allano, and M. Trinité, CCD recording method for cross-correlation PIV development in high speed flow. Experiments in Fluids, (to be published 1994).

(Symposium proceeding)
M. Mouqallid, B. Lecordier and M. Trinité, High speed tomography analysis of mixture no uniformity on flame propagation in simulated internal engine. (Proposed to SAE 1994)

(Symposium proceeding)
E. Rouland,S. Vottier,B. Lecordier and M. trinité, Cross-correlation PIV development for high speed flow with a standard CCD camera. The institute of Mechanical Engineers city, University London, 14-15 April 1994.

(Journal article)
C.E. Willert and M. Gharib, Digital Particle Image Velocimetry, Experiment In Fluids, Vol 10, (1991).

VELOCITY MEASUREMENTS IN TURBULENT PREMIXED FLAMES: DEVELOPMENT OF A PIV MEASUREMENT SYSTEM AND COMPARISON WITH LDV.

Nicola Paone

Dipartimento di Meccanica, Università di Ancona,
via Brecce Bianche, I-60131 Ancona, Italia.

ABSTRACT.

The development of a PIV system for measurements in premixed turbulent flames is presented; it is based on photographic acquisition of double exposed images, employing a doulble oscillator Nd-Yag laser. Seeding of the flow is discussed. The PIV system is applied to two different flames: its performance is optimized on a premixed unconfined LPG flame produced by a Bunsen burner, then it is applied to a larger confined CH_4 flame burning inside a transparent combustion chamber. Comparison with LDV measurements is presented. Processing of the velocity measurements by the two techniques allows observation of turbulent structures in space and time; results are presented with main attention to the measurement techniques and to the comparison of the results achievable by employing each of them.

1. INTRODUCTION.

Particle Image Velocimetry (PIV) has become at present a powerful measurement technique suitable for the experimental investigation of a large variety of flows. The study of turbulent flames, at industrial scale, is a field of great interest, due to the more and more demanding requirements for the decrease of pollutant production and emission from the combustor and to the necessity of increased efficiency. The measurement of the flame velocity field is significant for the evaluation of mass transport and heat transfer phenomena which act within the flame. A rather large experience is already available on velocity measurement in flames by Laser Doppler Velocimetry (LDV). This non-intrusive measurement technique can provide the three-dimensional velocity field, in terms of mean velocity components and turbulent fluctuations; measurements are local and are performed in time, according to an eulerian observation of the phenomena. Turbulent structures are measured by processing the time records of local velocity; time scales can be computed if velocity data are sampled at a sufficiently high repetition rate. Such an approach, although feasible, implies very high data rates which are rather difficult to achieve in combusting flows, where seeding problems are particularly difficult to solve.

PIV therefore appears as a very useful technique for measuring the velocity field in combusting flows, which can provide complementary results to those obtained by LDV. Some examples are reported in Armstrong et a. (1992), Lewis et a. (1987), Logan and Smith (1989), Reuss et a. (1989-1990). The measured vector field can be used to observe directly large turbulent structures in space and therefore exctract informations related to convective mass and heat transfer inside the flame. The inherently instantaneous nature of PIV velocity field data allows to freeze motion; measurements on a turbulent flow are therefore different from one image to another and clearly show how a turbulent flow is due to the convection of vortical structures superimposed to the mean flow. These structures, whose dimensions are spread across a wide range, are responsible of convective phenomena. Spatial resolution of PIV measurements constitutes the major limitation to the detection of spatial structures within the flow; in fact, by PIV it is only possible to resolve structures whose dimension is at least twice the distance among two adiacent measurement locations in the grid of points laid upon the measurement plane, according to the Shannon sampling theorem. PIV measurements are therefore low pass filtered in the spatial frequency domain of the image of the flow. This limitation is more and more stringent when PIV is applied to large scale flows and when seeding density is poor; this is the case of large industrial combustors.

With the aim to develop a PIV system suited for velocity measurements in flames of industrial interest and in order to develop the necessary experimental skill in performing such experiments, at University of Ancona it has been initiated a program devoted to LDV and PIV measurements on different premixed flames. It has been chosen to develop the PIV measurement chain on a small scale flame produced by a Bunsen burner and then to extend the application to a combustion chamber operating with a larger premixed combustor.

2. DEVELOPMENT OF A PIV SYSTEM FOR MEASUREMENTS IN FLAMES.

When considering the design of a PIV measurement system to be applied to a combusting flow, the weak block of the measurement chain clearly appears to be the image acquisition.

Being image acquisition the step in which information is recorded, all related measurement problems need to be addressed with particular attention; in fact it is fundamental to stress that, as in any other measurement procedure, no data processing technique will ever be capable of extracting information which was not previously recorded. Data processing will then be important in terms of minimum signal to noise level which can be processed, but the quality of the results, in terms of uncertainty and resolution, relies mostly on the quality of the recording at the very first stage in the measurement procedure. Therefore main attention in this work is devoted to the process of image formation and recording.

Three elements play their role in image formation: a)

seeding particles, b) pulsed light sheet illumination, c) photographic acquisition. They are closely related to each other and need to be addressed together.

As in any other large scale flow, PIV image acquisition in large flames suffers of limitations related to the necessity to resolve very small particle images over a rather large field of view. In this work the objective was to be able to measure velocity over flow fields having up to 200 mm width, employing standard 24x36 mm camera, therefore minimum magnification between image and object is M ≈ 1/6. In a combusting flow usually metal oxide particles are employed, which have the capability to survive to the high temperatures across the flame front and are available at diameters of the order of 1 μm, Witze and Baritaud (1986). Their aerodynamic behaviour is sufficient to follow turbulent velocity fluctuations in the frequency range which is measurable by LDV and therefore are also suited for PIV applications. Film resolution should be chosen after evaluation of average particle image dimension; diffraction, image blurring due to motion, focussing etc., impose the choice of films having at least 100 line pairs/mm. Particle dimension affects also scattering efficiency and the total amount of energy available to form a particle image depends on density of incoming energy, on scattering efficiency and again on M. In order to record images of small tracers with a small M it is necessary therefore to employ very high energy for the illuminating light source. Pulsed laser illumination is consequently the only possible choice.

In this work it has been employed a double oscillator Nd-Yag laser, which operates on its second harmonic, producing two green light pulses (λ=532 nm) having an energy of 105 mJ/imp and a duration of about 12 ns. The two lasers have been synchronized by controlling the cavity Q-switch by a variable delay pulse generator, which has an accuracy of 10^{-12}s, and can therefore produce light pulses with a variable time delay Δt which can be very precisely set to the desired value. The system is triggered by the flash signal of a standard photographic camera. In order to maximize light intensity, the light sheet is expanded to the minimum necessary lateral dimension and it is focussed in order to minimize its thickness; according to the dimension of the scene this implies the use of different cylindrical and spherical lenses.

For given particle dimension, image magnification and laser energy, other parameters can be used to improve sensitivity of the recording system; they are film sensitivity and recording optics numerical aperture. Previuos experience showed that a good compromise between film sensitivity and resolution is achieved with Kodak TMax 400 ASA, which is employed in all the following measurements; a 60 mm focal length macro objective has been employed at its maximum aperture f/2.8.

Special attention has to be paid to filtering out background illumination coming from flame radiation. In fact any flame produces a broad spectrum radiation, which constitutes background noise on the recorded images. As in LDV, it is necessary to remove unwanted light frequencies; therefore light is recorded only within a narrow band, about 10 nm wide, centered around the laser line, in this case at 532 nm, by adopting an interference filter on the receiving optics. There is still a residual amount of noise produced by the flame within this narrow band; it should be observed that it has some positive effects due to the non linear behaviour of film emulsion when exposed to incoming radiation. In fact at the opening of the camera shutter the film is esposed to light from the flame, which brings the eposure level towards the notch on the exposure curve, as reported in fig. 1; when the laser flashes the particles scatter light and images are recorded with an higher contrast than what would be produced by flashing the laser in absence of pre-exposure. Of course the pre-exposure duration has to be optimized for each experimental set-up.

All previous considerations have been employed for the design of a PIV measurement system which proved to effectively record particle images in combusting flows, (fig. 2). Light sheet dimensions and seeding particles were optimized for each case.

Once images are recorded, they are processed by an optical bench operating in the Young's fringe mode. Digitized fringes are analysed by an autocorrelation algorithm and velocity results are stored in files for further processing and visualization.

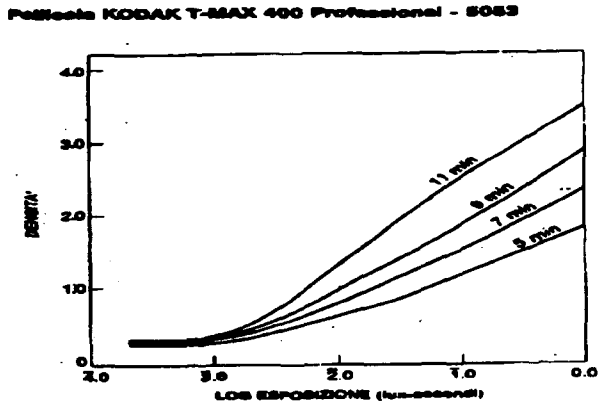

Fig.1-Film exposure curve.

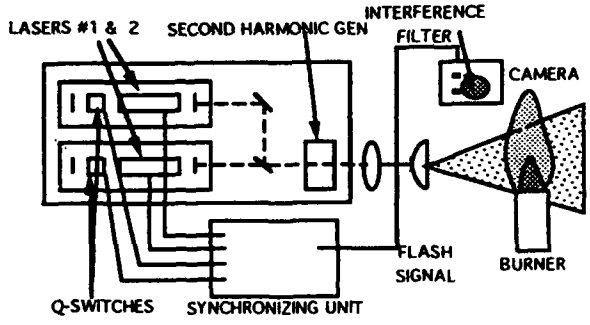

Fig.2- Scheme of PIV system.

3. MEASUREMENTS IN A BUNSEN BURNER.

The development of the PIV system has been accomplished on a simple combusting flow, a Bunsen burner operating with LPG coming from a pressurized bottle. The burner has a nozzle having 17 mm internal diameter; gas is injected upstream of a pipe whose length is 80 mm and air is driven into the flow by the negative pressure differential produced by the gas motion. Complete mixing of air and gas is achieved along the pipe. Fig. 3 shows the facility; it can be noticed the settling chamber around the air intake. Seeding particles are injected in the settling chamber, so that air is uniformly seeded before entering the pipe. Particles are therefore available all across the flame, due to the mixing of air and gas. In these experiments, seeding particles are introduced into the air flow by an atomizer, which produces a fine spray of liquid droplets containing sparse particles. Particle concentration and spray dilution are optimized for each experimental condition. Main criterium is to observe tracers both upstream and downstream the flame front. In fact,

when observing tracers in flames, it appears that image concentration drops when crossing the flame front; flame front can actually be identified by observing the change in particle number per unit image surface. This is due to the thermal and chemical action of the flame on the particle and to the large thermal expansion of the gas across the flame, which strongly reduces the volume concentration of residual tracers. Tracer concentration upstream the flame has therefore to be increased, in order to have particles also in the combusting region, but attention should be paid to avoid overlapping images in the unburned region, which could interfere and form speckles, rather noisy and difficult to process.

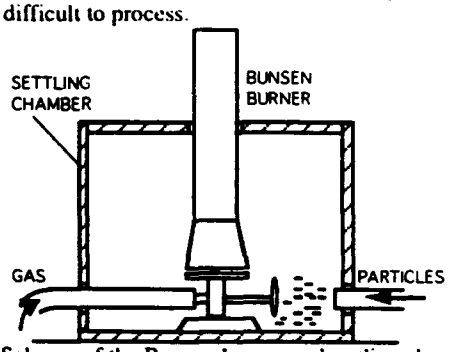

Fig. 3-Scheme of the Bunsen burner and settling chamber.

3.1 Measurements by PIV.

It has been used a series of lenses in order to shine a light sheet having 70 mm lateral width and about 100 μm thickness. The light sheet is shone across the symmetry plane of the exit nozzle. Images are recorded with magnification M=0.435 flashing the lasers at a time interval Δt=90μs. TiO_2 particles having polidisperse diameter around 0.2-2.0 μm are employed At this magnification ratio, with the PIV system described above, they produce about 50 particle image pairs per mm^2 upstream the flame front, each image having about 10 μm diameter. Fig. 4 shows a typical PIV picture; the flame front can be easily identified as the region across which the number of seeding tracers drops significantly. Its complex geometry, typical of premixed turbulent flames can be observed. It should be noticed that this is the two-dimensional section of a really three-dimensional flow field, which shows axial symmetry only when considering mean values computed over time windows much longer than the turbulent time scales.

A series of images has been acquired and processed; only some results will be shown here. Figs. 5-a and 5-b show two examples of absolute velocity measurement; on each picture it has been interrogated a regular grid of 31x61 points (1891 points), over an area equal to 69.0x34.5 mm^2 positioned 4.5 mm dowstream the nozzle of the burner. Measurement points are spaced 0.5 mm on the picture, therefore velocity samples are measured with a spatial resolution equal to 1.1 mm. Successfull measurements are obtained on about 70% of the grid points. Each velocity field differs significantly from the others, although it is possible to observe common features; in particular it is evident that the flow is accelerated across the flame front and velocity vectors show lower scatter in the burnt region. Although some simmetry is maintained in the instantaneous flow fields, it is visible the presence of large vortical structures which dominate the region upstream the flame front and also cause the significant loss of data in that region. The flow is dominated by convection; flow diverges from the axis at the exit of the nozzle; radial expansion continues across the flame front, but its effect is reduced by acceleration in vertical direction, which contributes to organize the flow along the burner axis. Processing of the images to yield relative velocity vectors offers a clearer insight into the flow structures. For this purpose, in all pictures, mean vertical velocity has been subtracted; figs. 6-a and 6-b show two examples of relative velocity field computed from data of figs. 5-a,b. The two vector fields show the uniformity of the flow downstream the flame front and the presence of vortices at the nozzle exit and at the lateral borders of the combusting flow. The dimensions of the vortices are of the order of several mm. They contribute to the entrainment of air from the outer region; only primary air was seeded, therefore measurements in the mixing region are not possible. Vorticity component perpendicular to the plane of measurement can be computed for each velocity field. Figs.7-a and 7-b show results of processing the previous velocity fields; vorticity is larger where vortical flow occurrs. Figs. 8-a, 8-b and 8-c show the results computed by averaging 10 different velocity fields; these plots therefore should be more representative of the steady state behaviuor of the flame. In fact flow symmetry appears enhanced by the averaging process and the whole flow field appears more homogeneous; vorticity is concentrated in the conical region upstream the flame front, where mixing between primary air and gas is still occurring. Crossing of the flame front produces a sharp decrease in turbulence intensity.

3.2 Comparison with LDV measurements.

In order to verify performance of the PIV system and to better describe the different observations that such measurement technique allows with respect to conventional techniques, results of instantaneous and averaged measurements have been compared to LDV measurements performed in the same flow. Axial velocity measurements by LDV have been performed along the vertical axis of the burner, while radial velocity component is measured along a radial direction 20 mm downstream the nozzle. Grid points are 2.5 mm apart from each other; 1000 LDV velocity samples are averaged at each measurement location. Uncertainty on LDV mean velocity data is evaluated to be about ±1%, while it is about ±3% for PIV data, Paone and Riethmuller (1989). Figs. 9-a and 9-b show comparison among instantaneous PIV data from fig.5 and LDV; differences are due to the convection of large eddies within the flame, as observed previosly. Comparison shows better agreement when PIV averaged data are used, as in figs. 10-a and 10-b although statistics of PIV data is still very poor, being available only 10 data sets. Nevertheless, comparison shows that PIV is capable of capturing instantaneous structures very effectively, and it shows that instantaneously the flow field structure can differ significantly from what observed as mean flow. Again this confirms that PIV and LDV are strictly complementary measurement techniques.

4. MEASUREMENTS IN A PREMIXED CH_4 COMBUSTOR.

In order to apply the developed PIV system to industrial combustors, it has been tested in a facility which operates with CH_4 inside a confined combustion chamber. The test rig is schematically represented in fig. 11. The gas flows through a nozzle of a Venturi pipe; air is driven into the flow by the low static pressure caused by gas motion. Mixing of air and gas occurrs along the diffuser of the combustor, whose outlet diameter is 60 mm. The flame develops inside a cylindrical

combustion chamber built in transparent silica, having internal diameter D_i=180 mm and length L=1000mm; its thickness is 5 mm, its refraction index is 1.46. Such a material can operate with no damage at temperatures of the order of 500°C, therefore is well suited for combustion measurements. Its optical coefficient of transmission for visible light is about 0.92 for 5mm thickness. The combustion chamber is connected to a vertical chemney 1 m high for smoke exhaust; it can therefore be considered as operating at atmospheric pressure. Gas flow rate is monitored and it results Q_g=1.52 Nm^3/h; the combustor operates at a power P=13700kcal/h=15.9kW.

4.1 Measurements by PIV.

Being the measurement area much larger than before, the PIV system must be operated at M≈0.12÷0.18, imaging on the photographic film a light sheet 200 mm wide. Air is seeded by tracer particles injected in the settling chamber upstream the combustor air intake; seeding is produced by atomizing water droplets in which ZrO_2 particles are diluted. Partcle diameter is polidispersed, with an upper limit about 5μm. PIV pictrures are acquired by firing the lasers at Δt=150μs with 105mJ/pulse.

Fig. 12 shows a typical PIV negative. The photograph shows the sudden decrease in particle concentration across the flame front, as already observed on the Bunsen burner. Large vortices, which entrain external unseeded air into the flame can be observed at the border of the flame. Noise due to reflections of the light sheet is present on the picture; it cannot be avoided, due to the fact that the combustion chamber is a cylinder. Quality of the images is therefore affected by these reflections and by background flare all over the field. Image is noisy also due to the larger amount of flame radiation; the use of the interference filter does not eliminate completely the problem.

When such images are processed resulting velocity fields look like fig. 13-a and 13-b, where absolute and relative velocity are represented respectively. Several similar measurements have been taken on the flame; in all cases processing was succesfull in about 50% of the measurement points of the regular grid laid on the pictures and about 400-600 velocity vectors are simultaneously measured on each picture. Again velocity fields show the presence of large vortices. The flow accelerates soon after the flame front, but velocity tends to decrease moving forward into the combustion chamber, due to the radial expansion of the jet. Velocity is maximum soon after the flame front. Disturbances are convected downstream the flame front and the flow shows three dimensional nature, which results in signal drop out even three diameters downstream the exit nozzle.

4.2 Comparison with LDV measurements.

Axial velocity measurements have been performed along several diameters into the combustion chamber by LDV, Paone (1994). Fig. 14 shows mean axial velocity profiles. Uncertainty in LDV mean velocity data is ±1%, while it is about ±5% for PIV. Their comparison to PIV measurements confirms the expansion of the jet inside the combustion chamber and the acceleration across the flame front. Turbulence intensity, which is not reported in this paper, is maximum at the jet boundaries; PIV pictures show that in those regions air is entrainmed by large vortices. Their passage determines high turbulence level. Data rate in LDV measurements is too low inside such a flame to perform frequency analysis; therefore time scales of such flow could not be efficiently investigated by LDV. On the other hand PIV pictures provide a very rapid evaluation of turbulent structures macroscale; therefore informations on mass transport in the flame can be derived by PIV data. These considerations again put in evidence complementarity of LDV and PIV.

5. CONCLUDING REMARKS.

This paper has presented criteria followed in the design and experimental test of a PIV measurement system for combusting flows. The choice of seeding particles, light source, image acquisition device is discussed. Measurements in a Bunsen burner are performed and compared to LDV results. They put in light the different information obtained by PIV, an instantaneous measurement of flow velocity, with respect to what normally observed by eulerian techniques, as LDV. The complementarity of the two approaches is enhanced. Measurements performed in a larger combustor, operating in a closed combustion chamber, show the difficulties in application of PIV to large combusting flows. Nevertheless results prove the potential that such measurement technique offers in the investigation of combusting flows. Again comparison with LDV data shows that PIV can measure very efficiently spatial flow structures responsible of mass transport phenomena connected to combustion.

6. REFERENCES.

Armstrong N.W.H., Shand A.M., Bray K.N.C., Ereaut P.R. 1992, PIV applied to premixed turbulent flames, Optical Meth. & Data Proc..in heat & Fluid Flow, The Inst. of Mech. Eng., London.

Lewis G.S., Cantwell B.J., Lecuona A. 1987, The use of particle tracking to obtain planar velocity measurements in an unsteady laminar diffusion flame, The Combustion Institute Western States Section, Spring Meeting, Paper No.87-35.

Logan P., Smith O. 1989 Particle Image Velocimetry in reacting flows, The Combustion Institute Western States Section, Fall Meeting, Paper No.89-56.

N.Paone 1994 Measurement of combusting flow field by laser Doppler velocimetry in premixed methane combustor, Proc. Int.Conf.Exp.Fluid Mech. 94, Torino, Italy.

N.Paone, M.L.Riethmuller 1989, Uncertainty analysis in a particle image displacement velocimetry experiment: measurements inside a centrifugal pump, Proc. 3rd Int. Conf. Laser Anem. Adv. & Appl., Swansea, Wales.

Reuss D.L., Bardsley M., Felton P., Landreth C., Adrian R. 1990 Velocity, vorticity and strain rate ahead of a flame in an engine using Particle Image Velocimetry, SAE paper n. 900053.

Reuss D.L., Adrian R., Landreth C. 1989 Two dimensional velocity measurements in a laminar flame using Particle Image Velocimetry, Comb.Sci.and Tech., vol.67 pp.73-83.

Witze P.O., Baritaud T.A. 1986 Particle seeding for Mie scattering measurements in combusting flows, Proc. 3rd Int.Symp.on Laser Anem. in Fluid Mechanics, Lisbon, Portugal.

7 ACKNOWLEDGMENTS.

The author thanks Apparecchiature e Bruciatori Speciali (ABS) of Cologno Monzese, Italy, for providing the combustor and V.Ponzio for the construction of the test facility. Experiments were performed with contribution of I.Cicoria, S.Evangelisti, G.Magri and E.Vita.

Fig. 4 Typical PIV picture on Bunsen burner.

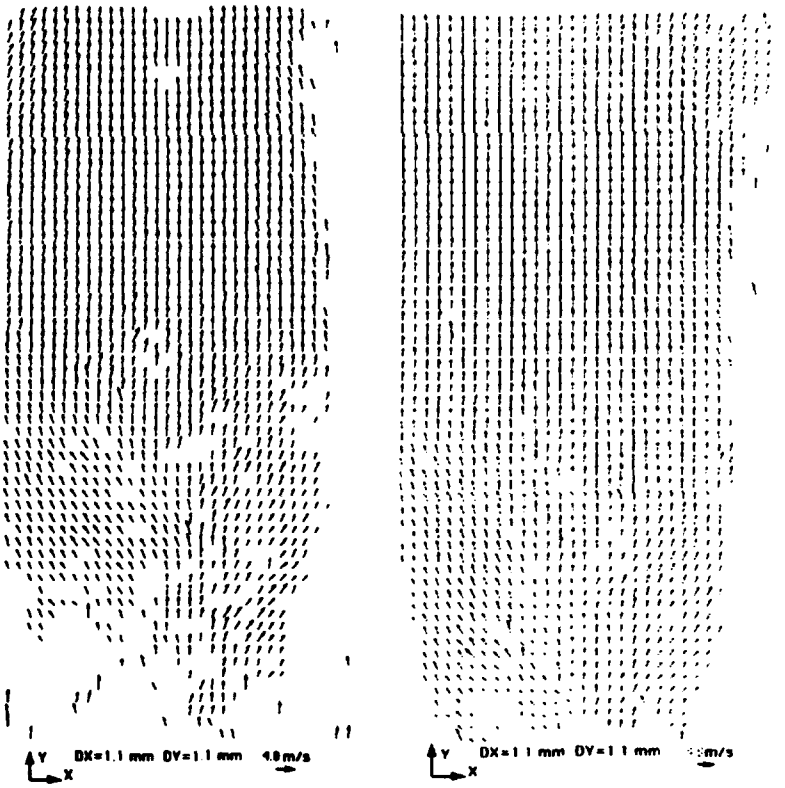

Fig. 5-a-b Two examples of absolute velocity measurement on Bunsen burner.

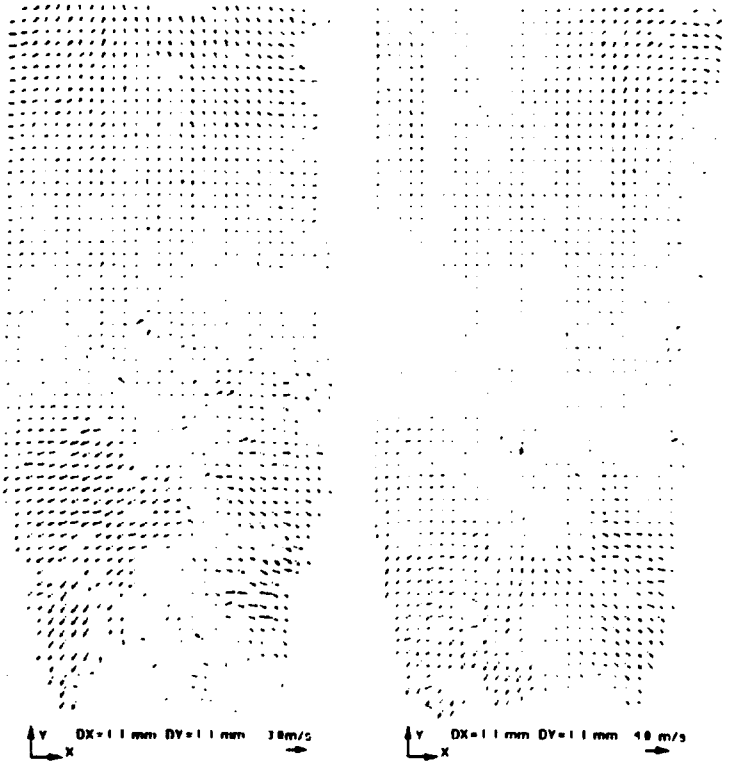

Fig. 6-a -b Relative velocity field on Bunsen computed from data of figs. 5-a,b.

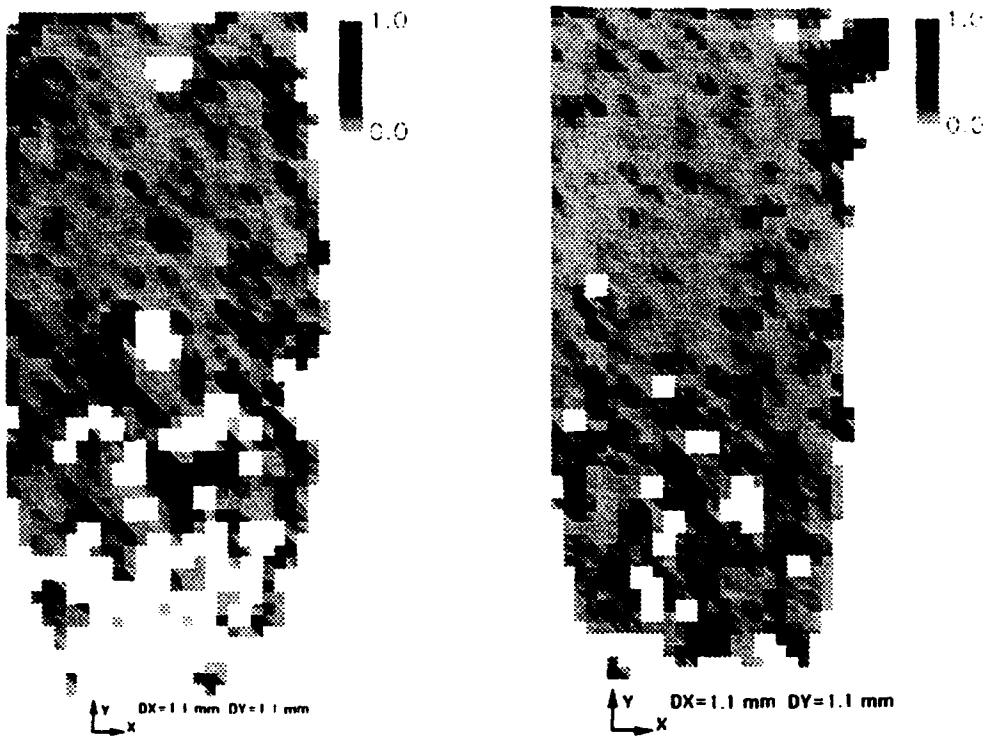

Fig.7-a-b Vorticity computed by processing the velocity fields of figs. 5-a,b.

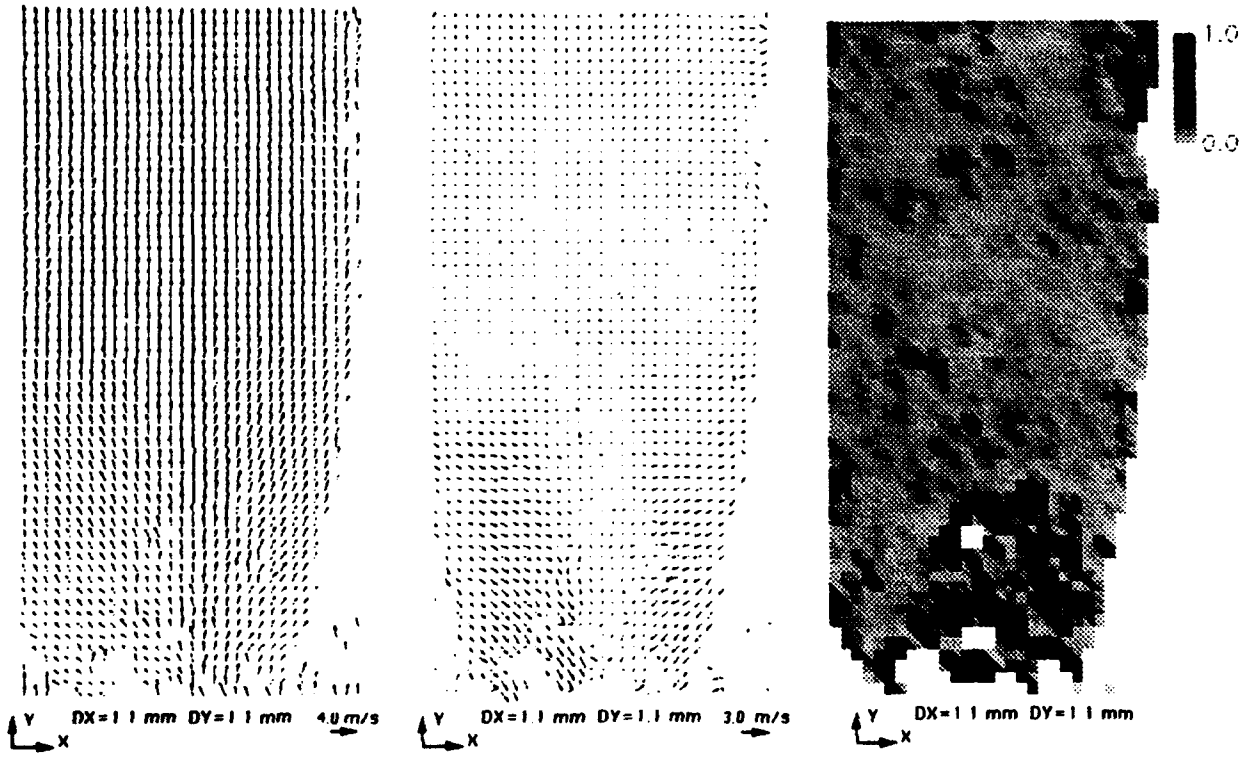

Figs. 8-a-b-c Results computed by averaging 10 different velocity fields: absolute, relative velocity and vorticity

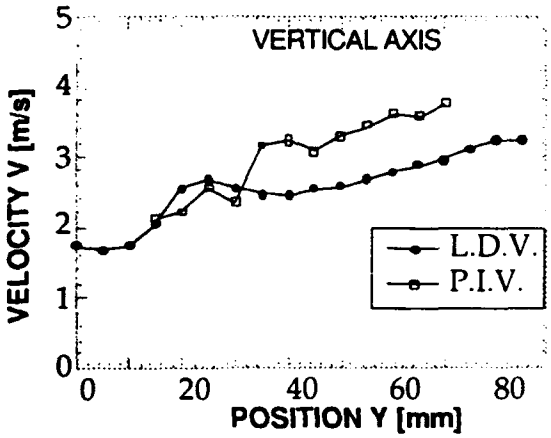

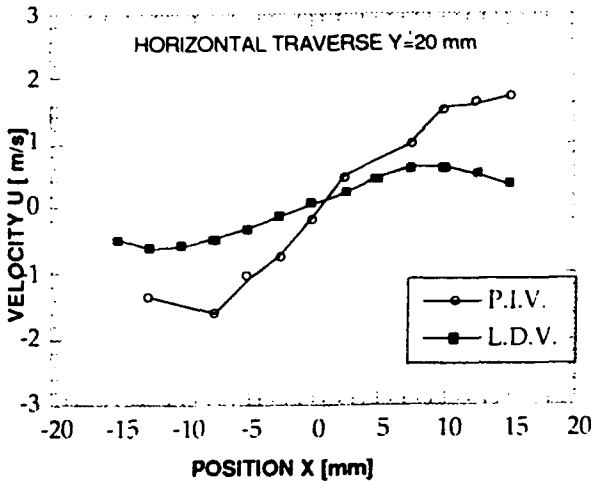

Figs. 9-a and 9-b show comparison among instantaneous PIV data and LDV from fig. 5 on Bunsen.

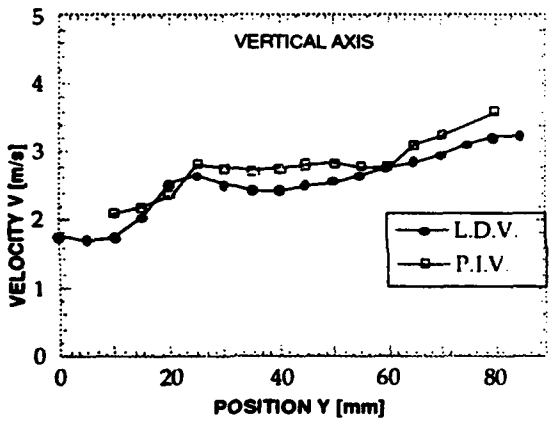

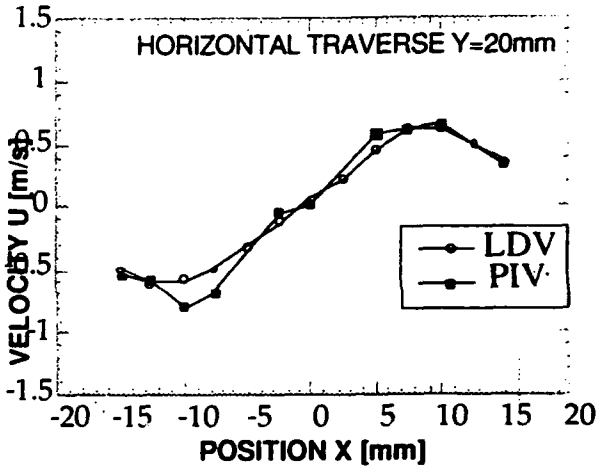

Figs. 10-a and 10-b Comparison PIV/LDV; PIV data are averaged over 10 pictures.

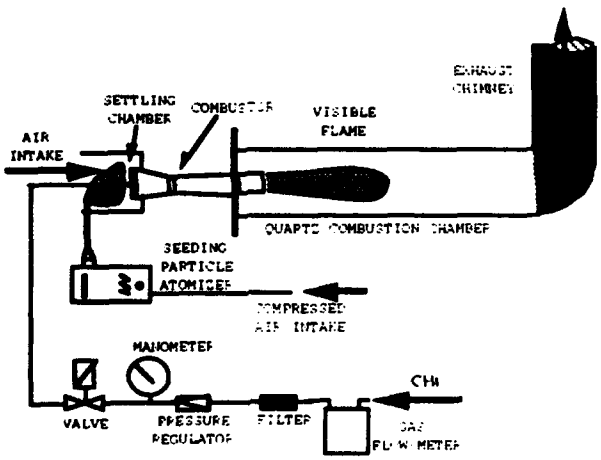

Fig. 11 Scheme of the CH_4 premixed combustor.

Fig. 12 Typical PIV negative in CH_4 combustor.

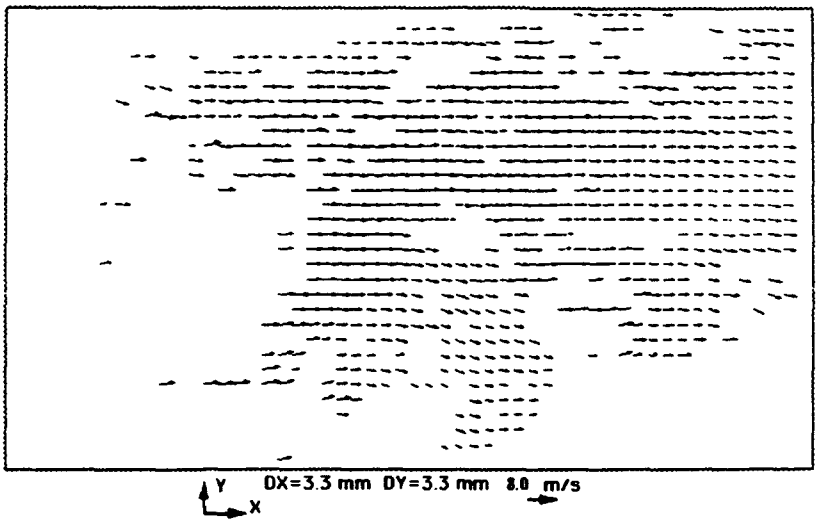

Fig. 13 - a - b. Velocity fields in CH_4 combustor.

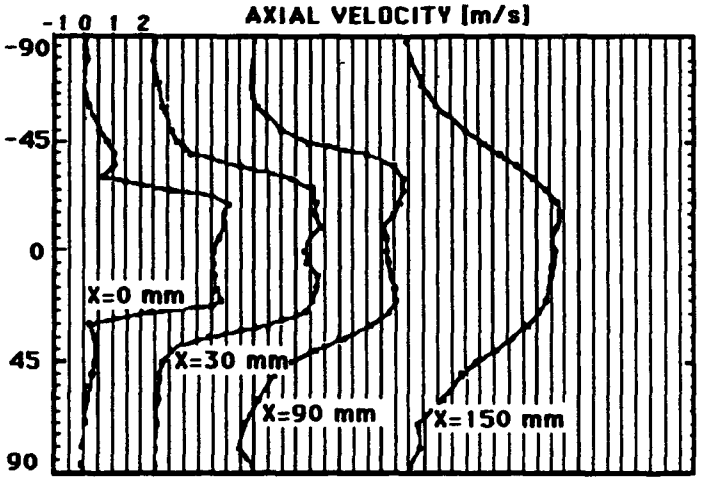

Fig. 14 - Axial velocity in CH4 combustor by LDV.

FLAME FRONT VISUALIZATION BY OH LIF AND C_2 SPONTANEOUS EMISSION IN AXISYMMETRIC LAMINAR METHANE-AIR PREMIXED FLAMES

K.MOKADDEM, M.Y.PERRIN and J.C.ROLON
Laboratoire EM2C, CNRS, Ecole Centrale de Paris
92295 Chatenay Malabry Cedex, France
M.PERRIN
Gaz de France, Research and Developement Division, CERSTA
BP 33, 93211 La Plaine St Denis Cedex, France
H.B.LEVINSKY
Gasunie Research, N. V. Nederlandse Gasunie,
P. O. Box 19, 9700 M A
Groningen, The Nederlands

ABSTRACT

Visualization of the location of the flame front is important in combustion studies, and is generally obtained by using natural C2 and OH emission. For a better understanding of the meaning of these two flame front tracers, and a more precise description of the flame front concept, two optical diagnostic techniques are compared in this work: Laser Induced Fluorescence of OH and Spontaneous Emission of C_2. These methods are applied to an axisymmetric laminar methane-air premixed flame for a range of flow rates and fuel-air ratios. Images of C_2 radicals in flames are obtained using an intensified CCD camera with a narrow band interference filter centered at the (0-0) band of the Swan system. The response of the camera has been calibrated with a uniform source, taking into account the actual local sensitivity of the imaging system as a whole (CCD, intensifier, lens, filter) from zero to the maximum level of illumination. The local intensity at the CCD is a function of the total C_2 emission integrated along the optical path. An Abel transformation is performed on each row of the instantaneous images after filtering with a spatial low pass filter to obtain an image of the cross section. A spectroscopic study relates the resulting amount of light to the C_2 concentration. OH images are obtained by Laser Induced Fluorescence. The Q1(7) line in the $X^2\Pi$ ($v''=0$) -> $A^2\Sigma^+$ ($v'=1$) transition is excited and the emission in the (1,1) band is detected. The OH signal is averaged over 100 laser pulses and collected on an intensified diode array. Finally, the images are generated by translating the laser beam and the diode array in the vertical direction in steps of 1 mm using precision positioners. The results show that, for low flow rates and fuel-air ratios, the location of the maximum of OH and C_2 intensities are in good agreement. In these lean reactive flows, the flame front is accurately defined by the two radicals. For higher flow rates and fuel-air ratios, OH is produced in the secondary diffusion reaction zone resulting from the reaction of the ambient oxygen with the hot fuel rich combustion products of the primary flame front. C_2 radicals are not preponderant in the outer diffusion flame. A comparison between OH and C_2 concentrations profils in the region where the inner and outer cones are seperated shows that the maximum of OH concentration is no longer representative of the primary premixed reaction zone location whereas it is more accurately determined by C_2 Spontaneous Emission method. Close to the burner, the OH distributions from the two cones merge to form a broad region of OH intensity, the C_2 image remains sharp. This study has compared the role of OH and C_2 radicals in flame front location. It has also shown that imaging of C_2 Spontaneous Emission is an accurate and easy experimental method for instantaneous flame front visualization. This technique does not require a large investement compared to LIF and gives quantitative tomographic information of C_2 concentration in axisymmetric laminar flames

INTRODUCTION

Flame imaging provide important new insights in the understanding of combustion processes and provide useful information on complex chemical and fluid mechanical phenomena typically found in combustion devices. Different techniques can be used to visualize reacting flow or to measure selected flowfield parameters. These parameters have to be related to some property that can be measured by means of a light beam. For many years the most common imaging techniques used in combustion have been schlieren, holographic interferometry and shadograph based on changes in refractive index and in flows of constant or nearly constant pressure. One may interpret the resulting images in terms of temperature gradients. The boundary separating the fresh and burnt gases may be located and can be used to identify the aprproximate position of the flame front. The major limitations of these visualisation methods concerns their spatial resolution in flows which are not two-dimensional with respect to the optical axis, and the difficult distinction of a simple interface between gases of different density from an active flame sheet. Other methods are based on the amount of light scattered by the fluid elements, Mie scattering (see Boyer (1980)) when particles are required and Rayleigh scattering (see Escoda (1983)) for molecules.

In most of hydrocarbon flames, the reaction zone is characterized by a luminous shape, which is associated to spontaneous emission of excited molecules and radicals produced by chemical reactions and the heat released by combustion. It is admitted that the maximum of this luminous regions zones correspond to the maximum of the heat release density and defines a flame front position. It is then possible to detect the flame front location by imaging the spontaneous emission of the flames.

This problem is solved for laminar or turbulent two dimensional flames using a time resolved camera (high speed camera or intensified CCD camera). In this case the flame front location is spatially well resolved.

For three dimensional flows, the information is integrated over the optical path along the line of sight and the image is not easily deconvolved. In axisymmetric flows the Abel transform is used to deconvolved the data (see Rolon and al (1991), Bennaghmouch and Perrin (1992)).

The geometry and motion of the flame front can also be gathered by LIF imaging. In this method the laser light illuminates the reactive flow and excites the fluorescence of a species which is present in the flow. The light radiated by this species may be detected by a diode array or a CCD camera (see Hanson (1986) and McManus and al (1993)).

In this paper, a new experimental method is investigated based on the imaging of spontaneous emission of C_2 radicals with a reconstruction algorithm based on the Abel transformation in order to obtain the quantitative C_2 concentration field in the flame. This technique is compared to results provided by OH Laser Induced Fluorescence.

The two diagnostics were applied on a laminar axisymmetric premixed methane-air flame for several flow rate and fuel air ratios. The C_2 Spontaneous Emission Spectroscopy Method (C_2 SES) is detailed in the first section of this study. A few elements of OH LIF spectroscopy are also briefly presented. Then the experimental apparatus and the calibration of the C_2 SES and OH LIF experiments are described in the second section. Finally the results are compared and discussed leading to a better understanding of the flame front behavior by C_2 and OH imaging techniques.

THEORETICAL STUDY OF C_2 SES AND OH LIF

The quantity of photons per unit volume emitted by excited radicals during the combustion reaction depends on the population of the chemical species produced.

To chose an efficient flame front tracer, a spectrum of a premixed laminar propane-air stretched flame has been performed.

The most intense emission corresponds to the (0-0) transition of the C_2 Swann system ($d^3\pi g$-$a^3\pi u$). The corresponding wavelength (516.5 nm) belongs to the visible spectrum and this transition can be efficiently isolated using a narrow bandwidth (1 nm) interference filter centered on 516.5 nm.

The image of a flame throughout the filter described below provides an integrated information in time and in space. The integration time corresponds to the exposure time of the optical system whereas the space integration deals with the optical path followed by the emitted beam of light (Figure 1).

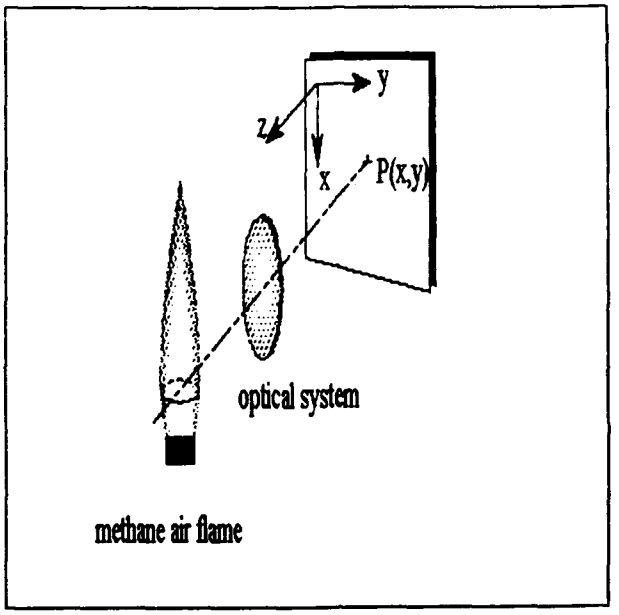

Figure 1 : Space integration of a beam of light throught the cross section of a flame

The number of photons reaching each pixel of the flame image has consequently the following expression:

$$P(x,y) = \tau \int_{\text{time}} \int_{\text{optical path}} I(x,y,z,t)\exp(-\alpha z)dzdt$$

I(x,y,z,t) is the number of photons emitted per second and unit volume by C_2 radicals in the solid angle determined by the aperture of the optics. The variations of this angle are less than 15% in the axial and radial directions of the flame. α takes into account the absorption of the beam throughout the flame and τ its attenuation throughout the optical apparatus. For stationary laminar and optically thin ($\alpha << 1$) flames this expression leads to:

$$P(x,y) = \tau \times \text{time exposure} \times \int_{\text{optical path}} I(x,y,z,t)dz$$

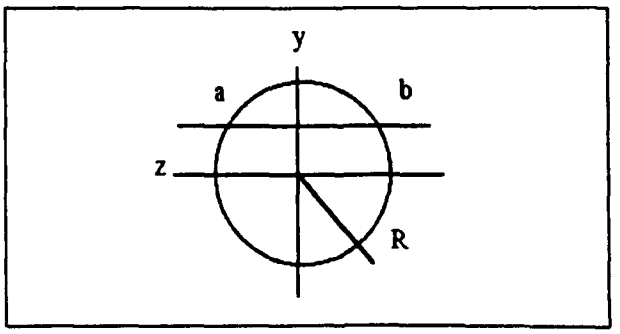

Figure 2 : Cross section of an axisymmetric flame

Finally for an axisymmetric flame the new variables showed in Figure 2 give the following result:

$$P(x,y) = 2 \times \tau \times \text{time exposure} \times \int_{x}^{R} I(x,r) \frac{r}{\sqrt{r^2 - y^2}} dr$$

The expression is known as Abel integral whose exact inversion gives:

$$I(x,r) = \frac{-1}{\tau \times \text{time exposure} \times \pi} \int_{r}^{R} \frac{\partial}{\partial y} P(x,y) \frac{dy}{\sqrt{y^2 - r^2}}$$

We can now obtain by image processing the intensity of light locally emitted by C_2 radicals. Due to the finite filter bandwidth, the collected light is composed by different rotationnal lines.

A spectroscopic study of C_2 spontaneous emission based on Boltzmann equilibrium and taking into account the spectral window of the inteference filter leads to this final expression:

$$I(x,r) = N_v \times \Psi(T)$$

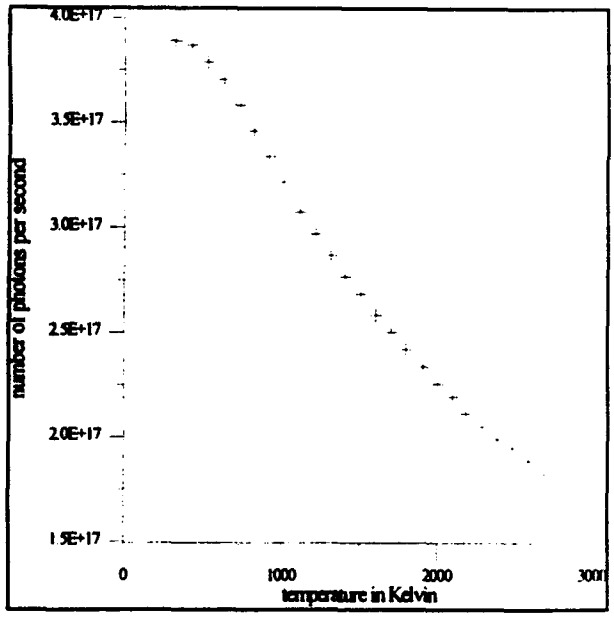

Figure 3 : Variations of ψ with the temperature

Using the spectroscopic constants already tabulated (see Piar (1993)), a study of $\psi(T)$ is possible. The curve in Figure 3 shows its variation with temperature. C_2 radicals are located in the flame front. In laminar premixed methane-air flows the temperature varies in this zone between 1500 K and 2200 K. For these values the dependence of ψ with T is slight (less than 15%). With these approximations quantitative values of C2 concentration can be obtained from the expression above.

For OH LIF, the $Q^1(7)$ line in the $X^2\pi(v''=0) \rightarrow A^2\Sigma^+$ ($v'=1$) manifold is excited with pulse energies in excess of 10 mj. The emission (1,1) band is isolated and detected. The broadband fluorescence includes contributions from other rotational states populated by collisionnal transfer. The emission from these other states is susceptible to quenching. The analysis made is restricted to regions where the temperature and the concentration are expected to vary slowly and quenching corrections have not been applied to the data. In addition, loss of population to the (0,0) is considered to have little effect on these results.

DESCRIPTION OF THE EXPERIMENTS

The C_2 SES and OH LIF diagnostic methods are applied in an axisymmetric premixed laminar methane air flame for fully rich (1.46) and slightly rich (1.25) fuel air ratios. The total flow rate has been adjusted in order to obtain a stable laminar flame. The flame is produced by a laboratory burner of 1 meter long and 9.5 mm inner diameter studied at Gaz de France Research Center and EM2C Laboratory for C_2 SES and Gazunie Research for OH LIF.

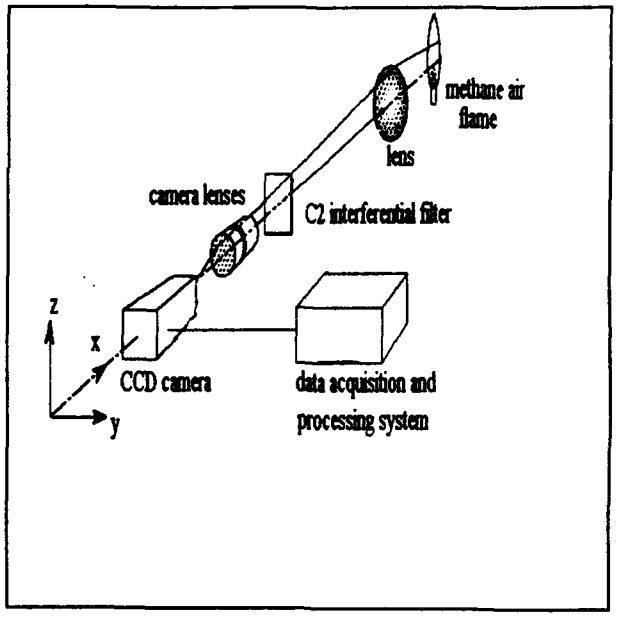

Figure 4 : Experimental set up for C_2 SES method

The images of C_2 radicals (Figure 4) are obtained using an intensified CCD video camera (Proxitronic HF1). The exposure time is 20 ms. The other elements of the experimental set up are:

- a narrow band (1nm) interference filter (Melles Griot) centered at the (0-0) band of the Swan system (516.5 nm)
- a video digitizer board Matrox PIP 1024 performing frame grabbing on the video signal from the camera. It has a resolution of 512×512 pixels with 8 bits ADC depth.
- an imaging software (Visilog 3.11) which incorporates both image processing and analysis libraries.

In order to obtain quantitative images of C_2 radicals, the response of the CCD camera has to be calibrated from zero to the maximum level of illumination. This calibration has been performed with the whole imaging system (CCD, intensifier, lenses, filter) to take into account the global system response. The experimental method used for this calibration consists in taking images of a uniform planar source of light. The offset and gain of the frame grabber is adjusted with the following procedure. The camera shutter is closed and the signal level (0.3 V) is digitized. The offset value is decremented until the corresponding digital value has the averaged value of 0.

The same procedure is performed for the gain adjustment. The level of the light source is increased until the signal level reaches 1V. The corresponding digital value is incremented until it has an averaged value of 255. Then the grabbed images are divided by the maximal value reached by the pixels leading to a corrected image taking into account the vignetting and the pixel response. This experiment provides also the conversion range between the level of gray scale and the number of photons reaching each pixel of the CCD by adding between the light source and the camera several calibrated density filters (Figure 5).

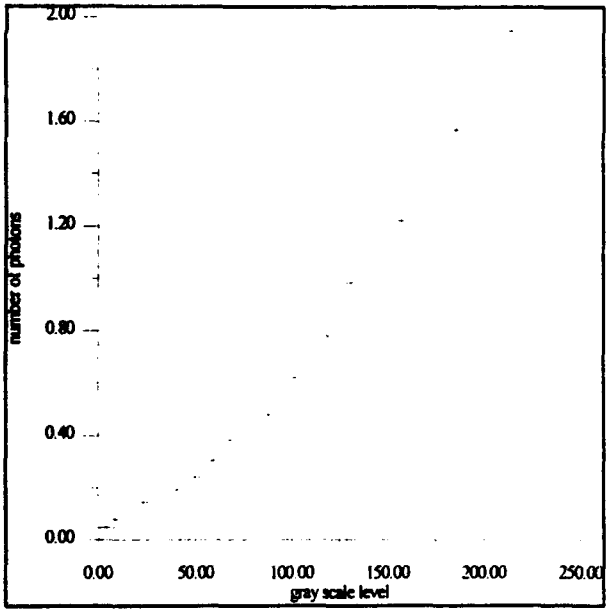

Figure 5 : C_2 SES imaging system calibration curve

In the theoretical study, we made the approximation that the light emitted by each probe volume along the flame's cross section is focussed at the same location on the image plane. This approximation eliminates the effect of depth of field. The actual phenomena is shown in Figure 6.

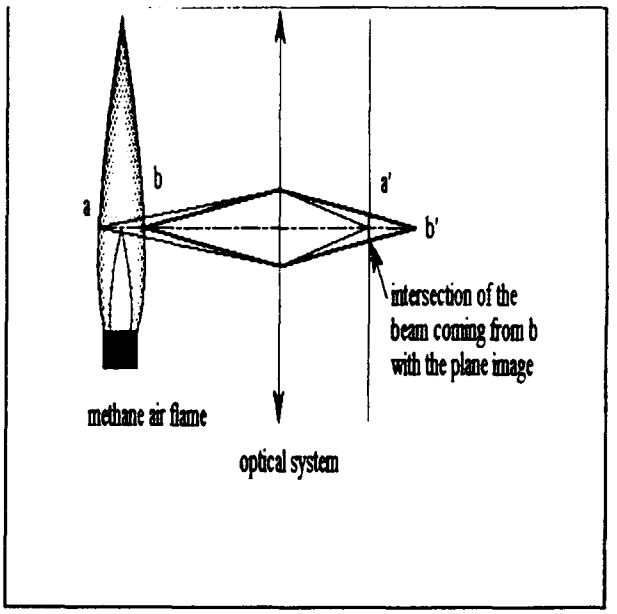

Figure 6 : View of the effect of the dept of field

The image of the collected light along the optical axis corresponds to an area of pixels. This area has been experimentally evaluated to 9 pixels. Aside from this effect, the information is blurred in the image plane due to the system resolution (less than 2 pixels).

OH images are obtained by laser induced fluorescence. The OH signal is averaged over 100 laser pulses and collected on an intensified diode array (Figure 7). Finally the images are generated by translating the laser beam and the diode array in the vertical direction in steps of 1mm using precision positioners.

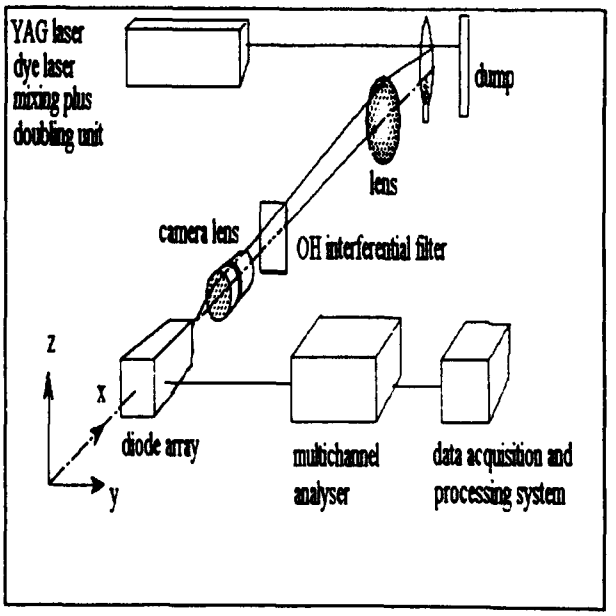

Figure 7 : Experimental set up of the OH LIF method

RESULTS AND DISCUSSION

In this study we have used C_2 spontaneous emission and OH LIF to vizualise the flame front. For C_2 SES we have shown that the local intensity on the CCD is a function of the total C_2 emission on the optical path integrated along the line of sight. The raw images are filtered with a spatial medium filter to take into account the diffusion effect described above. The convolution is performed on each raw of the axisymmetric image by the Abel integral transform.

The results (Figures 8 and 9) show that, for low flow rates and fuel-air ratios, the location of the maximum of OH and C_2 intensities are in good agreement. In such slightly rich reactive flows the flame front is accurately defined by these two radicals. We can notice that the better flame front resolution evaluated by the C_2 SES method is due to the short lifetime of these radicals compared to OH. This last specie are convected by the flow whereas C_2 emission is only detected in the flame front region.

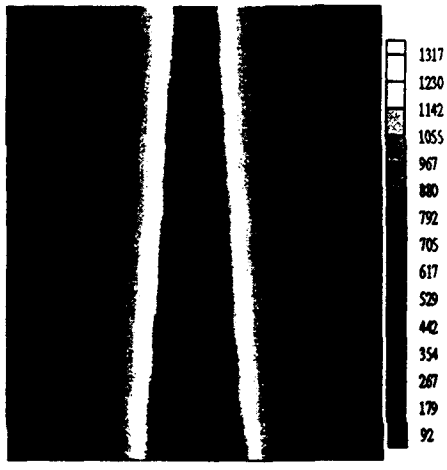

Figure 8 : OH image in an axisymmetric premixed methane air flame (total flow rate =6.75, fuel air ratio=1.25)

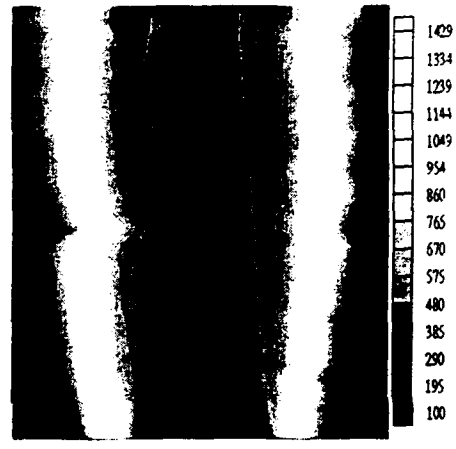

Figure 10 : OH image in an axisymmetric premixed methane air flame (total flow rate =6.78, fuel air ratio=1.46)

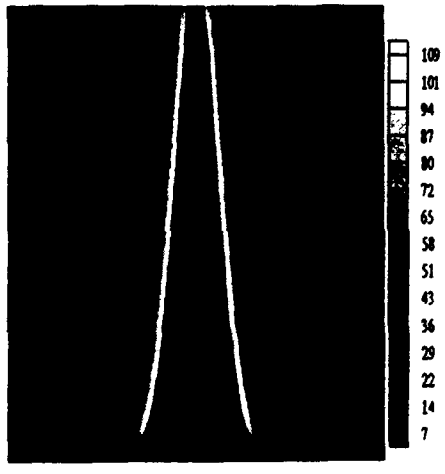

Figure 9 : C_2 image in an axisymmetric premixed methane air flame (total flow rate =6.75, fuel air ratio=1.25)

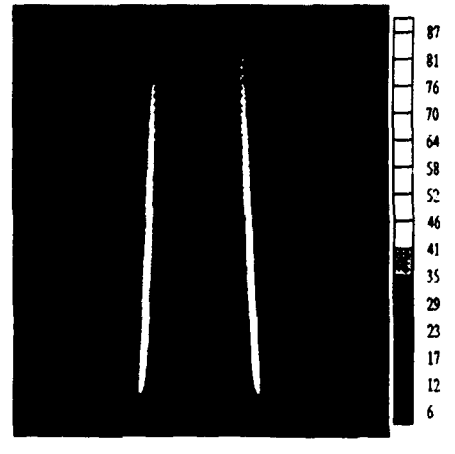

Figure 11 : C_2 image in an axisymmetric premixed methane air flame (total flow rate =6.78, fuel air ratio=1.46)

For higher flow rates and fuel ratios, OH is produced in the secondary diffusion reaction zone resulting from the reaction of the ambient oxygen with the hot fuel rich combustion products of the premixed flame front. C_2 radicals do not exist in the outer diffusion flame (Figures 10 and 11).

At a height where the inner and the outer cones are separated the maximum of OH concentration is not located in the premixed reaction zone but in the secondary zone (figure 12). On the opposite, C_2 peaks sharply in the primary zone where OH exihibits a small plateau.

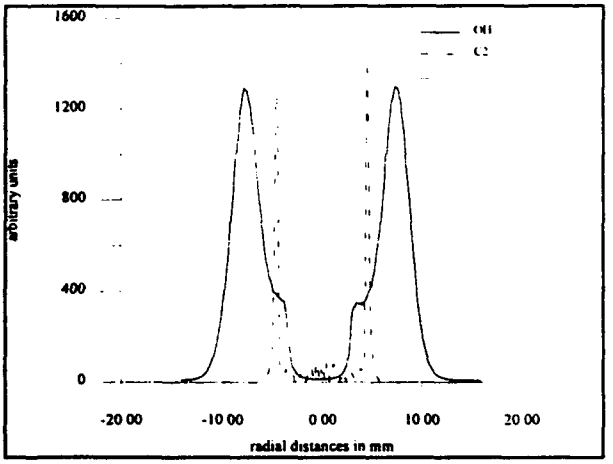

Figure 12 : OH and C_2 profiles at the upper region (15 mm from the burner) of an axisymmetric premixed methane air flame (total flow rate=6.78, fuel air ratio=1.78)

Close from the burner the OH distribution from the two cones merge to form a broad region of high OH concentration, the C_2 profile remains sharp (Figure 13). Then only C_2 is specific of the premixed flame front.

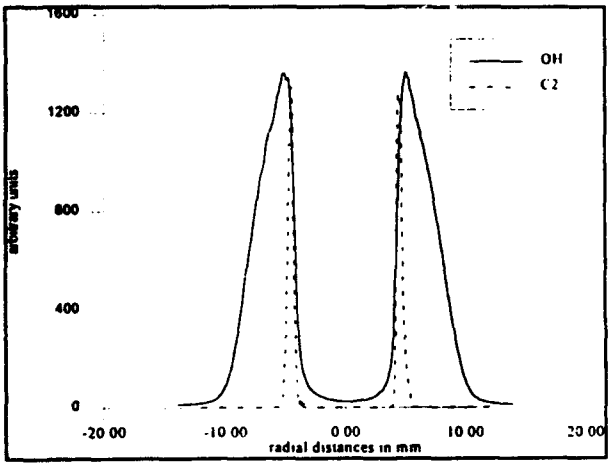

Figure 13 : OH and C_2 profiles at the basis region (2 mm from the burner) of an axisymmetric premixed methane air flame (total flow rate=6.78, fuel air ratio=1.78)

CONCLUSION

Spontaneous Emission Spectroscopy of C_2 radicals was shown to be, in combination with Abel integral transform, a good diagnostic technique for premixed flame front visualisation. This study has compared the distribution of OH and C_2 radicals in the flame.

The short chimical lifetime of C_2 compared to OH, which is convected by the flow, provides a better spatial resolution. In rich reactive flows OH is an accurate tracer of the secondary diffusion reaction zone whereas C_2 emission is only detected in the premixed flame front.

C_2 SES diagnostic can provide accurate quantitative tomographic information in flames and is an interesting complement to the information obtained by the LIF method.

ACKNOWLEDGEMENT

We wich to thank Tineke Van der Meij, Rob Jacobs, Anatoli Mokhov from Gazunie Research for performing the OH LIF experiments and P. Mahé from Gaz de France for their technical support during the experiments. Fruitfull discussions with Dr B. Piar on C_2 spectroscopy very much stimulated this work.

LIST OF THE SYMBOLS

I(x, y, z), I(x, r) : emitted intensity in each point of the flame in photons per second and unit volume in the solid angle of collection

τ : attenuation coefficient by to the optical system

P(x, y) : number of photons received by each pixel

α(x, y, z) : absorption coefficient

r and R : current and maximal radius of the flame

N_v: total fundamental vibrationnal population of C_2 (m^{-3})

λ : wavelength in nm

k : Boltzmann constant

c : celerity of light

REFERENCES

Baronavski A.P. and McDonald J.R, 1977, Measurments of C2 Concentrations in an acetylen flame, J. of chemical physics, Vol 66, Num7.

Bennaghmouch H. and Perrin M., 1992, Mesure de Temperature par Spectroscopie Infrarouge (Emission-Absorption) dans une Flamme Turbulente Stabilisée par un Obstacle, Gaz de France-DR-CERSTA Rept, N92.254

Boyer L.,1980, Laser Tomographic Method for Flame Front Movement Studies, Combustion and flame, Vol 39

Escoda M.C. and Long M.B., 1983. Rayleigh Scattering Measurments of the Gaz Concentration Field in Turbulent Jets, AIAA Journal, Vol 21.

Hanson R.K., 1988, Planar Laser Induced Fluorescence, Jour. of Quantitative Spectroscopy and Radiative Transfer, Vol 40.

Mambo-Caristan J.C., Philippe L.C., Perrin M.Y. and Martin J.P., 1989, Laser Beam Deviation as a Local Density Probe, Experiments in Fluids, Vol 7

McManus K., Yip B. and Candel S.M., 1993, Emission and Laser Fluorescence Imaging Methods in Experimental Combustion, Invited Lecture at the Third Conference on Experimental Heat Transfer, Fluid Mechanics and Thermodynamics, Honolulu.

Rolon J.C., Veynante D., Martin J.P., Jakob G.,Dornberg E. and Durst F., 1991, Laser Velocity and Density Measurments of a Flat Counter Flow Diffusion Flame, Aerothermodynamics in Combustors, IUTAM Symposium Taipai, Taiwan-Published by Lee R.S.L., Whitelaw J.H. and Wung T.S., 1992, Springer-Verlag Berlin heidelberg ed.

Tatum J.B. and Jarowski W.A., 1987, A Solution of Abel Equations, Journal Quant. Spectros. Radiat. Transfer, Vol 38, Num 4.

Tatarczyk T. and Becker K.H., 1976, Lifetime Measurments on Single Vibrational Levels of C2 bu Laser Fluorescence Excitation, Chemical physics letters, Vol 14, Num 1.

Piar B., 1993, Exploitation du spectre d'émission de molécules diatomiques, Ph. D. thesis, Ecole Centrale de Paris

Van Ooostendorp D.L., Borghols W.T.A.and Levinsky H.B., 1991, The Influence of Ambient Etrainement on Partially Premixed Burner Flames : LIF Imaging of CO and OH, Combustion Science and Technology, Vol 79.

Session 16.
Votices & Breakdown

TAYLOR VORTICES IN SHEAR-THINNING LIQUIDS

M P Escudier, I W Gouldson and D M Jones

University of Liverpool, Dept of Mechanical Engineering,
P O Box 147, Liverpool, L69 3BX, England.

ABSTRACT

The flow structure in a concentric annular geometry with a radius ratio of 0.506 has been investigated for inner cylinder (centrebody) rotation rates below and above the critical Taylor number for one Newtonian and two non-Newtonian fluids.

For the Newtonian fluid, an aqueous solution of glucose, the azimuthal (tangential) velocity component is in excellent agreement with theoretical predictions for Taylor number $Ta < Ta_c$ (i.e. plane Couette flow). The transition from plane Couette flow to a flow exhibiting toroidal vortices (Taylor vortices) is clearly identified by the abrupt development of a component of axial velocity. Detailed velocity mappings of one vortex pair in both the axial and tangential directions at one Taylor number above the critical value have been made, together with measurements of the magnitude of the maximum axial and tangential velocities at two other Taylor numbers. The tangential velocity component exhibited a periodic structure of the same wavelength as that observed for the axial component with the extrema corresponding to zero axial velocity. Higher values of the maximum axial velocity and velocity gradient are observed closer to the centrebody than at the outer wall whilst the radial location of zero axial velocity in the vortex interior (i.e. the eye of the vortex) moves towards the outer wall with increasing Taylor number.

The first non-Newtonian fluid, an aqueous solution of Xanthan gum, which is strongly shear thinning and slightly elastic, exhibited a slight deviation from the theoretical tangential velocity profile for a power-law fluid in plane Couette flow attributed to the sensitivity of the profile to the power-law index, n. The transition to Taylor flow determined by the increase from zero in the axial velocity component is much more gradual and less well defined than for the glucose solution. The detailed mapping of a vortex pair conducted at a single Taylor number revealed a similar structure to that observed for the Newtonian fluid although the asymmetry in the maximum axial velocities is more marked than for the Newtonian case with a significant radial shift in the location of the vortex eye towards the centrebody. It was also found that the vortices exhibit a slow axial drift in the direction opposite to the centrebody rotation vector whereas there was zero drift for the Newtonian case.

Due to the thixotropic nature of the second shear-thinning fluid, a Laponite/CMC aqueous blend, it was not possible to identify a transition point from plane Couette flow to Taylor flow. Three tangential velocity profiles measured in plane Couette flow at low Taylor numbers are characteristic of a yield-stress fluid, with a layer of gelled fluid surrounding a region of rotating fluid close to the centrebody. A detailed mapping of a vortex pair at one Taylor number revealed a vortex cell structure very similar to that for the Xanthan gum suggesting that the shear-thinning aspect of the fluid rheology for both non-Newtonian fluids was far more significant than either thixotropy or viscoelasticity. However, an axial drift was again apparent but in the opposite direction to that for the Xanthan gum suggesting that this effect is associated with the differences in the rheological characteristics of the two fluids.

1. INTRODUCTION

The cellular motion that develops in the fluid contained between two concentric cylinders when the rotation speed exceeds a critical value, strongly dependent upon the radius ratio, was discovered and analysed theoretically and experimentally by Taylor in 1923. The review of Stuart (1986) lists nearly a hundred subsequent papers concerned in one way and another with Taylor-vortex flows whilst Koschmieder (1993) puts the total at about three hundred. Although some quite remarkable experiments have been reported, starting with those of Taylor himself and including the definitive work of Donnelly (1958) and Coles (1965), almost all have been limited to either torque measurements or visualisation of flow structures through the outer cylinder wall with considerable emphasis on transitions between flow states rather than the internal details of a particular flow state.

Hot-film, laser Doppler anemometer and electrochemical current measurements of power spectra have also been employed to detect departures from the axisymmetric structure of the primary Taylor state to increasingly complex wavy vortices as the Taylor number is increased. In view of the interest in Taylor vortex flow which has continued for more than 70 years, it seems remarkable that no measurements of the internal structure of Taylor vortices have been reported hitherto.

So far as non-Newtonian fluids are concerned, the Taylor-vortex literature is very limited. Recent theoretical work includes the finite-element study of the stability of inelastic non-Newtonian fluids in Couette flow by Lockett et al (1992) based upon the far more extensive numerical work of Lockett (1992) which also includes the influence of an imposed axial flow and eccentricity. The latter topics are also being investigated experimentally in the wider research programme of which this study of Taylor vortices is a part. Previous experimental work on non-Newtonian liquids has been concerned either with detecting the critical rotation speed for the onset of Taylor motion or using the critical speed to determine rheological properties.

As was Lockett's (1992) work, the present study was motivated by the need for a more complete understanding of the flow of drilling fluids in the annulus created between drillpipe and wellbore during oil- and gas-well drilling operations. The selection of the two non-Newtonian fluids used for the work described here was strongly influenced by the viscometric characteristics of a typical drilling fluid: shear thinning, thixotropic, viscoelastic and formulated to gel below a critical shear (yield) stress. To permit the use of laser Doppler anemometry for the detailed flow measurements, it was essential that the fluids were also optically transparent. Of the two fluids selected, one, Xanthan gum, is shear thinning and elastic whilst the other, a Laponite/CMC blend, is shear thinning with a low yield stress and thixotropic. A second aspect of the present work which was influenced by the relevance to drilling situations is the geometry of the apparatus. The radius ratio is 0.506 and the aspect ratio (i.e. annulus length/gap width) is 233:1, which is considerably higher than any previous wide-gap Taylor-vortex apparatus. Such a high aspect ratio was essential since the main aim of the research programme was the investigation of fully developed flow through the annulus, i.e. a combination of the flow produced by an imposed axial pressure gradient and centrebody rotation.

Measurements are provided which reveal the influence of fluid rheology on the tangential velocity distribution for Couette flow and on the tangential and axial velocity distributions within Taylor vortices. Variations in the internal vortex structure with increasing Taylor number are investigated by determining the changes in the radial distributions of the maximum and minimum axial velocities within a Taylor cell.

2. EXPERIMENTAL RIG AND INSTRUMENTATION

The annular test section comprises six precision-bore borosilicate glass tubes (ID 100.4 ± 0.1mm) with a 50.8mm diameter thin-wall stainless steel inner tube giving a radius ratio of 0.506. The outer glass tubes are assembled into modules with matching male/female stainless steel flanges at alternate ends. There are five modules each of 1.027m length and one of 0.64m, which gives an overall length of 5.775m and a length-to-hydraulic diameter ratio of 116. The centrebody rotation speed may be infinitely varied up to a maximum of 126rpm.

Mean flow velocities were determined using a Dantec Fibreflow laser Doppler anemometer (LDA) system comprising of a 60X10 probe and 55X12 beam expander in conjunction with a Dantec BSA 57N10 Burst Spectrum Analyzer signal processor and Hewlett Packard 286/12 microcomputer. The length of the principal axis of the LDA measurement volume is estimated as 0.193 mm in water. Vortex mappings in the axial direction were made by traversing the probe head along the axis of the annulus at discrete radii within the annulus gap. Tangential vortex mappings were achieved by rotating the probe head through 90° and again traversing along the annulus axis at discrete radii. The traversing system was controlled by a microcomputer (IBM XT PS2 model 30) and had a spatial resolution of 0.015mm. A flat-faced optical box containing castor oil (R_n = 1.478) was positioned over the pipe at the measurement location to minimise refraction of the beams.

Rheological measurements were made on a CarriMed controlled-stress rheometer (CSL 100) using a combination of cone-and-plate and parallel-plate geometries and employing CarriMed's flow equilibrium software for the Laponite/CMC blend. Fluid refractive indices were determined using an ABBE 60/ED high accuracy refractometer.

3. TEST FLUIDS: PREPARATION AND RHEOLOGY

The first (purely polymeric) non-Newtonian fluid was an aqueous solution of Xanthan gum and the second a Laponite/CMC blend. For comparison purposes, a series of experiments was also carried out for a representative Newtonian fluid, a mixture of glucose syrup and water.

A working quantity of each fluid was prepared by filtering tap water prior to the addition of the glucose or polymer and, for the blend, the Laponite powder. To retard bacteriological degradation, a small quantity (80-200 ppm) of formaldehyde was added. Seeding particles (Timiron MP-1005, mean diameter ~20 μm) at a concentration of 1ppm were added to improve the LDA signal/noise ratio and the data rate.

Viscometric measurements were made at temperatures bracketing those observed in the experimental rig and

viscosity values used in data reduction arrived at by linear interpolation. Measurements were made immediately before and after each flow run to check whether degradation of the polymer solutions had taken place, and the fluids discarded if this was the case.

The Newtonian fluid used was a 2:1 w/w glucose syrup (Cerestar) and water mixture with an initial viscosity μ = 0.065 Pa.s at 20°C. Due to water evaporation, the viscosity gradually increased to a value of 0.08 Pa.s with no measurable change in either density or refractive index, which were 1,265 kg/m^3 and 1.436, respectively.

The purely polymeric non-Newtonian fluid was a 0.15% aqueous solution of Xanthan gum, for which the viscosity data (**Figure 1**) are well represented by the Sisko model:

$$\mu = \mu_{ref}(\lambda_S \dot{\gamma})^{n-1} + \mu_\infty$$

with λ_S = 11.0 s, n = 0.437, μ_∞ = 0.001 Pa.s and μ_{ref} = 1 Pa.s. For shear rates between about 1 and 1000 s^{-1}, Xanthan gum at the concentration used here essentially behaves as a power-law fluid.

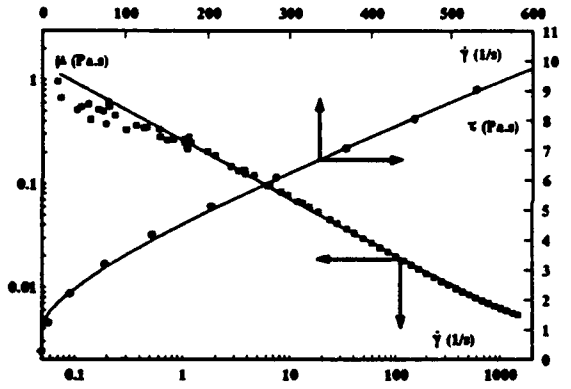

Figure 1. Viscometric characteristics of Xanthan gum and Laponite/CMC.

The Laponite/CMC blend solution was nominally a blend of aqueous solutions of 0.5% Laponite and 0.07% CMC which produces a thixotropic, shear-thinning fluid with a low yield stress (**Figure 1**). Due to the known difficulties of characterizing thixotropic fluids (Alderman et al, 1988), for this fluid the CarriMed flow-equilibrium procedure was adopted whereby a shear stress is selected and maintained and the shear rate monitored until steady-state conditions are achieved. In this manner, excellent reproducibility of viscometric data was obtained. The data are well modelled over the shear-rate range considered by the Casson equation:

$$\tau^{1/2} = \tau_y^{1/2} + \tau_{ref}^{1/2} (\lambda_C \dot{\gamma})^{1/2}$$

with τ_y = 0.99 Pa, λ_C = 7.55 x 10^{-3} s and τ_{ref} = 1 Pa.

The thixotropic behaviour of a typical Laponite/CMC blend is illustrated in **Figure 2** which shows two curves of viscosity versus time. The upper curve represents the response of the fluid to a sudden increase in imposed shear stress (from 0 Pa to 15 Pa) with a resulting breakdown of structure. The lower curve corresponds to the buildup of structure when the shear stress is suddenly decreased (from 35 Pa to 15 Pa). The timescales for both buildup and breakdown are seen to be about 3,000 s, so that the time to establish an equilibrium flow for this fluid is very long.

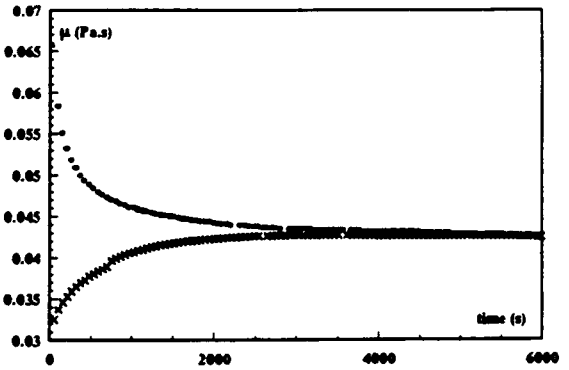

Figure 2. Viscosity vs time for Laponite/CMC.

4. EXPERIMENTAL RESULTS

4.1 Newtonian Fluid

For the glucose solution, monitoring the development of an axial velocity component at a fixed radial location close to the centrebody (ξ = 0.8) as the centrebody rotation rate was progressively increased proved to be a very sensitive and repeatable indicator for the onset of Taylor flow: the results of two separate runs for this fluid are shown in **Figure 3**. For a radius ratio of 0.506, a critical Taylor number of 4,500 would be consistent with the experiments of Donnelly (1958). The lower value of 3,700 found here is thought to be a consequence of the departures from straightness of slight centrebody geometry.

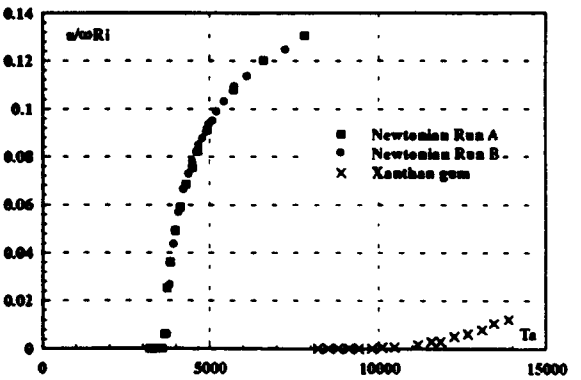

Figure 3. Axial velocity vs Taylor number.

Once the transition point had been identified, tangential velocity profiles were measured at sub-critical Taylor numbers of 427 and 2,910 and, as seen from **Figure 4** found to be in excellent agreement with the Newtonian Couette flow profile.

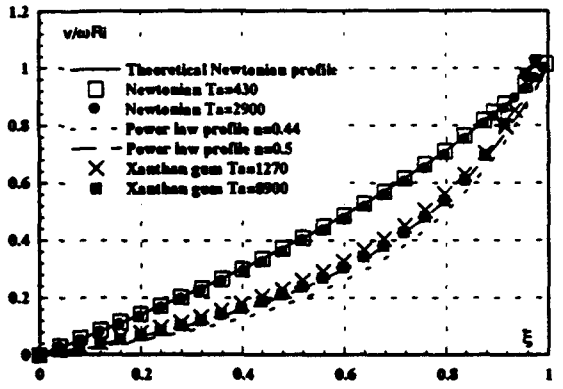

Figure 4. Tangential velocity profiles for Newtonian fluid and Xanthan gum.

A detailed mapping of the axial and tangential velocity components over an adjacent pair of counter-rotating vortices was carried out for a supercritical Taylor number of 15,400 which is well below the second critical Taylor number at which the axisymmetric Taylor vortex flow becomes unstable: for a radius ratio of 0.5, Synder and Lambert (1966) put the second critical value at at least an order of magnitude higher than the first. Flow was established by pre-setting the rotation speed to the required value and then switching the system on to produce a sudden start (full rotation speed reached in a few seconds). The mapping was then performed as a succession of traverses along the axis of the geometry at fixed radial locations. The vortices were found to be stable over the timescale of the experiment and to exhibit no drift along the axis of the geometry. The data are presented in **Figure 5** with a schematic diagram indicating the sense of axial-radial circulation within the vortices. The tangential velocity component (**Figure 5b**) exhibits an axial periodicity of the same frequency as the axial component (**Figure 5a**) but lags the axial component by 90° (i.e. the maximum and minimum tangential velocities correspond to zero axial velocity). From **Figure 5b** it is seen that the tangential velocity at any radial location is highest at the boundary between adjacent Taylor cells where there is radial outflow and lowest on the inflow boundary. This observation is consistent with considerations of angular-momentum transport with reference to the base Couette flow. In contrast with a potential vortex, fluid transported radially outward carries an excess of angular momentum leading to a velocity overshoot, whilst the reverse is true for fluid transported radially inward. It may also be remarked that at any radial location the departure of the tangential velocity from the theoretical Couette-flow variation exceeds the axial velocity at that location: it is clearly inappropriate to regard the Taylor vortex motion as a minor perturbation of the underlying Couette flow.

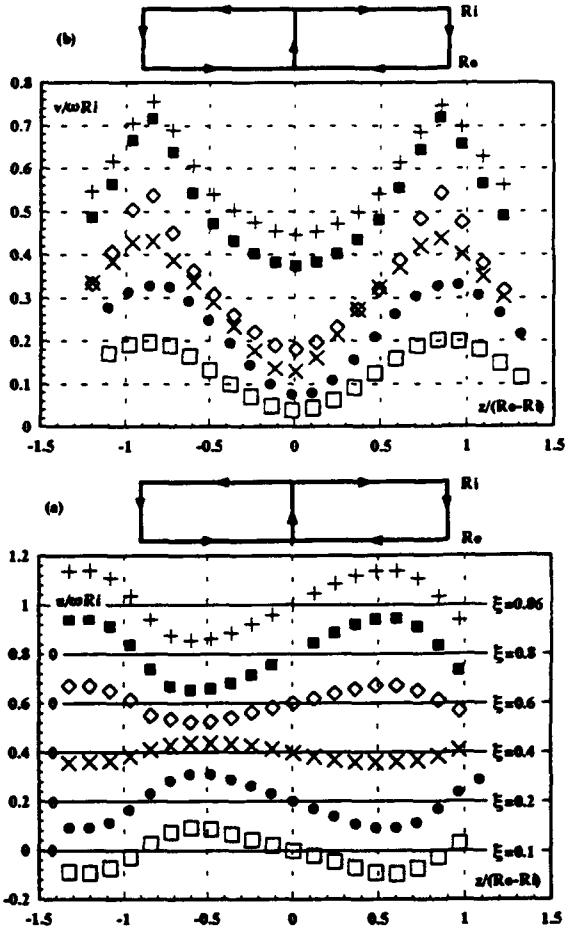

Figure 5. Velocity components within Taylor vortices for glucose solution at a Taylor number of 15400 (a) axial (b) tangential. The schematic diagram shows the sense of the radial/axial circulation.

The overall structure of the motion within a Taylor cell is clearly revealed by the streamlines (**Figure 6**), computed from the measurements shown in **Figure 5(a)**. The axial asymmetry with the eye of the vortex closest to the radial outflow boundary, would seem to be consistent with the asymmetry in the tangential velocity commented on above.

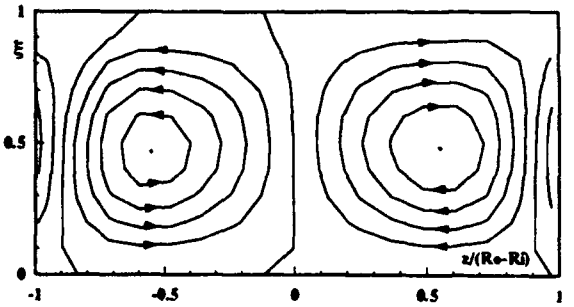

Figure 6. Streamline patterns within Taylor vortices for glucose solution at a Taylor number of 15400 (the stream function Ψ varies from 0 on the boundaries to a maximum of 1 in the vortex interior).

The maximum axial velocity components at Taylor numbers of 4,460, 15,400 and 25,100, presented in **Figure 7**, confirm that both velocities and velocity gradients are higher in the vicinity of the centrebody than at the outer wall of the annulus, and that with increasing Taylor number the position of zero velocity (the eye of the vortex) moves towards the outer wall.

4.2 XANTHAN GUM

Since Xanthan gum may be considered to be essentially a power-law fluid, the Taylor number was defined as suggested by Sinevic et al (1986) with the effective viscosity determined from the theoretical shear rate prevailing at the rotating surface for Couette flow of a power-law fluid, i.e. $\dot{\gamma}_C = (2\omega/n)\,[1 - \kappa^{2/n}]^{-1}$ with values of n in the range 0.44 to 0.47.

The critical Taylor number was again determined by monitoring the development of an axial velocity component at a fixed radius with changing centrebody rotation rates. The data shown in **Figure 3** reveal that the onset of Taylor flow is much more gradual than was the case for glucose. This is at variance with the conclusion of Green and Jones (1982) who found that the increase in torque which accompanies the onset of Taylor flow was just as abrupt for Xanthan gum and polyacrylamide as for a Newtonian fluid. From the present work it may be concluded that the critical Taylor number for 0.15% Xanthan gum is about 10,000.

The two tangential-velocity profiles measured in plane Couette flow (**Figure 4**) correspond to sub-critical Taylor numbers of 1,360 and 9,800. Agreement with the theoretical profile appropriate for a power-law fluid of index 0.44, is very good, although the data fall slightly closer to the curve for an index of n = 0.5.

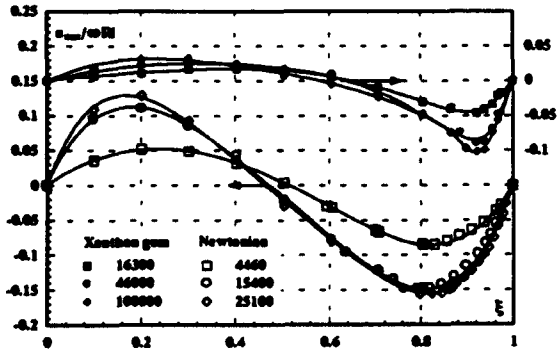

Figure 7. Radial variation of maximum axial velocity within a Taylor vortex for Newtonian fluid and Xanthan gum.

Mappings of the Taylor vortex structure in the axial and tangential planes were conducted at a supercritical Taylor number of 46,000 after a stabilization time of about 240 minutes. It became apparent during the mapping that the vortices were drifting at approximately 3-4 μm/s along the axis of the geometry opposite to the direction of the centrebody rotation vector. Due to the exceptionally long stabilization times predicted by Snyder for a geometry of this length and fluid viscosity it was initially thought that the drift might be due to inadequate settling times. Other possible causes were thought to be imperfections in the flow geometry or the rheological characteristics of the fluid, particularly its elasticity. However, as will be seen in the next section, vortex drift was also observed for Laponite/CMC, but in the opposite direction suggesting that fluid rheology rather than geometry or settling time was the underlying cause. As for the Newtonian case, the tangential velocity component (**Figure 8b**) exhibits a periodicity of the same frequency as the axial velocity component (**Figure 8a**) but lags the axial component by 90° (i.e. the maximum and minimum tangential velocities correspond to zero axial velocity).

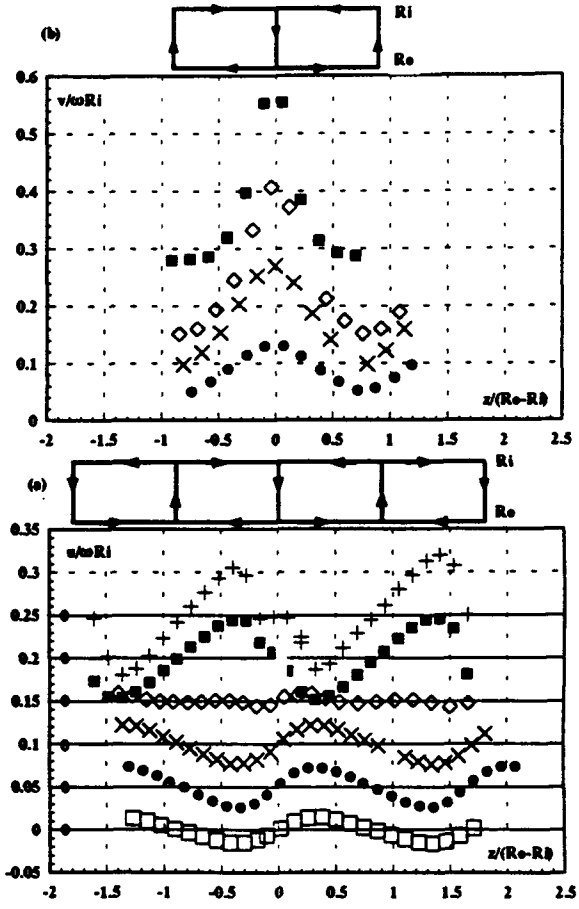

Figure 8. Velocity components within Taylor vortices for Xanthan gum at a Taylor number of 46000 (a) axial (b) tangential.

Streamline patterns, (**Figure 9**) determined from the axial velocity measurements again reveal the overall structure of the interior motion. The essential difference compared with the observations for glucose is the radial shift of the vortex eye towards the centrebody, i.e. in the direction of higher shear stress and lower viscosity. The maximum axial velocity components, also measured at two additional Taylor numbers (**Figure 7**), confirm the increased radial asymmetry compared with the Newtonian

fluid with significantly higher velocities and velocity gradients in the near centrebody region.

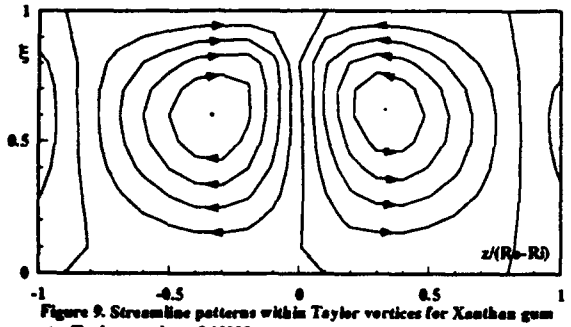

Figure 9. Streamline patterns within Taylor vortices for Xanthan gum at a Taylor number of 46000.

4.3 LAPONITE/CMC

Given the long equilibrium times associated with the thixotropic character of the Laponite/CMC blend, it was not practical to investigate the precise onset of Taylor flow by progressively increasing the rotation speed. Three profiles were measured in plane Couette flow together with one detailed vortex mapping at the highest possible centrebody rotation rate. As for Xanthan gum, the Taylor number has been defined by evaluating the apparent viscosity at the centrebody surface at a shear rate $\dot{\gamma}_C$ corresponding to Couette flow. The three velocity profiles in **Figure 10** are well represented by the theoretical results for a yield-stress fluid with flow restricted to the inner region of the annulus. stationary fluid in the outer annular region and the yield surface located progressively closer to the outer wall as the centrebody rotation rate increases.

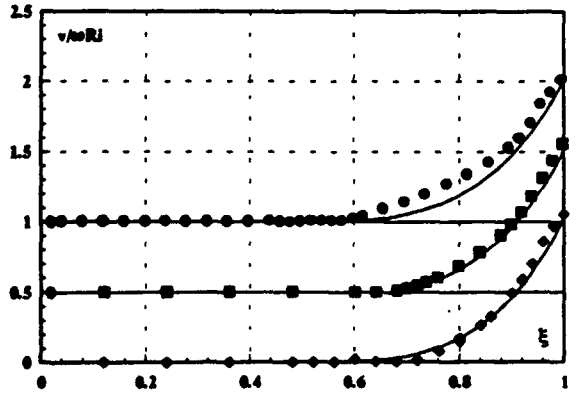

Figure 10. Tangential velocity profiles for 0.15% Laponite/0.07% CMC. Taylor numbers of ◆ 220 ■ 890 ● 1510

The vortex mapping conducted at a Taylor number of 54,000 (**Figure 11**) shows similar trends to those seen previously for the Newtonian fluid and Xanthan Gum, with no region of gelled fluid in evidence. Again the vortices were found to exhibit a slow drift (3-4 μm/s) along the axis of the geometry but now in the direction of the centrebody rotation vector. This contrast with the behaviour for Xanthan Gum suggests the drift is a consequence of the differences in fluid rheology, since all other influences were the same for the two fluids. The streamline patterns (**Figure 12**) are remarkably similar to those for Xanthan gum suggesting that the global structure of the Taylor vortices is determined by the shear-thinning characteristics of these two fluids and not significantly influenced by either elasticity or thixotropy.

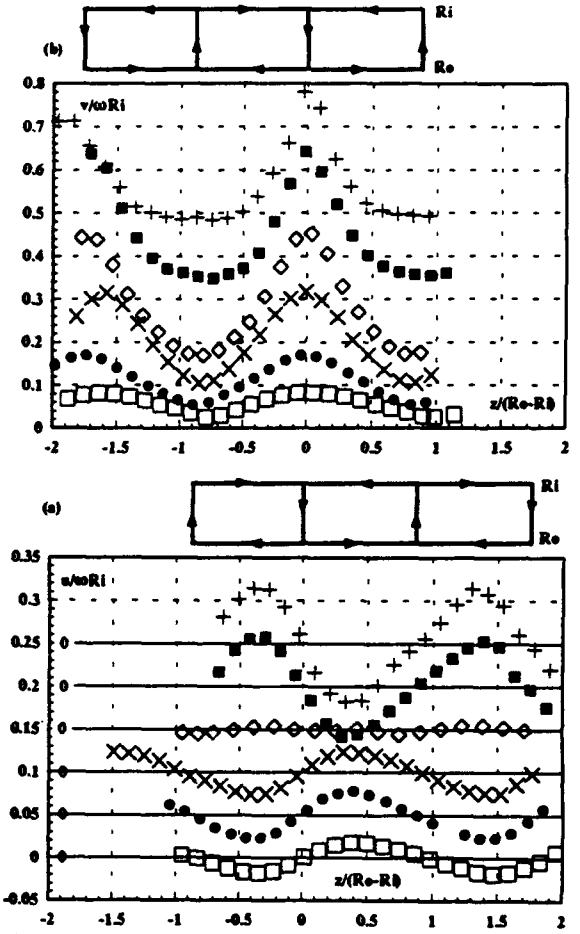

Figure 11. Velocity components within Taylor vortices for Laponite/CMC at a Taylor number of 54000 (a) axial (b) tangential.

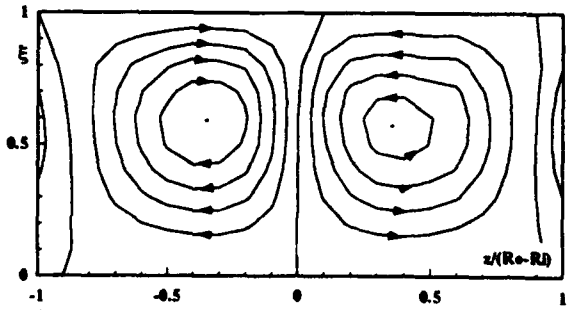

Figure 12. Streamline patterns within Taylor vortices for Laponite/CMC at a Taylor number of 54000.

5. CONCLUSIONS

For plane Couette flow of a Newtonian fluid, the measured azimuthal (tangential) velocity component is in excellent agreement with theoretical prediction and the transition from plane Couette flow to a flow exhibiting Taylor vortices is clearly identified by an abrupt increase from zero in the axial velocity. Detailed velocity mapping of a vortex pair showed the tangential velocity to exhibit a periodic structure of the same frequency as the axial component but out of phase by 90°. Higher values of the maximum axial velocity and velocity gradient are observed closer to the centrebody than the outer wall with the eye of the vortex moving towards the outer wall with increasing Taylor number. Streamline patterns determined from the measured axial velocities show that there is an appreciable axial asymmetry in the vortex structure, with the eye of the vortex closest to the radial outflow boundary where the tangential velocity was found to lie above the Couette-flow profile in contrast to the inflow boundary where it was lower.

Measurements for 0.15% Xanthan gum were again in close agreement with the theoretical tangential velocity profile for a power-law fluid in plane Couette flow although there was evidence of sensitivity to the power-law index, n. The transition to Taylor flow was marked by a more gradual increase from zero in the value of the axial velocity component. A slow drift of the vortices along the axis of the annulus was attributed to the elastic character of the fluid. The tangential and axial velocity components exhibited similar periodicity to that observed for the Newtonian fluid. The radial asymmetry in the vortex structure was more marked than for glucose with the eye of the vortex closer to the centrebody.

The thixotropic nature of the Laponite/CMC blend did not permit precise identification of the transition point from plane Couette flow to Taylor flow. Tangential velocity profiles measured in plane Couette flow are characteristic of a yield-stress fluid, with flow being restricted to inner region of the annulus. No region of gelled fluid was observed above the critical Taylor number and the vortex cell structure found to be remarkably similar to that for the Xanthan Gum suggesting that the shear-thinning aspect of the fluid rheology is far more important than either thixotropy or viscoelasticity whereas the axial drift, in the opposite direction to that of Xanthan gum, is more likely to be associated with thixotropy.

ACKNOWLEDGEMENTS

The work reported here represents part of a programme of research which has received financial support from SERC (GR/F 87813), BP Exploration Company Ltd, Shell Research BV and AEA Petroleum Services. This support is gratefully acknowledged. Frequent meetings with Professor J H Whitelaw, Imperial College of Science, Technology and Medicine, Dr C F Lockyear and Dr D Ryan, BP Research, Ms B Kampman, Shell Research BV and Dr W J Worraker, AEA Technology, were of considerable benefit to the research.

NOMENCLATURE

n	power-law exponent for fluid viscosity
r	radial distance from pipe centreline (m)
R_i	outer radius of centrebody (m)
R_n	refractive index
R_o	inner radius of outer tube (m)
R_y	radial location of yield surface (m)
Ta	Taylor number
Ta_c	critical Taylor number
u	axial component of velocity (m/s)
u_{max}	maximum axial velocity (m/s)
v	tangential component of velocity (m/s)
z	axial distance along annulus (m)
$\dot{\gamma}$	shear rate (s^{-1})
$\dot{\gamma}_C$	shear rate at centrebody (s^{-1})
κ	radius ratio R_i/R_o
λ_C	constant in Casson model (s)
λ_S	constant in Sisko model (s)
μ	dynamic viscosity (Pa.s)
μ_{ref}	reference viscosity (1 Pa.s)
μ_∞	infinite shear-rate viscosity (Pa.s)
ξ	non-dimensional radial location $(R_o - r)/(R_o - R_i)$
τ	shear stress (Pa)
τ_{ref}	reference shear stress (1 Pa)
τ_y	fluid yield stress (Pa)
ψ	non-dimensional stream function
ω	angular velocity of centrebody (rad/s)

7. REFERENCES

Alderman N.J., Ram Babu D., Hughes T.L. and Maitland G.C., 1988, The rheological properties of oil well drilling fluids, Proc. Xth Int. Cong.Rheology; Sydney, pp 140-142.

Coles, D., 1965, Transition in circular Couette flow. J. Fluid Mech., Vol 21, pp 385-425.

Donnelly R.J., 1958, Experiments on the stability of viscous flow between rotating cylinders. I. Torque measurements. Proc. R. Soc. Lond. A, Vol 246. pp 312-325.

Green, J. and Jones, W.M., 1982, Couette flow of dilute solutions of macromolecules : embryo cellos and overstability. J. Fluid Mech., Vol 119. pp 491-505.

Koschmeider, E.L., 1993, Bénard cells and Taylor vortices. Cambridge University Press.

Lockett, T.J., 1992, Numerical simulation of inelastic non-Newtonian fluid flows in annuli. PhD Thesis. Imperial College of Science, Technology and Medicine.

Lockett T.J., Richardson, S.M. and Worraker W.J., 1992, The stability of inelastic non-Newtonian fluids in Couette flow between concentric cylinders: a finite-element study. J. Non-Newtonian Fluid Mech., Vol 43, pp 165-177.

Sinevic V, Kuboi R and Nienow A.W., 1986, Power numbers, Taylor numbers and Taylor vortices in viscous Newtonian and non-Newtonian fluids. Chem. Eng. Sci., Vol 41. No 11, pp 2915-2923.

Synder H.A. and Lambert R.B., 1966, Harmonic generation in Taylor vortices between rotating cylinders. J. Fluid Mech. Vol 26, pp 545-562.

Stuart, J.T., 1986, Taylor-vortex flow: A dynamical system. SIAM Review, Vol 283, pp 315-342.

Taylor, G.I., 1923, Stability of a viscous liquid contained between two rotating cylinders. Phil. Trans. Roy. Soc., London, A., Vol 223, pp 289-343.

LDV MEASUREMENTS OF CONFINED VORTEX BREAKDOWN GENERATED BY A ROTATING CONE

D.F.G. Durão, J.C.F. Pereira, T.T.S. Pereira and J.M.M. Sousa

Instituto Superior Técnico/Technical University of Lisbon
Mechanical Engineering Department
Av. Rovisco Pais
1096 Lisbon Codex
Portugal

ABSTRACT

LDV measurements of the three-dimensional velocity flowfield in the confined swirling flow generated by a rotating cone are presented. The reported measurements covered two particular regimes exhibiting bubble-type of vortex breakdown. The corresponding Reynolds numbers were Re = 2200 and 2570, with values of the confinement parameter H/R = 2 and 3, respectively. The former regime displayed single breakdown, while the latter regime was characterized by double breakdown. The present measurements and flow visualization have corroborated the axisymmetry of the flowfield associated to bubble-type of vortex breakdown already observed in different flow geometries.

1. INTRODUCTION

The words "vortex breakdown" (VB) are nowadays assentingly used to describe an abrupt change in the structure of the core of a swirling flow. When a certain critical state, determined by the Reynolds number and the geometry of the swirl generator, is reached, the flow in the axis undergoes a drastic deceleration, leading to the occurrence of a stagnation point with the concomitant enlargement of the core, often associated to regions of recirculating flow. The phenomenon may, however, present distinctive features, depending upon the case, as it has been reported to occur in a panoply of circumstances.

The major general classification of the different forms of VB divides them into two categories: the "bubble-type" and the "spiral-type", the former usually displaying a high degree of axisymmetry and the latter being intrinsically non-axisymmetric. Nevertheless, since the first recognized observation of VB, by Peckham and Atkinson (1957), in the tip vortices of a delta-winged aircraft, the problem has received the attention of many other researchers, giving rise to the discovery of a number of sub-categories. The complexity of VB flows and its sensitivity to external disturbances advised the implementation of experimental apparatus where the phenomenon might be accurately investigated under controlled conditions. The tube flow with swirl generated by an upstream guidevane arrangement was widely used, first by Harvey (1962) and later by several others, e.g., Sarpkaya (1971), Faler (1976), Faler and Leibovich (1977), Escudier and Keller (1983), and Bornstein and Escudier (1984). Escudier and his co-workers have also used another apparatus (Escudier *et al*, 1980 and Escudier *et al*, 1982), the slit-tube arrangement, exhibiting the advantage of a resulting vortex core which was relatively thin, although the swirling flow has been found to be slightly asymmetrical. A third experimental device which has been employed in many investigations was the cylindrical container, where the fluid motion is produced by a rotating endwall (see, e.g., Escudier, 1984 and Spohn *et al*, 1993). Mainly due to the fact that for this configuration the boundary conditions are precisely specified, successful numerical simulations have been recently also performed for this geometry. These were reported in a series of papers by Lopez (1990), Brown and Lopez (1990), and Lopez and Perry (1992). Despite the fact that the flow visualization studies have probably played the dominant role in this line of research, detailed and very reliable measurements of bubble-type breakdown have also been carried out (Faler and Leibovitch, 1978 and Bornstein and Escudier, 1984) using a non-intrusive technique, laser-Doppler velocimetry (LDV). It is undeniable that the complete and accurate mapping of the internal structure of VB flows represents an invaluable contribution towards the understanding of the underlying mechanisms.

From the practical viewpoint, the relevance of the aforementioned studies cannot be neglected, as VB occurs not only in unconfined flows, as in the above cited case of delta wings, but particularly in numerous confined swirling flows, such as those inside furnaces and combustion chambers, in draft tubes of water turbines and in the outlet casing of axial turbomachinery. While in the mentioned cases where combustion is present the occurrence of VB may be beneficial, as the zones of turbulent recirculating flow are suitable for flame stabilization, in the remainder cases it has pernicious consequences as it results in undesirable pressure loss and structural vibrations.

The above referred variety of cases and associated geometries suggested the idea of investigating the behavior of VB structures generated inside a slightly more complicated geometry. In the present paper an experimental study of confined swirling flow generated by a rotating cone is described. The main objective of the reported investigations is to apply LDV techniques to accurately characterize the core structure of the flow, with special emphasis put on the occurrence of VB and its consequences in the surrounding flowfield.

Herein, detailed measurements of the three-dimensional velocity field associated to bubble-type VB are complemented with flow visualization. The next section describes the experimental arrangement, presents details of the flow configuration, of the laser-Doppler velocimeter and flow visualization. In Section 3, the results of the present work are shown and discussed. The last section summarizes the main findings of this study.

2. EXPERIMENTAL ARRANGEMENT

2.1 Flow Configuration

The essential features of the experimental setup are schematically shown in Fig.1. The swirling flow is generated inside a DURAN glass cylinder with an inner radius R = 50 mm and the length H may be adjusted, up to H/R = 4, using the screw fixed to the top wall. The rotating cone, $(H/R)_{cone}$ = 1, is driven by an electronically controlled motor which velocity is adjustable in a continuous range up to 1500 rpm (Ω = 157 rad/s). The working fluid employed for the LDV measurements was "baby oil", a colorless oil mixture, aiming to avoid the loss of applicability of LDV due by changes of position of the measuring volume which occur when the light passes through solids and fluids of different refractive index. By refractive index matching, this fluid allowed to eliminate the problem of distortion of the optical paths through the curved surfaces in the liquid flow, so that reliable measurements close to the walls could be carried out. In order to ensure stable operating conditions (constant viscosity and refractive index) it was necessary to immerse the cylindrical container in a thermostatically controlled bath of the same working fluid, with temperature adjusted up to ± 0.1 °C, using a GRANT TD immersion thermostat and water cooling. The viscosity values have been obtained employing a digital viscometer BROOKFIELD model DV-II. Due to the pureness of the working fluid, it was further necessary to add polystyrene spherical particles (d = 1 μm) to the oil, so that a reasonable signal-to-noise ratio could be obtained.

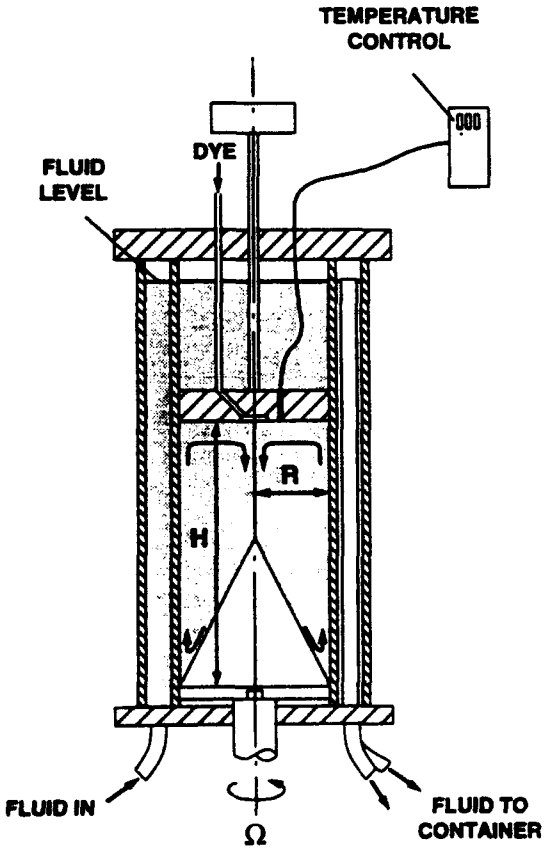

Fig. 1 Geometrical flow configuration

After flow visualization two regimes were selected to be studied in detail, covering the aspect ratios H/R = 2 and 3. The Reynolds numbers characterizing these cases were $Re = \Omega R^2/\nu$ = 2200 and 2570, respectively.

2.2 Instrumentation

The measurements were obtained using a two-component LDV system. A 3W (nominal) Ar-ion laser was employed as laser source for the velocimeter, which was operated in the dual-beam (two green and two blue) backward-scatter mode and included acousto-optic modulator to provide sensitivity to the flow direction. A shift frequency of 200 kHz was used. The principal characteristics of the velocimeter are summarized in Table 1.

Table 1 *Principal characteristics of the* laser-Doppler velocimeter

3W (nominal) Ar-ion laser — wavelengths: green: 514.5 nm blue: 488.0 nm
Virtual beam waist diameter, @ $1/e^2$ points: 1.4 mm
Focal length of focusing lens: 350 mm
Half-angle of beam intersection: measured (in air): 4.086° calculated (in working fluid): 2.774°
Fringe separation in working fluid: green: 5.315 μm blue: 5.042 μm
Number of fringes within the control volume: 31
Calculated dimensions of measuring volume, @ $1/e^2$ points, in working fluid: major axis of the ellipsoid: green: 3.384 mm blue: 3.210 mm minor axis of the ellipsoid: green: 0.164 mm blue: 0.155 mm
Velocimeter transfer constants: green: 5.315 (ms^{-1})/MHz blue: 5.042 (ms^{-1})/MHz

The backward-scatter light (green and blue) was collected through the transmitting and receiving lenses and focused into the multimode receiving fiber. The received light from the multimode fiber was collimated with the double-input coupler. The collimated received light was directed into a color separator to separate the light of the two velocity components. Then, the photomultiplier output signals were monitored in a two-channel oscilloscope, filtered and processed using a double counter (TSI 1990C) interface with

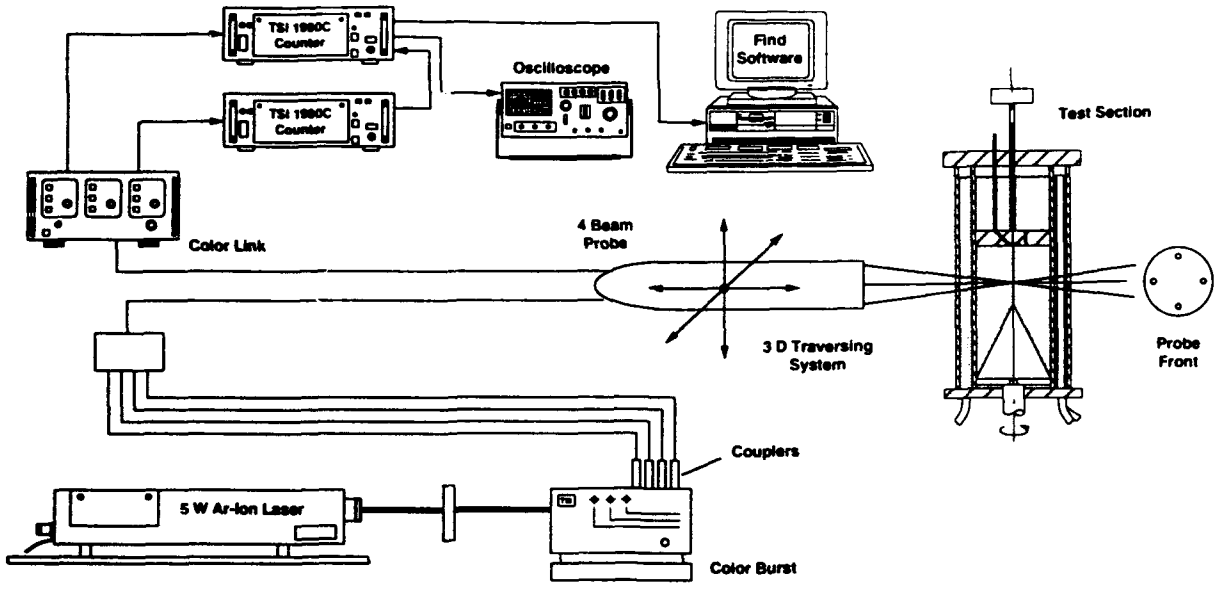

Fig. 2 Optical arrangement and signal processing

a digital computer, as shown in Fig. 2. The velocity values were evaluated by ensemble averaging, calculated from 5000 samples, using the TSI FIND Software. This software was also used to control an ISEL three-dimensional traversing system, where the fiberoptic probe containing the transmitting and receiving optics was mounted. The test section was held stationary. In order to map the three-dimensional velocity flowfield, two traversings through centerplanes of the test section were carried out for stations along the axial direction. In the first traversing, the axial and radial components (u and v) were measured, while during the second traversing, performed in a direction normal to the previous one, data to compute the swirl component (w) was acquired.

The velocity measurements may be affected by non-turbulent Doppler broadening errors, due to gradients of mean velocity across the measuring volume (see, e.g., Durst *et al*, 1981). The maximum error in the mean velocity value was estimated to be normally at least four orders of magnitude smaller than the maximum velocity in the flow. On the other hand, random errors associated to the statistical evaluation of the mean velocity values were found to be below 3%, according to the analysis referred by Yanta and Smith (1978) for a 95% confidence level.

2.3 Flow Visualization

The fluid motion inside the cylinder was made visible by light reflecting the seeding particles in the oil. A lateral laser light illuminated the cylinder centerplane and photographs were taken at right angle to the sheet of light. Still photographs were obtained with 3200 ASA film, using exposure times of 1/15 to 1/2 seconds.

3. RESULTS

The angular speed Ω of the cone was gradually increased, starting from rest. This originated the development of a rotating boundary layer on the cone surface which caused a centrifugal pump effect, sending the fluid radially outwards in spiral trajectories. Due to the presence of the cylinder walls, the fluid was then forced to spiral up them, giving rise to the establishment of a sidewall boundary layer. Except for the losses caused by viscous dissipation, the fluid conserved its angular momentum, until reaching the top stationary wall. Then, another boundary layer is formed, decelerating the fluid in the vicinity of the wall. As the radial pressure forces had to be compensated by the centrifugal forces, the fluid trajectory radius was reduced, directing the flow towards the axis. Then, by continuity, the spinning cone further sucked the fluid from the axis of the top wall, again in a spiral motion downwards to the tip of the cone. These features were observed during the flow visualization that was carried out prior to the detailed measurements. It guided the selection of the regimes to study and also the choice of the measurement locations.

Figures 3a and 3b show the flow patterns inside the cylinder, for $H/R = 2$, $Re = 2200$ (case 1), and for $H/R = 3$, $Re = 2570$ (case 2), respectively. The photographs reveal fully developed recirculation bubbles in the core flow, indicating single breakdown for case 1 and double breakdown for case 2. It was possible to observe that, close to $Re = 1350$, in case 1 (single breakdown), and $Re = 2240$ in case 2 (double breakdown, simultaneous), spiral structures were formed. With a small increase in Ω, these structures were radially stretched, giving place to the aforementioned recirculation bubbles, as a central stagnation point appeared.

Figures 4a and 4b display the velocity vectors formed by the measured axial and radial velocity components, corresponding to case 1 and case 2, respectively. As in the flow visualization study, case 1 was characterized by the presence of a significantly stretched (radially) single bubble, while case 2 exhibited a regular bubble near the top wall and a second more elongated (longitudinally) one closer to the cone. Throughout the bubbles interior it can be seen that the fluid velocities are very low, which implies that

these are regions of practically uniform pressure. The measurements further confirmed the axisymmetry of the present flow cases.

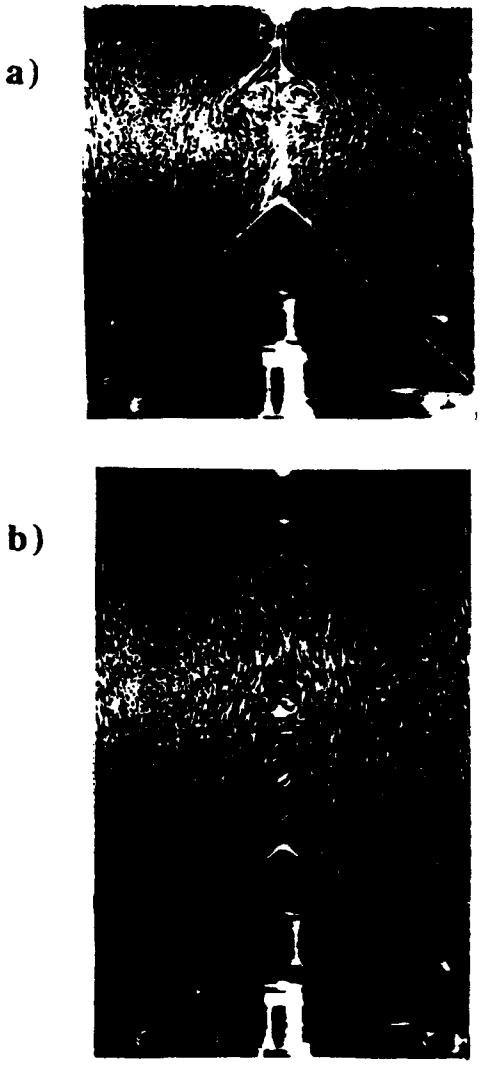

Fig. 3 Flow visualization
a) Studied regime for $H/R = 2$
b) Studied regime for $H/R = 3$

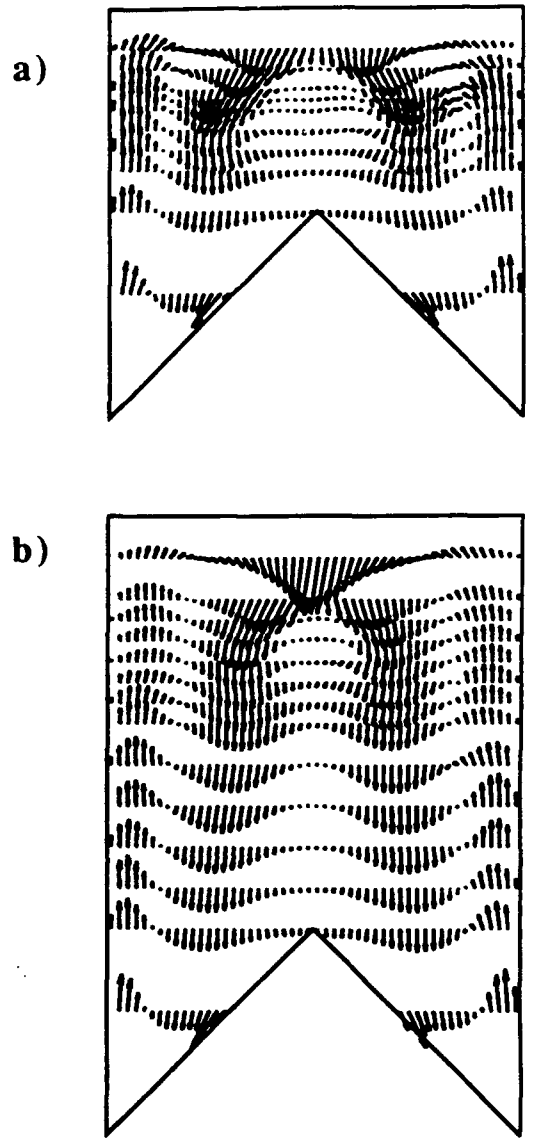

Fig. 4 Measured velocity vectors (u,v)
a) Studied regime for $H/R = 2$
b) Studied regime for $H/R = 3$

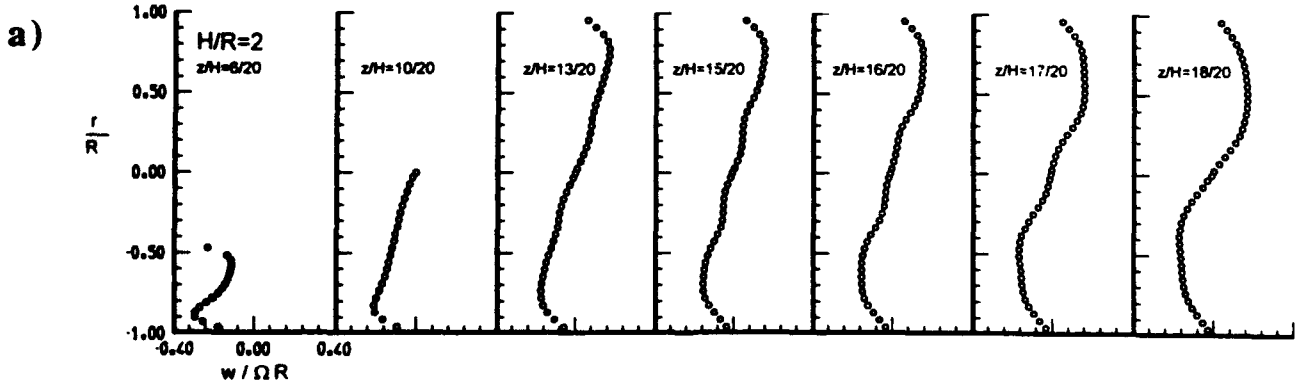

For caption see next page

b)

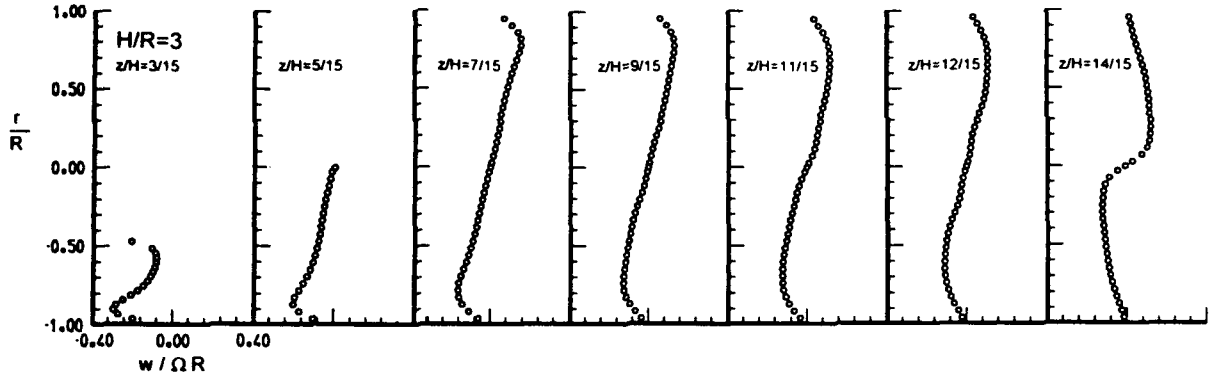

Fig. 5 Profiles of w-velocity component
a) Studied regime for $H/R = 2$; b) Studied regime for $H/R = 3$

The evolution of the swirl component along a centerplane is portrayed in Figs. 5a and 5b. The most remarkable features are the high gradients in the cone region and, moving upwards into vortex breakdown locations, the development of double-zoned velocity profiles. It is discernible that the presence of a recirculation bubble yields a region of low swirl velocity, while an outer region with higher swirl can also be identified in these profiles. Both regions display almost constant values of swirl velocity. The magnitude of this effect was observed to be correlated with the strength of the recirculation bubble.

4. CONCLUSIONS

Flow visualization and detailed LDV measurements of the three velocity components in the confined swirling flow generated by a rotating cone have been presented for two distinct flow conditions. These were characterized by the presence of bubble-type vortex breakdown. For $H/R = 2$ and $Re = 2200$, single breakdown was observed, while for $H/R = 3$ and $Re = 2570$ the flow displayed double breakdown. Both the flow visualization and the measurements have shown that the flowfield was axisymmetric.

The features exhibited by the present flow problem were similar to those reported for the rotating endwall (disk) problem. However, the investigated geometry have shown different stability characteristics.

REFERENCES

Bornstein, J. & Escudier, M.P. 1984, LDA Measurements within a Vortex Breakdown Bubble, Laser Anemometry in Fluid Mechanics, pp. 253-263, Ladoan-Instituto Superior Técnico.

Brown, G.L. & Lopez, J.M. 1990, Axisymmetric Vortex Breakdown. Part 2. Physical Mechanisms, J. Fluid Mech., vol. 221, pp. 553-576.

Durst, F., Melling, A. & Whitelaw, J.H. 1981, Principles and Practice of Laser-Doppler Anemometry, 2nd ed., Academic Press, New York.

Escudier, M.P. 1984, Observations of the Flow Produced in a Cylindrical Container by a Rotating Endwall, Exp. Fluids, vol. 2, no. 4, pp.189-196.

Escudier, M.P. & Keller, J.J. 1983, Vortex Breakdown: a Two-Stage Transition, AGARD CP-342, Paper 25.

Escudier, M.P., Bornstein, J. & Maxworthy, T. 1982, The Dynamics of Confined Vortices, Proc. R. Soc. Lond., Ser. A, no. 382, pp. 335-360.

Escudier, M.P., Bornstein, J. & Zehnder, N. 1980, Observations and LDA Measurements of Confined Turbulent Vortex Flow, J. Fluid Mech., vol. 98, no. 1, pp. 49-63.

Faler, J.H. 1976, Some Experiments in Swirling Flows: Detailed Velocity Measurements of a Vortex Breakdown using a Laser Doppler Anemometer, NASA CR-135115.

Faler, J.H. & Leibovich, S. 1977, Disrupted States of Vortex Flow and Vortex Breakdown, Phys. Fluids, vol. 20, no. 9, pp. 1385-1400.

Faler, J.H. & Leibovich, S. 1978, An Experimental Map of the Internal Structure of a Vortex Breakdown, J. Fluid Mech., vol. 86, no. 2, pp. 313-335.

Harvey, J.K. 1962, Some Observations of the Vortex Breakdown Phenomenon, J. Fluid Mech., vol. 14, no. 4, pp. 585-592.

Lopez, J.M. 1990, Axisymmetric Vortex Breakdown. Part 1. Confined Swirling Flow, J. Fluid Mech., vol. 221, pp. 533-552.

Lopez, J.M. & Perry, A.D. 1992, Axisymmetric Vortex Breakdown. Part 3. Onset of Periodic Flow and Chaotic Advection, J. Fluid Mech., vol. 234, pp. 449-471.

Peckham, D.H. & Atkinson, S.A. 1957, Preliminary Results of Low Speed Wind Tunnel Tests on a Gothic Wing of Aspect Ratio 1.0, Aero. Res. Counc. CP-508.

Sarpkaya, T. 1971, Vortex Breakdown in Swirling Conical Flows, AIAA J., vol. 9, no. 9, pp. 1792-1799.

Spohn, A., Mory, M. & Hopfinger, E.J. 1993, Observations of Vortex Breakdown in an Open Cylindrical Container with a Rotating Bottom, Exp. Fluids, vol. 14, no. 1/2, pp. 70-77.

Yanta, Z. & Smith, R.A. 1978, Measurements of Turbulent-Transport Properties with a Laser-Doppler Velocimeter, AIAA-73-169, Eleventh Aerospace Science Meeting, Washington.

7th International Symposium on Applications of Laser-Techniques to Fluid Mechanics, Lissabon, July 1994

LDV-MEASUREMENTS ON THE LAMINAR-TURBULENT TRANSITION IN SPHERICAL COUETTE FLOW

Christoph Egbers, Wolfgang Beyer, Alexander Meijering and Hans J. Rath

Center of Applied Space Technology and Microgravity (ZARM)
University of Bremen, 28359 Bremen, F.R.G.

ABSTRACT

The laminar-turbulent transition of a viscous incompressible fluid flow in the gap between two concentric spheres, where only the inner sphere rotates (spherical Couette flow), was investigated by laser-Doppler-velocimetry and simultanously flow visualization measurements for the case of two relatively wide gap widths (β = 0.33 and β = 0.5), where Taylor vortices do not exist. At the stability threshold, where the laminar basic flow loses its stability, the first instability manifests itself as a break of the spatial symmetry and non-axisymmetric secondary waves with spiral arms occur. They spread from the pole to the equator. With increasing the Reynolds number above the critical one, the number of secondary waves with spiral vortices decreases. During the laminar-turbulent transition, these secondary waves are periodic in time, quasi-periodic and then they lose their stability to turbulence.

1 INTRODUCTION

We consider the flow between two concentric spheres as illustrated in figure 1 with the inner sphere rotating and the outer one at rest. This flow can be characterized by the following control parameters: The aspect-ratio $\beta = (R_2-R_1)/R_1$ and the Reynolds number $Re = (R_1^2 \cdot \omega_1)/\nu$, where R_1 and R_2 are the inner and outer radii, ω_1 is the angular velocity of the inner sphere and ν is the kinematic viscosity.

Earlier experimental investigations on spherical Couette flow were restricted to small and medium gap widths, where Taylor vortices exist as reported by Sawatzki & Zierep (1970), Munson & Menguturk (1975), Wimmer (1976), Yavorskaya *et al.* (1980), Wimmer (1981), Bühler (1985) and Bühler & Zierep (1984, 1986).

Although spherical Couette flow is more relevant to astrophysical and geophysical applications, in comparison with the Taylor-Couette flow system (e.g. Fenstermacher *et al.* 1979, Andereck *et al.* 1986, Buzug *et al.* 1992, 1993, v. Stamm *et al.* 1993), the dynamic behaviour during the laminar-turbulent transition of the flow between two concentric spheres has been studied less (e.g. Belyaev *et al.* 1984, Nakabayashi &Tsuchida 1988).

In this study some new aspects of the dynamic behaviour in the spherical Couette flow during the transition to turbulence for a wide range of Reynolds numbers and for the case of wide gap widths are presented. The instabilities arising are in contrast to Taylor-instabilities (Taylor 1923). They occur in the form of non-axisymmetric secondary waves with spiral arms, which break the spatial symmetry-behaviour of the basic flow. With increasing the Reynolds number, the number of secondary waves with spiral arms decreases, before the flow loses its stability to turbulence (Egbers 1994). In earlier works, this transition was thought to be a direct transition into turbulence without the existence of instabilities (e.g. Munson & Menguturk 1975).

Therefore, in this work we want to give some additional quantitative estimates for the existance of a transition region during the laminar-turbulent transition and for the onset of turbulence.

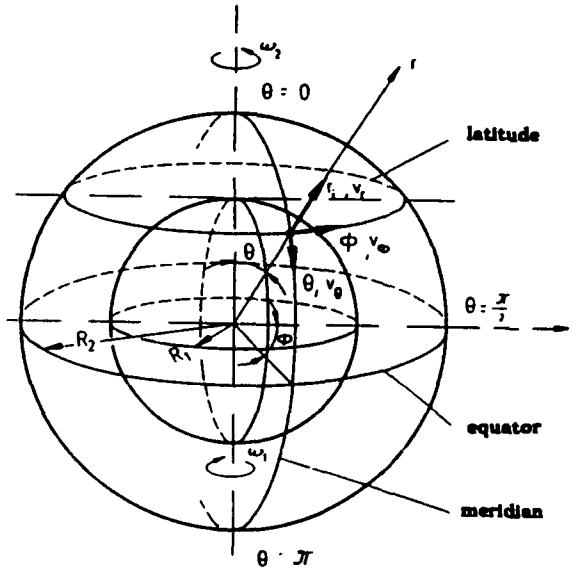

Fig. 1: Principle sketch of the spherical Couette flow

Experimental results connected with the problems of stability, bifurcation, non-axisymmetry, periodicity and turbulence in the spherical Couette flow will be discussed. These experiments can serve on one hand as a quantitative improvement of our previous experiments (Egbers 1994) and on the other hand as a test for future quantitative measurements connected with the characterization of period-doubling phenomena.

Nevertheless, the model of the concentric spherical Couette flow is of basic importance especially for the understanding of the chaotic behaviour as observed in geophysical and astrophysical motions.

2 EXPERIMENTAL METHODS

2.1 Experimental apparatus

An experimental set-up for spherical Couette flow was constructed, consisting of an inner sphere rotating concentrically inside another rotating outer spherical shell. A principle sketch of the experimental apparatus is illustrated in figure 2:

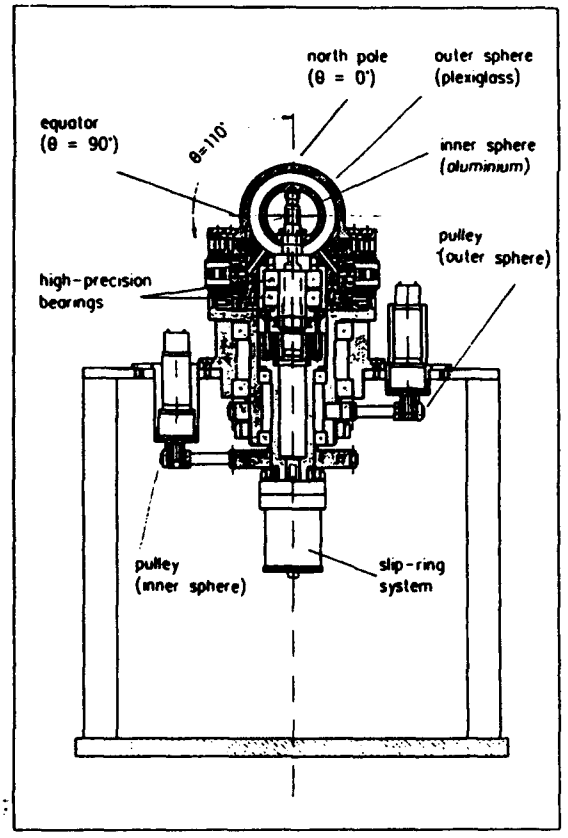

Fig. 2: Principle sketch of the experimental apparatus

The outer sphere (R_2 =40.00±0.02 mm) is composed of two transparent acrylic plastic hemispheres. The upper hemisphere has a spherical outer surface of about $0 \le \Theta \le 110^{\circ}$ to investigate whether the occuring flow patterns are symmetric with respect to the equatorial plane or not.The inner sphere is made out of aluminium having the five various radii R_1 shown in table 1, to variate the aspect ratio β in a range between $0.08 \le \beta \le 0.5$.

No.	radius R_1 of inner spheres [mm]	aspect ratio β $\beta = (R_2 - R_1)/R_1$
1	37.00 ± 0.01	0.08
2	33.96 ± 0.02	0.18
3	32.03 ± 0.02	0.25
4	29.95 ± 0.03	0.33
5	26.70 ± 0.01	0.50

Table 1: Dimensions of inner spheres and variation of aspect ratio (radius of the outer sphere: R_2 = 40.00±0.02 mm)

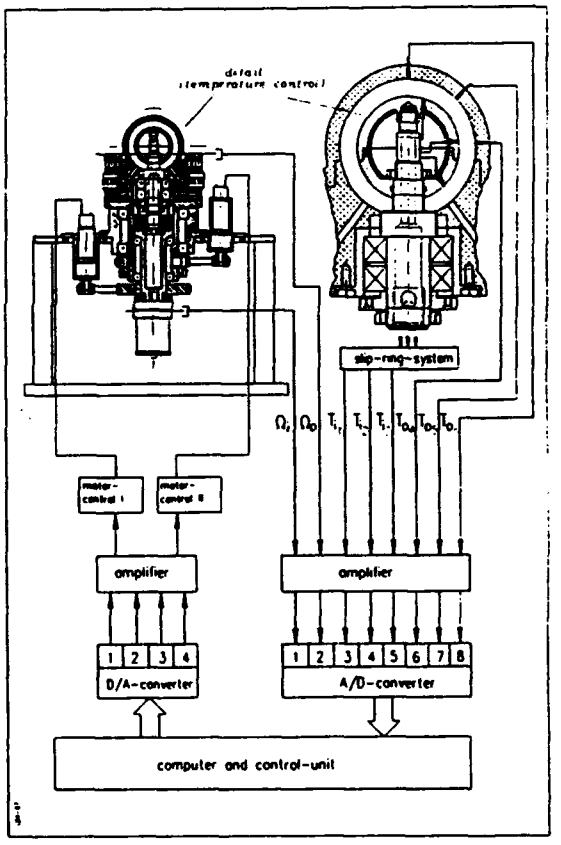

Fig. 3: Schematic view of the experiment control (principle of temperature control and rotation rate measurement)

Generally, both spheres can be rotated independently by means of two belt-drives. The eccentricity between outer and inner sphere could be minimized to ±0.015 mm using high precision bearings and shafts. Two different synchronous motor drives were adapted, which provide a uniform and stable rate of rotation up to n_{max} = 850 rev/min with fluctuations of less than 1.5%. They variate

the Reynolds numbers of the inner and outer sphere respectively in a range from 0 to Re = 10^5. The revolutions were calibrated using an optical tracking system (optical coupling). Most of our experiments were carried out by increasing the Reynolds number quasistationary from zero. However, because the occuring flow structures depend also on initial conditions, the acceleration rate for both spheres can be variated. A schematic view of the experiment control is illustrated in figure 3:

Experiments with the spherical Couette flow system were carried out in a laboratory condition, where the temperature could be kept uniformly up to ± 0.3 °C. Since the viscosity of the silicone oils, which were used as working fluids, vary by approximately 2% / ° C, the temperature must be precisely controlled and measured in order to have a well-defined Reynolds number. A temperature accuracy of ± 0.15 ° C was achieved for all six temperature sensors (PT 1000) used in our experiment: For measuring the fluid temperature, three temperature sensors are installed just below the outer surface of the inner sphere at latitudes $\Theta_{i1} = 10°$, $\Theta_{i2} = 80°$ and $\Theta_{i3} = 160°$. These temperature data were transferred from the rotating sphere to the stationary part by a slip-ring system. For investigations with only the inner sphere rotating three other temperature sensors are installed at the inner surface of the outer sphere at latitudes $\Theta_{o1}=0°$, $\Theta_{o2}=45°$ and $\Theta_{o3}=90°$ as depicted in fig. 3. Most of the measurements were made with the silicone oil M3 at a temperature of 25°C.

Fluid data			Baysilon-oil M3
density	ρ	[kg/m³]	910
kin. viscosity	ν	[10^{-6} m²/s]	3.30
refractive index	n	[-]	1.394

Table 2: List of characteristic fluid data (25°C)

As tracer particles small aluminium flakes were used. The concentration by weight was 0.05%. The viscosities of the working fluids with tracer particles were measured with a VOR-rheometer (BOHLIN-Reologi AB, Sweden). An effect on the viscosity was not detected. The physical properties of the working fluid M3 are listed in table 2 for the temperature of 25 °C.

2.2 Flow visualization technique

Because some of the observed flow structures appearing in the spherical Couette flow are non-axisymmetric and non-equatorialsymmetric, it was necessary to develop a new observation-technique, which provides a simultaneously flow visualization of both the azimuthal and the meridional flow. Therefore, a combination of the following two visualization methods was used:

To investigate the flow structures occuring in the meridional cross-section of the spherical annulus, a slit illumination technique is employed. In addition to the slit illumination technique, a system with a fiber-optic is applied to visualize the front flow region with azimuthal waves. Furthermore, for characterizing the non-axisymmetric instabilities in wide gap widths, two cameras were simultaneously used for the observation of the polar and equatorial region. In practice, the angle of observation of the azimuthal and meridional flows is of about 90°. In this way, the cellular structure of the occuring vortices in the meridional plane as well as the azimuthal and polar behaviour of the arising flow pattern can be obtained. Photographs or print sequences from video-records (videoprints) were taken.

2.3 Laser-Doppler-velocimeter measuring system

For the application of laser-Doppler-velocimetry (LDV) on the spherical Couette flow experiment, a special traversing system has been constructed to mount the optic probe on the spherical Couette flow experiment as depicted in figure 4 (a), while the laser and the transmitter are mounted apart from the experiment on a mounting bench. The traversing system consists of a high-precision bow with a traversing sledge and a traversing table. The traversing sledge is capable of moving the optic probe in meridional direction ($0 \le \Theta \le 110°$) and the traversing table is capable of

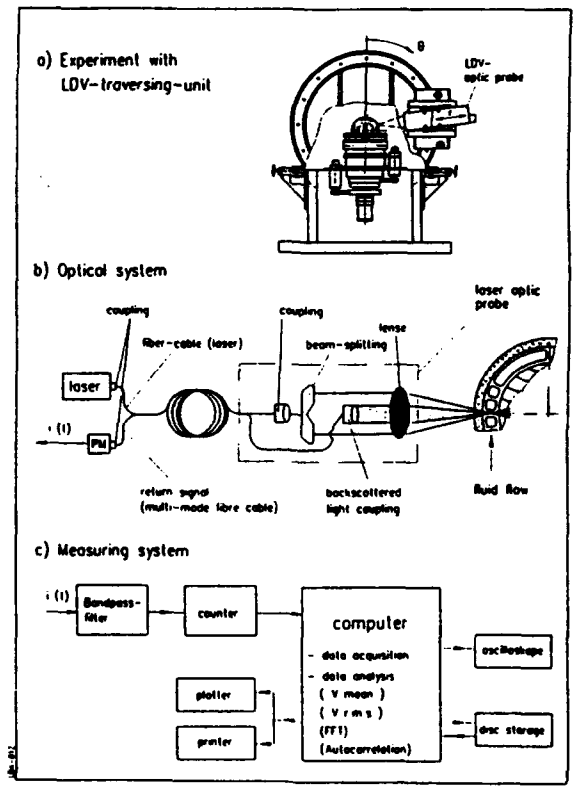

Fig. 4: Schematic diagram of the applied laser-Doppler-velocimeter (LDV) system:
(a): Traversing system for the LDV optic probe
(b): Optical system
(c): Measuring system

moving in radial direction over a range of 60 mm in order to determine the meridional dependence of the velocity and to obtain velocity profiles. The laser-Doppler-velocimeter system used in our experiments, consists of a 100 mW Ar-laser, a transmitter unit and a 1-D fiber-flow optic-probe (DANTEC-Electronics, Denmark). A frequency shift is added by the Bragg-cell-unit to one of the beam pair to allow for measurements of reversing flows. The optic probe with a fibre optic cable is connected to the transmitter via manipulators. The optical part of the laser-Doppler-system, which uses the dual beam backscatter geometry, is shown schematically in figure 4 (b). The backscattered light is focussed on a photomultiplier tube. All LDV measurements were made with the traversing system mentioned above. Data records of each measurement in the centre of the gap consisted of 32000 validated Doppler bursts, while for each location along the profile, a sequence of 8000 validated Doppler bursts was accumulated in the buffer interface. A principle sketch of the data processing technique with the laser-Doppler signal-processor, which is based on FFT-technique, is shown in figure 4(c). Parameters characterizing the laser-Doppler-velocimeter and traversing data are listed in table 3.

Ar-laser	100	[mW]
focal length	160	[mm]
wavelength	514.5	[nm]
beam spacing	38	[mm]
beam diameter	2.2	[mm]
number of fringes	22	[−]
probe volume: length	0.4	[mm]
diameter	0.05	[mm]
fringe spacing	2.18	[µm]
Bragg-cell frequency	40	[MHz]
meridional traversing angle	$0 \le \Theta \le 110°$	
radial traversing distance	$0 \le r \le 60$ mm	

Table 3: Parameters characterizing the laser-Doppler-velocimeter and traversing data

The application of the LDV-technique on the spherical Couette flow experiment requires an optical correction for the accurate determinations of the probe volume locations and for the interference fringe spacing due to refraction effects of the spherical outer surface. Because the probe is adjusted in radial direction, the optical axis of the front lense of the probe passes perpendicular through the spherical outer surface. Thus, the correction for the two laser beams, which are in the same plane, could be calculated for a cylindrical surface. However, the fact, that a small probing volume is needed to produce sufficient spatial resolution, which could be obtained only by a large intersection angle, the small-angle approximation cannot be used in this case. The correction method used in this work for the case of large intersection angles, is illustrated in figure 5. The ray tracing begins at the front lense of the LDV optics. The equations describing the beam propagation follow immediatly from Snells law and from geometric considerations. For further details, the reader might be referred to Kekoe & Desai (1987), Gardavský & Hrbek (1989) and Meijering (1993).

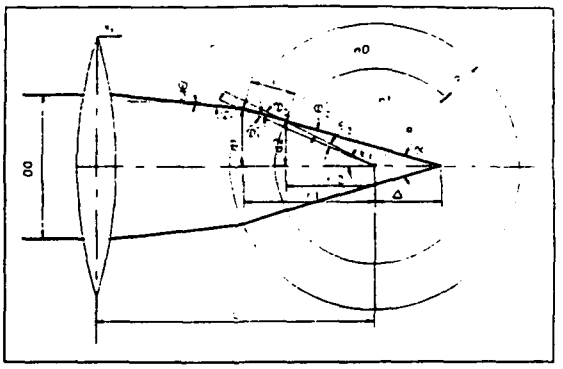

Fig. 5: Ray tracing for measuring the azimuthal and meridional velocity component (Meijering 1993)

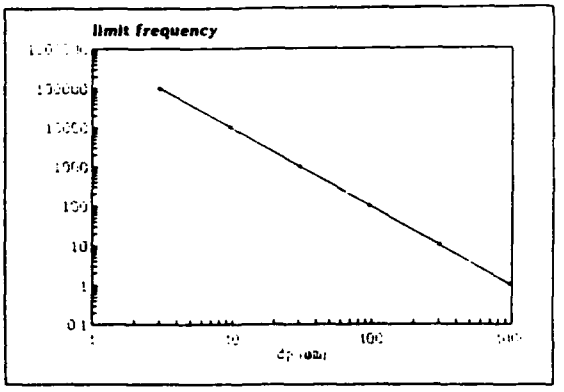

Fig. 6: Frequency limit as a function of particle diameter: Aluminium-flakes in silicone oil M3: $d_p \approx 50$ µm (Meijering 1993)

The LDV-technique requires the addition of particles to the working fluid. For this study of simultaneously LDV- and flow visualization-measurements, we were able to use the same small aluminium particles as tracer ranging between 10 and 50µm by calculating the particle adaption capability, which was improved with the formulas given by Ruck (1990). For an amplitude ratio η = 99%, which defines the accuracy with which the particles follow the fluid fluctuations, the calculated limitation frequency as a function of particle diameter and for the tracer/fluid combination used in the experiment is illustrated in figure 6. As can be seen from this calculation, the frequency limit for 50µm particles is only of about 500 Hz, which is 5 times higher as the measured frequencies of the power spectra. As a result of this calculation, the position Δ of the laser beam intersection relative to the centre of the sphere in radial direction is determined by Meijering (1993).

$$\Delta = d_2 / \tan(\alpha/2) - r_2.$$

The interference fringe spacing Δx at the laser beam intersection that is traversed in radial direction is

$$\Delta x = (\lambda / n_1) / 2\sin(\alpha/2).$$

The azimuthal velocity will be

$$v = f_D \cdot \Delta x.$$

The refraction corrections for the probe volume location and the fringe spacing are shown in figure 7.

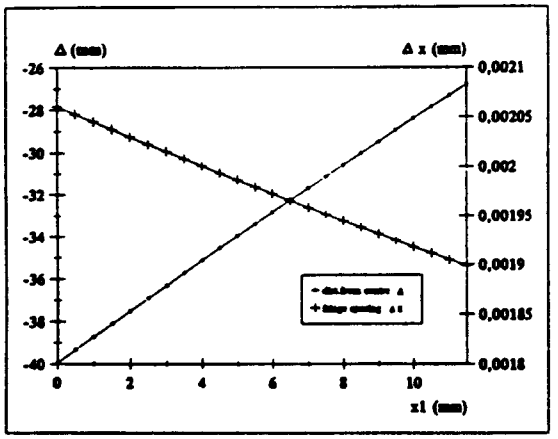

Fig. 7: Refraction correction for the optic probe volume location Δ and the interference fringe spacing Δx as a function of the radial traversing position (Meijering 1993)

Fig. 8: Visual observations of the secondary waves with spiral vortices (β = 0.5, Re = 1583, n = 5)

Furthermore, the spherical Couette flow in wide gap widths shows the well-known transition phenomena of hysteresis and non-uniqueness, depending on the acceleration rate of the inner sphere (Egbers 1994).

In order to give some quantitative estimates on the dynamic behaviour of these secondary wave instabilities, for a wide range of Reynolds numbers, the azimuthal velocity components were recorded as a function of time in the center of the gap. From these records, the mean azimuthal velocity component, velocity profiles, the turbulence intensity (r.m.s value), the autocorrelation coefficients and the power spectra were calculated. Some of the results will be presented in the following chapters.

3 EXPERIMENTAL RESULTS

3.1 Visual observations of wide gap instabilities

In a previous investigation on the stability of spherical Couette flow (Egbers 1994), it was found, that the laminar basic flow between two concentric spheres, where only the inner sphere rotates and the outer one is at rest, loses its stability not only in the form of Taylor-instability. The instabilities occuring depend strongly on the aspect ratio. For wide gap widths ($\beta \geq 0.33$) considered here, the first instability manifests itself as a break of the spatial symmetry and a new non-axisymmetric secondary wave mode was observed, which spreads from the pole to the equator. With increasing the Reynolds number, the number of secondary waves with n spiral vortices decreases. For $\beta = 0.33$, secondary waves with n = six, five and four spiral arms were found, while in the gap with an aspect ratio of $\beta = 0.5$ waves with n = five, four or three spiral arms exist. As an example for this type of instability, the secondary wave flow with n = five spiral arms - observed from the pole - is depicted in figure 8.

The flow regimes, their spatial states with non-axisymmetric and non-equatorial symmetric secondary waves were characterized by measuring the phase velocities and the displacement between the northern and the southern hemisphere of the arising secondary waves (Egbers 1994).

3.2 Velocity distributions

During the transition region, the azimuthal velocity profiles as a function of the radial coordinate were measured at Θ 48° ($\beta = 0.33$) and $\Theta = 52^0$ ($\beta = 0.5$) with increasing Reynolds numbers. As can be seen in figure 9, the non-dimensional mean velocity profiles become more concave (upward) with increasing the Reynolds number in comparison with the theoretical one for the laminar basic flow calculated from Ritter (1973). Furthermore, with increasing the Reynolds number, the profiles exihibit a typical boundary layer characteristic with a minimum near the inner sphere and a maximum near the outer sphere. The velocity gradients become greater near the inner sphere in comparison with the outer sphere.

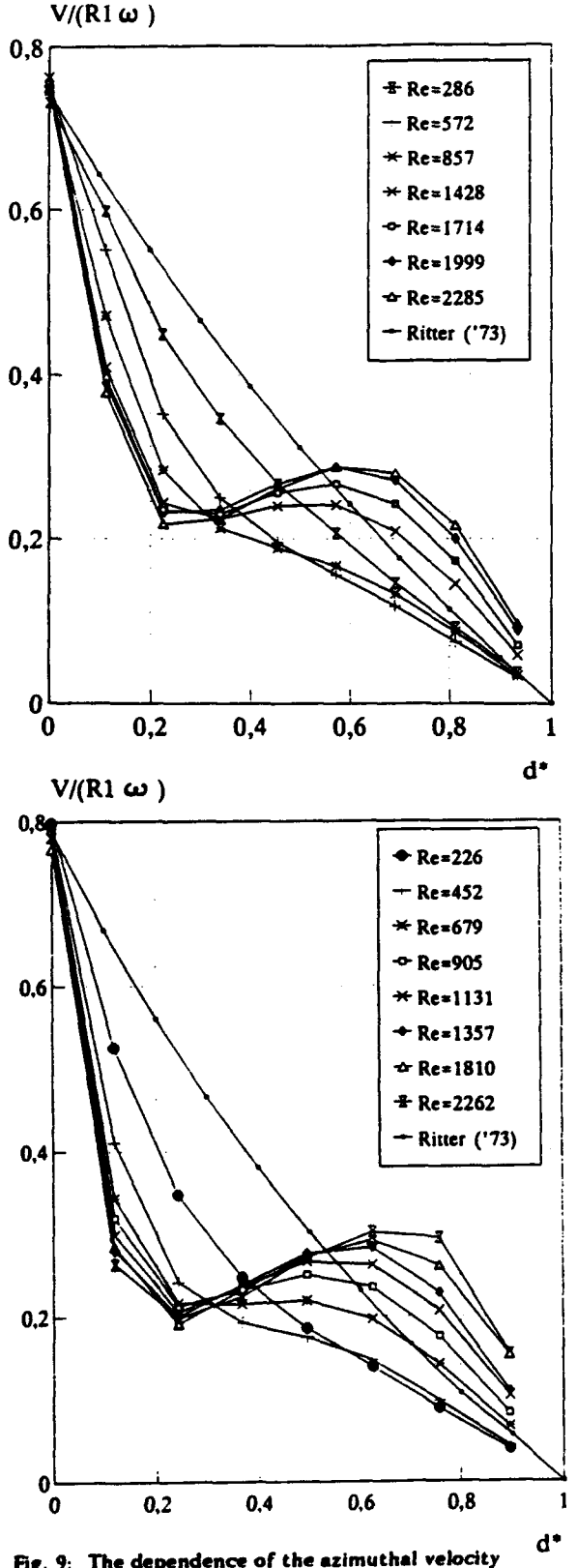

Fig. 9: The dependence of the azimuthal velocity profiles in the gap as a function of the Reynolds number in the transition region: (a) $\beta = 0.33$; $\Theta = 48°$ (b) $\beta = 0.5$; $\Theta = 52°$

3.3 Velocity fluctuations

The temporal dependence of the azimuthal velocity component in the centre of the gap ($d^* = 0.5$) as a function of the Reynolds number during the laminar/turbulent transition for the flow in the gap with an aspect ratio $\beta = 0.5$ and at the latitude $\Theta = 52°$ are illustrated in figure 10:

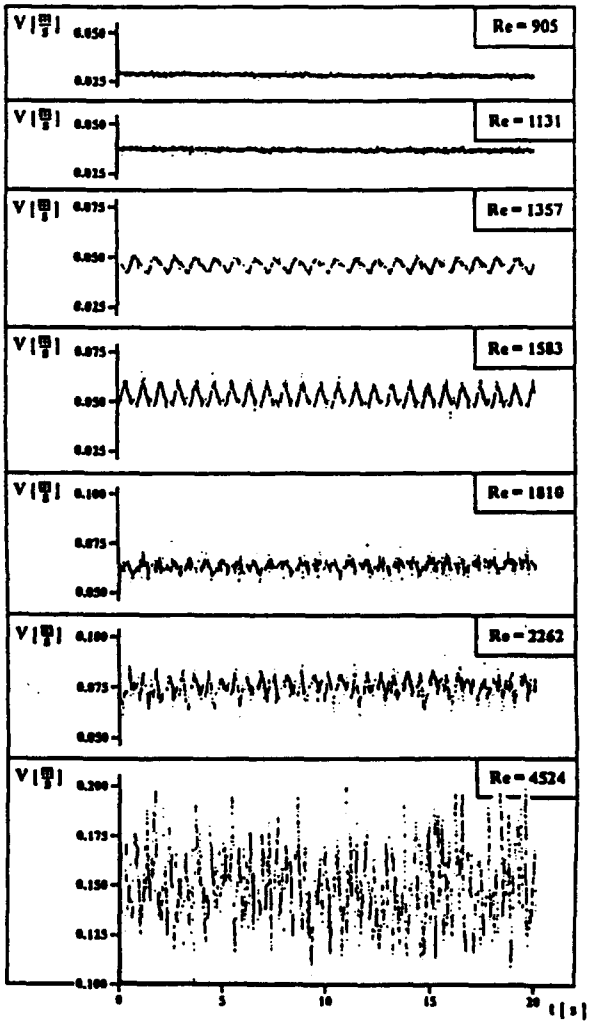

Fig.10: The temporal dependence of the azimuthal velocity components in the centre of the gap ($d^* = 0.5$) as a function of the Reynolds number during the laminar/turbulent transition ($\beta = 0.5$, $\Theta = 52°$)

For Re = 905 and Re = 1131 the flow is laminar stable. But with increasing the Reynolds number above the critical value ($Re_{crit} = 1244$) up to Re = 1357 (corresponding to visual observations shown in figure 8), the velocity shows a sinusoidale fluctuation, which corresponds to the phase velocity of the secondary waves. As already observed by flow visualization measurements, the secondary waves are periodic in time (Re = 1357, Re = 1583), quasi- periodic with noise (Re = 1810, Re = 2262)

and finally they are fully turbulent (Re = 4524). These results could be improved by calculating the corresponding autocorrelation coefficients as depicted in figure 11. From these records it can be seen, that the periodicity is also available for Re = 1357 and Re = 1583, but for Re ≥ 1810, the autocorrelation coefficients are quasi-periodic and damped, while for Re ≥ 2262 they are strongly damped.

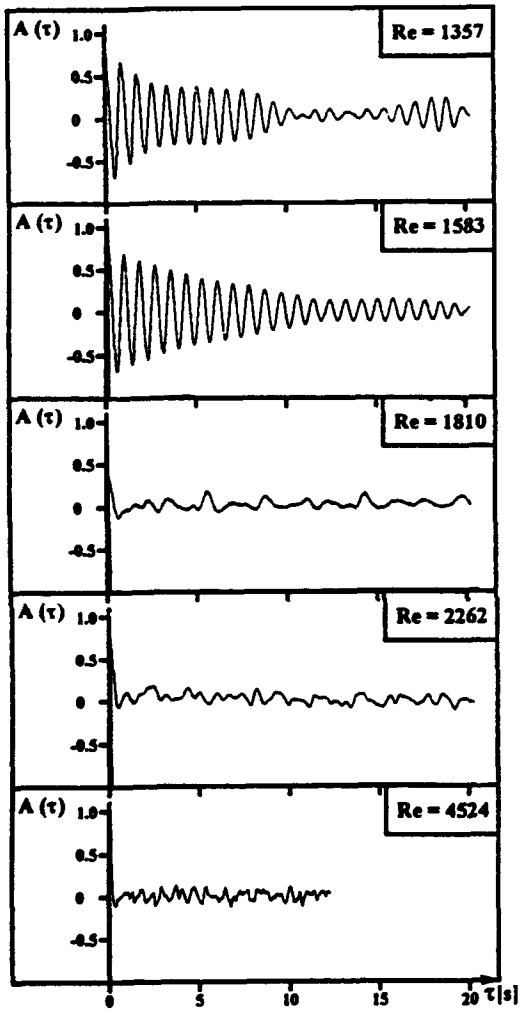

Fig.11: The autocorrelation coefficients of the azimuthal velocity components in the centre of the gap ($d^* = 0.5$) as a function of the Reynolds number during the laminar/ turbulent transition ($\beta = 0.5$, $\Theta = 52°$)

3.4 Power-spectra

The calculated power-spectra of the azimuthal velocity and the corresponding simultaneously observed flow pattern are illustrated in figure 12. For Re = 1583, where the secondary wave flow with five spiral arms exist, the power-spectrum contains a single frequency peak, which corresponds to the rotation frequency of the wave mode (Egbers 1994). The spectrum for Re = 1809 contains six frequency peaks, which corresponds to the quasi-periodic motion. For Re ≥ 2262, the frequency spectrum is filled continiously with noise and the flow becomes turbulent as it is shown in the corresponding visual observations. The transition to turbulence is characterized by the development of small scale structures.

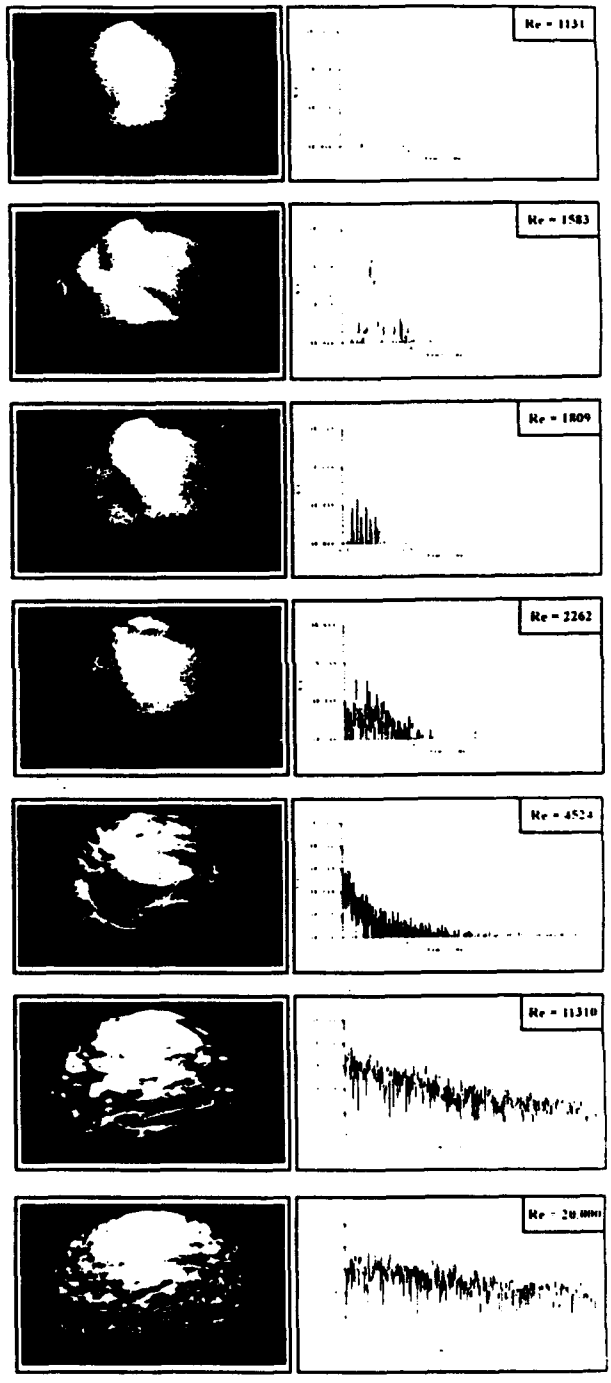

Fig. 12: Power-spectra of the azimuthal velocity components in the centre of the gap ($d^* = 0.5$) and corresponding observed flow regimes as a function of the Re-number during the laminar/ turbulent transition ($\beta = 0.50$; $\Theta = 52°$)

4 CONCLUSIONS

We have considered some characteristics of the laminar/ turbulent transition of the spherical Couette flow for wide gap widths. In contrast to previous investigations, we could detect a transition region, where instabilities in the form of secondary waves with spiral arms exist, which break the spatial symmetry. The LDV-technique could be applied successfully for measurements of the azimuthal velocity components. Their time-dependent behaviour during the transition to turbulence was obtained and shows the typical phenomena of periodicity, quasi-peridicity and stochastic regions. Further investigations must be carried out to give more informations about the dependence of the development of turbulence as a function of the meridional coordinate Θ.

ACKNOWLEDGEMENT

This work was supported by the Deutsche Agentur für Raumfahrtangelegenheiten (DARA) under grant number 50 QV 8898. The authors thank the students Jens Immohr and Sönke Seebacher for their assistence during this work.

REFERENCES

Andereck, C.D., Liu, S.S. and Swinney, H.L. (1986): Flow regimes in a circular Couette system with independently rotating cylinders. J. Fluid Mech., vol. 164, 155-183

Belyaev, Yu.N., Monakhov, A.A., Scherbakov, S.A. and Yavorskaya, I.M. (1984): Some routes to turbulence in spherical Couette Flow. in: Kozlov,V.V. (ed.): Laminar-TurbulentTransition. IUTAM-Symp. Novosibirsk/USSR, Springer, Berlin, Heidelberg, NewYork, Tokyo

Bühler, K. (1985): Strömungsmechanische Instabilitäten zäher Medien im Kugelspalt. VDI-Berichte, Reihe7: Strömungstechnik Nr.96

Bühler, K. and Zierep, J. (1984): New secondary instabilities for high Re-number flow between two rotating spheres. in: Kozlov,V.V. (ed.): Laminar-Turbulent-Transition. IUTAM-Symp. Novosibirsk/USSR, Springer, Berlin, Heidelberg, NewYork, Tokyo

Bühler, K. and Zierep, J. (1986): Dynamical instabilities and transition to turbulence in spherical gap flows. in: Comte-Bellot, G. and Mathieu, J.: Advances in turbulence. Proc. 1st Europ. Turb. Conf., Lyon, France, 1-4 July, Springer, Berlin, Heidelberg, NewYork, London, Paris, Tokyo

Buzug, Th., v. Stamm, J. and Pfister, G. (1992): Fractal dimensions of strange attractors obtained from the Taylor-Couette experiment. Physica A, 191, 559-563

Buzug, Th., v. Stamm, J. and Pfister, G. (1993): Characterization of period-doubling scenarios in Taylor-Couette flow. Physical Review E, 47, no. 2, 1054-1065

Egbers, C.(1994): Zur Stabilität der Strömung im konzentrischen Kugelspalt. Dissertation, Universität Bremen

Fenstermacher, P.R., Swinney, H.L. and Gollub, J.P. (1979): Dynamic instabilities and the transition to chaotic Taylor vortex flow. J. Fluid Mech., vol94, part1, 103-128

Gardavský, J. and Hrbek, J. (1989): Refraction Correction for LDV-Measurements in Circular Tubes within Rectangular Optical Boxes. DANTEC-inf. no. 8

Kekoe, A.B. and Desai, P.V. (1987): Compensation for refractive-index variations in laser-Doppler-anemometry. Applied Optics 26, 2582-2591

Meijering, A. (1993): Anwendung der Laser-Doppler-Anemometrie für Strömungsuntersuchungen im Spalt zwischen zwei konzentrisch rotierenden Kugeln. Diplomarbeit, Universität Bremen, FB 4, ZARM

Munson, B.R. and Menguturk, M. (1975): Viscous incompressible flow between concentric rotating spheres. Part 3: Linear stability and experiments. J. Fluid Mech., vol. 69, 705-719

Nakabayashi, K. and Tsuchida,Y. (1988): Spectral study of the laminar-turbulent transition in spherical Couette flow. J. Fluid Mech., vol. 194, 101-132

Ritter, C.F. (1973): Berechnung der zähen, inkompressiblen Strömung im Spalt zwischen zwei konzentrischen, rotierenden Kugelflächen. Dissertation. Universität Karlsruhe

Ruck, B. (1990) Lasermethoden in der Strömungsmeßtechnik. AT-Fachverlag , Stuttgart

Sawatzki, O. und Zierep, J. (1970): Das Stromfeld im Spalt zwischen zwei konzentrischen Kugelflächen, von denen die innere rotiert. Acta Mechanica 9, 13-35

v. Stamm, J., Buzug, Th. and Pfister, G. (199 : Frequency locking in axisymmetric Taylor-Couette flow. submitted to Physical Review E.

Taylor, G.J. (1923): Stability of a viscous liquid contained between two rotating cylinders. Phil.Trans. A223, 289-293

Wimmer, M. (1976): Experiments on a viscous fluid flow between concentric rotating spheres. J. Fluid Mech., vol.78, part2, 317-335

Wimmer, M. (1981): Experiments on the stability of viscous flow between two concentric rotating spheres. J. Fluid Mech., vol.103, 117-131

Yavorskaya, I.M., Belyaev,Yu.N., Monakhov, A.A., Astaf'eva, N.M, Scherbakov, S.A. and Vvedenskaya, N.D. (1980): Stability, non-uniqueness and transition to turbulence in the flow between two rotating spheres. IUTAM-Symposium

LDA AND LIF EXPERIMENTS ON THE QUASI-PERIODIC AND COMPLEX FLOW IN A CYCLONE

M.G.D. Fokke, T.L. Liem, J.J. Derksen[1] and H.E.A. van den Akker

Kramers Laboratorium voor Fysische Technologie, Delft University of Technology
Prins Bernhardlaan 6
2628 BW Delft; The Netherlands

ABSTRACT

An experimental study on the flow field in a reverse flow cyclone operating at Reynolds numbers of the order of 10^4 was performed. Under all circumstances the flow showed low frequency fluctuations due to so called vortex precession. With laser doppler anemometry (LDA) radial profiles of both axial and tangential velocity were measured. A laser induced fluorescence (LIF) experiment visualised the flow in the core region of the cyclone. In case the cyclone was fed through one inlet (i.e. at strongest swirl conditions) the experimental results demonstrate backflow from outside the cyclone near its centre.

INTRODUCTION

Swirl flows are important, both in science and in engineering. From a fluid dynamicist's point of view, swirl flows exhibit interesting phenomena such as precession, recirculation, and non-isotropic turbulence. Process industry utilises swirl flows in a wide range of applications (e.g. cyclone separators, burners, spray nozzles). When optimising such process equipment it is essential its fluid dynamics be well understood.

The separator performance of reverse flow gas cyclones strongly depends on details of the flow field. Computational fluid dynamics (CFD) can be a very helpful tool in cyclone optimisation (see e.g. Boysan *et al*, 1982). However, the complexity of the turbulent flow in cyclones necessitates experiments in order to guide and verify the computations. In this context we performed experimental studies on flow fields in reverse flow cyclones.

Most experiments were conducted in a water cyclone, completely filled with water due to water head. Its geometry is depicted in *figure 1*. With LDA and visualisation techniques the flow field was investigated at several flow rates fed through either one inlet or two inlets. A water instead of a gas

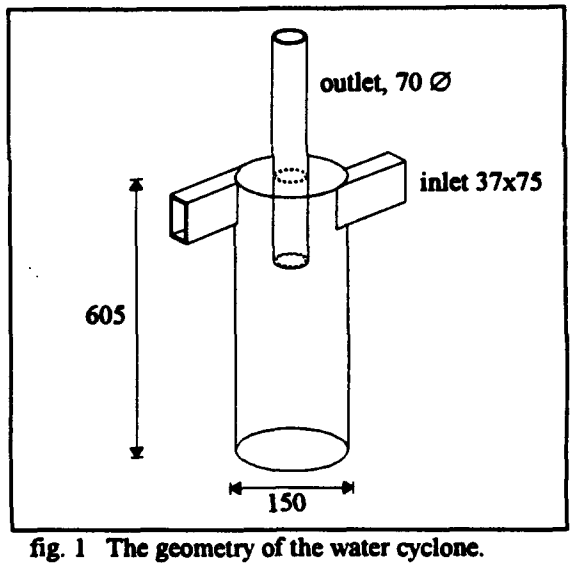

fig. 1 The geometry of the water cyclone. Sizes in mm.

cyclone was used because water facilitates visualisation and continuous LDA measurements. The flow can be roughly characterised with a Reynolds number and a swirl number (*Sw*), the latter being the ratio of axial flux of angular momentum and axial flux of axial momentum times cyclone radius. In general the (overall) swirl number is determined by the geometry of the cyclone. The water cyclone can be operated at Reynolds numbers between 1×10^4 and 4×10^4 with either *Sw=3* (one inlet) or

[1] author to whom correspondence should be addressed

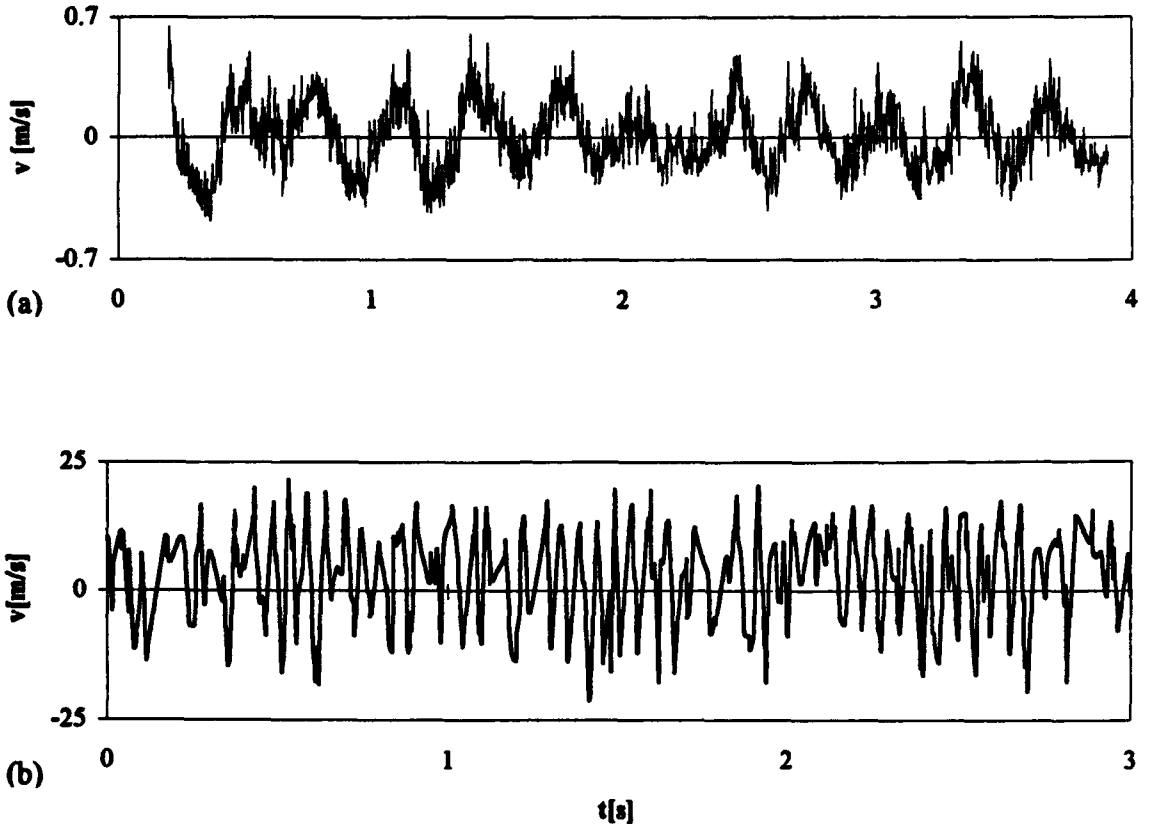

fig. 2 Two LDA time series. (a) Time series in the water cyclone at $Re=2\times10^4$, (b) time series in a gas cyclone at $Re=3\times10^4$.

Sw=1.5 (two inlets). In order to check the similarity with gas cyclone flow we also present experimental results from an air cyclone (with different geometry) operating at almost practical superficial velocities.

Under all circumstances the vortex core showed a low frequency precessing motion. Throughout the flow field the precession of the vortex core was felt. This is demonstrated in *figure 2* where typical LDA measurements are depicted. The first time series (*figure 2a*) was obtained in the water cyclone. Its low frequency fluctuations are due to vortex precession. For reference we also present a LDA time series measured in the gas cyclone at a much higher superficial velocity (*figure 2b*). The signals are *quasi*-periodic. Therefore we could not, as in truly periodic flows like the flows in stirred vessels or combustion engines, perform phase resolved measurements. Such techniques are useless given the random phase jumps of the precessing vortex core. However, detailed knowledge of the flow, particularly near the centre line of the cyclone, requires velocity profiles that are resolved for the vortex core position. The LDA experiments were supplemented with a visualisation study using LIF in order to obtain more insight in the flow near the vortex core.

LDA EXPERIMENTS

The LDA set up we employed was a one-component reference beam system manufactured by TPD. A laser beam emanating from a 32 mW HeNe laser was diffracted and frequency shifted at a rotating grating. A 400 mm focal length lens focused the beams into the measuring volume which had dimensions $4.2\times0.16\times0.16$ mm^3. Light from the reference beam mixed with scattered light was detected with a photodiode. The photodiode signal was processed by a frequency tracker. The tracker signal was sampled with a frequency of

512 Hz. At several flow rates through the cyclone fed through either one inlet or two inlets (ranging from 1×4.5 m^3/h to 1×16 m^3/h and from 2×4.5 m^3/h to 2×8 m^3/h) radial profiles of the axial and tangential velocity at two vertical positions were measured.

Spectral analysis of the LDA time series showed that the principal frequency of the fluctuations induced by vortex precession was proportional to the flow rate with a proportionality constant depending on the number of inlets, corresponding to results found in literature (e.g. Gupta *et al*, 1984). The Strouhal numbers, defined as $S=f_{prec}D^3/\phi_v$ (with f_{prec} the precession frequency, D the cyclone diameter and ϕ_v the volume flux through the cyclone) were found to be 5.22 and 2.92 for one inlet and two inlets respectively. The latter value corresponds quite well with $S=3.04$ for a cyclone with two inlets operating at $Re \geq 3\times10^4$ reported in Gupta *et al* (1984).

It is known (see e.g. Escudier & Zehnder, 1982) that under strong swirl conditions backflow in the core of the cyclone can occur. The time averaged axial velocity profiles we measured with LDA do not show backflow near the centre, i.e. the time averaged velocity in the cyclone core always had an upward component. Due to precession however these time averaged profiles are smoothed versions of the profiles centred on the actual (moving) vortex core position: backflow could have been obscured by spatial averaging.

Based on ideas presented by Liem & van den Akker (1992) a procedure to correct the time averaged profiles of the axial velocity for the influence of precession was developed. The assumption was made that an extremum in the velocity time series corresponds to a more or less fixed position of the vortex core relative to the measuring volume. The extrema in the LDA signals were determined by filtering the original time series with a double moving average filter, the second filter having a width about 1.5 times the width of the first filter (the width of a moving average filter equals f_s/N_{ma} with f_s the sampling frequency and N_{ma} the number of samples within the average). The filter's widths were chosen to lie within the spectral gap between precession induced and turbulent fluctuations. The average of a number of small sets of measurement points near the extrema is interpreted as an averaged velocity at a specific (yet unknown) position relative to the vortex core:

$$v_{corr} = \frac{1}{N(k+1)} \sum_{i=1}^{N} \sum_{j=-k/2}^{k/2} v(n_i + j)$$

with v_{corr} the corrected averaged velocity at an extremum (the minima yield $v_{corr,min}$, the maxima $v_{corr,max}$), $v(n_i+j)$ the individual velocity measurements and n_i the sample numbers of the extrema (minima *or* maxima) of the filtered signal.

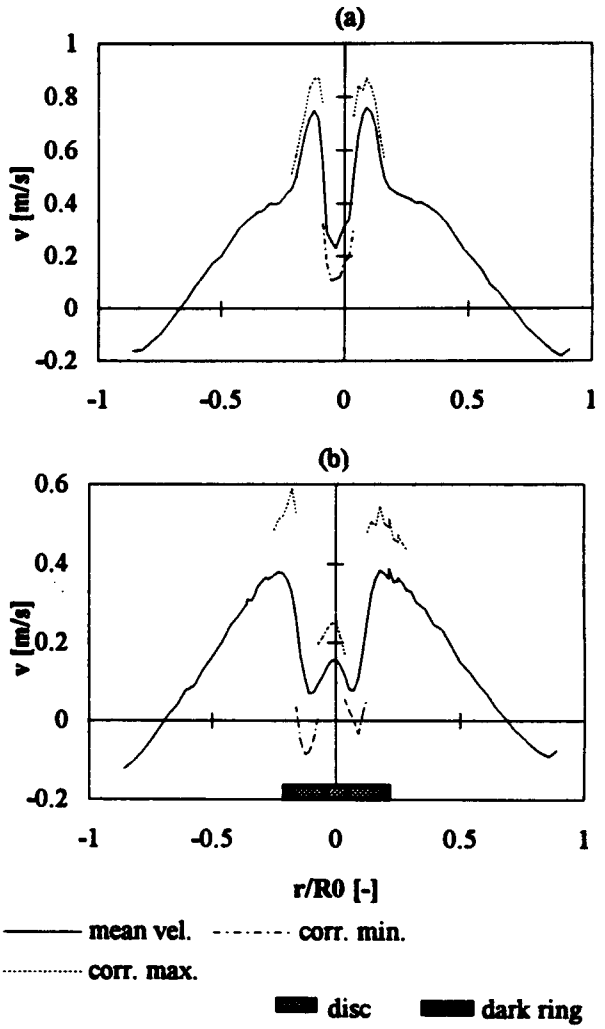

fig. 3 Radial profiles of axial velocity at z=228 mm. (a) Flow through two inlets (2×8 m^3/h).(b) Flow through one inlet (1×8 m^3/h). In the bottom part the dimensions of the disc observed with LIF are displayed.

The total number of points within the average equals $N(k+1)$, N is the number of extrema and $(k+1)$ the number of points per extremum. The choice of the parameter k is a compromise between accurate statistical estimates (large k) and sufficient temporal/spatial resolution (small k). In practice a value of about 20 sufficed.

VELOCITY PROFILES

Major differences between flow structures in the cyclone operating with one inlet ($Sw=3$) and two inlets ($Sw=1.5$) are observed. This is demonstrated in the *figures 3a* and *3b* which show radial profiles of the axial velocity in both operating modes. The results of the precession correction procedure are also depicted. Only for the one inlet case, i.e. for strongest swirl, the corrected LDA measurements show backflow near the vortex core. *Figure 4* is a radial profile of the time averaged axial velocity in the gas cyclone at $Re=3\times10^4$ and $Sw=3.1$. The data corrected for vortex precession indicate backflow.

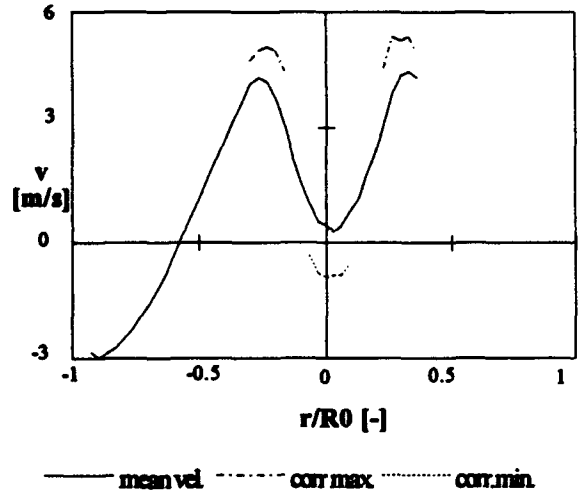

fig. 4 Radial profile of the axial velocity in the gas cyclone.

The radial profiles of the tangential velocity (*figure 5*) can be divided in a forced vortex (inner) and a free vortex (outer) region. The profiles in the outer region can be adequately described with

$$v_\theta = Cr^{-\alpha}$$

with v_θ the tangential velocity, r the radial position and C and α constants. The values of α range

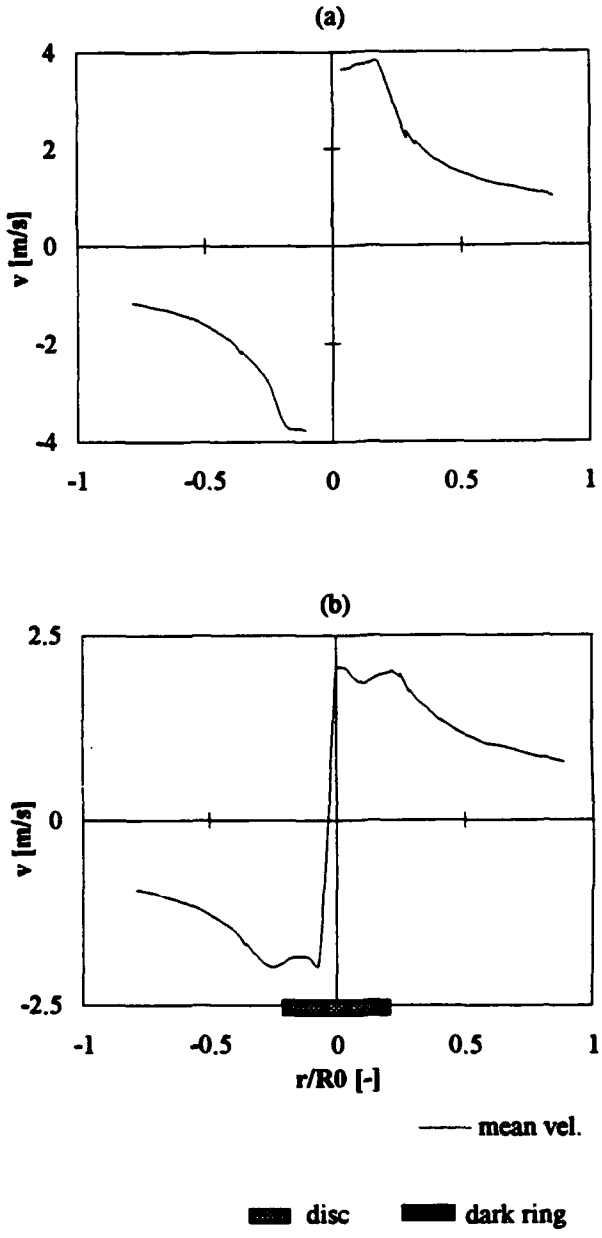

fig. 5 Radial profiles of tangential velocity at z=228 mm. (a) Flow through two inlets (2×8 m^3/h). (b) Flow through one inlet (1×8 m^3/h). In the bottom part the dimensions of the disc observed with LIF.

fig. 6 Grey value picture from a LIF visualisation in a horizontal plane in the cyclone. The centre of the picture roughly corresponds with the cyclone's centre

from 0.71 to 0.78, depending on operating conditions. The measurements very close to the core of the vortex were hindered by air bubbles which are trapped at this low pressure location and by very large velocity fluctuations due to steep gradients and vortex precession.

VISUALISATION

In addition to LDA, the cyclone flow was investigated with a LIF experiment. Fluorescent dye was injected at the bottom of the cyclone. A 488 nm lasersheet emerging from an Argon-ion laser excited the dye in a horizontal plane about halfway in the cyclone. The image was recorded with a digital camera (with a resolution of 254×252 pixels) from underneath the flat bottom of the cyclone. The flow rate in the cyclone was 8 m^3/h through one inlet. *Figure 6* is a typical example of a grey value picture we obtained with this set up. At first sight one would expect rapid mixing of the dye throughout the cyclone due to the turbulent conditions ($Re=2\times10^4$). To our surprise however, in the core of the cyclone a highly coherent structure was observed. There is a dark (low fluorescent dye concentration) outer region that can be clearly distinguished from a light (high fluorescent dye concentration) disc with a diameter of about 0.3 times the cyclone diameter. Within this disc is a dark ring. Apparently, the flow within the disc region hardly showed mixing in radial direction. Once the dye had entered this region it stayed there and was transported towards the exit pipe. The dye in the outer region mixed rapidly. We conclude that the flow can be divided in a laminar centre region and a turbulent outer region. The dark ring within the centre region suggests backflow from outside the cyclone near the vortex core. The three successive (binary) camera frames depicted in *figure 7* give a clear view on vortex precession.

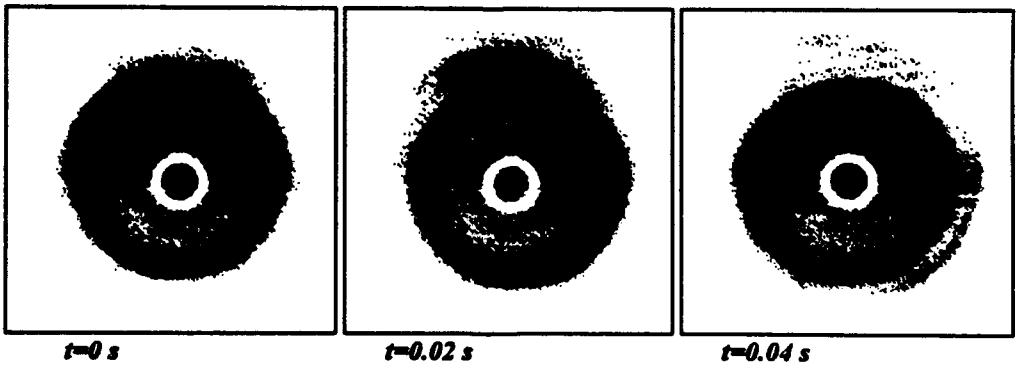

fig. 7 Sequence of three (binary) camera frames demonstrating precession of the vortex core.

DISCUSSION AND OUTLOOK

The precession of the vortex core, the velocity profiles obtained with LDA and the results of the visualisation experiment clearly demonstrate the complexity of the flow in a cyclone. The flow structure strongly depends on the cyclone geometry, e.g. the number of inlets employed. In case the water cyclone was fed through one inlet the strong swirl caused backflow near the vortex core.

For a flow rate of 8 m^3/h through one inlet we can compare the LDA data and the results of the LIF visualisation. In the *figures 3b* and *5b* the averaged position and dimensions of the disc, observed with LIF are drawn within the radial profiles of the axial and tangential velocity respectively. A simple stability analysis (Sloan *et al*, 1986) shows that rapid mixing in the free vortex region was to be expected. This is in good agreement with our result that the radial position of the transition between forced and free vortex measured with LDA corresponds with the radius of the stable disc (*see figure 5b*).

Figure 3b combines the axial velocity profile with the visualisation results. Here a clear discrepancy exists between the position and the size of the backflow region identified with the corrected LDA measurements and the visualisation experiment. The cause of this deviation is not yet clear. It might be that the flow structure within the disc region is still far more complex than we expect it to be and that for instance the ring within the disc is part of the backflow region only, the remainder of this region being obscured by local radial mixing. Experimental work on this intriguing problem is currently in progress.

REFERENCES

Boysan F., Ayers W.H. & Swithenbank J. 1982, A fundamental mathematical modelling approach to cyclone design. Trans IChemE, vol. 60, p 222.

Escudier M.P. & Zehnder J. 1982, Vortex-flow regimes, J. Fluid Mech., vol. 115, p. 105.

Gupta A.K., Lilley D.G. & Syred N. 1984, Swirl flows, Abacus Press, Tunbridge Wells.

Liem T.L. & van den Akker H.E.A. 1992, LDV measurements of the turbulent flow in gas cyclones. Thirteenth Symposium on Turbulence, Rolla Missouri, p B12.

Sloan D.G., Smith P.J. & Smoot L.D. 1986, Modelling of swirl in turbulent flow systems, Prog. Energy Comb. Sci., vol. 12, p. 188.

Session 17.
Optics II

SCANNING LASER DOPPLER PROBE FOR PROFILE MEASUREMENTS

V. Strunck, G. Grosche, D. Dopheide

Physikalisch-Technische Bundesanstalt
Laboratory for Fluid Flow Measuring Techniques
Bundesallee 100, D-38116 Braunschweig

ABSTRACT

To measure velocity profiles in a boundary layer, the measuring volume of common Laser Doppler Anemometers (LDA) has to vary its position in the layer. The spatial resolution of such velocity profile is limited in principal by the size of the probe volume. The method proposed reduces the positioning actions, increases the spatial resolution of the measuring volume by an order of magnitude and measures whole profiles inside the classical measuring volume while leaving the sensor fixed. Moreover, spreading fringe distances and similar distortions inside the measuring volume can be corrected.

1. THEORY

The method presented is a combination of a two illuminating beam dual-scatter Laser Doppler Anemometer (LDA) and a cross-beam reference-scatter LDA. Both LDA systems offer the possibility of measuring the speed of a scatterer, but the chronal appearence of both LDA signals is different. This time difference is determined by the time of flight of a scatterer from one 'fringe' system to the next. Assuming a one dimensional flow, the time lag of signals from both measuring volumes is proportional to their spatial separation and to the speed of the scatterer. By geometry, their separation is a function of the distance from the crosspoint of the two beams in the on-axes direction of the optical system.

1.1 Dual Beam and Reference Beam Method

Figure 1 shows the two measuring volumes, as they are 'seen' by the detecting photodiodes. The avalanche diode (outside the beams) detects only scatterers inside the crossing region of both beams. The main axis of the ellipsoidal volume is part of the optical axis of the dual beam LDA. The main axis also locates the maximum amount of light scattered from a particle crossing the volume.

The PIN diode heterodynes continous light from the reference beam with light scattered out of the illuminating beam to generate the Doppler signal. The main axis of the measuring volume in this reference-scatter set-up is the axis of the illuminating beam. The reference-scatter LDA volume is inclined by the half angle of the beam intersection to the dual-scatter LDA volume.

To operate a reference scatter LDA it is not necessary to form an intersection of both beams. But, using the reference beam method in combination with the dual beam method, the beams must intersect. Furthermore, the two beams should have equal intensities. Detecting Doppler signals in such a strong beam is made possible by PIN diodes, operating at a high optical power (≈1 mW), see Dopheide at al. 1991. In the configuration used both measuring volumes have the same fringe distance and the same fringe orientation.

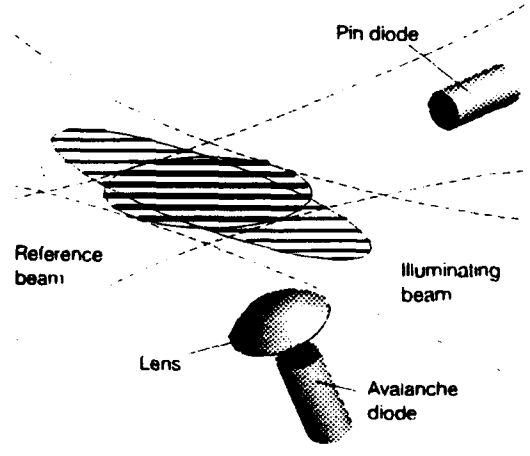

Fig. 1 Schematic of the measuring volumes of a combined dual-scatter reference-scatter LDA

As outlined by Strunck et al (1993), contributions from both measuring volumes are distinguishable due to different detector positions. The dual scatter LDA receiver generates Doppler signals with a pedestal. The reference scatter LDA receiver generates Doppler signals without a significant pedestal. Contributions of the dual scatter set-up to the reference-scatter LDA signal are some orders of magnitude lower and thus negligable.

Because the size of the dual beam LDA probe volume is bounded by the $1/e^2$ contour of both beams, the reference scatter LDA is seen to have a 1/e contour and is limited in addition by radiation alignment (Drain, 1972). Therefore, the strength of the heterodyned signal obtained depends on the angular separation of the scatterer in the illuminating beam and

the source of the reference beam, and of the diameter D of the light collecting aperture (detector area) and the distance l of the detector to the cross point. The maximum length y of the reference-scatter LDA probe measured in direction of the optical axis of the two beams is

$$y = \frac{2\,\lambda\,l}{D\,\varepsilon}.$$

λ is the wavelength of the laser and ε is the angle between the two beams. In our configuration, the probe volume spans up to about 3 mm along the optical axis of the set-up. Because of the 1/e contour, the reference probe volume is thinner, but longer than the dual beam probe as outlined in figure 1.

1.2 Considerations to the Combining Method

In order to measure the time of flight of a scatterer from one probe volume to the next, we have to evaluate the centre of the Doppler signals. This can be done by calculating the envelopes of the signals and finding the maxima. Instead, we prefer to use cross correlation to calculate the time lag. Cross correlation locks to the Doppler oscillations, the result of the procedure is the time of flight from the strongest fringe in the illuminating beam to the strongest fringe (i.e. the optical axis) in the dual-scatter LDA as shown in figure 2.

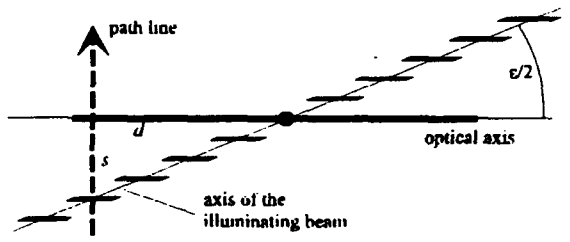

Fig. 2 Travel time and geometric considerations

While the dual-scatter probe can be reduced to a single fringe in figure 2, the reference-scatter probe is provided with a staircase-like geometry. The length of the travelled way s of a scatterer at a velocity u and a time of flight t is

$$s = u \cdot t.$$

The distance d to the cross point of both beams thus is

$$d = \frac{s}{\tan(\varepsilon/2)}.$$

Because the distance s is digitized by the correlation method in units of fringe distance, the distance d to the centre of both probes is, too. From measurements, we will not get a Gaussian type of density distribution of particles along the optical axis, but a distribution at discret points along the axis. Thus, other methods getting the centre of the Doppler signal by using the envelope (i.e. Hilbert transform) will result in a higher spatial resolution. Another simple method to increase resolution by a factor of two is to square the Doppler signal data before processing it, hence doubling the number of oscillations. For simplicity, we only use the cross correlation method.

1.3 Particle Size Effects

The curved surface of a scattering particle not only changes the direction of light, but also changes the phase of light. A summary of particle sizing effects is presented by Tayaly and Bates 1990. As the particles are small compared to the wavelength, maximum light is scattered from the axis of the beams (dashed line in figure 3) and the phase is not changed. With increasing size of the scatterer, the centre of the particle is virtually shifted to the beam axis by an amount of h (about one third of the radius of a water droplet in air):

$$h = s\tan\left(\varepsilon/2\right)\frac{n}{n-\cos\left(\varepsilon/2\right)}$$

This influences the reference-scatter signal and the travel time t of the particle in the combined probe. In figure 2 the time of flight gets longer on the left side from the crosspoint and shorter on the opposite side. In consequence, all positions measured on the optical axis are shifted (to the right).

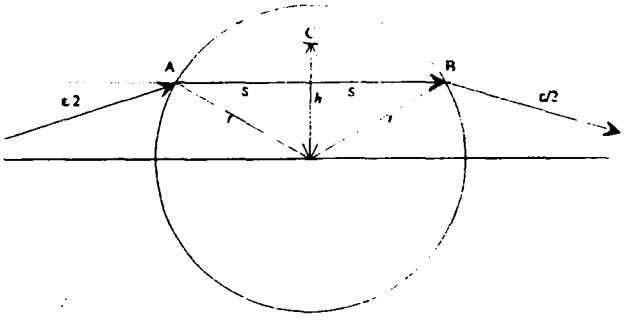

Fig. 3 Particle size effects on the time of fligth measurement

The dual-scatter method will only not be affected, when the light collecting system is located on the optical axis of the set-up. Therefore a time of flight measurement using the envelopes of the Doppler signals is sensitive to particle size.

How is the phase delay of large particles changing the time of flight evaluated by the cross correlation procedure? The cross correlation is extremely sensitive to phase changes in the Doppler signals. The phase dependence on particle radius r is well known for dual-scatter probes from phase Doppler anemometry (PDA). According to Bachalo 1987 and using geometric optics and figure 3, the path length difference Δ_1 of the beam in the reference-scatter system is

$$\Delta_1 = n^* \overline{AB} - \left(\overline{AC} + \overline{CB}\right), \quad n \text{ refractive index, or}$$

$$\Delta_1 = 2s\left(n - \frac{1}{\cos\left(\varepsilon/2\right)}\right) \text{ and}$$

$$s = r\cos\left[\arctan\left(\frac{\sin\left(\varepsilon/2\right)}{n-\cos\left(\varepsilon/2\right)}\right)\right]$$

In our set-up the phase path length is changed by about one third of the diameter d, i.e. a 3µm particle would shift the fringe system by a fringe spacing.

Compared to the phase shift Δ_2 of a dual-scatter component with a detector at the same place, the reference scatter probe is about 50 times more effective:

$$\Delta_2 = \Delta_1 - d(n-1).$$

Potentially, the probe is able to measure small sizes of particles, because the envelope of Doppler signals as well as the fringe system are shifted by curved surfaces.

However, for small particles not only refraction, but also diffraction must be considered. For this reason, only particle sizes smaller than the fringe distance will not stress to locate the trajectory of a scatterer through the optical axis in the method presented.

2. SET-UP AND CALIBRATION

The sensor was adapted to the nozzle used to calibrate high gas flow rates at the PTB. Figure 4 gives an impression on geometry and size.

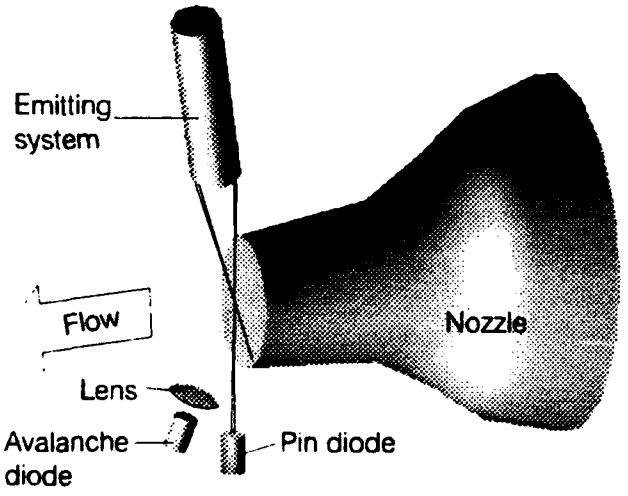

Fig. 4 Test nozzle and combined LDA system

The nozzle has a high contraction ratio of 11:1 to establish a flat profile in the nozzle except at its boundary. One beam of the emitting system is blocked inside the nozzle, the second beam is aligned parallel to the exit plane and 1 mm away from the plane in the streamwise direction. This is the reference beam of the reference-scatter system and inside there is the receiving PIN diode. The dual-scatter receiver has a light collecting lens, which focusses the scattered light from both beams to an avalanche diode. It is located outside the axis with an angle of twice the half angle of the crossing beams.

A second two-beam dual scatter system not shown in figure 4 has its probe volume orientated perpendicular to the combined probe to have the same spatial resolution when moving the systems vertically. We will proof the coincidence of both system when measuring the boundary layer.

The first step was to test the combined LDA in the middle of the nozzle. About 2000 velocities were attached to the distance from the cross point of the two beams in figure 5.

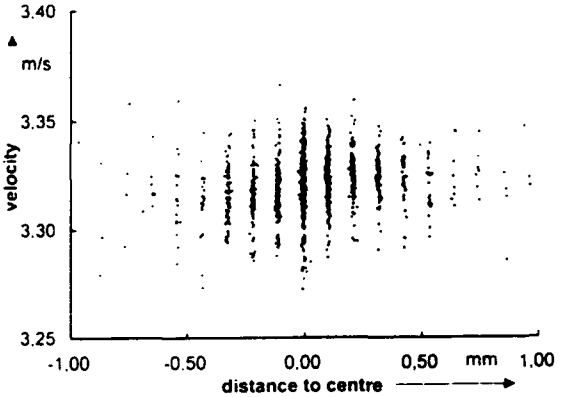

Fig. 5 Velocity distribution along the optical axis in the middle of the nozzle

Remark that the turbulence intensity measured is 0.4 %. Most of the velocities have been measured at the cross point. In steps of 106 µm from the cross point again velocities have been collected. Each step also can be expressed in terms of fringe units. A distance of 1 fringe unit means a travel way of the particle from one fringe in the first probe to the next fringe in the second probe. This distance is proportional to the location on the optical axis, i.e. one fringe step in direction normal to fringe system corresponds to a distance of 106 µm along the optical axis. The particle diameter was 3 µm ±10 %, no phase shift can be observed. The distribution appears rastered in space, the velocities distribute mainly at full fringe unit locations. The width of a single structure is about one tenth of a fringe unit. A better procedure than the one used to calculate the centre of both LDA signals would be able to increase the spatial resolution by a factor of ten.

To get an impression of the length of the combined probe, a velocity distribution based on 8000 velocities has been converted to a histogram (PDF) in figure 6:

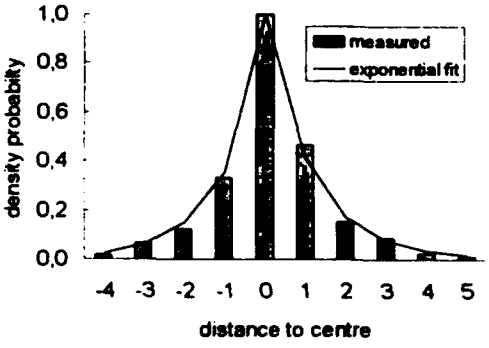

Fig. 6 Probability density distribution along the optical axis

Instead of a Gaussian envelope the distribution shows an exponential decay from the centre. For simplicity, the distances are now shown as fringe spacing units. A reason for this behaviour is the cross correlation method to calculate the time

of flight. Because the maximum of the envelopes of the Doppler signal is relatively flat, noise on the signal can shift the centre of a burst in terms of Doppler periods. Common mode noise on both signals will shift the locations to the centre at the expense of neighboured locations. Under this view the full width at half maximum of distribution is about 300 µm or half the length of the dual-scatter probe volume. Because the distribution is not constant all along the probe, to sample the same ensemble of velocities 300 µm away from the middle of the probe, acquisition time has to be increased by a factor of ten compared to the time needed in the middle of the probe.

Next we calculate the average velocity of each pattern of figure 5. Because we use two Doppler sensors, we compare the velocity from the dual-scatter probe and the velocity from the reference-scatter probe with the velocity of the flow in figure 7:

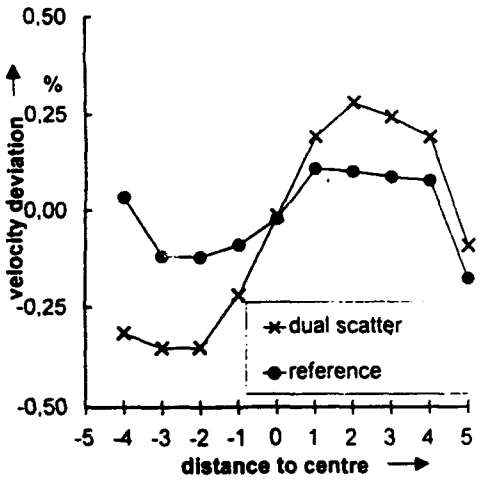

Fig. 7 Velocity deviation along the optical axis

As figure 7 shows, the velocity deviations are less than 0,3 % and lie within the turbulence intensity of the flow. As shown above, deviations outside ±300 µm from the centre are not as representative as deviations inside. The dual-scatter probe shows the fringe spreading of the 'real' fringe system, the reference-scatter probe 'virtual' fringe system depends on the angular position of the particle and the reference beam as shown by Strunck et al. (1993). This effect compensates partly and only in the experiment the fringe spreading of the 'real' fringe system.

The error curve can be used to calibrate fringe distance of the probe at each step along the optical axis. However, turbulence measured will not be effected by the calibration, as long as turbulence is higher than the deviation.

Inside a laminar and plane flow, the confidence in locating the passage of a particle in the probe volume cannot be approved, because all particles have nearly the same speed. To investigate exchanges of locations to be measured, we moved the probe into the boundary layer of the nozzle.

3. BOUNDARY LAYER MEASUREMENTS

The combined probe was moved in steps of 1 mm in the boundary layer at the exit plane of the nozzle 120 mm in diameter. The boundary layer itself has a thickness of 3 mm , when the main flow has a speed of 3,3 m/s. This takes place at a flow rate of 256 m^3/h. Figure 8 shows 8000 velocities, sampled in 4 steps along the optical axis.

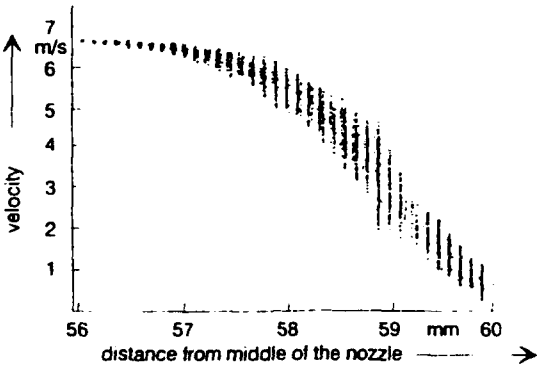

Fig. 8 Velocities sampled in four steps along the optical axis

Again the structured distribution generated by the cross correlation data reduction is exhibited. Because of moving the whole system in the boundary layer in steps of 1 mm, the structures nearly overlap. Looking at the outer flow (left side in figure 8), the velocity distribution is very small due to a small turbulence scale. Inside the boundary layer, spreading occurs with increasing turbulence towards the boundary.

Again we will look at the probability density distribution of the same ensemble of velocities in figure 9.

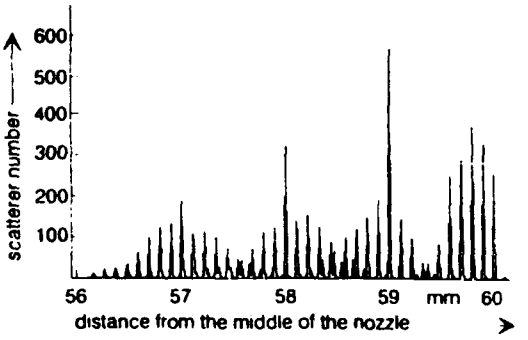

Fig. 9 Probability density distribution of the probe in the boundary layer

The density distribution shows, as already outlined in figure 6, four independent distributions of four sensor positions in the boundary layer. The distance in the plot is measured from the centre of the nozzle, the nozzle border is at 59,9 mm No velocities could be acquired outside the nozzle region, when the probe was 1 mm downstream the exit plane. The shape of the distributions with the probe centered at 59 mm and

more at 60 mm reflects the dilution of particle density at the nozzle boundary.

The peaks at 57, 58 and 59 mm can be seen as produced by common mode noise in the semiconductor GaAlAs laser. Reflected light from surfaces into the diode can result in an intensity modulation of the diode itself, thus shifting some velocity locations to the centre of the sensor. Common mode noise in the acquisition system will produce the same effect.

Compared to figure 6, the sensor exhibits now in figure 9 twice the full width at half maximum, especially at 57 mm. Here it has a total span of 2 mm.

After averaging the velocities at each part of the distribution in figure 8, we compare them with velocities obtained from a dual-scatter Doppler probe volume oriented perpendicular to the optical axis of the combined probe. This probe is a two-dimensional probe illuminated by the green and blue line of an Argon ion type laser. The thickness of the probe is about 100 µm and thus comparable with the spatial resolution of the combined probe. The length of the probe is 800 µm, but now oriented parallel to the boundary layer.We vary the location of the probe in 40 steps of 100 µm in the boundary layer. In figure 10 the results are exhibited.

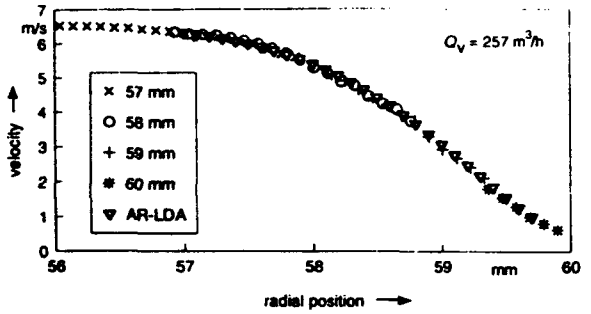

Fig. 10 Comparison measurement in the boundary layer

Both methods, the enhanced and the classical one using the AR-LDA, show a good agreement of the profiles measured. In the region of high turbulence the data of the combined probe exhibit greater deviations up to 5 %. This depends mainly on the smaller number of samples taken by the sensor far from its centre. Further deviations probably are due to noisy signals. As outlined above, the influence of the Doppler period is negligable, but the time of flight measurement is affected. Consider, the spatial position of the particle can change by ±1 'fringe' unit on the on-axis distance.

In the centre of the distribution, a particle shifted in one direction will be equalized by a particle shifted to the opposite direction. At positions far from the centre of the probe, only shifts away from the centre will succeed in being acquired by the data acquisition. Particle signals shifted by noise towards the centre have smaller amplitudes and signal to noise ratios compared to particle signals from positions shifted away from the centre. Far from the centre of the sensor, the boundary layer gradient is measured smaller in a system with noise present than without.

4. CONCLUSIONS

A new LDA method has been developed to measure (parts of) velocity profiles while leaving the measuring apparatus fixed. The technique described is able to resolve within the measuring volume and allows improvements by an order of magnitude. Using a cross beam LDA, the time lag of Doppler signals, corresponding to the time of flight from the dual-scatter probe to the combined reference-scatter probe, yields the on-axis distance from the centre of the probes.

The fringe distance of the system can be corrected individually along the optical axis of the probe to increase the accuracy of the sensor.

Particle sizing with the probe is possible, but needs further investigation. Therefore, the above application was restricted to monodisperse particles of less than 5 µm in diameter as well as to particle diameter distributions around 1,5 µm.

The enhanced system allows to measure boundary layers and whole profiles within a span of up to 2 mm. Potentially, the spatial resolution inside the measuring volume can be increased again by an order of magnitude (to 10 µm) using better data reduction methods than shown.

The poorer signal quality (SNR≈10 dB) of our reference-scatter system compared to the dual-scatter signal (SNR≈20 dB) and its influence on the time of flight measurement can be improved by selecting more noiseless lasing and sensing devices.

5. REFERENCES

Bachalo, W. D., 1987, Method for Measuring the Size and Velocity of Spheres by Dual-Beam Light-Scatter Interferometry, Appl. Opt. 19, pp. 363-370

Dopheide, D.,Faber, M., Yen-Bing-Yü, Taux, G., 1991, Semiconductor Long-Range Anemometer Using a 5 mW Diode Laser and a Pin Diode, 5th Int. Symp. on Applications of Laser Techniques to Fuid Mechanics, Springer Verlag Berlin, Heidelberg, pp. 385-399

Drain, L.E. 1972, Coherent and Noncoherent methods in Doppler Optical Beat Velocity Measurement, J. Phys. D: Appl. Phys. 5, pp. 481

Strunck, V., Grosche, G. & Dopheide, D., 1993, New Laser Doppler Sensors for Spatial Velocity Information, Proc. of the 15th Int. Congress. on Instrumentation in Aerospace Simulation Facilities, IEEE Pub. 93CH3199-7, 36, pp. 1-5

Tayali, N.E. & Bates, C.J., 1990, Particle Sizing Techniques in Multiphase Flows: A Review, Flow. Meas. Instrum, Vol. 1, pp. 7-105.

more at 60 mm reflects the dilution of particle density at the nozzle boundary.

The peaks at 57, 58 and 59 mm can be seen as produced by common mode noise in the semiconductor GaAlAs laser. Reflected light from surfaces into the diode can result in an intensity modulation of the diode itself, thus shifting some velocity locations to the centre of the sensor. Common mode noise in the acquisition system will produce the same effect.

Compared to figure 6, the sensor exhibits now in figure 9 twice the full width at half maximum, especially at 57 mm. Here it has a total span of 2 mm.

After averaging the velocities at each part of the distribution in figure 8, we compare them with velocities obtained from a dual-scatter Doppler probe volume oriented perpendicular to the optical axis of the combined probe. This probe is a two-dimensional probe illuminated by the green and blue line of an Argon ion type laser. The thickness of the probe is about 100 µm and thus comparable with the spatial resolution of the combined probe. The length of the probe is 800 µm, but now oriented parallel to the boundary layer. We vary the location of the probe in 40 steps of 100 µm in the boundary layer. In figure 10 the results are exhibited.

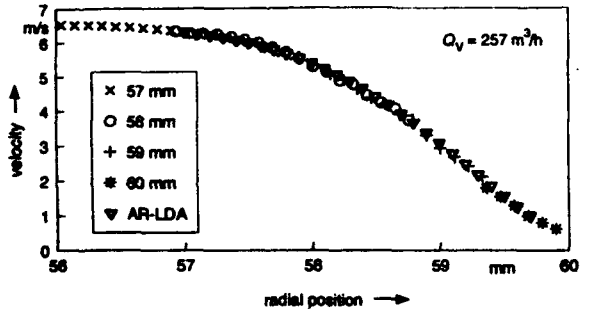

Fig. 10 Comparison measurement in the boundary layer

Both methods, the enhanced and the classical one using the AR-LDA, show a good agreement of the profiles measured. In the region of high turbulence the data of the combined probe exhibit greater deviations up to 5 %. This depends mainly on the smaller number of samples taken by the sensor far from its centre. Further deviations probably are due to noisy signals. As outlined above, the influence of the Doppler period is negligable, but the time of flight measurement is affected. Consider, the spatial position of the particle can change by ±1 'fringe' unit on the on-axis distance.

In the centre of the distribution, a particle shifted in one direction will be equalized by a particle shifted to the opposite direction. At positions far from the centre of the probe, only shifts away from the centre will succeed in being acquired by the data acquisition. Particle signals shifted by noise towards the centre have smaller amplitudes and signal to noise ratios compared to particle signals from positions shifted away from the centre. Far from the centre of the sensor, the boundary layer gradient is measured smaller in a system with noise present than without.

4. CONCLUSIONS

A new LDA method has been developed to measure (parts of) velocity profiles while leaving the measuring apparatus fixed. The technique described is able to resolve within the measuring volume and allows improvements by an order of magnitude. Using a cross beam LDA, the time lag of Doppler signals, corresponding to the time of flight from the dual-scatter probe to the combined reference-scatter probe, yields the on-axis distance from the centre of the probes.

The fringe distance of the system can be corrected individually along the optical axis of the probe to increase the accuracy of the sensor.

Particle sizing with the probe is possible, but needs further investigation. Therefore, the above application was restricted to monodisperse particles of less than 5 µm in diameter as well as to particle diameter distributions around 1,5 µm.

The enhanced system allows to measure boundary layers and whole profiles within a span of up to 2 mm. Potentially, the spatial resolution inside the measuring volume can be increased again by an order of magnitude (to 10 µm) using better data reduction methods than shown.

The poorer signal quality (SNR≈10 dB) of our reference-scatter system compared to the dual-scatter signal (SNR≈20 dB) and its influence on the time of flight measurement can be improved by selecting more noiseless lasing and sensing devices.

5. REFERENCES

Bachalo, W. D., 1987, Method for Measuring the Size and Velocity of Spheres by Dual-Beam Light-Scatter Interferometry, Appl. Opt. 19, pp. 363-370

Dopheide, D.,Faber, M., Yen-Bing-Yü, Taux, G., 1991, Semiconductor Long-Range Anemometer Using a 5 mW Diode Laser and a Pin Diode, 5th Int. Symp. on Applications of Laser Techniques to Fuid Mechanics, Springer Verlag Berlin, Heidelberg, pp. 385-399

Drain, L.E. 1972, Coherent and Noncoherent methods in Doppler Optical Beat Velocity Measurement, J. Phys. D: Appl. Phys. 5, pp. 481

Strunck, V., Grosche, G. & Dopheide, D., 1993, New Laser Doppler Sensors for Spatial Velocity Information, Proc. of the 15th Int. Congress. on Instrumentation in Aerospace Simulation Facilities, IEEE Pub. 93CH3199-7, 36, pp. 1-5

Tayali, N.E. & Bates, C.J., 1990, Particle Sizing Techniques in Multiphase Flows: A Review, Flow. Meas. Instrum, Vol. 1, pp. 7-105.

SIMULTANEOUS MULTI-POINT LASER VELOCIMETRY USING HOLOGRAPHIC OPTICAL ELEMENT LENS

Medhat Azzazy

Science Applications International Corporation
Torrance, California

ABSTRACT

A technique for simultaneous multi-point formation of measurement volumes has been developed. The technique, which uses a holographic optical element (HOE) lens, can be used in conjunction with any laser measurement system, including laser Doppler and laser transit anemometry, and laser induced fluorescence. The technique is based on recording the locations of the measurement volumes on a hologram. When the hologram is illuminated by a collimated beam, the images of the measurement volumes (foci) are reconstructed. The foci can be arranged to fall on a line, a plane, or within a volume. Two HOE lenses, 3 foci and 9 foci, were designed and fabricated. The measured spot size using the HOE lens was comparable to the diffraction limited spot size. The maximum laser intensity fluctuations were ±13% over the 9 foci.

Two sets of measurements were performed using the HOE lens. The first set included measuring the velocity using a wire attached to a rotating disc. The second set involved measuring the velocity profile in a fully developed turbulent pipe flow. The uncertainty of the measured velocity using the HOE lens compared to an achromatic lens was within ±0.1%.

1. INTRODUCTION

Simultaneous multi-point velocity measurements are desirable in many diverse applications such as studies of turbulent and unsteady flows, and measurements of volumetric flow rates. Investigations of turbulent flows, such as interference of jets, flow swirl, and associated fundamental eddy structure require knowledge of time-space correlation profiles. The spatial velocity profile must be measured instantaneously to resolve time-space correlations. Studies involving unsteady flows or in wind tunnel applications where steady state conditions exist only for a short period of time, e.g., shock tubes or blow down tunnels, require instantaneous measurements of the velocity at multi-points. Volumetric flow rate measurements which are essential to many applications such as custody transfer and distribution operations in gas pipelines, and air intake for the combustion process in gas turbine engines and internal combustion engines also require multi-point velocity measurements.

Techniques to measure velocity distribution rely on one of the following concepts: 1) illumination of the measurement area by a laser sheet, e.g., particle image velocimetry (PIV) [1,2], 2) scanning the probe volume over the measurement area, e.g., scanning laser Doppler velocimetry (LDV) [3], and 3) splitting the laser beam into a number of beams and duplicating the transmitter optics, e.g., diffraction grating method [4], and special beam splitter optics techniques [5]. The laser sheet illumination method is inefficient because it requires powerful lasers to illuminate an area much larger than required for the measurement points. The drawbacks of the scanning method include measurement position uncertainties, and measurement bias due to continuous movement of the measurement volume. The beam splitting method is limited to a few applications because the number of measurement volumes are restricted by the optics, and the quality of laser beam at the measurement volumes is insufficient for LDV measurements.

The present study reports on a new technique for multipoint formation that avoids the drawbacks of current methods. The technique depends on recording the locations of the foci on a hologram which, if illuminated by a collimated beam, reconstructs the images of the foci. Consequently, the measurement volumes are generated where they are needed, thus optimizing the laser power. The technique has the advantage of high laser beam splitting efficiency while maintaining equal laser intensity at the multiple foci. Simultaneous multiple measurement volumes are produced without any mechanically moving parts. The hologram lens can be used in conjunction with any laser measurement system such as laser Doppler and laser transit anemometry, and laser induced fluorescence.

The technique was first applied to measure the velocity in a controlled testbed using a wire attached to a rotating disc. The velocity profile in a fully developed turbulent pipe flow was then measured. In the following, the principle of multi-point formation will be discussed followed by an analysis of the probe volume characteristics using HOE. The experimental set-up is described and laboratory evaluation of HOE performance is given.

2. PRINCIPLE OF MULTI-POINT FORMATION

Simultaneous multiple foci are generated using a holographic optical element (HOE) lens. The function of the HOE lens is to focus a collimated laser beam into a number of foci. The foci can be arranged to fall on a line, a plane, or within a volume. The line arrangement can be either off-axis or on-axis, as shown in Fig. 1. The plane configuration is similar to a two-dimensional off-axis line application. The volume arrangement is a combination of plane configuration and on-axis line geometry. Other geometrical arrangements for the foci may be conceived.

The versatility of the HOE lens to achieve different geometries for the foci locations is due to the process by which the hologram is constructed. A light source located at the required focal point is used to record the hologram. By moving

the light source to the second focal point, a second picture can be recorded on the same hologram, and the process is repeated for all the focal points. When the hologram is reconstructed the images of the foci are reproduced.

The key issues in constructing the HOE lens are: (1) image quality at the focal point, (2) beam splitting efficiency, and (3) shadow effects for on-axis applications. In the following, an analysis of these key issues will be given.

2.1 Image Quality at the Focal Point

Image quality at the focal point is of particular importance to laser velocimetry optics because it determines the resolution and the signal to noise ratio (SNR) of the instrument. The ability of the HOE lens to generate diffraction-limited spot size requires special considerations during the fabrication of the hologram. First, the light source used to record the hologram must be free from spherical aberrations, and must be of a size equal to the diffraction-limited spot size. Second, the wavefront distortion introduced by the holographic material must be eliminated or reduced.

The amplitude A of the reconstruction wave in the primary focus of a HOE lens of focal length f is described by the relationship [6],

$$A(\xi,\eta,f) = C e^{\frac{jk}{2f}(\xi^2+\eta^2)} F(b(x,y)) \qquad (1)$$

where b(x,y) is the aperture function, F denotes Fourier transform, ξ and η are the coordinates in the focal plane, and x and y are the coordinates in the hologram plane.

During the holographic recording process, variations in the layer thickness of the holographic recording material introduces phase distortion $\varphi(x,y)$ to the original wavefront. Although φ is usually very small, it can result in a substantial deformation of the measuring volume. Introducing phase distortion to the primary focus of HOE modifies the amplitude described by equation 1 such that

$$A(\xi,\eta,f) = C e^{\frac{jk}{2f}(\xi^2+\eta^2)} \{F(b) + F(b) * F(j\varphi(x,y))\} \qquad (2)$$

The resolution of the holographic lens, described by equation (2), is determined from the aperture function and phase distortion of the reconstructed wave. For a top hat aperture function, equation (2) shows that if the distortion $\varphi(x,y)$ contains low spatial frequencies, i.e., order of the inverse of aperture diameter, the resolution of the spot size formed by the holographic lens will be equal to the diffraction limited spot size. The hologram spatial frequency S_f can be found from the relationship

$$S_f = \frac{n_H - n_0}{\lambda_0} \frac{\Delta x}{L} \qquad (3)$$

where λ_0 is the wavelength of incident wavefront, and $\Delta x/L$ is the thickness variation per unit length. Therefore, for a 1 cm diameter aperture, diffraction limited spot size can be obtained when the maximum thickness variation is ≤ 0.5 μm/cm. It has been demonstrated in the literature [7] that it is possible to fabricate HOE lens with a thickness variation of 0.2 μm/cm. Therefore, for most optical configurations it is possible to manufacture a HOE lens with a beam quality at the measurement volume approximately the same as an aberration free lens.

2.2 Beam Splitting Efficiency

The hologram diffraction efficiency is defined as the ratio of the useful image forming light intensity diffracted by the hologram to the total light intensity used to illuminate the hologram. The efficiency of splitting the incoming laser beam into multiple foci largely depends on the holographic recording material [8-10]. High efficiency HOE lens is obtained by recording the hologram on a dichromated gelatin (DCG) material. Efficiencies of approximately 75-80% have been reported in the literature [11]. The quality of the images formed by a DCG hologram is best when a visible light in the 400-500 nm range is used to record the hologram. When such a hologram is constructed using a laser diode in the 700-900 nm range, a correction of the location of the foci due to chromatic aberration must be made. Silver halides allow holograms to be recorded and reconstructed in the near infrared wavelength range, thus avoiding chromatic aberrations when laser diodes are used. However, silver halides have poor diffraction efficiency, i.e., 5-10%.

Since the signal-to-noise ratio of optical instruments is proportional to the square root of the laser intensity, a uniform laser intensity at the HOE foci is required. To achieve this condition, the exposure time for each foci must be adjusted to take into account the effects of subsequent exposures. Foci-to-foci intensity variations of the order of 10% are expected due to variations in the holographic plate modulation transfer function (MTF) which affects the exposure time. For a 10% laser intensity variation, the signal-to-noise ratio at the different foci will fluctuate by 5% which is well within the acceptable tolerance range of most optical instruments.

2.3 Shadow Effect

The building block for any geometrical arrangement of the foci is the on-axis and off-axis line configurations. For large off-axis angle applications, i.e., off-axis angles >5°, lens aberrations, including spherical aberrations, coma, and field curvature, result in large spot size. In these applications an additional lens can be used to correct the aberrations and generate a spot size about the same as the diffraction limited beam waist. The spatial resolution of the on-axis configuration is limited by the shadowing effect that occurs due to interference from the superposition of light generated by diverged beams upstream of the focal point (shown in Fig. 2). Beam divergence after the upstream focal point casts a shadow on the subsequent focal points. This effect is equivalent to the existence of background noise. Therefore, a signal to shadow ratio (SSR) can be defined as:

$$SSR|_i = \frac{I_i}{\sum_{k=1}^{NF} I_k|_i} \qquad (4)$$

where I_i is the laser beam intensity at point i, NF is the number of on-axis focal points, and $I_k|_i$ is the diverged laser beam intensity at point i due to a beam focused at point k. The tolerable level of the SSR, which is a function of the number and location of the focal points, varies with the applications depending upon the signal-to-noise ratio and the data acquisition and processing system. Experimentally, an SSR of about 100 is adequate for most applications; however, an analysis of acceptable SSR must be conducted.

3. HOE PROBE VOLUME CHARACTERISTICS

Two HOE lenses were designed and fabricated: 3-point and 9-point HOE. The optical quality of the measurement volumes is characterized by the size of laser spot, laser beam intensity variations and signal to shadow ratio (SSR). The laser spot size at the foci was determined using a ray tracing technique. The relative intensities of the foci were measured using a silicon photodiode. The SSR was calculated using equation 4.

Table 1 describes the characteristics of the probe volumes using the 9-point HOE. The maximum focal point to focal point laser intensity fluctuations was within ±13% resulting in maximum variation in the SNR of ±6.7%, which is well within the capabilities of most detectors' dynamic range and signal processing systems.

The spot size using HOE as determined from ray tracing was comparable to the diffraction limited spot size at the same location as described in Table 1. High optical beam quality (spot size is of the order of the theoretical diffraction limited spot size) at the measurement volume is important to the overall instrument signal to noise ratio. Spot sizes much larger than the diffraction limited spot size reduce both the laser power per unit area and the resulting signal, and degrades the instrument spatial resolution.

Table 1 shows that the SSR at the first focal point is the highest because the laser beam rays that are converging to form the focal points (downstream of the first focus) have smaller power per unit area than the laser beam that is in focus. The SSR decreases as the contribution from the upstream foci increases. At the 5th foci, a balance is achieved between the contribution of the out-of-focus and in-focus points. The minimum SSR occurred at the 8th foci, owing to its close location to the 7th and 9th foci (dictated by the nature of the fully developed turbulent pipe flow). In general, the SSR can be optimized by taking into consideration the nature of the fluid flow and the distance between the foci.

4. HOE PERFORMANCE EVALUATION

4.1 Velocity Measurement Technique

The HOE lens was combined with diode array velocimetry (DAV) technique to measure the velocity at multiple points [12]. The basic concept of DAV is to create a number of laser spots or sheets at the probe volume as shown in Fig. 3. As a particle crosses the optical pattern, it generates a signal analogous to that of fringe LDV. By measuring the frequency of the signal ω, and by knowing the spacing between spots δ, the velocity u is determined from the relationship

$$u = \delta \cdot \omega \qquad (5)$$

Measurements in the frequency domain allow the separation of the noise from the signal, thus improving the accuracy, repeatability and the detection of low SNR. The incoherence feature of the technique relaxes the stringent requirements imposed by LDV and, thus, permits the utilization of laser diode arrays.

The intensity distribution at the focal plane of a perfect lens, i.e., aberration free lens, due to laser diode array illumination is described by the relationship

$$I = B \cdot e^{-2(\omega \cdot t)^2} \cdot \sum_{i=1}^{NL} \mathrm{rect}\left(2\omega t - i\frac{\delta}{b_0} \right) \qquad (6)$$

where b_0 is the laser beam waist at the probe volume, NL is the number of laser spots (sheets), and rect is the rectangle function.

There are some similarities between the intensity described by equation (6) and LDV signals after completely removing the pedestal component through a high pass filter. First, the exponential term is the same; the origin of that term is the Gaussian intensity distribution characteristic of most lasers. Second, the periodic component in DAV is described as a summation of rectangle functions, while in LDV it is described by a cosine function. The summation term in equation (6) can be approximated by a cosine function when the beam waist b_0 equals the beam separation δ. In this case, the periodic term in LDV is modulated by an exponential factor, while in DAV, the periodic term is not modulated. Therefore, high signal visibility can be obtained with DAV, without the stringent requirements that have to be satisfied to achieve the same visibility using an LDV system.

4.2 Experimental Setup

The output of four individually addressable laser diodes (3 µm×1 µm) was collimated using a 12.5 mm focal length lens. The collimated laser beam was then used to illuminate the HOE lens. The separation of the laser beams at the foci was 85 µm. The DAV receiving optics, and data processing are similar to the LDV technique. The DAV optical system is schematically illustrated in Fig. 4. Combining the DAV technique and the HOE lens results in an optimum procedure for multi-point velocity measurement applications. The DAV optical transmitter does not need the stringent optical requirements of an LDV, and relies on the use of collimated beam to illuminate the HOE lens. However, the HOE technique can be integrated with the optical train of an LDV, a laser transit anemometry (LTA), or a laser induced fluorescence (LIF) system.

Two sets of velocity measurement experiments were conducted to determine the performance of the HOE lens: controlled tests and wind tunnel tests. The controlled tests were performed using a wire which was projected from the edge of a rotating wheel. The wire, which simulated particles passing through the probe volume, was 75 µm in diameter. The signals from the wire had fixed amplitude, frequency and arrival time.

The flow tests were performed in a low speed wind tunnel, schematically shown in Fig. 5. The test section was 10 cm in diameter and located 60 diameters downstream the tunnel inlet. Reynolds number, based on centerline velocity and test section diameter, varied from 3×10^4 to 2×10^5. The flow field at the test section was fully developed turbulent pipe flow.

5. RESULTS AND DISCUSSIONS

5.1 Rotating Wire Velocity Measurements

The velocity of the rotating wire was measured using the HOE lens and an achromatic lens at each focal point. The velocity statistics, i.e., average and standard deviation (RMS) of the rotating wire, were determined using 10,000 velocity samples. Since the sampling process is Poisson distributed, the corresponding statistical error was ±0.1%. The rotating wire RMS velocity using an achromatic lens was ±0.1%, i.e., within

the statistical error. The RMS velocity using the HOE lens was also ±0.1%. Therefore, the velocity uncertainty due to using the HOE was dominated by the repeatability of the experiment which was within ±0.1%. A conservative conclusion would be that the velocity error due to using the HOE lens is much less than ±0.1%.

5.2 Wind Tunnel Tests

The HOE-DAV method was used to measure the centerline velocity in the tunnel in the Reynolds number range 3×10^4 to 1.7×10^5, which corresponds to a velocity range of 4.5 to 25 m/sec. The particle average size was 5 μm. The tunnel velocity statistics were obtained using 4,000 velocity samples at each point. The tunnel centerline average velocity was measured using a HOE lens and an achromatic lens. The two velocities were within ±0.1%. Figure 6 shows the average velocity profile obtained by 3-points HOE lens at 5 mm, 15 mm and 50 mm from the pipe wall, at a Reynolds number of 1.7×10^5. The turbulence intensity was calculated from the ratio of the root mean square value of the velocity samples normalized by the local mean velocity. The measured centerline turbulence intensity using the HOE lens was compared to the intensity measured using an achromatic lens, showing that the two intensities were within ±0.1%. A plot of the turbulence intensity profile at 5 mm, 15 mm, and 50 mm from the pipe wall, at a Reynolds number of 1.7×10^5, using the HOE lens is shown in Fig. 7. The turbulence intensity profile using the HOE lens correlates to within ±0.1% of the profile measured using an achromatic lens.

6. CONCLUSIONS

A multi-point velocity measurement technique using a HOE lens has been developed. The location of the measurement volumes can be arranged to fall on a line, a plane, or within a volume. The HOE lens can be incorporated with a number of laser measurement techniques including LDV, LTA, and LIF to generate multiple foci. Two HOE lenses, 3-point and 9-point, were designed and fabricated. The performance of the HOE lenses was evaluated using a wire attached to a rotating disc and through wind tunnel tests. Fully developed turbulent velocity profiles in a pipe flow were obtained using these HOE lenses. The tests show that the HOE spot size was approximately the same as the theoretical diffraction limited value. The maximum laser intensity variations at all foci were ±13% and the hologram diffraction efficiency was 70%. The minimum SSR was 73:1 near the pipe wall where a large number of foci were required due to the steep velocity gradient. The velocity uncertainty using the HOE lens was less than the instrument's ±0.1% uncertainty.

NOMENCLATURE

A	Amplitude of reconstructed wave
B	constant
b	Aperture function
b_o	Laser beam waist at the probe volume
C	Constant
F	Fourier transform
f	Focal length of HOE lens
I_i	Laser beam intensity at focal point *i*
k	Wave number
L	Hologram thickness
n_0	Index of refraction in air
NF	Number of foci
n_H	Index of refraction of holographic material
NL	Number of laser sheets
S_f	Hologram spatial frequency
SSR	Signal to shadow ratio
t	time
u	velocity
x and y	Hologram coordinates

Greek

Δx	Thickness variation of holographic material
φ	Phase distortion introduced by the holographic recording material
λ_0	Wavelength of incident wavefront
ξ and η	Focal plane coordinates
δ	Laser sheet-to-sheet separation
ω	DAV signal frequency

ACKNOWLEDGEMENT

The work was supported in part by Gas Research Institute (GRI), under contract No. 5092-260-2449, Mr. Ferol Fish, Program Manager, and by the Gas Company of Southern California, Mrs. Claire Becker-Castle, Program Manager.

REFERENCES

1. Adrian, R.J., Offutt, P.W., Landreth, C.C., Liu, Z., and Hanratty, T.J., "Studies of Liquid Turbulence Using Double-Pulsed Particle Correlation," *Proc. 5th Int. Symp. on Appl. of Laser Tech. to Fluid Mech.*, 15.4 (1990).

2. Cenedese, A., Palmieri, G., and Romano, G.P., "Turbulent Intensity Evaluation with PIV," *Proc. 5th Int. Symp. on Appl. of Laser Tech. to Fluid Mech.*, 15.5 (1990).

3. Durst, F., Lehmann, B., and Tropea, C., "Laser Doppler System for Rapid Scanning of Flow Field," *Rev. Sci. Instrum.*, 52 (11), (1981).

4. Nakatani, N., Maegawa, A., Izumi, T., and Yamada, T., "Advanced Multi-Point Optical Fiber LDV's - Vorticity Measurement and Some New Optical Systems," *Proc. 3rd Int. Symp. on Appl. of Laser Tech. to Fluid Mech.*, 8.4 (1986).

5. Ikeda, Y., Kurihara, N., Nakajima, T., and Matsumoto, R., "Multipoint Simultaneous LDV Optics," Applications of Laser Anemometry to Fluid Mechanics, R.J. Adrian, T. Asanuma, D.F.G. Durao, F. Durst, and J.H. Whitelaw (Eds.), Springer-Verlag, New York, 361 (1989).

6. Goodman, J.W., "Introduction to Fourier Optics," Chap. 6, McGraw-Hill, New York, (1968).

7. Stojanoff, C.G., and Windeln, W., "Development of High Efficiency Holographic Optical Elements," *SPIE Progress in Holography*, Vol. 812:64 (1987).

8. Feldman, M.R., and Guest, C.C., "Computer Generated Holographic Optical Elements for Optical Interconnection of Very Large Scale Integrated Circuits," *Appl. Optics*, 26:4377 (1987).

9. Wang, L., Geng, W.Z., and Kostuk, R.K., "An Efficient Multiple-Image Holographic Optical Element," *SPIE Holographic Optics: Optically and Computer Generated*, Vol.1052:97 (1989).

10. Rallison, R.D., "Incoherent Multifocus Hololens Design and Fabrication," *SPIE Holography* , Vol. 1183:663 (1989).

11. Liang, Y.Z., Zhao, D., and Liu, H.K., "Multifocus Dichromated Gelatin Hololens," *Appl. Optics*, 22:3451 (1983).

12. Azzazy, M., Rosow, B., and Potts, R., "Flow Velocity Measurements Using Laser Diode Array," Submitted for publication at the Journal of Fluids Engineering (1994).

Table 1. Foci Location, Laser Intensity, and Spot Size

Foci Location (mm) (relative to hologram)	Foci Location (mm) (relative to pipe wall)	Relative Laser Intensity	Spot Size (μm)	SSR
60.00	50.00	113	4.8	664
68.42	43.18	102	5.4	411
76.04	35.56	109	5.9	321
83.66	27.94	135	6.5	252
91.28	20.32	121	7.1	144
96.36	15.24	131	7.5	105
101.44	10.16	149	7.9	94
106.52	5.10	146	8.3	73
110.33	1.27	149	8.5	101

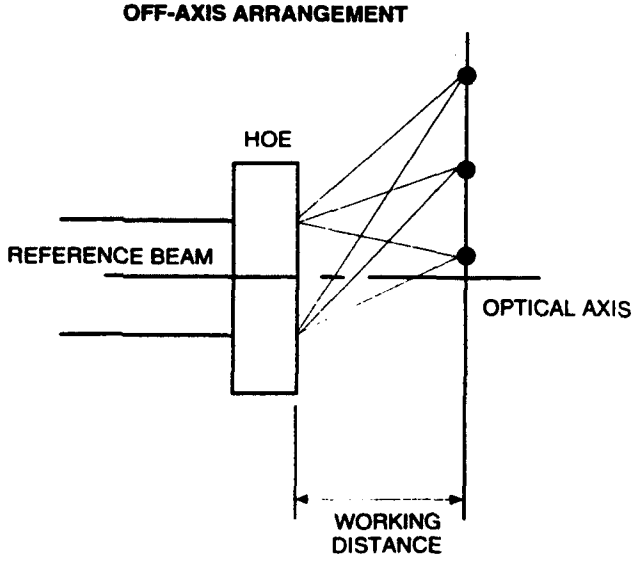

Figure 1-a. Off-Axis HOE Arrangement

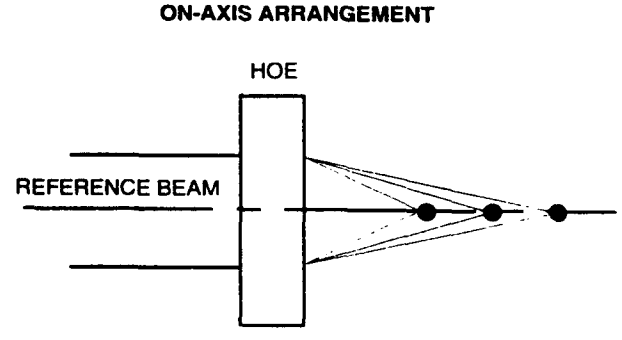

Figure 1-b. On-Axis HOE Arrangement

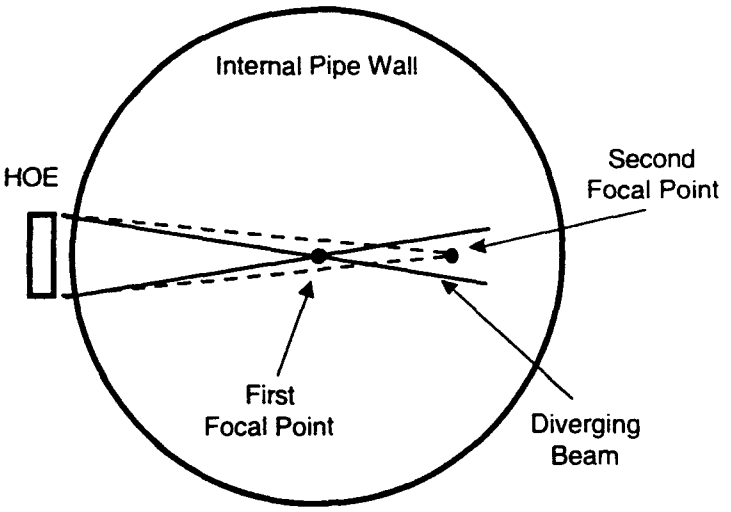

Figure 2. Schematic of Shadowing Effect

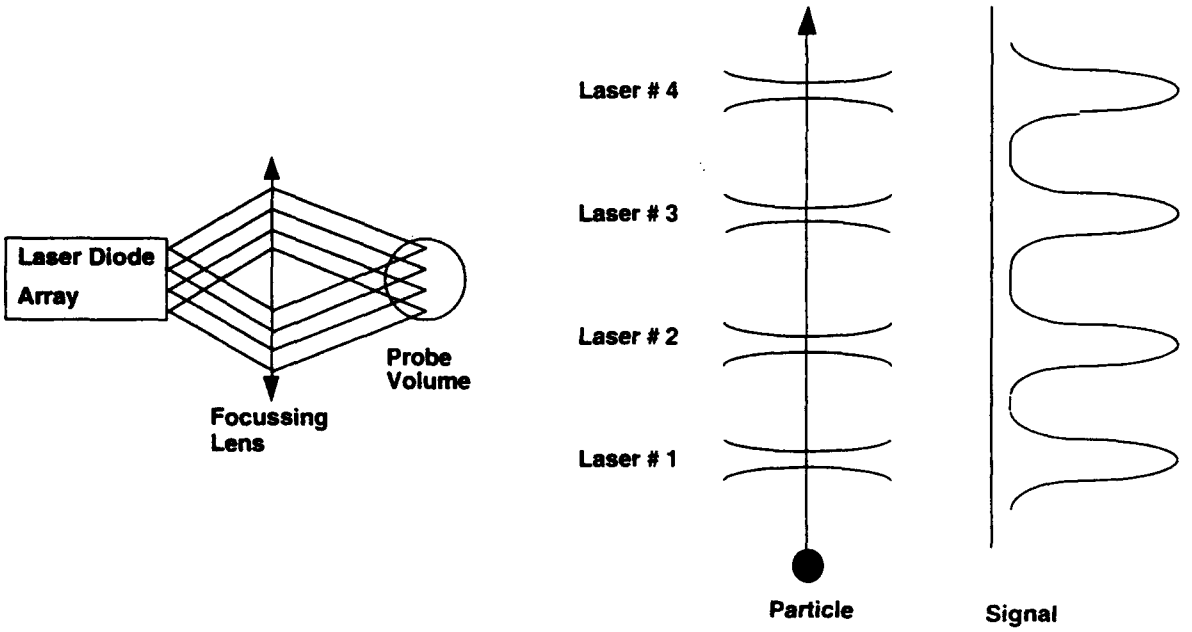

Figure 3. Schematic of DAV Technique

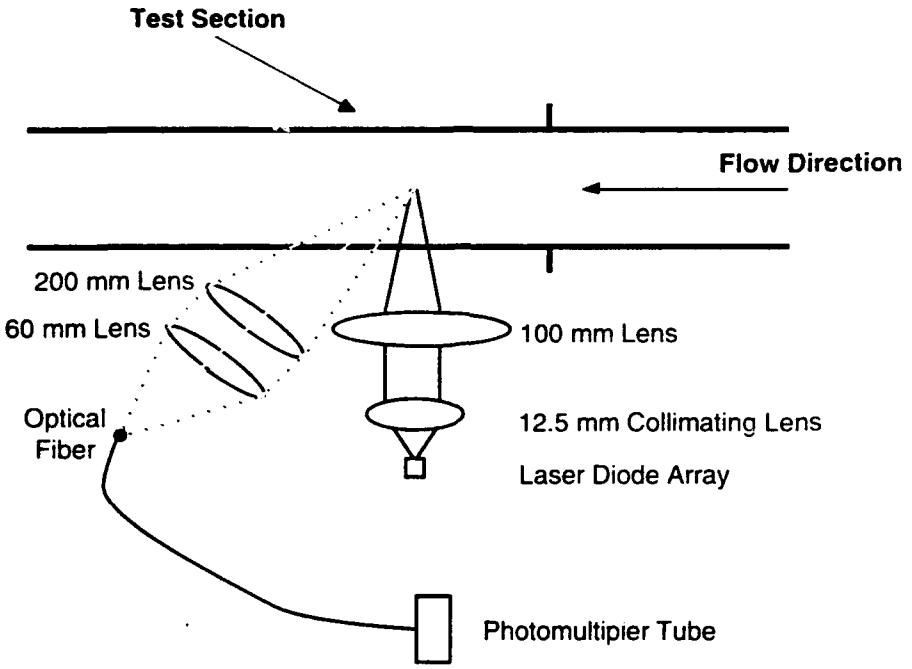

Figure 4. Schematic of the Optical System

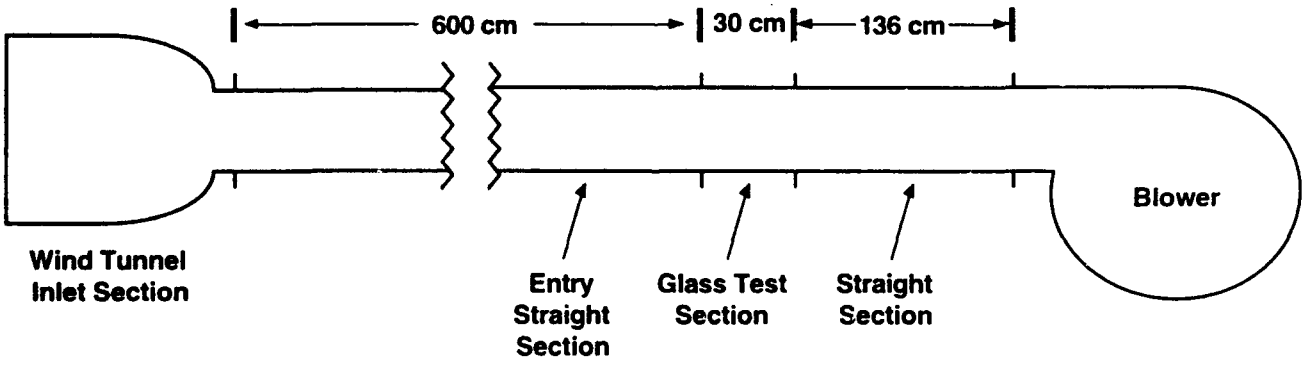

Figure 5. Schematic of the Wind Tunnel

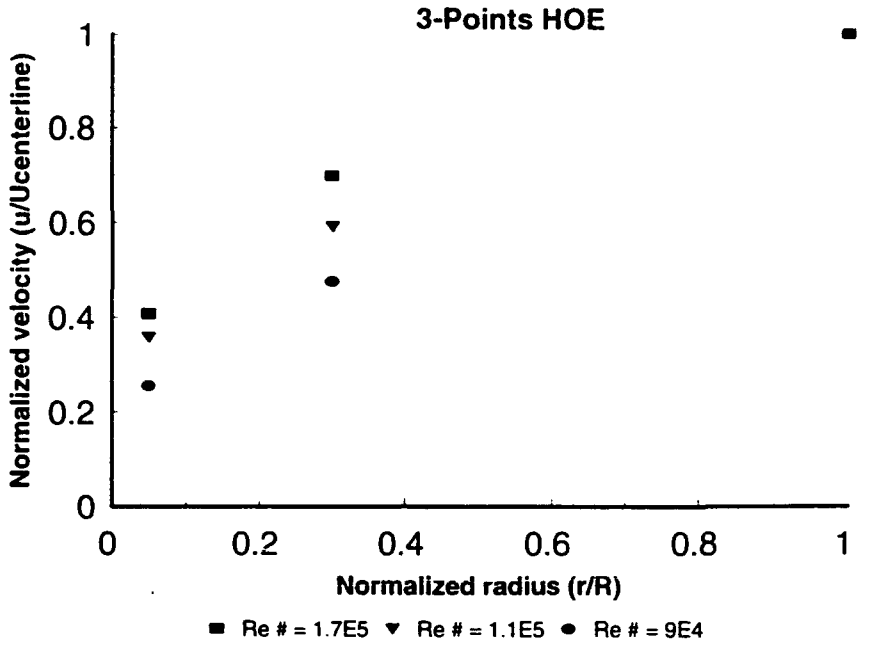

Figure 6. Three-Point HOE Velocity Profile

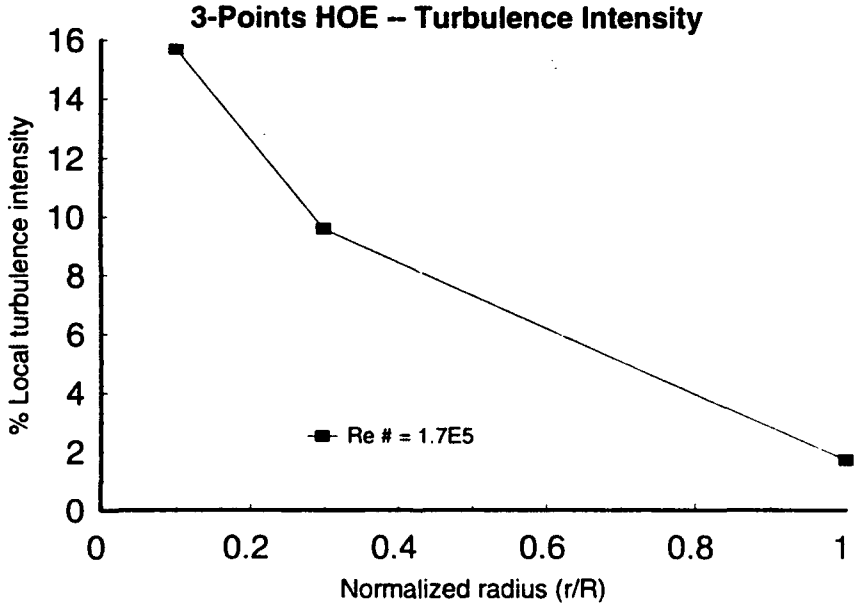

Figure 7. Local Turbulence Intensity at High Re #

THE EFFECT OF LASER BEAM ORIENTATION ON THE ACCURACY OF 3D LDA MEASUREMENTS WITHIN AN ANNULAR TEST FACILITY

J. F. Carrotte and K. M. Britchford

Department of Aeronautical Engineering,
University of Technology,
Loughborough, Leicestershire, LE11 3TU, U.K.

ABSTRACT

Often when making 3D coincident Laser Doppler Anemometry (LDA) measurements, restricted optical access means that the measured velocities have to be transformed into orthogonal components to fully define the flow field. This paper is concerned with the errors that can occur during this process. Errors in the derived orthogonal mean velocities are determined by the accuracy to which the laser beam alignment can be obtained. In addition the finite resolution, to which each processor determines the measured velocities, can lead to errors in the derived Reynolds stresses which may be amplified by the transformation process. A method is presented that estimates the relative experimental error that occurs as the direction of the measured velocity components is varied. These predictions are compared with measurements, obtained on a fully annular facility, in which these errors were observed. Whilst their magnitude is a function of the alignment of the measured velocity components, the significance of these errors depends upon the particular application and the flow field being measured.

INTRODUCTION

In a wide variety of applications a better understanding of the physical behaviour of turbulent flow may be obtained through more detailed and comprehensive measurements. At the same time this information may be used to validate and improve turbulence models for the accurate prediction of the flow. Thus, in addition to the mean velocities, it may be desirable to evaluate the time-averaged Reynolds stresses and higher order velocity correlations. Such information can be obtained using LDA, with an additional advantage being the non-intrusive nature of this measurement technique. Although a well established method, significant complications can arise since, in order to obtain all the time-averaged velocity data, it is necessary to simultaneously measure velocity components in 3 different directions. Furthermore, optical access to the measurement region is often limited, and so the measured velocity data has to be transformed in order to derive 3 mutually orthogonal components. One such application using these techniques is described by Carrotte et al. (1993), in which methods have been developed for obtaining coincident 3D LDA measurements on a facility that simulates the flow within gas turbine engines. These geometries are characterised by relatively small annular passages in which the optical access to the measurement region is severely restricted. Thus, both the transmitted light and the reflected signals have to pass through an outer casing with the measured velocity components being highly non-orthogonal. Of particular difficulty is the accurate definition of the velocity in the radial direction.

This paper concentrates on the errors which occur, in the derived quantities, due to transformation of the measured velocities into 3 orthogonal components. Particular attention is paid to the way in which the transformation process gives rise to a poorer resolution of the derived orthogonal velocities, compared with that of the components measured by each processor, which can lead to errors in the derived turbulence quantities. A theoretical analysis is presented and compared with measurements obtained in a fully annular S-shaped duct facility. This simulates the flow within a passage connecting the compressor spools of a gas turbine engine. Although these errors will be present in a wide variety of applications, they could be of particular significance for annular duct applications because of the limited access to the measurement region.

ANALYSIS OF TRANSFORMATION ERRORS

Various factors determine the direction of each measured velocity component and hence the transformation matrix that must be applied to convert the measured velocities (c_1, c_2, c_3) into the orthogonal components (u, v, w), i.e.,

$$\begin{Bmatrix} u \\ v \\ w \end{Bmatrix} = \begin{bmatrix} a_{11} & a_{12} & a_{13} \\ a_{21} & a_{22} & a_{23} \\ a_{31} & a_{32} & a_{33} \end{bmatrix} \begin{Bmatrix} c_1 \\ c_2 \\ c_3 \end{Bmatrix} \qquad (1)$$

Alternatively, this can be written as,

$$u_i = a_{ij}\, c_j \qquad (2)$$

where the i th. component of velocity is obtained by summing for j = 1, 3.

Clearly, errors in the derived velocity components will occur if the terms in the transformation matrix (a_{ij}) are not of the correct magnitude. Systematic errors of this type are a function of the orientation of the laser beams, with respect to the orthogonal axes of the rig, and the accuracy to which these can be measured. Knowledge of the limits to which laser beam alignment can be determined allows the terms in the transformation matrix (a_{ij}) to be varied to correspond with these limits and the effect on the mean orthogonal velocities (U, V, W) evaluated. However, this paper is more concerned with the errors that arise due to the finite resolution to which each velocity sample can be determined and the influence of the optical transformation upon these errors.

In converting each Doppler burst into a velocity measurement, the finite resolution (Δc_i) of the processor means that c_i can only be determined to within $\pm\Delta c_i$ of its true value. (N.B. This is common to all processors.) Hence, each derived orthogonal velocity will also be subject to a finite resolution (Δu_i), but this is of different magnitude to that determined by each processor and is given by,

$$\Delta u_i = \frac{\partial u_i}{\partial c_1}\Delta c_1 + \frac{\partial u_i}{\partial c_2}\Delta c_2 + \frac{\partial u_i}{\partial c_3}\Delta c_3 \qquad (3)$$

But $\partial u_i/\partial c_j = a_{ij}$ therefore,

$$\Delta u_i = a_{ij}\, \Delta c_j \qquad (4)$$

Since the resolution error of each processor is random it will have no effect on the mean orthogonal velocities (U_i) obtained from averaging over a number of bursts as $\overline{\Delta c_i} = 0$. However, since $\overline{(\Delta c_i)^2} \neq 0$ all the measured Reynolds stresses ($\overline{u_i u_j}$) will contain errors ($\Delta\overline{u_i u_j}$) which are given by the product $\overline{\Delta u_i \Delta u_j}$. Using equation (4) and assuming that $\overline{\Delta c_i \Delta c_j} = 0$ leads to,

$$\Delta\overline{u_i u_j} = a_{ik}\, a_{jk}\, \overline{(\Delta c_k)^2} \qquad \left[\sum_{k=1}^{3}\right] \qquad (5)$$

For example, the $\overline{uv}$ error ($\Delta\overline{uv}$) is given by,

$$\Delta\overline{uv} = (a_{11}\, a_{21})\overline{(\Delta c_1)^2} + (a_{12}\, a_{22})\overline{(\Delta c_2)^2} + (a_{13}\, a_{23})\overline{(\Delta c_3)^2}$$

and the $\overline{vv}$ error ($\Delta\overline{vv}$) is given by,

$$\Delta\overline{vv} = (a_{21})^2\overline{(\Delta c_1)^2} + (a_{22})^2\overline{(\Delta c_2)^2} + (a_{23})^2\overline{(\Delta c_3)^2}$$

The resolution is a function of the type of processor and the signal-to-noise ratio (SNR) associated with a given measurement. However, it should be noted that the Reynolds stress errors ($\Delta\overline{u_i u_j}$) are also determined by the magnitude of the terms in the transformation matrix (a_{ij}). Thus, although errors in the variance of each measured component will always occur, due to the finite processor resolution, the transformation process can give rise to errors in all the derived Reynolds stress components which may be amplified to much higher levels. The amplification is dependant upon the optical transformation and can be significantly larger for one Reynolds stress component compared with others. Further, equation (5) shows that the derived normal stresses are always greater than their true values, whereas the shear stresses may be subjected to errors of either sign.

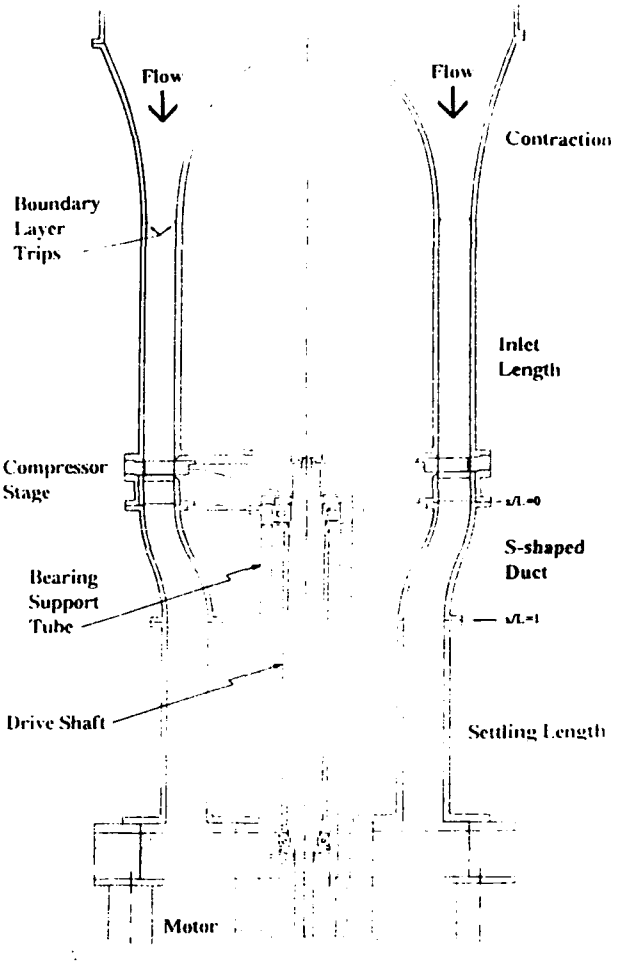

Figure 1 Experimental Facility

EXPERIMENTAL FACILITY

Measurements have been made on a fully annular facility which simulates the flow within the duct connecting the compressor spools of gas turbine engines. Optimisation necessitates that each spool is of different diameter and so the interconnecting duct takes the form of a complex S shape. The experimental facility (Fig. 1) is vertically mounted with air being drawn from atmosphere into a large plenum before

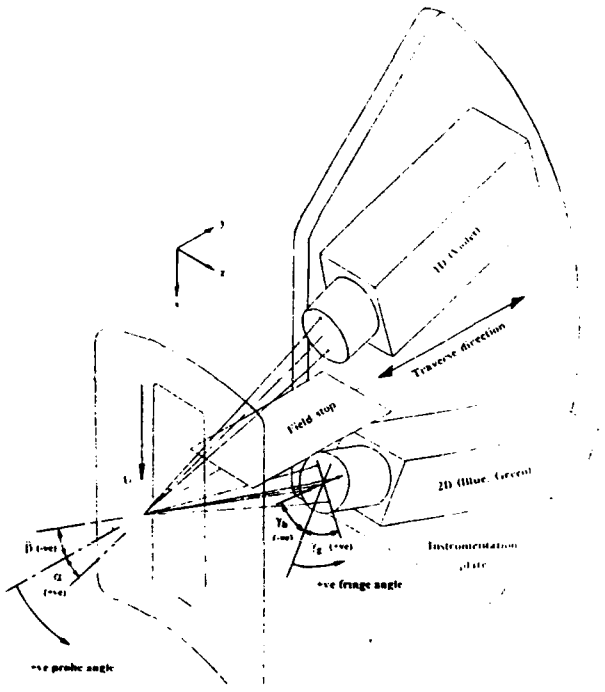

Figure 2 Optical Arrangement

passing through the intake which also contains a honeycomb flow straightener. At the end of the inlet section, 7 hydraulic diameters long, an axial compressor can be incorporated immediately upstream of the annular S-shaped duct to generate engine representative inlet conditions. However, all the measurements presented in this paper are with the compressor removed so that entry conditions to the duct are determined by turbulent boundary layer development along the inlet length. In this case air is drawn through the facility by two centrifugal compressors located in the exhaust system. The test section geometry is outlined in detail by Britchford et al. (1994) but is of constant area with an exit to inlet mean radius ratio of 0.8 and an axial length to inlet passage height of 3.4. Within the duct 4 laser windows allow measurements at up to 11 traverse stations. All results were obtained at a Reynolds number, based on inlet hydraulic diameter and mean passage velocity, of 2.8×10^5. Results have already been presented by Britchford et al. (1994) with the mean velocity profile indicating a central 'potential' core region, along the entire length of the duct, which isolates the boundary layers that develop along each wall. It should be noted, from consideration of the upstream geometry, that within the central core region the turbulence is isotropic (i.e. $\overline{uu} = \overline{vv} = \overline{ww}$) and that the shear stresses are all of zero magnitude (i.e. $\overline{uv} = \overline{uw} = \overline{vw} = 0$).

INSTRUMENTATION AND SIGNAL PROCESSING

Measurements have been obtained using a Dantec colour separated 3 channel LDA system incorporating the 60x fibreflow series of optical elements. Light from a 5 watt Argon Ion laser was separated into the green, blue and violet wavelengths within the transmitter box, each channel also incorporating a 40 MHz frequency shift to eliminate fringe bias. Fibre optic links connect the transmitter box to the optical probe heads, which are mounted on an instrumentation plate attached to the side of the test rig (Fig. 2). Both 1D (violet) and 2D (blue, green) probe heads, of diameter 14 mm, are simultaneously used to obtain 3 component measurements. In addition to the transmitting optics, each probe also incorporates receiving optics and a multi-mode fibre for signal transmission to the photomultipliers. For the data presented here beam expanders were also used resulting in each channel having a beam separation of 16 mm at exit from the expander, a focal length of 120 mm and a receiving optics aperture of diameter 22 mm. In back-scatter operation this gives a control volume size of approximately 0.1x0.1x1.5 mm. However, off-axis detection was used in all the results presented, with the 1D probe being used to detect signals from the blue, green velocity components and vice-versa. For the typical included angle used this gave an effective control volume size of 0.1x0.1x0.3 mm.

The fully annular test facility meant that both the transmitted light and the reflected signal have to pass through the outer casing with optical access being provided by several curved perspex windows as detailed by Carrotte et al. (1993). In order to initially align the laser beams each window, along with the instrumentation plate supporting the probes, must be removed from the test rig. All six beams are then projected through the window and aligned to simultaneously pass through a 50 µm diameter pin hole. In this way the required coincidence of the control volumes and receiving optics can be achieved. In addition, the pin hole was also used to track the path of each beam which allowed the beam alignment, relative to the rig axis, to be determined to within ±0.2°. This information is required for obtaining the value of the terms (a_{ij}) in the optical transformation matrix. As described by Carrotte et al. (1993), the ±0.2° angle variation can lead to errors in the measured mean orthogonal velocity components (U, V, W) of up to 0.1 m/s for data similar to that presented in this paper.

Seeding was provided by a TSI six-jet atomiser using a relatively low viscosity oil. The resulting particles of approximately 0.5 µm diameter were injected by a single radial pipe, with multiple outlet holes, located in the plenum above the measurement position. Signals received from each channel due to the passage of particles through the control volume were processed in the frequency domain using 57N10 Burst Spectrum Analysers (BSAs). All measurements were performed with hardware coincidence filtering i.e. data was only recorded when a burst was simultaneously registered by the detector circuits of all 3 BSAs. In this way the three velocity components recorded for each measurement were associated with the same particle passing through the control volume. However, after coincidence filtering some bursts were rejected by the internal validation tests conducted by each

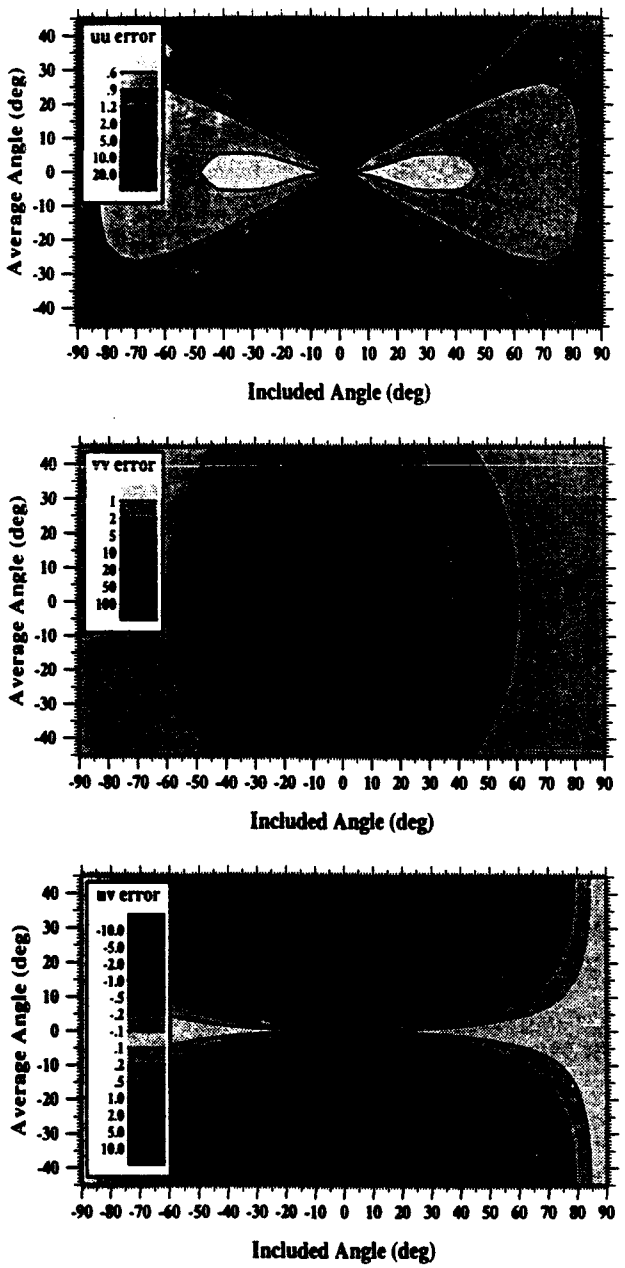

Figure 3 Variation of Reynolds Stress Errors (Unity Resolution) with Probe Angle Combination

processor. For this reason off-line software coincidence filtering was also performed in which a data point was only accepted as coincident if the arrival time registered by each channel was within the time estimated for the particle to pass through the control volume. Some 10,000 bursts were collected at each point but the internal validation process and software coincidence filtering meant that a reduced number (typically 4,000) of coincident velocity samples were available for deriving the time averaged quantities.

	Probe Angles ($\gamma_g=-\gamma_b=45°$)		Reynolds Stress Error (Unity Resolution)		
x/L	$(\alpha-\beta)$	$0.5(\alpha+\beta)$	$\Delta\overline{uu}$	$\Delta\overline{vv}$	$\Delta\overline{uv}$
-0.4	42.5°	1.8°	0.58	3.80	-0.08
0.02	-38.1°	-28.4°	1.48	3.76	1.72
0.125	42.6°	-3.6°	0.59	3.76	0.19
0.25	42.3°	4.1°	0.59	3.84	-0.24
0.375	42.3°	3.8°	0.60	3.88	-0.24
0.5	42.3°	4.0°	0.61	3.89	-0.26
0.625	42.0°	4.4°	0.61	3.94	-0.29
0.75	42.3°	4.1°	0.59	3.83	-0.23
0.875	-40.2°	-2.3°	0.57	4.24	0.15
1.0	-40.2°	-2.3°	0.57	4.24	0.15
1.4a	40.4°	-2.5°	0.57	4.15	0.14
1.4b	67.7°	-0.9°	0.73	1.62	0.02

Table 1 Probe Angle Combination and Reynolds Stress Errors (Unitv Resolution) for Each Traverse

RESULTS AND DISCUSSION

The flow field is to be defined relative to orthogonal axes in the axial (x), radial (y) and circumferential (z) directions (Fig. 2). However, the measured velocity components are determined by the alignment of the optical probe heads on the test facility. The 1D and 2D probes are at angles of α and β to the traverse direction and lie in the axial-radial plane. In addition, whereas the violet beams are constrained to also lie in this plane, the planes containing the green and blue beams are rotated about the 2D probe axis by angles γ_g and γ_b respectively. All the angles and associated sign conventions are defined in Figure 2 and produce a transformation matrix with terms,

$$a_{11} = -\frac{\sin(\alpha)\sin(\gamma_b)}{\sin(\alpha-\beta)\sin(\gamma_g-\gamma_b)} \qquad (6.1)$$

$$a_{12} = \frac{\sin(\alpha)\sin(\gamma_g)}{\sin(\alpha-\beta)\sin(\gamma_g-\gamma_b)} \qquad (6.2)$$

$$a_{13} = -\frac{\sin(\beta)}{\sin(\alpha-\beta)} \qquad (6.3)$$

$$a_{21} = \frac{\cos(\alpha)\sin(\gamma_b)}{\sin(\alpha-\beta)\sin(\gamma_g-\gamma_b)} \qquad (6.4)$$

$$a_{22} = -\frac{\cos(\alpha)\sin(\gamma_g)}{\sin(\alpha-\beta)\sin(\gamma_g-\gamma_b)} \qquad (6.5)$$

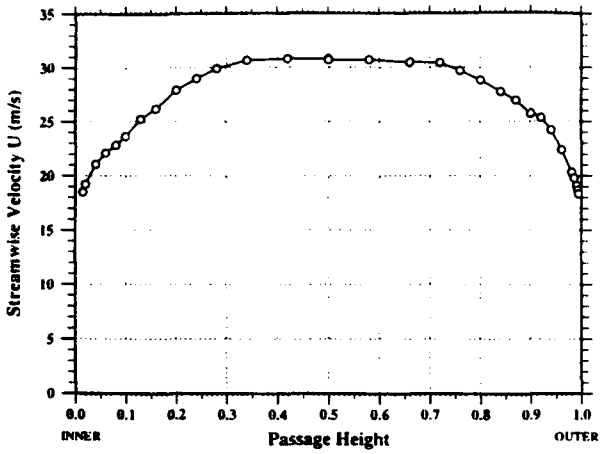

Figure 4 Streamwise Velocity Distribution (x/L = 1.4a)

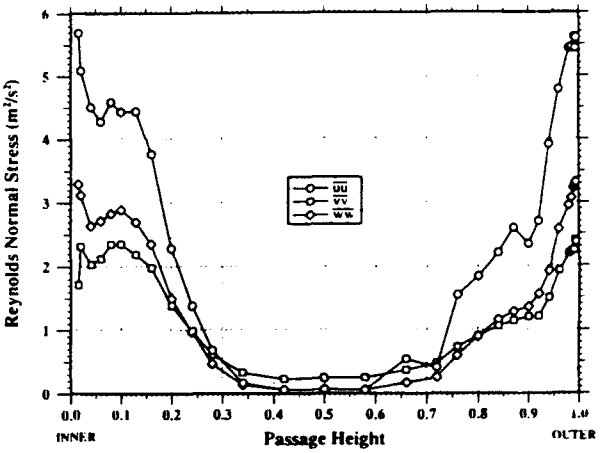

Figure 5 Normal Stress Distributions (x/L = 1.4a)

$$a_{23} = \frac{\cos(\beta)}{\sin(\alpha - \beta)} \tag{6.6}$$

$$a_{31} = \frac{\cos(\gamma_b)}{\sin(\gamma_g - \gamma_b)} \tag{6.7}$$

$$a_{32} = -\frac{\cos(\gamma_g)}{\sin(\gamma_g - \gamma_b)} \tag{6.8}$$

$$a_{33} = 0 \tag{6.9}$$

The measured velocities U_{BSA1}, U_{BSA2} and U_{BSA3}, which are associated with the green, blue and violet control volumes respectively, are then related to the orthogonal velocities u, v and w via,

$$\begin{Bmatrix} u \\ v \\ w \end{Bmatrix} = \begin{bmatrix} a_{11} & a_{12} & a_{13} \\ a_{21} & a_{22} & a_{23} \\ a_{31} & a_{32} & a_{33} \end{bmatrix} \begin{Bmatrix} U_{BSA1} \\ U_{BSA2} \\ U_{BSA3} \end{Bmatrix} \tag{7}$$

Predicted Probe Angle Effects

In order to asses the relative magnitude of the Reynolds stress error associated with each component, the actual terms in the transformation (6) were included in equation (5) and used to calculate $\Delta\overline{u_i u_j}$ for a wide range of probe angle combinations (α, β). The errors are presented as contour plots (Fig. 3), with each angle combination being defined in terms of the included angle between the probes (α–β) and the average angle made by the probes with respect to the traverse direction $0.5(\alpha+\beta)$. It was assumed that the green and blue fringe angles (γ_g, γ_b) were at 45° and –45° respectively, as was approximately the case in the experimental measurements, and that the resolution of each processor (ΔU_{BSAk}) was of unity magnitude (i.e. 1 m/s). This latter assumption is not realistic and so for the different angle combinations it is the relative size of the errors, rather than their absolute values, that can be assessed. Thus, a value of 1.0 (normal stresses) or 0.0 (shear stresses) indicates the error in the stress component that would occur, due to the finite processor resolution, if transformation were not necessary. However, angle combinations that give rise to errors much greater than these indicate a significant amplification of the resolution errors, due to transformation, leading to larger errors in the derived Reynolds stresses. For the case described, only the Reynolds stress errors $\Delta\overline{uu}$, $\Delta\overline{vv}$ and $\Delta\overline{uv}$ vary with α, β ($\Delta\overline{ww} = 1$ and $\Delta\overline{uw} = \Delta\overline{vw} = 0$ for all α, β) and therefore only these are presented in Figure 3. It should be noted that the contours are not at equal intervals and the values are different on each plot.

For the normal stresses it can be seen that the radial component ($\overline{vv}$) is subjected to a larger error compared with the axial component ($\overline{uu}$). For example, at zero average angle and an included angle of 20° the error in $\overline{vv}$ is 16.6 (for unity resolution) compared with 0.52 for $\overline{uu}$. However, halving the included angle to 10° will increase the $\overline{vv}$ error value to 65.8, whereas it will reduce to 4.27 if the included angle can be doubled. These errors reflect the nature of a fully annular facility, where access is through the outer casing, so that large differences in alignment occur between the measured velocity components and the radial direction. Thus the error in radial normal stress is mainly a function of the included angle between the probes, with closer alignment of the measured components to the radial direction occurring at larger included angles. For the axial normal stress ($\overline{uu}$) the average angle of the probe heads, as well as the included angle, can influence the error magnitudes. The shear stress ($\overline{uv}$) can have errors of both positive and negative magnitude which are mainly a function of the average probe angle. In this case, the error for a wide range of included angles can be minimised by having the probe heads

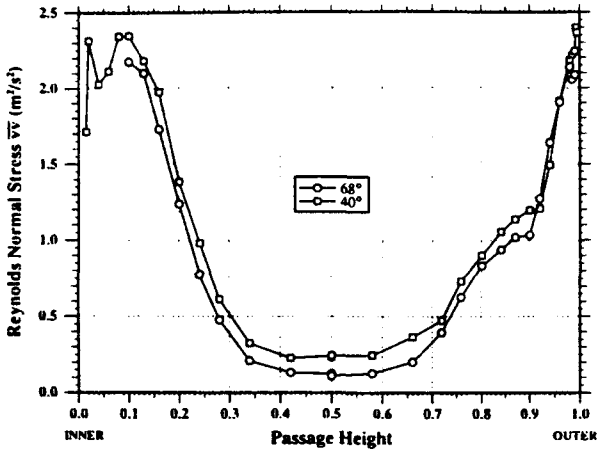

Figure 6 Effect of Increasing Included Angle on Radial Normal Stress Distribution (x/L = 1.4)

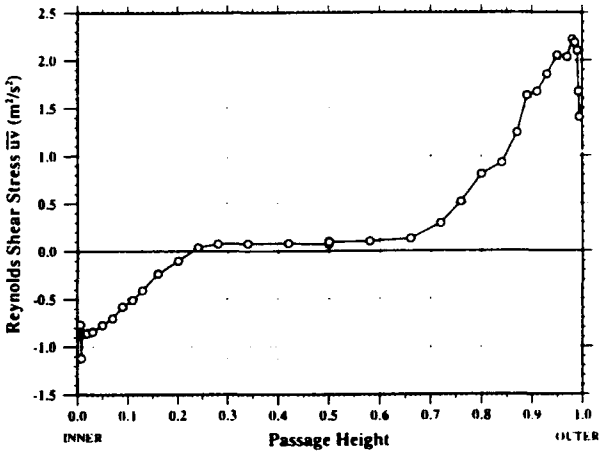

Figure 7 Shear Stress Distribution (x/L = 0.02)

symmetrically located about the traverse direction, resulting in a small average angle.

Although errors can be predicted for a large number of angle combinations, in reality the choice is restricted by the geometry of the optical windows and test facility. However, the above analysis is useful in assessing which combination of angles (α, β, γ_g, γ_b), that are practical, will minimise the errors associated with all 6 Reynolds stresses or those stresses which are of particular significance to an investigation.

Experimental Measurements

Measurements have been made at 11 stations within the annular S-shaped duct, with local variations in geometry resulting in several probe angle combinations (α, β) being used (Table 1). Within practical limitations these angles were chosen to minimise the effects of transformation on the Reynolds stresses, but errors are still evident in the experimental data.

At x/L = 1.4 the mean velocity profile (Fig. 4) indicates the presence of boundary layers which have been subjected to both streamwise pressure gradient and curvature effects during their development within the S-shaped duct. A central core region is also present and occupies some 35% of the passage height, with the turbulence in this region being of relatively low intensity and isotropic. Here, due to the higher transformation errors in the radial direction, the measured radial normal stress ($\overline{vv}$) is over twice that of the axial ($\overline{uu}$) and circumferential ($\overline{ww}$) values (Fig. 5). This was confirmed by increasing the included angle (α–β) from 40° to 68°, although this precluded measurements being obtained close to the inner wall. Figure 6 shows that with the larger included angle, lower radial normal stresses are obtained across a large portion of the passage due to the reduced transformation errors. This data also indicates how in regions of low turbulence the errors are of greatest significance, since they are of similar magnitude to the actual stress levels. However, within each boundary layer although the error magnitude may increase, due to changes in the processor resolution, the higher stress levels mean these errors are of relatively less significance. Hence the importance of processor resolution, and its amplification through the transformation matrix, needs to be assessed relative to the flow field being measured. For the shear stress component ($\overline{uv}$) values of finite magnitude were recorded within the central core region, as indicated at x/L = 0.02 (Fig. 7), despite the true values being zero. Here a probe configuration with a relatively large average angle was used and the errors are again thought to be due to the transformation error.

Estimate of Processor Resolution

In the central passage region it is known that the turbulence should be isotropic with normal stress components of equal magnitude ($\overline{uu} = \overline{vv} = \overline{ww}$) and a shear stress ($\overline{uv}$) of zero. With this information the actual resolution of each BSA processor can be calculated. For all the measurements, in the central region, resolutions of approximately 0.14 m/s, 0.21 m/s and 0.28 m/s were typically indicated for ΔU_{BSA_1}, ΔU_{BSA_2} and ΔU_{BSA_3} respectively. The original error plots (Fig. 3) were based on a 1 m/s resolution on all processors and therefore allowed only the relative errors between different probe angles to be assessed. Using the resolutions determined from the experimental data, the actual errors expected for each Reynolds stress component over a range of probe angles can calculated. The components corresponding to the original plot are presented here (Fig. 8), although now only the circumferential normal stress ($\overline{ww}$) is invariant with probe angle (α, β). Note also the change in contour magnitudes due to the actual resolutions being much smaller than the unity values originally assumed. Furthermore, the shape of the contours are modified since the resolution of each processor is different, with errors being relatively larger for Reynolds stress components that are more dependant on the velocity measured by the 3rd. processor

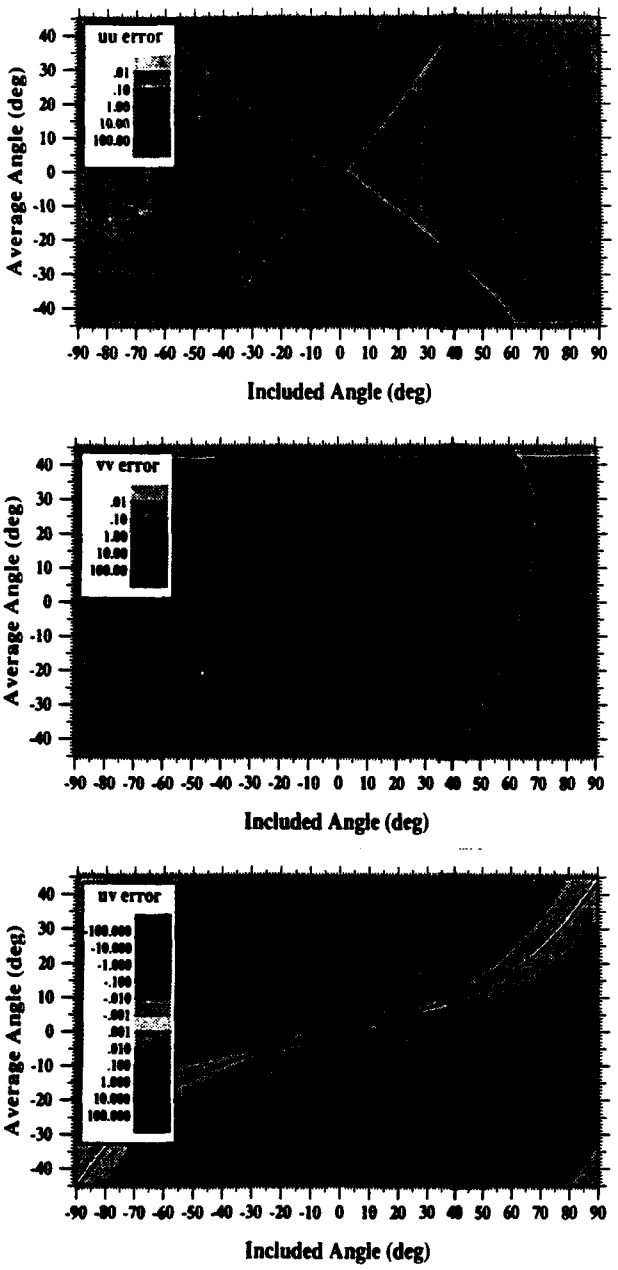

Figure 8 Variation of Reynolds Stress Errors with Probe Angle Combination

(U_{BSA1}). It can be seen that the minimum shear stress error no longer occurs at zero average angle but at some finite value dependent upon the included angle.

The resolution of each processor is a function of the record interval (RI), this being the period over which a Doppler burst is sampled and is therefore determined by the number of samples and the sampling frequency. Due to various signal analysis techniques used by the processor, the accuracy to which a particular burst can be resolved is a function of the RI, as given by,

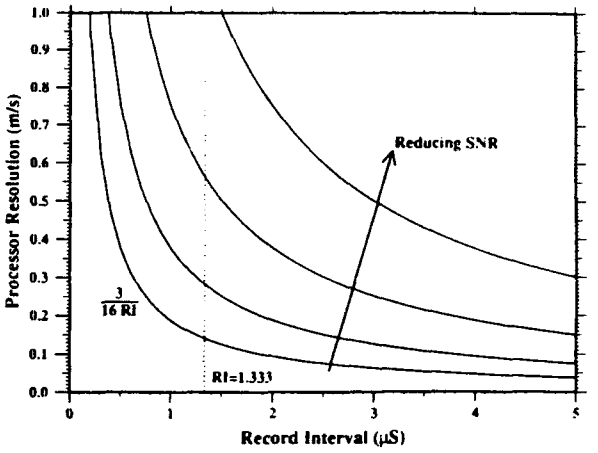

Figure 9 Variation of Resolution with Record Interval

$$\text{processor resolution} = \frac{C_a}{16\,RI} \qquad (8)$$

where C_a is the fringe spacing or calibration factor (m/s/MHz) and is determined by the light wavelength and the angle between the pair of beams forming the control volume. However, equation (8) only applies to regions in which a good signal-to-noise ratio (SNR) can be achieved, with the resolution becoming worse as the noise content of the signal increases (i.e. lower SNR). The relationship between record interval and resolution for various noise levels is indicated in Figure 9, with the calibration factor (C_a) used approximately corresponding to that in the present investigation. It should be noted that the record interval selected should reflect the time taken for the particles to cross the control volume and hence the duration of the bursts. Dantec (1991) recommend a value of two-thirds the transit time of the fastest particles. For the data presented here, this resulted in a record interval of 1.333 μs which for 3D coincident data, must be the same for all processors. For the green component (BSA_1), it can be seen (Fig. 9) that the calculated resolution corresponds to that which should be obtained at a good SNR and seems to confirm the analysis techniques used. However, the poorer resolution of the other processors appears to indicate operation at a lower SNR. This may be associated with the laser characteristics and the different amounts of light power present in each of the control volumes. As described by Carrotte et al. (1993) the green volume (BSA_1) contains the maximum power whereas the component with the least power is violet (BSA_3), containing only 10–20% of this value. It is also interesting to note that the poorer SNR may be reflected by the proportion of data validated by each processor during acquisition, this being 100%, 75% and 50% of the coincident bursts detected by BSA_1 BSA_2 and BSA_3 respectively.

Optimum Laser Beam Alignment

Errors will occur in the Reynolds normal stresses due to the finite resolution to which velocities can be measured, but if the measured data have to be transformed then such errors can be significantly amplified and affect all the Reynolds stresses. However, it should be noted that minimising these errors is difficult since the selected measurement directions, in addition to determining the transformation matrix, can also affect the processor resolution. For example, the magnitude of the terms (a_{ij}) in the transformation matrix can be minimised by measuring, if it were possible, along each orthogonal axis. However, the higher velocities associated with the measured streamwise component and the much lower values of the other two components changes the velocity signal analysed by each processor. The resulting alteration to processor filter settings and other parameters thereby affect the SNR of the bursts being analysed. Furthermore, the selection of certain measurement directions can also increase the noise content of the analysed signals due to reflection from nearby surfaces etc. (Carrotte et al., 1993) Thus, in addition to determining the transformation matrix, the selected measurement directions affect the signal-to-noise ratio at which each processor operates and the associated processor resolution. It also follows that not only is the quality of the data affected by the selected beam alignment, but also the ability to obtain any data in regions of high noise such as close to solid surfaces. Hence, in addition to the transformation errors consideration should be given to the likely SNR of the measured components. This is of particular significance for the violet component since, due to the relatively low power in the control volume, it has nominally the poorest SNR.

CONCLUSIONS

For 3D measurements restricted optical access usually results in the transformation of the measured velocities in order to fully define the flow field using orthogonal components. This may introduce errors into the derived quantities and the following conclusions are drawn:-

- Alignment of laser beams on the test facility can only be specified within certain limits. Hence, this effects the accuracy of the terms used in the transformation matrix and can lead to errors in the derived orthogonal mean velocities.

- The finite resolution associated with each measured velocity can be amplified, during the transformation process, and thereby significantly affect the derived Reynolds stresses. Such errors will increase the normal stress values recorded but the shear stress errors may be of either positive or negative magnitude.

- The magnitude of the errors is a function of the included angle between the measured velocity components and the average angle made by these components with each orthogonal axis.

- In a region of low isotropic turbulence errors due to transformation have been observed experimentally on a fully annular facility. In such a geometry access is restricted and results in the radial normal stress errors being of largest magnitude.

- Any experimental investigation of turbulent flow should be aware of the Reynolds stress errors that can occur and their significance should be assessed with respect to the level of turbulence present.

The effects of laser beam alignment on the quality of data obtained is the subject of a continuing investigation at Loughborough.

REFERENCES

Britchford, K. M., Carrotte, J. F., Stevens, S. J. and McGuirk, J. J., 1994, "The Development of the Mean Flow and Turbulence Structure in an Annular S-shaped Duct", ASME Paper No. 94-GT-457.

Carrotte, J. F., Britchford, K. M. & Wray, A. P., 1993, "Three Component LDA Measurements of Annulus Wall Boundary Layers Upstream of an Annular S-shaped Duct", Proceedings of the Fifth International Conference on Laser Anemometry Advance and Applications, Veldhoven, The Netherlands, pp. 111-118.

Dantec, 1991, "Burstware Software Guide", Dantec Elektronic, Denmark.

A GENERAL PROCEDURE FOR CALCULATING AND CORRECTING THE DISPLACEMENT OF LASER BEAMS PASSING THROUGH PLANE AND CYLINDRICAL WINDOWS USING A THREE COMPONENT LASER DOPPLER ANEMOMETER FOR TURBOMACHINERY APPLICATIONS

A.Doukelis, M.Founti*, K. Mathioudakis and K. Papailiou

Mechanical Engineering Department,
Fluids Section,
Lab. of Thermal Turbomachines
* Thermal Engineering Section,
Lab. of Steam Generators and Thermal Plants
National Technical University of Athens
Athens, Greece

ABSTRACT

The paper presents a general mathematical procedure for the calculation of the measuring location of three pairs of laser beams, their diplacement and corresponding velocity component inclination due to refraction of the laser beams at curved interfaces. The beam equations are solved, without any small-angle approximations, for an arrangement corresponding to a three component laser Doppler anemometer. Refractive index variations of the media, due to temperature or pressure variations, are taken into account.

The proposed formulation has been validated by comparison with experimental results. The correction procedure has been applied to a typical configuration for measurements in a turbomachinery passage and representative beam displacement calculations are presented. Possibilies offered by the method in designing experiments as well as correcting obtained results are discused.

1. INTRODUCTION

In laser-Doppler anemometry, when beams pass through transparent curved windows, it is necessary to make corrections for the refraction of the laser beams at the interface boundaries. Simplified or simple case calculations have been reported in the literature, e.g. Bicen and Whitelaw (1981), Boadway and Carahan (1979), Parry et al (1990) and the required correction has become a standard procedure for measurements performed with a single-component laser-Doppler anemometer.

In recent years the application of two and three-component laser-Doppler anemometers has become increasingly popular, especially with the advent of laser diodes and fibre-optic links which allow the production of small-size optical probes. Such three-component laser-Doppler anemometers find particular application in turbomachinery flows, where optical access and size of available window is normally limited, the measuring control volume has to be of small size and the resulting angle between the beam pairs forming the 3-D arrangement has to be generally small.

Additionally, in turbomachine applications alternative methods such as refractive index matching techniques, Durst et al (1993), or use of correction lenses, Durrett et al (1985), cannot be generally applied, due to the nature of the flows under investigation. It is, therefore, necessary to calculate the displacement of the beams due to refraction. Especially, with three-component laser-Doppler anemometers it is important to guarantee a priori coincidence in space of the three measuring volumes and to estimate the required velocity correction.

The passage of the three beam-pairs through a curved interface can affect:

a) the position of the intersection of each beam-pair (i.e of the measuring volume),

b) the relative position in space of the three measuring volumes, which in the general case may not cross any more after sucessive refractions,

c) the shape of each of the measuring volumes and, consequently, the fringe spacing (the calibration factor between fringe crossing frequency and seed particle velocity may change),

d) the orientation of the measured velocity component.

The radius of curvature and the thickness of the walls of the flow enclosure, the intersection angles of the laser beam-pairs, the angle of incidence of each beam on the interface surface influence the above four factors, together with the refractive indices of the inner/outer fluid(s) and of the wall. The resulting beam displacements can become significant in turbomachinery configurations, as for example reported by Strazisar (1986), where the three velocity components are generally resolved in non-orthogonal coordinate systems.

The analytical solution of the beam transmittance equations for the general case is difficult without, for example, small-angle approximations, employed by Bicen and Whitelaw (1981). Gardavsky et al (1989) reported corrections in three dimensions resulting by solving the general system of equations for a pipe configuration inserted in a rectangular box, an approach which is commonly applied together with refractive index matching of the fluid and enclosure walls.

It is the purpose of this work to present a mathematical procedure solving the general beam transmittance equations to allow calculation of the displacement in space due to refraction during simultaneous three-component LDA velocity measurements. The displacements result from the three pairs of laser beams meeting a curved window at different angles in three dimensions. The procedure examines coincidence in space of the three measuring control volumes and can provide estimates of the required corrections.

In order to validate the developed procedure, the calculated displacements have been experimentally verified in a simple configuration.

2. DESCRIPTION OF THE MATHEMATICAL PROCEDURE

The proposed correction procedure has been developed for a typical configuration of a three-component laser-Doppler anemometer comprising of two probes, as shown in Figure 1. The two-component (2-D) probe transmits two orthogonal pair of beams and the one-component probe (1-D) transmits the third pair of beams and it is positioned at a certain angle with respect to the 2-D probe. The optical parameters of the two probes and the system of coordinates used in the calculations are shown in Figure 1.

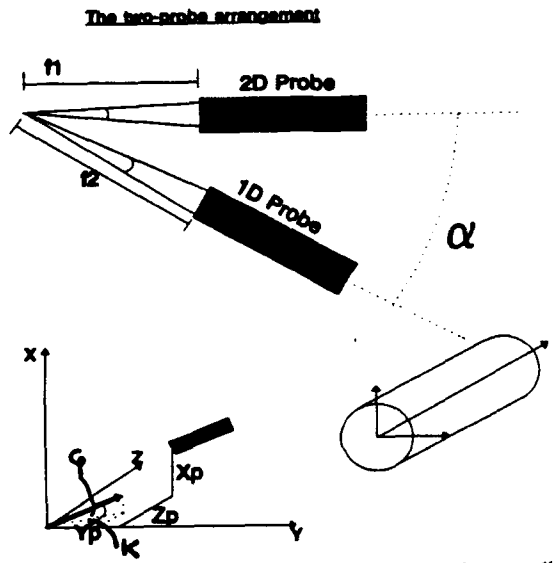

Figure 1: Layout of the probe configuration and the coordinate system used for the calculations

For the derivation of the general equations of the transmittance of the laser beams, the optical parameters of each probe, the geometry of the two-probe assembly and its position are known (Figure 1), namely:
- The focal lengths f_1 and f_2 of the focusing lens of the 2-D and of the 1-D probe and the respective half angles θ_1 and θ_2,
- the angle α between the two probes,
- the point (X_p,Y_p,Z_p) corresponding to the point of intersection of the horizontal and vertical lines connecting the four beams of the 2-D probe on the focusing lens and
-the angles ϕ and κ the 2-D probe forms with the horizontal and the vertical planes respectively.

The geometrical data and properties of the interface window are also known:
-its radius of curvature R_o,
-the thickness, t, and
-the refractive indices n_a, n_o, n_w, of the external, the internal fluid and of the wall material respectively.

The calculation of the refractive indices of the internal and external fluids, considered here to be air, takes into account the different conditions of the air inside and outside the window (namely the pressure, the temperature and the humidity ratio).

The refractive index of the air is related to its density according to (Allonso-Finn, 1967):

$$n_r = 1.0 + 0.00024\,\rho$$

The density, ρ, is calculated as a function of the pressure, p, the temperature, t, and the humidity ratio, H, providing values of n_a and n_o.

The proposed method involves two basic procedures:
a) The path of a single refracted beam, issuing from one incident laser beam with arbitrary orientation with respect to the interface wall, is determined.
b) Using the available geometrical parameters for the 2-D and 1-D probes, the refracted beams issuing from each individual incident beam are determined. From the corresponding equations the intersection points of the refracted beams are determined as well as the direction of their bisectors.

Each procedure is described below.

The following steps have been adopted for the calculation of the beam displacement due to refraction:

Step 1.1: Definition of the beam equations: The equation describing an incident beam is defined by the vector $\vec{r}_1(a_1,b_1,c_1)$ parallel to the beam and the point of origin $A(x_1,y_1,z_1)$, Figure 2. The equation of a line in 3-D space has the form:

$$(x-x_1)/a_1 = (y-y_1)/b_1 = (z-z_1)/c_1$$

The calculation of x_1,y_1,z_1,a_1,b_1,c_1 for one beam is done from the data of the corresponding probe and its position.

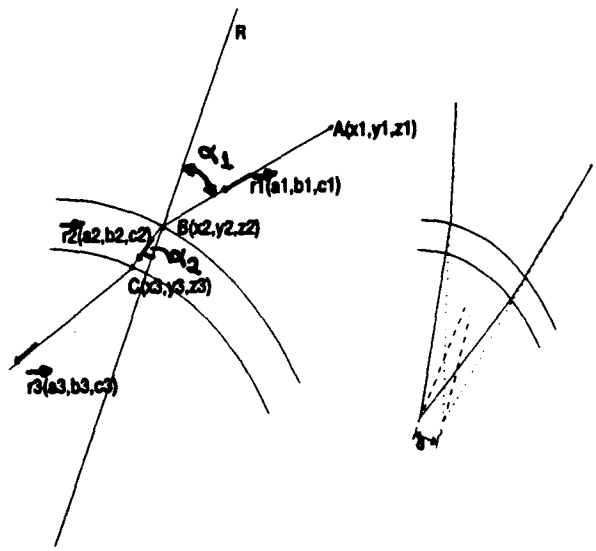

Figure 2: Path of a single refracted beam-Displacement between initial and final point of intersection

Step 1.2: Calculation of the point of intersection on the outer interface surface: The point of intersection, $B(x_2,y_2,z_2)$, of each beam with the outer wall of the window is calculated by solving the system of equations of the initial beam and of the curved surface, $S(x,y,z) = 0$. The equation of the curved (cylindrical) surface has the following form in the chosen system of coordinates:

$$x^2 + y^2 + c^2 = R_o^2$$

The resulting 3 X 3 system of equations is solved analytically, taking into account all possible cases for the parameters of the equations. This system of equations may have two solutions, corresponding to the two points of intersection of a cylinder and

a line. The point $B(x_2,y_2,z_2)$ which corresponds to the geometry of our problem is chosen as the correct solution.

Step 1.3: Calculation of the vector parallel to each beam: The unit vector $\vec{r_2}(a_2,b_2,c_2)$ parallel to each beam after the first refraction on the outer wall of the window is then calculated. This is done by solving again a system of equations, which are derived as follows:

- Refraction is considered to take place on the plane created by each original beam and the corresponding radius of curvature of the surface at the point of intersection $B(x_2,y_2,z_2)$. Thus, the inner product of the vector $\vec{r_2}(a_2,b_2,c_2)$ and the vector (L,M,N) perpendicular to this plane must equal zero:

$$L\,a_2 + M\,b_2 + N\,c_2 = 0$$

The vector (L,M,N) is calculated from the equation of the plane, which is known, since it is defined by the incident beam and the radius of curvature of the outer surface at the point of intersection with the beam. In this approach the definition of the plane is done by one point and two vectors parallel to the plane, namely the point $(0,0,z_2)$ and the vectors $(x_2,y_2,0)$ and (x_1,y_1,z_1-z_2).

- Snell's law, Durst et al (1976),relates the values of the angles α_1 and α_2, between each beam and the radius at the point of intersection before and after refraction, respectively.

$$n_a \cos(\alpha_1) = n_w \cos(\alpha_2)$$

This equation provides values for the unknown α_2, since α_1 can be calculated from the inner product between the initial beam and the radius of the curved surface at the point of intersection:

$$\cos(\alpha_1) = \frac{(x_2,y_2,0)\cdot(a_1,b_1,c_1)}{\|(x_2,y_2,0)\|\,\|(a_1,b_1,c_1)\|}$$

while

$$\cos(\alpha_1) = \frac{(x_2,y_2,0)\cdot(a_2,b_2,c_2)}{\|(x_2,y_2,0)\|\,\|(a_2,b_2,c_2)\|}$$

- The final equation employed is the trigonometric equation:

$$a_2^2+b_2^2+c_2^2 = 1$$

Solution of this system of equations provides the vector $\vec{r_2}(a_2,b_2,c_2)$. Again two solutions can be calculated and the one that is compatible with the given geometry is chosen.

Step 1.4: Calculation of the point of intersection at the inner surface. Steps 2 and 3 are similarly repeated for the inner surface of the curved wall,and the intersection point, as well as the direction of the refracted beams are derived.

The second procedure consists of the evaluation of the measuring volume position and orientation, for each pair of beams, after they have crossed the wall. This procedure is applied to each pair of beams of the two-probe arrangement and consists of two steps:

Step 2.1: Determination of the new point of intersection of each beam pair. By applying Procedure 1 to each one of the beams of one pair, the equation for each beam after passing through the window is determined. Having these equations, the intersection point is determined by solving the appropriate system of equations.

At this point it should be mentioned that the beam axes, after passing through the window, may not intersect any more. This is examined in the procedure, and if it happens, instead of defining the intersection point (which does not exist), the magnitude of the vertical distance between the two axes is determined.

Step 2.2: Calculation of velocity component inclination. The vector of the final bisector of each pair of beams is finally calculated, again by solving a system of equations. The bisector lies on the plane of the two beams and, as a result, the inner product of the vector (a_b,b_b,c_b) of the bisector and of the vector perpendicular to the plane of the beams must be equal to zero.

Calculations presented here have been performed in Cartesian coordinates, but the coordinate system can be transformed to a turbomachinery system of coordinates employing axial, radial and peripheral coordinates. The Cartesian system of coordinates has been chosen because it offers the lower complexity of the resulting equations in comparison to the corresponding equations in cylindrical coordinates.

3. VALIDATION OF THE PROPOSED CODE

The developed code has been compared with calculated beam diplacements provided by Bicen and Whitelaw (1981) and with our own experimental results obtained in a simple arrangement. For the theoretical verification the refraction correction equations provided by Bicen and Whitelaw (1981) have been considered. The beam displacement for axial, tangential and radial velocity measurements in a straight pipe configuration has been calculated and compared to the results of the current study. All calculations agreed very well but, for reasons of space, only the comparison between initial radius and final position of the point of intersection (radius and angle of displacement in cylindrical coordinates) for the case of radial velocity measurements are shown here in Figures 3 and 4 respectively. The optical parameters and wall thickness used for the calculations are shown in the respective figures.

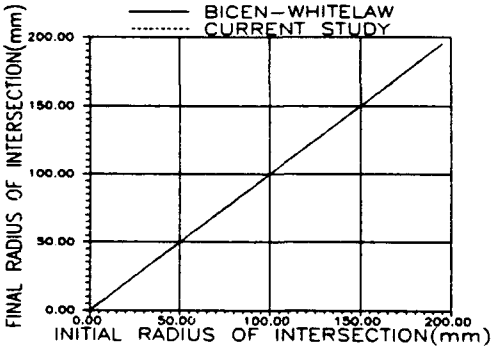

Figure 3: Calculated radius for radial velocity component measurements in a staight pipe - Comparison with results by Bicen & Whitelaw (1981). (f_1=200mm,t=2mm,Y_p=200mm,Z_p=0,ϕ=0,κ=0)

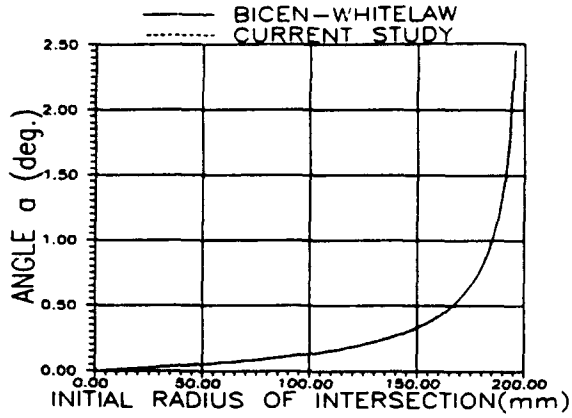

Figure 4: Calculated angle (cylindrical coordinates) for radial velocity component measurements in a straight pipe-Comparison with results by Bicen & Whitelaw (1981).

For the experiments, the two component (2-D) probe has been aligned as shown in Figure 5. A thin glass plate, fixed on the traversing mechanism, has been used as a scattering medium to produce an artificial Doppler burst. The beams have been initially focussed on the glass plate without the presence of the window. Subsequently, the window has been placed between the thin glass plate and the 2-D probe. The window could be rotated and translated in the vertical direction relative to the 2-D probe, with the use of a second traversing mechanism. After positioning of the window, the probe has been focussed again on the glass plate and the displacement has been recorded. This displacement corresponds to the displacement of the laser beams due to refraction as they cross the window.

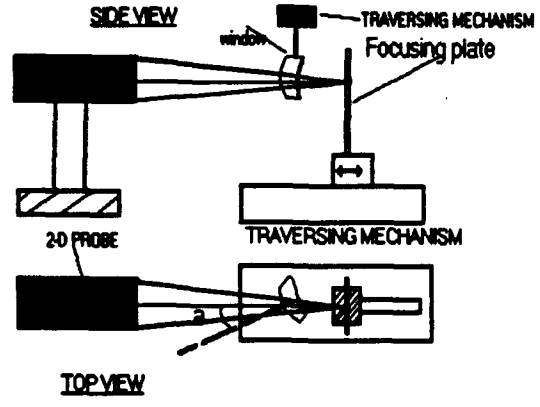

Figure 5: Layout of the experimental arrangement for the verification of the calculated displacement

In order to locate the centre of the measuring control volume, the backscattered signal has been recorded, time-averaged and stored on a digital oscilloscope. The point of focus has been defined as the point where the maximum amplitude has been measured on the oscilloscope.

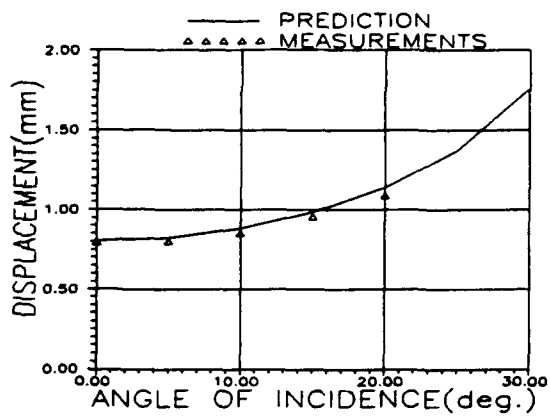

Figure 6: Comparison between calculated and measured displacement(f_1=120mm,t=5mm,R_o=324mm)

The angle of incidence of the laser beams to the curved window has been varied by rotating the window. Displacements have been recorded for various angles of incidence and are shown in Figure 6 in comparison to the calculated results with very good agreement.

4. APPLICATION OF THE DEVELOPED PROCEDURE IN A TURBOMACHINERY ANNULUS

The developed method has been applied to a configuration representative of an actual turbomachinery geometry (Figure 7). Calculations have been performed for an annular passage with 324 mm outer radius of curvature . Calculations are presented in Cartesian coordinates as a percentage of annulus height from the casing and towards the centreline where the hub is placed. The focal lengths of the 1-D and 2-D probes have been considered equal to 120 mm each and the angle between the two probes is 30 deg. The axial and circumferential velocity components are measured by the 2-D probe (U-beams and V-beams, respectively) and the third, non-orthogonal, velocity component is measured by the 1-D probe (W-beams) at the original positioning of the probe carriage(position 0:ϕ=0, κ=0)

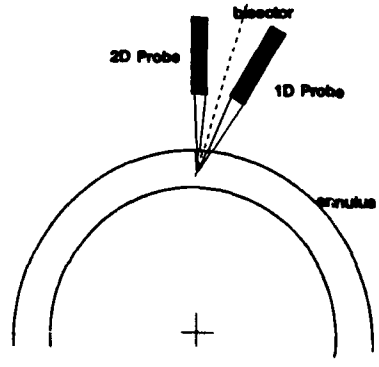

Figure 7: Layout of the configuration used for the calculations

Figures 8 and 9 present the effects of varying air temperature and pressure inside the configuration. The beams are considered to intersect at a fixed position inside the configuration(with the

absence of the window) and the total displacement is calculated. In both cases the effects on the calculated displacements are very small.

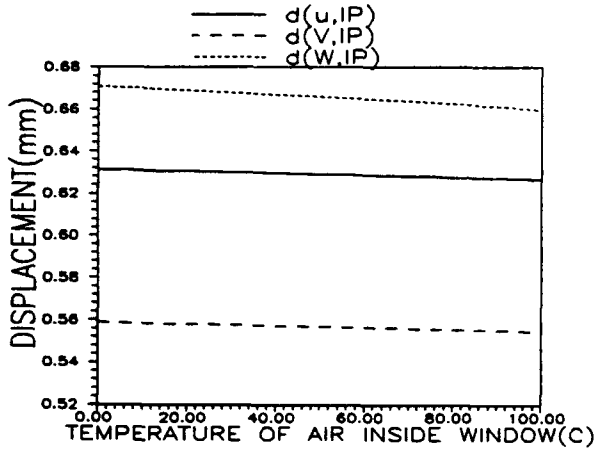

Figure 8: Effect of air temperature variations on the calculated beam displacement.
(X_p=40mm,Y_p=400mm,Z_p=0,ϕ=15deg.,κ=0,t=2mm)

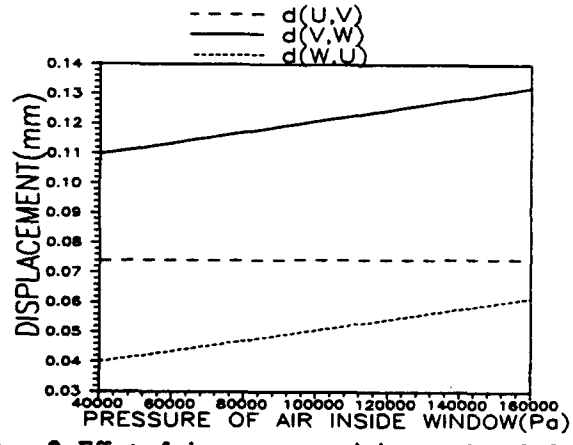

Figure 9: Effect of air - pressure variations on the calculated beam displacement
(X_p=40mm,Y_p=400mm,Z_p=0,ϕ=15deg.,κ=0,t=2mm)

Figure 10 presents the calculated displacement in space between every two beam-pairs, together with the displacement from the initial point of intersection for each beam-pair, as a function of the distance of the measuring volume from the hub of the annulus for the case where the bisector of the probes lies on Y-axis and the angle ϕ equals to -15 deg. Additional information is presented in Figure 11 showing the displacement for each of the three pairs of beams from their initial point of intersection, in Cartesian coordinates.

Similarly, Figures 12 and 13 present the same information for the case where the axis of symmetry of the 2-D probe lies on the Y-axis and ϕ = 0 deg. In both cases, beam non-coincidence in space becomes more significant as the two probes are traversed from the casing towards the hub, although relative diplacements for each beam-pair from the initial point of intersection are more important towards the casing.

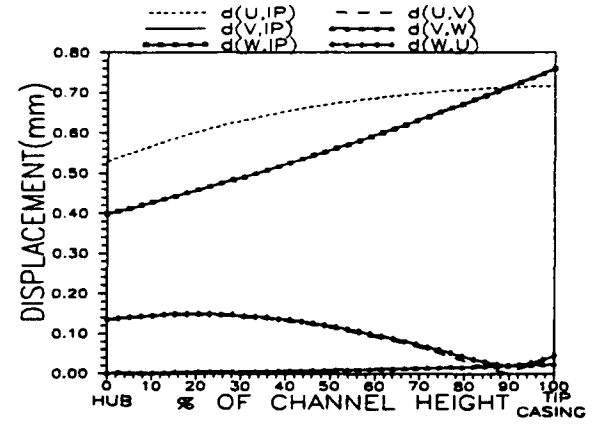

Figure 10: Calculated displacement in space between the three beam-pair points of intersection- Bisector of probes lies on Y-axis.(X_p=-31.058mm,Z_p=0,ϕ=-15deg.,κ=0,t=2mm)

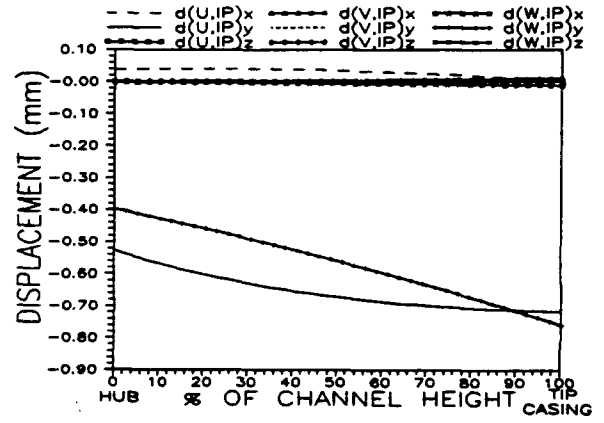

Figure 11: Calculated displacement of each beam-pair from its initial point of intersection -Bisector of probes lies on Y-axis.
(X_p=-31.058mm,Z_p=0,ϕ=-15deg.,κ=0,t=2mm)

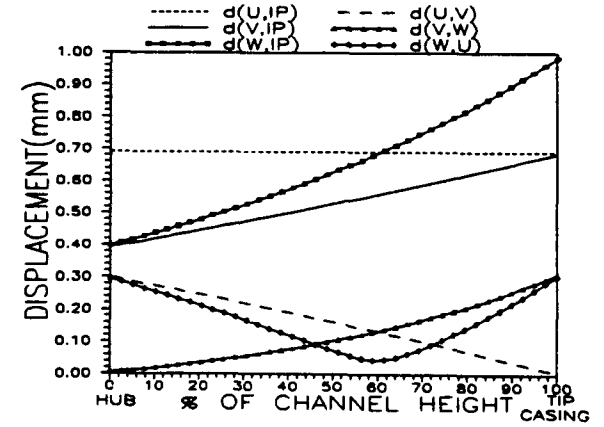

Figure 12: Calculated diplacement between points of intersection - Axis of symmetry of 2-D probe lies on Y-axis.
(X_p=0,Z_p=0,ϕ=0,κ=0,t=2mm)

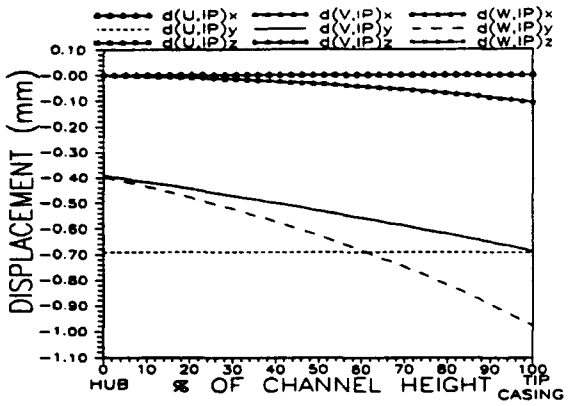

Figure 13: Calculated displacement in Cartesian coordinates - Axis of symmetry of 2-D probe lies on Y-axis. ($X_p=0, Z_p=0, \phi=0, \kappa=0, t=2mm$)

In Figures 14 and 15 the effect of increasing the curvature of the window on the calculated displacement is presented. In this case, the focal lengths of the two probes are equal to 200 mm. The Figures demonstrate that significant displacement occurs for the beams measuring the W - velocity component (1-D probe). As anticipated, higher values of displacement are calculated for the small radii of curvature.

Figure 16 shows the calculated angle between the initial and final bisector of the beam-pairs for the case of $\phi=15$ deg, which proves to be insignificant for the examined case, whereas Figure 17 shows the corresponding displacement.

Finally Figures 18 and 19 show the effect of the thickness of the window on the calculated angle between the initial and final bisector, as well as the corresponding displacement of the beams. Calculations of this kind are very useful during the design of an experiment. For example using figures 18 and 19 allows determination of the maximum acceptable window thickness for keeping displacements in predefined limits.

In all the above figures d is the distance between points of intersection and IP is the initial point of intersection.

A general remark that can be extracted from the current study is that, even when two beams cross between them, the three sets of beams do not coincide in the same point in space, and the displacement is quite significant (it can reach a value of 1mm for the presented cases). When the two beams of a pair are found not coincidental in space, this does not necessarily mean that they do not coincide in reality, because the beams are not mathematical lines but have a Gaussian shape. Thus the vertical distance between the beams should be compared, for instance, with the beam's diameter. In the current calculations, for a certain configuration a distance of 20 μm was found for the W-beams, that have a beam diameter of 44μm. This means that the beams are partly coincident, but the shape of the probe's volume is deformed.

CONLUSIONS

-A mathematical procedure for solving the general beam transmittance equations, in order to calculate beam displacement due to refraction, has been presented for a three component laser Doppler anemometer.

-The procedure has been validated with experimental data and other similar calculations.

-The procedure has been applied to a layout for measurements in an annular passage, where coincidence in space of the displaced beams has been examined.

-The code can serve as a tool in order to determine a priori coincidence in space of the three measuring volumes with three component laser Doppler anemometers. It can also serve for minimizing the refraction effects by optimizing the optical (e.g. focal length) and flow (e.g. thickness of wall) geometrical characteristics. Furthermore, by calculating the new velocity component inclination due to refraction effects , it is quite easy to correct the velocity components measured. In the cases presented this correction was not deemed necessary, because of the small angles calculated between the initial and final bisectors, but in several cases that were also examined for the verification of the applicability of the code in all possible geometries(e.g. very small radius of curvature), the angles calculated are quite significant(even more than 3-4 deg.) and, therefore, the corrections are necessary.

-Finally it should be quoted that the presented code can serve as a general tool for the calculation of refraction effects, since it can be applied to every possible geometry of window, if the equation of the surface of the window is known.

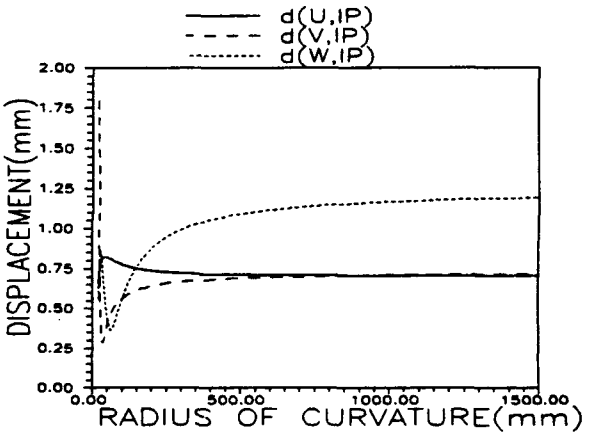

Figure 14: Effect of the radius of curvature on the calculated beam displacement ($t=2mm, \phi=10deg., \kappa=0$, distance between 2-D probe and window is constant)

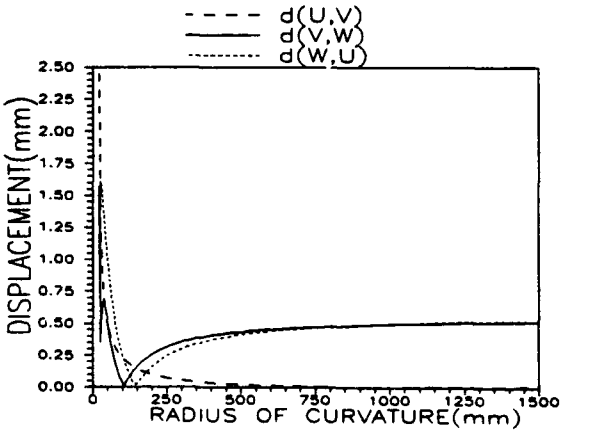

Figure 15: Effect of the radius of curvature on the calculated beam displacement ($t=2mm, \phi=10deg., \kappa=0$, distance between 2-D probe and surface of window is constant)

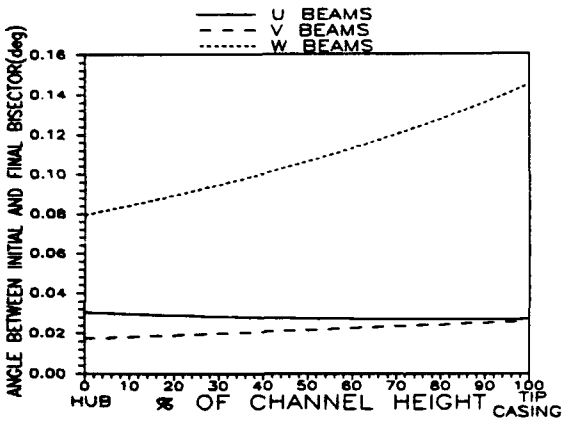

Figure 16: Calculated angle between initial and final bisector of the beams(X_p=50mm,Z_p=0,ϕ=15deg.,κ=0,t=2mm)

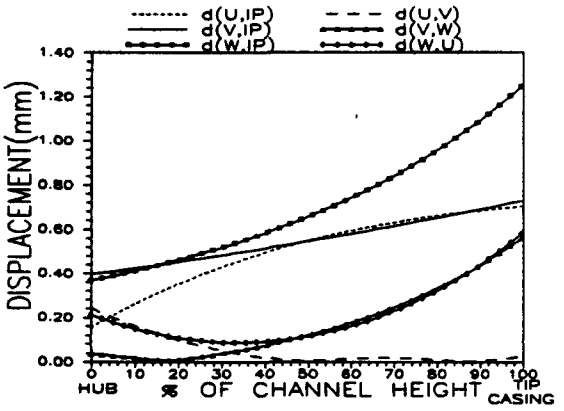

Figure 17: Calculated displacement between points of intersection
(X_p=50mm,Z_p=0,ϕ=15deg.,κ=0,t=2mm)

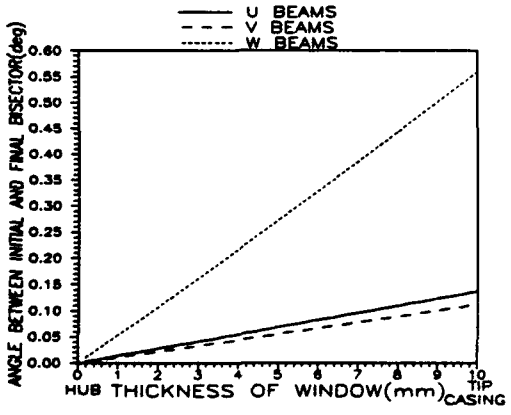

Figure 18: Effect of window thickness to the calculated angle between the initial and final bisector of the beams
(X_p=50mm,Y_p=400mm,ϕ=15deg.,κ=0)

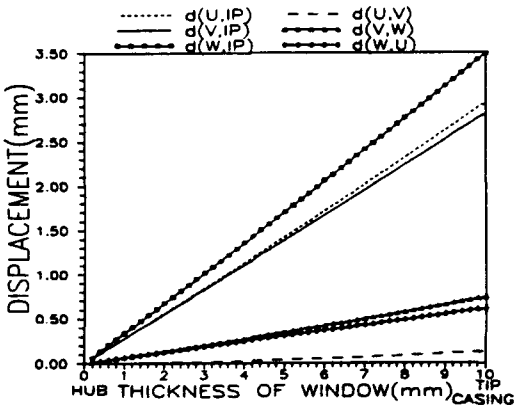

Figure 19: Effect of window thickness to the calculated displacement.(X_p=50mm,Y_p=400mm,ϕ=15deg.,κ=0)

REFERENCES

Allonso, M. - Finn, J.F. 1967, Fundamental Univesity Physics Volume 2, Fields and Waves, Addison-Wesley Publishing Company, pp.185

Bicen, A.F. & Whitelaw, J.H. 1981, Refraction Correction for LDA Measurements in Flows with Curved Optical Boundaries, Imperial College of Science and Technology, Dept. of Mechanical Engineering, Fluids Section, Report No. FS/81/17.

Boadway, J.D. & Karahan, E. 1979, Laser Doppler Anemometer Readings for Refraction at Cylindrical Interfaces, Letter to the editor, DISA Information, No. 26, pp. 4-6.

Durrett, R.P., Gould R.D., Stevenson W.H. & Thompson H. D. 1985, A Correction Lens for Laser Doppler Velocimeter Measurements in a Cylindrical Tube, AIAA Journal, vol. 23, No. 9.

Durst, F., Melling, A. & Whitelaw, J.H., 1976, Principles and Practice of Laser Doppler Anemometry, Academic Press, London.

Durst, F. Jovanovic, J. and Sender, J. 1993, Detailed Measurements of the Near Wall Region of Turbulent Pipe Flow, ASME FED, Vol. 146, Data for Validation of CFD codes, Edts. D. Goldstein, D. Hughe, R. Johnson, and D. Lankfort, Book No. H00786, pp.79 -87.

Gardavsky, J., Hrbek, J., Chara, Z. & Severa, M. 1989, Refraction Corrections for LDA measurements in Circular Tubes within Rectangular Optical Boxes, DANTEC Information, No. 8, pp. 2-5.

Parry, A.J., Lalor, M.J., Tridimas Y.D. and Woolley N.H. 1990, Refraction Corrections for Laser-Doppler Anemometry in a Pipe Bend, DANTEC Information, No. 9, pp. 4-6.

Strazisar, A.J. 1986, Laser Fringe Anemometry for Aero Engine Components, NASA Technical Memorandum 88798.

ACKNOWLEDGEMENTS

The work has been performed within the frame of the AERO-CT2-0039, PN2031 contract and the financial assistance of the C.E.U. is gratefully acknowledged.

Session 18.
Two Phase Flow Instrumentation I

EXPERIMENTAL INVESTIGATIONS ON THE EFFECT OF TRAJECTORY DEPENDENT SCATTERING ON PHASE DOPPLER PARTICLE SIZING WITH A STANDARD INSTRUMENT

M. Willmann, R. Kneer, L. Eigenmann, S. Wittig
Institut für Thermische Strömungsmaschinen, Universität Karlsruhe, Germany

E.D. Hirleman
Arizona State University, USA

ABSTRACT

The phase-Doppler particle sizing method is well established for the characterization of two phase flows. Originally the principle was developed based on the assumption of a uniform intensity profile of the laser beams forming the probe volume. However, recent studies pointed out the necessity to take into account the effects of nonuniform droplet illumination due to the Gaussian intensity profile of the laser beams. As a result, recent papers [Naqwi et al. (1990), Haugen et al. (1993)] have considered a range of different design parameters for the optical layout of a phase Doppler instrument.

In this study, layout criteria considering both uniform and nonuniform droplet illumination were applied to the standard AEROMETRICS counter-based equipment. Based on this analysis, experimental investigations with monodisperse droplets of known size will show, how reliable these basic methods are and which errors actually have to be expected from nonuniform droplet illumination.

NOMENCLATURE

d	m	droplet diameter
d_{min}	m	minimum droplet diameter with detectable scattered light from non-dominant modes
d_{max}	m	droplet diam. with same intensity in scattered light of dominant and non-dominant modes
d_Φ	m	droplet diam. with minimum in signal visibility
d_{sat}	m	largest diameter of measured distribution
d_v	m	diameter of probe volume
g	-	intensity ratio between scattering modes
n	-	real part of refractive index
Nr	-	number of lens/track combination
p	-	scattering mode
R	-	intensity range of detectors
v_s	m/s	offset velocity
Δy	m	distance between incident rays of different scattering modes
$\Delta\Phi$	°	angular extend of detectors
Φ	°	off-axis angle
$\psi_{1,2,3}$	°	elevation angle of detectors 1,2 and 3

1. INTRODUCTION

Phase Doppler particle sizers make use of the light pattern generated by a droplet illuminated by two crossed, focused laser beams. For this, a receiving unit with two or more detectors is used to determine the spacing of the scattered fringe pattern at a distinct position in the farfield of the droplets. With the known correlation between the fringe spacing and the droplet diameter, reliable particle sizing is possible.

From Naqwi et al. (1990) it is known that the performance of the phase Doppler instrument strongly depends on the optical layout. In the first part of the following analysis basic layout criteria applicable for uniform illumination of the droplets will be applied to the AEROMETRICS counter based standard instrument. Based on this analysis, in the second part of the paper extended criteria considering nonuniform illumination will be applied.

Finally, measurements with monodisperse droplets will illustrate the reliability of these methods and indicate which effects and errors actually can be expected from the Gaussian beam intensity profile.

2. BASIC PHASE DOPPLER LAYOUT

In the following the basic layout criteria of a phase Doppler configuration considering uniform droplet illumination will be discussed, specifically with respect to the AEROMETRICS instrument. This analysis is performed in order to understand the limitations of this specific instrument as a base for the further investigations considering nonuniform illumination of droplets.

2.1. Off-axis angle between transmitter and receiver

The off-axis angle between transmitter and receiver optics is the most relevant parameter of a phase Doppler configuration. It must be selected considering the optical properties of the participating fluids and the optical access to the flow regime under investigation. Fig. 1 illustrates the relative intensity distribution of scattered light around a water droplet (n=1.33) in air. Following van de Hulst (1981) it is calculated based on geometrical optics. From this approach, it is possible to distinguish between the different scattering modes p=0, 1, 2

and higher orders. Since the mode p=2 has two parts in the backscatter region, in Fig. 1 it is divided into the two submodes p=2a and p=2b.

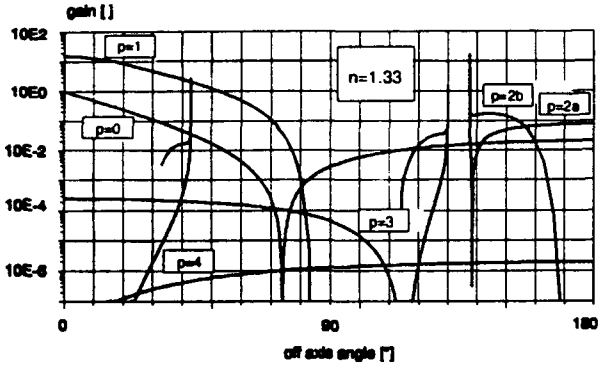

Fig. 1 Gain diagram for water droplets in air (n=1.33)

The light scattered from the two laser beams interferes in the farfield of the droplet and produces a fringe pattern on the detector plane. This scattered light consists of parts from different scattering modes produced by each of the two laser beams. A fixed, linear relation between the detected spacing of the fringe pattern and the droplet diameter only exists when the interference pattern is dominated by the light of one single scattering mode from both laser beams. Scattered light from other modes disturbs this linear correlation. Like most standard configurations, the receiver of the AEROMETRICS instrument detects the fringe pattern in an angular range of approx. $\Delta\Phi=10°$. From the above discussion, the following criteria have to be satisfied over this angular range:

- one dominant mode or submode
- high ratio of intensity to non-dominant modes

Forward scattering setups with $\Phi=30°$ or $\Phi=74°$ are therefore favorite configurations for sizing water sprays. The $\Phi=150°$ backscatter configuration has a great advantage when applied to complex, real machines, since limited optical access often precludes forward scattering configurations. [Kneer et al. (1993)]. Fig. 1 indicates that in backscatter the ratio of intensity from the dominant mode to the following modes is much lower than in forward scattering configurations. Therefore the light from non-dominant modes will disturb the fringe pattern of the dominant mode p=2b. However, all three configurations are considered in the following.

2.2. Polarization of the laser beams

The polarization of the laser beams strongly influences the scattering behavior of the droplets. The gain curves of Fig. 1 are valid only for light polarized parallel to the plane of the laser beams. This direction of polarization is used in the standard AEROMETRICS instrument, since it offers the most flexible configuration.

Nr	Coll.-Lens	Foc.-.Lens	Track	Intersect. Angle [°]	Fringe spacing [µm]	max . vel. [m/s]	max. Offset [m/s]	dΦ [µm] Φ=30° (p=1)	dΦ [µm] Φ=74° (p=1)	dΦ [µm] Φ=150° (p=2b)
1	160	200	1	1.49	19.8	200	31	720	1059	581
2			2	3.01	9.8	200	33	346	500	290
3			3	5.95	4.95	100	35	173	257	146
4		495	1	0.60	49.1	200	77	1800	2571	1385
5			2	1.23	23.9	200	80	857	1285	720
6			3	2.38	12.37	200	88	439	643	367
7		1016	1	0.30	98.2	200	154	3600	4500	3000
8			2	0.60	49.0	200	164	1800	2570	1500
9			3	1.19	24.7	200	166	900	1286	720
10	300	200	1	2.81	10.5	200	16	375	545	310
11			2	5.50	5.4	100	18	188	277	158
12			3	11.17	2.6	50	19	93	135	78
13		495	1	1.12	26.3	200	41	900	1385	783
14			2	2.20	13.4	200	45	473	692	391
15			3	4.48	6.6	100	47	234	333	194
16		1016	1	0.56	52.6	200	82	2000	2571	1636
17			2	1.10	26.8	100	89	947	1385	783
18			3	2.24	13.1	100	94	462	692	391

Table 1 Basic layout parameters of the AEROMETRICS standard instrument.

2.3. Beam Intersection angle

The intersection angle between the two laser beams forming the probe volume primarily controls the range for velocity measurements since it fixes the fringe spacing in the probe volume.

The AEROMETRICS transmitter uses a rotating grating as beamsplitter unit. Here, tracks with different numbers of grating line pairs can produce three different angles between the laser beams. These beams are made parallel by a collimating lens and then are focused in the probe volume by the focusing lens. With the standard lenses delivered with the

instrument and the three tracks on the rotating grating 18 different configurations are possible as listed in Table 1. The rotating grating is also used as frequency shift unit. The frequency shift between the two laser beams produces an offset velocity and is necessary to perform direction sensitive measurements. In Table 1 the resulting maximum velocities and maximum offset velocities are listed for the different configurations. Low values for the offset velocities often limit the applicability of the instrument to complex, highly-turbulent two phase flows.

2.4. Elevation angle and shape of detectors

Standard phase Doppler instruments make use of three detectors to analyze the scattered fringe pattern. These detectors are positioned at different elevation angles perpendicular to the scattered fringes in order to measure their spatial distance. The manufacturer of the AEROMETRICS Phase Doppler instrument fixed the elevation angles to approx. $\psi_{1,3} = \pm 3.8°$ for the outer pair of detectors and $\psi_2 = 1.1°$ for a single inner one, with slight differences between different instruments. The detailed shape of the detectors is described in Sankar (1991). Together with the selected fringe spacing, the position and shape of the detectors limit the resolution in diameter measurement of the instrument. Following Naqwi and Durst (1990), the local phase on the extension of one detector should not exceed 360° to avoid phase jumps in the calibration curve due to bad visibility of the integrated signals over the detector plane. Considering the dominant scattering mode of each off-axis configuration, (i.e. p=1 at Φ=30° and Φ=70° and p=2b at Φ=150°) the maximum diameters d_Φ have been determined from scattering calculations based on geometrical optics. These values are listed in Table 1 for the different off-axis configurations.
It is essential that the largest diameter in the measured size distribution does not exceed d_Φ. Nevertheless the range should be used as wide as possible to reach a high resolution in droplet sizing. The software of the AEROMETRICS instrument enables the operator to size up to approx. 2/3 of d_Φ.

3. EXTENDED PHASE DOPPLER LAYOUT

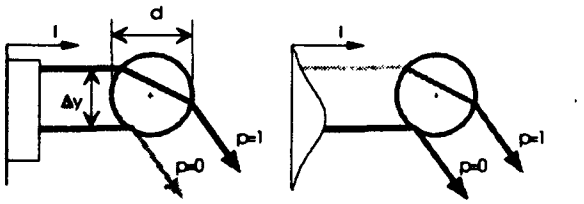

Fig. 2 droplet illumination a.) uniform b.) non-uniform

The analysis performed yet is based on the ideal assumption of uniform droplet illumination. The limits obtained from this analysis are valid in the following, but are supplemented by some more restrictive criteria concerning droplet sizing in a probe volume produced by laser beams with a nonuniform intensity profile.

Fig 2a shows a droplet which is illuminated with an ideal uniform intensity profile. The gain curves in Fig. 1 are calculated from this assumption for the incident light. Corresponding to Fig. 2b, real laser beams have a typically Gaussian intensity profile and therefore especially large droplets are illuminated non-uniformly. On critical trajectories through the probe volume, depending on the ratio between droplet diameter and probe volume diameter, the ratio of intensity between the different scattering modes may differ from that calculated from the ideal assumption of uniform illuminated droplets. Therefore the interference pattern will also differ from the expected ideal one and errors in the determination of droplet diameters occur. In the following, several parameters will be presented that characterize the effects of non-uniform droplet illumination. Since most of these parameters have a more estimative character, measurements will show how reliable these estimations are and how these effects actually influence measurements.

3.1. Beam diameter

It is obvious from Fig. 2 that the ratio between droplet diameter and Gaussian beam diameter of the probe volume is the most important parameter governing effects due to nonuniform illumination. In general, this ratio should be as high as possible. The increase of d_v on the other hand is limited especially in dense sprays, since the Phase Doppler instrument can only interpret the scattered light of one single particle. The maximum diameter of the probe volume therefore has to be found experimentally for each application. However, the parameters discussed in the following characterize the sensitivity of a chosen configuration to nonuniform droplet illumination. For the AEROMETRICS instrument, the beam diameter at the probe volume is mainly determined by the diameter of the laser beam entering the transmitter optic and the selected combination of lenses. With a typical laser beam diameter of approx 0.8 mm the resulting waist diameters d_v are listed in Table 3 for the different lens combinations. The following analysis will quantify the expected effects due to non-uniform droplet illumination for various beam diameters.

3.2. Intensity ratios of dominant and non-dominant modes

The critical maximum diameters d_{max} in Table 3 are based on the assumption that the dominant scattering mode is only disturbed by a less dominant mode when the intensity of the scattered light of both modes is in the same order of magnitude. Depending on the probe volume diameter d_v therefore a maximum particle diameter d_{max} can be calculated for which the two rays of Fig. 2b leave the droplet at the same level of intensity when the droplets pass the probe volume on a critical trajectory:

$$d_{max} = \sqrt{\frac{d_v^2}{8\left(\frac{\Delta y}{d}\right)^2}\ln(g)}$$

Following Fig. 2b $\Delta y/d$ is the distance Δy of tw7o incident rays of different scatter modes normalized by the droplet diameter. The ratio g of intensities between these two rays is calculated assuming uniform droplet illumination. It is obvious from Fig. 1 that especially at Φ=74° the value for the ratio g depends on the angular extension of the detectors. For the AEROMETRICS instrument with an extension of about $\Delta\Phi$=10°, the values for g and $\Delta y/d$ are listed in Table 2 for the dominant modes of the three off-axis configurations.

	Φ=30° (1/0)	Φ=74° (1/0)	Φ=150° (2b/0)	Φ=150° (2b/2a)
g	52	217	7	3
$\Delta y/d$	0.85	0.9	0.65	0.25
d_{max}/d_v	0.83	0.91	0.76	1.48
d_{min}/d_{sat}	0.21	0.42	0.08	0.05

Table 2: Ratio of intensity and normalized distance of incidence and resulting critical droplet diameters.

It can be seen, that the 74°-configuration has a slight advantage compared to the 30°-configuration. In backscatter configuration, all three dominant modes have to be considered, since here not the mode p=2a, but the mode p=0 limits the upper diameter of this configuration.

3.3. Dynamic range of detectors

Photomultipliers used as detectors have typically a dynamic range in intensity of R=1200. The upper limit of this range is fixed by scattered light from the dominant mode of the largest particles (d_{sat}) of a measured distribution. Errors due to nonuniform illumination certainly occur, when droplets larger than d_{max} pass the probe volume on critical trajectories, and when the intensity of scattered light from these trajectories is high enough to be detected. With the assumption, that the intensity of scattered light increases with d^2 of the droplets, the ratio d_{min}/d_{sat} can be calculated, which characterizes the range where errors may occur, when the critical diameter d_{max} is exceeded.

$$\frac{d_{min}}{d_{sat}} = \sqrt{\frac{g}{R}}$$

It is obvious, that this ratio should be as close as possible to unity. This could be reached with a lower dynamic range in detection, which on the other hand would result in a loss of information from small droplets in the spray and therefore is impractical. Especially for the backscatter range it can be seen from Table 2 that this ratio is very low. From this, non-dominant modes will disturb the fringe pattern of the dominant mode in a wide diameter range. From this point of view, the 74°-configuration is the most suitable configuration due to the high ratio of intensities between dominant and non-dominant modes.

3.5. Rejection algorithms

From the above discussion it is obvious, that wrong signals may be received due to non-uniform illumination of the droplets when dense sprays with a wide diameter distribution are under investigation. The performance of a phase Doppler instrument can be improved by the detection and rejection of signals from particles on critical trajectories. Here several suggestions from Bachalo et al. (1993), Aizu et al. (1993) or Grehan et al. (1993) exists, where most of them are not practical with a standard instrument. The equipment under investigation makes use of two algorithms to reject errors due to non-uniform illumination.

Nr	d_v [µm]	dmax [µm] 30° (1/0)	dmax [µm] 74° (1/0)	dmax [µm] 150° (2b/0)	failing phase comp. Φ=30° (1/0)		failing phase comp. Φ=74° (1/0)		failing phase comp. Φ=150° (2b/0)	
1	133	110	121	101	0-211	(542-284)	0-492	(828-426)	0-304	(456-377)
2	133	110	121	101	0-105	(271-141)	0-236	(392-203)	0-152	(228-186)
3	133	110	121	101	0-53	(135-70)	0-116	(201-104)	0-77	(115-94)
4	330	273	301	250	0-530	(1411-726)	0-1134	(2005-1030)	0-727	(1090-924)
5	330	273	301	250	0-263	(672-346)	0-574	(1012-520)	0-378	(566-460)
6	330	273	301	250	0-132	(343-177)	0-299	(503-259)	0-192	(288-237)
7	677	560	617	514	0-976	(2864-1471)	0-2323	(3581-1839)	0-1555	(2332-1826)
8	677	560	617	514	0-530	(1411-726)	0-1134	(2005-1030)	0-786	(1180-986)
9	677	560	617	514	0-275	(705-363)	0-625	(1012-520)	0-378	(566-460)
10	71	59	65	54	0-112	(293-152)	0-254	(428-220)	0-162	(243-199)
11	71	59	65	54	0-57	(146-76)	0-127	(217-112)	0-83	(124-101)
12	71	59	65	54	0-28	(71-38)	0-62	(105-55)	0-41	(61-50)
13	176	146	160	134	0-287	(705-363)	0-625	(1089-560)	0-410	(615-507)
14	176	146	160	134	0-143	(370-191)	0-327	(541-279)	0-205	(307-254)
15	176	146	160	134	0-70	(182-95)	0-156	(261-135)	0-101	(152-125)
16	361	299	329	274	0-574	(1566-805)	0-1134	(2005-1030)	0-857	(1285-1055)
17	361	299	329	274	0-287	(742-381)	0-687	(1089-560)	0-410	(615-507)
18	361	299	329	274	0-143	(361-186)	0-312	(541-279)	0-205	(307-250)

Table 3 Diameter of probe volume and characteristic diameters concerning non-uniform droplet illumination

In the first rejection algorithm a phase comparison between the two pairs of detectors is used to distinguish between the fringe pattern of different scattering modes. The diameter values determined from the signals of the two pairs of detectors must agree to within some specified tolerance. This tolerance is necessary to allow a slight ellipticity of the measured droplets. From Haugen et al. (1993) it is known that the phase comparison may fail for large tolerances in droplet-ellipticity check. For the AEROMETRICS instrument, the result of the analysis of this rejection algorithm is presented in Table 3 for the suggested 15% level in droplet-ellipticity check from the manufacturer. The values in brackets show the limits of the linear redistribution due to the erroneous interpretation of scattered light from non-dominant modes. In the 30° off-axis configuration of combination Nr. 1 for example, a very small droplet is interpreted as a 565 µm one and an actually 214 µm droplet as a 292 µm one, when they pass the probe volume on critical trajectories. It can be seen from the analysis, that this rejection algorithm fails up to almost the first half of the measuring range. For the backscatter configuration only the interaction between the p=2b and the p=0 mode is analyzed, since due to similar slopes of the modes p=2a and the p=2b phase-comparison fails here for the whole diameter range.

The second rejection algorithm, intensity validation, checks, if signal intensity and measured diameter correspond to each other. Usually many droplets pass the probe volume on non-critical trajectories away from the center, and therefore scatter light with the correct phase information but a low intensity. Since these particles should be validated, the intensity validation algorithm is suitable only to reject particles which are erroneously sized too small. From the values in brackets in table 3 it can be seen, that particles not rejected by phase comparison are usually sized too large, and therefore even with intensity validation no complete rejection will be accomplished.

4. EXPERIMENTAL INVESTIGATIONS

The above analysis clearly demonstrates the limits of the different optical configurations of the AEROMETRICS instrument. Since most of these parameters have a more estimative character, in the following, results will be presented from measurements, in order to analyze actually occurring errors. These measurements are performed with monodisperse droplets, where laser intensity and instrument setup are chosen in order to simulate measurements on a polydisperse spray. Three different droplet sizes of approx. 50 µm, 100 µm and 200 µm in diameter have been investigated, representing a polydisperse diameter distribution.

From the previously discussed layout criteria a focal length of 495 mm for the focusing lens offers a wide velocity measurement range and sufficient accuracy in droplet sizing with respect to the range of diameters studied here. With the selection of the 300mm collimating lens the probe volume diameter is limited to 176µm. This selection is chosen with respect to the discussed difficulties when sizing dense sprays. The instrument was used on track 2 of the rotating grating (Configuration Nr. 14). In every case detector sensitivity and laser intensity were selected such that saturation of the detectors just occurs for the 200µm particles passing through the center of the probe volume.

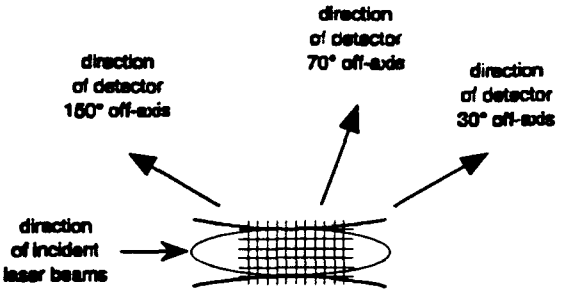

Fig 3 Experimental setup

Fig 3 shows a schematic of the experimental setup. The arrow on the left illustrates the direction of the incident laser beams which form the elliptic probe volume. A schematic grid is added to indicate the positions of investigated droplet trajectories. The arrows in the top of the probe volume show where the receiver optic is positioned for the three different configurations. The droplets were produced with a piezoelectric driven monodroplet generator, described by Anders et al. (1986), which is fixed on a microtraverse. A distance of approx. 50mm between droplet generator and probe volume ensured that the droplets were spherical when entering the probe volume.

4.1. 30°-off-axis configuration

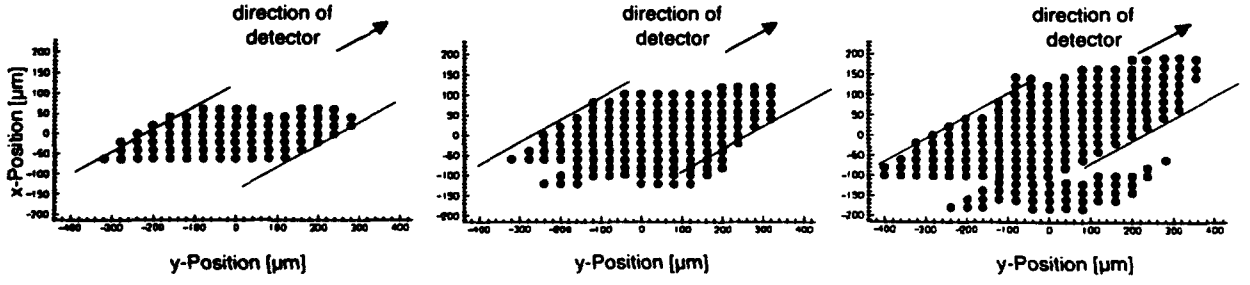

Fig. 4 Positions of validated trajectories (30° off-axis) a.) d=60µm b.) d=110µm c.) d=200µm

The data points in Fig. 4 illustrate for the 30° off-axis configuration trajectory positions for which droplets have been accepted by the instrument, regardless of acquisition rate, validation rate and measured diameter. The area from where signals can be obtained is limited due to several effects. The incident laser beams are parallel with the y-axis and for that reason the decreasing intensity of the beam profile limits the detection of signals in the x-direction. A limitation of the probe volume along the laser beams is obtained by a slit in the receiving optics. The projection of this slit is added schematically in Fig. 4. For the small droplets in Fig 4a. the probe volume is limited only due to these basic effects. The larger droplets show a different behavior which arises due to non-uniform droplet illumination. Here an additional area in the lower right edge can be observed where data are accepted by the instrument.

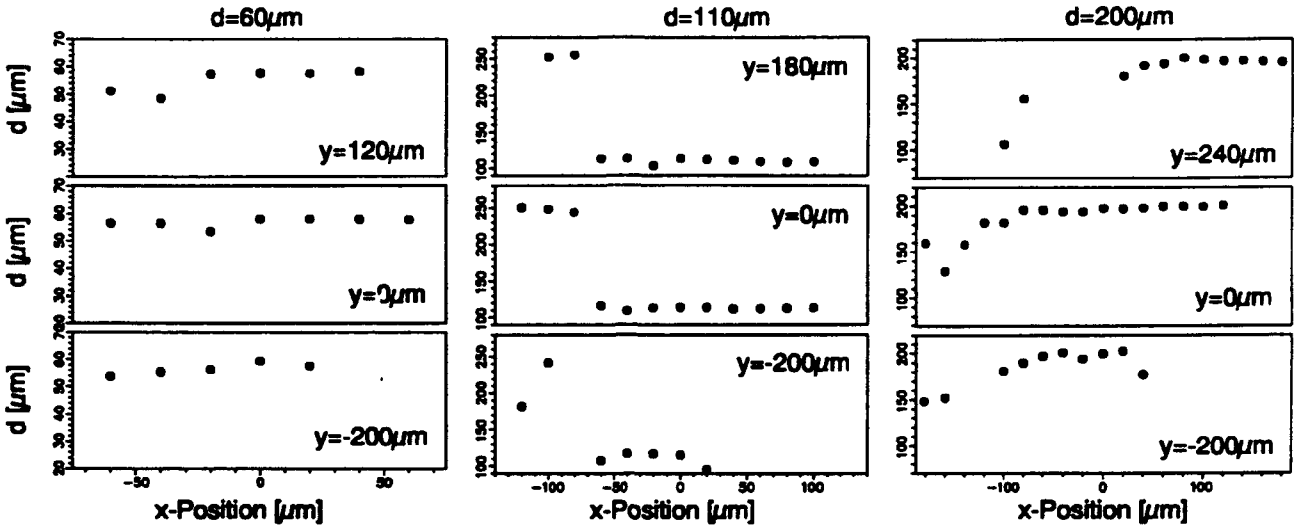

Fig. 5 Measured diameters for different droplets at different positions in probe volume (30° off axis)

In Fig. 5 the measured diameter values at different positions in the probe volume illustrate effects due to the Gaussian intensity distribution, As expected from the layout criteria no significant errors occur for the 60µm particles. These droplets are much smaller than d_{max} and therefore are sized correctly. Validation rates are reduced only slightly in the regions near the projections of the slit.

The most significant errors occur for the 110µm droplets, despite the fact that this diameter is lower than d_{max}. The erroneous diameter of 245 µm corresponds to the scattering mode p=0. Since the phase comparison fails for this size class, the validation rate is not reduced for these trajectories.

For the 200µm droplets, sizing errors are observed as well, but the validation rate is strongly reduced by the phase comparison algorithm. Therefore from the diameter range where phase comparison works, no statistically relevant errors are expected.

4.2. 74°-off-axis configuration

From the theoretical analysis it is clear that the 74° off-axis configuration shows many advantages in comparison to the 30° off-axis configuration.

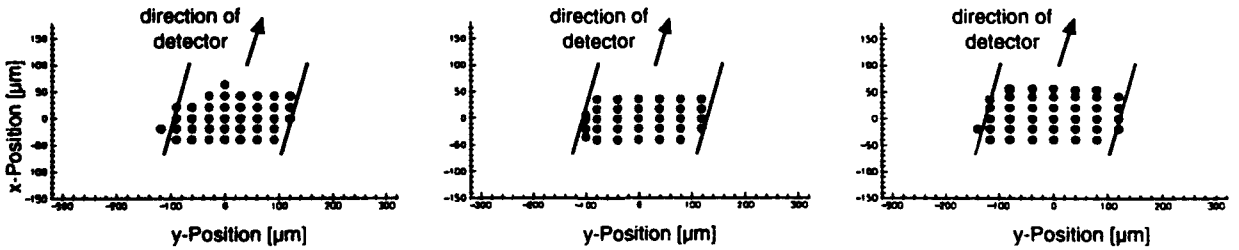

Fig. 6 Positions of validated trajectories (74° off-axis) a.) d=55µm b.) d=90µm c.) d=190µm

The diameter d_{max} is higher, which means that with the same diameter of probe volume larger droplets can be sized without Gaussian beam effects. In addition, the ratio d_{min}/d_{sat} is closer to one and therefore non-dominant modes will disturb the dominant ones only in a small diameter range when d_{max} is exceeded. In summary, this configuration should have a much better performance, even without rejection algorithms. It can be seen from the measurements that areas with uncertainties in the sizing result occur at the edges of the measuring volume. In contrast to the 30° off-axis configuration, erroneous values

do not correspond to the p=0 mode. In addition, for large droplets, the area of misinterpretation is not at the lower edge of the probe area but rather on the side nearest the receiver. It is obvious from Fig. 1 that the p=3 mode is the relevant mode, disturbing the fringe pattern of the dominant p=1 mode. Since both modes have almost the same slope factor, no rejection by phase comparison can be obtained.

With the relatively small area of misinterpretation, and since erroneous measured diameters do not differ much from actual values, this configuration seems to be suitable for spray measurements. On the other hand it is obvious that with standard instrumentation no significant improvement in accuracy can be obtained.

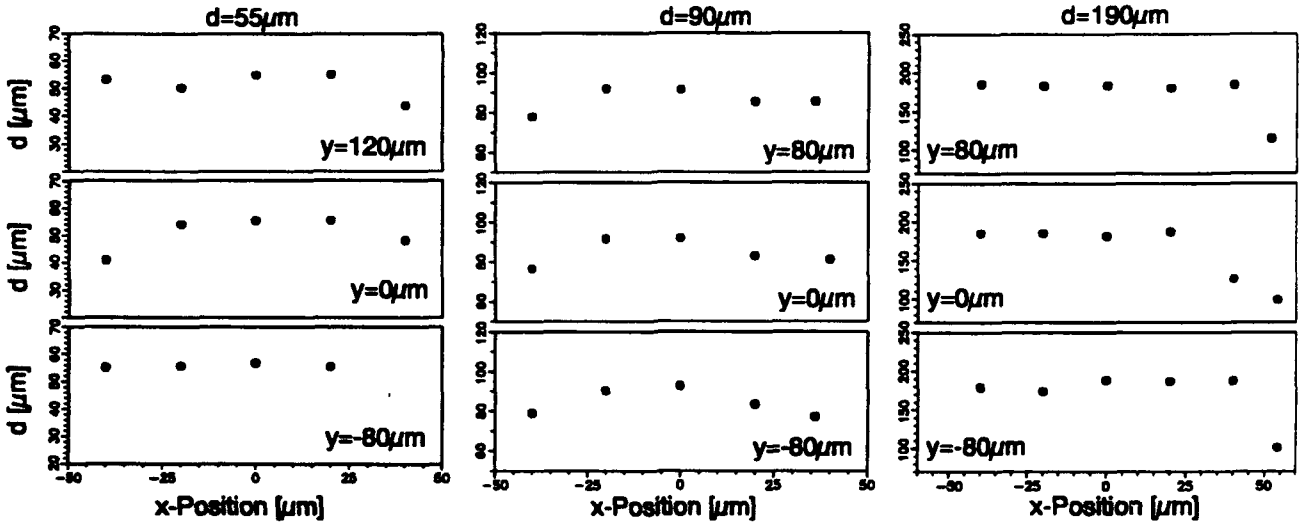

Fig. 7 Measured diameters for different droplets at different positions in probe volume (74° off axis)

4.3. 150°off-axis

As mentioned above the backscatter arrangement has its great advantages when applied to real machines with limited optical access. From the above discussed theoretical considerations, this configuration shows the worst results. dΦ and d_{max} show the lowest values and therefore the dominant mode is disturbed in a wide diameter range. Additionally, rejection algorithms for the two p=2 modes fail.

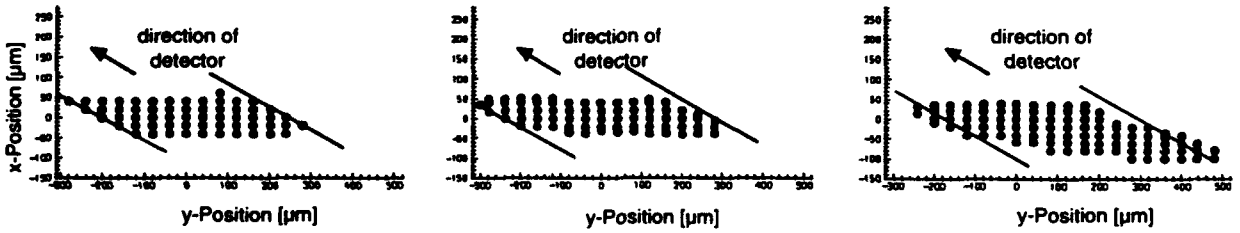

Fig. 8 Positions of validated trajectories (150° off-axis) a.) d=60µm b.) d=110µm c.) d=200µm

The area of validated trajectory positions for the backscatter configuration shows especially for the large droplets similar irregularities of the probe area as the 30° off-axis configuration.

The poor performance parameters of the backscatter configuration are manifested in sizing errors. For small droplets the measured values vary in the order of 50%, where in contrast to above discussed configurations no distinct area with misinterpretation occurs and no rejection can be observed. In addition, no distinct levels of erroneous measured diameters like the forward-scattering configurations can be observed. For large droplets rejection algorithms fail, since the two dominant modes p=2a and p=2b show similar slopes and can not be distinguished.

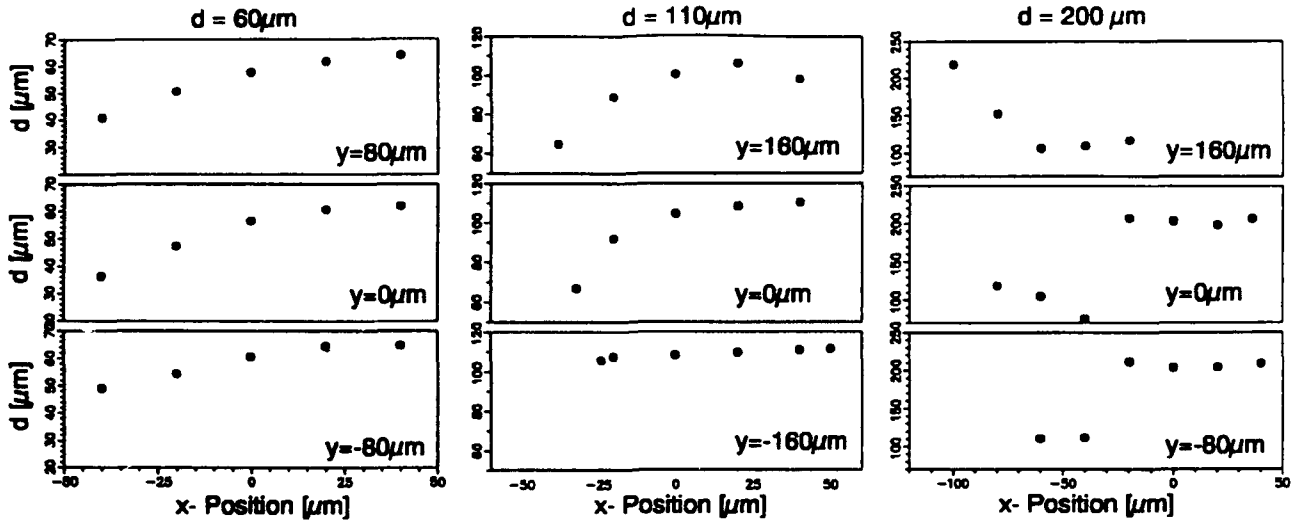

Fig. 9 Measured diameters for different droplets at different positions in probe volume (150° off axis)

CONCLUSIONS

The analysis of the AEROMETRICS standard instrument clearly demonstrates the limits of this instrument concerning errors due to non-uniform droplet illumination. Nevertheless, with the presented layout parameters it is possible to find a suitable configuration for most applications. The measurements performed here in general confirm the applicability of parameters from the layout procedure, which has a more estimative character.

Additional calculations have to be performed to analyze that range of trajectories where the dominance of different modes changes. The extent of this area strongly influences the performance of the instrument. However, with knowledge of these effects, algorithms may be developed which correct diameter distributions disturbed by Gaussian beam effects.

ACKNOWLEDGMENTS

This research was funded in part by SFB 167 "Hochbelastete Brennräume" of the "Deutsche Forschungsgemeinschaft". The participation of E.D.H. was made possible by a Fellowship from the Alexander von Humboldt Foundation. The droplet generator was made available for the measurements by a loan from K. Anders. Support from all sources is gratefully acknowledged.

BIBLIOGRAPHY

Aizu Y., Durst F., Grehan G., Onofri F., Xu T.H., 1993, PDA-System without Gaussian Beam defects, *The Third International Congress on Optical Particle Sizing*, August 23-26, Yokohama, Japan

Anders K., 1986, Monodisperse Droplet streams and their application in space, Proceedings of symposium: *'fluid dynamics and space,'* VKI, Rhode-Saint-Genese, 25 & 26 June (ESA SP-265, August 1986)

Bachalo W.D., 1993, The Phase Doppler Method: Analysis, Performance Evaluations and Applications to Atomization and Turbulent Two-Phase Flow Research, *3rd International Congress on Optical Particle sizing* , Yokohama, Japan, August 23-26

Haugen P.; von Benzon H.H., 1993, Phase Doppler measurement of the diameter of large particles -considerations for optimization, *The third International Congress on Optical Particle Sizing* August 23-26, Yokohama, Japan

Kneer R., Willmann M., Zeitler R., Wittig S., 1993, Phase Doppler particle sizing inside a production gas turbine combustor. *Non intrusive Combustion diagnostics*, Begell House, New York

Naqwi A.A., 1993, Innovative Phase Doppler Systems and their Applications, *The third International Congress on Optical Particle Sizing* August 23-26, Yokohama, Japan

Naqwi A.A.; Durst F. 1990, Light scattering Applied to LDA and PDA Measurements Part 1: Theory and Numerical Treatments, *Part. Part. Syst. Charact 8* pp. 245-258

Naqwi A.A.; Durst F. 1990, Light scattering Applied to LDA and PDA Measurements Part 2: Computational results and their Discussion, *Part. Part. Syst. Charact 9* pp. 66-80

Sankar S.V.; Bachalo W.D. 1991, Response characteristics of the phase Doppler particle analyzer for sizing particles larger than the light wavelength, *APPLIED OPTICS* ,Vol.30, No.12 ,20 April 1991

van de Hulst H.C. 1957 Light scattering by small particles. *Dover Publications, In., New York.*

Measurement of bubbles by Phase Doppler technique and trajectory ambiguity

G. Gréhan*, F. Onofri*, T. Girasole*, G. Gouesbet*
F. Durst+ and C. Tropea+

* Laboratoire d'Energétique des Systèmes et Procédés.
INSA de ROUEN, URA.CNRS.230, CORIA.
BP08, 76131, Mont-Saint-Aignan Cédex, France.
Tel: (33) 35 52 83 87, Fax: (33) 35 52 83 90

+Lehrstuhl für Strömungsmechanik
University of Erlangen-Nürnberg
Cauerstr. 4, 91058 Erlangen, Germany

1 Introduction

To measure particle velocity/particle size correlations, the phase Doppler Anemometer (PDA) represents one of the most versatile and accurate techniques available today.

Nevertheless, like any technique, the PDA is not without limitations:

- When the size of the particle under investigation is of the same order as the incident wavelength, the phase shift/diameter relationship is no longer linear because of Mie resonances. This leads to ambiguity in the size determination, see Sankar et al. (1990) and Naqwi et al. (1992).

- When the particle size is not small compared to the focused beam diameter, the phase shift/diameter relationship is also nonlinear because of the nonuniform incident intensity across the surface of the particle. The nonuniform illumination leads to a change in the ratio of refracted and reflected light received by the detectors and thus modifies the intended phase shift/diameter relationship. This effect is known as trajectory ambiguity or Gaussian beam defect, since the arising error depends on the particle positions or particles trajectory inside the measurement control volume.

The latter effect has been studied in detail by using geometrical optics (Bachalo & Sankar (1988), Sankar & Bachalo (1991)) and Generalized Lorenz-Mie Theory (GLMT) (Gréhan et al. (1991,1994)). Various solutions to remove or at least minimize the trajectory ambiguity have been proposed for classical geometries (Gréhan et al. (1992)) or using more original designs such as the Planar geometry (Aizu et al. (1993), Modified Standard geometry (Xu & Tropea (1994)) or the dual burst technique (Onofri et al. (1994)). Nevertheless, these studies have been focused on refractive particles, i.e. water droplets and PDA configurations in which refraction is the dominating scattering mechanism to be considered. In the present paper the trajectory ambiguity will be examined for reflective dominated systems, typically systems for the measurement of particles with a relative refractive index less than one, i.e. air bubbles in water.

This paper describes a study of trajectory effects in the phase Doppler technique taking into account all the properties of the optical signal (phase shift, visibility, and pedestal) and is organized as follows. Section 2 reviews the GLMT and simulation model as well as the geometry under

study. Then section 3 displays computational results for the classical geometry and discusses similarities and differences compared with the droplet case. Section 4 is devoted to modified standard geometries while section 5 is devoted to the dual burst technique. Section 6 is a conclusion.

2 GLMT, simulation model and geometry under study

2.1 GLMT

The classical Lorenz-Mie Theory (LMT), which is about one century old, describes the interaction between a plane wave and a homogeneous sphere. It has been widely used to design instruments and to analyze data in optical sizing. Unfortunately, most techniques use laser sources which produce finite cross-section light beams so that when the particle diameters are not small enough with respect to the beam width, LMT is inevitably misleading. Therefore, the research team at Rouen worked out a generalization of LMT. A description of the analytical work is given in Gouesbet et al. (1991), where earlier references may also be found.

The physics behind GLMT is very simple. It solves Maxwell's equations with the appropriate boundary conditions at the surface of the sphere and at an infinite distance from the sphere. GLMT introduces two new series of beam shape coefficients $g^m_{n,TM}$ and $g^m_{n,TE}$, which describe the incident beam. For practical computations special algorithms have been developed for the case of circular and elliptical Gaussian beams. The more powerful technique is based on the so-called localization principle (Gouesbet et al. (1990)), which has been recently rigorously demonstrated (Lock and Gouesbet (1994)). Only codes based on the localization principle are used to carry out computations in the present paper.

2.2 Simulation Model

The scattered light signal from a dual-beam system may be expressed in the following form (Naqwi & Durst (1991)):

$$P(t) = P_s[1 + \nu \cos(\Delta\omega\, t + \Phi)] \qquad (1)$$

where P_s, ν, Φ and $\Delta\omega$ are the signal pedestal, visibility, phase and heterodyne Doppler frequency, respectively. The parameters P_s, ν, and Φ are functions of the complex scattering amplitudes S_1 and S_2, which are provided by GLMT (Gréhan et al. (1994)).

2.3 PDA setup

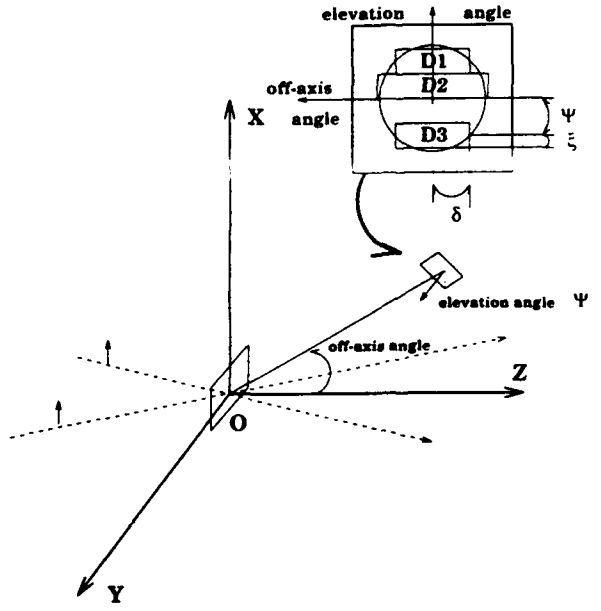

Figure 1: *Geometry of phase Doppler*

In order to be able to compare with results previously published, the geometry selected is as close as possible to the layout studied in Bachalo & Sankar (1988), Sankar & Bachalo (1991), using geometrical optics or Gréhan et al. (1991,1994), using GLMT. The optical layout is illustrated in Fig. 1, where various angles are defined, the size and location of the rectangular receiving apertures used for detectors D_1, D_2 and D_3, are also shown.

Two laser beams, polarized parallel to the OX axis, propagate in the (YOZ) plane. The two beam waists are centered at point O. The results presented here pertain to an angle of 1.35° between the two-beams. The beam waist diameter is 80 μm and the wavelength is 0.4747 μm. At the centre of the measuring volume, each beam has an intensity of 10^7 W/m^2.

Detector	Ψ	δ	ξ
D_1	4.1°	4.39°	1.57 °
D_2	1.27°	5.71°	1.27 °
D_3	-4.1°	4.39°	1.57 °

Table 1: *Elementary detector parameters*

Each detector is defined by: its center location, an off-axis angle θ in the plane (ZOX) and an elevation angle Ψ, and its aperture size. Parallel to the fringes, the receiving aperture subtends a half-angle δ, and normal to the fringes the half-angle is denoted by ξ. Table 1 gives the values used in this paper. Air bubbles in water with a complex refractive index of $0.75 - 0.0i$ are considered as the scattering particles.

2.4 Computation domain

The computation domain in this paper is limited to the plane (XOY), where the particle center was moved in steps of 16 μm parallel to the OX and OY directions, describing a square with each side of 160 μm using 121 grid points. For each of these 121 locations, the pedestal, visibility and phase recorded by each of the three detectors were computed.

Each component of this 11x11 matrix was interpolated onto a 25x25 grid and used to draw maps as in Gréhan et al. (1994).

3 Standard geometry

3.1 30° detection

The collection unit is in the plane (XOZ), with an off-axis angle of $\theta = 30°$. The main particle trajectory is parallel to the Y axis.

Figures 2 and 3 display iso-pedestal lines (more exactly iso-level of $\log_{10}(P_s)$, where P_s is expressed in Watt). corresponding to detector D_1, for bubbles of 1 and 40 μm diameter, respectively.

Figures 4 and 5 display iso-phase shift lines between detector pairs 1-2, Φ_{12} and 1-3, Φ_{13} respectively. for a bubble of 1 μm diameter. Figures 6

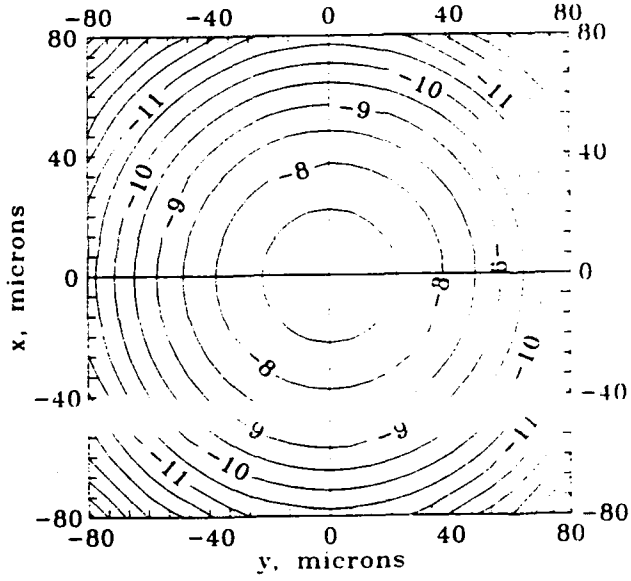

Figure 2: *Iso-pedestal lines for detector D_1 and a bubble of 1 μm diameter*

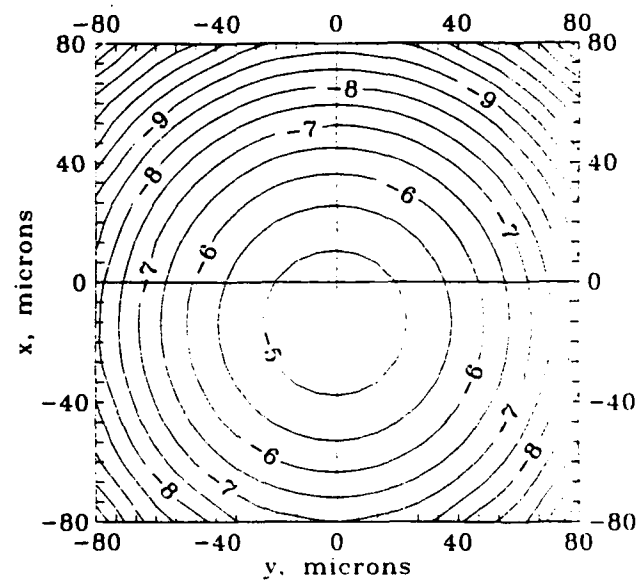

Figure 3: *Iso-pedestal lines for detector D_1 and a bubble of 40 μm diameter*

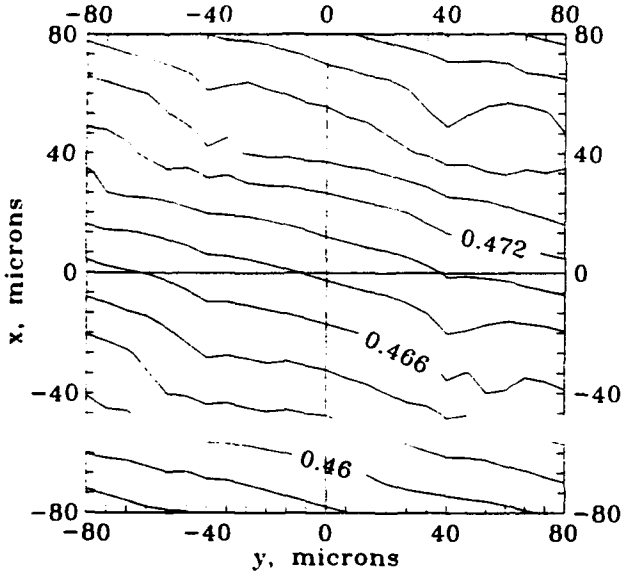

Figure 4: *Iso-phase shift lines Φ_{12} for a bubble of 1 μm diameter*

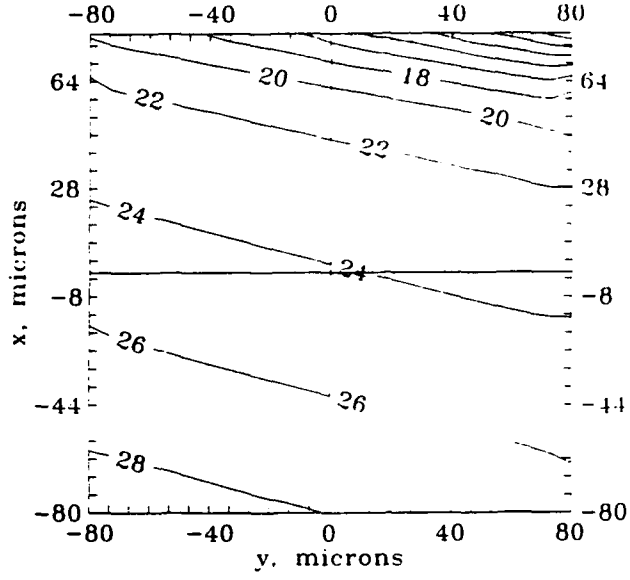

Figure 6: *Iso-phase shift lines Φ_{12} for a bubble of 40 μm diameter*

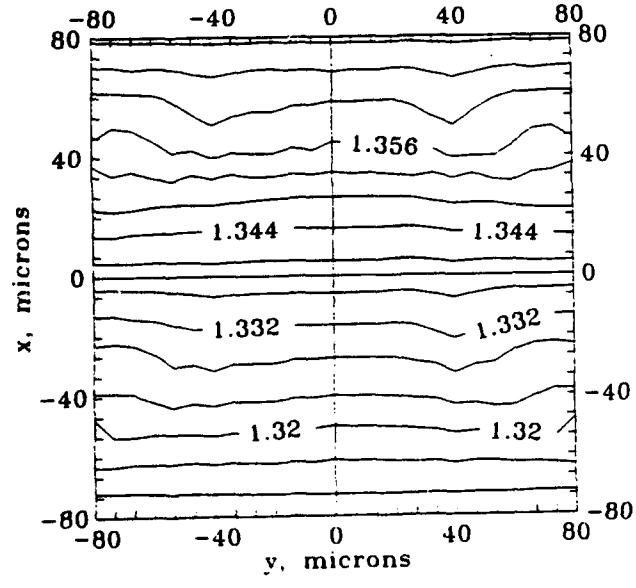

Figure 5: *Iso-phase shift lines Φ_{13} for a bubble of 1 μm diameter*

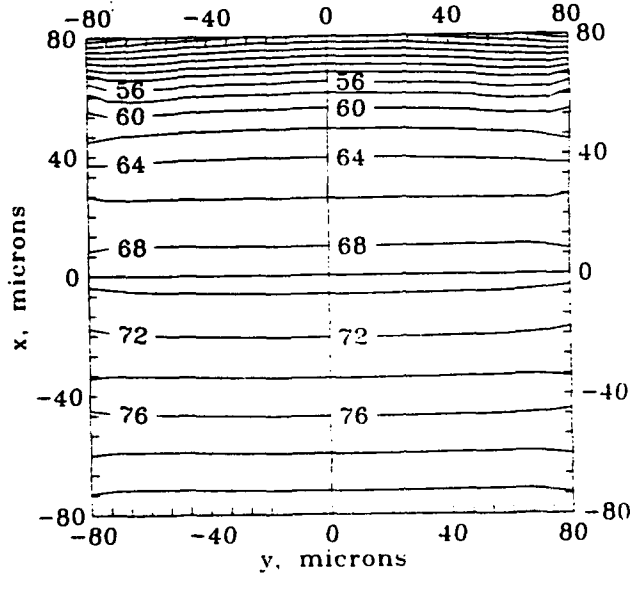

Figure 7: *Iso-phase shift lines Φ_{13} for a bubble of 40 μm diameter*

and 7 show Φ_{12} and Φ_{13} but for a 40 μm diameter bubble. Maps of visibility are not presented because the visibility is always very good.

Figure 2 and 3 show that the pedestal is a strong function of the bubble diameter and location in the control volume. Furthermore, the location of the maximum value of the pedestal depends on the particle size (and detector location). For example, for the 40 μm diameter bubble (Fig. 3), the maximum is located at ($Y = 0$, $x \approx -16$ μm). *The location of the maximum of the pedestal moves opposite than for the droplet case (Gréhan et al. (1994)).*

Figures 4-5, for 1 μm diameter bubble, show that the phase shift is nearly independent of the particle location in the control volume. The gradient of illuminating light intensity onto the particle is very small. Hence the assumption of a uniform illumination of the particle is verified and the classical Lorenz-Mie theory could be used successfully (the phase shifts predicted by LMT are $\Phi_{12} = 0.468°$ and $\Phi_{13} = 1.338°$).

Figures 6-7, for the 40 μm diameter bubble, show that the phase shift is strongly dependent on the particle location.

If we want to measure at the same time 1 μm and 40 μm diameter bubbles, the level of minimum pedestal must be -7.5 (see Fig. 2). Then from figure 3 and figures 6-7, the measured phase shift for a 40 μm diameter bubble evolves (i) from 20° to 28° for Φ_{12} (ii) from 58° to 82° for Φ_{13}. Note that the plane wave prediction for a 40 μm bubble are $\Phi_{12,LMT} = 24.10°$ and $\Phi_{13,LMT} = 69.17°$.

Then for this standard geometry, as the mean particle trajectory is parallel to the Y axis, the measured diameter for a 40 μm bubble could vary from about 37 to 53 μm, if the measured phase shift are interpreted with the plane wave relationships Phase shift/diameter ($d_p = 0.658\,\Phi_{13}$). *For bubbles, the trajectory ambiguity overestimates the bubble diameter in contrast with the droplet case where it corresponds to an underestimate at the droplet diameter (Gréhan et al. (1994)).*

Nevertheless, the trajectory effect is less important than for the droplet case. The difference can be explained as follows.

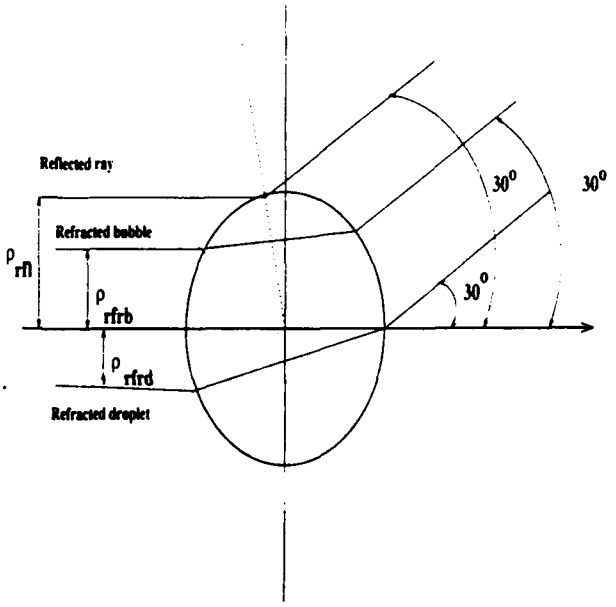

Figure 8: *Rays contributing to the scattering process at an off-axis of* 30°, *for a water droplet in air or an air bubble in water*

At 30°, for a water droplet as well as for an air bubble the two main contributions are due to refraction and reflection.

For example for a 40 μm diameter particle, by reflection, the ray which is collected corresponds to an impact parameter ρ_{rfl} of $\approx$ 19.3 μm for both cases (droplet or bubble). But by refraction, the ray which is collected corresponds to an impact parameter ρ_{rfrb} of $\approx$ 10.4 μm for the bubble, and ρ_{rfrd} of $\approx$ -9.7 μm for the droplet (see figure 8). Then the modification of the relative importance of rays reflected and refracted involves rays separated from $\approx$ 9 μm for the bubble, but $\approx$ 29 μm for the droplet.

3.2 70° detection

Nevertheless, a 30° detection is really only an attractive solution when the optical access is limited, it is not the best choice for measuring bubbles. When possible a location of the detector unit at $\approx$ 70° is recommended.

Figures 9 and 10 correspond to such a detection angle of 70°. From Figure 9 the shift of the lo-

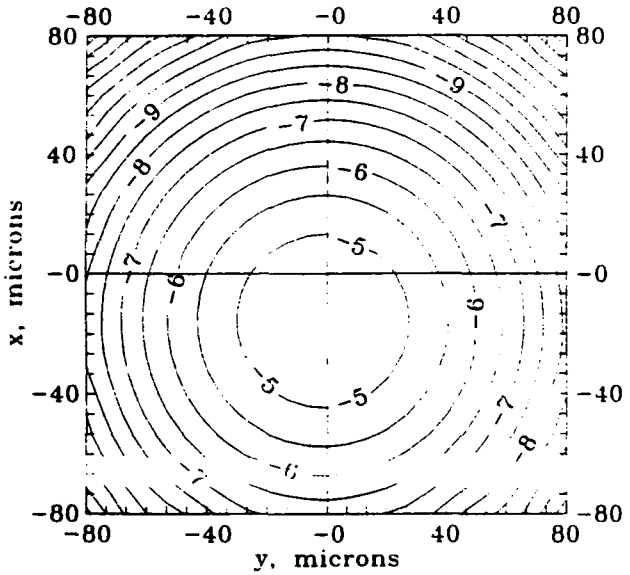

Figure 9: *Iso-pedestal lines for detector D_1 and a bubble of 40 μm diameter, 70° detection*

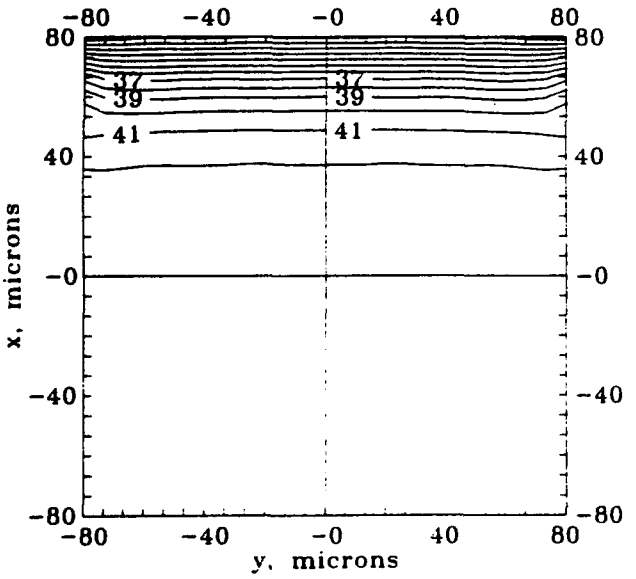

Figure 10: *Iso-phase shift lines Φ_{13} for a bubble of 40 μm diameter, 70° detection*

cation of the maximum of the pedestal toward negative X is close to the one predicted for a 30° detection. Comparing Figs 7 and 10, it is clear that the trajectory effect is much less severe for the 70° detection: contour lines are not present in the bottom of the figure due to the invariance of the phase shift. The phase shift predicted by LMT for a 40 μm bubble is of 42.79°. As the phase shift/particle relationship diameter is $d_p = 1.058\ \Phi_{13}$, the measured diameter of the 40 μm bubble varies from 42 μm to 45 μm across the measurement volume.

4 Modified standard Geometry

The modified standard geometry corresponds retaining the same optical design that was previously computed, but the main particle trajectory is now parallel to the X-axis, and the signal processing is only carried out on the part of the signal corresponding to the maximum of the pedestal (Xu & Tropea (1994)).

Re-interpreting the series of Figures 2-7, we conclude that when the mean particle trajectory is parallel to X, and the signal processing is limited to the maximum of the pedestal, the bubble diameter is measured with a good accuracy, including detection at an angle of 30°.

5 Dual burst technique

The aim of the dual burst technique is to measure the size, velocity, and refractive index of a particle by using only one detection unit and a continuous analysis of the phase shift evolution during each burst. The principal of the technique is fully described, in the case of refracting droplets, by Onofri et al.(1994). The aim of this section is to discuss the similarities and differences with the droplet case, in order to describe the applicability of the method to liquid flow with solid (refractive or strictly reflecting) particles and bubbles.

Fig. 11 displays the evolution of the phase shift and pedestal for three bubbles of different size travelling parallel to OX. Taking into account a variation of the intensity limited to 10^6,the pres-

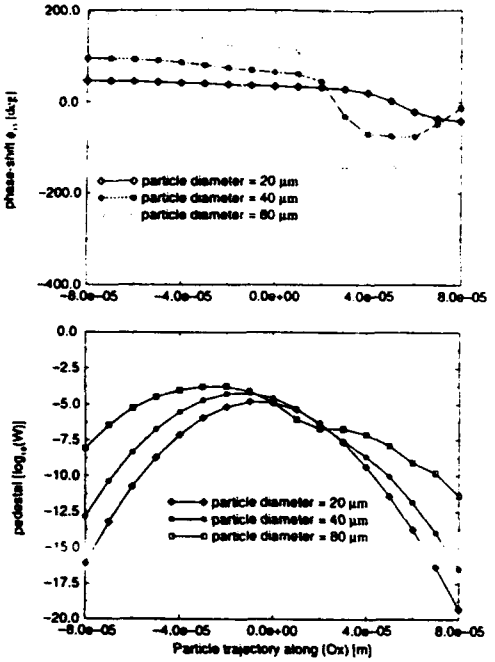

Figure 11: *Dual burst geometry, 2 $w_0 = 40\mu m$, (a) evolution of the phase shift along X (b) evolution of the pedestal, the particle diameter is the parameter: bubble case*

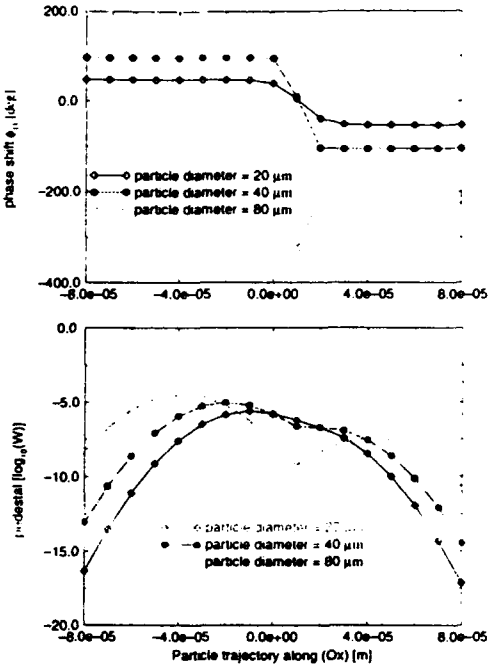

Figure 12: *Dual burst geometry, 2 $w_0 = 40\mu m$, (a) evolution of the phase shift along X (b) evolution of the pedestal, the particle diameter is the parameter: perfectly reflecting particle*

ence of a second burst is not clear, in contrast to the refracting droplet case, .

Nevertheless, from Fig. 11, GLMT phase shift predictions for $X = -80$ μm are 46.6, 95.4 and 192.7 ° , and for $X = 0$, 34.3, 64.6 and 119.2 ° for the bubbles of 20, 40 and 80 μm, respectively. To compare, the phase shifts predicted by geometrical optics for such bubbles with this geometry are (i) by reflection 48, 98, and 195 °, (ii) by refraction 30, 60, and 117 ° for the 20, 40, and 80 μm bubbles, respectively.

Then, for example with the 80 μm bubble, the phase evolves between approximately the value predicted by geometrical optics for a reflective scattering process to a refractive scattering process. The gradient of light on the particle is strong enough to shift the "refracted burst" and the "reflected burst" but not enough to separate them. This evolution is limited to the negative abscissa, for the positive abscissa another scattering process is prevailing, but not discussed here because the level of the corresponding pedestal is very low.

Fig. 12 displays the same evolution as Fig. 11 but for a perfectly reflecting particle (m=1.5-5i). The particle is so absorbing that no light can cross through it. Again, we limit our attention to the negative abscissa, as for Fig. 11. The main behaviour is that now the phase is exactly constant, corresponding to geometric optics predictions for a reflecting particle. Then, especially for big particles, the difference between bubbles and strictly reflecting particles can be extracted from the continuous evolution of the phase in the burst of bubbles.

6 Conclusion

In the present paper, the influence of the trajectory effect on size measurements of bubbles by phase Doppler technique has been discussed for a classical geometry, a modified standard geometry, as well as for the Dual Burst technique. In the later case, possibility of distinction between bubbles and perfectly reflecting particles has been dicussed. These results will help to understand the physical effects which are at the origin of the mea-

surements of ghost bubbles in some experimental set-ups (Moechti, 1993).

7 Acknowledgments

The authors are grateful to the Commission of the European Communities, the French government (PROCOPE program), the German Ministry of Research and Technology, and the Deutsche Forschungsgesellschaft for providing financial support for this work.

8 References

Aizu Y., Durst F., Gréhan G., Onofri F. & Xu T.H. 1993, A PDA system without Gaussian beam defects, *3rd Int. Cong. on Optical Particle Sizing, Yokohama, Japan*, pp. 461-470.

Bachalo W.D. & Sankar S.V. 1988, Analysis of the light scattering interferometry for spheres larger than the light wavelength, *Proc. 4th Intl. Symposium on Applications of Laser Anemometry to Fluid Mechanics, Lisbon* paper 1.8.

Gouesbet G., Maheu B. & Gréhan G. 1988, Light scattering from a sphere arbitrarily located in a Gaussian beam, using a bromwich formulation, *J.O.S.A. A*, vol. 5, pp. 1428-1443.

Gouesbet G., Gréhan G. & Maheu B. 1990, Localized interpretation to compute all the coefficients g_n^m in the generalized Lorenz-Mie theory, *J.O.S.A. A*, vol. 7, pp. 4003-4018.

Gouesbet G., Gréhan G. & Maheu B. 1991, Generalized Lorenz-Mie theory and applications to optical sizing, in *Combustion Measurements*, ed. Norman Chigier, pp.339-384, Hemisphere Publishing Corporation, New York.

Gréhan G., Gouesbet G., Naqwi A. & Durst F. 1991, Evaluation of a phase Doppler system using generalized Lorenz-Mie theory, *Int. Conf. on Multiphase flows'91, Tsukuba, Japan*, pp. 291-296.

Gréhan G., Gouesbet G., Naqwi A. & Durst F. 1992, Trajectory ambiguities in phase Doppler systems: Use of polarizers and additional detectors to suppress the effect, *6th intl. symp. on applications of laser techniques to fluid mechanics, Lisbon*, paper 12-1

Gréhan G., Gouesbet G., Naqwi A. & Durst F. 1994, Trajectory ambiguities in phase Doppler systems: study of a near-forward and a near-backward geometry, *To be published by Part. Part. Syst. Charact.*

Lock J.A. & Gouesbet G. 1994, A rigorous justification of the Localized approximation to the beam shape coefficients in generalized Lorenz-Mie theory. I: On-axis beams, *to be published by J.O.S.A. A*,

Moechti T.Y. 1993, Etude expérimentale des écoulements de Poiseuille à bulles plans. Thése. Grenoble le 20 Décembre 1993. Chapitre V.

Naqwi A. & Durst F. 1993, Analysis of laser light-scattering interferometric devices for in-line diagnostics of moving particles, Applied Optics, vol. 32, pp. 4003-4018.

Naqwi A., Ziema M. & Durst F. 1992, Fine particle sizing using an extended phase Doppler anemometer, *5th European Symp. Particle Characterization (PARTEC92), Nürmberg, Germany*, pp. 267-279.

Onofri F., Gréhan G., Gouesbet G., Xu T.H., Brenn G. & Tropea C. 1994, Phase-Doppler anemometer with dual-burst technique for particle refractive index measurements, *7th Intl. Symposium on Applications of Laser Anemometry to Fluid Mechanics, Lisbon*

Sankar S.V. & Bachalo W.D. 1991, Response characteristics of the phase Doppler particle analyzer for sizing spherical particles larger than the light wavelength. *Appl. Optics*, vol. 30, pp. 1487-1496.

Sankar S.V., Weber B.J. & Bachalo W.D. 1990, Sizing fine particles with the phase Doppler interferometric technique, *Proc. of the 2nd Int. congress on Optical particle sizing, Tempe, USA, pp. 277-287.*

Xu T.H. & Tropea C. 1994, Improving performance of two-component Phase Doppler anemometer, *To be published by Meas. Sci. Techn.*

Dual Mode Phase Doppler Anemometry

C. Tropea*, T.-H. Xu*, F. Onofri†, G. Gréhan†, P. Haugen‡

* Lehrstuhl für Strömungsmechnik, University of Erlangen. Germany
† Laboratoire d'Energétique des Systèmes et Procédés, INSA de Rouen, France
‡ Dantec Measurement Technology A/S, Skovlunde, Denmark

Abstract

A new PDA measurement system is introduced and analysed in this paper. The system has been called the *Dual-Mode* PDA, since it combines a conventional or standard PDA optical arrangement with a planar PDA system. Using four detectors and measuring two velocity components, the new system eliminates completely ambiguity in the size measurement due to particle trajectory. Design considerations and first results using mono-dispersed droplets are presented.

1 Introduction

Of increasing interest is the application of the phase Doppler anemometer technique to the measurement of mass flux and concentration, especially in sprays. Such measurements are essential when studying droplet evaporation, paint spray deposition, droplet splashing on a wall, etc., where a mass balance at different measurement planes is the primary quantity of interest. Experience in measuring mass flux with the PDA technique has however, been varied, notwithstanding the considerable effort required to integrate over numerous measurement points to obtain a total mass flux comparable to a reference value monitored at the spray input. Whereas some investigations have reported values which are too low, especially with very fine droplet distributions (Bulzan et al. 1992), an overestimation of the mass flux is more typical, sometimes reaching many hundreds of percent in simple pressure driven atomizers. It is therefore instructive to consider the primary measurement quantities required to compute the local mass flux, eg. for a uni-directional flow:

$$f_n = \frac{\pi\rho}{6\Delta t}\sum_{i=1}^{I}\frac{D_i^3 N_i}{A(D_i)_n}\cdot\frac{\overline{U_n(D_i)}}{\overline{|U_n(D_i)|}}$$

n	-	index of flux direction
i	-	index of droplet size
N_i	-	number of particles in size class i
$U_n(D_i)$	-	velocity of particles in size class i and direction n
$A(D_i)$	-	size dependent cross-sectional area
D_i	-	droplet size

Of these parameters, the droplet velocity and the number of droplets (N_i) are probably the most secure, although very low SNR values, for example through obscuration in dense sprays, may lead to non-validation and thus to counting errors in N_j. Recent work has attempted to extend signal processing to multiple scatterers in the measurement volume to improve this estimate (Sankar et al. 1993). The reference area over which the passage of particles is counted, $A(D_i)$, is size dependent and has led to a numer of algorithms for in-situ determination of the quantity (Saffman 1987). Recent work has shed doubt on how well defined the length dimension of $A(D_i)$ is for large particles, usually expected to correspond to the slit aperture image intersecting the beam crossing (Löffler-Mang 1992, Schöne 1993). The cross-sectional area may also lack in accuracy due to inaccuracy of the transit time or the particle trajectory being truncated by the projected slit. A promising approach to correctly estimating the effective area has been proposed by Qiu and Sommerfeld (1992, 1994) for a steady flow or for an unsteady flow.

Clearly however, the accurate measurement of droplet size (D_i) will be of utmost importance, since this parameter enters the computation to the third power. Unfortunately there are often conflicting demands on the layout of a PDA system to achieve high accuracy in size measurement. For dense sprays the single realization condition can only be met by decreasing the measurement volume size, examined in detail by Edwards and Marx (1992). On the other hand the *Gaussian beam defect* or *trajectory effect*, as

recognized by Saffman (1986) and outlined further by Gréhan et al. (1991) & Sankar et al. (1992) will lead to larger size errors as the ratio of droplet size to measurement volume diameter increases. Even without altering the measurement volume size, the trajectory effect may well vary significantly in its influence, as a spray evolves downstream through agglomeration (Domnick et al. 1993). It is therefore the elimination of the trajectory effect that was the prime motivation of the present paper, with the aim of improving concentration and mass flux measurements.

There have been many suggestions for eliminating trajectory effects in PDA, ranging from the judicious selection of system parameters (Haugen & von Benzon 1993, Naqwi 1993, Sankar et al. 1991) to more complex optical arrangements involving additional detectors (Gréhan et al. 1992). Two more recent suggestions appear to be more practical from an instrumentation point of view and form the basis for the present development.

The first of these is the planar PDA (PPDA), named for the fact that the detectors lie in the plane of the intersecting laser beam (Aizu et al. 1993). Although both reflective and refractive scattered light is received with the PPDA, the contributions come with a time-delay and furthermore the refractive contribution is much higher in amplitude. Thus a clear distinction at the signal detection stage can be made to eliminate sizing errors. A second method of eliminating trajectory effect when using a two-component system, is to change the flow direction of droplets perpendicular to the beam intersection plane, termed a modified standard PDA (MS-PDA) (Xu & Troea 1994). Both the PPDA and MS-PDA suffer however, from the constraint that the flow must be aligned either with the X or Y axis respectively. In a turbulent flow, trajectory errors can still be expected with these systems.

Before describing the new development, it should be mentioned that still another promising approach has been introduced to avoid trajectory errors. Proper orientation of the receiving optics and judicious choice of the measurement volume diameter can also lead to a more distinct separation of the reflective and refractive contributions over a large range of droplet diameters. This effect, used by Hess & Wood (1993) and Lading & Hansen (1992) in their Pulse Displacement Technique, has also been recently adapted to PDA as the *Dual Burst* Technique (DBT) (Onofri et al. 1994).

2 Description of the Technique

The *Dual Mode* PDA is a four beam, two-component system, which combines two detectors of a standard system with two detectors of a planar system in a single receiving unit. The optical layout is pictured in Fig. 1. The transmitting optics differ in no way from a conventional PDA. Typically, the main flow direction is along the Y-axis, however deviations from this direction do not lead to errors, but at most a non-validation of the size measurement.

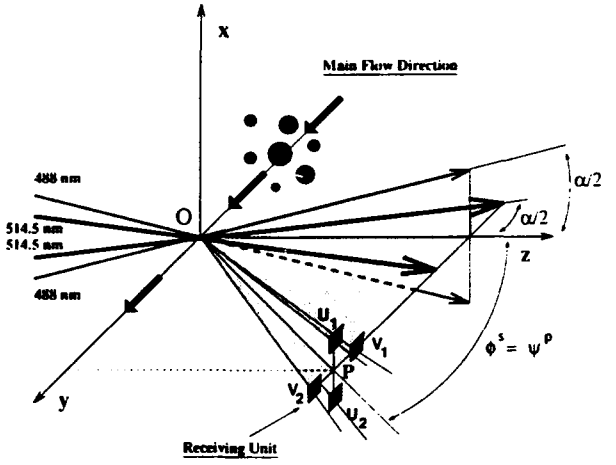

Figure 1: The optical geometry of the Dual mode PDA System.

The receiving unit provides four apertures for the four detectors, detectors V_1 and V_2 for the PPDA and the velocity component aligned with the Y-axis and U_1 and U_2 for a standard PDA (SPDA) and the velocity component aligned with the X-axis. Interference filters are used in front of the detectors to separate the scattered light from each of the beam pairs.

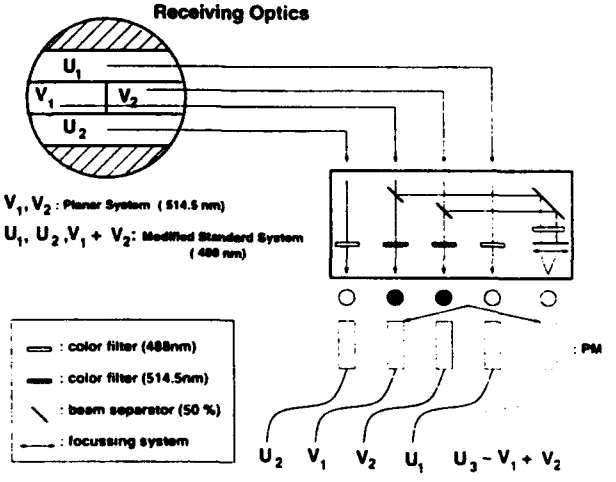

Figure 2: Schematic of receiving aperture and detector system.

The segmented collecting lens and the receiving optics is shown schematically in Fig. 2, using a fiber optic implementation. Conceptually, a fifth detector could easily be incorporated, for instance as U_3, providing redundancy in the 2π phase determination and thus the possibility of refractive index measurements in addition to a sphericity check. The receiving aperture sizes and shapes can be easily modified by placing a mask in front of the segmented lens. The optimization of the mask for a given application constitutes much of the design work in achieving the results presented below.

3 Design Computations

Having defined the DM-PDA, an optimization for a given size range and refractive index must consider the choice of:

- α - intersection full angle
- ϕ^S - off-axis angle (SPDA)
- Ψ^P - mean elevation angle (PPDA)
- $\Delta\Psi^P$ - detector separation angle (PPDA)
- $\Delta\Psi^S$ - detector separation angle (SPDA)

and the receiving aperture size and shape. The wavelengths are considered fixed at λ=514.5nm used for the PPDA and λ=488nm for the SPDA. The present study was limited to relative refractive indexes in the range $1.1 < m < 2.0$. Furthermore, only geometries of the transmitting optics corresponding to a standard DANTEC 60X11 probe have been considered, as summarized in Table 1. Other values are achievable through the use of beam expanders or alternative front lenses. The receiving apertures are more tedious to describe, however they are designed on the basis of a modified Dantec 57X40 FiberPDA receiving probe with a focal length of 160mm, as summarized in Table 2.

60X11 Probe		
Beam Separation[mm]	38	
Beam Diameter[mm]	1.35	
Focal Length[mm]	160	400
Intersection Half-Angle[°]	6.77	2.72
MV Diameter[μm]	75	190

Table 1: Specifications of transmitting optics used for computational study.

3.1 Computations According to Geometric Optics (G.O.)

Some initial computations were performed according to geometric optics, to have a general overview of the system characteristics. In Fig. 3 the phase conversion factors of a refracting particle for the SPDA and PPDA are shown as a function of relative refractive index (m) and off-axis angle (ϕ^S), whereby some caution must be given to these G.O. results at extreme values of m. This figure indicates that scattering angles beyond 40° would severely limit the PPDA system at low m. Values below 20° would lead to disturbances through diffraction. The scattering angle of 30° shows a flat behaviour for the PPDA for $1.3 < m < 2.0$, while the SPDA conversion factor decreases monotonically. This behaviour of the two systems may be attractive for future systems designed for the measurement of refractive index. At m=1.33 the ratio of phase conversion factors SPDA/PPDA is approximately 3.

Small Size Range: 0-40μm	f=160mm			
	U_1	U_2	V_1	V_2
Geometric Center[mm]	11.51	-11.51	10.5	-10.5
Area[mm^2]	407	407	200	200

Table 2: Optical parameters for receiving unit.

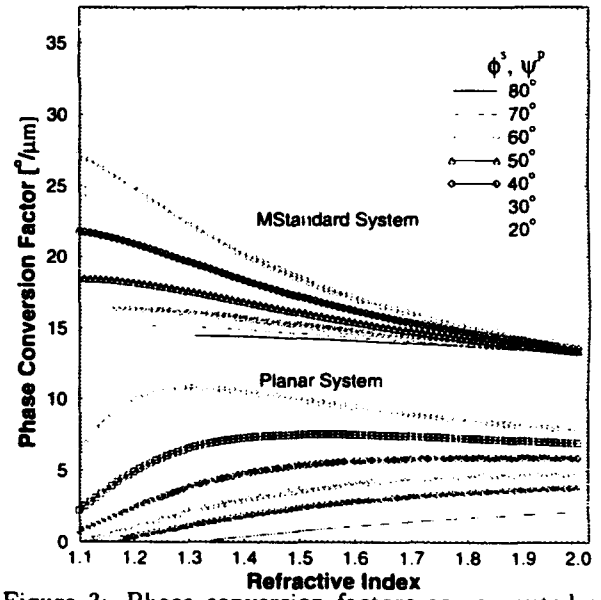

Figure 3: Phase conversion factors as computed according to geometric optics, (α/2=6.77°).

In Fig. 4 maps of constant phase conversion factor are given for the SPDA and PPDA as a function of off-axis/mean elevation angle and detector separation angle. Also from these figures it is clear that scattering angles near $\phi^S = \Psi^P$=30° are advantageous to allow good sensitivity in the PPDA receiving mask design. The SPDA will remain equally sensitive at all scattering angles.

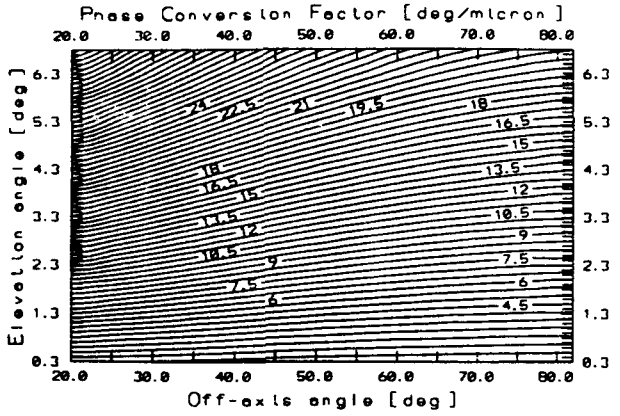

a) SPDA

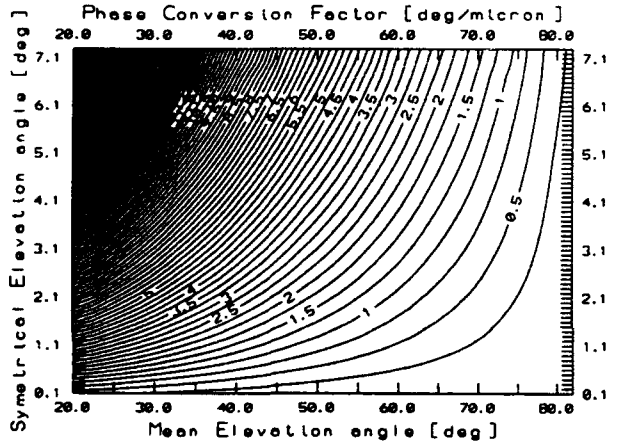

b) SPDA

Figure 4: Maps of iso-phase conversion factor ($\alpha/2$=6.77°, m=1.333).

3.2 Computations According to GLMT

Further computations have been performed with the Generalized Lorenz-Mie Theory (GLMT), described by Gouesbet et al. (1991), where earlier references may also be found.

With some optimization of the receiving mask, results like those shown in Fig. 5 have been obtained for the phase/diameter relations, the signal intensity and the signal visibility. These calculations were performed for a small size range, nominally 0-40μm. Therefore the short focal length transmitting lens was used (f=160mm) to achieve a higher light intensity in the measurement volume. Fig. 5 indicates that measurements up to 40μm should be achievable, with very linear behaviour of both the SPDA and PPDA phase/diameter relations. One exception is the PPDA behaviour for small particles, which is well known from Aizu et al. (1993). In this range the SPDA must be used for the size measurement. Similar results could be obtained for m=1.1 and 1.6 as well as for a medium size range, D < 240μm (see Table 2). At m=1.1, although a scattering angle of ϕ^S=25° was used, there was still some deviation of the phase/diameter relation from the G.O. result, calling for special treatment in the processing software.

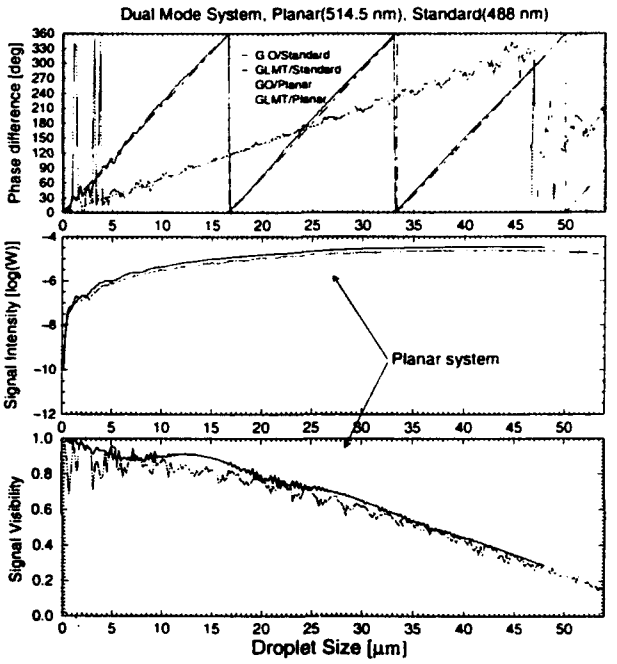

Figure 5: GLMT computations of the phase diameter relation: m = 1.333, $\phi^S = \Psi^P = 30°$.

One essential feature of the DM-PDA is to eliminate the trajectory effect. This is illustrated in Fig. 6, in which the spatial distribution of the SPDA/PPDA-phase ratio is mapped as a function of the position of the droplet center in the measurement volume. These computations have been carried out for a 40μm water droplet and for an optical arrangement similar to tat used in section 3.1. Droplets passing through the measurement volume parallel to the Y-axis (trajectory **A** in Fig. 6 will yield a constant SPDA/PPDA-phase ratio over the positive y half of the control volume. At negative y positions, this ratio will vary from the expected values according to refractive dominated scattering. Assuming however, that the phase differences are determined from those portions of the signal having the maximum amplitude, a correct size measurement will be made. Should a droplet pass through the volume at a glancing angle or parallel to the X-axis, but at a negative y position (trajectories **B** or

C in Fig. 6), the SPDA/PPDA phase ratio will deviate from the expected value and will not be validated. This validation step consists essentially of only accepting measurements for which the size determined using the SPDA agrees with the size determined using the PPDA, within tolerance limits. Note that the validation also effectively reduces the y dimension of the measurement volume.

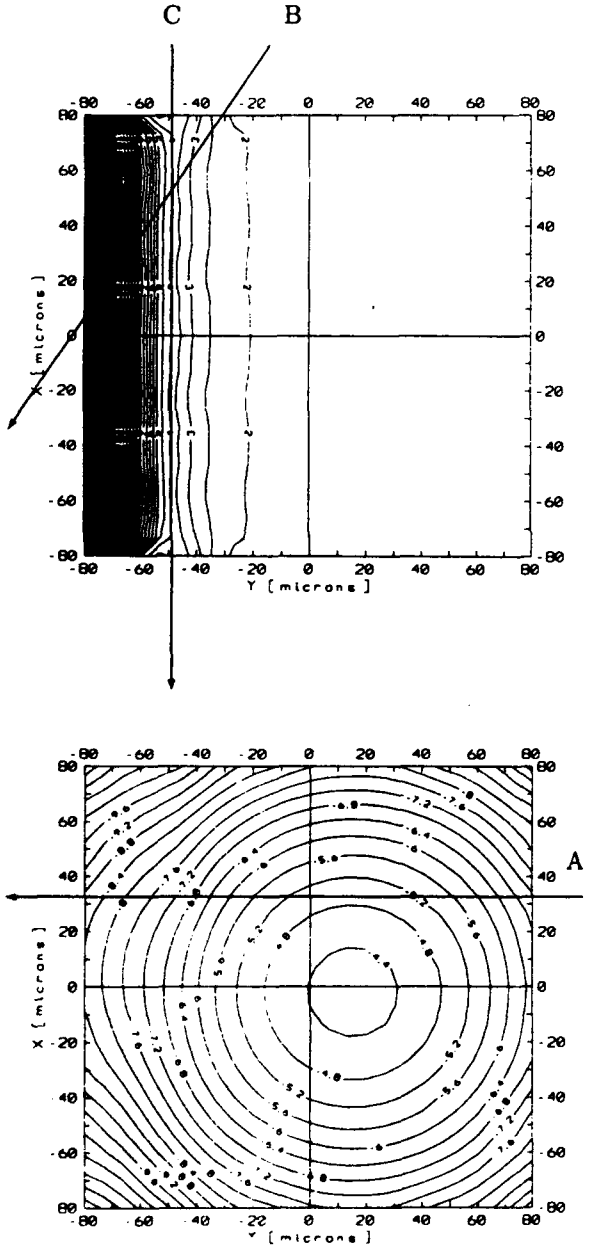

Figure 6: Iso-maps of a) SPDA/PPDA-phase ratio and b) SPDA signal intensity for 40μm water droplet.

4 Experimental Verification

Whereas the computations have been performed for a system based on a commercial PDA fiber probe, the initial experimental verification was carried out for a laboratory set-up. The specifications of this system are summarized in Table 3.

	Planar	Standard
Wavelength [nm]	514.5	488.0
Front Lens [mm]	310.4	310.4
Beam Spacing [mm]	21.68	21.68
Half Beam Angle [deg]	2	2
MV Diameter [μm]	130	125
Receiving Lens [mm]	310.4	310.4
Scattering Angle [deg]	0	30
Elevation Angle 1 [deg]	31.85	5.063
Elevation Angle 2 [deg]	28.15	-5.063
Phase Factor* [deg/μm]	1.225	6.942
Phase Factor Ratio* [-]	5.67	

* for m=1.333

Table 3: Specifications of DM-PDA for experimental verification.

To study the DM-PDA in more detail, a 4-channel transient recorder was used to record the signals from each of the four photodetectors(APD). It was then possible to track the phase difference of the SPDA and PPDA subsystems as the droplet traversed the measurement volume. This was done using a zero crossing detector.

In Fig. 7 the results of such an analysis for a 66μm water droplet crossing parallel to the Y-axis is shown. The y position is shown as traversing time with an arbitrary origin. This figure indicates that the portion of the burst with the maximum amplitude also yields an SPDA/PPDA size ratio of approximately one, and that the size determined at this position agrees well with the actual droplet diameter (63μm vs. 66μm). The portions of the signal used to determine the particle size are designated in Fig. 7b and correspond to the maximum signal amplitude.

In Fig. 8 similar results are shown for a 64μm water droplet traversing parallel to the X-axis, the first diagram corresponding to an invalid trajectory for which the SPDA/PPDA size ratio does not equal one and the second diagram resulting in a valid measurement with good agreement to the expected size (61μm vs. 64μm). The results in Fig. 8a show a situation in which the PPDA phase is very close to the 2π size period of the SPDA, causing sudden jumps in the size ratio for small variations in phase.

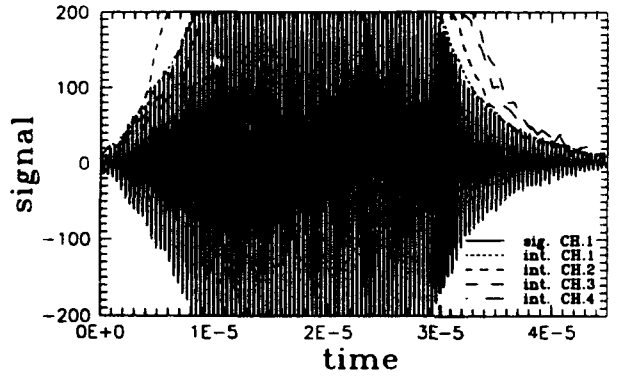

a) Doppler signal and envelopes

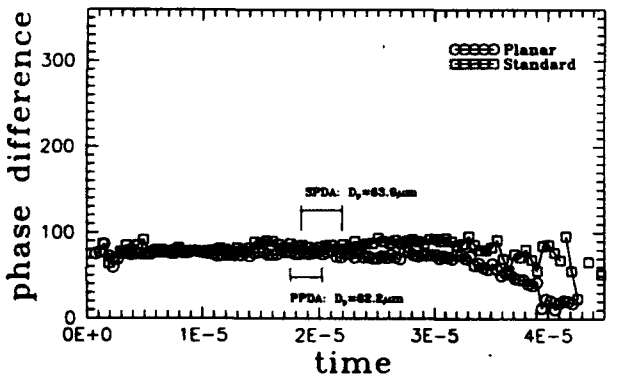

b) SPDA and PPDA phase difference

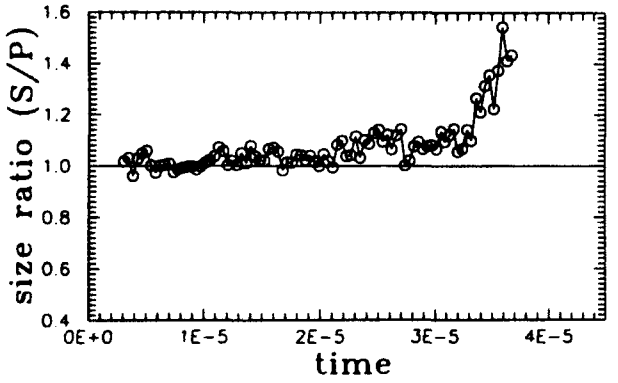

c) SPDA/PPDA size ratio

Figure 7: Signal analysis for a 66μm water droplet traversing parallel to Y-axis.

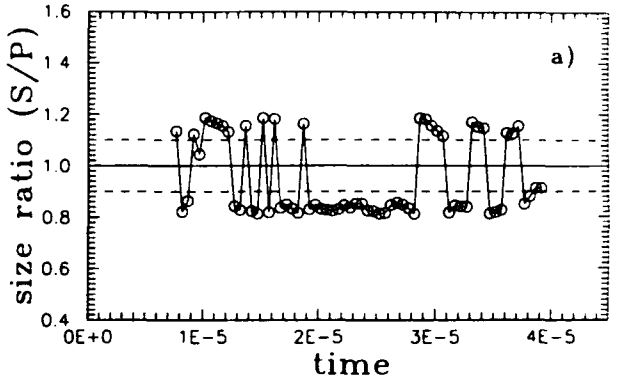

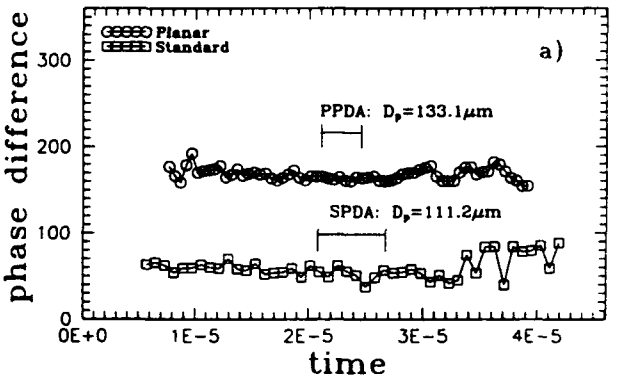

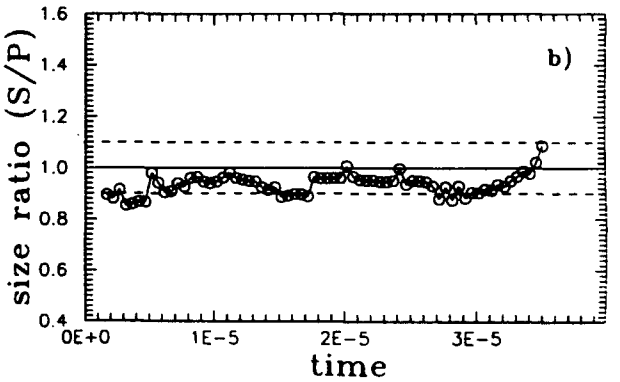

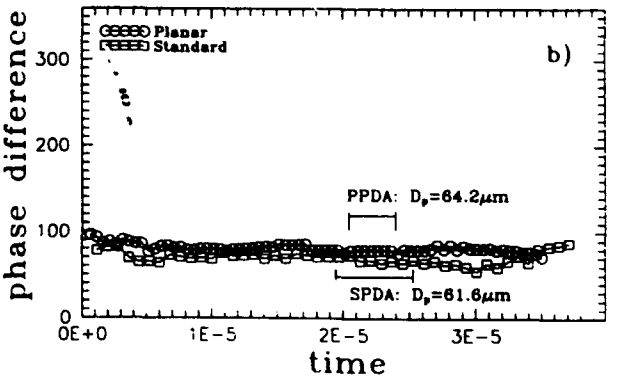

Figure 8: Signal analysis for a 64μm water droplet traversing parallel to X-axis: a) negative y value (invalid); b) positive y value (valid).

5 Conclusions and Final Remarks

A novel PDA optical arrangement has been introduced with the aim of eliminating the trajectory effect, thus improving concentration and mass flux measurements. Initial design work indicates that suitable layouts can be found to meet these requirements for particles in a wide range of relative refractive indexes. Validation in the system consists of comparing the measured size using a standard PDA system with the simultaneous size measurement of a planar PDA system. The system offers the advantage of combining the SPDA and PPDA in one receiving unit, thus simplifying alignment. The *dual mode* PDA has been demonstrated in a laboratory set-up, in which the elimination of the trajectory effect was confirmed. The modifications to a standard 2D PDA to implement the DM-PDA appear to be minor and are presently being undertaken with commercial equipment.

The authors wish to acknowledge the financial support of the Commission of the European Communities and the French and German governments through the PROCOPE program.

References

Aizu, Y., Durst, F., Gréhan, G., Onofri, F., Xu, T.-H. 1993, PDA-System Without Gaussian Beam Defects, *Proc. 3rd Int. Conf. Optical Part. Sizing '93*, Yokohama, Japan, pp. 461-470.

Bulzan, D.L., Levy, Y., Aggarwal, S.K., Chitre, S. 1992, Measurements and Predictions of a Liquid Spray from an Air Assist Nozzle, *Atom. & Sprays*, vol. 2, no. 4, pp. 445-462.

Domnick, J., Dorfner, V., Durst, F., Yamashita, M. 1993, Performance Evaluation of Different Phase Doppler Systems, in *Proc. 3rd Int. Conf. Optical Part. Sizing '93*, Yokohama, Japan, pp. 425-433.

Edwards, C.F. & Marx, K.D. 1992, Analysis of the Ideal Phase-Doppler System: Limitations Imposed by the Single-Particle Constraint, *Atom. & Sprays*, vol. 2, pp. 319-366.

Gouesbet, G., Gréhan, G., Maheu, B. 1991, Generalized Lorenz-Mie Theory and Applications to Optical Sizing, in *Combustion Measurements*, ed. N. Chigier, pp. 339-381, Hemisphere Publishing Corp., New York.

Gréhan, G. Gouesbet, G., Naqwi, A., Durst, F. 1991, Evaluation of a Phase Doppler System using Generalized Lorenz-Mie Theory, in *Int. Conf. on Multiphase Flows '91*, Tsukuba, Japan, pp. 291-296.

Gréhan, G., Gouesbet,G., Naqi,A., Durst, F. 1992, Trajectory Ambiguities in Phase Doppler Systems: Use of Polarizers and Additional Detectors to Suppress the Effect, in *Proc. 6th Int. Symp. on Appl. of Laser Anemom. to Fluid Mech.*, Lisbon, paper 12.1.

Haugen, P., von Benzon, H.H. 1993, Phase Doppler Measurement of the Diameter of Large Particles, in *Proc. 3rd Int. Conf. Optical Part. Sizing '93*, Yokohama, Japan, pp. 301-306.

Hess, C.F., Wood, C.P. 1993, The Pulse Displacement Technique - A Single Particle Counter with a Size Range Larger than 1000:1, *Proc. 3rd Int. Conf. Optical Part. Sizing '93*, Yokohama, Japan, pp. 475-482.

Lading, L., Hansen, B.H. 1992, A Complementary Method for Simultaneous Measurement of Size and Velocity, in *Proc. 6th Int. Symp. on Appl. of Laser Anemom. to Fluid Mech.*, Lisbon, paper 15.1.

Löffler-Mang, M. 1992, Düseninnenströmung, Tropfenentstehung und Tropfenausbreitung bei rücklaufgeregelten Drall-Druckzerstäubern, Ph.D. Thesis, University of Karlsruhe.

Naqwi, A.A. 1993, Innovative Phase Doppler Systems and Their Applications, *Proc. 3rd Int. Conf. Optical Part. Sizing '93*, Yokohama, Japan, pp. 245-260.

Onofri, F., Gréhan, G., Gouesbet, G., Xu, T.-H., Brenn, G., Tropea, C. 1994, Phase Doppler Anemometry with Dual Burst Technique for Particle Refractive Index Measurement, in *Proc. 7th Int. Symp. on Appl. of Laser Anemom. to Fluid Mech.*, Lisbon, paper 12.1.

Qiu, H.-H., Sommerfeld, M. 1992, A Reliable Method for Determining the Measurement Volume Size and Particle Mass Fluxes using Phase-Doppler Anemometry, *Exp. in Fluids*, vol. 13, pp. 393-404.

Qiu, H.-H., Sommerfeld, M. 1994, Particle Concentration Measurements by Phase-Doppler Anemometry in Complex Dispersed Two-Phase Flows, *Exp. in Fluids*, accepted for publication.

Saffman, M. 1987, Automatic Calibration of Measurement Volume Size, *Appl. Optics*, vol. 26, pp. 2592-2597.

Saffman, M. 1986, The Use of Polarized Light for Optical Particle Sizing, in *Anemometry in Fluid Mechanics-III*, LADOAN - Instituto Superior Técnico, Lisbon, pp. 387-398.

Sankar, S.V., Inenaga, A., Bachalo, WD. 1992, Trajectory Dependent Scattering in Phase Doppler Interferometry: Minimizing and Eliminating Sizing Error, *Proc. 6th Int. Symp. of Appl. of Laser Techn. to Fluid Mechanics*, LADOAN, Lisbon.

Sankar, S.V., Weber, B.J., Kamemoto, D.Y., Bachalo, W.D. 1991. Sizing Fine particles with the Phase doppler Interferometri Technique, *Appl. Optics*, vol. 30, no. 33, pp. 4914-4920.

Sankar, S.V., Ibrahim, K.M., Bachalo, W.D. 1993, Coherent Scattering by Multiple Particles in Phase Doppler Interferometry, *Proc. 3rd Int. Conf. Optical Part. Sizing '93*, Yokohama, Japan, late submission.

Schöne, F. 1993, Wichtung von Partikelgrößenverteilungen in der Phasen-Doppler-Anemometrie, Ph.D. Thesis, University of Bremen.

Xu, T.-H., Tropea, C. 1994, Improving Performance of Two-Component Phase Doppler Anemometers, *Meas Sci & Tech.*, accepted for publication.

CORRECTION OF PARTICLE SIZE DISTRIBUTIONS FROM PDA-MEASUREMENTS FOR CONTINUOUS DISTRIBUTIONS LESS THAN 10 µm

S. Schabel, A. Doicu, F. Ebert

Universität Kaiserslautern, Lehrstuhl für Mechanische Verfahrenstechnik und Strömungsmechanik, Postfach 3049, D-67653 Kaiserslautern

ABSTRACT

In the phase-Doppler-anemometry the diameter of a particle can be calculated from the measured phase difference of two signals. The phase response is given by the Lorenz-Mie theory. For particles less than about 10 µm this correlation is nonlinear but oscillating so that one phase difference can result from several diameters. Some PDA systems solve this problem by the use of three or more detectors. Here, two evaluation methods will be presented which can correct the measured particle size distributions in an appropriate way.

The first method is based on the assumption that the density distribution of the particle size has the form of a parametric continuous distribution. The parameters are calculated with a least-squares method. The criterion is that the phase density distribution calculated from the presumed distribution must fit to the measured phase density distribution.

The second method is based on the phase response resulting from Mie-calculations, too. Because this correlation is not single-valued all possible diameters should be equiprobable for each phase difference. With this condition a particle distribution is calculated in which each phase difference is attributed to all possible diameters. Both methods are compared with each other and with light-scattering-measurements.

1. INTRODUCTION

The phase-Doppler-anemometry is a modern method for simultaneous measuring of the size and the velocity of spherical particles. This measuring method is an extention of the laser-Doppler-anemometry which allows the measurement of the velocity only. The LDA is extended at least with one additional photodetector for detecting the particle diameter. The diameter of the particle is then calculated from the phase difference of these signals. The correct optical setup is one of the major problems with this measuring method. In the best case, the setup should result in a linear relation between phase difference and particle diameter. This condition can be realized, if one mechanism of light scattering dominates the others. This means either reflexion or refraction or diffraction dominates. It is usually not possible to get such a linear phase response for particles below 5 - 10 µm with commercial PDA-equipement. In this size-region the phase response is nonlinear and oscillating so that one phase difference can result from several particle diameters. This leads to a broadening of the size distribution in the case of evaluation with a linear approximation.

Previous solutions of this problem use additional photodetectors [1] what is coupled with extra costs and additional hard- and software. We have developed two evaluation methods which allow a correction of the measuring results. The first method is based on the assumption of a parametric distribution for the particle size distribution. The parameters of this distribution are calculated by a least-squares method and lead to sufficient values for the mean diameter and the standard deviation of a particle size distribution. The second method presumes the equiprobability of all possible particle diameters for each phase difference. This method leads to results which are comparable with those from computations with a linear phase response as it is known from the geometrical optics. Both methods are compared with optical particle counter measurements.

2. MATHEMATICAL FUNDAMENTALS

This section will be concerned with the description of two mathematical methods which are used for the particle size analysis. These are the parametric continuous distribution method, which assumes a parametric and continuous distribution for the particle sizes, and the equiprobability

method, which assumes the equiprobability of all possible particle diameters for each phase difference. Two variants are possible for the parametric continuous distribution method. The first one, the probability density function method, is a pointwise evaluation and the second one, the probability method, is an integral evaluation.

2.1 The Parametric Continuous Distribution Method.

We consider the continuous random variables ϕ and a, where ϕ is a continuous function of a:

$$\phi = \phi(a);\ \phi \in C^1([a_{min}, a_{max}]) \tag{1}$$

If $\phi(a)$ is a monotonic function we obtain

$$p_\phi(\phi) = p_a[a(\phi)]a'(\phi) \tag{2}$$

for the direct problem and

$$p_a(a) = p_\phi[\phi(a)]\phi'(a) \tag{3}$$

for the inverse problem.

In this case of phase-Doppler anemometric, we desired to compute the inverse problem which is the calculation of the probability density function (PDF) $p_a(a)$ respectivley the particle size distribution for a measured PDF $p_\phi(\phi)$ of the random variable ϕ (the phase distribution). In the case of a monotonic function $\phi = \phi(a)$ the evaluation of the direct and of the inverse problem is possible. Since $\phi(a)$ is a nonmonotonic function in our case of application, we can evaluate $p_\phi(\phi)$ from a given PDF $p_a(a)$ only. Thus we have to assume a particle size distribution resp. a PDF $p_a(a)$, compute the corresponding PDF $p_\phi(\phi)$ and compare the calculated and the measured $p_\phi(\phi)$. Two algorithms for this regression are available. The first one operates with the probability density function and the second one with the probability of the random variable ϕ.

We introduce

$$S_\phi = \left\{a_k(\phi),\ k = k(\phi) = 1..N_k\ /\ \phi(a_k) = \phi\right\} \tag{4}$$

for the PDF-method as the set of solutions for the equation $\phi(a) = \phi$ if ϕ is fixed. Then we find in each point ϕ_j, as ist is shown in Fig. 1

$$p_\phi(\phi_j) = \sum_{k(\phi_j)=1}^{N_k} p_a\left[a_k(\phi_j)\right] \cdot \frac{1}{\left|\phi'(a_k)\right|} \tag{5}$$

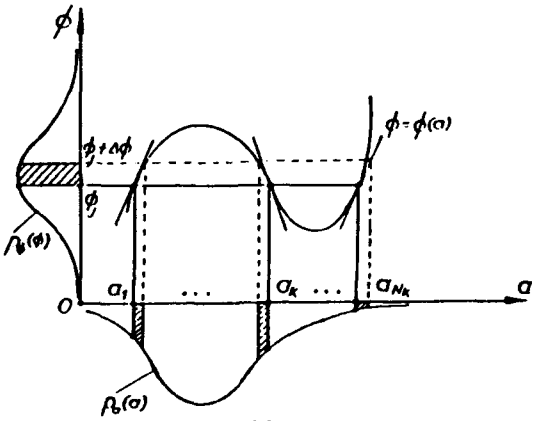

Figure 1: Probability Density Method

The probability method is based on the probability with which the random variable ϕ occures in the interval $[\phi_1, \phi_2]$:

$$P(\phi_1 < \phi < \phi_2) = \frac{\Delta N(\phi_1 < \phi < \phi_2)}{N} = h(\phi_1, \phi_2) = \int_{\phi_1}^{\phi_2} p_\phi(\phi)d\phi = \sum_{q=1}^{N_q} v(q) \int_{b_q}^{b_{q+1}} p_a(a)da \tag{6}$$

where

$$S_{\phi_1\phi_2} = \left\{b_q(\phi_1, \phi_2),\ q = q(\phi_1, \phi_2) = 1..N_q\right\} = S_{\phi_1} \cup S_{\phi_2} \tag{7}$$

is the ordered set of solutions for the equation $\phi(a) = \phi_1$ and $\phi(a) = \phi_2$. This is plotted in Fig. 2. The function v(q) is a validation function and is given by

$$v(q) = \begin{cases} 1 & \text{if } \left((b_q \in S_{\phi_1}) \wedge (b_{q+1} \in S_{\phi_2})\right) \vee \\ & \vee\left((b_q \in S_{\phi_2}) \wedge (b_{q+1} \in S_{\phi_1})\right) \vee \\ & \vee\left(\begin{array}{l}(b_q, b_{q+1} \in S_{\phi_1}) \wedge \\ \left(\phi([b_q, b_{q+1}]) \subseteq [\phi_1, \phi_2]\right)\end{array}\right) \vee \\ & \vee\left(\begin{array}{l}(b_q, b_{q+1} \in S_{\phi_2}) \wedge \\ \left(\phi([b_q, b_{q+1}]) \subseteq [\phi_1, \phi_2]\right)\end{array}\right) \\ 0 & \end{cases} \tag{8}$$

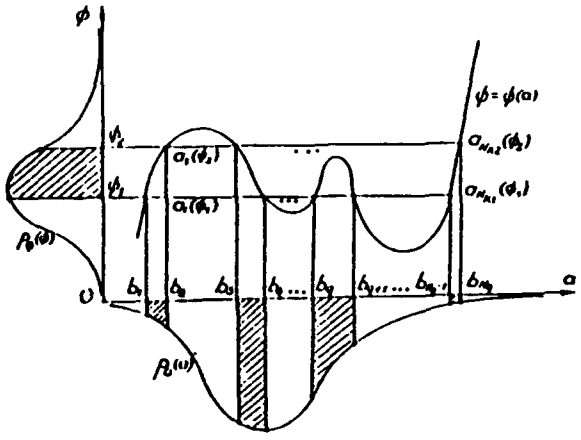

Figure 2: Probability Method

The inverse problem can be resolved if the form of the PDF $p_a(a)$ is apriori accepted. We assume the PDF of the particle size as a parametric continuous function $\tilde{p}_a(a, x_\alpha)$. The parameters x_α of this function are calculated with a least-squares method. This leads to a phase-PDF or a phase-probability histogram calculated from the presumed distribution which fits to the measured phase associated functions as follows:

$$L_1(x_\alpha) = \int_{-\infty}^{\infty} \left[p_\phi(\phi) - \tilde{p}_\phi(\phi) \right]^2 d\phi = \sum_{j=1}^{N_\phi} \left[p_\phi(\phi_j) - \sum_{k(\phi_j)=1}^{N_k} \tilde{p}_a\left[a_k(\phi_j), x_\alpha\right] \frac{1}{\left|\phi'\left[a_k(\phi_j)\right]\right|} \right]^2 \tag{9}$$

$$L_2(x_\alpha) = \sum_{j=1}^{N_\phi - 1} \left[h(\phi_j, \phi_{j+1}) - \tilde{h}(\phi_j, \phi_{j+1}) \right]^2 = \sum_{j=1}^{N_\phi - 1} \left[h(\phi_j, \phi_{j+1}) - \sum_{q=1}^{N_q} v(q) \int_{b_q}^{b_{q+1}} \tilde{p}[a, x_\alpha] da \right]^2 \tag{10}$$

Here, the assumed PDF is a combination of two Gaussian PDF and is defined as:

$$\tilde{p}_a(a, \bar{a}, \sigma_1, \sigma_2) = \frac{2}{\sqrt{2\pi}(\sigma_1 + \sigma_2)} \left[e^{-\frac{(a-\bar{a})^2}{2\sigma_1^2}} \theta(\bar{a} - a) + e^{-\frac{(a-\bar{a})^2}{2\sigma_2^2}} \theta(a - \bar{a}) \right] \tag{11}$$

The mean value of the random variable a in the PDF (11) is given by

$$a_m = \bar{a} + \sqrt{\frac{2}{\pi}}(\sigma_2 - \sigma_1) \tag{12}$$

The computer code developed for this calculations has two input parameters: the number of classes in the phase domaine N_ϕ and the increment of the particle diameter Δa. For a given phase distribution between ϕ_{min} and ϕ_{max} we compute the maximal searching interval $[a_{min}, a_{max}]$ with

$$a_{min} = \min_{k(\phi_{min})} \{a_k(\phi_{min})\}$$
$$a_{max} = \max_{k(\phi_{max})} \{a_k(\phi_{max})\} \tag{13}$$

Then for each interval of particle diameters

$$I_\alpha = I_{(m,n,p)} = [\bar{a} - 3\sigma_1, \bar{a} + 3\sigma_2] \subseteq [a_{min}, a_{max}]$$
$$\bar{a} = m\Delta a;\ 3\sigma_1 = n\Delta a;\ 3\sigma_2 = p\Delta a;\ m, n, p \in N \tag{14}$$

the functions (9) or (10) will be evaluated. The parameters of the distribution parameters assure the minimum of the functions L_1 respectivley L_2.

The probabilty density function $p_\phi(\phi)$ is approximated by the measured frequency density of the random variable ϕ. A realistic approximation of the PDF requires a great number of data points and a fine grid for the phase domain so that the phase oscillations are correctly pursuited. The PDF-method is practically a pointwise method and leads to sufficient results for tight size distributions.

This method was tested with a particle size distribution ($\bar{a} = 2\mu m, \sigma_1 = 0.2\mu m, \sigma_2 = 0.4\mu m$) for water droplets. We used the phase response for a planar PDA layout given by Naqwi [1] as shown in Fig. 3. This planar layout allows to obtain large phase shifts from small particles while maintaining small angles between the laser beams.

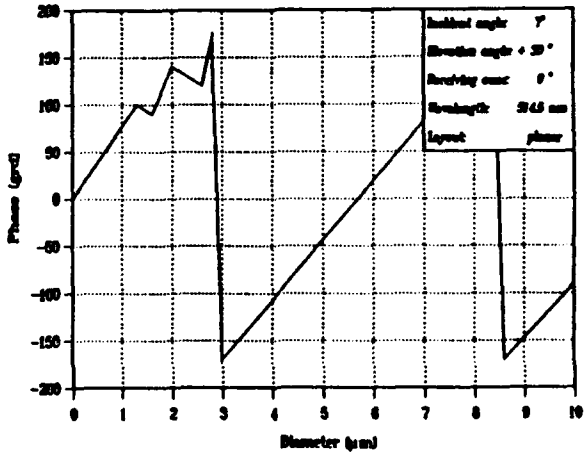

Figure 3: Phase Response for the Planar PDA Layout [2]

The phase distribution was calculated from the particle size distribution with this phase response and then taken as an input distribution for the PDF-method. As a result the mean square deviation of the input size distribution and the detected one

$$\sigma_p = \int_{-\infty}^{\infty} \left[p_{input}(a) - p_{det}(a) \right]^2 da \qquad (15)$$

is plotted in Fig.4. The results which we have obtained with the PDF-method are generally satisfactory for a large number of classes N_ϕ in the phase domain and small increments of particle diameters Δa. The detected distribution for $N_\phi = 40$ and $\Delta a = 0.116\mu m$ was

$\bar{a} = 2\mu m$; $\sigma_1 = 0.185\mu m$; $\sigma_2 = 0.416\mu m$

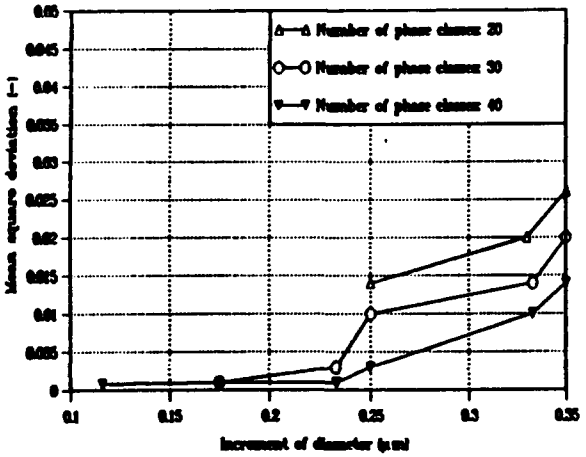

Figure 4: Mean Square Deviation of the Input Size Distribution and the Detected Distribution

The probability (P) method is based on the relative frequency of the random variable ϕ and can be considered as an integral method which leads to sufficient results even for a rough division of the phase domain. For the analysis with the P method we have considered a standard optical layout of a PDA system with a large angle between the laser beams. The phase response for water droplets was computed with a MIE computer code which was developed for axissymetrically particles in the generalized Lorenz-Mie theory. We have obtained identical results for spherical paricles with the STREU [2] computer code which is shown in Fig.5.

The example input distribution has the parameters $\bar{a} = 2.1\mu m$; $\sigma_1 = 0.5\mu m$; $\sigma_2 = 0.5\mu m$. The particle size distribution computed with a linear response characteristic leads to a detected size distribution which is broader than the input distribution. This effect does not have a great importance if the size distribution corresponds to the whole interval of analysis.

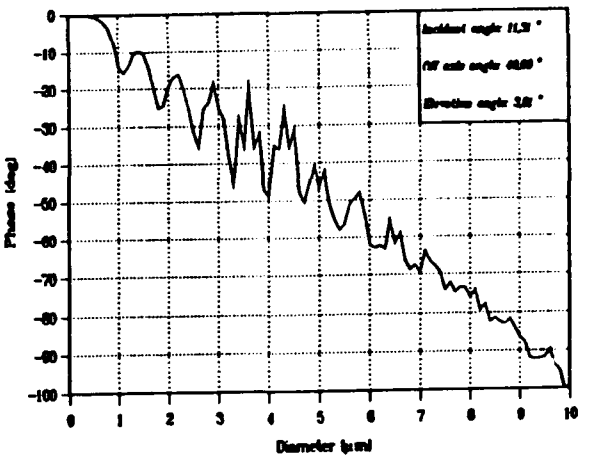

Figure 5: Phase Responses computed with STREU [2]

In this case the linear method and the probability method both lead to appropiate results. If the size distribution is tight, the influence of the particularity of the phase response becomes significant and the standard deviation of the distribution detected by the linear method is different. Fig. 6 shows the size distribution which was computed with the probabilty method. There is a good correspondence to the input distribution.

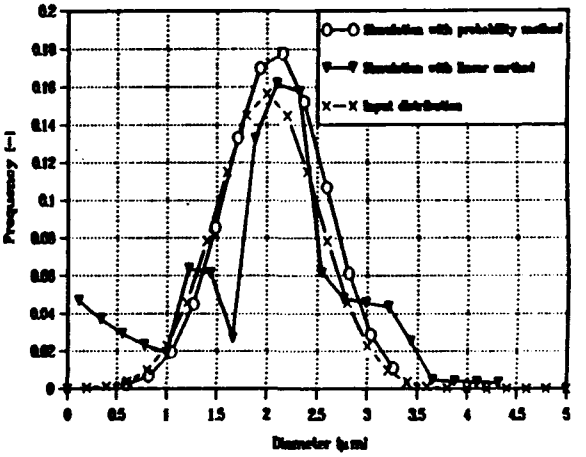

Figure 6: The Probability Method

2.2 The Equiprobable Distribution Method.

We build the size probability function for each measured phase difference

$$p_\phi(a,\tilde{\phi}) = \frac{1}{\sqrt{2\pi}\sigma_\phi} e^{-\frac{(\phi(a)-\tilde{\phi})^2}{2\sigma_\phi^2}} \phi'(a) \qquad (16)$$

so that the PDF $p_a(a)$ can be computed as follows:

$$p_a(a) = \int_{-\infty}^{\infty} p_\phi(\tilde{\phi}) p_a(a,\tilde{\phi}) d\tilde{\phi} \qquad (17).$$

In equation (16) the standard deviations of the uncertainties of the phase measurements are represented by σ_ϕ. These parameter should be set to the estimated experimental uncertainties in the phase measurements so that the process of computing the probability function will be realistic. We use $\sigma_\phi \to 0$ as a first approximation. Then

$$p_a(a,\tilde{\phi}) = \delta\left[\phi(a) - \tilde{\phi}\right] \cdot \phi'(a) \qquad (18).$$

With the assumption

$$\delta\left[\phi(a) - \tilde{\phi}\right] \cdot \phi'(a) = \frac{1}{N_k} \sum_{k(\tilde{\phi})=1}^{N_k} \delta\left[a - a_k(\tilde{\phi})\right] \qquad (19)$$

we can consider a as a discret random variable with the values

$$a_s = a_k(\phi_j) \qquad j = 1..N_\phi;\ k = k(\phi_j) = 1..N_k;\ s = 1,2,.. \quad (20)$$

and the associate probabilities

$$p_s = \frac{1}{N_k} \qquad (21).$$

With this assumption the particle size distribution is calculated in which each phase difference is attributed to all possible diameters. For each phase diffrence ϕ_j we consider that all roots of the equation $\phi(a) = \phi_j$ are equiprobable with the probabilty $1/N_k$.

3. APPLICATION TO DROPLET SIZE MEASUREMENT

Our application of the phase-Doppler-anemometry is the measurement of the size and the velocity of water droplets in a experimental setup for the separation of fine particles by heterogeneous condensation. In this experiments we like to measure the size of the droplets at any point within the cross section of the glass tube. In-situ measurement is absolutely necessary because sampling would cause additional evaporation or condensation and change the diameter of the droplets. We measured with an optical particle counter so far which allowed the measurement in the centre of the tube only. But this is not satisfactory because mass balances are only possible if the mass flow over the entire cross section can be measured. For this reason we developed the described evaluation methods. Those allow the measurement of the droplet sizes, which are between 1 and 10 µm, ant any point within the tube. Additionally we can compare the distribution with results from the optical particle counter

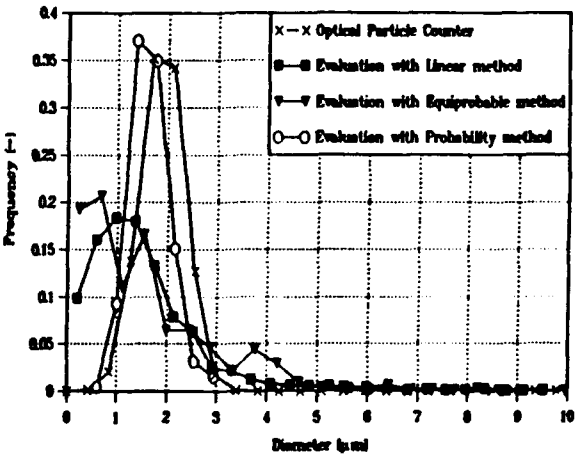

Figure 7: Application of the Evaluation Methods to Droplet Measurement

Fig. 7 shows a typical measurement result from the described condensation experiments. The commercial PDA-software evaluates the phase data with a linear method. In the case of small droplets and oscillations of the phase response this leads to a broadening of the particle size distribution. The use of such distributions for mass balances is problematic. Fig. 7 compares the described evaluation methods with an optical particle counter measurement. It is obvious that the equiprobable evaluation leads to the same results as the linear method. This is because the phase response oscillates around the linear approximation. The best result is obtained with the probability method. The broadening of the size distribution can be corrected and the method gives correct amounts for the droplet mean diameter and the standard deviation of the size distribution. This amounts are within the accuracy of the optical particle counter. The probability density method leads to similar results if the number of classes is sufficient. But because this is a pointwise method a lot more than 40 classes are necessary. Thus the probability method is the best one for practical application.

4. REFERENCES

[1] Naqwi, A., Ziema, M., Durst, F.:"Fine Particle Sizing using an extended Phase Doppler Anemometer" Symposium on Particle Characterization, Nuremberg, 1992

[2] STREU - A Computational Code for the Light Scattering Properties of Spherical Particles INVENT GmbH, D-8520 Erlangen, Germany

Session 19.
Swirling Flows

ROUTE TO CHAOS FOR A SWIRLING FLOW IN AN OPEN CYLINDRICAL CONTAINER WITH A ROTATING BOTTOM

Horn-Jiunn Sheen[1], Der-Liang Young[2] and Tzong-Yih Hwu[2]

[1]Institute of Applied Mechanics
[2]Department of Civil Engineering
National Taiwan University, Taipei 10764, TAIWAN

ABSTRACT

In this study, the *period-doubling* (subharmonic cascade) route to chaos is investigated for a swirling flow in an open cylindrical container driven by a rotating bottom disk after vortex breakdown has occurred. A glycerine-water mixture with about 85% glycerine in volume was used as the testing fluid. A non-intrusive optical method by using laser-Doppler velocimetry was used to investigate the physical characteristics of the swirling flow transition from the laminar to the turbulent regimes. Measurements were made for the circumferential velocity component with one of the parameters of the aspect ratio (height to radius) fixed at 2. The other relevant controlled parameter was the Reynolds number, which was allowed to vary by adjusting the rotating speed of the bottom disk. Results depicted that the flow was steady when the Reynolds number was below 1850. The onset of periodic flow was found when the Reynolds number ranged from 1850 to 1900. As the Reynolds number was increased to a value between 2100 and 2200, the flow was subharmonically bifurcated into a *period-doubling* motion. The flow bifurcated again through a subharmonic cascade mode with four peaks as observed in the power spectra diagrams when the Reynolds number reached between 2300 and 2400. With a further increase in Reynolds number, the flow finally became a chaotic motion.

1. INTRODUCTION

A swirling flow in cylindrical containers (closed or open) with a rotating bottom disk as the endwall is an advantageous model for investigating the phenomenon of a vortex structure and its breakdown. The superiority of studying a vortex break in a rotating container flow to investigating those commonly observed in delta wing trailing vortices (Peckham & Atkinson, 1957) or swirling vortex tubes (Sarpkaya, 1971) lies in its lower Reynolds number and aspect ratio. The aspect ratio, $As = H/R$, is defined as the ratio of the height of the fluid in the container above the bottom disk, H, to the inner radius of the container, R. The rotating speeds, Ω, are adjusted to obtain various Reynolds numbers, $Re = R^2\Omega/\nu$, where ν is the kinematic viscosity of the working fluid. Due to its technological relevance, the study of a swirling flow in a cylindrical container has drawn tremendous attention from both experimentalists and numerical modellers.

In the category of a closed rotating disk-cylinder flow system, Vogel (1968) and Escudier (1984) were the pioneers in conducting flow visualization experiments to establish the boundaries of steady separation vortices in a parameter space by using the laser-induced fluorescence technique. One, two, or three steady breakdown bubbles on the rotating axis were observed. On the other hand, Ronnenberg (1977) used laser-Doppler velocimeter to perform detailed measurement of flow structure for the case of one vortex breakdown bubble. The undulating flows were also reported for higher Reynolds numbers. From these results, the regimes for steady and unsteady vortex breakdown were classified according to the system parameters of Reynolds number and aspect ratio. Recently, Roesner (1990) re-examined the salient features of the recirculation bubbles for a wide range of nondimensional parameters. What distinguished Roesner's findings from those of previous studies was the existence of vortex breakdown under the unsteady or nonsymmetric modes for the onset of secondary flows. With the advent of computer technology, numerical solutions of finite geometry using the Navier-Stokes equations under the assumption of an axially symmetric characteristic of the flow were undertaken. For example, Lugt and his collaborators (1982, 1987) mainly confirmed the steady vortex bubbles observed from experiments, although some oscillating vortex cells were found. A similar steady and unsteady numerical simulation of recirculation bubbles of a vortex breakdown was also performed by Neitzel (1988). Lopez and his collaborators (1990a, 1990b, 1992) also simulated the steady as well as periodic modes of vortex breakdown for As=2.5 with Re up to 4000. To illustrate the chaotic behaviors, the concept of Lagrangian chaotic advection was introduced. Daube & Sorensen (1989) also found a critical Reynolds number (Re_c=2400 $\pm$ 15) for the criterion to distinguish the steady and unsteady vortex breakdown with As=2. When Re reached as high as 5000, oscillatory flow still prevailed. Besides the critical Reynolds number, they also reported findings for the period-doubling phenomenon as well as a hysteresis effect on the frequency of periodic oscillations. Young & Liao (1991) even extended Re to as high as Re=10000 and revealed the highly chaotic characteristics of a flow field through a supercritical Hopf bifurcation process.

As far as an open cylindrical container with a rotating disk is concerned, only a very few studies are available to the knowledge of the writers. Spohn *et al.* (1993) conducted a thorough investigation with a glycerine-water mixture via the flow visualization technique to establish a vortex breakdown diagram similar to Escudier's closed system. They found that when the aspect ratio was less than 2.5, the flow became unsteady as the Reynolds number reached a critical value of 2200. Similar trends were also found by Lin (1992). Hyun (1985) carried out a numerical calculation of an open tank with a free surface driven by a rotating bottom. No evidence for the formation of vortex breakdown was found for the case of As=0.5 and Re=100, however. Lin (1992) also extended his numerical simulation to the conditions of As=2.0 and Re=1325 and found one steady vortex breakdown, which compared favorably to his experimental results. Two steady separating vortex bubbles were simulated by Young & Liao (1992) when As=1.0 and Re=1000 was adopted. Both experimental measurements and numerical simulations also indicated that the free surface had a destablizing effect, in that it promoted the onset of periodic flows and chaotic motions.

Observation of the filling and emptying processes of the vortex breakdown bubbles conducted in flow visualization experiments in general precluded measuring quantitatively the unsteady coalescence and separation of the vortex structure as Re became higher and higher. This drawback was overcome by the introduction of an optical measurement method using laser-Doppler velocimetry (LDV). The non-intrusion and non-interference of the flow field made LDV very suitable for this study, since any ascertainable disturbance introducing any antifact of hydrodynamic instability in our swirling system would be minimized. LDV also has a relatively small measuring volume and offers precise measurement for the velocity component with a proper optical arrangement. Further, the LDV system has very high frequency response compared to the characteristic frequency of the flow motion in the present study. Unlike the axisymmetric vortex breakdown numerical models and flow visualization techniques (Lugt & Haussling, 1982; Neitzel, 1988), LDV provides more accurate detection of the flow field, as far as the unsteady and asymmetric characteristics of higher Reynolds number swirling flows were concerned. In the meantime, the measured velocity field enables us to study the flow transition from the laminar to the turbulent regimes. Therefore, the purpose of this study was to investigate the transient process from a steady laminar flow to chaotic motion and the associated route to chaos for a swirling vortex flow in an open cylindrical container with a rotating bottom.

2. EXPERIMENTAL

2.1 Experimental Set-up

The schematic diagram of the experimental set-up is shown in Fig. 1. A perspex cylindrical container, with an inner diameter of 184 mm, thickness of 8 mm and height of 563 mm, measuring from the bottom disk, was fixed on a flat perspex plate, which had a size of 550 × 470 mm. The plate was mounted on a table through six steel rods. The cylindrical container was surrounded by a rectangular tank, which was also fixed on a bottom plate with inner dimensions of 420 × 320 × 600 mm. The region between the test section of the cylindrical container, and the rectangular tank was filled with water. The water temperature is kept constant within $\pm 0.1^{\circ}C$ by using a constant temperature bath. A perspex plate was utilized as a cover to close the rectangular tank and, in the meantime, to prevent the testing fluid from coming in contact with ambient air. A rotary bottom disk with a diameter of 182 mm, also made of perspex, had a clearance of 1 mm to the container wall. The disk was driven by a 1/4 Hp DC motor connected to a worm-gear reducer to adjust the rotating speed. The rotating speed of the bottom disk, Ω, was varied from 25 to 500 rpm. For the measurements of rotating speed, burst counts were generated by an optical shaft encoder and fed into a frequency-to-voltage counter. The voltage was then compared with the command voltage closing the loop. The accuracy for the rotating speed readout was within ±0.5%.

A glycerine-water mixture with 85% glycerine in volume was used as the working fluid. During the measurements, the temperature of the surrounding water was kept at 25° C by using a constant temperature bath. The dynamic viscosity and mass density of the working fluid were 114.4 cP (P=$g/cm\ sec$) and 1.232 g/cm^3 with a probable error of 0.1 cP and 0.002 g/cm^3, respectively, at the beginning of the experiment. Since the dynamic viscosity of the testing fluid was sensitive to the variation in temperature, the value at the end of the experiment was carefully checked again. The aspect ratio was kept at 2 in this study. The

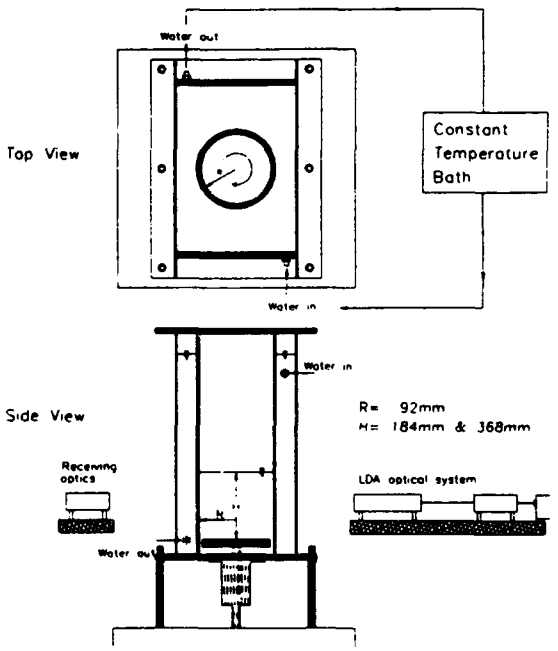

Fig. 1 The schematic diagram of the experimental set-up.

controlled parameter of the Reynolds number ranged from 1500 to 4000. Since we paid more attention to temporal response than to spatial variations, velocity measurements at a fixed position were performed. The measurement position for LDV was selected to be on the meridional plane about 50 mm above the rotating disk and 32 mm from the rotating axis of the container and away from the solid boundary and the free surface.

2.2 Measurement Technique

Dual-beam forward-scattering laser-Doppler velocimetry (LDV) was employed to measure the circumferential velocity component. We adopted a 300 mW Argon-ion laser as the light source with an output beam diameter of 0.82 mm. A green light beam with a wavelength of 514.5 nm was obtained by using an optical filter. The focusing lens had a focal length of 350 mm and half angle of 3.983°. A 2.27X beam expander was used to reduce the measuring volume dimensions and to increase the signal-to-noise ratio (SNR). The dimensions of the ellipsoidal measuring volume were estimated to be about 123 μm in diameter and 1.77 mm in length. A Bragg cell, frequency shifter, was utilized to extend the measurement range for low speed flow even with a reversed flow and, further, to minimize the fringe bias errors. A photomultiplier was used as the photo detector with proper amplification. One counter-type signal processor with DMA interface connected to a personal computer was then employed for data acquisition and data processing. The uncertainty for the LDV optical and electronic system was estimated to be less than 2%.

Measurements were made for the swirling flow with various Reynolds numbers. For each measurement, 5120 data were sampled. The typical sampling rates in this experiment were from about 100 to 200 data points per second, which was much higher than the characteristic frequencies in the flows. In other words, we had a very high Nyquist sampling rate in this study. Since the LDV signals were randomly sampled, the data recorded by the computer included both the velocity information and the duration between data. The histograms were then obtained by using the above-mentioned information. In order to perform spectral analyses, the data needed further processing. Equal time-interval data were retrieved by using a linear interpolation method. We employed 4096 points to calculate the power spectra of velocity fluctuation and applied the Hanning window to reduce the leakage effect of the Gibbs phenomenon.

3. RESULTS AND DISCUSSION

In this study, flow conditions with twelve Reynolds numbers ranging from 1500 to 4000 were faciliated. Figure 2 shows the histogram of the circumferential velocity in a clockwise direction, which coincides with the direction of the rotating bottom disk. In the figure, all data are depicted in a duration of fifteen seconds. The velocity power spectra are shown in Fig. 3. The diagrams of Poincaré sections diagrams, obtained from their phase planes, in which x and y coordinates are circumferential velocities and their associated accelerations, respectively, are sketched in Fig. 4. All Poincaré sections diagrams are plotted with the local maxima of their circumferential velocities for a duration of ten seconds. Detailed descriptions are given below.

3.1 Steady Flow

Figure 2.1 shows the histogram of the flow for Re = 1500, which confirms that the flow field can be regarded as a steady laminar one. The power spectrum in Fig. 3.1 only

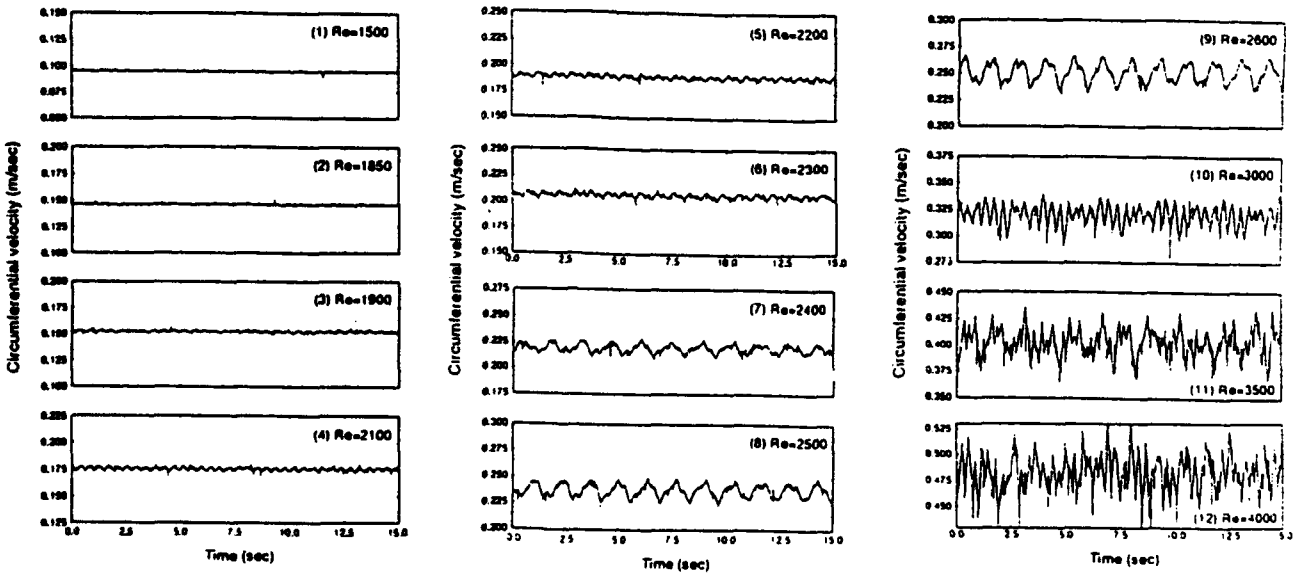

Fig. 2 The histograms of circumferential velocity with various Reynolds numbers.

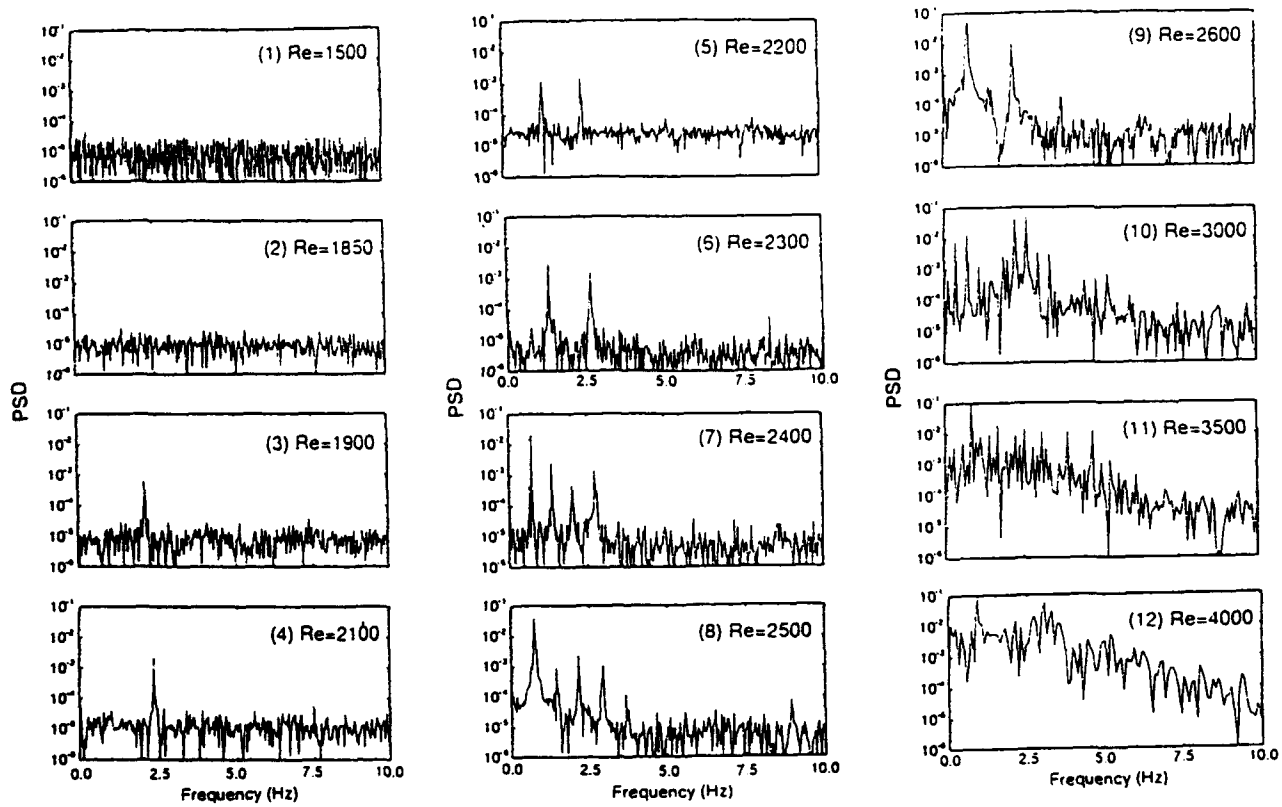

Fig. 3 The power spectra of circumferential velocity with various Reynolds numbers.

shows very low-level noise and, therefore, characterizes the steadiness of the flow pattern. The Poincaré section diagram for a steady flow should ideally have only one point. However, the Poincaré section in Fig. 4.1 provides other neighboring points since it was very difficult to obtain exactly one point as far as this experiment is concerned.

Results for Re=1850 similar to those for Re=1500 were obtained. The diagrams of the histogram, power spectrum and Poincaré section are shown in Figs. 2.2, 3.2 and 4.2, respectively. It can be seen that the fluid motion still maintains a laminar and steady regime.

3.2 Periodic Flow

The sinusoidal oscillation of circumferential velocity was observed for Re=1900. The histogram in Fig. 2.3 reveals a periodic motion with a small amplitude. An isolated peak with frequency f_1=2.094 Hz is clearly identified from the power spectrum diagram shown in Fig. 3.3. The Poincaré section diagram for this periodic flow should also theoretically possess exactly one point. Nevertheless, some neighboring points which are similar to those for steady flow cases can be seen in Fig. 4.3. The critical Reynolds number for the onset of periodic motion is conjectured to be in a range from 1850 to 1900.

Under the condition of aspect ratio 2, the critical Reynolds number associated with the onset of periodic motion for this measurement was found to be much lower than those of previous studies by Escudier (1984), who reported about 2500 for a closed container, and by Spohn *et al.* (1993), who reported about 2200 for an open container. The free surface had a destablizing effect and promoted the onset of periodic flows. Spohn *et al.*'s results may be attributed to the difficulty of exactly distinguishing the critical margin between steady and unsteady flow by using a flow visualization method.

As the Reynolds number increased to 2100, the periodic motion was more vividly observed from the histogram as shown in Fig. 2.4. The amplitude of the velocity oscillations increased gradually. In the power spectrum diagram of Fig. 3.4, one peak is found at a frequency of f_1=2.345 Hz and is higher than that of Re=1900. The Poincaré section diagram in Fig 4.4 shows a similar trend.

3.3 Period-doubling Flow

For Re=2200, a distinct period-doubling phenomenon through subharmonic bifurcation was observed. From the histogram, as displayed in Fig. 2.5, the period was found to be about twice that for the case of Re=2100. The power spectrum in Fig. 3.5 shows two distinguishable peaks at f_1=2.473 Hz and $f_{\frac{1}{2}}$=1.255 Hz. The value of $f_{\frac{1}{2}}$ is about half that of f_1. From the nonlinear dynamic system theory, the Poincaré section for this phenomenon should theoretically have only two isolated points. However, the result for this experiment, as shown in Fig. 4.5, has some extra

points. This may be due to the weak coherent relation between the flow's velocity and acceleration, which are used in the phase plane. When the Reynolds number ranged between 2100 and 2200, a critical Reynolds number should have existed wherein the periodic motion bifurcated into a double-period motion.

When Re reached 2300, the flow characteristics were the same as those for Re=2200. The amplitude of oscillating velocity further increased, and the period was almost invariant as shown in Fig. 2.6. The power spectrum, shown in Fig. 3.6, also identifies two peaks at f_1=2.645 Hz and $f_{\frac{1}{2}}$=1.322 Hz, while $f_{\frac{1}{2}}$ is exactly half of f_1. These two frequencies are slightly higher than those for Re=2200. The intensity of peak $f_{\frac{1}{2}}$ became higher as Re increased and eventually dominated f_1. The Poincaré section in Fig. 4.6 reflects a similar trend to that for Re=2200.

3.4 Period-quadrupling Flow

A conspicuous period-quadrupling phenomenon occurred when Re reached 2400. The histogram shown in Fig. 2.7 displays a composed wave form, and the period of the motion is about twice that for Re=2300. In addition to the original two peaks, f_1 and $f_{\frac{1}{2}}$, in the power spectrum, two extra ones, $f_{\frac{3}{4}}$ and $f_{\frac{1}{4}}$, are generated. The power spectrum in Fig. 3.7 obviously shows these four peaks with f_1=2.729 Hz, $f_{\frac{3}{4}}$=2.009 Hz, $f_{\frac{1}{2}}$=1.365 Hz and $f_{\frac{1}{4}}$=0.720 Hz, respectively. The values of f_1 and $f_{\frac{1}{2}}$ were also slightly higher than those for Re=2300. The intensity of the peak at $f_{\frac{1}{4}}$ became higher as Re increased and eventually dominated the flow. As discerned from this figure, $f_{\frac{1}{4}}$ and $f_{\frac{3}{4}}$ were about half of $f_{\frac{1}{2}}$ and $f_{\frac{1}{2}} + f_1$, respectively, and the results are in agreement with the period-doubling phenomenon. Similarly, the Poincaré section diagram in this case should theoretically have only four isolated points. The results as illustrated in Fig. 4.7 are approximately in agreement with the expected outcomes for this case. For a Reynolds number in the range between 2300 and 2400, there should also exist one critical Reynolds number from which the flow will bifurcate through subharmonic instability to excite another double-period motion.

When Re was increased to 2500, the histogram, power spectrum and Poincaré section diagrams were as depicted in Figs. 2.8, 3.8 and 4.8, respectively. The four peaks shown in the power spectrum are f_1=2.914 Hz, $f_{\frac{3}{4}}$=2.137 Hz, $f_{\frac{1}{2}}$=1.438 Hz and $f_{\frac{1}{4}}$=0.738 Hz, respectively. The results for this case are similar to those for Re=2400. Moreover, these four peaks also show a slight down-shift as compared to those for Re=2400. The intensities of the oscillating modes near $f_{\frac{1}{4}}$ obviously increase, and the distribution of the power spectrum density (PSD) around $f_{\frac{1}{4}}$ is broadened.

3.5 Chaotic Flow

The wave form of the histogram, shown in Fig. 2.9, lost regularity gradually as Re was increased to 2600. The broadband power spectrum shown in Fig. 3.9 indicates the behavior of chaotic motions. The Poincaré section in Fig. 4.9 also exhibits some nearly non-coherent points. For Re=3000, the histogram in Fig. 2.10 shows that the flow has almost lost its regularity. The power spectrum in Fig. 3.10 does not confirm any periodicity. The Poincaré section in Fig. 4.10 also reveals some random points. The flow develops into the chaotic regime.

For Re=3500, the wave form in the histogram in Fig. 2.11 has totally lost regularity. The power spectrum and Poincaré section, as shown in Figs. 3.11 and 4.11, respectively, obviously demonstrate that the flow moved in a random way.

When Re was increased to 4000, the fluctuations of velocity, as shown in Fig. 2.12, were further amplified. The power spectrum and Poincáre section results show clearly the chaotic characteristics of the swirling flow, as is shown in Figs. 3.12 and 4.12, respectively.

In the study of this swirling vortex flow, the inherent route to the onset of chaotic flow with successive period-doubling bifurcations exhibited phenomena similar to those observed in other flows, e.g. the Rayleigh-Bénard convection problem investigated by Gollub & Benson (1980).

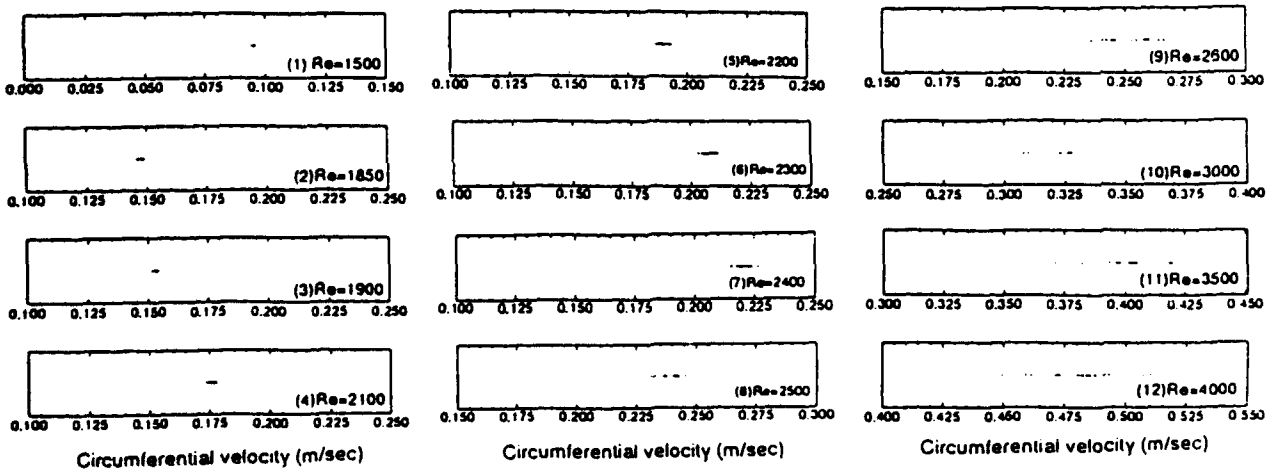

Fig. 4 The Poincaré section diagrams with various Reynolds numbers.

They explored the same scenario of route to chaos in one case in their experiments, which had an aspect ratio of 3.5, and a Prandtl number of 2.5 and used Rayleigh number as the control parameter. Other routes to chaos were also explored such as quasi-periodicity and phase locking, three frequencies and intermittency. Notably, in this study, the original frequency changed from 2.345 *Hz* to 2.729 *Hz* as the Reynolds number increased from 2100 to 2400. This frequency-shifting phenomenon was also found by Gollub & Swinney (1975) in their experimental study of a Taylor-Couette vortex flow system.

4. CONCLUSIONS

The period-doubling route to chaos for a swirling vortex flow in a open cylindrical container with a rotating bottom disk and an aspect ratio of 2 was studied by using laser-Doppler velocimetry. When Re was in a range between 1850 and 1900, the onset of periodic motion for this flow was found. The period for the flow with Re=2100 was 0.426 *sec*. The flow was subharmonically bifurcated into a double-period motion when Re was between 2100 and 2200. The period for the flow with Re=2300 was 0.756 *sec*. When the Reynolds number varied in the range from 2300 to 2400, the flow bifurcated again through the period-doubling mode with four peaks as observed from the power spectra diagrams. The period for the flow with Re=2400 was 1.389 *sec*. When the Reynolds number was further increased, the flow eventually showed chaotic motions.

ACKNOWLEDGMENTS

The authors would like to thank the National Science Council of the Republic of China for financial support under grant No. NSC-82-0410-E-002-191.

REFERENCES

Brown, G.L. & Lopez, J.M. 1990b, Axisymmetric vortex breakdown: Part 2. Physical mechanisms, J. Fluid Mech., vol. 221, pp. 553-576.

Daube, O. & Sorensen, J.N. 1989, Simulation numérique de l'écoulement périodique axisymétrique dans une cavité cylindrique, C.R. Acad. Sci., vol. 308, Ser. II, pp. 463-469.

Escudier, M. P. 1984, Observations of the flow produced in a cylindrical container by a rotating endwall, Exp. Fluids, vol. 2, pp. 189-196.

Gollub, J.P. & Swinney, H.L. 1975, Onset of turbulence in a rotating fluid, Phy. Rev. Lett., vol. 35, pp. 927-930.

Gollub, J.P. & Benson, S.V. 1980, Many routes to turbulent convection, J. Fluid Mech., vol. 100, pp. 449-470.

Hyun, J.M. 1985, Flow in an open tank with a free surface driven by the spinning bottom, J. Fluids Eng., vol. 107, pp. 495-499.

Lin, G.H. 1992, Vortex breakdown in a circular tank with free surface, M.S. Thesis, National Taiwan University, Taipei, Taiwan.

Lopez, J.M. 1990a, Axisymmetric vortex breakdown: Part 1. Confined swirling flow, J. Fluid Mech., vol. 221, pp. 533-552.

Lopez, J.M. & Perry, A.D. 1992, Axisymmetric vortex breakdown: Part 3. Onset of periodic flow and chaotic advection, J. Fluid Mech., vol. 234, pp. 449-471.

Lugt, H.J. & Haussling, H.J. 1982, Axisymmetric vortex breakdown in rotating fluid within a container, J. Applied Mech., vol. 49, pp. 921-923.

Lugt, H.J. & Abboud, M. 1987, Axisymmetric vortex breakdown with and without temperature effects in a container with a rotating lid, J. Fluid Mech., vol. 179, pp. 179-200.

Neitzel, G.P. 1988, Streak-line motion during steady and unsteady axisymmetric vortex breakdown, Phys. Fluids, vol. 31, pp. 958-969.

Peckham, D. H. & Atkinson, S. 1957, Preliminary results of low speed wind tunnel tends on a Gothic wing of aspect ratio 1.0, Aero. Res. Counc., CP-508.

Roesner, K.G. 1990, Recirculation zones in a cylinder with rotating lid, in Topological Fluid Mechanics, ed. H. K. Moffatt and A. Tsinober, pp. 699-708, Cambridge Univ. Press, London.

Ronnenberg, B. 1977, Ein selbstjustierendes 3-Komponenten Laserdoppleranemometer nach dem Vergleichsstrahlverfahren, angewandt für Untersuchungen in einer stationären zylindersymmetrischen Drehströmung mit einem Rückstromgebiet, MPI Bericht 20.

Sarpkaya, T. 1971, On stationary and traveling vortex breakdowns, J. Fluid Mech., vol. 45, pp. 545-559.

Spohn, A., Mory, M. & Hopfinger, E.J. 1993, Observations of vortex breakdown in an open cylindrical container with a rotating bottom, Exp. Fluids, vol. 14, pp. 70-77.

Vogel, H. U. 1968, Experimentelle Ergebnisse über die laminare Strömung in einem zylindrischen Gehäuse mit darin rotierender Scheibe, MPI Bericht 6.

Young, D.L. & Liao, C.B. 1991, The Hopf bifurcation in the cylindrical cavity, Numerical Methods in Laminar and Turbulent Flow, vol. 7, Part 1, pp. 729-739.

Young, D. L. & Liao, C. B. 1992, Axisymmetric vortex breakdown with free surface, Proc. of Computational Fluid Dynamics, Taichung, Taiwan, pp. 371-383.

CONFINED MIXING BETWEEN A COMPRESSIBLE CENTRAL JET AND A SWIRLING CO-FLOWING OUTER STREAM

by

S.C. Favaloro and E.A. Brizuela

Aeronautical and Maritime Research Laboratory
Defence Science & Technology Organisation
Melbourne, Australia

1. SUMMARY

The mixing between a compressible central jet and a swirling co-flowing outer stream in an axisymmetric isothermal rig has been studied using a two component laser Doppler velocimeter (LDV). The experimental results were compared with the predictions of a computational scheme which used the k - ε closure model. The comparisons confirmed the poor performance of the k - ε model in predicting mean velocities in recirculation regions and turbulence quantities across shear layers. The limitations of using on-axis LDV systems with long measurement volumes to perform measurements across flow regions with large velocity gradients and length scales comparable to the volume length was demonstrated. In addition it was found that LDV measurements of mean and fluctuating quantities may not be sufficient to describe and reproduce cases of strong shear; consideration of other stochastic properties of the measured ensembles is also required to separate large scale motions from conventional turbulence.

2. INTRODUCTION

The use of computer codes to predict the gas flow through gas turbine and ramjet combustion systems has been widely recognised as a valuable aid in the design of more efficient combustors. The flowfields in these systems can contain regions of highly turbulent recirculating flow and compressible free shear layers with large velocity and density gradients. In addition, swirl is usually implemented in these systems to improve overall combustor performance such as increased combustion efficiency and reduced formation of pollutants. Accurate numerical simulation of these flows still remains a problem due to their inherent complexity and the requirement for turbulence closure models, which are used in the time mean solution of the equations governing the flowfield. In experimental studies of these flows, it has been well documented that laser based methods, such as laser Doppler velocimetry (LDV), are the most viable for obtaining accurate data for code validation purposes, since the problems of directional ambiguity, flow disturbance and inadequate frequency response to high level turbulent fluctuations, which can occur with non-optical techniques, are avoided.

A common feature of the comparisons between LDV data and numerical predictions (eg, Nejad et al, 1989) is that in turbulent swirling flows, some computer codes underpredict the turbulent kinetic energy while making reasonable predictions of mean velocity components. These differences may not be entirely due to inadequacies in the computer code, since LDV systems themselves can contribute to the discrepancy by over predicting the turbulence levels, especially in regions of high shear. This effect is most pronounced when the experimental flow is either unstable, or the LDV system has a spatial resolution comparable with large turbulent length scales in the flow. The current study compares the predictions of a computer program, which uses the k - ε closure model, with LDV measurements obtained from experiments in a confined axisymmetric co-flowing rig, which has a compressible centre jet emanating from a bluff body and surrounded by an isothermal swirling flow.

3. EXPERIMENTAL ARRANGEMENT

A schematic of the axisymmetric experimental rig is shown in figure 1(a). Plots of the streamlines and velocity vectors from the numerical simulation (see below) are shown in figure 1(b) to illustrate the flow pattern along with the sign convention adopted in this study. The rig was designed to provide two independently controlled, co-flowing, axisymmetric air streams which mix with each other in a cylindrical test section of length 1.5 m and diameter 152.4 mm. The test section was fabricated from a number of different pipe lengths and an optical access section which enabled LDV and total pressure measurements to be performed at axial intervals of approximately 37 mm.

The central jet was formed from air issuing from a convergent nozzle, of exit diameter 14.7 mm, which was centrally located in an axisymmetric centre body of diameter 80 mm. The outer co-flowing stream passed through a swirler, fabricated from 12 circular arc guide vanes, and through a tapered annular passage, 500 mm in length and 25 mm in width, before passing over the centre body at the start of the test section. Rig total pressures were set to provide nominal axial velocities of 52 m/s (U2) in the outer flow and 200 m/s in the central jet.

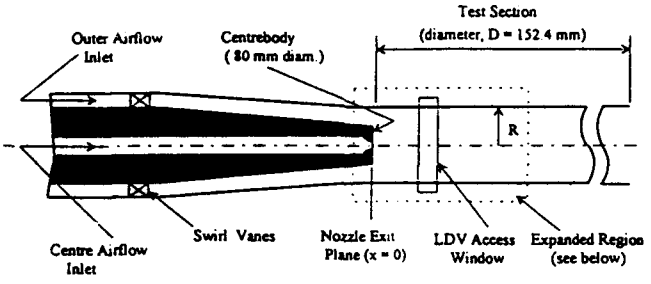

(a) - Schematic of experimental rig

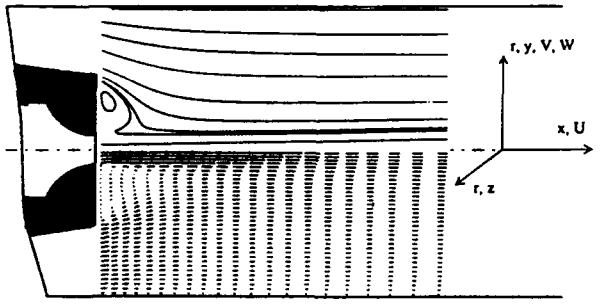

(b) - Expanded region showing flow pattern

Figure 1 -Experimental Rig and Flow Pattern

To enable LDV measurements to be performed, the outer flow was seeded with polydisperse sugar particles, which were generated by the atomisation of a 5 per cent sugar and water solution in a Thermo Systems Incorporated (TSI) model 9306 six jet atomiser. The seed was introduced to the flow in a settling chamber, well upstream of the test section, through a six-point manifold to provide a uniform particle distribution in the test section. Data published (Agarwal and Johnson, 1981) for the model 9306 atomiser suggests that atomisation of a 5 per cent salt/water solution will produce particles ranging in size from 0.5 to 3 micron, with a mean around 0.8 micron. - slightly larger particles can be expected with the equivalent sugar/water solution. A high pressure version of the TSI seeder was used to seed the central jet. A 50 cP Dow Corning fluid was used as the seed base, and was introduced to the flow upstream of the exit nozzle. To ensure equal concentrations of particles in both streams, the seeders were controlled so their output was in the same ratio as the volume flow ratio of the two streams.

4. LDV SYSTEM

The LDV used in the experiments was a TSI 9100-7 two channel, two colour system which was optimised for high speed flow measurement in the range -300 to 1100 m/s. The system operated in backscatter mode with frequency shifting on both channels. The combination of 13 mm beam spacing, 2.75 beam expansion and a 750 mm focussing lens gave ellipsoidal measuring volume dimensions of approximately 0.13 mm diameter and 4 mm length. The frequency/velocity conversions for both channels were usually around 8 m/s/MHz, but depended upon the final beam half angles that were measured once the crossing point was established. A 0.1 mm aperture in the field stop system reduced the measurement volume diameter seen by the photomultipliers, but the on-axis collection forced velocity realisations to be made over the full length of the measurement volume. Both channels had Bragg cells in one beam which provided a frequency shift of 40 MHz. The combination of 40 MHz frequency shifting against the mean flow direction and 45 degree beam orientation effectively eliminated any fringe bias, and allowed the maximum expected Doppler frequencies (around 55 MHz) to be well within the detectable range of the photomultipliers.

The whole system was mounted on a milling machine base which enabled the measurement volume to be located inside the test section with an accuracy of 0.05 mm. Radial and axial velocity components were obtained by locating the measurement volume on the rig centreline and traversing the milling machine along a vertical radius (y direction, figure 1b). Tangential and axial components were obtained by traversing the final focussing lens along a horizontal radius (z-direction, figure 1b), using a TSI model 9400 traverse table controlled by a TSI model 9430 positioner, .

Two TSI 1990 counter processors, a TSI 1998 interface and a PDP-11 computer constituted the data acquisition and processing system. The 1998 interface was set in 'non-priority' mode and provided coincident velocity measurements from both channels within a time interval of 1ms. The data transfer to the computer, via DMA, proceeded at a much faster rate than the velocity realisation rates in the two counters; hence, the data in most sections of the flowfield was fully velocity biased.

Corrections for velocity bias were made by particle interarrival time weighting (Nejad et al, 1989) with the time between velocity realisations transferred to the computer along with the velocity data. This was the preferred correction method, since the possibility of low data rates inhibited the use of constant time interval sampling, while the likelihood of zero velocity components in both channels (and the lack of simultaneous 3D velocity measurements) prevented the use of velocity magnitude weighting.

5. NUMERICAL SIMULATION

The flow situation was reproduced by means of solving the time-averaged conservation equations numerically. Turbulence closure was modelled by the two-equation k - ε model. Standard Dirichlet and Neumann conditions were applied at the boundaries. Logarithmic law-of-the-wall relations were enforced for the k - ε model at solid boundaries. The set of discretised conservation equations was solved using a finite volume technique (Cope, 1991, and Vanka et al, 1989), which features a co-located grid, the hybrid differencing scheme, and a pressure correction relation for the continuity equation (Patankar, 1980).

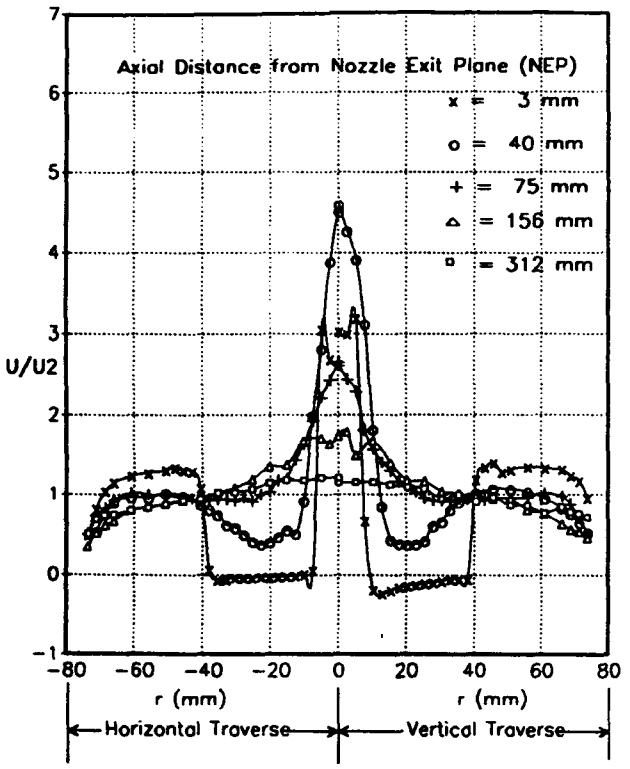

Figure 2 - Axial Mean Velocities

An attempt was made to improve the performance of the κ - ε model in the recirculation zones by modifying the constants in the ε equation using Richardson numbers. For a curved streamline the Richardson number, R_i, is defined by:

$$R_i = \frac{\textit{Production of turbulent KE due to curvature}}{\textit{Total production of turbulent KE}}$$

From Leschziner and Rodi (1981), the production terms on a curved streamline of radius R_c are :

$$\left(-2\overline{u_s u_n} + 4\overline{u_s u_n} + 2\overline{u_s^2} - 2\overline{u_n^2}\right)\frac{U_s}{R_c},$$

where s and n identify directions tangential and normal to the streamline respectively.

Retaining only the shear terms,

$$R_i = \frac{2\overline{u_s u_n}\, U_s / R_c}{G/\rho},$$

where G is the production of turbulent kinetic energy appearing in the standard k - ε model.

Substituting Boussinesq's hypothesis:

$$-\overline{u_s u_n} = \nu_t\left(\frac{\partial U_s}{\partial n} + \frac{\partial U_n}{\partial s}\right) = \nu_t \frac{\partial U_s}{\partial n}, \text{ for } U_n = 0$$

and assuming solid body rotation, ie., $\frac{\partial U_s}{\partial n} = \frac{U_s}{R_c}$, and for the case of axisymmetric swirl, where R_c = r, and U_s = W, then

$$R_{i\theta} = \frac{-2(W/r)^2}{G/(\rho\nu_t)}.$$

For a recirculation zone in the plane of motion, $U_s = \sqrt{U^2 + V^2}$. The radius of curvature is given by Durst and Rastogi (1979) as:

$$R_c^{-1} = \frac{UV\left(\frac{\partial V}{\partial y} - \frac{\partial U}{\partial x}\right) + U^2\frac{\partial V}{\partial x} - V^2\frac{\partial U}{\partial y}}{U_s^3},$$

whence the recirculation Richardson number (Srinivasan and Mongia, 1980) is

$$R_{ic} = \frac{-2\left[\left(UV\left(\frac{\partial V}{\partial y} - \frac{\partial U}{\partial x}\right) + U^2\frac{\partial V}{\partial x} - V^2\frac{\partial U}{\partial y}\right)/\left(U^2+V^2\right)\right]^2}{G/(\rho\nu_t)}$$

Then, following Rodi (1979), the constant C_1 in the κ - ε model is modified as:

$$C_1 = 1.42 e^{-\alpha_1 R_i \theta} e^{-\alpha_2 R_i c},$$

with empirical constants $\alpha_1 = 0.2$, and $\alpha_2 = 2.0$.

6. RESULTS and DISCUSSION

6.1 Measured Mean Velocities

Mean and turbulence data were collected by the LDV system at six axial locations at selected intervals in the parallel mixing region. Figure 2 shows profiles of mean axial velocity components at five of these locations which were gathered from traverses along horizontal radii (left side of the figure) and along vertical radii (right side of figure). The profiles illustrate the overall symmetry of the mixing flow field except for minor differences in the recirculation region close to the nozzle exit plane (x = 3mm). Other notable features include a centreline flow acceleration between 3 and 40 mm downstream of the nozzle exit, and a progressive broadening of the jet after 40 mm. In addition, there are high axial velocity gradients at the edge of the jet and the surrounding flow (65m/s/mm) and at the edge of the bluff centrebody (25m/s/mm).

Figure 3 shows profiles of tangential (left side of figure) and radial (right side) mean velocities at the same five axial locations. The swirl number of the flow entering the test section, calculated from the formula given in Nejad et al (1989), was approximately 0.3. The tangential velocity profiles for the outer flow are typical of free vortex flows (ie., W $\propto$ 1/r) and remain relatively constant throughout the measurement regime. The high levels of swirl still in evidence 300 mm from the nozzle exit plane indicates that the angular momentum of the outer flow has been maintained and relatively unaffected by the spread of the central jet. Near the boundary of the central jet the motion tends to a forced vortex

flow (ie., W ∝ r) which is then maintained to the centreline (ie., at r =0). Maximum tangential velocities of around 1.25 to 1.5 times the axial mean flow occur at the jet boundaries which is consistent with the large static pressure gradients observed therein. The radial mean velocity profiles correctly depict the flow in the recirculation region and its subsequent wake downstream of the bluff centrebody; ie.,radial outflow 3mm from the bluff body, inflow 40 mm downstream before reverting to a radial outflow as the central jet expands. In the outer region, the flow is directed towards the centreline up to 75 mm from the bluff body which is consistent with the approach angle of the flow entering the test section.

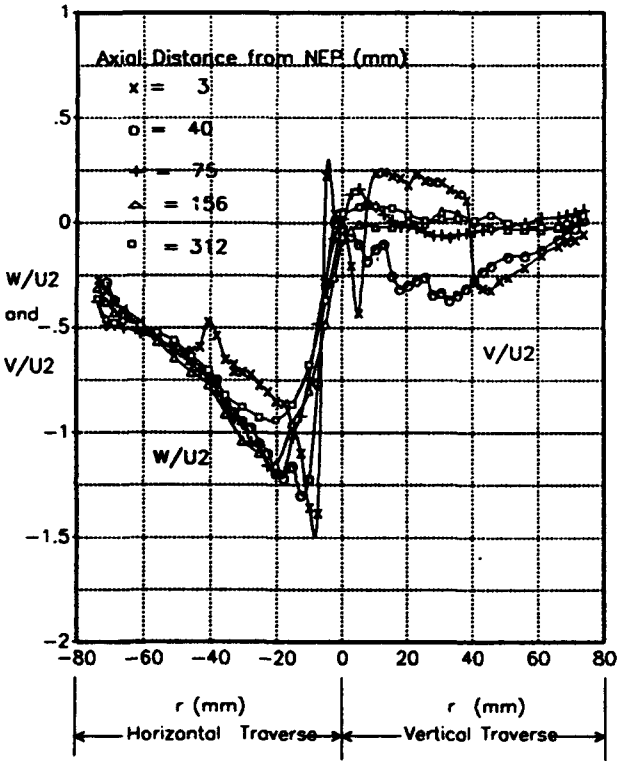

Figure 3 - Tangential and Radial Mean Velocities

Figure 4 shows an expanded view of the radial profiles in the centre section of the flow. On both sides of the centreline, the velocities are directed inwards in the central jet region up to an axial distance of 40 mm after which they are directed outwards. These features, along with the centreline axial flow acceleration (figure 2), indicate the presence of a vena contracta with minimum cross section between 40 and 75 mm from the nozzle exit.

6.2 Measured Turbulent Velocities

Figure 5 shows profiles of axial turbulent velocities at the same five axial locations normalised with respect to the outer flow inlet velocity. The levels of turbulent fluctuation are fairly low immediately downstream of the nozzle exit, but increase rapidly as the central jet expands, before decaying slowly in the streamwise direction.

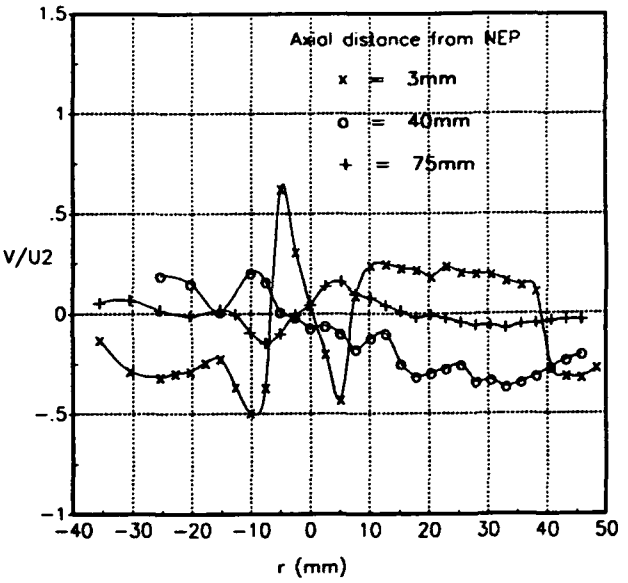

Figure 4 - Expanded View of Radial Mean Velocities

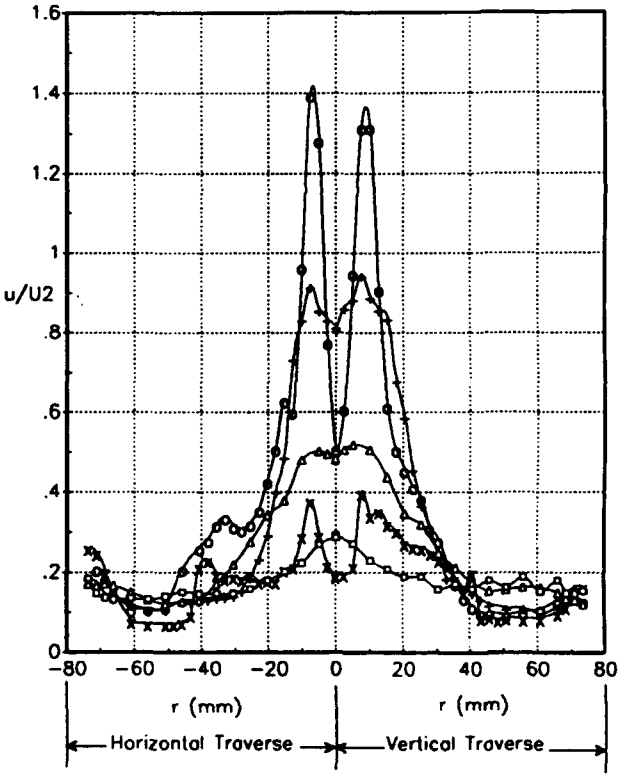

Figure 5 - Measured Axial Turbulent Velocities

Local maxima are evident in the shear layer between the central jet and the surrounding flow, and in the shear layer emanating from the edge of the bluff body. This latter feature is apparent only at axial locations up to one half of the centrebody diameter (40 mm) from the nozzle exit plane and is more pronounced in the results from the horizontal traverse.

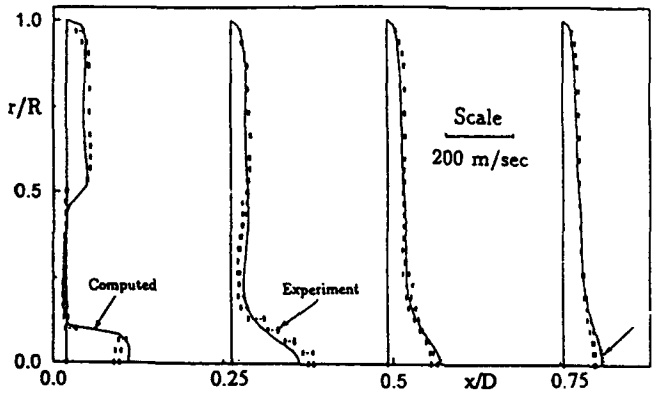

Figure 6 - Comparison of Mean Axial Velocities

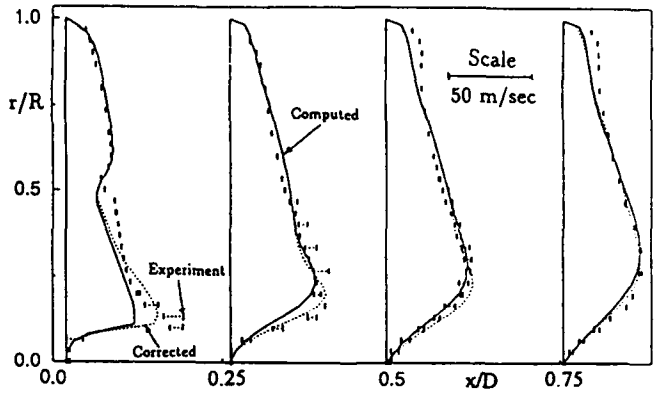

Figure 8 - Comparison of Mean Tangential Velocities

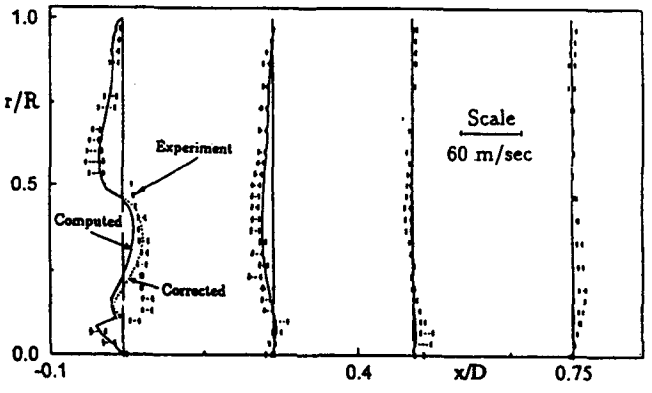

Figure 7 - Comparison of Radial Mean Velocities

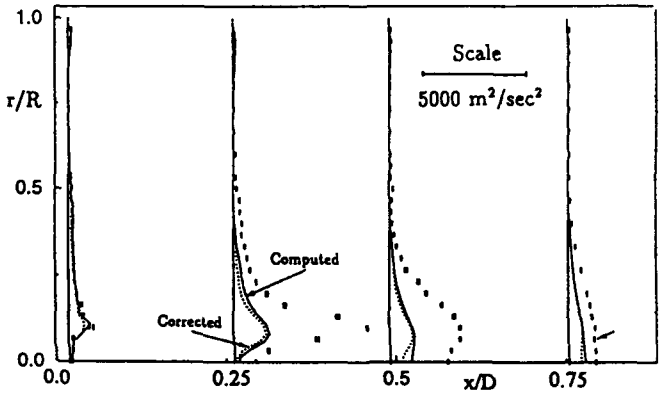

Figure 9 - Comparison of Turbulent Kinetic Energies

Rapid decay of turbulent fluctuations are usually indicative of high diffusion and dissipation rates. The apparent slow decay of the fluctuations in the shear layer at the boundary of the central jet suggest the presence of large scale turbulent structures which maintain their integrity and only dissipate slowly in the streamwise direction.

6.3. Numerical Comparisons

Figures 6, 7, & 8 show comparisons of calculated and experimental mean velocities up to x/D = .75 (x = 112 mm) from the nozzle exit plane. The numerical simulation of the axial mean motions (figure 6) was generally satisfactory, but the predictions of the radial and tangential mean velocities (figures 7 & 8) were unsatisfactory especially in the recirculation region. This was not unexpected since the poor performance of the k - ε model in strong recirculating flows is well documented.

The results of the simulation of the shear layer between the inner and outer flows were clearly unsatisfactory, as demonstrated in figure 9 which shows calculated and measured turbulent kinetic energy profiles. Maximum discrepancies between the calculated and experimental results occurred around 40 mm from the nozzle exit plane (ie., at x/D = .26) which corresponds to the region of maximum turbulence levels (figure 5) and maximum axial and tangential velocity gradients. Richardson number corrections (as outlined in the previous section) were attempted and are shown on figures 6 through 9 as dotted lines. Although the mean velocity predictions were somewhat improved, the corrections failed to yield levels of turbulent kinetic energy closer to the experimental data.

Figure 10 shows the LDV velocity histograms through the shear layer between the inner and outer flows 40 mm from the nozzle exit plane. Although the data has been corrected for velocity bias, the axial and tangential velocity distributions are skewed across the shear layer with very high turbulence levels. It is likely that these levels are not accurate indicators of the true local turbulence due to velocity realisations being achieved over the entire length of the measurement volume which spans a region of very high velocity gradient; ie., between r/R = .067 and r/R = .134 (which corresponds to a radial distance of 5 mm, only 1 mm longer than the measuring volume length) the measured mean velocities change by approximately 120 m/s (axial) and 48 m/s (tangential). Off-axis collection, in conjunction with smaller receiving apertures, would give greater spatial resolution and hence provide more accurate data on the shear layer structure.

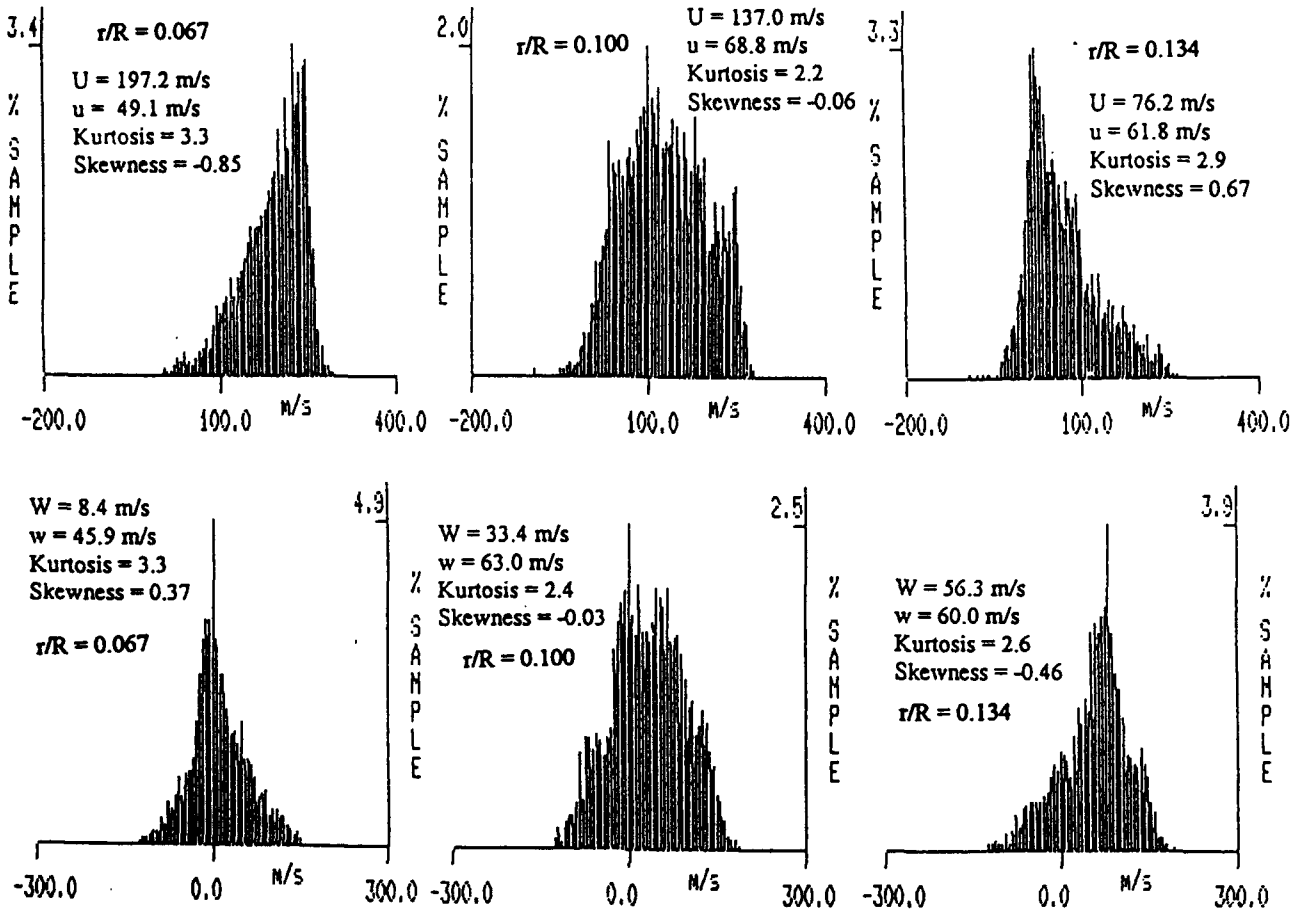

Figure 10 - Shear Layer Velocity Histograms at x = 40 mm

An additional cause for discrepancies between computed and measured results may possibly be found in the non-Gaussian nature of the histogram on the shear layer (r/R =0.1 , figure 10), wherein its stochastic properties depend on factors other than local factors. A phenomenon of this nature cannot be reproduced by a turbulence model which assumes the length scale to be determined by the local values of turbulent kinetic energy and its dissipation. The suggestion is that fluctuating quantities measured by the LDV system include elements of large scale structures. This is consistent with the pattern of turbulence decay discussed in 6.2 above.

7. CONCLUSIONS

The use of early generation LDV systems, which require long measurement volumes to measure high speed flows, can, in some flow situations, contribute to discrepancies between experimental results and the predictions of computer codes which model turbulence. As outlined above, artificially high turbulence in the measured values can arise when velocity realisations are made over shear layers with high velocity gradients and length scales comparable to measurement volume dimensions.

8. NOMENCLATURE

D	=	Test section diameter
k	=	Turbulent kinetic energy
r	=	Radial co-ordinate
R	=	Test section radius
U,V,W	=	Axial, radial, and tangential mean velocities
u,v,w	=	Axial, radial and tangential fluctuating velocities
x,y,z	=	Spatial co-ordinates
ε	=	Dissipation rate
ν_t	=	Turbulent viscosity
ρ	=	Density

REFERENCES

AGARWAL, J.K. and JOHNSON, E.M., 'Generating Aerosol for Laser Velocimeter Seeding', TSI Quarterly, Volume VII, Issue 3, pp 5 -12, July-Sept 1981.

COPE, W.K., 'On the Numerical Simulation of Turbulent Flows in Complex Geometries', M.S. Thesis, Department of Mechanical and Industrial Engineering, University of Illinois, Urbana-Champaign, 1991.

DURST, F and RASTOGI, A.K., 'Turbulent Flow over Two-dimensional Fences', *Proceedings*, Second Symposium on Turbulent Shear Flows, London, 1979.

LESCHZINER, M.A., and RODI, W., 'Calculation of Annular and Twin Parallel Jets Using Various Discretisation Schemes and Turbulence Model Variations', Transactions of the ASME, Journal of Fluids Engineering, Vol. 103, pp 352-360, June 1981.

NEJAD, A.S., VANKA, S.P., FAVALORO, S.C., SAMIMY, M., and LANGENFELD, C., 'Application of Laser Velocimetry for Characterisation of Confined Swirling Flow', Journal of Engineering for Gas Turbines and Power, Vol 111, No.1, pp 36-46, Jan., 1989.

PATANKAR, S.V., "Numerical Heat Transfer and Fluid Flow", Hemisphere Publishing Co., New York, 1980.

RODI, W., 'Influence of Buoyancy and Rotation on Equations for the Turbulent Length Scale', *Proceedings*, Second Symposium on Turbulent Shear Flows, London, 1979.

SRINIVASAN, R and MONGIA, H.C., 'Numerical Computations of Swirling Recirculationg Flow - Final Report', NASA Contractor Report CR-165196, NASA Lewis Research Center, 1980.

VANKA, S.P., KRAZINSKI, J.L., and NEJAD, A.S., AIAA Journal of Propulsion and Power, 5, 431, 1989

EXPERIMENTAL STUDIES OF CONFINED TURBULENT SWIRLING FLOWS

M. Wessman, J. Klingmann and B. Norén

Department of Heat and Power Engineering
Lund Institute of Technology
P.O. Box 118, S-221 00 Lund
Sweden

ABSTRACT

Two component LDV-measurements have been made in a turbulent flowfield following an axisymmetric confined sudden expansion, followed by a contraction. Three swirling flow cases and one non-swirling case are presented. Mean velocities and Reynolds stresses were measured at axial positions ranging from x/H= -2.1 to 19.5 and for a radial position range of r/R ± 0.99. For this radial range the corner eddy recirculation zone is clearly present in all cases. Its extension decreases with increasing swirl number. To characterise the influence of the periodic disturbances that are associated with swirling flows, an integration of an estimated power spectrum around the frequency of the periodic disturbances was made along the centre line. It was found that as much as 50 % of the turbulent kinetic energy is associated with the periodic disturbances.

1. INTRODUCTION

The application of this experiment is a simplified dump combuster. It is interesting to study how different inlet conditions influence the size of recirculation regions for flame holding, and how the mixing rate is enhanced by the swirl number. The objective of the present investigation is to provide an accurate database for turbulence model validation.

The swirling flow through a sudden axisymmetric expansion is a complex flow, pocessing several different flow regimes. The production of turbulence is increased above that of a non-swirling flow by the presence of the tangential velocity component, which results in additional velocity gradients. The flow phenomenon that is produced is found in a wide variety of important applications. In combustion systems, turbulent swirling flow is introduced to increase the mixing rate and reduce the flame size.

When the swirl is introduced, the wall bounded recirculation zone decreases and for a certain critical swirl number a central recirculation zone occurs, a phenomenon known as the vortex breakdown. The recirculating fluid generates regions of high turbulence in the shear layer between the reverse flow and the surrounding flow. There are at least four classes of mean flow fields, Gouldin et al (1985), that can be recognised in swirling flows, depending on the presence or absence of axial mean reversal flow in or near the vortex core: no reverse flow, a central recirculation zone, a torrodial recirculation zone, and a long backflow region or columnar flow. The central recirculation zone seems to occur at about a swirl number of 0.35, e.g. Hallet and Gunther (1984). The torrodial recirculation zone consists of cones having a hollow core shape, with positive axial mean velocity on the vortex centre line, e.g. Owen et al (1978), Juang et al (1990) and Yoon and Lilley (1984).

A further complex and little understood phenomenon which occurs in swirling flow, is an unsteady and periodic asymmetry in the flow field, known as the precessing vortex core (PVC), Gupta et al (1984). This periodic and unsteady behaviour has been observed by different investigators. Hallet and Gunther (1984) found the presence of a low frequency oscillation in the flow below the critical swirl and with increasing swirl the periodicity became weaker and less distinct, until just before the onset of the vortex breakdown it disappeared. Cassidy and Falvey (1970) found that the Strouhal number increases with increasing swirl number and that the Strouhal number appears to be independent of the Reynolds number above 10^5.

2. EXPERIMENTAL APPARATUS

2.1 Flow geometry

The test rig is a closed loop in which the test section is constructed of glass and is surrounded by a glass box. A picture of the test rig can be seen in figure 1. Both the expansion ratio and the contraction ratio are 1.93. Three different constant-angel axial flow-type generators have been used to generate the swirl. The vane angle for the three swirl generators is 26, 48 and 66 degrees and with a hub of 16 mm in diameter. For a Reynolds number of 10^4 the swirl generators produce a swirl number of 0.33, 0.58 and 0.99 in the inlet. The swirl number is defined as:

$$S = \frac{\int_0^R UWr^2 dr}{R_1 \int_0^R U^2 r dr}. \qquad (1)$$

To allow velocity measurements near the wall and measurements of the stresses of axial and radial velocities a refractive index matching fluid has been used, which means that the fluid has the same refractive index as the glass tube. This fluid is used both as working fluid and as surrounding fluid in the box. The fluid that has been chosen is a mixture of dibutyl phthalate (80 volume percent) and ethanol, which is a newtonian fluid. This makes the whole test section an optically homogeneous unit. For easy measurements at different locations, the probe is mounted on a traversing system. The resolution of the digital scale was 0.01 mm.

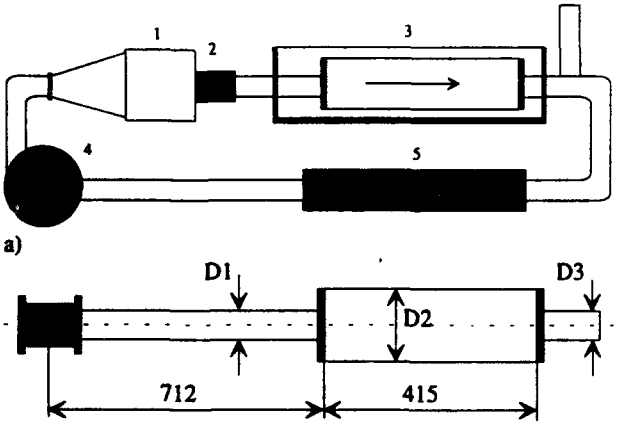

Fig. 1 a) Experimental setup. 1-Flow conditioner. 2-Swirl generator. 3-Test section. 4-Pump with an adjustable AC drive. 5-Heat exchanger.
b) Geometry of the test section. ($D_1 = D_3$, $D_2/D_1 = 1.94$).

2.2. LDV system

The velocity measurements were made with a two-component Dantec fiber-flow LDV system. The light source was a 4W Ar-ion laser operated at 0.5 W. The system operates in backscatter mode with a lens with a focal length of 310 mm. The size of the measuring volumes, based on $1/e^2$ intensity points, was roughly 50 microns in diameter and 600 microns in length, with a fringe spacing of 2.2 microns. For seeding material, metallic coated particles with a mean diameter of 4 µm were used. The signals from the photomultiplier were processed in Dantecs Burst Spectrum Analyser (BSA).

2.3. Experimental procedures

The measurements have been made with a data rate of about 200 Hz and with 20000 bursts in each location for each velocity component. To measure the stresses $\overline{uv}$ and $\overline{uw}$, the measurements were made in coincidence mode. The matching of the refractive index of the fluid makes it easy to measure the stresses, specially $\overline{uv}$. Another advantage is the linear relation between the translation of the probe and the translation of the measuring volume. The measurements have been made in a region of $-2.1 < x/H < 19.5$ and $-0.99 < r/R < 0.99$, where x is the axial direction from the expansion, H is the step high ($H=(D_1-D_2)/2$) and R the radius of the different sections. The inlet and outlet profiles have been measured in all cases and the condition for axisymmetry has been checked in four different cross-sections in each flow case. The measured variables are U, V, W, $\overline{uu}$, $\overline{ww}$, $\overline{vv}$, $\overline{uw}$ and $\overline{uv}$ in all cases. The values presented are the transit time weighted values. This is based on the standard deviation of the flow volume of each cross section. The standard deviation for flow volume is 4%. To obtain the volume flow of each section, an integration over velocities in each radial section has to be made. The transit time weighted value and time between data weighted value give almost the same results. The unweighted properties showed influences of velocity bias. The effect of the scattering light of the laser by the wall has not caused any trouble, but problems arose with particles attached to the surface. In the data this can be seen as a spike at zero velocity.

3. EXPERIMENTAL RESULTS AND DISCUSSION

3.1. Mean velocity distribution

In figures 2 to 5 the non-dimensional velocity vector plots are shown in the axial and radial plane for the non swirling case and for swirl numbers 0.33, 0.58 and 0.99. All velocity values have been normalised with the inlet axial bulk velocity, U_b. In the figures the recirculation zones are marked with a line for the axial zero mean velocities. For swirl number 0.33, no central recirculation zones occur. In figure 3 it can be seen how the velocity decreases after the expansion in the centre of the pipe, but the deceleration is not strong enough to cause vortex breakdown, which is in good agreement with the results of Samimy et al (1987). For swirl numbers 0.58 and 0.99, a torrodial central recirculation zone occurs, and the vortex breakdown occurs upstream in the inlet pipe. For these swirl numbers the flow consists of a reversed flow along the centre line followed by a second stagnation point, after which the central zone is surrounded by a reversed flow, which can be seen in figures 4 and 5. The fluid in the centre of the breakdown structure moves continuously downstream until a second, spiral, breakdown is reached. This has also been found by Bornstein and Escudier (1982). This secondary stagnation point occurs after the expansion for swirl number 0.58 and before the expansion for swirl number 0.99. The secondary breakdown of a spiral can exlpain the appearances of the velocity plots for the swirl number 0.58 and 0.99, where asymmetric behaviour can be seen, especially for swirl number 0.99.

The torrodial central recirculation zone that occurs for swirl numbers 0.58 and 0.99, has also been found by Yoon and Lilley (1984) and by Juang et al (1990). These experiments have a convergent exit in common.

The central recirculation zone occupies 31 per cent of the diameter (D_2) for swirl number 0.58 and 51 per cent for swirl number 0.99. The peak value in the reversed torrodial central recirculation zone also increases with increasing swirl number.

For swirl number 0.99, it reached a value of $0.59U_b$ located before the expansion.

The outer recirculation zone decreases with increasing swirl number. For no swirl the outer recirculation zone has a reattachment point at 10.4 steps and for swirl number 0.99 at 1.9 steps. The reversed axial mean velocity peak in the outer reciculation zone increases with increasing swirl number for the four cases. Figure 6 shows the extension of the outer recirculation zone as a function of swirl number, compared to other experiments. The extension of the outer recirculation zone in the non-swirling case is larger compared with the other experiments. One explanation can be the low Reynolds number compared with the other experiments. Durst and Tropea (1983) showed that in this range of Reynolds number there is a great Reynolds number dependency.

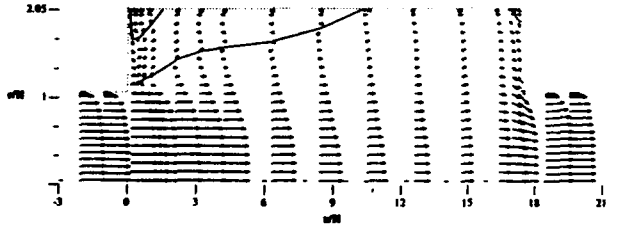

Fig. 2 Velocity vectors in axial and radial plane for swirl number zero.

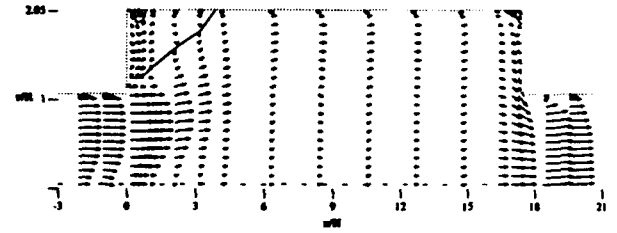

Fig. 3 Velocity vectors in axial and radial plane for swirl number 0.33.

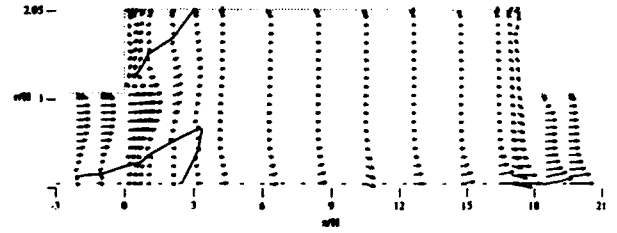

Fig. 4 Velocity vectors in axial and radial plane for swirl number 0.58.

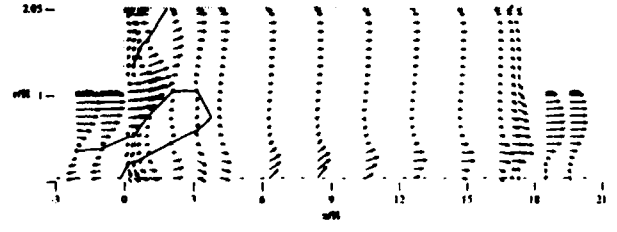

Fig. 5 Velocity vectors in axial and radial plane for swirl number 0.99.

In figure 2 to 5 a secondary recirculation zone -a corner eddy can be seen. The extension of the corner eddy for the non-swirling case is $0.09<x/H<1.56$ and the peak velocity in this area is $U/U_b=0.03$. For swirl number 0.99 the extension for the corner eddy recirculation zone is $0.11<x/H<0.42$ and the peak velocity in this area is $U/U_b=0.04$. In figures 2 to 5 it can be seen that the extension of the corner eddy decreases with increasing swirl number. The corner eddy recirculation zone has also been measured by Szczepura (1985) for a non-swirling case and by Ahmed et al (1992) for a swirling case.

In figure 7 the axial central velocities are plotted. The most significant part of this figure is the jet-like behaviour for swirl number 0.58. For swirl number 0.99, figures 5 and 7, a third breakdown can be recognised in the contraction.

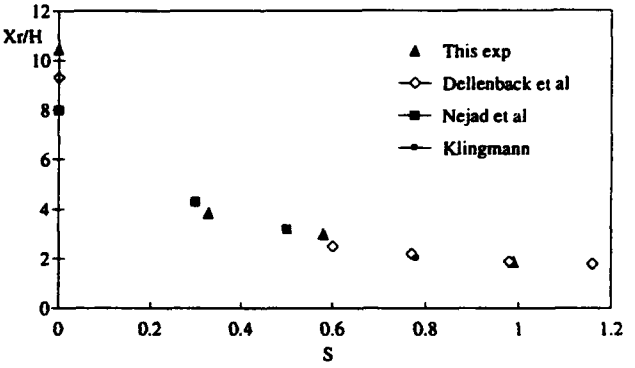

Fig. 6 The reattachment length of the outer recirculation zone as function of swirl number.

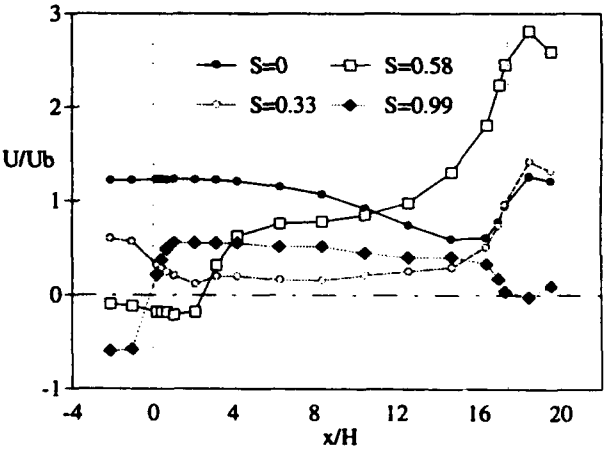

Fig. 7 Non-dimensional velocity at the centre line.

3.2. Turbulence distribution

Figures 8 to 11 show the evolution of the non-dimensional turbulent kinetic energy through the geometry. The turbulent kinetic energy is calculated as $k=(\overline{uu}+\overline{ww}+\overline{vv})/2$. The turbulent kinetic energy in the inlet increases with increasing

swirl number. At the core at the inlet, a peak value of 0.3% for the non-swirling flow and for swirl number 0.99 a peak value of 37% is reached. The kinetic energy after the expansion increases from 6% for the non-swirling case to 95% for swirl number 0.99. The location of this peak value moves upstream with increasing swirl number. After the contraction, behind the corner, there is a peak value near the wall in all cases.

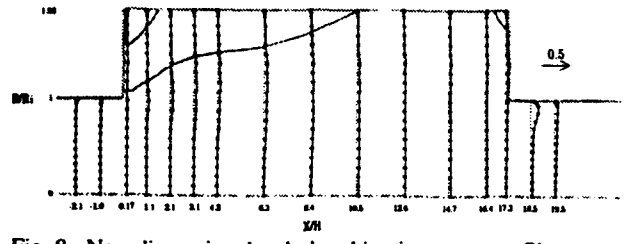

Fig. 8 Non-dimensional turbulent kinetic energy profiles (k/U_b^2) for the non-swirling case.

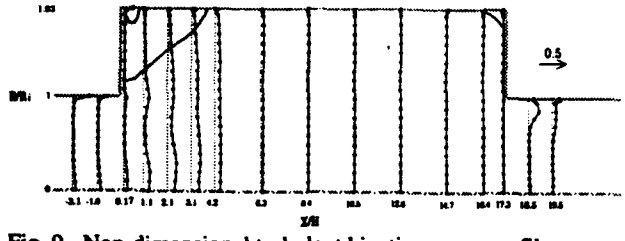

Fig. 9 Non-dimensional turbulent kinetic energy profiles (k/U_b^2) for swirl number 0.33.

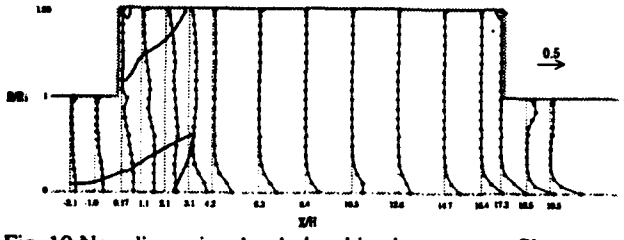

Fig. 10 Non-dimensional turbulent kinetic energy profiles (k/U_b^2) for swirl number 0.58.

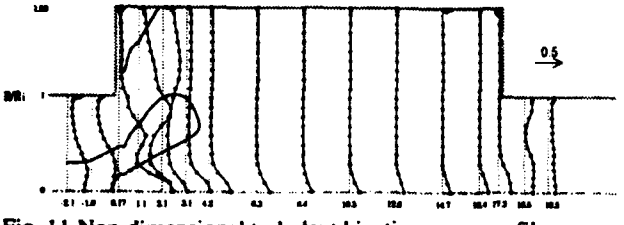

Fig. 11 Non-dimensional turbulent kinetic energy profiles (k/U_b^2) for swirl number 0.99.

The peak values of the turbulent kinetic energy are generally coincident and lie in the region bounded by the edge of the shear layer and main flow. It can be seen that the turbulent fluctuations have apparently dissipated faster for larger swirl numbers, but for swirl number 0.58 and 0.99 at the centre line, there seems to be a production of turbulent kinetic energy. The production of this turbulent kinetic energy at the centre line can depend on a secondary breakdown that occurs in a spiral and that a periodic disturbance precess about the axis. The axial mean velocity gradient is also great in the centre of the flow. In the non-swirling case, the production of turbulent kinetic energy is associated with an axial mean velocity gradient at the outer shear layer. In the swirling cases, the turbulent production of kinetic energy is also associated with the shear layer at the centre where the production is greater. Even for swirl number 0.33 the production of turbulent kinetic energy is greater in the centre than at the outer shear layer.

The effect of swirl on isotropy was examined. This is particularly important because the majority of the closure models assume isotropic turbulence. In the zero swirling case, it was found that the entire flow field was anisotropic. In the swirling case the magnitude of radial turbulent velocity was 25-300% of the axial turbulent velocity. The magnitude of the tangential turbulent velocity was 60-300% of the axial turbulent velocity. This implies the possibility of isotropic regions. For swirl number 0.33 small pockets of isotropic turbulent flow existed, particularly in the developing region. For swirl number 0.58 and 0.99 only small pockets of isotropic turbulent flow were found. Therefore one can conclude that these four flow cases were anisotrpic throughout the whole field.

3.3. Shear stresses

The value of the shear stress in the shear layer for the non-swirling case reaches a peak value of $\overline{uv}/U_b^2$=0.018. This result agree well with those obtained by Gould et al (1990) where a normalised peak value of 0.015 is measured. The shear stress $\overline{uw}$ remained insignificant. For the swirling flows two peaks were associated in the UV plane. The high stress values occurred at regions of maximum velocity gradients. For S=0.33, the shear stress is greater in the corner recirculation shear layer than in the core flow where there is a decrease in axial mean velocity. For S=0.58 and S=0.99, the peak value is located at the shear layer between the central recirculation zone and the main flow. The peak values located to the expansion increase with increasing swirl number from $\overline{uv}/U_b^2$=0.05 for S=0.33 to $\overline{uv}/U_b^2$=0.19 for S=0.99. The location of the peak value in the UV plane moves upstream with increasing swirl number , from x/H=2.1 for the non-swirling case to x/H=0.17 for swirl number 0.99. The peak value in the UW plane is of same magnitude as in the UV plane. In figures 12 and 13, the stress in the UV and UW planes is shown for swirl number 0.99. It is interesting to note that after the reattachment point the shear stress values are insignificant, apart from a small degree of stress at the centre line region for swirl number 0.58 and 0.99. This is probably associated with the spiral and the periodic disturbance. Peak values in $\overline{uw}$ and $\overline{uv}$ were also found in the area after the contraction. For increasing swirl number, the maximum peak value increases and the location of the peak value of the stress is moved upstreams in both the UV and UW plane.

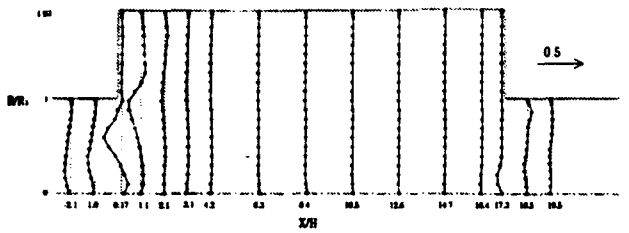

Fig. 12 Normalised shear stress profiles for swirl number 0.99 ($\overline{uv}/U_b^2$).

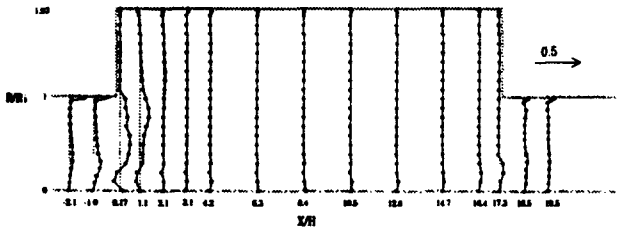

Fig. 13 Normalised shear stress profiles for swirl number 0.99 ($\overline{uw}/U_b^2$).

The correlation coefficients defined as $C_{uw}=\overline{uw}/u'w'$ and $C_{uv}=\overline{uv}/u'v'$ are shown in figures 14 and 14 for swirl number 0.33. The correlation coefficient describes whether or not a change, due to turbulence in one component of the velocity, depends on a change in the other component. For the non-swirling flow the correlation of C_{uw} is almost zero in the entire flow field and the correlation C_{uv} is positive except for small regions in the corner after expansion and before contraction. In the swirling cases the correlation coefficient peak value is higher compared with the non-swirling flow. In all cases there is a positive C_{uv} peak in the region of the outer recirculation zone. In the swirling cases there is a negative peak in C_{uv} that is associated with the central torrodial recirculation zone, or for swirl number 0.33 with the deceleration in axial mean velocity.

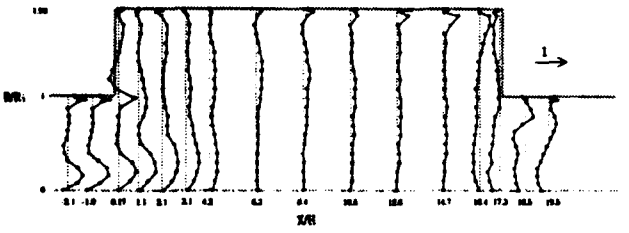

Fig. 14 Correlation coefficient C_{uw} for swirl number 0.33.

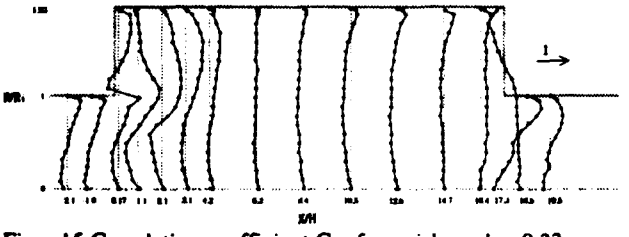

Fig. 15 Correlation coefficient C_{uv} for swirl number 0.33.

The C_{uw} positive peaks are associated with the central torrodial recirculation zone and with the deceleration of axial mean velocity for swirl number 0.33. For C_{uw} at the centre line, the correlation becomes negative after the secondary stagnation point.

3.4. PVC

A characteristic of swirling flows is the appearance of a large scale oscillation. The central part of the flow becomes unstable and a periodic distrubance starts to precess about the axis of symmetry. This is known as the precessing vortex core (PVC), Gupta et al (1984).

In order to characterise the influence of the periodic distrubances, the power spectrum was estimated as the cosine Fourier transform of the slotted auto correlation. Due to the low data density of the measurements, only the low frequency part of the spectrum could be obtained. Estimates of the auto correlation are sensitive to velocity bias where transit time weighting was used. An indication of the energy induced by the precessing can be obtained by integration of the power spectrum over frequencies near the frequency of the precessing, f_{PVC}, equation 2,

$$E_{PVC} = \int_{0.8f_{PVC}}^{1.2f_{PVC}} P(f)df \qquad (2)$$

where P(f) is the power spectrum of one velocity component.

This measure of the precessing strength is obviously crude in the sense that it does not differentiate between the energy induced by the precessing and the energy induced by the turbulence, but it has the advantage of being applicable without knowledge of a spectrum without the precessing.

Swirl number	0	0.33	0.58	0.99
fPVC (Hz)	5.5*	24.5	17.9	6.9

* A chosen value to calculate the E_{PVC}

Table 1. The frequency of periodic disturbances.

Through the auto correlation and the power spectrum, the frequencies for the three swirling cases were found and can be seen in table 1. Periodic disturbance is found in all the swirl cases. The low swirl number produced the highest PVC frequencies and for increasing swirl number the frequencies decrease. It seems that f_{PVC} would disappear if the swirl number were to increase further. The energy, E_{PVC}, for the central line measurements for the four cases were investigated. Figures 16-18 show the normalised E_{PVC}, where $E_{PVC}/u'u'$ is the axial and $E_{PVC}/w'w'$ is the radial respective the tangential energy component for the swirl cases. For the periodic disturbances most of the energy is located in the radial, respectively the tangential directions. For swirl numbers 0.33 and 0.58, the peak value for the radial and tangential energy is located at the expansion and for swirl number 0.58 it seems to have disappeared at the point where the central recirculation zone

disappears. For swirl number 0.99, the periodic disturbances seem to continue futher downstream.

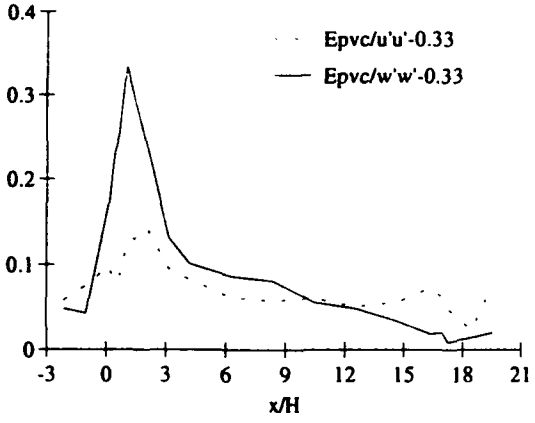

Fig. 16 Normalised E_{PVC} along the centre line for swirl number 0.33.

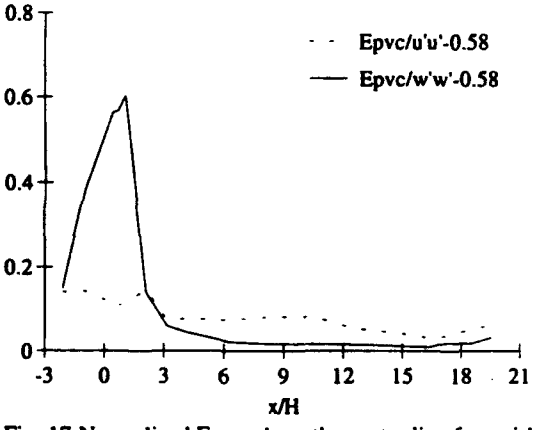

Fig. 17 Normalised E_{PVC} along the centre line for swirl number 0.58.

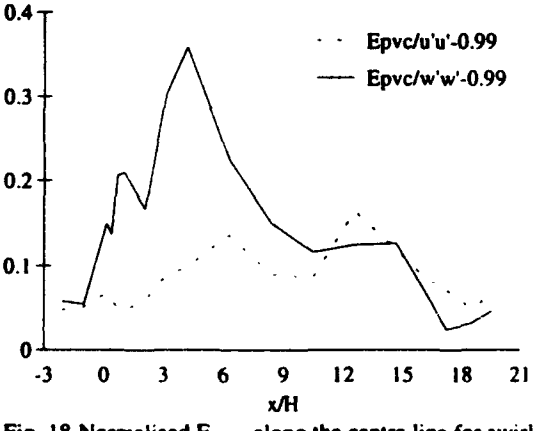

Fig. 18 Normalised E_{PVC} along the centre line for swirl number 0.99.

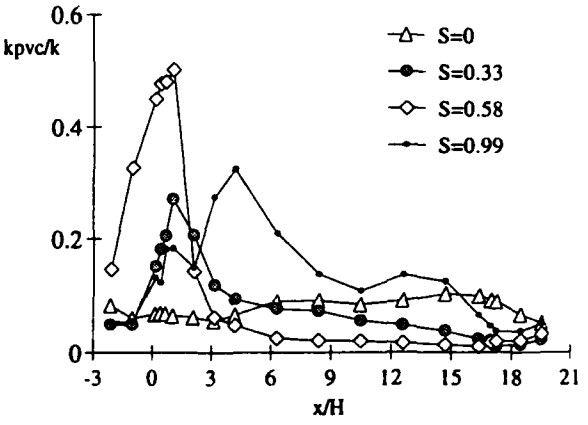

Fig. 19 k_{PVC}/k as function of x/H.

In figure 19 the normalised turbulent kinetic energy produced by the periodic disturbance is shown for all cases.

The strongest influence of the precession is found for swirl number 0.58 and it is located in the torrodial recirculation zone.

For swirl number 0.99 the peak of the PVC influence is not located in the torrodial recirculation zone, instead it is located in the spiral, see figures 5 and 11. For swirl number 0.58 the turbulent kinetic energy is large at the centre line, figure 10, but the influence of the PVC is rather small after the torrodial recirculation zone.

After the contraction, it seems that the influence of the PVC reaches the same level in all cases, figure 19, or that it has disappeared.

5. CONCLUSIONS

The purpose of the present study has been to obtain detailed experimental data for mean velocities and Reynolds stresses as a function of different inlet swirl numbers. For this purpose a refractive index matching fluid has been used, with good results. The measurements have indicated a number of interesting features of axisymmetric vortex breakdown. For swirl number 0.58 and 0.99, a central torrodial recirculation zone occurs, followed by a second stagnation point on the centre line.

The peak value of the turbulent kinetic energy increases dramatically in the swirling cases compared to the non-swirling case.

The influence of the PVC on the turbulent kinetic energy at the centre line has been investigated. The greatest influence is detected for swirl number 0.58. As much as 50% of the turbulent kinetic energy is associated with PVC influence.

ACKNOWLEDGEMENTS

Financial support from the Swedish Board for Technical Development, is gratefully acknowledged.

REFERENCES

Ahmed, S.A. and Nejad, A.S. 1992, Swirl effects on confined flows in axisymmetric geometries, Journal of Propulion and Power, vol. 8, no. 2, pp. 339-345.

Bornstein, J.& Escudier, M.P. 1982, LDA measurements within a vortex-breakdown bubble, First Int. Symp. on Applicatons of Laser-Techniques to Fluid Mechanics, Lisabon.

Cassidy, J.J. and Falvey, H.T. 1970, Observations of unsteady flow arising after vortex breakdown, J. of Fluid Mechanics, vol. 41, no. 4, pp. 727-736.

Dellenback, P.A., Metzger, D.E. & Neitzel, G.P. 1988, Measurements in turbulent swirling flow through a abrupt axisymmetric expansion, AIAA Journal, vol. 26, no. 6, pp. 669-681.

Durst, F.& Tropea, C. 1983, Flows over Two-Dimensional Backward- Facing Steps, Structure of Complex Turbulent Shear Flow, IUTAM Symposium Marseille 1982, Springer, pp. 41-52.

Gould, R.D., Stevenson, W.H. & Thompson, H.D. 1990, Investigation of turbulent transport in an axisymmetric sudden expansion, AIAA Journal, vol 28, no. 2, pp 276-283.

Gouldin, F.C., Depsky, J.S. & Lee, S-L. 1985, Velocity field characteristics of a swirling flow combustor, AIAA Journal, vol. 23, no 1, pp 95-102.

Gupta, A.K., Lilley, D.G. & Syred, N. 1984, Swirl Flows, Abacus press.

Hallet, W.L.H.& Gunther, R. 1984, Flow and mixing in swirling flow in a sudden expansion, The Canadian Journal of Chemical Engineering, vol. 62, pp. 149-155.

Juang, R-S, Ynag, S-C, Chang, W-C. & Chen, J-S. 1990, Flow characteristics of isothermal suddenly expanding swirling flow in an industrial burner with bluff body, Journal of Chemical Engineering of Japan, vol. 23, no. 6, pp. 722-727.

Klingmann, J. 1991, A strongly swirling flow through a sudden expansion; comparison between computations and LDA-Measurements, LUTMDN/(TMVK-7008)/1-65/(1991), thesis report

Nejad, A.S. & Ahmed, S.A., 1992 Flow field characteristics of an axisymmetric sudden-expansion pipe flow with different initial swirl distribution, Int. J. Heat and Fluid Flow, vol. 13, no. 4, pp. 314-321.

Owen, F.K., Spadaccini, L.J., Kennedy, J.B.& Bowman, C.T. 1978, Effects of inlet air swirl and fuel volatility on the structure of confined spray flames, 17TH International Symp on Combustion, Leeds, pp. 467-473.

Samimy, M., Nejad, A.S., Langenfeld, C.A., Craig, R.R. & Vanaka, S.P. 1987, Isothermal swirling flow in a dump combustor, AIAA-Paper-87-1352.

Szczepura, R.T. 1985, Flow characteristics of an axisymmetric sudden pipe expansion: results obtained from the turbulence studies rig. Part1 mean and turbulence velocity results, TPRD/B/0702/N85, CEGB report, Berkeley.

Yoon, H.K. & Lilley, D.G. 1984, Futher time-mean measurements in confined swirling flows, AIAA Journal, vol. 22, no. 4, pp. 514-515.

AXIAL AND TANGENTIAL VELOCITY COMPONENTS AT THE EXHAUST END OF A HIGHLY COMPLEX CYCLONIC FLOW

Mr. P. A. Yazdabadi, Dr. A. J. Griffiths, Prof. N. Syred

Division of Mechanical Engineering and Energy studies, University of Wales College of Cardiff, UK

ABSTRACT

A laboratory scale cyclone dust separator with swirl numbers varying from 3.043 to 1.790 was used to examine the effects of different downstream pipework configurations, flowrates and swirl numbers upon the size, shape, and position of the precessing vortex core (P.V.C.). Also examined was the effect the precessing vortex core had on the reverse flow zone, and the relationship between the two.

It was concluded that the reverse flow zone displaced the central vortex core, so that it is off-set from the geometric centreline, to create the precessing vortex core. The reverse flow zone would then provide feedback for the precessing vortex core, and precess around the central axis about 30 degrees behind the precessing vortex core.

The size and position of the P.V.C. was effected by changes in Reynolds number, and any additions of downstream systems to the cyclone would also affect the strength of the P.V.C.

The P.V.C. would squeeze and accelerate the flow through a constriction set up between the outer limits of the core and of the exit diameter wall.

Spiral engulfment vortices were produced on the outside of the flow and served as the initial entrainment mechanism for external flow.

1. INTRODUCTION

1.1 Cyclone Dust Separators

Cyclone dust separators are used in a wide variety of industrial and manufacturing sectors, where there is the need to separate dust from gas streams prior to the exhaust. In many petrochemical industries these devices are used in a continuous mode to improve both product recovery and conversion within a process.

The geometrical shape of the cyclone is simple; however Yazdabadi *et a. (1992)* have shown that the pattern of the gas flow is extremely complex. This flow is usually classified as swirling or cyclonic i.e. an axisymmetric turbulent flow in which both tangential or swirl and axial velocity components are important. The radial velocity component is an order of magnitude lower, as illustrated by Syred and O'Doherty (1993).

The resultant flow conditions have been accepted as being that of a Rankine or Burgers vortex superimposed on a mean flow in the axial direction. This model suggests that conservation of angular momentum exists according to the law w.r=constant. In practice the conservation follows the relationship $w.r^{\alpha}$= constant, where Douglas *et a.* (1983) state that $\alpha \approx 0.7$ typically for cyclonic flows.

Under particular flow conditions the vortex precesses at some frequency away from the central region. The structure is coherent and its offset from the central axis determines the extent of the reversed flow region (recirculation zone). This flow geometry is called the precessing vortex core (P.V.C.) and Yazdabadi *et a.* (1992) showed that its feedback mechanism is the reversed flow region.

The resultant effect of this type of flow regime, especially at the exhaust of a cyclone, is akin to a large out of balance mass of fluid / particles rotating at a high swirl velocity. Yazdabadi *et a.* (1993) highlighted that vibration may be encountered, caused or initiated by the flow instability set up by the P.V.C.

This paper, therefore, investigates the naturally occurring three dimensional time dependent instability associated with strongly swirling cyclonic flows, using laser doppler anemometry (L.D.A) techniques. Clarification is given to the "cause and effect" of the P.V.C., especially in relation to the reversed flow zone.

2. THE PRECESSING VORTEX CORE (P.V.C.)

The formation of the recirculation zones in a swirling flow device depends upon the swirl number of the device and its geometry. It is now well documented that the assumptions of axisymmetry in such flows are only true for a very low swirl and Reynolds numbers. At a critical swirl number of about 0.6 as the Reynolds number is increased an instability develops called the vortex breakdown phenomenon. As the Reynolds

number is further increased, a large three dimensional time dependent instability, called the precessing vortex core develops. In this the central forced vortex region of flow is displaced from the axis and starts to precess about the axis of symmetry. It has been reported by Syred and Beer (1972) and Syred *et a.* (1973) that this phenomenon is very regular in nature and can cause other instabilities to arise.

The P.V.C. appears to be a mechanism for the rapid transport of fluid from the wall opposite the exit of the swirling device to the downstream end of the reverse flow zone. For it to be a stable oscillation, there must be feedback, and it has been suggested by Chanaud (1965) that this is provided by the reverse flow zone. It has also been suggested by Syred and Beer (1973) that the reverse flow zone displaces the central vortex core giving rise to the P.V.C.

It is known that the P.V.C. has a regular frequency and amplitude, simply dependent upon the system configuration and flowrate. For certain steep cyclone cone wall angles it has been observed that the P.V.C. can be considerably excited making contact with the wall, stirring up fine dust and reducing dust / material separation. The 7 degree half angle cone used in the well known high efficiency Stairmand unit, described by Stairmand (1949), was noted by Shariet (1990) to minimise this vortex core precession.

The P.V.C. can also cause many other problems by locking onto other system instabilities and resonating (or driving) with them. This can be a severe problem in large installations where low frequency high amplitude oscillations can easily arise. Putnam (1971) and Gupta *et a.* (1984) stated that beside being undesirable from a 'noise' aspect, this may easily cause sufficiently large pressure fluctuations to overstress the outer shell of both the cyclone and the downstream interconnecting systems.

3. EXPERIMENTAL ANALYSIS

Experiments were carried out using a laboratory scale cyclone dust separator. Particular attention was paid to the exit of the cyclone and thus the effects of downstream pipe configurations on the velocity components of the swirling flow were examined. Table 1 highlights the equivalent lengths of those pipework configurations attached to the cyclone. The exit diameter was also varied by the application of inserts allowing the cyclone to have two distinct geometric swirl numbers, 1.790 and 3.043 respectively. Seven test configurations were executed, and are listed in table 2.

A laser probe was carefully aligned such that the control volume was located at the central axis of the exhaust / pipe bend configurations under consideration.

A hotwire probe, utilising linearising and filtering equipment, was positioned close to the outer edge of the exhaust nozzle. A clear sinusoidal P.V.C. signal was obtained, this was input into a triggering unit, which output a synchronised square wave, used to reset the LDA time base after each cycle of the P.V.C.

This meant that for a specific radial position the instantaneous velocity variations with time for several cycles of the P.V.C. could be superimposed over one another. Thus representative mean and r.m.s instantaneous rotating velocity values for an averaged single P.V.C. cycle could be produced. This is commonly termed phase averaging and is a technique derived from LDA work in reciprocating engines.

The laser control volume was traversed from the centre of the flow radially outwards to beyond the extremities of the cyclone exhaust/pipe bend configuration under consideration, taking axial and tangential velocity measurements every 1mm.

At each 1mm step axial and tangential velocity components of the flow were recorded, and the data was presented as a mean instantaneous velocity time curve for a complete cycle of the P.V.C. From this data derivations of rotating mean axial and tangential velocities were made by digitising each velocity / time curve for a complete P.V.C. cycle. Nine identical radial paths were chosen and velocity data tabulated as a function of radius.

Finally, the processed data was plotted as spatial distributions of rotating mean axial and tangential velocities in

Table 1. Dimensions and equivalent lengths of downstream pipework configurations

downstream pipework configuration	Equivalent length /cyclone exit diameters
Cyclone exhaust tube	1.3
Straight pipe	6.5
60° angled bend	2.7
90° angled bend	3.2

Table 2. Test apparatus set-up and flow conditions

test number	Sg	Re	experimental set-up
1	3.043	28500	cyclone only flowrate=1000 l/min
2	3.043	14250	cyclone only flowrate=500 l/min
3	1.790	25600	cyclone only flowrate=900 l/min
4	3.043	42750	cyclone only flowrate=1500 l/min
5	3.043	14250	cyclone + 6.5 exit diameter flowrate=500 l/min
6	3.043	28500	cyclone + 3.2 exit diameter flowrate=1000 l/min
7	3.043	28500	cyclone + 2.7 exit diameter flowrate=1000 l/min

a plane. Also derived were the associated r.m.s profiles, these have not been examined in detail in this paper as they are known to be prone to P.V.C. ' jitter ' causing slight changes in the trigger point from cycle to cycle. Obviously this also affected the mean rotating axial and tangential profiles as did the size of the control volume (effectively 2mm long). By using methods described by Kline and McClintok (1953) the accuracy of these rotating mean phased averaged velocity measurements is estimated to be ± 5 % for velocities > 4 m/s, ± 10 % for velocities < 4 m/s.

4. PRELIMINARY ANALYSIS OF RESULTS

As discussed in the last section the flows at the exhaust nozzle of the cyclone dust separator freely exhausting to atmosphere have been characterised for the mean rotating axial and tangential velocity for two swirl levels, a range of Reynolds numbers, and three different exhaust configurations as illustrated by the spatial distributions.in figures 2 to 8.

In order to interpret the data it is useful to be able to postulate a model which can explain the very unusual results obtained for the mean rotating tangential velocities, figures 2a to 8a, namely the area of negative tangential velocity extending from the geometrical centre of the device, to typically R≈0.25. Careful examination of data from work reported, herein, detailed measurements at various distances downstream of the exhaust and indeed from swirl burners (where similar phenomenon occur) reported by Claypole *et a.* (1986), Yazdabadi *et a.* (1992), and Sato *et a.* (1993) indicates that the problem is caused by an inappropriate choice of co-ordinate system.

Figure 1 illustrates a model for the motion of the vortex which explains the measurement of the negative tangential velocity close to the normal axis, this being due to the fact that the geometrical centre of the unit and the centre of the vortex

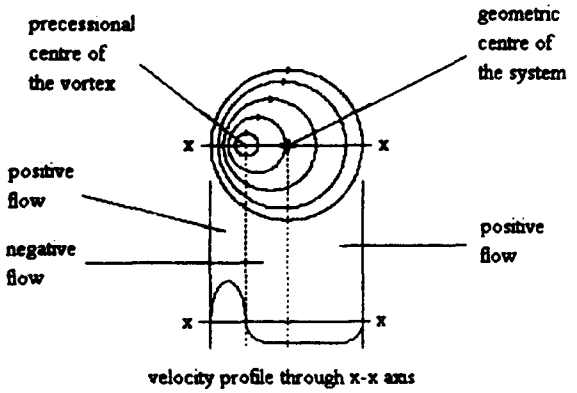

Figure 1. Schematic diagram of the off set vortex

do not coincide. It appears that the centre of the vortex is displaced to one side of the geometric centre of the system and precesses about this axis. This is well illustrated by figure 1, which shows mean rotating tangential velocities through the precessional centre of the vortex (P.C.O.V.) and the geometric centre of the device when allowance is made for a change in the sign of velocity as one passes through the true vortex centre.

Calculation of the angular momentum flux balance along this line clearly showed that there was a balance on both sides of the precessional centre of the vortex to within ± 0.2%. As discussed later this gives a clear explanation of the form of the mean rotating tangential velocity fields measured. For convenience the mean rotating tangential velocity has been collected, processed and presented using the geometric centre of the device as the centre of the co-ordinate system.

5. DISCUSSION OF RESULTS

Using the model of figure 1 detailed interpretations of the various results obtained can be undertaken. Figures 2a and 2b illustrate results from the normal cyclone configuration, with Sg=3.043 and Re=28500 with a precessional frequency of 150 Hz. Figure 2a shows the mean rotating tangential velocity field. The approximate centre of the vortex has been marked and it can be seen that this displacement from the geometric centre is sufficient to accelerate the tangential velocity to a maximum of 25 m/s from a typical mean level of 10 to 11 m/s. In effect the swirling flow is accelerated as angular momentum flux is conserved by being squeezed through a narrow region between the precessional centre of the vortex and the wall. The formation of reverse flow zones in swirling flow is well known to be caused by,

(a) The formation of strong radial pressure gradients due to the term $\frac{dp}{dr} = -\rho\frac{w^2}{r}$ which give for cyclonic units operating at near to atmospheric pressure sub atmospheric pressure levels on the axis

(b) Axial decay of tangential velocity level (as occur at sudden enlargements etc. as in this work) which translates via the radial pressure gradient term in (a) above into negative axial pressure gradients which induce reverse axial flow

Since the P.C.O.V. is clearly shown in figure 1 for tangential velocities, it must be logical to assume that the axial velocity profiles will have a similar centre of flow, i.e. displaced from the geometric centre. Indeed this does infact occur, as shown by figure 2b. The central reverse flow zone encompasses the P.C.O.V., as to be expected, and also extends to a non dimensional radius of up to 0.25 to 0.3R infront of the P.C.O.V. Several other very important flow features are evident in figures 2a and 2b viz.

(i) Not only are high mean tangential velocities generated

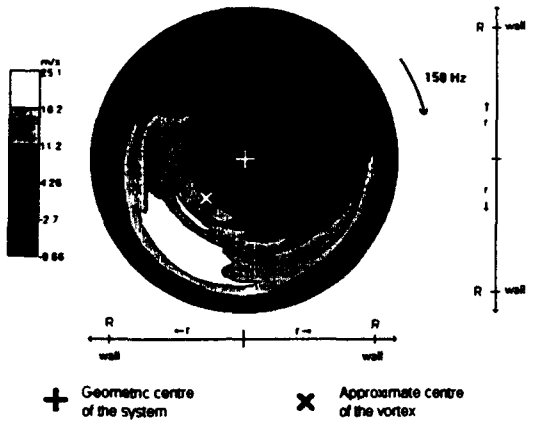

Figure 2a. Spatial distribution of rotating mean tangential velocities for test number 1. Re=28500, Sg=3.043

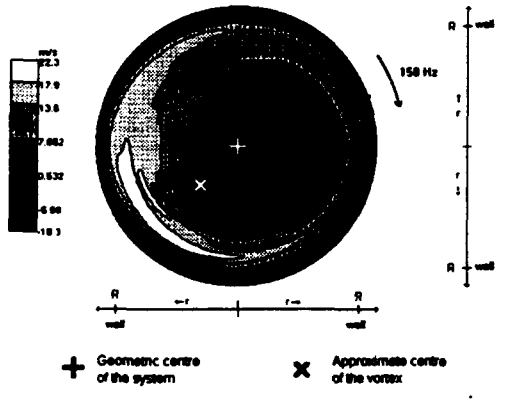

Figure 2b. Spatial distribution of rotating mean axial velocities for test number 1. Re=28500, Sg=3.043

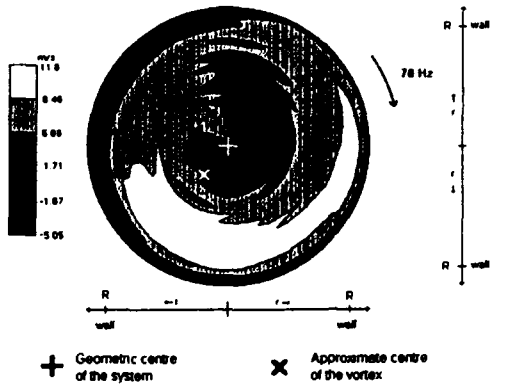

Figure 3a. Spatial distribution of rotating mean tangential velocities for test number 2. Re=14250, Sg=3.043

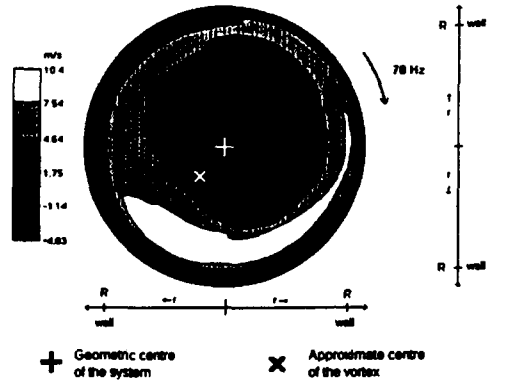

Figure 3b. Spatial distribution of rotating mean axial velocities for test number 2. Re=14250, Sg=3.043

by the P.C.O.V. effect over a sector extending some 20° ahead and 60° behind the P.C.O.V., but also are high mean axial velocities over a similar region. Clearly it is in this region that the largest mass fluxes of flow are occurring.

(ii) Just beyond the exhaust lip of the cyclone at R≥1.05 a sector of reverse axial flow extending over 340° on the outer periphery of the flow has developed as shown in figure 2b. Flow visualisation studies have revealed that this region is associated with the formation of engulfment vortices and high initial entrainment rates (a well known phenomenon with swirling flows). Indications are that these engulfment vortices are spiral or helical in nature and break-up after about 0.25 to 0.5 exit diameters.

Figure 3 shows the effect of halving the flowrate (or Reynolds number) on the flow. The broad features of the flow are similar to figure 2, although some important differences emerge

(a) The peak tangential velocity when compared to the average over the section is somewhat reduced, comparing figures 3a and 2a, whilst the region of negative tangential velocity is of similar area, but of a slightly different shape.

(b) The lower Reynolds number flow produces a slightly larger area of reversed axial flow, comparing figures 3b and 2b. For both regions it is noticeable how the largest area of reversed axial flow occurs behind the P.C.O.V.

(c) The reverse flow zone on the outer periphery of the flow has virtually disappeared at the lower Reynolds number, comparing figures 3b and 2b, this is because of the reduced velocity levels.

The effect of swirl number on the mean rotating flow fields is shown by comparing figures 4a and 4b (Sg=1.790) with figures 2a and 2b (Sg=3.043) for similar Reynolds numbers. The region of high tangential velocity (upto 26.9 m/s) for Sg=1.790, figure 4a, can be seen to extend over more than 180° as compared to 60° for the high swirl number result, figure 2a for Sg=3.043. The region of negative tangential velocity is reduced somewhat, but there are still clear indications of the presence of the P.C.O.V. effect. Again there is evidence of an uneven region of reverse flow in the centre of the flow, but

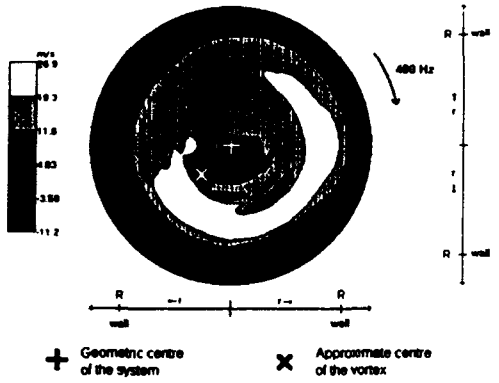

Figure 4a. Spatial distribution of rotating mean tangential velocities for test number 3. Re=25600, Sg=1.790

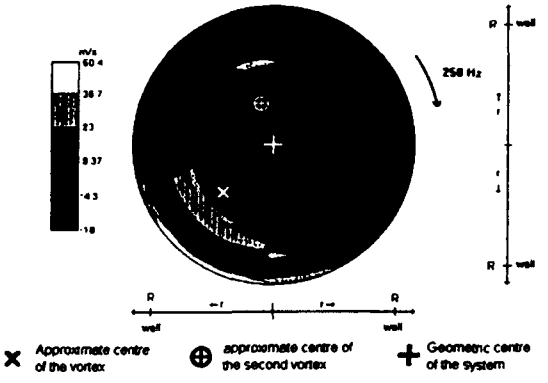

Figure 5a. Spatial distribution of rotating mean tangential velocities for test number 4. Re=42750, Sg=3.043

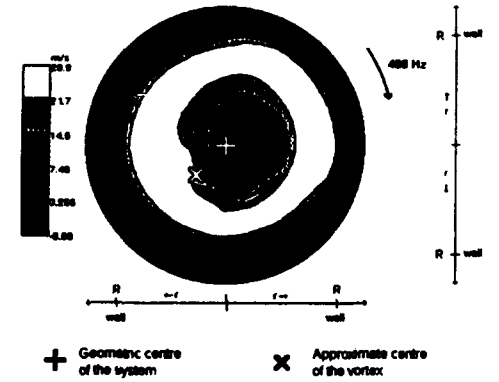

Figure 4b. Spatial distribution of rotating mean axial velocities for test number 3. Re=25600, Sg=1.790

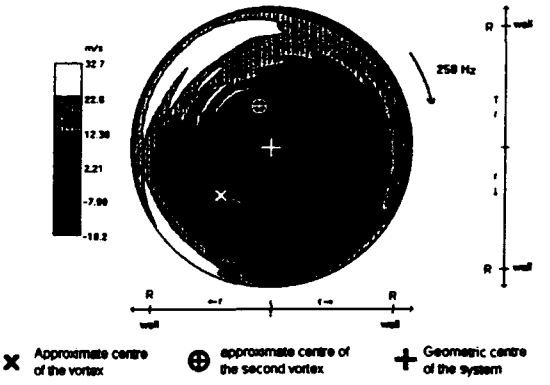

Figure 5b. Spatial distribution of rotating mean axial velocities for test number 4. Re=42750, Sg=3.043

again off axis, identified in figure 4b. The outer section of the flow between the wall and the P.C.O.V. is more uniform in the θ direction, figure 4b (1≤R≤0.6). There is again evidence of large scale engulfment vortices on the outside of the flow (R≥1), as shown by the intermittent (in the θ direction) reversed axial flow in this region, which is of far greater extent than with the higher swirl number; compare figures 4b and 2b.

The effect of increased Reynolds number from 28,500 to 42,750 for Sg=3.043 is shown by comparison of figures 2a and 2b, with 5a and 5b. Figure 5a shows that a substantial enlargement of the area of negative tangential velocity has occurred at the higher Reynolds number, compared to that shown in figure 2a. The highest tangential velocity region, figure 5a, is clearly located close to the outer wall in a thin narrow sector. Evidence of a second P.C.O.V. forming can be clearly seen in a region of flow 120° infront of the main P.C.O.V., figure 5a. Spectral analysis of the P.C.O.V. signal shows this to be a higher frequency or harmonic of the main P.C.O.V. This is more representative of the true flow due to better triggering by the now sharper P.C.O.V. signal (at higher velocity levels). The extent of the influence of the P.C.O.V. in the θ direction is more limited, but its relative magnitude is much greater. The pattern of axial velocities has also altered considerably, when comparing figures 5b and 2b, with an even larger area of off centred central reverse flow. Again the squeezing effect of this reverse flow on the forward axial flow is evident, figure 5b. However the flow is complicated by a further region of high axial velocity forward flow about 70° to 90° infront of the centre of the central reverse flow zone, again indicative of the formation of a second P.C.O.V.

The effect of a sharp 90° bend on the P.V.C. is illustrated by figures 6a and 6b for the same swirl and Reynolds numbers as figures 2a and 2b. This bend has smoothed out the axial velocities in the θ direction, creating a far more uniform profile as shown in figure 6b. But not so with the tangential velocity as seen in figure 6a, where there is still typically, close to the outer wall, a variation in tangential velocity by more than a factor of 2 in the θ direction over 360°. Large areas of negative

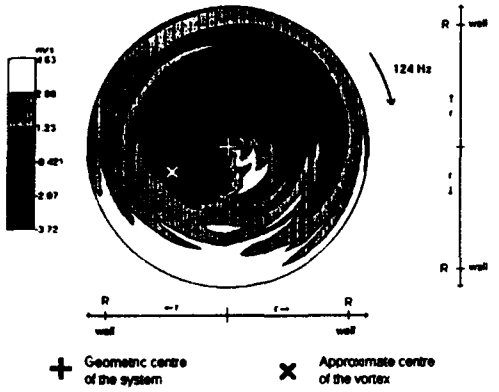

Figure 6a. Spatial distribution of rotating mean tangential velocities for test number 6. Re=28500, Sg=3.043

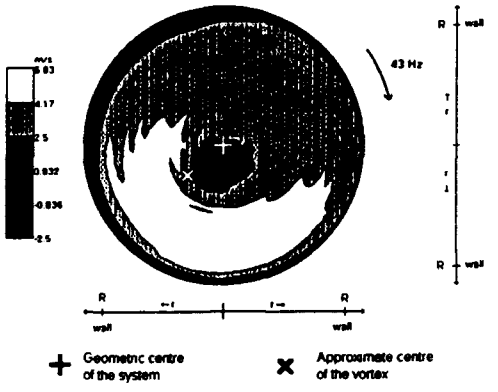

Figure 7a. Spatial distribution of rotating mean tangential velocities for test number 5. Re=14250, Sg=3.043

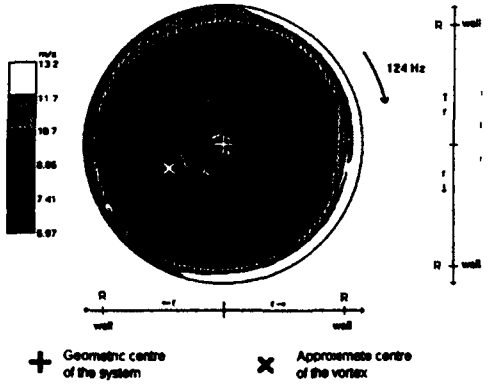

Figure 6b. Spatial distribution of rotating mean axial velocities for test number 6. Re=28500, Sg=3.043

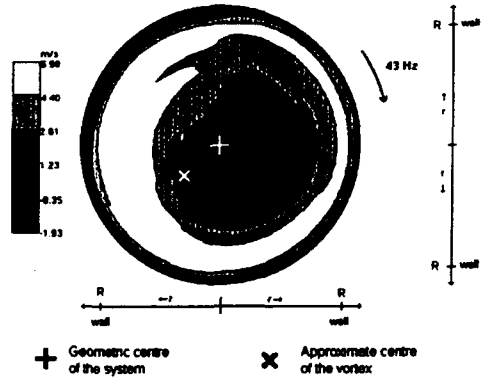

Figure 7b. Spatial distribution of rotating mean axial velocities for test number 5. Re=14250, Sg=3.043

tangential velocity still exist near to the central axis (infact larger than in figures 2a and 3a) indicating the presence of a precessing off centre vortex. The sharp bend has destroyed any axial reverse flow. Feedback mechanisms are difficult to identify but may arise from reverse flow in or just before this sharp bend and not detected by these measurements.

The effect of a 6.5 exit diameter straight pipe on the tangential flow field is illustrated in figures 7a and 7b for Sg=3.043 and Re=14,250 and is best compared to figure 3a and 3b. Although the actual maximum velocity levels have declined considerably, by a factor of 5 for tangential and nearly 4 for axial, the main features of the flow have scarcely altered, with a small region of negative tangential velocity combined with an outer high velocity area covering nearly 180°. Here the region of reversed axial flow is clearly off centre and closely correlates with the P.C.O.V., highlighted in figure 7b.

It has been previously shown that the length of straight downstream pipework does not effect the shape and existence of the P.V.C. The introduction of a 60° angled bend as shown in figures 8a and 8b has centralised the vortex region to that of the geometric centre of the pipework. Thus the precessing phenomenon has been destroyed across the bend. The velocity profiles are symmetric in both the tangential and axial planes. The peak velocities in both cases cover a greater percentage of the flow field, again indicating a redistribution of the momentum flux. Hence large flow reversal zone exists in the central core.

Table 3 highlights the radial position of the P.C.O.V. for the different Reynolds numbers, geometric swirl numbers, and exit pipe geometries under consideration. Most notable is that for a geometric swirl number of 3.043, an increase in Reynolds number from 14250 to 42750 moves the centre of the P.C.O.V. outwards from the geometric centre of the system by over 0.2R (0.28R - 0.49R).

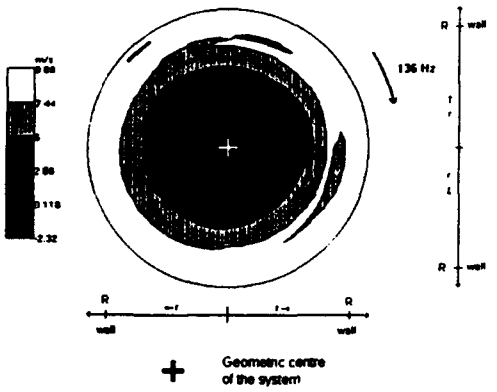

Figure 8a. Spatial distribution of rotating mean tangential velocities for test number 7. Re=28500, Sg=3.043

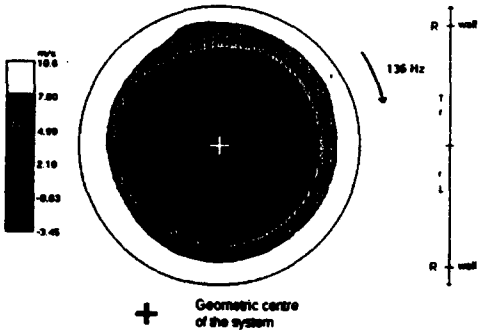

Figure 8b. Spatial distribution of rotating mean axial velocities for test number 7. Re=28500, Sg=3.043

Table 3. Radial position of the P.C.O.V. for the varying experimental parameters

Test	Re	Sg	cyclone attachments	P.C.O.V. radial position
1	28500	3.043	none	0.35R
2	14250	3.043	none	0.28R
3	25600	1.790	none	0.30R
4	42750	3.043	none	0.49R
5	14250	3.043	straight pipe	0.33R
6	28500	3.043	90° angled bend	0.44R

6. CONCLUSIONS

This paper has provided information via phase averaging techniques of the three dimensional time dependent flows formed in the exhaust region of a cyclone dust separator. The work has produced a new model to describe vortex core precession, clearly showing that the phenomena is caused by the actual displacement of the centre of the vortex from and precession around the geometrical centre of the system. For tangential velocities a new rotating co-ordinate centre is needed, based on the precessional centre of the vortex. Angular momentum flux considerations based on this new co-ordinate centre clearly show why the tangential flow is accelerated by the P.V.C. phenomena, thus creating the 'classic' P.V.C. signal. The central reverse flow zone is always associated with the centre of the vortex in swirling flow and this work has been clearly shown to be correlated with the rotating precessional centre of the vortex.

The addition of external pipework has been shown to affect the P.V.C. and unique new information on the effect of a hard bend produced. Axial velocity contours were shown to be much smoother in the θ direction; whilst reverse flow is destroyed. The P.V.C. phenomena propagated around the bend, albeit with much lower velocity levels.

The size and radial position of the P.V.C. is also effected by a change in Reynolds number. An increase in Reynolds number shrinking the P.V.C. size but increasing its amplitude and moving it further from the central axis of the exhaust.

Finally reverse flow on the outside of the flows points to the existence of large scale engulfment vortices on the outside of the flow, the level of this dependant upon the geometrical swirl number of the system. These can be concluded to cause vibration in the system which could increase the amplitude of the already present vibrations.

7. ACKNOWLEDGEMENTS

The authors wish to acknowledge the financial assistance provided by British Petroleum for this research. P. Yazdabadi acknowledges the award of a EPSRC Total Technology studentship.

8. NOMENCLATURE

Re - Reynolds number, defined as $\{4\,Q\,/\,(\pi\,D\,\nu)\}$
Sg - geometric swirl number, defined as $\{\pi\,R_x\,R_o\,/\,A_t\}$
A_t - tangential inlet area (m^2)
D - cyclone exhaust diameter (m)
Q - flowrate (m^3/s)
R - radius (m)
R_x - radius of exhaust (m)
R_o - radius of cyclone main body (m)
r - radial position (m)
w - time-mean swirl velocity (m / s)
ρ - density (kg/m^3)
ν - kinematic viscosity (m^2/s)
α - vortex exponent
P.C.O.V. - Precessional Centre Of the Vortex

P.V.C. - Precessing Vortex Core

9. REFERENCES

Chanaud, R. C., 1965, Observations of oscillatory motion in certain swirling flows, J. Fluid Mechanics, vol 21 part 1, pp. 111-127

Claypole, T.C., Evans, P., Hodge, J., Syred, N., 1986, The influence of the precessing vortex core on velocity measurements in swirling flows, 3rd international symposium on aplications of laser techniques to fluid mechanics, Lisbon, Portugal, July

Douglas J. F., Gasiorek, J. M., Swaffield, J. A., 1983, Fluid mechanics, Pitman Books Limited, London

Gupta, A. K., Lilly, D., Syred, N., 1984, Swirl flows, Abacus Press, Tunbridge Wells, Kent

Kline, S. J., McClintok, I. A., 1953, Describing Uncertanties in Single-Sample Experiments, Mechanical Engineering, January, p 3-8

Putnam, A., 1971, Combustion - driven oscillations in industry, American Elsevier publishing inc., New York

Sato, K., O'Doherty, T., Biffin, M., Syred, N., 1993, Analysis of strong swirling flow in swirl burner / furnaces, International symposim on combustion and emissions control, Cardiff, Wales, September

Shariet, R. A., 1990, A study of novel cyclone preheater towers, Ph.d Thesis, Cardiff University, p22

Stairmand, C. J, 1949, Pressure drop in cyclone separators, Engineering, 168, 4369, p 409

Syred, N., and Beer, J. M., 1972, Vortex core precession in high swirl flows, Proc. 2nd International Japanese Society of Mechanical Engineers Symposium on Fluid Machinery and Fluidics, Tokyo

Syred, N., Beer, J. M., 1973, The effect of combustion upon precessing vortex cores generated by swirl combustion, Proc. 14th Symp. (Int) on combustion, The Combustion Institute, Pittsburgh, USA

Syred, N., Hanby, V. I., Gupta, A. K., 1973, Resonant instabilities generated by swirl burners, Journal of the institute of fuel, vol 46, no. 387, p402-407

Syred, N., O'Doherty, T., 1993, Coherent structures in swirl burners and their interaction with the combustion process, Proc. Anglo-German Combustion symposium, Cambridge, pp. 116-119

Yazdabadi, P. A., Griffiths, A. J., Syred, N., 1992, Investigations into precessing vortex core phenomenon in cyclone dust separators, University of Wales College of Cardiff, internal report 1704

Yazdabadi, P. A., Griffiths, A. J., Syred, N., 1992, Axial and tangential velocity components at the exhaust end of a highly complex flow pattern generated by a precessing vortex core, University of Wales College of Cardiff, internal report 1782

Yazdabadi, P. A., Griffiths, A. J., Syred, N., 1993, Investigations into precessing vortex core phenomenon in cyclone dust separators, submitted to the IMechE for publication

Session 20.
Scalar Measurements I

PURE ROTATIONAL CARS METHOD FOR TEMPERATURE OF GAS MIXTURE

Y. Hara, S. Ito, T. Ni-imi and T. Fujimoto

Department of Electronic-Mechanical Engineering

Nagoya University, Japan

ABSTRACT

Q-branch vibrational Coherent Anti-Stokes Raman Scattering(CARS) has been often applied to high temperature measurement (about 2000K) of gas flow in combustion and plasma diagnostics and so forth(e.g., Taran, 1987; Eckbreth, 1988). To the contrary, or as a compensatory technique, pure rotational CARS is useful at low temperature range, particularly at room temperature and below. If the gas contains only one species, rotational lines of a pure rotational CARS spectrum are separated enough so that they are distinguishable. Consequently, rotational temperature can be calculated more easily from the pure rotational CARS spectrum by means of Boltzmann's plot. However, it's not the case for gas mixture which consists of some species, because the rotational lines of each species overlap each other partially in the spectrum.

In this paper, an easier method to deduce temperature from the pure rotational CARS spectrum of gas mixture is proposed. In order to investigate the effectiveness of our method, we apply it to evaluating of pure rotational CARS spectra taken along the centerline of supersonic free jets of air and gas mixture which consists of 50% nitrogen and 50% oxygen, using multiple four-color interaction method.

1. INTRODUCTION

Pure rotational CARS is very useful as a tool of gas thermometry in low temperature range(e.g., Murphy and Chang, 1981; Dick and Gierulski, 1986), because its rotational lines can be isolated with rather large line spacings even using multiplex method or relatively poor spectral resolution apparatus, when gas consists of single species dominantly. For example, the line spacings for nitrogen molecules are about 8 cm^{-1}. According to this fact, rotational temperature can be easily calculated from the slope of a Boltzmann's plot by using integrated line intensities(Murphy and Chang, 1981; Harashima, 1988). However, when the gas consists of multiple species like air which can be regarded as gas mixture of nitrogen and oxygen, the rotational lines of each species overlap each other partially in the spectrum. So, in that case, temperature could be deduced from the best fitting of the theoretical spectra to the experimental one, like the usual method used in Q-branch vibrational CARS. However, this fitting procedure is rather complicated and a set of the theoretical spectra must be calculated exactly in advance. By the way, when the gas consists of only a few species, the spectrum could be separated into the spectra of each species. Magens and Leipertz (1993) applied Fourier analysis technique to evaluating of pure rotational CARS spectra, where the different contributions of nitrogen and oxygen were able to be separated in the Fourier space. However, even with that technique, a best fitting procedure between experimental and calculated spectra has to be used in the Fourier space.

In this study, an easier method to deduce temperature from a pure rotational CARS spectrum of gas mixture is proposed assuming equal temperature values of constituent species. In addition, for simplicity, we assume that the ratios between number densities of constituent species are known in any other way. Particularly, air is selected as an example of gas mixture in this study, because it's considered to be very important as the carrier gas for experiments of compressible flow and so on. In our method, a spectrum of gas mixture is partitioned into some sections and the ratios of line intensities in each section are calculated theoretically

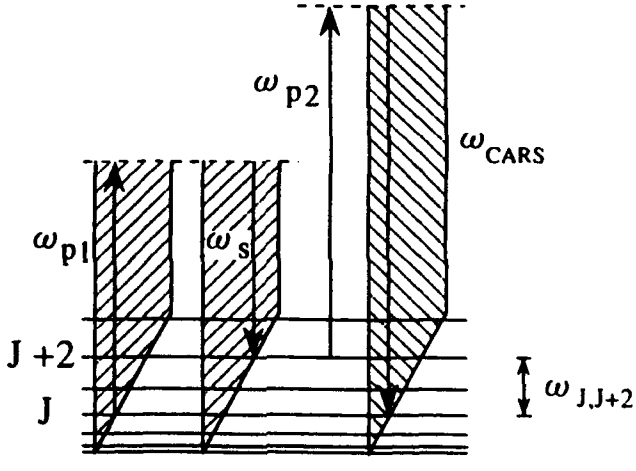

Fig. 1 Pure rotational CARS transition process

assuming a proper temperature. Once the spectrum of gas mixture is separated into the spectra of each species, temperatures of each species can be easily determined from the Boltzmann's plots by the iterative way, respectively.

2. PROCEDURE OF TEMPERATURE DEDUCTION

Figure 1 shows pure rotational CARS transition process in multiple four-color interaction method(Alden et al, 1986; Eckbreth and Anderson, 1986), where the rotational energies are excited with two photons of different frequencies (ω_{P1}, ω_S) from a broadband dye laser. If the frequency ω_{P2} of a narrowband laser is rather different from ω_{P1} and ω_S, the CARS signal with frequency ω_{CARS} ($\omega_{CARS} = \omega_{P1} + \omega_{P2} - \omega_S$) can be acquired very easily by separation of it from the broadband laser using a dichroic mirror. As well known, the CARS intensity is proportional to the square of the third-order nonlinear susceptibility and is given by

$$I(\omega_{CARS}) = \text{const.} \, |\chi^{(3)}(\omega_{P1} - \omega_S)|^2 I_{P1} I_{P2} I_S . \qquad (1)$$

where I_{P1}, I_{P2} and I_S are the laser intensities at the frequencies ω_{P1}, ω_{P2} and ω_S, respectively. The nonlinear susceptibility is the sum of resonant terms for transition $J \rightarrow J+2$ (here, J means rotational quantum number),

$$\chi_J^{(3)} = \frac{\gamma^2 \, n \, N(J) \, b(J) \left\{ 1 - \exp\left(-\hbar \omega_{J,J+2} / k_B T \right) \right\}}{\omega_{J,J+2} - (\omega_{P1} - \omega_S) - i \Gamma_J / 2} , \qquad (2)$$

and the nonresonant background (e.g., Dick and Gierulski, 1986). In Eq.(2), γ, n and Γ_J are the anisotropy of the molecular polarizability tensor, number density and the linewidth of the Jth's rotational line, respectively. Then, N(J), b(J) and $\hbar \omega_{J,J+2}$ are given by

$$N(J) = \frac{1}{Q_r} g_J (2J + 1) \exp\left\{ - E_r(J) / k_B T \right\} , \qquad (3)$$

$$b(J) = \frac{(J + 1)(J + 2)}{(2J + 1)(2J + 3)} \qquad (4)$$

and

$$\hbar \omega_{J,J+2} = E_r(J + 2) - E_r(J) , \qquad (5)$$

where Q_r, g_J, k_B and T are the rotational partition function, the nuclear spin degeneracy factor, Boltzmann's constant and rotational temperature, respectively. The rotational energy $E_r(J)$ is expressed by

$$E_r(J) = hcBJ (J + 1) , \qquad (6)$$

if the centrifugal effect can be neglected. In Eq.(6), B is molecular rotational constant, h is Planck's constant ($\hbar = h/2\pi$) and c is the speed of light. Neglecting the laser intensity distribution, the Jth's rotational line intensities I_J are given by

$$I_J = \text{const.} \int |\chi_J^{(3)}|^2 d(\omega_{P1} - \omega_S)$$

$$= \text{const.} \frac{\gamma^4 n^2 N(J)^2 b(J)^2 \left\{ 1 - \exp\left(-\hbar \omega_{J,J+2} / k_B T \right) \right\}^2}{\Gamma_J} . \qquad (7)$$

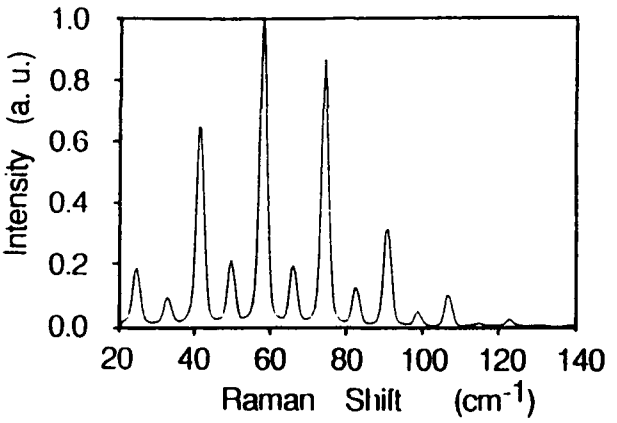

Fig. 2 Pure rotational CARS spectrum of nitrogen

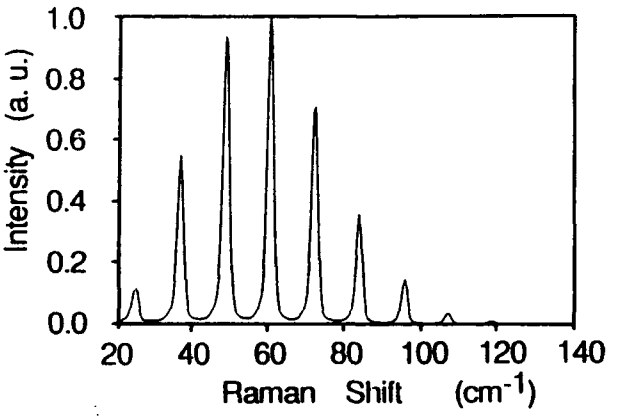

Fig. 3 Pure rotational CARS spectrum of oxygen

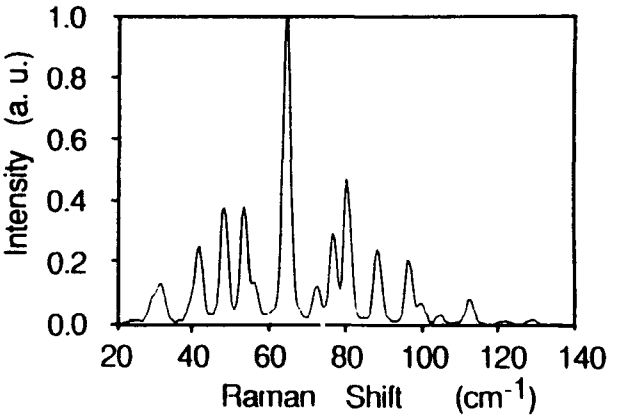

Fig. 4 Pure rotational CARS spectrum of air

Substituting Eq.(6) into Eq.(7) and transforming a little, the following equation can be obtained

$$F(J) = - aJ(J + 1) + \text{const.} , \qquad (8)$$

where

$$F(J) = \ln\left[\frac{I_J \Gamma_J}{b(J)^2 g_J^2 (2J+1)^2 \{1 - \exp(-\hbar\omega_{J,J+2}/k_B T)\}^2}\right] \quad (9)$$

and

$$a = \frac{2hcB}{k_B T} \quad (10)$$

Figure 2, 3 and 4 show the spectra of N_2, O_2 and air, respectively, taken at room temperature and atmospheric pressure. In the case where the gas contains only one species as Fig.2 or Fig. 3, the obtained spectrum is constructed of some isolated rotational lines and the line intensities are able to be calculated easily. Then, using the line intensities, the values of F(J) are calculated and are plotted to the values of J(J+1) as indicated in Fig. 5. The rotational temperature can be calculated from the slope (Eq.(10)) of a straight line which can be obtained by a least squares routine. This is called Boltzmann's plot method. This method is rather easy because the calculation of theoretical spectra and the best fitting procedure are not necessary.

However, as illustrated in Fig. 4, the spectra of gas mixture like air is complicated because of the superposition of the spectra of constituent species. In this case, the Boltzmann's plot method can not be applied as it is. Therefore, we propose to sectionalise the spectra of gas mixture as illustrated in Fig. 6. Figure 6 is a calculated spectrum of air, where the intensity distribution of a broadband laser and the line broadening due to slit function

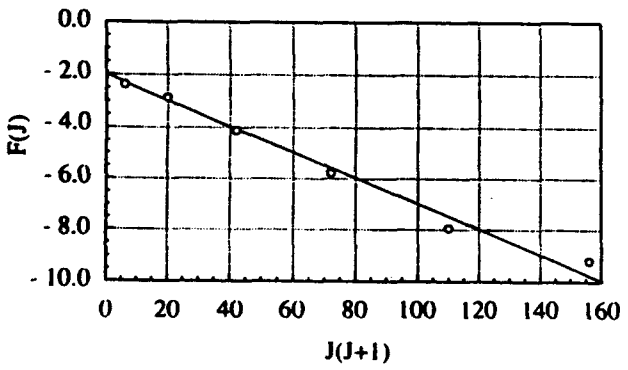

Fig. 5 Boltzmann's plot

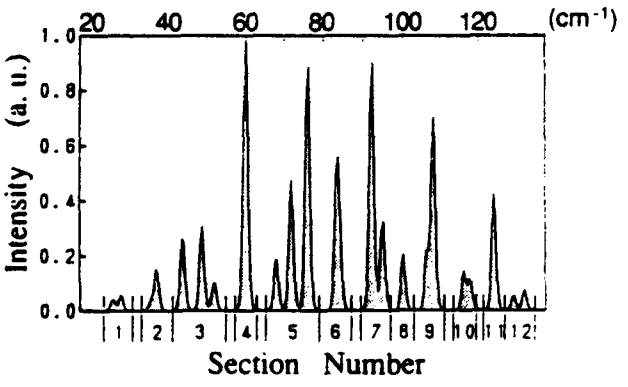

Fig. 6 Sectionalization of spectrum of gas mixture

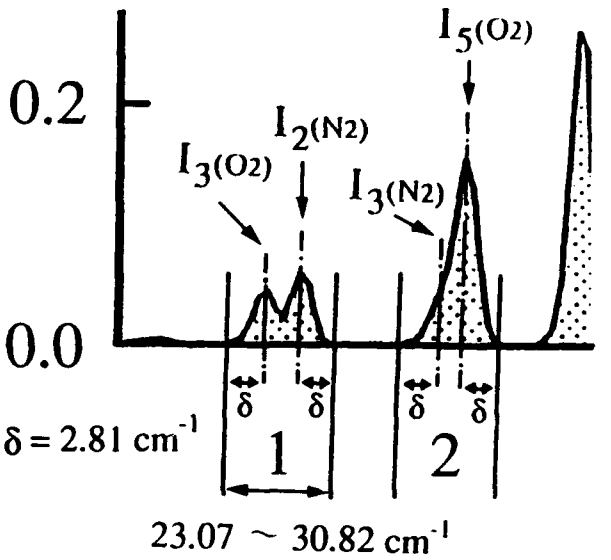

Fig. 7 Section 1 and section 2

are not considered. The spectrum is separated into 12 sections in Fig. 6 in accordance with the rules as follows: The adjacent rotational lines with less than 5 cm^{-1} separation are put in the same section and the both ends of each section are located at 2.81 cm^{-1} outwards from the each extreme rotational line in the section. Here, the value of 2.81 cm^{-1} accords with 6 elements of photodiode detectors in our apparatus. For example, as seen in Fig. 7, section 1 includes two rotational lines, i.e. the third O_2 line $I_3(O_2)$ and the second N_2 line $I_2(N_2)$, and its region is from 23.07 cm^{-1} to 30.82 cm^{-1} in Raman shift. The section 2 includes $I_3(N_2)$ and $I_5(O_2)$, having the region from 33.20 cm^{-1} to 40.19 cm^{-1}.

By the way, using the Eq.(7), the ratios between the line intensity of nitrogen and that of oxygen can be calculated by

$$\frac{I_J(N_2)}{I_{J'}(O_2)} = \left(\frac{\gamma(N_2)}{\gamma(O_2)}\right)^4 \left(\frac{n(N_2)}{n(O_2)}\right)^2 \left(\frac{\Gamma_J}{\Gamma_{J'}}\right) \times \frac{N(J)^2 b(J)^2 \{1 - \exp(-\hbar\omega_{J,J+2}/k_B T)\}^2}{N(J')^2 b(J')^2 \{1 - \exp(-\hbar\omega_{J',J'+2}/k_B T)\}^2} \quad (11)$$

if the proper temperature is given. The ratio between the anisotropy of N_2 and that of O_2 was calculated by comparison with a measured spectrum of air and several theoretical spectra with different ratios, and the value of $\gamma^2_{(N_2)} : \gamma^2_{(O_2)} = 1 : 2.6$ is gained. This value is in good agreement with the values quoted in the paper by Vaughan et al (1993). In this study, the values of linewidth Γ_J are taken from the literature by Jammu et al (1966), and are assumed, for simplicity, to be independent of temperature and pressure.

In our method, the integrated spectral intensity in each section is shared among the rotational lines in its section according to the ratios given by Eq.(11). After this sharing, all line intensities of each constituent species can be determined relatively, and like the case of simple gas,

Table 1 Regions of each section and ratios of sharing in the case of air with room temperature

Section No.	Region (cm^{-1})	Ratio of Sharing
1	23.07 ~ 30.82	$I_3(O_2) : I_2(N_2) = 1 : 1.34$
2	33.20 ~ 40.19	$I_3(N_2) : I_5(O_2) = 0.22 : 1$
3	41.18 ~ 54.81	$I_4(N_2) : I_7(O_2) : I_5(N_2) = 0.81 : 1 : 0.34$
4	57.19 ~ 63.17	$I_6(N_2) : I_9(O_2) = 1.3 : 1$
5	65.18 ~ 78.79	$I_7(N_2) : I_{11}(O_2) : I_8(N_2) = 0.38 : 1 : 1.89$
6	80.48 ~ 86.78	$I_{13}(O_2) : I_9(N_2) = 1 : 0.53$
7	89.15 ~ 97.12	$I_{10}(N_2) : I_{15}(O_2) = 2.55 : 1$
8	97.13 ~ 102.75	$I_{11}(N_2)$
9	103.36 ~ 110.73	$I_{17}(O_2) : I_{12}(N_2) = 1 : 3.25$
10	113.08 ~ 120.40	$I_{13}(N_2) : I_{19}(O_2) = 1.17 : 1$
11	121.06 ~ 126.67	$I_{14}(N_2)$
12	126.68 ~ 134.64	$I_{21}(O_2) : I_{15}(N_2) = 1 : 1.34$

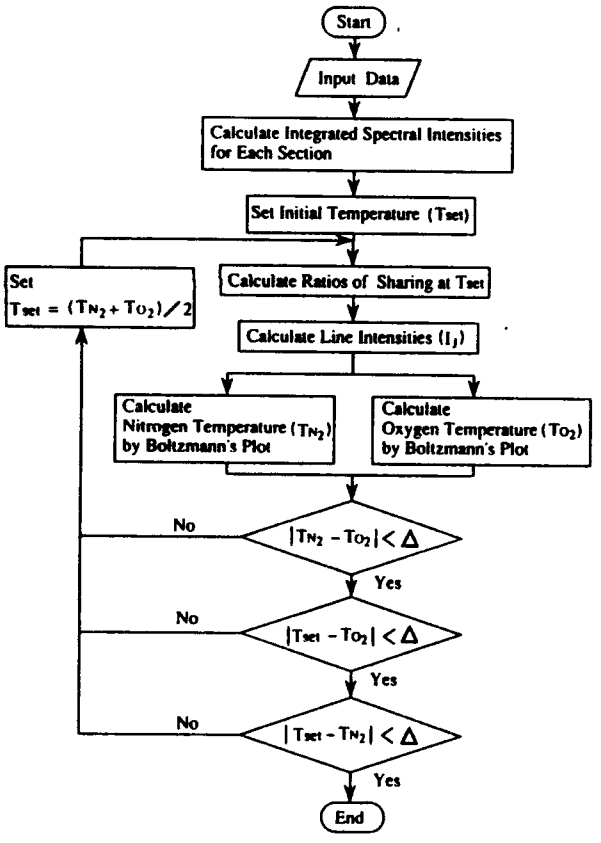

Fig. 8 Flow chart to determine temperature of gas mixture

rotational temperature can be calculated using the Boltzmann's plot method. As an example, the regions of each section and the ratios of sharing of spectral intensity between nitrogen and oxygen are shown in Table 1 in the case of air with room temperature.

Practically, a proper initial temperature selected with the rough shape of spectrum is set at first, and using it the ratios of sharing are calculated in each section. Then, the temperatures of nitrogen and oxygen are calculated from the slope of each Boltzmann's plot. However, usually, the three values of the calculated temperatures of nitrogen and oxygen and the initial temperature are different each other. Therefore, the initial temperature is replaced by the mean value of the calculated temperatures of nitrogen and oxygen, and the ratios of sharing are calculated again with the mean value. This process is repeated until the differences among the temperatures T_N, T_O and T_{set} become less than a temperature difference criterion Δ. Figure 8 displays the flow chart of this temperature determining process. Obviously, this method can not apply to the case when the temperatures of the constituent species are different like in non-equilibrium.

3. EXPERIMENTAL APPARATUS

In order to investigate the effectiveness of our method, we apply it to evaluating of the pure rotational CARS spectra taken along the centerline of a supersonic free jet of air or of gas mixture that consists of 50% nitrogen and 50% oxygen. Figure 9 illustrates our CARS apparatus. We adopt the multiple four-color interaction method by Alden et al (1986) or Eckbreth and Anderson (1986) to capture the pure rotational CARS spectra. A part of the frequency doubled output from a Nd:YAG laser (Quanta-Ray DCR-3D, 532 nm) pumps a broadband dye laser (Quanta-Ray PDL-2, 607 nm, bandwidth is about 60 cm^{-1}). The output of the dye laser is separated two beams ω_{P1} and ω_S by a beam splitter. The rest of the YAG laser output, i.e. ω_{P2}, is superimposed onto one of the dye laser beams using a dichroic mirror. The three beams are focused on a spot on the axis of the supersonic free jet by a 300 mm focal length lens. The signal CARS beam generated from the sample region can be separated from the incident laser beams with an aperture and a dichroic mirror, because the signal beam is scattered in a laser-like manner in a different direction from the YAG laser beam and its frequency is rather different from that of the dye laser beam superimposing it. The CARS signal dispersed by a double monochromator (JASCO, CT-40D, f = 400 mm) is detected by an optical multichannel analyzer (TN-6143, 512 channels). The crossed-beam configuration (i.e., BOXCARS) mentioned above gives a spatial resolution of about 2 mm in the direction of line of sight.

On the other hand, the gas is expanded from a source chamber with higher pressure to a expansion chamber with lower pressure through a nozzle whose diameter is D=1 mm and produces a supersonic free jet. In order to measure the temperature at different positions, the expansion chamber can be moved along the centerline of the jet using a motor-driven stage.

4. RESULTS AND DISCUSSION

Figure 10 and 11 show the examples of CARS spectra measured in the supersonic free jet of air. These spectra are accumulated by 250 laser shots. In this case, the pressure of

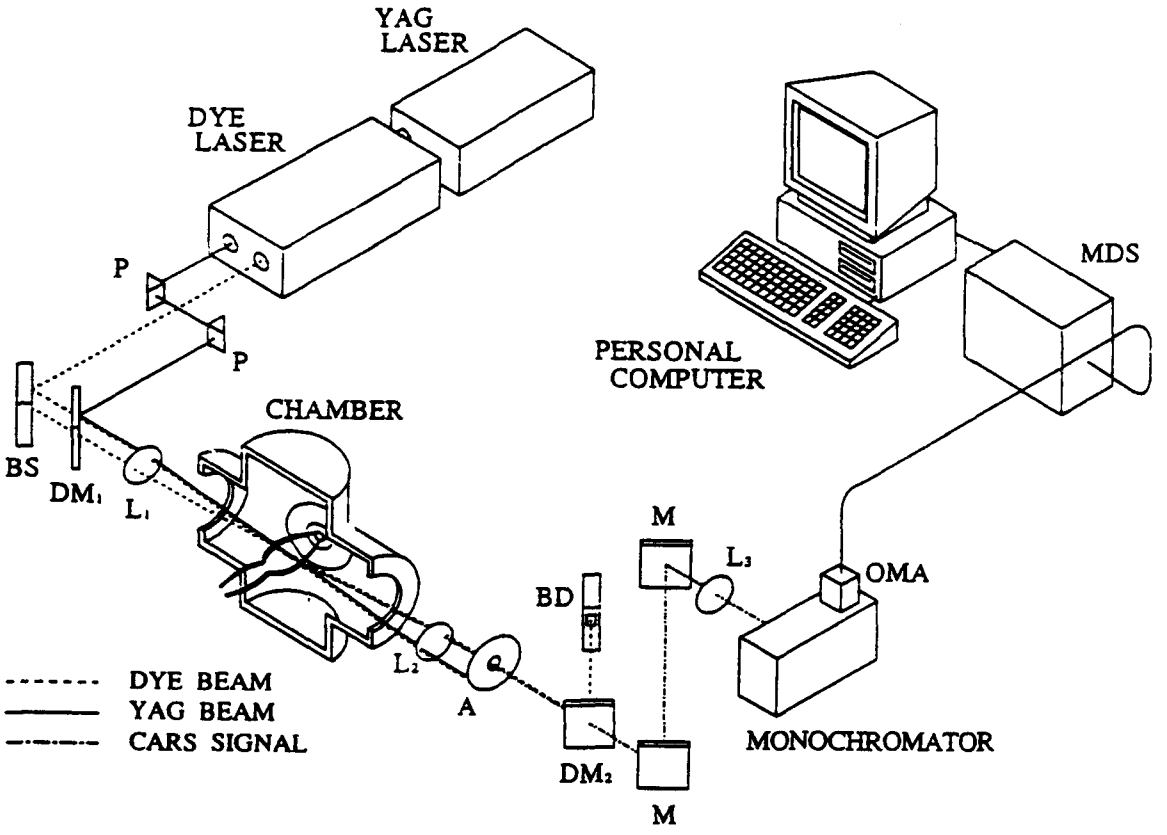

Abbreviations

P : Prism BS : Beam Splitter DM : Dichroic Mirror
L : Lenz A : Aperture M : Mirror BD : Beam Dumper
OMA : Optical Multichannel Analyzer
MDS : Multipurpose Data Processing System

Fig. 9 Experimental apparatus of pure rotational CARS

the source chamber is 8.66×10^4 Pa and that of the expansion chamber is 5.3×10^2Pa, respectively. Although the ratio between the number density of nitrogen and oxygen in air is 78 : 21, the polarizability anisotropy of oxygen is larger than that of nitrogen, therefore in the spectra of air the rotational line intensities of each species are comparable. The rotational temperatures along the centerline of the supersonic free jet are calculated from these spectra using our method after correcting the spectra with an averaged distribution of dye laser intensity. As seen in Fig. 10 and Fig. 11, the rotational lines hardly appears in high Raman shift region because of low temperature due to rapid expansion. In such cases, only the rotational lines with lower rotational quantum numbers are used for calculation of temperature in our code. The mean values of 5 measurements at the same position are designated by circles in Fig.12. Not indicated explicitly in the Figure, the differences between the maximum and minimum of measured temperatures at each position are less than 4 K. The dotted line indicates theoretical temperature given by Ashkenas and Sherman (1966) . The deviations of the mean values among the 5 measured temperatures from the theoretical values are found to be smaller than 6 K and the agreement between them is rather good. By the way, when the temperature difference criterion Δ is set to 1 K, non-convergence of temperature difference has occurred in some cases, therefore the value of Δ is set to 2 K in our study.

To confirm the effectiveness of our method when the ratio between the number density of nitrogen and oxygen is changed, we also measured the temperature of gas mixture that consists of 50 % nitrogen and 50 % oxygen. The spectra captured in the supersonic free jet of gas mixture are showed in Fig. 13 and Fig. 14. In this case, the pressure of the source chamber is 8.44×10^4 Pa and that of the expansion chamber is 5.3×10^2 Pa, respectively. Because of higher oxygen number density and large polarizability anisotropy for oxygen, the intensities of the rotational lines of oxygen are rather strong and dominant in the spectrum as seen in Fig. 13 or Fig.14. In addition, the S/N ratios in the spectra of gas mixture are larger than those in the spectra of air. As shown in Fig. 15, however, the result of the temperature measurement in gas mixture is almost the same as that of air. Therefore, our method for deduction of the rotational temperature from the

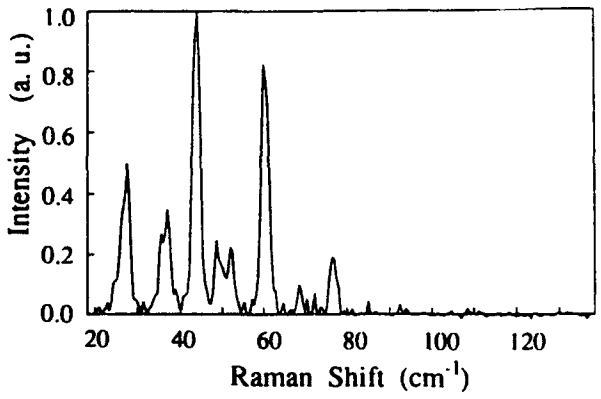

Fig. 10 Spectrum of air (x=0.75 mm, T=133.5 K)

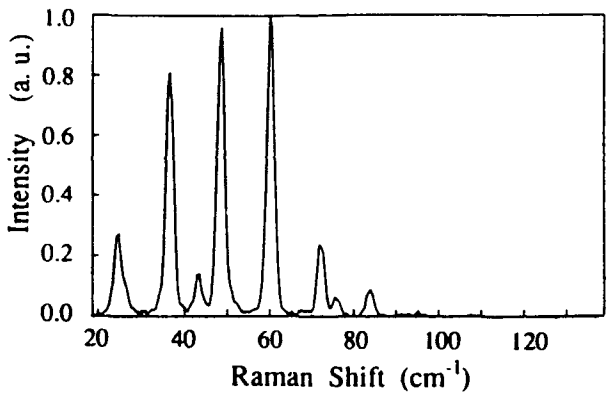

Fig. 13 Spectrum of gas mixture (x=0.65 mm, T=136.2 K)

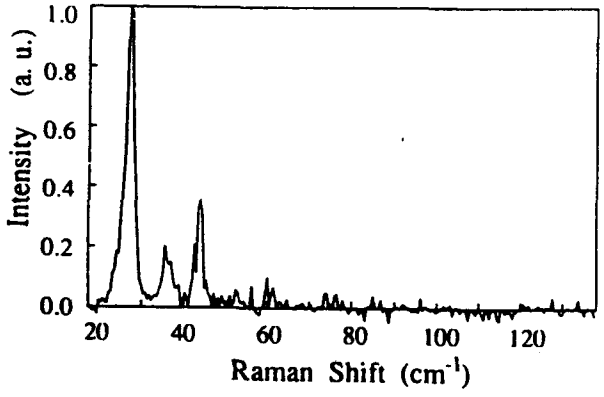

Fig. 11 Spectrum of air (x=4.25 mm, T=42.6 K)

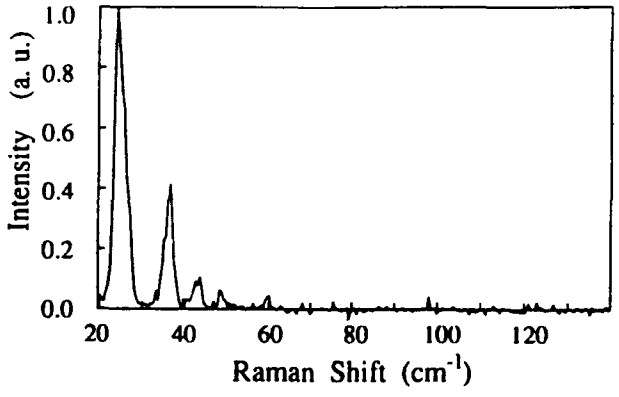

Fig. 14 Spectrum of gas mixture (x=4.65 mm, T=35.6 K)

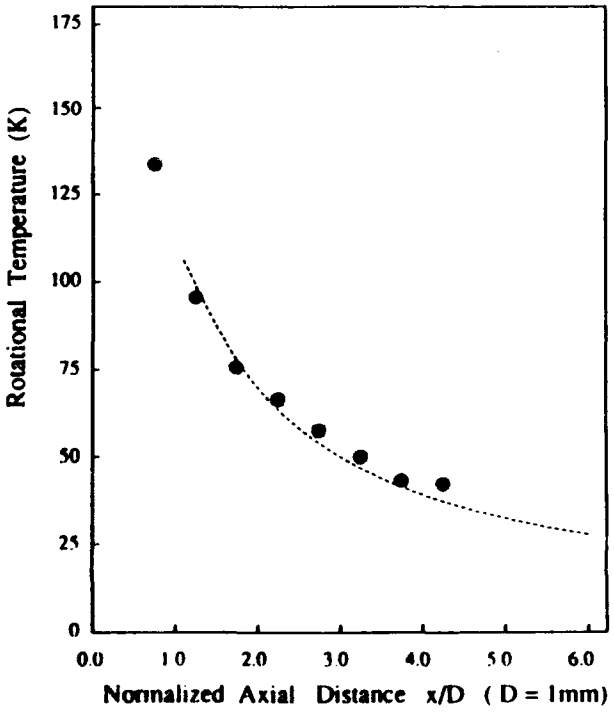

Fig. 12 Results of temperature measurement (Air)

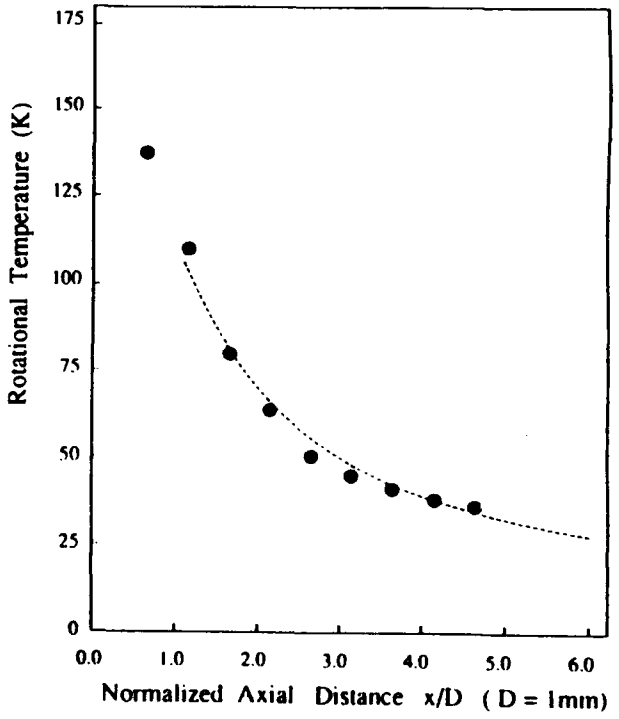

Fig. 15 Results of temperature measurement (Gas mixture)

pure rotational CARS spectra of gas mixture is effective in any ratio between the number densities of constituent species when the gas consists of only a few species.

5. CONCLUSIONS

We proposed a method for deduction of the temperature from the pure rotational CARS spectra of gas mixture. The method uses the sectionalization of spectra and Boltzmann's plot method. It is rather simpler than the fitting method used in general. The method was applied to the temperature measurement in the supersonic free jets in order to confirm its effectiveness and the experimental results agreed well with the theoretical ones. However, it is necessary to be conducted the verification in the high temperature range in future. Also in this study, the ratios between the number densities of the constituent species were known in advance and were constant, but the values should be dete mined from the identical spectra with any other method. For example, Fourier analysis technique may be used to determine the ratios between the constituent species.

REFERENCES

Alden, M., Bengtsson, P.-E. & Edner, H. 1986, Rotational CARS Generation through a Multiple Four-Color Interaction, Appl.Opt., vol.25, pp.4493-4500.

Ashkenas, H. & Sherman, F. S. 1966, The Structure and Utilization of Supersonic Free Jets in Low Density Wind Tunnels, in Rarefied Gas Dynamics, ed. J. H. de Leeuw, vol.2, pp.84-105, ACADEMIC PRESS.

Dick, B. & Gierulski, A. 1986, Multiplex Rotational CARS of N_2, O_2, and CO with Excimer Pumped Dye Laser: Species Identification and Thermometry in the Intermediate Temperature Range with High Temporal and Spatial Resolution, Appl. Phys. B, vol.40, pp. 1-7.

Eckbreth, A. C. & Anderson, T. J. 1986, Simultaneous Rotational Coherent Anti-Stokes Raman Spectroscopy and Coherent Stokes Raman Spectroscopy with Arbitrary Pump-Stokes Spectral Separation, Opt. Lett. vol. 11, pp. 496-498.

Eckbreth, A. C. 1988, Laser Diagnostics for Combustion Temperature and Species, pp. 220-300, ABACUS PRESS.

Harashima, Y. 1988, A Study on Gas Thermometry using Pure Rotational CARS Spectroscopy, Master's Degree Thesis, Tokyo Univ. of Agri. & Tech, Tokyo,Japan.

Jammu, K. S., John, G. E. St. & Welsh, H. L. 1966, Pressure Broadening of the Rotational Raman Lines of Some Simple Gases, Canadian J. of Phys., vol.44, pp. 797-814.

Magens, E. & Leipertz, A. 1993, Evaluation of Accumulated Pure Rotational CARS Spectra taken in Mixing Regions of Flames, in Coherent Raman Spectroscopy, ed. Castellucci, E. M. , Righini, R. & Foggi, P. , pp. 141-146, World Scientific.

Murphy, D. V. & Chang, R. K. 1981, Single-Pulse Broadband Rotational Coherent Anti- Stokes Raman Scattering Thermometry of Cold N_2 Gas, Opt. Lett., vol.6, pp. 233-235.

Taran, J. P. 1987, CARS (Coherent Anti-Stokes Raman Spectroscopy) Diagnostics of Discharges, Pure & Appl. Chem., vol.59, pp. 1295-1300.

Vaughan, G., Wareing, D. P., Pepler, S. J., Thomas, L. & Mitev, V. 1993, Atmospheric Temperature Measurements made by Rotational Raman Scattering, Appl. Opt., vol.32, pp. 2758-2764.

COMPARISON OF THE LIF AND DFWM TECHNIQUES FOR DETECTION AND IMAGING OF NITROGEN DIOXIDE

B. A. Mann and R. F. White

CSIRO, Division of Building Construction and Engineering, PO Box 56, Highett, Vic. 3190, Australia

ABSTRACT

The spectroscopic techniques of Degenerate Four-wave Mixing and Laser Induced Fluorescence have been applied to the detection of minor species for combustion diagnostics. In this paper we compare the results obtained from these techniques when used to detect the nitrogen dioxide molecule. Previous results have been obtained which show that DFWM signals increase for NO_2 when buffer gas is added (Mann *et al.* 1992), and that LIF signals are greatly reduced under the same circumstances (Mann and White 1993). In this paper we make direct quantitative comparisons of the two techniques in NO_2 and discuss the application of these techniques for making measurements in combustion environments.

1. INTRODUCTION

In recent years there has been a great deal of interest shown in methods of detecting minor species in combustion environments. Parameters of concentration and temperature are often required in these circumstances, but are traditionally difficult to obtain *in situ* in hostile environments. Optical methods offer the advantages of non-intrusive measurements, while laser methods offer in addition high spatial, temporal (pulsed lasers) and spectral resolution. In particular we are aiming to detect nitrogen dioxide, which is a combustion product known to cause air pollution, photochemical smog, acid rain, depletion of the ozone layer and respiratory complaints (Bowman 1992). Levels of NO_2 of 0.1-0.25 ppm by volume are considered dangerous for prolonged exposure (Streeton 1990).

To detect nitrogen dioxide *in situ* in a burner, in particular lox NOx burners, we need to be able to detect low concentrations of NO_2 in an environment at atmospheric pressure. Severe collisional quenching is known to occur in this molecule with the addition of modest pressures of buffer gas, reducing the effectiveness of fluorescence techniques. Techniques such as CARS (see for example, Greenhalgh 1987) are useful only at concentrations greater than 1%; in the case of NO_2 the suspected levels are less than 10 ppm, so this technique is not suitable.

In previous work (Mann *et al.* 1992) we have applied the non-linear laser method of DFWM to NO_2 in nitrogen at atmospheric pressure, achieving good detection limits in quantities ranging from 10,000 down to 1 ppm. In addition two-dimensional DFWM images were obtained of NO_2 seeded into a propane/air flame. An unexpected result of this work was the apparent insensitivity of DFWM to collisional quenching, since the addition of buffer gas increased the DFWM signals. Further work (Mann and White 1993) has established a qualitative comparison of the LIF and DFWM techniques for detection of nitrogen dioxide in increasing quantities of buffer gas. These results showed the expected reduction of the LIF signal with increasing buffer gas (up to 760 torr) and the corresponding increase of DFWM signal. In these particular measurements direct comparison could not be made as different detectors were used, so only the trends could be compared. In addition the DFWM results were taken under conditions of saturation, so these could not be compared directly to former results.

In this work we report quantitative measurements for both techniques using the same detector, so that the results can be directly compared. The DFWM experiment was established in a non-saturating format to enable comparison with previous results.

2. DFWM TECHNIQUE

DFWM is a third order non-linear technique, used primarily as a source of phase conjugation (see Fisher

1983). A typical beam geometry is shown in Figure 1. It is also an excellent spectroscopic technique, producing high resolution sub-Döppler spectra. The three input beams and the output phase-conjugate signal are all at the same wavelength, hence the term "degenerate". The probe beam may be at any convenient angle since phase-matching is automatic, hence the technique is suitable where optical access is limited. There is no need for a 90° window as is required in LIF.

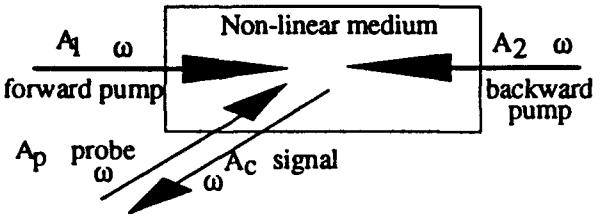

Fig. 1 Typical beam geometry for DFWM.

3. LIF TECHNIQUE

The LIF technique involves the resonant laser excitation of a molecular transition followed by isotropic fluorescent decay. The fluorescence may be detected over a known waveband by use of a suitable optical filter. In a typical experimental set-up the detection is at 90° to the laser excitation. Inherent problems with this technique are the occurrence of Rayleigh or Mie scattering at the resonant wavelength and the quantification of results, which requires a detailed knowledge of quenching rates and other spectroscopic terms. The problem of scatter can be eliminated by detecting off-resonance, although this reduces the signal intensity. Quantification requires a number of approximations and assumptions to be made. LIF has become a more common diagnostic in recent years due to simplicity of experimental set-up, detectibility of minor species and its more recent extension to a two-dimensional imaging format.

4. EXPERIMENTAL METHOD

The LIF experiment was set up as in Figure 2. Detection was achieved from the side window of the same cell used for DFWM. The DFWM experiment was set up using the format shown in Figure 3. A fused silica cell was used with a window at each end and one on the side to allow LIF detection. This cell was connected to a vacuum pump, pressure gauges and gas inlet manifold. A Questek XeCl excimer laser was used to pump a dye laser using Coumarin 460 dye in methanol giving a tunable range of 450-480 nm. The DFWM signal was redirected with a beam-splitter and detected using a photomultiplier tube (PMT) situated a few metres from the experiment. An improvement on previous signal to noise levels was obtained by using polarisation techniques. The laser light is polarised using a standard polariser. The back pump polarisation is then arranged to be orthogonal to that of the other in-going beams by use of a quarter wave plate, in this case a non-wavelength specific rhomb. The signal emerges with the polarisation at the same orientation as the back pump. Use of an analysing polariser in front of the detector allows efficient discrimination of the signal beam from any forward pump or probe light. Additional DFWM detection was performed using a gated (5 ns) dual micro-channel image-intensified CID camera (ITT F4573/11123) for comparison of signal strength and detectibility with the LIF signals. The LIF experiments were performed by blocking the DFWM probe beam and back-reflected pump and detecting the signal at 90° to the beam using the same PMT and two collection lenses. In the LIF detection a coloured glass filter (Schott OG590) was placed in front of the PMT to eliminate scatter from the exciting laser. Essentially the experiments were designed to investigate the effect of buffer gas (air or nitrogen) on the signal intensity of both DFWM and LIF in NO_2.

For both techniques the cell was initially filled with pure NO_2, to a pressure of 7.6 torr. Buffer gas (nitrogen) was then added in incremental steps and a measurement or image was recorded for each pressure. Previous DFWM buffer gas dependences have been carried out using nitrogen and air for comparison (Mann 1991). Further LIF experiments were then performed using air as buffer gas to see if the presence of oxygen modified the behaviour of NO_2 fluorescence.

In later experiments a PMT was used to detect both LIF and DFWM signals (Figures 2 and 3). A calibration of the PMT was performed to enable comparison of gain levels. LIF and DFWM experiments were performed as before, investigating the buffer gas dependence of the two techniques. In the case of DFWM the experiment was performed under conditions of non-saturation intensities and using polarisation discrimination to improve the signal to noise ratio.

Simultaneous DFWM and LIF spectra were taken by tuning the laser in increments of 0.001 nm and collecting a signal averaged over 32 shots. A photodiode was used for DFWM signal detection and the PMT for LIF detection. Both signals were processed via a boxcar and computer. The process was computer controlled using in-house developed software.

In a further experiment the intensified CID camera was used in place of the PMT to capture independently the images produced by the DFWM and LIF signals.

These were repeated for pure NO_2 and for NO_2 with buffer gas (nitrogen or air) at atmospheric pressure.

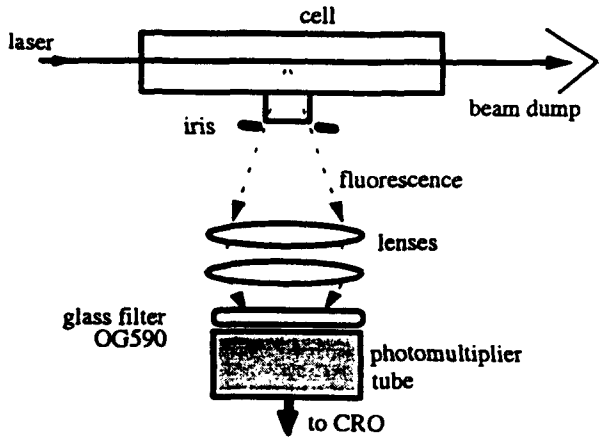

Fig. 2 Schematic of LIF experiment

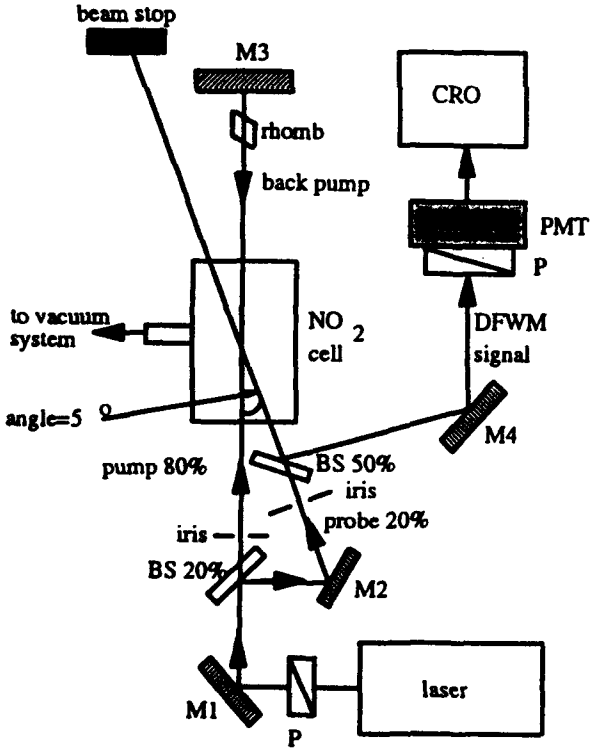

Fig. 3 Schematic of DFWM experiment. M1, M2, M4 are high reflectors at 45°, M3 at 90°. BS is a beam-splitter and P is a polariser.

5. RESULTS

A dependence of DFWM signal against laser intensity was performed using NO_2 in buffer gas at atmospheric pressure (best signal situation). It was found to have a gradient of 2.1 (not shown). The dependence of DFWM signal on laser intensity gives an indication of power saturation of the experiment. In DFWM a cubic dependence is expected in a non-saturated region due to the three input beams. The quadratic dependence of the DFWM signal on the laser intensity is consistent with that observed by Garman and Dunn-Rankin (1993) and is indicative of the regime where thermal gratings are the dominant source.

Figure 4 shows a calibration curve for the PMT used in the experiments. This has been used to compare signals obtained at different PMT gain settings.

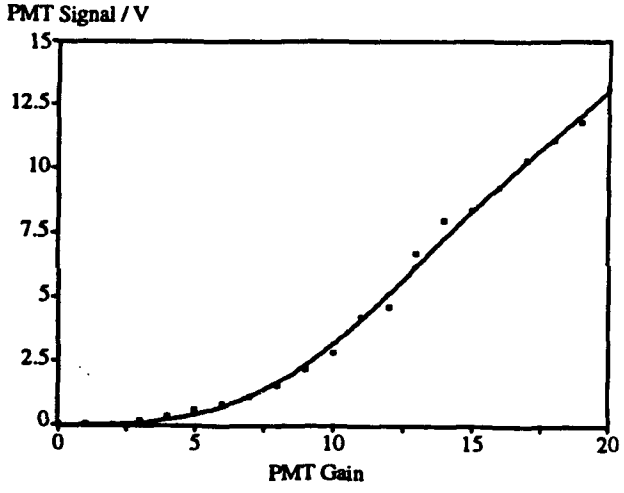

Fig. 4 Calibration curve for the PMT detector

Figure 5 shows the dependence of (a) DFWM signal and (b) LIF signal on buffer gas pressure for nitrogen dioxide. In DFWM experiments the PMT gain setting was only 7 compared with 20 required for the LIF detection. In terms of trends the DFWM signal increased slightly then decreased at low buffer gas pressures, then rises after 150 torr of buffer gas, increasing until measurements were stopped at atmospheric pressure. These results are consistent with those seen in previous experiments (Mann *et al.* 1992; Mann and Proctor 1992). The LIF signal decreases continuously as buffer gas is added. The effect is greater when nitrogen is replaced by air. At atmospheric pressure the signal to noise ratio (S:N) is ~1:1, compared with S:N of 1000:1 for DFWM at the same

pressure. However for pure NO_2 the signal to noise ratio was 5000:1 for LIF compared to ~4:1 for DFWM.

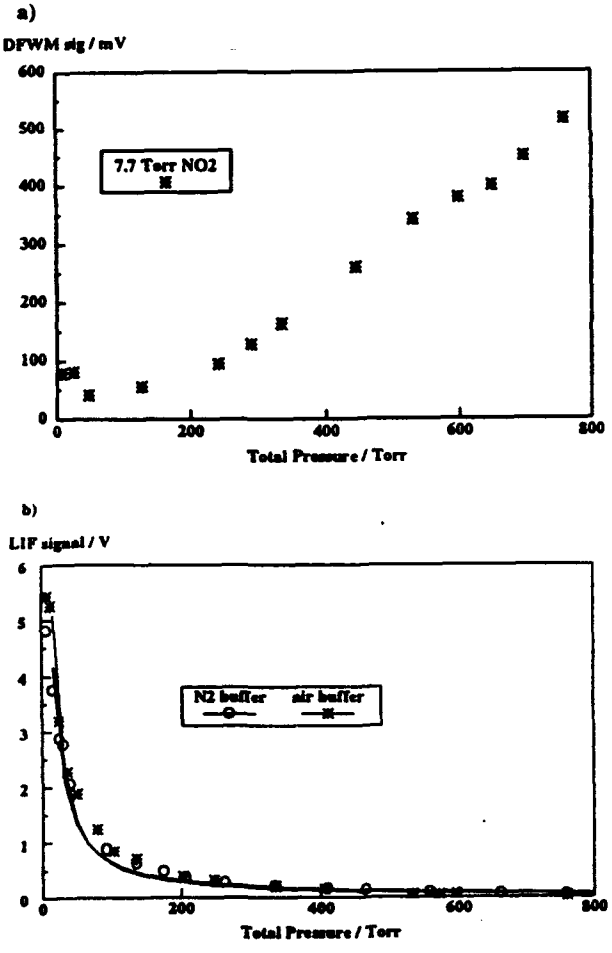

Fig. 5(a) Graph of dependence of DFWM signal in NO_2 on buffer gas (nitrogen) pressure, PMT gain 7. (b) Graph of dependence of LIF signal in NO_2 on buffer gas pressure (air or nitrogen), PMT gain 20. The lines shown are lines of best fit. In both cases the same quantity (7.6 torr) of NO_2 was used. Buffer gas was added in small increments up to 760 torr total pressure.

Figure 6 shows a DFWM spectrum of 5 torr of pure NO_2 taken over the 455 nm region, which appears to be consistent with previous DFWM spectra (Mann *et al.* 1992) in terms of line positions, although intensities appear to vary. A simultaneous LIF spectrum, recorded with the PMT, is shown on the same figure. Unfortunately it was not possible to monitor laser intensity simultaneously as only two channels were available on the boxcar and data collection system, so these spectra are not normalised to laser intensity. However previous individual spectra were normalised to laser intensity and tended to show the same spectral features with only slight intensity variations. The laser intensity variations were minimised by collecting data over 32 shots for each laser grating position.

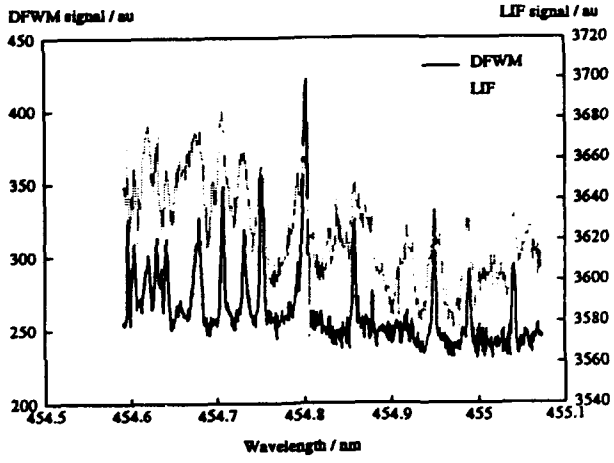

Fig. 6 Simultaneous DFWM and LIF excitation spectra in NO_2. The LIF lines are coincident with the DFWM at some peaks and are difficult to distinguish.

Figure 7 shows images taken of LIF and DFWM in NO_2 to demonstrate the signal to noise ratio obtained in each case. Figures 7a and b are LIF images in pure NO_2 and NO_2 with nitrogen buffer gas respectively. Camera gain has increased from 4.2 to 6.4 with an increased background noise level. When air was used as buffer gas the LIF signal could not be distinguished from background noise for pressures above 250 torr. Figures 7c and d show images of DFWM signal in pure NO_2 and NO_2 in atmospheric pressure of nitrogen respectively. In this case the gain of the camera was reduced from 4.0 to 1.4. Although the signal to noise ratio was poor (about 2:1) in Fig 7c, with the addition of N_2 in 7d the signal to noise ratio was greater than 2000:1.

6. DISCUSSION

The initial decrease in DFWM signal with increasing buffer gas pressure (Figure 5a) is thought to be due to the effect of pressure broadening. This effect has been qualitatively modelled (Mann 1991; Mann and Proctor 1992) and shows such a decrease for low pressures of buffer gas. The decreasing signal would continue with increasing buffer gas, but as more buffer gas is introduced the effect of thermal gratings becomes the dominant signal-producing process.

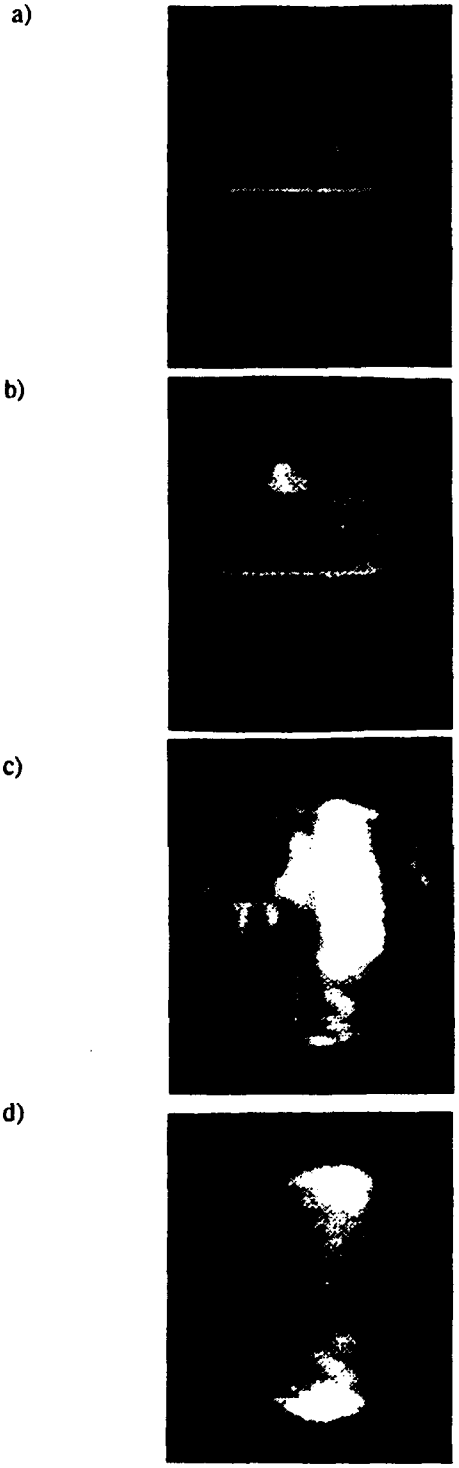

Fig. 7 Images taken with intensified CID camera. (a) Line LIF in 7.6 torr of NO_2, camera gain 4.2. (b) Line LIF in 1% NO_2 in nitrogen at 760 torr, gain 6.4. (c) DFWM signal in 7.6 torr NO_2, gain 4.0. It is difficult to distinguish the signal (brighter area) from the noise. (d) DFWM in 1% NO_2 in nitrogen at 760 torr, gain 1.4. In this image the central white zone is all signal.

These longer-lived gratings are produced by molecules in the ground state with different Boltzmann temperatures, and are not subject to the collisional de-excitation which is the dominant process in washing out the initial population grating. (The assumption made here is that the molecular motion is a slower process than collisional de-excitation. Calculations using our particular configuration suggest a forward-grating spacing of 6×10^{-6} m which is large compared with the mean distance between collisions for low pressures.) A model of these processes is being developed in conjunction with R. J. S. Morrison, Monash University.

While the exact process causing this increase in DFWM signal has yet to be definitively modelled, the result is the improved detection of NO_2 at higher buffer gas pressures up to atmospheric pressure. This increased signal gives DFWM an advantage over LIF detection of this molecule for higher pressure/atmospheric pressure environments. In particular applications such as imaging of NO_2 seeded into an atmospheric pressure flame/flow have been achieved (Mann *et al.* 1992), whilst LIF imaging and detection of this molecule have tended to be at low pressures or in rotationally cooled conditions (Sugimoto *et al.* 1984).

For low pressures of buffer gas, less than 100 torr for example, LIF would still be the preferred method of detection.

Figure 6 shows simultaneous DFWM and LIF spectra in pure NO_2. Both spectra are in good agreement with that of Mann *et al.* (1992) and Sugimoto *et al.* (1984), which was used to assign the original spectra in Mann *et al.* (1992). For spectroscopic purposes, DFWM gives sub-Döppler spectra, and the DFWM lines in Figure 7 are observed to be narrower than those of the LIF trace.

In Figure 7 we aim to show the advantages or disadvantages of the two techniques for imaging purposes. Although the LIF technique is the simplest to set up in an expanded form (we have just taken line LIF images here, not in a planar format) the signal to noise ratio deteriorates rapidly with increasing buffer gas (Figures 7a to 7b). The gain of the camera had to be increased from 4.2 to 6.4 in order to obtain an image for buffer gas pressure of 760 torr (Figure 7b). According to the camera gain information the gain indicated on the camera dial is equivalent to a gain increase by a factor of 10. In contrast the DFWM images, which were taken by aiming the signal beam into the camera, had an initial gain of 4.0 (Figure 7c) decreasing to 1.4 for the atmospheric pressure case (Figure 7d), which is a decrease in gain required by a factor of approximately 15. At atmospheric pressure this reflects the much better signals obtained for DFWM compared to LIF but for pure NO_2 the similar gains required for LIF and DFWM

indicate similar signal levels for the two techniques for this condition. However the background noise of the LIF in pure NO_2 is virtually zero, whereas with the DFWM some scatter has been observed. This scatter could be minimised by a more careful imaging set-up and the use of polarisation to eliminate forward scatter, as in the experimental arrangement shown in Figure 3.

7. CONCLUSIONS

The usefulness of LIF for certain molecules is limited by factors such as quenching, or lack of a fluorescing transition. In this case other techniques have to be adopted, and DFWM is currently being investigated by several groups as a useful alternative for minor species detection. In the particular case of NO_2 it has been demonstrated that LIF is not the preferred method for detection of minor concentrations in atmospheric pressure situations, particularly in air, due to collisional quenching. However DFWM appears to be a viable alternative, with increased sensitivity at atmospheric pressure. In addition DFWM provides a sensitive method for 2-dimensional imaging of NO_2 particularly under atmospheric pressure conditions. As a spectroscopic technique in pure NO_2 the DFWM spectrum shows narrow, easily identified lines when compared with the corresponding LIF spectrum.

REFERENCES

Bowman, C.T. 1992, Control of Combustion-generated Nitrogen Oxide Emissions, Technology Driven by Regulations, 24th International Symposium on Combustion, The Combustion Institute, Sydney.

Fisher, R.A. 1983, Optical Phase Conjugation, Academic Press.

Garman, J.D. and Dunn-Rankin D. 1993, Dependence of NO_2 Degenerate Four-Wave Mixing Signals on Buffer Gas Pressure. SPIE vol 1862, 133 .

Greenhalgh, D.A. 1987, Quantitative CARS Spectroscopy, Ch 5 of Advances in Non linear Spectroscopy, eds R.J.H. Clarke & R.E. Hester, John Wiley and Sons.

Mann, B.A. 1991, Novel Coherent Laser Spectroscopic Techniques for Minor Species Combustion Diagnostics, Ph.D. Thesis, Reading University, England.

Mann, B.A. O'Leary S.V. Astill A.G. & Greenhalgh. D.A. 1992, Degenerate Four Wave Mixing in Nitrogen Dioxide: Application to Combustion Diagnostics. Appl Phys B vol. 54, pp. 271-277.

Mann, B.A. & Proctor D. 1992, Poster presentation, 24th International Symposium on Combustion, The Combustion Institute, Sydney.

Mann, B.A. & White R.F. 1993, Detection of Nitrogen Dioxide Using LIF and DFWM: Effect of Buffer Gas, Proc. DSTO Workshop on Laser Diagnostics, Paper 15.

Streeton, J.A. 1990, Air Pollution Health Effects and Air Quality Objectives in Victoria, Victorian EPA, Australia.

Sugimoto, N. Takeuchi, N. Iijima, H. Arai, T. & Takezawa, S. 1984, Observation of Spin Splittings in the $^2B_1$ State of NO_2 by Means of Polarisation Spectroscopy. Chem Phys Letts vol. 106, pp. 403-407.

MULTIDIRECTIONAL LASER ABSORPTION TECHNIQUE FOR SIMULTANEOUS DETERMINATION OF TEMPERATURE AND CONCENTRATION WITHIN A SHOCKED GASEOUS INTERFACE

G. Jourdan, A. Touat, I. Chemouni and L. Houas

Université de Provence - IUSTI - CNRS ura 1168 - Dept. MHEQ
case 321- Faculté Saint-Jérôme 13397 Marseille cedex 20 - France

J. Fortes

Université d'Aveiro - Dept Physique
3800 Aveiro - Portugal

ABSTRACT

When a shock wave passes normally through an interface between two fluids of different densities, the hydrodynamic instability leads to turbulent three-dimensional mixing zone. Temperature and concentration are determinated through this mixing zone by a multidirectional laser absorption technique, in a double diaphragm shock tube. Absorption coefficients of two characteristic vibrational-rotational lines of the CO_2 bending mode are measured using a continuous wave CO_2 laser as a diagnostic probe. Average thermodynamic parameters have been previously determinated across the mixing zone by a monodirectional laser absorption method. Here, temperature and concentration within the mixing zone are obtained in different regions of shock tube cross section, in order to get some information on the influence of the wall effects on the development of the mixing zone.

1. INTRODUCTION

One of the fundamental problems of nuclear fusion by inertial confinement is the birth and growth of a turbulent mixing zone between the shell material and the combustible. This mixing zone, connected to the hydrodynamic instability, called Richtmyer-Meshkov instability, contributes to decrease the efficiency of the nuclear reaction. Our shock tube experiment is the monodimensional application of this phenomenon. We study the evolution of such a mixing zone originated from the shock wave acceleration of a plane interface, which initially separates two gases of different densities. Most of experimental works carried out in the framework of the Richtmyer-Meshkov instability give only qualitative informations of turbulent mixing zone such as Schlieren photographs. This technique has been used to observe the evolution and the thickness of the mixing zone. But the wall effects and the three dimensional nature of the phenomenon alter the thickness measurements. Up to the present time, to obtain quantitative informations, such as thermodynamic parameters, new techniques are undertaken as X-Ray densitometry (Bonazza et al. 1993 and Rodriguez et al. 1993) or Planar Laser Induced Fluorescence (Jacobs, 1993). In our experimental study, a multidirectional laser absorption technique (Wang, 1976) is developed for simultaneous determination of temperature and concentration profiles within a Richtmyer-Meshkov gaseous mixing zone. This experimental method is essentially based on the measurements of the absorption of 2 continuous wave CO_2 laser lines by the CO_2 in CO_2/Ar or CO_2/He mixing zones.

2. PRINCIPLE OF MEASUREMENT

The absorption of an isolated line (frequency ν) is related to the absorption coefficient α_ν by the relation $I=I_0 \exp(-\alpha_\nu L)$, where I_0 and I are the laser intensities before and after absorption respectively and L is the length of the absorbing medium. The absorption coefficient depends on the temperature and the density at a determinated frequency of the absorbing medium.

$$\alpha_\nu = \alpha(\rho, T, \nu)$$

With two measurements at 2 different frequencies, the resolution of a system of 2 equations with 2 unknowns (temperature and density) allows the determination of mean temperature and density profiles within the medium.

$$\begin{cases} \alpha_{\nu_1} = \alpha(\rho, T, \nu_1) \\ \alpha_{\nu_2} = \alpha(\rho, T, \nu_2) \end{cases}$$

Absorption coefficient calculation is made with a Voigt profile hypothesis for the CO_2 laser line. This expression also take into account the CO_2 hot bands absorption and is defined by (Fortes et al. 1994) :

$$\alpha_v(\rho,T) = \frac{8\pi^3 \nu_0}{3KT} \frac{a}{\pi \Delta\nu_D} \sqrt{\frac{\ln 2}{\pi}} g(j) |R_{12}|^2 Q_r^{-1} \left|R_{j\to j\pm1}\right|^2$$

$$\rho_{CO_2} \int_{-\infty}^{+\infty} \frac{\exp(-y^2)}{a^2 + (x-y)^2} dy \sum_i \alpha(j_i, T)$$

with

$$\alpha(j_i,T) = (B_1 - B_2)\left[1 + \frac{1}{1+4\left(\frac{k_i}{\Delta\nu_c}\right)^2} \frac{|R'_{i,12}|^2}{|R_{12}|^2}\right]$$

$$B_1 = b_1 \exp\left(\frac{-b_1 j_i (j_i+1)hc}{KT} - \frac{\theta_1}{T}\right)$$

$$B_2 = b_2 \exp\left(\frac{-b_2 (j_i + j')(j_i + j' + 1)hc}{KT} - \frac{\theta_3}{T}\right)$$

where ρ and T are the density and temperature of CO_2 respectively.

The different used symbols are : ν_0 the frequency of CO_2 laser line, $|R_{12}|^2$ a spectral characteristic equal to 1.37 10^{-39} erg cm^3 (Strilchuk & Offenberger 1974), j the rotational number,

$\left|R_{j\to j\pm1}\right|^2 = \frac{j+1}{2j+3}$ for a R line,

$\left|R_{j\to j\pm1}\right|^2 = \frac{j}{2j-1}$ for a P line,

$$Q_v^{-1} = \left\{1 - \exp\left(-\frac{\theta_1}{T}\right)\right\} \left\{1 - \exp\left(-\frac{\theta_2}{T}\right)\right\}^2 \left\{1 - \exp\left(-\frac{\theta_3}{T}\right)\right\}$$

the vibrational partition function of CO_2, a the Voigt coefficient (2<a<4), θ_i the i^{th} mode characteristic temperature, j_i the rotational number of i^{th} the hot band, j'=0 for a R line and j'=1 for a P line, k_i is the difference between the CO_2 laser line centre and hot band centre, $|R'_{12}|^2$ the power of i^{th} hot band (i=0 for the central band and then k_i=0), $\Delta\nu_c$ and $\Delta\nu_D$ the collisional and the Doppler spectral width respectively.

Previous temperature and concentration profiles have been determined within a CO_2/Ar mixing zone (Houas et al. 1987). But these thermodynamic parameters were integrated through the mixing zone, along a thin cylinder which represents, in fact, the laser beam across the test section In the present work, since the mixing zone is of course non homogeneous, we have divided the test chamber cross section into 9 regions where, in each one, we consider the mixing to be homogeneous. Figure 1 shows the different laser cross beams in the 9 regions with 5 different experimental configurations.

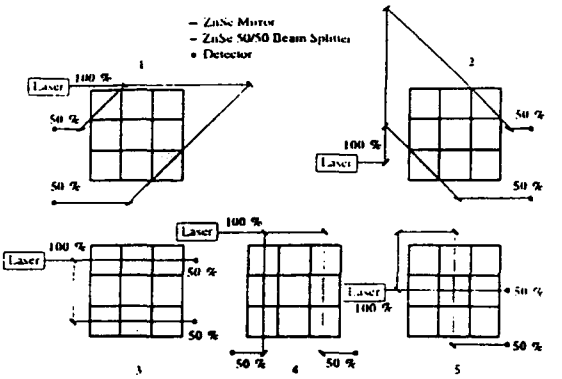

Figure 1 : The different cross beam configurations through the shock tube cross section

Using 2 different laser lines, the total experiment number is 10. The measurements must be solved in a proper order. For example, in the present arrangement, regions (1,1), (3,3), (3,1) and (1,3) can be solved independently, but the other zones (1,2), (3,2), (2,1), (2,3) and (2,2) may only be processed in that order. For the last case (2,2), we determine the absorbed energy through 2 different optical ways (Configuration 5), in order to evaluate the validity of the present diagnostic method.

3. EXPERIMENTAL SET-UP

Experiments are performed in a double diaphragm shock tube about 8 m total length. The test chamber is 8.5 cm by 8.5 cm square cross section and its length is variable from 80 to 150 cm. The test gases are CO_2, because of its spectroscopic properties, and Argon or Helium because they present no infrared absorption in the domain of our experiments. They are initially separated by a thin plastic membrane (1.5μm thickness). The SAT C7 continuous wave CO_2 laser (8Watts, beam diameter 2mm and 3.1mrd divergence) is stabilized on a suitable chosen line, Ge and ZnSe attenuators are used so that the incident beam power is less than 10mWatts. The infrared detectors type Cd_xHg_xTe centred on 10.6μm are cooled with liquid nitrogen. A frequency analyser gives a check on the used band (P20 and R12 lines). The absorption signals are recorded by a digitising oscilloscope and processed by an IBM PC 486 DX 50MHz for temperature and

concentration calculations. Figure 2 presents a sketch of the general experimental set-up.

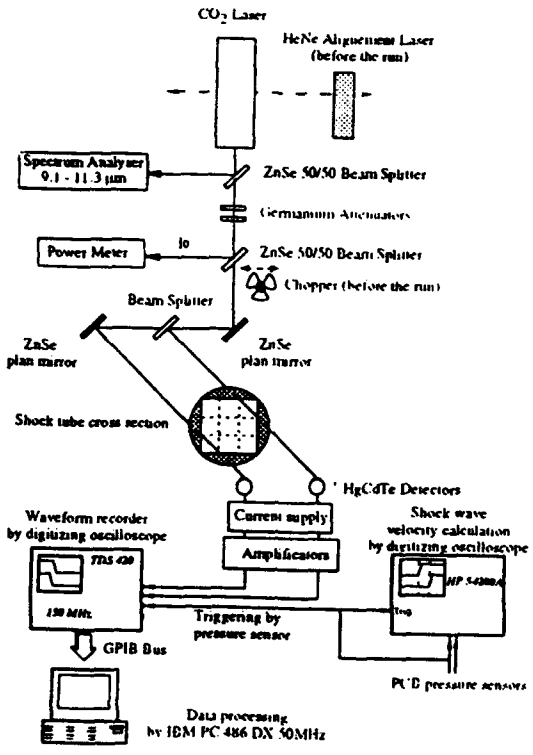

Figure 2 : Sketch of the experimental set-up

Figure 3 shows typical absorption signals.

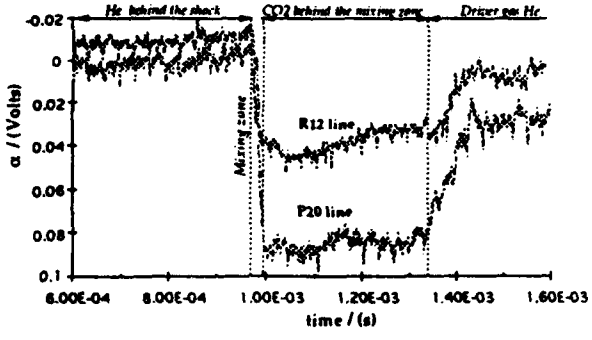

Figure 3 : Example of absorption signals for the CO_2/He mixing zone at Mach number 5

Figures 4a and 4b give the experimental wave diagrams, where x=0 and t=0 correspond to the initial interface position and the instant of oscilloscope triggering respectively. Absorption measurements have been realised at the 550 mm abscissa, for 2 couples of test gases : CO_2/Ar and CO_2/He with Mach number 5 in the CO_2.

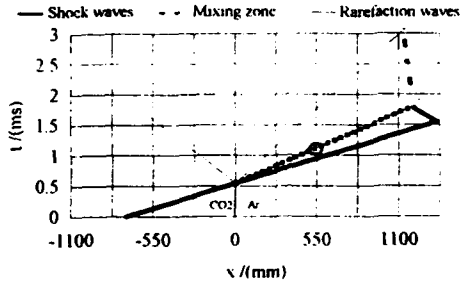

Figure 4a : (x,t) diagram CO_2/Ar Mach 5

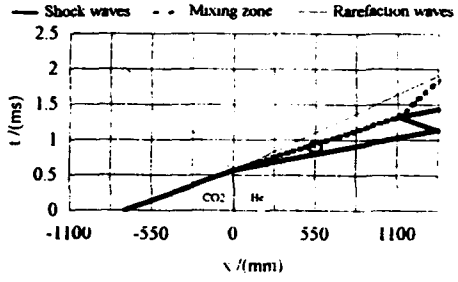

Figure 4b : (x,t) diagram CO_2/He Mach 5

4. RESULTS AND DISCUSSION

Figures 5 and 6 present mass concentration profiles and normalized temperature of CO_2 in the CO_2/Ar and CO_2/He mixing zones for an incident shock wave Mach number in CO_2 of 5. As preliminary results have shown that the mixing zone presents a significant symmetry in the 4 corners of the shock tube and near the walls (Touat et al. 1993), we present here only results obtained in one corner, near one wall and in the centre of the tube.

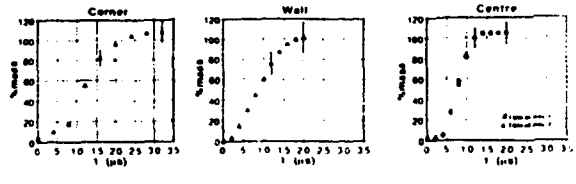

Figure 5a : Concentration profiles - CO_2/Ar Mach 5
Mixing zone velocity = 1100m/s
Initial pressure $P_{CO2} = P_{Ar} = 2000Pa$
Atwood number = -0.34

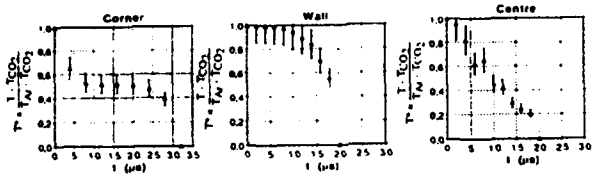

Figure 5b : Normalized temperature profiles
CO_2/Ar Mach 5

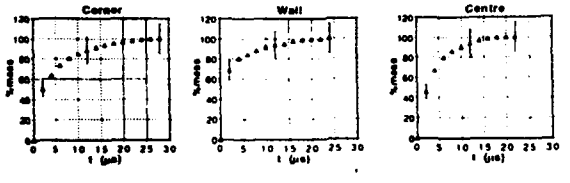

Figure 6a : Concentration profiles - CO_2/He Mach 5
Mixing zone velocity = 1485m/s
Initial pressure $P_{CO2} = P_{He} = 2000Pa$
Atwood number = -0.83

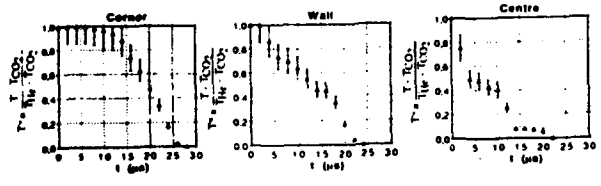

Figure 6b : Normalized temperature profiles
CO_2/He Mach 5

First, the 2 profiles obtained in the centre for 2 different optical ways in CO_2/Ar mixing zone, are very similar and validate the multidirectional diagnostic laser method. From an other hand, the different profiles obtained in each zone, give some information on the influence of the boundary layer and the three dimensional aspect of the turbulent mixing zone. Effectively, the mixing zone thickness is not homogeneous. As we can see, the thickness of the CO_2/Ar mixing zone is about 30 mm in the corner, 12 mm near the wall and 10 mm in centre. For the CO_2/He case, we obtain 25 mm in the corner, 16 mm near the wall and 15 mm in the centre. Furthermore, with this new technique, we can observe that thickness measurements by Schlieren visualizations were over evaluated (Houas et al. 1994).
Let us consider now the mass concentration profiles.

As we can see, each concentration profile in the centre of the tube (Figures 5a and 6a) can be devided in 3 different regions. In the first one, which corresponds to about 5% (for CO_2/He mixing zone) to 20% (for CO_2/Ar case) of the total thickness of the mixing zone, the monatomic gas is preponderant. The third region, about 40% for the 2 mixing zones tested, shows a preponderance of CO_2 since in this region we obtain more than 95% of CO_2. In the second region, which is between the first and the third one (approximately half of the mixing zone thickness for the 2 cases) we observe a variation of the concentration from 5% to 95%. In our opinion, this region corresponds to the effective mixing zone far from the influence of the wall effects. With these considerations, we can conceive 2 three dimensional aspects of the mixing zone shape in the shock tube compatible with the concentration profiles and which point out the wall effects. The mixing zone develops between 2 regions which are directly governed by the wall effects as show below :

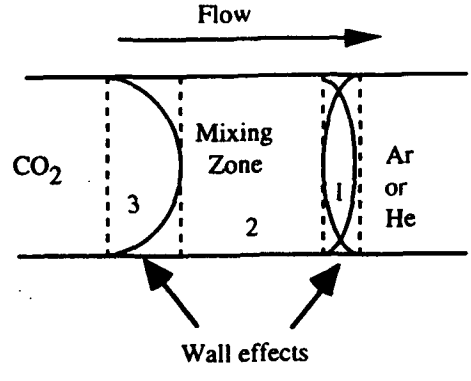

The normalized temperatures T* for the 2 tested mixing zones are presented on figure 5b and 6b, where T* is defined by : $T^* = \frac{T - T_{CO_2}}{T_X - T_{CO_2}}$, X = Ar or He. In the centre, the influence of shock tube walls is really negligible and the associated profile are almost linear. Near the walls, the influence of the boundary layer, probably turbulent for CO_2/Ar mixing and probably laminar for CO_2/He mixing, and the corner effects can explain the different temperature profiles in the first case and the similar ones for the CO_2/He mixing zone. Thus, it is probable that in the first case the laser beam near the walls (Configurations 3 and 4 - Figure 1) crossed close to boundary layer and is more far from it in the CO_2/He case. Presently, in the corner, the superposition of boundary layer and angle effects with the complexity of the laser cross beam do not warrant to explain correctly the results.

5. CONCLUSION

The multidirectional laser absorption technique is available for thermodynamic parameters study in shock tube experiments. The different profiles measured within different regions of the shock tube cross section give some informations on the wall boundary layer and shock tube corners influences. These profiles also constitute a data basis for Richtmyer-Meshkov instability numerical simulation codes. Moreover, mixing zone thickness measured at this abscissa by Schlieren technique can be corrected by a factor 0.5. The quantitative influence of wall effects, difficult to evaluate by Schlieren techniques, are clearly pointed out with the multidirectional laser absorption method. Simultaneous measurements with 3 detectors are presently undertaken to provide the time delay in the 3 signals and to obtain a real three dimensional view of the mixing zone thickness.

ACKNOWLEDGEMENTS

This work is supported by the Centre d'Etudes Nucléaires de Limeil-Valenton (C.E.A.) on contract N°1253/S 766 II Y.

REFERENCES

Bonazza, R. & Sturtevant, B. 1993, X-Ray Measurements of Shock-Induced Mixing at an Air/Xenon Interface, Proceeding of the 4th International Workshop on the Physics of Compressible Turbulent Mixing, Cambridge (U.K.), p194.

Fortes, J. Ramdani, A. & Houas, L. 1994, CO_2 Laser Absorption Measurements of Temperature and Density in Shock Induced Richtmyer-Meshkov Mixing Zone, to be published.

Houas, L. Farhat, A. Ramdani, A. Fortes, J. & Brun, R. 1987, Concentration and Temperature Profiles in a Shocked Gaseous Interface, Proceeding of the 16th International Symposium on Shock Tubes and Waves, Aachen (Germany).

Houas, L. Chemouni, I. & Touat, A. 1994, Remarks on Richtmyer-Meshkov Experiments in Shock Tubes, to be published.

Jacobs, J.W. Jenkins, D.G. Klein, D.L. & Benjamin, R.F. 1993, Experimental Study of Instability Growth Patterns of a Shock-Accelerated, Thin Fluid Layer, Proceeding of the 4th International Workshop on the Physics of Compressible Turbulent Mixing, Cambridge (U.K.), p223.

Rodriguez, G. Galametz, I. Croso, H. & Haas, J.F. 1993, Richtmyer-Meshkov Instability in a Vertical Shock Tube, Proceeding of the 4th International Workshop on the Physics of Compressible Turbulent Mixing, Cambridge (U.K.), p260.

Strilchuk, A.R. & Offenberger, A.A. 1974, High Temperature Absorption in CO_2 at 10.6 μm, Applied Optics, vol 13, n°11, p2643.

Touat, A. Chemouni, I. Jourdan, G. Labracherie, L. & Houas, L. 1993, Simultaneous Temperature and Concentration measurements in Richtmyer-Meshkov Mixing, Proceeding of the 19th International Symposium on Shock Tubes and Waves, Marseille (France).

Wang, J.Y. 1976, Laser Absorption Method for Simultaneous Determination of Temperature and Species Concentration through a Cross Section of a Radiating Flow, Applied Optics, vol 15, n°3, p768.

A SHOCK TUBE STUDY OF CN EMISSION IN TITAN RADIATIVE ENVIRONMENT

M. Billiotte, L. Labracherie, M.P. Dumitrescu, L.Z. Dumitrescu, R. Brun, D. Zeitoun and L. Houas

Université de Provence, IUSTI - CNRS URA 1168, Dept. MHEq, case 321, Faculté Saint Jérôme, 13397 Marseille cedex 20, France

M. Baillion

Aerospatiale, Division Espace et Défense, Departement Aerodynamique, B.P. 2 78133 Les Mureaux Cédex, France

ABSTRACT

The CN radical is present in a wide variety of complex gaseous environments at temperatures up to 10,000K and is of prime interest in many instances of astrophysical and terrestrial interests such as stellar atmospheres, afterglow discharges, combustion processes and planetary entry probes. The Huygens probe will enter the Titan atmosphere which is mainly composed of Nitrogen (up to 90%), Argon (more than 10%) and Methane (nearly 5%) and will be submitted to conditions corresponding to a Mach 20 flow. Emission and absorption measurements of the main electronic transitions of CN molecules have been planned to determine the different thermochemical properties such as non-equilibrium temperatures and concentration. Tests are performed in the shock-tube of the Marseilles free-piston hypersonic facility which allows to produce high Mach numbers without any combustion or pre-heater device that might contaminate the test gas.

1. INTRODUCTION

The NASA-ESA planetary mission "Cassini" planned to explore Saturn and its satellites, consists of an Orbiter and a Probe. The so-called Huygens probe will be released from the Orbiter and enter Titan's atmosphere at a velocity of about 6 km/s. The probe will be submitted, during its deceleration, to a high temperature environment that generates a severe radiating heat flux. Titan's atmosphere is composed of Methane in amounts that do not exceed 3 or 4% in the most portion of the atmosphere, but could reach 10 % near the ground. Argon is also present in the atmosphere but the exact concentration has not been exactly determined, and could be in the range of 0 to 20 %. The main component is Nitrogen which may be up to 90 % in Titan's atmosphere composition.

The temperature of the flow field behind the shock wave is high enough to transform the gas in the shock layer into an ionised plasma composed mainly of N_2, N, C, CH, CN, H, NH, Ar and their associate ionised species as well as electrons. The shock stand-off distance is small so that the shock layer plasma is not in thermal equilibrium (Park, 1992), and the assumption of thermal equilibrium leads to underestimated radiative heating compared to experimental data (Park, 1988). The CN molar fraction in the plasma is such that the radiative heat flux is mainly due to spontaneous emission of the so-called CN violet band ($B^2\Sigma^+ \rightarrow X^2\Sigma^+$).

The Marseille free-piston facility can be easily tuned to match the entry conditions of the Huygens probe. The non-equilibrium shock layer conditions are produced behind a normal shock wave propagating in the shock tube. An example of the non-equilibrium temperatures calculated behind a Mach 16 incident shock wave is given in figure 1 (Baillon et al., 1992).

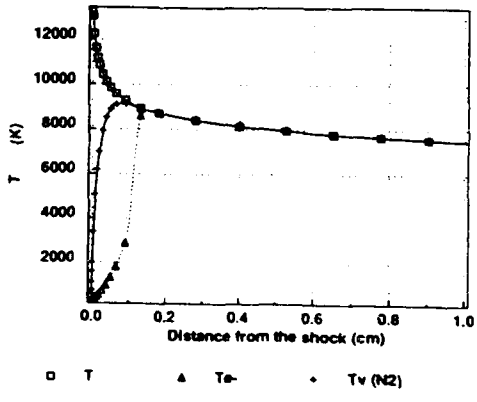

Figure 1: Evolution of the non-equilibrium temperatures in the normal shock layer

The aim of this work is to determine the non-equilibrium radiative heat-flux of the CN molecules in the shock layer and to deduce temperatures and concentration evolution for different mixtures by means of emission and absorption measurements. For moment, only emission measurements are conducted and a set of different mixtures are tested to find which can be the most severe radiative environment for the Huygens probe.

2. EXPERIMENTAL SET-UP

2.1 Facility description

Experiments are conducted in the TCM2 free-piston shock tube which is presented in figure 2. Initial pressures are 40 bar in the air reservoir and 3 bar of helium in the compression tube. The piston weight is 12 kg and the burst pressure of the diaphragm separating the shock tube from the driver tube is 120 bar. Different upstream compositions have been tested which correspond to four different concentration of Argon: 0%, 5%, 10% and 20%. The methane molar fraction is constant in each case and is equal to 3% and the nitrogen molar fraction correspond to the stœchiometric composition. The mixtures have been previously prepared with an accuracy of less than 2 % for the molar fraction of each species. Before the filling of the shock tube, a vacuum of 10^{-4} mb is generated by a turbo-molecular pump. The initial filling pressure of the test mixture is 2 mb so that the theoretical Mach number is about 18. Bursting pressures have been shown to be reproduced within 1% by a special scoring device (Labracherie et al., 1993). The test section is located in the shock tube 3.5 m downstream of the diaphragm. The shock tube is 70 mm internal diameter and 6 m long. The windows of the test chamber are BK7 glass 10 mm thick and 20 mm diameter.

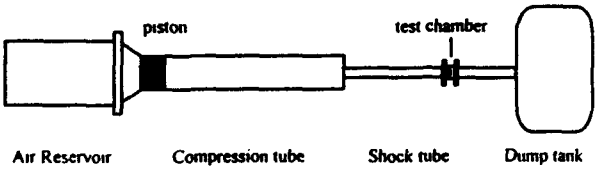

Figure 2: Scheme of the Marseille facility

The shock velocity at the test chamber location is measured with three wall-mounted platinum resistance gauges and the downstream pressure with a PCB piezoelectric gauge model A113-A21.

2.2 Optical system

The optical apparatus for emission recording is shown in figure 3. The emitted light is focused into an optical fibre through a rectangular slit of 500 µm width by a 50 mm focal lens. The solid angle of light collection is less than 15.10^{-3} sr and the spatial smearing at the centre of the shock tube is about 0.8 mm. The reception rectangular optical fibre, which is 200 µm width, is imaged on the entrance slit of the Cherny-Turner 640 mm monochromator.

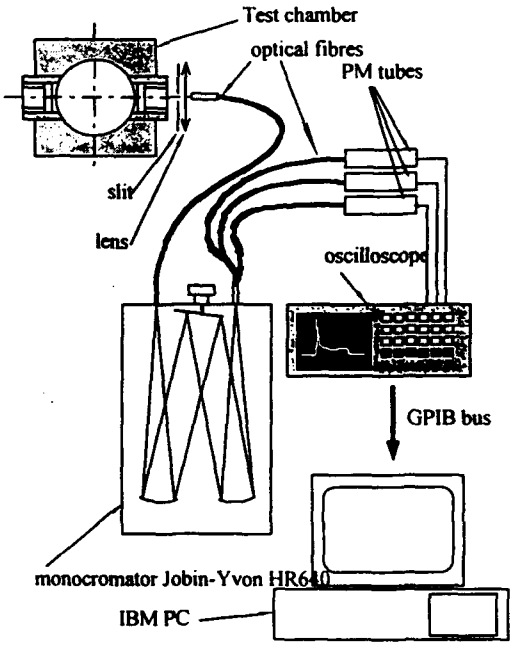

Figure 3: Optical apparatus

The dimension of the grating is 10 cm x 10 cm, ruled to 3200 lines/mm; thus the linear dispersion is about 3.7 Å/mm at 4000Å. A special apparatus has been designed for the monochromator exit and consists of three rectangular optical fibres which materialize three exit slits. This system is shown in figure 4. The width of each fibre is 200 µm and the horizontal spacing between the slits has been fixed to fit in with three spectral lines of interest. This system is particularly attractive in reducing the number of shots needed and especially because the three scanned wavelengths correspond to identical experimental conditions.

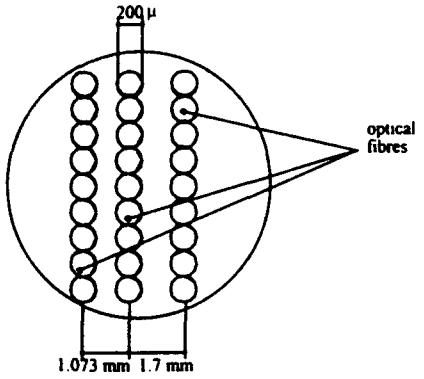

Figure 4: Exit slit system for simultaneous wavelength measurement

The light emission is measured with three photo-multipliers tubes Hamamatsu R105 UH which have been chosen for their great sensitivity in the ultraviolet region and because of their very fast rise time (< 10 ns). Amplifying circuits have been designed to produce a current/voltage conversion of 4 mV/µA on a 50 Ω load resistance with a rise time smaller than 100 ns. The PMT signals are recorded by a four channel Tektronix 150 MHz bandwidth oscilloscope.

3. EMISSION MEASUREMENTS

Emission measurements of the electronic transition $B^2\Sigma^+ \rightarrow X^2\Sigma^+$ of CN molecules are first conducted behind the incident shock wave propagating in different test mixtures. The $\Delta v=0$ band is especially recorded because of its emission magnitude compared to the other vibrational transitions. Moreover, no overlapping spectrum from other species is present in the violet system of CN except from the first negative band of N_2^+ which is very low due to the weak concentration of the ionised species (Baillon et al., 1992).

Figure 5 shows a typical signal obtained at 3880 Å with a 10% Ar mixture for typical run conditions with an initial low pressure of 2 mb. The emission signal increases until the electronic temperature reach a maximum. Then, the electronic temperature, just as the rotational and vibrational temperatures, decreases until a plateau value is reached. In fact, this plateau value cannot be explained by an equilibrium value because the distance behind the shock is too small to allow thermal equilibrium. Wall boundary layer and deceleration of the shock velocity seem to be the main cause for this early stationary plateau. The ratio of the peak value to the plateau value is about 4, which is in good agreement with previous analyses (Park C.S, 1991).

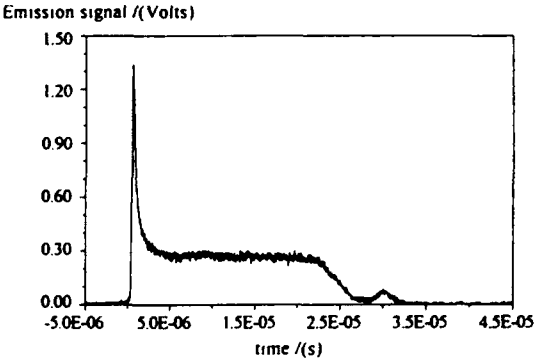

Figure 5: Typical emission signal

These measurements are used to calculate the rotational and vibrational temperature evolution within the shock layer. The three scanned wavelengths are set to belong for two of them to the (0.0) band and the third one to the (1,1) band so that the rotational temperature can be determined from the ratio of two intensities recorded in the same vibrational band and the vibrational temperature from ratio of intensities measured in different vibrational bands. The figure 6 shows the three simultaneous emission measurements.

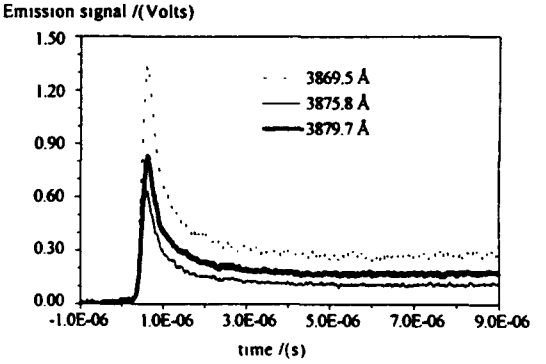

Figure 6: Simultaneous measurements of emission signals

The intensities ratio in the P branch of the (0,0) band depends theoretically only on the rotational temperature but practically, overlapping of the rotational lines prevents from obtaining a relationship between measured intensities ratio and

temperature. Thus, the ratio of measured intensities have to be compared with the calculated one for a given rotational temperature. The true emission spectrum of the molecule is calculated by a line by line method (Arnold et al., 1969) and is convoluted with the measured slit function of the optical system. The rotational temperature is iterated in the synthetic spectra calculation until the theoretical intensities ratio is equal to the experimental one. The ratio of experimental intensities ($I_{3879.7Å}/I_{3875.8Å}$) and ($I_{3879.7Å}/I_{3869.5Å}$) are plotted in figure 7.

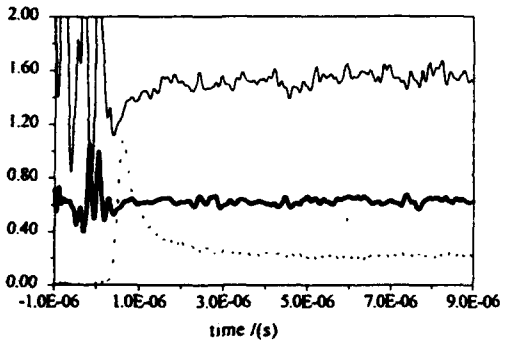

Figure 7: Experimental ratios $I_{3879.7Å}/I_{3875.8Å}$ (normal solid line) and $I_{3879.7Å}/I_{3869.5Å}$ (bold solid line). One of the emission signal is shown for time reference (dashed line)

In the same way, for a given rotational temperature, the ratio of two intensities that belong to different vibrational transitions, is a function of the vibrational temperature and of the rotational temperature which has been determined from the previous ratio.

At the present time, a disagreement in experimental intensities has been found and the total spectrum of the $\Delta v=0$ system is actually recorded to find the origin of the discrepancy.

5. CONCLUSION

As a provisional conclusion, the CN emission spectrum of the violet system is recorded but a disagreement in the comparison of experimental results with theoretical calculation prevents actually from determining rotational and vibrational temperature profiles. A new set of runs is needed in the $\Delta v=0$ range to give the complete qualitative spectrum in order to make a more accurate comparison with emission calculations of CN molecules.

Absorption measurements which allow to deduce both electronic temperature and CN concentration, will be conducted afterwards.

ACKNOWLEDGEMENT

This work is supported by AEROSPATIALE "Espace & Défense" (Contract 250064-32319Z)

REFERENCES

Arnold, J.O., Whiting, E.E., Lyle, G.C. 1969, Line by line calculation of spectra from diatomic molecules and atoms assuming a voigt line profile, Journal of Quant. Spectrosc. and Radiat. Transfer., Vol. 9, pp. 775-798.

Baillon, M., Soler J. and Taquin G., Huygens 1992 Probe Radiative Environment. Proc. of the IUTAM Symposium, pp. 3-12, Marseille, France.

Labracherie, L., Dumitrecu, M.P., Burtschell, Y. and Houas, L. 1993, On the compression process in a free-piston shock-tunnel, Shock Waves, Vol. 3, pp. 19-23.

Park, C. 1988, Assesment of a two-temperature kinetic model for dissociating and weakly ionizing nitrogen. Journal of thermophysics and heat transfer, Vol. 2, No. 1, pp. 8-16.

Park, C.S. 1991, Studies of radiative emission from the stimulated shock layer of the huygens probe, P.H.D, Stanford University.

Flow Density Visualization Enhancement to the Warwick Solid State 3DPIV System

M. Funes-Gallanzi

Optical Engineering Laboratory
Department of Engineering
University of Warwick, U.K.

1 Abstract

The work presented in this paper deals with the capture of a qualitative picture at the same time as stereo PIV data is being gathered. In this way, the quantitative data provided by PIV can be put into the qualitative framework provided by the flow density visualization image.

The third channel of a colour frame grabber system was used to capture a shadowgraph at the same time as the PIV data was gathered at a speed of 240m/s. The imaging system is capable of capuring PIV data in real time at a resolution of 576*768 pixels. The PIV data was measured on a RB-211 bypass model using a Nd/YAG double pulse laser. Other forms of flow density techniques are currently being investigated such as Schlieren and Sheareography.

2 Introduction

The development of a PIV system previously described [3] proved very successful and straight-forward to operate as a stereo PIV digital system. The results of the analysis, however, were still considered to be unsatisfactory; as they could not be set readily into an overall qualitative framework. It was noted that at least one extra channel was readily available for use together with the 3DPIV system, which could be used to give a wider perpective from which to evaluate the more quantitative data provided by PIV.

There is essentially three flow density visualisation techniques. These were considered, and the Shadowgraph/Schlieren technique was chosen to be added to the 3DPIV system. The system was tested at the new Warwick University transonic blowdown facility; recently instrumented and commisioned. First of all, the following is a short description of the flow density visualisation techniques. The experimental facility is then described. This is followed by a description of the experiment performed to test both the facility and the new setup 3DPIV system in conjunction; which involved measurements on a jet bypass model of an RB-211.

3 Shadowgraph/Schlieren techniques

The Shadowgraph technique is the simplest in terms of the complexity of the optical setup needed to generate the shadowgraph pictures. In this setup a parallel beam is generated by a lens whose focal point coincides with a point light source. The parallel light beam traverses the flow field under investigation. The intensity distribution in the light beam is then recorded in a plane some distance from the region of interest. Because of the refraction of the light rays in the flow field, the intensisty distribution in the recording plane will deviate by $\Delta I(x,y)$ from the intensity distribution $I(x,y)$ which would have been recorded in the absense of any refraction.

It can be shown that the shadowgraph technique responds to the second order derivatives of the density in the flow field. The shadowgraph technique can be applied to visualize shock wave geometries in high-speed flows. Shock waves localize surfaces in the flow over which the flow parameters vary discontinously (assuming inviscid flow). However, flow is in fact viscous, and so experimentally observed shock waves have a finite thickness. Shock waves will be reflected in the shadowgraph by local, strong intensity fluctuations. Another application of interest involves its ability to visualize density variations in turbulent flow. If the exposure time is suitably short, turbulent structures will be visible as a grany pattern. However, the technique has only limited ability to provide quantitative information. From the derived equations, it follows that this would require a double integration of the recorded intensity distribution. Nevertheless, the simplicity of the required optical setup has made it a widely applied diagnostic technique where a quick qualitative overview of the flow field is required.

With a few extra optical components, the shadowgraph system can be expanded to the Schlieren system of Figure 1. In this optical arrangement the light beam is focussed by a second lens to form an image of the light in its focal plane. A camera lens images a plane in the region of interest on the recording plane. In the presence of a variable density flow field, the light rays will have been refracted. Therefore, the image of the light source in the focal plane of the second lens will be displaced from the x-axis, the optical axis of the Schlieren system. If the refraction angle of a particular light ray is equal to ε and if the focal length of the second lens is equal to f, then the displacement will be equal to $f.\tan(\varepsilon)$. By positioning a spatial filter in the focal plane of the second lens, the refraction of the individual light rays in the light beam caused by the interaction with the flow field becomes visible in the recording plane as a midifield intensity pattern: the Schlieren picture. The intensity in the recording plane is proportional to the component of the density gradient in the flow field normal to the knife-edge.

In summary, the shadowgraph technique, the Schlieren technique and the interferometric technique respectively visualize the integrated value of the second order derivative of density, of the first order derivative of the density, and of the absolute density in a three dimensional flow field.

Only the interferometric technique is able to provide accurate

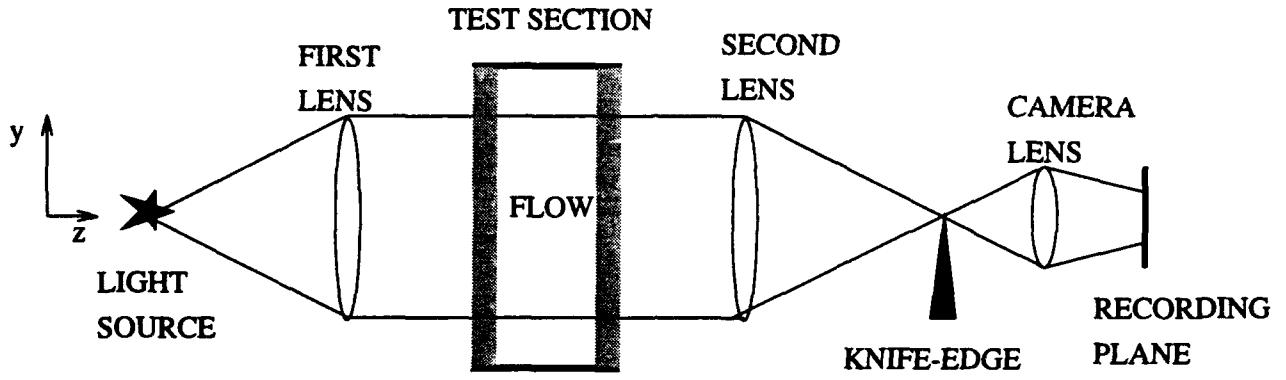

Figure 1 Optical Arrangement of Schlieren System

quantitative data (of the order of $\frac{\lambda}{10}$) about the density in the flow field because it visualizes the density distribution as a fringe pattern with known density difference between the fringes. On the other hand, it requires a high degree of skill and sophisticated equipment to perform, as well as being very difficult to carry out in an industrial environment. Therefore, since the solid state PIV system developed aims to be portable, quick and straight-forward to use, the Shadowgraph/Schlieren techniques were preferred for use to complement the stereo PIV approach.

4 Warwick University Transonic Blowdown Facility(TBF) Description

The Warwick University Transonic Blowdown facility is s transient tunnel surrounded by an Anacote chamber. The initial function of the test cell had been the evaluation of noise levels at the exit of a transonic jet.

The facility is described schematically in the diagram shown in Figure 2. The compressor supplies air directly into the presssure vessel, and takes approximately 20 minutes to achieve its design pressure of 26 bar; i.e. it holds 90kg of air. The run conditions are determined by the setting of valve M/R2 which switches on the pilot operated valve R18. The AG20 step down valve serves only to protect the M/R2 valve from excessive pressure. The flow then passes through the regulator valve R34. This is an electronically-controlled valve which can be set to maintain a fixed flow-rate downstream. Ultimately, as the mass of air in the pressure vessel is depleted (normally by no more than 20% to limit any changes in the Reynolds number), the pressure immediately upstream of the regulator falls. The electronic control on the regulator senses the pressure drop and compensates accordingly. The flow then passes through a dryer and a ball-bearing IVCO valve, solenoid operated through a Norbro pneumatic actuator, before entering the settling tank. The ball-bearing valve is computer-controlled by the imaging equipment and opened approximately 1 second before imaging begins to ensure the desired flow conditions have been achieved. The settling tank lies immediately before the sonic throat; the stagnation pressure at this point being the deteminant factor in the behaviour of the test flow. The seeding required for PIV experiments, is injected into the settling chamber as shown, at a pressure of approximately 8 bar.

The facility has only recently come under the control of the Optical Engineering Laboratory. A number of improvements are currently being studied. These include differential pressure transducer shut-down when the mass in the presssure vessel falls below a set point, placing the dryer before the pressure vessel, addition of a by-pass, and replacement of the current regulator arrangement to improve the available flow rate.

5 3DPIV/Schlieren Experimental Techniques

The nature of the Schlieren pictures obtained as part of a 3DPIV system, can be rather different from conventional Schlieren and provides further insight into the characteristics of the flow under consideration. Typically, a small percentage is bled from the main Nd/YAG beam to provide the light source for imaging. This light source, in a typical high-speed experiment, would be made up of two or three 10ns pulses μs apart. Thus, each pulse generates and almost instantaneous image of the flow. Therefore, if the flow within the sensing period is stable one image is visible. If the flow is highly turbulent, two or three distinct images obtain.

6 Overall System

The experimental system of Figure 3 was implemented in order to investigate the suitability of the Schlieren technique as a complement of the 3DPIV system. Approximately 5% of the light could be taken by a beam splitter from the main 3DPIV pulse laser beam and employed for the Schlieren image. The rest of the beam being employed for PIV imaging, as recently reported[2] at SPIE, to produce the 3DPIV data.

As a means of setting up the experiment and checking the system more easily, a shadowgraph configuration was setup first. This setup involved the use of white light source rather than bleeding the Nd/YAG and simplyfing the optics to image a shadowgraph rather than the extra work involved in setting up the spatial filter for the Schlieren image.

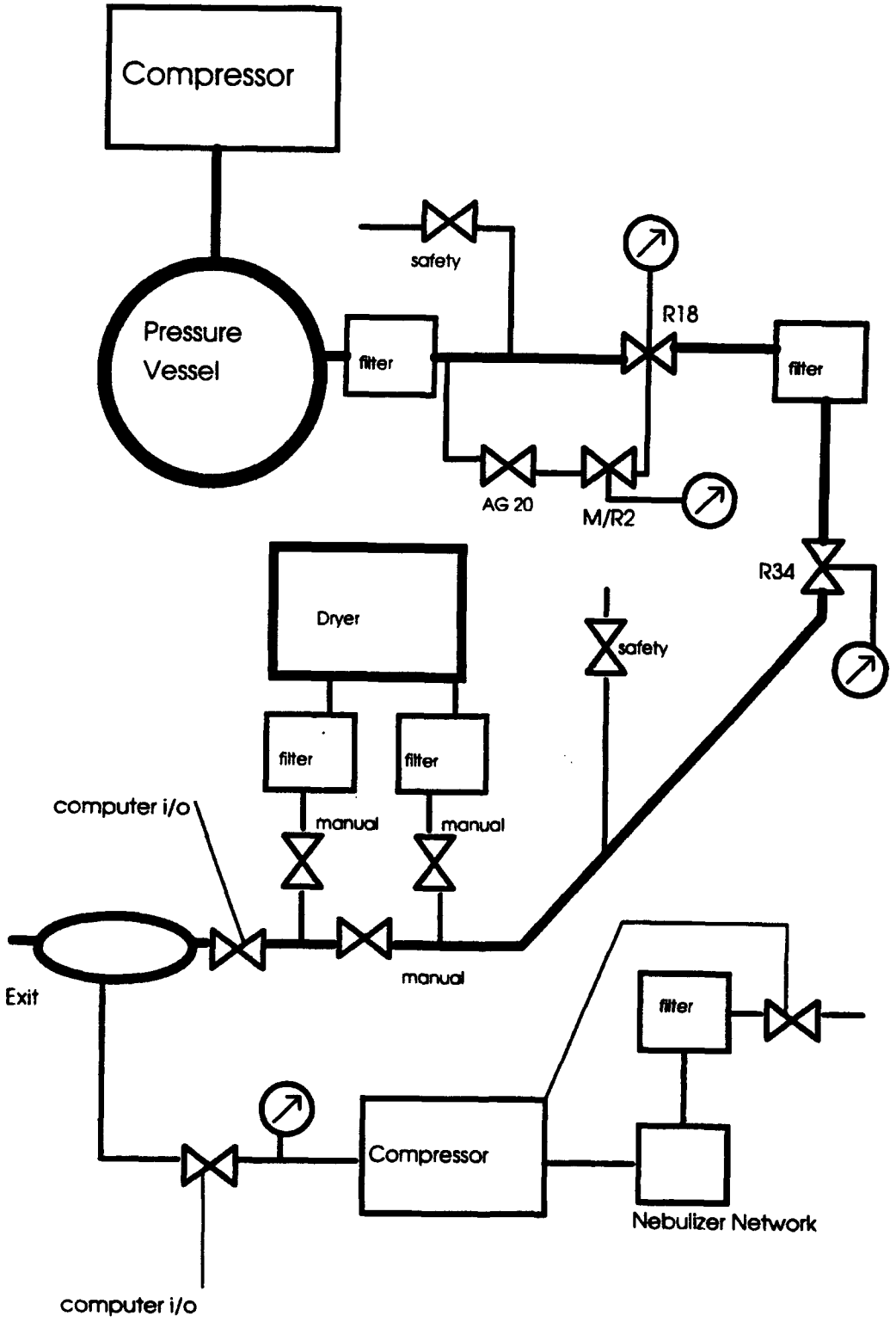

Figure 2 Schematic diagram of the TBF facility

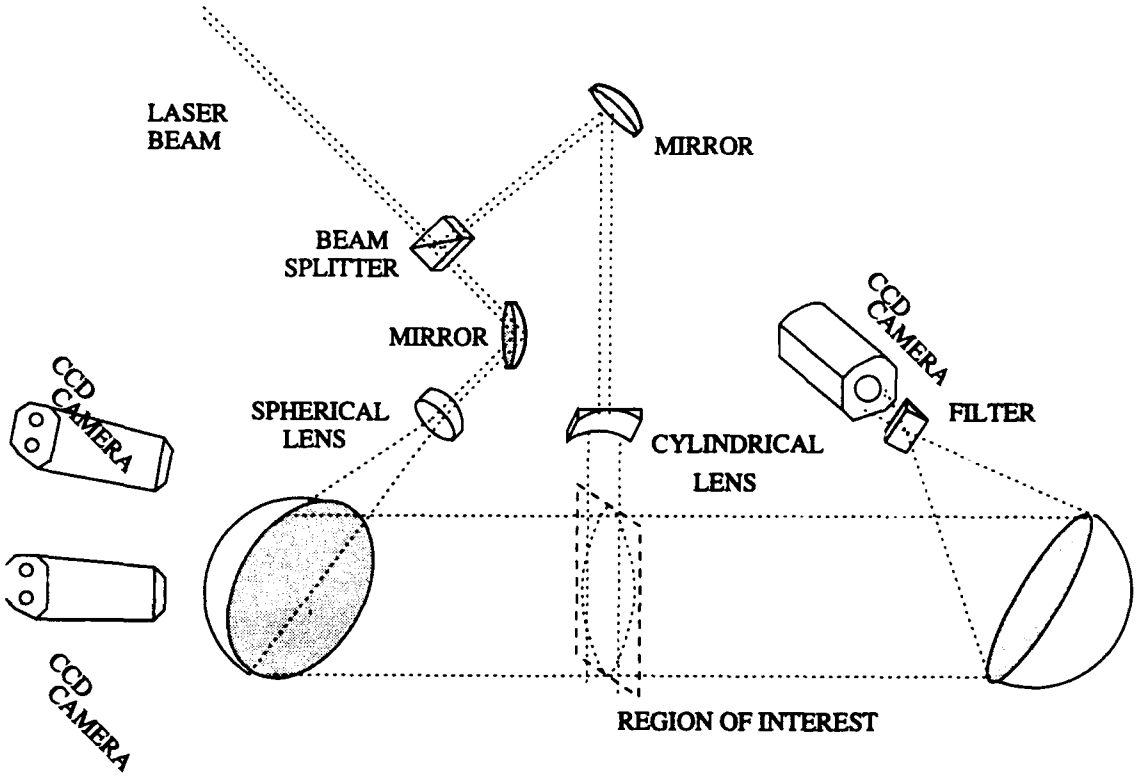

Figure 3 Schematic diagram of the overall system

7 PIV Imaging System

The PIV system includes a computer-controlled high-sensitivity CCD camera arrangement, together with image analysis tools which allow the user to asses the results of the test within a half hour period. The whole system being externally triggered, to allow the investigation of stator-rotor interactions for instance.

In fact, the system has been recently successfully tested at Mach 2. As soon as the ILPC is available, this video system will be tested at DRA Pyestock. It is designed to cope with the exacting requirements demanded by the stator/rotor interaction research currently under way. It is schematically described in figure 4 :

A high performance colour frame-grabber lies at the heart of the system. Thus, it is able to record stereo images as well as a third general-purpose camera; all genlocked. It is controlled by a PC which, through an I/O board, also controls the analog control circuitry. The analog control circuit generates the video sync. signals required by the CCD cameras (set to 768x576 non-interlace mode) and the LFS sync. which fires the laser; taking into account the external trigger generated by a rotor blade passing a position of interest downstream of the stator blade. Stepper drives are also available through the I/O board as required up to a maximum of 6. The oscilloscope is used for focussing purposes. The LFS is controlled by a second PC which intructs it as to the relative delay between the various operations it performs.

8 Data Processing and Analysis

The pre-processing of the data before computer analysis consisted of the following steps. The data was split into individual TIF images according to colour channel and frame. Computer enhancement of the PIV images was carried out employing the XV package under the UNIX operating system. They were then transformed to be viewed from a complementary position as the Schlieren image by the APWin package. APWin was then applied to the PIV data.

APWin is a computer program which is the result of a long period of research directed towards the automatic extraction of particle image data from stored digital images. A direct spatial digital processing method was adopted. This approach was taken after reviewing the work of Goss, 1989. The particle data at transonic speeds tends to be sparse, which makes the processing of individual particles far more attractive than the global processing usually applied to low speed flows. There are several significant advantages of working with a direct image as opposed to the more conventional Fourier domain approaches of Adrian[4], as described in the companion paper presented at this conference. The digitized particle field analyzed by APWin is a binary image. The images contain several features which need to be separated without ambiguity. These being:

- Images of the paired particles.
- Single unmatched particles.

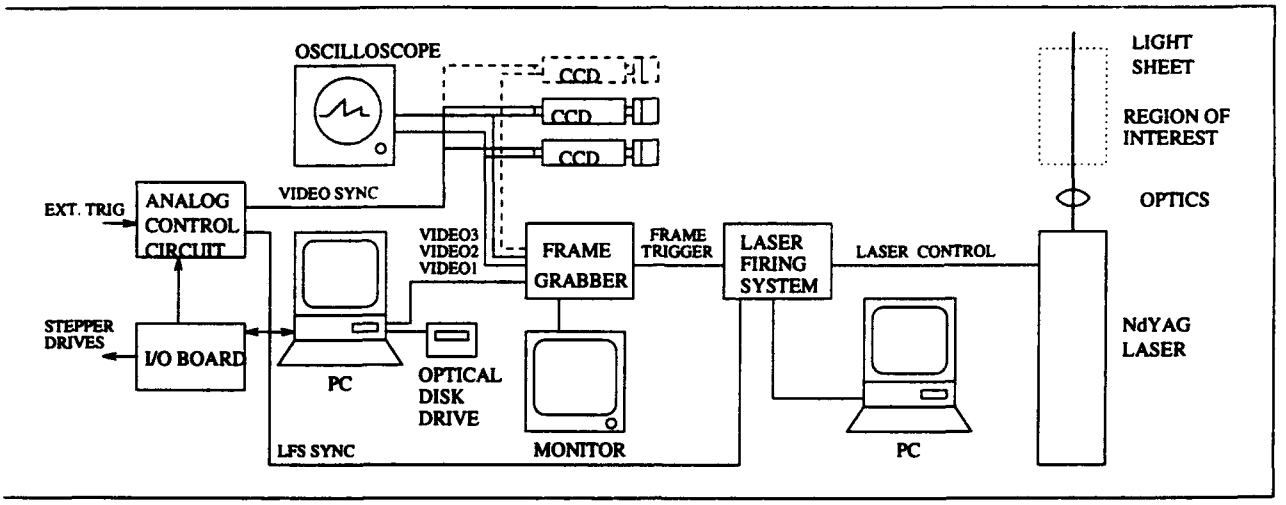

Figure 4 Schematic diagram of solid state system

- Glare from laser light reflection.
- Noise.

The processing must identify the spacing of the paired particles and translate them into velocities. An automatic spatial analysis strategy has been evolved to deal efficiently with the sparse data fields encountered. Aimed at reducing the effect of ambiguity in particle pairing, and accommodating the changing flow directions, this strategy incorporates the following steps in an iterative fashion until no new pairs are encountered.

- Initial particle pairing.
- Ambiguous pair recognition.
- Setting/updating a velocity and direction range.
- Removal of background flare and noise.
- Final particle sorting.

APWin was slightly altered to enable the user to implement a transformation of the image under consideration. This was required because the Schlieren mirrors lay in the path of view of the cameras and so the cameras were placed under the mirrors. Therefore, the PIV images had to be transformed to the same spatial position as the Schlieren. The Schlieren image was recorded by a third camera. Thus, the power required by the Schlieren picture could be kept to a minimum and so not lead to a loss of contrast of the main 3DPIV images. The Schlieren camera was connected to the blue channel of the frame grabber and sensed as part of a colour image.

9 Experimental Results

The experiment consisted, as previously decribed, of two stages. The first involved the use of a white light source and a shadowgraph to validate the system. The second part involved the use of laser light and Schlieren imaging. Figure 5 shows the results of the first stage of the experiment. The second part of the experiment was not completed due to equipment failure. Because the second stage of this test was not judged to be critical, and given some time constraints, this part was abandoned as not being worthy of the extra work involved.

Nevertheless, the availability of a diagnostic image to complement, and set into a qualitative framework, the PIV data has been shown to be a major step forward in the development of this technique. By providing the Shadowgraph picture as the background picture to the stero images, as shown in Figure 5, the interpretation and validation of the data is made clearer and easier respectively.

10Current Research

As shown in Figure 5, the PIV information is at the moment displayed in the form of two separate PIV images. These two images, however, if suitably combined yield a full three-dimensional plot of the velocity field. In order to achieve this result the following steps have to be taken. Firstly, the three images must be captured; as shown in this paper. Secondly, with the help of the REGISTER software described in the companion paper presented at this conference, an accurate - down to +/- 1° - estimate of all relative positions must be made to enable a reliable estimate of the out-of-plane component of velocity. Thirdly, an algorithm has to be implemented to identify particle pairs appearing in both PIV views; this topic being one of data analysis and display is currently the subject of some of the groups' research. Fourthly, using the technique described in the companion paper, the objective is that of combining geometric and photometric information to yield an estimate of the out-of-plane component with an accuracy comparable to that of the in-plane components of velocity. Lastly, the three-dimensional velocity field has to be displayed and combined with the flow density image to yield an overall picture of the region of interest; which is another area of current research.

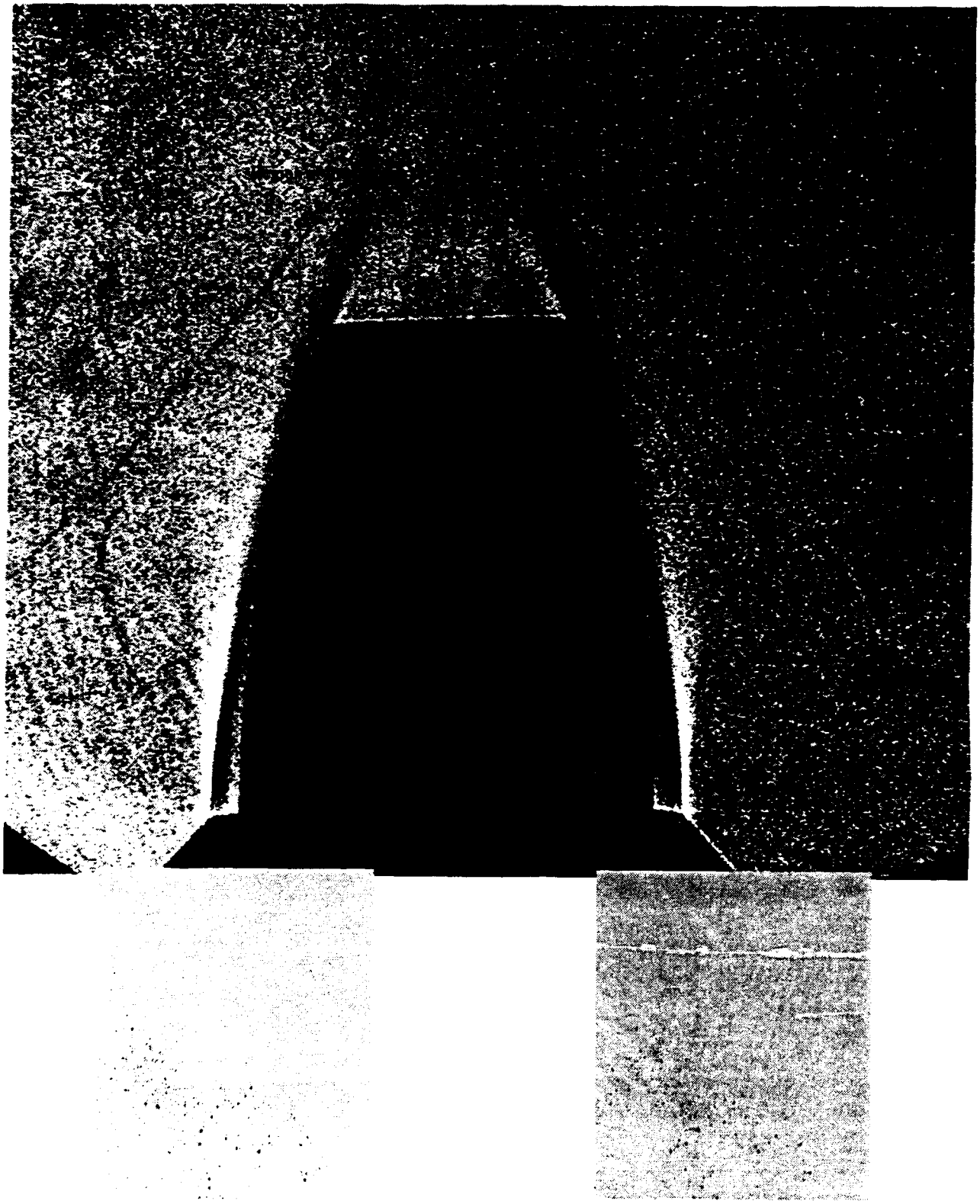

Figure 5 3DPIV/Shadowgraph experimental result

11Conclusions

The refinement of the 3DPIV system provided by the Schlieren image delivers a system which can be used to investigate unsteady transonic flow both from a qualitative and a quantitative standpoint at the same instant of flow.

The limitations of the imaging system are no longer one of science but merely of technology and price. With sufficient funds, it is theoretically possible to devise and implement a system of as much as 2048x2048 pixels resolution. At this resolution, the solid state approach begins to compare favourably with film, while providing greater sensitivity, at video rates for instant analysis.

Furthermore, it opens the possibility of providing a basis for extracting quatitative data from Schlieren pictures; by combining PIV and Schlieren density information or fringe information. Instantaneous information of a highly turbulent flow at approximately 240 m/s was obtained both of a qualitative and quantitative nature simultaneously; thus opening the door to a thorough non-intrusive investigation of the nature of turbulence and losses generated by unsteady flow in turbomachinery. The equipment, given its characteristics, being ideal fot real industrial applications, rather than merely laboratory use.

12Acknowledgements

The author would like to thank Dr. P.J. Bryanston-Cross for his general advice, and Mrs. D. Udrea and Mr. D. Barnsdale for their invaluable help in building the equipment described in this chapter. Also Dr. T.R. Judge for help in the programming aspects and helpful comments for the analysis of the experimental results.

13References

[1] H. Sheitle & S. Wagner, "A four colours line grid schlieren method for quantitative flow measurement", Exp. Fluids 9, 333-336, 1990.

[2] M. Funes-Gallanzi & P. Bryanston-Cross," Solid state visualization of a highly three dimensional flow using stereoscopic particle image velocimetry(3DPIV)", SPIE Conference, San Diego, vol. 2036, 1993.

[3] M. Funes-Gallanzi, P.J. Bryanston-Cross & D.D. Udrea, " High Accuracy techniques Applied to the Extraction of Absolute position Estimates in a 3DPIV System", VIIth International Symposium on Applications of laser Techniques to Fluid Mechanics, 11-14 July, Lisbon, Portugal, 1994.

[4] R.J. Adrian & C. Yao, "Pulse laser technique application to liquid and gaseous flows and the scattering power of seed materials", Applied Optics, Vol. 24 No1 Jan, 1985.

[5] L.P. Goss et al, "A novel technique for blade-to-blade velocity measurements in a turbine cascade",AIAA/ASME/SAE/ASEE 25th Joint Propulsion Conference, Monterrey CA July 10-12, 1989.

SEVENTH INTERNATIONAL SYMPOSIUM ON APPLICATIONS OF LASER TECHNIQUES TO FLUID MECHANICS

July 11- 14, 1994 in Lisbon, Portugal

AUTHORS' INDEX

Abe N., 13.4

Adrian R.J. , 1.4, 4.3

Adzic M., 27.1

Aguerre F., 9.2

Ainley S.B., 3.5

Aísa L., 18.5

Akamatsu F., 12.4

Akimoto H., 27.2

Akino N., 22.4

Akker H. den, 16.4

Alahyari A., 37.1

Albrecht H., 6.3

Almeida G.P., 13.1

Anders K., 21.2

Andersen K., 8.1

Anderson D., 14.6

Andrès N., 32.4

Andresen E., 25.4

Antonia R.A., 4.1

Arcoumanis C., 33.4

Ariga I., 3.3

Arndt V., 23.3

Aroussi A., 26.3, 35.4

Arrègle J., 33.2

Arroyo M.P., 32.4

Arts T., 7.2

Artt D.W., 3.1

Ayob R., 27.3

Azzazy M., 17.2

Bachalo W., 8.3, 12.3, 24.4

Baillion M., 20.4

Balabani S., 39.3

Balachandar R., 27.4

Baritaud T., 29.3

Barnhart D.H., 1.4

Barrett R., 10.1

Barrett R.V., 38.5

Bates C.J., 27.3

Behrens T., 6.3

Benedict L., 25.6

Bergeles G., 39.3

Bergmann H.W., 34.6

Bernd Leitl 25.5

Berton E., 10.3

Beyera W., 16.3

Billiotte M., 20.4

Bodegon M., 39.1

Bohan M., 24.3

Böhme L., 25.4

Bolik T., 6.3

Booij R., 28.5

Borée J., 36.4

Braun M.J., 39.5

Bremeyer R., 22.2

Bremhorst K., 34.3

Brenn G., 21.1, 21.4

Britchford K., 17.3

Brizuela F., 19.2

Brun K., 3.5

Brun R., 20.4

Bryanston-Cross P.J., 20.5, 35.7

Buchave P., 21.3

Buermann D.H., 12.3

Burchan C., 22.5

Burry D., 39.3

Bütefisch K., 7.3

Camporeale S., 8.2

Carr L.W., 38.3

Carrotte J., 17.3

Cartellier A., 31.5

Carvalho I. S., 27.1

Caspersen C., 11.2, 23.5

Catalano C., 29.3

Catalano G., 7.1

Cenedese A., 8.2, 22.1

Chandrasekhara M.S., 38.3

Chang K., 7.1

Charnay G., 36.4

Cheah S., 28.3

Chemouni I., 20.3

Ching C.Y., 4.1

Claypole T., 24.3

Coghe A., 36.3

Corbin F., 2.4

Cossali G.E., 36.3

Coton F., 10.5

Croonrnbroek T., 9.2

Czarske J., 14.4

Czarske J., 23.3

D'Amore M., 34.5

Dabiri D., 29.1

Daiber A.J., 32.1

Damp S.M., 23.4

Darabiha, N., 9.2

Derksen J., 16.4

Derou D., 35.3

Desantes J.M., 33.2

Desevaux P., 29.2

Dieter J., 22.2

Dinkelacker F., 6.3

Djenidi L., 4.1

Doieu A., 18.4

Domnick J., 21.1, 34.6

Donsi G., 34.5

Dopheide D., 14.1, 14.2, 14.4, 14.5, 17.1, 23.3

Doukelis A., 17.4

Draad A.A., 35.1

Duarte D., 2.3

Duclos J.M., 2.1

Dugué J., 6.1

Dumitrescu L., 20.4

Dumitrescu M., 20.4

Durão D., 13.1, 16.2, 25.3

Durst F., 2.2, 13.6, 18.2, 21.1, 24.2, 34.6

Duval A.L., 34.3

Dzodzo M., 39.5

Easson W., 14.6 , 31.4

Ebert F., 18.4

Edwards R.V. , 1.1

Egbers C., 16.3

Eigenbrod C., 6.3

Eigenmann L., 18.1

Eisele K., 38.4

Eriksson J.G., 13.3

Escudier M., 4.6, 16.1

Favaloro S., 19.2

Favier D., 10.3, 38.2

Ferrante A., 9.5

Ferrão P., 2.3

Finkelstein N., 26.6

Fischer M., 37.4

Fitzpatrick J., 8.4

Flack R.D., 3.5

Fokke M., 16.4

Forkey, J. 26.6

Foster D.P.E., 36.2

Founti M., 17.4

Freek C., 25.3

Frohn A., 21.2

Fu S., 10.5, 26.3

Fujimoto T., 20.1

Fujimura K., 22.3

Fujita H., 31.1

Fukuzato K., 31.1

Funes-Gallanzi M., 20.5, 35.7

Ganti G., 36.2

Garcia J., 18.5

Garib M., 29.1

Gaudio M., 9.5

Gee K., 22.5

Gieseke T., 26.1

Giordano P., 34.5

Girasole T., 18.2

Glass D.H., 31.4

Glovanevsky B., 12.1

Gouesbet ,G., 1.2, 18.2, 21.4

Gougat P., 34.1

Gould R., 25.6

Gouldson I., 4.7, 16.1

Graham L.J.W., 37.2

Grant I., 10.5, 26.3, 35.4

Greated C. A., 14.6, 31.4

Green R.M., 33.5

Grehan , G., 18.2, 18.3, 21.4

Griffiths A., 19.4

Grimley T.A., 4.4

Grosche G., 17.1

Guezennec Y., 26.1

Gutmark E., 6.2

Hanratty T.J., 4.3

Hanson-Parr D.M., 6.2

Hara Y., 20.1

Harano W., 31.1

Hardalupas Y., 1.3

Harris S., 22.5

Hassan Y.A., 37.5

Haugen P., 18.3

Haugland R., 22.5

Heitor M.V., 2.3, 9.3, 13.1, 27.1

Herault L., 35.3

Hering F., 22.2

Herschkorn C., 34.1

Hess C., 24.6

Hesselink L., 32.1

Higuchi M., 31.2

Hinrichs H., 26.2

Hinsch K., 26.2

Hirleman E., 18.1

Hirt F., 37.3

Hishida K., 24.7, 31.2

Hiwatika B., 31.3

Horner M., 10.4

Hornung K., 34.4

Host-Madsen A., 8.1, 11.1, 11.2, 26.4

Houas L., 20.3, 20.4

Houjung S., 28.1

Hull D., 33.4

Hwu T., 19.1

Hyun J., 22.3

Iacovides H., 28.3

Ibrahim K., 8.3, 12.3, 24.4

Ida T., 9.1

Ihalainen H., 11.4

Ikeda Y., 9.4

Imamot H., 28.2

Infield D., 10.5

Ishigaki T., 28.2

Ito S., 20.1

Itoh Y., 22.3

Jackson D., 28.3

Jähne B., 22.2, 29.4

Jakobsen M.L., 31.4

Ji H., 28.3

Johansson G., 25.2

Jones D., 16.1

Jones J., 14.6

Jourdan G., 20.3

Jow S., 13.5

Jud E., 37.3

Kaminaga F., 27.2

Kamino H., 28.4

Kampmann S., 2.5

Karlsson R.I., 13.3

Karini G., 27.2

Karvinen R., 11.4

Katsuki M., 12.4

Katsumata T., 13.4

Kawaguchi Y., 2.6

Kawahara N., 9.4

Kawaji M., 27.2

Kechemair D., 34.1

Khan M., 29.2

Klingmann J., 19.3, 25.2

Kneer R., 18.1

Koch R., 18.1

Koerber G., 38.1

Kompenhans J., 35.2, 35.5, 35.6, 38.1

König J., 6.3

Kononenko V., 24.5

Kontani K., 2.6

Koyama H., 22.3

Koyama T., 36.5

Kramer R., 14.4 , 14.5, 23.3

Krothapalli A., 15.1, 26.5

Krstic R., 39.5

Labracherie L., 20.4

Lacas F., 12.2

Lading L. , 1.1

Lagranja J., 18.5

Larsen P., 25.4, 39.4

Lascu J., 34.1

Lattime S.B., 39.5

Launder B., 28.3

le Coz J., 29.3

Lecordier B., 15.2

Lee D., 11.3

Lee H., 7.5

Lee K.C., 10.2, 36.2

Legi Img., 31.5

Leipertz A., 2.5, 12.6

Lekakis I., 13.6

Lempert W., 22.5, 26.6

Lepicovsky J., 3.6

Levinsky H., 15.4

Levy Y., 12.1

Liem T., 16.4

Lin C., 13.5

Liou T., 7.5

Liu Z.C., 4.3

Longmire E.K., 37.1

Lorencez C., 27.2

Lourenço L., 15.1, 26.5

Lowson M., 10.1

Macleod N., 32.2

Maeda M., 3.3, 24.7, 31.2

Magee K., 22.5

Mandel B., 12.5

Mann B., 20.2

Mannheimer R.J., 4.4

Maresca C., 10.3, 38.2

Martano M., 9.5

Martin J.P., 9.2

Martinez R., 37.5

Martins L., 7.4

Mathioudakis K., 17.4

Mathis J., 7.1

Mba M. Nsi, 10.3

Mbiock A., 6.1

McCluskey D.R., 26.4, 31.4

McDonnell C., 8.4

McGalbraith R., 10.4

Meijering A., 16.3

Meinhart C.D. , 1.4

Melling A., 2.2

Menon R., 24.1

Meyer K. E., 39.4

Miles P.C., 33.5

Miles R., 22.5, 26.6

Mizutani Y., 12.4

Mokaddem J. K., 15.4

Montazel X., 2.1

Moore A., 39.1

Moreira A.L., 9.3

Morikita H., 24.7, 31.2

Mouqallid M., 15.2

Muggli F., 38.4

Müller D., 6.3

Müller E., 23.2

Müller H., 14.1, 14.2, 14.4, 14.5, 23.3

Mulpuru S., 27.4

Münch K., 12.6

Mungal M., 15.1

Münsterer T., 29.4

Muto Y., 28.2

Nakabe K., 12.4

Nakajima T., 9.4

Nakatani N., 32.5

Naqwi A., 24.1, 24.2
Narayana P., 25.1
Nebrensky J.J., 32.2
Neichen B. I., 12.5
Neveu F., 2.4
Ni-Imi T., 20.1
Nigim H., 13.2
Nishida O., 31.1
Nobach H., 23.2
Nonn T., 21.3
Norén B., 19.3
Nuglisch H.J., 36.4

O'Rourke M.J., 3.1
Obi S., 3.3
Obokota T., 36.5
Ohba K., 28.4
Ohkawa H., 31.1
Ohtake K., 9.1
Okamoto S., 13.4
Ölçmen M.S., 4.2
Onofri F., 18.2, 18.3, 21.4
Oshio T., 32.5
Owens E., 10.5

Page N.W., 34.3
Pan X., 26.3, 35.4
Panday P., 29.2
Pani B., 7.3
Paone N., 3.2, 15.3, 36.1
Papailiou K., 17.4
Park J.T., 4.4
Parr T.P., 6.2
Pascazio M., 38.2
Passchier D., 25.1
Pastor J.V., 33.2
Peña F., 7.2
Pereira A.S., 4.5
Pereira J., 16.2, 25.3
Pereira T., 16.2
Perrin M., 2.4, 15.4
Perrini A., 9.5
Philip O.G., 37.5
Piana J., 2.1
Picher G., 33.1
Pinho F.T., 4.5
Pinotti M., 3.2
Pires A.C., 9.3
Posylkin M., 33.3
Prud'homme R., 34.1
Pun W., 27.2

Querzoli G., 22.1
Quintanilla M., 32.4

Raffel I.M., 35.5, 35.6, 38.1
Raso G., 34.5
Rath H., 6.3, 16.3

Reichel F., 35.2

Rickards J., 38.5

Riethmuller M., 21.5

Rinkevichius B., 14.3, 24.5

Rolon J., 9.2, 15.4

Roth N., 21.2

Roth P., 34.2

Rutherford K., 10.2

Saarenrinne P., 11.4

Sankar S.V., 12.3, 24.4

Santollini C., 36.1

Saunders C., 38.5

Saville D., 22.5

Schabel S., 18.4

Schadow K.C., 6.2

Schmidl W.D., 37.5

Schmitt N.P., 14.4

Schröder T., 6.3

Schubert E., 34.6

Seidel M., 24.2

Sender J., 13.6

Sheen H., 19.1

Shimizu L., 22.4

Shiono K., 28.2

Shirakawa T., 31.2

Simpson R.L., 4.2

Sivadas V., 7.3

Smirnov N., 6.3

Smith G., 10.5

Soini S., 11.4

Soranno A., 9.5

Soria J., 37.2

Sorrenti R., 9.5

Sousa J., 16.2

Speck P., 29.2

Squires D.D., 38.3

Stewart J., 10.4

Stoffel B., 3.4

Strecker J.J.F., 34.2

Stroud J., 39.2

Strunck V., 14.1, 17.1

Sudo Y., 27.2

Sugiyama A., 3.3

Sung H., 11.3, 22.3

Suzuki D., 13.4

Suzuki K., 22.4

Swales C., 10.1, 38.5

Syred N., 19.4

Tabata T., 12.4

Tagawa M., 1.3

Takegami T., 28.4

Tanaka H., 36.5

Taylor A.M.K.P. , 1.3, 33.3, 39.1

Timmerman B.H., 32.3

Többen H., 14.2, 23.3

Tomasini E.P. , 3.2, 36.1

Tong F., 28.1

Touat A., 20.3

Tridimas Y.D., 31.3

Triebel W., 6.3

Trimis D., 2.2

Trinite M., 2.4, 15.2

Tropea C., 13.2, 18.2, 18.3, 21.1, 21.4, 23.2

Tsunoda K., 13.4

Tukker J., 28.5

Tulleken H., 23.1

Tummers M., 25.1

Tyurnikov M., 6.4

Uemura T., 22.3

Ungurian H., 27.4

van Beeck J., 21.5

van der Hoeven J.G. Th., 35.1

van Maanen H., 23.2

van Oord J., 35.1

Versaevel P., 9.2, 12.2

Veynante D., 2.1, 36.4

Vienola S., 11.4

Vogt A., 35.2

von Benzon H., 21.3

Wang A., 13.5

Wang H., 14.1, 23.3

Wang X., 10.5, 26.3

Watt D.W., 32.3

Weber R., 6.1

Weiss K., 3.4

Wernert P., 38.1

Wessman M., 19.3

Westerweel J., 35.1

White F., 20.2

Whitelaw J.H., 7.4

Whitelaw J.H., 33.3, 33.4, 39.1

Wietrich F., 38.1

Wigley G., 33.1

Wilder M.C., 38.3

Willmann M., 18.1

Wishart D., 26.5

Wittig S., 18.1

Witze P.O., 33.5

Wood C., 24.6

Woolley N.H., 31.3

Wu Y., 7.5

Wung Tzong-Shyan, 22.6

Xu C.H., 33.4

Xu T., 18.3 , 21.1, 21.4

Yazdabadi P., 19.4

Yearling P. R., 25.6

Yianneskis M., 10.2, 36.2, 39.3

Young D., 19.1

Yu K., 6.2

Zeitoun D., 20.4

Zeller R., 34.6

Zerf G., 34.4

Zhang X., 29.1

Zhang Z., 37.3, 38.4

Zhao Y., 10.5, 26.1

Ziema M., 24.2